

AD-A229 590



VOLUME 163

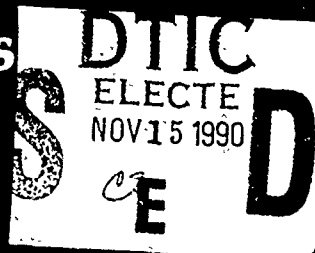
Impurities, Defects and Diffusion in Semiconductors: Bulk and Layered Structures

EDITORS

Donald J. Wolford

Jerzy Bernholc

Eugene E. Haller



DTIC FILE COPY

DISTRIBUTION STATEMENT A

Approved for public release;
Distribution Unlimited

REPORT DOCUMENTATION PAGE			Form Approved OMB No. 0704-0188	
<small>Public reporting burden for this collection of information is estimated to average 1 hour per response, including the time for reviewing instructions, searching existing data sources, gathering and maintaining the data needed, and completing and reviewing the collection of information. Send comments regarding this burden estimate or any other aspect of this collection of information, including suggestions for reducing this burden, to Washington Headquarters Services, Directorate for Information Operations and Reports, 1215 Jefferson Davis Highway, Suite 1204, Arlington, VA 22202-4302, and to the Office of Management and Budget, Paperwork Reduction Project (0704-0188), Washington, DC 20503.</small>				
1. AGENCY USE ONLY (Leave blank)	2. REPORT DATE	3. REPORT TYPE AND DATES COVERED		
		Final Report 22 Nov 89-21 Nov 90		
4. TITLE AND SUBTITLE			5. FUNDING NUMBERS	
1989 Materials Research Society Fall Meeting			2306/A2	
6. AUTHOR(S)				
Dr John Ballance				
7. PERFORMING ORGANIZATION NAME(S) AND ADDRESS(ES)			8. PERFORMING ORGANIZATION REPORT NUMBER	
Material Reserach Society 9800 McKnight Road, Suite 327 Pittsburgh, PA 15237-6005			AFOSR-TR-90-111	
9. SPONSORING/MONITORING AGENCY NAME(S) AND ADDRESS(ES)			10. SPONSORING/MONITORING AGENCY REPORT NUMBER	
AFOSR/NE Bldg 410 Bolling AFB DC 2033206448			AFOSR-90-0081	
11. SUPPLEMENTARY NOTES				
12a. DISTRIBUTION/AVAILABILITY STATEMENT			12b. DISTRIBUTION CODE	
UNLIMITED				
13. ABSTRACT (Maximum 200 words)				
<p>CONFERENCE WAS HELD ON THE FOLLWING AREA</p> <p>(158) In Situ Patterning: Selective Area Deposition and Etching</p> <p>(161) Properties of II-VI Semiconductors: Bulk Crystals, Expitaxial Films, Quantum Well Structures, and Dilute Magnetic Systems</p> <p>(163) Impurities, Defects and Diffusion in Semiconductors: Bulk and Layered Structures</p> <p>(168) Chemical Vapor Deposition of Refractory Metals and Ceramics</p> <p>(170) Tailored Interfaces in Composite Materials.</p>				
14. SUBJECT TERMS			15. NUMBER OF PAGES	
			16. PRICE CODE	
17. SECURITY CLASSIFICATION OF REPORT	18. SECURITY CLASSIFICATION OF THIS PAGE	19. SECURITY CLASSIFICATION OF ABSTRACT	20. LIMITATION OF ABSTRACT	
UNCLASS	UNCLASS	UNCLASS	UNLIMITED	

DTIC
ELECTE
NOV 15 1990

E

D

Impurities, Defects and Diffusion in Semiconductors: Bulk and Layered Structures

Accession For	
NTIS GRA&I	<input checked="" type="checkbox"/>
DTIC TAB	<input checked="" type="checkbox"/>
Unannounced	<input type="checkbox"/>
Justification	
By _____	
Distribution/	
Availability Codes	
Dist	Avail and/or Special
A-1	



90 11 15 116

Impurities, Defects and Diffusion in Semiconductors: Bulk and Layered Structures

Symposium held November 27-December 1, 1989, Boston,
Massachusetts, U.S.A.

EDITORS:

Donald J. Woford

IBM T.J. Watson Research Center, Yorktown Heights, New York, U.S.A.

Jerzy Bernholc

North Carolina State University, Raleigh, North Carolina, U.S.A.

Eugene E. Haller

University of California at Berkeley, Berkeley, California, U.S.A.



MATERIALS RESEARCH SOCIETY

Pittsburgh, Pennsylvania

This work was supported in part by the Office of Naval Research under Grant Number N00014-90-J-1286. The United States Government has a royalty-free license throughout the world in all copyrightable material contained herein.

This work was supported by the Air Force Office of Scientific Research, Air Force Systems Command, USAF, under Grant Number AFOSR 90-0081.

Single article reprints from this publication are available through University Microfilms Inc., 300 North Zeeb Road, Ann Arbor, Michigan 48106

CODEN: MRSPDH

Copyright 1990 by Materials Research Society.
All rights reserved.

This book has been registered with Copyright Clearance Center, Inc. For further information, please contact the Copyright Clearance Center, Salem, Massachusetts

Published by:

Materials Research Society
9800 McKnight Road
Pittsburgh, Pennsylvania 15237
Telephone (412) 367-3003
FAX (412) 367-4373

Library of Congress Cataloging in Publication Data

Impurities, defects, and diffusion in semiconductors : bulk and layered structures .
symposium held November 27-December 1, 1989, Boston, Massachusetts, U.S.A. /
editors, Donald J. Wolford, Jerry Bernholc, Eugene E. Haller.

p. cm. — (Materials Research Society symposium proceedings : ISSN 0272-9172 ; v. 163)

Includes bibliographical references.

ISBN 1-55899-051-8

1. Semiconductors—Impurity distribution—Congresses. 2. Semiconductors—Defects—Congresses. 3. Semiconductors—Diffusion—Congresses. I. Wolford, Donald J. II. Bernholc, Jerry. III. Haller, Eugene E. IV. Materials Research Society. V. Series: Materials Research Society symposium proceedings : v. 163.

QC611.6.D4148 1990
621.381'52—dc20

90-5584
CIP

Manufactured in the United States of America

Contents

PREFACE	xxi
ACKNOWLEDGMENTS	xxiii
MATERIALS RESEARCH SOCIETY SYMPOSIUM PROCEEDINGS	xxv
PART I: ELECTRONIC STRUCTURE - DEEP LEVELS	
*HIGH-RESOLUTION SPECTROSCOPY OF POINT DEFECTS IN SILICON H.G. Grimmeiss, M. Kleverman, and J. Olajos	3
INFRARED ABSORPTION STUDY OF ZINC-DOPED SILICON E. Merk, J. Heyman, and E.E. Haller	15
INFRARED STUDIES OF THE DOUBLE ACCEPTOR ZINC IN SILICON A. Dörnen, R. Kienle, K. Thonke, P. Stolz, G. Pensl, D. Grünebaum, and N.A. Stolwijk	21
PRESSURE DEPENDENCE OF A DEEP EXCITONIC LEVEL IN SILICON G.A. Northrop and D.J. Welford	27
ODMR OF SHALLOW DONORS IN Zn-DOPED LEC-GROWN InP J.M. Trombetta and T.A. Kennedy	33
*COMPLEX DEFECTS IN SEMICONDUCTORS B. Monemar	39
THE ELECTRONIC STRUCTURE OF INTERSTITIAL IRON IN SILICON A. Thilderkvist, G. Grossmann, M. Kleverman, and H.G. Grimmeiss	51
DISLOCATION RELATED D-BAND LUMINESCENCE; THE EFFECTS OF TRANSITION METAL CONTAMINATION Victor Higgs, E.C. Lightowers, and P. Kightley	57
PHOTOLUMINESCENCE EXCITATION SPECTROSCOPY OF MOCVD- GROWN: GaAs:V Y.J. Kao, N.M. Haegel, and W.S. Hobson	63
RADIATIVE AND NON-RADIATIVE RECOMBINATIONS AT Er CENTERS IN GaAlAs Taha Benyattou, Djelloul Seghier, Gerard Guillot, Richard Moncorge, Pierre Galtier, and Marie-Noelle Charasse	69

*Invited Paper

CHARACTERIZATION OF DEEP-LEVEL DEFECTS IN SEMI-INSULATING GaAs AND InP BY PHOTOINDUCED TRANSIENT SPECTROSCOPY (PITS) Pawel Kaminski	75
ELECTRONIC STRUCTURE OF Li-IMPURITIES IN ZnSe T. Oguchi, T. Sasaki, and H. Katayama-Yoshida	81
MODIFIED OPTICALLY DETECTED MAGNETIC RESONANCE TECHNIQUE FOR STUDIES OF DEFECTS IN Si AND GaAs W.M. Chen and B. Monemar	85
NITROGEN AND PHOSPHOROUS IMPURITIES IN DIAMOND Koblar Jackson, Mark R. Pederson, and Joseph G. Harrison	89
PART II: ELECTRONIC STRUCTURE - SHALLOW IMPURITIES	
*RADIATIVE RECOMBINATION AND CARRIER LIFETIMES IN SURFACE-FREE GaAs HOMOSTRUCTURES L.M. Smith, D.J. Wolford, R. Venkatasubramanian, and S.K. Ghandhi	95
EVIDENCE FOR STRONG TRAPPING BY IONIZED DONORS OF FREE EXCITONS IN EXCITED STATES FOR HIGH PURITY GaAs AND AlGaAs S. Zemon and G. Lambert	109
FORMATION OF THREE RED-SHIFT EMISSIONS IN HEAVILY GERMANIUM-DOPED P-TYPE GaAs GROWN BY MBE Y. Makita, A. Yamada, H. Shibata, H. Asakura, N. Ohnishi, A.C. Beye, K.M. Mayer, and N. Kutsuwada	115
ELECTRICAL PROPERTIES OF HEAVILY Be-DOPED GaAs GROWN BY MOLECULAR BEAM EPITAXY H. Shibata, Y. Makita, A. Yamada, N. Ohnishi, M. Mori, Y. Nakayama, A.C. Beye, K.M. Mayer, T. Takahashi, Y. Sugiyama, M. Tacano, K. Ishituka, and T. Matsumori	121
PHOTOLUMINESCENCE STUDY OF GaAs DIFFUSED WITH Li H.P. Gislason, E.Ö. Sveinbjörnsson, B. Monemar, and M. Linnarsson	127
LASER-THERMAL IMPURITY PUMPING OF SHALLOW DONORS IN ULTRAPURE GERMANIUM T. Theiler, F. Keilmann, and E.E. Haller	133
ELECTRICAL AND PHOTOLUMINESCENCE PROPERTIES OF Mg ⁺ AND C ⁺ IMPLANTED ACCEPTORS IN InP A.C. Beye, A. Yamada, A. Shimizu, H. Shibata, H. Tanoue, K.M. Mayer, H. Sugiyama, K. Kamijoh, T. Oda, O. Arriga, I. Akiyama, N. Kutsuwada, T. Matsumori, S. Uekusa, and Y. Makita	139

*Invited Paper

PART III: ELECTRONIC STRUCTURES - NATIVE
DEFECTS, COMPLEXES, TRANSITION METALS IN COMPOUNDS

OPTICALLY DETECTED MAGNETIC RESONANCE OF SULFUR DOPED GALLIUM PHOSPHIDE K.L. Brower	145
THE ROLE OF OXYGEN IN p-TYPE InP J. Michel, J. Jeong, K.M. Lee, and L.C. Kimerling	151
MID-INFRARED SPECTRAL PHOTORESPONSE OF SEMI-INSULATING GaAs G.J. Brown and W.C. Mitchel	157
CORRELATION OF THE 0.8 eV EMISSION BAND WITH THE EL6 CENTER IN GaAs S. Alaya, M.A. Zaidi, G. Marrakchi, H. Maaref, H.J. von Bardeleben, and J.C. Bourgoin	163
THE ELECTRONIC STRUCTURE OF THE "0.15 eV" Cu ACCEPTOR LEVEL IN GaAs E. Janzén, M. Linnarsson, B. Monemar, and M. Kleverman	169
OPTICAL ABSORPTION OF DEEP DEFECTS IN NEUTRON IRRADIATED SEMI-INSULATING GaAs M.O. Manasreh and P.J. Pearah	175
NEW, GERMANIUM - RELATED DEFECT IN NEUTRON - IRRADIATED GALLIUM PHOSPHIDE J. Barczynska and E. Goldys	179
DEEP LEVEL LUMINESCENCE IN InP: PHONON FEATURE ANALYSIS S. Banerjee, A.K. Srivastava, and B.M. Arora	185
THE NATURE OF NATIVE DEFECTS IN LEC GROWN SEMI- INSULATING GaAs BY THERMALLY STIMULATED CURRENT SPECTROSCOPY Zhaoqiang Fang, Lei Shan, T.E. Schlesinger, and A.G. Milnes	189
ANOMALOUS LUMINESCENCE PROPERTIES OF GaAs GROWN BY MOLECULAR BEAM EPITAXY I. Szafranek, M.A. Plano, M.J. McCollum, S.L. Jackson, S.A. Stockman, K.Y. Cheng, and G.E. Stillman	193
COMPARATIVE OPTICAL STUDIES OF Cu, Mn, AND C IMPURITIES IN BULK LEC GROWN GaAs BY ELECTRON BEAM ELECTROREFLEC- TANCE (EBER) AND PHOTOLUMINESCENCE (PL) M.H. Herman, P.J. Pearah, K. Elcess, and I.D. Ward	197
Ge RELATED DEEP LEVEL LUMINESCENCE IN InGaAs LATTICE MATCHED TO InP S.S. Chandvankar, A.K. Srivastava, B.M. Arora, and D.K. Sharma	203
THE DEEP 0.11eV MANGANESE ACCEPTOR LEVEL IN GaAs M. Kleverman, E. Janzén, M. Linnarsson, and B. Monemar	207

IDENTIFICATION OF SURFACE-RELATED ELECTRON TRAPS IN UNDOPED GaAs BY DEEP LEVEL TRANSIENT SPECTROSCOPY Ki-Chul Shin and In-Shik Park	211
LUMINESCENCE DUE TO Mn DOPED GaP Teresa Monteiro and Estela Pereira	215
PART IV: ELECTRONIC STRUCTURE - COMPLEXES IN SILICON	
*HIGH PERFORMANCE PHOTOLUMINESCENCE SPECTROSCOPY USING FOURIER TRANSFORM INTERFEROMETRY M.L.W. Thewalt, M.K. Nissen, D.J.S. Beckett, and K.R. Lundgren	221
GENERATION AND DISSOCIATION OF IRON-BORON PAIRS IN SILICON Masashi Suezawa and Koji Sumino	233
PHOTOCONDUCTIVITY STUDY OF CrB AND Cr _i IN SILICON A. Schlette, R. Kienle, A. Dörnen, W. Kürner, and K. Thonke	239
*FORMATION OF In-Cu PAIRS IN SILICON DURING CHEMO- MECHANICAL POLISHING Th. Wichert, R. Keller, M. Deicher, W. Pfeiffer, H. Skudlik, and D. Steiner	245
STRAIN INDUCED INTRINSIC QUANTUM WELLS AS THE ORIGIN OF BROAD BAND PHOTOLUMINESCENCE IN SILICON CONTAINING EXTENDED DEFECTS H. Weman and B. Monemar	257
OPTICAL PROPERTIES OF NOVEL VIBRONIC BANDS IN ELECTRON- IRRADIATED TIN DOPED SILICON J.H. Svensson, B. Monemar, and B.G. Svensson	261
A NEW METASTABLE DEFECT IN SILICON, OPTICAL PROPERTIES AND AN INVESTIGATION OF THE MECHANISM CAUSING THE CONFIGURATIONAL CHANGE J.H. Svensson and B. Monemar	265
NOVEL LUMINESCENCE BAND IN SILICON IMPLANTED WITH PHOSPHORUS AND BORON A.K. Srivastava, D.K. Sharma, K.L. Narasimhan, D. Sarkar, and V. Premchandran	269
UNIAXIAL STRESS AND ZEEMAN MEASUREMENTS ON THE 943 meV LUMINESCENCE BAND IN SILICON M.C. Carmo, K.G. McGuigan, M.O. Henry, G. Davies, and E.C. Lightowlers	273
IDENTIFICATION OF RADIATION-INDUCED DEFECTS IN Si:Al Ya.I. Latushko and V.V. Petrov	277

*Invited Paper

DEFECT-FORMATION DEPENDENCE ON GROUP V-DOPANT ATOMS IN ELECTRON-IRRADIATED SILICON O.O. Awadelkarim, A. Henry, B. Monemar, and J.L. Lindström	283
ELECTRONIC STRUCTURE OF VACANCY-PHOSPHORUS IMPURITY COMPLEXES IN SILICON Hongqi Xu and U. Lindefelt	287
NEW DLTS PEAKS ASSOCIATED WITH NEW DONORS AND RODLIKE DEFECTS IN CZOCHRALSKI SILICON Yoichi Kamiura, Fumio Hashimoto, and Minoru Yoneta	291
MULTICONFIGURATIONAL CARBON-GROUP V PAIR DEFECTS IN SILICON E. Güreer and B.W. Benson	295
EXCITONIC RECOMBINATION AT A TRANSITION-METAL RELATED DEFECT IN SILICON K.G. McGuigan, M.O. Henry, E.C. Lightowers, and M.H. Nazare	299
ELECTRONIC STRUCTURE OF TWO SULPHUR-RELATED BOUND EXCITONS IN SILICON STUDIED BY OPTICAL DETECTION OF MAGNETIC RESONANCE W.M. Chen, A. Henry, E. Janzén, B. Monemar, and M.L.W. Thewalt	303
AN ELECTRON PARAMAGNETIC RESONANCE INVESTIGATION OF IRON-INDIUM PAIRS IN SILICON P. Emanuelsson, W. Gehlhoff, P. Omling, and H.G. Grimmeiss	307
PART V: ELECTRONIC STRUCTURE - SUPERLATTICES	
*LIGHT- AND HEAVY-HOLE BOUND EXCITON TRANSITIONS AND FREE TO BOUND TRANSITIONS IN $\text{Ga}_x\text{Al}_{1-x}\text{As}/\text{GaAs}$ QUANTUM WELLS Donald C. Reynolds and K.K. Bajaj	313
DECAY MEASUREMENTS OF FREE AND BOUND EXCITON RECOM- BINATION IN DOPED $\text{GaAs}/\text{GaAlAs}$ QUANTUM WELLS J.P. Bergman, P.O. Holtz, B. Monemar, M. Sundaram, J.L. Merz, and A.C. Gossard	325
EFFECTS OF CONFINEMENT ON THE OPTICAL PROPERTIES OF A SHALLOW ACCEPTOR AND ITS BOUND EXCITON IN NARROW $\text{GaAs}/\text{AlGaAs}$ QUANTUM WELLS P.O. Holtz, M. Sundaram, G.C. Rune, B. Monemar, J.L. Merz, and A.C. Gossard	331
INTRINSIC LUMINESCENCE OF $\text{GaAs}/\text{AlGaAs}$ HETEROJUNCTIONS IN A TRANSVERSE ELECTRIC FIELD Q.X. Zhao, J.P. Bergman, P.O. Holtz, B. Monemar, C. Hallin, M. Sundaram, J.L. Merz, and A.C. Gossard	337

*Invited Paper

DEFECT INDUCED LUMINESCENCE FROM MBE PREPARED Si/Si _{1-x} Ge _x SUPERLATTICES G.A. Northrop, S.S. Iyer, and D.J. Wolford	343
DEEP LEVELS IN SUPERLATTICES John D. Dow, Shang Yuan Ren, Jun Shen, and Min-Hsiung Tsai	349
QUALITATIVE PHYSICS OF DEFECTS IN QUANTUM WELLS: INTERFACE ROUGHNESS Harold P. Hjalmarson	361
PART VI: HYDROGEN IN SILICON	
*FERMI RESONANCE EFFECTS ON THE VIBRATION MODES OF HYDROGEN-PASSIVATED BORON IN SILICON G.D. Watkins, W.B. Fowler, G.G. Deleo, M. Stavola, D.M. Kozuch, S.J. Pearton, and J. Lopata	367
OPTICALLY DETECTED MAGNETIC RESONANCE OF A HYDROGEN- RELATED COMPLEX DEFECT IN SILICON W.M. Chen, O.O. Awadelkarim, B. Monemar, J.L. Lindström, and G.S. Oehrlein	377
*HYDROGEN IN CRYSTALLINE AND AMORPHOUS SILICON Guido L. Chiarotti, F. Buda, R. Car, and M. Parrinello	383
HYDROGEN DIFFUSION IN BORON-DOPED SILICON C.P. Herrero, M. Stutzmann, and A. Breitschwerdt	395
MODELING OF THE DIFFUSION OF HYDROGEN IN SILICON D. Mathiot, D. Ballutaud, P. De Mierry, and M. Aucouturier	401
*STRUCTURE AND METASTABILITY OF MUONIUM CENTERS IN SEMICONDUCTORS AND THEIR SIMULATION OF ISOLATED HYDROGEN CENTERS T.L. Estle, R.F. Kiefl, J.W. Schneider, and C. Schwab	407
ELECTRONIC STRUCTURE AND HYPERFINE PARAMETERS FOR HYDROGEN AND MUONIUM IN SILICON Chris G. Van de Walle	419
HYDROGEN IN CRYSTALLINE SILICON UNDER COMPRESSION AND TENSION C.S. Nichols and D.R. Clarke	425
ANALYSIS OF REAL-TIME HYDROGENATION DATA FROM P AND N-TYPE SILICON Carleton H. Seager and Robert A. Anderson	431
HYDROGEN SEGREGATION AT THE Al/Si INTERFACE STUDIED USING A NUCLEAR RESONANT REACTION Joyce C. Liu, A.D. Marwick, and F.K. Legoues	437

*Invited Paper

DISSOCIATION KINETICS OF SHALLOW-ACCEPTOR-HYDROGEN PAIRS IN SILICON T. Zundel and J. Weber	443
HYDROGEN INDUCED DEFECTS AT SILICON SURFACES AND BURIED EPITAXIAL MISFIT DISLOCATION INTERFACES Tian-Qun Zhou, Zbigniew Radzinski, Zhigang Xiao, Bhushan Sopori, and George A. Rozgonyi	449
SURFACE AND BULK PROPERTIES WHICH INFLUENCE ION-BEAM HYDROGENATION OF SILICON Robert A. Anderson and Carleton H. Seager	455
HYDROGEN PASSIVATION STUDIES IN DISLOCATED CZ AND FZ SILICON C. Dubé, J.P. Kalejs, and S. Rajendran	459
PART VII: HYDROGEN IN III-Vs	
*HYDROGEN COMPLEXES IN III-V SEMICONDUCTORS Bernard Pajot	465
Sn-H COMPLEX IN HYDROGEN PASSIVATED GaAs D.M. Kozuch, Michael Stavola, S.J. Pearton, C.R. Abernathy, and J. Lopata	477
REASSESSMENT OF ACCEPTOR PASSIVATION MODELS IN p-TYPE HYDROGENATED GaAs I. Szafranek and G.E. Stillman	483
HYDROGEN PASSIVATION OF INTERFACIAL DEFECTS IN MOCVD GROWN GaAs/InP V. Swaminathan, U.K. Chakrabarti, W.S. Hobson, R. Caruso, J. Lopata, and S.J. Pearton	489
PASSIVATION OF Zn-ACCEPTORS IN InGaAs DURING RIE WITH CHF ₃ /H ₂ AND CH ₄ /H ₂ Martin Möhrle	495
SURFACE PROTECTION DURING PLASMA HYDROGENATION FOR ACCEPTOR PASSIVATION IN InP J. Lopata, W.C. Dautremont-Smith, S.J. Pearton, J.W. Lee, N.T. Ha, and H.S. Luftman	501
PART VIII: DIFFUSION IN SILICON AND GERMANIUM	
*ATOMIC DIFFUSION PROCESSES IN SILICON Sokrates T. Pantelides	511
PRESSURE AND STRAIN EFFECTS ON DIFFUSION A. Antonelli and J. Bernholc	523
LOW-TEMPERATURE DIFFUSION OF DOPANTS IN SILICON P. Fahey and M. Wittmer	529

*Invited Paper

DETERMINATION OF DIFFUSION PARAMETERS FOR ARSENIC Michael Heinrich, Matthias Budil, and Hans W. Pötzl	535
MEASUREMENTS OF ENHANCED DIFFUSION OF BURIED LAYERS IN SILICON MEMBRANE STRUCTURES DURING OXIDATION Scott T. Dunham, Anuradha M. Agarwal, and Nanseng Jeng	543
MIGRATIONS OF INTERSTITIAL ATOMS IN SEMICONDUCTORS (SURFACE DIFFUSION AND KICK-OUT MECHANISM) Takao Wada, Akihiro Takeda, Masaya Ichimura, and Michihiko Takeda	549
MEASUREMENTS OF ENHANCED OXYGEN DIFFUSION IN SILICON DURING THERMAL DONOR FORMATION: NEW EVIDENCE FOR POSSIBLE MECHANISMS A.R. Brown, R. Murray, R.C. Newman, and J.H. Tucker	555
A STEADY-STATE MODEL FOR COUPLED DEFECT IMPURITY DIFFUSION IN SILICON F.F. Morehead and R.F. Lever	561
HIGH AND LOW TEMPERATURE MEASUREMENTS OF THE CHROMIUM DIFFUSIVITY IN SILICON J. Zhu and D. Barbier	567
THE FORMATION OF SILICON-RICH SILICIDES Maria Ronay and R.G. Schad	573
PRECIPITATION OF COPPER AND COBALT AT GRAIN BOUNDARIES IN SILICON U. Jendrich and H.J. Möller	579
ANNEALING OF ION IMPLANTED TIN IN SILICON: A RBS/ CHANNELING, MÖSSBAUER SPECTROSCOPY AND TEM INVESTIGA- TION OF SOLUBILITY AND RESIDUAL DEFECTS P. Kringhøj, A. Nylandsted Larsen, and J.W. Petersen	585
EXTREME SUPERSATURATION OF OXYGEN IN LOW TEMPERATURE EPITAXIAL SILICON AND SILICON-GERMANIUM ALLOYS P.V. Schwartz, J.C. Sturm, P.M. Garone, and S.A. Schwarz	591
AN ANOMALOUS VACANCY DIFFUSION IN SILICON DURING THE ANTIMONY DRIVE-IN DIFFUSION W. Wijaranakula and J.H. Matlock	597
A COMPARISON OF THE DIFFUSIVITY OF As AND Ge IN Si AT HIGH DONOR CONCENTRATIONS K. Kylliesbech Larsen, P. Gaiduk, and A. Nylandsted Larsen	601
ANOMALOUS TRANSIENT TAIL DIFFUSION OF BORON IN SILICON: KINETIC MODELING OF DIFFUSION AND CLUSTER FORMATION N.E.B. Cowern, H.F.F. Jos, K.T.F. Janssen, and A.J.H. Wachters	605

FAILURE OF THE "KICK-OUT" MODEL FOR THE DIFFUSION OF Au INTO Si WHEN TESTED BY MONTE CARLO SIMULATION U. Schmid, J.A. Van Vechten, N.C. Myers, and U. Koch	609
DIFFUSION OF POINT DEFECTS IN A STRESSED SIMPLE CUBIC LATTICE Dimitrios Maroudas and Robert A. Brown	615
THE ENHANCEMENT OF THE INTERDIFFUSION IN Si/Ge AMORPHOUS ARTIFICIAL MULTILAYERS BY ADDITIONS OF B AND Au B. Park, F. Spaepen, J.M. Poate, and D.C. Jacobson	621
DIFFUSION OF Au IN AMORPHOUS Si MEASURED BY THE ARTIFICIAL MULTILAYER TECHNIQUE E. Nygren, B. Park, L.M. Goldman, D.T. Wu, A.V. Wagner, and F. Spaepen	627
HYDROGEN DIFFUSION AND COMPLEX FORMATION IN SILICON J.T. Borenstein, D. Tulchinski, and J.W. Corbett	633
PART IX: DIFFUSION IN COMPOUNDS	
*DIFFUSION AND INTERDIFFUSION IN MULTILAYERED SEMI- CONDUCTOR SYSTEMS A. Ourmazd, Y. Kim, and M. Bode	639
ATOMIC LAYER EPITAXY OF GaAs ON Ge SUBSTRATES J. Ramdani, B.T. McDermott, and S.M. Bedair	647
DIFFUSION OF ION IMPLANTED Mg AND Be IN GaAs H.G. Robinson, M.D. Deal, and D.A. Stevenson	653
DEFECT FORMATION DURING Zn DIFFUSION INTO GaAs Martina Luysberg, W. Jäger, K. Urban, M. Perret, N.A. Stolwijk, and H. Mehrer	659
ROOM-TEMPERATURE DIFFUSION OF Mn IN CdTe AND THE FORMATION OF $\text{Cd}_{1-x}\text{Mn}_x\text{Te}$ A. Wall, A. Raisanen, G. Haugstad, and A. Franciosi	665
AN EXAMINATION OF THE MECHANISMS OF Si DIFFUSION IN GaAs Shaofeng Yu, Ulrich M. Gosele, and Teh Y. Tan	671
DIFFUSION OF Ga VACANCIES AND Si IN GaAs K.B. Kahan, D.J. Lawrence, D.L. Peterson, and G. Rajeswaran	677
MECHANISM FOR THE DIFFUSION OF ZINC IN GALLIUM ARSENIDE K.B. Kahan	681
DIFFUSION OF ION-IMPLANTED TIN IN GALLIUM ARSENIDE E.L. Allen, M.D. Deal, and J.D. Plummer	685

*Invited Paper

THE ROLE OF CHARGED POINT DEFECTS ON THE DIFFUSION BEHAVIOR OF SILICON IN GaAs Jeffrey J. Murray, Michael D. Deal, and David A. Stevenson	691
PART X: DIFFUSION IN SUPERLATTICES	
*IMPURITY-INDUCED LAYER DISORDERING: CURRENT UNDER- STANDING AND AREAS FOR FUTURE INVESTIGATION L.J. Guido and Nick Holonyak, Jr.	697
BEHAVIOR OF DOPANT-RELATED DEFECTS IN AlGaAs SUPER- LATTICES N.D. Theodore, P. Mei, S.A. Schwarz, C.B. Carter, C. Palmstrom, J.P. Harbison, and L.T. Florez	709
*DIFFUSION IN GALLIUM ARSENIDE AND GaAs-BASED LAYERED STRUCTURES U. Gösele, T.Y. Tan, and Shaofeng Yu	715
PART XI: DX CENTERS	
*THE DX CENTER: EVIDENCE FOR CHARGE CAPTURE VIA AN EXCITED INTERMEDIATE STATE Thomas N. Theis and Patricia M. Mooney	729
EFFECT OF LOCAL ATOMIC CONFIGURATION ON DX ENERGY LEVEL T. Baba, M. Mizuta, T. Fujisawa, J. Yoshino, and H. Kukimoto	741
ELECTRIC FIELD ENHANCEMENT OF ELECTRON EMISSION FROM DX CENTERS AND CONSEQUENCES J.C. Bourgoin, M. Zazoui, S.L. Feng, H.J. von Bardeleben, S. Alaya, and H. Maaref	747
OPTICALLY DETECTED MAGNETIC RESONANCE OF GROUP IV AND GROUP VI DONORS IN $\text{Al}_{0.6}\text{Ga}_{0.4}\text{As}/\text{GaAs}$ HETEROSTRUCTURES E. Glaser, T.A. Kennedy, B. Molnar, and M. Mizuta	753
PHOTOLUMINESCENCE AND BANDGAP NARROWING IN HEAVILY DOPED n-GaAs H.D. Yao and A. Compaan	759
*THEORY OF DX CENTERS IN $\text{Al}_x\text{Ga}_{1-x}$ ALLOYS D.J. Chadi and S.B. Zhang	765
A PHOTOCAPTURE TEST OF DX-CENTER MODELS Harold P. Hjalmarson, S.R. Kurtz, and T.M. Brennan	773
DX-CENTER IN Se-DOPED $\text{Al}_x\text{Ga}_{1-x}\text{As}$ Thomas R. Hanak, Assem M. Bakry, Richard K. Ahrenkiel, and Michael L. Timmons	781

*Invited Paper

POOLE FRENKEL EFFECT ON THE DX CENTERS IN III-V TERNARY ALLOYS	785
H. Altelaarrea, J. Bosch, A. Perez, J. Samitier, and J.R. Morante	
TRANSIENT CURRENT AND TRANSIENT CAPACITANCE MEASUREMENTS OF DEFECTS IN AlGaAs HEMTS	789
R. Magno and R. Shelby	
ELECTRONIC AND OPTICAL PROPERTIES OF DEEP DONORS IN HYDROGENATED $\text{Al}_x\text{Ga}_{1-x}\text{As:Si}$	793
R. Mostefaoui, R. Legros, J. Chevallier, C.W. Tu, and R.F. Kopf	

PART XII: EL2 CENTERS

THE METASTABILITY OF THE EL2 AND DX DEFECTS IN GaAs AND 3-5 ALLOYS	799
H.J. von Bardeleben and J.C. Bourgoin	
*PROGRESS IN UNDERSTANDING THE OPTICAL PROPERTIES OF EL2	805
G.A. Baraff	
THE DOUBLE DONOR ISSUE OF THE EL2 DEFECT IN GaAs	909
M.O. Manasreh and G.J. Brown	
ABSOLUTE PRESSURE DEPENDENCE OF THE SECOND IONIZATION LEVEL OF EL2 IN GaAs	815
D.E. Bliss, W. Walukiewicz, D.D. Nolte, and E.E. Haller	
*THE SYMMETRY OF THE EL2 DEFECT IN GaAs	821
P. Trautman and J.M. Baranowski	
RECOVERY FROM THE METASTABLE EL2 DEFECT IN GaAs UNDER MONOCHROMATIC LIGHT ILLUMINATION	827
M.O. Manasreh and D.W. Fischer	
EL-2 DEFECT FORMATION AND CARBON INCORPORATION IN GaAs GROWN BY ORGANOMETALLIC VAPOR PHASE EPITAXY	831
R. Venkatasubramanian, J.M. Borrego, and S.K. Ghandhi	
THE ROLE OF EL2 FOR THE MOBILITY-LIFETIME PRODUCT OF PHOTOEXCITED ELECTRONS IN GaAs	837
G.C. Valley, H.J. von Bardeleben, and H. Rajbenbach	

PART XIII: DOPING IN III-Vs

*ELECTRON SCATTERING BY NATIVE DEFECTS IN UNIFORMLY AND MODULATION DOPED SEMICONDUCTOR STRUCTURES	845
W. Walukiewicz	

*Invited Paper

ACCEPTOR DELTA-DOPING IN GaAs W.S. Hobson, S.J. Pearton, C.R. Abernathy, and G. Cabaniss	855
PRECIPITATION PHENOMENA ASSOCIATED WITH ULTRA-HIGH Be DOPING IN $\text{Ga}_{0.47}\text{In}_{0.53}\text{P}$ LAYERS GROWN BY MBE C.M. Coteil, M.B. Panish, R.A. Hamm, L.C. Hopkins, and J.M. Gibson	861
CHARACTERISTICS OF DOPING AND DIFFUSION OF HEAVILY DOPED N AND P TYPE InP AND InGaAs EPITAXIAL LAYERS GROWN BY METAL ORGANIC CHEMICAL VAPOR DEPOSITION C.J. Pinzone, N.T. Ha, N.D. Gerrard, R.D. Dupuis, and H.S. Luftman	867
EFFECTS OF Si INCORPORATION AND ELECTRICAL ACTIVATION ON INTERSUBBAND OPTICAL ABSORPTION IN MBE-GROWN GaAs/AlGaAs MULTIPLE QUANTUM WELL STRUCTURES J.D. Ralston, H. Ennen, M. Maier, M. Ramsteiner, B. Dischler, P. Koidl, and P. Hiesinger	875
BERYLLIUM DOPING IN MBE-GROWN GaAs AND AlGaAs Joseph Pellegrino, James Griffin, Leary Myers, and Michael Spencer	881
CARBON DOPING IN InGaAs GROWN BY MBE Hiroshi Ito and Tadao Ishibashi	887
PART XIV: ORDERING IN ALLOYS	
*ORDERING IN III/V ALLOYS G.B. Stringfellow	893
COMPARISON OF ORDERED AND MODULATED STRUCTURES IN InGaP ALLOY SEMICONDUCTORS GROWN BY MOCVD, CHLORIDE- VPE AND LPE METHODS O. Ueda, T. Kato, T. Matsumoto, M. Hoshino, M. Takechi, and M. Ozeki	901
ATOMIC ORDERING AND ALLOY CLUSTERING IN MBE-GROWN $\text{InAs}_y\text{Sb}_{1-y}$ EPITAXIAL LAYERS Tae-Yeon Seong, A.G. Norman, C.R. Booker, R. Droopad, R.L. Williams, S.D. Parker, P.D. Wang, and R.A. Stradling	907
PART XV: PROCESSING OF SILICON AND GERMANIUM	
RAPID THERMAL PROCESS-INDUCED DEFECTS: GETTERING OF INTERNAL CONTAMINANTS Bouchaib Hartiti, Wolfgang Eichhammer, Jean- Claude Muller, and Paul Siffert	915

*Invited Paper

OXYGEN AND IRON REDISTRIBUTION UPON THERMAL TREATMENT IN IRON IMPLANTED SILICON B. Pivac, A. Borghesi, L. Ottolini, M. Geddo, A. Piaggi, and A. Stella	919
ION BEAM ETCHING OF SILICON: IMPLANTATION AND DIFFUSION OF NOBLE GAS ATOMS, AND GETTERING OF COPPER William D. Sawyer, Jörg Schmälzlin, and Jörg Weber	923
ANGLE RESOLVED XPS ANALYSIS OF SURFACE REGION DEFECTS IN RAPID THERMAL ANNEALED ANTIMONY IMPLANTED SILICON S.N. Kumar, G. Chaussemy, A. Laugier, B. Canut, and M. Charbonnier	927
DEFECTS IN MBE-GROWN SILICON EPILAYERS STUDIED WITH VARIABLE-ENERGY POSITRONS P.J. Simpson, P.J. Schultz, I.V. Mitchell, T.E. Jackman, and G.C. Aers	931
A HVEM STUDY OF THE ELECTRON IRRADIATED DEFECTS IN NITROGEN DOPED FZ-Si SINGLE CRYSTAL Gao Yuzun and T. Takeyama	937
MOLECULAR DYNAMICS STUDIES OF DISLOCATIONS IN Si M.S. Duesbery, D.J. Michel, and B. Joos	941
A TEM INVESTIGATION OF SECONDARY DISLOCATIONS IN GRAIN BOUNDARIES IN GERMANIUM M. Griess, M. Seibt, and H.J. Möller	945
AC PHOTOVOLTAIC INSPECTION OF P-N JUNCTIONS HAVING HIGH LEAKAGE CURRENT N. Homma, H. Shimizu, C. Munakata, and M. Ogasawara	951
TWINNING STRUCTURE OF {113} DEFECTS IN HIGH-DOSE OXYGEN IMPLANTED SILICON-ON-INSULATOR MATERIAL S. Visitserngtrakul, J. Barry, and S. Krause	955
STRUCTURAL TRANSITIONS IN TITANIUM/AMORPHOUS-SILICON MULTILAYERS E. Ma, L.A. Clevenger, C.V. Thompson, R.R. DeAvillez, and K.N. Tu	961
STUDIES OF THE EARLY OXIDATION OF SILICON (111) IN ATOMIC OXYGEN Bhola N. De, Jane Hruska, Jane Peterkin, Yong Zhao, and John A. Woollam	965
ENHANCEMENT OF OXYGEN PRECIPITATION IN QUENCHED CZOCHEWSKI SILICON CRYSTALS A. Hara, T. Fukuda, I. Hirai, and A. Ohsawa	969

PART XVI: PROCESSING OF COMPOUNDS

BURIED AMORPHOUS LAYER IN GALLIUM ARSENIDE D. Sengupta, M.C. Ridgway, J.M. Zemanski, and S.T. Johnson	975
DEFECT LEVELS IN THE NEAR-SURFACE REGION OF 2.0 MeV ¹⁶ O ⁺ ION IMPLANTED n-GaAs C.C. Tin, P.A. Barnes, T.T. Bardin, and J.G. Pronko	979
CORRELATION OF VOID FORMATION WITH THE REDUCTION OF CARRIER ACTIVATION AND ANOMALOUS DOPANT DIFFUSION IN Si-IMPLANTED GaAs Kei-Yu Ko, Samuel Chen, S.-Tong Lee, Longru Zheng, and T.Y. Tan	983
SURFACE AND INTERFACE DAMAGE CHARACTERIZATION OF REACTIVE ION ETCHED MBE REGROWN GaAs M.W. Cole, M. Dutta, J. Rossabi, D.D. Smith, and J.L. Lehman	987
Pd/Au:Be OHMIC CONTACTS TO p-TYPE GaAs K.M. Schmitz, K.L. Jiao, R. Sharma, W.A. Anderson, G. Rajeswaran, L.R. Zheng, M.W. Cole, and R.T. Lareau	993
IMPROVED HOLE DIFFUSION LENGTHS IN BULK n-TYPE GaAs FOR HIGH EFFICIENCY SOLAR CELLS D. Wong, T.E. Schlesinger, and A.G. Milnes	997
THE STUDY OF CONTAMINATION OF CARBON, BORON, AND OXYGEN IN LEC-GaAs Y. Itoh, M. Takai, H. Fukushima, and H. Kirita	1001
IN-SITU SYNTHESIS AND MAGNETICALLY STABILIZED KYROPOULOS GROWTH OF UNDOPED INDIUM PHOSPHIDE Stephen Bachowski, Brian S. Ahern, Robert M. Hilton, and Joseph A. Adamski	1007
DEEP-LEVEL DOMINATED CURRENT-VOLTAGE CHARACTERISTICS OF NOVEL SEMICONDUCTOR HETEROSTRUCTURES K. Das	1011
SURFACE STRUCTURE OF SULFUR COATED GaAs Yoshihisa Fujisaki and Shigeo Goto	1017
ELECTRICAL AND MATERIAL CHARACTERIZATION OF THE STABILITY OF AlGaAs AND GaAs PLANAR DOPED STRUCTURES Larry P. Sadwick and Dwight C. Streit	1021
PHOTOLUMINESCENCE STUDIES OF IMPURITIES AND DEFECTS IN MERCURIC IODIDE X.J. Bao, T.E. Schlesinger, R.B. James, A.Y. Cheng, and C. Ortale	1027

DEPTH SENSITIVE IMAGING OF DEFECTS IN EPILAYERS AND SINGLE CRYSTALS USING WHITE BEAM SYNCHROTRON RADIATION TOPOGRAPHY IN GRAZING BRAGG-LAUE GEOMETRY M. Dudley, G.-D. Yao, J. Wu, and H.-Y. Liu	1031
AUTHOR INDEX	1037
SUBJECT INDEX	1043
MATERIALS RESEARCH SOCIETY SYMPOSIUM PROCEEDINGS	1051

Preface

This volume of proceedings contains manuscripts from Symposium G, entitled "Impurities, Defects, and Diffusion in Semiconductors: Bulk and Layered Structures." It was held November 27-December 1, 1989, in Boston, MA, as part of the 1989 Fall Meeting of the Materials Research Society. Historically, Symposium G was the seventh in a series of MRS-sponsored symposia which focused on various aspects of defects and defect properties in semiconducting materials. The program lasted four-and-one-half days and two evenings, and consisted of 21 invited talks, 75 contributed oral presentations, and 104 posters, making it the most ambitious symposium held to date by MRS on semiconductor defects. Symposium G received gratifying response from the international defects, diffusion, and superlattice communities, with work originating from some 25 countries, led (in descending order) by the United States, Sweden, Japan, West Germany, and France. As organizers, we therefore owe this proceedings to the enthusiasm and expertise so many brought to Symposium G.

This symposium was conceived from the view that impurities, defects, and diffusion play key roles in modern-day research and development of semiconducting materials, structures, and devices. Recent breakthroughs in materials preparation with monolayer control, in diversity and sensitivity of characterization techniques, and in new theoretical methods, have collectively led to great advances in the understanding of defect- and impurity-related phenomena. They have also resulted in the formulation of new, more complex and insightful questions. Since related questions may arise in studies of bulk semiconductors, quantum wells, superlattices, and homo- and heterostructures, the intent of this symposium was to bring together, from around the world, experimentalists and theorists working on defect problems from throughout these various semiconductor systems. Papers were originally solicited in the following broad topical areas:

- Electronic structure of shallow and deep-level impurities, impurity complexes, native defects, and atomically ordered alloys
- Self-diffusion, and diffusion of shallow and deep-level impurities and native defects
- Defect and impurity reactions and thermochemistry, stoichiometry, and alloy-ordering phenomena
- Interdiffusion and segregation in compounds and layered structures
- Hydrogen-related phenomena and impurity passivation in semiconductors

To encourage the symposium attendees to emphasize these keynote themes, experienced contributors from each major topical area were invited to participate. Their talks helped define the intended conference's emphasis and flow.

Correspondingly, this proceedings volume is organized into 16 parts, generally following the symposium order. The first 5 parts deal with the Electronic Structure of various defect types

in both elemental and III-V materials, as deduced largely by spectroscopies and theory. Highlights include Prof. Grimmeiss' comprehensive, lead-off talk on recent progress made using high-resolution PTIS techniques applied to point defects in Si. Other detailed spectroscopy talks then follow, re-emphasizing the power of optical spectroscopies in defect identification. These include: Prof. Monemar's review talk on complex defects explored by absorption, luminescence, and ODMR in Si and III-Vs; Dr. Smith's review of novel optical aspects resulting from heavy shallow doping in homostructures; talks on level structure of a wide variety of native defects and transition metals; Prof. Thewalt's review of high-resolution Fourier-transform luminescence in defect characterization; Prof. Wichert's talk on perturbed angular correlation (PAC) techniques for impurity-pair identification in Si; numerous contributed talks on transition-metal complexes and radiation defects in Si; and Dr. Reynold's review of defect spectroscopy in quantum wells, as well as contributed talks on the same topic. This was followed by Prof. Dow's review of the recent theory of defect levels in superlattices, and a contributed paper.

Next, the proceedings deal with topics related to Hydrogen, with Si hosts presented in Part 6 and III-Vs presented in Part 7. Prof. Watkins sets the tone by describing elegant infrared experiments and theory detailing H-B pairs in Si as Fermi resonances. This is followed by other talks on experiments and theory concerning microscopies of H behavior, including: Dr. Chiarotti on molecular dynamics simulations of H motion in crystalline and amorphous Si; Prof. Estle on the structure and stability of muonium centers in semiconductors; Prof. Pajot on infrared spectroscopy of H-impurity complexes in III-Vs; and a variety of authors on H-related passivation phenomena of dopants in III-Vs.

The next major theme is Diffusion, with the corresponding papers being presented in Part 8 on Si and Ge, Part 9 on compound semiconductors, and Part 10 on superlattices. These are led off by a review of first-principles calculations of self-diffusion and dopant diffusion in Si by Dr. Pantelides. This is followed by numerous contributed presentations on both theoretical and experimental studies in Si and Ge. Topics covered include the influence of pressure and strain on diffusion; transition-metal motion; silicide formation; impurity precipitation; the elucidation of kick-out mechanisms; and anomalous diffusion mechanisms and interactions in elementals. Dr. Ourmazd then carries this theme into compounds by describing TEM studies of self- and interdiffusion in multilayer structures; which is followed by various experimental talks on both intrinsic and extrinsic diffusion in both III-Vs and II-VIs. The diffusion theme is concluded with presentations by Prof. Guido on experimental aspects of impurity-enhanced disordering of superlattices, and by Prof. Goesele on the theory of such impurity disordering.

The fourth major theme is DX and EL2 Centers, contained in Parts 11 and 12, respectively. These topics are introduced by Dr. Theis who reviews the current status of experiments aimed at the microscopic and electronic properties of DX centers, including those needed to test DX theories. This presentation is followed by related talks on optical and transport experiments of both shallow and deep DX properties, and new theoretical predictions for DX photocapture; and Dr. Chadi's review of current prominent DX models, including negative-U and large-lattice-relaxation aspects. This section is concluded with possible connections

between DX and EL2 centers in a variety of measurement and crystal-growth talks, with recent microscopic theory of EL2 being reviewed by Dr. Baraff, and recent experiments related to EL2 symmetry being reviewed by Dr. Trautman.

The fifth theme centers on III-V Doping, as presented in Part 13. It is highlighted by Dr. Walukiewicz who discusses recent thermochemical models of amphoteric native defects used to interpret successfully numerous transport experiments in GaAs and metal-semiconductor interface studies. This is complemented by additional talks on dopant activation and precipitation in bulk and in structures.

Theme six is Alloy Ordering, as reviewed by Prof. Stringfellow. Here he presents strong experimental and thermochemical evidence to prove that spontaneous, atomic ordering during crystal growth occurs broadly and quite commonly in mixed semiconductor systems, and often arises in systems displaying miscibility gaps. This was followed by TEM studies of related alloys showing strong intrinsic ordering.

The seventh and final theme is Processing, with Si- and Ge-related papers contained in Part 15 and compound-related papers contained in Part 16. Here, some 26 presentations describe such diverse aspects of processing as, for example, reactive-ion etching, rapid-thermal annealing, ion-beam etching, ion implantation, electron irradiation, oxidation, thermal quenching, ohmic-contact formation, amorphous-layer formation, and surface-passivation methods.

Symposium G, described above and documented in the following Parts, achieved the main goals we, as organizers, set down. The most important of those was the bringing together, in one meeting, researchers from the areas of bulk defects, diffusion and processing, and layered materials. High standards were maintained throughout, and the symposium was well attended and well received. We thank all the participants who made this possible.

April 1990

D.J. Wolford
J. Bernholc
E.E. Haller

Acknowledgments

We would like to thank all the presenters, chairpersons, and the audience for their often enthusiastic participation in this symposium.

Since the names of all the authors are listed in the Table of Contents, we only list the chairpersons here. They were K.K. Bajaj, D.J. Chadi, H.G. Grimmeiss, L.C. Kimerling, R.C. Newman, M.L.W. Thewalt, S.G. Bishop, J. Furdyna, H.P. Hjalmarson, P.M. Mooney, M. Stavola, and J.A. Van Vechten. We are much indebted to them for stimulating the discussions, for their own expert comments, and for keeping the program on track.

We are very much obliged to the many reviewers of the papers in this volume, each of whom reviewed a substantial number of papers on very short notice. Their contributions have much improved the quality of these Proceedings.

The financial support for this symposium was provided by the Air Force Office for Scientific Research, Dr. Cole Litton, Program Director; and by the Office of Naval Research, Dr. Larry R. Cooper, Program Director. By stimulating interdisciplinary presentations and attendance, their support has been instrumental to making this symposium a success.

A substantial amount of administrative costs have been carried by the Co-organizers' institutions. We wish to thank IBM Corporation, Lawrence Berkeley Laboratories, and North Carolina State University for providing personnel and other services essential to the planning and the smooth running of the symposium.

Finally, we would like to thank the MRS staff for invaluable assistance in preparing and running the symposium, and for their patience, indulgence, and care in the preparation of this proceedings volume.

MATERIALS RESEARCH SOCIETY SYMPOSIUM PROCEEDINGS

Recent Materials Research Society Symposium Proceedings

- Volume 145—III-V Heterostructures for Electronic/Photonic Devices, C.W. Tu, V.D. Matterna, A.C. Gossard, 1989, ISBN: 1-55899-018-6
- Volume 146—Rapid Thermal Annealing/Chemical Vapor Deposition and Integrated Processing, D. Hodul, J. Gelpey, M.L. Green, T.E. Seidel, 1989, ISBN: 1-55899-019-4
- Volume 147—Ion Beam Processing of Advanced Electronic Materials, N.W. Cheung, A.D. Marwick, J.B. Roberto, 1989, ISBN: 1-55899-020-8
- Volume 148—Chemistry and Defects in Semiconductor Heterostructures, M. Kawabe, T.D. Sands, E.R. Weber, R.S. Williams, 1989, ISBN: 1-55899-021-6
- Volume 149—Amorphous Silicon Technology-1989, A. Madan, M.J. Thompson, P.C. Taylor, Y. Hamakawa, P.G. LeComber, 1989, ISBN: 1-55899-022-4
- Volume 150—Materials for Magneto-Optic Data Storage, C.J. Robinson, T. Suzuki, C.M. Falco, 1989, ISBN: 1-55899-023-2
- Volume 151—Growth, Characterization and Properties of Ultrathin Magnetic Films and Multilayers, B.T. Jonker, J.P. Heremans, E.E. Marinero, 1989, ISBN: 1-55899-024-0
- Volume 152—Optical Materials: Processing and Science, D.B. Poker, C. Ortiz, 1989, ISBN: 1-55899-025-9
- Volume 153—Interfaces Between Polymers, Metals, and Ceramics, B.M. DeKoven, A.J. Gellman, R. Rosenberg, 1989, ISBN: 1-55899-026-7
- Volume 154—Electronic Packaging Materials Science IV, R. Jaccodine, K.A. Jackson, E.D. Lillie, R.C. Sundahl, 1989, ISBN: 1-55899-027-5
- Volume 155—Processing Science of Advanced Ceramics, I.A. Aksay, G.L. McVay, D.R. Ulrich, 1989, ISBN: 1-55899-028-3
- Volume 156—High Temperature Superconductors: Relationships Between Properties, Structure, and Solid-State Chemistry, J.R. Jorgensen, K. Kitazawa, J.M. Tarascon, M.S. Thompson, J.B. Torrance, 1989, ISBN: 1-55899-029
- Volume 157—Beam-Solid Interactions: Physical Phenomena, J.A. Knapp, P. Borgesen, R.A. Zuhr, 1989, ISBN 1-55899-045-3
- Volume 158—In-Situ Patterning: Selective Area Deposition and Etching, R. Rosenberg, A.F. Bernhardt, J.G. Black, 1989, ISBN 1-55899-046-1
- Volume 159—Atomic Scale Structure of Interfaces, R.D. Bringans, R.M. Feenstra, J.M. Gibson, 1989, ISBN 1-55899-047-X
- Volume 160—Layered Structures: Heteroepitaxy, Superlattices, Strain, and Metastability, B.W. Dodson, L.J. Schowalter, J.E. Cunningham, F.H. Pollak, 1989, ISBN 1-55899-048-8
- Volume 161—Properties of II-VI Semiconductors: Bulk Crystals, Epitaxial Films, Quantum Well Structures and Dilute Magnetic Systems, J.F. Schetzina, F.J. Bartoli, Jr., H.F. Schaake, 1989, ISBN 1-55899-049-6
- Volume 162—Diamond, Boron Nitride, Silicon Carbide and Related Wide Bandgap Semiconductors, J.T. Glass, R.F. Messier, N. Fujimori, 1989, ISBN 1-55899-050-X
- Volume 163—Impurities, Defects and Diffusion in Semiconductors: Bulk and Layered Structures, J. Bernholc, E.E. Haller, D.J. Wolford, 1989, ISBN 1-55899-051-8
- Volume 164—Materials Issues in Microcrystalline Semiconductors, P.M. Fauchet, C.C. Tsai, K. Tanaka, 1989, ISBN 1-55899-052-6
- Volume 165—Characterization of Plasma-Enhanced CVD Processes, G. Lucovsky, D.E. Ibbotson, D.W. Hess, 1989, ISBN 1-55899-053-4
- Volume 166—Neutron Scattering for Materials Science, S.M. Sharf, S.C. Moss,

MATERIALS RESEARCH SOCIETY SYMPOSIUM PROCEEDINGS

- Volume 167—Advanced Electronic Packaging Materials, A. Barfknecht, J. Partridge, C-Y. Li, C.J. Chen, 1989, ISBN 1-55899-055-0
- Volume 168—Chemical Vapor Deposition of Refractory Metals and Ceramics, T.M. Besmann, B.M. Gallois, 1989, ISBN 1-55899-056-9
- Volume 169—High Temperature Superconductors: Fundamental Properties and Novel Materials Processing, J. Narayan, C.W. Chu, L.F. Schneemeyer, D.K. Christen, 1989, ISBN 1-55899-057-7
- Volume 170—Tailored Interfaces in Composite Materials, C.G. Pantano, E.J.H. Chen, 1989, ISBN 1-55899-058-5
- Volume 171—Polymer Based Molecular Composites, D.W. Schaefer, J.E. Mark, 1989, ISBN 1-55899-059-3
- Volume 172—Optical Fiber Materials and Processing, J.W. Fleming, G.H. Sigel, S. Takahashi, P.W. France, 1989, ISBN 1-55899-060-7
- Volume 173—Electrical, Optical and Magnetic Properties of Organic Solid-State Materials, L.Y. Chiang, D.O. Cowan, P. Chaikin, 1989, ISBN 1-55899-061-5
- Volume 174—Materials Synthesis Utilizing Biological Processes, M. Alper, P.D. Calvert, P.C. Rieke, 1989, ISBN 1-55899-062-3
- Volume 175—Multi-Functional Materials, D.R. Ulrich, F.E. Karasz, A.J. Buckley, G. Gallagher-Daggitt, 1989, ISBN 1-55899-063-1
- Volume 176—Scientific Basis for Nuclear Waste Management XIII, V.M. Oversby, P.W. Brown, 1989, ISBN 1-55899-064-X
- Volume 177—Macromolecular Liquids, C.R. Safinya, S.A. Safran, P.A. Pincus, 1989, ISBN 1-55899-065-8
- Volume 178—Fly Ash and Coal Conversion By-Products: Characterization, Utilization and Disposal VI, F.P. Glasser, R.L. Day, 1989, ISBN 1-55899-066-6
- Volume 179—Specialty Cements with Advanced Properties, H. Jennings, A.G. Landers, B.E. Scheetz, I. Odler, 1989, ISBN 1-55899-067-4

MATERIALS RESEARCH SOCIETY MONOGRAPH

Atom Probe Microanalysis: Principles and Applications to Materials Problems, M.K. Miller, G.D.W. Smith, 1989, ISBN 0-931837-99-5

Earlier Materials Research Society Symposium Proceedings listed in the back.

PART I

Electronic Structure -
Deep Levels

HIGH-RESOLUTION SPECTROSCOPY OF POINT DEFECTS IN SILICON

H.G. GRIMMEISS, M. KLEVERMAN AND J. OLAJOS

University of Lund, Dept. of Solid State Physics, Box 118, S-221 00 Lund, Sweden

ABSTRACT

The paper briefly outlines recent developments in high resolution spectroscopy of point defects in silicon. One of the methods, namely, photothermal ionization spectroscopy (PTIS) is discussed in detail. Impurities induced by selenium and several transition metals are used as examples in order to illustrate the powerful scope of both transmission and PTIS measurements. These measurements are capable of providing unique information on the electronic properties of point defects, even when the defects exhibit complex excitation spectra.

INTRODUCTION

The great advances in semiconductor electronics can be traced to a unique combination of basic conceptual advances, the perfection of new materials and the development of new device principles. Ever since the invention of the transistor, we have witnessed a fantastic growth in silicon technology, leading to more complex functions and higher densities of devices such as the mega bit memories. This development would hardly be plausible without an increased understanding of semiconductor materials and a better insight into the important role, defects play in most currently used devices. It is therefore not surprising that a variety of techniques for the characterization and identification of defects in semiconductors have evolved during the last few decades. Some of the earlier methods comprise electrical and magnetic measurements, photoconductivity, absorption and various forms of luminescence [1]. All these methods allowed the study of thermal "activation energies" and/or optical threshold energies but only very rarely could absolute values of fundamental electronic parameters be determined [2]. This situation has changed considerably with the introduction of junction space charge techniques (JSCT) such as photocurrent [3] and dark capacitance [4] measurements. Most of these methods, in particular deep level transient spectroscopy (DLTS) [5], allows the determination of defect concentrations with sufficient accuracy and the direct measurement of electronic parameters such as emission and capture rates. Once these parameters are known, the energy position of defects within the band gap can be determined in terms of enthalpies and/or threshold energies deduced from the distribution of a single optical cross section. There is no doubt that these measurement methods provided an important breakthrough in the characterization of defects in semiconductors.

In parallel with this development fundamental improvements were achieved in defect identification [6]. If the chemical origin of the defect is unknown, defect characterization is rather meaningless. It was therefore of utmost importance to combine experimental methods for defect identification with those for defect characterization [7].

There are several basic differences between JSCT and other characterization methods which have been previously reviewed [8] and will therefore not be discussed further in this paper. Instead an attempt is made to outline, very briefly, recent developments in the characterization and identification of point defects in silicon which have been made possible by the application of methods other than JSCT. The focus here will in particular be limited to two methods, namely transmission and PTIS. These two techniques are capable of providing unique information on the electronic properties of defects. PTIS and transmission

measurements possess many common features but nevertheless have interesting differences. It is these differences, which among other aspects will be discussed in further detail.

BASIC PROPERTIES OF PHOTOTHERMAL IONIZATION SPECTROSCOPY

PTIS has been used to study shallow centers for more than 20 years [9]. Only recently has the method been applied to investigate deep defects. Basically, PTIS is a thermally enhanced photoconductivity method, consisting of an optical excitation of

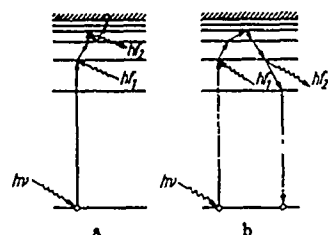


Fig. 1. Scheme of the thermal transitions in an impurity atom excited by light. (a) ionization (b) return to the ground state. $h\nu$ energy of light quantum, h_f phonon energy [9].

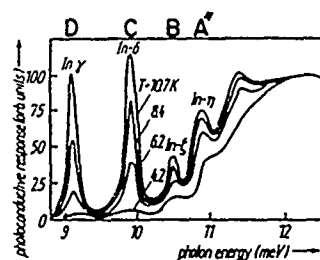


Fig. 2. PTIS spectra of indium-doped germanium (p-type) at different temperatures from Ref. [9].

charge carrier from the ground state into excited states of a defect followed by thermal ionization of the excited defect (Fig. 1). The absorption of a photon may or may not result in a positive PTIS signal depending on whether or not the charge carrier is finally excited into the band continuum. Typical spectra obtained already in 1967 for indium-doped germanium at different temperatures [9] are shown in Fig. 2. Indium has a binding energy of 11.7 meV in germanium. Transitions from the ground state into the valence band continuum are clearly seen as a broad, featureless spectrum at energies greater than the binding energy. On the low-energy side of the continuum threshold, five lines are observed which are caused by two-step excitation processes via excited states. Due to the two-step excitation processes the peak heights of the lines increase with increasing temperature, implying that the signal of shallower levels is favoured over the signal from deeper levels. This interesting property and the good signal-to-noise ratio obtained with Fourier transform spectroscopy is more convincingly demonstrated in Fig. 3, which shows a recent study by Kahn [10] on the $A(\text{Cu}, \text{H}_2)$ acceptor in high purity germanium. Apart from the hydrogenated copper center, the sample also contained residual impurities, such as aluminium, gallium and boron. The

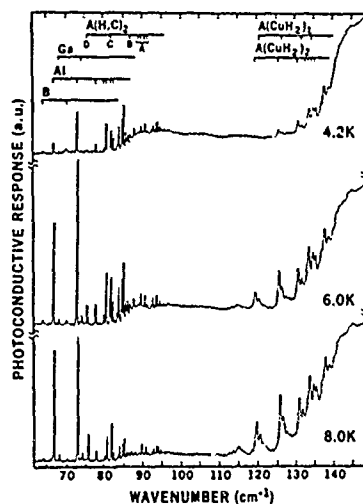


Fig. 3. PTIS spectrum of germanium containing the shallow acceptors B, Al, Ga and $A(\text{H}, \text{C})_2$ and the acceptor $A(\text{Cu}, \text{H}_2)$ [10].

concentration of these impurities was of the order of 10^9 cm^{-3} . A closer inspection of the spectrum due to the $\text{A}(\text{Cu}, \text{H}_2)$ center clearly shows that the peak height of lines due to deeper excited states increase with increasing temperature. This particular property of PTIS can be used to obtain information on the electronic properties of a defect which would be otherwise difficult to obtain by absorption measurements.

Another interesting difference between PTIS and absorption is the high sensitivity of PTIS. From previous investigations of shallow centers it is known that under certain conditions, especially in a particular temperature range, the PTIS signal is independent of the concentration of defects down to very low values [9]. It has been shown that, depending on the defect it should be possible to study impurities in germanium with concentrations as low as 10^5 cm^{-3} [9]. Since the solubility of impurities often decreases with increasing binding energy [11], PTIS is particularly important in the study of deep impurities. Furthermore, the method is inexpensive and simple since the sample studied acts as a photon detector itself which has great advantages for measurements in certain wavelength regions.

THERMAL AND OPTICAL STUDIES OF INDIVIDUAL EXCITED STATES

It has already been pointed out that in a certain temperature range the strength of a PTIS signal may be strongly temperature dependent. This unique property has recently been used [12] to provide additional experimental evidence that the center responsible for the so-called C line in silicon is donor-like and that all lines observed in photoluminescence and absorption [13-17] are associated with this donor. In this paper we will demonstrate that PTIS can be used to determine thermal activation energies of individual excited states with an accuracy better than 1 meV. This may offer new possibilities for the investigation of recombination processes via such states. For this study selenium doped silicon was used.

The isolated neutral selenium donor in silicon has been previously characterized in detail [18]. The PTIS spectra of this center which has a ground state binding energy of 306.6 meV, were collected at 20 different temperatures between 8.1 K and 114 K [19]. A spectrum taken at 24.7 K is shown in Fig. 4. The assignment of the lines is the same as in Ref. 18. The energy positions of the lines studied are in excellent agreement with Effective Mass Theory (EMT) [18]. Plotting the logarithm of the integrated peak intensity versus $1/T$, a linear relationship is obtained for all lines seen in Fig. 4. A typical result for the

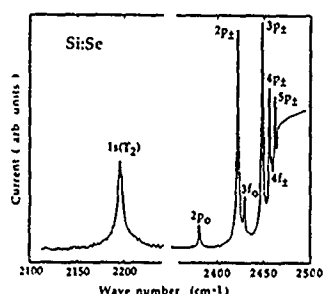


Fig. 4. Photocurrent due to Si:Se^0 as a function of photon energy. The spectrum between wave number 2360 cm^{-1} and 2500 cm^{-1} was recorded at 24.7 K and that between wave numbers 2110 and 2230 at 65.8 K, since all lines cannot be seen at one single temperature.

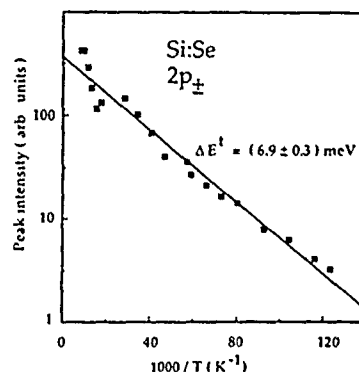


Fig. 5. The integrated amplitude of the $2p_{\pm}$ line as a function of reciprocal temperature. The thermal activation energy is calculated from the slope of the regression line and the standard error is estimated from the scatter in the data.

$2p_{\pm}$ line is shown in Fig. 5. The linear relationship suggests that the PTIS signal is governed by detailed balance [20]. It can be seen that the activation energy ΔE_{th} calculated from these linear relationships is close to the value of the change in enthalpy ΔH needed to excite an electron from an excited state into the conduction band [20]. It is interesting to note that the scatter in the measured data, presented in Fig. 5 for the $2p_{\pm}$ line, is small and seemingly below 1 meV. Furthermore, the value obtained for ΔE_{th} differs from the optical binding energy only by 0.5 meV, which is almost within the experimental error. For lines shallower than $2p_{\pm}$ the difference is even smaller.

The ΔE_{th} values for all lines studied are plotted in Fig. 6 as a function of the optical transition energy ΔE^o . All ΔE_{th} values lie more or less on a straight line (dotted line in Fig. 6). It is therefore not surprising that the extrapolation of the ΔE_{th} values to zero, intercepts the ΔE^o axis at an energy which differs from the ground state binding energy of the center by only a few tenths of meV. It is interesting to note that within the limits of experimental error the thermal activation energies of all lines shallower than $2p_0$ are in good agreement with their optical binding energy. In contrast, the ΔE_{th} value of the $2p_0$ line (and probably also the one for the $1s1_2$ line) deviates from the optical binding energy, shown by the solid line of slope 1 in Fig. 6. Since the optical binding energies of all p lines studied are in excellent agreement with their EMT values [18], this implies that within the experimental error, the ΔE_{th} values of all p lines are equal to their EMT values, except for the value of the $2p_0$ line. Future experiments with other chalcogens have to be performed in order to determine whether the deviation of the ΔE_{th} from the EMT binding energy of the p line is due to particular properties of the PTIS method, or whether the deviation reflects certain properties of the capture process.

Comparing the spectrum of Fig. 4 with a spectrum of a group V donor, it is immediately realized that optical spectra of chalcogen double donors bear close resemblance with corresponding spectra of group V donors in silicon. For both groups of impurities the ground state is a $1sA_1$ singlet state and the binding energies of the final states, except for the s-line states, are well accounted for by EMT. The spectra of chalcogens and group V donors are therefore easy to analyze. There is, however, one important difference between the chalcogen donors and group V donors in silicon. The group V donors show only transitions from the ground state to p states, whereas chalcogen donors exhibit additional transitions to EMT forbidden (but symmetry allowed) valley-orbit split ns states. This behaviour is a direct consequence of the increased binding energy of the chalcogen donors. As the ground state gets deeper, the selection rules are further relaxed and are instead governed by the symmetry of the center. It has been observed that this trend is still more pronounced for very deep centers. One such example is the silver donor in silicon [21].

SILVER DONOR IN SILICON

The ground state of the neutral isolated silver donor in silicon lies about 340 meV above the valence band [22]. The transmission spectrum of the center is shown

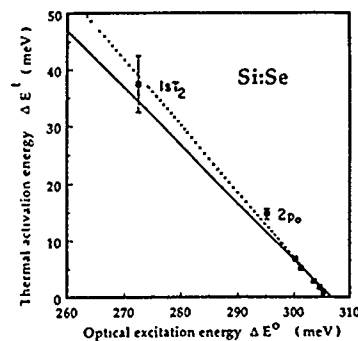


Fig. 6. The thermal activation energy as a function of optical excitation energy for the different lines shown in Fig. 4. The dotted line, which goes through the experimental points, gives a continuum value of around 307 meV. The solid line is obtained from the Effective Mass Theory values as a function of the optical excitation energies.

in Fig. 7 along with the spectra of the phosphorus and neutral tellurium donor in silicon. A comparison of the spectra shows that the general feature of the silver spectrum is quite different from the other two spectra. The assignment of the silver spectrum was considerably facilitated due to clearly observed phonon assisted Fano resonances which convincingly demonstrated the donor character of the center [21]. A striking feature of the silver spectrum is the fact that the p lines are very weak (in fact the $2p_{+}$ line was never observed) and that the spectrum is dominated by ns lines. In the case of tellurium strong spin-orbit interactions mix the $1sT_2$ levels originating from the singlet $T_2(^1T_2)$ and triplet $T_2(^3T_2)$ states so that both the singlet and the otherwise forbidden triplet T_2 level become visible [23]. Assuming, that there is also an exchange interaction between the loosely bound excited electron and the electrons of the silver donor core, it is believed that the A, B and IC lines may originate from similar many-particle and spin-orbit effects as in the case of tellurium. Following this assignment, the four closely spaced lines of the $1s(E+T_2)$ structure suggest a lower symmetry than T_d for the silver donor, although the ground state is assumed to be $1sA_1$ [21].

The different feature of the excitation spectra of chalcogen donors and the silver donor stems from the increased localization of the ground state. With increasing strength of the central-cell potential the binding energy of the $1sA_1$ ground state increases and a larger part of the conduction band minima in k space contributes to the wavefunction of the $1sA_1$ ground state. This implies that the overlap between the wavefunctions of the ground state and excited Coulomb states decreases and thus the electric-dipole matrix elements. This effect is strongest for p states, since s states are more delocalized in k space. With increasing deviation from EMT the relative intensities of transitions to s states become increasingly stronger compared with transitions to p states and finally the s lines will dominate the excitation spectrum.

The two examples of impurities discussed thus far are characterized in the case of the selenium donor by simple spectra which, except for $1s$ states, are in excellent agreement with those for the group V donors, and in the case of the silver donor by a strong dominance of transitions to s-like states with energies which are no longer predicted by EMT. The next example to be discussed is the interstitial iron which exhibits a different kind of excitation spectrum due to a splitting of the final states.

INTERSTITIAL IRON IN SILICON

Typical transmission spectra of interstitial iron which seemingly show little resemblance to the selenium spectrum of Fig. 4 are presented for two different temperatures in Fig. 8. The identity of the center giving rise to the spectra was established by photo-EPR measurements [23], which clearly showed that the center is

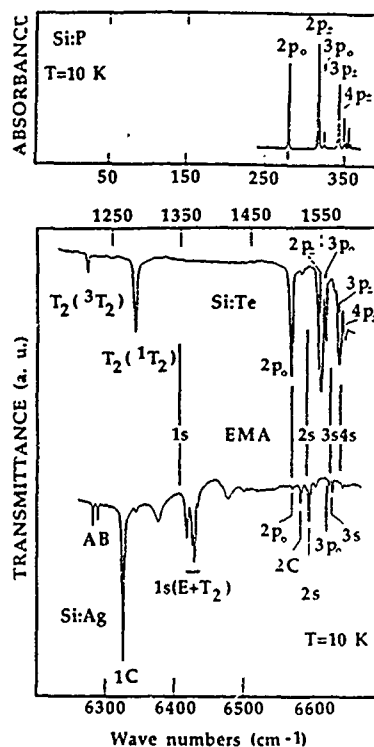


Fig. 7. Absorption spectra in silicon for (a) the shallow P donor and (b) the deep Te and Ag donors.

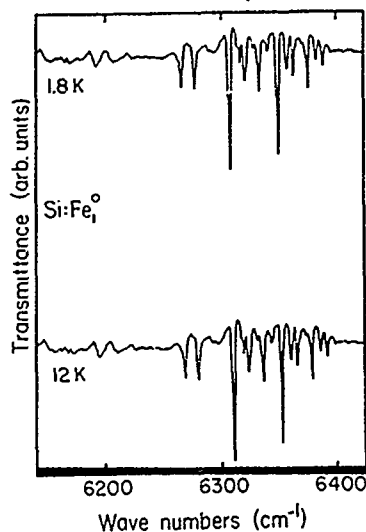


Fig. 8. High resolution spectrum of Fe_i^0 in silicon at two different temperatures.

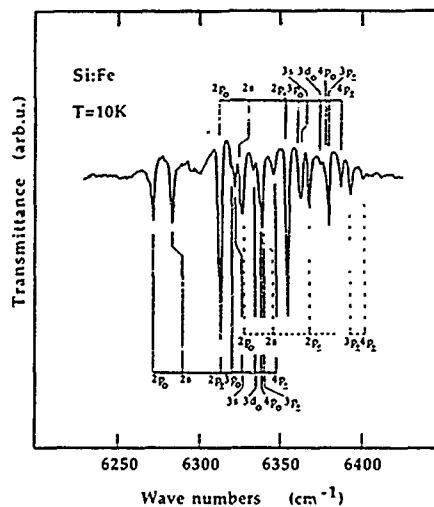


Fig. 9. High resolution spectrum of Fe_i^0 in silicon.

that they consist of three overlapping EMT-donor series as shown in Fig. 9. It is interesting to note that within each series, the positions of the p-lines are in excellent agreement with those predicted by EMT and their relative intensities are similar to those shown for the selenium donor in Fig. 4. However, in contrast to the selenium spectrum no sharp transitions between 1s valley-orbit split states are detected, although the spectrum obviously includes 2s and 3s lines. Though the split 1s lines are not directly observed, there are good reasons to believe that some of the lines observed as phonon-assisted Fano resonances can be attributed to the split 1s states. Since annealing experiments provide convincing evidence that the three series belong to the same center, one may wonder whether they are caused by a splitting of the ground state or the final states. A splitting of the ground state can be disregarded due to the results presented in Fig. 8, which clearly show that neither the total intensity nor the relative intensity of the lines change within the temperature range of 1.8K to 12K. In a separate paper to be presented at this symposium a detailed analysis of the iron spectra will be given, which will provide convincing evidence that the three EMT series of the interstitial iron originate from a splitting of the final states.

Excitation spectra may not only be affected by a splitting of the final states but may also be influenced by a splitting of the ground state. One such example is the neutral interstitial manganese center in silicon [25].

INTERSTITIAL MANGANESE IN SILICON

Interstitial manganese has been previously studied by EPR, Hall-effect measurements and JSCT [26-28]. These investigations showed that the defect has three different charge states (Mn^+ , Mn^0 and Mn^-) and that the transition Mn^{+0} has a thermal activation energy of about 120 meV (Fig. 10). In contrast to the interstitial iron where the excitation of an electron from the ground state into shallow donor states was studied, hole transitions from the neutral manganese center into shallow acceptor-like states are now discussed in more detail.

Silicon samples diffused with manganese at 1250° and rapidly quenched, showed a series of four sharp lines at 2 K. The lines are superimposed on a background spectrum. The ratio of the original Mn-doped Si spectrum to the background is shown in Fig. 11. With increasing photon energy the energy separation between the four lines at 2K decreases, indicating that the lines probably originate from excited states of a screened Coulomb potential. From the high-energy limit of the line series a ground state energy of about 1050 meV is deduced for the transition $Mn^{0/-}$. This is in fair agreement with the previously measured energy of 120 meV for the transition $Mn^{0/-}$ considering that the band gap energy of silicon is about 1170 meV at low temperatures.

The strength of the EPR signal for the Mn^0 and Mn^- charge states did not change with illumination, and therefore photo-EPR could not be applied to correlate the EPR spectra with the transmission measurements. Instead isochronal annealing experiments were performed for obtaining information on the chemical identity of the center causing the line spectra of Fig. 11. A comparison of the total transmission intensity and the Mn_i^0 integrated EPR signal (Fig. 12), as a function of the annealing temperature shows that both signals anneal out at the same temperature, supporting our assumption that the spectra of Fig. 11 originate from hole transitions of the Mn_i^0 center. It is worth mentioning that all lines shown in Fig. 11 exhibited the same annealing characteristics. This is also true for the Mn_i^0 and Mn_i^- EPR signals which may indicate that no shift of the Fermi level position occurred during the annealing experiments.

For temperatures above 2K, the intensity of the transmission lines (Fig. 11) decreases and new lines are observed at slightly lower energies. The energy distance between the lines in each group is almost identical for all groups and has a mean value of 1.3 meV. Fig. 11 also shows

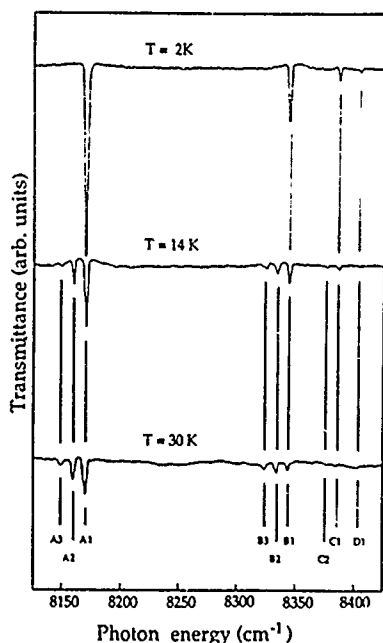


Fig. 11. Transmittance spectra of Si:Mn measured at different temperatures.

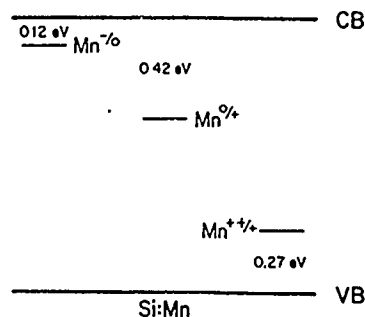


Fig. 10. Energy positions of interstitial manganese in silicon.

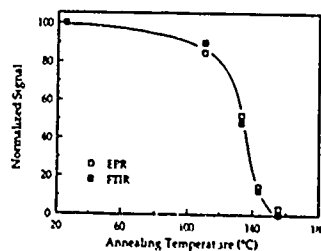


Fig. 12. The sum of the integrated intensities of the A-lines (solid squares) and the EPR signal of the neutral interstitial manganese (open squares) of the same sample as a function of the isochronal annealing (15 min) temperature. Both signals are normalized to their unannealed value.

that the relative intensities of the lines within each group are similar for all groups and that this behaviour does not change with temperature. These observations, together with a more detailed analysis [25] suggest that the spectra originate from a splitting of the initial state in the optical transitions and that the splitting is caused by a local phonon (Fig. 12). The energy of 1.3 meV for the local phonon is in agreement with the isochronal annealing experiment and is much smaller than those previously observed for transition metal related impurities in silicon, which is indicative of a much smaller spring constant. Fig. 13 shows the energy transition level model for all lines which have been experimentally observed according to Fig. 11.

Before discussing the model in more detail it is worth mentioning that the observed line spectrum due to the transitions $Mn_i^{0/-}$ fits reasonably well into the trend previously found for the group III acceptors in silicon if it is assumed that the line with the lowest energy is caused by transitions to the second s state ($2\Gamma_8^+$). The binding energies of the even parity s states for the group III acceptors which have been determined experimentally [29] show a considerable central-cell shift which increases with increasing ground state binding energy (Fig. 14).

One of the reasons for the final hole states being assigned as different even parity excited s states stems from an analysis of the relative intensities of the main lines in each group and previous results obtained for the isolated silver donor in silicon [21]. For s-like final states it is expected that the transition intensity is proportional to the square of the electric dipole matrix element. Since the initial state is strongly localized, the matrix element is essentially given by the amplitude of the wave function of the hole at the center of the impurity potential. For a hydrogen-like center the amplitude of such an s wave function scales as $n^{-3/2}$ where n is the principle quantum number. One would therefore expect that irrespective of the measurement temperature, the following relation should be valid for the intensities of the no-phonon lines A1, B1 and

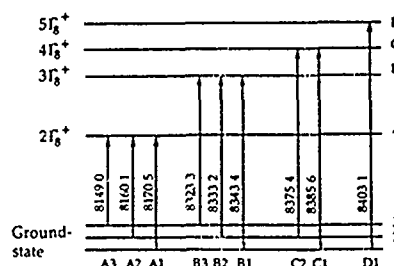


Fig. 13. Scheme of the level structure and the observed transitions with their corresponding energies in cm^{-1} .

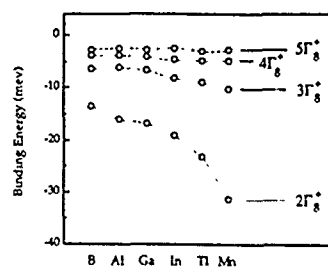


Fig. 14. Experimental s-like even-parity-state energies of Tl, In, Ga, Al and B acceptors in silicon (ref. 29) compared with the neutral interstitial manganese.

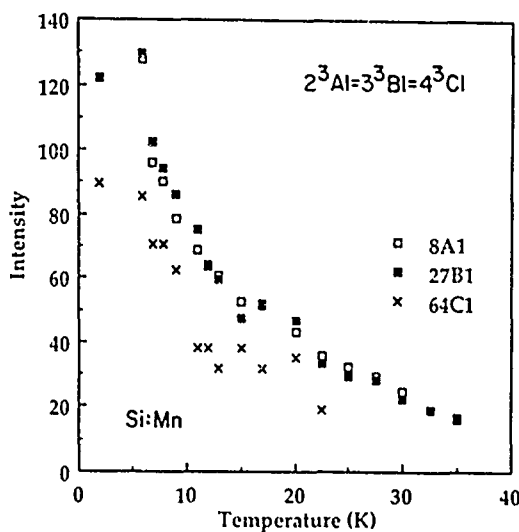


Fig. 15. Intensities of the A1, B1 and C1 lines multiplied by 8, 27 and 64, respectively. All intensities are measured in the same arbitrary units.

C1: $2^3 A_1 = 3^3 B_1 = 4^3 C_1$. Fig. 15 shows that these considerations are in reasonable agreement with experimental findings.

So far only transmission measurements of the Mn_i^0 center have been discussed. Due to the higher sensitivity of the PTIS technique further details of the Mn_i^0 center could be studied using photoconductivity measurements. Apart from these details PTIS studies revealed one particular property of the Mn_i^0 center which we are unable to explain at present. The PTIS signal is expected to be thermally stimulated and should therefore increase exponentially with temperature within a certain temperature range. In the case of the chalcogen donors (and other centers) in silicon this particular feature of PTIS was used to gain further insight into the electronic properties of the centers. Interestingly, no such thermal enhancement of the PTIS signal is observed for the Mn_i^0 center. As demonstrated in

Fig. 16 the intensity of the PTIS signal shows a similar temperature dependence as the corresponding transmission signal, which decreases with increasing temperature over the entire temperature region studied. The observed PTIS signal is positive and is therefore a true contribution to the photoconductivity. A similar temperature dependence of the transmission and PTIS signal clearly shows that the photoconductivity signal of the Mn_i^0 center is not thermally stimulated.

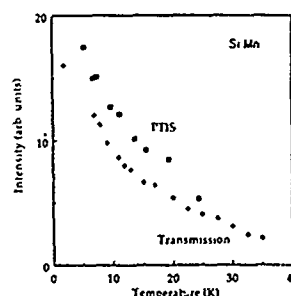


Fig. 16. Intensity of the A1 line in silicon measured in transmission and PTIS as a function of the temperature.

PLATINUM DOPED SILICON

Although the Mn_i^0 center was the first defect not showing a thermally stimulated PTIS signal, it is not the only center which exhibits such a behaviour. Similar observations have also been made for a platinum related center in silicon.

Platinum doped silicon has previously been studied in detail [30]. From these studies it is known that single substitutional platinum has different charge states with an acceptor-like ground state 0.23 eV below the conduction band and a donor-like ground state 0.32 eV above the valence band. PTIS measurements showed not only the $P_{3/2}$ and $P_{1/2}$ line spectrum of the Pt acceptor, but also phonon-assisted Fano resonances of the $P_{3/2}$ states and, in particular, three strong unidentified positive lines which were labeled T lines (Fig. 17). It could be demonstrated that the T lines are not part of the platinum acceptor spectrum. Furthermore, the three T lines are always observed with the same relative intensities suggesting a common origin of these lines.

In addition, recent investigations [31] showed that the center, causing the T-lines has T_d symmetry and is only observed in Pt doped silicon samples. Since the T lines are almost not affected by annealing temperatures up to 1000°C and the impurity responsible for the T lines is a very slow diffuser, it is believed that the T line center is the isolated Pt center and is most probably the single substitutional Pt center.

It has already been pointed out that the T lines are not due to hole transitions of the neutral platinum acceptor. In order to find out whether the final states of the T

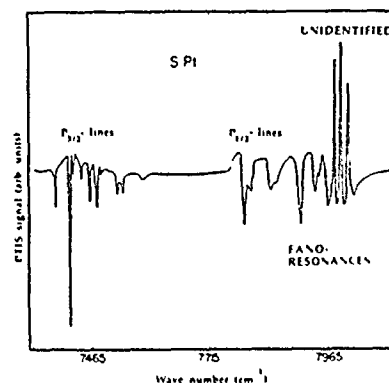


Fig. 17. Spectrum of Si:Pt obtained in PTIS at 10K.

lines are associated with the conduction band minima or valence band maxima, uniaxial stress experiments were performed (Fig. 18). No splittings and only a small center-of-gravity shift were observed for stress parallel to the $[111]$ direction, whereas large splittings and stress-induced linear shift rates at higher stress were observed for the $[001]$ and $[110]$ directions. The close agreement of the shifts with the stress response of the six-fold degenerate conduction band minima suggests that the final states in the transitions of the T lines involve shallow donor states, which can be described by EMT and the deformation-potential approximation.

Further evidence that the initial state of the T lines lies in the lower half of the energy gap and therefore cannot be associated with hole transitions, is obtained from doping experiments. Fig. 19 shows the transmission spectra of three different samples with similar platinum concentrations but different positions of the Fermi level. The peak heights of the T lines increase steadily with a lowering of the Fermi level, and are strongest in heavily doped p-type samples with the platinum acceptor lines nearly absent.

Comparing the excitation energies of the T lines with the energy position of the neutral platinum donor (Fig. 20), it is quite obvious that the T lines are not associated with $Pt^{0/+}$ transitions. A comprehensive study of the T lines, including Zeeman and piezo spectroscopy, shows [31] that the T lines are caused by transitions from the $\Gamma_7(T_2)$ ground state of the single positively charged, platinum donor to donor-like 1s excited states. The lines due to excited p states have not been detected since their excitation energies are too close to the band gap energy. Assuming that the binding energy of

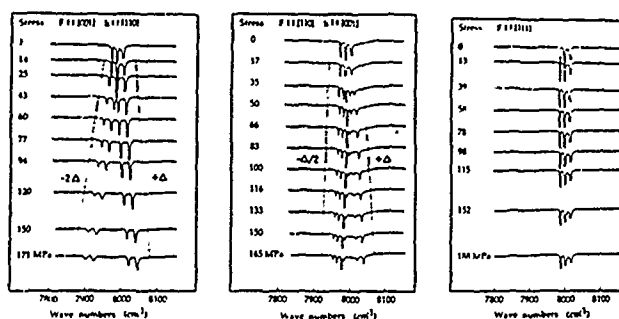


Fig. 18. Transmission spectra showing the response of the T lines to uniaxial stress. The straight lines indicate the stress shifts of the six fold degenerate conduction band minima.

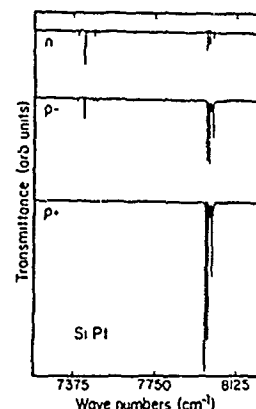


Fig. 19. Transmission spectra of Si:Pt for three different positions of the Fermi level.

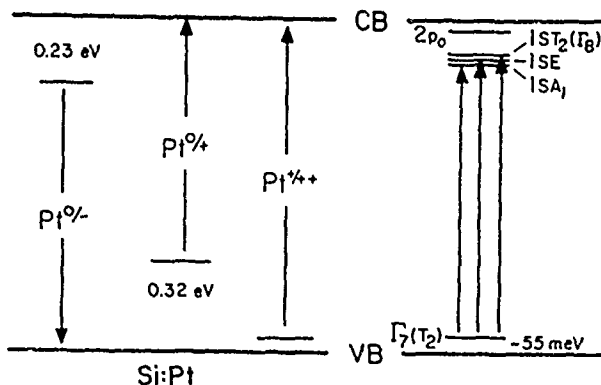


Fig. 20. Energy positions of isolated platinum in silicon [32].

the $1sT_2$ excited state of the charged platinum donor is close to the $1s$ EMT value, i.e. about 120 meV, the $\Gamma_1(T_2)$ ground state is expected to lie about 55 meV above the valence band.

As in the case of the Mn_i^0 center, the PTIS signal of the T lines is not thermally stimulated for temperatures above 6K. This is clearly seen in Fig. 21 where three spectra taken at 6K, 14K and 20K, are presented. Various explanations have been put forth for this behaviour, but none of these can really account for all experimental results available on the T lines. The sample is p type and the PTIS signal of the T lines is positive. One may therefore speculate that the PTIS signal is not only due to a thermalization of excited states, but also, due to the proximity of the ground state to the valence band edge, influenced by a thermalization of the ground state which could be more effective than the thermalization of the excited states. This model would explain the decrease of the PTIS signal of the T lines with increasing temperature, but could hardly account for the absence of the thermal enhancement of the PTIS signal for the Mn_i^0 center since for the Mn_i^0 center the energy difference between the ground state and the band edge is more than twice as much as for the charged platinum donor.

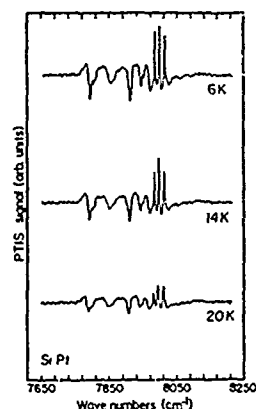


Fig. 21. PTIS spectra of T lines in Si:Pt.

CONCLUSION

The intention of this short review was to briefly outline recent developments in high resolution spectroscopy of defects in silicon, which have provided complementary methods for a more detailed understanding of such defects. One of these methods, namely PTIS, can be used to study not only the optical but also thermal properties of individual energy levels. Highly resolved line spectra have been observed for an increasing number of defects in silicon. The spectra of donors with small binding energies are dominated by transitions to p-like states, but the dielectric dipole selection rules and relative intensities of excitation lines may change with increasing binding energies resulting in spectra with completely different features. This implies that the spectra of some of the very deep centers are dominated by transitions to EMT-forbidden s-like states as in the case of the silver donor, the neutral interstitial manganese center and the substitutional charged platinum donor in silicon. Interestingly, the observed p states of such spectra always have binding energies which are in good agreement with their EMT values, whereas the s-like states are not predicted by EMT and are determined by the localized central cell potential. Lines due to bound-to-bound transitions into s-like states therefore cannot be used as "fingerprints" for the identification of the defect type, i.e. to establish whether the lines are due to bound-to-bound transitions of donor or acceptor levels. For the assignment of such spectra, additional information is needed, which quite often can be obtained by applying perturbation spectroscopy. Due to the limited scope of this paper it is not possible to discuss these possibilities in more detail.

References

- [1] See for example R.H. Bube, Photoconductivity of Solids, John Wiley & Sons, Inc., New York, 1960

- [2] See for example W. Hoogenstraaten, Ph.D. Thesis, University of Amsterdam (1958)
- [3] G. Björklund and H.G. Grimmeiss, *Phys. Status Solidi* **42**, K1 (1970)
- [4] C.T. Sah, L. Forbes, L.L. Rosier and A.F. Tasch, *Solid State Electron.* **13**, 759 (1970)
- [5] D.V. Lang, *J. Appl. Phys.* **45**, 3023 (1974)
- [6] See for example G.W. Ludwig, *Phys. Rev.* **137**, A1520 (1965)
- [7] H.G. Grimmeiss, E. Janzén, H. Ennen, O. Schirmer, J. Schneider, R. Wörner, C. Holm, E. Sirtl and P. Wagner, *Phys. Rev.* **B24**, 4571 (1981)
- [8] H.G. Grimmeiss, M. Kleverman and J. Olajos, *Mater. Sci. Forum* **38-41**, 341 (1989)
- [9] T.M. Lifshits, N.P. Likhtman and V.I. Sidorov, *Fiz. Tekh. Poluprov.* **2**, 782 (1968)
- [10] J.M. Kahn, PhD Thesis, University of California at Berkeley (1986)
- [11] H.J. Queisser, *Festkörperprobleme* **XI**, 45 (1971)
- [12] M. Kleverman, J.O. Fornell, J. Olajos, H.G. Grimmeiss and J.L. Lindström, *Phys. Rev.* **B37**, 10199 (1988)
- [13] G.D. Watkins and J.W. Corbett, *Phys. Rev.* **121**, 1001 (1961)
- [14] J.W. Corbett, G.D. Watkins, R.M. Chrenko and R.S. McDonald, *Phys. Rev.* **121**, 1015 (1961)
- [15] J. Wagner, K. Thonke and R. Sauer, *Phys. Rev.* **B29**, 7051 (1984)
- [16] C.P. Foy, *J. Phys. C* **15**, 2059 (1982)
- [17] K. Thonke, A. Hangleiter, J. Wagner and R. Sauer, *J. Phys. C* **18**, L 795 (1985)
- [18] E. Janzén, R. Stedman, G. Grossmann and H.G. Grimmeiss, *Phys. Rev.* **28**, 1907 (1984)
- [19] J.O. Fornell and H.G. Grimmeiss, to be published
- [20] O. Engström and A. Alm, *Solid-State Electron.* **21**, 1571 (1978)
- [21] J. Olajos, M. Kleverman, B. Bech Nielsen and H.G. Grimmeiss, *Inst. Phys. Conf. Ser.* No 95, p. 101 (1989)
- [22] N. Baber, H.G. Grimmeiss, M. Kleverman, P. Omling and N. Zafar, *J. Appl. Phys.* **62**, 2855 (1987)
- [23] K. Bergman, G. Grossmann, H.G. Grimmeiss and M. Stavola, *Phys. Rev. Lett.* **56**, 2827 (1986)
- [24] J. Olajos, B. Bech Nielsen, M. Kleverman, P. Omling, P. Emanuelsson and H.G. Grimmeiss, *Appl. Phys. Lett.* **53**, 2507 (1988)
- [25] T. Bever, P. Emanuelsson, M. Kleverman and H.G. Grimmeiss, *J. Appl. Phys.* (?)
- [26] G.W. Ludwig and H.H. Woodbury, *Solid State Phys.* **13**, 223 (1962)
- [27] R. Czaputa, H. Feichtinger and J. Oswald, *Solid State Commun.* **47**, 223 (1983)
- [28] L.C. Kimerling, J.L. Benton and J.J. Rubin in: *Defects and Radiation Effects in Semiconductors 1980*, *Inst. of Physics Conf. Ser.* **59**, 217 (1981)
- [29] J. Wagner and R. Sauer, *Phys. Rev.* **B26**, 6, 3502
- [30] M. Kleverman, J. Olajos and H.G. Grimmeiss, *Phys. Rev.* **B37**, 2613 (1988) and references therein.
- [31] J. Olajos, M. Kleverman and H.G. Grimmeiss, *Phys. Rev.* **B40**, 6196 (1989)
- [32] M. Pugnet, J. Barbolla, J.C. Brabant, F. Saint-Yves and M. Brousseau, *Physica Status Solidi A* **35**, 533 (1976)

INFRARED ABSORPTION STUDY OF ZINC-DOPED SILICON.

E. MERK, J. HEYMAN and E. E. HALLER

Center for Advanced Materials, Materials and Chemical Sciences Division, Lawrence Berkeley Laboratory, and University of California
Berkeley, CA 94720.

ABSTRACT

We report high resolution infrared absorption spectra associated with the deep zinc acceptor in silicon. The optical transitions between ground and bound excited "p-like" states of the neutral helium-like double acceptor Zn^0 center have been observed for the first time. The absorption cross section for the hole transition is found to be very small, of the order of 10^{-17} cm^2 . Energy spacings of the $P_{3/2}$ Rydberg series are very similar to the spacings of the group-III acceptors, suggesting that, in spite of the large ground state binding energy, effective mass approximation still applies to the bound excited states. This represents one more case where the strong central cell potential does not significantly disturb the neutral helium-like bound excited states. Similar observations have been made for the less deep neutral double acceptor Be, and for the chalcogens donors S, Se and Te.

The optical ionization energy of Zn^{0+} has been determined to be 2575 cm^{-1} (319 meV).

Two additional sets of absorption lines related to zinc have been observed at 2130 cm^{-1} and 2758 cm^{-1} . Their origin will be discussed.

INTRODUCTION

The knowledge of the electronic structure of group-II impurities in silicon lags behind our understanding of these impurities in germanium [1-4]. This is in part related to the fact that in silicon the group-II impurities give rise to much deeper, more localized electronic states in the bandgap compared to the case of germanium. In addition the concentration of electrically active group-II acceptors lies around 10^{16} cm^{-3} , a factor of 100 smaller than in Ge. In combination these properties make the observation of line spectra originating from ground to bound excited state transitions much more difficult in Si than in Ge. Indeed most of the levels related to group-II impurities in silicon have been determined from resistivity and Hall effect measurements or junction space charge techniques, e.g. Deep Level Transient Spectroscopy (DLTS). The activation energies of the two charge states of the double acceptor zinc were determined as early as in the late fifties [5,6] to be $E_v + 0.31 \text{ eV}$ for the first ionization stage and $E_c - 0.55 \text{ eV}$ for the second one. Since that time and despite numerous attempts, no structured absorption features due to bound hole transitions were reported [7].

In this work we report the first observation of bound to bound transitions in the neutral double acceptor Zn in silicon which allows an accurate determination of its optical activation energy. Further motivation for this work is related to an interest in the study of the mechanism of hydrogen passivation of a double acceptor which are expected to become partially or fully passivated. Preliminary results of hydrogen passivation of zinc in silicon are presented: a new complex related to zinc and hydrogen is observed as well as a strong isotope effect at this center upon substitution of hydrogen with deuterium.

EXPERIMENTAL PROCEDURE

The silicon wafers used in the present investigation of the neutral acceptor zinc were float-zone material ranging from high purity (N-type $\sim 5000 \Omega \text{ cm}$) to moderately phosphorus doped

($\sim 60 \Omega\text{cm}$). Some boron doped specimens have been used for DLTS measurements. Samples with dimensions $1 \times 1 \times 0.3 \text{ cm}^3$ suitable for IR absorption analysis were cut from these wafers. The sample preparation has been reported in details elsewhere [8]. Zinc was diffused for a few hours at temperatures close to 1200°C . The diffusion processes have been performed under various ambients: helium, hydrogen or deuterium. Once the diffusion was completed, the ampoule containing the sample was either quenched in mineral oil or furnace cooled in order to investigate the possible clustering of zinc atoms. Quenching led to cooling rates of approximately 200°C/s while furnace cooling gave rates of 2°C/min .

SIMS measurements performed on several diffused samples yield a concentration of Zn in the 10^{15} cm^{-3} range. DLTS and Hall effect measurements have given the same concentrations suggesting that most of the zinc incorporated was electrically active.

We used a rapid-scan Fourier transform spectrometer (Digilab FTS-20E) in the mid-infrared range for the absorption spectral analysis. The sample was mounted on the cold finger of a Janis cryostat with variable temperature control. A cooled indium doped silicon photodetector was found most suitable for the detection of the Zn^0 excitation spectrum.

In every stage of this study, reference specimens submitted to the exact same sample preparation and heat treatments were used for comparison.

EXPERIMENTAL RESULTS AND DISCUSSION

In Fig.1 we show a typical low temperature mid-infrared absorption spectrum taken from a sample of float-zoned silicon diffused with zinc at 1200°C in a helium atmosphere. At high energy it is dominated by the strong absorption transitions from the neutral zinc ground state to valence band continuum. On the low energy side of the continuum threshold, around 2500 cm^{-1} , a set of lines is observed. The ratio in absorption intensities of these lines compared to the continuum emphasizes the small fraction of oscillator strength which goes into the transitions to the bound excited states compared to the transitions from the $1s$ ground state to the continuum. This is a consequence of the large spreading in k -space of the ground state wavefunction due to the depth of the level. It enables a more efficient coupling with the extended states of the valence band continuum than with the less extended shallow excited states. By using the values of the zinc concentration determined by SIMS and Hall effect, we deduce an optical cross-section for the ground to bound excited states hole transitions of the order of 10^{-17} cm^2 .

Fig.2 displays on a more expanded scale the sequence of lines which is identified with the Lyman series of the neutral helium-like double acceptor zinc. The excitation lines represent one-hole excitations from the $(1s)^2$ ground state to the $(1s)(np)$ excited states of the neutral double acceptor. We have numbered these excitation lines according to the scheme proposed by Baldereschi and Lipari [9]. The energy spacings and relative intensities are very similar to those obtained for the group-III shallow acceptors in silicon. We note that such a similarity had been reported for an other neutral helium-like double acceptor, beryllium [10]. This is illustrated in Table I where we present the ionization energies and the energy spacings observed for the two well known single acceptors boron and indium as well for the double acceptor beryllium (set I) together with our results for zinc.

By adding the binding energy of the final state leading to line 2, 11.7 meV [12], to the transition energy of this line, we estimate the optical ionization energy of zinc $E(\text{Zn}^{0/})$ to be 319 meV .

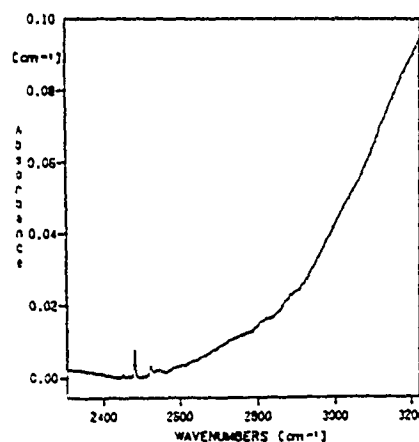


Fig.1: Absorption spectrum of Zn doped Si at $T = 4.5\text{K}$. Resolution is 0.5 cm^{-1} .

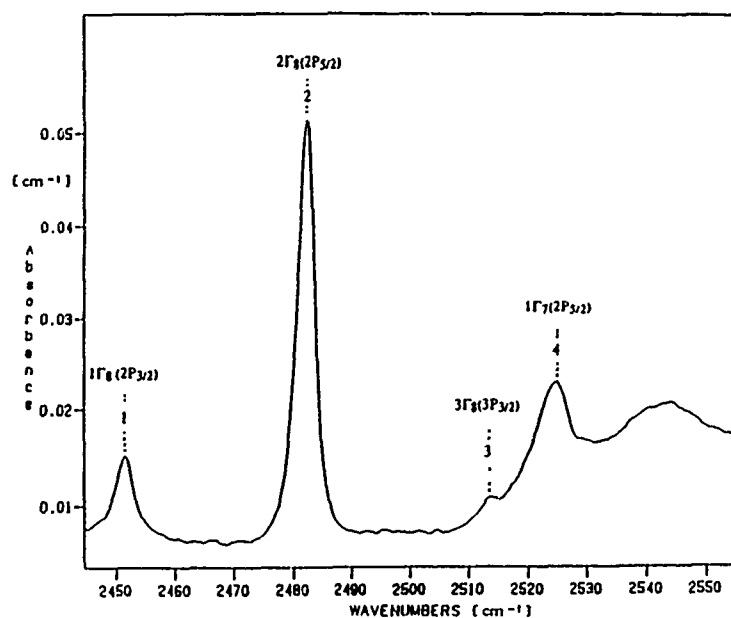


Fig.2: Excitation spectrum of neutral helium like double acceptor Zn in Si at $T = 4.5\text{K}$. Resolution is 0.5 cm^{-1} .

The effective mass-like character of the bound excited states of this deep double acceptor indicates a very effective screening of the central cell potential by the second hole remaining in the $1s$ -like state near the impurity center. It is worthwhile to note that recently several deep impurities such as the acceptors gold and platinum and several chalcogens related double donors were shown to have effective mass-like excited states [13]. This behavior is understandable since the wave functions of the p -like excited states have zero amplitude at the site of the impurity, whereas the wave functions of the s states have a finite amplitude. Therefore the former are expected to be rather unaffected by the central cell potential, in contrast to the s states.

The excitation spectra of neutral Zn at two different temperatures are shown in Fig.3. In the extra-structure which grows dramatically with increasing temperature on the low energy side of each of the four lines we were able to discern unambiguously four components in the case of the line 2 related structure. In Table II, we present the results of the thermal activation analysis of these components. We observe both a split ground state and additional excited states splitting.

Table I: Ionization energies and energy spacings between the excitation lines of various acceptors and Zn^0 in silicon (the values relative to B and In have been taken from [11])

lines	B	In	Be^0	Zn^0
energy locations of lines (meV)				
1	30.38	141.99	176.4	304.01
2	34.49	145.79	180.3	307.83
3	38.35	149.74	184.3	311.72
4	39.57	150.80	185.6	313.10
energy spacings between lines (meV)				
Δ_{12}	4.11	3.80	3.70	3.82
Δ_{23}	4.36	3.95	4.00	3.89
Δ_{24}	5.08	5.01	5.30	5.27

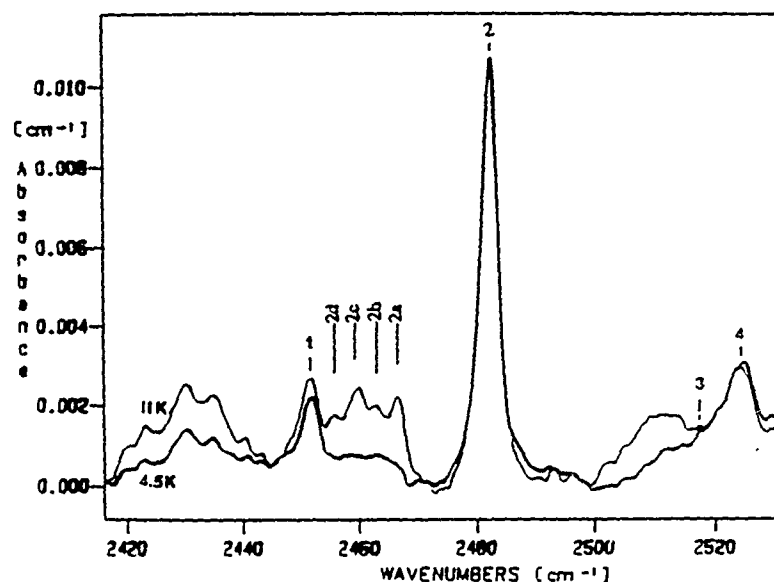


Fig.3: High resolution excitation spectra of Zn^0 in Si at two different temperatures: lower curve for $T = 4.5\text{K}$, upper curve for $T = 11\text{K}$.

Table II: Positions E_i , energy spacings $\Delta E_{\text{optical}}$ from line 2, and Boltzman factors $\Delta E_{\text{thermal}}$ for the 4 identified components on the low energy side of line 2 (307.83 meV):

lines	E_i (meV)	$\Delta E_{\text{optical}}$ (meV)	$\Delta E_{\text{thermal}}$ (meV)
2a	305.98	1.85	2.0 ($\pm 20\%$)
2b	305.35	2.48	2.1 ($\pm 20\%$)
2c	304.98	2.85	3.0 ($\pm 20\%$)
2d	304.67	3.16	2.1 ($\pm 20\%$)

From these results we conclude that the ground state of Zn^0 is split into at least 3 components. Under time reversal symmetry, the ground state of a single acceptor can split into two components. Our results prove that the 319meV level is not due to a single acceptor. It is interesting to note that a large splitting (2.4 meV) of the ground state of the zinc double acceptor in germanium was reported some years ago by Thewalt et al. [14]. Additional infrared spectroscopy studies using stress and polarized light are needed to investigate further the splitting.

Depending on the cooling rate of the specimens after the high temperature diffusion of Zn, a set of smaller absorption lines on the high energy side of the Zn^0 excitation spectrum was observed. The energy spacings between these lines are again in agreement with effective-mass like excited states of an acceptor. This quenching dependent behavior is illustrated in Fig.4 where it is seen that an as-diffused Si:Zn sample, furnace cooled (curve A) exhibits a definite structure with the strongest line located at 2758 cm^{-1} , whereas in the quenched sample (curve B) none of the lines are clearly discernable. Subsequent annealing at high temperature of a furnace cooled sample followed by rapid quenching in mineral oil causes the complete disappearance of these features. Further high temperature annealing not followed by rapid quenching has been found to restore them. This reversible behavior which depends strongly on the cooling rate suggests that some complex formation is involved in the center responsible for this set of absorption lines.

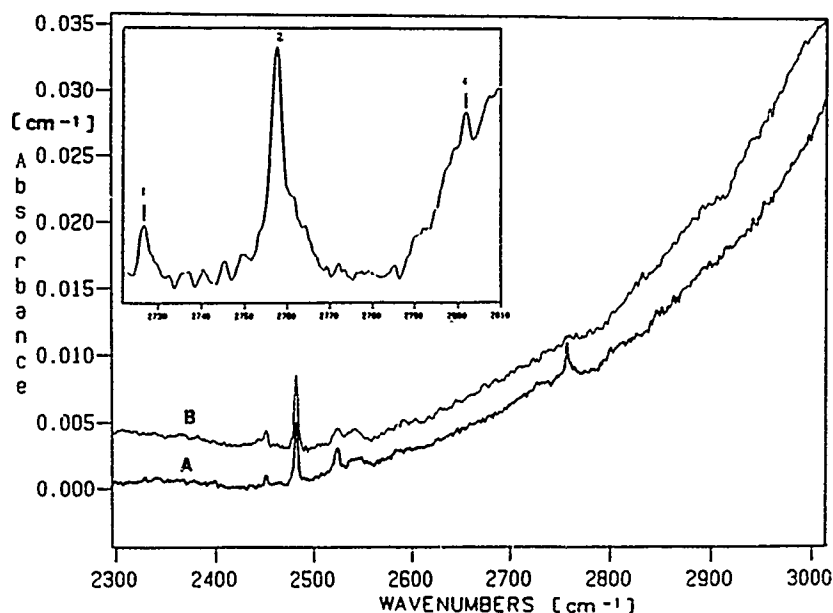
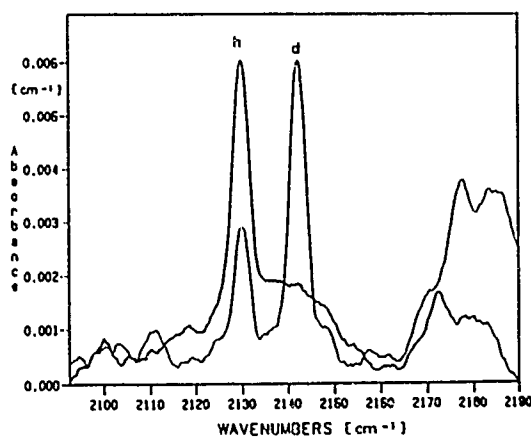


Fig.4: High resolution low temperature absorption spectra of Zn diffused Si samples: (A) furnace cooled, (B) quenched from high temperature. Insert shows the 2758 cm^{-1} sequence of lines on an expanded scale.

Further studies are required to identify the exact structure of this zinc related complex. It is worthwhile to note that no discernable influence of the cooling rate on the Zn^0 excitation spectrum has been detected.

In order to investigate the hydrogen passivation of the zinc centers, the high temperature diffusion process was repeated in an hydrogen ambient, followed by rapid quenching. In Fig.5 we show the spectrum of such a zinc diffused silicon sample. It displays a new sequence of lines on the low energy side of the Zn^0 excitation spectrum, with its strongest line located at 2130cm^{-1} .

Fig.5: Effect of deuterium substitution to hydrogen on the 2130 cm^{-1} set of absorption lines: Zn has been diffused in Si samples: (h) in H_2 ambient, (d) in D_2 ambient.



The spacings between the observed lines again are very similar to the spacings of bound excited states of single acceptors (see Table 1). These lines were not found in samples which were not quenched, as well as in samples quenched but re-annealed at high temperature after diffusion.

When deuterium was used instead of hydrogen for the ambient of the diffusion process a second sequence of lines shifted by 12 cm^{-1} appeared towards the high energy side. This isotope shift is even larger than the significant shift of 7.8 cm^{-1} reported for (Be,H) and (Be,D) [15]. The large shift suggests strong interaction between the electronic ground state of the hole and the proton for this deep level center which we tentatively identify with the (Zn,H) complex. Current work is in progress to ascertain this identification.

CONCLUSIONS

The excitation spectrum of the neutral helium-like double acceptor Zn has been measured and interpreted. The effective mass-like character of the bound excited states associated with this deep state has been established. The optical ionization energy of $\text{Zn}^{0/-}$ has been determined to be 319 meV with an optical cross-section for the hole transition of the order of 10^{-17} cm^2 . The temperature dependent study of this excitation spectrum has revealed a large splitting of both the ground state and the excited states.

There is strong evidence that the " 2758 cm^{-1} " set of lines is related to the formation of a complex involving zinc, and that the " 2130 cm^{-1} " features are related to electronic transitions from a center involving zinc and hydrogen.

ACKNOWLEDGMENTS

It is a pleasure to acknowledge L.M. Falicov and A. Gieseckus for very stimulating discussions, and W.L. Hansen and J. Beeman for their expert advice on numerous experimental aspects. This work was supported in part by the US National Science Foundation Grant DMR-8806766, and by the US DOE under contract DE-AC03-76SF00098. E. Merk is grateful to the Swiss National Foundation for research assistantship.

REFERENCES

1. E. E. Haller, W.L. Hansen and F. S. Goulding, *Adv. in Physics* **30**, 93 (1981).
2. M.L.W. Thewalt, D. Labrie, I. J. Booth, B. P. Clayman, E. C. Lightowers and E. E. Haller, *Physica* **146B**, 47 (1987).
3. W. J. Moore, *J. Phys. Chem. Solids* **32**, 93 (1971).
4. T. A. Callot and J. W. MacKay, *Phys. Rev.* **161**, 698 (1967).
5. C. S. Fuller and F. J. Morin, *Phys. Rev.* **105**, 379 (1957).
6. R. O. Carlson, *Phys. Rev.* **108**, 1390 (1957).
7. B. V. Kornilov, *Soviet Physics-Solid State* **5**, 2420 (1964).
8. E. Merk, J. Heyman and E.E. Haller, *Sol. State Commun.* **72**, 851 (1989).
9. A. Baldereschi and N. Lipari, *Phys. Rev.* **B9**, 1525 (1974).
10. R.K. Crouch, J. B. Robertson and T. E. Cilimier, *Phys. Rev.* **B5**, 3111 (1972); see also J. Heyman, L. M. Falicov and E.E. Haller, *Bull Am Phys. Soc. SeriesII* **34N3**, 834 (1989).
11. Landolt & Bornstein, *III/17a*, p.55, ed. by O. Madelung, M. Schulz and H. Weiss.
12. N. Binggeli and A. Baldereschi, *Sol. State Commun.* **66**, 323 (1988).
13. M. Kleverman, J. Olajos and G. Grossmann, H. G. Grimmeiss, *Mat. Res.Soc. Symp. Proc.* **104**, 141 (1988); H. G. Grimmeiss, *Helv. Phys. Acta*, **56**, 317 (1983).
14. M.L.W. Thewalt, B.P. Clayman and D. Labrie, *Phys. Rev.* **B32**, 2663 (1985).
15. K. Muro and A. J. Sievers, *Phys. Rev. Lett.* **57**, 897 (1986).

INFRARED STUDIES OF THE DOUBLE ACCEPTOR ZINC IN SILICON

A. Dörnen^{*}, R. Kienle^{*}, K. Thonke^{*}, P. Stolz^{**}, G. Pensl^{**}, D. Grünebaum^{***}
and N.A. Stolwijk

^{*}4. Physikalisches Institut, Universität Stuttgart, D-7000 Stuttgart 80, FRG

^{**}Institut für angewandte Physik, Universität Erlangen, D-8520 Erlangen, FRG

^{***}Institut für Metallforschung, Universität Münster, D-4400 Münster, FRG

ABSTRACT

In the present paper, optical absorption studies on the neutral charge state of the double acceptor zinc in silicon are presented. Measurements were carried out in the mid infrared (MIR) and in the near infrared (NIR) region. The MIR absorption spectra show the excitation series of an effective-mass-like hole, from which the Zn^0 level position is calculated to be at $E_v + 319.1$ meV. A splitting of the ground state into 3 sublevels is assigned to hole-hole coupling and crystal-field splitting. Absorption spectra obtained in the NIR are interpreted in terms of an A^0X -type bound exciton.

INTRODUCTION

Double acceptors in germanium are widely investigated by means of optical spectroscopy [1]; but detailed information on double acceptors in silicon is still rare. Beryllium e.g. introduces several centers when it is diffused into silicon [2,3]. One of these centers (BeI), is believed to be the substitutional Be double acceptor [2,3] though a second charge state has not yet been reported [4]. The only double acceptor in silicon identified so far is zinc. Two levels at $E_v + 0.31$ eV and $E_c - 0.55$ eV are identified with the $0/-$ and $-/--$ charge state transitions, respectively [5,6]. In recent work the thermal-emission rates and capture rates of carriers were characterized by transient-capacitance technique [7,8]. Optical investigations were dealing with photoionization only, so that still some uncertainty remained about the exact level positions [9,10].

By observation of effective-mass-(EM)-like excited states of the Zn^0 center, we are able to calculate precisely the ground state to be 319.1 ± 0.3 meV above the valence band. In a second part, spectra, obtained in the NIR spectral region, are discussed with regard to excitons bound to Zn^0 .

EXPERIMENTAL

Samples from boron doped float zone material (10^{13} cm^{-3}) and phosphorus doped Czochralski crystals ($2 \cdot 10^{15} \text{ cm}^{-3}$ and $4 \cdot 10^{15} \text{ cm}^{-3}$) were prepared for the zinc diffusion. Samples were sealed in evacuated quartz ampoules together with zinc ingots and heated to 1200°C for 40 hours. The diffusion was finished by quenching the ampoule in water. An additional heat treatment at 600°C was applied, to move most of the incorporated zinc atoms into the double acceptor configuration. Optical surfaces were achieved by polishing.

A Fourier spectrometer (Bomem DA3 series) was used to record the absorption spectra. The setup was equipped alternatively with a cooled InSb detector for the MIR and with a germanium diode for the NIR.

The zinc concentration was determined by Hall measurements to be $(9 \pm 3) \cdot 10^{16} \text{ cm}^{-3}$. Spreading resistance profiles were taken on similarly treated samples to control the zinc distribution. Over the whole sample the homogeneity was found to be better than 10% of the total zinc concentration. All samples resulted in p-type conductivity after zinc diffusion.

MID INFRARED ABSORPTION SPECTRA

For temperatures above 40 K all samples investigated show a strong absorption band beginning at around 2500 cm^{-1} extending up to the band-band absorption. A similar spectrum is also observed in photocurrent measurements. Previous absorption [9] and photocurrent studies [10] on zinc diffused silicon have shown that photoionization of neutral zinc ($\text{Zn}^0 \rightarrow \text{Zn}^+ + h$) is the underlying process. Since in all our samples the zinc concentration is much higher than the shallow background doping, phosphorus is compensated in the originally n-type samples. Hence, we observe the photoionization of Zn^0 in boron doped and phosphorus doped samples as well. The maximum optical cross section is calculated to $\sigma_{\text{max}} = (0.5 \pm 0.2) \cdot 10^{-16} \text{ cm}^2$. This value is in fairly good accordance with the previously reported values $\sigma_{\text{max}} = (1 \dots 2) \cdot 10^{-16} \text{ cm}^2$ [9] and $\sigma_{\text{max}} = 1 \cdot 10^{-16} \text{ cm}^2$ [10].

At temperatures lower than 40 K sharp line spectra appear, located close to the photoionization onset. These lines, labelled I_1^a through I_4^a , are displayed in Fig. 1a together with the photoionization onset mentioned above. The line spectrum appears in all investigated samples with the same absorption ratio to σ_{max} of photoionization. Hence, we assign these lines to bound-to-bound transitions at Zn^0 . It is the typical "fingerprint" of transitions between a Γ_8 ground state into a series of odd-parity EM-like excited states. Similar spectra are known, e.g., for the (shallow) acceptor indium [11] and deep acceptor centers related to gold [12], platinum [12] and several beryllium related centers [2,3]. For each of these defects the characteristic absorption spectrum indicates shallow EM-like excited states originating from the $P_{3/2}$ valence band. These states are satisfactorily described by the effective-mass theory (EMT) developed by Baldereschi and Lipari [13]. Adding the theoretical binding energy of a specific excited state to the corresponding transition energy - observed from the absorption spectrum - results in the ionization energy of the Zn^0 center. We find the Zn^0 level position at $319.1 \pm .3 \text{ meV}$ above the valence band and obtain an excellent agreement between the binding energies of the excited states and the EMT values, see table 1. Level positions obtained from electrical measurements [5-8] with a larger uncertainty are in accordance with the optical data presented here. The EM series limit as indicated in Fig. 1 is shifted by about 6 meV to lower energies compared to the photoionization

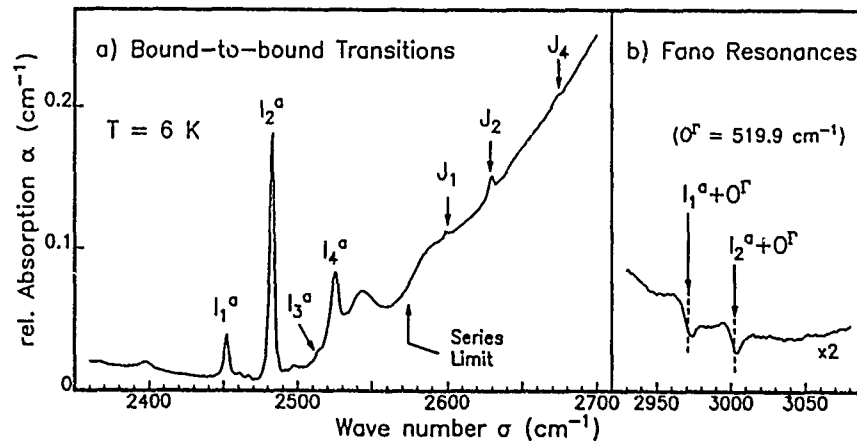


FIG. 1. a) Zn^0 absorption lines (I series), due to the excitation into EM-like states; EMT series limit, as indicated. J lines see text and Ref. 16, b) Fano resonances of lines I_1^a and I_2^a .

TABLE 1: Spectroscopic values ($\bar{\nu}$) of the Zn° center and the $\text{Zn}(\text{X2})$ center [16], binding energies (E_b) of the EM-states, and ground state position relative to the valence band.

Zn°			$\text{Zn}(\text{X2})$			EMT [13]	
$\bar{\nu}$ (cm^{-1})	E_b (meV)		$\bar{\nu}$ (cm^{-1})	E_b (meV)		E_b (meV)	
I ₁	2451.1	15.2	J ₁	2598.6	15.3	15.5	$1\Gamma_8$
I ₂	2482.5	11.3	J ₂	2629.0	11.5	11.4	$2\Gamma_8$
I ₃	2513.9	7.4				7.3	$3\Gamma_8$
I ₄	2524.7	6.1	J ₄	2673.6	6.0	6.0	$1\Gamma_7+1\Gamma_6$
$E_{\text{ion}} = 319.1 \text{ meV}$			$E_{\text{ion}} = 337.5 \text{ meV}$				

onset. This shift might be caused by a relaxation of the center following to the ionization as discussed e.g. in Ref. 14. The EM-like character of the excited states is confirmed by Fano resonances, observed for the lines I₁^a and I₂^a, see Fig. 1b. These resonances are caused by interference between EMT levels and free conduction band states via an O¹ phonon (519.9 cm^{-1}). This coupling is characteristic of shallow group-III acceptors in silicon [15]. For the BeI center, Fano resonances as displayed in Fig. 1b are found, too [3].

Another EMT spectrum comprising the lines labelled J₁, J₂ and J₄ is assigned to a different zinc-related center (named $\text{Zn}(\text{X2})$ [16]), with an ionization energy of 337.5 meV, see table 1.

The ground state of neutral zinc is split into three substates as temperature dependent measurements show. With raising the temperature from 6 K to 10 K and 18 K two sets of lines (I^b and I^c) show up, see Fig. 2. The

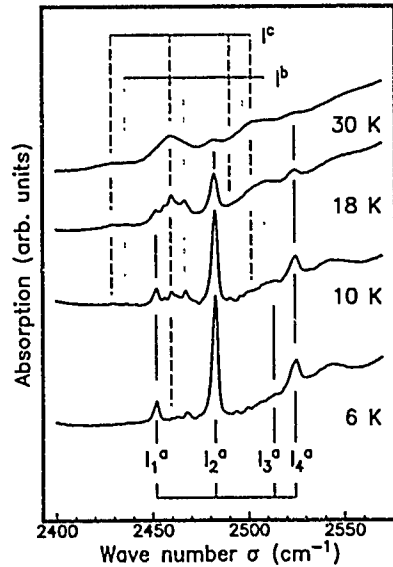


FIG. 2. Thermally activated absorption of the Zn° center. All lines with corresponding transitions starting from the same ground state are lumped together. See level scheme in Fig. 3

lines in each set are found to have the same spectroscopic spacings as the lines in the low temperature spectrum I^a. The absorption of the lines I₂^a, I₂^b, and I₂^c as a function of the temperature was measured quantitatively. Since I₂^b and I₂^c are not resolvable over a sufficient temperature range the sum (I₂^b+I₂^c) was evaluated. In Fig. 3 the ratio (I₂^b+I₂^c)/I₂^a is plotted versus 1/T. As can be seen, the ratio is governed by a Boltzmann factor with

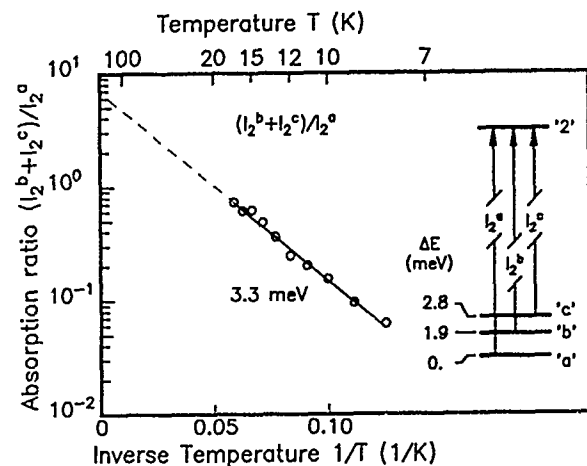


FIG. 3. Thermalisation of the lines I_2^a , I_2^b and I_2^c ; see text. Scheme of the ground-state levels in terms of hole energy.

an activation energy of 3.3 meV. This clearly shows, that the absorption strength reflects the thermal population of the ground-state levels. From the shifts of the three sets I^a , I^b , and I^c , a level scheme of the ground state levels as depicted in Fig. 3 can be drawn. A small deviation of the thermal-activation energy from the expected value 1.9 - 2.8 meV is not understood presently.

The ground-state splitting observed for several double acceptors in germanium is attributed to the exchange interaction of the two holes; see Ref. 17 for discussion and further references. In the present case hole-hole interaction seems to be important, too, since a threefold split ground state cannot originate from a single hole state (Γ_8). Because of Kramers degeneracy, a Γ_8 state can split into 2 levels only; e.g. when the atom relaxes from the substitutional site to a position of lower symmetry. In terms of a j-j coupling scheme the two hole states $j = 3/2$ (Γ_8) of the double acceptor couple to $J = 0$ (Γ_1) and $J = 2$ ($\Gamma_3 + \Gamma_5$), when the Pauli principle is taken into account. A crystal field with T_d symmetry may split the $J = 2$ state into Γ_3 and Γ_5 states which are 2-fold and 3-fold degenerate, respectively. A splitting into $J=0$ and $J=2$, observed for the systems Ge:Hg (0.7 meV) [18], Ge:Zn (2.4 meV) [19] and Ge:Mg (1.8 meV) [17] was explained by the mutual influence of exchange interaction and crystal field splitting.

The 3 sublevels of the Zn^0 ground state found here agree with the model outlined above. From the high-temperature limit of $(I_2^b + I_2^c)/I_2^a = 6.9 \pm 1.5$ (Fig. 3) follows clearly that Γ_1 is the lowest ground state sublevel of Si:Zn 0 . The same case was assumed for Ge:Zn, too [19]

NEAR INFRARED ABSORPTION SPECTRA

Further absorption features appear close to the region of band-band absorption. As depicted in Fig. 4 (lower spectrum), a group of 3 lines (α , β and γ) with some additional fine structure can be resolved around 8850 cm^{-1} . The lines are observable in all investigated samples after zinc diffusion. Their integral absorption correlates with the intensity of the I^a lines, reported in the previous section. Comparing these lines with spectra of acceptor bound excitons (A^0X) motivates the assignment of α , β , and γ to the no-phonon-assisted generation of an exciton bound to neutral zinc (Zn^0X).

The group III acceptors Al, Ga, and In exhibit a bound-exciton-(BE)-absorption spectrum similar to the lines under discussion. Three A^0X lines are observed as well, reflecting a 3-fold split excitonic state. Still unclear is the origin of the excitonic state structure. Two different models are

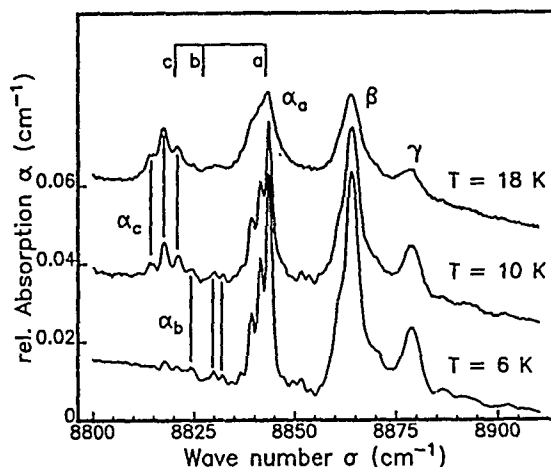


FIG. 4. Lines α_a , β , and γ assigned to Zn^0X transitions, see text. Thermalization of α_a , α_b , and α_c resembles behavior of lines I^a , I^b , and I^c . Bracket represents ground-state splitting as evaluated from Fig. 2.

considered [20,21]. Both models suppose the interaction of the 2 holes in the excitonic state but lay additional emphasize on crystal field effects [20] and electron hole coupling [21]. Since for the Zn^0X an additional hole can couple to the exciton, this case becomes even more complicated. Thus we restrict ourselves to comparison of our findings with experimental results available for group-III acceptors.

Taking the high energy component of α_a , the localization of the BE is calculated to 58.7 meV. Thallium as the deepest group-III acceptor binds the exciton with 43.8 meV [21]. Compared to the ionization energies (Zn^0 : 319.1 meV; Tl: 255 meV [22]) the value of 58.7 meV is reasonable as exciton-binding energy.

BE transition are known to couple to TO phonons. The ratio of absorption strength between the TO replica and the no-phonon lines (NP) $\alpha(\text{TO})/\alpha(\text{NP})$ decreases with an increasing localization of the exciton. For the group -III acceptors this ratio varies from 127 for boron down to 1/10 for thallium [21]. Replica of α_a and β due to TO phonons are found (not shown here) with $\alpha(\text{TO})/\alpha(\text{NP}) \approx 1/40$, being in accordance with the values mentioned above. Possible TA replicas, also found for A^0X , are not observable because of a too low signal to noise ratio.

A link between the NIR and MIR spectra is the Zn^0 ground-state splitting, which should be seen in both types of spectra. Like in the hole excitation spectra, thermally activated lines grow in with raising temperature. Two sets of lines α_c and α_b each with a three-fold fine structure like line α_a can be identified. There is no significant thermalization observable within the fine structure of α_a , α_b , and α_c . The thermalization of the 3 groups α_a , α_b , and α_c resembles the behavior of the lines I_2^a , I_2^b , and I_2^c , as shown in Fig. 2. Hence, the ground state of these transitions also must consist of 3 sublevels. The bracket in Fig. 4 represents the splitting of the Zn^0 ground state as evaluated from Fig. 2. Neglecting the fine structure, hole excitation spectra and bound exciton spectra give an accordant view of the Zn^0 ground state.

SUMMARY

Optical absorption spectroscopy on neutral zinc in silicon shows the excitation of a hole into odd-parity EM states. This fact allows to calculate the ground state to $E_v + 319.1 \pm .3$ meV. Absorption spectra measured in the NIR are most probably due to excitonic transitions. Both types of spectra show that the Zn^0 ground state consists of three sublevels that arise from

hole-hole interaction and crystal-field splitting. Future work will focus on both absorption experiments carried out under uniaxial stress and on photoluminescence to confirm this model.

ACKNOWLEDGEMENTS

For many helpful discussions we are grateful to R. Sauer.

REFERENCES

1. for an overview and further references see: A.K. Ramdas and S. Rodriguez, Rep. Prog. Phys. 44, 1297 (1981).
2. R.K. Crouch, J.B. Robertson, and T.E. Gilmer Jr., Phys. Rev B 5, 3111 (1972).
3. M. Kleverman, and H.G. Grimmeiss, Semicond. Sci. Technol. 1, 45 (1986).
4. H. Tomokage, H. Nakashima, and K. Hashimoto, Jap. J. Appl. Phys. 21, 805 (1982).
5. C.S. Fuller and F.J. Morin, Phys. Rev. 105, 379 (1957).
6. R.O. Carlson, Phys. Rev. 108, 1390 (1957).
7. H. Lemke, phys. stat. sol. (a) 72, 177 (1982),
A.C. Wang, L.S. Lu, and C.T. Sah, Phys. Rev. B 30, 5896 (1984).
8. P. Stolz, G. Pensl, D. Grünebaum, N. Stolwijk, to be published in Materials Science and Engineering, 1989.
9. B.V. Kornilov, Soviet Physics - Solid State 5, 2420 (1964),
Y.I. Zavadskii and B.V. Kornilov, phys. stat. sol. 42, 617 (1970).
10. A.F. Slensky and R.H. Bube, Phys. Rev B 6, 1328 (1972),
J.M. Herman III and C.T. Sah, J. Appl. Phys. 44, 1259 (1973).
11. A. Tardella and B. Pajot, J. Physique 43, 1789 (1982).
12. G. Armelies, J. Barrau, M. Brousseau, B. Pajot, and C. Naud, Solid State Commun. 56, 303 (1985).
13. A. Baldereschi and N.O. Lipari, Proc. 13th Int. Conf. on Physics of Semiconductors, Ed: F.G. Fumi (Tipografia Marves, Rome, 1976), p. 595.
14. S. Mayo, J.R. Lowney, and M.I. Bell, in "Microscopic Identification of Electronic Defects in Semiconductors", Ed.: N.M. Johnson, S.G. Bishop and G.D. Watkins, Mat. Res. Soc. Symp. Proc. 46, (Pittsburgh 1986), p. 297
15. G.D. Watkins and W. Beall Fowler, Phys. Rev. B 16, 4524 (1977).
16. The binding energy of this center is close to the value obtained for the electrically active center Zn(X2), observed in DLTS [12]. Therefore we accept this nomenclature for the optically active center. Additional correlations will be reported elsewhere.
17. M.L.W. Thewalt, D. Labrie, I.J. Booth, B.P. Clayman, E.C. Lightowers, and E.E. Haller, Physica 146B, 47 (1987).
18. R.A. Chapman, W.G. Hutchinson, and T.L. Estle, Phys. Rev. Lett. 17, 132 (1966).
19. M.L.W. Thewalt, B.P. Clayman, and D. Labrie, Phys. Rev. B32, 2663 (1985).
20. K.R. Elliot, G.C. Osbourn, D.L. Smith, and T.C. McGill, Phys. Rev. B 17, 1808 (1978).
21. M.A. Vouk and E.C. Lightowers, J. of Luminescence 11, 357 (1977).
22. J.H. Nevin and H.T. Henderson, J. Appl. Phys. 46, 2130 (1975).

PRESSURE DEPENDENCE OF A DEEP EXCITONIC LEVEL IN SILICON*

G.A. Northrop and D.J. Welford
IBM Thomas J. Watson Research Center, Yorktown Heights, NY 10598.

ABSTRACT

Certain optically active defects in silicon provide a unique opportunity to observe, in detail, the effect of hydrostatic pressure on a deep level. We present a photoluminescence (5 - 100K) study of one such defect, the I_1 radiation-damage center, under high hydrostatic pressures (1-50 kbar). While the energy variation of this level indicates the expected multi-band nature typical of a deep level, a severe and continuous reduction in the observed luminescence intensity was also observed. Temperature dependence, time resolved photoluminescence, and photoluminescence excitation spectroscopy are employed to attempt to discern the mechanism involved.

INTRODUCTION

Over the last 10 years a number of defects have been reported in silicon which exhibit strong no-phonon lines in photoluminescence, often with remarkably high efficiency [1]. These are deep excitonic levels that show some lattice coupling (vibronic side bands) but have a strong enough no-phonon line that makes the precise energy level clearly identifiable. Some are complexes produced by radiation damage, followed by low temperature annealing, of which most involve impurities such as oxygen and carbon normally found in CZ silicon. Another group occurs when transition metals, such as iron and chromium, are diffused into Si. Most of these are assumed to be dopant - transition metal complexes. A third group can be formed by rapid thermal quenching of heated In or Tl doped Si. As a group, these defects are well suited to the study of the effects of high pressure on deep levels in silicon due to their strong signatures and narrow linewidths.

The I_1 center [2], produced by radiation damage, was selected for this study primarily due to its strong luminescence, and the fact that it can be produced easily in high purity silicon. Although its microscopic structure is not known, its occurrence doesn't correlate with any impurity, thus, it is likely a complex of intrinsic defects produced by the radiation damage. It is most efficiently produced by ion or neutron bombardment, but can also be produced by other forms of radiation. Magnetic field and uniaxial stress measurements have shown that the I_1 ground state is non-degenerate, and that the defect has C_{3v} symmetry [3-5]. It has a total binding energy of 137 meV, and the temperature dependence of the PL intensity has an Arrhenius quench energy (\sim thermal binding energy) of about 50 meV [4].

PHOTOLUMINESCENCE ENERGY VS. PRESSURE

The samples used in this study were taken from boron doped ($\sim 10^{15} \text{ cm}^{-2}$) CZ grown wafers. These wafers were damaged by implantation with $3 \times 10^{12} / \text{cm}^2 \text{ Si}^+$, at 50 keV, and then annealed at 200 °C to produce the I_1 centers. Chemical etch profiling of samples prepared this way indicates that the I_1 centers are confined to within 0.3 μm of the surface, however, there is no good estimate of the defect density created this way. A thinned piece of this material was placed in a diamond anvil cell (DAC) for the high pressure measurements, along with a small chip of ruby used to determine the pressure. The cell was cooled to 15 K in a flowing He cryostat for PL measurements, but was raised to room temperature for each pressure adjustment. Excitation was typically 10 mW from

and Ar⁺ ion laser (5145 Å), and the PL analyzed by a conventional double scanning monochromator and a cooled Ge PIN photodiode.

The spectra in Figure 1 show both band edge (free exciton) and I₁ luminescence from atmospheric pressure to almost 50 kbar. The FE_{T0} replica of the free exciton

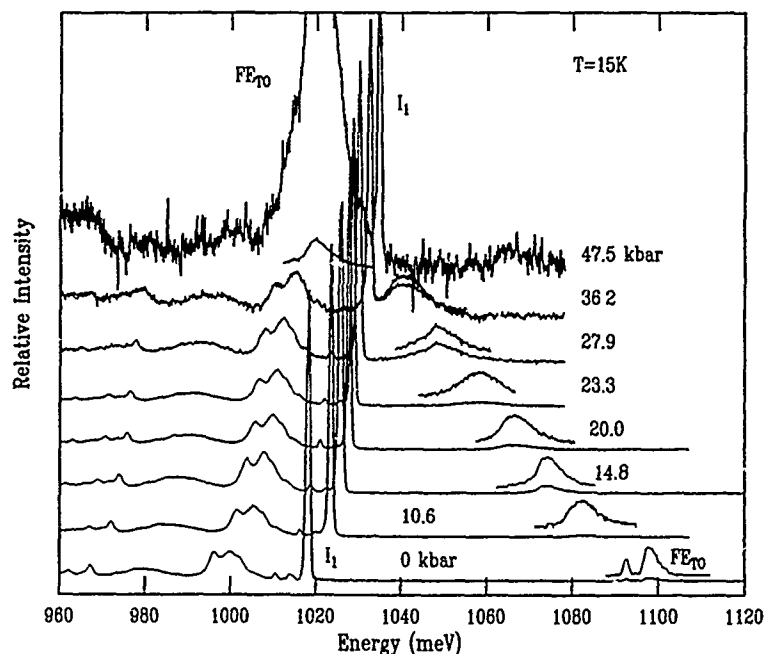


Figure 1. Photoluminescence spectra versus hydrostatic pressure. The full spectra are plotted with the I₁ intensity normalized, while the FE region is additionally plotted at constant FE intensity.

moves down in energy, following the X-band edge with which it is associated. The I₁ spectra consist on an intense no-phonon line (at 1018 meV in the atmospheric pressure spectrum), and a vibronic structure on the low energy side produced by emission of a photon with a lattice vibration. As expected for a deep level, the I₁ energy doesn't follow the band minimum, and in fact goes up with pressure, reflecting contributions to the I₁ electronic state from the other band minima. Figure 2 summarizes these energy shifts. A linear fit of the FE_{T0} line gives a slope of $-1.68 (\pm 0.05)$ meV/kbar. This gives the most accurate value to date for the pressure dependence of the X band edge [6,7]. The full spectra in Fig. 1 are plotted normalized to the I₁ intensity, while the short insets show the FE_{T0} line at fixed intensity. Over this pressure range the I₁ intensity drops by more than 3 orders of magnitude (right axis of Fig. 2), while the FE intensity remains about constant. This change was reversible, with the I₁ intensity returning upon returning to low pressure. Above 50 kbar I₁ became unobservable, well before the anticipated crossing with the FE edge at about 70 kbar. That, coupled with the steady nature of this decrease, suggests that something quite unanticipated is happening to the I₁ level under applied pressure.

Due to the complexity of optical excitation and recombination, there are a number of factors which may contribute to a change in photoluminescence intensity such as is observed for I₁ under pressure. They can be broken into three groups : 1) reduced

radiative efficiency of I_1 , 2) reduced capture rate for I_1 , and 3) reduced steady state carrier density due to other recombination channels. The remainder of this paper will attempt to analyze the possible sources of this effect in the light of several additional experiments, and to relate to what this might indicate about the I_1 bound exciton.

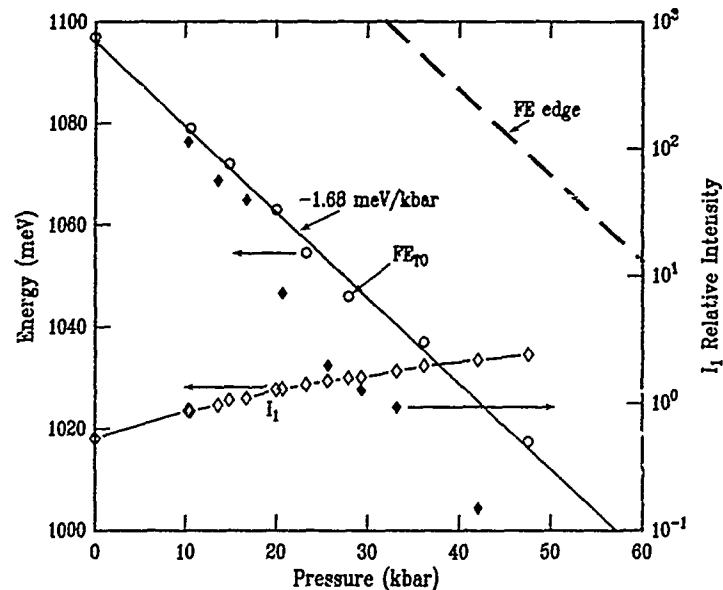


Figure 2. Variation in FE_{TO} and I_1 energies with pressure. The dotted line shows the FE edge, which is 15 meV below the X band edge, based upon a TO phonon energy of 58 meV. The drop in I_1 intensity, shown on the right axis, shows the demise of I_1 well before crossing the band edge.

ELECTRONIC STRUCTURE OF I_1

One potential signature for changes in the I_1 ground state could be observed directly in the PL spectra of Figure 1. A significant change in the wave function could change the lattice relaxation associated with the exciton, thus changing the vibronic coupling. The vibronic structure in these spectra does not vary over this pressure range. This suggests that the exciton doesn't undergo a significant change which might, in turn, cause a change in the radiative efficiency.

Another internal mechanism for reduction of the I_1 radiative efficiency is the possible involvement of a low lying excited state. This has been suggested by others based upon a highly nonlinear uniaxial stress dependence and multiple activation energies used in fits to PL temperature dependences [4]. The clear change in the pressure derivative of the I_1 energy (Fig. 2) is also suggestive of an interaction with such a low lying excited state. If such a state was non-radiative, then populating it would reduce the overall radiative efficiency of the defect. A good test of this, however, is found in the temperature and pressure dependence of the PL intensity found in Figure 3. For three different pressures, the I_1 luminescence begins to quench between 20 K and 30 K, and more importantly, the intensity in the low temperature limit is independent of temperature, but still strongly dependent upon pressure. If a pressure induced reduction of the energy separation of such an excited state was causing the quenching of I_1 , one would expect to see a significant change with temperature, even at 10 to 15 K. The solid lines in Fig. 3 are fits to an expression for thermal partition between the radiative I_1

ground state and the nearest band. The activation energy from these fits varies from 45 meV at 22 kbar to 35 meV at 44 kbar. Although this variation may be experimentally significant, it is not sufficient to explain the loss of intensity in the low temperature limit.

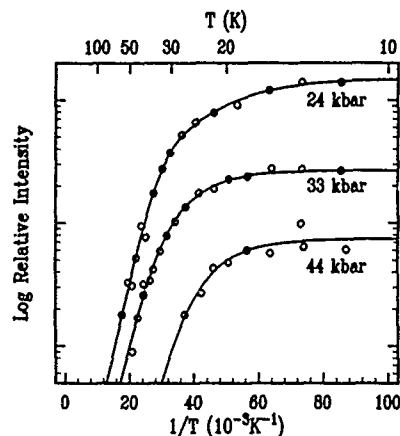


Figure 3. Temperature and pressure dependence of I_1 PL intensity. The large variation in intensity with pressure in the low temperature limit and the fixed quenching temperature and slope indicate that the I_1 thermal binding energy doesn't vary significantly with pressure.

I_1 PL intensity, with a usable average power of about 10 mW and a linewidth of about 0.5 meV (4 cm^{-1}). Figure 4 presents both PL and PLE spectra for I_1 at atmospheric pressure. Unfortunately, the signals were not strong enough to perform this measurement in the diamond anvil cell. For the PLE the luminescence detected was the integral of the no-phonon line, and the laser was scanned toward higher energies. All of the structure in this PLE spectrum is identifiable as the anti-stokes vibronic structure resulting from excitation into the I_1 ground state plus creation of a phonon. No extra lines could be found which might result from resonant excitation into a no-phonon excited excitonic state. Resonant excitation of the no-phonon line and detection of PL in the TA phonon band provided a relative measure of the I_1 absorption. The thick vertical bar in Fig. 4 represents the strength of an equivalent excitation in the PLE. No excited states appear on this scale, although, any with an oscillator strength a factor of 10 less than the ground state would be difficult to distinguish from the vibronic background.

Excited states have been observed for two similar defects in silicon, the C radiation damage center [8], and the P defect associated with oxygen precipitation [9]. Both of these defects revealed a series of lines in PLE very similar to the spectrum for excitation of an effective mass donor. The model presented for the excitonic state at these centers was of a hole bound tightly ($\sim 300\text{ meV}$) to the neutral defect, and an electron then bound to the positively charged center by its Coulomb potential. The PLE lines resulted from resonant excitation of a hole bound to the defect and an electron in an excited hydrogenic state. The lack of such lines for the I_1 center may indicate that this pseudo-donor (or pseudo-acceptor) picture may not fit I_1 at all. This apparent difference may involve the fact that the I_1 level is shallow enough that neither electron or hole may be bound that strongly, and neither may be effective mass like.

The possibility of a low lying non-radiative excited state is not the only mechanism for excited states to effect the photoluminescence from I_1 . Although the capture mechanism for this type of defect is entirely unknown, it is expected that excited states, particularly shallow ones, play a significant role in capture processes. If application of pressure changed the presence, or depth, of such states, it might greatly effect capture at the center. This might be expected to happen for I_1 as its ground state moves closer to the band edge. A search for excited states has been performed using photoluminescence excitation spectroscopy (PLE). Since the spectral range required (1018 meV and up) is inaccessible to conventional dye lasers, the optical source used was a LiNbO_3 optical parametric oscillator, using a Cu-vapor pumped dye laser as a pump source. This system provides continuously tunable 15 nsec pulses at 5

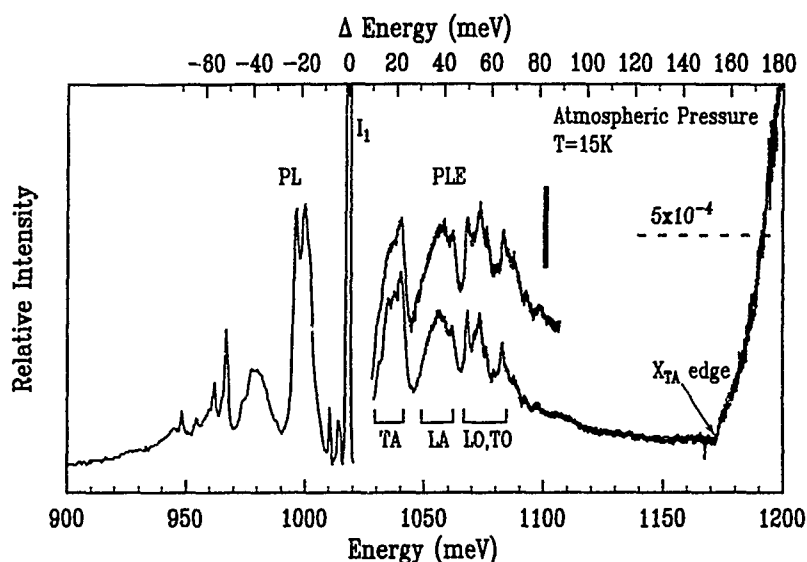


Figure 4. Photoluminescence and PLE spectra of I_1 at atmospheric pressure. The two PLE spectra are different runs under the same conditions. Most of the vibronic structure in both the PL and PLE is associated with the denoted bulk phonons; no excited states were discernible in the PLE. The heavy line is the expected strength for an excited state with oscillator strength equal to the ground state. The dashed line marks an estimated fractional absorption based upon $\alpha=0.15 \text{ cm}^{-1}$ at 1190 meV and a length of $30 \mu\text{m}$, the approximate exciton diffusion length.

One other technique which might help discern whether the pressure induced change in the I_1 exciton is internal or not is that of luminescence lifetime. If the oscillator strength of the transition is changing with pressure then this should be reflected in the lifetime. Figure 5 shows the luminescence decay time for the I_1 center at atmospheric pressure. This data was taken using pulsed excitation from a cavity-dumped Ar^+ -ion laser and time correlated photon counting with an S-1 photomultiplier tube. This is the only photocathode with any sensitivity at the I_1 wavelength (1217 nm), and there its quantum efficiency is about 10^{-6} . This poor sensitivity made its application to the diamond anvil cell impossible. The three decay curves shown are for the free exciton, the I_1 no-phonon line, and the direct response to the laser. The 200-400 nsec lifetime of the free exciton is most likely coming from the bulk of this $400 \mu\text{m}$ thick sample. The 40 nsec decay time observed for I_1 is therefore an upper limit on its lifetime. This is the first reported decay time for this defect, and it is noteworthy that it is significantly shorter than has been reported for a number of similar defects, which range from around 10 to more than $1000 \mu\text{sec}$ [1]. If the radiative efficiency is high, then this defect could have a large oscillator strength. If the measured lifetime is entirely radiative, then the oscillator strength would be greater than 0.1. This must serve as an upper limit, however, as the radiative efficiency of this transition is not known.

The final mechanism that might cause the loss of I_1 luminescence with pressure is the possibility of increased capture and nonradiative recombination at other defects in the damage layer. This competitive recombination channel could reduce the local density of carriers available for capture at I_1 centers.

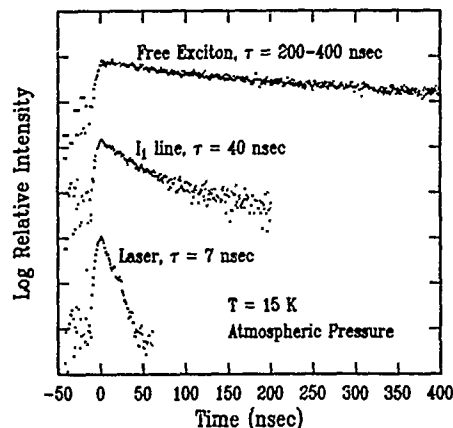


Figure 5 Photoluminescence time decays for I_1 sample at atmospheric pressure. Each vertical division is one decade.

A key indicator of the steady state electron-hole density in the sample is the free exciton intensity. The fact that this remains approximately constant as pressure increases suggests that competitive recombination channels are not affected by pressure. However, this is made uncertain by the fact that this is an inhomogeneous system; the luminescing centers are confined to a thin layer near the surface. The free exciton luminescence comes from the 30 μm thick bulk portion of the sample, and could only be reduced significantly by increased recombination in the surface layer if the surface recombination velocity were not already quite high. Based upon this, one cannot rule out increased recombination at defects other than I_1 created by the implantation damage.

SUMMARY

We report the first study of low temperature photoluminescence in crystalline silicon at high hydrostatic pressure. This has produced a more accurate value for the pressure dependence of the X-band edge and demonstrated the multi-band contributions to a deep excitonic level (I_1). The photoluminescence from this level is quenched by pressure well before the projected crossing with the band edge. Luminescence lifetime, photoluminescence excitation spectroscopy, and PL temperature dependence have been employed to try to discern the cause of this effect. Although the mechanism for this unusual behavior is still not certain, the results have provided new information about I_1 in the determination of its luminescence lifetime (40 nsec), and the apparent lack of an excited state spectrum.

*Supported in part by the U.S. Office of Naval Research under contract N00014-85-C-0868.

REFERENCES

1. For a recent review of luminescing deep levels in silicon see: Gordon Davies, *Physics Reports* **176**, 84 (1989).
2. C.G. Kirkpatrick, J.R. Noonan, and B.G. Streetman, *Radiation Effects* **30**, 97 (1976).
3. N. Burger, K. Thonke, and R. Sauer, *Phys. Rev. Lett.* **52**, 1645 (1984).
4. N. Burger, E. Irion, A. Teschner K. Thonke, and R. Sauer, *Phys. Rev.* **B35**, 3804 (1987).
5. Gordon Davies, E.C. Lightowers, and Zofia E. Ciechanowska, *J. Phys.* **C20**, 191 (1987).
6. B. Welber, C.K. Kim, Manuel Cardona, and Sergio Rodriquez, *Solid State Communications* **17**, 1021 (1975).
7. William Paul and G.L. Pearson, *Phys. Rev.* **98**, 1755 (1955).
8. J. Wagner, K. Thonke, and R. Sauer, *Phys. Rev.* **B29**, 7051 (1984).
9. J. Wagner, A. Dornen, and R. Sauer, *Phys. Rev.* **B31**, 5561 (1985).

ODMR OF SHALLOW DONORS IN Zn-DOPED LEC-GROWN InP

J. M. TROMBETTA* AND T. A. KENNEDY
 Naval Research Laboratory, Washington, DC 20375

ABSTRACT

ODMR spectra observed while monitoring the shallow donor-shallow acceptor pair emission in Zn-doped LEC-grown InP display strong features in the region near the conduction electron value of $g=1.20$. In addition to a previously observed narrow line, we observe a much broader resonance which dominates at low photoexcitation intensity. This broader line is interpreted as the unresolved exchange split resonances of electrons bound to residual shallow donors. The exchange broadening arises from interactions with nearby paramagnetic centers. Both resonances result in a decrease in the shallow-donor-to-shallow-acceptor radiative recombination and give evidence for pair recombination processes which compete with this emission.

INTRODUCTION

Recombination in bulk semiconductors is generally influenced by the presence of defects. The use of ODMR (Optically Detected Magnetic Resonance) has, in many cases, identified a participating deep level species through signature structure such as a strong hyperfine interaction[1,2]. In contrast, only a few shallow centers have been unambiguously identified by this technique. One such example is the In donor in ZnO[3]. In several II-VI semiconductors, ODMR has been utilized to study the electron-hole exchange interactions present in donor-acceptor close-pair recombination[4,5]. Recently, an extensive optically detected electron nuclear double resonance study has demonstrated the effective-mass-like character of a donor in GaP[6].

Shallow donor magnetic resonance in InP has received limited attention to date. The theoretical g -value obtained by Lawaetz[7] using $k \cdot p$ perturbation theory is $g = 1.20$. A narrow electron paramagnetic resonance line with $g = 1.20$ was observed in slightly n-type InP by Goltzene *et al.*[8] and ascribed to residual shallow donors. In two recent observations a very narrow conduction electron spin resonance at $g = 1.2042 \pm 0.0005$ has been assigned to electrons in a shallow donor impurity band[9,10]. The resonance of conduction electrons has also been observed through the polarization of photoluminescence in epitaxial n-type InP[11]. The g -value of shallow electrons is thus well understood and distinct due to its considerable shift from the free electron value of 2.0023. An early ODMR observation of a narrow line (20mT) near this g -value was made by Yan Dawei *et al.*[12] in a study of InP:Mn. This feature was assigned to electrons either in the conduction band or bound to donors. Robins *et al.*[13] observed a similar feature in LEC-grown InP:Zn. Both of these works emphasized deep centers.

In this work we report a detailed study of two donor-like resonances observed in lightly Zn-doped InP. The new resonance, which is strongly inhomogeneously broadened, can be assigned to electrons bound to residual shallow donors. The dependence of these resonances upon photoexcitation intensity, microwave modulation frequency, and other parameters provides information about the recombination processes which involve the shallow donor.

EXPERIMENTAL DETAILS

The sample used in this study was a single crystal of Zn-doped LEC-grown InP with a room temperature hole concentration of $5 \times 10^{15} \text{ cm}^{-3}$. The ODMR measurements were performed at microwave frequencies of 24 GHz or 35 GHz in superfluid helium at 1.6 K within an Oxford Instruments optical split-pair magnet system. The 50 mW microwave power sources were on - off modulated at 35 Hz to 80 kHz. The optical excitation was achieved with either a He-Ne laser (633 nm) or a Kr^+ ion laser (647 nm). The photoluminescence was detected along the magnetic field with a Si photodiode with the exciting light filtered out using a 780 nm (Schott RG780) long pass filter. In this configuration the collected luminescence was dominated by the emission at 1.37 eV. To obtain the spectral dependence of the ODMR, a Bausch and Lomb high intensity monochromator was inserted in the luminescence collection path. ODMR was detected synchronously with the microwave modulation as a change in either the total or the circularly polarized component of the photoluminescence. The ODMR spectra were then obtained by subtracting off the linear component of the non-resonant background.

RESULTS

The optical recombination properties of Zn-doped InP have been studied by Robins *et al.* [13] using the ODMR technique. The resonance due to P_{In} antisites was detected as an increase in the emission at 0.8 eV and as a decrease in the shallow-donor-to-shallow-acceptor emission at 1.37 eV. Their results supported an identification of the 0.8 eV emission as antisite-to-acceptor pair recombination. These processes are summarized in the energy level diagram shown in Fig. 1. Other possible deep level processes (Fig. 1) will also be discussed.

ODMR spectra obtained at 24 GHz in the magnetic field region near $g = 1.2$ while monitoring the total shallow-donor-to-shallow-acceptor (DA) pair emission are presented in Fig. 2 for three different photoexcitation intensities. The spectra contain a narrow (16 mT) line with $g = 1.20 \pm 0.01$ as a decrease in the total luminescence. Measurements performed with 35 GHz microwaves have confirmed this g - value. A new, much broader (80 - 140 mT) feature appears with decreasing photoexcitation intensity, also causing a decrease in the emission. Both resonances are isotropic within the experimental error. From the g value of these lines it is likely that they both arise from effective mass - like electrons. Both signals contribute their largest fractional change in luminescence at low photoexcitation intensity. As the photoexcitation intensity is increased, however, the broad line decreases sharply while the narrow line decreases only slightly. Above 0.1 W/cm^2 the broad line cannot be distinguished from the wings of the narrow line but the narrow line does not decrease in strength up to at least 10 W/cm^2 . Whereas the process giving the broad line is substantially saturated by a high excitation density, the narrow line process is not. This result suggests that the recombination rate for the process giving the broad line is considerably lower than that of the narrow line.

It is possible to obtain information about the recombination rates from a study of their characteristic response times under the on - off modulation of the microwaves. The in-phase and quadrature components of the two ODMR signals as a function of the modulation frequency are shown in Fig. 3. Both in-phase signals decay in amplitude as the frequency increases, but the broad resonance disappears at frequencies roughly an order of magnitude lower than the narrow resonance. The in-phase and quadrature components become equal when the signal lags the modulation by 45° , which, for the broad resonance, occurs at a much lower frequency than for the narrow resonance. Thus, the overall response rate of the broad resonance is considerably lower than that of the narrow resonance. It is likely that this results from a difference in recombination rates as was evidenced by the difference in photoexcitation intensity dependence.

A study of the intensity of the narrow line and the shallow DA pair photoluminescence

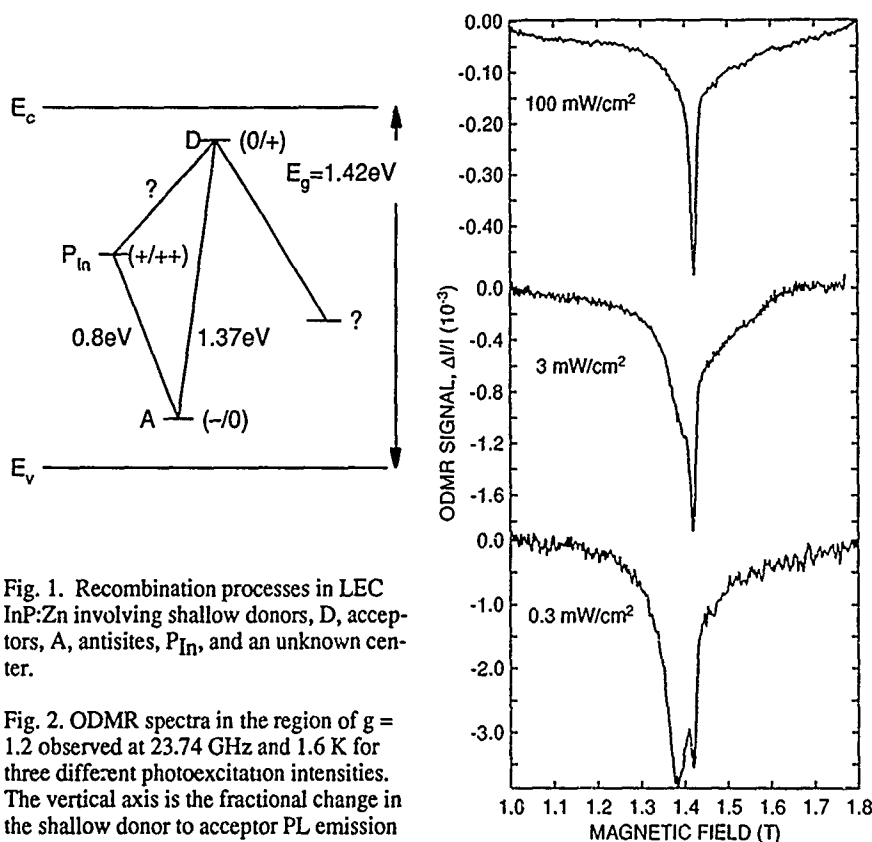


Fig. 1. Recombination processes in LEC InP:Zn involving shallow donors, D, acceptors, A, antisites, P_{In} , and an unknown center.

Fig. 2. ODMR spectra in the region of $g = 1.2$ observed at 23.74 GHz and 1.6 K for three different photoexcitation intensities. The vertical axis is the fractional change in the shallow donor to acceptor PL emission at 1.37 eV.

(PL) intensity versus the emission wavelength is shown in Fig. 4. The ODMR and the PL intensities were measured with a resolution of 12 nm and a photoexcitation intensity of 100 mW/cm². The PL intensity is peaked at $\lambda = 901 \pm 1$ nm while the peak of the wavelength distribution of the ODMR resonance is at $\lambda = 911 \pm 2$ nm. The ODMR is observed only for the long wavelength tail of the PL distribution. In particular, only the most distant DA pairs present, having the longest emission wavelength as well as the lowest recombination rate [14], participate in the ODMR process. As is discussed below, this result provides a clue to the nature of the spin dependent process involved. The broader resonance was not of sufficient intensity to be studied in this manner.

DISCUSSION

The spin dependence of a donor-acceptor-pair recombination has been considered thoroughly elsewhere [4], but the basic principles will be briefly reviewed here. We consider a simple DA pair excited state in which both the electron localized on the donor and the hole localized on the acceptor have spin 1/2. The corresponding energy levels in a magnetic field are shown in Fig. 5 with the states designated by the spins of the donor and acceptor. The large arrows represent the allowed radiative optical recombinations while the small arrows in-

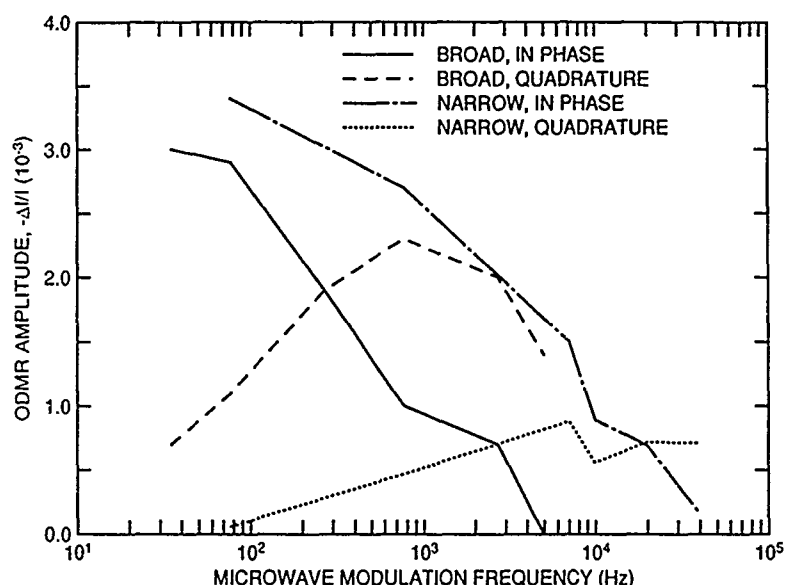


Fig. 3. Microwave modulation frequency dependence of both narrow and broad shallow-electron resonances while monitoring the shallow donor to shallow acceptor PL emission. The in-phase and quadrature components are both shown.

dicating the microwave transitions which change the spin of the donor electron. A weak electron-hole exchange interaction, J , splits the resonance into two lines separated by $\Delta B = J/2g\mu_B$. If the spin-lattice relaxation is much slower than the optical recombination (non-thermalized spins), then the states corresponding to the forbidden transitions ($++$ and $--$) will have populations which are greater than the states corresponding to the allowed transitions ($+-$ and $-+$). In this case both microwave transitions result in an increase in the emission. It should be noted that a decrease in a given emission can result from the increase of a competing process. Such a "shunt" process could be a recombination involving another center or a nonradiative component of the recombination under study. A distribution of exchange splittings is anticipated when a distribution of donor-acceptor separations is present.

ODMR of shallow donors in several other semiconductors such as GaP[6], CdS[5], and AlAs[15] has previously been reported and for most of these observations, the resonance linewidth was below 20 mT. Cox and Davies [5] have studied shallow donor resonances on donor-acceptor recombination in CdS with exchange splittings from 10 to 1000 mT. Due to its inhomogeneous broadening relative to the narrow line, the broader resonance observed here is assigned to electrons bound to residual shallow donors of an unknown species and not to conduction electrons. It is likely that this resonance arises from the recombination of a donor paired with another center and its lineshape arises from exchange interactions with this center. The average exchange interaction in this picture can be estimated from the linewidth to be roughly 3 μeV , a value similar to those measured for the shallow DA pair emission in CdS [5]. Other possible broadening mechanisms include shallow donor-shallow donor exchange interactions.

The two resonances observed here cause a decrease in the total emitted intensity from shallow DA pairs, while the resonant change in the polarization of this emission was measured to be nearly zero. Thus in consideration of the model described by Fig. 5, these resonances cannot simply arise from the spin dependence of the radiative recombina-

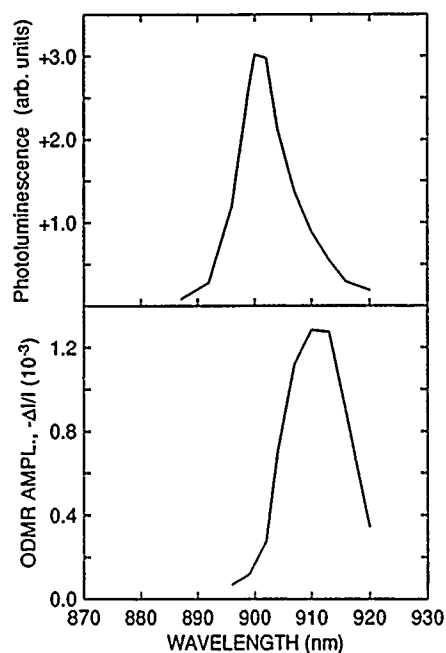


Fig. 4. Photoluminescence intensity of the 1.37eV shallow donor to shallow acceptor recombination and spectral dependence of narrow shallow electron ODMR amplitude under the same conditions.

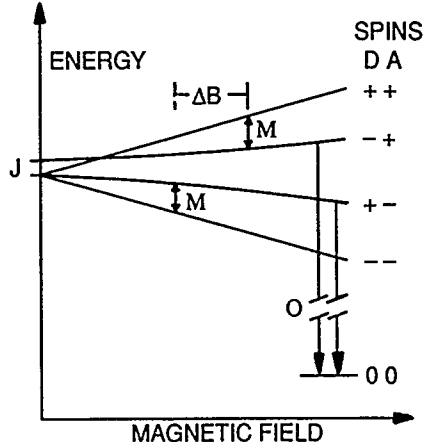


Fig. 5. Energies of the four spin levels of the luminescence excited state for a donor acceptor pair with a weak exchange interaction, J . The microwave (M) and optical (O) transitions are shown.

tion of shallow-donor-shallow-acceptor pairs. They therefore originate from competing or "shunt" recombination processes. Photoluminescence measurements on this sample reveal the antisite to acceptor emission and an unidentified band near 1.0 eV (Fig. 1). Temkin *et al.* [16] have assigned a broad PL band at 1.0 eV in LEC InP to the P vacancy and Skolnick *et al.* [17] have observed a PL emission at this energy in Cu diffused material. The ODMR measurements by Robins *et al.* [13] on the same material included a broad resonance at $g = 2.0$ having a photoexcitation intensity dependence quite similar to that of the broad donor resonance observed in the present studies. Thus it is plausible that both of these resonances arise from the same recombination, and constitute the two partners in a pair recombination.

The narrow resonance arises from a process which is considerably slower than the average shallow DA pair recombination in this material as evidenced by the data of Fig. 4. For example, this resonance could arise from a pair recombination involving a deep center such as the P_{In} antisite. A slower process such as this could effectively compete only with the most distant DA pairs, causing the wavelength dependence observed. It is also possible that a nonradiative component of the shallow donor - shallow acceptor pair recombination gives rise to this resonance. The lack of participation of the closest (fastest) DA pairs in the ODMR (Fig. 4) might result if the microwave excitation rate is not high enough to affect the spin populations of these pairs.

Finally we note that in Fig. 2 the broad resonance peaks at a lower field than the narrow resonance at $g = 1.20$, apparently shifting to lower fields and narrowing with decreasing

excitation intensity. The position of the peak of the broad resonance is 36 mT below that of the sharp resonance at the lowest excitation intensities employed here. It is possible that the slower, more distant pairs observed at lower excitation intensity have more nearly equal populations in the (+ +) and (- +) states, due to spin thermalization, compared with the faster pairs observed at higher excitation intensity. The result would be a decrease in the intensity of the high field-split lines (Fig. 5) for these pairs, and thus an apparent shift to lower field. Further studies of this effect are in progress.

SUMMARY

ODMR studies of two isotropic resonances at the shallow electron g-value of $g = 1.20$ in Zn-doped LEC-grown InP are reported. While the broader resonance appears only at low photoexcitation intensity and low modulation frequency, the narrow resonance can be observed under high excitation and at high frequencies. Both resonances result in a decrease in the shallow donor - shallow acceptor pair emission at 1.37 eV. Because of its inhomogeneous broadening relative to the narrow line the broader line is assigned to the unresolved exchange-split resonances of electrons bound to residual shallow donors. The results reveal an additional recombination process involving the residual shallow donors in this material.

ACKNOWLEDGEMENTS

We would like to thank R. L. Henry for providing this sample and E. R. Glaser for helpful discussions. This work was supported in part by the U. S. Office of Naval Research.

* NRC-NRL RESIDENT RESEARCH ASSOCIATE

REFERENCES

1. B. C. Cavenett, *Adv. Phys.* **30**, 475 (1981).
2. J. J. Davies, *J. Crys. Growth* **72**, 317 (1985).
3. D. Block, A. Hervé, and R. T. Cox, *Phys. Rev. B* **25**, 6049 (1982).
4. D. J. Dunstan and J. J. Davies, *J. Phys. C* **12**, 2927 (1979).
5. R. T. Cox and J. J. Davies, *Phys. Rev. B* **34**, 8591 (1986).
6. D. Y. Jeon, J. F. Donegan, and G. D. Watkins, *Phys. Rev. B* **39**, 3207 (1989).
7. P. Lawaetz, *Phys. Rev. B* **4**, 3460 (1971).
8. A. Goltzené, B. Meyer, and C. Schwab, *J. Appl. Phys.* **62**, 4406 (1987).
9. B. Clerjaud, F. Gendron, H. Obloh, J. Schneider, and W. Wilkening, *Phys. Rev. B* **40**, 2042 (1989).
10. B. Gotschy, G. Denninger, H. Obloh, W. Wilkening, and J. Schneider, *Sol. St. Commun.* **71**, 629 (1989).
11. C. Weisbuch and C. Hermann, *Sol. St. Commun.* **16**, 659 (1974).
12. Yan Dawei, B. C. Cavenett, and M. S. Skolnick, *J. Phys. C* **16**, L647 (1983).
13. L. H. Robins, P. C. Taylor, and T. A. Kennedy, *Phys. Rev. B* **38**, 13227 (1988).
14. P. J. Dean, in *Progress in Solid State Chemistry*, Vol. 8, edited by J. O. McCaldin and G. Somorjai (Pergamon Press, New York, 1973), p. 1.
15. E. R. Glaser, T. A. Kennedy, R. S. Sillmon, and M. G. Spencer, *Phys. Rev. B* **40**, 3447 (1989).
16. H. Temkin, B. V. Dutt, W. A. Bonner, and V. G. Keramidas, *J. Appl. Phys.* **53**, 7526 (1982).
17. M. S. Skolnick, E. J. Foulkes, and B. Tuck, *J. Appl. Phys.* **55**, 2951 (1984).

COMPLEX DEFECTS IN SEMICONDUCTORS

B. MONEMAR¹

Max-Planck-Institut für Festkörperforschung
Heisenbergstr. 1, D-7000 Stuttgart 80, Federal Republic of Germany

ABSTRACT

Complex defects in semiconductors are briefly reviewed, with emphasis on the electronic structure. Classes of such defects with a varying degree of complexity are discussed, with reference to recent optical data for neutral defects in GaP and silicon. These include P_{Ga} -antisite related substitutional complexes in GaP, Ga_i -acceptor complexes in GaP, substitutional chalcogen complex defects in silicon and vacancy-impurity complexes in silicon.

I. INTRODUCTION

The importance of defects in determining relevant properties of semiconductors was realized at an early stage, and already in the 1950's a considerable amount of work was carried out on defect characterization, in particular concerning shallow dopants. Ever since there has been a steady increase in the activity in this research area, and most physical aspects of shallow impurities are now understood, at least on a practical level. [1] The more detailed studies of deep levels in semiconductors started later (in the 1960's and 1970's), but a great deal of progress has been done, particularly on point defects. [2] There is another class of defects, however, where progress has been much slower, namely complex defects, which typically consist of more than one defect site, and have a low symmetry. [3] Such defects commonly occur in most semiconductors, particularly as a result of various processing steps, and are of practical importance as residual defects that very significantly affect various properties like carrier recombination, lifetimes and degradation behavior. The problems of calculating properties of such defects from first principles with a sufficient accuracy are not yet commonly addressed, although a few cases have been attempted. [4,5,6]

Experimentally there are two major pieces of information to be extracted in order to obtain a satisfactory understanding of complex defects: (a) the identity of the defect, i.e. the local geometrical arrangement of the atoms participating in the defect structure, and (b) the electronic structure of the defect, i.e. the bound electronic states and their properties. The first problem seems to be a real bottleneck, since there are, so far, no generally applicable techniques developed with a sufficient sensitivity to selectively study the structure of a specific complex defect, which is often of lower concentration than other defects (or impurities) in the material. Recent advances on this problem will be exemplified below. The electronic structure can in many cases be studied with optical perturbation spectroscopy [3,7], including the recently developed optically detected magnetic resonance (ODMR) technique. [8,9]

This paper summarizes briefly some recent developments in the study of physical properties of complex defects, with emphasis on the electronic structure. Different classes of complex defects are briefly discussed, demonstrating the degree of complexity that occurs. Simple models for the electronic structure are discussed, in relation to optical data for neutral defects from excited state perturbation spectroscopies. A number of recently studied experimental cases are demonstrated, for complex defects in GaP and silicon.

¹Permanent address: Department of Physics and Measurement Technology, Materials Science Division, Linköping University, S-58183 Linköping, Sweden.

II. CATEGORIES OF COMPLEX DEFECTS

The very simplest example of a complex defect is just an impurity atom that is relaxed from a normal T_d lattice symmetry. For substitutional atoms such relaxations may be large and lead to rebonding, as recently suggested e.g. for the DX donor centers in III-V materials [6], and possibly also for some donors in II-VI materials. [10] Similarly, interstitial atoms may also be relaxed from high symmetry positions, as suggested e.g. for Li donors in GaP [11], and for O and N impurities in silicon, in which case a rebonding and relaxation to lower symmetry occurs. [12,13]

The next step in complexity is a pair of point defects or impurity atoms. The divacancy [14] and the V-O center (A-center) [12] in silicon are well known such examples involving intrinsic defects, with rebonding occurring so that the defect symmetry is lower than the lattice symmetry. Simpler cases are the substitutional impurity pairs, where the impurity atoms often approximately occupy the regular lattice positions (Fig. 1a). Well known examples are the radiative N-N pairs in GaP [16]. Another class of simple complex defects is the substitutional-interstitial impurity pair (Fig. 1b). Good examples of these are shallow acceptor-interstitial transition metal pairs, such as Fe_i-B_s or Cr_i-B_s pairs in silicon. [17] This latter category is also relatively simple in the way that the atoms occupy approximately high symmetry positions, and no rebonding occurs. Further examples of such defects will be discussed below. When substantial rebonding occurs the defect structure becomes more

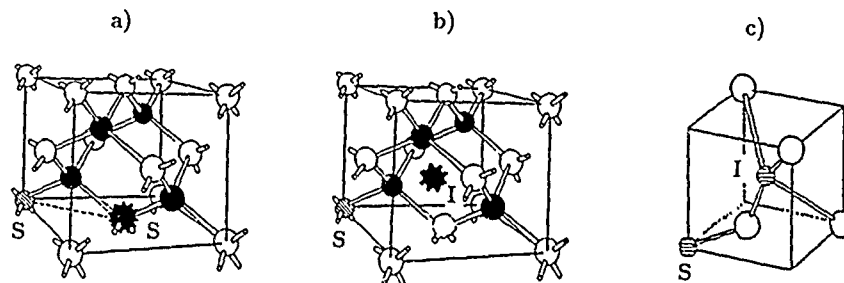


Figure 1: Examples of different complex defects: (a) a substitutional pair, (b) a substitutional-interstitial pair, (c) a rebonded defect containing a split interstitial.

complicated. Relatively simple defects like the C-C_i G-line defect (Fig. 1c) or the C_i-O, C-line defect in silicon [18,19] become complicated by metastability via switching of bonds related to such rebonded configurations, which gives rise to a multiplicity of both the geometrical and the electronic structure of the defect. [20] Even more complex defects occur as preages of precipitation. The so called thermal donors in silicon have been studied experimentally and theoretically for over 30 years, but no firm conclusion exists as yet for the structure of these defects, which are assumed to be a family of O-related aggregates. [21]

III. ELECTRONIC STRUCTURE OF NEUTRAL COMPLEX DEFECTS

We shall here limit our discussion of the electronic structure of complex defects to the neutral charge state of such defects. This case in fact covers most of the experimentally

encountered situations at low temperature, and also shows the richest variety in properties. Also, neutral defects can be studied by a number of optical techniques. Complex defects often have several charge states though, which can be stabilized by a suitable position of the Fermi level, or by excitation.

A neutral complex defect can in its ground state usually be characterized via a $(o/+)$ 'donor' level of a $(-/o)$ 'acceptor' level, where the labelling 'donor' and 'acceptor' is commonly used in literature, in analogy with the similar charge states for shallow donors and acceptors. Actually many defects have both a $(-/o)$ and a $(o/+)$ level in the gap, in fact (as will be shown below) more than one $(-/o)$ or $(o/+)$ level may be present for the same defect. Often $(o/+)$ levels occur close to the valence band and $(-/o)$ levels close to the conduction band, i.e. in general we are dealing with genuine deep level properties.

Reliable theoretical calculations of the electronic structure of complex defects, in general, do not yet exist, so it is useful to refer to simple physical models. A neutral defect is characterized by a potential, that may or may not have a Coulomb part. We shall schematically illustrate the problem with the example of a complex neutral defect, which has a deep $(o/+)$ level in the gap. A deep complex single donor e.g. has an electron-attractive local potential, which contains as one part the Coulomb field from the donor core (Fig. 2a). The potential is otherwise dominated by the local atomic potentials of the defect atoms and the local strain field, which is often quite strong. [7] The result is a deep $(o/+)$ donor level in the gap, which characterizes the electronic ground state.

On the other hand there are other neutral defects which have a deep $(o/+)$ level in the gap, but have a quite different potential, and consequently different properties. If e.g. the electron active in this level is localized to a bond related to an impurity atom at the defect (see e.g. Fig. 1c), there will be no hydrogenic Coulomb potential present in the defect core (Fig. 2b). Excitations of the defect simply involves taking away the electron from the local bond, either to the valence band (hole capture) or to higher energy states.

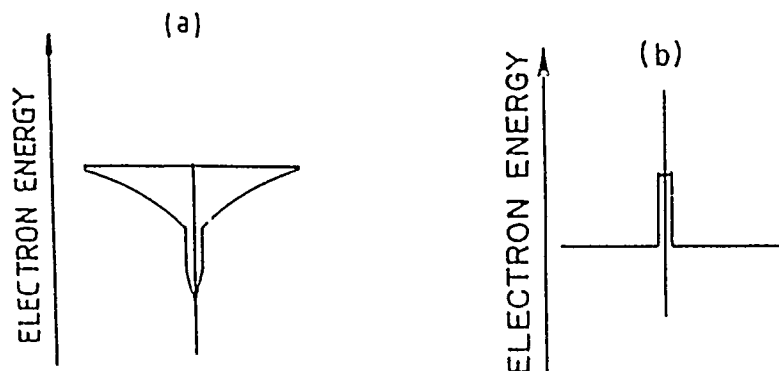


Figure 2: Schematic defect potential for (a) a defect with a $(o/+)$ deep donor level, (b) a neutral defect with a $(o/+)$ level, but lacking a donor Coulomb potential.

The excited states corresponding to these two different cases of $(o/+)$ levels are also different. The deep donor ground state can be optically excited from the $1sA_1$ ground state to higher more or less effective mass (EM) like states close to the conduction band (Fig. 3a), as demonstrated e.g. for deep chalcogen donors in Si. [22] Donor bound excitons can also be

created, due to the presence of a $(-/o)$ level at higher energies. In the second case discussed above an optical excitation means the creation of a bound exciton (BE) state, either directly by below band gap absorption, or by hole-capture followed by a secondary capture of an electron in the Coulomb potential of the bound hole. The latter case is a 'pseudo-donor' case, where the Coulomb potential is only present due to the excitation (not before), and the $1sA_1$ pseudo-donor level is separated from the $(o/+)$ ground state by the BE electronic energy (Fig. 3b).

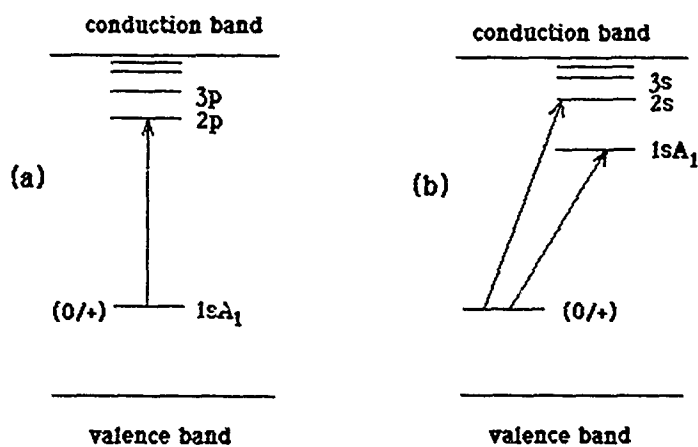


Figure 3: Comparison between excited states of (a) a deep donor $(o/+)$ level and (b) a deep neutral defect $(o/+)$ level, which gives rise to pseudo-donor states.

The case presented above in connection with Figs. 2 and 3 concerned $(o/+)$ ground state levels, associated with either donor-like or pseudo-donor-like excitations. Similarly for $(-/o)$ levels, one can in an analogous way expect acceptor-like and pseudo-acceptor-like excitations, respectively, for different types of neutral defects. Following the above mentioned example, a local bond electron would typically tend to be acceptor-like, i.e. produce (EM) like excited acceptor states close to the valence band, while an electron-attractive neutral potential would tend to give rise to pseudo-acceptor states via the $(-/o)$ ground state level.

The above scheme may for some cases be oversimplified, but is believed to cover a quite large range of complex defects giving rise to deep $(o/+)$ and $(-/o)$ levels in the band gap.

IV. EXAMPLES OF ELECTRONIC STRUCTURE OF NEUTRAL COMPLEX DEFECTS

In the following some recent experimental data on complex defects will be reviewed, with emphasis on the electronic structure obtained. We concentrate on some relatively simple cases of non-rebonded defects, but will also mention some preliminary results on a vacancy-related complex in silicon.

IV.A. P_{Ga} antisite-related complexes in GaP

P_{Ga} in GaP is rather well documented in literature, and is a deep double donor with levels around midgap. [23] If this donor is made part of a complex with a double acceptor such as Cu_{Ga} , a neutral substitutional complex defect is expected to be formed with symmetries corresponding to the relative Ga-site lattice positions occupied. In recent experiments on

optical detection of magnetic resonance (ODMR), three different spectra corresponding to one (110) and two (111)-oriented such defects were in fact observed and tentatively identified as due to $\text{Cu}_{\text{Ga}}\text{P}_{\text{Ga}}$ pairs. [24,25] (Fig. 4) These correspond to excited triplet BE states,

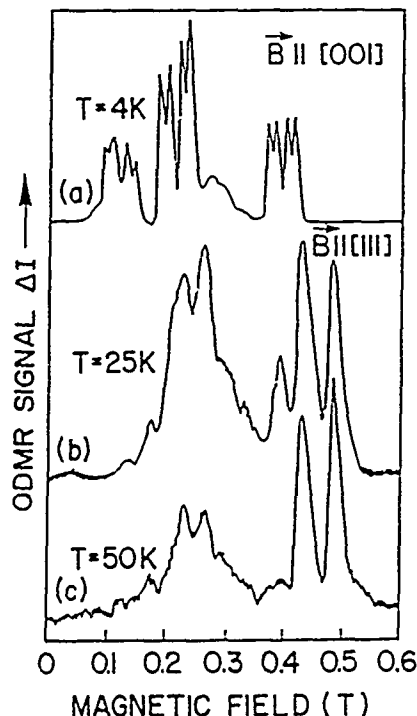


Figure 4: ODMR spectra for Cu-Li diffused GaP, showing triplet resonances for three different $\text{P}_{\text{Ga}}\text{-Cu}_{\text{Ga}}$ related complex defects. The central hyperfine interaction for P_{Ga} is clearly resolved in all cases, but is of varying magnitude for the different defects.

formed via exchange interaction between a spin-like electron and a spin-like hole. [7] The ground state is in all cases deep around midgap, and is diamagnetic, $S=0$. This means that the two extra electrons in the P_{Ga} can be assumed to fill in the missing bond electrons due to the nearby Cu_{Ga} . In the excited BE state there is evidence that both carriers are strongly localized, the electron probably more than the hole. [26] Therefore, in fact, these ODMR data do not give a clear indication whether the ground state observed is connected with a $(o/+)$ level or a $(-/o)$ level, in the absence of theoretical calculations. The fact that rather strong hyperfine (HF) splitting from P_{Ga} is observed for the electron in the BE (Fig. 4), and no such splitting for the hole, argues for a $(-/o)$ ground state level above midgap.

IV.B. Ga-interstitial related complexes in GaP

Some years ago a triplet resonance ODMR signal was reported in O-doped GaP [27,28], and tentatively related to the O^- charge state of the substitutional O donor, in a relaxed configuration. The resonance shows a clear HF splitting for a single Ga atom, and was recently reinterpreted as due to a complex involving Ga_i , $\text{Ga}_i\text{-X}$. [29] Here X is an unknown acceptor-like component, possibly a shallow acceptor. The experiences with this defect show the importance of excitation transfer in interpreting ODMR spectra for excited states of

complex defects. [30,31,32] The defect gives rise to a deep PL band with a near-midgap ground state level, presumably a $(-/o)$ level due to the strong potential of the Ga_i atom. A similar deep PL band was recently reported for Cu-doped GaP, (Fig. 5) with an even larger Ga_i -related HF splitting in the ODMR triplet resonance spectrum. [33] Thus there seems to be a family of Ga_i -related complexes with deep $(-/o)$ levels just above midgap in GaP.

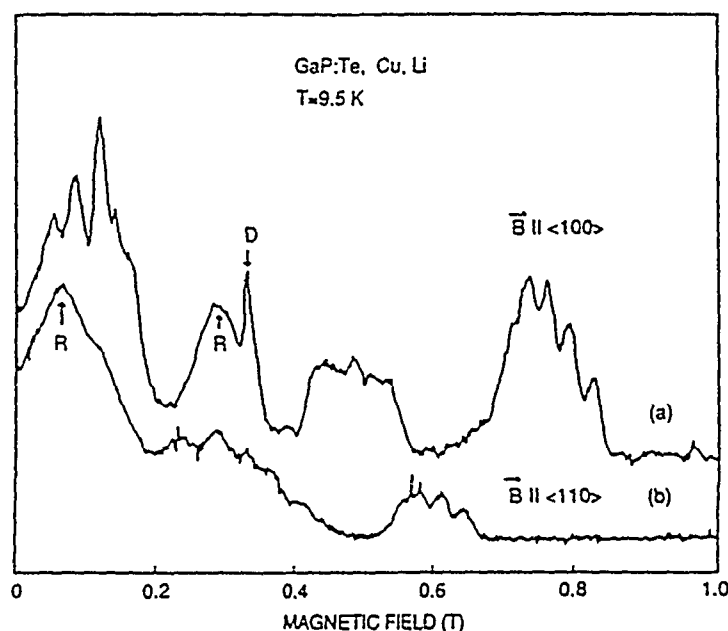


Figure 5: ODMR spectra for the Ga_i -Y defect in GaP taken at 9.5K and 9.2 GHz. A triplet resonance is observed where the Ga_i -related central hyperfine splitting is clearly resolved. Features D and R do not belong to the triplet spectrum.

IV.C. An S-related complex defect in silicon

Chalcogen donors in silicon have been studied in great detail in recent years, as model deep donors, both theoretically [3,4] and experimentally. [35,36] Complexes occur as pairs of such deep donors, and it has been shown theoretically that these chalcogen pairs are substitutional pairs. [34] Experimentally it has been shown e.g. that the S_2 pair donor is a trigonal deep double donor, with an energy $1sA_1^+$ ($o/+$) at 187.61 meV at low temperature. [36] Theoretically another deep $1sA_1^-$ ($o/+$) level is predicted in the lower part of the energy gap [38], since, in fact, in total four electrons are left over in the neutral S_2 -donor, i.e. they are not needed for bonding to the surrounding silicon atoms (Fig. 6a). It has recently been discovered that S-doped silicon appears to have novel interesting optical properties. Two BE spectra have been observed at low temperature, with no-phonon triplet energies $S_A^o=968.24$ meV and $S_B^o=811.96$ meV, respectively. [38] It has been shown that these BE's belong to two different configurations of the same S-related defect. [39] The defect has recently been tentatively identified as the S_2 pair defect [40], from the spectroscopic fingerprint that $S_A^o-S_B^o=156.28$ meV is indeed very close to the energy difference between the previously studied levels for the A_1^+ ($o/+$) donor level, i.e. $1s(E^-)-1sA_1^+=156.35$ meV. [36] Preliminary ODMR data have shown that the excited BE states have slightly different symmetries [41], but the binding energies for the pseudodonor electrons are in both cases very similar, close to 66

meV. [38] The ground state is supposed to have the trigonal symmetry of S_2^+ , although in fact for the S_B BE the ground state has one of the donor electrons excited to the $1sE^-$ state, stabilized by an additional distortion. If this tentative model is correct, it leads to an accurate determination of the $1sA_1^-$ ($o/+$) level as $E_v + 0.137$ eV (Fig. 6b). Similar optical properties seem to be present for the Se_2 pair in silicon. [42]

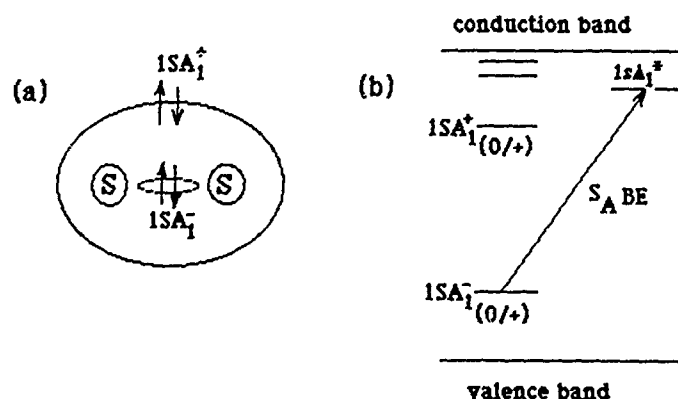


Figure 6: (a) Schematic picture of the neutral ground state configuration of the S_2 pair in silicon. (b) Simplified one-electron energy level diagram for the S_A excitation of the neutral S_2 pair defect.

IV.D. The deep 0.615 meV pseudodonor BE in silicon

Another deep BE spectrum in highly C-doped electron-irradiated Cz silicon has recently been studied in some detail. It has a BE zero phonon line at 0.615 eV at 2K, belonging to a metastable configuration that can be created by optical band gap excitation below 70K. [43] The defect is tentatively identified as a C_iO_i -related neutral complex, with a ($o/+$) energy level at about $E_v + 0.34$ eV, very similar to the ($o/+$) energy level of the C-line defect, also C_iO_i -related. [48] The mechanism of the transfer into the metastable configuration at low T is suggested to be the free exciton Auger recombination, which assists in the reorientation of the defect. [45] An interesting aspect of the optical spectrum of this defect, as shown in Fig. 7, is the demonstration of a deep ($o/+$)* pseudo-donor level. The $1sA_1$ level of the pseudodonor is situated at 0.615 eV above the ($o/+$) ground state level, but higher s-like excited pseudodonor states are observed at around 0.780 eV, $1s(E+T_2)$, at 0.784 eV, $2s(A_1)$ and at 0.802 eV, $2s(E+T_2)$. The splitting pattern of these states is consistent with a low-defect symmetry. The ionization edge is determined as 0.811 eV, meaning a pseudo-donor binding energy of 0.196 eV at 2K, the deepest pseudo-donor state so far established in silicon.

The defects discussed above under IV C and D have the property in common that they have a ($o/+$) level deep in the gap, which is not a normal deep donor state, but rather a state related to the capture of a hole to the defect, in the process of creating the BE. This strongly localized hole in low symmetry is then naturally spin-like giving rise to a BE

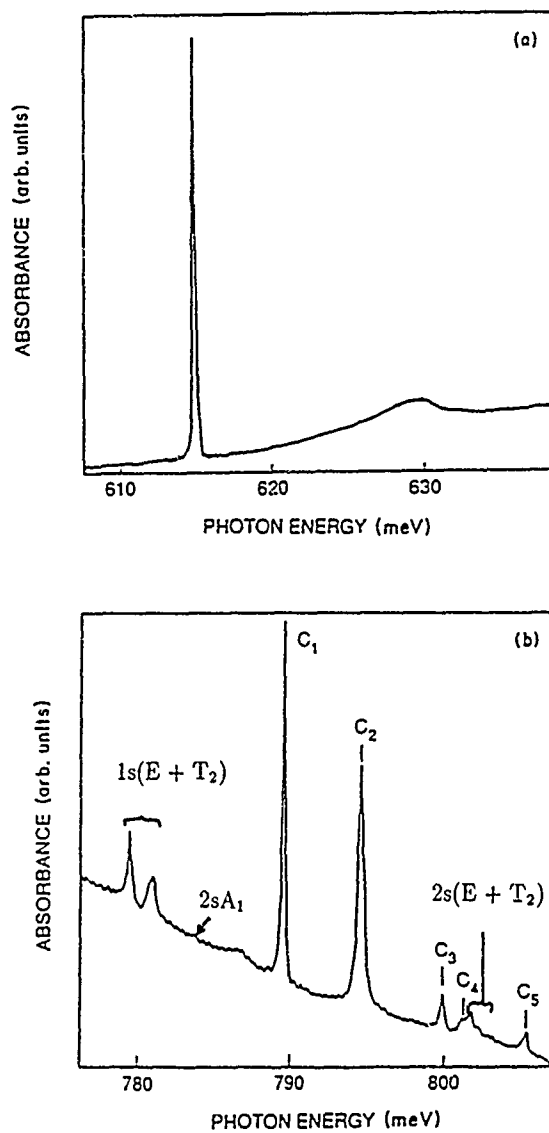


Figure 7: Absorption spectrum of an electron-irradiated Cz silicon sample after 30h excitation at 4K with band gap light. (a) The no-phonon region showing the 0.615 eV no-phonon BE line. (b) Excited states related to the pseudo-donor $1sA_1$ ground state. The lines marked C_1 - C_5 belong to another defect, the so-called C-line defect [19].

electronic structure as a triplet-singlet (TS) pair at lowest BE energy. [7] The fact that in many cases for BE's in silicon only the singlet (and not the triplet) is observed in PL spectra is not yet fully explained, but may be due to either a small TS energy splitting, so that the weak T-state is always thermalized into the S-state, or the T-state may sometimes have a completely forbidden optical transition probability to the ground state. [46] The majority of defect BE lines observed in silicon are within this BE category, i.e. they show either triplet or singlet character for the lowest electronic BE PL line.

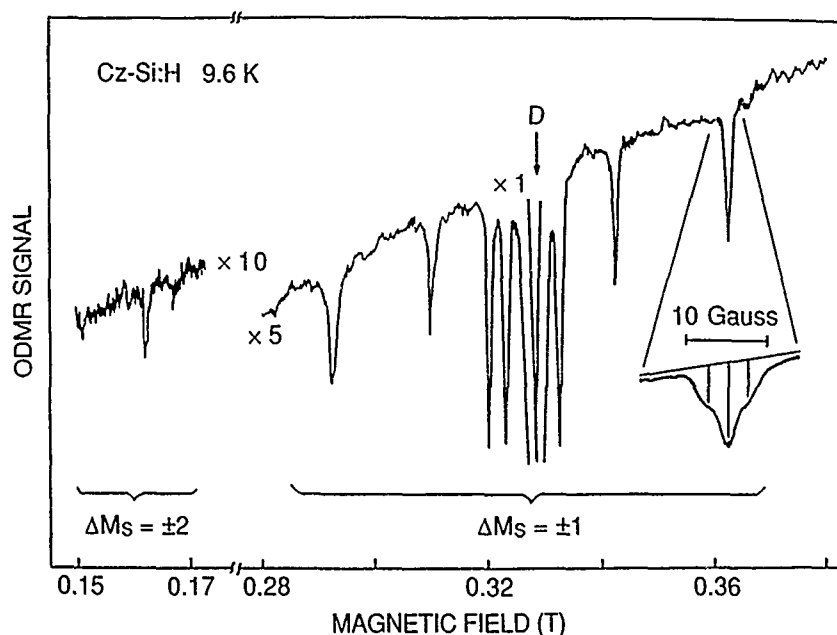


Figure 8: ODMR spectrum for the so-called HVH complex in silicon, showing a negative triplet spectrum, with resolved hyperfine splitting tentatively assigned to two ^1H atoms (see inset).

IV.E. A hydrogen-vacancy complex in silicon?

Hydrogen is known to passivate both shallow and deep defects in silicon, by complex formation. Only in a few cases have the structure of these complexes been suggested from experimental data, however. [47] Recent ODMR studies of the H_2 plasma-treated silicon reveals a strong triplet ODMR spectrum (Fig. 8), with rather sharp lines, which have hyperfine (HF) satellites suggested to be due to interaction of the electronic spin with two hydrogen nuclei. [48] The spectrum also reveals a C_{2v} symmetry, as expected for a vacancy in the neutral charge state, if two of the dangling bonds are rebonded, and the other two are saturated with two H atoms, i.e. the HVH configuration schematically depicted in Fig. 9a. It should be pointed out that this model is still tentative, and further experiments are in progress. The electronic structure of the defect can be understood in terms of an excited $(\sigma/+)^*$ level, where a hole is created in the distorted bond of the defect, and the corresponding electron is instead occupying an antibonding state. (Fig. 9b) The position in the energy gap of these levels has so far not been obtained experimentally, so even the model of the electronic structure should be regarded as tentative.

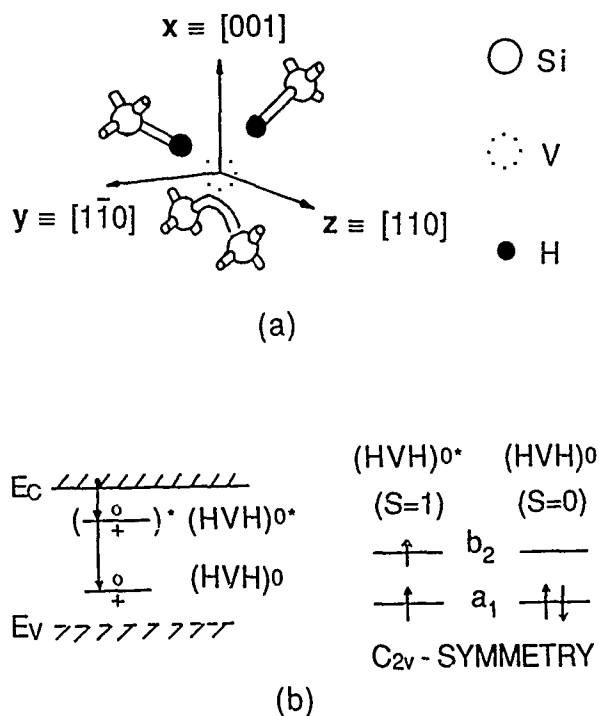


Figure 9: (a) Schematic model for the geometry of the so-called HVH defect in silicon (b) Suggested electronic structure for the HVH defect, related to the ODMR observations.

V. SUMMARY AND CONCLUSIONS

The above discussion of some simple elements of the electronic structure of complex defects, exemplified by a set of recent experimental data for a number of neutral such defects, is intended to give the impression that complex defects must be discussed within the framework of deep level theory. There is in general a lack of sufficiently accurate determination of the geometrical and electronic structure of such defects. Recently progress has been made on both the identification part and the electronic structure, in particular from accurate experiments on ir transmission and ODMR, as partly demonstrated in this work. We feel we are, in fact, rapidly approaching the situation where a number of simple examples of complex defects will be identified with a reasonable degree of confidence, regarding both their geometrical and electronic structure.

ACKNOWLEDGEMENTS

It is a pleasure to acknowledge the cooperation of a large number of people in the research work behind this report. Apart from the supply of the experimental data presented and referred to here, useful discussions were held particularly with W.M. Chen, H.P. Gislason, E. Janzén, M. Godlewski, P.O. Holtz, J. Svensson, O.O. Awadelkarim and A. Henry.

References

- [1] For an update on the present status of research on shallow impurities see e.g. Proc. 3rd Intl. Conf. on Shallow Impurities in Semiconductors, Linköping, Sweden, Aug. 1988, Inst. Phys. Conf. Ser. 95, 1988, ed. B. Monemar.
- [2] For a recent review on deep levels see e.g. S.T. Pantelides, Deep Centers in Semiconductors (Gordon and Breach, New York, 1986).
- [3] B. Monemar, CRC Critical Reviews on Solid State and Materials Sciences 15, 111 (1988).
- [4] G.A. Baraff and M. Schlüter, Phys. Rev. B33, 7346 (1986).
- [5] R. Car, P. Kelly, A. Oshiyama, and S.T. Pantelides, Phys. Rev. Lett. 52, 1814 (1984).
- [6] J. Dabrowski and M. Scheffler, Phys. Rev. Lett. 60, 2183 (1988); D.J. Chadi and K.J. Chang, Phys. Rev. Lett. 60, 2187 (1988).
- [7] B. Monemar, U. Lindefeit, and W.M. Chen, Physica 146B, 256 (1987).
- [8] B.C. Cavenett, Adv. in Phys. 30, 475 (1981).
- [9] W.M. Chen, B. Monemar, and M. Godlewski, Defect and Diffusion Forum, 62/63, 133 (1989).
- [10] K. Khachatryan, M. Kaminska, E.R. Weber, P. Becla, and R.A. Street, Phys. Rev. B40, 6304 (1989).
- [11] P.J. Dean, "Luminescence of Crystals, Molecules and Solutions", ed F. Williams, (Plenum, New York, 1973) p. 538.
- [12] G.D. Watkins and J.W. Corbett, Phys. Rev. 121, 1001 (1961); J.W. Corbett, G.D. Watkins, R.M. Crenko, and R.S. McDonald, Phys. Rev. 121, 1015 (1961).
- [13] K.L. Brower, Phys. Rev. Lett. 44, 1627 (1980); Phys. Rev. B26, 6040 (1982).
- [14] G.D. Watkins and J.W. Corbett, Phys. Rev. 138, A543 (1965).
- [15] D.G. Thomas and J.J. Hopfield, Phys. Rev. 155, 680 (1966).
- [16] T.N. Morgan, B. Welber, and R.N. Bhargava, Phys. Rev. 166, 751 (1968); C.H. Henry, P.J. Dean, and J.D. Cuthbert, *ibid.*, 166, 754 (1968).
- [17] G.W. Ludwig and H.H. Woodbury, Solid State Physics, Vol. 3 (Academic Press, New York, 1962) p. 223.
- [18] R. Sauer in Microscopic Identification of Electronic Defects in Semiconductors, edited by N.M. Johnson, S.G. Bishop, and G.D. Watkins (Materials Research Society Proc. 46, Pittsburgh, PA 1987) p. 507.
- [19] G. Davies, Physics Reports 176, 83 (1989).
- [20] G.D. Watkins, Proc. 15th Int. Conf. on Defects in Semiconductors, Budapest, Aug. 22-26, 1986, G. Feenczi, ed., Materials Science Forum 38/41, p. 39.
- [21] G.D. Watkins, Proc. 14th Int. Conf. on Defects in Semiconductors, Paris, Aug. 18-22, 1986, H. von Bardeleben, ed., Materials Science Forum 10/11, p. 953.
- [22] G. Grossman, K. Bergman, and M. Kleverman 146B, 30 (1987).
- [23] U. Kaufmann, J. Schneider, and A. Räuber, Appl. Phys. Lett. 29, 312 (1976).

- [24] W.M. Chen, H.P. Gislason, and B. Monemar, Phys. Rev. B36, 5058 (1987).
- [25] W.M. Chen, B. Monemar, and M. Godlewski, Phys. Rev. B37, 2564 (1988).
- [26] M. Godlewski, W.M. Chen, and B. Monemar, Defect and Diffusion Forum, 62/63, 107 (1989).
- [27] M. Gal, B.C. Cavanett, and P. Smith, Phys. Rev. Lett. 43, 1611 (1979).
- [28] M. Gal, B.C. Cavanett, and P.J. Dean, J. Phys. C14, 1507 (1981).
- [29] M. Godlewski and B. Monemar, Phys. Rev. B37, 2752 (1988).
- [30] M. Gal, Phys. Rev. B39, 10422 (1989).
- [31] M. Godlewski and B. Monemar, B39, 10424 (1989).
- [32] M. Godlewski, W.M. Chen, and B. Monemar, Phys. Rev. B37, 2570 (1988).
- [33] W.M. Chen and B. Monemar, Phys. Rev. B40, 1365 (1989).
- [34] C.M. Weinert and M. Scheffler, Phys. Rev. Lett. 58, 1456 (1987).
- [35] G.W. Ludwig, Phys. Rev. 137, A 1520 (1965).
- [36] E. Janzèn, R. Stedman, G. Grossmann, and H.G. Grimmeiss, Phys. Rev. B29, 1907 (1984).
- [37] O.F. Sankey and J.D. Dow, Phys. Rev. B26, 3243 (1982); G. Kim, J.D. Dow, and S. Lee, Phys. Rev. 1340, 7888 (1989).
- [38] D.S. Beckett, M.K. Nissen, and M.L.W. Thewalt, Phys. Rev. B40, 9618 (1989).
- [39] M. Singh, E. C. Lightowlers, and G. Davies, Proc. E-MRS 1989 Spring Meeting, May 30-June 2, Strasbourg, France, (in press).
- [40] E. Janzèn, A. Henry, W.M. Chen, and B. Monemar, (unpublished).
- [41] W.M. Chen, A. Henry, E. Janzèn, B. Monemar, and M.L.W. Thewalt, (these proceedings).
- [42] P.L. Bradfield, T.G. Brown, and D.G. Hall, Phys. Rev. B38, 3533 (1988).
- [43] J.H. Svensson and B. Monemar, Phys. Rev. B40, 1410 (1989).
- [44] K. Thonke, G.D. Watkins, and R. Sauer, Solid State Commun. 51, 127 (1984).
- [45] J.H. Svensson and B. Monemar, (these proceedings).
- [46] K. Thonke, A. Hangleiter, J. Wagner, and R. Sauer, J. Phys. C18, L795 (1985).
- [47] S.J. Pearton, J.W. Corbett, and T.S. Shi, Appl. Phys. A43, 153 (1987).
- [48] W.M. Chen, O.O. Awadelkarim, B. Monemar, J.L. Lindström, and G.S. Oehrlein, (unpublished).

THE ELECTRONIC STRUCTURE OF INTERSTITIAL IRON IN SILICON

A THILDERKVIST, G GROSSMANN, M KLEVERMAN, AND H G GRIMMEISS
Department of Solid State Physics, University of Lund, Box 118, S-221 00 Sweden

ABSTRACT

A donor-like spectrum in Fe-doped silicon has been studied by means of high-resolution Zeeman spectroscopy. Previous work had unambiguously identified the center as the interstitial iron impurity and the spectrum was interpreted as due to the transitions $\text{Fe}_i^0 + h\nu \rightarrow \text{Fe}_i^+ + e^-$, where an electron is excited to shallow effective-mass-like donor states. In this paper, we can, by studying the transitions in a magnetic field, verify the effective-mass-like character of the loosely bound electron. Furthermore, we also obtain information on the impurity core whose level structure is reflected in the observed superposition of donor-like Rydberg series and whose g values determines the Zeeman splitting pattern.

INTRODUCTION

The electronic properties of the transition metal (TM) impurities in silicon have attracted considerable interest, both experimentally and theoretically, since the pioneering electron-paramagnetic resonance (EPR) work by Ludwig and Woodbury in the early 60's [1]. The theoretical understanding of TM impurities has increased during the last years and it is no exaggeration to state that a basic understanding has been achieved [2]. Nevertheless, experiments reveal many finer structures which are still impossible to predict on theoretical grounds, e. g. symmetry-breaking lattice distortions; nor can the energy-level structure be calculated with an accuracy comparable to experimental observations. Transmission spectroscopy has proven to be a valuable tool for gaining deeper insight into the electronic structure of TMs in silicon. No internal d transitions have yet been identified and the optical transitions so far assigned are from a localized ground state to shallow donor or acceptor like states.

Recently, the observation of a Fe-related line spectrum in silicon was reported [3]. An isochronal annealing experiment performed on the same sample in both EPR and transmission showed that the lines originate from transitions at the neutral charge state of interstitial Fe, Fe_i^0 . Furthermore, the photoionization cross section for electrons was measured by photo-EPR and photoconductivity, and compared with previously published junction space charge results. The excellent agreement between the different results showed that the same center was probed by the three methods. The most intense lines were well accounted for by assuming two superimposed shallow donor-like spectra. Additional, weaker lines, indicated that also a third series may be involved.

Considering the delocalization of the electron in one of the shallow-donor states, it is reasonable to assume that the interaction between the core and the excited electron is negligible. Therefore, it should be feasible to consider the final state as built up from two decoupled systems: a shallow-donor electron and the Fe_i^+ core. The origin of the superimposed spectra was tentatively assigned to shake-up effects in the final core state, i.e. different energy levels of the core may be reached in the optical transitions.

In this paper we report on new transmission studies of the interstitial iron impurity in silicon using Zeeman spectroscopy. The objective is to identify the origin of the different superimposed spectra by studying their behavior in a magnetic field, i.e. to identify the donor character of the excited states and to obtain information on the g -values of the initial and final core states.

EXPERIMENTAL

Sample preparation

Iron was introduced into orientated and polished silicon samples by means of sol-

id state diffusion. After evaporation of Fe onto one of the optically inactive sample surfaces, the samples were put into quartz ampoules which then were evacuated and sealed off. After heat treatment in 1250 °C for 2h the samples were quenched in pump oil or ethylene glycole.

Experimental methods

The transmission spectra were obtained with a Bomem DA3-02 FTIR spectrometer equipped with a liquid-nitrogen cooled InSb-photodiode detector. The appodized resolution was 0.5 or 1 cm^{-1} . A Leybold-Heraeus continuous-flow cryostat was used. In the Zeeman experiments, an Oxford Instruments spectromagnet was used in the Voigt configuration and the maximum magnetic field was 6.5T. Different optical filters and polarizers were made use of when necessary. The absorption signal is about 0.2% and therefore, the original transmission spectrum was divided by an artificial background in order to increase the transparency of the spectrum.

THEORY

The EPR spectra of Fe_i^0 and Fe_i^+ are well understood in terms of the Ludwig-Woodbury (L-W) model [1]. According to this model, the atomic d-state is split by the crystal field into an e and a t_2 state, the e state being found at an energy Δ_{CF} above the t_2 state and these orbitals are filled successively in such a way that the electron configuration gives maximum spin (Hund's rule) while obeying the exclusion principle. In the case of Fe^0 , the configuration is $t_2^6 e^2$. The t_2 subshell is filled and the six t_2 electrons form an 1A_1 term, whereas the two e electrons result in a 3A_2 term. Altogether, a 3A_2 term is found as the ground state for Fe^0 . In the case of Fe^+ , one of the t_2 states is unoccupied and the five t_2 electrons give rise to a 2T_2 term and, hence, the ground state is 4T_1 (Hund's rule). This model has proven to give a satisfactory interpretation for the observed EPR spectra of interstitial TM impurities in silicon.

Recent calculations [2,4] show that the success of this model is more or less accidental in the case of the t_2 state. The dt_2 state is hybridized with p-like t_2 valence-band states and, hence, the t_2 gap level has both d and p character and the latter increases with decreasing atomic number of the impurity. This leads to a delocalization of the t_2 gap state. On the other hand, the e state is localized and d like. The L-W model may still be used but the hybridization leads to e.g. a quenching of the orbital g value.

Including spin-orbit interaction, the 3A_2 term results in a three-fold degenerate T_2 level as the ground state for Fe_i^0 whereas the 4T_1 term of Fe_i^+ is split into three levels: Γ_6 ($J=1/2$), Γ_8 ($J=3/2$), and $\Gamma_7 + \Gamma_8$ ($J=5/2$). Here the Γ_i 's are irreducible representations of the tetrahedral double group and the J values are given for comparison with an atomic P level spin-orbit coupled to a spin $S=3/2$. The g values of T_2 (3A_2) and Γ_6 (4T_1) have been experimentally determined by EPR whereas theoretical estimates exist for all levels of 4T_1 [2,4].

Zeeman effect for shallow donors

In silicon, due to the anisotropy of the effective mass of the conduction band minima, only parity and the projection of angular momentum along the principal axis of the ellipsoidal constant-energy surface remain good quantum numbers for the eigenfunctions of the effective-mass Hamiltonian. Thus the hydrogenic degeneracy of e.g. the np_0 ($m=0$) and the np_{\pm} ($m=\pm 1$) states is lifted. In the following analysis we will focus on these p-like states as the valley-orbit interaction is expected to be

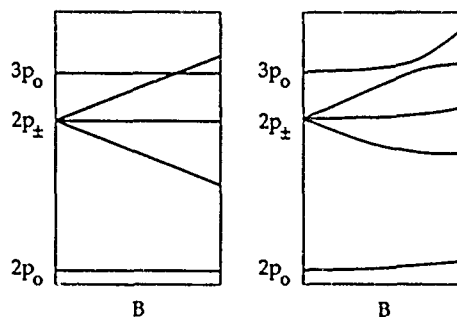


Fig. 1. Schematic linear (left) and quadratic (right) Zeeman splitting pattern of shallow donor states in a magnetic field B. For clarity splittings due to spin are omitted.

negligible for these states, in contrast to s-like states, and thus their characteristic energy spacing, well predicted by effective-mass theory (EMT), is important for the identification of Rydberg series of a donor.

In a homogeneous magnetic field, the p_{\pm} states of a given valley will suffer a linear splitting which is proportional to the projection of the field direction along the principal axis of the ellipsoid [5]. This splitting, inversely proportional to the transverse effective mass, is large and thus easily distinguished from the expected splitting of the Fe core states.

At higher magnetic fields, terms quadratic in B become increasingly important and lead, in lowest order, to quadratic shifts of all states. Pajot *et al.* [6,7] have studied the quadratic Zeeman effect for phosphorus in silicon and find a satisfactory agreement between experiment and theory, when evaluating the effect of the magnetic field by perturbation theory. Higher order terms are small and only become important when they couple states shifted into near-resonance, where they lead to a characteristic avoided-crossing behavior. The linear and quadratic behavior of np states is shown schematically in Fig. 1, where the additional splittings due to spin are excluded for clarity. (For the shallow donor spectra reported for phosphorus these spin splittings cancel.)

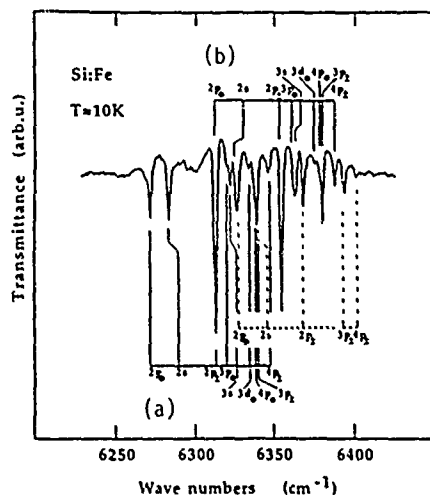


Fig. 3. Transmission spectrum of Si:Fe for zero magnetic field taken from Ref. 3. (a) and (b) denote the two main Rydberg series, while the assignment of the third series (dashed lines) is less certain.

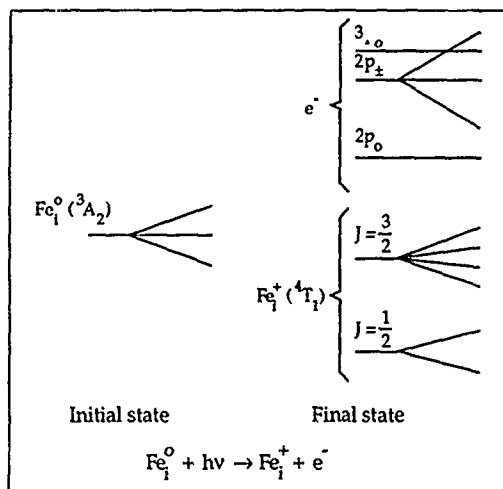


Fig. 2. Schematic Zeeman splitting pattern for the Fe core in its initial and final states and for the excited electron in shallow donor states. For clarity, spin splittings for these donor states have been omitted, also not shown is the $J=5/2$ level of the $4T_1$ term.

Zeeman effect for Fe donor

Superimposed on the Zeeman splitting of the shallow donor states of the excited electron, which also must include the splitting due to its spin, we expect to observe the Zeeman effect for the Fe core in both initial and final states ($\text{Fe}_i^0 + h\nu \rightarrow \text{Fe}_f^+ + e^-$) as shown schematically in Fig. 2. Different core levels may lead to a superposition of Rydberg series. Assuming the behavior of the shallow donor electron known, one can thus from the observed Zeeman pattern deduce information on the Zeeman splitting of those levels of the Fe core, which are involved in the transition responsible for a given line.

EXPERIMENTAL RESULTS

In Fig. 3 the transmission spec-

trum at zero magnetic field is presented as well as the previous assignment of the lines [3]. From the line spacings, we can identify two main Rydberg series superimposed, which are very similar also in their relative intensities. The $2p_0$ line of the higher series (b) and the $2p_{\pm}$ line of the lower (a) series coincide and are not resolved. The third series is less certain and also the present Zeeman results, although rather ambiguous for these lines, raise further doubts.

Fig. 4 shows the transmission spectra for increasing magnetic fields. The $2p_{\pm}$ lines are seen to split strongly as do the corresponding lines of shallow donors, whereas the smaller splittings, e.g. of the $2p_0^a$ state, must be attributed to the Fe core. As the measurements were done at very low temperature ($T=1.8K$) and extend to rather high magnetic fields, in general only the lowest split component of the initial core state will be populated. We thus do not expect to observe the initial state splitting, only its shift. For the lowest fields and their correspondingly small splittings we do, however, observe weak thermalization effects, i.e. weaker lines lying towards lower energies and rapidly decreasing in intensity. Hence, the multiplicity of the Rydberg series and the Zeeman shifts and splittings observed - apart from those of the shallow donor states and the shift of the initial state component which is common to all lines - should reflect the electronic structure of the final state of the core.

To analyze the data we assume the first Rydberg series to be due to transitions to the $J=1/2$ level of the final state core, i.e. the ground state of Fe_i^+ observed in EPR. The g values for the initial state core (3A_2) and all levels of the final state core (4T_1) have been calculated by Katayama-Yoshida and Zunger [2,4] and agree in those cases they have been observed, (3A_2) and $J=1/2(^4T_1)$, well with experiment. We first consider the $2p_0^a$ line. The shallow $2p_0$

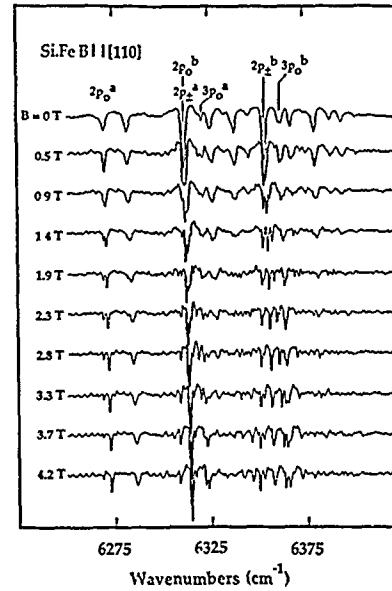


Fig. 4. Transmission spectra of Si:Fe for increasing magnetic fields.

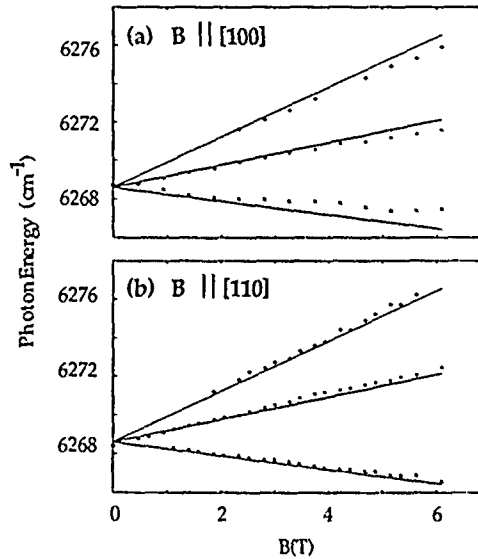


Fig. 5. Zeeman splitting of the $2p_0^a$ line for magnetic field (a) $B \parallel [100]$ and (b) $B \parallel [110]$. The lines show the behavior expected from the model explained in the text.

state only splits due to the electronic spin, its quadratic Zeeman shift is negligible. The two spin states and the two $J = 1/2$ states lead to four possible transitions with different energies. Given that the initial state is a single shifted component of (3A_2), however, only three have non-vanishing matrix elements and of these the central line is expected to be the strongest by about a factor of four. Fig. 5 shows the line positions as a function of magnetic field in two directions ([100] and [110]) together with the parametrization of our model based

on the core g factors. The $2p_{\pm}^a$ line splitting is found to be closely isotropic and well accounted for, and also the relative intensities follow the expected trends.

To account for the splitting of the $2p_{\pm}^a$ line shown in Fig. 6 we have to include the quadratic shift of the shallow $2p_{\pm}$ state which we assume to be equal to that obtained for phosphorus in silicon by Pajot *et al.* [7]. Furthermore, the interaction with the $3p_0$ state is simply modeled by an effective coupling constant obtained by fitting to the data. The $2p_0^b$ line is expected to lie very close to the $2p_{\pm}^a$ line and its splitting pattern will be superimposed on that of the central $2p_{\pm}^a$ lines. For these lines the data are not as clearly resolved and their detailed interpretation remains ambiguous. Thus, Fig. 6 only shows the predicted behavior of those lines, which result from the split $2p_{\pm}$ donor states, and their interaction with the $3p_0$ lines. Not all lines are resolved in experiment but the lines expected to be strong are clearly identified. The fact that the quadratic behavior, including the $2p_{\pm} - 3p_0$ interaction, agrees well with that of phosphorus confirms that we observe a donor in its neutral charge state. For a donor in its positive charge state with its less extended excited states, the quadratic shifts become much smaller, as is indeed observed for Si:Mg⁺ [8]. Furthermore, all three lines, $2p_0^a$, $2p_{\pm}^a$, and $3p_0^a$, agree in their energy spacing with neutral donor states and the fact that their Zeeman behavior can be understood by taking into account the g factors of the assumed core states, strongly favors our interpretation that the transitions lead from a 3A_2 component to a $J=1/2(^4T_1)$ core state.

Also for the $2p_{\pm}^b$ and $3p_0^b$ lines the energy spacing was the basis for their assignment, and in Fig. 7 we again observe the same quadratic shifts as for the corresponding (a) lines and also the characteristic interaction between the $2p_{\pm}^b$ and $3p_0^b$ lines. Although the $2p_0^b$ line is not observed distinctly, there thus seems to be little doubt as to the identification of the second series (b). If we take the same initial state as for the (a) series discussed above and assume the final state of the core to have $J = 3/2$, an analysis of matrix elements predicts each shallow-donor line to split into five lines, of which two are expected to be stronger than the others. As seen in Fig. 7, this model seems to be able to account for the observed lines, but lack of resolution makes a definite assignment impossible. An immediate question raised by this interpretation is, of

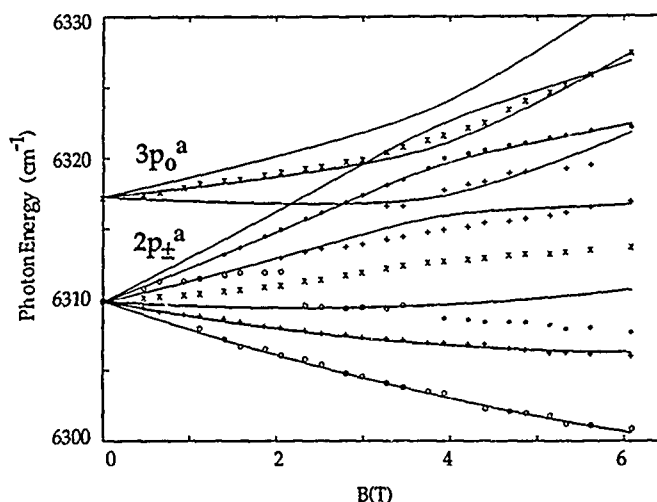


Fig. 6. Zeeman splitting of the $2p_{\pm}^a$ and $3p_0^a$ lines for magnetic field $B \parallel [110]$. The solid lines show the splitting expected for transitions involving the $3p_0$ and the split $2p_{\pm}$ donor states assuming a $J=1/2$ final-state core as explained in the text. The only adjustable parameter, the $2p_{\pm}^a - 3p_0^a$ coupling, was obtained by fitting to the data.

course, why the final-state core level with $J=5/2$ is not seen. While the assignment of the (b) Rydberg series thus is quite certain, the detailed interpretation of the core states involved in the transitions must remain tentative.

DISCUSSION

The present study gives strong evidence for two Rydberg series, (a) and (b), associated with the neutral charge state of the Fe_i donor. Both energy spacings and Zeeman patterns of well-resolved lines agree in detail with the shallow donor phosphorus. No characteristic $2p_{\pm}$ splitting associated with a third series, however, is observed.

The overall Zeeman behavior supports the assumption that the initial state of the transitions involves one component of the 3A_2 term which is shifted towards lower energy by the magnetic field and the data are consistent with the g value obtained in EPR. Assuming further a $J=1/2$ (4T_1) final-state core, its experimental g value can account for the $2p_o^a$, $2p_{\pm}^a$, and $3p_o^a$ lines (only disregarding their weak interaction), the most prominent features of the (a) series. For the (b) series a $J=3/2$ final-state core seems possible but no definite statement can be made at present.

ACKNOWLEDGMENTS

The authors would like to thank J. Olajos for experimental assistance, L. Timby and E-L Hellquist for preparing the samples, and the Swedish Board for Technical Developments and The Swedish Natural Science Research Council for financial support.

REFERENCES

1. G. W. Ludwig and H. H. Woodbury, *Solid State Phys.* 13, 223 (1962)
2. A. Zunger, *Solid State Phys.* 39, 275 (1987)
3. J. Olajos, B. Bech Nielsen, M. Kleverman, P. Omling, P. Emanuelsson, and H.G. Grimmeiss, *Appl. Phys. Lett.* 53, 2507 (1988)
4. H. Katayama-Yoshida and A. Zunger, *Phys. Rev.* B31, 8317 (1985)
5. R.R. Haering, *Can. J. Phys.* 36, 1136 (1958)
6. B. Pajot, F. Merlet, G. Taravella, and Ph. Arcas, *Can. J. Phys.* 50, 1106 (1972)
7. B. Pajot, F. Merlet, G. Taravella, *Can. J. Phys.* 50, 2186 (1972)
8. M. Kleverman, A. Thilderkvist, G. Grossmann, and H.G. Grimmeiss (unpublished)

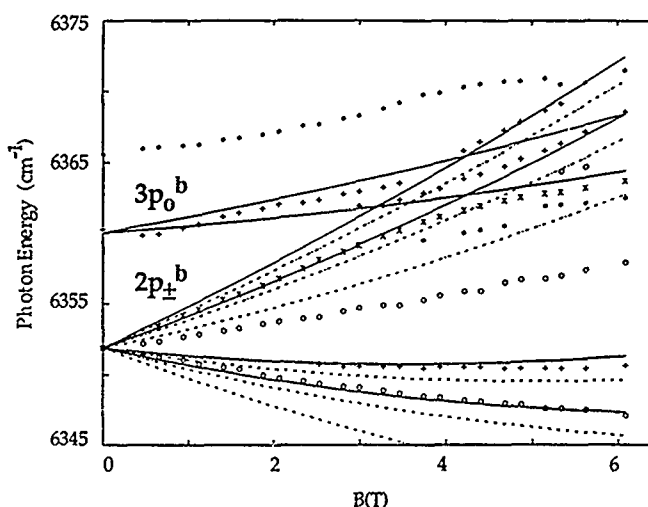


Fig. 7. Zeeman splitting of the $2p_{\pm}^b$ and $3p_o^b$ lines for magnetic field $B \parallel [110]$. The solid (dashed) lines show the splitting expected for stronger (weaker) transitions involving $3p_o$ and the split $2p_{\pm}$ donor states assuming a $J=3/2$ final-state core as explained in the text. For $3p_o^b$ only the stronger lines are indicated (solid) and no $2p_{\pm}^b - 3p_o^b$ interaction is included.

DISLOCATION RELATED D-BAND LUMINESCENCE; THE EFFECTS OF TRANSITION METAL CONTAMINATION

VICTOR HIGGS*, E.C. LIGHTOWLERS* AND P. KIGHTLEY**

*Physics Department, King's College London, Strand, London WC2R 2LS, UK

**Plessey Research (Caswell) Ltd, Caswell, Towcester, Northants NN12 8EQ, UK

ABSTRACT

Photoluminescence measurements have been made on plastically formed silicon, free from metal contamination, with dislocation densities in the range 10^4 - 10^8 cm^{-2} . Only after deliberate contamination with Cu, Fe or Ni were the dislocation related D-bands the dominant spectral features observed. TEM analysis has revealed that there are no differences in the dislocation structures before and after contamination and that there is no evidence for precipitation on the dislocations or in their strain fields. The D-band features may, therefore, be due to impurities (metal atoms or point defect complexes) trapped in the strain fields of the dislocations.

INTRODUCTION

A considerable effort has been devoted to the study of the D-band luminescence features which are associated with the presence of dislocations in silicon. This work has been directed mainly towards relating particular luminescence features with particular dislocation types and understanding the nature of the electronic transitions involved^[1]. A similar but more limited investigation has been made of dislocation related luminescence in germanium^[2] and very recently in Si/Ge alloys.^[3]

D-band features are observed in silicon containing dislocations, either as grown in, or generated by plastic deformation produced by uniaxial stress or bending. Four principal bands are observed: D1 at 812meV, D2 at 875meV, D3 at 934meV and D4 at 1.0eV ^[4]. Detailed luminescence studies^[1] have shown that the bands D1 and D2 exhibit similar behaviour and also D3 and D4. It has been suggested that D1 and D2 may be either associated with point defects in the strain fields of the dislocation or related to kinks on the dislocations^[5], whereas D3 and D4 have been ascribed to electronic transitions within the dislocation core structure.

Dislocation luminescence has been observed in silicon grown by MBE and has been investigated in some detail by Robbins et al^[6]. In a more recent investigation of epitaxial layers grown by MBE^[7], where the dislocation densities were found to be in the range 10^3 - 10^5 as determined by defect etching, we were puzzled by the absence of any of the D-band luminescence features in the as-grown material. In the course of this work it became clear that the D-band luminescence could be produced by deliberate contamination with transition metals, in particular Cu, Fe and Ni. Although the nature of the transition metal did not have a significant effect on the shapes and energies of the D-bands, it was suggested that the luminescence might be associated with transition metal decorated as distinct from undecorated dislocations.

In turn this suggested that published results on D-band luminescence from plastically deformed silicon (and possibly germanium) might also be strongly influenced by the presence of transition metals and that this might explain some of the lack of reproducibility apparent in this work. In order to explore this, a stress cell has been constructed in which a sample can be subjected to uniaxial stress up to 15MPa at temperatures up to 800°C with all the heated parts made from quartz. Plastically deformed material produced with this equipment has been investigated by photoluminescence, preferential etching and TEM.

EXPERIMENTAL

Several ingots of high purity FZ silicon were first examined for the presence of transition metals. This was achieved by heating thin slices in the temperature range 600-900°C and then rapidly quenching to room temperature. This type of treatment is known to give rise

to specific luminescence features associated with Cu, Ni and Fe complexes^[8] if these impurities are present or introduced by surface contamination. For copper this method^[9] has been shown to be sensitive to surface concentrations as low as 10^{10} cm^{-2} . One ingot in particular of high purity FZ material showed no trace of transition metal contamination and a number of (111) slices were cut from this material and $2 \times 4 \times 10 \text{ mm}^3$ samples produced with a $\langle 312 \rangle$ stress axis^[10]. Before the deformation process both the sample and the quartz stress cell were subjected to an RCA clean.

Following deformation, the samples were preferentially etched to determine the homogeneity and density of the dislocations. Three or four sections were cut from each sample and these were etched in $\text{HNO}_3/10\% \text{ HF}$ in preparation for photoluminescence measurements. These were carried out with the samples immersed in liquid helium at 4.2K and excited by 514.5nm radiation from an Ar laser. The luminescence was analysed by a Nicolet 60 SX Fourier transform spectrometer fitted with a cooled Ge diode detector. Following PL analysis some of the same samples were hand lapped from the back to a thickness of $100 \mu\text{m}$ and then chemically etched to form a disc shaped hole that is electron transparent. These were examined with TEM with an accelerating voltage of 120keV in bright field and dark field and weak beam diffracting conditions.

RESULTS

In spite of considerable care with RCA cleaning of both the stress samples and the quartz stress equipment, many of the plastically deformed samples did show D-band luminescence of varying intensity without further treatment. We did however manage to produce several samples which had a dislocation etch pit density between 10^4 - 10^8 cm^{-2} which showed negligible D-band luminescence. The spectra obtained from a sample before and after stressing at 15MPa at 750°C , which produced an etch pit density of 10^7 cm^{-2} , are shown in figures 1 and 2. There is some very weak D-band luminescence and there is some evidence for contamination by lithium (source unknown) but the major effect is a severe broadening of the free and bound exciton luminescence features indicating the presence of considerable strain.

This sample was deliberately contaminated with copper by stroking the surface with a pure copper wire and heating for 30 minutes at 900°C . Figure 3 shows that the D-bands are now the dominant luminescence features present. An adjacent section of this sample was heated at 900°C following an RCA clean and this produced only a minor increase in the strength of the D-bands. A similar set of measurements were carried out on a similar sample in which the contaminating metals were iron and nickel instead of copper. The spectral features were virtually identical with those produced by copper contamination and the energies of the features were unchanged within the limit that they can be determined.

Copper contaminated and uncontaminated samples have been examined by TEM. The majority of dislocations observed are 60 degree dislocations aligned along the $\langle 110 \rangle$ direction in the major glide plane^[10]. In both cases all the dislocations are dissociated into two Shockley partials connected by a stacking fault ribbon. The dissociation widths of the stacking fault ribbon vary from 100-500Å. A typical dissociated dislocation is shown in figure 4. On comparison of the contaminated and uncontaminated samples there appear to be no structural changes in the dislocations and no differences in the average widths of the stacking faults. Also there is no evidence for precipitation on the partials or the stacking fault ribbon in the contaminated sample. TEM analysis of Fe and Ni contaminated samples is currently in progress and the initial results are the same.

The TEM measurements have shown that there is no evidence for precipitation in the metal contaminated samples. However it is well known that the stress fields around a dislocation can be relieved by a suitable arrangement of nearby solute atoms (Cottrell atmosphere). The metal atoms introduced by contamination may be playing a direct role in the formation of such an atmosphere or a secondary role by interacting with point defects clusters which are known to form in such samples. This type of interaction may be responsible for the observation of the D-band features.

Controlled introduction of metal contamination

It is not clear from the wire stroking method how much metal is being introduced on

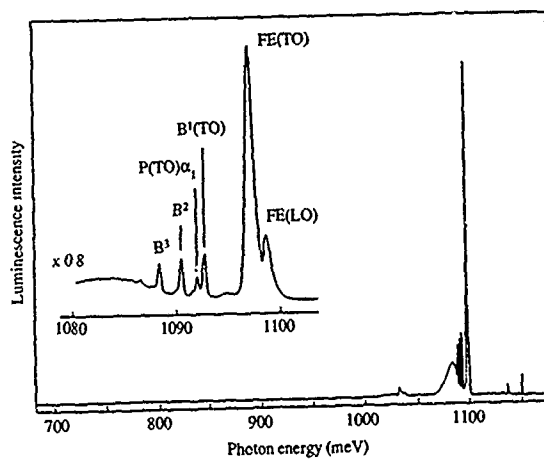


Figure 1. Photoluminescence spectrum of the high purity FZ Si starting material before plastic deformation.

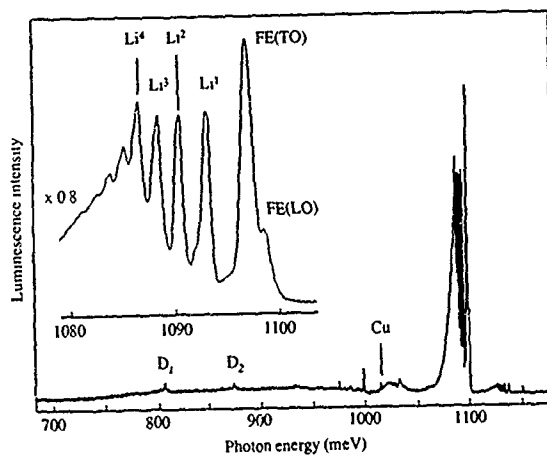


Figure 2. Photoluminescence spectrum of a sample plastically deformed at 15MPa and 750°C.

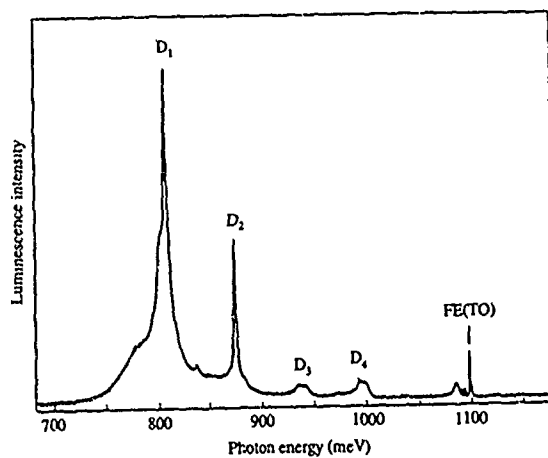


Figure 3. Photoluminescence spectrum of the same sample as figure 2 after deliberate copper contamination by a single wire stroke and heating at 900°C.

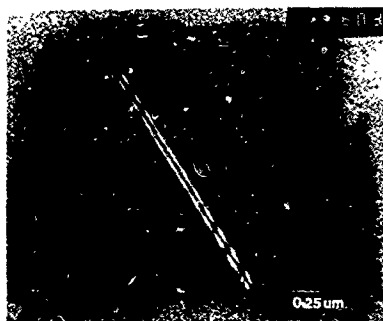


Figure 4. A TEM picture of a typical dissociated dislocation.

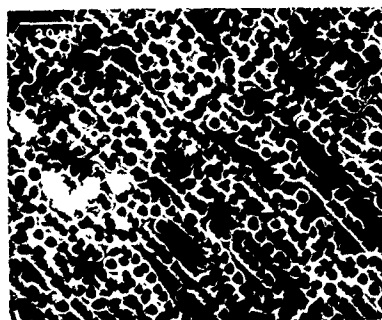


Figure 5. An SEM micrograph of a preferentially etched sample plastically deformed at 800°C.

the silicon surface before annealing. A more controllable way of introducing metal contamination on silicon surfaces is the use of back plating from high purity HF solutions which has been investigated in detail by Kern^[11]. We have applied this technique to the contamination of plastically deformed samples to provide some indication of the metal concentrations necessary to produce the D-band luminescence.

Several samples plastically deformed at 700 or 750°C, with dislocation densities in the range 10^6 - 10^7 cm^{-2} , were first RCA cleaned and then soaked in high purity HF (49%) for 30 minutes. This was followed by a rinse in 18 MΩ deionised water and heating for 30 minutes at 900°C in an RCA cleaned quartz tube. The copper concentration in the HF employed was found to be 3.8 ppb by atomic absorption measurements, and other electropositive metals which would be expected to plate out, such as gold and silver, were below the detection limits. Using the data produced by Kern^[11], this concentration of copper should have produced a surface concentration on the samples $\sim 4 \times 10^{12} \text{ cm}^{-2}$. The increase in the D-band luminescence produced by this treatment was similar to that obtained by a single wire stroke as illustrated in figure 3. It is clear that a surface copper concentration of only ~ 0.003 of a monolayer is sufficient to induce strong D-band luminescence.

Effect of deformation temperature

In order to check the dependence of the D-band features on the concentration of dislocations, a set of samples was produced at a constant uniaxial stress of 15 MPa with deformation temperatures in the range 600°C to 800°C. This gave rise to dislocation densities between 10^4 and 10^8 cm^{-2} . An SEM micrograph of a preferentially etched sample deformed at 800°C is shown in figure 5. Without further treatment all the samples showed very weak D-band features, the strength of the luminescence tending to increase with the dislocation density. Annealing without deliberate contamination produced a small increase in the D-band luminescence in some of the samples. The back plating technique was then used to introduce copper into the samples which in all cases produced up to an order of magnitude increase in the D-band luminescence relative to the free and bound exciton features.

The positions of the D-bands did not change with the concentration of dislocations present but there was a significant change in their relative intensities. The D1 and D2 bands were dominant in all the spectra but the peak height ratio D1/D2 decreased from ~ 4.2 at 600°C to ~ 2.8 at 800°C. The D3 and D4 bands increased in their relative intensities as a function of increasing dislocation density and were strongest in the sample deformed at 800°C.

Effect of annealing temperature

During the initial experiments the most efficient temperature for deliberate contamination was found to be 900°C. At lower temperatures the D-band luminescence was

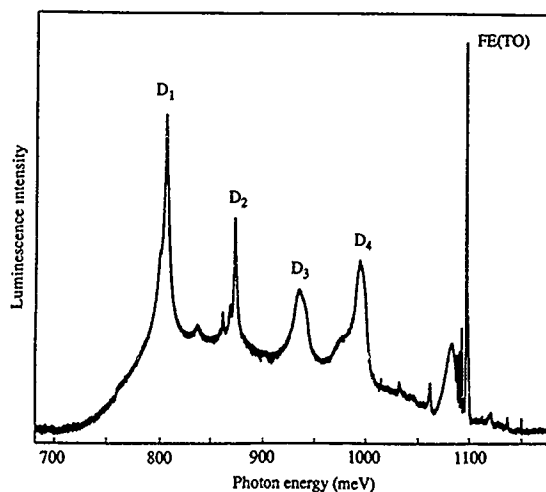


Figure 6. Photoluminescence spectrum of a sample plastically deformed at 700°C, copper contaminated by back plating from HF and annealed at 600°C.

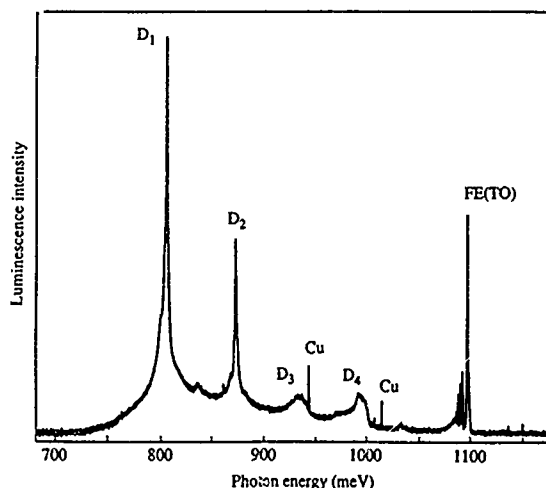


Figure 7. Photoluminescence spectrum of a sample plastically deformed at 700°C, copper contaminated by back plating from HF and annealed at 700°C.

generally much weaker. In order to check the effect of annealing temperature a sample deformed at 700°C, giving rise to a uniformly distributed etch pit density of $\sim 5 \times 10^5 \text{ cm}^{-2}$, was cut into four sections which were back plated in HF and annealed at 600, 700, 800 and 900°C. Spectra obtained from the samples annealed at 600 and 700°C are shown in figures 6 and 7. At 600°C there is a large underlying continuum and the D3 and D4 bands have intensities comparable with the D1 and D2 bands. The sub-structure particularly in D2 is also more apparent. Increasing the anneal temperature increased the overall strength of the D-bands relative to the free and bound exciton luminescence and the dominance of the D1 and D2 bands.

Other techniques have shown that point defect aggregates are produced during deformation [12, 13] and it has been inferred that the concentration increases with increasing strain and deformation temperature. In addition, it has also been shown that such centres anneal out in the temperature range 750-900°C. The changes in the luminescence spectra observed in the work reported here may be connected with this process. However the role played by metal contamination is not all clear. All the metals investigated are fast diffusers in silicon but exhibit quite different chemical properties [14].

These preliminary results show that both the deformation temperature and the annealing temperature have significant effects on the photoluminescence spectra. However, further characterisation (EBIC, TEM and cathodoluminescence imaging) is required before the results described can be fully understood.

SUMMARY

We have shown that high purity FZ silicon, which is free of transition metal contamination, that has been carefully cleaned and is then plastically deformed in a metal free environment to produce dislocations densities in the range 10^4 - 10^8 cm^{-2} , does not show significant D-band luminescence. Strong D-band luminescence features can be created by deliberate contamination with Cu, Fe and Ni. It has been shown that surface copper levels less than 0.01 monolayers are sufficient to produce the D-band features. TEM investigations have revealed that there are no differences in the dislocation structures before and after contamination. In addition there is no evidence of precipitation on the dislocations or in the strain fields around the dislocation. The D-band features may be due to impurities (point defect clusters or point defects or metal atoms) trapped in the strain fields of the dislocations.

ACKNOWLEDGEMENTS

This work was supported by the Science and Engineering Council. We are very grateful to A. Brinklow (Plessey) for carrying out the atomic absorption measurements.

REFERENCES

1. R.Sauer, J.Weber, J.Stolz, E.R.Weber, K.H. Kuslers and H. Alexander, Appl. Phys.A 36, 1 (1985).
2. S.Lelikov, T.Rebane and G. Schreter, Inst. Phys. Conf. Series 104, 119 (1989).
3. J.Weber and M.I.Alonso, Proc. Int. Conf. on the Science and Technology of Defect Control in Semiconductors, Yokohama, September 1989.
4. N.A.Drozdzov, A.A.Patrin, V.D.Tkachev, Sov. Phys. JETP. Lett. 23, 597 (1976).
5. M.Sueaza, K.Sumino, Y.Nishina, Jpn. J. Appl. Phys. 21, L518 (1982).
6. D.J.Robbins, D.B. Gasson, R.W.Hardeman, N.G.Chew, A.G. Cullis and C.A.Warwick, Electrochem. Soc. Proc. 85-7, 57 (1985).
7. V.Higgs, E.C.Lightowers, G.Davies, F.Schaffler and E.Kasper, Semicond. Sci. Technol. 4, 593 (1989).
8. M.C.Do Carmo, M.H.Nazare, M.F.Thomaz, I.Calao, F.Cerqueira and G.Davies Mat. Res. Soc. Symp. Proc Vol. 138, 221 (1989).
9. L.T.Canham, M.R. Dyball and K.G.Barracough, J.Appl. Phys. 66, 920 (1989).
10. K.Wessel and H. Alexander, Phil. Mag. 35, 1523 (1977).
11. W.Kern, RCA Review, June 1970, p. 234.
12. E.R.Weber and H.Alexander, Proc. Int. Sym. on Structure and Properties of Dislocations in Semiconductors, Aussios, 1983, J. Physique 44C (1983).
13. L.C. Kimerling and J.R. Patel. Appl. Phys. Lett. 38, 73 (1979).
14. K.Graff, Aggregation Phenomena of Point Defects in Silicon, edited by E.Sirtl and J.Gorissen (The Electrochem. Soc., Pennington, NJ 1981) p.121.

PHOTOLUMINESCENCE EXCITATION SPECTROSCOPY OF MOCVD-GROWN: GaAs:V

Y.J. KAO, AND N.M. HAEGEL

Dept of Materials Science and Engineering, University of California - Los Angeles, Los Angeles, CA 90024;

W.S. HOBSON,

AT&T Bell Laboratories, Murray Hill, NJ 07974.

ABSTRACT

Photoluminescence excitation spectra have been obtained at 4.2 K for the characteristic V^{3+} intra-center emission (0.65 – 0.75 eV) of MOCVD-grown GaAs:V. Oscillatory structure of the PLE spectrum with above-band-edge excitation has been observed in GaAs:V for the first time. The oscillatory period is found to be 41.3 ± 0.5 meV, corresponding to $[1 + (m_e^*/m_{hh}^*)]\hbar\omega_{LO}$, and is due to energy relaxation of conduction band electrons through LO phonon emission. Our results suggest capture by a shallow donor as an intermediate step in the luminescence from the V center.

INTRODUCTION

Vanadium is a substitutional impurity in GaAs which is known to have a characteristic crystal-field luminescence band in the 0.65 – 0.75 eV energy range [1]. It has been shown that vanadium gives rise to a deep acceptor level at $E_c - 0.15$ eV [2,3,4]. Figure 1 shows the substitutional vanadium levels in GaAs [4].

In this study, photoluminescence (PL) and photoluminescence excitation (PLE) spectroscopies have been used to study the characteristic V^{3+} emissions of MOCVD-grown GaAs:V. One of the results that emerged from this study is that an oscillatory structure in the PLE spectrum with above-band-edge excitation has been observed.

EXPERIMENTAL

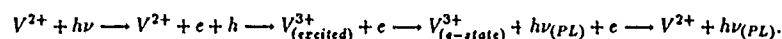
A barrel-type OMVPE reactor operated at atmospheric pressure was used for all the GaAs growth runs. Trimethylgallium (TMG) and arsine (AsH_3) were employed as the source chemicals with a V/III ratio of 15. Both H_2 and He carrier gases were used with qualitatively similar results. The typical growth rate and temperature were $3.7 \mu\text{m/h}$ and 675°C , respectively. The ultra-high-purity $VO(OC_2H_5)_3$ source was held at 10°C in a thermostatic bath. The detailed processes of the growth and chemical analysis were described in a previous report [5]. Some of the samples were additionally doped with Si and/or Be in order to systematically vary the Fermi levels in the epitaxial layer and change the charge state of the vanadium.

In the PL measurements, samples were immersed in liquid He and excited with an Ar ion laser at $\lambda = 514.5$ nm. The luminescence was detected using a cooled PbS detector. The spectra were calibrated for the spectral response of the system with a blackbody source. In the PLE measurements, the excitation source was replaced by a combination of a 75 W tungsten lamp and a 0.25 m grating monochromator. The output intensity of the excitation source was normalized for constant lamp intensity. The 0.65 – 0.75 eV luminescence band was selected by using a $1.6 \mu\text{m}$ long-pass filter or a monochromator.

RESULTS AND DISCUSSION

All of the n-type and semi-insulating (SI) vanadium-doped GaAs exhibited the same infrared PL band centered at 0.65 – 0.75 eV, although the ratio of band edge of deep level PL intensity varied. A typical PL spectrum from these samples is shown in Figure 2 and is similar to previous reports from bulk GaAs: V [1].

In the n-type samples, which are Si doped in addition to the vanadium, the V should exist in the V^{2+} charge state. This is the ionized acceptor state at $E_c - 0.15$ eV and would be expected due to compensation by the shallow donors. The following mechanism has previously been proposed [3] for excitation of the V^{3+} intracenter transition via electron-hole production:



GaAs:V

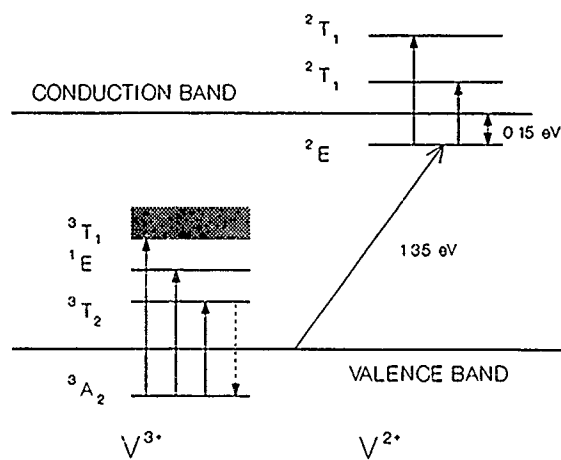


Fig. 1 Energy levels of the substitutional vanadium in GaAs.

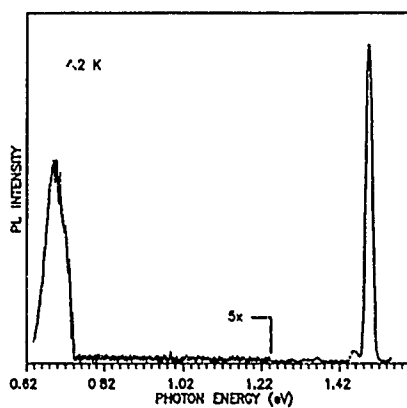


Fig. 2 A typical PL spectrum.

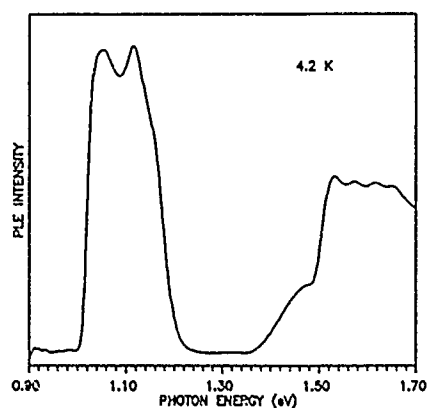


Fig. 3 A PLE spectrum from SI bulk samples.

In an attempt to study the PL and PLE of V in p-type GaAs, several samples were implanted with Be in order to dope the epitaxial layer. Multiple implants with varying energies were used to attain a uniform implantation profile to a depth of $\sim 1\mu\text{m}$. The characteristic V PL was observed in these samples, but was very weak. This may be due to the increased presence of V in the V^{3+} neutral state, in which the intracenter transition may not be as likely to occur as a result of capture of free carriers. However, the high Be concentration as a result of the implantation may also lead to factors such as damage or V-Be pairing, which could also affect the PL intensities.

The PLE measurements were performed on a series of n-type and SI MOCVD-grown samples. No structure was found in the PLE spectra with below-band-edge excitation for the epitaxial layers. This is partly due to the small thickness and relatively low absorption cross section for the intracenter transitions. In contrast, a strong excitation band centered around 1.1 eV was measured from a SI bulk sample, shown in Figure 3. This 1.1 eV band is the same as the one observed by conventional absorption measurements [3]. This PLE observation confirms the assignment of the absorption transition.

With the above-band-edge excitation, oscillatory structure was observed in the PLE spectra, as shown in Figure 4. This was observed for the epitaxial n-type samples, as well as the bulk materials. Figure 4 also indicates that the intensity of these oscillatory bands diminished as the concentration of Si in the sample was increased. The period of this oscillatory structure is determined to be $41.3 \pm 0.5\text{ meV}$, as indicated in Figure 5. This is in excellent agreement with the theoretical prediction:

$$\Delta E = [1 + (m_e^*/m_{hh}^*)]\hbar\omega_{LO}$$

for the cooling of hot electrons via LO phonon emission. Here m_e^* is the electron effective mass, m_{hh}^* is the heavy-hole effective mass, and $\hbar\omega_{LO}$ is the longitudinal-optical (LO)-phonon energy at Γ point (36.74 meV). These oscillatory structures are well-known in photoconductivity (PC) spectra [6,7], and have been observed in PLE spectra [8,9] on $(e - A^\circ)$ and $(D^\circ - A^\circ)$ luminescences due to shallow acceptors, and EL2-related emission in GaAs [10,11]. The enhancement factor of $[1 + (m_e^*/m_{hh}^*)]$ is a result of the curvature of the conduction and valence bands.

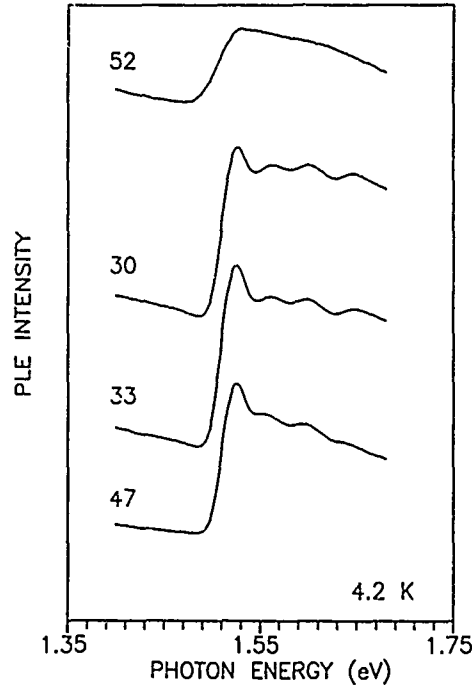


Fig. 4 PLE spectra. Sample 52: n-type, $[V] \sim 2 \times 10^{18}$, $[Si] \sim 5 \times 10^{16}$. Sample 30: n-type, $[V] \sim 4 \times 10^{18}$, $[Si] \sim 10^{16}$. Sample 33: n-type, $[V] \sim 3 \times 10^{18}$, $[Si] \sim 10^{16}$. Sample 47: SI, $[V] \sim 2 \times 10^{18}$, $[Si] \sim 2 \times 10^{15}$ [All concentrations in cm^{-3}].

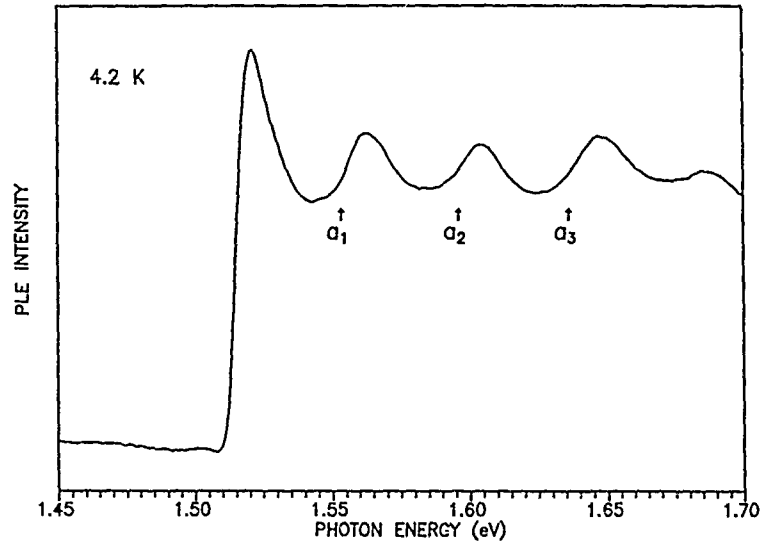


Fig. 5 Oscillatory structure of PLE spectrum obtained from sample 30-1.

Several mechanisms could be proposed to explain the oscillatory structure. The variation of the V PL intensity as a function of incident wavelength indicates some energy-dependent electron capture mechanism in the luminescence process. Three possibilities would include 1) energy-dependent capture of the electron directly into the V^{3+} , 2) competition for electrons from some other energy-dependent mechanisms, such as donor-acceptor pair recombination, and 3) capture into a shallow donor state as an intermediate step in the capture of the electron to V^{3+} .

Since deep centers are not expected to show such strong dependence on the energy of the electron, capture into shallow donors must play some role in the oscillation. Ulrich [8] has shown that the capture of hot electrons by ionized donors via LO phonon emission is observed in GaAs. The threshold for relaxation is given by

$$a_n = E_g + (n\hbar\omega_{LO} - E_D)(1 + m_e^*/m_{hh}^*)$$

Applying this to our data, with $E_g = 1.519$ eV and $E_D = 5.7$ meV, we see that the energies described by a_n correspond to thresholds for the increase of PL intensity. Thus, we propose that capture by a shallow donor plays an intermediate role in the vanadium PL. This is in agreement with results from Shanabrook [10] and Yu [11], who also reported oscillation in the PLE of deep levels.

CONCLUSIONS

In summary, we observe, for the first time, oscillations in the PLE of GaAs: V. Our results are in excellent agreement with energy-dependent capture of hot electrons via LO phonon emission and indicate capture by a shallow donor as an intermediate step in the V PL. We intend to perform PLE measurements on the band edge luminescence transitions in these samples to obtain direct confirmation of the mechanism.

ACKNOWLEDGMENTS

This work was supported in part by a grant from the David and Lucile Packard Foundation.

REFERENCES

- [1] U. Kaufmann, H. Ennen, J. Schneider, and R. Worner, *Phys. Rev. B* **25**, 5598 (1982).
- [2] C. D. Brandt, A. M. Hennel, L. M. Pawlowicz, F. P. Dabkowski, J. Lagowski, and H. C. Gatos, *Appl. Phys. Lett.* **47**, 607 (1985).
- [3] B. Clerjaud, C. Naud, B. Deveaud, B. Lambert, B. Plot, G. Bremond, C. Benjeddou, G. Guillot, and A. Nouailhat, *J. Appl. Phys.* **58**, 4207 (1985).
- [4] A. M. Hennel, C. D. Brandt, K. Y. Ko, J. Lagowski, and H. C. Gatos, *J. Appl. Phys.* **62**, 163 (1988).
- [5] W. S. Hobson, S. J. Pearton, V. Swaminathan, A. S. Jordan, H. Kanber, Y. J. Kao, and N. M. Haegel, *Appl. Phys. Lett.* **54**, 1772 (1989).
- [6] R. E. Nalory, *Phys. Rev.* **178**, 1293 (1961).
- [7] R. W. Shaw, *Phys. Rev. B* **3**, 3283 (1971).
- [8] R. Ulrich, *Phys. Rev. Lett.* **27**, 1512 (1971).
- [9] C. Weisbuch, *Solid-State Electron.* **21**, 179 (1978).
- [10] B. V. Shanabrook, P. B. Klein, E. M. Swiggard, and S. G. Bishop, *J. Appl. Phys.* **54**, 336 (1983).
- [11] Phil Won Yu, *Phys. Rev. B* **29**, 2283 (1984).

RADIATIVE AND NON-RADIATIVE RECOMBINATIONS AT Er CENTERS IN GaAlAs

TAHA BENYATTOU *, DJELLOUL SEGHER * AND GERARD GUILLOT *
RICHARD MONCORGE**

PIERRE GALTIER*** AND MARIE-NOELLE CHARASSE ***

* INSA de Lyon, LPM, Bat 502, 69621 Villeurbanne cedex, France.

**UCB, Bat 205, Laboratoire de Physico-Chimie des Matériaux Luminescents, 69622
Villeurbanne cedex, France

***Thomson CSF/LCR, 91404 Orsay cedex, France.

ABSTRACT

Photoluminescence (PL) of Molecular Beam Epitaxy grown Er doped $\text{Ga}_{0.55}\text{Al}_{0.45}\text{As}$ has been studied under continuous and pulsed laser excitation. The observed PL lines are attributed to transitions from the first excited state $^4I_{13/2}$ to the ground state $^4I_{15/2}$. The life time of the $^4I_{13/2}$ level is found to be 1 ms at 10K, which is comparable to the decay time observed in insulators.

Using two-beam experiments we show that there are losses (Auger effect) that occur during the PL excitation. We propose the following model for the Er PL excitation process: excitons bound to Er are created and decay non radiatively by energy transfer to the rare earth (which is the cause of the Er related PL) or to free carriers by Auger effect (which is the cause of the observed losses).

INTRODUCTION

Incorporating rare earth (RE) in III-V compounds is very interesting because of their internal transitions which give rise to narrow emission lines in the near infrared region that are practically independent of the III-V host. In particular, erbium doping [1- 7] seems very attractive due to the possibility of realising new emitting devices at 1.54 μm which corresponds to a minimum of absorption of silica based optical fibers. However, there is a poor knowledge of the excitation-deexcitation processes of these luminescent centers. The aim of this work is to investigate these processes with PL and two-beam experiments. We propose a simple PL excitation model which accounts for the observed experimental results and show that Auger losses [8] are predominant.

MATERIAL AND TECHNIQUES

Our study was made on one sample of $\text{Ga}_{0.55}\text{Al}_{0.45}\text{As}$ doped with an Er concentration of $3 \times 10^{17} \text{cm}^{-3}$. It was grown by Molecular Beam Epitaxy at the Laboratoire Central de Recherche THOMSON CSF. Details concerning the growth technique used here are reported elsewhere [5].

For the PL study the excitation was provided, in the CW excitation experiments, by the 5145Å line of an Argon ion laser or the 6328Å line of an He-Ne laser. The luminescence was then analysed through a 0.6m JOBIN YVON HRS2 monochromator and detected with Ge photodetector cooled to 77K coupled to a lock-in amplifier.

Pulsed excitation experiments were also performed. For that we used a YAG : Nd pumped dye laser from QUANTEL which delivered excitation pulses of 15ns duration at 6200Å. The PL signal was selected through an adapted broad band interferential filter ($\lambda = 1.545 \pm 0.024 \mu\text{m}$) and detected with a fast response Ge photodetector cooled to 77K. The signal was then analysed with a digital oscilloscope.

EXPERIMENTAL DATA

Figure 1(a) shows the PL spectrum recorded at 10K under CW Argon ion laser. It consists of two sets of characteristic narrow lines located around 1.54 and 1.56 μm . They are attributed to $^4I_{13/2} \rightarrow ^4I_{15/2}$ optical transitions within Er^{3+} ions in two kinds of sites. The PL decay obtained at 10K under pulsed excitation is shown in figure 1(b). It is made of two exponential components with time constants of 260 μs and 1.17ms. Because of the large spectral width of

the interferential filter used to select the fluorescence, we attribute each component to one kind of Er^{3+} site.

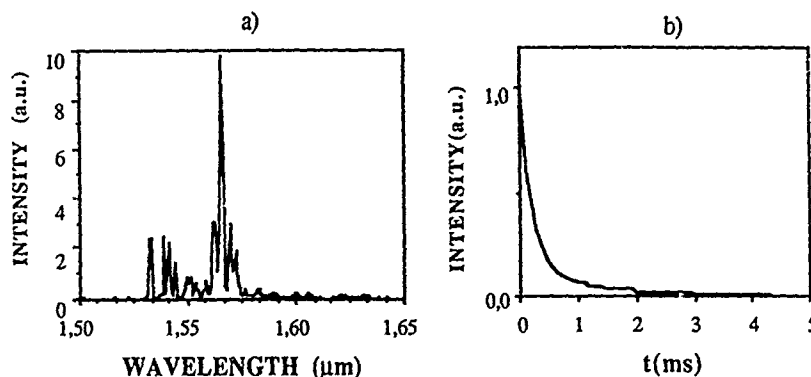


FIGURE 1

- a) Photoluminescence spectrum of $\text{Ga}_{0.55}\text{Al}_{0.45}\text{As}:\text{Er}$ at 10K under Argon laser excitation
 b) Er PL decay at 10K under pulsed laser excitation at 5200 Å

The PL intensity presents a square root dependence on the excitation pump power (Figure 2). Assuming that this behavior can be accounted for by the optical losses induced by the creation of electron-hole pairs, we decided to check it with the aid of two-beam experiments.

A first beam, called pump beam, populates the erbium excited state $^4\text{I}_{13/2}$ which is monitored by its characteristic PL at 1.54 μm . A second beam, the probe beam, is used to create the electron-hole pairs. A decrease in the $^4\text{I}_{13/2}$ PL intensity would thus be a measure of the probe beam induced optical losses on the pump beam.

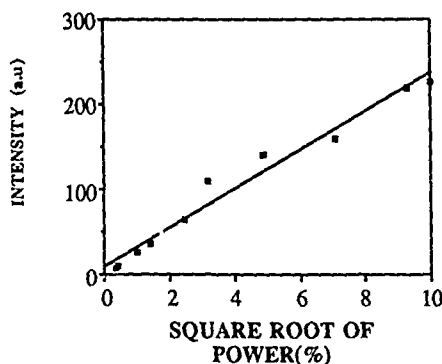


FIGURE 2

Photoluminescence intensity versus square root of the excitation power

Experiments with a CW pump laser were performed at 300K. The pump and the probe beams were provided by a 10mW He-Ne laser and a 200mW Argon ion laser respectively. In order to avoid any direct pumping effect caused by the probe beam, we chopped the pump beam and the PL was detected with a lock-in amplifier.

When the probe beam and the pump beam spots overlap, the PL signal decreases with the power of the probe beam. This is shown in Figure 3. For 200mW the PL decreases by about a factor of 3.

Transient experiments were also performed using the pulsed laser (pulses of less than

1mJ over 0.4 cm²) described as the pump beam. The probe beam was provided by the same Argon ion laser used for the CW experiment. The sample was cooled down to 14K. Recording the PL decay we see that the probe beam induces a decrease of the PL signal, the profile shape remaining the same (i.e. with the same time constants).

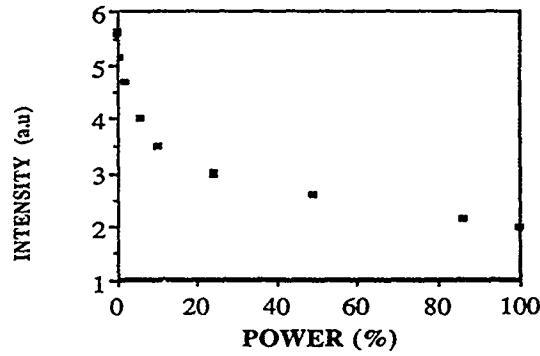


FIGURE 3

Photoluminescence intensity of Er as a function of the power of CW laser pump beam

In the case of the CW pump laser experiments we can say that for Er³⁺ doped GaAlAs the optical losses are due to the probe beam photogenerated carriers. This effect seems to be very important (decrease by about a factor 3 at the maximum probe beam power). So it could be the origin of the PL intensity sublinear dependence mentioned at the beginning. These losses could occur during the PL excitation or deexcitation processes and are likely related to some kind of Auger process.

In the pulsed laser pump experiments we do not see any effect on the PL decay mode ; therefore, we can conclude that the losses do not occur during the PL deexcitation but only during the excitation process.

DISCUSSION

Some recent results [6-7] show that rare earth impurities such as Yb³⁺ and Er³⁺ can act as traps for electrons in the III-V compounds. We can therefore think that erbium centers could bind excitons (directly or by successive capture of carriers). We have seen that losses occur during the excitation process and are related to the free carrier concentration. This leads us to think that there are two paths for the non radiative recombination of the bound excitons : (i) Auger recombination (energy transfer to free carriers), (ii) Energy transfer to erbium ions, the losses come here from the Auger process [8] (c.f., Figure 4).

The population equation according to these hypotheses can be written. The probability for one bound exciton to transfer its energy to an erbium ion is given by :

$$P = \frac{P_e}{P_e + Bn} \quad (1)$$

where P_e is the erbium excitation rate, Bn is the Auger recombination rate, n is the electron concentration and B a transfer constant. We can write :

$$\frac{d n_e^*}{dt} = A\phi \frac{P_e}{P_e + Bn} - \frac{n_e^*}{\tau_f} \quad (2)$$

where n_e^* is the excited erbium ion concentration, $A\phi$ the number of created bound excitons, ϕ the light flux and τ_f the ⁴I_{13/2} fluorescence decay time constant.

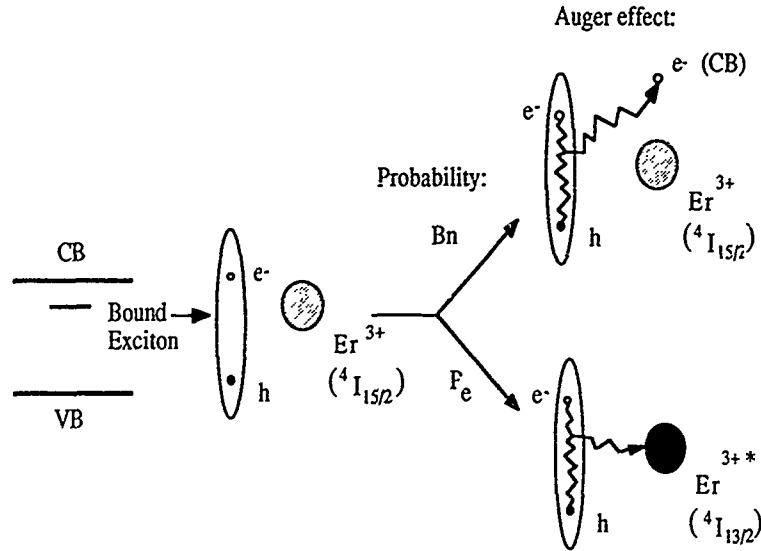


FIGURE 4
Er PL excitation model

If we assume a bimolecular recombination of the photogenerated carriers so that $n=B\sqrt{\phi}$ then we can write (2) in the following form :

$$\frac{d n_{e^*}}{dt} = A\phi \frac{P_e}{P_e + C\sqrt{\phi}} - \frac{n_{e^*}}{\tau_f} \quad (3)$$

where $C=BB'$

At high flux ϕ the Auger process can be dominating ($C\sqrt{\phi} \gg P_e$) :

$$\frac{d n_{e^*}}{dt} \approx \frac{A P_e}{C} \sqrt{\phi} - \frac{n_{e^*}}{\tau_f} \quad (4)$$

Then in the steady state situation we obtain :

$$n_{e^*} = \frac{\tau_f A P_e}{C} \sqrt{\phi} \quad (5)$$

The density of excited erbium ions is proportional to the square root of the pump power. Let us see if this model works also for the two-beam experiments.

If ϕ_{pump} and ϕ_{probe} stand for the pump and the probe beam flux respectively and if we assume that $\phi_{\text{pump}} \ll \phi_{\text{probe}}$ so that the carrier concentration depends essentially on the probe beam we can write the following population equation (cf(3)) :

$$\frac{d n_{e^*}}{dt} = A\phi_{\text{pump}} \frac{P_e}{P_e + C\sqrt{\phi_{\text{probe}}}} - \frac{n_{e^*}}{\tau_f} \quad (6)$$

n_{e^*} is the density of erbium ions created by the pump beam that we detect by chopping the pump beam in the CW laser experiment and recording the signal with a lock-in amplifier.

In this case we obtain in the steady state situation :

$$n_{e*} = u \phi_{\text{pump}} \left(\frac{1}{1 + v \sqrt{\phi_{\text{probe}}}} \right) \quad (7)$$

where $u = \tau_f A$ and $v = C/P_e$
 ϕ_{pump} is constant and ϕ_{probe} is varying, we can then write (7) in the following form :

$$n_{e*} = n_{e0*} \left(\frac{1}{1 + v \sqrt{\phi_{\text{probe}}}} \right) \quad (8)$$

where n_{e0*} is the excited erbium population when $\phi_{\text{probe}} = 0$. Then we find:

$$\left(\frac{1}{n_{e*}} - \frac{1}{n_{e0*}} \right)^2 \propto \phi_{\text{probe}} \quad (9)$$

In figure 5 we have plotted $(1/I - 1/I_0)^2$ versus ϕ_{probe} where I is the recorded PL intensity and I_0 is the intensity without probe beam. It can be seen that the experimental data are well fitted by relation (9).

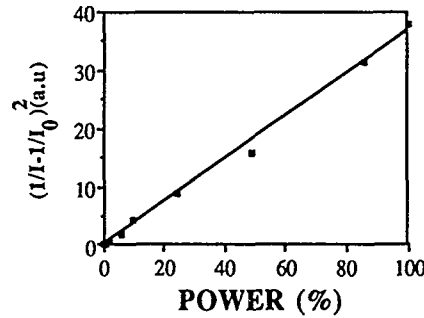


FIGURE 5

Plot of $(1/I - 1/I_0)^2$ as a function of the power of the laser probe beam (I_0 , I are respectively the Er PL intensity without and with the probe beam)

In conclusion we have shown that in erbium doped GaAlAs there are significant optical losses occurring during the PL excitation process and these losses are related to the free carriers. The PL excitation model presented here : formation of bound excitons at the erbium centers and non-radiative decay through two main channels, Auger recombination and energy transfer to erbium ions, is in good agreement with the experimental results. The Auger losses occurring during the PL excitation could be the origin of the very low efficiency of the GaAlAs : Er LED[4]. It appears now that a deeper understanding of the excitation and deexcitation processes in this type of material is necessary to evaluate the technological performances of such devices.

Our approach could be extended to other rare earth doped III-V compounds since in most of them the PL intensity presents a sublinear variation with the excitation pump power.

References

1. S.Pomrenke, H.Ennen and W.Haydl, J.Appl.Phys. 59,601 (1986)
2. W.T.Tsang and R.A.Logan, Appl.Phys.Lett 49,1686 (1986)
- 3.H.Ennen, J.Wagner, H.D. Muller and R.S. Smith, J.Appl.Phys. 61,4877 (1987)

4. P.Galtier, J.P.Pocholle, M.N.Charasse, T.Benyattou, G.Guillot, B.DeCremoux and J.P.Hirtz (unpublished)

5. P.Galtier, M.N.Charasse, J.Chazelas, A.M.Huber, C.Grattepain, J.Siejka and J.P.Hirtz , in Gallium Arsenide and Related Compounds 1988 edited by J.S. Harris (IOP Pub. Ltd 96 , Atlanta ,1988) pp. 61-64.

6. P.S.Whitney, K.Uwai, H.Nakogome and K.Takahei , Appl.Phys.Lett. 53,2074 (1988)

7. B.Lambert, A.LeCorre, Y.Toudic, C.Lhomer, G.Grandpierre and M.Gauneau (unpublished).

8. J.M Langer J. of Lum. 40/41 ,589 (1988)

CHARACTERIZATION OF DEEP-LEVEL DEFECTS IN SEMI-INSULATING GaAs AND InP BY PHOTOINDUCED TRANSIENT SPECTROSCOPY (PITS)

PAWEŁ KAMINSKI

Institute of Electronic Materials Technology, ul. Konstruktor-ska 6, 02-673 Warsaw, Poland

ABSTRACT

Deep states in semi-insulating (SI) materials: GaAs:Cr, undoped GaAs and InP:Fe are investigated by Photoinduced Transient Spectroscopy (PITS). The relationship between the Hall mobility in undoped SI GaAs and occurrence of the EL2-related peak in the PITS spectrum is shown.

INTRODUCTION

Semi-insulating (SI) GaAs and InP are substrate materials for manufacturing high speed electronic devices. However, quality of these materials in terms of device performance is strongly affected by deep-level impurities and native defects. So, monitoring of deep states in SI GaAs and SI InP is of great practical importance. Because of the high resistivity of the material and hence the difficulty of filling the traps by change in electrical bias, conventional capacitance-mode Deep Level Spectroscopy (DLTS) is not applicable. The technique employed in this study, often referred to as Photoinduced Transient Spectroscopy (PITS) [1,2], relies on filling the traps by optical pulse and analysing the photocurrent transient as a function of temperature while the light is off. The time variation of the excess electron concentration related to the change in trap occupancy is given by [1]

$$n(t) = N_T \tau_n e_n \exp(-e_n t) \quad (1)$$

where N_T is the trap concentration, τ_n is electron lifetime and e_n is the thermal emission rate for electrons. The temperature dependence of e_n is given by [2]

$$e_n = \tau_n^{-1} = \gamma_n \sigma_n T^2 \exp(-E_a/kT) \quad (2)$$

where k is Boltzmann's constant, T is the absolute temperature, E_a is the activation energy, σ_n is the apparent capture cross-section for electrons and γ_n is material constant (for GaAs $\gamma_n = 2.0 \times 10^{20} \text{ cm}^{-2} \text{ K}^{-2} \text{ s}^{-1}$). For hole traps, the value of material constant γ_p differs from that of γ_n because of the difference

between the effective mass values for electrons and holes (for GaAs $\tau_p = 1.8 \times 10^{21} \text{ cm}^{-2} \text{ K}^{-2} \text{ s}^{-1}$).

This paper is aimed at showing the potentialities of PITS technique for characterization of deep states in semi-insulating III-V compounds grown in various conditions. The spectra were obtained by processing the photo-induced transient current using the double-gated boxcar integrator similarly as in DLTS technique.

RESULTS AND DISCUSSION

The GaAs and InP crystals were grown in $\langle 100 \rangle$ direction by liquid-encapsulated Czochralski (LEC) method.

The resistivity of Cr-doped GaAs samples, measured at 300 K, was $5 \times 10^8 \Omega \text{ cm}$ and Hall mobility about $1500 \text{ cm}^2/\text{Vs}$. Since the crystal was pulled from the quartz crucible, the low value of mobility is probably due to its strong contamination with silicon. The chromium concentration in the samples, determined by optical absorption, was $3 \times 10^{16} \text{ cm}^{-3}$. Figure 1 shows the PITS spectrum for the Cr-doped GaAs samples and the activation energies for

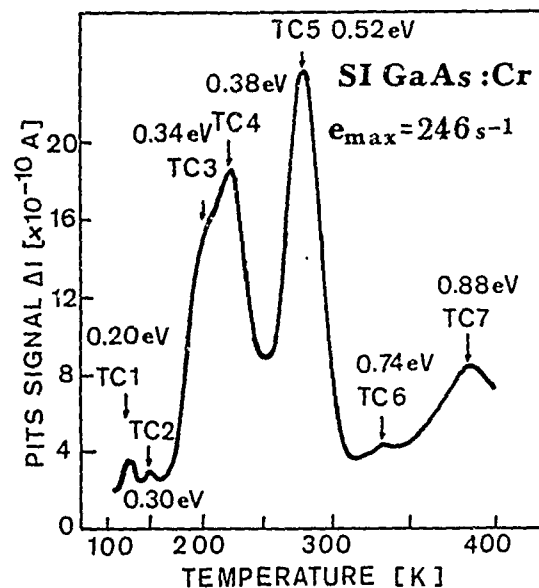


Fig.1 .PITS spectrum for Cr-doped LEC SI GaAs .
Hall mobility :
 $1500 \text{ cm}^2/\text{Vs}$.

the traps observed. A number of traps labeled TC1 - TC7 were detected what indicates that defect structure of the material is very complex. Based upon previous DLTS and PITS measurements [1-3], we can perform a tentative identification of the observed defect centers. Thus, traps TC1 ($E_a = 0.20\text{eV}$, $\sigma_n = 2 \times 10^{-15}\text{cm}^2$), TC2 ($E_a = 0.30\text{eV}$, $\sigma_p = 3 \times 10^{-14}\text{cm}^2$), TC3 ($E_a = 0.34\text{eV}$, $\sigma_n = 4 \times 10^{-16}\text{cm}^2$) and TC4 ($E_a = 0.38\text{eV}$, $\sigma_n = 5 \times 10^{-16}\text{cm}^2$) can be assigned, respectively, to the previously observed centers EL17, HL12, EL6 and EL5 whose atomic configuration, however, still remains unknown [1-3]. The mid-gap traps: TC5 ($E_a = 0.52\text{eV}$, $\sigma_p = 4 \times 10^{-15}\text{cm}^2$), TC6 ($E_a = 0.74\text{eV}$, $\sigma_n = 5 \times 10^{-13}\text{cm}^2$) and TC7 ($E_a = 0.88\text{eV}$, $\sigma_p = 3 \times 10^{-13}\text{cm}^2$) can be identified with the centers known as HL8, EL2 and HL1 respectively [1-3]. The hole trap HL8 (TC5) is considered to be attributed to iron-related defect [1-3]. However, recent work of Dobrilla [4] suggests that it may be related to stoichiometric conditions. The EL2 (TC6) is a well known defect responsible for semi-insulating properties of undoped SI GaAs. According to recent models [5], it is a complex involving As antisite and another native defect. The hole trap HL1 (TC7) is attributed to substitutional chromium in the $\text{Cr}^{2+}/\text{Cr}^{3+}$ state which produces a deep acceptor level that compensates shallow donors giving rise to the high resistivity of the samples [1-3]. The small amplitude of both TC6 and TC7 peaks is probably due to substantial decrease of charge carriers lifetime above 300K.

In the PITS spectrum for undoped SI GaAs pulled from the quartz crucible eight traps labeled T1- T8 are observed (Fig.2). The Hall mobility in the samples was $2500\text{cm}^2/\text{Vs}$. Trap T1 ($E_a = 0.21\text{eV}$, $\sigma_n = 3 \times 10^{-14}\text{cm}^2$) can be assigned to EL17 center [2]. Trap T2, similarly as trap TC2 in the case of GaAs:Cr, is presumably HL12 center. Trap T3 ($E_a = 0.30\text{eV}$, $\sigma_p = 1 \times 10^{-15}\text{cm}^2$) is likely to be a defect center known as HL6 [1-3]. Trap T4 ($E_a = 0.40\text{eV}$, $\sigma_p = 4 \times 10^{-13}\text{cm}^2$) can be identified as the HL4 center which is related to the common contaminants in LEC GaAs such as Cu or Ni [1-3]. Trap T5 ($E_a = 0.36\text{eV}$, $\sigma_n = 8 \times 10^{-15}\text{cm}^2$) is attributed to the EL6 center that also occurs in Cr-doped material. The parameters of mid-gap traps: T6 ($E_a = 0.55\text{eV}$, $\sigma_n = 4 \times 10^{-13}\text{cm}^2$), T7 ($E_a = 0.69\text{eV}$, $\sigma_p = 1 \times 10^{-13}\text{cm}^2$) and T8 ($E_a = 0.74\text{eV}$, $\sigma_n = 5 \times 10^{-13}\text{cm}^2$) are consistent with the signatures of EL3, HL9 and EL2 centers respectively [1-3]. The center HL9, frequen-

Fig.2 .PITS spec-
trum for undoped
LEC SI GaAs with
low Hall mobility
($\mu_H = 2500 \text{ cm}^2/\text{Vs}$).

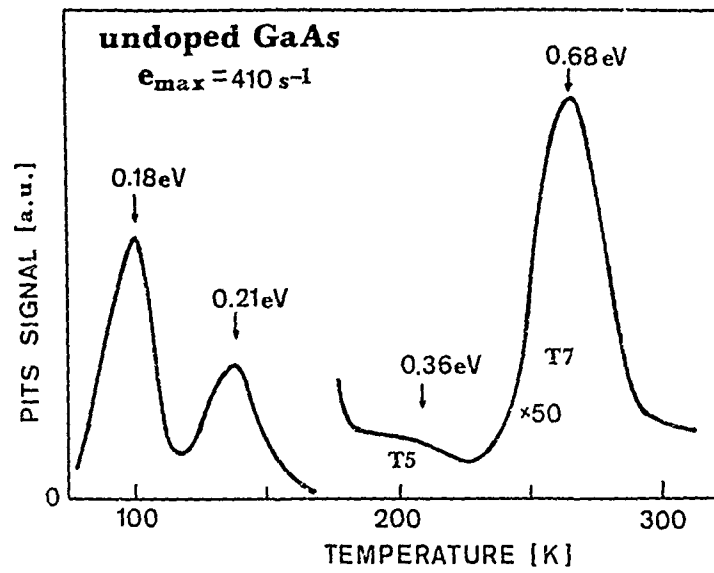
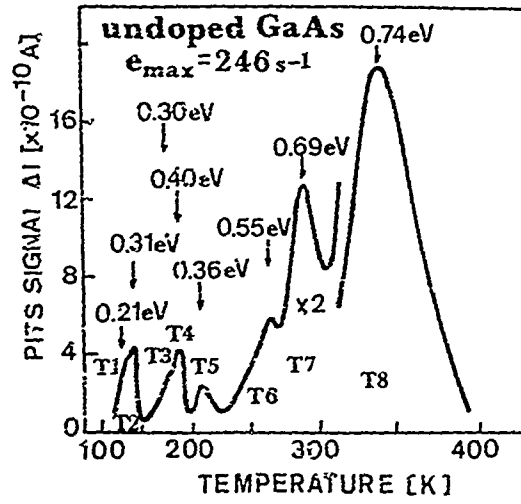


Fig.3 .PITS spectrum for undoped LEC SI GaAs with high
Hall mobility ($\mu_H = 5500 \text{ cm}^2/\text{Vs}$).

tly observed in undoped SI GaAs, is considered to be related to the B_2O_3 encapsulant conditions [1-3].

Figure 3 shows the PITS spectrum for the undoped SI GaAs crystal in growth of which the pyrolytic boron nitride (pBN) crucible was utilized. The Hall mobility in the samples was about $5500 \text{ cm}^2/\text{Vs}$. It is worth noting that in this spectrum a peak corresponding to EL2 center is not observed, while in the spectrum for undoped SI GaAs with low Hall mobility (Fig. 2) the peak related to EL2 is dominant. This fact can be explained through the difference in the Fermi level position in materials with different Hall mobility. According to the diagrams shown by Walukiewicz *et al.* [6], the Fermi level in undoped SI GaAs with Hall mobility of $2500 \text{ cm}^2/\text{Vs}$ is located at 0.73 eV below the conduction band and 70% of the EL2 concentration is unoccupied. In undoped SI GaAs with Hall mobility exceeding $5000 \text{ cm}^2/\text{Vs}$ the Fermi level is located at $E_c - 0.64 \text{ eV}$ and only 2% of the EL2 concentration remains unoccupied. Since the filling efficiency is proportional to the concentration of unoccupied EL2 states, occurrence of the EL2 peak in the PITS spectrum is controlled by the Fermi level position in the sample.

Figure 4 shows the PITS spectrum for Fe-doped InP and the values of activation energies for detected deep-level defects. The activation energy for the dominant trap TF3 ($E_a = 0.64 \text{ eV}$) is in good agreement with the energy corresponding to transition $\text{Fe}^{2+} (3d^6) \rightarrow \text{Fe}^{3+} (3d^5) + e^- (\text{CB})$ [7]. Moreover, our temperature-dependent Hall effect measurements gave an activation energy of 0.64 eV and the variation of resistivity

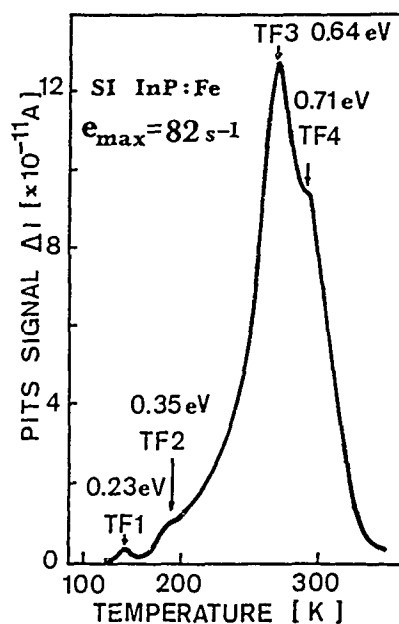


Fig. 4 . PITS spectrum for Fe-doped InP .

with temperature showed an activation energy of 0.65 eV . Hence, the trap TF3 is identified with Fe in $(-/0)$ charge state that produces deep acceptor level responsible for high resistivity of InP. Trap TF4 (0.71 eV) is presumably related to hole emission $\text{Fe}^{3+} \rightarrow \text{Fe}^{2+} + h$ (VB) [7]. Trap TF2 (0.35 eV) is likely to be related to transition $\text{Fe}^{+}(3d^7) \rightarrow \text{Fe}^{2+}(3d^6) + e^{-}$ (CB) [7]. Trap TF1 (0.23 eV) is probably associated with some Fe-related complex [7].

To sum up, the PITS technique was shown to be a very effective tool for monitoring deep-level defects in semi-insulating III-V materials. For undoped SI GaAs, occurrence of peak related to EL2 was found to be dependent on the Fermi level position in the sample .

REFERENCES

1. D.C. Look, in Semiconductors and Semimetals , edited by R.K. Willardson and A.C. Beer (Academic Press, New York, 1983), Vol.19, p.76 .
2. G.M. Martin, in Semi-Insulating III-V Materials :Nottingham 1980 , edited by G.J. Rhee (Shiva, Orpington UK,1980), p.13.
3. P. Kaminski and H. Thomas , in Defects in Crystals, edited by E.Mizera (World Scientific, Singapore, 1988), p.438 .
4. P. Dobrilla ,J.Appl.Phys. 64 , 6767 (1988) .
5. J.C. Bourgoin and H.J. von Bardeleben ,J.Appl.Phys. 64 ,R 65 (1988) .
6. W. Walukiewicz, J. Lagowski and H.C. Gatos , Appl.Phys.Lett. 43 ,192 (1983) .
7. S.G. Bishop , in Deep Centers in Semiconductors , edited by S.T.Pantelides (Gordon and Breach, New York, 1985), p.541 .

ELECTRONIC STRUCTURE OF Li-IMPURITIES IN ZnSe.

T. OGUCHI*, T. SASAKI* AND H. KATAYAMA-YOSHIDA**

*National Research Institute for Metals, Nakameguro, Meguro-ku, Tokyo 153, Japan

**Department of Physics, Tohoku University, Aramaki-Aoba, Sendai 980, Japan.

ABSTRACT

Electronic properties of ZnSe with a Li impurity are investigated with use of the local-density-functional approach. The electronic structures are calculated for different impurity sites by taking the neighboring lattice relaxation into account. By comparing their total energies, the stability of the Li impurity in ZnSe is discussed. It is proposed that the Li impurity at the substitutional Zn site might be unstable to the tetrahedral interstitial site with an ionization of Li and a vacancy at the Zn site.

INTRODUCTION

Properties of Li impurity in zinc selenide (ZnSe) is recognized as a crucial problem in fabricating a p-type material for the blue light-emitting-diode. The experimental result shows that substitutional Li at the Zn site (Li_{Zn}) seems to be unstable at room temperatures[1]. Although Li_{Zn} is expected to work as a shallow acceptor, only little is known on the electronic structure of the Li impurity in ZnSe.

For elemental semiconductors, detailed information on the electronic structure and the atomic configuration of various defects are now available from theoretical and experimental studies. Similar situation is being achieved for III-V semiconductors but less attention has been paid to II-VI systems.

The electronic structure of an acceptor has been investigated successfully with the effective-mass theory in most semiconductors, particularly, Si and Ge. An application of the effective-mass theory to the electronic structure of an acceptor in ZnSe is probably doubtful since the effective Bohr radius of a shallow acceptor state calculated within the theory is 13.7Å which is much larger than the corresponding observed value (4.7Å) for the Na acceptor[2,3]. Chacham *et al.* have calculated the Li_{Zn} system using a cluster model and have obtained the activation energy of the acceptor level in good agreement with the experimental value[4]. However, no lattice relaxation has been taken into account in their calculation.

In this Symposium, we present results of the electronic structure calculation for a Li impurity in ZnSe using the local-density-functional formalism taking the lattice relaxation into account and discuss the stability of the Li impurity. In particular, we focus on the following reaction:



where Li_i and V_{Zn} denote a Li impurity at an interstitial site and a vacancy at the Zn site, respectively. In order to clarify the reaction of Eq. (1), the total energies of these systems have been calculated.

MODEL AND METHODS

We applied the local-density approximation of the density-functional theory to supercell model systems[5]; a defect is introduced into an fcc unit cell which contains eight Zn and eight Se atoms with the zinc-blend structure. The norm-conserving pseudopotential method without the spin-orbit interaction [6] was used and the wave functions were expanded with the plane-wave basis set up to the kinetic energy of 9.0Ry. A new set of pseudopotential has been developed for the Zn atom to get good convergence of the plane wave by keeping the 3d states core. As for Se and Li, the pseudopotential listed in Ref. 6 was adopted. The exchange-correlation energy was calculated with use of the Ceperley-Alder-Perdew-Zunger form[7,8].

The lattice relaxation of the nearest neighbor atoms around the defect was taken into account with the dynamical-simulated-annealing scheme[9] which provides a simultaneous optimization for both the electronic state and the lattice configuration. No symmetry was

assumed except the translational one. The Brillouin-zone sampling of the occupied states was represented by the summation at the Γ point of the supercell. In this investigation, calculations for the neutral state of each defect are presented.

RESULTS AND DISCUSSIONS

Substitutional Zn Site

When all remaining atoms are located at their ideal bulk positions, the force acting on the nearest neighbor Se atoms (denoted as Se(I)) is 1.41eV/\AA toward the Li atom substituted to the Zn site; the electrostatic (Madelung) force is 12.79eV/\AA while the force from band structure energy is -11.38eV/\AA . Consequently, the lattice relaxation occurs so that the distance between Li and Se(I) decreases. When only the breathing mode of the Se(I) motion is permitted, the equilibrium distance is 2.15\AA , being smaller than its ideal value by 0.21\AA .

The calculated electron density after the breathing relaxation is shown in Fig. 1. The valence electrons are distributed almost spherically around the Se sites. The density around the Li site is slightly enhanced in comparison with that around the Zn sites.

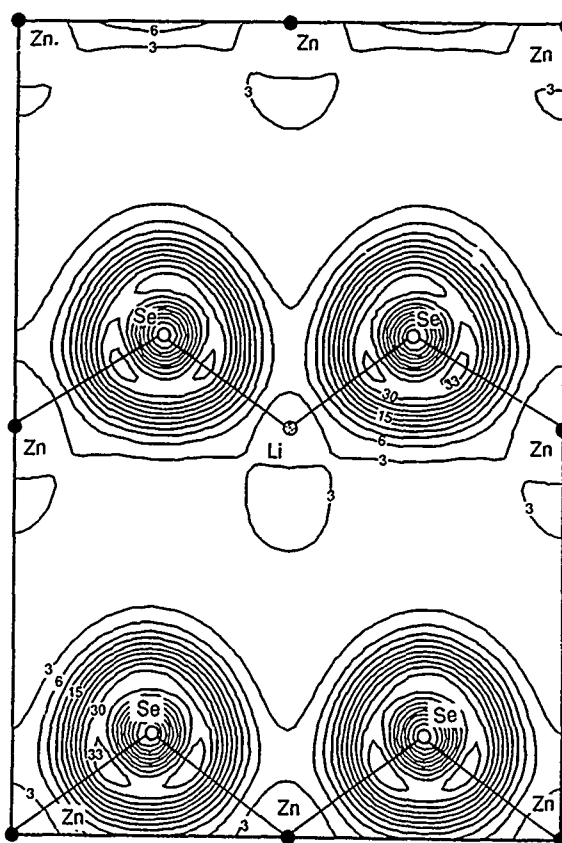


Fig. 1 Contour plot of the valence charge density of ZnSe with Li_{Zn} after the breathing-mode relaxation. The values are given in units of electrons per unit cell of $(5.456\text{\AA})^3$.

Figure 2 shows the energy levels calculated at the Γ point. The most drastic change due to the breathing relaxation can be seen near 2 eV below the valence-band maximum (VBM); the fourfold degeneracy appearing at the perfect crystal is eliminated in such a way that a state with A_1 symmetry is lifted up in energy and the remaining states keep the degeneracy at the original energy position. This change is due to that the A_1 resonance has most of its amplitude between Li and Se(I) while the latter states do between the Zn and Se atoms.

In the electronic structure of this atomic configuration, there is a threefold T_2 state with one hole at the Fermi energy. The T_2 state corresponds to the top of the valence band which is perturbed by the potential difference between the Li and Zn atoms. Such a partially filled state is subject to a Jahn-Teller (JT) distortion to another lower symmetry. When the symmetry constraint is removed, a JT distortion actually occurs, resulting the energy gain of 0.1 eV. The final symmetry around Li is not well identified because the JT displacements are too small. Reflecting such small movements, the change of the energy levels due to the relaxation is quite small, as seen in Fig. 2.

No distinct shallow acceptor level has been observed in the present calculation. A larger supercell might be necessary to explain the activation energy if a shallow level exists.

Interstitial Sites

In this investigation, two kinds of the tetrahedral interstitial sites (T_d) are considered; one is surrounded by the Se atoms, $T_d(\text{Se})$, and the other by Zn, $T_d(\text{Zn})$. In both cases, the lattice relaxation is found to be very small.

Concerning the energy levels calculated for both interstitial cases, there is the highest occupied state with one electron at the vicinity of the conduction band minimum (CBM), shown in Fig. 2. Furthermore no deep level appears in the energy gap for both systems. Thus the Li impurity at the T_d interstitial sites works as a donor center.

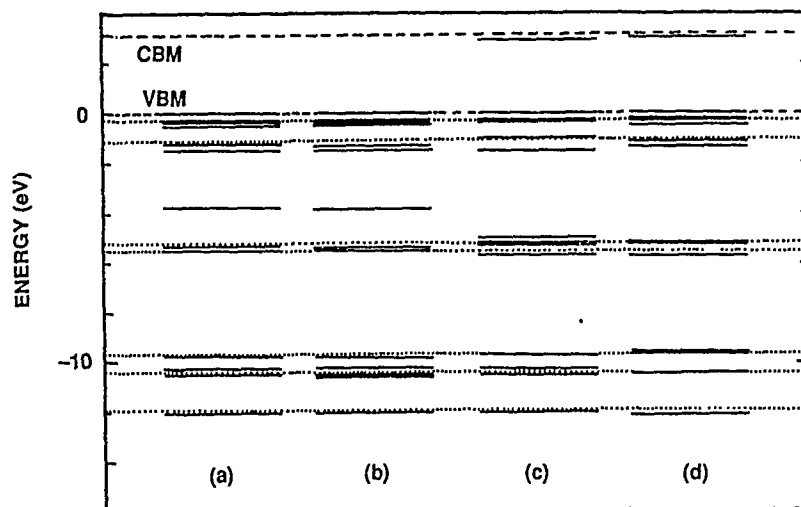


Fig. 2 Calculated energy levels of ZnSe with different Li impurities at the Γ point of the supercell: (a) after the breathing relaxation of ZnSe with Li_{Zn} , (b) after the full relaxation of ZnSe with Li_{Zn} , (c) ZnSe with Li at the $T_d(\text{Se})$ site and (d) ZnSe with Li at the $T_d(\text{Zn})$ site. Only the occupied states are shown. Broken and dotted lines represent the energy levels of perfect ZnSe.

Table I Calculated total energies per cell relative to perfect ZnSe.

Defect	Total Energy (eV)
Li_{Zn}	24.3
Li_i at $T_d(\text{Se})$	-8.9
Li_i at $T_d(\text{Zn})$	-6.7
V_{Zn}	34.7

Stability of Li_{Zn}

The calculated total energies relative to that of the perfect ZnSe are listed in Table I, together with the result for V_{Zn} . Details on the calculation for the vacancy will be appeared in elsewhere[10]. Using the values in Table I, one can estimate the energy needed for the reaction of Eq. (1) to be 1.5eV when the charged state of each defect is all neutral. Since the highest occupied state can be regarded as a shallow donor-like state as shown in Fig. 2, the ionization energy of the Li_i can be approximated with its orbital energy. Furthermore the total energy difference between charged states of V_{Zn} is considered to be small enough to neglect since V_{Zn} can be regarded as a divalent acceptor. When the chemical potential equals to VBM which is a relevant region in p-type semiconductors, the total energy of the r.h.s in Eq. (1) is reduced by about 3eV. Therefore Li_{Zn} becomes unstable to the creation of ionized Li_i and V_{Zn} and the self-compensation occurs. For more quantitative discussion the calculation for such charged states of the defects should be done.

CONCLUDING REMARKS

We have calculated the total energies and the electronic structure of a Li impurity and a Zn-site vacancy in ZnSe, by taking the lattice relaxation into account. It has been found that Li at $T_d(\text{Se})$ is stable and a shallow donor-like state appears. Finally, it has been proposed that Li_{Zn} could be self-compensated in such a way that Li at the Zn site migrates to the tetrahedral interstitial site with ionization, producing the vacancy at the Zn site.

The numerical calculations were performed with use of the Numerical Simulation System at National Aerospace Laboratory. This work is supported in part by a Grant-in-Aid for Scientific Research from the Ministry of Education, Science and Culture of Japan.

REFERENCES

1. Y. Yamada, I. Kidoguchi, T. Taguchi and A. Hiraki, Japan. J. Appl. Phys. 28 (1989) L837.
2. A. Baldereschi and N.O. Lipari, Phys. Rev. B8 (1973) 2697.
3. M. Ohishi, Japan. J. Appl. Phys. B25 (1986) 1546.
4. H. Chacham, J.L.A. Alves and M.L. De Siquiera, Solid State Commun. 64 (1987) 863.
5. Y. Bar-Yam and J.D. Joannopoulos, Phys. Rev. B30 (1984) 1844.
6. B.B. Bachelet, D.R. Hamann and M. Schlüter, Phys. Rev. B26 (1982) 4199.
7. D.M. Ceperley and B. Alder, Phys. Rev. Lett. 45 (1980) 566.
8. J. Perdew and A. Zunger, Phys. Rev. B23 (1981) 5048.
9. R. Car and M. Parrinello, Phys. Rev. Lett. 55 (1985) 2471.
10. T. Oguchi, T. Sasaki and H. Katayama-Yoshida, (unpublished).

MODIFIED OPTICALLY DETECTED MAGNETIC RESONANCE TECHNIQUE FOR STUDIES OF DEFECTS IN Si AND GaAs

W.M. CHEN* AND B. MONEMAR*,**

*Department of Physics and Measurement Technology, Linköping University, S-581 83 Linköping, SWEDEN

**Present address: Max-Planck-Institut für Festkörperforschung, Heisenbergstrasse 1, D-7000 Stuttgart 80, FRG.

ABSTRACT

We discuss one of the major difficulties, namely the strong free carrier induced background signal, in studies of defects in Si and GaAs by optically detected magnetic resonance (ODMR) technique. A modified ODMR technique, namely delayed ODMR, is presented and is shown to be very successful in overcoming this difficulty.

INTRODUCTION

ODMR has been proven to be a powerful technique for studies of electronic structure and microscopic identification of defects in many semiconductors over the past decade [1,2]. However, the application of the ODMR technique to the technologically important materials Si and GaAs as well as their related heterostructures has unfortunately been very limited so far [3-8]. In this work, we wish to expose one of the major difficulties responsible for this limitation, and we also present a modified ODMR technique which successfully overcomes this problem.

DIFFICULTIES IN ODMR STUDIES OF DEFECTS IN Si AND GaAs: ORIGIN AND CONSEQUENCE

One of the major problems in ODMR studies of defects in Si and GaAs is the presence of a strong background signal [9-15]. This background signal often dominates in an ODMR spectrum and obscures any possible detection of defect-related ODMR signals, as shown in the upper part of Fig.1.

The origin of this background signal has been a great concern, and has been discussed to be manifold [9-15], closely related to the properties of the materials. Some obvious differences between the materials like Si and GaAs and other materials in which ODMR has been very successful include the dielectric constant and the free-carrier mobility. A Si or GaAs crystal with a higher dielectric constant disturbs the microwave (MW) pattern more when placed in a MW cavity. This results in a strong effect on the crystal by a non-vanishing MW electric field (E-field), which should not be the case in an ideal ODMR experiment. Furthermore, free carriers of higher mobility in Si and GaAs are much easier to accelerate and consequently heated in the MW E-field as a cause of MW power loss. The heating of carriers varies the density of electronic excitations localized at defects (e.g. bound exciton (BE)) and thereby affects defect-related PL emission, via altering the capture probability of free carriers by defects or impact ionizing these electronic excitations

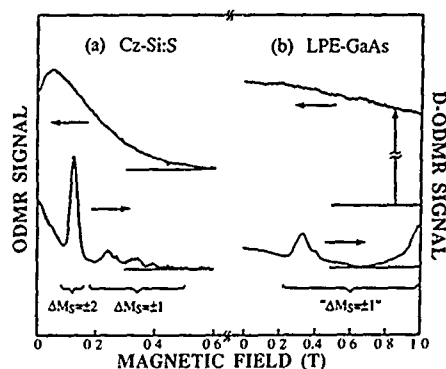


Fig. 1 The standard ODMR and the D-ODMR spectra at 4 K and 9.16 GHz : (a) from the S-related defect in Cz-grown Si, with $\tau_L = 0.3$ ms, $\tau_d = 0.4$ ms, $\tau_{MW} = 0.4$ ms and $T = 2$ ms; and (b) from the deep triplet center in LPE GaAs layer, with $\tau_L = 0.3$ ms, $\tau_d = 0.32$ ms, $\tau_{MW} = 0.4$ ms and $T = 2$ ms. The parameters τ_L , τ_d , τ_{MW} and T are defined in Fig.2.

by hot carriers when a certain threshold of the MW power is reached.

The intensity and the lineshape of the background signal as appearing in an ODMR spectrum depend largely on the specific configuration of the MW E-field with respect to a static magnetic field B . Unlike the case of a standard cyclotron resonance (CR) experiment when the MW E-field is preferably polarized perpendicular to B (either linearly or circularly polarized), the MW E-field in a common MW cavity for ODMR measurement usually contains components polarized both perpendicular and parallel to B . In the former case the background signal is customarily referred to as the optically detected CR (ODCR) signal when $\omega\tau \gg 1$. On the other hand, it seems to be more appropriate to describe the background signal as optically detected MW conductivity when $\omega\tau \ll 1$. In an ODMR experiment when there exists a subcomponent of the MW E-field polarized along B , a non-resonant MW power loss should also be considered. Therefore the background signal in an ODMR spectrum from Si and GaAs results not only from the CR heating of the free carriers but also from the non-resonant MW-induced heating of the free carriers damped by the magnetically-induced resistance.

OVERCOMING THE DIFFICULTIES BY D-ODMR: PRINCIPLE AND EXPERIMENTAL

Knowing the role of free carriers as a medium converting the MW power absorption to a variation of the defect-related PL emission, a way to overcome the background signal in the ODMR experiment is apparently to avoid the photo-excited free carriers. Some common methods to do so include below bandgap resonant optical excitation of a defect or the introduction of carrier traps. There are experimental difficulties in achieving resonant excitation of various defect systems by an infrared (IR) or near IR laser, preferably a tunable laser since various defects possess quite different excitation characteristics. Besides, the presence of a two-step excitation process [16] questions a general application of the first method. On the other hand, introduction of carrier traps by a special treatment, such as irradiation by high-energy particles, change the characteristics of the materials, which might affect or even destroy the defect systems of interest.

Another way to avoid the free carriers which has not been explored so far is to take the advantage of usually very different dynamical properties between the free carriers and the defect-related electronic excitations (e.g. deep BE's). It is well

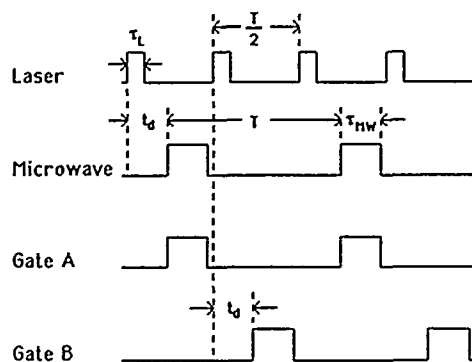


Fig.2 Pulse sequence of the laser, the microwave and the sampling gates A and B.

known that the free carriers usually decay much more quickly than the deep BE's. Therefore a modified ODMR technique, namely delayed ODMR, can be developed to overcome the ODCR background signal, by applying the MW pulse some time after

the optical excitation pulse when the free carrier density has significantly decreased. In Fig.2 we show a pulse sequence in such D-ODMR experiments for the optical excitation source (e.g. a laser), the MW radiation, and two sampling gates A and B. Here t_d denotes the delay time of the MW radiation and optical detection (gate A and B) after the laser pulse. The so-called D-ODMR signal corresponds to the difference between the two sampled signals, i.e. (A-B).

Our D-ODMR spectrometer is based on a modified Bruker ESR X-band spectrometer (Bruker 200D-SRC), with a cylindrical TE_{011} MW cavity (possessing a response time of about 100 ns or less) with optical access from all directions. Above bandgap optical excitation was achieved by using an Ar^+ laser, pulsed by an acousto-optic modulator (with a response time of about 100 ns) at a repetition rate $f_L = 2/T$. The delayed pulse, produced by an HP 8004A Pulse Generator (with a resolution of about 1 ns for the delay time and the pulse width) at a repetition rate $f_{MW} = 1/T$, triggered a PIN diode to amplitude modulate the MW power sent into the MW cavity. The PL signal was collected by a cooled North-Coast Ge detector (with response time of about 1 μ s), and then sampled with two gates (A and B) by a Boxcar Averager (including a gated integrator). The subtraction (A-B) in our case was simply performed by a lock-in amplifier, in phase with the pulsed MW radiation. The resulting ODMR spectrum was recorded by either an X-Y recorder or a computer.

A similar technique, named as pulsed ODMR [17] or time-resolved ODMR [18], has been employed to study defect systems with varying transient behaviour, such as differently distant donor-acceptor pairs [17,18]. The potential of the technique to overcome the ODCR background signal in the ODMR experiments in materials like Si and GaAs was not discovered in previous work, however.

RESULTS FOR SPIN-TRIPLET CENTERS IN Si AND GaAs

We have applied the D-ODMR technique to a number of defect systems in Si and GaAs, which turns out to be very successful. In Fig.1 we show two spin-triplet centers as examples. Both of them were not detectable in conventional ODMR due to the presence of a strong background signal, as shown in the upper part of the figure. By D-ODMR we were able to obtain the electronic structure of a S-related defect in crystalline silicon. The lowest electronic excited state has been revealed to be a spin-triplet ($S=1$), evidenced by its characteristic ODMR spectrum (lower part of Fig.1(a)) where both $\Delta M_S = \pm 2$ and $\Delta M_S = \pm 1$ transitions can be clearly seen. The

transition from the spin-triplet to the crystal ground state gives rise to the deep photoluminescence emissions [19]. A weak anisotropy of the spin-triplet, which could not be resolved in Zeeman spectroscopy [20], has been uncovered. This leads directly to a distorted trigonal symmetry of the S-related defect. The deep spin-triplet center, which has been previously seen in bulk GaAs materials [5,6], was observed for the first time to be present as a contamination in LPE-grown epitaxial GaAs layers by the D-ODMR technique (Fig.1(b)).

The D-ODMR technique presented in this work is not at all limited only to Si and GaAs. Its application to other high-dielectric-loss materials is highly relevant. The technique presented in this work may therefore represent a breakthrough in a general application of ODMR for studies of defects in semiconductors.

REFERENCES

1. B.C. Cavenett, Adv. in Phys. **30**, 475 (1981).
2. W.M. Chen, B. Monemar and M. Godlewski, in Defect and Diffusion Forum, Vol.62/63, edited by H.J. von Bardeleben (Trans. tech. Publications, Aedermannsdorf, 1989) p.133.
3. K.M. Lee, K.P. O'Donnell, J. Weber, B.C. Cavenett and G.D. Watkins, Phys. Rev. Lett. **48**, 37 (1982).
4. J. Weber and G.D. Watkins, in Proc. 13th Int. Conf. on Defects in Semiconductors, Coronado, edited by L.C. Kimerling and J.M. Parsey, Jr. (The Metallurgical Society of AIME, Warrendale, PA, 1985) p.661.
5. T.A. Kennedy and N.D. Wilsey, Phys. Rev. **B32**, 6942 (1985).
6. H.P. Gislason and G.D. Watkins, Phys. Rev. **B32**, 6945 (1985).
7. H.P. Gislason and G.D. Watkins, Phys. Rev. **B33**, 2957 (1986).
8. H.W. van Kesteren, E.C. Cosman, F.J.A.M. Greidanus, P. Dawson, K.J. Moore and C.T. Foxon, Phys. Rev. Lett. **61**, 129 (1988).
9. R. Romestain and C. Weisbuch, Phys. Rev. Lett. **45**, 2067 (1980).
10. B.C. Cavenett and E.J. Pakulis, Phys. Rev. **B32**, 8449 (1985).
11. E.J. Pakulis and G.A. Northrop, Appl. Phys. Lett. **50**, 1672 (1987).
12. M. Godlewski, H. Weman, F.P. Wang, B. Monemar, W.M. Chen and Q.X. Zhao, in Defects in Electronic Materials, edited by M. Stavola, S.J. Oearton and G. Davies (Mat. Res. Soc. Symp. Proc. **104**, 1988) pp.117-120.
13. W.M. Chen, Q.X. Zhao, M. Ahlström and B. Monemar, in The Physics of Semiconductors, edited by W. Zawadzki (Institute of Physics, Polish Academy of Sciences, Warsaw, 1988) p.279.
14. F.P. Wang, B. Monemar and M. Ahlström, Phys. Rev. **B40**, 11195 (1989).
15. W.M. Chen, P.O. Holtz, B. Monemar, M. Sundaram, J.L. Merz and A.C. Gossard, these proceedings.
16. B. Monemar and L. Samuelson, Phys. Rev. **B18**, 809 (1978).
17. P. Dawson, B.C. Cavenett and G. Sowersby, Solid State Electronics **21**, 1451 (1978).
18. J.J. Davies, R.T. Cox and J.E. Nicholls, Phys. Rev. **B30**, 4516 (1984).
19. M.L.W. Thewalt, M. Nissen, D.J.S. Beckett and S. Charbonneau, in Proc. 3rd Int. Conf. on Shallow Impurities in Semiconductors, ed. B. Monemar (Inst. of Phys. Conf. Series Vol.95, Bristol, 1989) p.505.
20. M. Singh, E.C. Lightowers and G. Davies, in Proc. E-MRS 1989 Spring Meeting, Strasbourg, May 30-June 2, 1989.

NITROGEN AND PHOSPHOROUS IMPURITIES IN DIAMOND

Koblar Jackson[†], Mark R. Pederson and Joseph G. Harrison^{*}, Complex Systems Theory Branch, Naval Research Laboratory, Washington D.C. 20375-5000. [†]NRC-NRL Research Associate. ^{*}University of Alabama-Birmingham, Birmingham, AL 35294.

ABSTRACT

In this paper we use a first-principles local density approximation-based approach to study the properties of the n-type impurities nitrogen and phosphorous in diamond. We determine impurity donor level positions of 0.90 eV and 1.09 eV, respectively for C:N and C:P, measured relative to the bottom of the conduction band. We also study the energetics of impurity atom relaxation along the $\langle 111 \rangle$ direction in the diamond lattice. While experimental observations indicate a trigonal distortion about the impurity site, we find the on-center position for both impurity atoms to be stable against the simple $\langle 111 \rangle$ relaxation.

INTRODUCTION

Substitutional nitrogen and phosphorous, with five valence electrons, are prototype n-type impurities in diamond. In this paper we study the properties of C:N and C:P using a first-principles quantum mechanical approach based on the local density approximation (LDA), performing self-consistent LDA calculations on finite clusters of atoms. In these calculations we seek first to determine the positions of the impurity donor levels relative to the host conduction band (CB). A second issue of interest is the position of the impurity atom in the diamond lattice. Experimental evidence clearly shows[1] a trigonal distortion at the impurity site. A simple model for this distortion has the the nitrogen atom moving off-center in the $\langle 111 \rangle$ direction as a result of a Jahn-Teller effect. Four equivalent anti-bonding orbitals centered on the C-N bonds are available to the donor electron. Stretching one of the bonds lowers the energy of the corresponding anti-bonding orbital, and placing the donor electron in this state gives a non-degenerate ground state for the C:N system. From the point of view of a one-electron theory such as LDA, however, such a picture is problematic. The lowest one-electron state available to the donor electron is a symmetric combination of the four anti-bonding orbitals. Any off-center relaxation in LDA must then be due to higher order effects. We investigate the off-center relaxation of the impurity atom in the diamond lattice by performing LDA total energy calculations as the impurity atom is systematically moved off-center.

COMPUTATIONAL METHOD

The local density approximation[2] is the starting point for most current first-principles condensed-matter calculations, and detailed expositions of the theory are abundant in the literature. In our calculations we employ the Kohn-Sham exchange functional, with Ceperly-Alder correlation as parametrized by Perdew and Zunger.[3] We solve the LDA one-electron Schroedinger equations in a Gaussian-orbital based, linear combinations of atomic orbitals framework, using a recently developed[4] variational mesh to evaluate the Hamiltonian matrix elements numerically. We investigate the properties of localized impurities by performing parallel calculations on finite clusters of atoms with

and without an impurity atom replacing the central host atom. Electronic properties are taken from the LDA eigenvalues and structural properties are determined by minimizing cluster total energies with respect to the appropriate nuclear coordinates. Independent total energy calculations for each configuration ensure that all orbital relaxation effects are included self-consistently.

RESULTS

A. Electronic properties

The clusters used in our calculations consist of successive shells of nearest neighbor (n.n.) carbon atoms around a central site, with bond lengths set equal to the C-C bond distance in diamond, 2.92 a.u. Four-fold coordination of surface carbons is achieved by adding hydrogen atoms at the appropriate sites, with a C-H distance of 2.08 a.u. Capping the clusters with hydrogen atoms ties off dangling bond states that would otherwise appear in what corresponds to the bulk crystal band gap. The simplest cluster for studying substitutional impurities is C_5H_{12} , consisting of a central atom, one n.n. shell of carbons, and the appropriate surface hydrogen atoms. In $C_{17}H_{36}$, second n.n. C atoms are included, and 36 hydrogen atoms used to cap the cluster.

The energy band gap and the VB width, taken as differences in the appropriate LDA eigenvalues, are convenient quantities for gauging the bulk-like character of a cluster. The values for the diamond band gap and VB width from LDA bandstructure calculations are 4.2 eV and 22.1 eV, respectively.[5] As shown in Table I, we found 7.5 eV and 12.6 eV for the gap and VB width in

Table I. Calculated values for the band gap and valence band width of diamond taken from hydrogen-terminated carbon cluster calculations.

System	Band Gap (eV)	VB width (eV)
C_5H_{12}	7.5	12.6
$C_{10}H_{22}^a$	5.0	16.3
$C_{17}H_{36}$	4.5	17.7
$C(\text{bulk})^b$	4.2	22.1

^aDiamond film calculations of Pederson, Jackson and Pickett[6].

^bBulk band structure calculations of Erwin[5].

the C_5H_{12} cluster, while for $C_{17}H_{36}$ we found 4.5 and 17.7 eV, respectively. In a separate calculation[6] of a $C_{10}H_{22}$ cluster model of the diamond (111) surface, we found 5.0 and 16.0 eV for the energy gap and VB width. The results in Table I clearly show that both the band gap and VB width uniformly approach the bulk crystal values with increasing numbers of atoms in the clusters; in the $C_{17}H_{36}$ cluster the band gap is within 10% of the bulk LDA value, suggesting that the electronic environment in this cluster is already reasonably bulk-like.

When the central atom in the C_5H_{12} and $C_{17}H_{36}$ clusters is replaced by N or P, two impurity related states appear in the vicinity of the host band gap. An anti-bonding donor state of A_1 (s-like) symmetry appears in the band gap just below the CB edge, and an unoccupied state of T_2 (p-like) symmetry appears just above the CB onset. For the N impurity, the position of the donor level

is essentially identical in the two clusters studied, at $E_c - 0.91$ eV and $E_c - 0.90$ eV in the smaller and larger clusters, respectively, where E_c is the bottom of the CB. The T_2 level is found just above the CB edge, 1.4 eV and 1.0 eV above the donor level in the two nitrogen impurity clusters. The P donor level lies at $E_c - 1.17$ eV and $E_c - 1.09$ eV in the two clusters studied, indicating some sensitivity of the result to cluster size. The greater sensitivity of the C:P result is probably due to the greater size of the P atom relative to C and N. The atomic radii are 1.28, 0.91 and 0.92 Å, respectively for P, C, and N. In C:P the T_2 impurity state is lower in energy than the corresponding state in C:N, and is essentially degenerate with the lowest CB state. The donor level results are collected in Table II.

Table II. The defect levels for on-site substitutional nitrogen and phosphorous defects in hydrogen-terminated clusters are presented as a function of cluster size. Energies are with respect to the lowest unoccupied state.

System	Energy (eV)
$C_5H_{12}:N$	0.91
$C_{17}H_{36}:N$	0.90
$C_5H_{12}:P$	1.17
$C_{17}H_{36}:P$	1.09

B. Structural properties

We investigated the on-center stability of the central atoms in the clusters by calculating cluster total energies while moving the central atom off the tetrahedral site in the $\langle 111 \rangle$ direction. This relaxation is the simplest distortion giving rise to the experimentally observed lowering of the symmetry from tetrahedral to trigonal at the impurity site. The total energy vs distortion plots for these calculations appear in Fig.1 where the relaxation is given as a percentage of the n.n. bond length (2.92 a.u.). Positive values correspond to bond-shrinking distortions and negative values to a stretching of the n.n. bond. The curves in Fig.1 indicate that the on-center site is stable for both the N and P impurity atoms, as well as for the central C atom in the "pure" clusters.

Because atomic P is significantly larger than atomic C or N (the atomic radii are 1.28, 0.91 and 0.92 Å), we expect lattice relaxation to be important in C:P but not in C:N. We calculated the total energy of the $C_{17}H_{36}:P$ cluster while allowing the first n.n. C atoms to relax symmetrically outward from the impurity atom, holding the remaining atoms in the cluster fixed. We find the minimum energy configuration to correspond to a 6% outward relaxation of the n.n. atoms, making the C-P distance 3.10 a.u. The position of the C:P donor level was insensitive to the n.n. relaxation, increasing by only 0.04 eV for a 10% relaxation. The A_1 impurity state remains well below the T_2 state in all these calculations.

SUMMARY

In this work we have performed self-consistent LDA cluster calculations on the C:N and C:P impurity systems. We found the donor levels in both systems to be deep, lying well below the unoccupied states. We find the activation

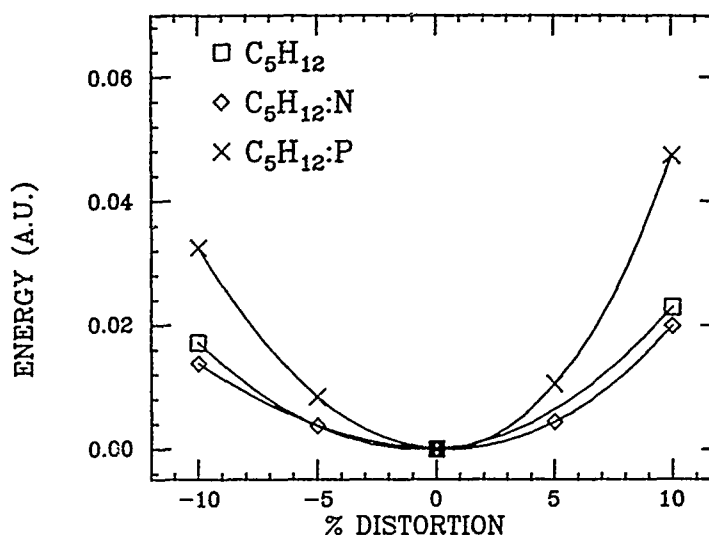


Fig.1 Total energy vs distortion curves for the relaxation of the central atom along the $\langle 111 \rangle$ trigonal axis for the indicated clusters. The distortion is given as a percent of the n.n. distance (2.09 a.u.), and energies are with respect to the on-center configuration for each cluster.

energy for the C:P donor state (1.09 eV) to be nearly the same as for the C:N donor (0.90 eV), suggesting that other group V elements such as As are also likely to have deep donor levels in diamond.

We have also investigated the structural properties of the N and P impurity atoms in the diamond lattice. For both C:N and C:P, we found the ideal tetrahedral substitutional impurity site to be stable against simple off-center relaxation of the impurity atom in the $\langle 111 \rangle$ direction. This suggests that the experimentally observed trigonal distortion at the impurity site in C:N is due to a more complicated relaxation mode than the simple relaxation of the impurity atom off the ideal substitutional site. Calculations on larger clusters are needed to investigate trigonal distortions involving more than the impurity atom.

ACKNOWLEDGEMENTS

This work was supported in part by the Office of Naval Research. The calculations were carried out in part on the CRAY computers at the Pittsburgh Supercomputer Center and the Alabama Supercomputer Center.

REFERENCES

- [1] J. Walker, Rep. Prog. Phys. **42**, 108 (1979), and references therein.
- [2] P. Hohenberg and W. Kohn, Phys. Rev. **136**, B864 (1964); W. Kohn and L.J. Sham, Phys. Rev. **140**, A1133 (1965).
- [3] J.P. Perdew and A. Zunger, Phys. Rev. B **23**, 5048.
- [4] M.R. Pederson and K.A. Jackson, submitted to Phys.Rev.B.
- [5] S.C. Erwin (private communication).
- [6] M.R. Pederson, K.A. Jackson and W.E. Pickett, in Technology Update on Diamond Films, Ed. R.P.H. Chang, D. Nelson and A. Hiraki, (Mat. Res. Soc., Pittsburgh, 1989).

PART II

Electronic Structure -
Shallow Impurities

RADIATIVE RECOMBINATION AND CARRIER LIFETIMES IN SURFACE-FREE GaAs HOMOSTRUCTURES

L. M. Smith and D. J. Wolford
IBM T. J. Watson Research Center
Yorktown Heights, NY 10598

R. Venkatasubramanian and S.K. Ghandhi
Rensselaer Polytechnic Institute
Troy, NY 12180

ABSTRACT

We show that the radiative efficiencies and lifetimes of photoexcited carriers in epitaxial GaAs may be enhanced by 3 to 4 orders-of-magnitude by the preparation of n^+ , doped layers at surface and substrate interfaces. Samples were prepared by Organo-Metallic Vapor Phase Epitaxy (OMVPE), with n -region thicknesses of 3-10 μm , and narrow layers Si-doped to n^+ concentrations of $5 \times 10^{18} \text{ cm}^{-3}$. Time-resolved luminescence in such structures, under both surface and bulk (near-band-edge) excitation conditions, reveal near-edge-excitonic or band-to-band-dominated recombination spectra, with carrier lifetimes ranging from 1.5 nsec at 1.5 K to nearly 1 μsec at room temperature. This is in contrast to the sub-nanosecond lifetimes typical in conventionally prepared bulk GaAs, but is comparable to the best reported for high-purity LPE-prepared GaAs/ $\text{Al}_x\text{Ga}_{1-x}\text{As}$ double heterostructures. The spatial distributions of photoexcited carriers in these structures are observed to expand by over an order of magnitude during their 1 μsec room temperature lifetime. The expansion is diffusive, with a measured diffusion constant of 14 cm^2/sec at 300 K. This corresponds to a room temperature mobility of 525 cm^2/Vsec , comparable to previously measured hole mobilities in bulk p -type GaAs of similar purity. These results are clear evidence that the narrow, heavily doped layers effectively "shield" minority carriers from the interfaces, thereby reducing interface recombination.

INTRODUCTION

Direct-gap semiconductors, such as GaAs, have always been recognized as the material of choice for optoelectronic devices. Since the radiative band-to-band transitions are dipole allowed and non-radiative Auger processes are nearly negligible, the theoretical quantum efficiency for the production of light in GaAs approaches 100%. In "real" structures, however, this limit is rarely, if ever, attained, because of non-radiative recombination at defects both in the bulk and at surfaces and interfaces. While non-radiative bulk defects have been rendered virtually negligible by modern epitaxial growth techniques, robust solutions to the problems of surface and interface states have remained elusive.

In fact, recombination of carriers in GaAs may, in practice, be completely dominated by nonradiative recombination at the crystal surface. The surface recombination velocity - generally greater than 10^4 cm/sec in GaAs - limits the minority carrier lifetime to less than a nanosecond. Many novel methods for passivation of these surface states have been attempted in recent years.[1-7] However, the standard against which all methods are compared are GaAs/ $\text{Al}_x\text{Ga}_{1-x}\text{As}$ heterostructures,[8-16] where the larger band gap $\text{Al}_x\text{Ga}_{1-x}\text{As}$ layers serve to confine the carriers to the GaAs layers inside the structure, and away from the crystal surface.

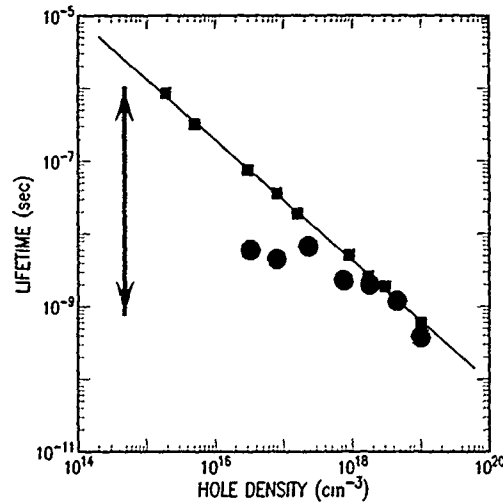


Figure 1. Dependence of minority carrier lifetime on impurity density from Refs. 8 (circles) and 9 (squares). Arrow shows variation in lifetime measurements from Refs. 9-16.

It was not until such double heterostructures were prepared that the physics of intrinsic radiative recombination processes in GaAs could be studied. In 1978 Nelson and Sobers [9] achieved a record minority carrier lifetime at room temperature of just over 1 μ sec in high-purity p-type GaAs ($N_A = 2 \times 10^{15} \text{ cm}^{-3}$) prepared by Liquid Phase Epitaxy (LPE). By varying the acceptor concentration in a series of samples, Nelson and Sobers verified (squares and solid line, Fig. 1) that the minority carrier lifetime varies inversely with the impurity density, $1/\tau = Bn$, a property earlier predicted in 1964 by Lasher and Stern [17], and first measured at higher doping levels in 1976 by Casey and Stern.[8]

Over the past decade, with the development of monolayer-precise growth techniques like Molecular Beam Epitaxy (MBE) and OMVPE, the purity of epitaxial GaAs has increased by well over an order of magnitude. If the trend predicted by Lasher and Stern, and demonstrated by Nelson and Sobers, holds at lower impurity levels, the room-temperature minority carrier lifetimes in present day ultra-high purity GaAs double heterostructures (DH) should be greater than 10 μ sec - an order-of-magnitude larger than Nelson and Sobers' record. In sharp contrast, however, recent results obtained in DH [9-16] do not generally exceed 1 μ sec, and in fact, sample-to-sample variations (arrow, Fig. 1) of room temperature minority carrier lifetimes extend over three orders-of-magnitude.

It is therefore clear that these poor results and, in particular, these extreme sample-to-sample variations observed in GaAs/ $\text{Al}_x\text{Ga}_{1-x}\text{As}$ heterostructures must be due to non-radiative recombination centers at heterointerfaces. However, quantitative descriptions of interface quality and its effect on carrier lifetimes has not been available because the intrinsic recombination processes in GaAs and the effect of bulk impurities is poorly understood. What is needed is an all-GaAs structure which confines carrier to the epilayer, and thus free of the perturbing influences of surfaces or heterointerfaces.

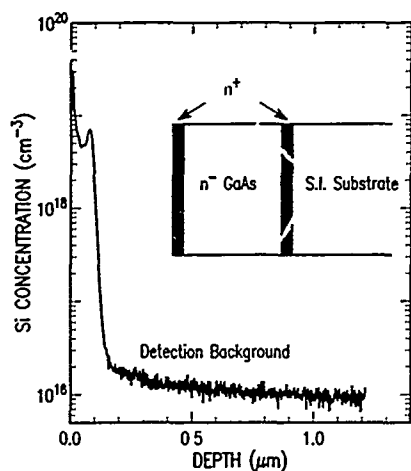


Figure 2. SIMS profile of the 10- μm $n^+/n/n^+$ sample. Inset is a schematic diagram of the GaAs homostructures used in these measurements.

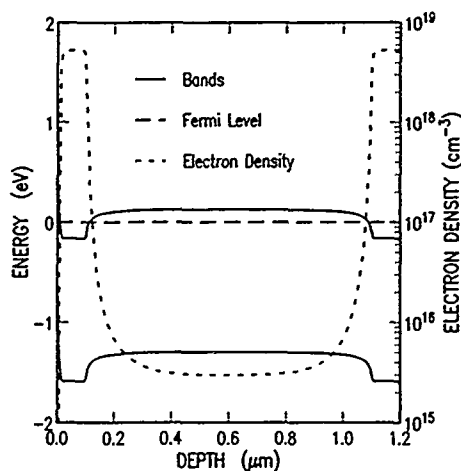


Figure 3. Solution to Poisson's equation for the $n^+/n/n^+$ GaAs homostructure at room temperature.

In this work, we report on time-resolved photoluminescence experiments in GaAs homostructures. We find that the radiative efficiency and lifetimes of photoexcited carriers in epitaxial GaAs may be enhanced by 3 to 4 orders-of-magnitude by the preparation of n^+ , heavily doped layers at surface and substrate interfaces.[18] Samples (inset, Fig. 2) were OMVPE-prepared with n-region thicknesses of 6- and 10- μm , with a narrow 1000 Å layer at the surface and a 2500 Å layer at the substrate interface Si-doped to n^+ concentrations of $5 \times 10^{18} \text{ cm}^{-3}$. The residual impurity density of the bulk layers was $3 \times 10^{15} \text{ cm}^{-3}$. In Fig. 2, the SIMS profile of the 10- μm structure reveals the sharply defined doping spike.

We believe that the mechanism confining the carriers to the bulk, undoped material is related to the band-bending at the homo-interface between the degenerate and non-degenerate regions of the crystal. Solutions to Poisson's equation for these structures shown in Fig. 3, reveal that the surface and substrate doping spikes provide a natural 200 meV barrier to hole migration to the sample surface or to the substrate.

TEMPERATURE DEPENDENCE OF MINORITY CARRIER LIFETIMES

In these experiments, carriers were photoexcited by a synchronously pumped, cavity dumped Styrl-8 dye laser which produced 8 psec pulses every 10 μsec . The wavelength of the excitation light was near-resonant with the band edge (approximately 8000 Å), to minimize absorption in the doped layers. The samples were mounted with rubber cement to a copper block in a variable temperature Janis Super Vari-Temp cryostat, and the temperature was monitored by a Si diode. The laser beam was focused to a 1 mm spot onto the samples and the average power density kept below 5 mW/cm² in order to minimize the effects of carrier diffusion and keep the initial density of electron-hole pairs as low as possible.

In Fig. 4 (a) the room temperature photoluminescence spectrum of a 10 μm epilayer with doped layers at the front and surface interfaces is compared with the same sample, but with the doped surface layer etched away. In both samples the Maxwell-Boltzmann distribution typical of band-to-band transitions is observed. However, in surprising contrast to the "etched" sample, the photoluminescence intensity from the untreated sample is over 3000 times stronger. The corresponding time decays of the photoluminescence intensity in these two samples (Fig. 4 (b)) show that the minority carrier lifetime in the spike-doped sample is also greatly enhanced. The time decays in the unetched sample are single exponential, with a 0.8 μsec lifetime which is independent of sampled wavelength. In fact, the 0.8 μsec lifetime observed in the unetched sample is comparable to the best LPE-prepared GaAs/Al_xGa_{1-x}As double heterostructures, while the 2 nsec lifetime of the etched sample is typical of "surface-dominated" GaAs. (Note that the buried doped layer is still effective in shielding carriers from the semi-insulating substrate.)

In Fig. 5 are shown the temperature dependence of photoluminescence time decays in a 6- μm epilayer. Note that the room temperature lifetime of 800 nsec is the same as is observed in the 10- μm sample (Fig. 4 (b)). The time decay is a single exponential over 4 decades, and the lifetime decreases monotonically with temperature down to 50 K. These single exponential decays also do not depend on spectral position. At temperatures between 50 and 25 K, the time decays become non-exponential, with a long-lived exponential tail which becomes correspondingly weaker and longer as the temperature is decreased. At temperatures below 25 K, the photoluminescence time decays are again exponential (see Fig. 6), with the derived lifetime decreasing from 25 nsec to 1.5 nsec as the temperature decreases. This temperature region precisely coincides with the appearance of sharp structure in the photoluminescence spectra (see Fig. 7), thus signaling the formation of excitonic states from free electrons and holes. However, we find that the lifetimes obtained from these decays do not depend on which of the excitonic species, free or bound, is sampled.

If these samples are indeed free of interface effects, the temperature dependence of the minority carrier lifetime at high temperatures should be understood by Lasher and Stern's calculation of the transition rates for band-to-band recombination in GaAs [2]. Following from Fermi's Golden Rule and assuming a temperature independent matrix element, they calculate the total spontaneous emission rate for a non-degenerate electron-hole gas to be $R_{\text{spont}} = Bnp(300/T)^{3/2}$, where n (p) is the free electron (hole) density and B , the radiative constant appropriate to GaAs, is approximately $2 \times 10^{-10} \text{ cm}^3/\text{sec}$. Taking the case of n-type GaAs with donor density of N_D , acceptor density of N_A , and a photoexcited electron-hole gas of density $n = p$, we may immediately write the governing time-dependent differential equation, $dp/dt = B(300/T)^{3/2} (n_0 + p) p$, where n_0 is the background density of thermally excited free electrons. This expression yields the simple solution,

$$p(t) = \frac{Ae^{-t/\tau}}{1 + C[1 - e^{-t/\tau}]}, \quad (1)$$

where $A = p_i$ is the initial photoexcited electron-hole pair density, $C = p_i/n_0$ is a measure of the bimolecular component of the decay, and

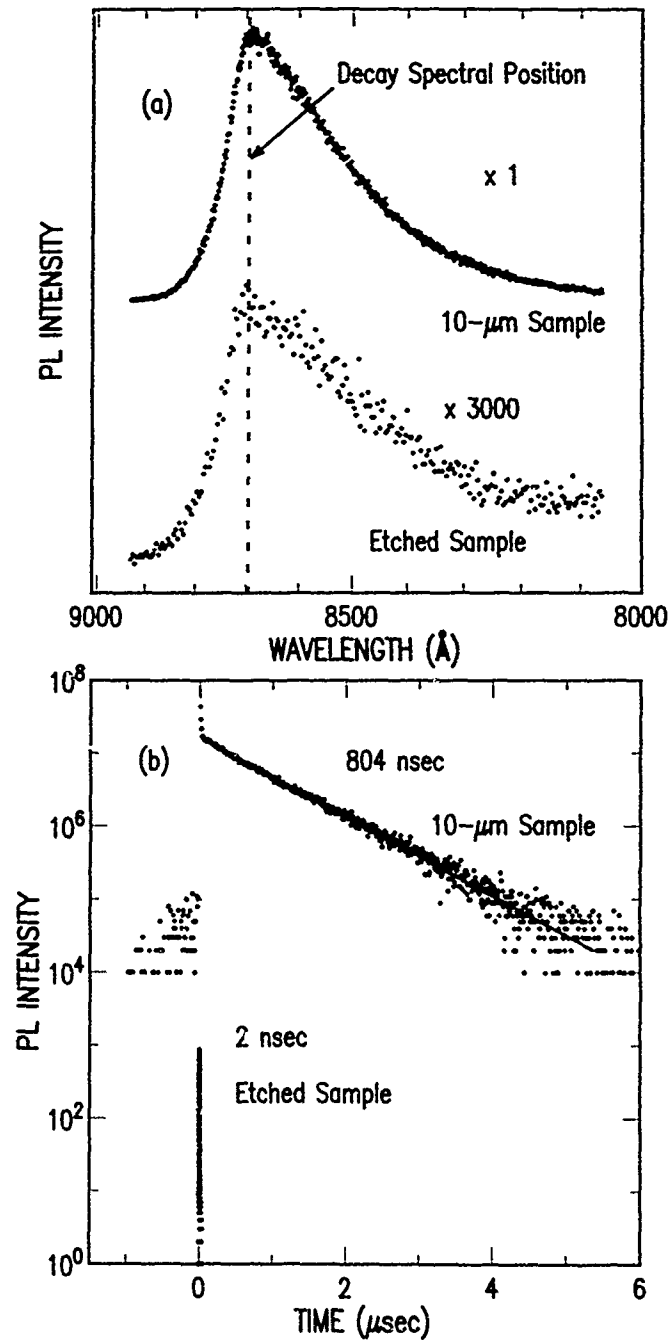


Figure 4. (a) Photoluminescence spectra of the 10- μm sample with the surface doping layer intact, and chemically removed (1500- \AA etched). (b) Time decay of the photoluminescence intensity at the wavelength marked by the dotted line in part (a), after pulsed laser excitation for the etched and unetched 10- μm samples.

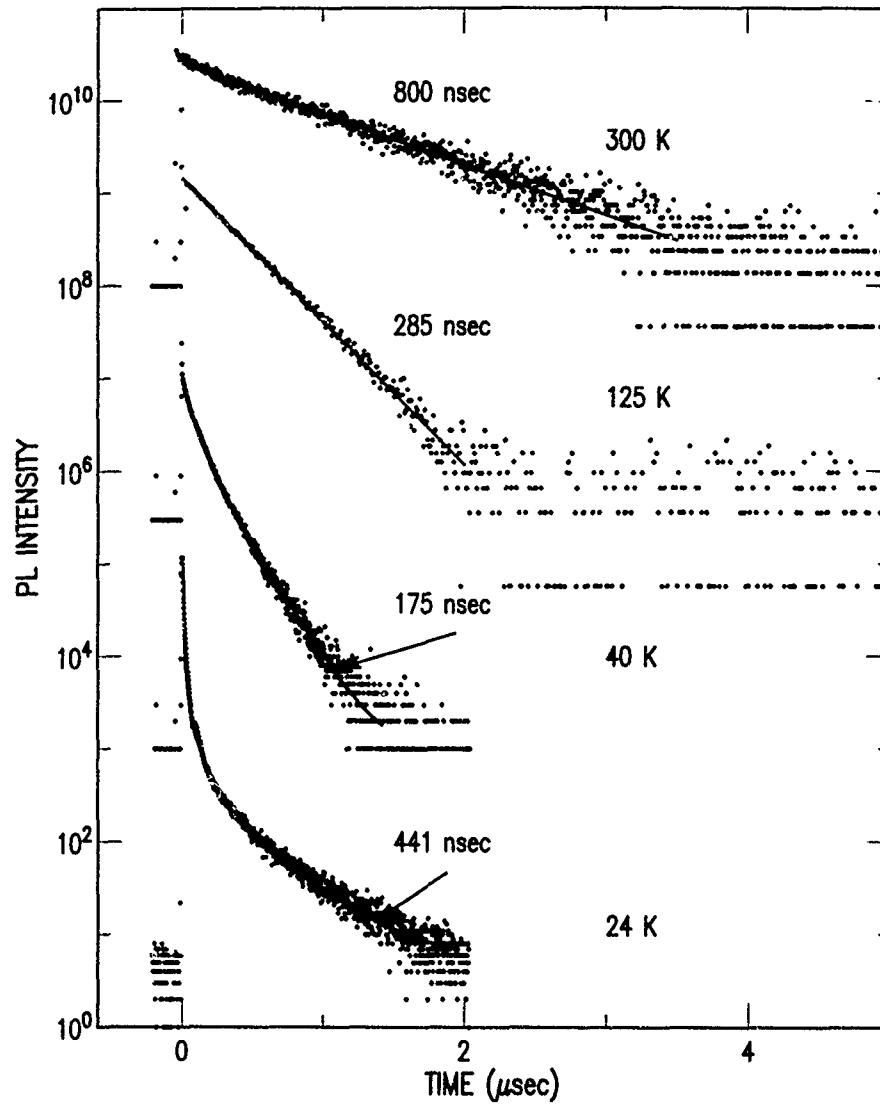


Figure 5. Temperature dependence ($T > 24$ K) of the time decays at the spectral peak of the photoluminescence intensity after pulsed laser excitation of the 6- μm sample. Solid lines are best fits to the data using Eq. 1, as described in the text; Lifetimes shown are those obtained from the fits. The time decays are independent of the spectral position sampled.

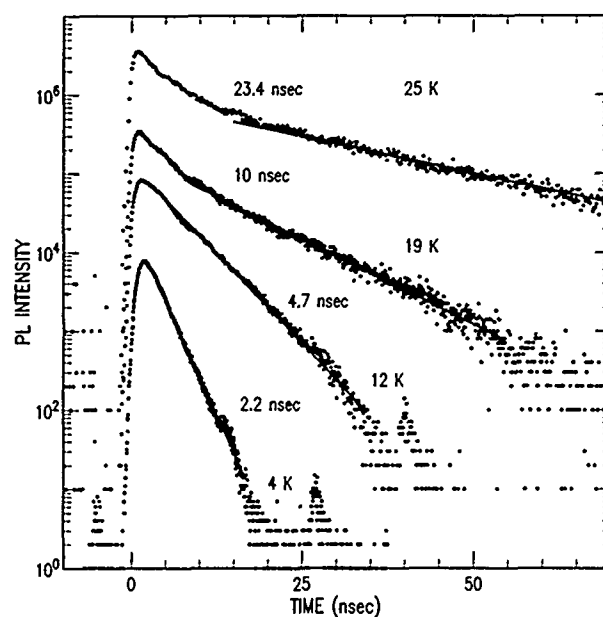


Figure 6. Temperature dependence ($T < 28$ K) of the time decays at the spectral peak of the photoluminescence intensity after pulsed laser excitation of the 6- μ m sample. Solid lines are best fits to the data to exponential time decays; lifetimes shown are those obtained from the fits.

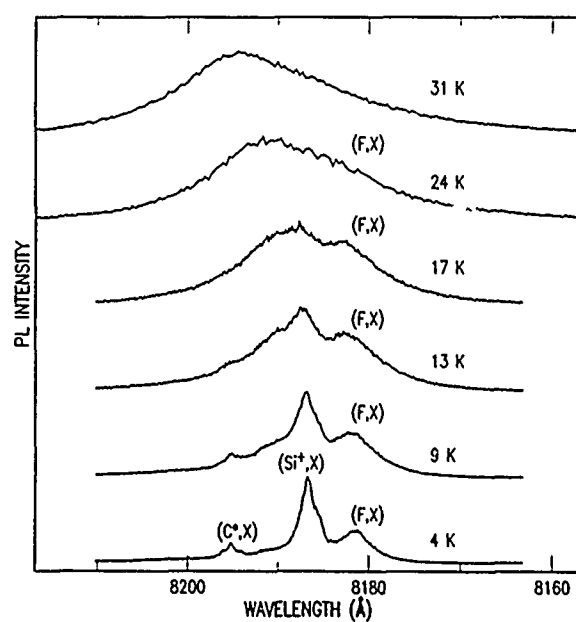


Figure 7. Temperature dependence of photoluminescence spectra at low temperatures for the 6- μ m sample.

$$\tau^{-1} = B(300/T)^{3/2}n_0 \quad (2)$$

is the minority carrier lifetime. Note that the thermal electron density, $n_0 = N_C e^{(E_F - E_g)/k_B T}$, where E_g is the band-gap energy and E_F is the Fermi energy, is calculated by determining the Fermi energy self-consistently by requiring charge neutrality. Thus, at room temperature, if $n = p \ll n_0 = N_D - N_A$, the resulting time decay is exponential with a decay time which depends on temperature as $T^{3/2}$. As the temperature drops below the donor-ionization energy, however, the electrons freeze out onto the donors and the recombination process becomes bimolecular, $dp/dt \sim p^2$, and non-exponential. In addition, the bulk radiative lifetime increases as the free electron density decreases. However, because the n^+ layers are degenerately doped, hole confinement is still effective at low temperatures.

The solid lines in Fig. 5 are best fits to the data using Eq. 1 with A , C and τ as free parameters (C set equal to zero for $T > 50$ K). The lifetimes obtained in the 6- μm (crosses) and 10- μm (plusses) samples are plotted in Fig. 8. Note that the temperature dependence of the lifetimes in both of these structures are nearly identical, but that the surface-etched 10- μm sample (triangles) exhibits short photoluminescence decays - under 3 nsec - over the entire temperature range. Data from the unetched samples may be fit to Eq. 2, with $B = 2 \times 10^{-10} \text{ cm}^3/\text{sec}$, $N_D - N_A = 3.5 \times 10^{15} \text{ cm}^{-3}$, and donor and acceptor ionization energies of 5.84 and 27 meV, respectively; the only free parameter used in the fit is the compensation ratio, N_A/N_D . In Fig. 8(a), the curves A, B and C show the calculated minority carrier lifetime temperature dependence for N_A/N_D equal to 0, 0.4 and 0.8 - the curves A, B and C in Fig. 8(b) show the corresponding temperature variation of the free electron density. We find that the best fit to the data is obtained for a compensation ratio of 0.4. While this is consistent with OMVPE GaAs of this purity prepared under identical conditions, we could not verify this directly because of the lack of Hall data. The lifetimes obtained at higher temperatures is lower than expected from the assumed value of B , and appears to approach a limit of 1 μsec . We believe that this reflects the true non-radiative recombination rate. Since the data does not appear to depend on the epitaxial thickness of the 6- or 10- μm samples, we assume that the non-radiative process results from defects in the bulk, and not at the surface.

As temperatures is reduced below 25 K, the time decays can no longer be fit simply to a bimolecular decay process (Eq. 1, above), and a short, exponential component increasingly begins to dominate the decays. By 20 K, the longer, bimolecular component is no longer observed and the photoluminescence time decays are purely single exponential (Fig. 6). This rapid change in the decay process is accompanied by the appearance of sharp excitonic structure in the photoluminescence spectra (Fig. 7). If we suppose that the decay dynamics are determined by the formation of free excitons at low temperatures, then the temperature dependence of the excitonic lifetime may be derived from consideration of the radiative selection rules. While momentum conservation requires that only excitonic states of near-zero momentum are able to decay radiatively, this condition is relaxed a somewhat because of homogeneous broadening of the excitonic states by interaction with acoustic phonons. For free excitons in a parabolic band, and an assumed Maxwell-Boltzmann distribution, the fraction r , of free excitons with kinetic energy smaller than Δ is given by [19]:

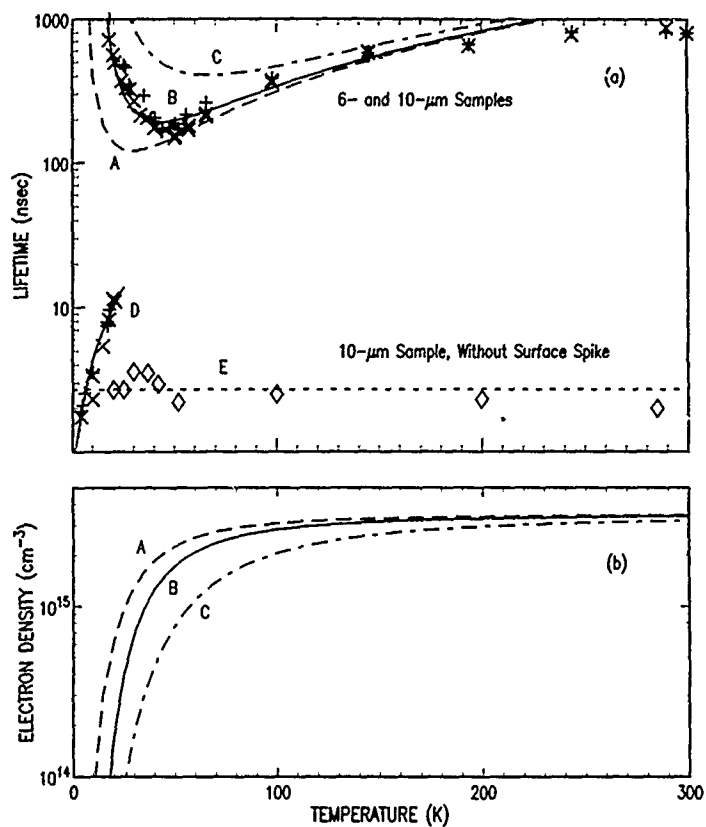


Figure 8. (a) Temperature dependence of the minority carrier lifetime from fits of time decays from the 6-μm (crosses) and 10-μm (pluses) samples. Triangles are those lifetimes observed in the 10-μm sample with the surface spike etched away. Curves A, B, and C are computations of the minority carrier lifetime using Eq. 2 and assuming $N_A/N_D = 0, 0.4$ and 0.8 , respectively. Curve D is best fit to the low temperature data assuming exciton dominated recombination as described in the text; excitonic homogeneous linewidth of 0.5 meV is assumed. (b) Curves A, B, and C are the temperature dependent free electron density corresponding to the curves A, B, and C in part (a).

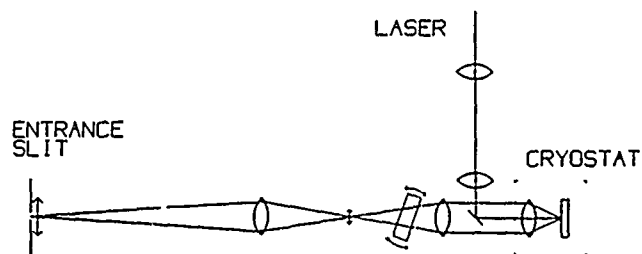


Figure 9. Schematic diagram of experiment used to measure time-resolved expansion of photoexcited carriers in GaAs $n^+/n/n^+$ structures.

$$\tau(T) = \frac{2}{\sqrt{\pi}} \int_0^{\Delta/kT} \sqrt{\epsilon} e^{-\epsilon} d\epsilon \quad (3)$$

From this expression, the temperature-dependent radiative lifetime may thus be derived derived: $\tau(T) = \tau_0/r(T)$. Therefore, the decreasing radiative lifetime in this temperature region may reflect the increasing population of excitons with near-zero center-of-mass momentum as the temperature is decreased. Thus, the low temperature data obtained in these samples is accurately described (curve D, Fig. 8(a)) by this temperature dependence with $\Delta = 0.5$ meV. However, we note that the low temperature photoluminescence spectra in these materials are not dominated by free exciton emission. Rather, photoluminescence spectra (Fig. 7) at 4 K exhibits excitons bound onto both ionized donors (Si) and neutral acceptors (C). Why lifetime data in these samples should be described, perhaps fortuitously, by this temperature dependence is not currently understood.

SPATIAL DIFFUSION OF PHOTOEXCITED CARRIERS

If these homostructures do indeed shield photoexcited carriers from non-radiative recombination at the surface and substrate interfaces, spatial diffusion of carriers away from the laser excitation point should be dramatic. In Fig. 9, a schematic diagram of a system to temporally and spatially resolve photoluminescence from these GaAs homostructures is displayed. In these experiments, carriers are photoexcited by a synchronously pumped, cavity dumped Styryl-8 dye laser which produces 8 psec, 8000-Å pulses every 10 μ sec. The laser beam is focussed to a 15- μ m spot onto the sample using a short focal length lens inside the cryostat. By using a microscope-like imaging system, a 40-times magnified image is projected onto the entrance slit of the spectrometer. Thus, with a rectangular lucite block mounted to a galvanometer, this image of the excitation region may be scanned across the slit, so that photoluminescence may be collected at variable distances away from the excitation point. The spatial resolution of this system is less than 4 microns. By collecting photoluminescence time decays at different positions, the changing spatial distribution of carriers may be directly imaged and measured.

In Fig. 10, the spatial profiles of the photoexcited carriers in the 6- μ m sample is displayed at several times after the excitation pulse. The distribution at the peak of the laser pulse ($t=0$ nsec) is 15- μ m wide and reflects the spatial width of the focussed laser beam. Following this 15- μ m wide excitation, the measured distributions expand rapidly with time, achieving a spatial width nearly 20 times the initially photoexcited distribution.

If the spatial transport of these carriers away from the excitation region is diffusive, then the spatially and temporally varying density, $n(r,t)$, should obey the diffusion equation

$$\frac{\partial n}{\partial t} = -\frac{n}{\tau_f} + D\nabla^2 n, \quad (4)$$

where the diffusion constant D , and lifetime τ_f , are assumed to be independent of the photoexcited carrier density, and the symbols r and ∇ are respectively the position and gradient in the two dimensional plane parallel to the epilayer. Solution to this equation is given by the expression:

$$n(r,t) = \frac{1}{4\pi Dt} e^{-r^2/4Dt} e^{-t/\tau_t}. \quad (5)$$

Thus, in a time-resolved measurement of the spatial distributions of photoexcited carriers, the decay of carriers affects only the overall intensity of the distributions, while the full-width at half-maximum, Δ , is given by

$$\Delta^2 = 11.08Dt + \Delta_0^2. \quad (6)$$

Thus, a plot of the square of the full-width at half-maximum should vary linearly with time, with a slope that is proportional to the diffusion constant, D .

The solid curves in Fig. 10 are fits of expanding Gaussians to the spatial distributions. The square of the full-width at half-maximum of these distributions obtained from the fits are plotted against time in Fig. 11, and demonstrates that the expansion occurs diffusively. The solid line in Fig. 11 is a best linear fit to the data, and the slope yields a diffusivity of 14 cm²/sec. Thus, from the Einstein relation, $\mu = D/k_B T$, the mobility of carriers in this material is calculated to be 526 cm²/Vsec. This derived value is fully consistent with the ambipolar mobility determined from electrical measurements of the electron and hole mobilities in bulk GaAs of similar purity.

From these measurements of the room temperature minority carrier lifetime and diffusivity, we note that the diffusion length of photoexcited holes in this material is nearly 40 μ m. Thus, considering that the width of the epilayer is just 6 μ m, we may conclude that the minority carriers must scatter many times from the n^+/n interface before recombining - a conclusion which confirms the extraordinary shielding properties provided by this structure.

CONCLUSIONS

We have demonstrated that both the luminescence quantum efficiency and minority carrier lifetime may be enhanced in $n^+/n/n^+$ GaAs homostructures by 3- to 4-orders-of-magnitude over typical surface-dominated high-purity GaAs. These results are equivalent to the best obtained for GaAs/ Al_xGa_{1-x} As heterostructures, but are more consistent due to the absence of unpredictable heterointerfaces. While such homostructures shows technological promise in the production of ultra-high efficiency optoelectronic devices and solar cells, they also clearly assist in the understanding radiative and non-radiative recombination in bulk GaAs and their dependence on dopants, defects, and compensation ratios. By direct comparison between these structures and GaAs in double heterostructures (prepared under equivalent conditions), it may be possible to finally understand the physics of defects and disorder at heterointerfaces and their effect on transport and radiative efficiency of minority carriers.

ACKNOWLEDGEMENTS

We thank F. Cardone for the SIMS measurements, and A. Warren for use of his computer program HETMOD. We also acknowledge helpful discussions with G. D. Gilliland. This work was supported in part by the Office of Naval Research under contract N00014-85-C-0868; the Solar Energy Research Institute, Golden, CO under contract XL-5-05018-2; and the New York State Energy Research and Development Authority under agreement 970-ERER-ER-87.

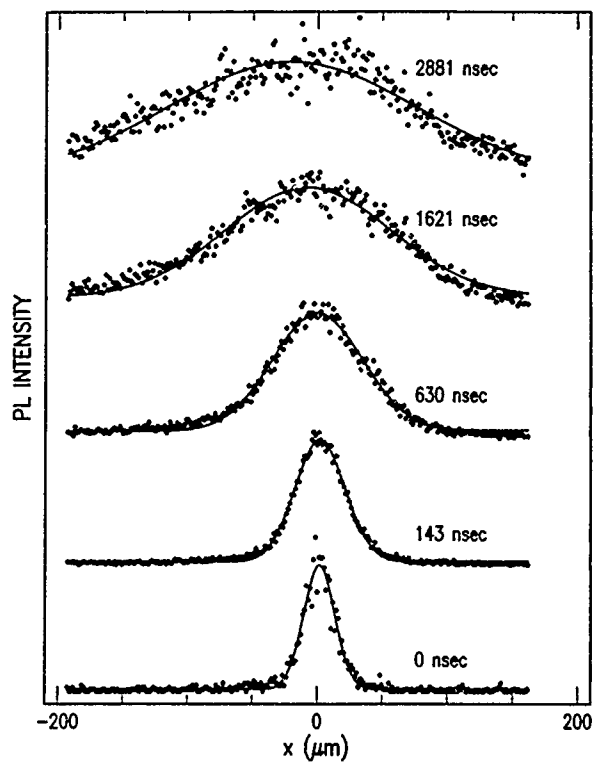


Figure 10. Time-resolved spatial expansion of photoexcited carriers in the 6- μm sample at 300 K. Solid lines are fits of the spatial distributions to expanding Gaussians.

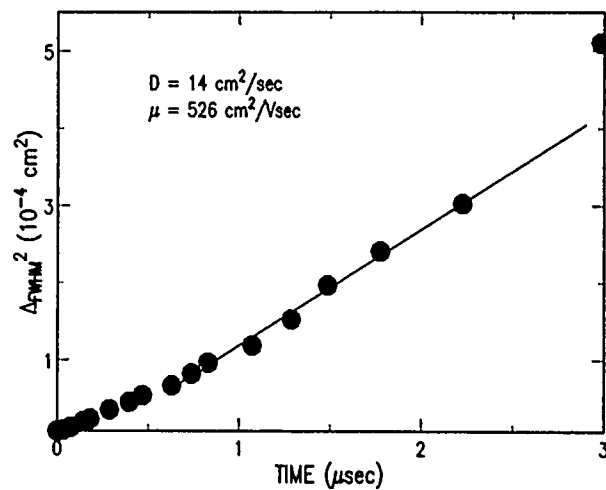


Figure 11. Plot of FWHM of spatial distributions shown in Fig. 10, as described in the text. Solid line is best fit to data, with slope which corresponds to a diffusion constant of 14 cm^2/sec .

REFERENCES

1. E. Yablonovitch, C.J. Sandroff, R. Bhat, and T. Gmitter, Appl. Phys. Lett. 51, 439 (1987).
2. D. Liu, T. Zhang, R.A. LaRue, J.S. Harris, Jr. and T.W. Sigmon, Appl. Phys. Lett. 53, 1059 (1988).
3. B.A. Parkinson, A. Heller, and B. Miller, Appl. Phys. Lett. 33, 521 (1978).
4. R.J. Nelson, J.S. Williams, H.J. Leamy, B. Miller, H.C. Casey, Jr., B.A. Parkinson, and A. Heller, Appl. Phys. Lett. 36, 76 (1981).
5. T.J. Gmitter, E. Yablonovitch, and A. Heller, J. Electrochem. Soc. 135, 2391 (1988).
6. S.K. Ghandhi, S. Tyagi, and R. Venkatasubramanian, Appl. Phys. Lett. 53, 1308 (1988).
7. J.M. Olson, R.K. Ahrenkiel, D.J. Dunlavy, Brian Keyes, and A.E. Kibbler, Appl. Phys. Lett. 55, 1208 (1989).
8. H.C. Casey, Jr. and Frank Stern, J. Appl. Phys. 47, 631 (1976).
9. R.J. Nelson and R.G. Sobers, J. Appl. Phys. 49, 6103 (1978).
10. J.E. Foquet and R.D. Burnham, IEEE J. of Quantum Elect., QE-22, 1799 (1986).
11. Dawson and Woodbridge Appl. Phys. Lett. 50, 1227 (1984).
12. H. Matsueda and K. Hara Appl. Phys. Lett. 55, 362 (1989).
13. A. Hariz, P. Daniel Dapkus, H.C. Lee, W.P. Menu and S.D. DenBaars, Appl. Phys. Lett. 54, 635 (1989).
14. H. Iwata, H. Yokoyama, M. Sigumoto, N. Hamao and K. Onabe, 11th Inter. Semicond. Laser Conf. Aug. 29 - Sept. 1, Boston, SPIE, p. 42 (1988).
15. E. Yablonovitch, R. Bhat and J.P. Harbison, Appl. Phys. Lett. 50, 1197 (1987).
16. L.W. Molenkamp and H.F.J. van't Blik, J. Appl. Phys. 64, 4253 (1988).
17. G. Lasher and F. Stern, Phys. Rev. 133, A553 (1964).
18. Leigh M. Smith, D.J. Wolford, R. Venkatasubramanian and S.K. Ghandhi. Electronic Materials Conference, Massachusetts Institute of Technology, Boston, Massachusetts, 1989. Leigh M. Smith, D.J. Wolford, R. Venkatasubramanian and S.K. Ghandhi. Bulletin of the American Physical Society 34, 958 (1989).
19. G.W. t'Hooft, W.A.J.A. van der Poel, L.W. Molenkamp, and C.T. Foxon, in "Excitons in Confined Systems," R. Del Sole, A. D'Andrea and A. Lapicciarella, eds., Springer-Verlag, p. 59, 1988.

EVIDENCE FOR STRONG TRAPPING BY IONIZED DONORS OF FREE EXCITONS IN EXCITED STATES FOR HIGH PURITY GaAs and AlGaAs

S. ZEMON AND G. LAMBERT

GTE Laboratories Incorporated, 40 Sylvan Road, Waltham, MA 02254

ABSTRACT

Striking increases in the intensity of donor-related, photoluminescence transitions are observed in undoped (10^{14} - 10^{15} cm $^{-3}$) GaAs for excitation energies (E_c) in the vicinity of the band-gap energy (E_g). The enhancement has maxima at E_c consistent with excitation of the $n=2$ and 3 states of the free exciton ($X_{n=2,3}$) and appears to be correlated to the concentration of ionized donors, suggesting that the effects are related to capture of electron-hole pairs by ionized donors through trapping of $X_{n=2,3}$. The enhancement decreases monotonically as E_c increases to values as much as 12 meV above E_g .

INTRODUCTION

A striking enhancement has been observed in the intensity of donor-related, photoluminescence (PL) transitions in undoped (10^{14} - 10^{15} cm $^{-3}$), epitaxial GaAs for excitation energies (E_c) in the vicinity of the band-gap energy (E_g). In some cases dramatic intensity increases of over two orders of magnitude have been found with donor-related transitions dominating acceptor-related ones in the excitonic region of even low-compensation, p-type material. At $T=4.2$ K the effect was maximum when pumping within the gap at $E_c=E_g-0.6$ meV (consistent with excitation of the $n=3$ state of the free exciton ($X_{n=3}$) [1]) and decreased monotonically as E_c was increased to values as much as 12 meV above E_g . For $T>4.2$ K the maximum occurred at an E_c corresponding to the $n=2$ state of the free exciton ($X_{n=2}$) [1,2]. The enhancement was most readily observed for transitions involving recombination of a free hole with an electron bound to a donor and/or radiative decay of an ionized-donor-bound exciton [$(D^0, h)/(D^+, X)$] and appears to be correlated to the concentration of ionized donors (N_D^+). Enhancements were also observed in a variety of other samples, including GaAs heterostructures and substrates as well as AlGaAs. We suggest that for $E_c < E_g$ these phenomena may be attributed to capture of electron-hole pairs by ionized donors through trapping of $X_{n=2,3}$.

EXPERIMENTAL DETAILS

The nominally undoped, (100)-oriented, GaAs epilayers were grown by both low-pressure organometallic vapor phase epitaxy (OMVPE) and molecular beam epitaxy (MBE) on semi-insulating GaAs substrates [3-5]. The OMVPE layers were low-compensation, n-type material {donor concentration (N_D) $\approx 10^{14}$ cm $^{-3}$ \gg acceptor concentration (N_A) $\approx 10^{13}$ cm $^{-3}$ [4]} as well as n- and p-type, compensated material ($N_D \approx N_A \approx 10^{14}$ cm $^{-3}$ [3]). The sharpness of the 4.2 K PL and magnetophotoluminescence (MPL) lines confirmed the high purity of the OMVPE layers [3,4,6]. The layer thicknesses were 1.5-17 μ m. The MBE sample was 2.5- μ m thick and p-type. Typical MBE layers grown under conditions similar to those of this sample were p-type with $N_A \approx 10^{15}$ cm $^{-3}$ [5]. The low intensity of the donor-related PL features observed during nonresonant excitation of this sample suggests that $N_A \gg N_D \approx 10^{14}$ cm $^{-3}$.

The selective PL and PLE measurements were made at 4.2 K with the sample freely

suspended in an immersion cryostat as well as at temperatures up to 25 K in a cold finger cryostat. The excitation source was an argon-laser-pumped dye laser (Styryl 9 dye) with a 0.1-nm bandwidth. Wavelengths were measured with a wavemeter and selected values were calibrated with a spectrometer. When required, the laser polarization was adjusted to be circularly polarized and the PL analyzed for right circularly polarized (RCP) and left circularly polarized (LCP) components. Power densities of 0.2-200 mW/cm² were employed. The signal was dispersed with a 0.85-m, double-grating spectrometer (0.04-nm resolution) and detected with a photon counting system using a cooled GaAs photocathode photomultiplier. The MPL system has been described in the literature [6].

EXPERIMENTAL RESULTS AND DISCUSSION

In Fig. 1 we show 4.2 K PL in the excitonic spectral region excited both at 804 nm (spectra labeled as 1) and 816.2 nm (spectra labeled as 2). The identifications of the features are shown at the top of the figure [2]. The laser line due to scattered pump light is indicated by an arrow in spectrum 2 of Fig. 1(a). Also indicated there as a dashed line is the position of the band gap at $\lambda_g=815.9$ nm (1.5192 eV [7]). Figure 1(a) shows spectra for the p-type, low-compensation, MBE sample. In spectrum 1 of Fig. 1(a) we observe only two peaks, one at the intrinsic free exciton feature $X_{n=1}$ and the other at the extrinsic acceptor feature (A°, X) [neutral-acceptor-bound exciton], as expected for nonresonant excitation of a high purity sample with $N_A (\approx 10^{15} \text{ cm}^{-3}) \gg N_D$. No donor-related features were detected. However, for excitation at 816.2 nm in spectrum 2 a dramatic change is found to occur with the donor feature (D°, h)/(D^+, X) emerging as dominant and the neutral donor feature (D°, X) becoming detectable. [Donor-to-carbon-acceptor transitions, to be discussed later, also become detectable.] Since all the donors are ionized (D^+) in this p-type material, the D^+ concentration $N_{D^+}=N_D \approx 10^{14} \text{ cm}^{-3}$. The ionized donors are clearly playing a crucial role in the enhancement process both by becoming photo-neutralized and, possibly, by becoming incorporated into bound excitons. In contrast, for a thick (9 μm), n-type, low-compensation layer, where donor-related PL features dominate for nonresonant excitation (as expected), only a relatively small increase in (D°, h)/(D^+, X) occurs for excitation at 816.2 nm. This reduced effect is consistent with the fact that most of the donor concentration ($\approx 10^{14} \text{ cm}^{-3}$) is expected to be neutral. However, for a layer similar to the latter but with a reduced thickness of 1.5 μm , a substantial enhancement effect is observed. This is shown in Fig. 1(b) where we note that (D°, h)/(D^+, X) undergoes an increase of $\approx 50\times$. (D°, X) also increases but to a lesser extent, similar to the trend found in Fig. 1(a). This enhancement effect is also consistent with the picture of the importance of N_{D^+} . Here the presence of a significant ionized donor concentration is explained by the fact that the 1.5- μm -thick layer is thin enough so that depletion effects would be expected to be substantial.

Enhancements of donor-related PL features were observed in a variety of other samples, e.g., (1) low compensation and compensated, n-type layers (thicknesses 0.5-2 μm) capped with AlGaAs window layers (thicknesses 0.3-7.5 μm), (2) the 1.5- μm -thick, GaAs layer of a selectively-doped heterostructure [8], (3) undoped GaAs substrates capped with AlGaAs, (4) GaAs grown on Si substrates [9], and (5) $\text{Al}_{1-x}\text{Ga}_x\text{As}$ layers with $x \leq 0.02$. Figure 2 displays 4.2 K excitonic spectra for $\text{Al}_{0.1}\text{Ga}_{0.9}\text{As}$ excited ≈ 25 meV above the band edge at 794.8 nm and within the band gap at 809.8 nm. The features are identified in analogy to those for GaAs shown in Fig. 1 and a significant enhancement of (D°, h)/(D^+, X) is observed. Other details will be reported elsewhere.

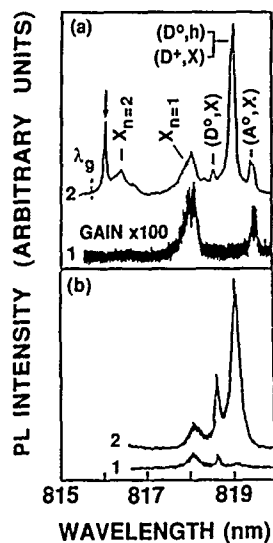


FIG. 1. 4.2 K, PL excitonic spectra for low-compensation samples. (a) p-type epilayer excited with 200 mW/cm². (b) Thin, n-type epilayer excited with 20 mW/cm². $\lambda_c=804$ nm for spectra 1 and 816.2 nm for spectra 2.

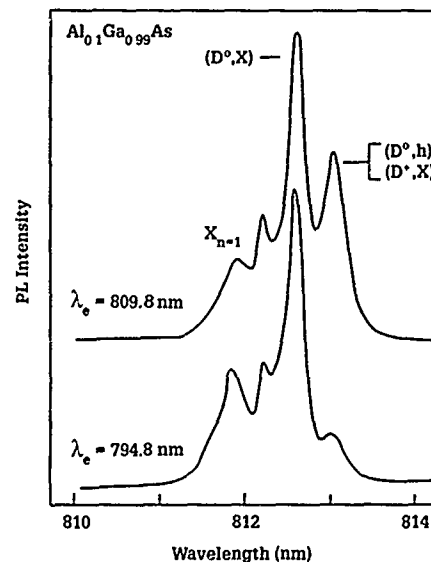


FIG. 2. 4.2 K, excitonic spectra for Al_{0.1}Ga_{0.9}As with the excitation wavelengths (λ_c) indicated.

In a magnetic field, where the degeneracy between the (D^0, h) and (D^+, X) peaks is substantially removed, the two types of transitions can be distinguished for samples with sufficiently sharp PL features, e.g., the high purity OMVPE epilayers [10]. A compensated, OMVPE sample was tested in a magnetic field of 6.4 T at 4.2 K and an enhancement was found in (D^+, X) , in addition to (D^0, h) , for E_c in the vicinity of the lowest, Landau-level, interband transition energy.

When exciting the samples of Fig. 1 with circularly polarized light (say LCP) at 4.2 K, the luminescence was unpolarized for excitation wavelengths $\lambda_c < 812$ nm. However, for 812 nm $< \lambda_c < 816.2$ nm the RCP component of $(D^0, h)/(D^+, X)$ was greater than the LCP component while the $X_{n=1}$, (D^0, X) and (A^0, X) features remained unpolarized. For example, at $\lambda_c = 816.2$ nm (the peak of the polarized PLE spectra) the RCP component of $(D^0, h)/(D^+, X)$ was $\approx 40\%$ greater than the LCP as shown in Fig. 3 for the thin n-type sample. A similar result was observed for the sample of Fig. 1(b). This polarization memory indicates that there is strong coupling between a state initially photoexcited and the corresponding emission state [11].

To examine the wavelength dependence of the enhancement in detail, we present in Fig. 4(a) a PLE spectrum of the sample of Fig. 1(a) where the spectrometer is set at $\lambda_s = 819.1$ nm for $(D^0, h)/(D^+, X)$ and, for comparison, in Fig. 4(b) at $\lambda_s = 819.6$ nm for (A^0, X) in the $J=3/2$ state. For reference the wavelength dependence of the dye laser output is included in Fig. 4(b). The major features are labeled [1,2]. As expected for the PLE of (A^0, X) , the spectrum of Fig. 4(b) has prominent peaks at the excitonic features $X_{n=2}$, $X_{n=1}$, (D^0, X) , and (A^0, X) in the $J=1/2$ state as well as a weak feature at $X_{n=3}$ [1,2]. [The $X_{n=2}$ and $X_{n=3}$ peaks are observed as well on the PLE spectra for $X_{n=1}$ and (D^0, X) .] In marked contrast, the spectrum of Fig. 4(a) rises monotonically [i.e., the $(D^0, h)/(D^+, X)$ feature grows] with increasing excitation wavelength to a maxi-

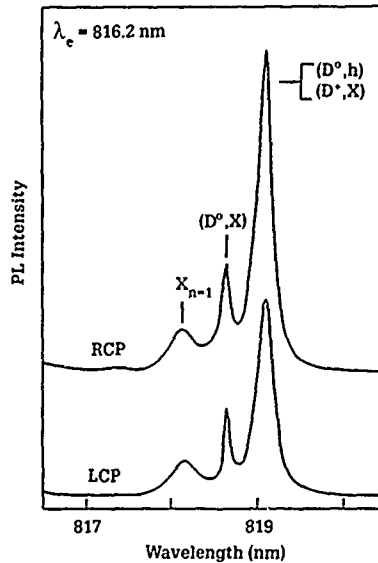


FIG. 3. 4.2 K, circularly polarized PL spectra for thin, n-type GaAs. The sample is excited with LCP light at the indicated λ_c .

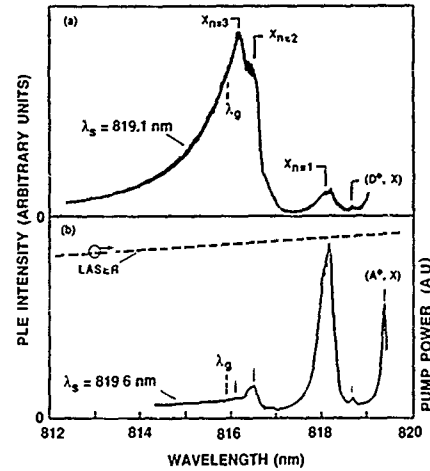


FIG. 4. 4.2 K, PLE spectra for p-type GaAs where λ_s denotes the spectrometer setting. The wavelength dependence of the excitation power ($\approx 200 \text{ mW/cm}^2$) is included in (b).

mum at 816.2 nm which is equivalent to an energy 0.6 meV below E_g [λ_g is denoted by a dashed line in Fig. 4(a) and (b)] and, as discussed below, is identified with excitation of $X_{n=3}$. The full width at half maximum of the main PLE band is $\approx 2 \text{ meV}$, the enhancement first becoming detectable as much as 12 meV above E_g . Similar spectra were observed for power densities as low as 0.2 mW/cm^2 . The prominent shoulder at $\approx 816.5 \text{ nm}$ is better resolved in the higher purity OMVPE samples and can be assigned to excitation of $X_{n=2}$. The low-amplitude shoulder at $\approx 816.9 \text{ nm}$, which is in close correspondence to a PLE feature in Fig. 4(b) and a PL feature observed in Fig. 1(a), appears to be $\approx 0.2 \text{ nm}$ longer than $(D^\circ_{n=2}, h)$. Finally, low-amplitude peaks are seen for $X_{n=1}$ and (D°, X) . No resonant enhancement of the $(D^\circ, h)/(D^+, X)$ feature was observed, in agreement with earlier observations [12]. From selectively excited PL spectra we find that pumping the $X_{n=2}$ transition has a stronger enhancement effect for $(D^\circ, h)/(D^+, X)$ than for the other excitonic features, while the opposite is true when pumping the $X_{n=1}$ transition. PLE data similar to Fig. 4(a) were observed for all the other homoepitaxial layers studied (with some differences for thick layers of low compensation, n-type material where the enhancement effect was small). Variations, however, occurred in the strength of the enhancement.

Within experimental error a PLE feature at 816.2 nm is consistent not only with excitation of $X_{n=3}$ (as indicated above) but also with excitation of an electron from the valence band into an $n=3$ state of a donor [13]. However, little or no response was found in the PLE spectrum of $(D^\circ_{n=1}, h)/(D^+, X)$ when pumping at the wavelength corresponding to $(D^\circ_{n=2}, h)$ at 816.8 nm [e.g., see Fig. 4(a)] or resonant excitation of the line itself [12]. Furthermore, no $(D^\circ_{n=1}, h)$ absorption peaks have been reported for high purity GaAs [1]. Thus, we assume that direct excitation of $(D^\circ_{n=3}, h)$ makes no significant contribution to the PLE spectrum of Fig. 4(a).

One explanation for the two main PLE features observed in Fig. 4(a) is that they represent enhancement of donor transitions due to trapping of $X_{n=2,3}$ by D^+ . Subsequently, this complex can transform into $(D^+, X_{n=1})$ as well as $(D^\circ_{n=1}, h)$. The long range attraction between D^+ and X_n

is due to interaction with the induced dipole. The interaction would be expected to be stronger as the exciton radius, i.e. n , increases (the Bohr radius goes as n^2 [14]). This is consistent with the observation that the trapping of $X_{n=3}$ is apparently more effective than that of $X_{n=2}$, which, in turn, is much more effective than $X_{n=1}$. It is interesting to note that strong overlap exists between the line shapes of $X_{n=3}$ and $(D^{\circ}_{n=3}, h)$ transitions (the peaks are less than 0.1 nm apart), a slightly reduced overlap between $X_{n=2}$ and $(D^{\circ}_{n=2}, h)$ [the peaks are ≈ 0.2 nm apart], and weak overlap between $X_{n=1}$ and $(D^{\circ}_{n=1}, h)$ [the peaks are 1 nm apart]. Thus, a resonant interaction may be operative between X_n and (D°_n, h) for $n=2$ and 3.

The $X_{n=3}$ PLE peak at 816.2 nm in Fig. 4(a) disappears by $T=11$ K. Presumably this is because of thermal dissociation due to the small (0.6 meV) binding energy. However, a reduced enhancement effect remains, exhibiting a peak at $X_{n=2}$ along with the tail previously observed in Fig. 4(a) at short wavelengths. By 25 K, the tail has essentially disappeared. A typical PLE spectrum at 11 K is shown in Fig. 5 for a compensated GaAs layer along with the 4.2 K spectrum. The explanation for the enhancement effect for $E_c > E_g$ is still under study. Perhaps it is related to creation of excitonic excited states with finite kinetic energies although such transitions are expected to be weak, requiring interactions with phonons in order to satisfy conservation of momentum [15].

A further demonstration of the enhancement of donor-related transitions can be obtained from Fig. 6. Here we show 4.2 K PL in the acceptor spectral region for an OMVPE, compensated layer with prominent, acceptor-related, PL features. The excitation wavelengths are $\lambda_c=805$ nm (spectrum 1) and 816.2 nm (spectrum 2), similar to those used in Fig. 1. The excitation power density and the signal gain were held constant. The two main peaks both involve transitions which terminate in a carbon-acceptor state (A°_C), one from the conduction band $[(e, A^{\circ}_C)]$ and the other from a neutral donor $[(D^{\circ}, A^{\circ}_C)]$, as indicated in the figure. Comparing

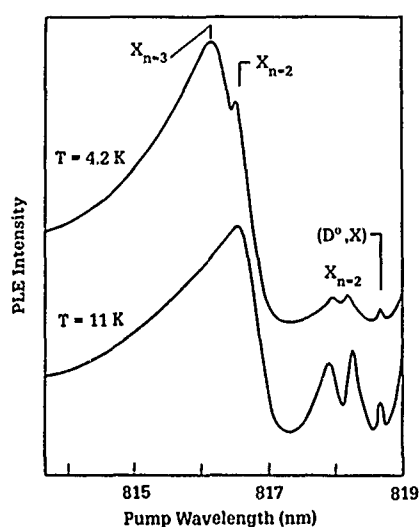


FIG. 5. PLE spectra at 4.2 K and 11 K for a compensated GaAs sample.

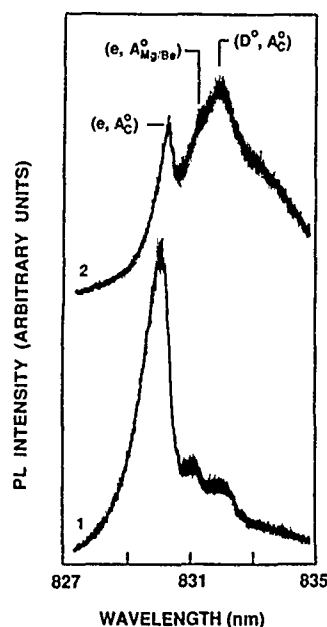


FIG. 6. 4.2 K acceptor PL for a compensated sample. $\lambda_c=805$ nm for spectrum 1 and 816.2 nm for 2. The excitation power (≈ 200 mW/cm²) and signal gain are kept constant.

the two spectra it can be seen that for $\lambda_e=816.2$ nm there is a substantial increase in the amplitude of (D^0, A^0C) while that of (e, A^0C) , in fact, decreases. These data along with the corresponding PLE spectra provide strong evidence that the concentration of photo-neutralized donors is increasing while that of photoexcited free electrons is decreasing as λ_e increases toward 816.4 nm.

We note that for the uncapped samples where the enhancement was strong, the PL intensity increased for all transitions [e.g., see Fig. 1(a)], indicating that the total luminescence intensity had increased. Presumably this is doing so at the expense of competing nonradiative recombination occurring at the surface. Possibly, for sufficiently small E_c , excitations are created which do not lead to energy loss due to nonradiative processes. Instead the excitations ($X_{n=2,3}$) are efficiently trapped by localized centers (D^+) and subsequent energy transfers to radiative states ensue.

In summary, we report the observation of an increase in the intensity of donor-related PL features in a variety of undoped GaAs layers (10^{14} - 10^{15} cm $^{-3}$) during excitation in the vicinity of the band edge. In particular, dramatic enhancements of over two orders of magnitude have been found for a low compensation, p-type sample where, over a range of excitation values, the $(D^0, h)/(D^+, X)$ feature actually dominated the (A^0, X) features in the excitonic region. The strong effects observed for this sample as well as for a thin, low-compensation, n-type layer have been correlated to the presence of ionized donors. The peaks observed in the PLE spectra of $(D^0, h)/(D^+, X)$ are interpreted in terms of enhancement of donor-related transitions by trapping of $X_{n=2,3}$ by ionized donors. Possibly, a resonant interaction is operative between X_n and (D^0, h) for $n=2,3$. The enhancements first become detectable for excitation energies as much as 12 meV about the band gap energy.

REFERENCES

1. For an absorption spectrum of high purity GaAs, see in C. Weisbuch, Ph. D. thesis, University of Paris, 1977 and M. D. Sturge, in *Excitons*, edited by E. I. Rashba and M. D. Sturge (North-Holland, Amsterdam, 1982), Chap. 1, p.11.
2. U. Heim and P. Hiesinger, Phys. Stat. Sol. B 66, 461 (1974).
3. J. Black, P. Norris, E. Koteles, and S. Zemon, Inst. Phys. Conf. Ser. 74, 683 (1985).
4. S. K. Shastri, S. Zemon, and P. Norris, Inst. Phys. Conf. Ser. 83, 81 (1987); S. K. Shastri, S. Zemon, D. G. Kenneson, and G. Lambert, Appl. Phys. Lett. 52, 150 (1988).
5. Jack P. Salerno, E. S. Koteles, J. V. Gormley, B. J. Sowell, E. M. Brody, J. Y. Chi, and R. P. Holmstrom, J. Vac. Sci. Technol. B 3, 618 (1985).
6. S. Zemon, P. Norris, and G. Lambert, J. Cryst. Growth 77, 321 (1986).
7. D. D. Sell, Phys. Rev. B 6, 3750 (1972).
8. S. K. Shastri, S. Zemon, D. Dugger and M. DeAngelis, Inst. Phys. Conf. Ser. 91, 307 (1988).
9. S. Zemon, C. Jagannath, S. K. Shastri, W. J. Miniscalco, and G. Lambert, Appl. Phys. Lett. 53, 213 (1988).
10. S. Zemon and G. Lambert (to be published).
11. See, for example, S. Zemon, C. Jagannath, S. K. Shastri, and G. Lambert, Solid State Commun. 65, 553 (1988).
12. R. Ulbrich and B. Moreth, Solid State Commun. 14, 331 (1974).
13. G. E. Stillman, C. M. Wolfe, and J. O. Dimmock, Solid State Commun. 7, 921 (1969).
14. John O. Dimmock, in *Semiconductors and Semimetals*, edited by R. K. Willardson and Albert C. Beer (Academic, New York, 1967), Vol. 3, p. 259.
15. See, for example, R. J. Elliot, in *Polarons and Excitons*, edited by C. G. Kuper and G. D. Whitfield (Oliver and Boyd, Edinburgh, 1963), pp. 269-293.

Formation of Three Red-Shift Emissions In Heavily Germanium-Doped P-Type GaAs Grown By MBE

Y. MAKITA*, A. YAMADA*, H. SHIBATA*, H. ASAKURA**, N. OHNISHI***, A. C. BEYE*, K. M. MAYER*, and N. KUTSUWADA****

* Electrotechnical Laboratory, 1-1-4 Umezono, Tsukuba-shi, 305, Japan.

** Tokai University, 1117 Kitakaname, Hiratsuka-shi, 259-12 Japan.

*** Informex Incorporated, Limited, 3-15-10 Hiyoshi, Kohoku-ku, Yokohama-shi, Kanagawa-ken 223, Japan

**** Nippon Institute of Technology, 1-1 Gakuendai, Miyashiro-machi, Saitama-ken.

ABSTRACT

Molecular beam epitaxy (MBE) of Ge-doped GaAs was made, in which As₄ to Ga flux ratio γ and Ge concentration $[Ge]$ were used as growth parameters. Photoluminescence (PL) spectra at 2K for slightly Ge-doped GaAs revealed that for $\gamma=1$ the emission of excitons bound to neutral Ge acceptors (A^0, X) was the dominant one. With increasing γ , (A^0, X) was found to be steeply suppressed and at around $\gamma=1.1$, (A^0, X) was totally quenched. For γ higher than 1.1, the emission of excitons bound to neutral Ge donors (D^0, X) was gradually enhanced and for $\gamma=1.1$, (D^0, X) became the principal one. Through van der Pauw measurements, samples with $[Ge]$ around $1 \times 10^{17} \text{ cm}^{-3}$ presented type conversion at around $\gamma=1.7$. In this series, the sample with $\gamma=1.0$ indicated a strong specific emission, [g-g], which is formed just below (A^0, X) and exhibited a strong energy shift towards lower energy sides (red shift) with increasing $[Ge]$. [g-g] was theoretically attributed to the pairs between excited-state acceptors. Since [g-g] is known to be easily quenched by small amount of donors, the formation of predominant [g-g] for $\gamma=1$ assures that very low-compensated p-type GaAs were grown by using this typically amphoteric impurity. We fabricated a series of p-type Ge-doped GaAs by keeping $\gamma=1$ in which the net hole concentration, $|N_A - N_D|$ as high as $1 \times 10^{20} \text{ cm}^{-3}$ was attained. We found four emissions which exhibited significant energy shifts with increasing $|N_A - N_D|$. From $|N_A - N_D| \sim 1 \times 10^{16} \text{ cm}^{-3}$, [g-g] begins to appear as a dominant emission and at $|N_A - N_D| \sim 1 \times 10^{17} \text{ cm}^{-3}$, another red shift emission, [g-g]₂ begins to be formed parallelly on the higher energy side of [g-g]. It is interesting to note that both [g-g] and [g-g]₂ seem to be totally quenched by the further increase of $[Ge]$. The emission due to band to Ge acceptor, (e, Ge) does not change its central energy until $[Ge] = 5 \times 10^{15} \text{ cm}^{-3}$ and for larger $[Ge]$ it turned into a new broad emission, [g-g] β showing a steep red energy shift. [g-g] α was formed on the higher energy side of (e, Ge) and indicated a systematic blue energy shift with growing $[Ge]$ larger than $1 \times 10^{19} \text{ cm}^{-3}$. [g-g] α was theoretically explained to be the emission due to the pairs between ground-state acceptors.

INTRODUCTION

Germanium is a typical amphoteric impurity in GaAs but its features are not well documented due to the difficulty of controlling the substitutional sites of Ge atoms. In molecular beam epitaxy (MBE) it was suggested that one can control the location of Ge atoms either at Ga (donor) or As (acceptor) sites by accurately adjusting Ga to As₄ flux ratio (γ) [1-4]. By making use of this feature one can possibly grow extremely low-compensated both n- and p-type Ge-doped GaAs [2]. We here present the results of Ge-doped GaAs made by MBE according to the above method. For the samples, photoluminescence (PL) were measured at 2K, together with van der Pauw at room temperature. Results indicated that low compensated p- and n- GaAs can be successfully fabricated for the wide range of net hole, $|N_A - N_D|$, and electron $|N_D - N_A|$ concentration, which presented the formation of altogether 5 emissions.

EXPERIMENTAL

MBE growth of Ge-doped GaAs was carried out at substrate temperatures (T_s) between 500°C and 650 °C for the wide range of γ from 1 to 11 [2]. The growth rate was usually 1.5 $\mu\text{m/h}$ and the typical thickness was 3 μm . At two extremal values of γ (=1 and 11), the temperature of Ge effusion cell (T_{Ge}) was varied between 700 °C and 1150 °C. Through van der Pauw measurements at room temperature this T_{Ge} range was found to correspond to the Ge concentration ($[\text{Ge}]$) from $1 \times 10^{15} \text{ cm}^{-3}$ to $1 \times 10^{20} \text{ cm}^{-3}$. Principal characterization was made by PL at 2K using 514.5nm line of Ar laser. Cooled GaAs and Ge photodetectors were used for PL measurements from 700nm to 900nm and from 800nm to 2000nm, respectively. Low excitation condition was sufficed for PL measurements during the course of whole PL investigation.

RESULTS

PL spectra for slightly Ge-doped GaAs are demonstrated in Figs.1 and 2 as a function of γ , together with that of not-intentionally doped sample. The net hole, $|\text{Na}-\text{Nb}|$, and electron, $|\text{Nb}-\text{Na}|$ concentration obtained from van der Pauw measurements are indicated in Fig.1, which reveals that the conversion of the conduction-type takes place at approximately $\gamma=1.4$. In the figures, the higher energy-side peaks can be classified as free (F. E.) and bound (B.E.) exciton emissions. The well-resolved observation of $n=1$ and 2 states for F.E. emissions indicates that the purity of the undoped sample is extremely high [5,6]. When a small amount of donor impurities are presented, the $n=1$ state of F.E. usually splits into two components, i.e. the upper- (UPB) and the lower (LPB) polariton branches as is shown in Fig. 2-a) [7]. Among B.E. emissions two emissions are related with donor impurities. They are (D^0, λ) and (D^+, λ) which are attributed due to the excitons bound to neutral and ionized donors, respectively. The exciton

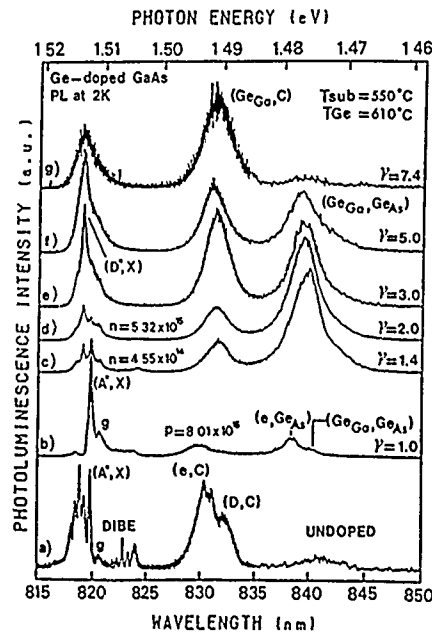


Fig.1 Photoluminescence spectra of Ge-doped GaAs.

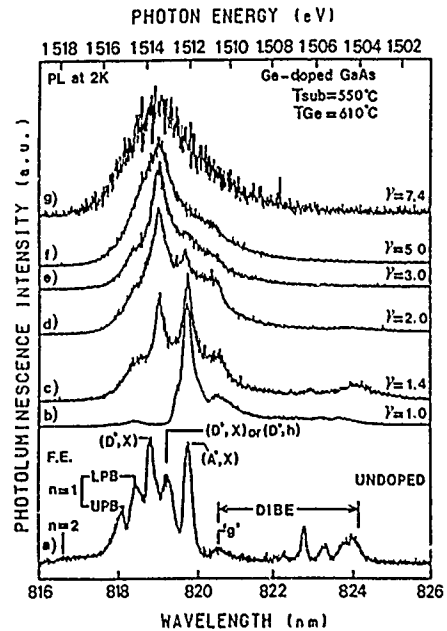


Fig.2 Photoluminescence spectra of Ge-doped GaAs near free and bound exciton emissions as a function of γ .

emission associated with acceptor impurity is designated by (A^0, λ) [5]. Exciton emissions bound to defects and their complexes with acceptor impurities are denoted by DIBE [8].

As is clear from Fig.2, the spectral features near B.E. drastically change with increasing γ . At $\gamma=1.0$, the dominant emission is (A^0, λ) and a slight quenching of DIBE seems to occur due to acceptor atom doping. For γ larger than 1.4 after type-conversion occurs, (A^0, λ) is totally suppressed and instead the formation and enhancement of (D^0, λ) is observed where D^0 should be neutral GeGa donor. These results tell that the typical amphoteric impurity, Ge can be precisely addressed at either acceptor(GeAs) or donor-(GeGa) lattice sites in the crystal. Results of Fig.2 are the direct indication by optical method that the type conversion occurs at around $\gamma=1.4$ and Ge works as neutral donor for the binding of excitons. For γ higher than 2, the principal emission is (D^0, λ) and fine structures of other exciton emissions are completely quenched to form finally one broad emission. This feature was commonly observed in donor-doped GaAs made by MBE [9]. A little shift of the center emission energy pertinent to (D^0, λ) was observed for the increment of γ . When γ is at high extremum, the surface becomes slightly degraded and the PL intensity is somehow weakened.

In Fig.1, the emissions lower than B.E. consist of band-to-acceptor transition, (e, A) and donor-acceptor pair emissions, (D, A) [5]. The increment of GeGa donors can be confirmed by the formation and evolution of two sorts of (D, A) , (GeGa, C) and $(\text{GeGa}, \text{GeAs})$ in which GeGa and GeAs are donors and acceptors due to Ge doping, respectively. The transition between conduction band to two kinds of acceptors, C and GeAs are denoted by (e, C) and (e, GeAs) , respectively. It is clear that $(\text{GeGa}, \text{GeAs})$ is strongly enhanced when the compensation is at its highest ($\gamma=1.1$) due the type-conversion [2].

PL spectra for the above series as long as $1.8 \mu\text{m}$ reveal that in the rather highly compensated samples ($1.4 \leq \gamma \leq 5.0$), upto 3-LO phonon replicas of (GeGa, C) and $(\text{GeGa}, \text{GeAs})$ were obtained together with three deep emissions at 1.38, 1.33 and 1.27 eV. They were not obtained in non-amphoteric

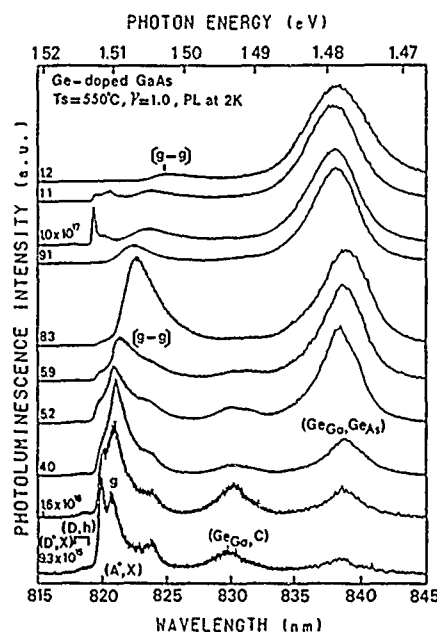


Fig.3 Photoluminescence spectra of Ge-doped GaAs as a function of $|N_A - N_D|$.

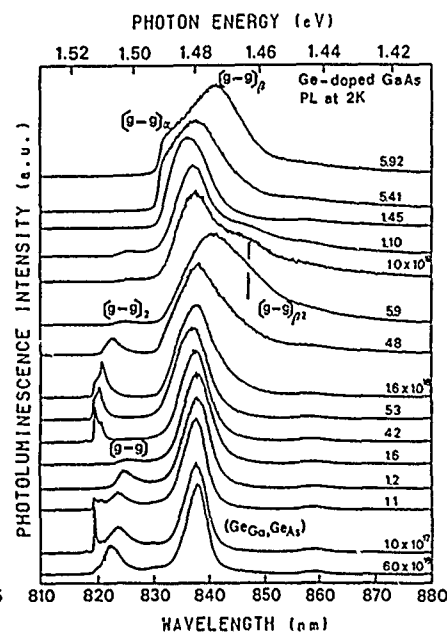


Fig.4 Photoluminescence spectra of Ge-doped GaAs for medium and high range of $|N_A - N_D|$.

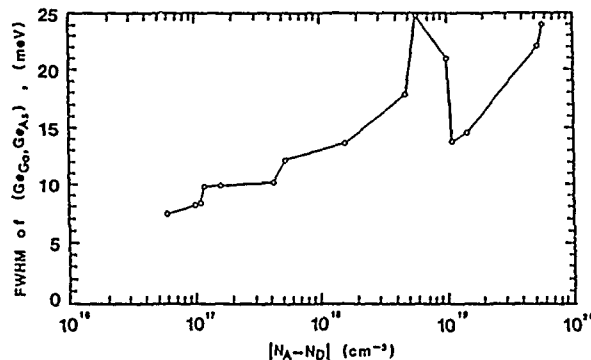


Fig.5 The full width of half maximum, FWHM, for (Ge_{Ga}-Ge_{As}) emission in Ge-doped GaAs.

produced at some range of γ when competing two processes to locate Ge at either Ge_{Ga} or Ge_{As} sites are existing. Details should be discussed in terms of excitation-power dependence and time-decay behaviors.

Ge-doped GaAs grown at constant $\gamma=1$, with $|N_A-N_D|$ from $1 \times 10^{15} \text{ cm}^{-3}$ to $1 \times 10^{20} \text{ cm}^{-3}$ presented five specific emissions denoted by 'g', [g-g] and [g-g]₁ ($i=2, \alpha, \beta$ and $\beta 2$). PL spectra as a function of net hole concentration, $|N_A-N_D|$ are shown in Figs.3 and 4 for rather light, and medium and heavy dose regime, respectively. It has been demonstrated that they can be substantially observed only when the concentration of background donors is at least by a factor of 30 smaller than that of acceptors [13]. Results indicate that during the doping of acceptor atoms, the incorporation of undesired impurities being effective for quenching these specific emissions was practically suppressed. The present observation is an obvious pointing that the prepared samples are truly p-type and very low-compensated ones.

In Fig.3 we notice [g-g] which is located below 'g' and displays a systematic energy shift with increasing $|N_A-N_D|$. [g-g] can be explained as a radiative transition due to the pairs between excited acceptors. It begins to be formed from $|N_A-N_D| = 5 \times 10^{16} \text{ cm}^{-3}$ and is suppressed at about $|N_A-N_D| = 4.2 \times 10^{17} \text{ cm}^{-3}$, whose feature is common in acceptor-doped GaAs [6,10,11]. The several near band-edge emissions for the samples with $|N_A-N_D|$ between 9.1×10^{16} and $1.2 \times 10^{17} \text{ cm}^{-3}$ can be partly ascribed to the emission coming from the underlying undoped buffer-layer.

A novel feature on the higher energy side of [g-g] is the appearance of an emission denoted by [g-g]₂. It showed red energy shift with increasing $|N_A-N_D|$ almost parallel to [g-g]. This emission was formed from $|N_A-N_D| = 4.2 \times 10^{17} \text{ cm}^{-3}$ and was quenched at around $|N_A-N_D| = 1.45 \times 10^{19} \text{ cm}^{-3}$. No similar emission was produced either in amphoteric or non-amphoteric acceptor-doped GaAs prepared by MBE, LPE and ion-implantation [6,10,11]. This feature can not be explained for the moment by a simple model previously-proposed [14].

When $|N_A-N_D|$ exceeds $5.41 \times 10^{19} \text{ cm}^{-3}$ an emission denoted by [g-g] α appears on the higher energy side of (e, Ge_{As}) which was also commonly obtained in acceptor-doped GaAs. [g-g] α indicates energy shift towards higher side (blue shift) by almost 30 meV with increasing $|N_A-N_D|$ higher than $1.0 \times 10^{19} \text{ cm}^{-3}$ and was theoretically explained as the radiative transition due to the pairs between ground-state acceptors [15]. On the lower energy side of (e, Ge_{As}), an emission labeled by [g-g] β is formed for the same $|N_A-N_D|$ range, which on the contrary presents red shift with increasing $|N_A-N_D|$. Due to the experimental difficulties, doping with $|N_A-N_D|$ higher than $5.9 \times 10^{19} \text{ cm}^{-3}$ was unable in the present samples and we missed to observe a dditional red-shift emission [g-g] β' which was universally observed in the

impurity-doped p-type GaAs made by MBE like Be-, Mg- and Zn-doped ones [10,6,11]. The formation of plural (D,A)-like emissions have been reported in the n-type Ge-doped GaAs when these samples are annealed [12]. The deep emissions suggests that transient energy states are presumably

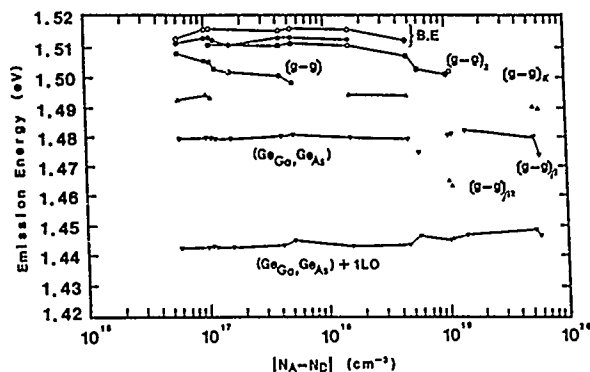


Fig.6 Emission energies in Ge-doped GaAs as a function of $|N_A - N_D|$.

$-Ge_{As}$) intensity, which makes 1.473 emission more (e, Ge_{As}) -like. From $|N_A - N_D|$ around $1.6 \times 10^{18} \text{ cm}^{-3}$, the energy full width of half maximum (FWHM) pertinent to (Ge_{Ga}, Ge_{As}) begins to be gradually growing and finally forms a hump. This evolution is displayed explicitly in Fig.5, where the variation of FWHM for (Ge_{Ga}, Ge_{As}) is given as a function of $|N_A - N_D|$. One can notice an anomalous FWHM feature at $|N_A - N_D| = 5.9 \times 10^{18} \text{ cm}^{-3}$. It is then reasonable to consider that at $|N_A - N_D|$ around $1.0 \times 10^{19} \text{ cm}^{-3}$, a novel emission denoted by $[g-g]\beta_2$ is formed on the higher energy side of (Ge_{Ga}, Ge_{As}) , the central energy of which presents red shift with increasing $|N_A - N_D|$. One should note that no such feature was obtained in the conventional acceptor-doped GaAs [6,10,11].

The emission energy dependence on $|N_A - N_D|$ for the present sample series is displayed in Fig.6. One can remark altogether three red-shift emissions, two on the higher and one on the lower energy sides of (Ge_{Ga}, Ge_{As}) , respectively. The remaining emissions do not present any energy dependence.

The spectral features of the emissions presenting both red and blue shift, denoted by $[g-g]$, $[g-g]\alpha$ and $[g-g]\beta$ are almost identical to those observed in the Be-doped GaAs [10,15]. Their radiative mechanism can be consistently ascribed to the pairs between excited-state acceptors for $[g-g]$ and those between ground-state acceptors for $[g-g]\beta$, respectively, as were described previously. The binding energy of Ge acceptor in GaAs is 36meV and by 7 to 10meV larger than those of other acceptors. This big Ge binding energy brings about less larger orbital diameter necessary to form the acceptor-acceptor pairs. This gives rise to the observation of $[g-g]$ and its associated emissions at higher concentration of $|N_A - N_D|$ than in other-type acceptor-incorporated sample. We have, however, observed no decisive spectra to confirm this speculation. We could tentatively presume that the bigger acceptor binding energy is potential to produce plural energy levels for the pairs, to which the formation of $[g-g]_2$ and $[g-g]\beta_2$ could be ascribed.

CONCLUSION

We successfully fabricated exclusively p- and n-type Ge-doped GaAs by molecular beam epitaxy in which the position of the amphoteric Ge atom was addressed by precisely controlling the As₄ to Ga flux ratio, γ . Low temperature photoluminescence and van der Pauw measurements as a function of γ revealed that p- to n-type-conversion occurs at $\gamma \sim 1.4$. The growth of low compensated, p-type GaAs doped with Ge was confirmed by the observation of the emission of excitons bound at Ge neutral acceptors, (A^0, X) . We made p-type Ge-doped GaAs by keeping $\gamma = 1$ and could attain the net hole carrier concentration, $|N_A - N_D|$ as high as $1 \times 10^{20} \text{ cm}^{-3}$. We found three red shift and one blue shift emissions with increasing $|N_A - N_D|$. $[g-g]$ appeared as a dominant

acceptor-doped GaAs (both for the group II and IV elements as dopants).

The emission at 1.473 eV is presumably a composite one between (e, Ge_{As}) and $(Ge_{Ga} - Ge_{As})$. The relatively large number of Ge_{Ga} to that of Ge_{As} for large γ brings about the reduction of $(Ge_{Ga}$

red shift emission from $|N_A-N_D| \sim 1 \times 10^{16} \text{ cm}^{-3}$ and at $|N_A-N_D| \sim 1 \times 10^{17} \text{ cm}^{-3}$ another red shift emission, $[g-g]_2$ was formed parallelly on the higher energy side of $[g-g]$. The emission due to band to Ge acceptor, (e, Ge) does not change its central energy until $|N_A-N_D| = 5 \times 10^{15} \text{ cm}^{-3}$ and for larger $|N_A-N_D|$ it turned into a new broad emission, $[g-g]_\beta$ showing a steep red energy shift. $[g-g]_\alpha$ was formed on the higher energy side of (e, Ge) and indicated a systematic blue energy shift with growing $[\text{Ge}]$ larger than $1 \times 10^{19} \text{ cm}^{-3}$. $[g-g]_\alpha$ was identified to be the emission due to the pairs between ground-state acceptors.

Authors wish to express their gratitude to J. Shimada and Y. Mitsuhashi.

References

1. Ai-zhen Li, A.G. Milnes, Z.-i. Chen, Y.F. Shao, and S.B. Wang, *J. Vac. Sci. Technol.*, **B3**(2), 629 (1985).
2. Y. Makita, H. Tanaka, M. Mori, N. Ohnishi, P. Phelan, S. Shigetomi, H. Shibata, and T. Matsumori, *J. Appl. Phys.*, **65**, 248 (1989).
3. M. Satoh, K. Kuriyama, and Y. Makita, *J. Appl. Phys.*, **65**, 2248 (1989).
4. R. Hechingbottom and G.J. Davies, *J. Crystal Growth*, **50**, 644 (1980).
5. H.B. Bebb and E.W. Williams, *Semiconductors and Semimetals Vol. 8*, ed. R.K. Willardson and A.C. Beer (Academic Press, New York, 1972), p. 181.
6. Y. Makita, Y. Takeuchi, N. Ohnishi, T. Nomura, K. Kudo, H. Tanaka, H.-C. Lee, M. Mori, and Y. Mitsuhashi, *Appl. Phys. Lett.*, **49**, 1184 (1986).
7. E. S.oteles, L. Johnson, J.P. Salerno, and M.O. Vassel, *Phys. Rev. Lett.*, **55**, 867 (1985).
8. Y. Makita, T. Nomura, M. Yokota, T. Matsumori, T. Izumi, Y. Takeuchi, and K. Kudo, *A.P.L.*, **47**(5), 623 (1985).
9. Y. Makita, M. Mori, H.-C. Lee, T. Kanayama, N. Ohnishi, P. Phelan and T. Matsumori, *Mat. Res. Soc. Symp. Proc. Vol. 126*, 171 (1988).
10. Y. Makita, M. Mori, N. Ohnishi, P. Phelan, T. Taguchi, Y. Sugiyama, M. Iacano, *Mat. Res. Soc. Proc. Vol. 102*, p. 175 (1988).
11. N. Ohnishi, Y. Makita, K. Irie, T. Nomura, H. Tanaka, M. Mori, Y. Mitsuhashi, *J. Appl. Phys.*, **60**, 2502 (1986).
12. P. Phelan, Y. Makita, H. Shibata, A. Yamada, N. Ohnishi, and A.C. Beve, *Proceedings of the International Conference of the Science and Technology of Defect Control in Semiconductors* (Sep. 1989 Yokohama).
13. T. Nomura, Y. Makita, K. Irie, N. Ohnishi, K. Kudo, H. Tanaka, and Y. Mitsuhashi, *Appl. Phys. Lett.*, **48**, 1715 (1986).
14. N. Ohnishi, Y. Makita, M. Mori, K. Irie, Y. Takeuchi, and S. Shigetomi, *J. Appl. Phys.*, **62**, 1843 (1987).
15. N. Ohnishi, Y. Makita, H. Shibata, A.C. Beve, A. Yamada, and M. Mori, to be published in *Mat. Res. Soc. Proc.* (1989, May, San Diego).

ELECTRICAL PROPERTIES OF HEAVILY Be-DOPED GaAs
GROWN BY MOLECULAR BEAM EPITAXY

H. SHIBATA*, Y. MAKITA*, A. YAMADA*, N. OHNISHI**, M. MORI*, Y. NAKAYAMA*,
A. C. BEYE*, K. M. MAYER*, T. TAKAHASHI*, Y. SUGIYAMA*, M. TACANO*,
K. ISHITUKA*** and T. MATSUMORI****

* Electrotechnical Laboratory, 1-1-4 Umezono, Tsukuba-shi, 305 Japan.

** Informex Incorporated Limited, 3-15-10 Hiyoshi, Kohoku-ku,
Yokohama-shi, 225 Japan.

*** Nippon Institute of Technology, 4-1 Gakuendai, Miyashiro-machi,
Saitama-ken, 345 Japan.

**** Tokai University, 1117 Kitakaname, Hiratsuka-shi, 259-12 Japan.

ABSTRACT

Electrical properties of heavily Be-doped GaAs grown by molecular beam epitaxy were investigated systematically in a wide range of Be-concentration from 1×10^{14} up to $2 \times 10^{20} \text{ cm}^{-3}$ by using van der Pauw technique. Probable carrier scattering mechanisms observed in this work are discussed by taking into account the radiative mechanisms of several new photoluminescence emissions previously observed in the band-edge-emission region of the samples. All samples were checked their electrical properties first at room-temperature. Five selected samples out of them were measured from 10° K up to room-temperature. Samples having the carrier concentration from 10^{14} to 10^{18} cm^{-3} presented typical semiconductor-like conduction with finite carrier excitation energy. For samples having carrier concentration $7 \times 10^{16} \text{ cm}^{-3}$, the conduction mechanism at high temperature region above 30° K was dominated by holes thermally excited into valence band. At low temperature region below 30° K , it was dominated by holes hopping from neutral to ionized acceptors with the assistance of phonons. Hole mobilities of samples having the carrier concentration from 10^{17} to 10^{18} cm^{-3} showed an anomalous behavior in the low temperature region, which suggests the presence of a new type of carrier scattering mechanism. A radiative center denoted by [g-g] observed in this concentration region will be a candidate scattering center to explain these electrical behaviors. Samples having the carrier concentration larger than 10^{19} cm^{-3} demonstrated typically metallic electric conduction not owing to thermally excited carriers, which means that an impurity band is formed but merged with valence band. The density of state of this combined valence band mixed with impurity band can be supposed to reflect carrier concentration dependence of the PL emission bands observed in this region, i.e. [g-g] α , [g-g] β and [g-g] γ .

INTRODUCTION

Systematic study on both optical and electrical properties of impurity doped GaAs for a wide range of impurity concentration is necessary for the fabrication of opto-electronic devices. Photoluminescence (PL) is one of the most important optical properties of semiconductors, but intrinsic PL features of p-type GaAs have not yet been revealed sufficiently compared with those of n-type GaAs, particularly in the heavily-doped regime [1]. In the near-band-edge emission region, a blue shift of the main broad PL emission with increasing donor concentration ([D]) has been usually observed in the case of n-type GaAs [2]. This "Burstein-Moss shift" can be easily explained as a consequence of conduction band filling with increasing [D] [3,4], and we may naturally expect that this theory can be applicable also for p-type materials. In heavily acceptor-doped GaAs, however, a red shift of the main PL emission band has been usually observed with increasing acceptor concentration against our expectation [5]. Recently we found several new strong PL emissions in the near-band-edge emission region for heavily acceptor-

doped GaAs [6-10]. These emissions were easily quenched by the incorporation of very small amount of compensating donor impurities [11]. Because of this "optical compensation effect" inherent to p-type GaAs, samples with low background donor concentration are indispensable to reveal real intrinsic optical properties of p-type GaAs.

Beryllium has proved to be an almost ideal p-type dopant in GaAs grown by molecular beam epitaxy (MBE) [12,13]. Optical and electrical properties of Be-doped GaAs have been reported by many authors up to Be concentration ($[Be]$) as high as $5 \times 10^{19} \text{ cm}^{-3}$ [12-19]. In this paper, we extended $[Be]$ further up to $2 \times 10^{20} \text{ cm}^{-3}$ by carefully avoiding unintentional donor incorporation. We here report on electrical properties of samples for the temperature between room-temperature and 10° K by taking into account their PL results obtained at 2° K [8-10]. We observed several new PL emissions in the near-band-edge emission region for heavily Be-doped, low-compensated GaAs, which were labeled by $[g-g]$, $[g-g]\alpha$, $[g-g]\beta$ and $[g-g]\gamma$ [8-10]. The new emissions indicated strong $[Be]$ dependence of the emission energy, but their emission mechanisms are not clearly understood up to now. We previously proposed a new concept which is based on a radiative recombination due to acceptor-acceptor pair [8-10,20]. By combining newly obtained results on electrical properties and those on PL, we describe the mechanisms of electronic conduction and optical transition. The validity of the previously proposed concept will be also discussed.

EXPERIMENTAL

A. SAMPLE FABRICATION : Samples used in this study were grown by commercial MBE system (RIBER 2300) on Cr-doped semi-insulating (100) GaAs wafers. For all samples, substrate temperature and the V/III flux ratio of As₄ to Ga were kept at 550°C and 2.0, respectively. The growth duration of Be-doped layer was 2 hours, after the growth of undoped buffer layer during 30 minutes. Total thickness of obtained layers was about $5.4 \mu\text{m}$ which was constant at all $[Be]$ range. The doping level was controlled by changing the temperature of Be effusion cell (T_{Be}) from 417°C to 870°C . We also fabricated undoped GaAs layer under the same growth condition to check the concentration of background contaminants in the MBE chamber.

B. CHARACTERIZATION : PL measurements were performed at 2° K using 514.5 nm Ar laser line under a condition of extremely low excitation density. PL signal was analyzed by a SPEX 1704 monochromator ($f/9.0$, 1m). For electrical measurement, Au-Zn alloy was used as an Ohmic contact material. Hall effect measurements were carried out at RT to determine hole concentration ($p(\text{RT})$) and hole mobility ($\mu(\text{RT})$) for all samples by van der Pauw technique. Five samples were selected to investigate the electrical properties as a function of T from 10° K up to RT.

RESULTS

A. PHOTOLUMINESCENCE SPECTRA : Peak energies of PL emission bands at $T = 2^\circ \text{ K}$ are shown in Fig.1 as a function of $p(\text{RT})$ [9,10]. $[g-g]$ can be observed from $p(\text{RT}) = 2.11 \times 10^{16}$ up to $1.94 \times 10^{18} \text{ cm}^{-3}$, showing remarkable red shift with increasing $p(\text{RT})$. Since it has been demonstrated that the intensity of $[g-g]$ can be easily quenched by the incorporation of small amount of donor [11], the appearance of this band ensures us that the compensation of our samples is very small [9,10]. $[g-g]\alpha$ appears at $p(\text{RT}) = 2.93 \times 10^{18} \text{ cm}^{-3}$ just after the disappearance of $[g-g]$ and can be observed until the highest $p(\text{RT})$ studied, showing strong blue shift with increasing $p(\text{RT})$ similar to the Burstein-Moss shift. $[g-g]\beta$ appeared at $p(\text{RT}) = 1.94 \times 10^{18} \text{ cm}^{-3}$ just after the disappearance of $[g-g]$ and can be clearly recognized at least until $p(\text{RT}) = 7.36 \times 10^{19} \text{ cm}^{-3}$, showing a strong red shift with increasing $p(\text{RT})$. Also, we can recognize another new wide emission band denoted by $[g-g]\beta'$ overlapping to $[g-g]\beta$.

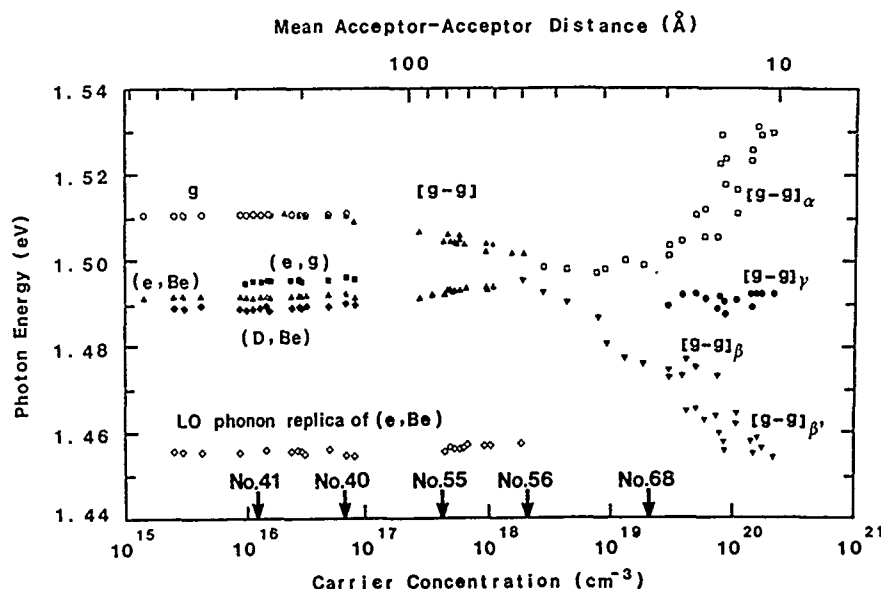


Fig. 1 The energy positions of emission bands observed at high concentration region as a function of room-temperature carrier concentration and corresponding mean distance between neighboring acceptors. Carrier concentration of selected five samples are also shown using arrows on the horizontal scale.

$[g-g]\gamma$ becomes recognizable at $p(\text{RT}) = 3.04 \times 10^{19} \text{ cm}^{-3}$ and can be observed until the highest $p(\text{RT})$ studied. $[g-g]\gamma$ does not show any remarkable energy shift with increasing $p(\text{RT})$.

B. ELECTRICAL PROPERTIES AT ROOM-TEMPERATURE : The highest $p(\text{RT})$ achieved was $2.13 \times 10^{20} \text{ cm}^{-3}$ which is remarkably higher than the highest value ever reported using Be [12]. For $p(\text{RT})$ between 1×10^{15} and $2 \times 10^{20} \text{ cm}^{-3}$, we observed a linear relation between the logarithm of $p(\text{RT})$ and $1/T_{\text{Be}}$ [13,14,17]. This implies that Be incorporated into GaAs by MBE is electrically active nearly 100% for $p(\text{RT})$ up to $2 \times 10^{20} \text{ cm}^{-3}$. The deviation from the linear relation at $p(\text{RT})$ below $1 \times 10^{15} \text{ cm}^{-3}$ may be due to Zn diffusion from the electrodes into GaAs during alloying after Au-Zn deposition. Dependence of $\mu(\text{RT})$ on $p(\text{RT})$ agreed well with "Brooks-Herring formula" [18,19] except low $p(\text{RT})$ region [8], where $\mu(\text{RT})$ decreased with decreasing $p(\text{RT})$. This anomaly may be due to the compensation of acceptors by unintentionally incorporated donors.

C. CARRIER CONCENTRATION AS A FUNCTION OF TEMPERATURE : $p(\text{RT})$ for selected five samples and variation of $p(T)$ as a function of $1/T$ are shown in Figs. 1 and 2, respectively. With decreasing T from RT to 30° K , $p(T)$ of sample No.40 exhibits monotonic decreasing, but it shows a minimum around 30° K and turns to increase with decreasing T . This demonstrates that the conduction mechanism above 30 K is governed by holes thermally activated into valence band and below 30 K it is by those hopping from neutral to ionized acceptors with the assistance of phonons [21,22]. This transition of transport mechanism to "impurity conduction" is a characteristic of lightly-doped semiconductors. $p(T)$ of sample No.68 exhibits no remarkable T dependence. This demonstrates that the carrier conduction mechanism of this sample is "metallic impurity conduction" [21,22]. The impurity band merges with valence band and conduction takes place without thermal excitation of

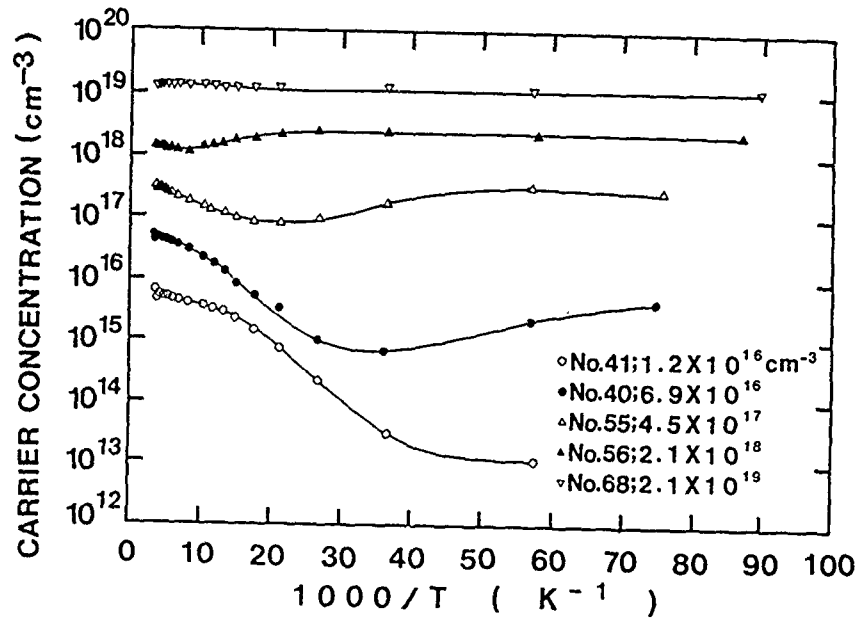


Fig. 2 Variation of carrier concentration as a function of temperature.

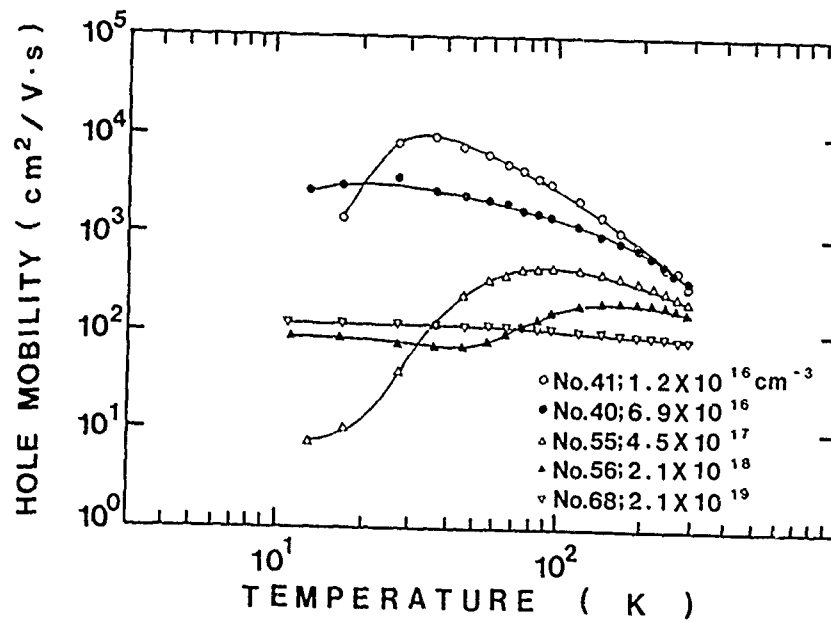


Fig. 3 Variation of hole mobility as a function of temperature

carriers in this sample. $p(T)$ of samples No.55 and 56 seems to show intermediate status between samples No.40 and 68. The initial negative slope and distinct minimum in $p(T)$ become unclear and disappear finally with increasing $p(RT)$.

D. HOLE MOBILITY AS A FUNCTION OF TEMPERATURE : Variation of $\mu(T)$ as a function of T is shown in Fig.3. Initially, $\mu(T)$ of samples No.41, 40, 55 and 56 increases with decreasing T , since the main carrier scattering center at high T region is polar optical phonon [12,17,18,21-23]. At low T region, $\mu(T)$ reaches to a maximum at certain critical T , and decreases with decreasing T below the this critical temperature, because the main carrier scattering centers at low T region are ionized impurities [12,17,18,21-23]. $\mu(T)$ of samples No.55 and 56 again increases with decreasing T at further lower T region [18,21,22]. One probable explanation is to introduce a new kind of carrier scattering center which is effective at low T region and become ineffective at further lower T region.

DISCUSSION

Previously we reported a novel concept to deal with newly discovered energy states associated with acceptors in heavily p-type doped GaAs from 10^{17} to 10^{20} cm^{-3} , which correspond to hole states bound to "acceptor-acceptor pair" formed by the overlapping of hole wave functions [9,10,19]. Recently Haufe et al. proposed alternative idea to treat the same subject, whose central considerations are directed to the formation of the impurity band [24].

Electronic properties of heavily-doped samples having $[\text{Be}]$ larger than 10^{19} cm^{-3} were found to be metallic because the impurity band is formed and merged with valence band. Therefore density of state of the combined impurity-valence band is essential to understand the PL properties of the emission band observed in this region, i.e. $[\text{g-g}]\alpha$, $[\text{g-g}]\beta$ and $[\text{g-g}]\gamma$. Hence the theory of Haufe et al. is considered to be valid in this $[\text{Be}]$ region. The mechanism of observed blue shift of $[\text{g-g}]\alpha$ may be the same as that of the Burstein-Moss shift. However the shift is not so strong compared with n-type materials, because the density of state of valence band is remarkably larger than that of conduction band.

Electronic properties of intermediately-doped samples having $[\text{Be}]$ from 10^{17} to 10^{19} cm^{-3} were demonstrated to be typically semiconductor-like with discrete acceptor energy level in the band gap. Hole mobilities of these samples presented peculiar increase with decreasing T at low T region, which implies an existence of a new type of carrier scattering center. As was previously described, this $[\text{Be}]$ region is dominated with $[\text{g-g}]$ emission in PL spectra, therefore it might be reasonable to consider that $[\text{g-g}]$ is responsible for this scattering center.

CONCLUSIONS

Electrical properties of heavily Be-doped GaAs grown by MBE were investigated systematically in a wide range of $p(RT)$ from 1×10^{14} cm^{-3} up to 2×10^{20} cm^{-3} using van der Pauw technique. Electric properties were semiconductor-like at $p(RT)$ from 10^{14} to 10^{18} cm^{-3} and metallic at $p(RT)$ higher than 10^{19} cm^{-3} . $\mu(T)$ of the samples having $p(RT)$ from 10^{17} to 10^{18} cm^{-3} showed peculiar increase with decreasing T at low T region. The introduction of a new type of acceptor energy level was suggested to be necessary to explain this transport mechanism of these samples. The energy state associated with $[\text{g-g}]$ will be one of the candidates to understand the present transport mechanisms. Density of state of the combined impurity-valence band observed in samples having $p(RT)$ larger than 10^{19} cm^{-3} was found to have a close relation with PL emission bands $[\text{g-g}]\alpha$, $[\text{g-g}]\beta$ and $[\text{g-g}]\gamma$ observed in these samples.

REFERENCES

1. D. J. Ashen, P. J. Dean, D. T. Hurle, J. B. Mullin, A. M. White and P. D. Green, *J. Phys. Chem. Solids* 36 1041 (1975).
2. D. S. Jiang, Y. Makita, K. Ploog and H. J. Queisser, *J. Appl. Phys.* 53, 999 (1982).
3. E. Burstein, *Phys. Rev.* 83, 632 (1954).
4. T. S. Moss, *Proc. Phys. Soc. London* B67, 775 (1954).
5. J. I. Pankov, *J. Phys. Soc. Japan* 21, Suppliment 298 (1966).
6. Y. Makita, T. Nomura, M. Yokota, T. Matsumori, T. Izumi, Y. Takeuchi and K. Kudo, *Appl. Phys. Lett.* 47, 623 (1985).
7. Y. Makita, Y. Takeuchi, N. Ohnishi, T. Nomura, K. Kudo, H. Tanaka, H. C. Lee, M. Mori and Y. Mitsuhashi, *Appl. Phys. Lett.* 49, 1184 (1986).
8. Y. Makita, M. Mori, N. Ohnishi, P. Phelan, T. Taguchi, Y. Sugiyama and M. Takano, *Mat. Res. Soc. Symp. Proc.* 102, 175 (1988).
9. N. Ohnishi, Y. Makita, H. Shibata, A. C. Beye, A. Yamada and M. Mori, to be published in *Proc. of Mat. Res. Soc. Symp.* 1989 Spring Meeting, San Diego.
10. H. Shibata, Y. Makita, M. Mori, T. Takahashi, A. Yamada, K. M. Mayer, N. Ohnishi and A. C. Beye, to be published in *Proc. of the 16th International Symp. on GaAs and Related Compounds*, 1989, Karuizawa.
11. T. Nomura, Y. Makita, K. Irie, N. Ohnishi, K. Kudo, H. Tanaka and Y. Mitsuhashi, *Appl. Phys. Lett.* 48, 1745 (1986).
12. M. Ilegems, in *The Technology and Physics of Molecular Beam Epitaxy*, edited by E. H. C. Parker (Plenum Press, New York, 1985) p.83.
13. M. Ilegems, *J. Appl. Phys.* 48, 1278 (1977).
14. K. Ploog, A. Fisher and K. Kunzel, *J. Electrochem. Soc.* 128, 400 (1981).
15. G. B. Scott, G. Duggan, P. Dawson, G. Weimann, *J. Appl. Phys.* 52, 6888 (1981).
16. N. Duhamel, P. Henoc, F. Alexandre and E. V. K. Rao, *Appl. Phys. Lett.* 39, 49 (1981).
17. P. K. Bhattacharya, H. J. Buhlmann, M. Ilegems and J. L. Staehli, *J. Appl. Phys.* 53, 6391 (1982).
18. J. D. Wiley, in *Semiconductor and Semimetals*, Vol.10, edited by R. K. Willardson and A. C. Beer (Academic Press, New York, 1975) p.91.
19. D. C. Look, in *Electrical Characterization of GaAs Materials and Devices* (John Wiley & Sons, 1989).
20. N. Ohnishi, Y. Makita, M. Mori, K. Irie, Y. Takeuchi and S. Shigetomi, *J. Appl. Phys.* 62, 1833 (1987).
21. F. Ermanis and K. Wolfstein, *J. Appl. Phys.* 37, 1963 (1966).
22. H. C. Casey, F. Ermanis and K. B. Wolfstein, *J. Appl. Phys.* 40, 2945 (1969).
23. G. E. Stillman and C. M. Wolfe, *Thin Solid Films* 31, 69 (1976).
24. A. Haufe, R. Schwabe, H. Fieseler and M. Ilegems, *J. Phys. C : Solid State Phys.* 21, 2951 (1988).

PHOTOLUMINESCENCE STUDY OF GaAs DIFFUSED WITH Li

H. P. GISLASON, E. Ö. SVEINBJÖRNSSON, B. MONEMAR* AND M. LINNARSSON*

Science Institute, University of Iceland, Dunhaga 3, IS-107 Reykjavik, Iceland

*Linköping University, Department of Physics and Measurement Technology,
S-581 83 Linköping, Sweden

ABSTRACT

We present a detailed study of the photoluminescence (PL) properties of a wide range of GaAs material diffused with the group I element Li. The effects of the Li diffusion are investigated through its effects on existing photoluminescence bands in the as-grown material as well as the appearance of new such bands. Among new PL bands resulting from the Li doping of n-type and semi-insulating material the most pronounced ones are a strong deep band at 1.34 eV and shallower bands at 1.45 and 1.48 eV. The origin of these PL bands will be discussed.

INTRODUCTION

Passivation of shallow impurities in semiconductors by atomic hydrogen has been found to result from the formation of complexes including the shallow donor or acceptor species and atomic hydrogen. Recent example of this effect in GaAs is the Be-H complex, where the hydrogen is a donor passivating the Be acceptor [1, 2]. There have also been studies of donor-H complexes, where the hydrogen acts as an acceptor [3]. In view of the interest in the properties of hydrogen in semiconductors, we focus our attention on the behaviour of another group-I element in GaAs, namely Li.

Li is a fast interstitial diffuser in GaAs with a high solubility at 800 °C both in undoped GaAs, $1.6 \times 10^{19} \text{ cm}^{-3}$, and in n- and p-type GaAs, $2.3 \times 10^{19} \text{ cm}^{-3}$ [4]. Nominally undoped GaAs samples which are diffused with Li at temperatures greater than 500 °C and cooled to room temperatures show a high resistivity. This has been explained by the action of Li^+ which rapidly diffuses through the crystal forming donor-acceptor complexes, thus compensating the crystal [5]. In this way Li compensates n-type Te-doped GaAs with concentrations as high as $5 \times 10^{18} \text{ cm}^{-3}$ [5]. Li is, however, also found to compensate strongly p-type material, in which case the interstitial Li donor is a natural candidate for the compensation mechanism.

Studies of Li in GaAs were quite extensive in the early seventies, but little work has been done on this topic recently. The information from earlier work mainly comprises solubility and diffusion data and local mode energies from IR spectroscopy [6]. More recently, photoluminescence studies of Cu- and Li-codoped GaAs were reported [7]. There Li diffusion was found to reduce the intensity of the 1.36 eV PL band resulting from the primary Cu diffusion [8] at the same time as a new PL band at 1.41 eV emerged. The intensity of this new PL band was found to be correlated with the Li-diffusion procedure. In the same study a preliminary investigation of Li-doping alone was reported. A strong PL band at 1.34 eV as well as shallower bands in the photon energy range 1.46 - 1.49 eV were observed in two samples [7]. These optical spectra have been studied in detail in the present investigation. A large variety of different GaAs samples have been studied and different properties of the PL bands investigated in samples where feasible. These properties include temperature dependence and the relation between excitation and PL intensities.

SAMPLE PREPARATION

The GaAs samples used in this study were prepared from a wide range of different starting material. The GaAs material includes Horizontal Bridgman (HB) and liquid encapsulated Czochralski (LEC) bulk crystals. The starting material used for the Li diffusions was either n-type Si, Se or Sn doped, p-type Zn doped, or semi-insulating (s.i.). Table I summarizes the properties of a small selection of typical starting material used for the Li diffusions.

The Li diffusion was performed in two different ways, in sealed evacuated quartz ampoules, on the one hand, and in open tubes in an inert gas atmosphere on the other hand. High purity quartz tubes were used for the ampoules which were evacuated to better than 10^{-5} mbar. The

TABLE I

Examples of different GaAs starting material used for Li doping in the present study.

sample number	crystal type	dopant type	concentration at 300K [cm^{-3}]	mobility at 300K [$\text{cm}^2/\text{V s}$]	epd [cm^{-2}]
WK11360	HB	un	$n = 2.2 \times 10^{16}$	4455	6500
X4702	HB	Sn	$n = 0.8-1.2 \times 10^{17}$	3460-3550	5000
X3545/2	LEC	Se	$n = 2.1 \times 10^{17}$	3320	8000
XK5549	HB	Zn	$p = 6.0 \times 10^{16}$	230	10000
830520	LEC	un	semi-insulating	low	$1-3 \times 10^4$

metallic Li was cleaned and placed in quartz cups inside the ampoules in order to avoid direct contact between the Li and the walls of the ampoules. The samples were brought in contact with the Li metal pellets for best results. If a concentration gradient of the Li in a sample was desired one end of the sample was kept free of Li during the diffusion, however. Typical diffusion temperatures were 400 - 600 °C and the diffusion time was on the order of one hour. The samples were rapidly cooled to room temperature after heat treatment, either in air or by immersing the quartz ampoules into water.

In the open-tube diffusions different Li source, metallic Li powder imbedded in grease was smeared on one side of the samples, either covering the whole of its surface or a part of it. The samples were placed in a quartz boat and Ar gas was flowed through the system during the diffusion. Similar diffusion times and temperatures were used as in the sealed-ampoule diffusions for best results.

Both the above Li-diffusion methods give similar results. In all cases reference samples were made from the starting material used for the Li diffusions. The reference samples were given identical heat treatment as the Li-diffused ones, without the Li source, however.

EXPERIMENTAL TECHNIQUES

The photoluminescence measurements were performed at liquid He temperatures using different closed cycle He refrigerators. One of them operates at 14 K and was used for most spectral analyses. Another one operates at temperatures between 3.6 K and room temperature and was used for measurements of the temperature dependence of the PL intensity. The samples were glued to the cold fingers of the cryostats with a liquid silver solution for a good thermal contact. In order to avoid sample heating care was taken not to use excessive excitation intensities.

For excitation the 5145 Å line of an Ar⁺ ion laser was used. Typical excitation power did not exceed 10 mW. Also the 6328 Å line of a He-Ne laser was used. The PL intensity variation was measured for excitation intensity variation over several orders of magnitude between 0.01 and 100 mW. The photoluminescence signal was detected via a double 0.85 m Spex 1404 grating monochromator using either a cooled North Coast Optics Ge detector or a cooled Hamamatsu R943 GaAs PM tube. The signal was amplified with a Stanford SR510 lock-in detector and recorded with an AT computer which controlled the measurements. The spectra presented in this paper were not corrected for the spectral response of the instruments since such corrections were of minor importance for the results.

EXPERIMENTAL RESULTS

Figure 1 shows PL spectra from sample WK11360, which is nominally undoped and n-type in as grown condition, see table I. The spectra are typical for low-doped n-type samples. The reference sample of figure 1a was heat treated at 600 °C for 60 minutes in vacuum. In addition to the characteristic near band-edge bound exciton peak at 1.513 eV and DA pair luminescence at 1.492 eV the well known Cu PL band at 1.36 eV is present in the sample. This luminescence

originates from recombination to the 0.15 eV level of the Cu acceptor which is a common contaminant in as grown and heat treated GaAs samples [8, 9]. The 1.36 eV Cu PL is the strongest band in the spectrum of figure 1a, but a weak Cu band was present already in the as-grown sample. At lower photon energies there are broad bands at 0.99 and 1.19 eV in the as grown sample. Heat treatment shifts the former to 1.02 eV and causes the latter to disappear. Li diffusion under similar conditions causes no further change in the deep PL bands, but changes all other PL bands in the spectrum.

There is a strong concentration gradient observed in samples Li diffused from one end of the sample. The approximately 2 cm long sample was Li diffused at 600 °C for 60 minutes in vacuum. After the diffusion a surface layer of about 10 μm was removed from the sample by etching. The strong Li concentration gradient is obvious from figures 1b, which was measured in a point at the opposite end from the Li source, through 1e, measured in a point where Li was in contact with the sample during diffusion. We observe the gradual appearance of the 1.34 eV PL band at the low energy wing of the no-phonon peak of the 1.36 eV Cu band. The 1.34 eV band is never observed in as-grown or heat treated samples in the absence of Li, but consistently present after Li diffusion with intensities ranging from weak as in 1b to strong as in 1e.

The intensity of the new 1.45 eV PL band varies with concentration, but Li diffusion under the conditions described here usually produces a strong such band. Its intensity relative to the new 1.485 eV peak varies across the sample, but generally changes in favour of the latter with increased Li doping. The 1.485 eV peak shows a similar correlation with the 1.492 eV DAP band as the one observed for the 1.36 and 1.34 eV PL bands. The 1.492 eV PL band is present in as-grown samples. In a point distant from the Li source, representing a low Li concentration, the 1.485 eV peak is of similar strength as the 1.492 eV peak. This is shown in figure 1b. As the Li concentration increases the latter gradually disappears and the 1.485 eV peak becomes stronger. Table II summarizes the observations of the four Li-related PL bands in the samples of table I.

Figure 1. a) PL spectra at 14 K from a reference sample heat treated at 600 °C for 60 minutes in vacuum and b-e) Li-diffused at 600 °C for 60 minutes. The total PL intensity and the Li concentration are strongest in e)

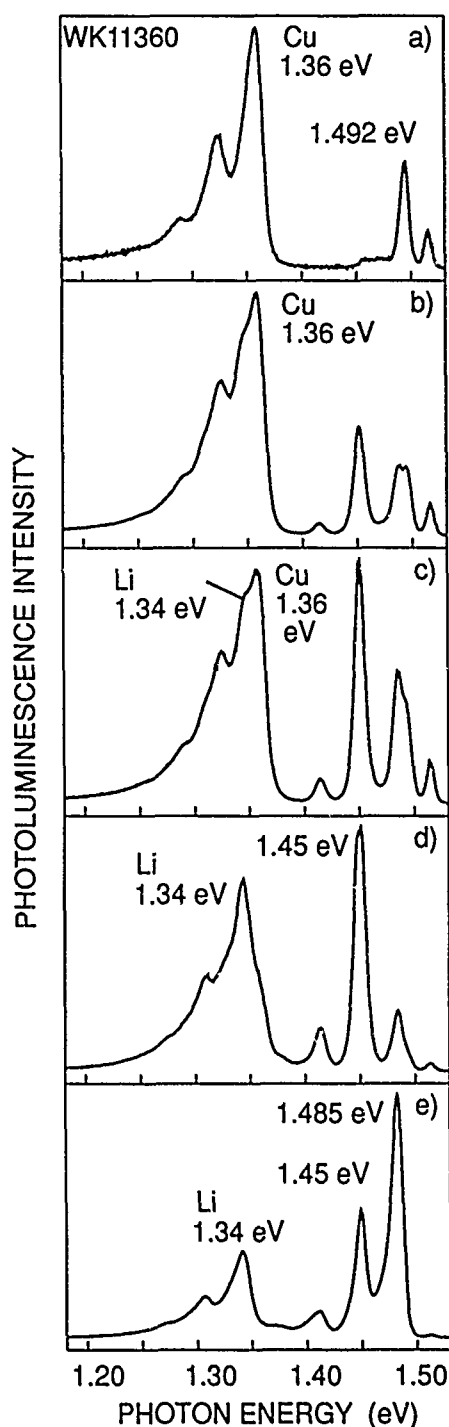


TABLE II

Li-related PL bands in typical GaAs starting material in the present study.

sample number	carrier type and concentration [cm ⁻³]	1.485 eV	1.45 eV	1.41 eV	1.34 eV
WK11360	n = 2.2 x 10 ¹⁶	yes	yes	yes	yes
X4702	n = 0.8-1.2 x 10 ¹⁷	yes	yes	yes	yes
X3545/2	n = 2.1 x 10 ¹⁷	broad PL at 1.46 eV		no	yes
XK5549	p = 6.0 x 10 ¹⁶	no	no	no	no
830520	semi-insulating	yes	no	yes	no

The 1.485 eV photoluminescence band

In view of its energy position and the fact that it seems to replace the shallow donor to acceptor PL bands we attribute the 1.485 eV PL band to a DAP recombination. We have observed a PL band close to this energy in all moderately doped n-type and some semi-insulating samples in this study, but not in p-type material. There is a slight shift of the peak position between samples of different origin, however. An experimental evidence for a DAP model is the fact that the PL intensity shows clear signs of saturation with excitation intensity in contrast to the 1.513 eV bound exciton peak which is linear. Also, the peak position shifts with excitation intensity from 1.482 eV for 0.01 mW to 1.487 eV for 100 mW excitation at 5145 Å. The diameter of the laser spot on the sample was 0.5 mm. The observed shift supports the identification of this PL band as a DAP recombination, the combined binding energies of the donor and acceptor being 1.52 - 1.482 = 0.038 eV in the limit of a negligible Coulomb term according to

$$E_g - (E_D + E_A) + e^2 / 4\pi\epsilon^2 r \rightarrow E_g - (E_D + E_A) \quad (1)$$

Typical donor binding energy in GaAs is slightly less than 6 meV which leaves 32 meV for the acceptor. The measured temperature quenching of this PL band has an activation energy of 28 ± 2 meV. This value is almost identical to the effective mass value for acceptors in GaAs. A room-temperature value of 23 meV has been reported for acceptor complexes involving Li_i and causing the p-type compensation of Li [5]. Another acceptor level, at $E_v + 44$ meV, has been reported in n-type GaAs compensated by Li [4]. Hall and conductivity measurements are needed in order to correlate the present PL results with level positions in the bandgap.

The temperature dependence of the 1.485 eV PL band as well as that of other Li-related bands is shown in figure 2. Figure 3 shows the PL spectrum in the bandgap region at excitation intensities ranging over 4 orders of magnitude. The shift of the 1.485 eV PL band is clearly demonstrated in the picture. Figure 4 illustrates the PL intensity for all four PL bands as a function of excitation intensity including the 1.513 eV BE for comparison. Table III summarizes the above experimental data.

The 1.45 eV photoluminescence band

The 1.45 eV PL band is only observed in n-type samples. It corresponds to a combined donor-acceptor binding energy of 73 meV which compares favourably with the measured activation energy of 66 meV if the latter is interpreted as an acceptor binding energy. The experimental data for the 1.45 eV PL band presented in figures 2 through 4 and summarized in table III are generally similar to those of the 1.485 eV one and hence we attribute it to another DAP recombination involving a Li-related acceptor. We note that the 1.45 eV band shows no shift between samples of different origin, whereas other Li-related bands have slightly different energies. This together with the fact that no DAP luminescence is found to correlate with the 1.45 eV PL, as is the case for other Li-related PL bands, indicates that the 66 meV Li acceptor neither involves the shallow doping nor deep contaminants.

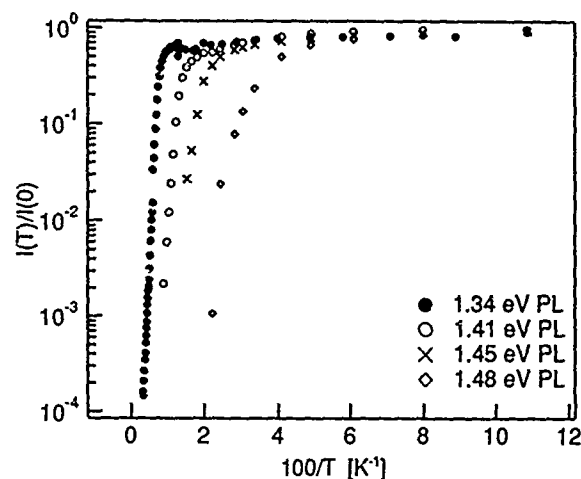


Figure 2. Temperature dependence of the PL intensity from a WK11360 sample measured with 2 mW excitation intensity at 5145 and 1 mW at 6328 Å. The PL intensity is normalized to the extrapolated value at $T=0$ K and plotted against $100/T$. The intensity is described as $I(T)/I(0) = [1 + C_0 \exp(-E_0/kT) + C_1 \exp(-E_1/kT)]^{-1}$ [10] where the activation energy E_0 describes the thermal quenching at elevated temperatures and E_1 the smaller slope at low T . Values of E_0 deduced for the different Li-related PL bands are listed in table III.

The 1.41 eV photoluminescence band

After Cu doping and a subsequent Li diffusion a competition between the Cu band and the 1.41 eV peak, attributed to a CuGaLi_i acceptor, has been reported [7]. This peak is weakly present in figure 1e, but generally this PL band is stronger after diffusion at higher temperatures. It is not

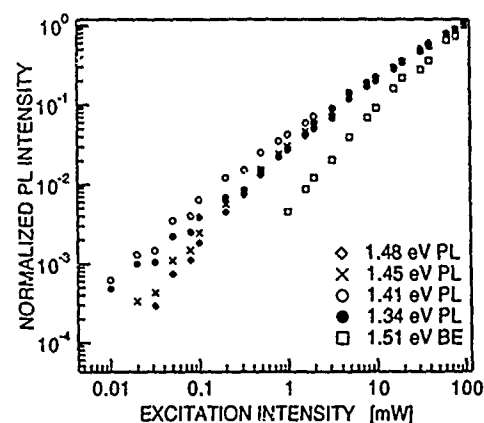
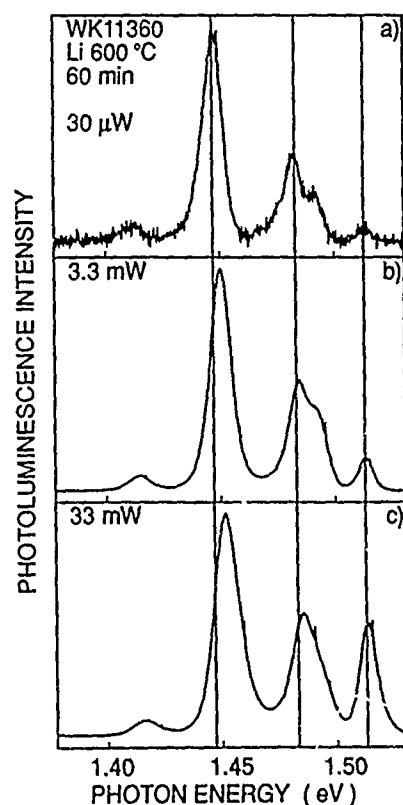


Figure 3. Normalized PL intensity of the four Li bands as a function of excitation intensity at 4K and 5145 Å. The 1.51 eV BE peak shows a linear relation. Other peaks saturate. The 1.34 eV PL shows a near-linear behaviour, however.

Figure 4. PL spectra at 14 K in the band-edge region at three different excitation intensities. The shift with excitation intensity is clear for both the 1.485 and 1.45 eV PL bands. As a contrast, the 1.513 eV BE peak does not shift. The deeper bands at 1.41 eV and 1.34 eV, not shown in the figure, do not shift with excitation intensity.

TABLE III

Summary of experimental data for the four Li-related PL bands measured at 14 K.

Energy position at $P_{exc}=10$ mW	1.485 eV	1.45 eV	1.41 eV	1.345 eV
$E_g - (E_D + E_A)$ [eV]	1.482	1.447	1.410	1.345
$E_D + E_A$ [meV]	38	73	110	175
Activation energy [meV]	28 ± 2	66 ± 2	98 ± 4	148 ± 4
Shift with P_{exc} [meV]	5 ± 1	5 ± 1	0	0
PL intensity versus P_{exc}	non-linear	non-linear	non-linear	nearly linear

clear at present whether the inadvertent Cu contamination always observed at high temperatures causes the 1.41 eV PL band to become strong, or whether high temperatures favour the complexing of this centre. An indication supporting the former is the fact that in the presence of a Cu source the 1.41 eV peak seems to increase without bounds, while in our case the limited access of Cu seems to present an upper bound. Instead the 1.34 eV PL band grows strong and dominates over the Cu-Li spectrum. The bulk of information collected from the present investigation supports the conclusion from earlier work that there is an anti-correlation between the intensities of the 1.36 eV Cu luminescence and the 1.41 eV PL band and its assignment to a $Cu_{Ga}Li_i$ acceptor with binding energy around 100 meV [7]. The experimental data are shown in figures 2 and 4 and summarized in table III.

The 1.34 eV photoluminescence band

Intentionally Cu-doped samples never show this peak strongly, but rather the 1.41 eV Cu-Li PL band. In the samples used in the present study the Cu concentration is limited to accidental contamination during sample growth and heat treatment. In this case the 1.34 eV PL band can become quite intense, although the Li-related band-edge luminescence usually dominates the spectra in heavily doped samples. The binding energy deduced from the peak position is in good agreement with the measured activation energy, but does not allow for a significant lattice relaxation, however, or about 30 meV. In view of the above evidence we suggest a deep Li acceptor as the origin of the 1.34 eV PL band, presumably a double Li_{Ga} acceptor. The model requires experimental verification, however. Work is in progress to provide additional information from far infrared studies.

This work was supported by the Icelandic Natural Science Foundation.

REFERENCES

1. P.S. Nandhra, R.C. Newman, R. Murray, B. Pajot, J. Chevallier, R.B. Beall, and J.J. Harris, *Semicond. Sci. Technol.* **3**, 356 (1988).
2. M. Stavola, S.J. Pearton, J. Lopata, C.R. Abernathy and K. Bergman, *Phys. Rev. B* **39**, 8051 (1989).
3. B. Pajot, R.C. Newman, R. Murray, A. Jalil, J. Chevallier, and R. Azoulay, *Phys. Rev. B* **37**, 4188 (1988).
4. C.S. Fuller and K.B. Wolfstirn, *J. Appl. Phys.* **33**, 2507 (1962).
5. A.G. Milnes, *Advances in electronics and electron physics* **61**, 63 (1983).
6. See e.g. M.E. Levy and W.G. Spitzer, *J. Phys. Chem. Solids* **6**, 3223 (1973).
7. H.P. Gislason, Z.G. Wang and B. Monemar, *J. Appl. Phys.* **58**, 240 (1985).
8. Z.G. Wang, H.P. Gislason and B. Monemar, *J. Appl. Phys.* **58**, 230 (1985).
9. E. Janzén, M. Linnarsson, and B. Monemar, these proceedings.
10. M.D. Sturge, E. Cohen and K.F. Rodgers, *Phys. Rev. B* **15**, 3169 (1977).

LASER-THERMAL IMPURITY PUMPING OF SHALLOW DONORS IN ULTRAPURE GERMANIUM

T. THEILER*, F. KEILMANN* AND E. E. HALLER**

* Max-Planck-Institut für Festkörperforschung, Heisenbergstr. 1, 7000 Stuttgart 80, FRG

** University of California at Berkeley and Lawrence Berkeley Laboratory, 1 Cyclotron Road, Berkeley, CA 94720

ABSTRACT

Extremely narrow far-infrared lines [1] of OH-donors in ultrapure germanium are used to probe the fundamental dynamic processes of impurities. We examine the 1s-2p transition as a function of laser intensity, using photothermal ionization spectroscopy (PTIS) modified by Zeeman tuning with frequency-fixed lasers. We observe a change of the resonance line shape in the intensity region near 10^{-4} W/cm². This effect can be quantitatively understood in a rate equation model which shows that at the critical intensity the ground state becomes depleted and the dependence of the recombination on the degree of ionization becomes important. Therefore the critical intensity depends also on compensation.

EXPERIMENT

An ultrapure Ge single crystal with the dimensions $1 \times 3 \times 7$ mm³ grown at the Lawrence Berkeley Laboratory is studied. The long axis is orientated in the [111] direction, the 7×3 mm² faces are

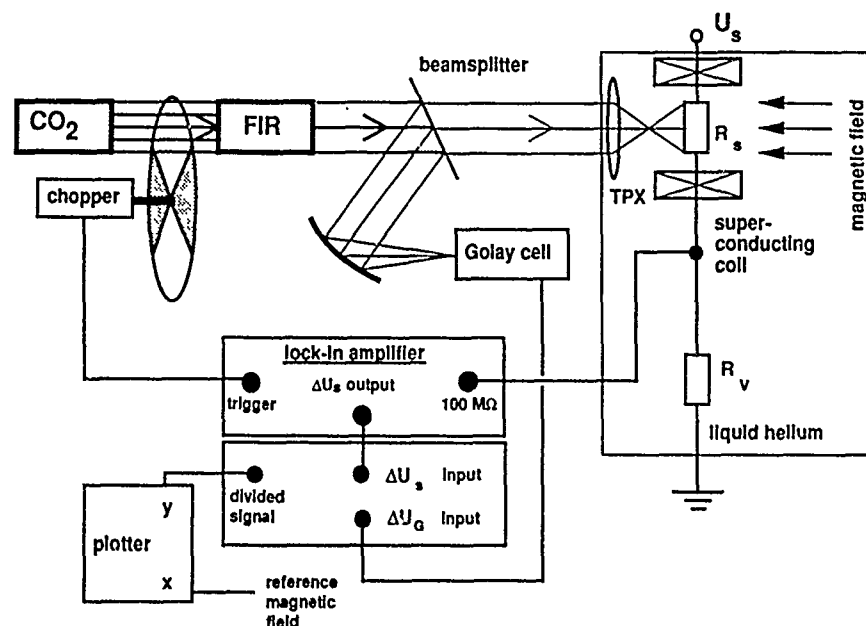


Fig. 1 Experimental setup

normal to the $[11\bar{2}]$ direction. The two $7 \times 1 \text{ mm}^2$ faces are ion-implanted with P (25keV, $4 \times 10^{14} \text{ cm}^{-2}$) and annealed at 300°C for 2 h in Ar to form good ohmic contacts. The sample has an OH-concentration of about 10^{11} cm^{-3} and a P concentration of 30 - 60% of that value. The concentration of the residual acceptors is of the order of 10^{10} cm^{-3} . The crystal is mounted in a liquid He bath cryostat at 4.2K with the electric field in $[111]$ direction and the magnetic field in $[11\bar{2}]$ direction. The $1s-2p_A$ transition of the D(OH) centre is Zeeman-tuned and excited with a CO_2 pumped alcohol laser at $117.227 \mu\text{m}$. The intensity of the c.w. laser is varied between 10^{-6} and 10^{-2} W/cm^2 . Figure 1 shows the experimental setup: The photothermal current of the sample is measured with and without radiation using a lock-in technique. The difference signal divided by the actual laser intensity, which is measured by a Golay cell via a beam splitter, is plotted versus the magnetic field. In this way small variations of the laser intensity are eliminated. A typical line shape is shown in fig. 2. The decreasing background photoconductivity arises from the magnetoresistance.

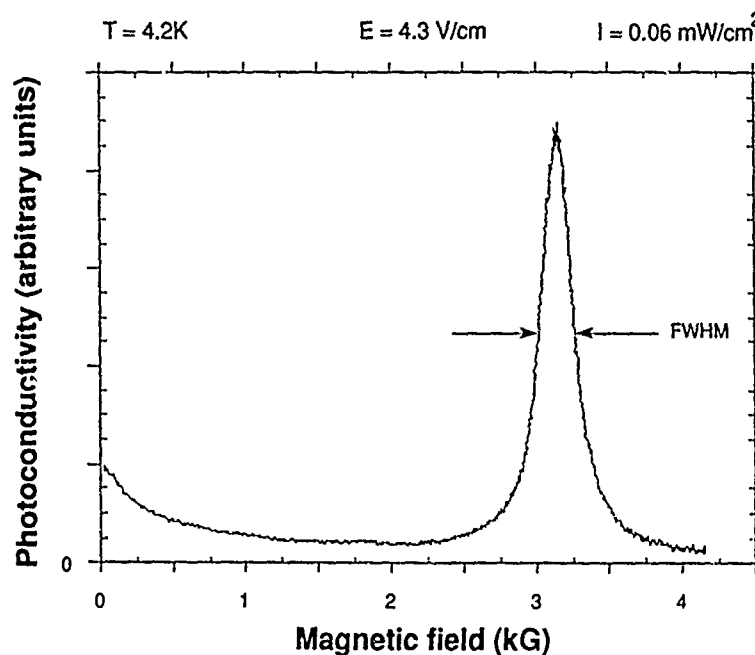


Fig. 2 Line shape of the $1s-2p_A$ transition as function of the magnetic field

RESULTS

Figure 3 shows the $1s-2p_A$ -resonance width at 4.2K measured at half maximum (FWHM) as a function of laser intensity for two different applied fields ($E = 1.86 \text{ V/cm}$ and $E = 2.86 \text{ V/cm}$). The frequency shift of the $1s-2p_A$ -resonance is directly proportional to the applied magnetic field up to 5 kG [2] and therefore the linewidth can be calculated directly from the line shape of the transition as function of the magnetic field. We find that the resonance starts to broaden at intensities as low as $10 \mu\text{W/cm}^2$. When plotting the peak photoconductivity in the $1s-2p_A$ resonance as function of intensity (fig. 4) we find that already above $1 \mu\text{W/cm}^2$ the signal scales less than linearly with intensity. How can this behaviour be explained?

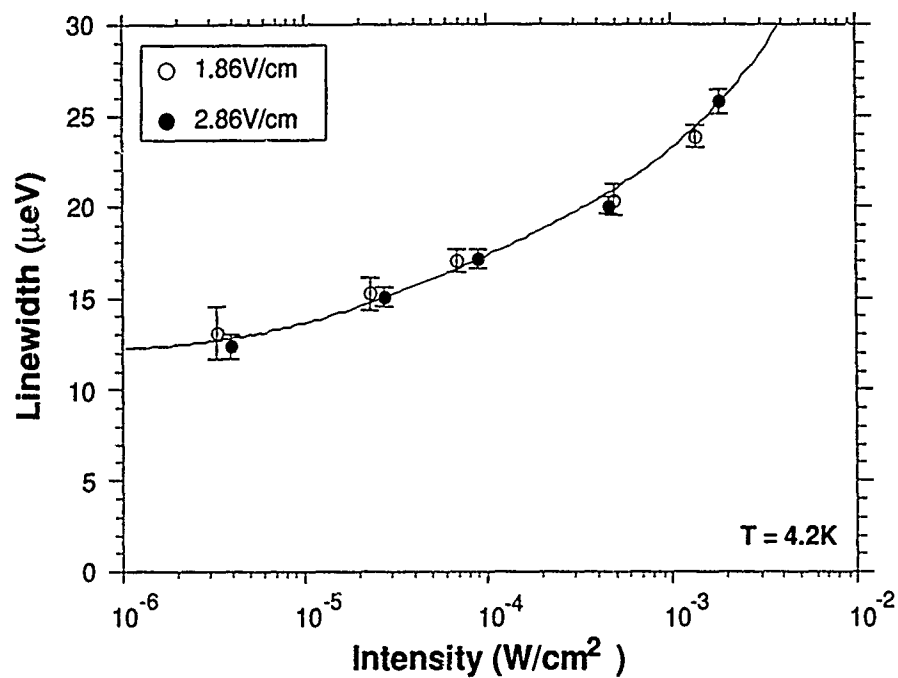


Fig. 3 Linewidth of the photothermal $1s-2p_A$ signal as function of intensity; solid line: theoretical curve

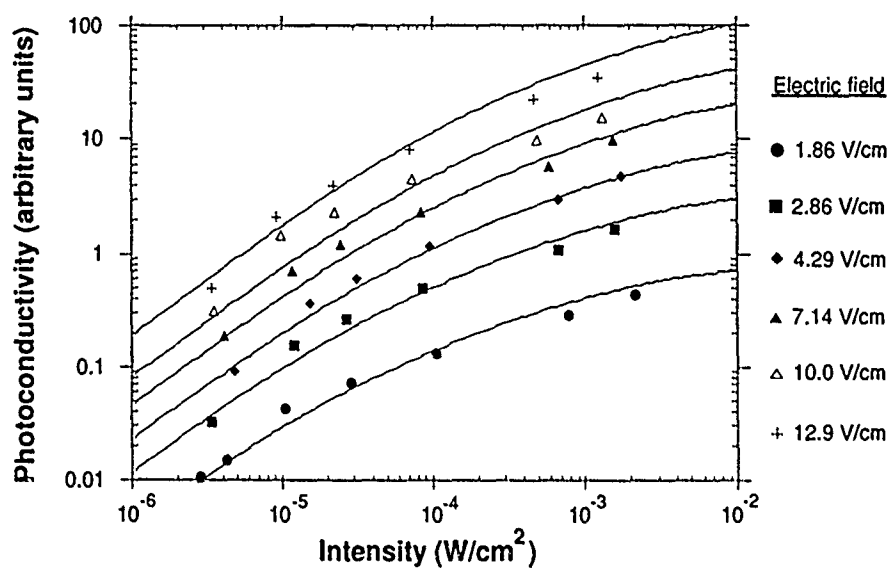


Fig. 4 Photothermal conductivity of the $1s-2p_A$ transition at 4.2K in resonance; solid lines: calculated curves

MODEL

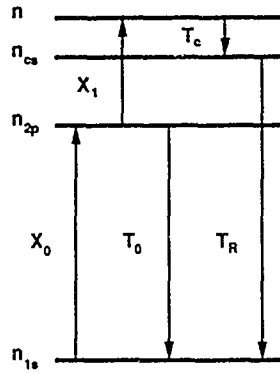


Fig. 5 Dynamics of the photothermally measured 1s-2p excitation

Figure 5 shows the dynamics of the photothermal ionization in Ge:D(OH): The 2p state is excited optically with a rate X_0 . From there the electrons are either ionized directly by acoustic phonons with a rate X_1 or they fall back into the ground-state with rate T_0 , due to both stimulated emission X_0 and phonon relaxation T_p . Once in the conduction band the electrons can become captured into excited s states [3] (population n_{cs}) of an ionized donor at a rate T_c . At 4K nearly all electrons that have reached a p state become ionized (98.6% for the 2p-state) while electrons in s-states are ionized with much smaller probability (47% for the 2s-state)[4]. Therefore the recombination takes place via s-states. The electrons quickly lose their energy on the way to the 2s-state [3]. There they remain longer, because the last relaxation step T_R requires a phonon of high energy.

The occupation density of the particular states as function of intensity can be calculated with the following rate equation model:

$$\frac{dn}{dt} = X_1 n_{2p} - T_c n$$

$$\frac{dn_{cs}}{dt} = T_c n - T_R n_{cs}$$

$$\frac{dn_{2p}}{dt} = X_0 n_{1s} - T_0 n_{2p} - X_1 n_{2p}$$

$$n_{1s} = N_D - N_A - n_{2p} - n_{cs} - n$$

with:

$$T_c = \sigma_c(T) v_D(E, T) (N_A + n)$$

$$T_0 = X_0 + T_p$$

$$X_0 = \frac{\sigma_{1s2p}(v) I}{h\nu}$$

$$v_D = \frac{2v_s}{\pi} \arctg\left(\frac{\pi\mu_{n,p}E}{2v_s}\right)$$

The last formula [5] describes the drift velocity v_D , where v_s is the maximum velocity of electrons in the conduction band, limited by the kinetic energy necessary for spontaneous emission of optical phonons ($v_s \approx 3 \times 10^7$ cm/sec). The mobility $\mu_{n,p}$ is limited only by acoustic phonon scattering. Because of the low compensation of the sample (acceptor concentration of the sample $N_A \approx 10^{10}$ cm⁻³) we use the electron mobility μ_n after Zylberstejn [6], which is given as a function of temperature by $\mu_n = 2.4 \times 10^7 \times T^{-3/2}$.

The optical cross section $\sigma_{1s2p}(\nu = \nu_{1s2p})$ can be derived from the integrated one as calculated in [7], by inserting the linewidth $\Delta\nu = 12 \mu\text{eV}$ for the 1s-2p-transition in the formula:

$$\int_{\text{line}} \sigma_{1s2p}(\nu) d\nu \approx \sigma_{1s2p}(\nu = \nu_{1s2p}) \Delta\nu$$

The absorption coefficient is obtained by multiplication with N_D . Using $N_D = 10^{11} \text{ cm}^{-3}$ we get a peak absorption $\alpha_{\text{max}} = 0.86 \text{ cm}^{-1}$. This number is a factor of 4 to 8 higher than the extrapolated values of experimental data from higher doped samples [8], assuming that the oscillator strength remains constant. Since the absorption in our sample was too small to be measured reliably we use the theoretical value in the calculation.

With $X_1 = 5.7 \times 10^8 \text{ sec}^{-1}$ [4], $T_p = 8.3 \times 10^6 \text{ sec}^{-1}$ [4], $T_R = 10^9 \text{ sec}^{-1}$ [9] and the cascade capture cross section $\sigma_c = 2.9 \times 10^{-11} \text{ cm}^2$ [3, 10] all parameters are known. In equilibrium the time derivation vanishes and only a set of simple equations remains to be solved. The results are plotted in fig. 6.

DISCUSSION

The intensity where stimulated 2p \rightarrow 1s emission processes begin to broaden the resonance is predicted by our model ($n_{2p} \rightarrow n_{1s}$ in fig. 6) to be above 50 mW/cm^2 as is experimentally verified (for a discussion see [11]). This range, however, cannot be reached with the c.w. laser system used in the present experiment.

Nearly all carriers in fig. 6 are contained in the ground state and in the conduction band. Two independent mechanisms of line-broadening can now be predicted from the curves:

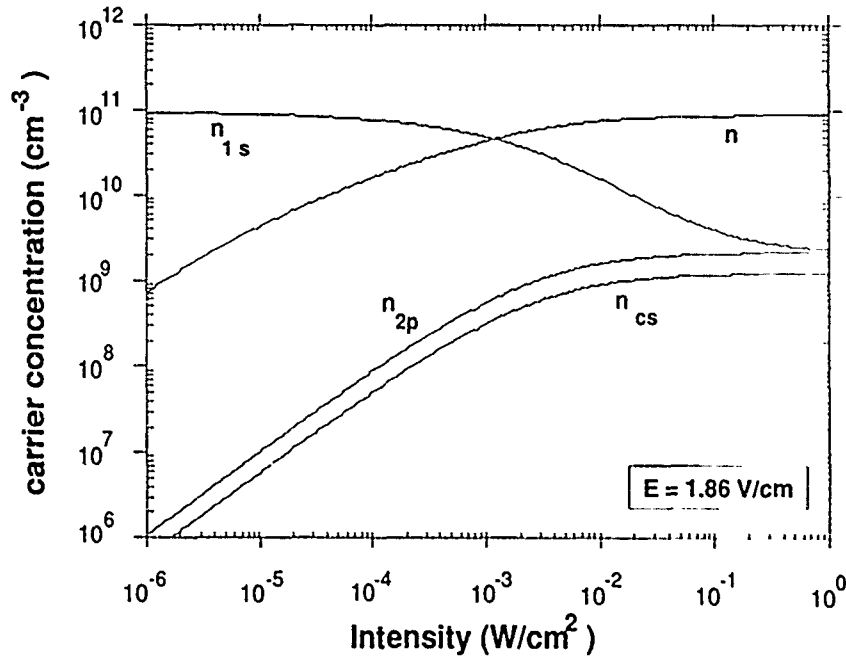


Fig. 6 Occupation density calculation of the particular levels

At about 1 mW/cm^2 the 1s-level is half depleted with the consequence that the carrier absorption coefficient comes down to half of its maximum value. Because the ground state population decreases with pump rate, which itself reduces on detuning from resonance, the 1s-2p absorption line begins to broaden above about $100 \text{ } \mu\text{W/cm}^2$.

The line broadening of the photothermal ionization signal (PTIS) below $100 \text{ } \mu\text{W/cm}^2$ in fig. 3 is dominated by a second mechanism: As shown in fig. 6 the concentration in the 2p-state is directly proportional to intensity up to at least $100 \text{ } \mu\text{W/cm}^2$, while on the other hand the density of electrons in the conduction band increases less than linearly already above $1 \text{ } \mu\text{W/cm}^2$. The latter results from an increase in the concentration of capture centres. Thus the photothermal conductivity line does not directly reflect the absorption line of the 1s-2p transition. The PTIS line rather appears broadened compared to the absorption line.

The total line broadening can be derived from the model. Assuming that the optical cross section yields a lorentzian line shape the photothermal linewidth Δv_{PTIS} is given by

$$\Delta v_{\text{PTIS}} = \Delta v \sqrt{1 + \frac{N_D n}{(N_A + n/2)(N_D - N_A - n)}}$$

which is in excellent agreement with the experimental results (solid line in fig. 3).

The sublinear increase of the photoconductive signal as function of intensity can now be explained accordingly:

1. The capture rate T_C of electrons in the conduction band increases with the number of ionized donors. Only when there are many more compensating acceptors than photoconducting electrons, T_C can be taken as constant and the photothermal signal is linear in intensity. In our case this is fulfilled only for very small intensity below 10^{-6} W/cm^2 .
2. Above 10^{-4} W/cm^2 the depletion of the ground state becomes important and yields an additional nonlinearity.

When we compare the calculated photoconductivity (solid lines in fig. 4), which is directly obtained from n in fig. 6, we find good agreement with the experimental set of data points. Therefore we have a model which satisfactorily explains the line broadening of the photothermal ionization signal at low intensities.

REFERENCES

1. H. Navarro, E. E. Haller and F. Keilmann, *Phys. Rev. B* **37**, 10822 (1988).
2. H. Navarro, J. Griffin and E. E. Haller, *J. Phys. C* **21**, 1511 (1988).
3. M. Lax, *Phys. Rev.* **119**, 1502 (1960).
4. F. Beleznyay and G. Pataki, *phys. stat. sol.* **13**, 499 (1966).
5. R. M. Westervelt and S. W. Teitsworth, *J. Appl. Phys.* **57**, 5457 (1985).
6. A. Zylberstein, *Phys. Rev.* **127**, 744 (1962).
7. E. Burstein, G. Picus and N. Sclar, *Photoconductive Conference Atlantic City 1954*, edited by R.G. Beckenridge, B. R. Russel and E. E. Hahn (John Wiley, New York 1954), p. 353.
8. E. Rotseart, P. Clauws, J. Vennik and L. van Goethem, *Physica* **146B**, 75 (1987).
9. G. Ascarelli and R. Rodríguez, *Phys. Rev.* **127**, 167 (1962).
10. V. N. Abakumov and I. N. Yassievich, *Sov. Phys. JETP* **44**, 345 (1976).
11. T. Theiler, F. Keilmann and E. E. Haller, *Proceedings of the Third International Conference Linköping 1988*, edited by B. Monemar (Institute of Physics Conference Series Number 95, Bristol and Philadelphia, 1989), p. 179.

ELECTRICAL AND PHOTOLUMINESCENCE PROPERTIES OF Mg^{+} and C^{+} IMPLANTED ACCEPTORS IN InP.

A.C. BEYE, A. YAMADA, A. SHIMIZU¹, H. SHIBATA, H. TANOUE, K.M. MAYER, H. SUGIYAMA, K. KAMIJOH², T. ODA³, O. ARRIGA³, I. AKIYAMA⁴, N. KUTSUWADA⁴, T. MATSUMORI⁵, S. UEKUSA¹ and Y. MAKITA.

Electrotechnical Laboratory, 1-1-4 Umezono, Tsukuba, Ibaraki-ken, 305 Japan.

1. Meiji University, Higashi-mita 1-1-1, Tama-ku, Kawasaki-shi, 214 Japan.

2. O. T. R. L., 5-5 Tokodai, Tsukuba-shi, Ibaraki-ken, 300-26 Japan.

3. Nippon Mining Co., Ltd., 3-17-35 Niizo-Minami, Toda-shi, 335 Japan.

4. N. I. T., Gakuendai 4-1, Miyashiro-cho, MinamiSaitama-gun, 345 Japan.

5. Tokai University, 1117 Kitakaname, Hiratsuka-shi, 259-12 Japan.

ABSTRACT

Implantation of Mg^{+} and C^{+} ions is carried out in bulk InP substrates using single or several energies up to 400 keV. The net carrier concentration profile at 300K is measured by capacitance-voltage (C-V) method. The ground and excited states binding energies of Mg and C acceptors are determined by low-temperature selective excitation of photoluminescence (PL). Additional sharp exciton-like emissions are detected after annealing of the samples. Their intensity is found to decrease with increasing Mg^{+} or C^{+} dose. Annealing-induced activation and/or formation of complex defect are the likely candidate mechanisms for the involved defect.

INTRODUCTION

Optoelectronic device applications [1-4] require the characterization of impurities in semiconductors such as InP and its related compounds [5-14]. Ion implantation is one of the commonly used method for the identification of involved chemical species.

In this paper, results of selective-excitation of photoluminescence (SPL) of Mg^{+} and C^{+} -implanted bulk InP grown by liquid encapsulated Czochralski are reported. The SPL spectra exhibit two-hole replica of Mg-acceptor bound exciton (BE) and PL lines involving DAP transitions to the Mg acceptor excited states. The emission properties of some annealing-induced defects are also discussed.

EXPERIMENTAL

Nominally undoped InP wafers are used for flat-profile ion-implantation with Mg^{+} as well as C^{+} with several energies up to 400 keV. Another series are implanted with Mg^{+} using single energy of 100 keV. Samples are then encapsulated with 1500Å thick SiN_x using plasma chemical vapor deposition at 370°C. Furnace annealing is done at 700°C during 15 or 20 min under H_2 flow.

After removal of the encapsulant in HF, the carrier concentration at 300K is measured by C-V method using Schottky contacts of electrolytic acid solution HCl (5%) + H_2O (95%) acting as etchant.

PL measurements are performed at 2K. Chemical etching down to 1 μm from the surface is used in order to reach part of the sample where the carrier concentration is comparable to that of the unimplanted wafer. The PL excited with an Ar^{+} pumped dye laser, is collected from the etched area, to resolve acceptor -BE and -excited state emissions.

RESULTS AND DISCUSSION

The PL spectra (fig.1) of Mg^+ -implanted InP exhibit an acceptor bound exciton (Mg^0X), free to bound e-Mg^0 and donor acceptor pair $\text{D}^0\text{-Mg}^0$ emissions. Estimation of Mg-acceptor binding energy (40.6 meV) is done from the position of e-Mg^0 band, in agreement with previously published data [10,13]. Additional emissions X_1 , X_3 , and X_4 are observed at 1.4083 eV (8801.5Å), 1.3974 eV (8870.1Å) and 1.3960 eV (8879Å). The excitonic nature of these recombination lines is suggested from their sharp spectral width and strong excitation intensity dependence. A partial quenching of these lines is observed with increasing Mg atomic concentration from $1 \times 10^{16} \text{ cm}^{-3}$ to $1 \times 10^{18} \text{ cm}^{-3}$.

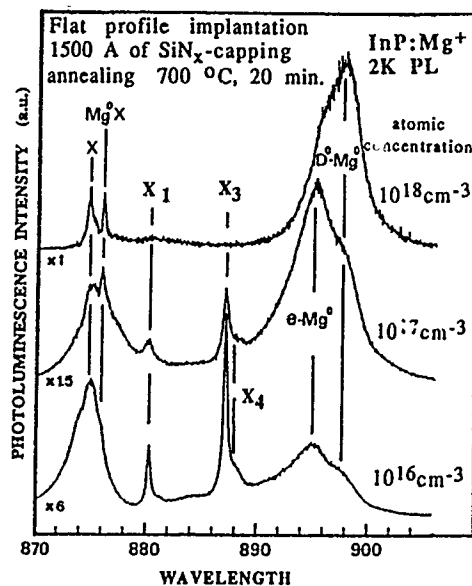


Fig.1: PL spectra of Mg^+ -implanted InP. Note the enhancement of Mg-related emissions and the quenching of X_1 , X_3 and X_4 emissions with increasing atomic concentration.

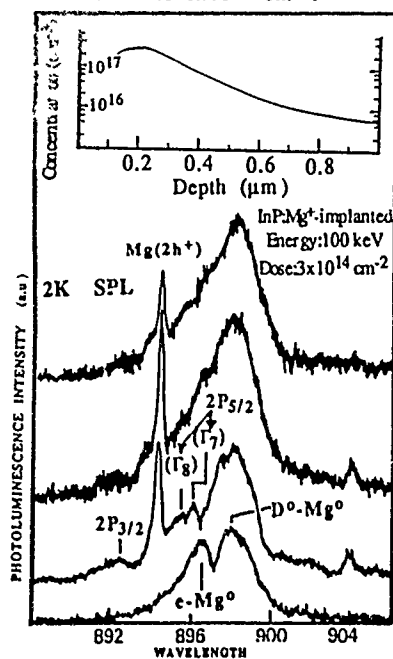


Fig.2: Set of SPL spectra excited around Mg^0X showing transitions involving Mg-acceptor excited states.

The insert of fig.2 shows the concentration profile of 100 keV Mg^+ -implanted InP used for SPL experiments. This single-energy implantation at an ion-dose of $3 \times 10^{14} \text{ cm}^{-2}$ leads to a net carrier concentration varying from $3 \times 10^{17} \text{ cm}^{-3}$ down to $5 \times 10^{15} \text{ cm}^{-3}$ respectively at 0.2 μm and 1.0 μm from the surface. In order to resolve the emission lines arising from transitions involving ground and excited states of Mg-acceptor, the PL is collected from this etched area where the carrier concentration is comparable to that of the unimplanted wafer. The PL spectrum (not recorded here) from such etched area is dominated by a strong acceptor bound exciton doublet (Mg^0X) at 1.4155 eV and 1.4152 eV [14].

A set of SPL spectra, excited around Mg^0X doublet, is shown in fig. 2. From the bottom to the top, the excitation energy is tuned above, close on and below the two components of Mg^0X .

These spectra show the resonant enhancement of $Mg(2h^+)$, the two-hole replica of Mg^0X , i.e. recombination of exciton bound to Mg acceptor leaving the remaining hole in its first $2S_{3/2}$ excited state. DAP transitions to the $2P_{3/2}$, $2P_{5/2}(\Gamma_8)$ and $2P_{5/2}(\Gamma_7)$ excited states of Mg-acceptor are also observed.

Fig.3 shows the PL spectra of C^+ -implanted InP (concentration of $1 \times 10^{16} \text{ cm}^{-3}$) as a function of excitation intensity. At low excitation, the spectrum (Fig.3.a) is dominated by DAP emission (D^0-C^0) involving C acceptor. With increasing excitation intensity, this emission band becomes broader owing to the emergence of FB emission $e-C^0$. The energy position of $e-C^0$ leads to an estimation of the binding energy of C acceptor of about 43.9 meV close to the already reported value (44.3 meV) obtained from temperature dependence of the PL [10]. The exciton-like PL peaks X_1 , X_3 and X_4 are strongly dependent upon the excitation intensity and quenched with increasing C concentration, as in the case of Mg^+ -implantation.

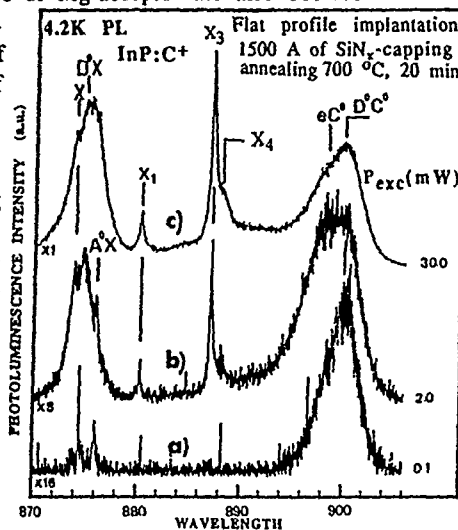


Fig.3: PL spectra of C^+ -implanted InP showing the strong dependence of X_1 , X_3 and X_4 emissions upon the excitation intensity.

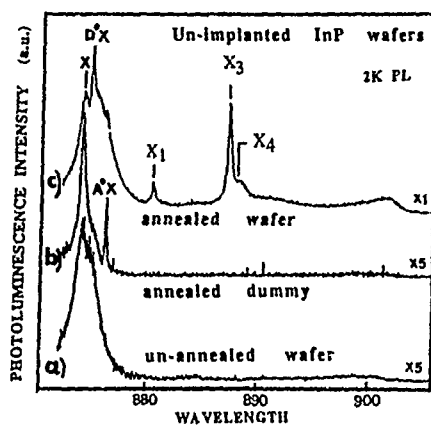


Fig.4: PL spectra of annealed and unannealed InP wafers (with different quality) showing the emergence of X_1 , X_3 and X_4 emissions.

The energy position of X_3 and its spectral shape (with a low energy shoulder X_4) are similar to those of isoelectronic Bi bound exciton line well characterized in Bi-doped InP [15]. Its detection in annealed and/or unimplanted bulk InP suggests at first an annealing induced-activation process of displaced Bi impurity off to regular substitutional site. Such hypothesis is ruled out after careful comparison. In fact, the Bi bound exciton line Bi^0X is exactly located at 1.3968 eV (8874 Å) in the 2K PL-spectra, i.e. about 0.6 meV below the X_3

The modifications of the emission properties of unimplanted InP that result from the annealing treatment, are analyzed in fig.4. The PL spectra of such virgin wafers before annealing (fig.4.a) and after annealing (fig.4.c) are compared with that (fig.4.b) of an InP dummy used for capping the samples during annealing. The peaks X_1 , X_3 and X_4 are not detected in the PL spectra of un-annealed wafer or in that of the annealed dummy. Besides the near bandedge emissions, these PL peaks are clearly detected in the PL spectrum of annealed wafers.

emission line. Furthermore, the similar annealing-behaviours of X_1 , X_3 and X_4 support a possible participation of annealing-induced-vacancies for the formation of the involved defect. A complex defect involving such vacancies and other impurities or point defects (already present in the starting material) is a likely candidate. Revisiting some PL studies of heat-treated InP [16-18], it should be noticed that X_1 , X_3 and X_4 emissions have been observed in annealed InP (respectively lines I, III and IV at 1.7K in ref.16 and lines A, D, and E at 4.2K in ref.17). Low-temperature (400°C-500°C) capless-annealing [16,17] or higher-one (700°C) in our case of coated samples, seem to be prerequisite for the defect-formation strengthening the possible role of phosphorus vacancies.

CONCLUSION

Implantation of Mg^+ and C^+ ions is carried out into undoped bulk InP substrates to perform acceptor spectroscopy. The $2S_{3/2}$, $2P_{3/2}$, $2P_{5/2}$ (Γ_8) and $2P_{5/2}$ (Γ_7) excitation from the $1S_{3/2}$ state of Mg acceptor in InP. The measured values are respectively 27.8 meV, 25.2 meV, 29.6 meV and 31.0 meV.

PL spectra of annealed wafers show additional exciton-like luminescence peaks. The involved defects that are induced by the annealing procedure, are suggested to be association of residual impurities and point defects or vacancies.

REFERENCES

1. H. Nagai and Y. Noguchi, *Appl. Phys. Lett.* **29**, 740 (1976).
2. C.C. Shen, J.J. Hsieh, and T.A. Lind, *Appl. Phys. Lett.* **30**, 353 (1977).
3. N.K. Dutta, T. Vessel, N.A. Olsson, R.A. Logan, L.A. Koszi, and R. Yen, *Appl. Phys. Lett.* **46**, 525 (1985).
4. N.K. Dutta, S.G. Napholtz, R. Yen, T. Vessel, T.M. Shen, and N.A. Olsson, *Appl. Phys. Lett.* **46**, 1036 (1985).
5. E.W. Williams, W. Elder, M.G. Astles, M. Webb, J.B. Mullin, B.Sraughan, and P.J. Tufton, *J. Electrochem. Soc.* **120**, 1741 (1973).
6. K. Hess, N. Stath, and K.W. Benz, *J. Electrochem. Soc.* **121**, 1208 (1974).
7. P.J. Dean, D.J. Robbins, and S.G. Bishop, *J. Phys.* **C12**, 5567 (1979).
8. P.J. Dean, D.J. Robbins, and S.G. Bishop, *Solid State Commun.* **32**, 379 (1979).
9. G.S. Pomrenke, D.C. Reynolds, and Y.S. Park, *J. Lumin.* **24/25**, 189 (1981).
10. B.J. Skromme, G.E. Stillman, J.D. Oberstar, and S.S. Chan, *Appl. Phys. Lett.* **44**, 319 (1984).
11. P.J. Dean and M.S. Skolnick, *J. Appl. Phys.* **54**, 346 (1983).
12. A.M. White, P.J. Dean, L.L. Taylor, R.C. Clarke, P.J. Ashen, and J.B. Mullin, *J. Phys.* **C5**, 1727 (1972).
13. T.S. Cheng, V.M. Airaksinen, and C.R. Stanley, *J. Appl. Phys.* **64**, 6662 (1988).
14. A.C. Beye, A. Yamada, T. Kamijoh, H. Tanoue, K.M. Mayer, N. Ohnishi, H. Shibata and Y. Makita, *Appl. Phys. Lett.*, Vol.56, No.4 (Jan.22,1989).
15. P.J. Dean, A.M. White, E.W. Williams and M.G. Astles, *Solid State Commun.* **2**, 1555 (1971).
16. J. Frandon, F. Fabre, G. Bacquet and F. Reynaud, *J. Appl. Phys.* **59**, 1627 (1986).
17. T.S. Kim, S.D. Lester and B.G. Streetman, *J. Appl. Phys.* **61**, 4598 (1987).
18. H. Shimakura, K. Kainosho, T. Inoue, H. Yamamoto and O. Oda, in Proceedings of the International Conference on the Science and Technology of Defect Control in Semiconductors, Yokohama 1989, Japan (to be published).

PART III

Electronic Structures -
Native Defects, Complexes,
Transition Metals in Compounds

OPTICALLY DETECTED MAGNETIC RESONANCE OF SULFUR DOPED GALLIUM PHOSPHIDE

K. L. BROWER

Sandia National Laboratories, Albuquerque, NM 87185-5800

ABSTRACT

An isotropic optically detected magnetic resonance (ODMR) having a Lorentzian lineshape at $g = 2.050 \pm 0.003$ and linewidth (FWHM) of 67.3 mT is observed in GaP doped with $6 - 9 \times 10^{17}$ S/cm³. The ODMR at $g = 2.050$ is believed to arise from free electrons (or holes) in the conduction (valence) band. This ODMR is completely quenched due to non-radiative recombination in the vicinity of $g = 1.99$.

INTRODUCTION

We have recently extended our magnetic resonance capabilities to include optically detected magnetic resonance (ODMR) for purposes of studying defects in III-V compound semiconductor systems. Some of the systems of particular interest with regard to defect studies are samples implanted with particular isotopes. For example, this technique may allow one to observe the hyperfine structure of impurity donors in GaP. Other interesting material systems are the strained layer superlattices and their interfaces. GaP is one of the III-V compound semiconductors of particular interest for ODMR studies. In this paper we report the results of our preliminary ODMR observations on as-grown sulfur doped GaP.

EXPERIMENTAL TECHNIQUES AND RESULTS

A schematic of the 20 GHz ODMR spectrometer used in these studies is shown in Fig. 1. The samples are illuminated with either a Ar laser or a dye laser. This spectrometer is sensitive to the intensity of the luminescence at magnetic resonance.

As the result of a preliminary survey, we observed the ODMR spectrum shown in Fig. 2 from a crystal of n-type GaP doped with $6 - 9 \times 10^{17}$ sulfur/cm³. This spectrum is observable under illumination with either the 514.5, 488, or 457.9 nm lines of the Ar laser. The ODMR signal is not observed under laser illumination at 800 nm (subbandgap light). The intensity of this ODMR is maximum with approximately 50 mW of incident laser power and 50 mW of incident microwave power. The peak in the luminescence of this ODMR signal as deduced using narrow band interference filters (10 nm, FWHM) is approximately 800 nm; however, the ODMR signal is observable at least between 680 and 1050 nm (no GaAs filter). Ordinarily, only a GaAs filter was used to screen the optical detector from the laser radiation. This ODMR signal was detected using narrow-band lock-in techniques and a liquid nitrogen cooled Ge detector. This spectrum appears isotropic with respect to the direction of the applied magnetic field. The microwaves were square-wave chopped at typically 280 Hz.

DISCUSSION

The dashed line in Fig. 2 is a Lorentzian curve least squares fitted to the observed ODMR spectrum between 620 and 712 mT and 776 and 800 mT. This Lorentzian curve is centered at 711.8 mT corresponding to a g value of 2.050 ± 0.003 with a linewidth (FWHM) of 67.3 "

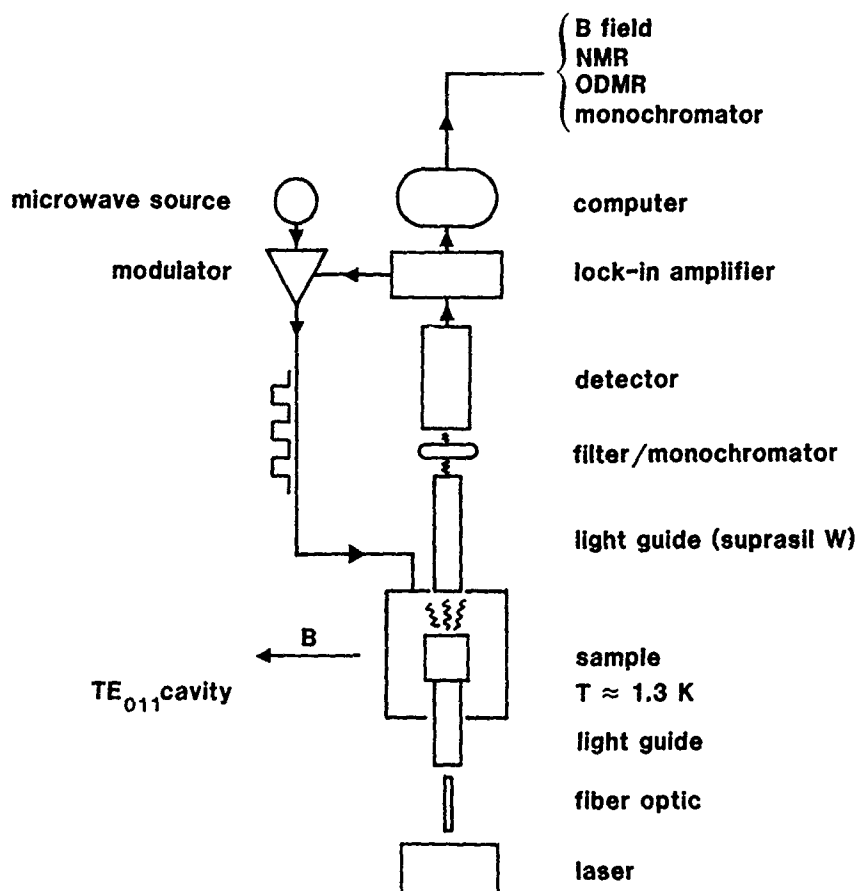


Fig. 1. Schematic of the 20 GHz ODMR spectrometer.

The ODMR response relative to the Lorentzian lineshape is enhanced between 712 and 731 mT and quenched due to non-radiative transitions between 731 and 760 mT. The point at which this derivative-like response crosses the Lorentzian curve in Fig. 2 corresponds to 731 mT and a g value of 1.996 ± 0.003 . The peak-to-peak width of this perturbing signal is 16.7 mT. This perturbing signal is attributed to the donor resonance which is known to have a g value of 1.99 ± 0.01 [1,2,3], a linewidth ranging from 12 to 25 mT [1,3], and spin dependent processes indicative of either non-radiative transitions [4] or a combination of enhanced and quenched spin dependent luminescence [5] as in our case. The donor resonance has been observed by ODMR in GaP doped with either O, Te [2], or S [3] and was first observed by EPR in crystals doped with S, Se, or Te [1]. Observation of the donor hyperfine spectrum has not yet been reported, although the ligand hyperfine spectrum in the case of oxygen doped GaP has been investigated with ENDOR showing that the donor is centered on the P sublattice [4].

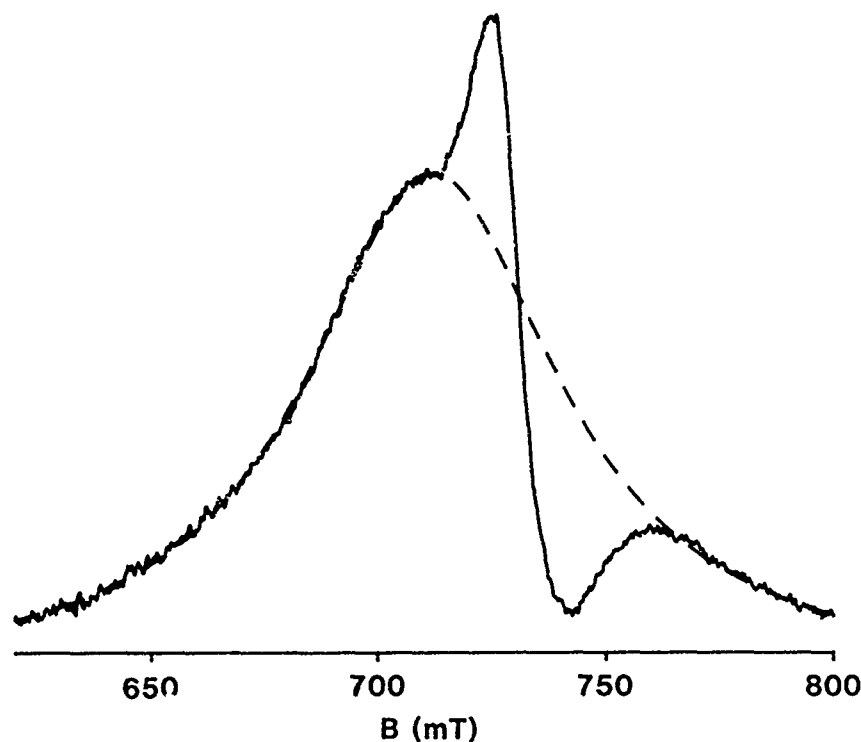


Fig. 2. ODMR of sulfur doped GaP at a microwave frequency of 20.4219 GHz at 1.3 K. The dashed line corresponds to a Lorentzian curve least squares fitted to the observed spectrum.

With regard to the identity of the resonance in Fig. 2 with $g = 2.050$, Cavenett observed an ODMR at $g = 2.05$ with a linewidth (FWHM) of approximately 125 mT in Cr doped GaP [6]. This resonance exhibited structural features which Cavenett suggested were consistent with an unpaired spin centered on a Ga site interacting with four P neighbors. This resonance also showed a relatively small donor resonance due to non-radiative recombination at $g = 1.996$.

In the case of the ODMR at $g = 2.050$ in Fig. 2, the luminescence responsible for the ODMR is subbandgap. This suggests that either a free electron is captured by a trapped hole center, a free hole is captured by a trapped electron, or both the electron and hole are trapped and radiative recombination occurs providing their wavefunctions overlap.

Consider the case in which the radiative recombination is enhanced by microwave induced spin flips of an unpaired electron localized on a defect. Since the linewidth of the ODMR we observe at $g = 2.050$ (Fig. 2) is significantly smaller than that observed by Cavenett [6], it is conceivable that the hyperfine structure is not resolved. We examined this possibility for three different ligand hyperfine models in which the lineshape was dominated by the ligand hyperfine interactions with a single shell of host lattice atoms. This calculation was based on the solution to a spin Hamiltonian with $S = 1/2$ and a dominant isotropic hyperfine interaction with

a shell of neighboring host lattice atoms. The positions of the hyperfine lines were calculated to second order, and the final lineshape was a superposition of Gaussian lineshapes with linewidths (FWHM) ranging from 10 to 30 mT representing the balance of the ligand hyperfine interactions. This calculated lineshape was least squares fitted to the Lorentzian curve representing the experimentally observed ODMR at $g = 2.050$ in terms of the isotropic g value and the isotropic ligand hyperfine tensor, a . The results of these calculations for three ligand models, assuming a linewidth of 30 mT for each of the hyperfine lines, is shown in Fig. 3; other solutions with Gaussian or Lorentzian linewidths ranging from 10 to 30 mT were also examined. In no case is it possible to reconstruct the observed Lorentzian lineshape by assuming a single dominant ligand hyperfine interaction. Furthermore, it may not be possible to account for the linewidth of this resonance from only ligand hyperfine interactions assuming only one unpaired electron unless one invokes strong spin polarization effects.

The Lorentzian lineshape of the observed ODMR resonance is suggestive of motional effects or lifetime broadening. It is conceivable that the Lorentzian lineshape could arise from motional averaging of the spin localized on a defect; however, this model seems unlikely because the motional effects required to account for a Lorentzian linewidth of 67.3 mT are expected to be quenched at 1.3 K.

An alternative model for the resonance at $g = 2.050$ as observed in Fig. 2 is that it is due to microwave induced spin flips of the free conduction (valence) electrons (holes). ODMR from the radiative recombination center is not observed. In this model the linewidth is dominated by spin-spin interactions, and the Lorentzian lineshape is due to

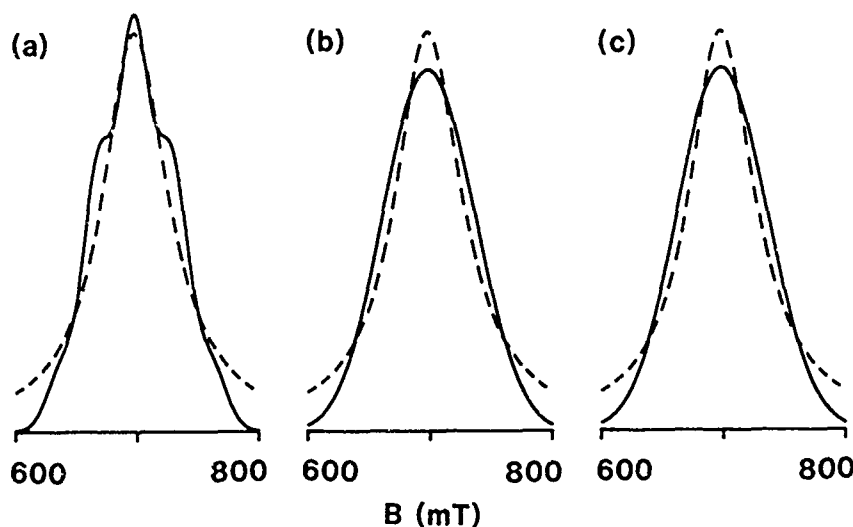


Fig. 3. Lorentzian representation of the ODMR at $g = 2.050$ (dashed curve) compared with calculated lineshapes assuming a dominant shell of ligand hyperfine interactions. The Gaussian linewidth (FWHM) of each hyperfine component comprising the composite spectrum is 30 mT. (a) Four neighboring P atoms with $a(^{31}\text{P}) = 0.0289 \text{ cm}^{-1}$. (b) Four neighboring Ga atoms with $a(^{69}\text{Ga}) = 0.0124 \text{ cm}^{-1}$. All isotopic configurations are included in this calculation. (c) Transferred hyperfine interaction with 12 P atoms with $a(^{31}\text{P}) = 0.0185 \text{ cm}^{-1}$.

motional/exchange effects. The fact that the ODMR is completely quenched at resonance in the vicinity of 742.5 mT suggests that all of the electrons (holes) contributing to the $g = 2.050$ resonance undergo electron-hole recombination by means of a spin-dependent non-radiative decay process at the donor center. The complete quenching of the ODMR is consistent with the freedom that the electrons (holes) have in reaching the donor centers. The nature of the radiative recombination center remains unknown.

CONCLUSIONS

An isotropic ODMR at $g = 2.050 \pm 0.003$ has been observed in n-type GaP doped with $6 - 9 \times 10^{17} \text{ S/cm}^3$. This resonance has a Lorentzian lineshape and linewidth (FWHM) of 67.3 mT. It is difficult, if not impossible, to account for the lineshape and linewidth of this resonance in terms of a dominant ligand hyperfine interaction. Furthermore, it is very unlikely that the Lorentzian lineshape can be attributed to motional effects of a localized spin since significant motional effects are expected to be quenched at 1.3 K. However, the Lorentzian lineshape and linewidth are consistent with motional/exchange effects of free electrons (or possibly holes) in the conduction (valence) band. This model suggests that the linewidth is dependent upon the concentration of free electrons (or holes). This ODMR may be important with regard to the study of motional and exchange effects in GaP.

REFERENCES

1. R. S. Title, Phys. Rev. 154, 668 (1967).
2. S. Toyotomi and K. Morigaki, J. Phys. Soc. Japan 29, 800 (1970).
3. M. Godlewski, W. M. Chen, and B. Monemar, Phys. Rev. B 33, 8246 (1986).
4. D. Y. Jeon, J. F. Donegan, and G. D. Watkins, Phys. Rev. B 39, 3207 (1989).
5. M. Gal, B. C. Cavenett, and P. Smith, Phys. Rev. Lett. 43, 1611 (1979).
6. B. C. Cavenett, Adv. Phys. 30, 475 (1981).

THE ROLE OF OXYGEN IN p-TYPE InP

J. MICHEL, J. JEONG, K.M. LEE, AND L.C. KIMERLING
AT&T Bell Laboratories, 600 Mountain Ave., Murray Hill, NJ 07041

ABSTRACT

We have studied the influence of oxygen on the optical properties of Be implanted InP. Be implanted p-type InP without oxygen shows a strong deep photoluminescence (PL) band at 0.82 eV following anneal. As the oxygen concentration increases, the 0.82 eV PL-band disappears. We attribute the disappearance of this PL-band to the formation of oxygen complexes with the implantation induced defects. In epitaxial grown, nominally undoped InP a new PL-line is observed at ~1.2 eV. The paramagnetic state of the phosphorus on indium P_{In} antisite is observed by optically detected magnetic resonance (ODMR) as a modulation of the photoluminescence in all Be implanted samples without oxygen. The antisite resonance is detected as a reduction of the 0.82 eV PL-band and the 1.2 eV PL-band. The observation of the Fe^{3+} resonance by ODMR spectroscopy is reported for the first time.

INTRODUCTION

InP is of considerable interest for its applications in optoelectronic and microwave devices. Ion implantation has proven to be an important doping technique which provides very good doping control and is used to realize n-type as well as p-type layers in semi-insulating InP substrates [1-4]. Little is known about defects and defect reactions due to implantation damage in these materials. Because implantation damage is confined to a layer of 2000 to 3000 Å, spectroscopic techniques like photoluminescence (PL) spectroscopy and optically detected magnetic resonance (ODMR) spectroscopy, detected as a change in intensity of the emission, are uniquely suitable to study processing.

Only a few PL investigations [e.g. 5-7] have been reported on implanted InP. Band edge luminescence due to the implanted dopants and deep luminescence due to implantation damage have been observed. The only deep center in InP which has been studied by ODMR is the P_{In} antisite defect [8-10]. It was found to be associated with a broad emission at 0.89 eV in electron irradiated InP:Zn. Recently, the P_{In} antisite was reported in P implanted InP [11].

In this paper we report on the effect of oxygen co-implantation in implanted p-type InP and the observation of a new antisite defect in implanted InP. To determine the quality of the implanted material PL measurements were performed. ODMR spectroscopy was used to investigate the implantation and heat treatment process using the P_{In} antisite as a defect fingerprint.

EXPERIMENTAL

As starting material semi-insulating InP:Fe and nominally undoped epitaxial InP was used. Be was implanted at 20 keV with a dose of $3 \times 10^{13} \text{ cm}^{-2}$ for epi InP and $6 \times 10^{13} \text{ cm}^{-2}$ for InP:Fe. O was implanted at 30 and 70 keV with various doses up to $4 \times 10^{13} \text{ cm}^{-2}$. The implantation temperature for O was 200° C, Be was implanted at room temperature. After capping with 100 nm thick borosilicate glass, the samples were activated at 850° C for 15 sec. using a rapid thermal annealer.

A 0.3 m monochromator was used for the PL measurements. The luminescence was excited by an Ar^+ ion laser at 488 nm at a sample temperature of ~1.7 K and was detected by using a cooled germanium detector. To obtain good resolution an excitation intensity of ~80 mW/cm² was used for most PL spectra.

The ODMR measurements were performed in a K-band spectrometer at 24 GHz. The microwave induced change of the photoluminescence signal was detected. The sample was mounted in a wall-less microwave cavity for optical access and cooled to ~1.7 K. Various optical long-pass and band-pass filters were used to detect the ODMR signal on different PL lines.

RESULTS AND DISCUSSION

Figure 1 shows the PL spectra of Be implanted epitaxial and iron-doped InP. All spectra were taken at 1.7 K. At this temperature almost all conduction-band electrons are frozen out on residual donor levels, located at 7.4 meV below the conduction band. Three features could be observed in these spectra: (1) an edge emission band at 1.382 eV, which can be identified as donor-acceptor (DA) recombination due to the Be_{In} acceptor ($\text{Be}(\text{DA})$) [6], accompanied by a LO phonon replica at 1.336 eV, (2) a weak emission band at ~ 1.2 eV and (3) a broad deep luminescence peaking around 0.82 eV, which has been observed earlier in Be-implanted InP and was tentatively assigned to the phosphorus vacancy (V_{P}) [7]. All spectra were optimized for the 0.82 eV luminescence. Under these conditions the 1.2 eV luminescence also has a maximum intensity. The starting material of the epitaxial InP showed no PL lines below 1.37 eV, but a strong line at 1.418 eV which is due to a group of unresolved bound excitons [12], and a weak shallow donor-acceptor recombination at ~ 1.39 eV.

Co-implantation with oxygen changes the PL spectrum considerably. Figure 2 shows that with increasing oxygen content the deep PL band decreases while the low energy emission at 1.2 eV increases and becomes the dominant line in the low energy part of the PL spectrum. Although the energy position of this band in the PL spectrum varies, we will refer to it as the 1.2 eV band in the subsequent text.

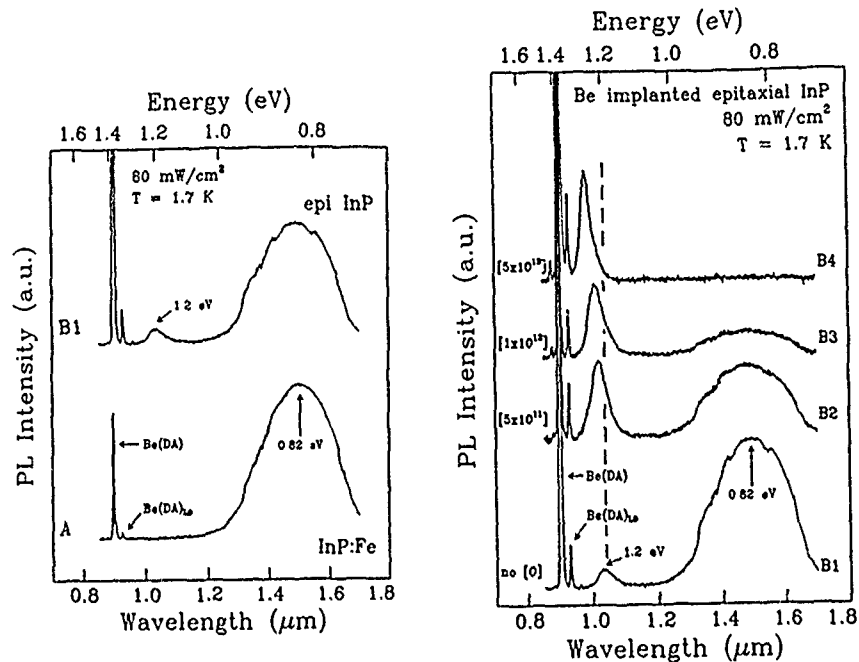


FIG. 1. Photoluminescence spectra of Be implanted InP following rapid thermal anneal. Sample A is semi-insulating InP:Fe, sample B1 is epitaxial grown, nominally undoped InP. The excitation power and detector gains are identical for both spectra.

FIG. 2. Photoluminescence spectra of Be implanted epitaxial InP with additional O implantation following rapid thermal anneal. The Be implantation dose is $3 \times 10^{13} \text{ cm}^{-2}$, the O implantation dose in $[\text{cm}^{-2}]$ is given by the numbers in brackets on the left of the spectra. Temperature, excitation power, and detector gains are as in Figure 1.

Implantation of oxygen alone in the starting material resulted only in a very weak deep PL, with little change in the near band-edge luminescence. No new PL lines of shallow defects due to oxygen were found.

For DA pair recombinations the recombination energy ($h\nu$) is increased due to Coulombic interactions between the donor and acceptor. This is described by

$$h\nu(r) = E_g - (E_A + E_D) + \frac{e^2}{\epsilon r} \quad (1)$$

where E_g is the band gap, E_A and E_D are the ionization energies of acceptor and donor respectively, e the electronic charge, ϵ the static dielectric constant and r the separation between the donor and acceptor.

A characteristic feature for a DA emission is the shift of the PL line to higher energies with increasing excitation energy because of the saturation of long distance pairs with high r values [13]. The experimental energy shift per decade of excitation intensity, α , for the 1.382 eV line was in the range of a few meV, which is typical for pair bands in InP, involving shallow donors and acceptors. On the contrary, for the band at 1.2 eV, we found α to be 29 meV in the lower excitation regime as is shown in Figure 3. This unusually large shift has formerly been observed in Cd and Zn diffused InP samples at a PL band at 1.28 eV [14]. From their investigation of this PL band Swaminathan *et al.* concluded that this band was due to a deep donor-to-acceptor recombination where the acceptor was Cd and Zn respectively.

While the Be(DA) recombination shows little dependence of the peak position on the oxygen content, the influence of oxygen on the 1.2 eV band is obvious and results in a shift of the peak position. In Figure 2, a steady shift to high peak energies with increasing O-dose can be observed. Such a behavior is predicted for the concentration dependence of DA pairs. A higher concentration of donors or acceptors leads to a closer distance of these

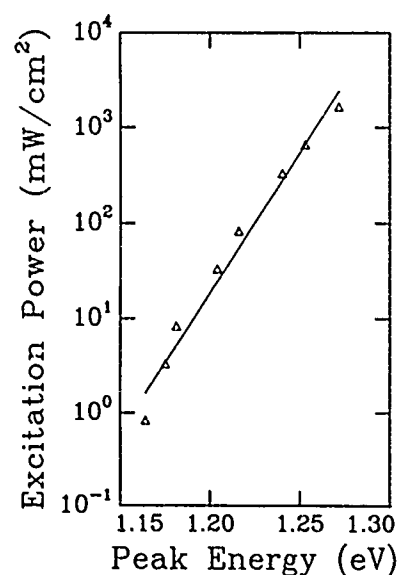


FIG. 3. Peak position of the 1.2 eV PL band as a function of the excitation power. $T = 1.7$ K.

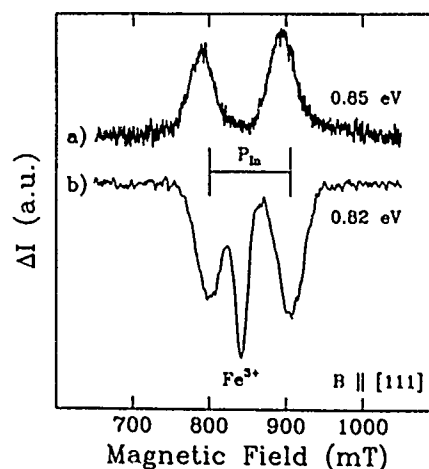


FIG. 4. ODMR spectrum of the P_{1n} antisite and Fe^{3+} for the magnetic field parallel to $[111]$. a) shows the antisite spectrum in as-grown InP:Zn, b) the antisite and Fe^{3+} spectrum, measured in sample A (Be implanted InP:Fe) on the 0.82 eV PL band. $T = 1.7$ K.

pairs and, according to equation (1), to a shift to higher energies. Nevertheless, the observed shift is too large to be explained as an increase in concentration. In other materials a concentration change of one order of magnitude results in a peak shift of ~ 5 meV [15] compared to 49 meV measured for the 1.2 eV band. Even an additional saturation effect of distant pairs due to the excitation energy cannot explain this large shift.

The origin of the 1.2 eV band is not known. If we assume that it is a DA pair then equation (1) leads to $E_A + E_D \approx 240$ meV for very low excitation energies. If Be is involved in this DA pair, then a deep donor with $E_D \approx 200$ meV should participate in this recombination. In an investigation of oxygen in InP, it was found that oxygen creates deep donors at 0.78 eV below conduction band [16]. In the PL emission we did not find any evidence for this oxygen-donor. Because there is experimental evidence that oxygen is involved in this defect, it is possible that complexes of O and intrinsic defects like the phosphorus vacancy are formed during annealing. These complexes can give rise to electrically active defects with slightly different energy levels modified by the local environment. The energy shift could then be explained as the observation of different DA recombinations.

The observed deep luminescence band is very similar to the PL band at 0.89 eV reported by Cavenett *et al.* [17] in e-irradiated InP:Zn. ODMR measurements by these authors showed that this PL band could be assigned to the P_{In} antisite defect. This conclusion was based on the observation that the ODMR signal was detected as an increase in the 0.89 eV emission, which indicates that the spin dependent recombination involves an unthermalized pair process. Similar observations were made for as-grown InP:Zn [18].

We measured the positive ODMR spectrum of the P_{In} antisite in InP:Zn grown under P overpressure as shown in Figure 4a. Figure 4b shows the antisite ODMR-signal detected on the 0.82 eV PL-band in Be implanted InP:Fe. The antisite signal could be observed in all Be-implanted samples without oxygen. Furthermore we were able to detect the antisite signal in the epi-InP on the 1.2 eV emission. The spin-Hamiltonian parameters of the antisite determined by our ODMR-measurements were $g = 1.99 \pm 0.01$ and $A = 0.099 \text{ cm}^{-1} \pm 0.005$. They are identical with the parameters, measured in as grown and electron irradiated InP [9,19]. Contrary to as-grown InP:Zn the antisite signal in ion-implanted InP was always detected as a decrease in the emission, which means that the antisite-to-acceptor recombination emission was not detected in PL.

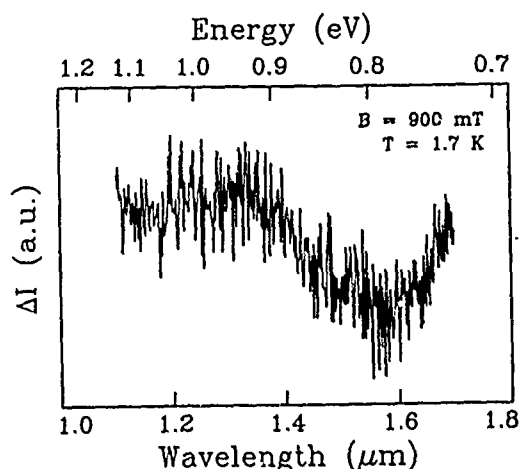


FIG. 5. Emission spectral dependence of one antisite ODMR line, observed in Be implanted InP:Fe (Figure 4b, also see Figure 1A). The magnetic field was held at $B = 900$ mT.

In Figure 5 the optical emission spectral dependence of the antisite ODMR signal in Be implanted InP:Fe is shown. No increase in PL intensity was observed to a low energy detector cut-off of 0.7 eV. Therefore the antisite-to-donor recombination emission must be below 0.7 eV, compared to 0.8 eV observed in as-grown InP. We conclude that the energy level of the antisite ($P_{In}^{+/++}$) state in Be implanted material is at least 0.1 eV deeper than that in e-irradiated or as-grown material.

Figure 4b shows the ODMR spectrum of Fe^{3+} ($3d^5$) in InP which has not previously been reported in the literature using ODMR-spectroscopy. The characteristic angular dependence of Fe^{3+} in InP, a $S = 5/2$ center, was detected using the out-of-phase signal so that the antisite-signals disappeared but the Fe^{3+} resonance was still visible. The Fe^{3+} ODMR is, like the antisite ODMR, observed as a decrease in the PL. This result is expected because the Fe^{3+} emission is known to be at 2.4 μm [20], which is beyond the detection range of our IR-detector. Therefore the Fe^{3+} ODMR is indirectly observed as a competing process at shorter wavelengths.

Because the antisite signal was detectable on the deep 0.82 eV PL band and on the 1.2 eV PL band we had the opportunity to observe, whether oxygen had any effects on the intensity of the antisite ODMR-signal. Except in sample B2, where a weak antisite-signal was measured, no antisite resonance was observed in any of the oxygen-implanted samples. This means that although both low-energy PL bands had reasonable intensities as in samples B2 and B3, the antisite signal decreased much faster than the 0.82 eV PL band. A change in the charge state of the antisite due to a shift of the Fermi level must be ruled out since sample B4 is still p-type. Furthermore there is no evidence that oxygen acts differently than other implants preventing the formation of antisite defects. PL spectra of reference samples implanted with oxygen, phosphorus and arsenic, respectively, showed no difference. Therefore it is likely that oxygen influences the paramagnetic antisite states by forming complexes with the P_{In} antisite. Since oxygen does change the properties of the antisite defect, it is very likely that oxygen also changes the properties of other intrinsic and implantation-induced defects.

SUMMARY

Oxygen co-implantation in Be implanted p-type InP changes the emission due to defects considerably. The implantation damage related deep luminescence at 0.82 eV is quenched, while a DA-like recombination at 1.2 eV is enhanced by O implantation. The 1.2 eV PL band shows a large energy shift with the excitation intensity. Such a shift is very unlikely for a DA pair recombination. Therefore we assign this PL band to a recombination between a series of oxygen related donors and Be.

With ODMR spectroscopy we showed that the P_{In} antisite, formed in implanted InP, has an energy level below 0.7 eV, contrary to the antisites, found in as-grown InP. Furthermore we reported the Fe^{3+} resonance, observed for the first time in ODMR.

References

- [1] J.P. Donnelly and C.E. Hurwitz, Appl. Phys. Lett. 31, 418 (1977).
- [2] T. Inada, S. Taka and Y. Yamamoto, J. Appl. Phys. 52, 6623 (1981).
- [3] A.N.M. Masum Choudhury, K. Tabatabaie-Alavi, C.G. Fonstad, and J.C. Gelpey, Appl. Phys. Lett. 43, 381 (1983).
- [4] U. Konig, J. Hilgarth, and H.-H. Tiemann, J. Electron. Mater. 14, 311 (1985).
- [5] P.K. Bhattacharya, W.H. Goodman, and M.V. Rao, J. Appl. Phys. 55, 509 (1984).
- [6] B.J. Skomme, G.E. Stillman, J.D. Oberstar, and S.S. Chan, Appl. Phys. Lett. 44, 319 (1984).
- [7] M.V. Rao, O.A. Aina, A. Fathimulla, and P.E. Thompson, J. Appl. Phys. 64, 2426 (1988).

- [8] M. Deiri, A. Kana-ah, B.C. Cavenett, T.A. Kennedy, and N.D. Wilsey, *J. Phys. C* **17**, L793 (1984).
- [9] A. Kana-ah, M. Deiri, B.C. Cavenett, N.D. Wilsey, and T.A. Kennedy, *J. Phys. C* **18**, L619 (1985).
- [10] L.H. Robins, P.C. Taylor, and T.A. Kennedy, *Phys. Rev. B* **38**, 13227 (1988).
- [11] T.A. Kennedy, E. R. Glaser, B. Molnar, and M.G. Spencer, submitted to ICS&T DCS 1989, Yokohama, Japan
- [12] K. Hess, N. Stath, and K.W. Benz, *J. Electrochem. Soc: Solid State Sci. Technol.* (Sept. 1974) 1208.
- [13] K. Maeda, *J. Phys. Chem. Solids* **26**, 595 (1965).
- [14] V. Swaminathan, V.M. Donnelly, and J. Long, *J. Appl. Phys.* **58**, 4565 (1985).
- [15] E.H. Bogardus and H.B. Bebb, *Phys. Rev.* **176**, 993 (1968).
- [16] S.H. Chiao and G.A. Antypas, *J. Appl. Phys* **49**, 466 (1978).
- [17] B.C. Cavenett, A. Kana-ah, M. Deiri, T.A. Kennedy, and N.D. Wilsey *J. Phys. C* **18**, L473 (1985).
- [18] T.A. Kennedy and N.D. Wilsey, *J. Cryst. Growth* **83**, 198 (1987)
- [19] T.A. Kennedy and N.D. Wilsey, *Appl. Phys. Lett.* **44**, 1089 (1984).
- [20] P.R. Tapster, M.S. Skolnick, R.G. Humphreys, P.J. Dean, B. Cockayne, and W.T. MacEwan, *J. Phys. C: Solid State Phys.* **14**, C5069 (1981).

MID-INFRARED SPECTRAL PHOTORESPONSE OF SEMI-INSULATING GaAs

G.J. BROWN AND W.C. MITCHEL

Materials Laboratory (WRDC/MLPO), Wright Research and Development Center, Wright-Patterson AFB, Ohio 45433-6533

ABSTRACT

We have developed a characterization technique using spectral photoconductivity that is capable of identifying deep energy levels in gallium arsenide. Our technique requires less sample processing than deep level transient spectroscopy (DLTS) and can be used on semi-insulating (si) gallium arsenide. The technique uses a mid-infrared fourier transform spectrometer for rapid photoresponse versus wavelength measurements. Using this technique we have observed evidence of several below mid-gap energy levels in undoped si gallium arsenide by the spectral PC technique. Spectral PC measurements were made on si GaAs before and after illuminating the cooled samples with high intensity white light at 8K. The PC spectrum typically showed a broad photoresponse that was attributed to multiple energy levels being present in the material. The observed energy levels were: 0.54 eV, 0.44 eV, 0.25 eV, 0.17 eV, 0.14 eV and ~0.10 eV. The shallow photoresponse from the carbon acceptor was not observed. The most striking spectral feature was a sharp ionization edge at about 0.44 eV in all of the samples studied. This energy level correlates to the 0.43 eV intrinsic defect level that has been observed by temperature dependent Hall effect measurements. The 0.44 eV level was also observed in our PC spectrum of a n-type Bridgman grown sample that had shown the 0.43 Hall effect level. The presence of additional deep levels in concentrations comparable to those of EL2 and carbon indicates that the simple model for compensation in si GaAs which invokes only EL2 and shallow impurities needs revision.

INTRODUCTION

Semi-insulating (si) GaAs substrates are a key material in the development of improved compound semiconductor microelectronic devices. The semi-insulating property of these substrates is strongly dependent upon the nature of the native defects and impurities in the material. These defects and impurities, or their complexes, can introduce a wide range of energy levels in the GaAs bandgap. The midgap levels, such as EL2, are believed to have the dominant role in the compensation of the material. For instance, the standard compensation model for si GaAs uses only a deep donor level (EL2) and a shallow acceptor level (carbon)[1]. In this model, the shallow acceptor levels would become uncompensated when the EL2 donor is photoquenched to its metastable state, if this metastable state is electrically inactive.

In order to study the uncompensated levels in si GaAs after photoquenching, we chose to use an FTIR spectral photoconductivity technique. Previously we had used this spectral PC technique to observe the acceptors levels in p-type GaAs[2]. Based on the above compensation model, we had expected to observe only the spectral photoresponse of the shallow acceptor impurities after the EL2 donor was photoquenched in si GaAs. However, the shallow acceptor spectrum was not observed. Instead, a range of deeper energy levels were observed in the post-quench spectrum. These same energy levels were also observed in n-type GaAs without photoquenching.

EXPERIMENTAL TECHNIQUE

The undoped semi-insulating samples were cut from boules of liquid encapsulated Czochralski (LEC) GaAs. The undoped n-type sample was cut from a boule of horizontal Bridgman (HB) grown GaAs. Ohmic contacts were made on the ends of the samples by a furnace anneal of indium solder. The samples were mounted on an electrical insulator on the coldfinger of a closed-cycle cryogenic refrigerator. The sample temperature could be varied from 8K up to 290K.

The photoconductivity experiments were performed using a Digilab model FTS-20CVX mid-infrared fourier transform spectrometer. Although the spectrometer was optimized for mid-IR measurements, there was a small amount of higher energy radiation in the beam that was detected by a near-IR lead selenide detector. The recorded spectral range was from $10,000\text{ cm}^{-1}$ to 200 cm^{-1} . Most of the spectra were collected at a resolution of only 2 cm^{-1} because the spectral features were so broad. The extrinsic photoresponse was measured in the voltage mode with the sample biased at 9 volts. The photoquench at 8K was performed using a quartz halogen white light source.

RESULTS

The first samples studied were undoped si GaAs samples that had exhibited a persistent photocurrent after optical quenching. Initially, there was no measurable photoresponse at 8K for these samples. While still at 8K, the sample was then optically quenched with a white light source for usually about 15 minutes, although some longer excitation times of up to 1 hour were also tried. After this optical excitation, the coldhead was returned to the FTIR spectrometer. The measured photoresponse versus wavenumber (cm^{-1}) is shown in figure 1. There is a broad photoresponse from about 500 to 5000 cm^{-1} . No deeper levels (ie above $5,000\text{ cm}^{-1}$) are observed although they were observed in other si GaAs samples we studied.

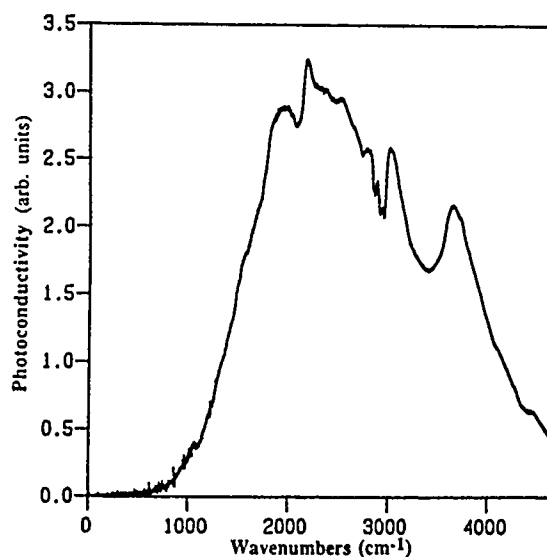


Figure 1. The photoconductivity spectrum for si GaAs at $T = 8\text{K}$.

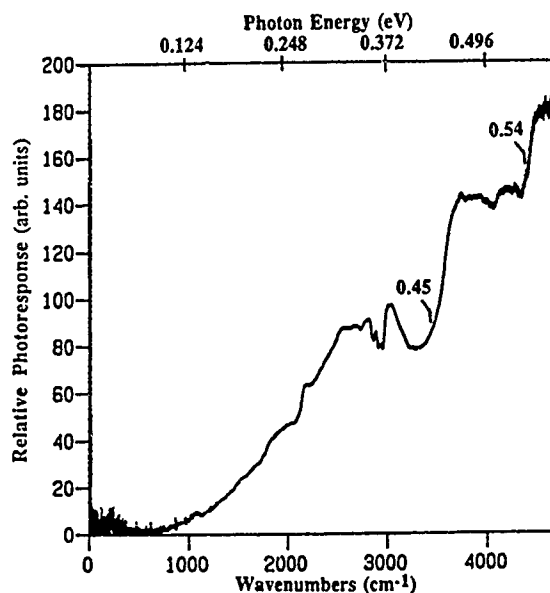


Figure 2. The photoconductivity spectrum for si GaAs at $T= 8K$ corrected for the number of photons per wavenumber.

The absence of any photoresponse below 500 cm^{-1} indicates that the shallow carbon acceptor level was not optically active after the photoquench. Although the ionization energy of the carbon level ($E_i = 0.026\text{ eV}$) is below the 200 cm^{-1} cut off of the spectrometer, the optical cross section of this level does extend into the range of the spectrometer and should be observed when the carbon impurity is ionized by higher energy photons. The 77/203 meV double acceptor is also not observed in this spectrum[2].

To better see what levels are responsible for the broad photoresponse, the spectrum in figure 1 was ratioed with a reference spectrum of the spectrometer's optical characteristics. This ratioed spectrum is shown in figure 2. With this correction, two dominant levels in the spectrum become obvious above 3500 cm^{-1} . To estimate the ionization energy of these two levels, one-tenth of the cut off energy was selected. By this estimate the measured ionization energies are 0.44 eV and 0.54 eV. PC thresholds at 0.46 eV and 0.42 eV have been reported for oxygen doped n-type GaAs[3-5]. However, large Franck-Condon shifts, of 0.11 eV and 0.24 eV, were proposed in two of the papers[4,5], while the third paper found that there was little lattice relaxation in connection with the electronic transition[3]. The 0.44 eV PC level is also in good agreement with temperature dependent Hall effect (TDH) measurements of a 0.43 eV donor level in n-type GaAs[6]. In addition, the 0.44 eV and 0.54 eV PC levels are a good match to two electron traps, at 0.44 eV (EL5) and 0.57 eV (EL3), reported for deep level transient spectroscopy (DLTS) measurements on undoped LEC GaAs[7]. These comparisons lead us to believe that the PC energy levels are due to two deep donor levels that are 0.44 eV and 0.54 eV below the conduction band.

In addition, four shallower donor levels are observed in the PC spectrum. To separate these levels out of the broad lower energy photoresponse, the temperature dependence of the PC spectrum was used. As is shown in figure 3, the photoresponse from 500 to $3,000\text{ cm}^{-1}$ gradually decreases as the temperature is increased from 8 to 110K. The PC signal is lost at

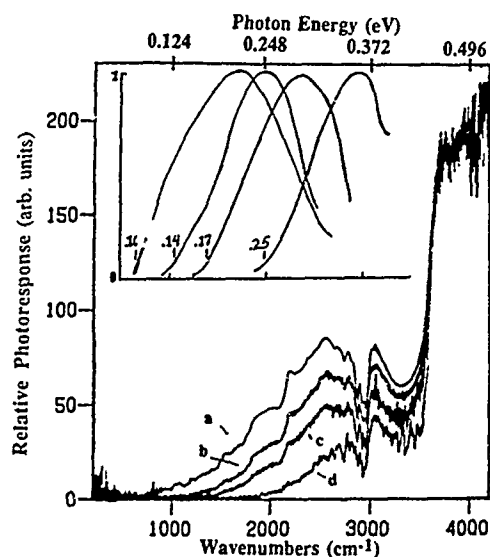


Figure 3. The photoresponse spectra for different temperatures: a) $T = 8\text{K}$ b) $T = 40\text{K}$ c) $T = 70\text{K}$ and d) $T = 110\text{K}$. The inset shows the normalized differences between the four spectra.

$\sim 120\text{K}$ when EL2 recovers. By subtracting spectra at two different temperatures, the levels that are masked in the overall broad response can be separated from each other. The normalized differences between the four spectra in figure 3, taken at different temperatures, give four photoresponse cross sections with ionization energies of $\sim 0.10\text{ eV}$, 0.14 eV , 0.17 eV and 0.25 eV . Again, comparing our levels to DLTS data, we find there is good agreement with the electron traps that were reported at 0.14 , 0.16 and 0.27 eV below the conduction band[7]. These electron traps were attributed to intrinsic defect levels in the GaAs with suggested identifications of EL11, EL9 and EL6 respectively. Temperature dependent Hall effect measurements also have shown a range of activation energies from 0.13 to 0.20 eV for a donor level(s) in n-type GaAs[8].

Since the reported DLTS and Hall effect measurements were made on undoped n-type GaAs, we decided to check for the above PC levels in n-type GaAs. A horizontal Bridgman sample was selected that had been previously measured by our temperature dependent Hall effect facility. The Hall results gave a donor activation energy of 0.43 eV . The PC results in figure 4 show the same 0.44 eV and 0.54 eV levels that had been seen in the si GaAs (figure 2). The 0.44 eV PC level was observed in every si or n-type GaAs sample we studied. The Hall effect level is an intrinsic defect level and a possible connection with the 0.35 eV EL6 level observed by DLTS[10] was postulated by Look[9]. Although the 0.44 eV (EL5) DLTS level is a better match to the Hall level, Look chose the 0.35 eV (EL6) DLTS level as possibly related to the Hall level. The reasons for choosing this DLTS level were: 1) EL6 is commonly observed in the $10^{15} - 10^{16}\text{ cm}^{-3}$ range in undoped GaAs, while 2) EL5 is seldom observed at concentrations $> 10^{15}\text{ cm}^{-3}$ in as-grown GaAs. If the 0.43 eV Hall level is the 0.35 eV DLTS level, then a Franck-Condon shift of 0.08 eV is required. However, the PC measurements should also see a FC shift and therefore would not match the Hall activation energy. The close agreement of DLTS, Hall effect and PC on the presence of a 0.44 eV level implies that this level has very little, if any, Franck-Condon shift. The DLTS EL5 level seems a better choice

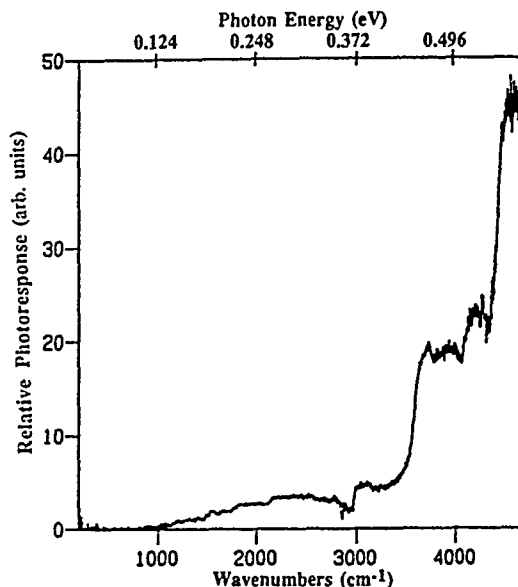


Figure 4. The spectral photoresponse for n-type GaAs at $T=8\text{K}$.

than the EL6 level, but is EL5 common enough or found in high enough concentrations to justify this assignment? The recent paper by Hashizume and Nagabuchi reported a trap concentration of $\sim 10^{16}\text{ cm}^{-3}$ for their 0.44 eV EL5 level in as-grown undoped GaAs[7]. But this level has not generally been reported at such high concentrations by other DLTS experiments. It is therefore difficult to make a choice between the two possible assignments for the 0.43 eV level.

CONCLUSIONS

We have used a rapid Fourier Transform mid-infrared photoconductivity technique to identify a series of deep levels in si and n-type GaAs. The six PC levels were 0.10, 0.14, 0.17, 0.25, 0.44 and 0.54 eV. By comparing these levels to reported DLTS and Hall effect levels, the levels were determined to be deep donors due to intrinsic defects in GaAs. The 0.44 eV PC level is in close agreement with the 0.43 eV Hall effect level. However, the possible association of the 0.44 eV PC level with EL6 was not determined.

In agreement with several other recent papers, we have found that the defect level scheme for si GaAs is much more complicated than the simple EL2 and carbon model. The effects of these additional levels needs to be addressed when modelling the compensation mechanism which produces semi-insulating GaAs.

REFERENCES

1. R. Bray, K. Wan and J.C. Parker, Phys. Rev. Lett. 57, 2434 (1986).
2. W.C. Mitchel, G.J. Brown, D.W. Fischer, P.W. Yu and J.E. Lang, J. Appl. Phys. 62, 2320 (1987).

3. H.G. Grimmeis and L-A Ledebø, J. Appl. Phys. 46, 2155 (1975).
4. M.C. Arikian, C.B. Hatch and B.K. Ridley, J. Phys. C.: Sol. St. Phys. 13, 635 (1980).
5. R.A. Malinaukas, L. Ya. Pervova and V.I. Fistul', Sov. Phys. Semicond. 13, 1330 (1979).
6. D.C. Look, S. Chaudhuri and J.R. Sizelove, Appl. Phys. Lett. 42, 829 (1983).
7. T. Hashizume and H. Nagabuchi, Semicond. Sci. Technol. 4, 427 (1989).
8. D.C. Look, D.C. Walter and J.A. Meyer, Sol. St. Comm. 42, 745 (1982).
9. David C. Look, in Semi-Insulating III-V Materials, Malmo 1988, edited by G. Grossmann and L. Ledebø (Adam Hilger, Bristol, 1988) p.1 .
10. G.M. Martin, A. Mitonneau and A. Mircea, Electronics Lett. 13, 191 (1977).

Correlation of the 0.8 eV emission band with the EL6 center in GaAs

S. ALAYA*, M. A. ZAIDI*, G. MARRAKCHI^(a), H. MAAREF*
H. J. VON BARDELEBEN **and J. C. BOURGOIN**

*Faculté des Sciences, Monastir 5000 TUNISIA

**Groupe de Physique des Solides de L'ENS, Centre National de la Recherche Scientifique^(b), Tour 23, 2 place Jussieu Paris Cedex 05 -75251. FRANCE

ABSTRACT

Combined photoluminescence and DLTS investigations of semi-insulating and n-type GaAs before and after a 15min, 850°C heat treatment under AsH_3 reveal that the treatment which anneals the EL6 center leads also to a disappearance of the 0.8eV PL band. The suggested correlation between EL6 and the 0.8eV PL is confirmed by the determination of the electron capture barrier of EL6 and the Franck-Condon shift deduced from the temperature dependence of the PL band leading to a consistent Configuration Coordinate diagram of this defect.

1. INTRODUCTION

The electrical characteristics of a semiconductor such as its free carrier concentration, mobility and minority carrier lifetime are determined by the interplay of the electrically active point defects. In the case of undoped semiconductors, such as the technologically important semi-insulating (S.I.) GaAs, this role is taken by the native defects [1]. Numerous defects have been detected in this material. The so-called EL2 center, commonly considered to be the most important defect in GaAs because of its strong influence on the electrical properties of the material, has been extensively studied [2] and was found to be present in all bulk-grown GaAs. The EL6 center at $E_c-0.35\text{eV}$ [3] which is commonly seen in both Liquid Encapsulated Czochralski (LEC) and Horizontal Bridgman (H.B.) grown GaAs, has received much less attention. Deep Level Transient Spectroscopy (DLTS) measurements have allowed to determine its thermal activation energy $E_c-0.35\text{eV}$ and its photoionization threshold of 0.8eV is obtained by optical excitation of DLTS (DLOS) [4]. The large difference between the electron thermal activation energy and the photoionization threshold is explained by an abnormally large lattice relaxation. To our knowledge, no photoluminescence studies of the EL6 defect have been reported. Windscheif et al [5] reported a 450°C annealing step for the 0.8eV PL and attributed it from this to the EL2 defect. This is however incorrect as shown by the high thermal stability of the As_{Ga} defect up to 1200°C. The apparent disappearance of the charged As_{Ga} defect in neutron irradiated SI GaAs being due to a Fermi level shift.

A different aspect, which we have not studied here, is the defect profile of EL6 and the 0.8eV PL into the bulk. Our study was limited to the correlation of EL6 and the 0.8eV PL in the near surface region.

II- EXPERIMENTAL

Samples used in the present work were SI and n-type bulk GaAs. The n-type samples were Se doped LEC and Si doped HB grown crystals with a carrier concentration of the order of 10^{17}cm^{-3} . The semi-insulating samples were grown by the LEC method.

a) present adress: Laboratoire de physique de la Matière, INSA, Lyon, France

b) laboratoire associé à l'Université Paris VII

For thermal treatment the samples were submitted to a 850°C for 15 min under AsH_3 atmosphere.

DLTS measurements were carried out on the Se doped samples. Schottky barriers were deposited by Au evaporation after the ohmic contact has been realized on the back of the wafer. PL excitation was made with an Ar ion laser (5145Å). Photoluminescence was dispersed with a monochromator and detected with a liquid nitrogen cooled PbS cell using a lock-in technique. The samples were mounted on a coldfinger of a closed cycle helium circulation cryostat. PL spectra were corrected for spectrometer and detector responses. DLTS studies were performed using a double lock-in amplifier and a PAR 410 capacitance meter and recorded in the temperature range 77- 430 K. A rate window of 20s^{-1} , a reverse bias of -1V and a filling pulse of 1V were used.

III-RESULTS AND DISCUSSION

Figure 1 shows the deep centers emission characteristics at 10K obtained from an undoped LEC Si sample before 850°C thermal annealing. The spectrum consists of three overlapping broad emission bands peaking at 0.64, 0.68 and 0.8eV respectively. The 0.68eV band has been associated to the EL2 center [6,7] while the 0.64eV emission has been related to both EL2 and to the presence of Oxygen [7].

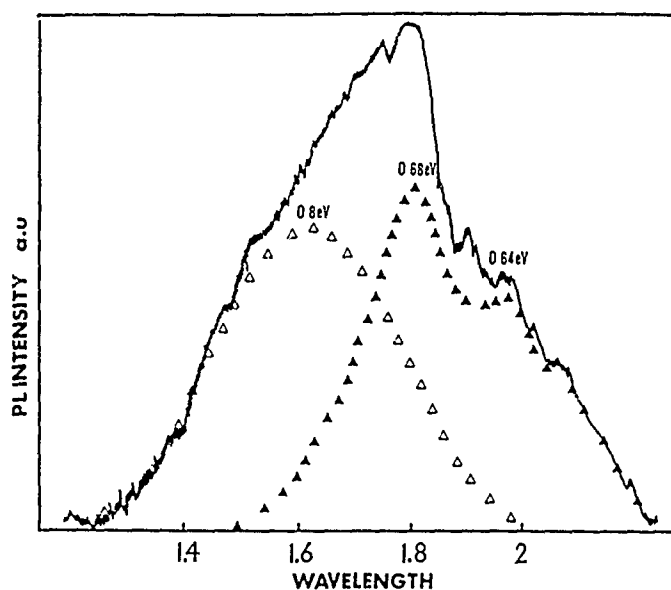


Fig. 1 10K PL spectra of undoped Si LEC GaAs before 850°C thermal annealing.

The global PL spectrum can be decomposed in three bands at 0.64, 0.68 and 0.8eV respectively. This decomposition is verified by a simple lineshape analysis of the 0.64 and 0.68eV PL bands and of the 0.8eV in p-type Ga rich samples where the two other bands are very weak (fig.2). From the temperature dependence of the half width of the 0.8eV band, we deduce a Franck-Condon shift of (0.35 ± 0.02) eV assuming a LO phonon energy of 32meV. Photoluminescence excitation measurements on the 0.8eV emission band have been done for p-type LEC grown sample. We found a PLE threshold E_i of 1.48eV. According to the fact that $h\nu_{lum} + 2d_{FC} = E_i$, we obtain a Franck-Condon shift d_{FC} of 0.34eV which is in good agreement with the last value. We attribute this luminescence to a radiative transition between the filled EL6 level and the valence band.

The luminescence spectrum of an annealed LEC SI GaAs is shown in Fig.3. The 0.8eV PL band has disappeared while the other bands remain nearly constant.

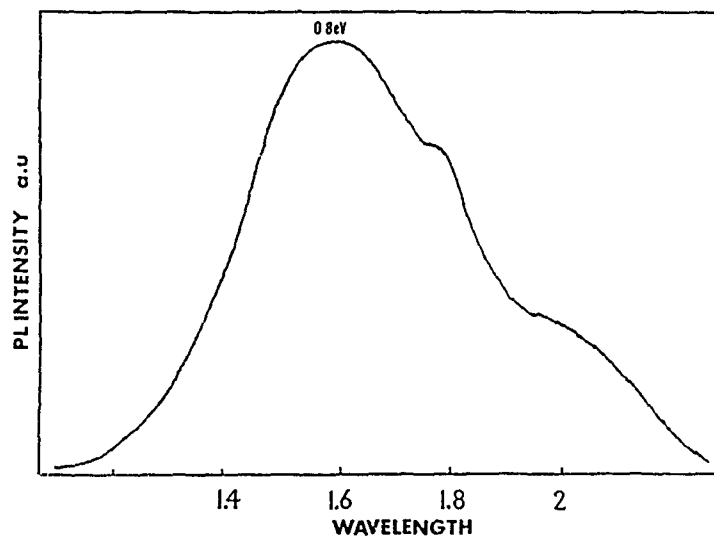


Fig. 2. 10K PL spectra of undoped LEC p-type GaAs

DLTS spectra of LEC Se doped GaAs before and after annealing are shown in fig. 3. The spectrum of an unannealed sample is composed of three distinct DLTS peaks corresponding to EL6, EL3 and EL2 respectively. The EL6 signal vanishes after thermal annealing at 850°C (fig.3b) in agreement with previous studies [8,9]. We have verified that the electron emission of the EL6 center is not sensitive to the electric field and we have determined a capture barrier which is smaller than 10meV ; this implies that the EL6 center is located at 0.35eV below the conduction band.

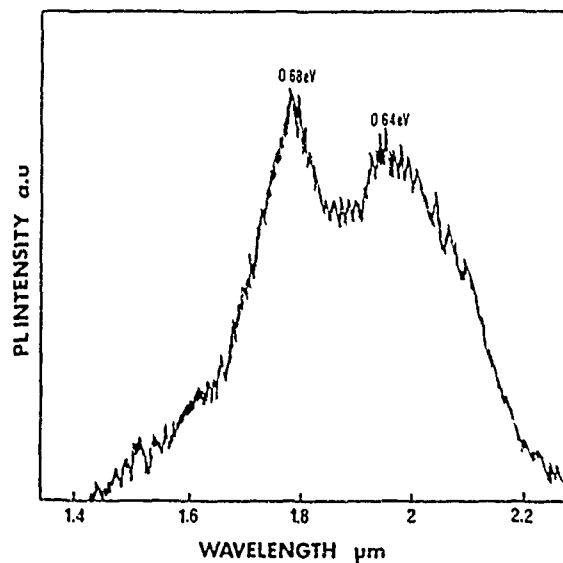


Fig. 3 10K PL spectra of undoped SI LEC GaAs after 850°C thermal annealing.

Our results show that the thermal annealing has the same effect on the the EL6 center concentration as on the 0.8eV PL emission intensity. Further, the electrical characteristics of the EL6 center, namely the energy level position ($E_T = E_c - 0.35\text{eV}$) and Franck-Condon shift ($d_{FC} \sim 0.45\text{eV}$) are similar those of the 0.8 eV emission.

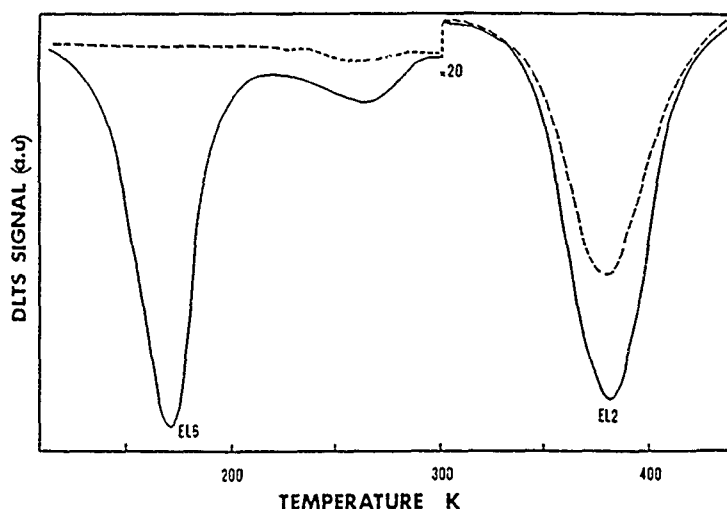


Fig. 4 DLTS spectra of electron traps in LEC n-type GaAs before (a) and after (b) annealing at 850°C. DLTS conditions: bias -1V, filling pulse amplitude 1V, filling pulse duration 2ms, rate window 20s^{-1} .

The attribution of the 0.8eV PL to the EL6 defect permits to construct a coherent C.C model for this defect (fig.5):

we have used the following results:

1. The difference between the thermal ionization energy (DLTS) E_T and the PL emission energy $h\nu_{lum}$ should be equal to the measured Franck Condon shift ($d_{FC} \sim 0.35 \pm 0.02\text{eV}$) since $E_T + d_{FC} = E_g - h\nu_{lum}$
2. The electron photoionization energy threshold E_0 (DLOS) should be between 0.7 and 0.8eV and the PLE threshold about 1.48eV .

Our model allows also to understand the results of Chantre et al [4] on the hole photoionization cross section σ_p^o . They concluded that $\sigma_p^o(\text{EL6}) \sim 0$. As it is seen in fig.4, the onset of the σ_p^o is 1.48eV that is higher than the energy range explored in their work. PL measurements have also been performed on the n type samples. Unfortunately, in these samples, where the Fermi level is pinned by the shallow donor (Si or Se) level at about $E_c - 0.005\text{eV}$, none of the three deep PL emissions (0.64, 0.68 and 0.8eV) was observed.

In order to give a complete description of EL6, one should establish a detailed picture of the atomic structure of the center. Unfortunately, techniques used in this work, i.e DLTS and photoluminescence, are not suited to give such microscopic structure.

Some speculations have been made about the atomic nature of EL6 and it has been assumed that this center is related to a defect containing the arsenic antisite [10]. However, the vanishing of this defect under thermal annealing at such a low temperature as 450°C [11] rules out the possibility of an arsenic antisite defect. Consequently, the microscopic structure of the EL6 center is still an open question. More experimental investigations are needed to give an exact microscopic picture of EL6 center.

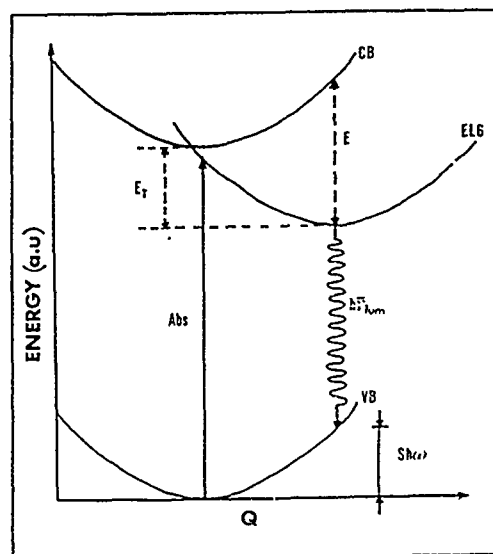


Fig.5 Configuration coordinate model for the EL6 center with a schematic illustration of the 0.8eV optical transition.

CONCLUSION

The Results obtained on SI and n type GaAs by combined DLTS and photoluminescence studies suggest that the 0.8eV band is associated with the EL6 center. This band has been explained as a radiative transition between the filled EL6 center and the valence band. We have found that the presence of the 0.8eV PL band is related to the Fermi level position. On the basis of these data a new Configuration Coordinate diagram has been proposed. However a detailed microscopic nature of this center is not yet reached.

REFERENCES

1. J. C. Bourgoin, H. J. Von Bardeleben and D. Stiévenard, J. Appl. Phys. **64**, R65 (1988).
2. For recent review see J. M. Martin and S. Makram Ebeid, in Deep Centers in Semiconductors, Ed. S. T. Pantelides (Gordon & Breach, New York) **6**, 399 (1986).
3. G. M. Martin, A. Mitonneau and A. Mircea, Electron. Lett. **13**, 191 (1977).
4. A. Chantre, G. Vincent and D. Bois, Phys. Rev. **B23**, 5335 (1981).
5. J. Windcsheif, H. Ennen, U. Kaufmann, J. Schneider and T. Kimura, Appl. Phys. **A30**, 47 (1983).
6. P. W. Yu, Solid state commun. **43**, 953 (1982).
7. M. Tajima, Jpn. J. Appl. Phys. **26**, L885 (1987).
8. Z. Q. Fang, T. E. Schlesinger and A. G. Milnes, J. Appl. Phys. **61**, 5047 (1987).
9. F. D. Auret, A. W. R. Leitch and J. S. Vermaak, J. Appl. Phys. **59**, 158 (1986).
10. M. Levinson, in Gallium Arsenide and Related Compounds, IOP. Conf. Proc. No **91**, 73. Heraklion, Greece 1987 (IOP Publishing 1988).
11. G. M. Martin, E. Esteve, P. Langlade and S. Makram-Ebeid, J. Appl. Phys. **56**, 2655 (1984).

THE ELECTRONIC STRUCTURE OF THE "0.15 eV" Cu ACCEPTOR LEVEL IN GaAs

E. JANZÉN *, M. LINNARSSON **, B. MONEMAR *, AND M. KLEVERMAN**

*Linköping University, Dept. of Physics and Measurement Technology
S-581 83 LINKÖPING, Sweden

**Dept. of Solid State Physics, University of Lund, S-221 00 LUND, Sweden

ABSTRACT

Cu diffused GaAs samples have been investigated using different kinds of FTIR techniques and photoluminescence. The results suggest that the "0.15 eV" level originates from the ionization of a neutral, nearly substitutional Cu acceptor at a Ga site. Furthermore, the results indicate a distortion in the [100] direction. The ground state binding energy obtained from the effective-mass-like excited states is 157.8 meV at 6K.

INTRODUCTION

Doping of GaAs with Cu gives rise to a number of Cu-related centers. The acceptor levels at 0.15 and 0.45 eV have been attributed to the two ionization levels of the double Cu acceptor at a Ga site. The observation of double compensation of n-type GaAs when doped with Cu supports this interpretation [1]. In the simplest model, Cu at a Ga site is supposed to be a double acceptor since two more holes are available when the bonds to the nearest As neighbors have been formed. However, no clear evidence has been presented that relates the 0.15 and the 0.45 eV defects with the two levels of a double acceptor. On the contrary, electrical measurements have suggested that the concentrations of these levels are different [2]. The interpretation of these kinds of measurements is not straight-forward, however.

In recent papers it was suggested that the 0.15 eV center was the second ionization level of the double acceptor [3-5]. This could explain the absence of a bound exciton for this center. On the other hand in Ref. 6 an absorption spectrum of the center was presented, showing three peaks which were interpreted as transitions from an unsplit ground state to "symmetry-split" p-like states of a neutral acceptor. The low number of excited states seen made the interpretation questionable.

Using stress and magnetic field in conjunction with photoluminescence it has been argued that the luminescence at 1.36 eV arises from the capture of a free electron to a Cu_{Ga} acceptor Jahn-Teller distorted along [001], containing two loosely bound holes [7-13]. The random-alloy splitting of the corresponding luminescence line in $\text{GaAs}_{1-x}\text{P}_x$ is consistent with an isolated Cu-atom at a Ga-site [14].

In this paper we will present evidence that the "0.15 eV" level is related to the neutral version of a double acceptor Cu^0 . The results suggest that the center is distorted in the [001] direction due to Jahn-Teller effect (JTE), although alternative models will be presented. The distortion of the Cu^0 centers is tentatively described in terms of a static distortion along [001], whereas when exciting one of the holes, the center is considered to have a dynamic JTE. In the dynamic limit, the remaining hole may be left in an excited vibronic state 0.8 meV above the ground state which may be the cause of the doublet structure for all lines in the spectrum of Cu^0 .

EXPERIMENTAL

Sample preparation

The GaAs wafers used were undoped horizontal Bridgman (HB) from MCP and semi-insulating liquid encapsulated Czochralski (LEC) from Sumitomo and Semitronic. Cu was evaporated on one face. The wafer was then put in a quartz ampoule together with a protective Ga melt saturated with GaAs at high temperature. The ampoule was sealed in vacuum. The wafers were diffused at temperatures from 600 to 850 °C for 4h.

Reference samples without Cu were fabricated at the same time. 4h was sufficient to diffuse Cu through the whole 500 μm thick wafer. After diffusion the ampoules were quenched in water. The remaining Cu film was removed by mechanical polishing. Both sides of the wafers were polished about 50 μm and then heavily etched (10-15 min in warm (80 °C) $\text{H}_2\text{SO}_4:\text{H}_2\text{O}:\text{H}_2\text{O}_2$ (5:1:1) etch).

The ohmic contacts of the photoconductors were made either by evaporating Zn, Au and Cr and alloying 30 s at 550 °C or by rubbing Al-Ga contacts. The photoconductors were mounted on isolated TO-5 headers with weak adhesive.

Experimental methods

The absorption and photoconductivity measurements were performed with FTIR-technique (BOMEM.DA3). The temperatures could be varied from 2 K to room temperature using two cryostats, a He-bath cryostat and a He-flow cryostat. A He-cooled Ge:Cu detector was used for the absorption measurements. Channel spectra were removed by filling suitable parts of the interferograms with zeros. In absorption the spectra at room temperature were taken as the reference spectra. For the low-temperature-photoluminescence measurements a SPEX 1404 monochromator was used. The samples were immersed in liquid helium (1.8 K) and excited by an Argon laser (5145 Å) with the power of 10-100 mW. Doping profiles were measured both with a Polaron PN 4200 Semiconductor Profiler and with a SIMS Cameca ims 4f. The SIMS data were obtained using O_2^+ ions. As reference we used a ^{63}Cu -implanted sample, 250 keV and a dose of $5 \times 10^{14} \text{ cm}^{-2}$.

EXPERIMENTAL RESULTS AND DISCUSSION

Non-perturbation data

In Fig. 1 a typical photoluminescence spectrum of a Cu-diffused sample is shown. The diffusion was carried out at 800 °C for 4 h. The carrier concentration measured with a Polaron Profiler was $1 \times 10^{17} \text{ cm}^{-3}$ and is assumed to be equal to the concentration of the Cu 0.15 eV level. The total Cu concentration as measured with SIMS was five times higher. The peak energy of 1.36 eV corresponds to a mixture of transitions from the conduction band and shallow donor states to the Cu acceptor level. Two LO phonon-replicas are clearly visible. As can be seen the "Cu-transitions" dominate the low energy part of the spectrum.

The ir-absorption spectrum of the same sample is shown in Fig. 2a, b. The peaks between 145 meV and 155 meV are due to transitions from the ground state to shallow EMT-like excited states. The structure around 185 meV is due to phonon-assisted Fano replicas of the same excited states. The ionization edge is blown up in Fig. 2 b showing the excited states in detail. The three dominant peaks at 150.50 meV, 151.34 meV and 152.42 meV, respectively, have been reported earlier [6]. The peaks at 146.48 meV, 150.50 meV and 152.41 meV can be assigned to transitions from the ground state to $2\text{P}_{3/2}(\Gamma_8)$, $2\text{P}_{5/2}(\Gamma_8)$ and $2\text{P}_{5/2}(\Gamma_7)$ states, respectively of a neutral acceptor. By adding the calculated binding energy of the $2\text{P}_{5/2}(\Gamma_8)$ state, 7.27 meV, [19], we arrive at a ground state binding energy of 157.8 meV.

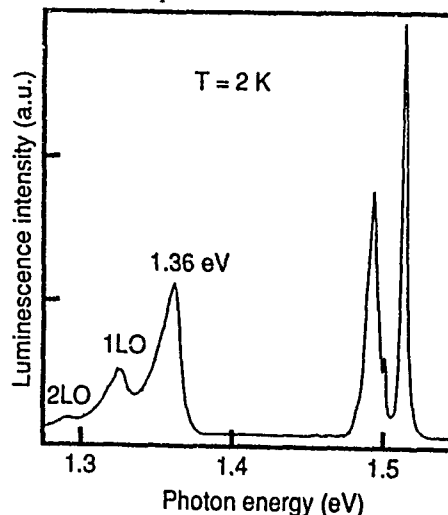


Fig.1 Photoluminescence spectrum of a Cu-diffused GaAs sample.

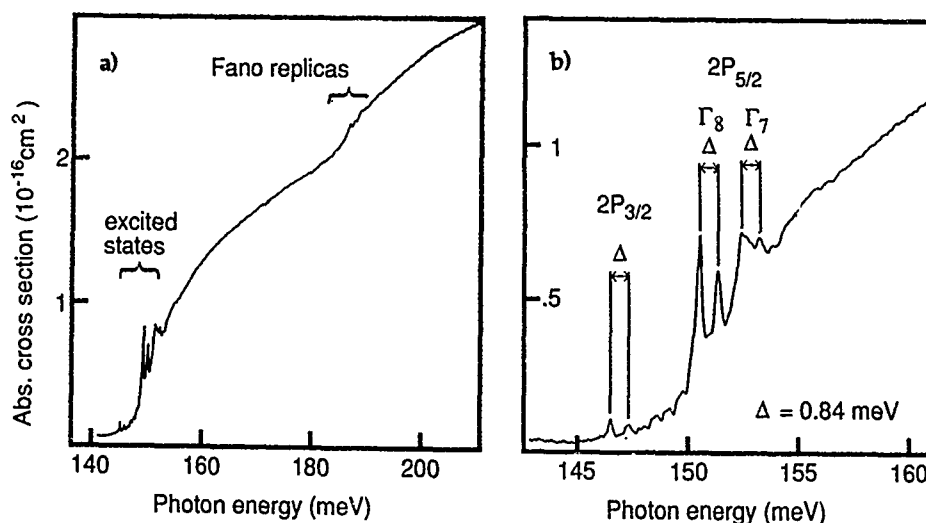


Fig. 2 a) Absorption spectrum of a Cu-diffused GaAs sample. b) Blow-up of the spectrum close to the ionization edge.

It is believed that the Cu^0 center is a double acceptor. A hole in an excited p-like state has only a small amplitude at the center. Thus, when exciting one of the holes to an excited state, the center may be regarded as $\text{Cu}^- +$ a shallow hole. The two subsystems may interact due to the exchange interaction although only to a minor extent when the excited hole enters a p state.

Each of the above assigned peaks has a replica 0.84 meV higher in energy. Previous luminescence measurements have been interpreted in terms of the center being Jahn-Teller distorted in the [001]-direction [7-9]. The distortion together with the existence of two holes at the center might split both the ground state and the excited states. However, the splittings are found to be identical for different excited states. This implies that

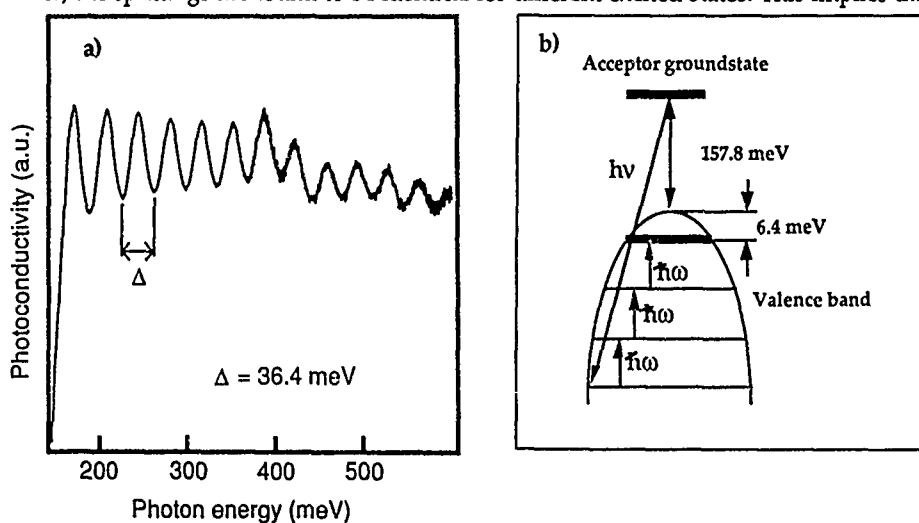


Fig. 3 a) The ratio of the photoconductivity spectra at 6K and 19K. b) Capture model of highly excited holes.

it cannot be the Coulomb excited states themselves that are split by a potential of lower than tetrahedral symmetry, since the probability to find the excited hole in the central-cell region decreases with the principal-quantum number of the hole. If, on the other hand, the ground state is split it should be possible to see thermalization effects. We measured the absorption spectrum between 1.8 K and 20 K, but we could not find any evidence for a thermalization. We therefore assign the splitting to different final core states that can be reached in the optical transition. With this model in mind, one conclusion may be drawn from the relative intensities between the replica and the main peaks. It is experimentally found to be about 2, an observation that strongly suggests that the ground state of Cu^- contains twice as many states as the first excited state. Cu^- binds only one hole and we assume that the lowest state has Γ_8 symmetry and that the higher one has Γ_6 (Γ_7) symmetry.

At low temperatures, Cu-diffused sample show oscillating photoconductivity above the ionization limit. The oscillations are temperature dependent. By dividing spectra at 6 K with spectra at 19 K the oscillations can be seen more clearly, see Fig. 3a, where up to 12 oscillations are visible. One interpretation of the oscillations is that a dip occurs in the photoconductivity when the excited hole via one or more LO-phonon emissions can reach a state from which it quickly can be captured by the center, see Fig. 3b.

If the energy positions of the six first dips of the oscillations at 6 K are used to obtain a linear fit, we get a phonon energy of 36.4 meV - similar to the energy of the LO phonon - and a final state for the phonon cascade 164.2 meV below the acceptor ground state. Since the binding energy of the ground state is 157.8 meV, this final state corresponds to an energy position 6.4 meV up in the valence band. The interpretation of this energy position is unclear. The hole might be captured to an unknown excited state ($2S_{3/2}(\Gamma_8)$) with a binding energy of $36.4 - 6.4 = 30.0$ meV, or the energy might be related to a Jahn-Teller distortion.

Stress and magnetic field

In Fig. 4 the uniaxial-stress induced splitting of the $2P_{3/2}(\Gamma_8)$, $2P_{5/2}(\Gamma_8)$, and $2P_{5/2}(\Gamma_7)$ lines are presented with $F \parallel [001]$ and $[111]$. The experimentally observed splitting is very different for the two directions. The final excited states are unambiguously identified as shallow p-like hole states and has in general similar properties to those of shallow acceptors in GaAs and in particular their response to uniaxial stress and magnetic fields is expected to be shallow-hole like. A Γ_8 state may split into two components in a stress field whereas a Γ_7 state, being a Kramers doublet, only can show a hydrostatic shift. It is interesting to note that with $F \parallel [111]$, a similar splitting pattern is seen for all lines, especially when accounting for the polarization of the $2P_{3/2}(\Gamma_8)$ line. No thermalization is observed and we therefore ascribe the common splitting as due to the different final core states. It is also notably that only a

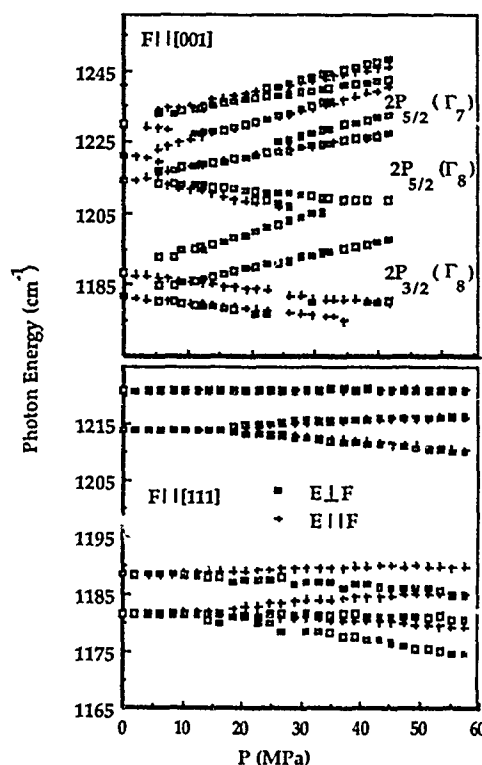


Fig. 4 The splitting for the lowest Cu lines with $F \parallel [001]$ and $[111]$.

small hydrostatic shift is observed suggesting that no splitting takes place in the initial state or that no re-orientation of the centers is induced by the uniaxial stress along [111]. We can therefore tentatively conclude that the Cu^0 center has no axis in parallel to [111] or [110] directions.

The splitting pattern is considerably more dramatic with $\mathbf{F} \parallel [001]$ (see Fig. 4). Larger splittings are observed and also stress induced changes in the relative intensities of the lines. With increasing stress, the intensity decreases for all lines that show a negative energy change. This shows that the ground state of Cu^0 has a degeneracy of electronic and/or orientational nature that may be partly lifted by stress in the [001] direction.

The stress response for $\mathbf{F} \parallel [110]$ becomes strongly non-linear for higher stresses. This may be due to interaction with the Γ_7 partner state from the $p_{1/2}$ valence band.

The splitting of the $2P_{5/2}(\Gamma_8)$ lines with the magnetic field $\mathbf{B} \parallel [001]$ is depicted in Fig. 5. The lines are calculated in accordance with the assumption that the core states of Cu^+ is a Γ_8 and a Γ_6 state and by using the g values for the excited state reported in Ref. 18. As expected, the lower $2P_{5/2}(\Gamma_8)$ show much richer features than the upper one due to the higher degeneracy of its corresponding core state. It is to be noted that the excited hole state is the same for both lines $2P_{5/2}(\Gamma_8)$. The g factors for the excited hole state is $g_{3/2}=0.6$ and $g_{1/2}=-2.4$ and for the core states $g_{3/2}=-0.11$ and $g_{1/2}=3.0$.

Models for Cu_{Ga}

Calculations show that the t_2 -gap level of the Cu_{Ga} impurity in GaAs is Ga-vacancy like whereas the Cu d levels are found deep in the valence band [15-17]. The t_2 level is occupied by two holes with spin 1/2. Several effects have to be considered, i.e., exchange, spin orbit, and lattice distortions, JTE in turn according to strength. The spin-orbit interaction splits the t_2 level into a Γ_8 and a Γ_7 state. If the two holes occupy the Γ_8 orbital (and assuming small exchange and JTE effect) the problem to be solved becomes similar to that for a shallow Γ_8 hole previously discussed in Refs. 7-9. In that case one may identify the final core states of Cu^+ as the Γ_8 and the Γ_7 one-particle states, being the spin-orbit split t_2 state with $s=1/2$. The electric-dipole transitions are induced by an one-particle operator and, hence, the occupancy of only one state can be changed. Since we observe transitions to both final core states, the ground state of Cu^0 must contain both the Γ_8 and the Γ_7 one-particle states and hence it seems not feasible to only consider one interaction only.

If we instead assume that the spin-orbit coupling is the strongest interaction, the two holes in the initial state will be in a Γ_8 state. A static Jahn-Teller distortion in the [001] direction will split this state into two two-fold degenerate states, X_6 and X_7 , the X_6 state is assumed to be the lowest. The Cu^0 ground state will be three-fold degenerated when the distortion is nearly static. The two holes both occupy the X_6 state and forms a $A_1(D_{2d})$ state and the three-fold degeneracy is due to the [001]-orientational degeneracy. In the final state, the remaining hole will still be in the X_6 state. Assuming that the distortion is less static now, the X_6 states belonging to different [001] directions may interact leading to a lifting of the accidental six-fold degeneracy of the Cu^0 ground state. The ground state will split into a fourfold Γ_8 and a twofold Γ_6 tunneling state which may be identified as those observed in the Cu spectrum. The g values of the Cu^+ core found in the fitting of the experimental data in Fig. 5 are surprisingly large for a JTE system

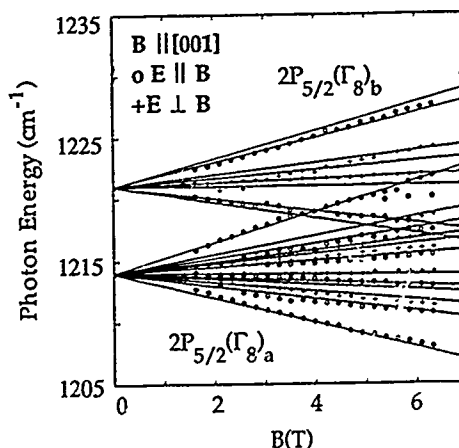


Fig. 5 Zeeman splitting of the $2P_{5/2}(\Gamma_8)$ line with $\mathbf{B} \parallel [001]$.

since a strong quenching of the g factors is expected for a JTE center [23].

It is not possible on the basis of the experimental results presented in this paper to draw any definite conclusions about the nature of the Γ_8 and a Γ_6 states of Cu^+ . However, a comparison between our results and those of other work favors the JTE model.

CONCLUSION

The experimental data presented in this paper strongly suggest that the 0.15 eV Cu level is a double acceptor. Furthermore, a structure in the lowest states of Cu^+ is established and identified in terms of a Γ_8 ground state and a Γ_6 (Γ_7) nearby state and they are tentatively assigned to be of vibronic origin.

ACKNOWLEDGMENTS

The authors would like to thank L. Timby for help with some of the sample preparations. We acknowledge financial support from the Swedish Natural Science Research Council and the Swedish Board of Technical Development.

Present address: The Royal Institute of Technology, Solid State Electronics, Box 1298, S-164 28 KISTA, Sweden

REFERENCES

1. R.N. Hall and J.H. Racette, *J. Appl. Phys.* **35**, 379 (1964)
2. N. Kullendorff, L. Jansson and L.-Å. Ledebo, *J. Appl. Phys.* **54**, 3203 (1983)
3. B. Monemar, H.P. Gislason and Z.G. Wang, *Phys. Rev.* **B31**, 7919 (1985)
4. Z.G. Wang, H.P. Gislason and B. Monemar, *J. Appl. Phys.* **58**, 230 (1985)
5. H.P. Gislason, B. Monemar, Z.G. Wang, Ch. Uihlein and P.L. Liu, *Phys. Rev.* **B32**, 3723 (1985)
6. F. Willmann, M. Blätte, H.J. Queisser and J. Treusch, *Solid State Commun.* **9**, 2281 (1971)
7. N.S. Averkiev, T.K. Ashirov and A.A. Gutkin, *Sov. Phys. Semicond.* **15**, 1145 (1981).
8. N.S. Averkiev, T.K. Ashirov and A.A. Gutkin, *Sov. Phys. Solid State* **24**, 1168 (1982)
9. N.S. Averkiev, T.K. Ashirov and A.A. Gutkin, *Sov. Phys. Semicond.* **17**, 61 (1983)
10. N.S. Averkiev, V.A. Vetrov, A.A. Gutkin, I.A. Merkulov, L.P. Nikitin, I.I. Reshina and N.G. Romanov, *Sov. Phys. Semicond.* **20**, 1014 (1986)
11. N.S. Averkiev, A.A. Gutkin, E. B. Osipov and V. E. Sedov, *Sov. Phys. Semicond.* **21**, 258 (1987)
12. N.S. Averkiev, Z.A. Adamiya, D.J. Aladashvili, T.K. Ashirov, A.A. Gutkin, E.B. Osipov and V.E. Sedov, *Sov. Phys. Semicond.* **21**, 262 (1987)
13. N.S. Averkiev, A.A. Gutkin, E.B. Osipov, V.E. Sedov and A.F. Tsatsulnikov, *Sov. Phys. Solid State* **30**, 841 (1988)
14. L. Samuelson, S. Nilsson, Z-G. Wang and H.G. Grimmeiss, *Phys. Rev. Lett.* **53**, 1501 (1984)
15. G. Delerue, G. Allan and M. Lannoo, *Proceedings of the 14th International Conference on Defects in Semiconductors*; edited by H.S. von Bardeleben (Trans Tech, Aedermansdorf, Switzerland, 1986), Vols. 10-12, p. 37.
16. C. Delerue, M. Lannoo and G. Allan, *Phys. Rev.* **B39**, 1659 (1989).
17. L.A. Hemstreet, *Phys. Rev.* **B22**, 4590 (1980).
18. M. Kleverman, E. Janzén, M. Linnarsson, and B. Monemar, at this conference.
19. The value was obtained by interpolating the data of Ref. 20 using the valence-band parameters of Refs. 21 and 22.
20. M. Said, M.A. Kanehisa, M. Balkanski and Y. Saad, *Phys. Rev.* **B35**, 687 (1987)
21. A. Baldereschi and N.O. Lipari, *Phys. Rev.* **B8**, 2697 (1973)
22. A. Baldereschi and N.O. Lipari, *Phys. Rev.* **B9**, 1525 (1974)
23. T. N. Morgan, *Phys. Rev. Lett.* **24**, 887 (1979)

OPTICAL ABSORPTION OF DEEP DEFECTS IN NEUTRON IRRADIATED SEMI-INSULATING GaAs.

M. O. MANASREH* and P. J. PEARAH**

*Electronic Technology Laboratory (WRDC/ELRA), Wright Research and Development Center, Wright-Patterson Air Force Base, Ohio 45433-6543,

**Spectrum Technology Incorporated, 6 October Hill Drive, Holliston, MA 01746.

ABSTRACT

Two defects were observed in thermal neutron irradiated semi-insulating liquid-encapsulated Czochralski (LEC) GaAs materials by using the infrared absorption technique. The first defect was observed before thermal annealing and it has a broad peak at ~ 0.83 eV. The second defect was observed after annealing the sample at 250°C for 15 min. The latter defect is an EL2-like defect, but is thermally unstable at 400°C with a concentration of about an order of magnitude larger than [EL2] observed in as grown LEC materials. Both defects were found to photoquench with white light or 1.1 eV monochromatic light at 9 K and thermally recovered at 150 K. The concentration of the EL2-like defect is reduced from $8.5 \times 10^{16} \text{cm}^{-3}$ after annealing the sample at 300°C for 15 min to $2 \times 10^{16} \text{cm}^{-3}$ after annealing at 400°C for 15 min. This defect becomes unquenchable after the latter annealing conditions. An explanation for this behavior is offered.

INTRODUCTION

Recent reports¹⁻³ show that high-dose neutron irradiation decomposes completely the atomic structure of the EL2 defect in semi-insulating GaAs while an EL2-like defect is generated after thermal annealing at certain temperatures. The disappearance of the EL2 defect in irradiated samples may rule out the speculation of identifying EL2 with the isolated arsenic antisite (As_{Ga}). The exemption of As_{Ga} as being the candidate for the EL2 atomic structure is supported by the absence of the metastability of As_{Ga} in neutron irradiated materials⁴⁻⁷ in which the concentration of As_{Ga} is increased as a function irradiation dose as detected by the electron paramagnetic resonance technique. In addition, metastability was not observed⁸ for As_{Ga} present in a large concentration in As-rich GaAs grown by molecular beam epitaxy.

In this article we report the optical absorption spectra of two deep defects in thermal neutron irradiated GaAs material. It was found that these defects have similar photoquenching and thermal recovery properties to those of EL2, but are different from EL2 in many other aspects.

EXPERIMENTAL TECHNIQUE

Several samples were cut from a LEC semi-insulating GaAs boule. The thermal neutron irradiation was performed at Chalk River Nuclear Laboratory, Ontario, Canada in a flux of $\sim 2 \times 10^{13}$ neutron/cm²-s. The thermal/fast neutron ration is $\sim 5 \times 10^3$. The resistivity and free carrier concentration of the irradiated samples were $8.83 \times 10^7 \Omega\text{-cm}$ and $9.29 \times 10^7 \text{cm}^{-3}$, respectively, prior to thermal annealing. After thermal annealing one sample at 850°C for 30 min, the resistivity and free carrier concentration become $3.16 \times 10^{-3} \Omega\text{-cm}$ and $8.22 \times 10^{17} \text{cm}^{-3}$, respectively. The free carrier concentration of $8.22 \times 10^{17} \text{cm}^{-3}$ was taken to indicate the radiation dose which is a measure of Ge and Se concentrations introduced in the sample during neutron transmutation doping. Infrared (IR) absorption measurements were

obtained using a CARY 2300 spectrophotometer. A closed-cycle refrigerator was used to cool the sample in the dark to 9 K. The monochromatic spectrophotometer light was weak enough ($\sim 5 \times 10^{-5}$ W/cm²) so that a noticeable photoquenching effect was not induced. Quenching of EL2 and the defects observed in the present study was achieved with an external 100 W quartz-halogen lamp or 1.12 eV monochromatic light with an intensity of 4 mW/cm². Thermal annealing was performed in an inert gas atmosphere. The upper temperature limit of the furnace was 850 °C. The temperature was controlled within ± 10 °C. No encapsulation was made and the loss of As from the GaAs surface at the upper temperature limit and short periods of time (< 30 min) did not introduce any noticeable effect on the EL2 defect in the control samples.

RESULTS AND DISCUSSION

The IR absorption spectra of the first defect (we will refer to this defect as FD) before and after photoquenching is shown in Fig. 1(a). The difference between the spectra in Fig. 1(a) is shown in Fig. 1(b). It is clear from Fig. 1(b) that the broad peak at ~ 0.83 eV is similar to the broad peak of EL2 observed at 1.18 eV. FD was observed before any thermal annealing.

Annealing the sample for 15 min at 250 °C reveals more interesting information. A defect identical to EL2 is observed as shown in Fig. 2. In this figure, we plotted the spectra before and after photoquenching [Fig. 2 (a)] and the difference between the above spectra [Fig. 2 (b)]. This defect was previously observed¹ and labeled DL2. The defect responsible for the quenchable component (DL2) in Fig. 2 is identical to the EL2 defect in two respects. First, it can be quenched with white light or 1.12 eV monochromatic light at low temperatures. Second, it is thermally recovered at temperatures ≥ 150 K. It is found, however, DL2 is different from EL2 in LEC SI GaAs in several respects. First, the DL2 concentration is much higher than the EL2 concentration. Martin *et al.*⁹ observed that the EL2 concentration is increased by increasing the neutron irradiation dose after annealing the samples for 15 min at 600 °C. We argue that the EL2 defect observed by Martin *et al.* is not the EL2 defect, but the DL2 defect. Second, the DL2 defect does not possess a ZPL at 1.039 eV. We found that samples irradiated with low doses do not show the ZPL before annealing. However, the ZPL is observed in these samples after annealing. Third, the DL2 defect is thermally unstable at 250 °C while EL2 is thermally stable up to 1000 °C. This is in agreement with Satoh and Kuriyama³. However, DL2 in other samples¹ irradiated at

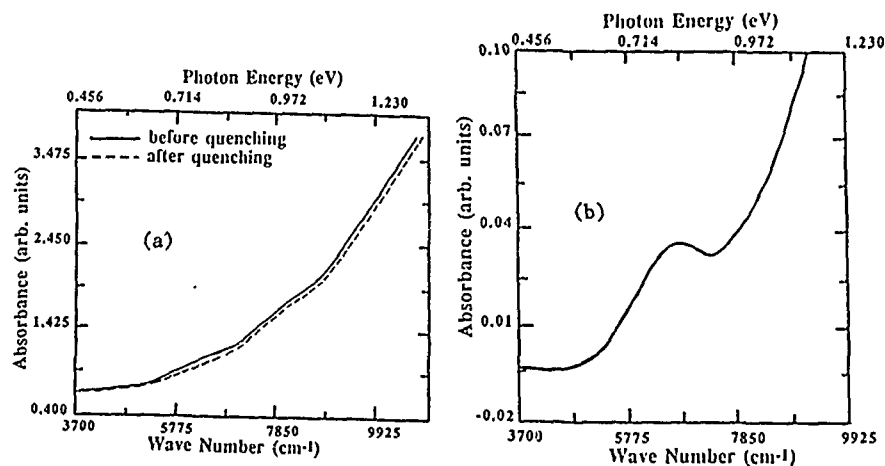


FIG.1. The IR absorption of the defect (FD) observed before thermal annealing in high dose irradiated samples. The spectra taken before and after photoquenching are plotted in (a) and the difference between them is plotted in (b).

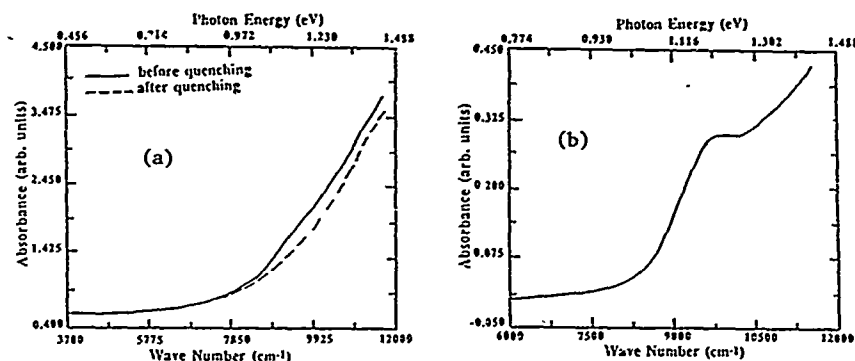


FIG. 2. The IR absorption spectra taken before and after photoquenching and after thermal annealing the sample at 250 °C for 15 min (a) The difference between spectra in (a) represents an EL2-like defect designated as DL2 and it is plotted in (b). the DL2 concentration was reduced from $8.5 \times 10^{16} \text{cm}^{-3}$ after annealing the sample at 300 °C for 15 min to $2 \times 10^{16} \text{cm}^{-3}$ after annealing at 400 °C for 15 min.

different reactor was found to be thermally stable up to 600 °C.

It was observed that the DL2 defect can be photoquenched completely during the isothermal annealing at 600 °C for the first 35 min¹. After this annealing time, DL2 was found not to photoquench completely. The situation is different in the present study where DL2 was not found to photoquench after annealing the sample for 15 min at 400 °C. The unquenchable DL2 defect is plotted in Fig. 3. The DL2 defect was observed to be quenchable after leaving the sample for several weeks at room temperature. This behavior was also observed in other samples with high irradiation dose, but the annealing temperature at which DL2 becomes unquenchable was found to be sample dependent.

There are two possible explanations for the above anomalous behavior. First, the DL2 defect is apparently composed of more than one simple point defect. These point defects can be antisites (As_{Ga}) and interstitials (vacancies). It is possible that one of these point defects, which may be responsible for the transformation of the DL2 defect from the normal state to the metastable configuration, may anneal out before the other two, preventing DL2 from photoquenching. This point defect could be generated during long time annealing at room temperature from nearby clusters (dislocations) formed during the neutron irradiation. The

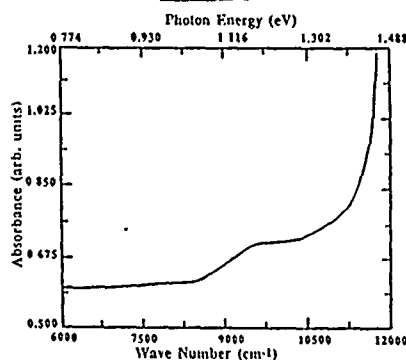


FIG. 3. The IR absorption spectrum of the unquenchable DL2. This behavior is observed after annealing the sample at 400 °C for 15 min.

second speculation is based on the results of Samuelson and Omling.¹⁰ They found that EL2 does not quench in $\text{GaAs}_{1-x}\text{P}_x$ when $x \geq 0.3$. Samuelson and Omling speculate that at this value of x the excited state of EL2 emerges from the conduction band and prevents the transformation of EL2 to the metastable configuration. We offer an alternative explanation. It is well known that shallow impurities such as Si, S, Te, etc. exist in GaAs and its alloys. These shallow impurities, especially Si, become deep centers when the band gap is increased by

alloying or applying hydrostatic pressure. The deep centers (known as DX centers) are very sensitive to light and can be ionized to give n-type persistent photoconductivity. The electrons that are released from the DX centers can be captured by the metastable EL2 defect causing an Auger type recovery.¹¹ The above explanation can be applied to explain the unquenchable DL2 defect in Fig. 3. Internal stress caused by dislocations and band bending due to clusters formed during the neutron irradiation may play an important role in the formation of defects (such as the DX centers) that emit electrons when the sample is irradiated by photons. The emitted electrons will be captured by the metastable DL2 (EL2) defect causing the recovery. Long term annealing at room temperature may affect the electron emitting defects in a way that they are either annealed out or no longer capable of emitting electrons.

Both FD and DL2 defects may be related to the EL2 defect, because of the resemblance between their IR absorption spectra. One possibility is that the atomic structure of the EL2 defect is formed by high neutron irradiation dose, but this atomic structure interacts with other defect complexes and clusters that were formed during irradiation. This interaction may modify or alter the behavior (such as thermal stability and IR absorption spectrum) of EL2 to give either FD or DL2. Therefore, understanding the DL2 defect may reveal important information about the EL2 defect.

CONCLUSION

We have shown that high dose neutron-irradiation decomposes EL2 completely and generates an EL2-like defect labeled as DL2. This defect is thermally unstable at temperatures less than 600 °C. A second defect labeled FD was also observed in high dose irradiated samples before any thermal annealing. Both DL2 and FD possess photoquenching and thermal recovery properties identical to those of EL2 but differ from EL2 in other aspects. The destruction of EL2 in high dose irradiated samples in which the isolated AsGa was found with a high concentration strongly suggests the EL2 cannot be a simple point defect.

ACKNOWLEDGMENT -- This work was supported in part by the Air Force Office of Scientific Research.

REFERENCES

1. M. O. Manasreh and D. W. Fischer, *Phys. Rev. B* **39**, 3239 (1989).
2. M. O. Manasreh, D. W. Fischer, and B. C. Covington, *Phys. Rev. B* **37**, 6567 (1988).
3. M. Satoh and K. Kuriyama, *Phys. Rev. B* **40**, 3473 (1989).
4. M. O. Manasreh, P. F. McDonald, S. A. Kivlighn, J. T. Minton, and B. C. Covington, *Solid State Commun.* **65**, 1267 (1988).
5. R. Worner, U. Kaufmann, and J. Schneider, *Appl. Phys. Lett.* **40**, 141 (1982).
6. J. Schneider and U. Kaufmann, *Solid State Commun.* **44**, 285 (1982).
7. A. Goltzene, B. Meyer, and C. Schwab, *Appl. Phys. Lett.* **54**, 907 (1989).
8. M. Kaminska *et al.* *Appl. Phys. Lett.* **54**, 1881 (1989).
9. G. M. Martin, E. Esteve, P. Langlade, and S. Makram-Ebeid, *J. Appl. Phys.* **56**, 2655 (1984).
10. L. Samuelson and P. Omling, *Phys. Rev. B* **34**, 5603 (1986).
11. A. Mittonneau and A. Mircea, *Solid State Commun.* **30**, 157 (1979).

NEW , GERMANIUM - RELATED DEFECT IN NEUTRON - IRRADIATED GALLIUM PHOSPHIDE

J. BARCZYNSKA AND E. GOLDYS

Institute of Experimental Physics, Warsaw University, Hoza 69, 00-681
Warszawa, Poland

ABSTRACT

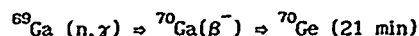
GaP crystals were irradiated with thermal neutrons with a fluence $1.4 \cdot 10^{19}$ neutrons / cm^2 . The isochronal annealing at temperatures up to 800°C resulted in n - type conductivity of irradiated samples. After 800°C anneal 10% of transmuted Ge atoms become neutral donors. Simultaneously the absorption spectrum shows a broad band centered at λ eV. The similar feature is observed in photoconductivity. The origin of the absorption band is discussed. The band is most likely due to germanium - related defect.

Introduction

Thermal neutron irradiation and annealing is a standard method to produce n-type silicon. The method takes advantage of the phenomenon of transmutation. When a semiconductor crystal is irradiated with neutrons a small fraction of lattice nuclei capture the neutrons. The nuclei undergo the transformation into the nuclei of atoms occupying nearby position in the periodic table (e.g. Si transmutes into P). The transmuted nuclei are not in substitutional position in crystalline lattice. An additional effect accompanying the neutron irradiation is formation of various structural defects due to recoil processes . The introduced defects lower the Fermi level into the midgap region and thus alter the electrical and optical properties of the semiconductor. In the course of annealing the removal of structure defects takes place, transmuted atoms move to their final, often substitutional positions and become electrically active.

Thermal neutron irradiation of III-V semiconductor leads in principle to its n- or p-type conductivity, because the atoms from the III group transmute to IV group amphoteric dopants. After annealing the IV group dopant moves to the cation or anion sublattice when it acts as a donor or an acceptor. In the case of GaAs [1] and InSb [2] neutron transmutation doping leads to predominant donor introduction.

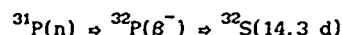
We have studied the thermal neutron irradiated GaP. The transmutation processes for Ga and P atoms follow the reactions:



$$\sigma_{\text{th}} = 1.68 \pm 0.07 \text{ b}$$



$$\sigma_{\text{th}} = 4.86 \pm 0.025 \text{ b}$$



$$\sigma_{\text{th}} = 180 \pm 7 \text{ mb.}$$

The comparison of the transmutation cross sections shows that the main dopant introduced into GaP is Ge. Former papers [3] indicate that all transmuted Ge atoms in thermal neutron irradiated GaP act as substitutional donors on Ga site. We report on more complicated behaviour of transmuted Ge in GaP.

Experiment

As samples we used polished GaP single crystal wafers of (110) orientation grown by LEC method. They were doped during growth with S with neutral donor concentration was $7 \cdot 10^{17} / \text{cm}^3$. The irradiation was carried out at Swierk reactor in Poland. The ratio of thermal to fast neutrons was 1000 : 1. The thermal neutron fluence ($1.4 \cdot 10^{19} / \text{cm}^2$) led to creation of $1.1 \cdot 10^{19}$ Ge nuclei/ cm^3 and $7 \cdot 10^{16}$ S nuclei / cm^3 [3]. We measured the absorption of irradiated samples at 300 and 150 K. Then the samples were annealed isochronally for 1h in vacuum at 300, 450, 600, 700 and 800° C. The unirradiated samples were annealed in the same conditions. Before measurements we removed from the samples the surface layer of thickness $\sim 50 \mu$ from each side. We examined the absorption of all annealed samples at 300 and 150°K. After 800° anneal we have measured the electron concentration vs T via Hall effect. The measurements were made in the Van der Pauw contact configuration in magnetic field of 1 T. We have measured also the resistance vs T and the photoconductivity (PC) spectrum. As ohmic contacts for irradiated and 800° annealed material served Au - Ge - Ni evaporated dots annealed at 550°C for 3 min. The results are presented in fig. 1a,1b,2,3.

Discussion

The side effect of neutron irradiation is the creation of different

structural defects like vacancies, interstitials, Frenkel pairs etc. Electrically an irradiated sample is semi-insulating. The majority of defects disappear after 700°C anneal [3]. Our samples after 800°C anneal acquire n-type conductivity. The concentration of electrons is thermally activated with the activation energy of 200 ± 10 meV (fig 3). The reported ionisation energy of substitutional Ge_{Ga} is 201.5 meV [4]. The agreement between these two values suggests that the observed activation energy is due to Fermi level pinning by the 201.5 meV level of Ge_{Ga} . At the same time the S level (106 meV below the c.b [5]) remains empty due to sulphur compensation by radiation defect levels remaining after 800°C anneal. If the sulphur level were filled with electrons in concentration $\sim 1 \cdot 10^{17}/\text{cm}^3$, the activation energy of ~ 100 meV would be noticed in fig 3. The electron

electrons in concentration $\sim 1 \cdot 10^{17}/\text{cm}^3$, the activation energy of ~ 100 meV would be noticed in fig 3. The electron concentration saturates at temperature higher than 300°K and reaches $5 \cdot 10^{16}/\text{cm}^3$ at 600 °C. We can estimate then the concentration of neutral Ge_{Ga} at about $1 \cdot 10^{17}/\text{cm}^3$. The remaining Ge occupies either Ga site (and is ionised), or P site (where it forms acceptors) or finally it remains in some other position inside the unit cell. Regardless of its position Ge may form complexes with other defects. The concentration of these remaining Ge atoms is $1 \cdot 10^{18}/\text{cm}^3$.

The neutron irradiation changes optical properties of GaP. The density of

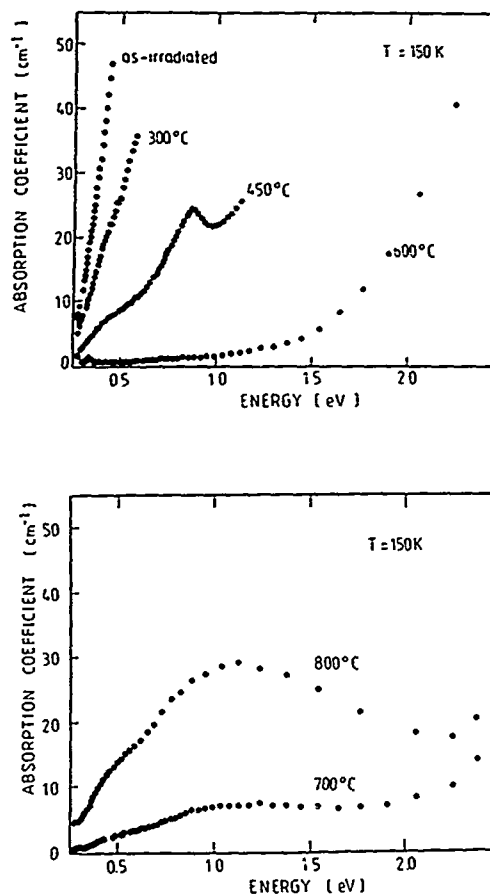


Fig 1a,1b. The absorption spectrum at 150 K of irradiated GaP after isochronal annealing at various temperatures. The annealing temperature is marked in the figure

defect states created by irradiation is manifested in optical gap reduction and in band tailing like in amorphous semiconductors [6]. When the annealing temperature increases, part of the defects are annihilated, the optical gap increases and attains the value close to the gap for nonirradiated samples after 700° anneal (fig 1a,1b). When the annealing temperature reaches 800°C the thermal energy is sufficient for the transformation of existing defects into new, optically active ones. After 800° anneal in the absorption spectrum a broad band with the maximum at 1 eV appears. The spectrum is similar at 150 and 300°C. An additional broad shoulder centered near 0.4 eV is seen on the low energy side of the main band. We verified that the nonirradiated samples after similar annealing do not show any traces of such absorption band. The absorption band is accompanied by similar band in photoconductivity. The photoconductivity spectrum (fig 2) however starts at 0.5 eV. The results of absorption and PC can be explained in terms of the optical transition of a defect. The defect is created during annealing at 800°C. The absorption band and a similar band in photoconductivity can be due to the optical transition within the defect when the final state is resonant with the band or by photolionisation of a defect. In both cases the shape of the spectrum (fig 1b) indicates that the defect is strongly coupled to the lattice. The optical cross sections of deep defects are often of the order of $10^{-16}/\text{cm}^2$ - $10^{-17}/\text{cm}^2$, therefore the defect responsible for the main

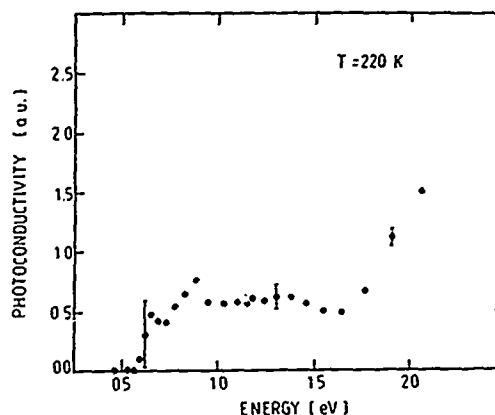


Fig 2. The photoconductivity spectrum at 220°K after 800°C anneal.

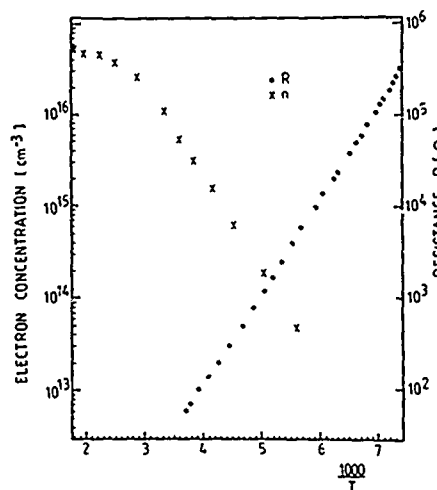


Fig 3. The electron concentration (crosses) and the sample resistance (dots) as a function of temperature.

band or by photolionisation of a defect. In both cases the shape of the spectrum (fig 1b) indicates that the defect is strongly coupled to the lattice. The optical cross sections of deep defects are often of the order of $10^{-16}/\text{cm}^2$ - $10^{-17}/\text{cm}^2$, therefore the defect responsible for the main

absorption band is present in large concentration $\sim 10^{17}/\text{cm}^3 - 10^{18}/\text{cm}^3$. Thus it is possible that a part of Ge atoms which do not form neutral donors during anneal approach other structural defects and form complexes. Such complexes give rise to the observed optical absorption and photoconductivity. The tendency to form complexes was observed in neutron transmutation doped GaAs [7]. It can be excluded that the 1 eV band comes from the optical transition from Ge_{Ga} defect level. Ge_{Ga} is considered a defect without any lattice relaxation [8]. We can not exclude that the 1 eV band is connected with purely structural defect. However some simple defects can be ruled out. The defect is not produced in large concentration during irradiation, because after 700°C anneal the absorption spectrum does not show the 1 eV band. This practically eliminates P_{Ga} antisite as a candidate for the defect. In neutron - irradiated GaAs arsenic antisite disappears in the course of annealing, so its concentration does not grow with annealing temperature. Other simple defects like vacancies which are found after neutron irradiation in large concentration also anneal out at temperatures lower than 800°C , so do Frenkel pairs [9].

Summary

The optical and electrical measurements of thermal neutron irradiated and annealed GaP were carried out. It has been noticed that after 800°C anneal 10 % of Ge (main dopant introduced via transmutation) forms neutral donors. The absorption spectrum after 800°C anneal reveals the dominant defect which is coupled to the lattice. We argue that the defect is germanium - related.

Acknowledgements

The authors express their thanks to Ms E. Kaminska and Ms A. Piotrowska from Warsaw Institute of Electron Technology for contact preparation and to D. Wasik from Institute of Experimental Physics, Warsaw University for help with Hall effect measurements.

References

- [1] M. Satoh, K. Kuriyama and Y. Makita, J. Appl. Phys, 65, 2248, (1989).

- [2] W. Gilbert Clark and R.A. Isaacson, J. Appl. Phys, 38, 2284, (1967).
- [3] A. Huber, F. Kuchar and J. Casta, J. Appl. Phys. 55, 353, (1984).
- [4] A.T. Vink, R.L.A. Van der Heyden and J.A.W. Van der Does de Bye, J. Lumin, 8, 105, (1973).
- [5] A.A. Kopylov and A.N. Pikhtin, Sov. Phys. Semicond. 5, 867, (1977) (in Russian)
- [6] T. Pankey Jr and J.E. Davey, J. Appl. Phys., 41, 697 (1970)
- [7] R. Rentzsch and K.J. Friedland, J. Lumin, 40 & 41 , 357 (1988).
- [8] M. Scheffler, J.P. Vigneron and G.B. Bachelet, Phys. Rev. Lett., 49, 1765, (1982).
- [9] T.A. Kennedy and N.D. Wilsey, Phys. Rev. Lett. 41, 977, (1978).

DEEP LEVEL LUMINESCENCE IN InP: PHONON FEATURE ANALYSIS

S. BANERJEE, A.K. SRIVASTAVA, AND B.M. ARORA
Tata Institute of Fundamental Research, Homi Bhabha Road,
Bombay 400005, India

ABSTRACT

The phonon features in the deep level luminescence (PL) bands related to Fe and Mn and native defects in InP have been clearly identified and the lineshape of the bands are analysed using configuration coordinate model. A consistent set of phonon parameters are determined for the first time.

INTRODUCTION

Presence of impurities and native defects in semiconductors are mainly responsible for the deep levels in the band gap region affecting the electrical and optical properties. Photoluminescence (PL) spectroscopy has been widely used to identify defects that modify the optical properties of the material. In undoped InP the deep level PL is characterized by several broad bands between 0.9 - 1.3 eV. The identification of the deep level components in undoped InP is quite difficult due to the very low intensity of the deep level PL emissions. The deep level PL in undoped InP has been associated with residual Fe and Mn [2,5], In- and P- vacancies, P-interstitial (native defects) and their complexes [2,5,6]. Distinct phonon related structures have been observed in the PL bands due to the strong interaction of the defects with the lattice. However, there is a lack of consensus on the parameters (such as zero-phonon transition energy, phonon energy and the phonon coupling strength) that describe the individual bands related to Fe and Mn and the native defects [1-5]. The main problem in obtaining a consistent set of parameters for a given defect is 1) often the phonon related features are broad and not distinct, and 2) the spectral features are modified due to many impurity bands present in the same energy range. We have observed distinct phonon related features in the PL bands related to Fe and Mn, and the band C (for the first time) in bulk grown LEC InP and analysed them using configuration coordinate model. We have obtained a set of sample independent parameters which can describe the deep level PL features in many samples consistently.

EXPERIMENTAL TECHNIQUES

Bulk grown LEC InP doped with Fe and Mn, and undoped InP before and after heat treatment (in an open tube set-up at 500-550°C with flowing H₂) are used in this study. The samples mounted in a closed cycle He refrigerator are excited by 488nm line of Ar ion laser. The luminescence from the samples (at 10K) is analysed by a 0.67m grating monochromator and detected using a liquid nitrogen cooled Ge detector together with a lock-in amplifier.

RESULTS AND DISCUSSION

Deep level PL spectra of InP doped with Fe and Mn are shown in Fig.1 and Fig.2, respectively. The Fe band in Fig.1 is centered near 1.08 eV and has a full width at half maximum (FWHM) of about 0.15 eV. The spectrum clearly shows the phonon features (indicated by arrows in Fig.1). In Fig.2 the main feature is a broad band with peak at nearly 1.15 eV and FWHM of 0.12eV. A shoulder is also seen on the high energy side of the spectrum.

This shoulder could be identified as the band B for the InP samples diffused with Mn [3].

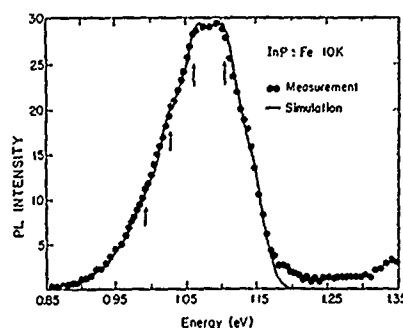


Fig.1. Deep level PL spectrum for InP:Fe. Energy of phonon replicas are indicated by arrows.

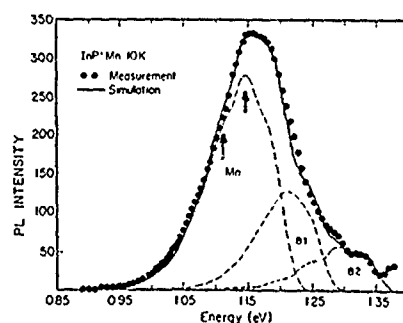


Fig.2. Deep level PL spectrum for InP:Mn. Energy of phonon replicas are indicated by arrows.

The spectra are analysed using configuration coordinate (CC) model for the defects. With the assumption of linear electron-phonon coupling and a single phonon mode of energy E_p the model predicts a luminescence line-shape at low temperatures, given by [7]

$$L(E) = \sum_{N=0}^{\infty} [e^{-S} S^N / N!] \sigma_{EL}(E + NE_p) \quad (1)$$

where N denotes the number of emitted phonon quanta each of energy E_p and S is the Huang-Rhys coefficient which is related to the electron-phonon coupling strength. The function σ_{EL} can be a Lorentzian for purely atomic like transitions or an asymmetric function for donor-acceptor like transitions. In our analysis the zero phonon line is assumed to be gaussian in shape and is given by

$$\sigma_{EL}(E) \sim \exp[-\{(E - E_0)/\sigma\}^2] \quad (2)$$

The position of this line and the phonon energy can be accurately determined from the experimental spectrum since the phonon features are clearly visible. The width of the zero phonon line σ and the Huang-Rhys coefficient S are used as fit parameters. Using the above expression, the convoluted spectrum is calculated to provide the best fit to the measured spectrum.

The solid line in Fig.1 represents the simulated spectrum which provides the best fit to the measurement. The parameters that give the best fit to the experimental data for Fe band are listed in Table 1. The width of

TABLE I

Simulation parameters giving best fit to the InP PL data

Band	Zero Phonon Line		Phonon Energy	Huang-Rhys Coefficient
	Energy E_0 (eV)	Width σ (eV)	E_p (eV)	(S)
Fe	1.142	0.026	0.039	2.0
Mn	1.185	0.025	0.039	1.4
B1	1.246	0.026	0.039	1.3
B2	1.330	0.025	0.043	1.2
C	1.113	0.030	0.039	1.6

the zero phonon line could be related to either non-homogeneities in the material producing level broadening or the presence of a strongly coupled low energy local mode phonon [7] or due to the presence of different states of the defect [4]. For InP:Mn the analysis of the data was performed by first fitting the lower energy part of the spectrum including the peak. Subsequently two other CC bands (B1 and B2) are added on the higher energy side to account for the shoulder. The three components fitted to the data are also individually shown in Fig.2. The parameters that describe the most prominent Mn band along with the parameters describing the bands B1 and B2 are also listed in Table 1.

Thus having obtained the parameters of the individual bands they can be used to fit the composite spectra by only changing the relative intensities of these well characterised bands. Fig.3 shows the PL spectrum of another Fe doped InP sample where the peak is shifted to higher (nearly 1.12eV) energy and has a larger width compared to that shown in Fig.1. The simulated spectrum along with the two components is also shown in Fig.3. The simulated spectrum is generated by using the previously determined parameters for Fe and Mn bands with relative strengths of the two peaks as the fit parameters. Excellent fit to the data for different samples were obtained. It is known that Mn is a common impurity in InP [2]. The presence of Mn in different amounts could shift the luminescence band continuously between the Fe and Mn peak energies. A similar argument has been supported by Eaves et.al [2] and Bishop [8] to explain the shift in the peak position or the

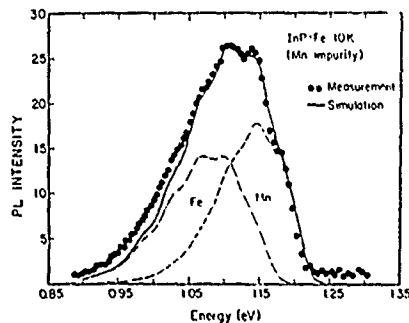


Fig.3. Deep level PL spectrum for InP:Fe with Mn impurity

composite spectrum rather than an unphysical variation in the coupling strength proposed by Yu [1].

In the case of undoped InP heat-treated at 500°C for 1 hr. a prominent band peaking at 1.07eV (band C[2,5,6]) is typically observed (Fig.4). This

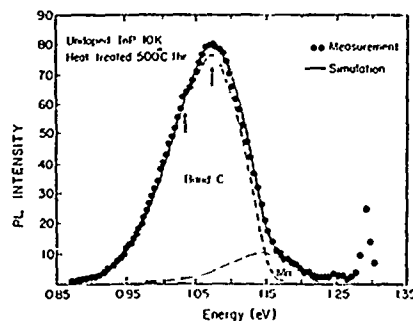


Fig.4. Deep level PL spectrum for undoped InP. Well resolved phonon features of band C have been marked with arrows.

band has been associated with a complex involving P-vacancy (native defect). Clear phonon features are indicated by arrows in the figure. The fit parameters for this band are listed in Table 1. In addition, there is a high energy shoulder present in the spectrum. This is due to the presence of Mn impurity and can be explained by incorporating an additional Mn peak in the simulation as shown in the simulated spectrum in Fig.4. The same defects with very small intensities have been observed in our virgin undoped samples.

In summary, we have analysed the measured PL spectra associated with deep levels related to Fe and Mn and native defects in InP. The lineshape analysis of the spectra using a configuration coordinate model resulted in a unique set of parameters for the individual bands. These parameters were used to explain the experimental data in several different samples quite consistently.

REFERENCES

1. P.W. Yu, Solid State Commun. 34, 183 (1980)
2. L.Eaves, A.W. Smith, M.S.Skolnik and B. Cockayne, J.Appl.Phys. 53, 4955 (1982)
3. M.S.Skolnick, E.J.Foulkes and B. Tuck, J.Appl.Phys. 55, 2951 (1984)
4. B. Plot-Chan, B. Deveaud, A. Rupert, and B. Lambert, J.Phys. Solid State Phys. C18, 5651 (1985)
5. H.Temkin and B.V.Dutt, Mat.Res.Soc.Proc. 14, 253 (1983)
6. H.Temkin and W.A.Bonner, J.Appl.Phys. 52, 397 (1981)
7. B.Nonemar and L.Samuelson, J.Luminescence 12/13, 507(1976) and Phys. Rev. B12, 809 (1978).
8. S.G.Bishop, "Deep Centers in Semiconductors: A state-of-the-art approach" (Edited by Sokrates T.Pantelides) p.541 Gordon and Breach Science Publishers, New York (1986)

THE NATURE OF NATIVE DEFECTS IN LEC GROWN SEMI-INSULATING GaAs BY THERMALLY STIMULATED CURRENT SPECTROSCOPY

ZHAOQIANG FANG, LEI SHAN, T. E. SCHLESINGER AND A. G. MILNES

Department of Electrical and Computer Engineering
Carnegie Mellon University, Pittsburgh, PA 15213

ABSTRACT

Traps have been studied by thermally stimulated current spectroscopy (TSC) with intrinsic (1.96 eV) and extrinsic (1.15 eV) light for both In doped and undoped LEC materials grown under various non-stoichiometric conditions. Significant differences are seen in the bulk trap spectra associated with Ga-rich and As-rich material and with isoelectronic In doping. Proximity wafer-annealing at 950° C has been shown to improve minority carrier lifetime in n-type GaAs and we show that in semi-insulating GaAs this causes changes in trap structure. From such thermal studies and the effects of non-stoichiometric growth, the probable nature of the traps commonly seen is inferred.

TYPICAL TSC SPECTRA

Five kinds of SI-GaAs were used in the study. Four are as-grown SI-GaAs: As-rich melt grown, Ga-rich melt grown, In doped and undoped. The other is a SI-GaAs wafer proximity-annealed at 950° C for 16 hr. in a sealed pure quartz ampoule. Both 1.96 eV light from a He-Ne laser and 1.15 eV light from a tungsten lamp via a monochromator were used for the excitation at 90 K. The details of sample preparation, experimental set-up and measurement conditions have been described elsewhere [1]. From typical TSC spectra (1.96 eV) for as-grown undoped SI-GaAs, shown in Fig. 1 and 2, it can be found that 1) at least six traps designated T_1 to T_6 can be observed in the temperature range from 90 K to 250 K, 2) T_2 dominates T_3 in the SI-GaAs with As-rich stoichiometry and T_3 dominates T_2 in the SI-GaAs with Ga-rich stoichiometry and 3) the peak T_3 in the "Ga-rich" sample appears to be composed of several traps with a main one at $T_m = 190$ K. But from the comparison of spectral structure between In doped and undoped SI-GaAs (Fig. 2), it can be seen that 1) in addition to the six traps observed in undoped SI-GaAs the other traps T_A and T_D can be clearly observed in In-doped SI-GaAs, 2) the T_A at 168 K dominates T_2 and T_3 and becomes the main trap in In-doped SI-GaAs and 3) although the etch pit density (EPD) in the In-doped sample ($2 \times 10^3 \text{ cm}^{-2}$) is much lower than the EPD in undoped sample. The estimated density of T_A is in 10^{17} cm^{-3} range, which is higher than for T_2 and T_3 in undoped SI-GaAs.

Three methods were used to determine the trap depths for main traps. They are 1) calculation by an approximate equation, $E_i = kT_m \ln T_m^4 / \beta$ [2], where E_i is the trap depth of a given trap, k is Boltzmann's constant, T_m is the temperature at the TSC peak and β is the heating rate during the thermal scan, 2) determination from Arrhenius plots of $\ln T_m^2 \beta$ vs. $1/T_m$ [3] and 3) determination from an initial rise slope or low temperature exponential edge for a given trap, which is measured after removing all emissions from traps shallower than the test one by raising the temperature to T ($T < T_m$ for a given trap), waiting for a long time (~35 min) and starting the thermal scan again from 90K [4]. The low temperature exponential edges for the main traps are shown in Fig. 3 with the results of trap depths obtained by the three methods in the inserted table. Acceptable values are 0.49 eV, 0.35-0.42 eV, 0.33 eV, 0.27 eV and 0.21 eV for T_2 , T_3 , T_A , T_5 and T_6 , respectively. The trap depth for T_D is calculated to be 0.17 eV.

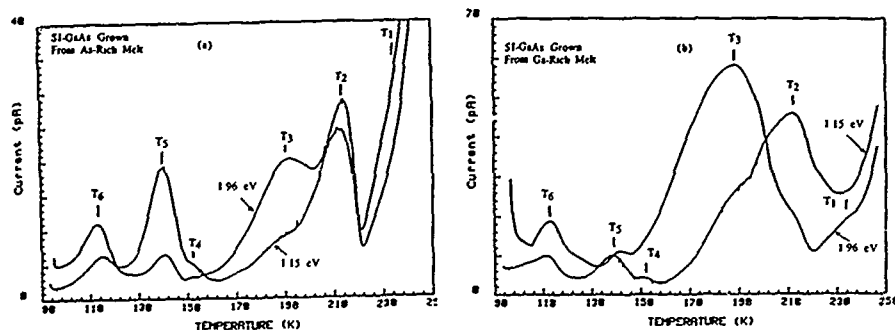
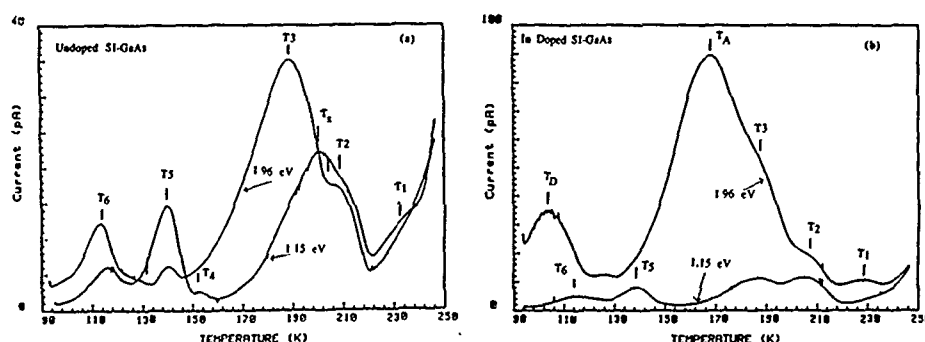


Fig. 1 (a)(b) Typical TSC Spectra

Fig. 2 (a)(b) In Doped GaAs Shows Traps T_A and T_D for 1.96 eV Illumination

In terms of the usual criterion for the type assignment of traps by using intrinsic light and changing bias polarities [5], T_2 , T_5 and T_6 are hole traps and T_1 is an electron trap. T_3 and T_A cannot be simply assigned as a hole or electron trap since they appear in both biasing polarities with a small peak shift. The estimated trap densities for the main traps T_2 , T_3 , T_A , T_5 and T_6 for different samples are in the mid- 10^{15} to 10^{17} cm^{-3} range. The traps are believed to be due to native defects because of the dependencies on stoichiometry and the low concentration of Cu, Fe and Mn in current undoped SI-GaAs.

EFFECTS OF 1.15 eV LIGHT

To study the effects of extrinsic light on TSC spectral structure, 1.15 eV light was chosen for the excitation at 90K, since the IR light is very effective for various kinds of quenching behavior. Indeed, a photocurrent quenching has been observed in as-grown SI-GaAs samples with As-rich and Ga-rich stoichiometry by using 1.15 eV excitation. This is in contrast with the photocurrent enhancement, which was observed at 90K by using 1.96 eV excitation on similar samples [1]. Comparisons of TSC spectra of 1.96 eV light vs. 1.15 eV light on two as-grown SI-GaAs with different stoichiometry are given in Fig. 1. It can be seen that 1) both 1.96 eV and 1.15 eV light can reveal all traps (T_1 to T_6), which implies that all TSC peaks observed by using 1.96 eV excitation are due to the carrier emission from the bulk traps 2) the ratio of peak height for T_2/T_3 and T_5/T_6 were increased by using 1.15 eV light due to the reduction of T_3 and T_6 and the increase in T_2 and T_5 . The results indicate that the occurrence of T_3 and the development of T_6 in 1.96 eV TSC spectra are related to electron capture, since the photo-excited carriers by 1.15 eV light are mainly holes, while those excited by 1.96 eV light are both electrons and holes. Therefore T_3 can be assigned as an electron trap.

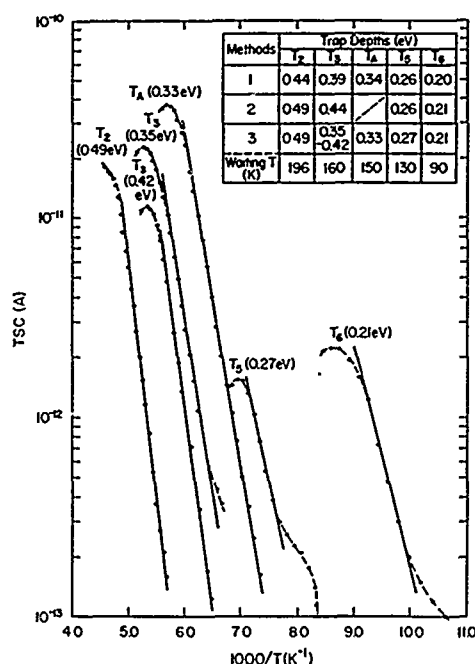


Fig. 3 Initial TSC Rise Curves and a Table of Trap Depths Determined by Various Methods

Comparisons of TSC spectra of 1.96 eV light vs. 1.15 eV light on In-doped and undoped SI-GaAs are shown in Fig. 2. It is found that 1) for undoped SI-GaAs traps T_3 and T_6 observed by 1.96 eV light are suppressed by 1.15 eV light and 2) for In-doped SI-GaAs traps T_A and T_D are suppressed by 1.15 eV light, which means that T_A and T_D are also related to electron capture and can be assigned as electron traps. Similar to the behavior of T_3 in undoped SI-GaAs, using 1.96 eV light, T_A and T_D can be revealed under both positively and negatively biasing polarities with a small peak shift.

TSC STUDY OF PROXIMITY ANNEALED SI-GaAs

Proximity wafer annealing, in which the wafer is covered by an identical one in a small sealed ampoule at 950°C for 16 hr, has been shown to improve minority carrier lifetime in n type Si or Te doped GaAs and to suppress many electron traps.[6] The same anneal causes significant changes in trap structure in the SI-GaAs. The TSC spectra of an annealed SI-GaAs, using 1.96 eV and 1.15 eV light with different illumination times are shown in Fig. 4. The photocurrent responses at 90K are inserted in both figures. A significant quenching effect can be observed in the 1.15 eV light case, which contrasts with the slight enhancement in the 1.96 eV light case. Before anneal, the TSC spectra (1.96 eV) of the sample can be found in Fig. 1(a). After anneal, a huge TSC peak at 132 K labeled T_5^* is revealed by long term illumination of 1.96 eV light and the ratio T_2/T_3 is changed from >1 to <1 . The large TSC signals measured after anneal might be due to the improvement in the lifetime of photo-excited carriers.

Increasing illumination times under 1.96 eV and 1.15 eV excitation causes an interesting difference: under 1.96 eV excitation the long term illumination results in a significant development of T_5^* with slight change in T_2 and T_3 , but under 1.15 eV

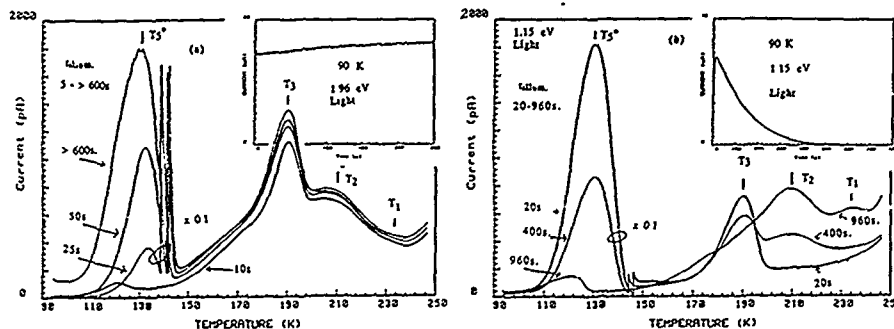


Fig. 4 (a)(b) TSC For a Specimen Proximity Anneal at 950°C with 1.96 and 1.15 eV Illumination. Photocurrent Is Shown in the Insets.

excitation the long term illumination results in a significant suppression of T_5^* with obvious change in the ratio of T_2/T_3 . Once again, the use of 1.15 eV excitation for long term causes the increase in the ratio of T_2/T_3 , which is similar to the observation on the as-grown Si-GaAs.

The trap depths of T_3 and T_5^* in annealed Si-GaAs were determined by the method of low temperature exponential edge to be 0.34 eV and 0.27 eV, respectively. The result means that the T_3 and T_5^* in annealed Si-GaAs are basically the same as T_3 and T_5 in as-grown Si-GaAs only with some difference in their capture cross section, since T_5 and T_5^* have slightly different peak temperatures.

POSSIBLE NATURE OF MAIN TRAPS

The above experiments provide some information as to the nature of the traps seen, although definitive identifications cannot be made. Traps T_2 ($E_v+0.49$ eV), T_3 and T_A ($E_c-0.33-0.42$ eV), T_5 and T_5^* ($E_v+0.27$ eV) and T_6 ($E_v+0.21$ eV) are tentatively identified as As_{Ga}^{+} , a V_{As} -related complex, a V_{Ga} -related complex and Ga_{As}^- , respectively through the comparison with main deep centers observed in LEC grown n and p type GaAs by DLTS.

REFERENCES

- [1.] Z. Q. Fang, L. Shan, T. E. Schlesinger and A. G. Milnes, to be published in Mater. Sci. & Engr., vol. B (1989).
- [2.] D. C. Look, Semiconductors and Semimetals **19**, 75 (1983).
- [3.] R. H. Bube, *Photoconductivity of Solids*, (Wiley, New York 1960).
- [4.] A. G. Milnes, *Deep Impurities in Semiconductors*, (Wiley, New York 1973), p. 236.
- [5.] G. M. Martin and D. Bois, Electrochem. Soc. Ext. Abstr. **78-3**, 32 (1978).
- [6.] D. Wong, H. K. Kim, Z. Q. Fang, T. E. Schlesinger and A. G. Milnes, J. Appl. Phys. **66**, 2002 (1989).

ACKNOWLEDGMENT

Supported in part by U.S. Army Research Grant DAAL03-86-K0066.

ANOMALOUS LUMINESCENCE PROPERTIES OF GaAs GROWN BY MOLECULAR BEAM EPITAXY

I. SZAFRANEK, M.A. PLANO, M.J. MCCOLLUM, S.L. JACKSON, S.A. STOCKMAN,
K.Y. CHENG and G.E. STILLMAN

Center for Compound Semiconductor Microelectronics, Materials Research Laboratory and
Coordinated Science Laboratory, University of Illinois at Urbana - Champaign, IL 61801.

ABSTRACT

A shallow acceptor-like defect labeled "A" is frequently incorporated in molecular beam epitaxial GaAs. We report here anomalous photoluminescence effects that are induced by this defect. With increasing concentration of the "A" defect: (1) neutral and ionized donor-bound exciton peaks disappear almost completely even for donor concentration as high as $7 \times 10^{14} \text{ cm}^{-3}$ and compensation ratio $N_D/N_A \approx 0.3$; (2) a new, sharp line emerges at 1.5138 eV, and (3) the relative intensity and line shape of the free exciton transition change dramatically. These observations are discussed in the perspective of previous reports, where similar effects were, in our opinion, misinterpreted.

INTRODUCTION

GaAs layers grown by molecular beam epitaxy (MBE) often exhibit unique photoluminescence (PL) features associated with unidentified shallow defects. The best known are the series of lines in the 1.504-1.511 eV range due to defect-bound excitons (d,X), first reported by Künzel and Ploog¹ and denoted hereafter as K-P peaks. Recently, we have found that the g(d,X) peak at the high energy limit of the K-P series originates in an exciton bound to the shallowest known acceptor-like defect in GaAs, labeled "A".² The activation energy of this defect is $\sim 24.8 \text{ meV}$, about 1.7 meV less than that of C_{As} acceptors.

In the present paper further investigation of the "A" defect is reported. We have characterized a set of MBE grown GaAs samples in which the relative PL intensities of the "A" defect-induced transitions, g(d,X) at 1.5112 eV and the free electron-to-"A" defect $A(e,A^0)$ at 1.4946 eV, varied over a wide range, allowing for study of anomalous effects induced by this defect in the exciton recombination luminescence. Our observations are important, because they demonstrate that if some commonly used methods of semiquantitative assessment of semiconductors with PL spectroscopy are used indiscriminately, they may provide an entirely misleading indication of purity and compensation in GaAs grown by MBE.

EXPERIMENTAL

Nominally undoped, p-type layers were grown in Phi 430P MBE system using solid Ga and As sources. A Phi As cracker with a rhenium baffle was operated at a current of 4 A (no temperature calibration has been available). Approximately 10 μm thick layers were grown under the As-stabilized (2x4) surface reconstruction conditions on semi-insulating, undoped liquid-encapsulated Czochralski GaAs substrates oriented 2° off the (100) orientation.

The samples were characterized electrically with van der Pauw Hall-effect measurements at a magnetic field of 0.66 T. The ohmic contacts on these p-type samples were formed with alloyed In-Zn spheres. Concentrations of electrically active donor and acceptor impurities were determined by numerical curve fitting of Hall carrier concentration measured over the temperature range of 15-300 K.³

Residual acceptor impurities and shallow defects in the layers were assessed with low temperature PL. The samples were measured over the temperature range of 1.7-21 K, being immersed strain-free in either superfluid He⁴ or flowing gaseous He. An unfocused 5145 Å line from an argon ion laser was used for the photoexcitation. The emitted radiation was spectrally resolved by an Instruments SA 1 m double spectrometer and detected by a thermoelectrically cooled GaAs photomultiplier tube, using the photon counting technique.

RESULTS AND DISCUSSION

A typical example of evolution of photoluminescence from MBE GaAs as a function of the "A" defect concentration is shown in Fig. 1. Sample No. 104 is a high purity and high mobility layer, and, accordingly, it exhibits a very well resolved exciton recombination spectrum. A notch between the upper and lower polariton branches of the free exciton band, FE,⁴ is clearly discernible and the neutral donor-bound exciton peak $(D^0, X)_{n=1}$ is very sharp, with a line width FWHM=0.13 meV. Although the sample is p-type the donor-related transitions, $(D^0, X)_{n=1}$, ionized donor-bound exciton (D^+, X) and neutral donor-to-valence band (D^0-h) , are more intense than the peaks due to recombination of the excitons bound to neutral acceptors, $(A^0, X)_{n=1}$. This pattern results from a high compensation ratio N_D/N_A , as confirmed by the Hall-effect data in Table I. Inspection of the two lower spectra in Fig. 1 reveals that the increase in the intensity of the "A" defect-induced transition $g(d, X)$ is accompanied by remarkable changes in the exciton recombination luminescence.

We first discuss the effect of a gradual quenching of donor-related peaks, (D^0, X) , (D^+, X) and (D^0-h) . As demonstrated in Fig. 2, this trend occurs regardless of the actual donor concentrations listed in Table I for the layers studied here. Fig. 2 shows the donor concentrations N_D and the amplitudes of donor-bound exciton peaks normalized to the luminescence intensity of the lower polariton branch of the free exciton FE,⁴ as a function of the "A" defect concentration given by the $g(d, X)/FE$ ratio. Two separate branches, one for low and one for high compensation, can be distinguished. The general trend is similar in each branch: as the $g(d, X)/FE$ ratio increases, amplitudes of the donor-induced transitions decrease and eventually almost completely disappear for the defect rich Samples Nos. 155 and 157, regardless of the fact that the electrically measured donor concentration increases. On the other hand, in the same PL spectra the amplitudes of both the $g(d, X)$ and $C(A^0, X)$ peaks, normalized to the FE intensity, are directly related to the acceptor concentration N_A . Consequently, the assessment of the compensation based, for example, on frequently used $(D^0, X)/(A^0, X)$ intensity ratio becomes impossible, though such ratios are frequently used to indicate sample compensation in the absence of reliable electrical measurements.

TABLE I: Electrical properties of unintentionally p-type doped GaAs layers grown by MBE

Sample No.	μ_{77} [cm ² /V·sec]	μ_{300} [cm ² /V·sec]	p77 [10 ¹⁴ cm ⁻³]	p300 [10 ¹⁴ cm ⁻³]	N_A [10 ¹⁴ cm ⁻³]	N_D [10 ¹⁴ cm ⁻³]	N_D/N_A
104	9070	270	0.57	4.93	2.6	2.1	0.80
108	8060	315	0.94	4.09	4.2	3.3	0.79
164	8900	430	2.79	3.61	3.0	0.4	0.12
157	7800	415	5.30	8.83	7.3	2.0	0.27
155	6350	410	15.6	27.7	26.	6.7	0.26

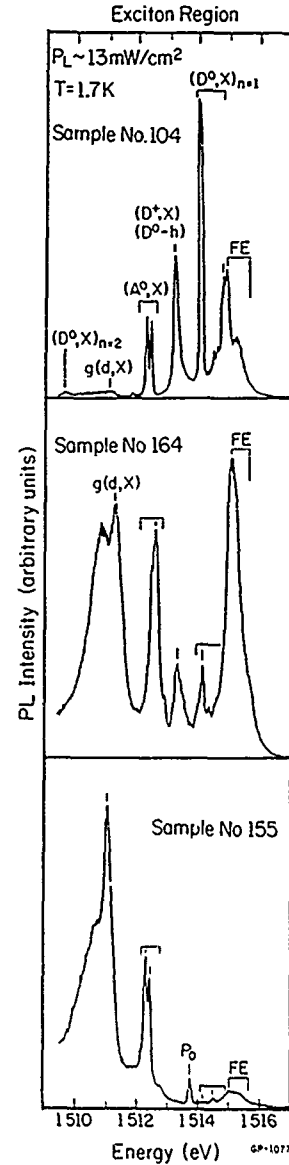


FIG. 1: PL spectra of three representative GaAs layers grown by MBE: No. 104- high purity and mobility; No. 164- intermediate "A" defect concentration; No. 155- relatively high "A" defect concentration. The quenching of the donor-related peaks and the appearance of a new line P_0 are apparent in the defect-rich sample.

The neutral and ionized donor-bound excitons are known to have very large oscillator strengths,⁵ as also evident here for Sample No. 104 in Fig. 1, where the corresponding transitions dominate the PL excitonic region of this high-purity p-type material. Therefore, the absence of these lines in the spectra of the defect-rich GaAs samples implies that the donor-bound exciton complexes are formed at extremely low concentrations. To account for this effect the following observations should be noticed. The dominant PL emission gradually shifted from the near band-edge range of FE, (D^0, X) and (D^+, X) transitions in high purity samples to the lower energy $C_{As}(A^0, X)$, $g(d, X)$ and other K-P bound exciton recombination processes in the defect-rich layers. Further, after reanalyzing PL data of a large variety of p-type GaAs layers grown by different epitaxial techniques, we cannot recall a single example of a similar quenching of donor-bound exciton peaks in samples with comparable N_D and N_D/N_A values, except for other MBE grown GaAs layers where the $g(d, X)$ peak was very pronounced. Finally, the defect-rich Samples Nos. 157 and 155 were exposed to 13.56 MHz hydrogen plasma that caused a very extensive neutralization of the "A" defects compared to other impurities present in these epitaxial layers. Whereas in the PL spectra of the as-grown samples the (D^0, X) and $(D^+, X)/(D^0-h)$ peaks were almost completely extinguished, the reduction in the concentration of the electrically active "A" defects after hydrogenation resulted in very well resolved, "normal" exciton recombination spectra, with sharp and intense donor-bound exciton lines. These observations have led us to conclude that it is the presence of large concentrations of the "A" defects in the material that suppresses the steady-state concentrations of the donor-bound exciton complexes and results in quenching of the corresponding luminescence peaks.

An additional PL feature clearly observed in the spectra where the donor-related transitions are almost fully quenched is a sharp line at 1.5138 eV, labeled P_0 (Sample No. 155 in Fig. 1). A similar peak has been previously observed in MBE GaAs,⁶⁻⁸ although never so intense as detected in Sample No. 157 (not shown). The origin of the P_0 line is not known; its appearance in our spectra in obvious conjunction with the large amplitude of the $g(d, X)$ band suggests that these two transitions may be related. The line width of the P_0 peak, FWHM=0.10 meV, is even narrower than for bound exciton transitions in GaAs. There is a possibility that the P_0 peak is due to the (D^0-h) transition, which is the lowest dissociation energy path of about 0.4 meV for the (D^+, X) complex.⁹ The (D^0-h) emission has a line width comparable to bound-exciton peaks, because of the donor-bound electron wavefunction confinement in the k-space.⁹ The (D^+, X) and (D^0-h) lines have not been so far mutually resolved in GaAs.

Other effects that have been observed in the excitonic region are pronounced changes in the line shape and relative intensity of the FE peak as a function of the "A" defect concentration. As the $g(d, X)$ peak becomes more dominant the two polariton branches of the FE band can no longer be resolved. A single, relatively narrow FE peak grows to prominence in the excitonic region at intermediate acceptor concentrations (Sample No. 164, Fig. 1). Similar observations have been reported previously.^{10,11} However, when the "A" defect concentration is still higher the FE band gradually diminishes, and eventually, for the excitation level of 13 mW/cm² it is weaker than the new P_0 peak (Fig. 1). Concurrently, the (A^0, X) and particularly $g(d, X)$ transitions become dominant.

Based on similar observations of the FE peak intensity and line shape evolution with disappearing donor-related excitonic transitions, the exciton-polariton photoluminescence has been reinterpreted.¹⁰ In that work the absence of the (D^0, X) and $(D^+, X)/(D^0-h)$ peaks was

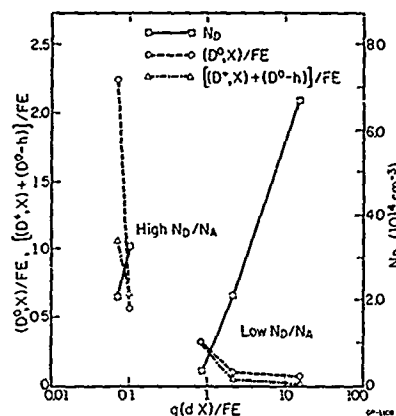


FIG. 2: The normalized amplitudes of donor-related transitions (dashed lines, left ordinate) as a function of the "A" defect concentration, shown in terms of the normalized $g(d, X)$ peak intensity. The actual concentration of shallow donors in these MBE GaAs layers is also shown.

attributed to exceptionally low donor concentrations in the MBE GaAs samples studied.¹⁰ The other authors¹⁰ inferred that the single narrow FE peak dominating their (and some of ours) excitonic PL spectra represents the true line shape of the intrinsic free exciton-polariton distribution, while the usually observed broad doublet structure derives from the modification of the intrinsic line shape due to elastic scattering of exciton polaritons by neutral impurities, in general, and by shallow donor species, in particular. No additional data were provided to support the claim of a very low compensation, which is the fundamental underlying assumption of the revised FE line shape model.¹⁰ The results of the present study seriously question the validity of these conclusions. First, we have demonstrated that because of an anomalous quenching of the donor-related transitions the corresponding peak intensities do not necessarily correlate with the presence and the relative concentration of shallow donor species in p-type MBE GaAs. Second, this supposedly intrinsic line shape of the FE peak has been observed so far only in GaAs grown by MBE, with impurity concentrations in the high 10^{14} - 10^{15} cm⁻³ range and the defect peaks usually also present in the PL spectra. In the highest purity and mobility GaAs grown by MBE¹² and by other epitaxial techniques, where $N_D \approx 1 \times 10^{13}$ cm⁻³ and $N_D/N_A \approx 0.1$, the familiar broad doublet structure has been always observed. Finally, when the defect-rich samples with the intense single FE peak were exposed to hydrogen plasma the doublet structure reappeared, although it is obvious that the hydrogenation process neutralizes electrically active impurities and defects, and the "A" defect in particular.¹² These results suggest that the single, narrow line shape of the FE peak is probably a consequence of some perturbation of the intrinsic exciton-polariton interaction by a relatively large concentration of the substitutional impurities and shallow defects incorporated during the MBE growth of GaAs.

CONCLUSIONS

The salient result of this study is that apparently "donorless" PL spectra may be obtained even for significantly compensated p-type GaAs layers grown by MBE. This behavior is attributed to large concentrations of the "A" defects and C_{As} acceptors. Therefore, the neutral and ionized donor-bound exciton transitions should be used with caution in attempts at semiquantitative assessment of defect-rich GaAs epitaxial layers.

Technical assistance of R. MacFarlane and R.T. Gladin in preparation of this manuscript is appreciated. This work was supported by the Joint Services Electronics Program, under contract N00015-84-C-0149, by the National Science Foundation, under grants DMR 86-12860 and CDR 85-22666 and by SDIO/IST under contract No. DAAL 03-89-K-0080 administered by the Army Research Office.

REFERENCES

1. H. Künzel and K. Ploog, *Appl. Phys. Lett.* **37**, 416 (1980).
2. I. Szafrank, M.A. Plano, M.J. McCollum, S.L. Jackson, K.Y. Cheng and G.E. Stillman, 1989 Electron. Mater. Conf. Boston, MA, June 1989 (unpublished).
3. G.E. Stillman and C.M. Wolfe, *Thin Solid Films* **31**, 69 (1976).
4. D.D. Sell, S.E. Stokowski, R. Dingle and J.V. DiLorenzo, *Phys. Rev. B* **7**, 4568 (1973).
5. E.I. Rashba, *Fiz. Tekh. Poluprovodn.* **8**, 1241 (1974) [*Sov. Phys. Semicond.* **8**, 807 (1975)].
6. J.P. Contour, G. Neu and M. Leroux, *J. Vac. Sci. Technol.* **B1**, 811 (1983).
7. N. Pan, S.S. Bose, M.H. Kim, G.E. Stillman, F. Chambers, G. Devane, C.R. Ito and M. Feng, *Appl. Phys. Lett.* **51**, 596 (1987).
8. M.S. Skolnick, T.D. Harris, C.W. Tu, T.M. Brennan and M.D. Sturge, *Appl. Phys. Lett.* **46**, 427 (1985).
9. E.W. Williams and H.B. Bebb, in *Semiconductors and Semimetals*, edited by R.K. Willardson and A.C. Beer, vol.8, p. 321 (Academic Press, New York, 1972).
10. E.S. Koteles, J. Lee, J.P. Salerno and M.O. Vassell, *Phys. Rev. Lett.* **55**, 867 (1985).
11. T.M. Kerr, C.E.C. Wood, S.M. Newstead and J.D. Wilcox, *J. Appl. Phys.* **65**, 2673 (1989).
12. I. Szafrank, M.A. Plano, M.J. McCollum, S.L. Jackson, S.A. Stockman, K.Y. Cheng and G.E. Stillman (unpublished).

COMPARATIVE OPTICAL STUDIES OF Cu, Mn, AND C IMPURITIES IN BULK LEC GROWN GaAs
BY ELECTRON BEAM ELECTROREFLECTANCE (EBER) AND PHOTOLUMINESCENCE (PL).

M. H. HERMAN*, P. J. PEARAH**, K. ELCESS*, AND I. D. WARD*

* Charles Evans & Associates, Redwood City, CA 94063

** Spectrum Technology, Holliston, MA 01746

ABSTRACT

We have used 300K Electron Beam Electroreflectance (EBER) and 4.2K photoluminescence (PL) to measure optical transitions in a series of LEC grown GaAs samples. The contaminants primarily consisted of the individual elements Cu, Mn, and C at levels above $10^{16}/\text{cm}^3$. In unmodified control samples we find evidence of strong excitonic effects in the EBER lineshape even at 300K. For the contaminated samples, we find characteristic impurity transitions below the E_0 bandgap of the GaAs in both optical spectroscopies. However, in general the estimated impurity binding energies by EBER are not equivalent to established PL or DLTS values. Specifically, from EBER data we find below E_0 (1.424eV at 300K) a Cu peak near 49meV (1.375eV) and a C peak about 39meV (1.385eV) below E_0 . An EBER spectrum of the Cu-contaminated sample at 124K shows an asymmetric Cu impurity peak 47meV below E_0 . The C feature has been ascribed to either Si or Ge from corresponding PL energies by several earlier researchers. Two samples which had been implanted with Mn and annealed show a peak about 43meV below E_0 (1.381eV), and what appears to be a sharp, excitonic transition 10 to 16meV above the E_0 . Although these features may be due to Mn alone, the latter observation is suggestive of strain-induced valence band splitting.

The correlated appearance of impurity peaks below the split-off $E_0+\Delta_0$ band may allow their assignment to either donors or acceptors in modulated reflectance studies [1,2]. None of the present cases showed corresponding transitions below $E_0+\Delta_0$, suggesting that the observed impurity features arise only from acceptor transitions. Alternatively, the reduction of light penetration into the GaAs above the E_0 bandgap, reducing the sample interaction volume, may also explain this null observation.

INTRODUCTION

The detection and characterization of elemental impurities and crystalline defects in compound semiconductors by optical spectroscopies has been fundamental to the development of solid state technologies. Especially in the GaAs system, photoluminescence (PL) has been extensively researched for the purpose of characterization of impurities [3]. However, PL alone is not sensitive to all defect types and is often complemented with DLTS and Hall measurements for further investigations of electrically active levels which do not luminesce. Other optical spectroscopies are also used to supplement PL studies of GaAs, such as IR transmission for detection of the EL2 concentration near midgap, and those of the electroreflectance (ER) modulation spectroscopy family, which are increasingly used to assess both bulk crystals and epitaxial heterostructures [4].

The identification of impurities in ER spectra began with the earliest discovery of the technique in 1966 by Seraphin [5,6]. Insightfully, Seraphin associated with impurities the higher temperature coefficient of some observed energy peaks (-0.61meV/K) compared to that of the E_0 band gap itself (-0.415meV/K). The impurities or defects responsible were not determined, however. Cardona *et al* [1] suggested in 1967 that a donor impurity may show peaks of identical binding energy below both the E_0 and the $E_0+\Delta_0$ band gaps, whereas acceptors would not appear below $E_0+\Delta_0$. Thus, the potential for optical ER detection and assignment of impurities was anticipated.

Several subsequent studies attempted to identify impurity peaks after their observation [7,8,9] by comparison of binding energies to those of photoluminescence (PL), concluding that close-lying energies must be due to the same impurities. Unfortunately, ER, with absorption associated features, and luminescence do not necessarily have the same energy levels [10]. We feel that this conceptual discrepancy makes ER identification of impurities inaccurate if based upon PL experience.

Incipient controlled studies were conducted by Williams and Rehn [11], who estimated the GaAs impurity detection limits by ER at $10^{16}/\text{cm}^3$. Further work by Williams [2] on the study the impurities Mn, Si, Cd, Te, and Ge in GaAs indicated that the impurity energy levels were functions of dopant concentration and possibly of the electric field used to modulate the sample. His studies of Mn in GaAs suggested a shift of the Mn impurity peak to lower energy with increased doping. Williams considered such energy shifts to be incommensurate with use for identification purposes. Of interest was his observation that the ER impurity peaks always occurred at energies lower than those expected from PL binding energies.

However, these studies were done before lineshape analysis was available, and it is possible that changes in signal phase, rather than actual shifts in peak energy, made the impurity signals appear to shift. To assess whether advances in impurity detection and determination can be made, we have therefore initiated an investigation of impurities in GaAs by recent ER methods. Below we report on the use of a contactless form of ER modulation spectroscopy - electron beam electroreflectance (EBER) - with PL to study the energy levels of Cu, Mn, and C contaminants in LEC grown GaAs. This material, as shown below, contains C signals in the PL spectra of each sample. Nevertheless, we observe strong similarities between samples which have been likewise contaminated, which we discuss below.

EXPERIMENTAL PROCEDURE

Photoluminescence (PL) and electron beam electroreflectance were performed on several LEC GaAs samples with known impurity concentrations. For PL, samples were cooled to 4.2K with a Janus optical cryostat and excited by the 647.1 nm line of a Kr^+ laser with a power density of about $1\text{W}/\text{cm}^2$. After passing through a 0.75 meter Spex spectrometer, the luminescence was detected with a cooled GaAs photocathode photomultiplier with photon counting electronics [12]. All samples showed a sharp free or bound exciton peak in addition to one or more impurity peaks.

Electron beam electroreflectance (EBER) [13] was performed on the same samples at room temperature. Variation of the surface electric field was accomplished by an incident 240eV electron beam, using square wave modulation at 190-235 Hz, and using a variety of current densities from $32\text{ A}/\text{cm}^2$ to $445\text{ A}/\text{cm}^2$. The light source was either a tungsten-halogen (WH) or a xenon (XE) lamp which was then passed through a PTI 0.25 meter monochromator and using appropriate cutoff filters to eliminate transmission of higher orders. The reflected monochromatic light was detected with either an InGaAs (IR) or a Si (visible and UV) diode detector.

RESULTS AND DISCUSSION

Unfortunately for comparative purposes, all of the samples in this study contained to some degree C, generally present in LEC material. The average binding energy as determined by 4.2K PL was 26meV, the well-established C acceptor level in GaAs. Therefore, we have compared several "control" samples to other wafers from the same boule, intentionally contaminated with either Cu or Mn, or having much higher C concentration than the control.

The Control samples:

The two control samples provided consistent EBER spectra at 300K. The spectrum of one, shown in Figure 1, has Franz-Keldysh oscillations (FKOs) extending above the E_0 bandgap in energy. We also observe a sharp discontinuity in the EBER spectra at the excitonic transition in the GaAs - even at 300K. This feature is thought to represent the free, $n=1$ exciton in GaAs, as observed earlier in absorption measurements [14]. If an impurity feature does lie close in energy to the E_0 transition, it is difficult to distinguish from the extension of the Franz-Keldysh oscillations below the E_0 bandgap - a limitation of ER techniques in the study of shallow impurities whenever there is a large built-in surface field. We consider the EBER spectrum to be free from obvious impurities. The concentrations of various trace impurities in the control GaAs are estimated from GDMS measurements to be as follows: [Se] $<10^{14}/\text{cm}^3$, [In] $<10^{13}/\text{cm}^3$, [Si] $<10^{14}/\text{cm}^3$, [Zn] $<10^{14}/\text{cm}^3$, [S] $<10^{14}/\text{cm}^3$, and [B] $<10^{15}/\text{cm}^3$. Finally, [EL2] $\sim 1.2 \cdot 10^{16}/\text{cm}^3$ as determined by FTIR and the 78meV acceptor is estimated to be $<10^{13}/\text{cm}^3$. Other parameters of the control and experimental samples appear in Table I. We currently have no estimates for Mn, but the experimental samples have been intentionally implanted with Mn and annealed and are thought to contain at least 100 times that of the control samples.

Table I: Experimentally varied contaminants and defects:

Sample	[C]	[Cu]	[Mn]
control	$<3 \cdot 10^{14}/\text{cm}^3$	$<10^{14}/\text{cm}^3$	N.A.
C	$2 \cdot 10^{16}/\text{cm}^3$		
Cu		$>10^{16}/\text{cm}^3$	
Mn implanted			$>100 \times \text{control}$

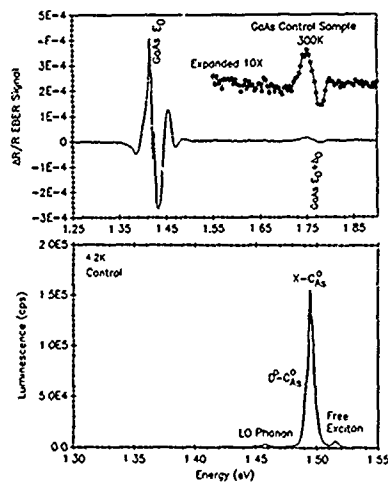


Figure 1: (a) 4.2K PL and (b) 300K EBER spectra of LEC GaAs control sample.

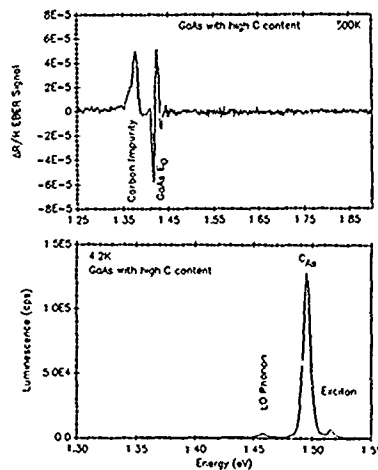


Figure 2: (a) 4.2K PL and (b) 300K EBER spectra of LEC GaAs sample having high C content.

C contaminated sample:

As C is an impurity present to an extent within all of the samples, we examine its effects first. The 4.2K PL spectrum of a sample with high C content appears in Figure 2a, and the corresponding 300K EBER spectrum is shown in Figure 2. The established PL peak associated with C appears 26meV

below the E_0 . Figure 2b shows a strong impurity peak observed by EBER at 300K nearly 39meV [15] below the GaAs E_0 , 13meV further below E_0 than the PL value. This seems to be the same large impurity peak reported by earlier researchers [7,8,16] and attributed to Si [8] or Ge [7], even possessing the same lineshape which extends broadly to low energy yet cuts off sharply at the upper peak energy. We note in passing that this lineshape is quite unusual from that theoretically expected [17].

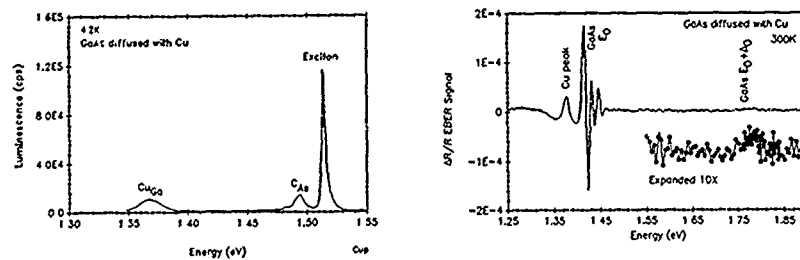


Figure 3: (a) 4.2K PL and (b) 300K EBER spectra of an LEC GaAs sample contaminated with Cu.

Cu contaminated samples:

Figure 3 shows PL and EBER spectra of two samples intentionally contaminated by Cu. The concentration of Cu in both samples is thought to be in the range of $10^{16}/cm^3$, compared to $10^{14}/cm^3$ for the control samples. The 4.2K PL spectrum in Figure 2a shows a C_{As} peak 25meV below E_0 , and a feature attributed to Cu_{Ga} nearly 150meV below E_0 [18].

The EBER spectrum of Figure 3b shows a clear impurity feature at about 47 \pm 3meV below E_0 at 300K. At 124K, an EBER spectrum of the same sample possesses an asymmetric peak 49meV below E_0 . This 47meV feature has a different energy from C (39meV) discussed above, and we believe that the absence of such a peak in the control samples and its clear observation in both intentionally Cu contaminated samples supports its identification as a Cu-related feature in the EBER. Again, the EBER impurity energy is not commensurate with that of PL.

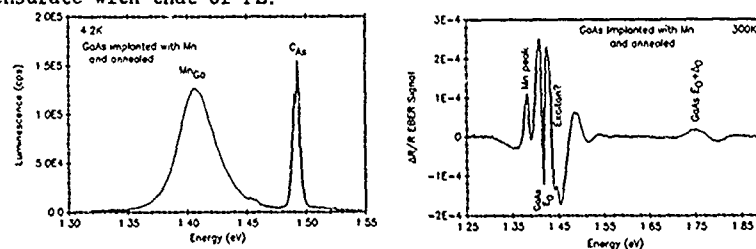


Figure 4: (a) 4.2K PL and (b) 300K EBER spectra of LEC GaAs sample implanted with Mn and annealed.

The Mn contaminated samples:

Figure 4 shows the PL and EBER spectra of one of the samples intentionally contaminated by Mn by implantation and then annealed. The concentration of Mn in both samples is believed to be many orders of magnitude larger than for the control samples, but the concentration is not known. The

4.2K PL spectrum in Figure 4a shows a C_{As} peak 25meV below E_0 and a feature attributed to Mn_{Ga} 108meV below E_0 (1.519eV).

Figure 4b, consistent with the EBER spectrum of another Mn doped sample, shows a very complex structure near E_0 at 300K. We observe an impurity peak about 43meV below E_0 (1.381eV), distinct from possible Franz-Keldysh oscillations near E_0 . We also note an apparent downward shift or smearing of the $E_0 + \Delta_0$ split-off band signal, compared to Figure 1 of the control sample. There appears to be an exciton-like peak above the GaAs E_0 , about 16meV above the E_0 at 1.424eV, which appears in EBER spectra of both samples. Although one may hypothesize that peaks below the $E_0 + \Delta_0$ can arise from donor-related transitions to the split-off valence band (VB), we can suggest no mechanism which can generate an exciton or impurity peak above the GaAs E_0 except due to an inhomogeneous strain splitting of the light and heavy hole valence bands. Strain can also explain the shift of the $E_0 + \Delta_0$. Indeed, there also appears to be a slight reduction of the PL C_{As} energy in the Mn sample compared to that of the control. Such a strain may arise in the surface layer from either the incorporation of large amounts of Mn or may be a residual effect of the implantation treatment, which we cannot at present distinguish, but which further experiments with X-ray diffraction may provide.

CONCLUSION

For the first time, EBER has been used to study impurities in GaAs, and the results compared to those of low temperature PL. Though it is clear that the presence of impurities modifies the EBER spectra in a reproducible way, the assignment of shallow impurity transitions is obscured by the presence of C in all samples and by the existence of the low energy Franz-Keldysh oscillation tail. Nonetheless, by comparison to our semi-insulating "control" samples, we find evidence for definite impurity peaks and signatures corresponding to C, Cu, and Mn. The feature observed from a high C containing sample shows a strong, assymetric peak at nearly 39meV binding energy. Likewise, samples of GaAs intentionally diffused with Cu show a consistent peak about 47meV below the E_0 transition. This binding energy contrasts with the 147meV value observed from PL at 4.2K. The binding energy of the C peak is discernably different from that of the Cu samples and is quite far below the 26meV value observed from PL. We have also noted that the symmetry of the Cu impurity features contrasts strongly to the dramatically assymetric signature attributed to C.

Quite different results are observed for two samples of GaAs intentionally implanted with Mn and annealed. These two samples both show evidence of a splitting of the E_0 into what appear to be two extra peaks and a shift or broadening of the split-off band $E_0 + \Delta_0$. Although the very reproducible EBER signature from the two Mn samples may have another origin, we alternatively suggest that the observed features originate from inhomogeneous strain splitting of the VB. The origin of this strain cannot be determined from the optical data alone, as it may arise from a concentration of Mn atoms in a surface layer, or from residual implantation damage.

Although the conceptual framework provides the possibility of sorting donor/acceptor impurity transitions by their simultaneous presence/absence below the split-off $E_0 + \Delta_0$ bandgap, we are unable to confirm this hypothesis with the present study. We have not observed such donor-related transitions in the C, Cu, or Mn samples, though we do observe a downward shift of $E_0 + \Delta_0$ from the Mn contaminated samples. We suggest that the latter effect is a result of strain, rather than a distinct impurity feature. Alternatively, the impurities studied may only have large optical densities for their acceptor levels. Stronger is the possibility that the interaction volume for impurities - limited only by the electric field modulation volume for energies below E_0 - is more strongly limited by the light penetration depth for energies close to

$E_0 + \Delta_0$. This latter effect would reduce the potential for donor-splitoff VB observations in semi-insulating materials.

Finally, we conclude that various impurities in semi-insulating GaAs may potentially be screened at room temperature optically by EBER. The impurity or defect-related features are clearly evident in the EBER data at 300K. Further, like samples demonstrate quite similar EBER spectra, showing that reproducibility of the impurity characterization by EBER is possible. We have also shown that the energy levels determined by PL are incommensurate with those observed by EBER, which implies that the identification of specific species by EBER and similar ER methods must await a more thorough study.

ACKNOWLEDGEMENTS

We gratefully acknowledge the assistance of Dr. C. Colvard of Charles Evans & Associates and J. Tower of Spectrum Technology in the preparation of the data. The EBER research has been supported in part by the Defense Advanced Research Projects Agency under contract DAAH01-88-C-0873.

REFERENCES

- 1 M. Cardona, K. L. Shaklee & F. H. Pollak, Phys. Rev. 154(3) 696, 1967.
- 2 E. W. Williams, Solid State Comm. 7, 541, 1969.
- 3 See for example D. J. Ashen, P. J. Dean, D. T. J. Hurle, J. B. Mullin, A. M. White & P. D. Greene, J. Phys. Chem. Solids 36 1041-1053, 1975.
- 4 See for example M. H. Herman, I. D. Ward, S. E. Buttrill, Jr. and G. L. Franke, "Characterization of III-V Semiconductor Structures Using Electron Beam Electroreflectance (EBER) Spectroscopy," MRS 144, 21-26, 1989. Also see M. H. Herman and I. D. Ward, "Characterization of GaAs-based Heterostructures Using Electron Beam Electroreflectance (EBER) Spectroscopy," proceedings of the 16th International GaAs and Related Materials Conference, Karuizawa Japan, 1989, in press.
- 5 B. O. Seraphin, J. Appl. Phys. 37(2) 721, 1966.
- 6 B. O. Seraphin, Proc. Phys. Soc. London 87, 239, 1966.
- 7 O. J. Glembocki, N. Bottka, & J. E. Furneau, J. Appl. Phys. 57(2) 432, 1985.
- 8 A. N. Pikhtin, V.-M. Airaksinen, H. Lopsanen, & T. Tuomi, J. Appl. Phys. 65(6) 2556, 1989.
- 9 M. H. Herman, R. C. Bowman, D. D. Smith, and S. C. Moss, and N. Chand, "Observation of Impurities in GaAs by Electron Beam Electroreflectance (EBER)," presented at the American Physical Society meeting in St. Louis, MO during March 20-24, 1989.
- 10 See for example the discussion by R. H. Bube, Electrons in solids Academic Press: New York, pp 126-127.
- 11 E. W. Williams & V. Rehn, Phys. Rev. 172(3), 1968.
- 12 P. J. Pearah, R. Tobin, J. P. Tower, R. M. Ware, L. Sargent, J. S. Blakemore, Proc. of Semi-Insulating III-V Materials, G. Grossmann and L. Ledebro, eds., Adam Hilger, Bristol, 1988, p. 195.
- 13 P. M. Raccach, J. W. Garland, S. E. Buttrill, Jr., L. Franke, J. Jackson, Appl. Phys. Lett. 52(19) 1584, 1988.
- 14 See the excitonic peak present in the 300K absorption data, discussed by J. S. Blakemore, J. Appl. Phys. 53(10) R123-R181, 1982.
- 15 The 39meV peak has been ascribed to C in earlier ER studies. See for example R. L. Tober, J. Pamulapati, P. K. Bhattacharya & J. E. Oh, Journal of Electronic Materials 18(3) 379-384, 1989.
- 16 R. C. Bowman, Jr., P. M. Adams, M. H. Herman, & S. E. Buttrill, "Effects of rapid thermal anneals on boron implanted GaAs," Materials Research Society, MRS 144, 471-6, 1989.
- 17 D. M. Eagles, J. Phys. Chem. Solids, 16 76, 1960.
- 18 E. W. Williams, Solid State Comm. 4, 585, 1966.

Ge RELATED DEEP LEVEL LUMINESCENCE IN InGaAs LATTICE MATCHED TO InP

S.S. CHANDVANKAR, A.K. SRIVASTAVA, B.M. ARORA and D.K. SHARMA
Tata Institute of Fundamental Research, Homi Bhabha Road,
Bombay 400005, India

ABSTRACT

Photoluminescence and Hall measurements are reported on Ge doped InGaAs layers lattice matched to InP. Ge doping of these samples results in highly compensated material, with the highest Ge content sample giving a p type conductivity with carrier concentration of $5 \times 10^{17} \text{ cm}^{-3}$. Low temperature PL spectra of these samples show a broad peak from 0.55 to 0.77 eV due to Ge. The peak of luminescence shifts to lower energy with increasing Ge content. The peak position shifts to higher energy with increasing excitation like in a D-A pair transition. The PL spectra have been explained on the basis of a model which assumes tail states near the band edges due to disorder produced by the presence of Ge in the lattice.

INTRODUCTION

$\text{In}_{0.53}\text{Ga}_{0.47}\text{As}$ alloy semiconductor is used in fabricating photodetectors used in modern Fibre-Optic Communication systems. n-type and p-type doping are generally achieved by incorporating group VI elements like Se, Te and group II elements like Zn, Cd respectively [1-3]. Group IV dopants such as Si, Ge and Sn may be preferable because of their low vapour pressures at the growth temperatures employed in Liquid Phase Epitaxy (LPE). However, these group IV dopants are amphoteric in nature and they can occupy either the cation or anion sites. Their electrical behaviour then depends on the lattice sites which they occupy. For example, in LPE GaAs, Sn behaves as a donor, Ge as an acceptor, and Si as either a donor or an acceptor depending upon the temperature of LPE growth [4]. On the other hand, in LPE InP, Si, Ge and Sn all behave as donors [5]. Hence, it is of interest to explore the behaviour of group IV atoms in InGaAsP which is a mixture of GaAs and InP lattices. We have earlier found that Ge in $\text{In}_{0.72}\text{Ga}_{0.28}\text{As}_{0.6}\text{P}_{0.4}$ behaves predominantly as a donor [6]. On the other hand, in InGaAs, Ge introduces both donors and acceptors with some preference for the acceptor like behaviour. As a result the materials are highly compensated with net p type conduction [7]. In addition to these electrical changes, Ge introduces a broad band of luminescence which is red shifted with respect to the band edge [8]. In this communication we report the results of electrical and luminescence measurements on Ge doped LPE grown $\text{In}_{0.53}\text{Ga}_{0.47}\text{As}$.

LIQUID PHASE EPITAXIAL GROWTH

The layers have been grown at 600°C in H_2 ambient, details of which are described elsewhere [7]. We have used two different solution baking schemes (I) 650°C, 5h and (II) 675-700°C, 24h. Ge is added to the growth solution after bakeout. Close lattice matching is observed between the epi layer and the substrate from X-ray diffraction measurements. The layers are characterised by Optical transmission measurement for the band edge at about 0.74 eV. Composition of some layers is also checked by energy dispersive X-ray measurement.

ELECTRICAL RESULTS

Resistivity and Hall measurements show that Ge produces net p type

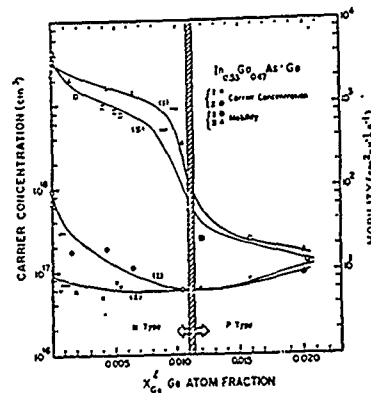


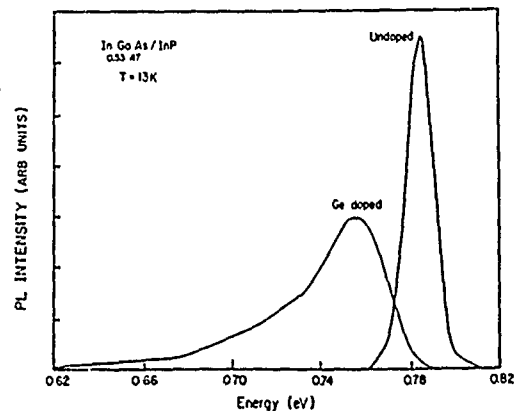
Fig.1. Carrier concentration and mobility versus atomic fraction of Ge in growth melt.

conduction. Fig.1 shows a plot of carrier concentration and mobility vs atom fraction of Ge in growth melt. It is seen that addition of Ge reduces the free electron concentration. The effect of Ge doping is dramatic as seen in the reduction of mobility of the samples in both sets I and II. The conductivity type changes at the Ge atom fraction of 0.010 - 0.015 in the solution as observed from the sign of the Hall voltage. However, the maximum hole concentration is about 10^{17} cm^{-3} . This indicates that although the samples do become p type, Ge doping produces strong compensation i.e. the amphoteric behaviour is quite predominant with Ge atoms occupying both the cation and anion sites.

PHOTOLUMINESCENCE RESULTS

The photoluminescence measurements are done at 12K by using closed cycle He refrigerator, a He-Ne laser source, a liquid nitrogen cooled InAs detector and lock-in amplifier. The set up used in the measurement is described elsewhere [9]. Figure 2 shows PL spectra of an undoped n type sample and a sample lightly doped with Ge. The spectrum of the undoped sample is similar to that reported in the literature [10] while the broad band introduced by Ge is seen for the first time. Figures 3 and 4 show that higher Ge doping produces a continuous shift of the broad band position to lower energies. The nature of the spectra does not depend significantly upon the conductivity type as seen from the samples which contain very similar amounts of Ge but have opposite conductivity types. An important and common property of this broad band in

Fig.2. Photoluminescence spectra of undoped and lightly doped InGaAs samples.



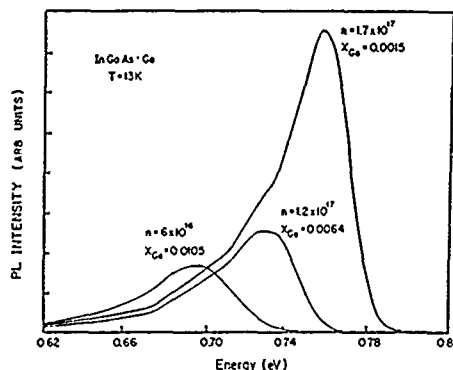


Fig.3

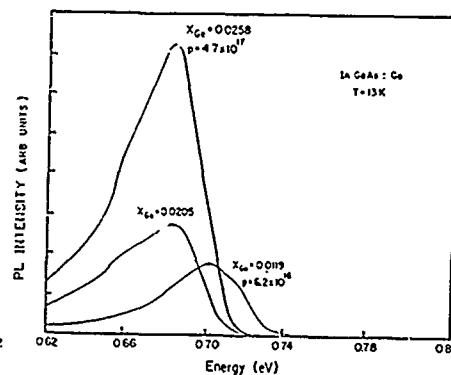


Fig.4

all the samples is that its shape depends on the level of excitation of the sample as seen from Fig.5.

On increasing the excitation intensity the peak shifts to higher energy irrespective of the Ge content and the conductivity type. This behaviour is characteristic of donor-acceptor pair transitions. Other features in the spectrum of sample with low Ge concentration can be attributed to the presence of 4 peaks at .76, .74, .71, .66 eV obtained by a sum of Gaussians to the experimental data (Fig.6). As the Ge content is increased, the broad band progressively shifts to lower energies. To account for this, we notice that the Ge doping produces heavy compensation (~ 100) leading to disorder and random potential fluctuations. Very low mobilities are one result of this disorder. We now postulate that this disorder produces tail states both near the conduction and valence band edges whose density and penetration into the gap energy increase with increase in the Ge content [11]. We further assume that the radiative recombination proceeds by transitions from the conduction band tail states occupied with electrons to the valence band tail states occupied with holes much in the same way as the donor-acceptor pair transitions [10]. Within this model, the shift of the PL bands to lower energies occur because the occupied state lie deeper in the gap at larger Ge concentration. On the other hand, states lying closer to the band edges fill at higher excitation intensity, leading to shift of the peak to higher energy as seen experimentally. Further support for the above model is obtained from the

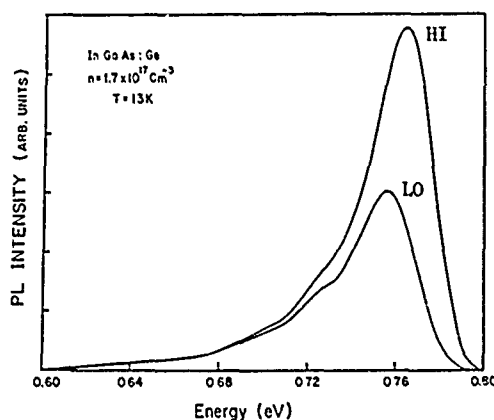
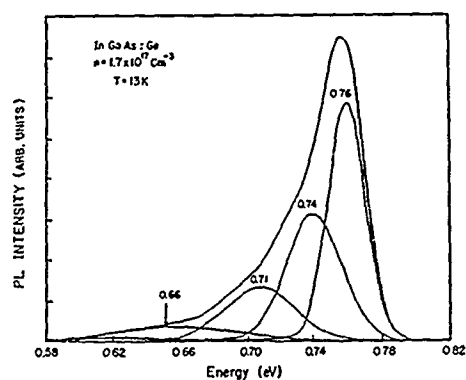


Fig.5. Photoluminescence spectra of lightly Ge doped InGaAs sample with low and high excitation powers.

Fig.6. Photoluminescence spectrum of lightly Ge doped InGaAs sample resolved into a set of Gaussian peaks.



nearly identical spectral shapes of the samples which have opposite conductivities with similar carrier densities. Ge content of these two samples is very similar, such that the tail state densities are expected to be similar, leading to the observed similarity of the spectral shapes. Details of the model will be further tested by the spectral shapes as well as from time dependence and temperature dependence of the PL spectra.

REFERENCES

1. InGaAsP Alloy Semiconductors, ed. by T.P.Pearsall (Wiley, New York, 1982)
2. P.A.Houston, *J. Mater. Science* **16**, 2935 (1981)
3. G.A.Antypass and L.Y.L.Shen, *Inst. Phys. Conf. Ser.* **33b**, 96 (1977)
4. K.H. Zschau in Festkorper Probleme XV, edited by H.J.Queisser (Pergamon, Braunschweig, 1975) p.1.
5. E.Kuphal, *J. Cryst. Growth* **54**, 117 (1981)
6. S.S.Chandvankar, R.Rajalakshmi, A.K.Srivastava, and B.M.Arora, *J. Cryst. Growth* **88**, 303 (1988)
7. S.S.Chandvankar and B.M.Arora, *J. Cryst. Growth*, **94**, 270 (1989)
8. B.M.Arora, S.Chakravarty, S.S.Chandvankar, R.Rajalakshmi and A.K.Srivastava, *Mate. Res.Soc.Symp. Proc.* **104**, 505 (1988)
9. A.K.Srivastava, *Ind. J. of Pure and Appl. Phys. Spl. Issue* **26** (1989)
10. K.H.Goetz, D.Bimberg, H.Juigensen, J.Selders, A.V.Solomonov, G.F.Glinskii and M.Razeghi, *J. Appl. Phys.* **54**, 4543 (1983)
11. B.I.Shlovskii and A.L.Efros, in Electronic Properties of Doped Semiconductors (Springer-Verlag, Berlin, 1984)

THE DEEP 0.11eV MANGANESE ACCEPTOR LEVEL IN GaAs

M. KLEVERMAN*, E. JANZÉN**, M. LINNARSSON**#, B. MONEMAR**

*Lund University, Dept. of Solid State Physics, S-221 00 LUND, Sweden

**Linköping University, Dept. of Physics and Measurement Technology, S-581 83 LIN-KÖPING, Sweden

ABSTRACT

The 0.11 eV Mn acceptor has been investigated using different kinds of FTIR techniques, Zeeman spectroscopy, and photoluminescence. The results clearly fits into the $3d^5$ + shallow hole model for Mn^0 and show that the 0.11 eV level originates from the ionization of a neutral, substitutional Mn acceptor at a Ga-site. The ground state binding energy obtained from the effective-mass like excited states is 112.4 meV.

INTRODUCTION

Manganese as a dopant in GaAs gives rise to an acceptor level about 0.11eV above the valence band. The level has been observed by Hall measurements [1], photoluminescence [2,3], absorption [4] and by space charge techniques [5]. EPR measurements showed a spectrum characteristic for ^{55}Mn with nuclear spin 5/2 [6,7]. The hyperfine interaction was found to be isotropic. The fine structure lines which are influenced by the 3d electrons were not resolvable.

Atomic manganese has the electronic configuration (Ar) $3d^5 4s^2$. On a substitutional Ga site three electrons would be used for the bonds to the nearest As atoms leaving the neutral manganese atom in a $3d^4$ configuration. Alternatively, it may be favorable energetically to form a $3d^5 (Mn^-)$ + loosely bound hole configuration. Recent EPR [8] and MCD [9] results favor the $3d^5$ configuration.

In this paper we will present absorption and photoconductivity data showing excited states of a neutral acceptor in great detail. The binding energy is 112.4 meV. The Zeeman data to be presented clearly favors the shallow hole model.

EXPERIMENTAL

The sample preparation is described in detail in Ref. 13, concerning Cu doped GaAs and only details specific for the fabrication of the Mn samples will be described here. Crushed manganese lumps and crushed GaAs wafers were mixed and put into a quartz ampoule together with the GaAs wafer. The samples were diffused at temperatures from 700 to 800 °C for 2-5h. After diffusion the ampoules were allowed to cool in the furnace or quenched in air. Both sides of the wafers were polished about 10 μm and then slightly etched 1 μm . About 500 μm were polished away from the surfaces of the samples used for the Zeeman experiments.

The SIMS data were obtained using O_2^+ ions. As reference we used a ^{55}Mn -implanted sample - 250 keV and a dose of $5 \times 10^{14} cm^{-2}$.

EXPERIMENTAL RESULTS AND DISCUSSION

Non-perturbation data

In Fig. 1 typical photoluminescence spectrum of a Mn-diffused sample is shown. The diffusion was carried out at 800 °C for 2h 40 min. The carrier concentration measu-

red with a Polaron Profiler was $1 \times 10^{18} \text{ cm}^{-3}$ and was equal to the total Mn concentration as measured with SIMS. However, the SIMS data showed that 100 μm below the surface the Mn concentration decreased sharply nearly two orders of magnitude and was then constant through the interior of the sample. It might be this interior part that gives rise to the detailed structure reported in this paper. The peak wavelength of 8800 Å corresponds to a mixture of transitions from the conduction band and shallow donor states to the Mn acceptor level. LO- and TA-phonon replicas are clearly visible. As can be seen the Mn-related transitions dominate the low energy part of the spectrum.

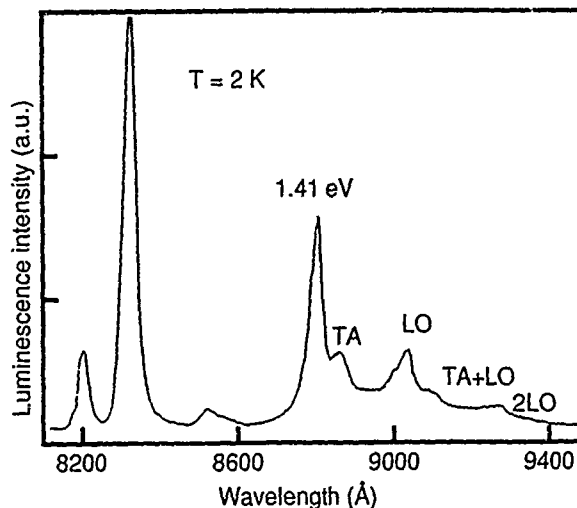


Fig.1 Photoluminescence spectrum of Mn-doped GaAs.

The absorption spectrum of the same sample is shown in Fig. 2. The peaks between 100 meV and 110 meV are due to transitions from the ground state to shallow EMT-like excited states. The structure around 140 meV is due to phonon-assisted Fano replicas of the same excited states. The dominant peaks at 101.20 meV, 105.16 meV, 107.07 meV and 108.5 meV can be assigned to transitions from the ground state to $2P_{3/2}(\Gamma_8)$, $2P_{5/2}(\Gamma_8)$, $2P_{5/2}(\Gamma_7)$ and $3P_{5/2}(\Gamma_8)$ states, respectively of a neutral acceptor. By adding the calculated binding energy of the $2P_{5/2}(\Gamma_8)$ state, 7.27 meV [13], we arrive at a ground state binding energy of 112.43 meV, which is in good agreement with 113 meV inferred from photoluminescence [3].

In the inset of Fig. 2 a photoconductivity spectrum of the continuum part is shown. Both in absorption (main figure) and photoconductivity (inset) LO-Fano replicas of the $2P_{5/2}(\Gamma_8)$ and $2P_{5/2}(\Gamma_7)$ lines are clearly visible. The strongest LO-replica in photoconductivity is that of the $2P_{3/2}(\Gamma_8)$ state whereas it is hardly discernible in absorption. The dip at 123.63 meV can be interpreted as the LO-Fano replica of an excited state not observed in absorption. Its binding energy would be 25.3 meV. A tentative assignment is the $2S_{3/2}(\Gamma_8)$ state, although the binding energy is considerably larger than the EMT-value of 7.7 meV [13]. This large shift may very well be understood in terms of a central-cell shift since it is expected to affect s states more strongly than the p states.

Another set of replicas is also visible in the inset of Fig. 2. The difference between the sets is $\Delta = 2.88 \text{ meV}$ which is nearly identical to the difference between the LO and the TO phonons given in [11] (2.89 meV). A plausible interpretation of the se-

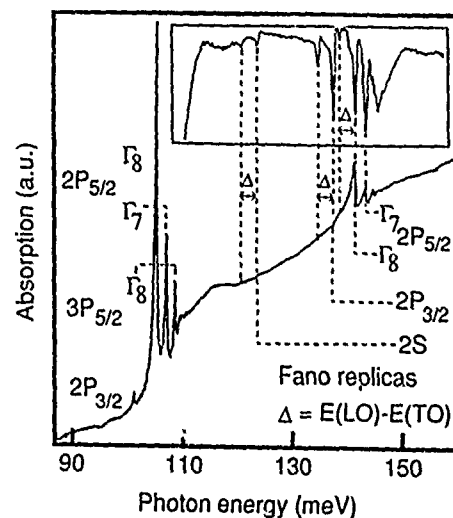


Fig. 2 Absorption (main figure) and photoconductivity (inset) of GaAs:Mn.

cond set of replicas would then be that they are TO-Fano replicas. According to the model presented in Ref. 8 there should be an excited state 2-3 meV above the ground state. An alternative explanation to the second set would then be that it is related to this excited state. However, we could not see any thermalization effect and the structure was not sensitive to changes in the intensity of the room temperature radiation.

Another puzzling fact is that there is a 3 meV difference between the excited state transitions reported in this paper and those of Ref. 4. The spectrum of Ref. 4 is smeared out but the three lowest excited states are still resolvable.

We also find oscillating photoconductivity above the ionization limit. The oscillations are temperature dependent. One interpretation of the oscillations is that a dip occurs in the photoconductivity when the excited hole via one or more LO-phonon emissions can reach a state from which it quickly can be captured by the center [13]. If the energy positions of the six lowest dips are used to obtain a linear fit, we get a phonon energy of 36.3 meV - similar to the energy of the LO phonon - and a final state for the phonon cascade 110.2 meV below the acceptor ground state. Since the binding energy of the ground state is 112.4 meV, this final state corresponds to an energy position 2.2 meV above the valence band. The interpretation of this energy position is at present unclear.

Zeeman results

In Fig. 3 the Zeeman results for the $2P_{5/2}(\Gamma_8)$ line with $B \parallel [001]$ is presented. Two components are observed when the electric-field vector E is parallel and three when perpendicular to B . The fourfold degeneracy of a Γ_8 (row index $m_j = \pm 3/2, \pm 1/2$) state is lifted by a magnetic field and the linear splitting is given by two g factors - $g_{3/2}$ and $g_{1/2}$ for each direction of B . The analysis of the experimental results is based on the model that Mn^0 has the ground state configuration $3d^5 + \Gamma_8$ and Mn^- has $3d^5$ (see Fig. 4). The observed hole spectrum is then due to excitation of the loosely bound hole at Mn^0 to excited p like shallow-hole states. The ground state for Mn^- is $6A_1$. The exchange interaction between the Γ_8 hole and $6A_1$ results in levels having $J=1, 2, 3$, and 4. The exchange interaction is expected to be small when the hole is in an excited p state considering their small amplitude at the impurity site. Furthermore, it is assumed that the $J=1$ level is the ground state of Mn^0 and in magnetic field exceeding about 1T only the $M_J=-1$ is thermally populated. The isotropic g factor of $6A_1$ is 2.003 and that for $J=1$ is 2.77 as deduced from EPR [8]. The $J=1$ component $|1, -1\rangle$ is given by

$$|1, -1\rangle = -\frac{\sqrt{2}}{2} |-\frac{5}{2}, \frac{3}{2}\rangle + \frac{\sqrt{30}}{10} |-\frac{3}{2}, \frac{1}{2}\rangle - \frac{\sqrt{15}}{10} |-\frac{1}{2}, -\frac{1}{2}\rangle + \frac{\sqrt{5}}{10} |\frac{1}{2}, -\frac{3}{2}\rangle \quad (1)$$

when expressed in the basis $|S=5/2, M_S\rangle |j=3/2, m_j\rangle$. The 12 allowed optical transitions for $B \parallel [001]$ are depicted schematically in Fig. 4. All four hole states are contained in the $|1, -1\rangle$ although with different weights (see Eq. 1) which accordingly affects the relative intensities of the lines experimentally observed. Since the state of the $6A_1$ core is not

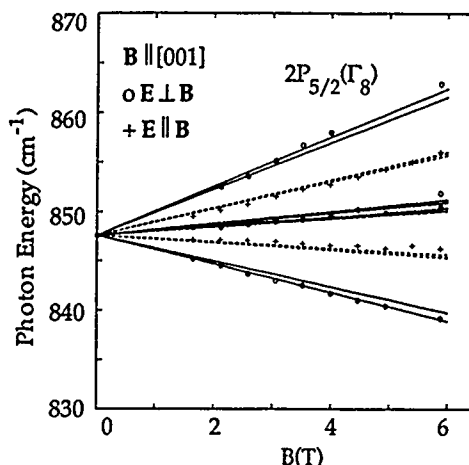


Fig. 3 Zeeman spectrum for the $2P_{5/2}(\Gamma_8)$ line with $B \parallel [001]$.

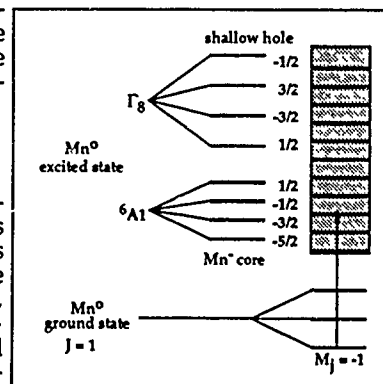


Fig. 4 Schematic figure showing the hole transitions when $B \parallel [001]$ according to the $3d^5 +$ hole model.

changed by the hole transition and only the $|1, -1\rangle$ is populated in the Zeeman experiment, only those $|S=5/2, M_S\rangle$ states found in Eq. 1 could be reached in the transitions. For longitudinal polarization, $E \parallel B$, four lines may be visible according to the selection rules for the $\Gamma_8 - \Gamma_8$ hole transitions: $\pm 3/2 \rightarrow \mp 1/2, \pm 1/2 \rightarrow \mp 3/2$ [12]. When $E \parallel B$, the relative intensity of the two lines experimentally observed is about 3.5. Assuming that in Ref. 10, the signs of the calculated g values for $2P_{5/2}(\Gamma_8)$ line is correct and that the absolute values are approximately correct it is found that the two lines contain two final states each (see Fig. 2). We find for $B \parallel [001]$: $g_{3/2} = -2.4$ and $g_{1/2} = 0.5$. Using these values, a satisfactory agreement is also obtained for $B \parallel [110]$ and $[111]$. It is interesting to note that the g values found for the $[001]$ directions implies that the g values for the $[110]$ and $[111]$ directions have about the same absolute values but different signs for $g_{3/2}$. The Zeeman spectrum is thus almost identical for all three main directions of the magnetic field since both the ground state and the $S=5/2$ core show isotropic splitting. In the fitting to the experimental data a g factor of 3 is used for the initial state which is somewhat larger than the value found from EPR. This may be explained by the much larger magnetic field used in this investigation compared with that used in EPR, considering that interaction between different spin-orbit levels of Mn^0 could be important for higher magnetic fields.

CONCLUSIONS

The experimental data presented gives strong additional evidence for the $3d^5 +$ shallow hole model for Mn^0 . However, yet puzzling facts exists e.g. the g value of 3.0 found in this work for the Mn^0 ground state compared that of 2.77 found in EPR. Furthermore, the additional Fano resonances observed in the photoconductivity experiment as well as the 2.2 meV "shift" of the valence-band edge deduced from the oscillating photocoductivity may have a common origin, although still unidentified.

ACKNOWLEDGMENTS

The authors would like to thank S. Ghatnekar for assistance with the Zeeman experiments and L. Timby for help with some of the sample preparations. We acknowledge financial support from the Swedish Natural Science Council and the Swedish Board for Technical Development.

Present address: The Royal Institute of Technology, Solid State Electronics, Box 1298, S-164 28 KISTA, Sweden

REFERENCES

1. L. J. Vieland, J. Appl. Phys. 33, 2007 (1962)
2. T. C. Lee and W. W. Anderson, Solid State Commun. 2, 265 (1964)
3. W. Schairer and M. Schmidt, Phys. Rev. B10, 2501 (1974)
4. R. A. Chapman and W. G. Hutchinson, Phys. Rev. Lett. 18, 443 (1967)
5. L. Montelius, S. Nilsson, L. Samuelson, E. Janzén, M. Ahlström, J. Appl. Phys. 64, 1564 (1988)
6. N. Almeleh and B. Goldstein, Phys. Rev. 128, 1568 (1962)
7. R. Bleekrode, J. Dieleman and H. J. Vegter, Phys. Lett. 2, 355 (1962)
8. J. Schneider, U. Kaufmann, W. Wilkening, M. Baeumler and F. Köhl, Phys. Rev. Lett. 59, 240 (1987)
9. M. Baeumler, B. K Meyer, U. Kaufmann, and J. Schneider, Materials Science Forum, 38-41, 797 (1989)
10. R. F. Kirkman, R. A. Stradling, and P. J. Lin-Chung, J. Phys. C: Solid-State, 11, 419 (1978)
11. A. Mooradian and G.B. Wright, Solid State Commun. 4, 431 (1966)
12. A. K. Bhattacharjee and S. Rodriguez, Phys. Rev. B6, 3836 (1972)

IDENTIFICATION OF SURFACE-RELATED ELECTRON TRAPS IN UNDOPED GAAS BY DEEP LEVEL TRANSIENT SPECTROSCOPY

KI-CHUL SHIN AND IN-SHIK PARK
GoldStar Cable Research Lab., 555 Hogye, Anyang, Kyungki, Korea,
430-080

ABSTRACT

Using undoped GaAs containing grain boundary, we performed annealing test to identify the processes occurring during heat treatment. We propose EL2 as a complex of double vacancy, As_{Ga} and As_i . From the concentration change at grain boundary region we temporarily conclude that EL3 is a simple intrinsic defect.

INTRODUCTION

In the processing of GaAs device, it is important to understand the nature of defects present to make best use of them or to get rid of them, if possible. The most dominantly found defect, EL2, has been studied very extensively, but the origin of it is not clear yet. Also the origin of EL3 level which is said to be related with the surface damage [1] is not verified.

It is well known that grain boundary in semiconductors works as a potential barrier. In the measurement of DLTS, this barrier has been used instead of surface Schottky barrier to study grain boundary region in GaAs [2]. Since a grain boundary acts as a sink for point or line defects, the annealing behavior of defects can easily be seen near grain boundary and this can be used to understand the annealing mechanism and the composition of deep level defects in GaAs.

EXPERIMENT

Samples were cut from horizontal Bridgman (HB) grown undoped GaAs crystal which is slightly As-rich. Measured carrier concentration was $6 \times 10^{16} / \text{cm}^3$, n-type. Sample was chosen such that grain boundary runs through the middle of the sample with size of $8 \times 1.2 \text{ mm}$. Sample thickness was $420 \mu\text{m}$. Annealing was performed at 200°C , 350°C , and 500°C for one hour in the flowing argon gas. Ohmic contacts were prepared by evaporating small dots of Au:Ge. DLTS measurement was done with Bio-Rad model number DL4600.

RESULTS AND DISCUSSION

Peak intensity change due to annealing

Figure 1 shows DLTS peak intensity change of observed traps in undoped GaAs grain sample for different annealing temperatures. According to Dannefefer et al's positron annihilation experiment [3], the most dominant point defect in undoped GaAs is double vacancy ($V_{Ga}V_{As}$) which anneals at $350^\circ\text{C} - 400^\circ\text{C}$. Therefore, in samples annealed below 350°C (hereafter called stage A anneal), point defects consist mostly of double vacancies, and in samples annealed at or above 350°C (hereafter called stage B

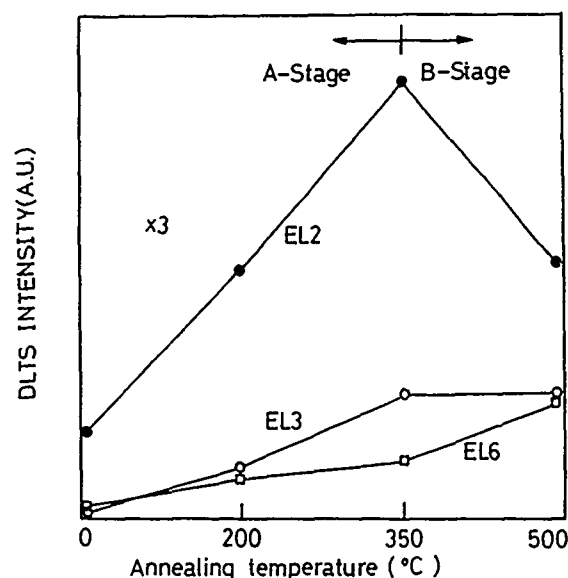


Fig. 1 Peak intensity change after annealing

anneal), double vacancy is no more prevailing species and single vacancy-related defect ($V_{Ga}As_{Ga}$) is the dominant one. From this argument, Wager et al [4] proposed that EL2 is a double vacancy-related defect ($V_{Ga}As_{Ga}V_{Ga}$ or $V_{As}V_{Ga}As_{Ga}$) and that EL2 forms a group of family. To explain the outdiffusion of EL2 under annealing, Min et al [5] suggested $V_{As}As_iV_{Ga}As_{Ga}$ to be a plausible model for EL2 on the basis of Wager's model. Then the annealing behavior of EL2 in Fig. 1 is well understood with Min's model. Under low temperature anneal (below 500°C), As_i gathers around grain boundary by long range migration [6] to produce EL2 level by combining with double vacancy (stage A), and in the stage B anneal, double vacancy concentration decreases resulting in reduced EL2 concentration, [EL2].

EL3 and EL6, on the other hand, show different behavior, i. e., EL3 is very stable through our annealing test and EL6 is the only species that increases in the stage B anneal. Only $V_{Ga}As_{Ga}$ can increase in concentration in the stage B anneal and it is reported that As_{Ga} anneals at considerably high temperature [6]. Therefore, we believe that EL6 is related with $V_{Ga}As_{Ga}$. EL3 which shows very stable behavior in stage B anneal is not considered to be one of V_{As} -related defects because most of V_{As} disappear in the stage B anneal [6].

Depth Profile

Depth profile of DLTS peaks for different annealing temperature is shown in Fig. 2. [EL2] increases near grain boundary while [EL3] and [EL6] decrease. Grain boundary acts as sink for point defects [6,7] and forms a highly distorted region. The increase of [EL2] near grain boundary suggests that EL2 is a high order complex of intrinsic defects. From the observation

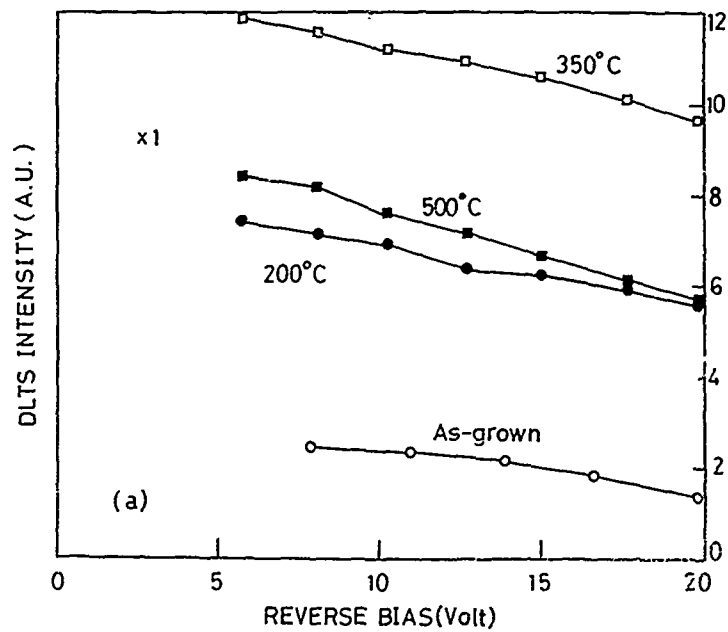


Fig. 2(a) Depth profile of EL2

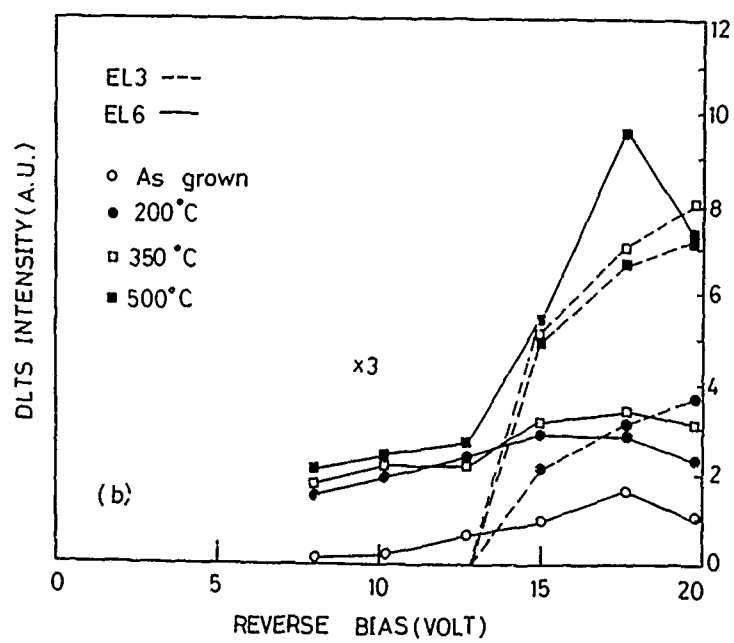


Fig. 2(b) Depth profile of EL3 and EL6

that [EL3] and [EL6] decrease near grain boundary we assume that these traps are either intrinsic or relatively simple defect complexes. The drastic decrease of [EL3] near grain boundary suggests that EL3 is a very simple defect. Defect which is simple in nature and thermally stable in the stage B anneal is one of the two antisite defect, As_{Ga} or Ga_{As} [6]. As we used crystal grown slightly As-rich, we temporarily conclude EL3 is As_{Ga} . This assumption also explains the sharp decrease of [EL3] near surface by outdiffusion of As under annealing at 800°C [1].

CONCLUSION

EL2 is a relatively complicated defect and the annealing behavior can best be explained by double vacancy model, $\text{V}_{\text{As}}\text{As}_i - \text{V}_{\text{Ga}}\text{As}_{\text{Ga}}$. We propose EL3 to be a simple intrinsic defect (probably As_{Ga}) since it is thermally stable in the temperature range 350°C-500°C and decreases drastically near grain boundary. EL6 is assumed to be a simple complex, $\text{V}_{\text{Ga}}\text{As}_{\text{Ga}}$.

REFERENCES

1. F.D. Aurret, A.W.R. Leitch, and J.S. Vermaak, J. Appl. Phys. 59, 158 (1986).
2. M. Spencer, R. Stall, L.F. Eastman, and C.E.C. Wood, J. Appl. Phys. 50, 8006 (1979).
3. S. Dannefear and D. Kerr, J. Appl. Phys. 60, 591 (1988).
4. J.F. Wager and J.A. Vechten, Phys. Rev. B36, 2330 (1987).
5. S.K. Min, E.K. Kim, and H.Y. Cho, J. Appl. Phys. 63, 4422 (1988).
6. J.V. Bourgoin and H.J. von Bardeleben, J. Appl. Phys. 64, R65 (1988).
7. J. Marek, A.G. Elliot, V. Wilke, and R. Geiss, Appl. Phys. Lett. 49, 1732 (1986).

LUMINESCENCE DUE TO Mn DOPED GaP

TERESA MONTEIRO AND ESTELA PEREIRA

Departamento e Centro de Fisica (INIC), Universidade de Aveiro, Portugal

ABSTRACT

In n-type GaP doping with Mn gives rise to a deep centre due to Mn^{+2} . Its luminescence occurs in the near infrared.

The behaviour of this centre is studied as a function of temperature and the thermal quenching of the luminescence interpreted as due to a non-radiative process to the ground state. The behaviour of another band that appears upon doping with Mn is also discussed.

INTRODUCTION

The growing interest in III - V compounds have rendered important the knowledge of the effect of the presence of transition metals in these crystals. GaP is the only III - V material where Mn originates a deep centre due to Mn^{+2} . The luminescence and EPR spectra of this centre is known [1,2]. Mn is the transition metal with higher solubility in GaP (ca. $10^{-19} cm^{-3}$), but has a small diffusion coefficient. Therefore it is easier to obtain Mn doped samples by an in-growing process than by diffusion into the crystal.

The Mn^{+2} luminescence occurs in the near infrared and is due to a ${}^4T_1 \rightarrow {}^6A_1$ transition. A splitting of the 4T_1 level of 9.5 meV is observed with an identical transition probability to the ground state as shown by the temperature behaviour of the two corresponding ZPL, and the corresponding lifetime of the luminescence up to 77 K [1].

In order to get a more detailed knowledge about the Mn^{+2} luminescence in GaP we studied the behaviour of this luminescence as a function of temperature and time. In all Mn doped samples an extra unstructured luminescence band (red band) at higher energies is observed although its intensity does not correlate with the Mn^{+2} intensity. The luminescence excitation spectra of the two bands is also different for excitation within the band gap although for both the more efficient process of excitation is above band gap.

EXPERIMENTAL DETAILS

The samples used in this work were of two different origins: in one Mn has been grow-in in the presence of excess of donors (mainly sulphur) with a Mn concentration of 10^{-5} g/g, in the others n-type LEC grown GaP (sulphur and carbon present) has been doped by vapour deposition of Mn followed by diffusion in an evacuated quartz ampoule 23h at $1100^\circ C$, giving a lower Mn concentration.

Time resolved luminescence spectra and lifetime measurements were carried out with a Spex 1934C phosphorimeter; luminescence excitation was observed using a W-lamp. Steady state spectra were measured using an Ar-Laser as excitation source. The samples were held in the cold tip of a closed cycle He cryostat.

EXPERIMENTAL RESULTS

In Fig. 1 the steady state luminescence of a Mn doped GaP sample is shown.

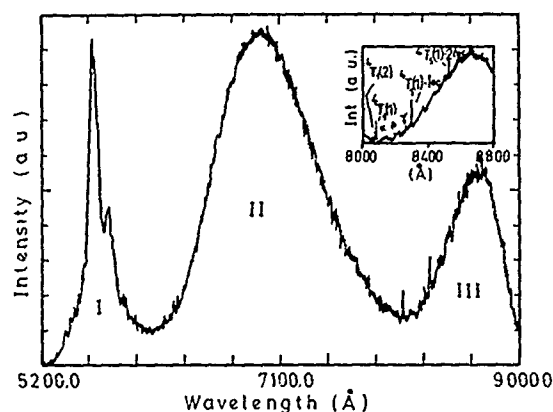


Fig. 1 - Uncorrected luminescence spectrum of Mn doped sample at 11 K, excited by the 488 nm Ar laser line. Insert: luminescence spectra of Mn^{+2} .

Besides the D-A luminescence (S-C) (region I) two bands are observed: a broad band in the red with maxima at 1.80 eV (region II) and the Mn^{+2} luminescence (region III). This latter agrees with the previously reported Mn^{+2} luminescence [1]. Although the red band occurs only in Mn doped samples it doesn't correlate with Mn luminescence for different samples. Upon increasing temperature the Mn^{+2} luminescence decreases (above 60 K) and the red luminescence changes, showing a new maximum at 1.72 eV (above 80 K) while the band with maximum at 1.80 eV decreases.

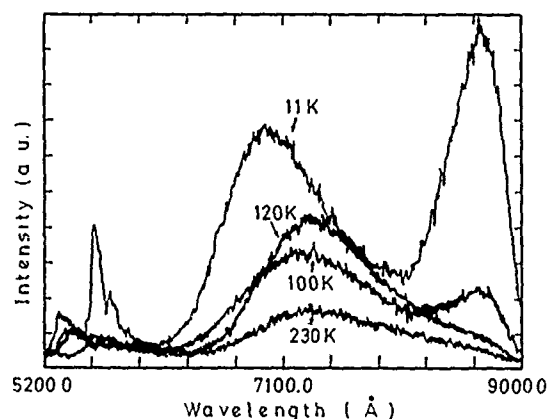


Fig. 2 - Uncorrected steady state luminescence spectra at several temperatures.

Time resolved spectra show a single exponential decay behaviour for the Mn^{+2} luminescence, according to previous results [1]. The decrease in intensity (Fig. 3a) matches the decrease in decay time above 60 K (Fig. 3b). The red band shows a non-exponential decay, that may be fitted to two exponentials. The different decays are also shown in Fig. 3b.

Monitoring at different wavelengths over the band gives the same decays but with different intensity ratios of the two components (Fig. 3a). The ratio of the two components intensities shows that the faster decay corresponds to a band shifted slightly towards higher energies and that amounts at most to 10% of the luminescence at low temperature. Above 100 K the band with maximum at 1.80 eV is nearly completely quenched and the new band with maximum at 1.72 eV shows a lifetime of the order of 200 ms. This band increases up to 150 K decreasing then slightly up to room temperature. Time resolved spectra are shown in Fig. 4.

Both red band and Mn luminescence are more efficiently excited by above band gap excitation, but the Mn excitation shows three other excitation bands one of which is nearly the mirror image of luminescence.

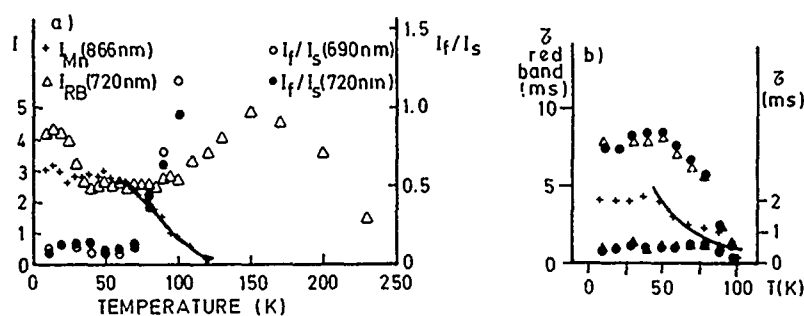


Fig. 3a - Temperature dependence of the intensity: + Mn luminescence, Δ red band luminescence. Intensity ratio of the two decay components: ○ at 1.80 eV and ● 1.72 eV; b - Temperature dependence of lifetimes: + Mn²⁺ lifetime, Δ red band lifetime monitored at 1.80 eV, ● red band lifetime monitored at 1.72 eV

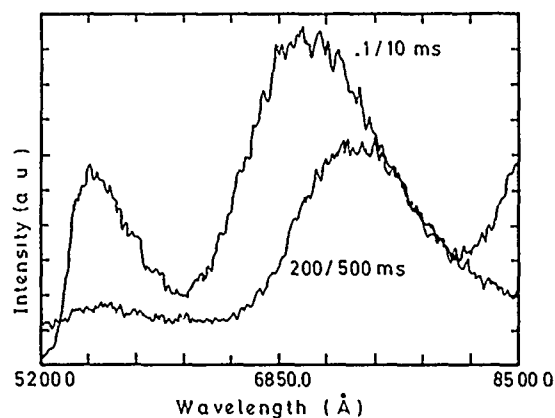


Fig. 4 - Time resolved spectra taken between .1/10 ms and 200/500 ms at 110 K

DISCUSSION

The Mn²⁺ centre in GaP is an efficient luminescing centre at low temperature, but at temperatures above 60 K non-radiative processes become dominant. A study of the relative intensity and decay behaviour shows that it is a non-radiative process internal to the centre that causes the quenching of the luminescence. The decay at low temperature is of the order of magnitude found in other Mn²⁺ centres in different hosts [3] and also what would be expected from a spin forbidden transition. Therefore it may be taken as the radiative decay from the centre. Our value is somewhat larger than the previously reported value of 1.4 ms [1]. It has been checked by time resolved spectra, allowing for any tail of the red band luminescence. The thermal quenching can be accounted for in a classic model assuming that quantum mechanical tunneling is not significant (quantum efficiency of one at low temperature). A best fit to both decay and intensity is given by $W_{nr} = W_0 \exp(E_a/KT)$ with $W_0 = 10^4 \text{ s}^{-1}$ and $E_a = 30 \text{ meV}$. W_0 is of the order of magnitude to be expected for a non-radiative transition between states with different spin multiplicity indicating that the non-radiative decay takes place to the ground state.

Although the origin of the red luminescence can not be definitely assigned to Mn, one interesting fact is that it only occurs in Mn doped

samples. In GaP several broad bands are known in the same spectral region [4], but this band has a different behaviour.

Unfortunately no ZPL could be observed even at 11 K. However the experimental results may be interpreted assuming that the red luminescence originates into different centres at low temperatures. This explains the two exponential decays found, the difference in its intensity, and different temperature behaviour. The results indicate that the faster band has a maximum shifted slightly towards higher energies (change of intensity ratios when monitoring at lower energies). However its low intensity prevents a meaningful time resolved spectral analysis. The new band that occurs above 100 K has quite a different behaviour. The most striking feature is the long lifetime.

These bands, although broad don't show the characteristic behaviour of D-A pair recombination [5]. On the other hand it is known that Mn makes readily complexes in GaP identified by EPR and ENDOR [2,6,7,8]. Therefore these luminescence may be due to complex formation. It is interesting to note that also in $\text{Al}_x\text{Ga}_{1-x}\text{As}$ Mn doped samples above 100 K a broad band at higher energies occur [9]. Although the 1.72 eV band appears when Mn^{+2} luminescence is most strongly quenched its long lifetime makes it unlikely that it is due to thermal population of another Mn^{+2} excited level, eg. the 4T_2 . An hypothesis that is currently being tested is the possibility that this new band involves ionization of the excited 4T_1 level of Mn^{+2} .

CONCLUSIONS

The radiative and non-radiative processes due to the presence of transition metal ions in III - V materials has not been extensively studied. Mn^{+2} in GaP is an efficient luminescence centre at low temperatures, but becomes a non-radiative centre at higher temperatures. Therefore it competes with other deexcitation processes like D-A recombination.

The new band, upon Mn doping, in the red has a behaviour that excludes D-A pair luminescence.

All these luminescence bands are more efficiently excited by above band gap excitation, although the Sulphur exciton also may transfer energy to these centres.

Further work is under way to get detailed information about the other excited levels of Mn in order to get a more precise value of the energy levels of Mn^{+2} in GaP.

ACKNOWLEDGEMENTS

Financial support from INIC and JNICT is acknowledged. One of us T.M. thanks INIC for a maintenance grant. We are grateful to Dr. Kaufman for the loan of a Mn doped sample, Dr. Gumlich for making available some unpublished results and Dr. Curie for his interest in this work. Mr. J. Januário and Mrs. I. Calao helped in the experiments.

REFERENCES

1. A.T. Vink and G.G.P. Van Gorkom, *J. Lum.* **5**, 379 (1972)
2. G.G.P. Van Gorkom and A.T. Vink, *Solid St. Comm.*, **11**, 767 (1972)
3. D. Fournier, A.C. Bocara and J.C. Rivoal, *J. Phys. C: Solid St. Phys.* **10**, 113 (1977)
4. J.M. Disham and D.F. Daly, *J. Appl. Phys.* **43**, 11 (1972)
5. P.J. Dean, *Progress in Solid St. Chemistry* **8**, 1 (1973)
6. R.S. Title and T.S. Plaskett, *Appl. Phys. Lett.* **14**, 2 (1969)
7. P. Van Engelen and S.J. Sie, *Solid St. Comm.* **30**, 515 (1979)
8. P. Van Engelen, *Phys. Rev. B* **22**, (7), 3144 (1980)
9. F. Bautien, J. Weber, *Phys. Rev. B* **37** (17), 10111 (1988)

PART IV

Electronic Structure -
Complexes in Silicon

HIGH PERFORMANCE PHOTOLUMINESCENCE SPECTROSCOPY USING FOURIER TRANSFORM INTERFEROMETRY

M.L.W. THEWALT, M.K. NISSEN, D.J.S. BECKETT AND K.R. LUNDGREN
Department of Physics, Simon Fraser University, Burnaby, BC, Canada V5A 1S6

ABSTRACT

We present recent results on the applications of Fourier transform techniques to photoluminescence spectroscopy as it relates to both basic and characterization-related semiconductor research. The emphasis here is on demonstrating the advantages of these methods in situations requiring very high spectral resolution and/or very high sensitivity. We also provide an example of the utility of interferometry in performing photoluminescence excitation spectroscopy in spectral regions where broadly tunable laser sources are not readily available.

INTRODUCTION

Fourier transform (FT) spectroscopy using variations of the Michelson interferometer has long been accepted as the technique of choice for absorption measurements in the mid- to far-infrared (MIR to FIR). More recently, Fourier transform photoluminescence spectroscopy (FTPLS) has been recognized as having certain advantages over the more customary dispersive PLS in the near-infrared (NIR) to MIR region, where sensitive photon-counting detectors, such as photomultiplier tubes are as yet unavailable (e.g.: $\lambda \geq 1\mu\text{m}$).¹⁻⁴ Here we refer for example to the work of McL Colley and Lightowers² on Si characterization using FTPLS, to the existence of a commercial FTPLS system dedicated to Si characterization³, and to the recent well-resolved and noise-free FTPLS spectra of the narrow-gap semiconductor InSb presented by Rowell⁴. It is also becoming evident that various manufacturers of interferometer systems are increasingly interested in FTPLS as a new applications area for their products.

Even so, it seems to us that practitioners of PLS have not yet fully explored and appreciated the major benefits of the FT techniques, in that most of the work reported so far could also have been done on readily available dispersive spectrometers. In addition, very little FTPLS has been done at all in the shorter wavelength region ($\lambda \leq 900\text{nm}$), where highly sensitive photon-counting detectors exist, and FTPLS is therefore commonly thought to offer no advantages over dispersive spectrometry.

In this paper we will demonstrate some of the unique capabilities of FTPLS with a number of examples of spectroscopy which would range from very difficult to next to impossible using any practical dispersive spectrometer. Special emphasis is placed on high-resolution FTPLS in the shorter wavelength region ($\lambda \leq 900\text{nm}$), since it is here that the capabilities of interferometry are least appreciated. We will also demonstrate the utility of FT techniques for performing photoluminescence excitation spectroscopy (PLES) in spectral regions where widely-tunable laser sources are not readily available. Before turning to the experimental results, we begin with a brief review of the potential advantages of interferometry over dispersive spectroscopy.

ADVANTAGES (AND DISADVANTAGES) OF INTERFEROMETRY

The two benefits of FT interferometry which are often referred to are the multiplex or Fellgett⁵ advantage, and the throughput or Jacquinot⁶ advantage. The multiplex advantage arises from the fact that in interferometry the detector simultaneously records all of the optical signals, while in single channel dispersive spectrometry it sees only a

single spectral channel at any given time. This results in a (theoretical) multiplex improvement in the signal-to-noise ratio (SNR) of \sqrt{N} , where N is the number of resolution elements collected in the spectrum, *provided that the system noise is dominated by detector noise* (i.e. the noise level coming out of the detector is unaffected by the presence or absence of the optical signal being measured). This is in fact often the case when measuring weak signals with inherently noisy detectors such as photodiodes or photoconductors. On the other hand, when measuring intense spectra, or when using essentially zero-background-noise detectors such as photomultiplier tubes, the noise level is dominated by noise in the signal itself, in which case there are two limiting regimes. In the ideal case of shot noise, the noise increases as the square root of the signal intensity, and the multiplex advantage favouring interferometry is exactly cancelled out. If, however, the noise amplitude increases linearly with increasing signal level (flicker noise), then interferometry actually has a multiplex *disadvantage* of \sqrt{N} .

Fortunately, interferometry offers another significant advantage over dispersive spectroscopy, namely the throughput advantage, which is particularly important when very high spectral resolution is required. For example, we can compare our interferometry with a high quality grating instrument (1 m double spectrometer, f8 optics, 1800 grooves/mm gratings) operated under identical conditions (say $\lambda \approx 800\text{nm}$, resolution = $13\mu\text{eV}$, or 0.10 cm^{-1}). Under these conditions the interferometer entrance aperture is 1.7 mm in diameter, while the spectrometer entrance slit is $30\text{ }\mu\text{m}$ wide as calculated from the reciprocal linear dispersion. Even assuming that the entire 2 cm height of the slit can be illuminated by the signal, the interferometer still has a much greater entrance area (2.3 mm^2 vs. 0.6 mm^2) as well as a greater solid angle (f4 vs. f8). Furthermore, in most practical PL experiments, one can usually focus a far greater fraction of the PL through a round aperture than through a slit with a $\sim 600:1$ length/width ratio.

In addition to the above two considerations, interferometry offers the following more general advantages:

1. Broad spectral capabilities - modern interferometers can now offer high performance from the FIR to the ultraviolet (UV) in a single compact instrument, using only a small number of interchangeable beamsplitters.
2. Wide spectral capability in a single scan - modern beamsplitters offer high efficiency over more than a decade of wavelength range, so one can in principle collect a PL spectrum from $10\,000\text{ cm}^{-1}$ to 1000 cm^{-1} in a single scan (detector permitting!) without any problems of aliasing or order sorting. This range is of course unattainable in a grating instrument. It should be emphasized that interferometry automatically collects the entire spectrum falling within the detector/beamsplitter/filter passband - there is no acquisition time penalty in collecting very wide spectra, as there is with dispersive spectrometry. This point is easily forgotten when looking at a figure which shows only a tiny segment of the FTPLS spectrum, but it can be of major significance when collecting broad survey-type spectra.
3. High spectral accuracy - since modern interferometers are typically referenced against frequency-stabilized He:Ne lasers, they provide very high spectral accuracy (better than 0.02 cm^{-1} at $10\,000\text{ cm}^{-1}$) without any need for calibration, or particular care in the measurement. Similar accuracy in dispersive spectrometry can only be obtained by frequent and painstaking calibration against known spectral lines.
4. Tradeoffs - interferometers offer very wide latitude in selecting the tradeoffs between spectral resolution, collection time, and SNR. Thus the same instrument performs well when collecting quick, wide, low resolution scans and lengthy high resolution scans. The same is not generally true of grating spectrometers.

EXPERIMENT

The spectra recorded here were collected on a Bomem DA3 interferometer system which was unmodified except for the mounting of external detector systems and PL collection optics. We chose to run the PL signal through the interferometer in the opposite direction of the normal internal light paths for practical reasons; thus our detector optics are mounted at the 'emission port'. The PL is collected from the sample by an off-axis parabolic mirror, and the collimated beam enters the interferometer through a 4 inch clear aperture quartz vacuum window. The spectral resolution is controlled by an adjustable aperture located at the focus just outside the 'emission port' window. The detector focusing optics include space for filters which are needed to block the scattered light from the excitation laser, as well as leakage light from the internal He:Ne laser and the white-light reference interferometer beams.

The Si and GaAs PL was detected by a 1 mm diameter liquid nitrogen (LN_2) cooled InGaAs diode sensitive from ~ 800 nm to $1.5 \mu\text{m}$, while the Ge PL was detected by a LN_2 cooled InSb detector shielded by a LN_2 cooled $2 \mu\text{m}$ short-pass filter. The Si and Ge PL was excited by an Ar-ion laser, while the GaAs results were obtained with excitation from a continuous-wave Ti-sapphire laser. In all cases the samples were immersed in superfluid He. A more detailed account of the apparatus will be given elsewhere.

RESULTS

Copper-doped Germanium

We begin with an example demonstrating the sensitivity advantage of FTPLS in an experiment requiring only moderate resolution, but in which the very weak signal is comparable in intensity to the detector noise. Substitutional Cu in Ge is the prototypical triple acceptor impurity, and its MIR electronic absorption spectrum has been thoroughly studied⁵, but until now there has been no report of bound exciton (BE) PL from this (or any other) triple acceptor. We had looked for such PL for several years using dispersive spectrometry and never observed anything, presumably due to the low radiative quantum efficiency of triple acceptor BE and to the exciton-scavenging effects of Cu complexes and precipitates.

When observing the *total* (no spectral selection) chopped PL signal of typical Ge:Cu samples passed through the interferometer the signal was found to be at most 2 to 3 times the detector noise level. In a single scan, the interferogram center-burst was almost invisible in the noise, but after sufficient averaging excellent spectra could be obtained, as shown in Fig. 1. The new BE transition, whose phonon replicas are labelled Cu_{LA} etc. (the stronger no-phonon line Cu_{NP} , is not shown) can be conclusively identified as being due to the Cu triple acceptor since the 2-hole transitions at the left of Fig. 1 (2S, 3S,...) converge to an ionization energy of 43.26 ± 0.03 meV, in excellent agreement with the value of 43.25 ± 0.01 meV determined for Cu by MIR absorption.⁵ A more detailed account of the Ge:Cu results will be published elsewhere, including higher resolution spectra which reveal unexpected structure in the NP transition.

Bound Multiexciton Complexes in Silicon

For our second example we will consider the ultra-high resolution FTPLS of a system which has been widely studied at lower resolution using dispersive spectroscopy, namely Si doped with P. Si:P has a rich spectrum consisting of PL due to the BE line, α^1 , as well as lines due to bound

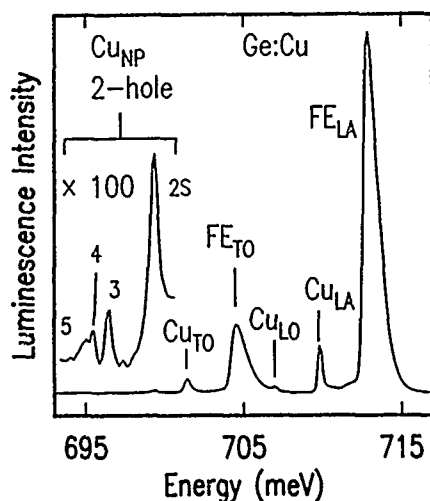


Fig. 1 Photoluminescence spectrum of Cu-doped Ge. FE_x represents the x-phonon replica of the free exciton, while Cu_x similarly refers to Cu BE replicas. At the left the Cu BE no-phonon (NP) 2-hole transitions are shown on an expanded scale.

multiexciton complexes (BMEC's) containing two to five electron-hole (e-h) pairs (α^2 to α^5).⁶ In Fig. 2 we show a 'normal' high resolution scan (res. = 0.5 cm^{-1} or $\approx 0.06 \text{ meV}$) taken with the interferometer which shows the usual Si:P BE and BMEC spectrum in the NP region. Even in this spectrum it is apparent that the BE line is narrower than any of the BMEC lines.

In fact, the α^1 line is expected to consist of a single component, while the BMEC transitions can have complicated initial and final state splittings due to e-e, e-h and h-h interactions. The search for this fine structure has been impossible using dispersive spectrometers, since almost all lack the needed resolution, and in any case the throughput would be too low to allow for an adequate SNR. BMEC fine structure has been detected previously in tour-de-force experiments in which moderate resolution grating spectrometers were used to select a given α^n line, and a scanned Fabry-Perot interferometer was used to provide high resolution spectral information over the selected region.^{8,9} These demanding measurements required a special purpose apparatus which is difficult to align and by its very nature is limited to fairly narrow regions of spectral coverage.

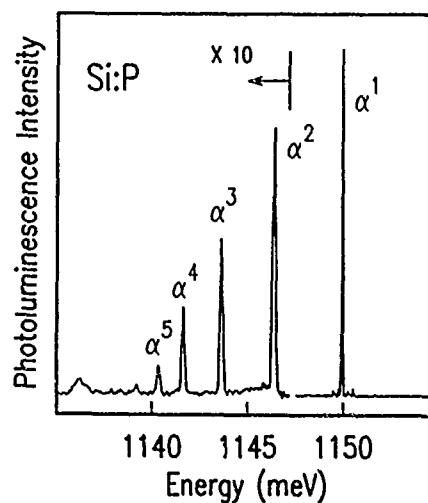


Fig. 2 Typical no-phonon photoluminescence spectrum of Si:P.

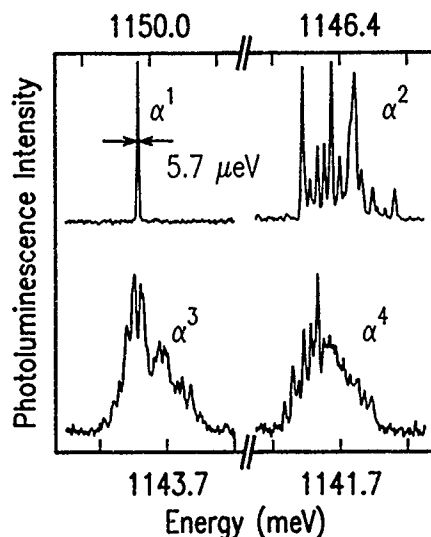


Fig. 3 Very high resolution spectra of four of the Si:P lines shown in Fig. 2. The energy interval between tick marks is 0.2 meV.

In Fig. 3 we show spectra of $\alpha^1 - \alpha^4$ obtained by FTPLS at an instrumental resolution of 0.02 cm^{-1} ($2.5 \mu\text{eV}$), far beyond that used in the earlier studies. We emphasize that these spectra were collected quickly and without any particular 'tricks' on an unmodified interferometer, which by its very nature can provide similar performance at any arbitrary wavelength. The resolution \cdot SNR product of our spectra is more than an order of magnitude better than that achieved through the previous painstaking non-FT methods,^{8,9} and we can therefore resolve a wealth of new structure. There are at present no theoretical predictions with which this fine structure can be compared. The observed $5.7 \mu\text{eV}$ full-width at half-maximum (FWHM) of the α^1 BE line (not corrected for instrumental broadening) is to our knowledge the sharpest non-resonantly excited BE transition ever reported. The $E/\Delta E$ of 200 000 is remarkable considering that such transitions are fully sensitive to inhomogeneous broadening effects due to shifting or splitting of the band edges resulting from random strains etc.

Magneto-photoluminescence in Gallium Arsenide

The last application of FTPLS we consider here is the high resolution PLS of GaAs epilayers, including magneto-photoluminescence (MPL) for shallow donor identification.¹⁰⁻¹⁴ This is a more unusual area for the FT method, since spectroscopy in this area is dominated by grating spectrometers and high-quantum-efficiency, low-dark-count, cooled photomultiplier tubes using GaAs photocathodes. Thus there is no multiplex advantage for FTPLS, but we will nevertheless demonstrate that it is competitive in this spectral region, primarily due to the throughput advantage. Other advantages of FTPLS in this application include its high spectral accuracy, and its ability to provide extremely high spectral resolution from a compact, general purpose instrument.

In Fig. 4 we show a wide portion of the medium resolution (0.25 cm^{-1} or 0.03 meV) FTPLS spectrum of a high quality MOCVD GaAs sample ($\mu_{77} = 115 \text{ 000 cm}^2/\text{V}\cdot\text{s}$) non-resonantly excited at 720 nm. It should be emphasized that the spectrum was actually collected out to the detector cutoff of $\sim 1.5 \mu\text{m}$ (830 meV). The total time for collection and transformation of such a typical 'normal' resolution spectrum is about 3 minutes. We identify some of the usual GaAs PL features: the C and Zn donor-acceptor-pair bands,

(D^0, C^0) and (D^0, Zn^0), the C free-to-bound transition (e, C^0), and in the rather compressed excitonic region only the acceptor BE (A^0, X) and donor BE (D^0, X). In Fig. 5 the excitonic region of the same spectrum is expanded to better reveal the structure of the (A^0, X) and (D^0, X) regions.

The (A^0, X) and (D^0, X) regions are further expanded in Figs. 6 and 7, which are taken from very high resolution FTPLS spectra (instrumental resolution 0.02 cm^{-1} or $2.5 \text{ } \mu\text{eV}$), again using excitation at 720 nm . These are to our knowledge the most highly resolved non-resonantly excited GaAs PL spectra yet reported. In Fig. 6 we can refer for example to the uncorrected $10.4 \text{ } \mu\text{eV}$ (A^0, X) line FWHM, and the complete separation of the C BE $j = 5/2$ component from the Zn BE $j = 3/2$ component. This spectrum was obtained from a single interferometer scan, with a total acquisition plus FT time of under 10 minutes. The (D^0, X) spectrum shown in Fig. 7 reveals to our knowledge the best reported resolution of the splitting between the (D^0, X) ground state (0) and the first non-rigid rotator excited state (1),¹⁵ which we measure to be 0.052 meV . The apparent FWHM of the 0 and 1 (D^0, X) transitions are $\sim 0.027 \text{ meV}$, but unresolved shoulders on the high energy sides of both lines may in fact be due to the presence of more than one donor species in this sample, as revealed in more detail in the next section. The 'X' label in the figure refers to the free exciton or polariton.

The identification of different shallow donor species in GaAs and other III-V materials is one of the most difficult tasks in the field of semiconductor characterization via optical techniques, due to the extremely small chemical shifts between different donors. The technique of choice in the past has been photothermal ionization spectroscopy (PTIS) in the FIR region, with the addition of a magnetic field to somewhat enhance the magnitudes of the chemical shifts between donor species.¹⁶ More recently, magneto-photoluminescence (MPL) has been shown to be a promising technique for donor identification in GaAs.¹⁰⁻¹⁴ It has several advantages over PTIS, not the least of which is the elimination of the need for sample preparation and the forming of ohmic contacts. All of the previous MPL work has relied on dispersive spectrometry.

The MPL spectra recorded here were obtained under the same conditions used in the recent study by Skromme *et al.*,¹⁴ namely a field of 12 T in a bottom-access magnet with samples in the Faraday configuration and at a temperature of $\sim 1.7 \text{ K}$. In contrast to Skromme *et al.* we were able to use a very simple optical system for collecting the PL, namely a single large plano-convex glass lens located outside the dewar to collimate the PL and four flat Al-coated mirrors to direct the collimated beam from the magnet dewar to the interferometer entrance window over a path length of $\sim 5 \text{ m}$. This simple system performs adequately, thanks to the large, circular entrance aperture of the interferometer.

In Fig. 8 we show a fairly broad section of a medium resolution (0.25 cm^{-1} or 0.03 meV) FTPL spectrum of the same GaAs sample used for the zero-field spectroscopy. In addition to the acceptor BE (A^0, X) and the principal donor BE (D^0, X) transitions (considerably complicated by magnetic splittings), we have shown the (D^0, X) two-electron transitions (tet) which leave the donor in the $2p_0$ or $2p_1$ final state after the PL transition. It is the tet which are used for donor identification in MPL, since these show a much larger chemical shift than do the principal (D^0, X) transitions.¹⁴ In Fig. 9 the principal (D^0, X) transitions of Fig. 8 are shown on an expanded scale, and labelled according to the scheme of Skromme *et al.*¹⁴

In Fig. 10(a) we show a high resolution spectrum (0.05 cm^{-1} or 0.006 meV) of the principal (D^0, X) lines of this sample when excited at the $n = 2$ polariton energy. Excitation at the polariton energy or at one of the BE excited states increases the PL intensity as compared to the previous examples where 720 nm excitation was used, but raises the problem of preventing the laser light from reaching and saturating the detector. This was achieved by a high performance four cavity interference filter having FWHM $= 1 \text{ nm}$ and a center $\lambda = 820 \text{ nm}$ at normal incidence. This filter could

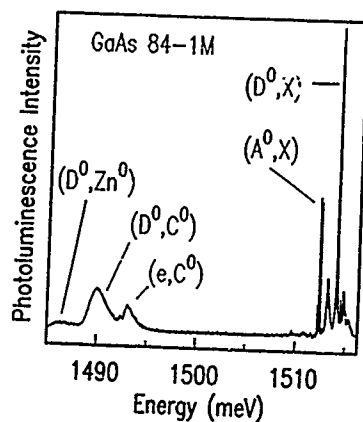


Fig. 4 Wide photoluminescence spectrum of high purity GaAs. The labels are described in the text.

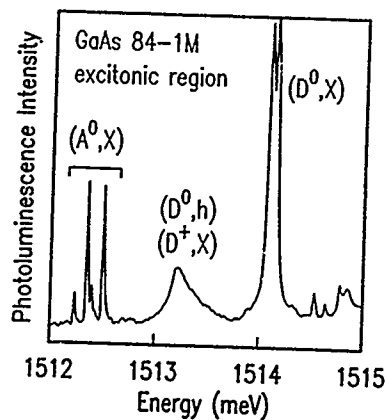


Fig. 5 Expanded view of the excitonic region from Fig. 4.

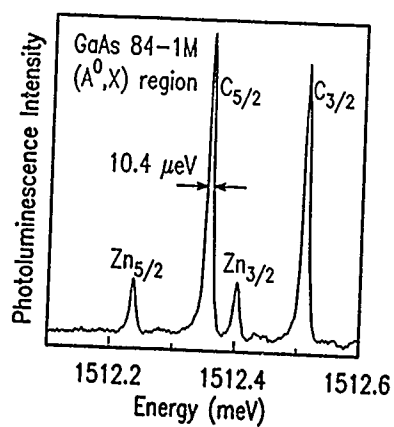


Fig. 6 High resolution photoluminescence spectrum in the acceptor bound exciton region for the same sample.

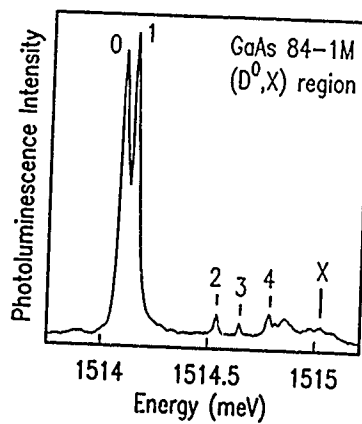


Fig. 7 High resolution photoluminescence spectrum in the donor bound exciton region for the same sample.

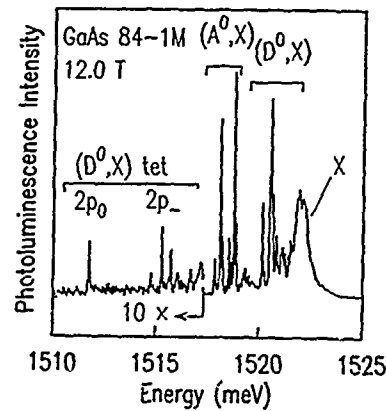


Fig. 8 Magneto-photoluminescence spectrum of the same sample taken at 12 T. The donor bound exciton two-electron transitions (tet) are shown on an expanded scale at the left.

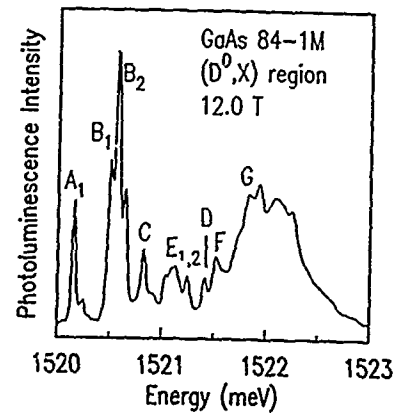


Fig. 9 Expanded view of the principal donor bound exciton transitions from Fig. 8.

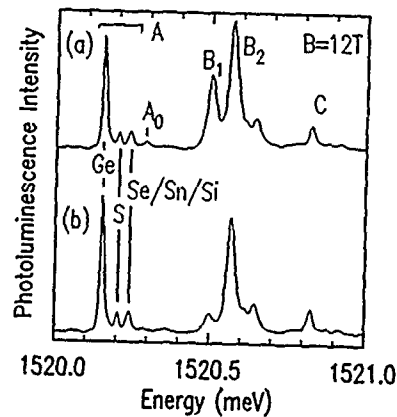


Fig. 10(a) High resolution magneto-photoluminescence spectrum over the principal donor bound exciton region with excitation into the $n = 2$ polariton. (b) As (a) but with a circular polarizer to reduce A_0 and B_1 intensities.

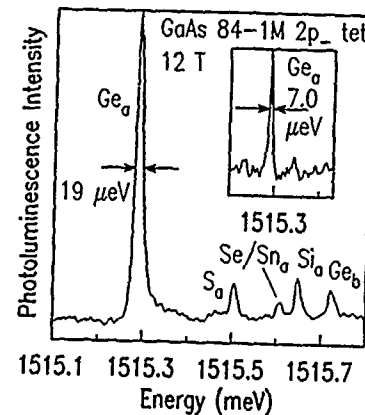


Fig. 11 High resolution photoluminescence spectrum over the $2p_-$ two electron transition region under the same conditions as Fig. 10(b). The inset shows the narrowing of the Ge_a $2p_-$ line when resonantly pumping the center of the principal Ge A line.

be angle-tuned to pass a ~ 1 nm band anywhere from the $2p_0$ tet to the principal (D^0, X) excited states at 12 T, and was very effective in blocking scattered excitation light even when the laser was tuned to only 4 meV above the PL region being observed. One could in general also use a small, high-throughput spectrometer as a tunable detector filter in situations where high rejection is needed such as in the resonantly excited PL studies reported here. The best choice might be a subtractive dispersion double spectrometer which would offer very high rejection outside the rectangular passband and whose high- and low-energy edges could be separately adjusted as desired.

In Fig 10(b) the same spectrum is shown with the addition of a circular polarizer in the PL path, which has been shown to considerably simplify the spectrum in the $2p_0$ and $2p_-$ tet region.^{12,14} In Fig 10(b) we see that the circular polarizer also has the same effect on some of the principal (D^0, X) transitions, primarily in reducing the A_0 and B_1 peaks. The comparison of Figs. 10(a) and 10(b) make it clear that the three lowest energy peaks all have the same polarization character, and are thus all A-type peaks. Skromme *et al.* have previously reported structure in the A-line region which they could attribute to transitions involving different donor BE, but these were not so well resolved as the peaks shown in Fig. 10. Watkins *et al.*¹³ had previously noticed signs of donor-specific structure in the A-line region when resonantly pumping these transitions with a tunable laser and monitoring the $2p_-$ tet PL. By comparing with the tet spectra described next, the strongest A peak is identified as due to Ge, the middle A peak to S, and the highest energy peak to a superposition of Se/Sn/Si transitions.

The shifts in transition energies between the different donor species are of course much more evident in the (weaker) tets.¹⁰⁻¹⁴ Here we discuss only the $2p_-$ tet, since the $2p_0$ lines were found to be considerably broader.

In Fig. 11 we show the $2p_-$ tet PL collected under the same conditions as for Fig. 10, except of course for the tuning of the interference filter. The transitions labelled Ge_a , S_a , Se/Sn and Si_a are the a-type $2p_-$ transitions (in the notation of Skromme *et al.*¹⁴) of the respective donor BE. Ge_b is a b-type $2p_-$ tet of the dominant Ge donor impurity (Ge_a and Ge_b differ in that they originate from two different Ge donor BE initial states). Again, the resolution between the various donor peaks achieved here is considerably better than that achieved in any of the previous MPL studies. The 19 μ eV width of the Ge_a line is remarkable considering that the inhomogeneous linewidth of the donor BE is not being narrowed by resonant excitation. One can of course achieve such narrowing by directly exciting into the middle of the Ge A-line. Under these conditions the Ge_a $2p_-$ tet was narrowed to only 7 μ eV, as shown in the inset to Fig. 11. These results compare favourably with the best $2p_-$ tet linewidths previously reported using dispersive spectroscopy, namely 35 μ eV (non-resonant) and 20 μ eV (resonant).¹⁴

Photoluminescence Excitation Spectroscopy

The last example of the utility of the FT techniques in PL spectroscopy is quite different, in that it involves photoluminescence excitation spectroscopy (PLES). In normal PLES the PL from some system is monitored over a fixed range of wavelengths while a tunable laser is scanned over the region to be studied, thus mapping out the absorption transitions which can give rise to the PL being monitored. In regions where tunable laser sources were unavailable, PLES has in the past been performed using excitation provided by monochromatizing an incoherent light source with a dispersive spectrometer.

However, one can instead perform FTPLES, in which the incoherent light source is modulated by passing it through an interferometer. Since non-laser PLES is usually performed in the low-signal limit, FTPLES can offer both multiplex and throughput advantages over dispersive PLES. This has already been pointed out by Hamilton and Clarke,¹⁷ but the advantages of FTPLES are not yet widely appreciated. The method may in fact have advantages over laser PLES even in regions where laser sources are available, in that arbitrarily wide spectral regions can be covered in a single scan without changing optics, dyes, etc.

As in resonantly excited PL, the main problem in FTPLES is that the interferometer itself has no rejection, and filter elements must therefore be used to block the direct throughput of photons at the PL wavelength region being monitored. This can be done by using, for example, short-pass interference filters, highly-reflecting blocking filters, or a subtractive dispersion double spectrometer in the excitation path. The PL can be selected with either a spectrometer or filters.

For our example we will study the FTPLES of the C-line defect in electron irradiated Si, which has previously been observed in PLE using a tunable colour center laser in the 1.5 - 1.6 μm region.¹⁸ The PL of this defect is dominated by a strong NP line, C_0 , as shown in Fig. 12(a). Below C_0 lies a broad, weak, phonon replica band which we use to monitor the PL through a 1.7 μm interference filter with a 100 nm FWHM. Our incoherent light source for this experiment is simply the standard internal tungsten-halogen lamp of the interferometer. The excitation light passes through a 1.5 μm 100 nm FWHM interference filter, which defines the region of the PLE spectrum, and blocks components at the PL wavelength. The resulting FTPLE spectrum shown in Fig. 12(b) is of very high quality, directly comparable to the previous¹⁸ colour center laser PLES. The collection of this spectrum would have been impossible using a dispersively monochromatized incandescent source.

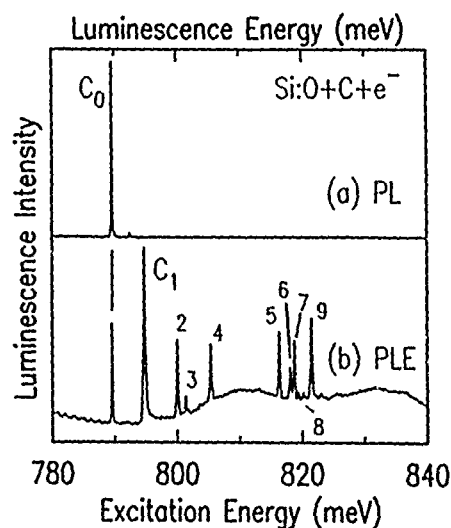


Fig. 12(a) Photoluminescence of the C_0 line in Si containing O and C after electron irradiation. (b) Fourier transform photoluminescence excitation spectrum of the same sample as described in the text.

The primary advantage of FTPLES is of course that it can cover any desired spectral region, unlike laser sources which have much more limited tuning ranges. This will prove useful not only in obtaining PLE spectra of defect systems such as the one considered here, but also for studying quantum wells and superlattices, particularly in the longer wavelength region ($\lambda \geq 1 \mu\text{m}$).

In conclusion, we feel confident in predicting a rapid growth in the application of FTPLS and FTPLES techniques to the challenges of semiconductor spectroscopy in the years ahead.

ACKNOWLEDGEMENTS

This work was supported by the Natural Sciences and Engineering Research Council of Canada and by the SFU Center for Systems Science. In addition, MLWT thanks the B.C. Advanced Systems Institute for the support of a Fellowship. We are also indebted to S. Watkins of American Cyanamid for providing a number of high quality GaAs samples.

REFERENCES

1. For a recent review of FT applications in the NIR and visible see: R. Williams, *App. Spectrosc. Rev.* 25, 63 (1989).
2. P. McL Colley and E.C. Lightowers, *Semicond. Sci. Technol.* 2, 157 (1987).
3. MIDAC Corp. Costa Mesa, CA, USA.
4. N.L. Rowell, *Infrared Phys.* 28, 37 (1988).
5. E.H. Salib, P. Fisher and P.E. Simmonds, *Phys. Rev. B* 32, 2424 (1985).
6. For a review of BMEC's see: M.L.W. Thewalt, in *Excitons*, edited by E.I. Rashba and M.D. Sturge (North Holland, Amsterdam, 1982) pp. 393-458.
7. G. Kirczenow, *Can. J. Phys.* 55, 1787 (1977).
8. R.R. Parsons, *Solid State Commun.* 22, 671 (1977).
9. A.S. Kaminskii, V.A. Karasyuk and Ya. E. Pokrovskii, *Zh. Eksp. Teor. Fiz.* 83, 2237 (1982) [*Sov. Phys. JETP* 56, 1295 (1982)].
10. D.C. Reynolds, P.C. Colter, C.W. Litton and E.B. Smith, *J. Appl. Phys.* 55, 1610 (1984).
11. S.S. Bose, B. Lee, M.H. Kim and G.E. Stillman, *Appl. Phys. Lett.* 51, 937 (1987).
12. S.K. Shastri, S. Zemon, D.G. Kenneson and G. Lambert, *Appl. Phys. Lett.* 52, 150 (1988).
13. S.P. Watkins, G. Haacke, H. Burkhard, M.L.W. Thewalt and S. Charbonneau, *J. Appl. Phys.* 64, 3205 (1988).
14. B.J. Skromme, R. Bhat, H.M. Cox and E. Colas, *IEEE J. Quant. Electr.* 25, 1035 (1989).
15. W. Rühle and W. Klingenstein, *Phys. Rev. B* 18, 7011 (1978).
16. G.E. Stillman, C.M. Wolfe and J.O. Dimmock, *Solid State Commun.* 7, 921 (1969).
17. B. Hamilton and G. Clarke, *Materials Science Forum* 38-41, 1337 (1989).
18. J. Wagner, K. Thonke and R. Sauer, *Phys. Rev. B* 29, 7051 (1984).

GENERATION AND DISSOCIATION OF IRON-BORON PAIRS IN SILICON

MASASHI SUEZAWA AND KOJI SUMINO

Institute for Materials Research, Tohoku University, Sendai 980,
Japan

ABSTRACT

The generation and dissociation processes of Fe-B pairs in Si crystal are investigated by means of the measurements of electron paramagnetic resonance of Si crystals of various B concentrations doped with Fe. Fe-B pairs are generated due to annealing of the crystals at temperatures around 300 K obeying to the first order reaction kinetics. The activation energy for pair generation is determined to be about 0.65 eV which is almost equal to the migration energy of Fe impurity in a Si crystal. Fe-B pairs are found to be dissociated at temperatures higher than 150°C leading to the precipitation of Fe.

1. INTRODUCTION

Studies of impurity Fe in Si crystals may be divided into two categories. Those belonging to the first category, which probably started in 1956 [1], have been undertaken as a part of the work to clarify the properties inherent to a variety of impurities in silicon crystals such as the energy level, solubility and diffusivity. Studies belonging to the second category deal with reactions of Fe impurity with other kinds of impurities or defects. One of the most interesting facts in conjunction with the latter is that an Fe atom forms a pair with an acceptor impurity atom at relatively low temperatures [2]. This type of studies was renewed whenever new experimental methods were invented or experimental techniques were improved.

On the other hand, in the course of quenching experiments of Si crystals from high temperatures with the aim to clarify the properties of intrinsic point defects in Si, the most common quenched-in "defect" was identified to be Fe impurity with the use of electron paramagnetic resonance method (EPR) [3], in spite of that Fe was not intentionally doped into Si. This result tells us how important to clean the environment of a Si crystal is when it is treated especially at an elevated temperature since Fe impurity often degrades the performance of electronic devices. Thus, the behavior of such unintentionally doped Fe impurity in Si crystals is attracting a great deal of attention in conjunction with the development of VLSI technology. The harmful action of Fe impurity in Si may disappear when it reacts with some other appropriate impurity such as a chemical acceptor. Complexes including Fe atoms may have electrical or optical properties which may be positively utilized in device engineering. So, understanding the detailed process of the reaction between Fe impurity and other impurities is important from both fundamental and practical viewpoints.

As our first study based on such an idea, we investigate here the generation and dissociation processes of Fe-B pairs in Si and clarify the temperature ranges for the pairing and depairing as well as the kinetics of pairing process in order to establish the fundamental knowledge for control of material property of Si.

2. EXPERIMENT

Table 1 gives the characteristics of Si crystals used in this work. All of them were grown by the float-zone technique. Crystals were cut into a rectangular shape $3.5 \times 3.0 \times 2.5$ mm³ in size. After polishing surfaces with CP-4, Fe was doped with the method first adopted by Collins and Carlson [1]; namely a specimen was sealed into an evacuated quartz capsule together with a piece of high purity Fe wire, heated for 1 hr at 1300°C, and then quenched into ice water. In order to keep the uniform distribution of Fe and B which is realized at a high temperature, a high quenching rate is needed. Ice water is known to be the most efficient cooling medium and quenching of a heated specimen into ice water fulfills the above requirement. Quenched specimens were stored in liquid nitrogen till the time of measurement in order to keep the specimens in the as-quenched state.

The concentration of Fe-B pairs was determined by means of EPR measurements. The advantage of this experimental technique lies in its nondestructive and contactless nature. The former nature makes it possible to follow the processes occurring during isochronal or isothermal annealing with one specimen, resulting in a small scatter of data, and the latter makes it possible to shorten the duration which the quenched specimen is kept at room temperature. Such duration was shorter than 2 min, which is short enough to keep the specimen in the as-quenched state as will be seen later in Fig. 2. The shortcoming of the technique lies in the difficulty in determining the absolute value of the concentration of concerned impurity. EPR was measured at 10 K with a JEOL X-band spectrometer. The modulation amplitude and frequency were 80 μ T and 100 kHz, respectively.

Table 1 Characterization of used crystals

Specimens	Dopant, (atoms/cm ³)
FP-1	B 8.2×10^{15}
FP-2	B 2.9×10^{15}
FP-3	B 4.7×10^{14}
FN-1	P 1.0×10^{15}

3. EXPERIMENTAL RESULTS

Figure 1 shows EPR spectra related to neutral Fe (Fe°), singly plus-charged (Fe^+), and neutral Fe-B of a specimen FP-2. The EPR signals of Fe° and Fe^+ were taken with an as-quenched specimen and that of Fe-B with a specimen after annealing at 100 °C for 10 min. The $[1\bar{1}0]$ axis of the specimen was parallel to the direction of the static magnetic field. The Fe-B bond of a Fe-B pair is directed along one of the $\langle 111 \rangle$ directions of the Si crystal. The signals at $H = 0.215$ and 0.232 T have the same line shape and originate from Fe-B pairs directed along the $[111]$ and $[1\bar{1}\bar{1}]$ directions and the signal at $H = 0.158$ T probably originates from the pairs directed along $[111]$ and $[1\bar{1}\bar{1}]$ directions, two signals being overlapping in the latter [4]. The signals around 0.1835 and 0.3135 T are due to Fe^+ and Fe° , respectively [5]. One of the advantages of EPR experiments lies in the ability to determine the concentrations of Fe^+ and Fe° independently of each other. As will be shown soon, EPR ab-

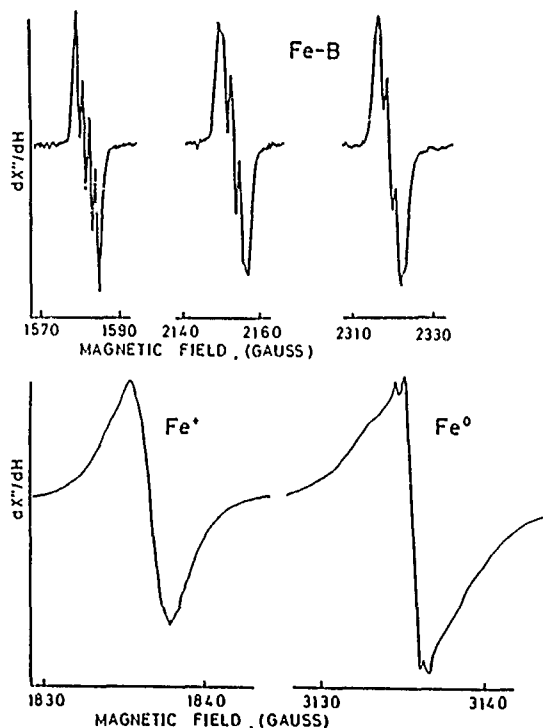


Fig. 1 EPR, absorption spectra related to Fe-B, Fe° and Fe^+ . The ordinate shows the first derivative of absorption and the abscissa the strength of static magnetic field. The microwave frequency is about 9.0741 GHz.

sorptions related to Fe^0 , Fe^+ and Fe-B were observed in each specimen. Since the donor levels of Fe and Fe-B are located at about 0.39 and 0.1 eV, respectively, above the valence band [6], this observation suggests that the Fermi level at 10 K is almost pinned at the Fe^0/Fe^+ level.

Figure 2 shows variations in the concentrations of Fe^+ , Fe^0 and Fe-B in a quenched specimen FP-2 due to isochronal annealing for 10 min at each temperature.

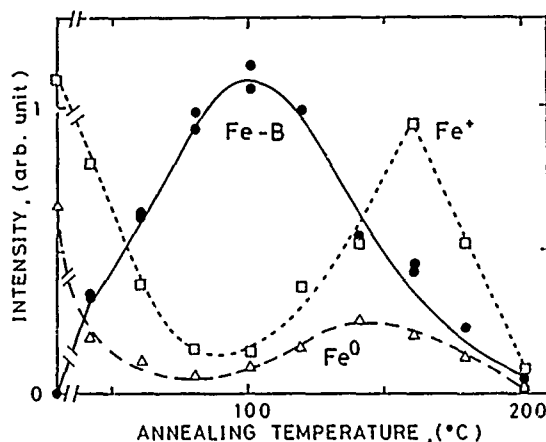


Fig. 2 Variations of the concentrations of Fe^+ , Fe^0 and Fe-B in isochronal annealing of an Fe-doped specimen of FP-2. Annealing duration is 10 min at each temperature. The ordinate shows the peak-to-peak intensity of the EPR absorption.

The ordinate shows the peak-to-peak intensity of EPR absorption at 10 K in the case that the $[1\bar{1}0]$ direction of the specimen is nearly parallel to the static magnetic field. The units of intensities in the ordinate for different absorptions are taken different for different absorptions. Therefore, the change in the intensity of each signal due to annealing is important and the relative magnitudes of the absorptions related to different kind of signals bear no significant meaning. The concentration of quenched-in Fe atoms is estimated to be around $1 \times 10^{16} \text{ cm}^{-3}$ from the condition of heat treatment. The concentration of B is around $2.9 \times 10^{15} \text{ cm}^{-3}$ in the specimen FP-2. Therefore, actually the absolute magnitude of the concentration of Fe^0 is higher than that of Fe^+ in contrast to the impression given by Fig. 2. We detected

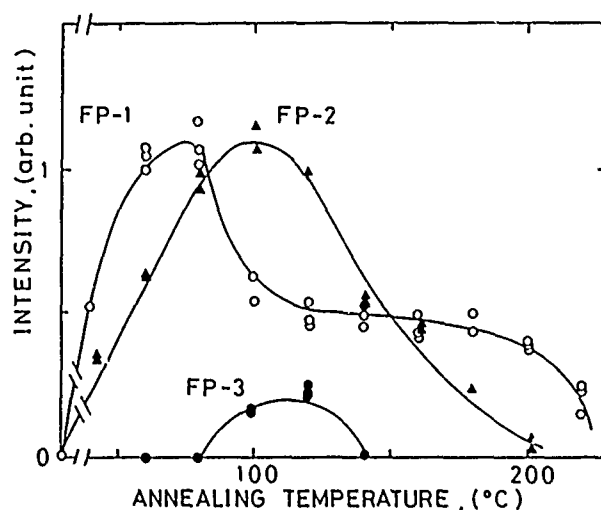


Fig. 3 Isochronal generation of Fe-B in specimens with various concentrations of B.

only signals of Fe^+ and Fe^0 in our as-quenched specimens. This suggests that the duration the quenched specimens were kept around room temperature before they were subjected to EPR measurements was so short that no detectable concentration of Fe-B was generated. The change in the Fe-B concentration against the annealing temperature is just the reverse of those of Fe^0 and Fe^+ in the annealing temperature range lower than about 150°C . This clearly shows that the generation and dissociation of Fe-B take place due to reactions among Fe^+ , Fe^0 , B- and B^0 in the temperature range between 40 to 150°C . As pointed out above, though the Fermi level

is pinned at $\text{Fe}^\circ/\text{Fe}^+$ and all B atoms are in the B^- state at 10 K, there may be a small amount of neutral B at room temperature. At temperatures above 150°C, Fe^+ and Fe° are thought to agglomerate into precipitates which are supposed to be EPR-inactive.

Figure 3 compares generation and annihilation behavior of Fe-B in specimens of FP-1, FP-2 and FP-3 (see Table 1). Pair generation begins at a lower temperature in a specimen of a higher B concentration. This effect is thought to reflect a decrease in the distance between an individual Fe atom and a B atom with an increase in the concentration of B. On the other hand, the peak temperature is determined by the balance of the generation process and the dissociation process of Fe-B. As will be discussed later, we can determine, in principle, the binding energy of a Fe atom and a B atom from the measurement of the peak temperature as a function of the initial concentrations of Fe and B atoms.

The kinetics of Fe-B generation was followed by means of isothermal annealing of quenched specimens at an appropriate temperature.

Figure 4 shows the generation curve of Fe-B at 40°C. The generation rate of Fe-B is the highest at the beginning of annealing and becomes lower with increasing duration of annealing, and finally the concentration of Fe-B is seen to be saturated. The annealing duration $t_{1/2}$ at which a half of the saturation value of the Fe-B concentration is attained is about 16 min at 40°C. The diffusion length $(D t_{1/2})^{1/2}$ of Fe atoms during such a duration is estimated to be about 3.8×10^{-6} cm with the use of the diffusion constant of $D = 1.3 \times 10^{-3} \exp(-0.68 \text{ eV}/kT) \text{ cm}^2 \cdot \text{s}^{-1}$ [7]. This length is of the same order of magnitude as the mean separation of B atoms in the specimen. This result suggests that Fe and B atoms are distributed independently of each other in our as-quenched specimens.

Figures 5 and 6 show the changes in the concentrations of Fe° and Fe^+ with the duration of isothermal annealing shown in Fig. 4. It is interesting to note that the concentration of Fe^+ shows a rapid increase followed by the maximum in the early stage of annealing. We interpret this initial increase to be caused by

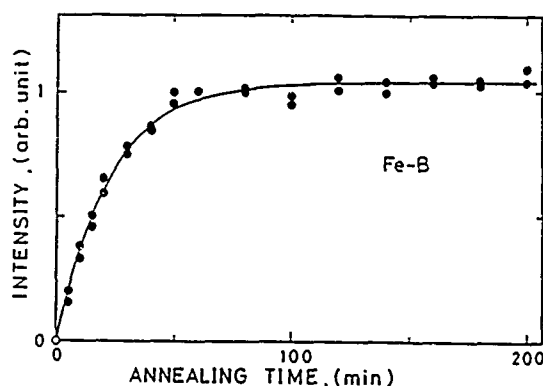


Fig. 4 Generation curve of Fe-B in isothermal annealing at 40°C. The full line is the fitting curve with Eq.(5).

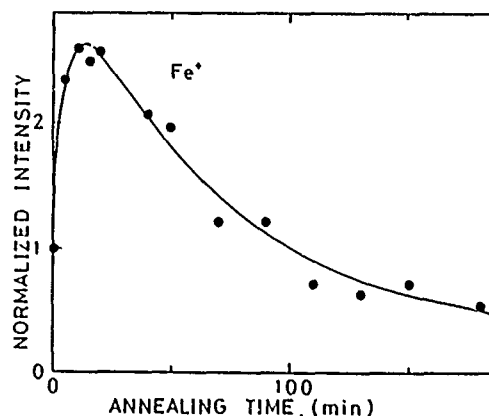


Fig. 5 Variation of the Fe^+ concentration due to isothermal annealing at 40°C.

thermal ionization of Fe° during annealing. The emission rate of electrons e_n in a unit of s from Fe° is estimated from the following equation :

$$e_n = C_n \cdot N_c \cdot g^{-1} \exp [(E_T - E_c) / k T] \approx 1.1 \times 10^7 T^2 \exp (-0.7 \text{ eV} / k T). \quad (1)$$

where $C_n (= \sigma_c \cdot v_{th})$ is the capture rate for electrons, $v_{th} = (3k T / m^*)^{1/2}$ is the thermal velocity of conduction electrons, $N_c (= 6.1 \times 10^{18} \text{ cm}^{-3}$ at room temperature) is the effective density of states of the conduction band, g is the degeneracy of the level (assumed to be unity), $\sigma_c (= 6 \times 10^{-15} \text{ cm}^2 [8])$ is the capture cross section for an electron of an Fe° , $E_T - E_c$ is the energy level measured from the bottom of the conduction band and m^* is the effective mass of an electron. The value of e_n is estimated to be of the comparable order of magnitude to that of jumping rate of an Fe atom. In other words, some of Fe° may be ionized during diffusion motion in the course of isothermal annealing.

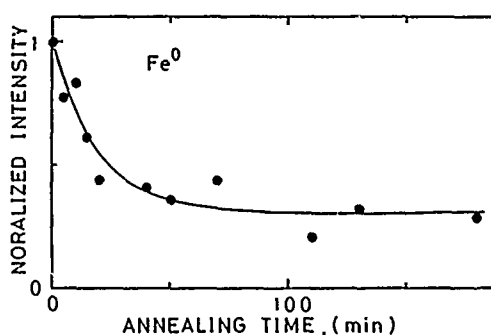
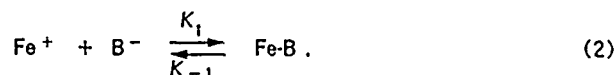


Fig. 6 Variation of the Fe° concentration due to isothermal annealing at 40°C .

4. ANALYSIS AND DISCUSSION

The observation in the preceding section has shown that Fe and B atoms are distributed independently of each other in our as-quenched specimens. In such a case, the generation process of Fe-B is well described with following chemical rate equation :



K_1 and K_{-1} are the reaction constants in the forward and backward directions, respectively. We have not yet succeeded in describing all the data in Figs. 4, 5, and 6 simultaneously. So, we give the analysis of the result in Fig. 4 in the following. The pairing process of Fe° and B° (neutral boron) is ignored since the concentration of B° is supposed to be very low. The rate equation for the pair generation is given as follows :

$$dp/dt = K_1 \cdot F \cdot B - K_{-1} \cdot p. \quad (3)$$

here, p , F and B are the concentrations of Fe-B, Fe^+ and B^- , respectively. We solve Eq.(3) under the following two assumptions ;

$$1) \quad F = F_0 - p, \quad B = B_0 - p. \quad (4)$$

F_0 and B_0 are the initial concentration of Fe^+ and B^- , respectively. The first equation of Eq.(4) does not necessarily in agreement with the result in Fig. 5 which shows an initial increase in the Fe^+ concentration. We do not take into account of this increase because it takes place much earlier than Fe-B is generated.

2) The p^2 term is neglected after putting Eq.(4) into Eq.(3).

The solution of Eq.(3) is given as follows :

$$p = p_\infty \{ 1 - \exp [- (K_1 [F_0 + B_0] + K_{-1}) t] \}. \quad (5)$$

here, p_{∞} is the saturation value of Fe-B. The solid line in Fig. 4 is the fitting curve with Eq.(5). The fitting is seen to be fairly good.

According to Eq.(5), $t_{1/2}$ is proportional to $1/[K_1(F_0+B_0)+K_{-1}]$. In the case of low temperature annealing such as the case of Fig. 4, the reverse reaction may be neglected (i.e. $K_{-1}=0$). The activation energy of K_1 is, then, determined to be about 0.65 eV, which is close to the migration energy of Fe in Si [6].

Under an ideal isochronal annealing in which the specimen temperature is raised linearly with the annealing time, the peak temperature for the Fe-B concentration is attained by the condition of $dp/dt=0$; namely $K_1 \cdot F \cdot B = K_{-1} \cdot p$ from Eq.(3). Therefore, we are able to determine, in principle, the energy of binding between an Fe atom and a B atom from a plot of the logarithm of K_1/K_{-1} , which is determined from $p/F \cdot B$ at the peak temperature, against the inverse of annealing temperature for various values of F_0 and B_0 . Such a work is now in progress.

5. CONCLUSION

The generation and dissociation processes of Fe-B in Si were investigated with the use of the EPR technique in determining of the concentrations of Fe-B, Fe^0 and Fe^+ . Random distribution of both Fe and B atoms was realized by rapid quenching of Fe-doped Si crystals from 1300°C. Isochronal annealing of quenched specimens showed that the generation of Fe-B took place in the temperature range below 100 °C while dissociation above this temperature. The kinetics of Fe-B generation process was well described with the first order reaction. The activation energy for the reaction was determined to be about 0.65 eV which coincided with the migration energy of Fe in Si.

REFERENCES

1. C.B. Collins and R.O. Carlson, Phys. Rev. **108**, 1409 (1957).
2. W.H. Sheperd and J.A. Turner, J. Phys. Chem. Solids **23**, 1697 (1962).
3. Y.H. Lee, R.L. Kleinhenz and J.W. Corbett, Appl. Phys. Lett. **31**, 142 (1977).
4. W. Gehlhoff, K.H. Sogsa and C. Meyer, Phys. Stat. Sol.(b) **105**, K91 (1981).
5. G. Ludwig and H.H. Woodbury, in *Solid State Physics* **13**, edited by F. Seitz and D. Turnbull (Academic Press, New York and London, 1962) pp.223 - 304.
6. K. Wunstel and P. Wagner, Appl. Phys. A **27**, 207 (1982).
7. E.R. Weber, Appl. Phys. A **30**, 1 (1983).
8. L.C. Kimerling, J.L. Benton and J.J. Rubin, Inst. Phys. Conf. Ser. No.59, 217 (1981).

PHOTOCONDUCTIVITY STUDY OF CrB AND Cr_i IN SILICON

A. Schlette, R. Kienle, A. Dörnen, W. Kürner, and K. Thonke; Universität Stuttgart, 4. Phys. Institut, Pfaffenwaldring 57, D 7000 Stuttgart 80

ABSTRACT

We observe in photoconductivity (PC) measurements EMT-like excited states of the pseudodonor CrB, which are responsible for the capture of free electrons due to their short lifetime. The energetic position of the ground state can be located at $E_v + (292 \pm 5)$ meV. A finestructure of the $(\text{CrB})^0$ transition consisting of at least 15 components is observed in PC and high-resolution Fourier transform photoluminescence. In acceptor-free silicon a step in photoconductivity at 205 ± 10 meV is ascribed to interstitial Cr, whereas a second step at ~ 425 meV could be due to substitutional Cr.

INTRODUCTION

Chromium is a transition metal which diffuses fast into silicon, tends to form complexes with different acceptors [1], and acts as efficient recombination center [2]. Especially the chromium-boron pair was studied in some detail by EPR [1], Photoluminescence (PL) [3,4], and DLTS [4,5]. This CrB complex is made up of a boron atom residing on a substitutional site, being negatively charged in the ground state, and an interstitial positively charged chromium atom with electron configuration $3d^5$ [1]. It acts as deep donor with binding energy $E_v + 0.27$ eV [4]. The process giving rise to PL spectra was interpreted as recombination of a shallow bound electron (binding energy ~ 15 meV) according to thermal data, into the strongly localized donor state. It remained unclear if the charge state of Cr or B is altered during this step [3]. In both EPR and PL a [111] axis was found for the CrB-pair.

Isolated chromium on interstitial sites was also detected first by EPR [1]. It gives rise to a donor state 0.23 eV below the conduction band [4,6]. No luminescence signal was reported for this defect.

Similar to iron, chromium seems to prefer interstitial sites and was found in a substitutional configuration only after codiffusion with copper [1] or irradiation [7]. From photoconductivity measurements a donor level at $E_c - 0.4$ eV was ascribed to Cr_s [7].

EXPERIMENTAL

The samples used in this study were prepared as described in Ref. 4. The chromium concentration is estimated to vary between 10^{13} and 2×10^{15} [4]. Photoconductivity spectra were recorded with a Bomem DA3 Fourier transform spectrometer equipped with a quartz beamsplitter and halogen light source for the near infrared wavelength region, and a KBR beamsplitter and globar source for the mid infrared. The samples were placed in a gas flow type cryostat, and the sample current was amplified by a transimpedance amplifier.

RESULTS: CHROMIUM BORON PAIRS

For boron concentrations of $\sim 2 \times 10^{15} \text{ cm}^{-3}$ in the starting material and chromium diffusion at 1200 °C both atomic species are abundant in about the same concentration. So the concentration of CrB pairs should already be high and most boron acceptors are expected to be compensated. A typical spectrum obtained on such samples in the energy range between 0.85 eV and the bandgap is depicted in fig. 1. Superimposed on a smooth background we find a negative peak at 843.8 meV, the position of the $(\text{CrB})^0$ no-phonon (NP) transition in photoluminescence [3]. Some 33 meV higher in energy we observe a step in the spectrum, followed by several weak modulations. Close to the bandgap, at

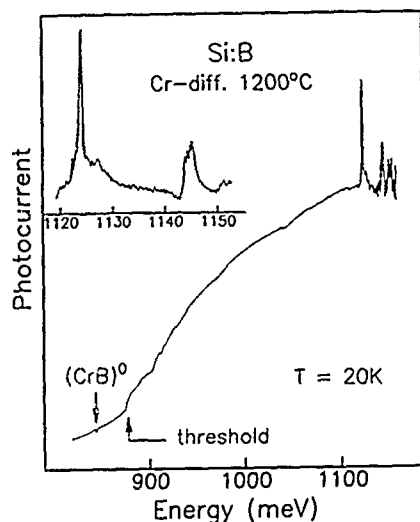


Fig. 1: Photoconductivity spectrum of a sample codoped with boron and chromium. Inset: The sharp-line spectra close to E_g in more detail.

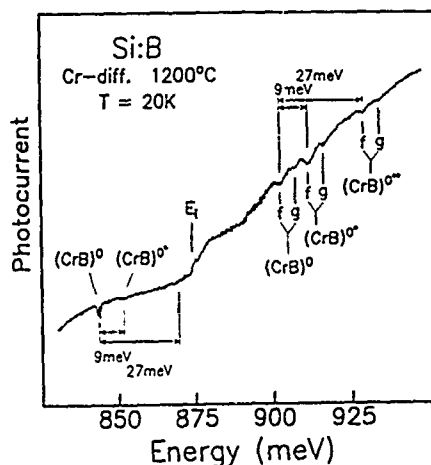


Fig. 2: The PC spectrum related to CrB: Beside the $(\text{CrB})^0$ line and a first excited state we observe fano resonances beyond the ionization threshold.

energies of 1124.4 meV and 1145 meV, two sharp positive resonances show up. We will discuss these peaks later.

Fig. 2 shows the region of the $(\text{CrB})^0$ transition in more detail. Shifted by one $f(\text{TO})$ and $g(\text{LO})$ phonon energy respectively, fano resonances [8] of $(\text{CrB})^0$ are detected. Again 9 meV higher in energy, a second pair of these resonances is observed. The corresponding no-phonon (NP)-transition is only weakly allowed and results in a small dip 9 meV above $(\text{CrB})^0$. A third pair of fano resonances 27 meV higher in energy has no counterpart in the NP region. The occurrence of these fano resonances is a clear indication that the excited states of CrB, into which the electron is ejected by absorption of light, are essentially shallow donor like in their character. The step in the PC spectrum ~ 33 meV above $(\text{CrB})^0$ corresponds to the ionization threshold; photons of energy higher than ~ 877 meV can remove electrons from CrB and eject them directly into the conduction band (CB).

These findings are fully consistent with PL uniaxial stress data published by Conzelmann et al. [3]. The gross shifting rate of the $(\text{CrB})^0$ NP line under stress corresponds to the rate which applies to the lower substate projected out of the conduction band multiplicity. Superimposed is an additional smaller splitting due to a defect induced trigonal axial field. A thermalizing 'hot line', which is observed for $X \parallel [100]$, was estimated to origin in a state 8 meV higher in energy. This must be the first excited state at +9 meV which is found in our PC spectra. We interpret these states as valley-orbit sublevels of the 1s donor ground state. Since for stress $X \parallel [100]$ and $X \parallel [110]$ nonlinearities in the shift of one of the subcomponents occur, the lowest state must be the A_1 (or E) state, mixing under stress with the E (or A_1) excited state. The 'hot line' component shows no nonlinearities and must therefore arise from a T_2 level, which does not mix with other states. Assuming the ground state to be of character A_1 , we expect both the E and T_2 state to be hidden in the peak at +9 meV. We ascribe the state at +27

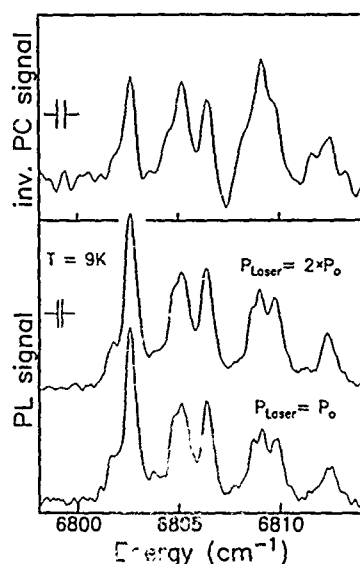


Fig. 3: Finestructure of the $(\text{CrB})^0$ line.
Upper trace: Photocoductivity spectrum at a resolution of 0.4 cm^{-1} . The y-axis is inverted for better comparison to PL spectra.
Lower trace: Photoluminescence spectra at two different laser excitation densities; res. = 0.2 cm^{-1} .

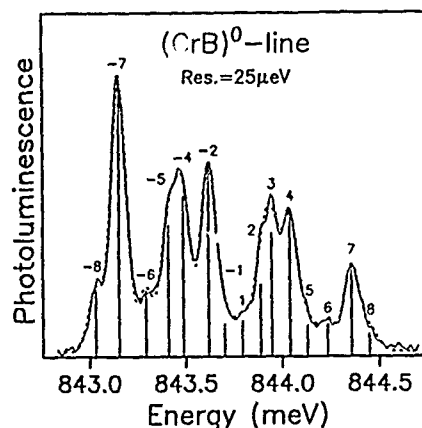


Fig. 4: Decomposition of the $(\text{CrB})^0$ PL spectrum into 15 symmetrical Gaussian lines. For parameters see table I. Numbers designate a tentative symmetrical ordering of components.
(solid line: experiment; broken line: fit)

meV to the $(2s, 2p)$ EMT states. If the $1s(E, T_2)$ states are assumed to be located at the energies predicted by a hydrogen model, the ionization threshold calculated from the spacing $(1s, 2s)$ is 33 meV. The whole situation encountered here is similar to the one found for the 'C-line' defect in irradiated silicon [9], which acts as pseudodonor with Effective-Mass-Theory (EMT)-like states perturbed by an axial defect field.

So the CrB pair also must act as a pseudodonor, binding as primary particle a hole in a strongly localized state, which in turn via Coulombic forces binds an electron in EMT-like states. The binding energy of the hole is calculated to be

$$E_{\text{gap}} - E_{\text{threshold(PC)}} = 1.169 \text{ eV} - 0.877 \text{ eV} = 292 (\pm 5) \text{ meV}.$$

This value for the CrB deep donor binding energy is close to the one determined by DLTS ($E_v + 270 \text{ meV}$ [4]). The luminescent process giving rise to the $(\text{CrB})^0$ line corresponds to the recombination of the shallow bound electron residing in the lowest $1s$ substate with the strongly localized hole. The smaller superimposed stress splitting components observed must be due to the weak response of the deeply bound hole. The fact, that in PC measurements the $(\text{CrB})^0$ lines remain negative even for sample temperatures up to 60K indicates, that the lifetime of electrons excited into the $1s$ pseudodonor states is very short. For these electrons the probability to drop back into the ground state is much higher than the probability to be ejected into the CB. We conclude therefore, that the shallow EMT like pseudodonor states are mainly responsible for the capture of free electrons, leading to the short free carrier lifetime observed in time resolved PL measurements.

Table 1: Decomposition of the high-resolution $(\text{CrB})^0$ spectrum recorded at higher excitation power: result of a fit comprising 15 symmetrical Gaussian lines of halfwidth $0.64 \pm 0.14 \text{ cm}^{-1}$. The last column gives the line positions (error: $\pm 0.1 \text{ cm}^{-1}$) relative to the middle between lines no. -7 and +7.

line no.	position (cm^{-1})	rel. amplitude (%)	rel. position
-8	6801.58	4.51 ± 0.22	-5.83
-7	6802.56	19.06 ± 0.24	-4.85
-6	6803.68	4.45 ± 0.22	-3.73
-5	6804.63	8.90 ± 0.42	-2.77
-4	6805.25	10.88 ± 0.42	-2.15
?			
-2	6806.31	13.09 ± 0.40	-1.10
-1	6806.97	2.18 ± 0.38	-0.43
1	6807.71	2.41 ± 0.34	+0.30
2	6808.48	4.88 ± 1.50	+1.08
3	6808.95	8.36 ± 1.60	+1.55
4	6809.72	9.25 ± 0.36	+2.31
5	6810.43	2.10 ± 0.32	+3.03
6	6811.25	2.23 ± 0.28	+3.85
7	6812.26	6.13 ± 0.26	+4.85
8	6813.01	1.57 ± 0.28	+5.62

Under high resolution the $(\text{CrB})^0$ line reveals a finestructure (see fig. 3), which resembles closely the one observed in previous photoluminescence work [3]. For easier comparison with PL spectra, we have inverted the negative PC peaks. Since all $(\text{CrB})^0$ lines superimposed on a broad background band are negative for all sample temperatures, the spectrum obtained here by photoconductivity is identical to a conventional absorption spectrum. In absorption, in turn, carried out on the same sample with $\sim 2 \text{ mm}$ thickness, the dip at the $(\text{CrB})^0$ position was almost undetectable, so that photoconductivity in this specific case due to favorable conditions offers much better signal to noise ratio. Although we could resolve substructures more clearly than in previous PL work [3], the halfwidth for individual components is still limited by resolution. So we investigated this line group by high resolution Fourier transform photoluminescence. The spectra in the lower part of fig. 3 were recorded with a cooled Germanium diode detector, mounted to the Bomem FT spectrometer (resolution setting 0.2 cm^{-1}). Due to the much better signal to noise ratio than in PC measurements, further details could be resolved. The $(\text{CrB})^0$ spectrum tends to saturate in all our samples (with maximum attainable CrB pair concentration) already at powers of the exciting 647 nm laser line of $\sim 0.1 \text{ Watt}$ focused onto $\sim 1/4 \text{ mm}^2$. Further increase of excitation power leads to a gain in intensity of the high energy components relative to the lowest strong line, presumably due to heating up of the sample in our gas flow cryostat. The $(\text{CrB})^0$ spectrum consists roughly of 4 equidistant thermalizing main groups of lines with at least 4-fold substructure in each group. Since in absorption (i.e. in the PC spectrum with negative peaks) all high energy components are stronger than in PL, the main 4-fold splitting must occur in the upper state of the transition.

For a more detailed analysis we tried to decompose the whole $(\text{CrB})^0$ spectrum into a set of symmetrical Gaussian lines with equal halfwidth. A satisfactory fit to either of the PL spectra in fig. 3 requires at least 15 components (see fig. 4). Table I contains the result for the upper PL spectrum of fig. 3. Except for two weak components (No. 5 and 6 in table I) the decompositions of both PL spectra give the same line positions, with stronger high-energy lines for the spectrum recorded with higher excitation power. It is not evident, in which way the whole complicated line pattern can be resolved into a combination of simple structures. Within the error margins

of our decomposition, the component positions seem to be grouped symmetrically around the middle of the pattern, defined by half way between the strong lines -7 and +7 (see table I). But for some pairings the counterpart line is missing or shifted too far for a convincing assignment.

Since it is not clear, if the chromium or boron atom changes its charge state when the CrB pair is excited, and due to numerous interactions involved, theoretical predictions are not straightforward. EPR determined the final charge state (i.e. when the electron is recombined) as Cr^+B^- , so chromium is in the $3d^5$ state with $S = 5/2$, $L = 0$. The $S = 5/2$ state is split by a D-term of 0.0806 cm^{-1} , resulting in a splitting of $6D = 0.48 \text{ cm}^{-1}$, a value which is about the halfwidth of the spectral components of $(\text{CrB})^0$ in PL. Therefore, and because of the thermalization behavior, the major part of the splitting must originate in the excited state. When during excitation chromium loses one electron more, its charge state is then Cr^{2+} ($3d^4$) with $S = 2$, $L = 2$. Several interactions affect the energy of the remaining d-electrons: The T_d crystal field splits $L = 2$ into E and T_2 states, where the latter is split further by the trigonal defect field. Spin-orbit interaction leads to splitting up of T_2 , and to a minor degree, of E as well. Finally the interaction of the bound EMT-like electron ($s=1/2$) with Cr^{2+} has to be considered. The negatively charged boron atom has filled shells and does not contribute to splittings.

If in turn boron is ionized to B^0 , the hole localized at B is subject to a trigonal crystal field and spin-orbit interactions leading together with coupling to the loosely bound electron to a maximum of 5 levels [10]. Only in the unlikely case of strong coupling between Cr d-shell electrons and B bound hole a more complicated level scheme could emerge. Therefore we consider the first mechanism



to be the more probable one. A final decision between the two alternative processes has to await further experimental work like high resolution Zeeman or stress experiments.

Complicated finestructure is also observed in the positive PL peaks located at $\sim 1.124 \text{ eV}$ and $\sim 1.145 \text{ eV}$ close to the bandgap energy (see inset fig. 1). This spectrum was found only in samples of a boron content around $5 \cdot 10^{15} \text{ cm}^{-3}$, a concentration where all boron atoms are expected to form pairs with chromium. Samples which have undergone the same preparing procedure, but

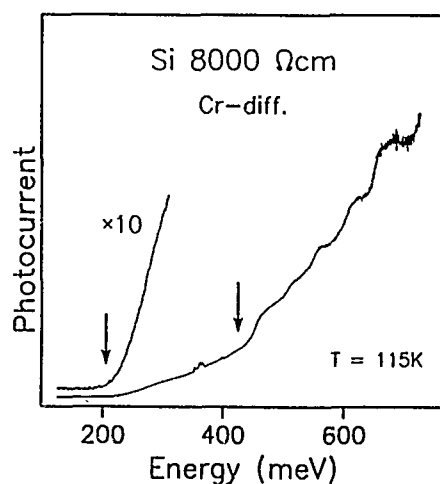


Fig. 5:
Photoconductivity
spectrum of chromium
in high resistivity
material. Arrows
indicate two thresh-
olds at 0.2 and
0.43 eV

with different boron content, showed the CrB features only. Both lines decrease rapidly in intensity for sample temperatures above 20 K, along with the background signal. We estimate a dissociation energy of ~ 30 meV for the 1.124 eV line, a value close to the energetic distance from the excitonic bandgap. Presumably, both lines can be ascribed to excitonic processes involving either Cr or CrB.

INTERSTITIAL AND SUBSTITUTIONAL(?) CHROMIUM

When chromium is diffused at 1200°C into pure silicon, a photoconductivity spectrum as depicted in fig. 5 is obtained. After diffusion, these samples were n-type due to interstitial chromium acting as deep donor [4, 7]. The first ionization threshold occurring in fig. 5 at 205 ± 10 meV must be linked to the $0/+$ transition of Cr_i . This value is in accordance with previous DLTS and PC work, where an activation energy between 0.21 and 0.23 eV was determined [4, 7]. No sharp lines below the threshold energy were observable even at sample temperatures around 120 K, so that for Cr_i either there exist no EMT-like excited states or their lifetime is extremely small. Since Cr_i is the dominant dopant in our sample, all carriers freeze out at $T \leq 140$ K as found in $C(T)$ measurements. $C(V)$ data recorded at $T = 250$ K give a Cr_i concentration of $5 \cdot 10^{14} \text{ cm}^{-3}$.

In fig. 5 a second step in the PC spectrum at 425 ± 15 meV shows up. The step is followed by a series of humps, which could be caused by coupling of the electronic transition to phonons of ~ 51 meV. We observe this defect related threshold in several samples, which were n-type after diffusion. DLTS measurements on the same sample as used in fig. 5, making use of Cr_i as dominant background doping, indicate that two hardly resolvable levels at ~ 410 meV exist in a total concentration of $\sim 5 \cdot 10^{13} \text{ cm}^{-3}$. Zolotukhin and Milevskii [7] ascribed this step to substitutional chromium, an assignment that seems plausible in view of the low concentration of the underlying defect.

Acknowledgements: We thank A. Hangleiter and H. Conzelmann for the loan of samples and helpful discussions. The support of this work by the BMFT under contract no. 13 AS 1027 is gratefully acknowledged.

LITERATURE

- 1 G.W. Ludwig, H.H. Woodbury, Solid State Physics, Seitz/Turnbull 13, 223 (1962)
- 2 A. Hangleiter, Phys. Rev. B 35, 9149 (1987)
- 3 H. Conzelmann, J. Weber, Physica 116b, 291 (1983)
- 4 H. Conzelmann, K. Graff, E.R. Weber, Appl. Phys. A 30, 169 (1983)
- 5 K. Graff, H. Pieper, in "Semiconductor Silicon 1981", ed. H.R. Huff and R.J. Kriegler, The Electrochemical Society, 331 (1981)
- 6 E. Feichtinger, R. Czaputa, Appl. Phys. Lett. 39, 706 (1982)
- 7 A.A. Zolotukhin, L.S. Milevskii, Sov. Phys. Solid State 13, 1598 (1972)
- 8 E. Janzén, G. Grossmann, R. Stedman, H.G. Grimmeiss, Phys. Rev. B 31, 8000 (1985)
- 9 K. Thonke, A. Hangleiter, J. Wagner, and R. Sauer, J. Phys. C 18, L795 (1985)
- 10 J.v.M. Morgan, T.N. Morgan, Phys. Rev. B 1, 739 (1970)

Formation of In-Cu Pairs in Silicon during Chemomechanical Polishing

TH. WICHERT*, R. KELLER, M. DEICHER, W. PFEIFFER, H. SKUDLIK
AND D. STEINER

Fakultät für Physik, Universität Konstanz, D 7750 Konstanz, FRG

ABSTRACT

Using the perturbed $\gamma\gamma$ angular correlation technique (PAC) the pairing of Cu with the radioactive acceptor atom ^{111}In in Si is detected. Because of the identity of the electric field gradients the so-called X defect, observed after chemomechanical polishing of Si wafers and known of neutralizing acceptor atoms in Si, is identified as a Cu atom. It is also shown that as-delivered Si wafers already contain Cu atoms which neutralize acceptor atoms if the wafers are annealed at 1173 K.

INTRODUCTION

During the past years a growing attention has been given to the problem of unintentional deactivation of dopant atoms in semiconductors.¹ Here, hydrogen plays a prominent role since it was discovered that acceptor atoms in Si are passivated by hydrogen atoms. Meanwhile, a fair number of device processing steps has been identified that all lead to the incorporation of H atoms into p-Si followed by the deactivation of acceptor atoms and the formation of acceptor-hydrogen pairs.

Among these processing steps also chemomechanical polishing of Si wafers in alkali-based solutions was found to neutralize the acceptor atoms B, Al, Ga, and In and again H was reported to be responsible for this process.² This interpretation has meanwhile become part of the current literature though two significant differences are evident if one compares the dynamics and thermal stability of the neutralization of the acceptor atoms effected by either chemomechanical polishing³ or by the other processing steps¹: i) polishing at ambient temperatures effects a passivation of acceptors across the whole sample of 1 mm thickness within a few hours (for an acceptor concentration of typical $1 \cdot 10^{16} \text{ cm}^{-3}$) whereas H atoms are known of passivating only the first 10 μm of the Si wafer at typically 400 K; this implies a substantially higher mobility of the passivating defect X in the polished wafer than of the H atom. ii) The complex formed after polishing dissociates already at room temperature as determined by the decrease of the electrical resistivity of the sample whereas acceptor-H pairs are known to dissociate not below 400 K. A third, direct evidence for the non-identity of the acceptor-X complex induced by polishing and

the acceptor-H pairs is the difference of the electric field gradients observed by perturbed $\gamma\gamma$ angular correlation experiments (PAC).⁴ Therefore, it has to be concluded that the defect X induced by chemomechanical polishing has to be different from H atoms.

Using the radioactive probe atom ^{111}In we shall determine the chemical identity of the X defect and demonstrate that chemomechanical polishing of Si leads to the formation of In-Cu pairs. In addition, we shall show that as-delivered Si wafers already contain Cu. The consequences of the identification of the X defect as a Cu atom will be discussed in the context of other investigations which also dealt with this X defect.

EXPERIMENTAL PROCEDURE

The PAC-Technique

In PAC experiments, the chemical nature of a particular defect is characterized by its electric field gradient that can be measured at the site of a radioactive probe atom. Here, the radioactive isotope ^{111}In (lifetime 4 days) will serve as the probe atom because it allows the study of the interaction of an acceptor atom with different types of defects in Si.

At the time of the decay of ^{111}In into ^{111}Cd the electric field gradient is measured by detecting in coincidence the two γ quanta that are emitted as a $\gamma\gamma$ cascade by the excited ^{111}Cd nucleus. If the two γ quanta are recorded at the relative angle Θ as a function of time t , elapsed between the emission of the first and second γ quantum, the coincidence rate reads⁵

$$I(t, \Theta) = I_0 \cdot \exp(-t/\tau) \cdot (1 + A_{22} \cdot G_2(t, \Theta)) \quad (1)$$

where I_0 denotes the coincidence rate at $t = 0$, $\tau = 123$ ns is the lifetime of the intermediate states within the $\gamma\gamma$ cascade, and $A_{22} = -0.12$ describes the spatial anisotropy of the $\gamma\gamma$ coincidence probability. The information on the electric field gradient is contained in the three frequencies ω_i of the perturbation function

$$G_2(t, \Theta) = S_0 + \sum_{n=1}^3 S_n \cdot \cos(\omega_n t) \quad (2)$$

In case of an electric field gradient tensor, which is axially symmetric about its largest component V_{zz} , i.e. the asymmetry parameter $\eta = (V_{xx} - V_{yy})/V_{zz}$ of the tensor is zero, the frequencies are given by

$$\omega_1 = (3\pi/10) \cdot eQV_{zz}/h = (3\pi/10) \cdot \nu_Q \quad (3a)$$

$$\omega_2 = 2 \cdot \omega_1 \quad \text{and} \quad \omega_3 = \omega_1 + \omega_2 \quad (3b)$$

The diagonalized, traceless electric field gradient tensor is completely described by two parameters: The quadrupole coupling constant $\nu_Q = eQ \cdot V_{zz}/h$, which via the nuclear quadrupole moment $Q = 0.83 \cdot 10^{-24} \text{ cm}^2$ is directly proportional to the component V_{zz} , and the asymmetry parameter η . (Note, that a non-zero value of η would be easily recognized because of the changed ratios of the frequencies ω_i .) The coefficients S_n in eq.(2) contain the information on the orientation of the electric field gradient and thereby on the orientation of the probe atom-defect complex with regard to the host lattice. Using four γ detectors twelve coincidence spectra are simultaneously recorded and combined into a single, so-called PAC time spectrum $R(t) = A_{22} \cdot G_2(t)$.

Thus, using PAC ^{111}In -defect complexes can be studied whereby their formation and thermal stability is determined by the chemical properties of the isotope ^{111}In and their defect specific electric field gradient is measured at the isotope ^{111}Cd . Different ^{111}In -defect complexes are easily distinguished because of their different electric field gradients.

Sample preparation

The Si samples were doped with the ^{111}In probe atoms by implantation with 350 keV and the depth profile can be described by a Gaussian distribution centered 1600 Å underneath the surface with a maximum local concentration of about $5 \cdot 10^{16} \text{ cm}^{-3}$. Annealing at $T_A = 1173 \text{ K}$ for 600 s under flowing N_2 is used to remove the implantation induced lattice disorder. The implanted p-type Si samples consisted either of floatzone material with doping levels ranging between 10^{12} and $1.6 \cdot 10^{17} \text{ B cm}^{-3}$ or of epi-Si layers grown on top of Si substrates. For the PAC experiments the samples were kept at $T_M = 78 \text{ K}$ because the electric field gradients of the here discussed defects vanish at room temperature.

CHEMOMECHANICAL POLISHING

It was shown that chemomechanical polishing of (111) p-Si wafers leads to the formation of $^{111}\text{In-X}$ pairs which are characterized by the three coupling constants $\nu_Q = 237 \text{ MHz}$ (In-X1), 334 MHz (In-X2), and 408 MHz (In-X3); the electric field gradients are axially symmetric ($\eta = 0$) with their symmetry axes along $\langle 111 \rangle$ directions of the Si lattice.⁴ Fig. 1 illustrates the experimental conditions: The ^{111}In doped Si wafers were protected by a lacquer on the implanted site and subsequently polished on the opposite site for 3 to 5 hours at room temperature. Fig. 2 (top) shows the result of a PAC experiment at a Si:B ($1 \cdot 10^{15} \text{ cm}^{-3}$) wafer; in the Fourier transform of the PAC time spectrum the frequencies characterizing In-X1 and In-X2 are visible, whereby each complex is connected

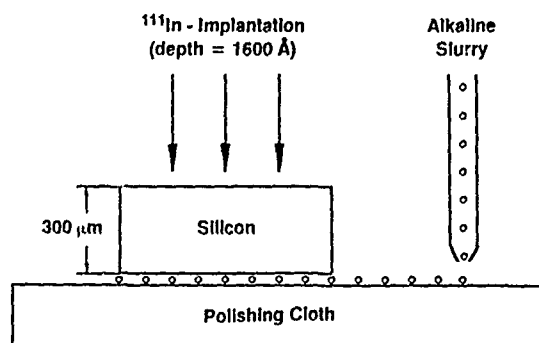


Fig. 1. Experimental conditions leading to the formation of ^{111}In -X pairs during chemomechanical polishing of (111) p-Si wafers at ambient temperature.

with the three frequencies ω_1 , ω_2 and $\omega_3 = \omega_1 + \omega_2$. The predominance of In-X1 and In-X2 is typical for Si samples in which the doping level is determined by the local ^{111}In acceptor

concentration. Since neither of the three coupling constants of the In-X complexes agrees with those three characterizing the In-H pairs, $\nu_Q = 360$ MHz, 480 MHz and 270 MHz⁵, it can be concluded that the X is not H. It should be noted, however, that the electric field gradients of the In-X complexes exhibit qualitatively close similarities with those of the In-H and also of the In-Li pairs: In each case, three different field gradients are observed whereby the occurrence of the third one always requires a higher acceptor concentration than the one given by the local ^{111}In concentration. In addition, the pairs formed with either the X defect, H or Li atoms all exhibit axial symmetry about the $\langle 111 \rangle$ lattice direction. The formation of ^{111}In -X pairs was also observed by Reislöhner et al. in PAC experiments at chemomechanically polished p-Si wafers in which the ^{111}In probe atoms were not introduced by implantation but by a modified silicon direct bonding process.⁶ Nonetheless, the chemical identity of the X defect remained unknown. It is interesting to note that also the experiment sketched in Fig. 1 testifies the above mentioned high mobility of the X defect: During polishing for about 4 hours, the defect crossed the Si wafer what gives an order of magnitude estimate for the diffusion coefficient of $D = 6 \cdot 10^{-8} \text{ cm}^2 \text{ s}^{-1}$ at 293 K.

DETECTION OF In-Cu PAIRS

For the determination of the chemical identity of the X defect ^{111}In doped Si samples were implanted with the elements Ar, Fe, Ni and Cu at low energies of 200 eV to look for a possible formation of the In-X pairs.⁷ The range of these elements in Si, covered with 15 to 20 Å of SiO_2 , is about 20 Å. That means, the implanted impurities have to diffuse about 1500 Å at the implantation temperature in order to reach the ^{111}In probe atoms and to form pairs. The element Cu was chosen because neutron activation analysis of Si wafers after chemomechanical polishing showed a correlation between the concentration of neutralized acceptor atoms and the Cu content of the polished sample.⁸

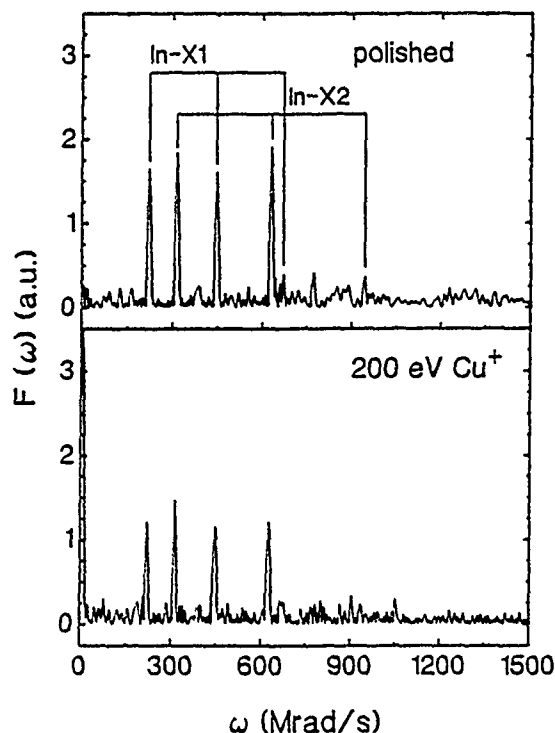


Fig. 2. Fourier transforms $F(\omega)$ of PAC spectra measured at ^{111}In doped Si after chemomechanical polishing of a Si:B ($1 \cdot 10^{15} \text{ cm}^{-3}$) wafer and after 200 eV Cu^+ implantation of an epi-Si:B ($4.5 \cdot 10^{14} \text{ cm}^{-3}$) layer. The identity of the observed frequencies shows that X is Cu.

Implantation of Cu atoms resulted in the formation of In-X pairs what is shown in Fig. 2 (bottom). After implantation of $3 \cdot 10^{14} \text{ Cu cm}^{-2}$ at 277 K into an epi-Si layer ($4.5 \cdot 10^{14} \text{ B cm}^{-3}$, $11 \mu\text{m}$ thick) on top of a Si:B ($4 \cdot 10^{18} \text{ cm}^{-3}$) wafer two electrical field gradients were visible and a comparison with the results after polishing (top of Fig. 2) reveals the identity of the frequencies with those characterizing In-X1 and In-X2.

PAC experiments at 78 K after doping with ^{111}In and annealing at 1173 K, ensured that before the implantation of the different elements no In-X complexes were already formed (see next section). When the Si samples contained a B concentration being comparable with or exceeding that of the ^{111}In concentration, also In-X3 was observed. An identification of X as an intrinsic defect, like a Si vacancy or a Si self-interstitial atom, would be possible, in principle, because the maximum transferred energy to a Si host atom by the different 200 eV projectiles is in the range 194 eV to 170 eV, what is still sufficient for the displacement of a few Si atoms. Such an assignment can be excluded, because

implantation of Ar, Fe and Ni with 200 eV produced no In-X pairs. Therefore, the PAC data prove that the X defect consists of Cu atoms and that chemomechanical polishing of p-type Si leads to the formation of acceptor-Cu pairs thereby deactivating the acceptor atoms.

Because of the $\langle 111 \rangle$ axial symmetry of the field gradient tensor characterizing the In-Cu

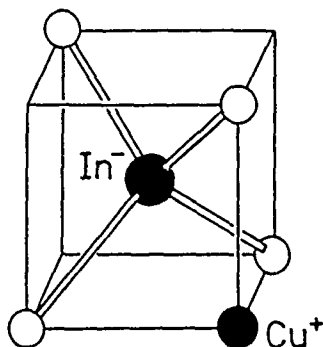


Fig. 3. Proposed configuration of an $\text{In}^- \cdot \text{Cu}^+$ pair in Si which fulfills the by PAC determined $\langle 111 \rangle$ symmetry.

complexes and the donor character of interstitial Cu atoms, we propose a complex with a Cu^+ atom located at a tetrahedral interstitial site next to the substitutional In^- acceptor as sketched in Fig. 3. The tetrahedral interstitial site is chosen because of the close resemblance of the ^{111}In -Cu pairs with ^{111}In -Li pairs observed in PAC experiments.⁵ Also Estreicher, based on theoretical calculations, proposed for the Cu and the Li atom a tetrahedral interstitial site next to the acceptor atom.⁹

The identification of the X defect as Cu is seemingly in contradiction to the results of two experiments in Si which studied the diffusivity of the X defect around 250 K and of Cu atoms around 800 K, respectively (Fig. 4). Zundel et al.¹⁰ investigated the diffusion of the X defect in a Si:In ($1.2 \cdot 10^{15} \text{ cm}^{-3}$) wafer that was chemomechanically polished to form the In-X pairs. By C-V profiling the change of the electrically active dopant concentration was measured as a function of sample temperature under different bias conditions. From these profiles the diffusion coefficient was extracted in the temperature range 220 K to 280 K (see X in Fig. 4). Hall et al.¹¹ measured the diffusion of Cu in Si:B ($5 \cdot 10^{20} \text{ cm}^{-3}$) between 673 K and 973 K using radioactive ^{64}Cu (see Cu in Fig. 4). Assuming an Arrhenius type behavior of the diffusion coefficient both sets of data obviously do not agree. Therefore the identification of X as Cu was refused and rather an identification as a Si self-interstitial atom was proposed¹⁰. However, when comparing both sets of data it should be taken into account that the doping level differed by 5 orders of magnitude. Hall et al. reported in

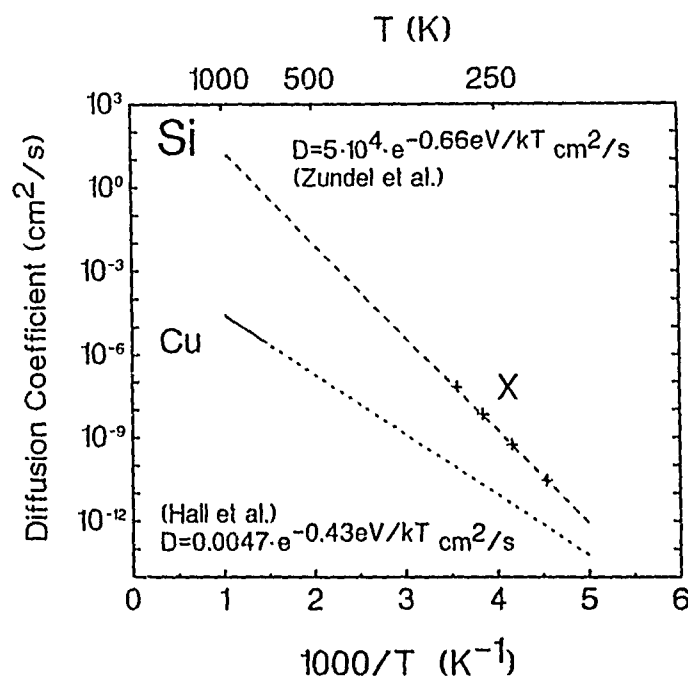


Fig. 4. Comparison of the diffusion coefficients of Cu in Si:B ($5 \cdot 10^{20} \text{ cm}^{-3}$)¹¹ and of the X defect in Si:In ($1.2 \cdot 10^{15} \text{ cm}^{-3}$)¹⁰.

their paper that according to their analysis interstitial Cu atoms do not form pairs with acceptor atoms and that the diffusion coefficient is independent of the acceptor concentration. Our PAC data directly prove the physical association of Cu atoms with the acceptor In in contrast to this analysis. Pairing, however, leads to a decrease of the effective diffusion coefficient of the more mobile species, i.e. Cu in this case¹². Therefore, the observation of a larger diffusion coefficient by Zundel et al. is reasonable because of the lower acceptor concentration. In a more recent C-V experiment on Cu diffused Si by Prescha et al.¹³ an involvement of Cu in the generation of the X defect is considered as being probable.

Cu CONTAMINATION IN Si WAFERS

Si Wafers

In the preceding paragraph we mentioned that check experiments have to ensure that no In-Cu pairs had been formed already after doping the Si sample with ¹¹¹In and annealing at 1173 K. For the formation of In-Cu pairs had turned out to be detectable in virtually all Si wafers as received from the suppliers. It should be remarked that these wafers were neither polished in the alkaline slurry nor intentionally contaminated with Cu atoms in any other way. Only at high B concentrations (above $6 \cdot 10^{16} \text{ cm}^{-3}$) no ¹¹¹In-Cu pairs could be detected by PAC any longer because the high B concentration represented such a strong competitive trap to the ¹¹¹In atoms under our experimental conditions that it suppressed the fractions of ¹¹¹In-Cu pairs to a level below 1%, the detection limit in our PAC experiments.

Fig. 5, which on its left shows the PAC time spectra and on its right their Fourier transforms, illustrates this effect that merely annealing of ¹¹¹In doped Si samples is sufficient for decorating, in this case, up to 40% of the ¹¹¹In atoms with Cu atoms. The wafer, whose resistivity of 6.5 to 8.5 Ωcm corresponds to a concentration of about $2 \cdot 10^{15} \text{ B cm}^{-3}$, was doped with 350 keV ¹¹¹In atoms and annealed for 600 s under flowing N_2 gas at step by step increasing temperatures T_A ; shown are the PAC data for $T_A = 1073 \text{ K}$, 1173 K and 1373 K . At the end of each annealing cycle the wafer was removed from the hot zone of the oven, still being under flowing N_2 , and cooled down to room temperature during 300 s. The Fourier transforms in Fig. 5 shows this procedure to effect a pronounced formation of In-Cu pairs. The occurrence of the three electric field gradients characterizing the ¹¹¹In-Cu pairs was also observed in PAC experiments by Reislöhner et al.⁶ who quenched p-Si wafers which were doped with the ¹¹¹In probe atoms by a silicon direct bonding process. In these experiments the radioactive probes resided within the first μm of the interface of the two bonded wafers and it turned out that pairs were only observed after quenching the samples into water with quenching rates exceeding 10^3 K s^{-1} . The fact that in the present

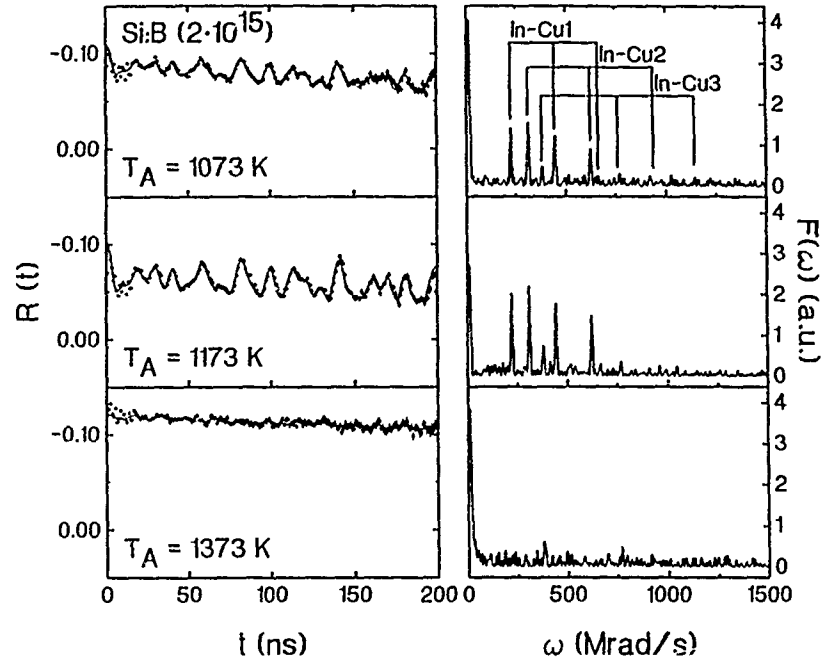


Fig. 5 PAC time spectra (left) along with their Fourier transforms (right) showing the occurrence of $^{111}\text{In-Cu}$ pairs in ^{111}In implanted Si wafers after annealing at temperatures T_A .

experiments $^{111}\text{In-Cu}$ pairs were observed for much lower cooling rates points to a strong enrichment of Cu towards the surface of the Si wafers because the probe atoms resided close to the wafer surface, in this case.

In Fig. 6 the fractions of In-Cu pairs i.e. the sum of In-Cu1 to In-Cu3, is plotted versus annealing temperature T_A . The increase in the fraction of In-Cu pairs with rising sample temperature corresponds to an increasing solubility of Cu in Si. At 973 K the solubility is $1.1 \cdot 10^{16} \text{ Cu cm}^{-3}$ and becomes comparable with the local ^{111}In concentration.¹⁴ Accordingly, the fraction of In-Cu pairs now rises sharply with T_A . At temperatures above 1173 K the probability for pair formation does not benefit any longer from the increased solubility of Cu and additional effects lead to a strong decrease of the pair fraction. (It should be noted that the retrograde solubility of Cu in Si possesses its maximum value at a higher temperature occurring near 1573 K.)

Using a four-point probe also the resistivity of the wafer used for the PAC experiment was measured in parallel. Plotted in Fig. 6 is the ratio between the resistivity R , measured after annealing at a temperature T_A , and the resistivity R_0 , measured at the as-delivered sample. The correlation between the increasing neutralization of electrically active atoms and the increasing formation of In-Cu pairs is evident. The identical behavior of the

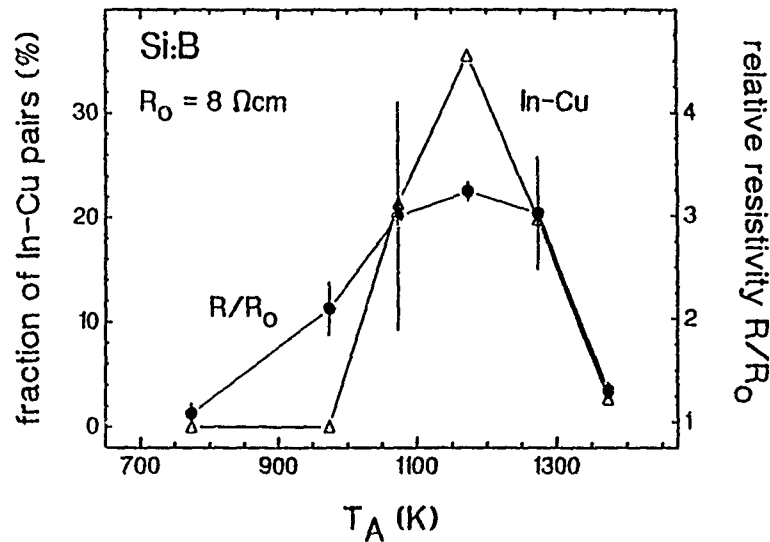


Fig. 6. Comparison of the fraction of ^{111}In -Cu pairs with the resistivity increase of the same Si:B ($2 \cdot 10^{15} \text{ cm}^{-3}$) wafer for different annealing temperatures T_A .

electrical resistivity was also found in Si:B wafers which had not been implanted with ^{111}In atoms, but only annealed at the respective temperatures. One should take into account that in this experiment the PAC probe atoms are sensitive to the first 2000 Å of the wafer, whereas the four-point probe is sensitive to the whole wafer and mainly observes the neutralization of B atoms. There are about $5 \cdot 10^{11} \text{ }^{111}\text{In cm}^{-2}$ implanted what has to be compared with $1 \cdot 10^{14} \text{ B cm}^{-2}$ in the whole wafer of about 600 μm thickness. Under the assumption that Cu^+ forms pairs with acceptors in general the comparison between PAC and resistivity measurement shows that the pairing effect is not restricted to the surface region of the wafer and that the decrease of both curves above 1173 K points to a declining ability of the acceptor atoms to trap Cu atoms, possibly because of a too high concentration of dissolved Cu atoms what leads to a pronounced mutual interaction between Cu atoms, or because of a too small binding energy of the acceptor-Cu pairs. From the resistivity data in Fig. 6 a lower limit of the Cu concentration is obtained assuming that the resistance was measured across the whole wafer: Since at $T_A = 1173 \text{ K}$ the resistivity increased from 7 Ωcm ($2 \cdot 10^{15} \text{ cm}^{-3}$) to 21 Ωcm ($6.5 \cdot 10^{14} \text{ cm}^{-3}$) the number of acceptor-Cu pairs or Cu atoms was $3.6 \cdot 10^{13} \text{ cm}^{-2}$.

With help of the PAC technique we have started a scan of differently doped Si wafers received from four suppliers. Fig. 7 presents preliminary results of this scan having the B doped Si wafers grouped according to their doping level. The shaded areas indicate the averaged fraction of In-Cu pairs found in the respective material. (The number next to

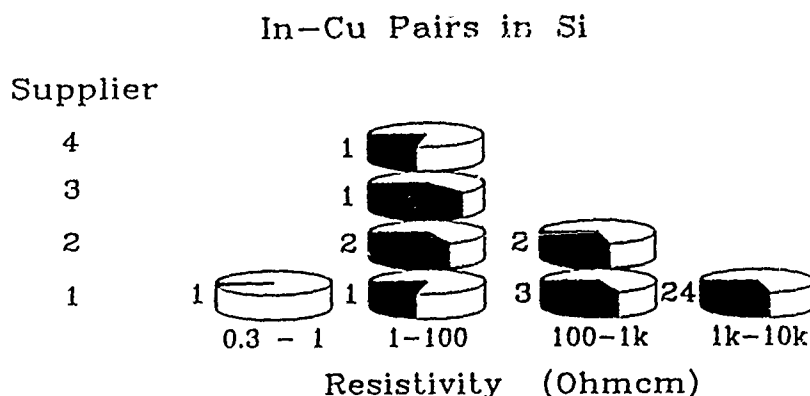


Fig. 7. Relative fraction of ^{111}In probe atoms, indicated by the shaded areas, which are decorated with Cu atoms after annealing Si:B wafers at 1173 K for 600 s. The strong reduction of visible Cu in case of the material having the lowest resistivity is caused by the high B concentration that exceeds the local probe atom concentration. The numbers next to the wafers indicate the number of investigated wafers.

each wafer is the number of investigated wafers.) Between 1 Ωcm and 10 $\text{k}\Omega\text{cm}$ the observed fractions of In-Cu pairs stayed constant because the B concentration is small compared with the local ^{111}In concentration; this situation changes when both concentrations become comparable as it is the case for resistivity values below 1 Ωcm . It is obvious that Cu is found in all Si wafers disregarding of the respective supplier. This observation points to a general step of wafer processing at which the Si is contaminated with Cu, like sawing of the bulk material.

Si Epi-layers

Because of this problem of an uncontrolled Cu contamination of Si wafers we had performed the experiments for the identification of the X defect (see Fig. 2) in undoped Si layers which were epitaxially grown on low resistivity Si wafers. As Fig. 8 (top) proves no fraction of ^{111}In -Cu pairs detectable by PAC exists in the ^{111}In implanted and annealed ($T_A = 1173\text{ K}$) epi-Si layers, in this case. The suppression of the ^{111}In -Cu pairs is effected by gettering the epi-layer free of Cu through the highly B doped Si substrate. That this effect is really in operation shows the result of the PAC experiment at an epi-layer which was grown on a Si substrate with a low B concentration ($1.3 \cdot 10^{15}\text{ cm}^{-3}$). Now, a pronounced formation of In-Cu pairs is observed because the gettering by the Si substrate is less efficient; here, In-Cu3 ($\nu_Q = 408\text{ MHz}$) is observed because the epi-layer contained $3 \cdot 10^{16}\text{ B cm}^{-3}$, what is known to favor the formation of In-Cu3.

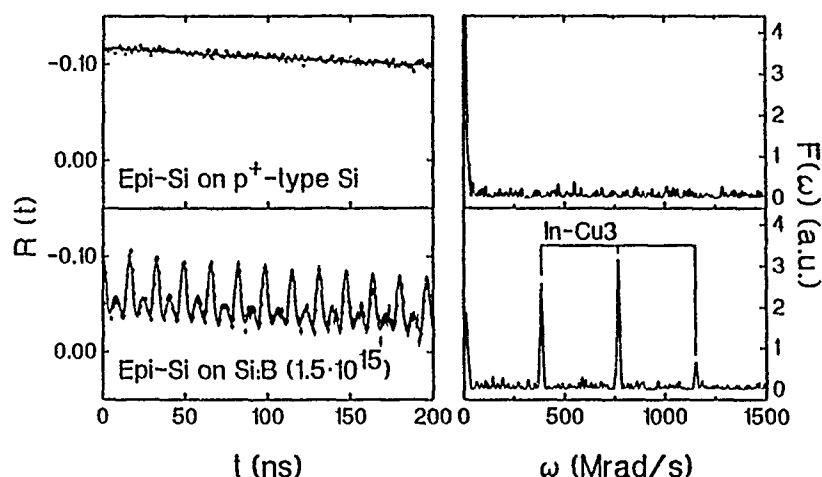


Fig. 8. Comparison of the formation of ^{111}In -Cu pairs in either an epi-Si:B ($4.5 \cdot 10^{14} \text{ cm}^{-3}$) layer on a low resistivity Si:B ($4 \cdot 10^{18} \text{ cm}^{-3}$) substrate (top) or in an epi-Si:B ($3 \cdot 10^{16} \text{ cm}^{-3}$) layer on a high resistivity Si:B ($1.3 \cdot 10^{15} \text{ cm}^{-3}$) substrate (bottom). Gettering of the low resistivity substrate is the reason for the strong reduction of the pair formation in the first epi-layer.

In the course of unravelling the chemical identity of the X defect, Forkel et al. presented PAC data¹⁵ which showed the formation of the $^{111}\text{In-X1}$ and $^{111}\text{In-X2}$ pairs after electron irradiation of Si:B ($2 \cdot 10^{15}$ and $1.6 \cdot 10^{17} \text{ cm}^{-3}$) wafers at 4.2 K and they proposed an identification of the X defect as an intrinsic defect, like a Si interstitial atom. In these investigations the conditions were quite similar to those of the present experiment which showed the formation of ^{111}In -Cu pairs already in the annealed Si wafers: The ^{111}In atoms were introduced via 80 keV implantation, the lattice damage was annealed at 1000 K, and only the wafer with the lower B concentration showed the formation of the pairs. Since the authors did not mention PAC spectra measured at 78 K before the electron irradiation which might have proven the absence or presence of the pairs at that stage of the experiment, it is quite probable that the annealing of the implanted Si wafers already produced the pairs rather than the electron irradiation. It should also be noted, that the pairs were not found in the wafer with the high B concentration in agreement with our observations.

Summarizing, the X defect produced by chemomechanical polishing of Si was identified as a Cu atom. The highly mobile interstitial Cu^+ forms pairs with the negatively charged acceptor and passivates it. Using the radioactive acceptor ^{111}In , it was also shown that as-delivered Si wafers are contaminated with Cu and annealing of the wafers leads to the formation of ^{111}In -Cu pairs paralleled by a passivation of the acceptor atoms. Considering that Cu is the transition element with the highest mobility and solubility in Si, the observed Cu contamination might have not been too surprising, afterwards. However, the processing step that introduces Cu into Si is still not yet identified.

The experimental assistance by Dr. Kohji Yamakawa is gratefully acknowledged. This work was financially supported by the Bundesminister für Forschung und Technologie and by the Deutsche Forschungsgemeinschaft (SFB 306).

REFERENCES

- * Present address: Technische Physik, Universität des Saarlandes, 6600 Saarbrücken, FRG.
- 1 S.J. Pearton, J.W. Corbett and T.S. Shi, *Appl. Phys. A* **43**, 153 (1987).
- 2 A. Schnegg, H. Prigge, M. Grundner, P.O. Hahn and H. Jacob, *Mat. Res. Soc. Symp. Proc.* **104**, 291 (1988).
- 3 A. Schnegg, M. Grundner and H. Jacob, in: *Semiconductor Silicon 1986*, ed. H.R. Huff, T. Abe and B. Kolbesen (Electrochemical Society, Pennington, N.J., 1986) p. 198.
- 4 M. Deicher, G. Grübel, R. Keller, E. Recknagel, N. Schulz, H. Skudlik, Th. Wichert, H. Prigge and A. Schnegg, *Inst. Phys. Conf. Ser. No. 95*, 155 (1989).
- 5 Th. Wichert, M. Deicher, G. Grübel, R. Keller, N. Schulz and H. Skudlik, *Appl. Phys. A* **48**, 59 (1989).
- 6 U. Reislohnner, S. Deubler, P. Dohlus, D. Forkel, G. Pensl, H. Plank, H. Wolf and W. Witthuhn, in: *Proceedings of the E-MRS-Europe 1989 Strasbourg Meeting, Symposium B*, in press.
- 7 R. Keller, M. Deicher, W. Pfeiffer, H. Skudlik, D. Steiner and Th. Wichert, to be published.
- 8 H. Prigge, P. Gerlach, P.O. Hahn and A. Schnegg, *Proc. 89, Electrochemical Society 1989*, p. 372.
- 9 S.K. Estreicher, to be published.
- 10 T. Zundel, J. Weber, B. Benson, P.O. Hahn, A. Schnegg and H. Prigge, *Appl. Phys. Lett.* **53**, 1426 (1988).
- 11 R.N. Hall and J.H. Racette, *J. Appl. Phys.* **35**, 379 (1964).
- 12 H. Reiss, C. Fuller and J.F. Morin, *Bell System Tech. J.* **35**, 535 (1956).
- 13 Th. Prescha, T. Zundel, J. Weber, H. Prigge and P. Gerlach, in: *Proceedings of the E-MRS-Europe 1989 Strasbourg Meeting, Symposium B*, in press.
- 14 E.R. Weber, *Appl. Phys. A* **30**, 1 (1983).
- 15 D. Forkel, S. Deubler, U. Reislohnner, K. Spörl, W. Witthuhn and H. Wolf, *Materials Science Forum* **38-41**, 1251 (1989).

STRAIN INDUCED INTRINSIC QUANTUM WELLS AS THE ORIGIN OF BROAD BAND PHOTOLUMINESCENCE IN SILICON CONTAINING EXTENDED DEFECTS

H. WEMAN* AND B. MÖNEMAR

Department of Physics and Measurement Technology, Linköping University, S-581 83 Linköping, SWEDEN

*Present address: Center for Quantized Electronic Structures (QUEST), University of California at Santa Barbara, Santa Barbara, California, 93 106, USA

ABSTRACT

A new recombination mechanism occurring in semiconductors containing extended defects is presented. The model is based on experimental data both from hydrogen plasma treated silicon, containing extended defects like platelets, and from oxygen precipitated silicon. The broad photoluminescence bands from these samples are attributed to the heavily damaged regions surrounding the extended defects, where electrons and holes can be localized in the strain-induced potential wells. From a theoretical calculation it is shown that the compressive strain field surrounding [111] and [100] platelets are sufficient to cause a local band gap reduction of as much as 0.3 eV, consistent with the experimental data.

INTRODUCTION

Low-temperature photoluminescence (PL) studies of defects in silicon have become a field of great interest in the past fifteen years, as recently reviewed by Davies [1]. Most of the work has been concentrated on bound exciton spectra of various impurities in the crystal, introduced both intentionally (by doping) or non-intentionally (process induced).

The PL from these centres usually gives rise to very sharp PL lines whereby the properties of the defects can be analyzed quite accurately. However in some cases broad featureless PL bands are observed which have been almost neglected [2-4]. It is the purpose of this paper to present a model which can explain the origin of these broad PL bands which are based on the local strain fields that surrounds the defects, as we tentatively suggested recently [5]. These broad bands are commonly observed in samples where more extended defects are seen. This includes oxygen precipitated [2,4], antimony precipitated [3] and hydrogen plasma treated silicon [5]. Most of our data presented in this paper are based on the experimental data from hydrogen plasma treated silicon where the geometry and dimensions of the extended defects (platelets, gas bubbles) are well known from transmission electron microscopy (TEM) viewgraphs. It has been shown that these platelets are commonly occurring as [111] planar defects with an extension of about 100 Å causing a 20 to 30 % dilation of the silicon interplanar separation [6].

EXPERIMENTAL RESULTS

The details of the experimental setup used in the PL experiments can be found elsewhere [4,5].

Typical broad PL bands that we will be discussing are shown in Figs. 1 and 2. The PL spectrum in Fig. 1 is taken at 2 K of a boron doped Si sample reactive ion etched (a), or plasma etched (b), in a 25 mTorr deuterium plasma for 10 min. The broad PL bands peaking at 0.9 eV with a halfwidth of 100 meV (FWHM), Fig. 1 (a), and 0.92 eV with a halfwidth of 75 meV (FWHM), Fig. 1 (b), is due to the etching treatment of the samples, while the other peaks are due to different replicas of the boron bound exciton [5]. The cross-sectional lattice image of this sample showed a heavily damaged region with [111] and [100] platelets.

The PL spectrum in Fig. 2 is taken at 2 K of a Cz-Si sample annealed at 450 °C for 504 h. Several sharp excitonic lines are observed due to various C-O related complex defects. However the dominating feature is the broad PL band peaking at about 0.9 eV [4]. From high resolution electron micrographs of similarly treated samples the agglomeration of oxygen into precipitates of various types (ribbons and platelets) have been observed [7].

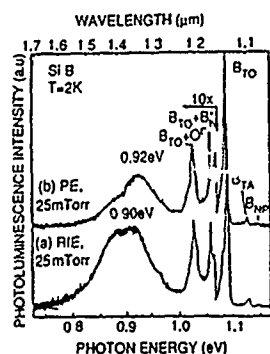


Fig. 1. PL spectra at 2 K of boron doped Si reactive ion etched (a), and plasma etched (b), in a 25 mTorr deuterium plasma for 10 min.

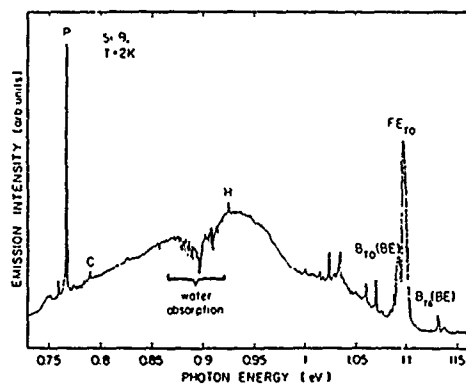


Fig. 2. PL spectrum at 2 K of a Cz-Si sample annealed at 450 C for 504 hours.

DISCUSSION OF THE IQW MODEL

The model which explains the behaviour of the broad PL bands associated with extended H-related defects in the near surface region (as shown in Fig. 1) is based on the fact that the silicon around such defects is highly strained. If we consider e.g. a platelet defect, as shown in Fig. 3, it is known from TEM data, that the hydrogen-saturated split which forms the platelet, separates the silicon boundary layer by a distance exceeding the normal lattice distance by about 20 to 30 % [6].

This means that there is a strong compressive strain field perpendicular to the platelet, so that the lattice constant could be considerably reduced in this direction. The strain field has an extension of about 70 to 100 Å, as judged from TEM data [8]. This compressive strain field will lead to a considerable reduction of the bandgap and then to a localized "quantum well" confinement of both electrons and holes, as will be shown in detail below.

In order to make quantitative estimates of the local shifts in the valence and conduction bands around a platelet defect, some simplifying assumptions are made. The strain-induced change in lattice constant perpendicular to the plane of the platelet is supposed to be much larger than the change parallel to the platelet, and the latter is therefore neglected.

From the known values of the deformation potentials in silicon one can estimate the shift of both the valence band top and the lowest conduction band minima, and in addition the contribution to the average band gap shift from the hydrostatic components of the strain field [9,10].

For the upshift of the valence band due to strain splitting one can derive an expression like

$$\Delta E_{v1} = -1/6 \Delta_0 + 1/4 \delta E + 1/2 [\Delta_0^2 + \Delta_0 \delta E + 9/4 (\delta E)^2]^{1/2} \quad (1)$$

valid for a uniaxial stress along [001] or [111] [10, 11].

Here Δ_0 is the spin-orbit splitting at $\Gamma_{25'}$ in unstrained silicon ($\Delta_0 = 0.044$ eV) and δE is the linear component of the strain induced splitting of the multiplet of the valence band top. For [111] oriented platelets the splitting δE_{111} can be expressed as

$$\delta E_{111} = 2\sqrt{3} \delta E_{xy} \quad (2)$$

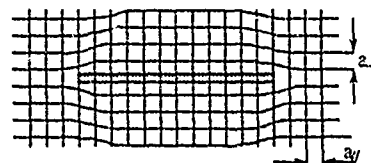


Fig. 3. Schematic picture of a hydrogen platelet defect, where the strain field induced by the platelet, have expanded the Si planes perpendicular to the plane of the platelet a.L. ($\Delta a_{\perp}/a_0 \sim 3\%$ and $\Delta a_{\parallel}/a_0 \sim 0$ assumed).

where d is the approximate deformation potential constant ($d = -4.85$ eV [12]) and the component ϵ_{xy} of the strain tensor in this case may be approximated by $\epsilon_{xy} \sim 1/3 \Delta a_1/a_0$ [11], where Δa_1 is the change of the lattice parameter perpendicular to the platelet. Similarly, for [100] oriented platelets δE_{100} is given by

$$\delta E_{100} = 2b(\epsilon_{zz} - \epsilon_{xx}) \quad (3)$$

where b is the approximate deformation potential parameter ($b = -2.1$ eV [11]), and in this case $\epsilon_{xx} \sim 0$, $\epsilon_{zz} \sim \Delta a_1/a_0$ [11].

For the conduction band there is no splitting in first order of the lowest Δ conduction band for [111] oriented platelets, while for [100] orientation there will be a downward shift of the magnitude

$$\Delta E_c^\Delta = \frac{2}{3} \Xi_u^\Delta (\epsilon_{zz} - \epsilon_{xx}) \quad (4)$$

where again Ξ_u^Δ is the approximate deformation potential constant ($\Xi_u^\Delta \sim 8.6$ eV [11]), $\epsilon_{xx} \sim 0$ and $\epsilon_{zz} \sim \Delta a_1/a_0$. In addition there is an average hydrostatic change ΔE_g^0 in the energy gap given by

$$\Delta E_g^0 = \alpha \bar{I} \bar{\epsilon} \quad (5)$$

where \bar{I} is the unit dyadic tensor, $\bar{\epsilon}$ is the strain tensor and α is given as 1.50 ± 0.3 eV [12].

From the above it is easily calculated, that for a maximum strain $\Delta a_1/a_0$ of 3 % the valence band top would be raised about 0.17 eV compared to unstrained material for [111] oriented platelets, while the conduction band would be lowered by an unknown partition of ΔE_g^0 , which is about 0.05 eV in this case. For [100] oriented platelets the upward shift ΔE_{v1} [100] is about 0.13 eV, for $\Delta a_1/a_0 = 3\%$. Similarly the Δ conduction band is lowered by a similar amount ~ 0.17 eV in this case (in addition to the hydrostatic shifts of 0.05 eV). Therefore the strain field induced reduction of the band gap is much larger for [100] oriented platelets, for the same perpendicular deformation.

The above estimates serve to demonstrate the main features of the proposed model for the electronic structure of the hydrogen-induced extended defects in silicon. Clearly for a compressive stress field the valence band will be pushed up while the conduction band will come down, compared to unstrained silicon. This means that there will be notches in both band edges at the interface towards the platelets, so that both electrons and holes can be localized in the same region, as shown in Fig. 4. This is in contrast to the case of a heterostructure interface, where typically only one carrier can be localized. The present case therefore represents a novel structure which is here realized by nature itself and which we here call "intrinsic quantum well" (IQW) induced by the strain field.

The extent of the potential notches is connected to the extent of the strain field. We have not attempted any self-consistent calculation of the spatial variation of this strain field, but the contrast observed in TEM pictures of these platelets [8], indicate an extension of about 100 Å. This rather wide potential may give rise to only one bound level for electrons and holes, respectively, at rather small distances Δ_e and Δ_h from the respective band edges (Fig. 4).

Comparing with the experimental spectrum in Fig. 1 (a), we may associate the PL band peaking around 0.9 eV to [100] oriented platelets, where the recombination process is supposed to be dominated by a TO-phonon assisted recombination between electrons and holes both localized in the potential wells close to the interface. The emission (at 2 K) would be expected to peak at

$$h\nu = E_g - E_p(\text{TO}) - (\Delta E_c + \Delta E_v) + (\Delta_e + \Delta_h) \quad (6)$$

Using the values $E_g = 1.17$ eV, $E_p(\text{TO}) = 0.06$ eV, and $(\Delta_e + \Delta_h) \sim 0.05$ eV, a value $(\Delta E_c + \Delta E_v) \sim 0.26$ eV is obtained. This would then be consistent with a maximum value of $\Delta a_1/a_0$ of about 3 %. Unfortunately the TEM data available are not sufficiently accurate to resolve such a shift. It is however of a reasonable magnitude, if it is assumed that the observed total strain is accommodated gradually over the strained region.

The bands observed at higher energies could be accounted for by [111]-oriented platelets, and in addition by other hydrogen-induced inclusions of a different geometry.

The latter would be more difficult to model exactly, but the above analysis shows that it is sufficient to have a compressive stress field in some region around such a defect to achieve localization of both electrons and holes in that region, i.e. IQW's.

One should also keep in mind a number of effects that would serve to broaden the observed spectra. It is well known from studies of electronic levels in 2D potentials in heterostructures that the localized levels are considerably broadened [13]. In addition, and perhaps more importantly, we have to assume that the ensemble of platelets in a sample exhibits some variations in size, shape and consequently in strain field profiles, making the potentials varying among the platelets. Further, overlap between different types of hydrogen related defects will also contribute to the observed broadening.

We believe that this strain-induced IQW recombination also is the origin of the broad PL bands observed in oxygen precipitated Si, such as in Fig. 2, and antimony precipitated Si [3]. This recombination mechanism should also be valid for other semiconductors where local strain fields are present, since the model is not related to the electrical potentials of the defects, but is of "intrinsic" nature. For instance it is possible that the broad PL bands observed in strain adjusted Si/Ge superlattices [14] are due to the IQW recombination mechanism.

CONCLUSION

We have presented a new recombination mechanism occurring in semiconductors containing extended defects which is based on experimental data, from plasma treated Si where [111] and [100] platelets have been observed by TEM. The observed broad PL bands are attributed to the strain surrounding these defects, where electrons and holes can be localized in potential wells. From a theoretical calculation we have shown that the compressive strain field surrounding these platelets, compressing the Si lattice normal to the plane of the platelet with about 3 %, is sufficient to cause a local bandgap reduction of as much as 0.3 eV, consistent with our data.

ACKNOWLEDGMENTS

We want to thank G. S. Oehrlein and J. L. Lindström for the hydrogen plasma treated samples and for valuable discussions.

REFERENCES

1. G. Davies, *Physics Reports*, **176**, 83 (1989).
2. N. Magnea, A. Lazrak, and J. L. Pautrat, *Appl. Phys. Lett.* **45**, 60 (1984).
3. J. Wagner, J. C. Gelpey, and R. T. Hodgson, *Appl. Phys. Lett.* **45**, 47 (1984).
4. H. Weman, B. Monemar, and P. O. Holtz, *Appl. Phys. Lett.* **47**, 1110 (1985).
5. H. Weman, J. L. Lindström, and G. S. Oehrlein, *Proc. E-MRS 1989 Spring Meeting, "Science and Technology of Defects in Silicon"*, Strasbourg, 1989, *Mat. Sci. Eng. B.* (1989).
6. F. A. Ponce, N. M. Johnson, J. C. Tramontana, and J. Walker, *Inst. Phys. Conf. Ser.* No. **87**, 49 (1987).
7. A. Bourret, J. Thibault-Dessaux, and D. N. Seidman, *J. Appl. Phys.* **55**, 825 (1984).
8. S. J. Jeng, G. S. Oehrlein, and G. J. Scilla, *Appl. Phys. Lett.* **53**, 1735 (1988).
9. C. Herring and E. Vogt, *Phys. Rev.* **101**, 944 (1956).
10. F. H. Pollak and M. Cardona, *Phys. Rev.* **172**, 816 (1986).
11. C. G. Van de Walle and R. M. Martin, *Phys. Rev. B* **34**, 5621 (1986).
12. L. D. Laude, F. H. Pollak, and M. Cardona, *Phys. Rev. B* **3**, 2623 (1971).
13. I. Kukushkin, V. Timofeev, K. v. Klitzing, and K. Ploog, *Festkörperprobleme*, **28**, 21 (1988).
14. R. Zachai, E. Friess, G. Abstreiter, E. Kasper, and H. Kibbel, *Proc. 19th Int. Conf. on the Physics of Semiconductors*, Warsaw, Poland, Aug. 1988.

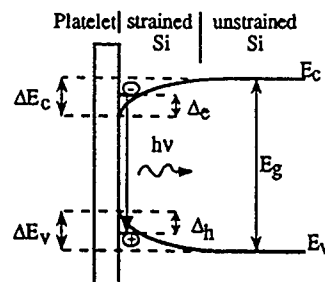


Fig. 4. The strain induced IQW model describing the origin of the broad PL bands. ΔE_c and ΔE_v denotes the strain induced shifts of the conduction and valence bands, respectively, while Δe and Δh denotes the distance of the electron and hole bands from the notches.

OPTICAL PROPERTIES OF NOVEL VIBRONIC BANDS IN ELECTRON-IRRADIATED TIN DOPED SILICON

J. H. SVENSSON, B. MONEMAR, B. G. SVENSSON*

Department of Physics and Measurement Technology, Institute of Technology, Linköping University, S-581 83 Linköping, Sweden

*Department of Solid State Electronics, The Royal Institute of Technology, P. O. Box 1298, S-164 28 Kista, Sweden

ABSTRACT

The optical absorption of two new electronic transitions in silicon doped with tin has been investigated. At low temperatures two no-phonon lines are observed at 2755.3 and 4112.2 cm^{-1} , each with strong coupling to a single quasi-localized vibration in the excited electronic state. These vibrations have quantum energies of 69.6 and 70.2 cm^{-1} , respectively. At higher temperatures coupling to thermally excited vibrational states in the ground electronic states is observed for both lines. The transition with the no-phonon line at 4112.2 cm^{-1} has been studied in detail and is found to be well described using the adiabatic and Condon approximations. The optical properties of the two transitions are found to be quite similar. Moreover the relative intensities of the two lines are found to be dependent on the optical excitation conditions.

INTRODUCTION

It has been demonstrated [1] that vacancies created by electron-irradiation of silicon at room temperature are highly mobile in the lattice. Impurity elements such as tin and germanium have been found to trap vacancies efficiently in silicon. The tin-vacancy defect has been found to be stable at room temperature [2,3], whereas the germanium-vacancy complex dissociates at approximately 200 K [4]. The electronic ground state of the tin-vacancy defect has been studied directly with Electron Paramagnetic Resonance (EPR) [3]. Moreover the defect has been found to be stable at temperatures up to approximately 470 K, observed both directly via the decrease in the EPR signal, and indirectly as the cause of an increase in the intensity of infrared absorption bands due to other vacancy related defects [5].

In this work we present results from infrared absorption studies of electron-irradiated silicon doped with tin. The ordinary tin-vacancy defect is found to be inactive with respect to infrared absorption, but during isochronal annealing of the samples previously unreported transitions are observed. The transitions emerge at annealing temperatures higher than 470 K, and are found to disappear at temperatures exceeding 580 K. We have focused on the optical properties of these transitions.

EXPERIMENTAL

The samples are Czochralski-grown phosphorus-doped silicon with a concentration of tin atoms of approximately $5 \times 10^{18} \text{ cm}^{-3}$. Irradiation with 2 MeV electrons with a dose of $2 \times 10^{18} \text{ e}^-/\text{cm}^2$ was done at room temperature. All absorption measurements were performed with a BOMEM DA3.26 Fourier Transform Infrared Spectrometer (FTIR) fitted with a liquid nitrogen cooled indium-antimonide detector. A halogen lightbulb source was filtered with silicon and germanium wafers held at room temperature.

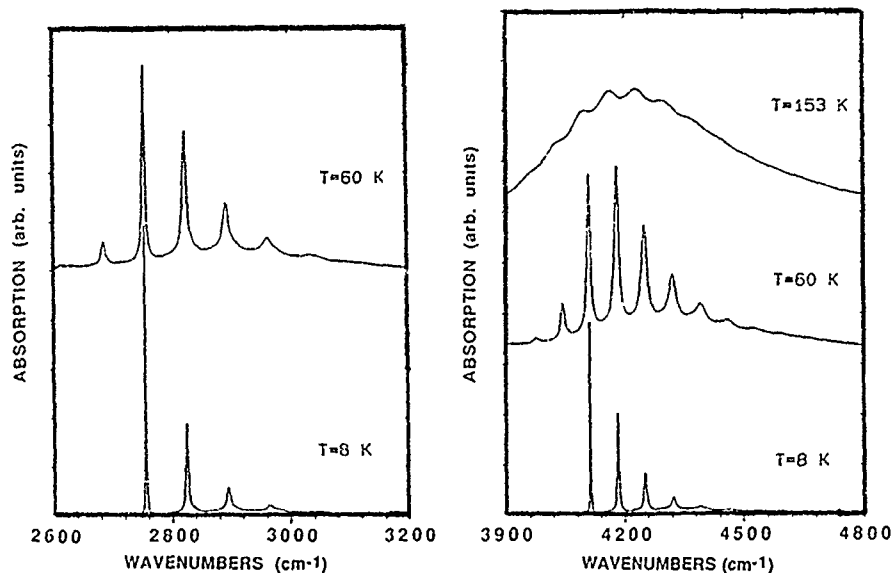


Figure 1.
Absorption spectrum of a sample showing the two no-phonon lines and their phonon replicas at different temperatures. No filtering of the source was done.

EXPERIMENTAL RESULTS AND DISCUSSION

A typical absorption spectrum at different temperatures is shown in figure 1. Two electronic transitions are observed with the no-phonon lines at 2755.3 and 4112.2 cm^{-1} , respectively. In the excited electronic states rather strong coupling to quasi-localized vibrations is observed with phonon energies of 69.6 and 70.2 cm^{-1} , respectively, at a sample temperature of 7 K. These values are deduced from the first vibrational excited states. The deviation from these values is within the margin of experimental error for excitation to vibrational levels with quantum numbers up to $n=4$ for the vibrational coupling to the 4112.2 cm^{-1} no-phonon line. The spectra will be referred to as "vibronic" bands.

The line at 4112.2 cm^{-1} does not split in magnetic fields up to 7 Tesla, and therefore corresponds to a singlet-to-singlet transition, while the line at 2755.3 cm^{-1} has not yet been investigated in a magnetic field. We will assume that the high energy vibronic band can be treated within the adiabatic and the Condon approximations [6,7]. Comparisons will be made concurrently with the low energy band, keeping in mind that the degeneracy of these electronic states is yet unknown.

Using the approximations above, the transition probability between the electronic ground state and the excited vibrational states, X_n , of the electronic excited state is :

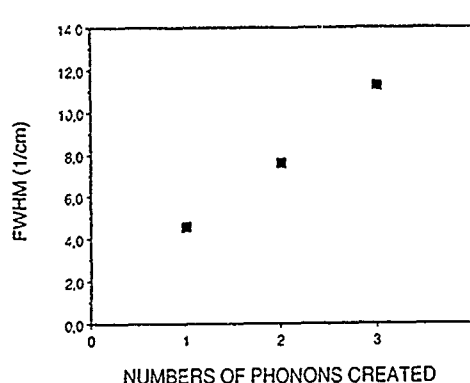


Figure 2. The full width at half maximum (FWHM) of the phonon replicas of the no-phonon line at 4112.2 cm^{-1} , versus numbers of phonons created.

$$M_{0n} = \int dQ X_n^*(Q-Q_0) X_0(Q)$$

where Q_0 is the displacement of the vibration equilibrium point between the two states. The harmonic oscillator state, X_n gives

$$|M_{0n}|^2 = e^{-S} S^n / n!$$

where S is the "Huang-Rhys" factor.

The optical transitions have relative intensities lying in a Poisson distribution and the argument, S , is measurable from the fraction of the transition probability lying in the no-phonon line.

Neglecting coupling to the broad band lattice vibrations and estimating the transition probability from the integrated intensity of the peaks gives the factor $S=1.3 \pm 0.05$ in the limit of low temperature. This value can fairly well reconstruct the intensities of the different vibrational replicas with respect to the no-phonon line. The value gives an energy relaxation ("Frank-Condon" shift) of 11.3 meV.

At elevated temperatures vibrational states in the ground electronic state become populated, as can be seen in figure 1. The value of the vibrational energies in the electronic ground state is lower than in the excited state. A larger degree of anharmonicity of the ground state potential is also indicated by the decreasing energy spacing between the $n=1$ and $n=2$ vibrational levels in the electronic ground state for both transitions.

The thermal population of the vibrational levels in the ground state will lead to a decrease of the no-phonon intensity if $S < 2$ [7], and this expected decrease is observed for both bands. The two vibronic bands broaden when the temperature is increased, and at 190 K no discrete structure from the vibrational transitions can be discerned. The total integrated intensity of the two vibronic bands, however, is independent of temperature, as predicted by theory, using the adiabatic and Condon approximations.

In figure 2 the broadening of the vibrational replicas of the no-phonon line is shown versus the number of phonons created in the excitation process. The relationship is close to linear, as is expected when a quasi-localized single vibration can decay directly into band phonons [6]. This result exposes the limitations of the relatively simple assumptions above and shows that interaction with low energy lattice band phonons can not be neglected.

Isochronal annealing of the samples for 20 minutes with 20 degree temperature intervals shows that the two bands appear at 470 K, the same temperature that the tin-vacancy defect is found to disappear at, and that the bands disappear at 590 K. A possible identification of the defect is a tin-vacancy defect trapped at a substitutional tin atom. Due to the close similarities between the two transitions with respect to their optical and thermal properties and due to the annealing results it is reasonable to assume that the transitions originate from the same defect.

Finally, it should be noted that the two no-phonon peaks exhibit an interesting dependence on the optical excitation energy during the cooling process. When the source is filtered with a germanium wafer held at room temperature, the intensity of the low energy line decreases and the intensity of the high energy line increases.

compared with the intensities when the source is unfiltered. These intensities do not, however, change in a 1:1 relation as expected for an ordinary change in relative population of two different charge states. The transformation process changing the intensity of the transitions has a very low or no thermal barrier. A detailed investigation with different perturbation spectroscopic methods such as a Zeeman study of the 2755.3 cm^{-1} line in combination with uniaxial stress and/or electron paramagnetic resonance is necessary to reveal the symmetries of the electronic states and to understand fully the behaviour discussed above.

CONCLUSION

Two new vibronic transitions have been observed in optical absorption for tin-doped silicon. A transition with a no-phonon peak at 4112.2 cm^{-1} couples to a single quasi-localized vibrational mode. A value of the Huang-Rhys factor of 1.3 describes the vibronic band well at low temperatures. At elevated temperatures transitions from thermally populated vibrational excited states in the ground state are found. The phonon replicas in the excited state are approximately energetically equidistant, while the energies of the replicas in the ground state decrease with increasing quantum number, thus indicating a larger degree of anharmonicity in the ground state. Increasing width of the phonon replicas indicates that the single vibrational mode can decay into band phonons and that a more detailed theoretical treatment is necessary to describe the vibrational properties accurately. A vibronic band with a no-phonon peak at 2755.3 cm^{-1} has very similar optical properties. According to the annealing kinetics a possible defect model is a tin-vacancy defect trapped at a substitutional tin atom. An interesting dependence on the optical excitation range of the relative intensity of the two transitions is found. The results indicate that the two transitions do not originate from different charge states of the same defect state. Information from perturbation spectroscopic methods is necessary to draw any further conclusions.

REFERENCES

1. G. D. Watkins, Lattice Defects in Semiconductors 1974 (Institute of Physics, London, 1975), p. 1.
2. A. Brelet, IEEE Trans. Nucl. Sci., NS-19, p. 220 (1972)
3. G. D. Watkins, Physical Review B, 12, p. 4383 (1975)
4. A. Brelet and J. Charlemagne, Radiation Effects in Semiconductors, edited by J. W. Corbett and G. D. Watkins, (Gordon and Breach, New York, 1971), p. 161
5. B. G. Svensson, J. H. Svensson, J. L. Lindström, G. Davies and J. W. Corbett, Appl. Phys. Lett., 51 (26), p. 2257, (1987)
6. K. K. Rebane, Impurity Spectra of Solids, Plenum Press, New York, 1970
7. G. Davies, Rep. Prog. Phys., Vol. 44, p. 787, (1981)

A NEW METASTABLE DEFECT IN SILICON, OPTICAL PROPERTIES AND AN INVESTIGATION OF THE MECHANISM CAUSING THE CONFIGURATIONAL CHANGE

J. H. SVENSSON, B. MONEMAR

Department of Physics and Measurement Technology, Institute of Technology,
Linköping University, S-581 83 Linköping, Sweden

ABSTRACT

A new optical transition with a no-phonon energy of 0.615 eV discovered in electron-irradiated silicon grown by the Czochralski technique is investigated, revealing metastable properties of the related defect. The investigation is focused on the optical properties of the transition and its associated structure and on the mechanism governing the change of defect configuration. The transformation of the defect to the metastable state is suggested to be induced by excitonic Auger recombination. A pseudo-donor model is presented as an explanation of the optical spectrum.

INTRODUCTION

A number of optical no-phonon transitions with varying coupling strength to phonons have been investigated in electron-irradiated silicon grown by the Czochralski-technique. The most prominent of these transitions have no-phonon energies at 0.790, 0.969 and 0.489 eV, respectively [1-6]

In the case of the 0.790 eV transition, electronic excited state structure is clearly observed [4]. The excitation structure has been explained as due to electronic excited states of an electron, that in its excited states is bound by the Coulomb field of a tightly bound hole. The electron and the bound hole are envisioned as a pseudo-donor [5].

The defect causing the no-phonon line at 0.969 eV has been proposed to be an interstitial-substitutional carbon pair; moreover the defect is believed to have two stable geometrical configurations [6]. Transformation between the two configurations was observed when the sample was optically excited with a YAG-laser at temperatures below 50 K.

Recently a new no-phonon transition in irradiated silicon was found at 0.615 eV [7]. Additional structure is observable at higher photon energies, approximately 165 meV above the no-phonon line. This line and the structure are only observed when the sample is optically excited at temperatures below 65 K. The entire structure disappears when the sample is heated to temperatures exceeding 70 K [7] and the thermal activation energy for the disappearance is 0.21 eV. A model explaining the results as being caused by a carbon-related defect with two configurations in the neutral charge state was put forward.

In the present work we have investigated the kinetics of the growth in intensity of the 0.615 eV no-phonon line using two different optical excitation sources to induce the growth. We also present results from an optical investigation of the absorption structure.

EXPERIMENTAL

The samples are Czochralski-grown phosphorus-doped silicon crystals, with an initial resistivity of 40 Ωcm at room temperature. The samples were polished to

obtain optical surfaces and then irradiated at room temperature with 2 MeV electrons. After the irradiation the samples were highly resistive.

All measurements were made with a BOMEM DA3.26 Fourier Transform Infrared Spectrometer (FTIR), with the source filtered with a silicon wafer at room temperature.

The samples were cooled with a helium bath cryostat with a temperature controller. The optical excitation sources were a halogen lightbulb or a Nd-doped yttrium aluminium garnet (Nd-YAG) laser, with a photon energy of 1.165 eV. The laser line was filtered through a bandpass filter to avoid excitation of the sample with other laser background lines.

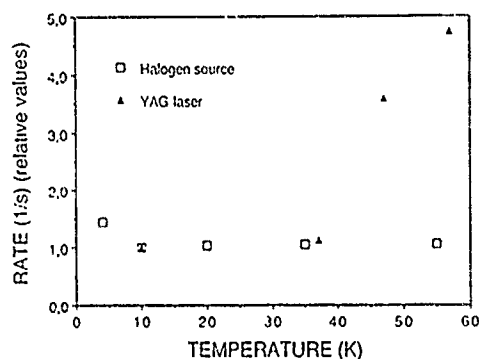


Figure 1.

The temperature dependence of the transformation rate to the metastable configuration using a halogen lightbulb or a YAG laser as excitation source. The intensity of the no-phonon line was evaluated at 4-11 K.

RESULTS AND DISCUSSION

Independent of the particular excitation source, the 0.615 eV (4960 cm^{-1}) line and its associated structure increased monotonically versus time at all sample temperatures. In figure 1 we show the rate of increase in intensity for optical excitation with both the YAG laser and a halogen lightbulb as a function of temperature. All measurements were made with a sample temperature between 4 and 11 K. As can be seen the transformation rate is approximately constant for temperatures between 10 and 55 K when the continuous light source is used. An increase of the rate is observed for the lowest temperature, 4.2 K.

A totally different temperature dependence is found when the discrete laser energy is used. An increase of the rate is observed when the sample temperature is increased.

The appearance of the optically active defect state only when the sample is exposed to above band gap excitation, or in the case of the laser excitation with a photon energy that is close to resonant with the bandgap energy, means that the transformation of the defect configuration occurs via recombination processes at the defects with either electrons, holes or free excitons. No transformation occurs when the continuous source is filtered with a silicon wafer held at room temperature during excitation times of the same order as displayed in figure 1.

Of the three different classical models for recombination mechanisms, multiphonon capture, cascade capture and Auger-type capture mechanisms, only Auger-type processes can account for the temperature dependence at low temperatures of the transformation rate. A new kind of Auger capture, the excitonic Auger capture process, has recently been put forward [8,9]. It differs from the other types of Auger processes in that the excess energy released when one carrier is captured is transferred to the remaining carrier of the exciton, whereas for a regular

Auger process, a second free carrier is needed to absorb the excess energy. The latter process would give a quadratic dependence of the recombination rate on carrier density. Thus a quadratic dependence of the conversion rate on the optical excitation effect is expected. Instead, a linear relationship is found, as expected for the excitonic Auger mechanism. The approximate independence of the rate on temperature between 10 and 55 K is in agreement with the results obtained by Hangleiter for excitonic Auger capture in the limit of low excitation [9].

The increase in rate versus temperature found when YAG laser excitation is used we attribute to the increase in absorption of the laser line due to the temperature dependence of the bandgap. An increase in rate is also expected due to the screening of Coulomb interaction at high carrier densities for exciton Auger capture [8].

It should be noted that we have neglected the influence of other recombination channels present in the sample and that we have assumed that the probability of transformation to the optically active state is independent of temperature.

The 0.615 eV no-phonon line and its associated structure is shown in figure 2. The sharpest peaks at higher energies are shown in detail. We tentatively assign these transitions to excitations from the deep non-degenerate electron ground state to excited hydrogen-like states according to the effective mass approximation (EMA), perturbed by the central-cell potential. The defect state with the electron in the excited state is referred to as a pseudo-donor. The electron is then described as bound in the Coulomb field of a hole tightly bound to the defect.

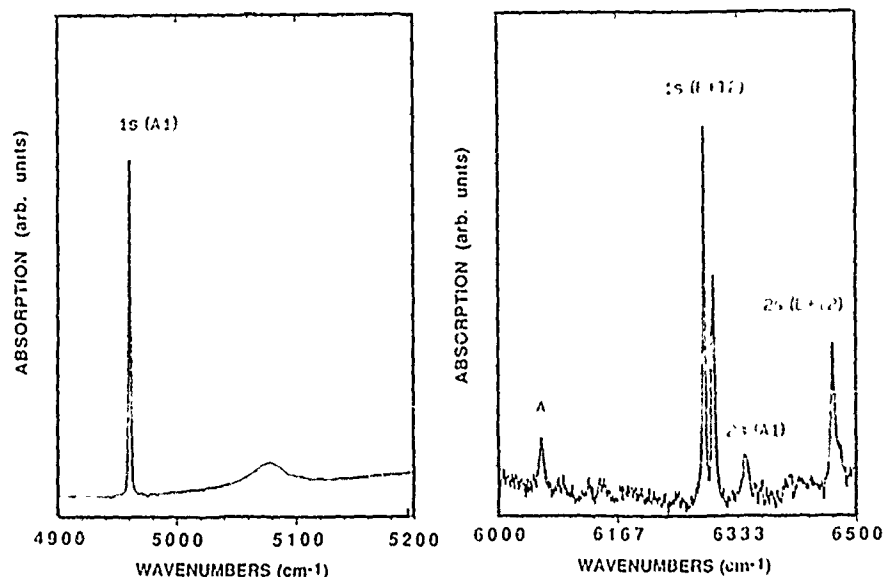


Figure 2. Absorption spectrum of the sample, showing the structure related to the line at 0.615 meV (4960 cm^{-1}).

We assign the no-phonon line at 0.615 meV (4960 cm^{-1}) to a transition to the $1s (A1)$ symmetric state and the structure at 0.780 eV (6291 cm^{-1}) as transitions to $1s (E+T2)$ states. The structure at higher energies in figure 2 is attributed to

transitions to 2s states [10]. A previously unreported line, labelled A in figure 2, emerges with optical excitation and is also most likely related to the defect.

It has been found that the binding energies of the 1s(E) and 1s(T2) states that have a node at the impurity site are relatively close to the theoretical binding energy value of the 1s-state according to EMA. According to our assignments above, the transition at 0.780 eV should approximately correspond to an 1s electron state with a theoretical binding energy of 31.26 meV. The ionisation edge would then be $780+31=811$ meV. This means that the binding energy of the electron in its lowest excited state, the 1s (A1) pseudo-donor state, is $811-615=196$ meV. This value locates the 0/+ electronic ground state of the optically active configuration of the defect at approximately $E_V+0.34$ eV.

The no-phonon line couples to lattice phonons (figure 2). The temperature dependence of the transition gives a constant integrated intensity of the whole absorption structure related to the transition for sample temperatures between 4.2 and 65 K.

CONCLUSIONS

We have presented results for the temperature dependence of the transformation rate of a metastable defect in silicon. The optically active metastable state is populated when the sample is optically excited at temperatures below 65 K. The process governing the change to the active defect state is found to be in agreement with free excitonic Auger recombination at the stable optically inactive defect state. The optical spectrum is also tentatively interpreted as due to a pseudo-donor. In this case the defect is neutral in the metastable state with a deep 0/+ donor level at $E_V+0.34$ eV and the electron of the pseudo-donor has a binding energy in its 1s (A1) ground state of 196 meV.

REFERENCES

1. A. V. Yuknevitch, Fiz. Tverd. Tela (Leningrad) **7**, 322 (1965) [Sov. Phys. Solid State **7**, 259 (1965)]
2. V. D. Tkachev, A. V. Mudryi, Radiation Effects in Semiconductors, ed. by N. B. Urii, Institute of Physics Conference Series, Vol. **31** (IOP, London, 1977), 231
3. G. Davies, E. C. Lightowers, M. Stavola, K. Bergman, B. G. Svensson Phys. Rev. B, **35**, 2755, (1987)
4. J. Wagner, K. Thonke, and R. Sauer, Phys. Rev. B, **31**, 5561, (1985)
5. K. Thonke, A. Hangleiter, J. Wagner, R. Sauer, J. Phys. C., **18**, L795, (1985)
6. L. W. Song, X. D. Zhan, B. W. Benson, G. D. Watkins, Phys. Rev. Lett., **60**, 460, (1988)
7. J. H. Svensson, B. Monemar, Phys. Rev. B, **40**, 1410, (1989)
8. A. Hangleiter, Phys. Rev. B, **37**, 2594, (1988)
9. A. Hangleiter, Phys. Rev. B, **35**, 9149, (1987)
10. J. H. Svensson, E. Janzén, B. Monemar, (unpublished)

NOVEL LUMINESCENCE BAND IN SILICON IMPLANTED WITH PHOSPHORUS AND BORON

A.K.SRIVASTAVA*, D.K.SHARMA*, K.L.NARASIMHAN*, D.SARKAR**
AND V. PREMCHANDRAN**

*Tata Institute of Fundamental Research, Homi Bhabha Road,
Bombay-400005, India

**Indian Telephone Industries, Doorvani Nagar, Bangalore
560016, India.

ABSTRACT

Photoluminescence measurements on silicon implanted with boron, phosphorus, and dual implanted with phosphorus and boron are reported. A high intensity luminescence band between 0.9-1.03 eV is observed in the samples with dual implantation of boron and phosphorus. The luminescence band has similar spectral characteristics as that of the 1.018 eV W or I1 band which is observed in silicon samples irradiated with neutrons or ions. However the annealing behaviour of the luminescence band observed in our samples differs considerably from that of the W band, whose intensity increases on annealing at 525 K and is quenched on heating to 600 K. The luminescence band in our samples is not annealed out even at 900 C. The temperature dependence of the intensity of the luminescence band is also studied. It shows excitonic behaviour with an activation energy of 52 meV.

INTRODUCTION

Defects induced by modern processing techniques in silicon are a subject of current interest. Ion-implantation is one of the most commonly used techniques in silicon technology. The technique is inherently defect prone due to the high energy ion bombardment. The simple defects generated during the bombardment can give rise to more complex defects during post implantation annealing. Some of these defects can participate in radiative recombinations giving rise to luminescence[1]. We report the results of low temperature photoluminescence measurements on thermally annealed phosphorus and boron implanted silicon. The samples subjected to dual implantation of boron and phosphorus show a very strong luminescence peak at 1.018eV and satellite peaks at lower energies. The intensity of this peak drops rapidly above 40K with an activation energy of 52 meV.

EXPERIMENTAL TECHNIQUES

The phosphorus and boron doped silicon substrates with resistivities 3-5 ohm-cm are implanted with P (180 keV, 10^{15} ions cm^{-2}) and B (80 keV, 10^{15} ions cm^{-2}). Some samples are dual implanted with P and B. The implantation energies for boron and phosphorus are adjusted to give very similar doping profiles for both impurities. The samples are thermally annealed at 900 C for 30min. followed by slow

cooling to 450C over 8 hrs. A control sample (virgin substrate) was also annealed in a similar fashion for comparison. For the photoluminescence measurements the samples cooled to 12 K in a close cycle He refrigerator are excited by a He-Ne laser (632nm) or an Ar ion laser (488nm). The luminescence from the samples are analysed by a 0.67m grating monochromator and detected by a liquid N₂ cooled Ge photodiode connected to a lock-in amplifier.

RESULTS AND DISCUSSION

A typical luminescence spectrum for the control sample shown in Fig. 1 consists of TO phonon line of B-acceptor at 1.1 eV. In this measurement the sample is excited by 100mW power from Ar ion laser. Photoluminescence spectra of samples with P and B single implants and subsequent annealing at 900°C are shown in Fig. 2. , the intensity of the 1.1 eV line reduces by nearly a factor of ten. There is no other significant change in the spectrum. The samples singly implanted with either P or B and annealed at 1050°C show similar behaviour. From these results we conclude that the implantation damage in these samples is almost completely annealed. The reduction in the luminescence intensity in the implanted samples is most probably due to the presence of a highly doped nearly 1 micron thick region in front of the sample. This layer acts as a dead layer which attenuates the luminescence intensity from the bulk region. No signal from the heavily doped region in the front of the sample could be observed.

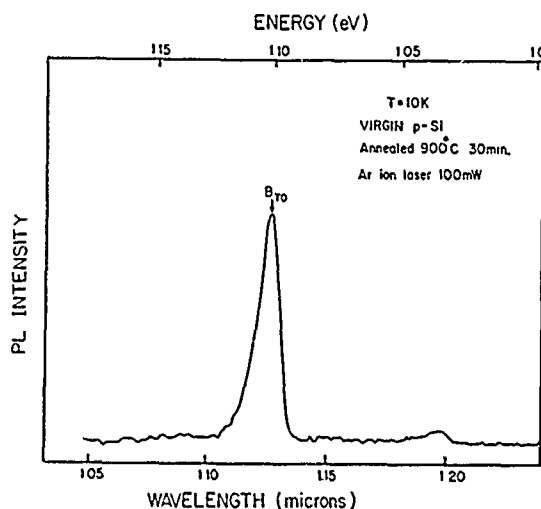


Fig.1 PL spectrum of unimplanted p type annealed Si.

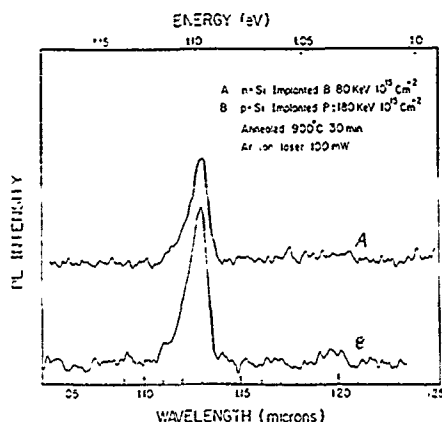


Fig. 2 PL spectra of Si implanted with boron and phosphorus after 900°C anneal.

The double implanted sample after annealing at 900°C shows a very strong luminescence line at 1.018 eV with phonon replicas at 0.999, 0.981 and 0.968 eV as shown in Fig.3. The spectrum is obtained by using a 2 mW He-Ne laser excitation. The TO phonon line is absent most probably due to very weak intensity. The luminescence intensity of the no phonon (NP) 1.018 eV line is nearly a factor of fifty larger than the TO phonon line in the control sample. The temperature dependence of the NP line shown in Fig.4. has an excitonic behaviour. The intensity is nearly constant upto 40 K and then falls rapidly with an activation energy of 52 meV in the 50-100K range. The singly implanted samples do not show this line in the luminescence spectra.

A similar luminescence feature with strong line at 1.018 eV (W and II bands) has been reported in Si bombarded with high energy particles like neutrons and ions[2-3]. Post implantation laser annealing of Si also gives rise to this luminescence line[4]. The intensity of this band is maximised by annealing at 525K for 30min. The line is nearly quenched by annealing above 600 K [1].

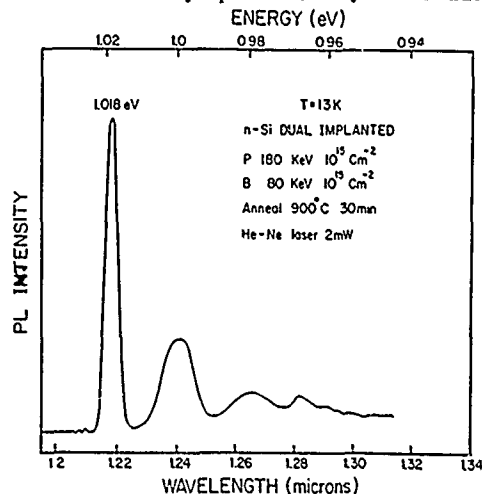


Fig. 3 PL spectrum of Si with dual implant and 900°C anneal

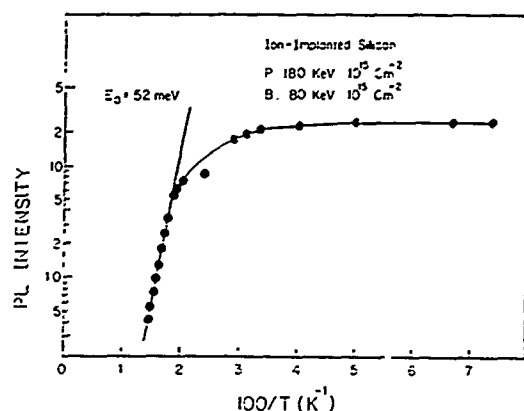


Fig. 4 Temperature dependence of 1018 meV line intensity

Our dual implanted samples continue to show this emission even after a 900 C anneal. On sequential etching we find that the intensity of the 1.018 eV line reaches a maximum at a depth of about 1-2 micron below the surface. From these results we think that there is a complex involving both the P and B which is responsible for this luminescence band.

The temperature dependence of the luminescence intensity shows excitonic behaviour. The intensity $I(T)$ was fit to the following relation [1] :

$$1/I(T) = A + BT^{3/2} \exp(-E_a/kT)$$

The fit gave an activation energy of 52 meV.

CONCLUSIONS

The damage caused by heavy implants of boron and phosphorus in silicon has been studied using photoluminescence. A deep level band with peak at 1.018 eV is observed in the sample which received both implants. The band has spectral features similar to radiation damage bands W and II reported in literature. However, it has a different annealing behaviour in that it is not quenched even after annealing to 900 C.

REFERENCES

1. G.Davies, Phys. Rep. 176, 84 (1989)
2. V.D.Tkachev and A.V.Mudryi, Inst. Phys. Conf. Ser. 31, 231 (1977)
3. C.G.Kirkpatrick and J.R.Noonan, Rad.Effects 30, 97 (1976)
4. M.S.Skolnick, A.G.Collis and H.C.Webber, J. Lumin. 24/25 39 (1981)

UNIAXIAL STRESS AND ZEEMAN MEASUREMENTS ON THE 943 meV LUMINESCENCE BAND IN SILICON

M.C. CARMO*, K.G. MCGUIGAN**, M.O. HENRY**, G. DAVIES# AND E.C. LIGHTOWLERS#

* Departamento de Física, Universidade de Aveiro, 3800 Aveiro, Portugal

** Physics Department, Dublin City University, Ireland

King's College, Physics Department, London WC2R 2LS, UK

ABSTRACT

The photoluminescence from silicon lightly doped with copper and rapidly quenched from $\sim 1100^\circ\text{C}$ is dominated by a vibronic band with zero-phonon lines (ZPL) in the region of 943 meV. We have studied the effect of external fields on the electronic properties of this band and the results are consistent with the luminescence occurring at a defect with T_d symmetry. The Zeeman measurements indicate that the luminescence is due to the recombination of excitons in $J = 1$, $J = 2$ states with the normal ordering of these levels reversed. This reversal is explained by the different response of these states to hydrostatic strains, and it is also argued that strain at the defect provides the binding potential for the exciton.

1. INTRODUCTION

The general properties of the 943 meV luminescence band, here identified as Cu^* have already been described [1]. Fig. 1 shows a low temperature spectrum of this band. Copper doped, oriented silicon samples were prepared in the usual manner and immersed in liquid helium cryostats. Uniaxial stresses up to 50 MPa were applied along the main crystallographic axis [100], [110] and [111] as well as magnetic fields up to 5 Tesla. Luminescence was picked up with either a dispersive Spex monochromator or a Fourier Transform Spectrometer fitted with germanium detectors.

In the present paper we report the results of applied uniaxial stresses (section 2) and magnetic fields (section 3) on the electronic properties of the 943 meV system. In section 4 we compare the results with other closely related transition metal centres in silicon and we discuss a possible stabilization mechanism for the Cu^* centre.

2. UNIAXIAL STRESS MEASUREMENTS

Experimental results of applied stresses are presented in Fig. 2. For low stresses (< 50 MPa) the data is reasonably fitted considering that transitions α and β are $T \rightarrow A$ transitions at a tetrahedral centre. At high stresses the data clearly deviates from straight lines due to strong interactions between neighbouring electronic states (except for $P//111$ where the shift rates remain linear due to symmetry reasons). The fits of Fig. 2 (bold lines) were obtained using the stress parameters shown in Table I, where the notation follows Kaplyanskii [2]. A describes the response to hydrostatic stresses, B measures the response to stresses transforming as $2s_{zz} - s_{xx} - s_{yy}$ and $s_{xx} - s_{yy}$ under T_d and C measures the response of the centre to stresses transforming as $S_{ij}(i \neq j)$ under T_d . From Table I we notice the large differences in the stress parameters A and B for the two electronic states α and β .

Table I: Stress parameters for Cu^* system (meV/GPa)

Line	A	B	C
α	- 6.5	- 3.7	18.0
β	- 2.1	- 13.6	14.9

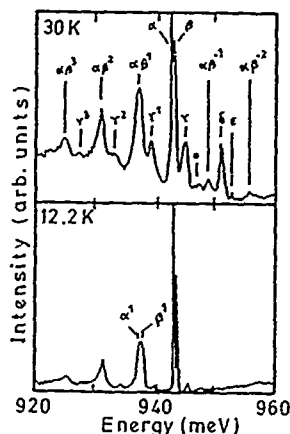


Fig. 1 - 943 meV luminescence band

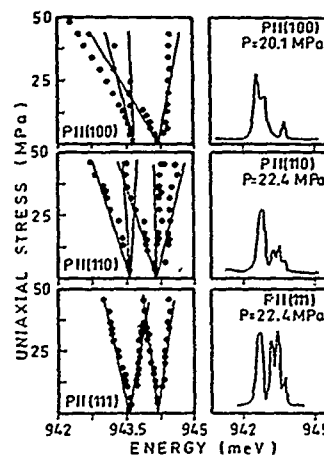


Fig. 2 - Uniaxial stress effects on the 943 meV electronic states α and β . Dots: experimental points. Bold lines: theoretical fits

3. ZEEMAN MEASUREMENTS

Zeeman measurements were carried out in Faraday and Voigt configurations. Fig. 3a shows the magnetic splitting of lines α and β . Fig. 3b shows the angular dependence of the split components when B is rotated in a $[110] - [001]$ plane. Line α clearly splits isotropically in 3 components and line β is clearly seen to split isotropically in five components under $B//100$ and $B//110$. With $B//111$ the splitting pattern of this line is not so clear due to the lower intensities of two components. The splitting pattern of these lines is similar to the Si:Fe-B system reported by Mohring et al [3] except for the inversion in the energy order of the electronic states α and β . In the system discussed here the triplet state α is at lower energy.

The temperature dependence of the split components is consistent with the splitting occurring in the excited states. The relative increase of the integrated intensities of α lines and β with magnetic field shows the typical dependence in B^2 (Fig. 4) due to the linear admixture of the wavefunctions in the interaction matrix. The fittings shown in Figs. 3a and 3b were obtained using the Zeeman interaction matrix for the states $J = 1$ and $J = 2$ of an exciton bound to an isoelectronic impurity discussed by Merz et al [4].

The Merz matrix was diagonalized for eigenvalues and eigenvectors and the energies and relative intensities of the split components calculated. A reasonable agreement with the experimental values can be obtained provided we use the measured relative transition probabilities of lines α and β , instead of taking the transition probability of line β equal to zero. The fitting parameters shown in table II are a least square fit among the experimental points. The case discussed here is however remarkable because, to our knowledge, it is the first reported case of a bound exciton showing an inversion in energy of the $J = 2$ and $J = 1$ excited states. We recall that due to exchange splitting the $J = 2$ state should appear at lower energy.

Other types of fittings were tried, including the possibility of a strong axial field, but a reasonable fitting could not be obtained.

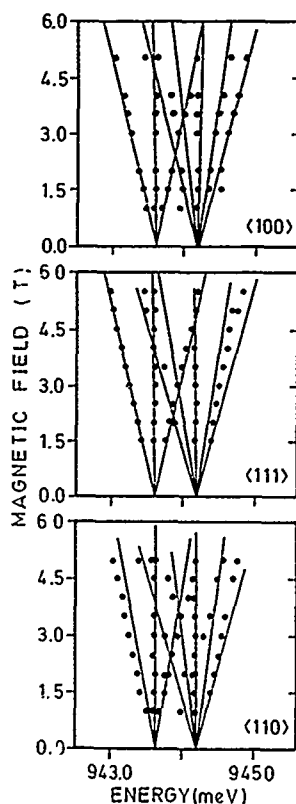


Fig. 3a - Splitting of states α and β under magnetic fields. Dots: experimental points. Lines: fittings

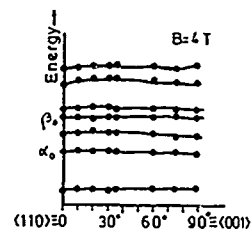


Fig. 3b - Angular dependence of split components at $B = 4$ Tesla

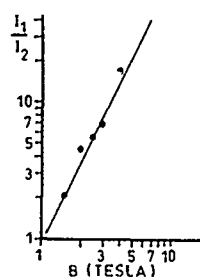


Fig. 4 - Relative intensities of lines α and β v.s. B

The Merz fitting parameters shown in table II yield a g_e factor for the electron close to zero ($g_e = 2\gamma_3 - 1/2(3\gamma_1 - \gamma_2)$). The g factor for the hole K_1 is 1.6 ($K_1 = 1/2(\gamma_1 + \gamma_2) + 1/3(\gamma_2 - \gamma_3)$) and the anisotropy factor of the hole ($L_1 = 4/3(\gamma_3 - \gamma_2)$) is zero. To our knowledge this is the smallest g factor of the electron reported for a bound exciton. The g factor of the hole is slightly larger than some of the values measured for shallow acceptors (e.g. 1.2 for boron). We also notice that the "effective g factor" of the system is 2.0.

Table II: Zeeman fitting parameters

γ_1	γ_2	γ_3	δ_1	δ_2
2.0	1.22	1.26	0	0

4. DISCUSSION

In a previous paper [5] we argued that some of these transition metal defects are highly unstable in the silicon lattice. As an example we pointed out that the 735 meV centre, attributed to an iron complex, is stabilized by a spin-orbit interaction and the 1067 meV system, attributed to an iron-boron defect, is stabilized by a pseudo Jahn-Teller effect with a strength of 10 meV. In the case of the Cu* system described here we propose that a stabilization mechanism can be provided by hydrostatic strain.

We have shown that transitions α and β are $T \rightarrow A$ transitions at a tetrahedral defect. Zeeman data provides isotropic splittings, consistent with tetrahedral symmetry. The Zeeman splittings and the angular dependence of the split components can be fitted using the model of an exciton bound to an isoelectronic impurity, the electron g factor is far from 2 showing that the electron is the strongly bound particle. An explanation for the inversion in energy of the excited states $J = 1$ and $J = 2$ has to be found. Based on the difference in response of these two levels to hydrostatic strains (symmetry conserving and thus having the only effect of shifting the energy of the states) we can calculate the local strain necessary to invert the relative order of the two states by the amount measured experimentally (0.5 meV at zero field). Taking a value of 2 meV for the normal exchange splitting of an exciton and the perfect lattice elastic constants (as a first approach) as $C_{11} = 168$ GPa, $C_{12} = 65$ GPa and $C_{44} = 80$ GPa the relative change in the lattice volume $\Delta V/V = \text{Tr } \epsilon_{ij}$ smaller than 0.2% (contraction) would be sufficient to account for the observed inversion of the two states. Zunger [6] predicted lattice distortions of this magnitude around 3d interstitial impurities in silicon. We also point out that the temperature dependence of the total intensity of the Cu* luminescence band decreases rapidly above 80 K (normally for excitons bound to isoelectronic impurities this decrease occurs at ~ 25 K [3,5]). This particular behaviour [7] supports the view that the defect is stabilized by strain due to the lattice compression around the defect. In fact the coefficient of linear expansion of the silicon lattice increases rapidly above 75 K [8] thus destroying the stability of the defect and allowing the exciton to be released.

ACKNOWLEDGEMENTS

We are grateful to INIC and JNICT in Portugal, EOLAS in Ireland and SERC in the UK for the financial support for this work. The authors also wish to thank EEC for the support given to us under a twinning program of two of the laboratories involved in this work.

REFERENCES

1. K.G. McGuigan, M.O. Henry, E.C. Lightowers, A.G. Steele, M.L. Thewalt, *Solid state commun.* **68** (1), 7 (1988)
2. A.A. Kaplyanski, *Optik. Spectrosk.* **16**, 1031 (1964)
3. H.D. Mohring, J. Weber, R. Sauer, *Phys. Rev. B* **30**, 894 (1984)
4. J.L. Merz, R.A. Faulkner, J.P. Dean, *Phys. Rev.* **188** (5), 1288 (1968)
5. M.C. Carmo et al, *Mat. Res. Soc. Symp. Proc.* **138**, 221 (1989)
6. A. Zunger, *Sol. State Phys* **39**, 275 (1986)
7. K.G. McGuigan (private communication)
8. G. Davies, *Phys. Reports* **176**, 83 (1989)

IDENTIFICATION OF RADIATION-INDUCED DEFECTS IN Si:Al

Latushko Ya.I. and Petrov V.V.

Lenin Byelorussian State University, Lenin Avenue 4, 220080 Minsk, USSR

ABSTRACT

Radiation-induced defects (RD) in Si:Al have been investigated by means of infrared absorption (IRA) and photoluminescence (PL) methods. It has been found that the main Al containing RD in electron-irradiated Si is an interstitial Al atom (Al_i). In the process of annealing at about 225 °C the production of Al_i-Al_i pairs takes place. The activation energy of this RD production is 0.95 eV, which corresponds to Al_i migration energy along hexagonal interstitials. Al_i is shown to be a two - charge donor with the energy level $E(+/++) = E_v + 0.20$ eV. Besides the above mentioned defect as well as acceptor type defect with $E_v + 0.21$ eV level a number of other defects has been revealed in neutron-irradiated Si:Al. These centers give rise to a great number of IRA and PL lines in the spectral range from 0.1 to 1.2 eV. The classification of the observed defects has been done on the basis of the annealing results and uniaxial stress measurements.

INTRODUCTION

Silicon doped with Al appeared to be a classical material while investigating RD formation in Si. The mechanism of interstitial atom formation by means of elastic collision of an electron with Al atom was suggested by Watkins [1]. However, the information concerning the properties of RD in Si:Al is far from being exhaustive. For instance, there is no complete information on the energy levels of interstitial aluminium (Al_i). Specifically, for the Al_i $E(+/++)$ level the value $E_v + 0.25$ eV was obtained in [2], and the value $E_v + (0.17 \pm 0.04)$ eV was obtained in [3]. On the basis of IRA data we obtained the value $E_v + 0.20$ eV [4]. In this work we present more detailed data on optical measurements of the properties of interstitial aluminium as well as the other RD, which are produced in Si:Al by neutron irradiation.

EXPERIMENT

Monocrystalline Si:Al with Al content from 1.3×10^{15} to 3×10^{17} cm⁻³ produced by means of floated-zone melting and Czochralski method was investigated. The content of oxygen and carbon impurities was 3×10^{16} - 1.0×10^{17} cm⁻³ and 1×10^{15} - 2×10^{17} cm⁻³, respectively. The irradiation by 4.5 MeV electrons was carried out at 30°C by fluences (Φ) up to 1×10^{18} cm⁻², and by reactor neutrons at $T \leq 70$ °C by $\Phi \leq 5 \times 10^{18}$ cm⁻². IRA and PL spectra were recorded at temperatures 1.8 - 80 K. The resolution was ≤ 2 cm⁻¹. Uniaxial stress measurements were made at 4.2 and 35 K.

RESULTS AND DISCUSSION

Interstitial aluminium

In Si:Al irradiated by fast electrons one could observe a characteristic helium - like series AM1 in IRA spectra when $E_f \geq E_v + 0.20$ eV. This series may be attributed to electron transitions on Al_i center [4]. Taking as a basis the effective mass theory (EMT) and knowing the location of spectral lines, it is easy to determine the location of $E(+/++)$ level of the given defect as $E_v + 0.20$ eV. This value is close to the values obtained by other less accurate methods [2,3] and may be considered as the most reliable.

During the annealing at $\sim 225^\circ\text{C}$ one could observe the disappearance of AM1 series and the appearance of a completely identical AM2 series, shifted to a higher energy region by ~ 2 meV. The intensity of AM2 series lines was approximately twice as small as the intensity of AM1 series.

The location of spectral lines and the transitions between the corresponding levels are shown in Fig.1. The transitions leading to the emission of radiation, which were observed in PL spectra are also shown in this figure. The value of the annealing activation energy of the defect responsible for AM1 series is 0.95 ± 0.1 eV. It is very close to the value obtained for the activation energy of Al diffusion along hexagonal interstitials [5,6]. That's why it seems quite probable that at 225°C the diffusion of Al_i takes place that results in the production of pair complexes. The interaction of Al_i atoms leads to some decrease in the ground state energy. One of the atoms in a pair retains its interstitial position, but the second one may occupy a substitutional position, too. In this case, however, more appreciable changes in the energy level system of Al_i center should take place. Therefore, one might suggest that both atoms remain in interstitials. The pairing of Al_i atoms results, probably, in the formation of a common orbit for outer electrons and in the compensation of their spins. As a result of this there disappears the EPR signal from Si-G18 center, which is an interstitial aluminium [1]. Its annealing also takes place at $200 - 225^\circ\text{C}$.

The process of changing Al_i atomic configuration at 225°C was also accompanied by some changes in the phonon wing and the splitting pattern of the lines due to $1s1s(\text{A}_1) - 1s1s(\text{T}_2)$ transitions. Fig.2 shows IRA spectrum region which corresponds to the transitions with the phonon excitation. Optical transitions connected with the excitation of TA, TO, LO phonons and also of a local phonon with the energy of $\Phi_1 = 27.9$ meV were observed in the configuration corresponding to AM1 series. These lines disappeared after changing the defect configuration. Thus, after the annealing at 225°C there occurs the decrease in the lattice deformation, caused by the center.

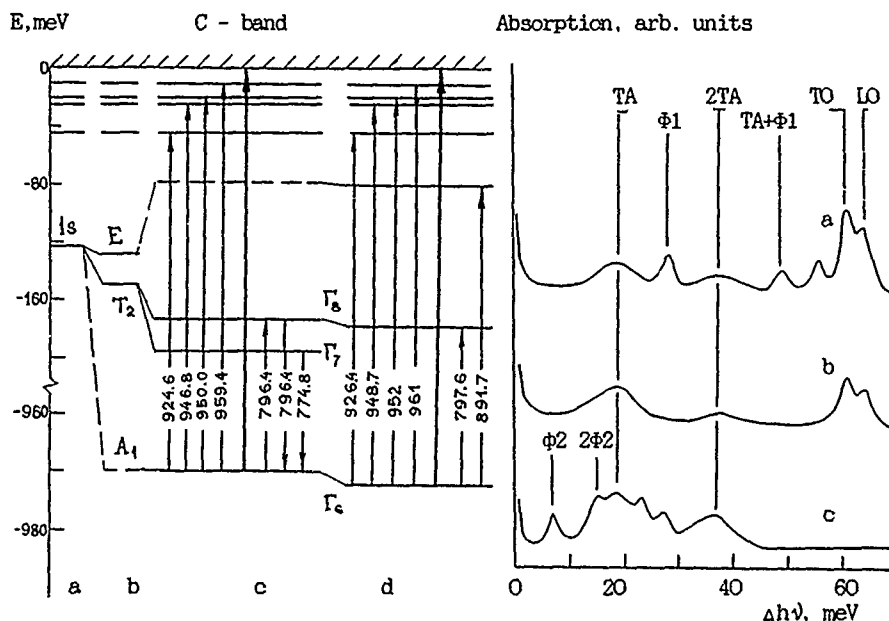


Fig.1. Shallow donor energy diagram based on EMT (a) and on valley-orbit interaction effect (b). Lines series AM1 (c) and AM2 (d).

Fig.2. IRA spectra in the phonon excitation region for lines 797.6 (a), 796.4 (b) and 939.3 meV (c).

The uniaxial stress measurements on IRA lines of both series revealed the following. The lines due to the transition into excited states np_0 , np_2 ($n = 2 \dots 4$) splitted according to the EMT for lines of hydrogen- and helium-like centers, the splitting being the same for lines of both series. The splitting of the line due to $1s\Gamma_8(A_1) - 1s\Gamma_8(T_2)$ transition caused by the stress was identical to the splitting of the lines due to the transition into excited states for AM1 series, the difference being in the smaller value of the splitting. For AM2 series, however, the splitting pattern of this line was essentially different (Fig.3), this testified to the change in the center symmetry.

Some additional information was obtained from the analysis of PL spectra. Fig.4 shows a section of IRA and PL spectrum in the region of 1.6 μm . At 80 K in PL spectrum there appeared a line, the energy position and annealing temperature of which were consistent to a great extent with the analogous parameters of IRA lines due to $1s\Gamma_8(A_1) - 1s\Gamma_8(T_2)$ transition. The decrease of measuring temperature led to the shift of PL and IRA lines to a lower-energy region. While shifting the IRA line narrowed and increased in intensity, PL line, however, shortened. Simultaneously, PL line appeared that was located 21.6 meV (774.8 meV) apart from the above mentioned line. The intensity of PL line at 4.2 K was, however, more than by an order of magnitude less than at 80 K. These facts can be interpreted as follows: 796.4 meV IRA and PL lines are due to $1s\Gamma_8(A_1) - 1s\Gamma_8(T_2)$ transitions, but 774.8 meV PL line is due to $1s\Gamma_7(T_2) - 1s\Gamma_8(A_1)$ transition. At high temperature (80 K) both levels (Γ_7 and Γ_8) are occupied as the result of the excitation, but because the probability of $\Gamma_8 - \Gamma_8$ transition is much greater than of $\Gamma_7 - \Gamma_8$, one can only observe 796.4 meV line. When T reduces only Γ_7 level appears to be occupied (as the result of nonradiative $\Gamma_8 - \Gamma_7$ transitions), and only 774.8 meV line is present in the spectrum, the intensity of which is very small owing to a small probability of this transition. Thus, one can detect $1s\Gamma_7(T_2)$ level of interstitial aluminium from PL spectra.

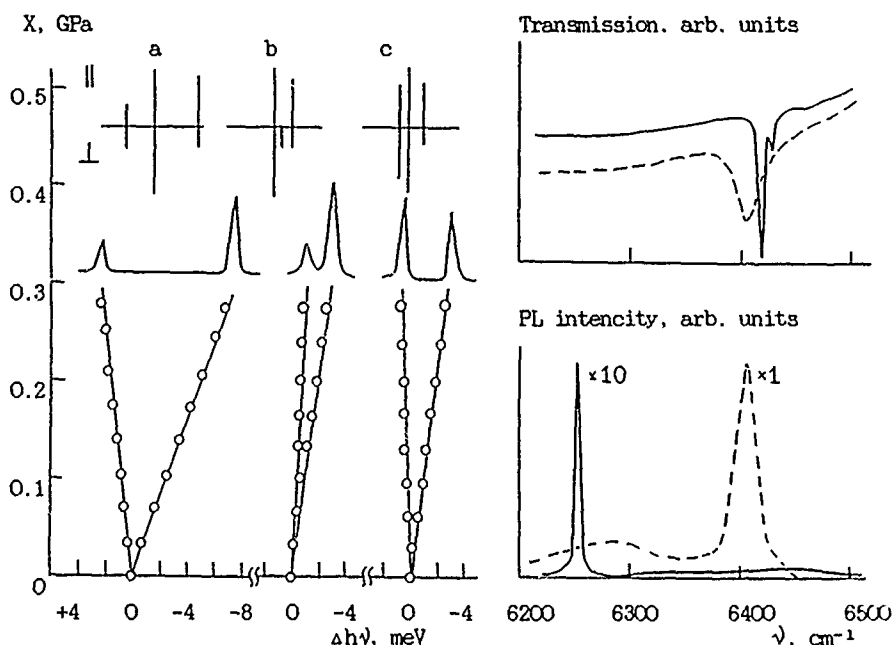


Fig. 3. Splitting of the 797.6 meV line. X II [100] (a), [111] (b) and [011] (c).

Fig. 4. IRA and PL spectra in the 1.6 μm region. T, K: 4.2 (—) and 80 (---).

RD with $E_v + 0.21$ level

As it was shown in [4] this defect containing two atoms of Al is of an acceptor type. Here in this paper we present detailed results of piezospectroscopic studies for 939.3 and 1202.6 meV IRA lines due to the transitions on this RD. The application of stress along [100] axis led to the splitting of the 1202.6 meV line into two components. For [111] and [011] stress there was no splitting, only the shift of the line into lower-energy region. This splitting pattern is characteristic for the tetragonal center with the symmetry axis oriented along [100] according to Kaplyanski theory [7]. The piezospectroscopic coefficients have the following values:

$$A_1 = -24.4 \pm 1.5 \text{ meV/GPa}, A_2 = +8.6 \pm 1.5 \text{ meV/GPa}.$$

The splitting pattern of 939.3 meV line was just the same, this gives an additional evidence that both lines belong to one center.

It is characteristic that in a phonon wing of 939.3 meV line alongside with the bands due to the excitation of TA phonons the lines due to the generation of local phonons with energies of $\Phi_2 = 7.6$ meV were also present (Fig.2).

Optical properties of RD in neutron-irradiated Si:Al

In spectra of neutron-irradiated Si:Al one could observe the lines due to the transitions at Al₁. Owing to high defect concentration they were broadened, that's why not all the transitions into excited states were resolved. Moreover, immediately after the irradiation one could observe the AM2 series lines, which, however, were appreciably less intensive than AM1 series lines.

939.3 and 1202.6 meV lines were not observed because after the irradiation the samples were considerably compensated, the Fermi level was localized near the center of the forbidden band and RD of an acceptor type with $E_v + 0.21$ eV level causing these lines was not occupied by the holes.

Transmission, arb. units

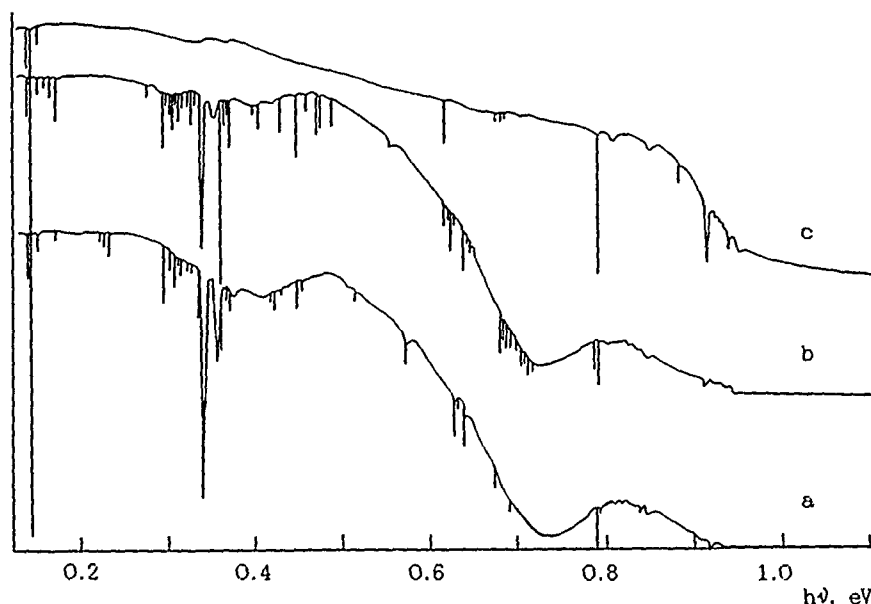


Fig. 5. IRA spectra of neutron-irradiated Si:Al. Annealing temperature. °C: 100(a), 175(b) and 225 (c).

Besides the above mentioned lines more than one hundred IRA lines in the range of 0.1 - 1.0 eV (Fig.5) as well as a number of PL lines in the energy region of 0.5 - 1.15 eV were recorded in neutron-irradiated Si:Al spectra. Most of these lines coincided in spectral location and annealing temperature of the centers that caused them with IRA lines [8]. All IRA lines as well as the majority of PL lines disappeared after the annealing at 350°C. certain PL lines including Al1(836.8 meV) [9] disappeared after the annealing at 450 °C.

On the basis of the intensity dependence analysis of IRA and PL lines on annealing temperature and the results of piezospectroscopic effect studies the majority of lines was divided into groups attributing to different defects.

Concise results of uniaxial stress measurements

The measurements of the splitted lines at uniaxial stress were made at 1.8 - 4.2 K in the energy range of 0.4 - 1.2 eV and at 35 K in the range of 0.1 - 0.4 eV. The splitting of some lines defied interpretations in terms of well-known theories [9,10]. Below, we present the results of the experiments on uniaxial deformation for some of the most intensive IRA lines, the interpretation of which was the simplest.

363.3 meV (2930 cm⁻¹) line was one of the most intensive. It was observed in the annealing temperature range of 50 - 250 °C, its maximum intensity being reached after the annealing at 200 °C. This line was characterized by strong temperature dependence of the intensity and half-width. When measuring temperature decreased from 80 to 35 K the width of this line decreased from 11 to < 3 cm⁻¹. The application of uniaxial stress along [100], [111] and [011] led to the line splitting into 2, 3 and 4 components, respectively. In the stress region under investigation ($X < 0.3$ GPa) the component shift dependence on X was linear. The number of the components and their polarization indicate that the defect responsible for this line is the center of monoclinic I symmetry type with piezospectroscopic coefficients (here and below in meV/GPa units):

$$A_1 = +1.75, \quad A_2 = -5.25, \quad A_3 = -23.75, \quad A_4 = +3.75.$$

373.7 meV (3014 cm⁻¹) line also reached its maximum intensity after the annealing at 200 °C. The uniaxial stress applied along [100] led to the line splitting into three components of equal intensity. The [111] stress also led to the splitting into 3 components, but their intensity was different, moreover, the highest energy component had a considerably greater width. It is quite possible that this very component is a superposition of several lines, which, however, were not resolved in our experiment. The number of the splitting components for $X \parallel [011]$ stress was 6, but three of them (with the highest energy) had small intensity, that's why it was not possible to determine the dependence of spectral shift magnitude on the stress exactly. The center responsible for this line is likely to possess a threeclinic symmetry. It was difficult to determine $A_4 \dots A_6$ piezospectroscopic coefficients, and for $A_1 \dots A_3$ coefficients the values were the following:

$$A_1 = +4.1, \quad A_2 = 0, \quad A_3 = -4.1.$$

406.8 meV (3282 cm⁻¹) line was observed after the annealing at 150 - 225 °C, its maximum intensity being reached after the annealing at 200 °C. It was splitted to 2, 2 and 3 components for [100], [111] and [011] stress, respectively, i. e. it is due to the center of rhombic I type symmetry. The values of piezospectroscopic coefficients are as follows:

$$A_1 = +8.6, \quad A_2 = -4.4, \quad A_3 = +8.1.$$

433.3 meV (3495 cm⁻¹) line had the analogous properties but for the energy shift magnitude of the components, that was ~10 % greater. The calculated values of the components of piezospectroscopic tensor are as follows:

$$A_1 = +10.2, \quad A_2 = -5.1, \quad A_3 = +5.0.$$

573 meV (4627 cm⁻¹) line was observed immediately after the irradiation, its intensity being decreased during the annealing. The uniaxial stress did not lead to the splitting of the line into separate components and the change of its shape. This can give evidence to the fact that the corresponding center has a crystal lattice type symmetry, and the electron transitions take place between its undegenerated levels.

621.9 meV (5016 cm⁻¹) and 622.5 meV (5021 cm⁻¹) lines were the narrowest ($\Delta\nu < 1.5 \text{ cm}^{-1}$). For X II [100] two components were observed, which had different polarization and were shifted into low-energy region. For X II [111] the components were not polarized and were shifted in the opposite directions. The magnitude of the component shift was very small ($\leq 0.5 \text{ meV/GPa}$), for X II [011] it was impossible to resolve the components.

650.8 meV (5249 cm⁻¹) line was also very narrow, but the magnitude of energy shift on applying uniaxial stress was somewhat greater ($\leq 1 \text{ meV/GPa}$). For the stress along three main crystallographic directions one could observe the splitting into two components, but it was not possible to calculate the values of piezospectroscopic coefficients on the basis of the theory [10].

687.1 meV (5542 cm⁻¹) line and 688.5 meV (5553 cm⁻¹) line as the three previous ones were the narrowest ($< 1.5 \text{ cm}^{-1}$) and were observed in the annealing temperature range of 175 - 300°C. For stress along [100], [111] and [011] the lines were splitted into 2, 3 and 3 components, respectively.

Three last groups of lines can be due to one or to three different defects. In all cases the observed splitting pattern is likely to be due to the removal of electron degeneration, and the lines investigated are due to the transitions either between $A_1 - T_1$ or $A_2 - T_2$ levels.

Thus, the analysis of piezospectroscopic effect also gives evidence to the presence in irradiated Si:Al of a large number of different defects. One of the possible causes for the presence of different FD is fact that Al atoms take part in the formation of ordinary defects (divacancies, multi-vacancy complexes, etc.), replacing one of more of the nearest Si atoms.

REFERENCES

1. G.D.Watkins, in Radiation Damage in Semiconductors, edited by P.Baruch. (Paris, 1964), p.97.
2. L.C.Kimerling in Radiation Effects in Semiconductors, (Bristol - London, 1977), p.221.
3. J.R.Troxell, A.P.Chatterjee, G.D.Watkins, *Phys. Rev. B* **19**, 697 (1979).
4. Ya.I.Latushko, V.V.Petrov in Defects in Semiconductors, edited by G.Ferenczi (Aedermannsdorf, 1979) p.1269.
5. G.A.Baraff, M.Schluter, *Phys. Rev. B* **30**, 3460 (1984).
6. Y.Bar-Yam, J.D.Joannopoulos, *Phys. Rev. Lett.* **52**, 1129 (1984).
7. A.A.Kaplijansky, *Opt. Spectrosc.* **16**, 329 (1964).
8. V.A.Bykovsky, Ya.I.Latushko, V.V.Petrov, *Fiz. Tekh. Poluprov.* **21**, 2039 (1987).
9. E.Iron, N.Burger, W.Kurner e.a., *Appl. Phys. A*, **48**, 25 (1989).
10. A.E.Hughes, W.A.Runciman, *Proc. Phys. Soc.* **90**, 827 (1967).

DEFECT-FORMATION DEPENDENCE ON GROUP V-DOPANT ATOMS IN ELECTRON-IRRADIATED SILICON

O.O. AWADELKARIM*, A. HENRY*, B. MONEMAR* AND J.L.
LINDSTRÖM**

* Department of Physics and Measurement Technology, Linköping University,
S-581 83 Linköping, SWEDEN

**National Defence Research Establishment, P.O. Box 1165, S-581 11
Linköping, SWEDEN

ABSTRACT

The defect states introduced in P-, As- and Sb-doped silicon upon room-temperature electron-irradiation are studied by deep-level transient spectroscopy (DLTS). Evidence is provided for the involvement of the P-atom and the vacancy in the defect complex giving rise to the prominent electron trap commonly observed at $\approx E_C - 0.4$ eV (E_C being the edge of the conduction band). This electron trap together with another at $E_C - 0.30$ eV, apparently phosphorus related, exhibit configurationally metastable behaviour. Other electron traps observed at $E_C - 0.27$ eV and $E_C - 0.51$ eV in Sb-doped material and $E_C - 0.34$ eV in As-doped material are attributed to complexes involving Sb and As atoms, respectively.

INTRODUCTION

Irradiated silicon crystals are expected to contain vacancies (V) and self interstitials (Si_i). However, complexes of intrinsic defects and impurity atoms can also be formed rendering the system more complicated. In irradiated n-type material complexes comprising column V donors (P, As, Sb, Bi) have been a subject of intensive studies [1-4]. Among such complexes P-V (E centre), As-V and Sb-V centres were observed by electron paramagnetic resonance (EPR) [1,2]. From DLTS studies the E-centre has been assigned an electron trap observed at $E_C - 0.4$ eV [4]. However, as more DLTS data became available this assignment has become progressively weaker. Several other defects, some of which are configurationally multistable, are reported to have electron traps at $E_C - 0.4$ eV [5,6]. Notably, these traps anneal out at temperatures below 200 °C where the E-centre is known to disappear [1]. In this study we investigate the role of group V impurities, namely P, As and Sb atoms, in the defect formation and stability in irradiated n-type silicon.

EXPERIMENTAL PROCEDURE

The samples used in this study were n-type P-, As- and Sb-doped silicon cut from float-zone (FZ) and Czochralski (Cz) single crystals. The dopant concentrations were in the range $\approx 10^{14}$ - 10^{16} cm⁻³. The samples were irradiated by 2.0 MeV electrons at room temperature to a total dose of 1.0×10^{16} e⁻/cm². Heat treatments on the samples were performed at 100, 200 and 300 °C for durations of 60 minutes. Schottky barrier structures on the samples were prepared by gold evaporation at a pressure of $\approx 1.0 \times 10^{-8}$ Torr. The DLTS measurements were carried out using a standard experimental setup [7]. The configurational stability of the traps is observed by cooling down the diodes from room temperature to liquid nitrogen temperature under zero- or reverse-bias conditions, as discussed by Benton and Levinson [8].

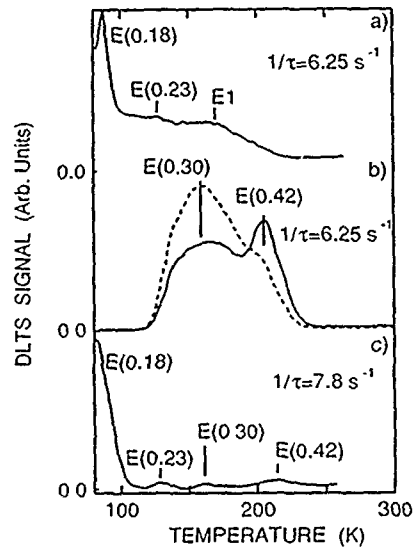


Fig.1: DLTS spectra taken at the rate windows indicated in irradiated (a) FZ Si:P ($n=5.5 \times 10^{14} \text{ cm}^{-3}$), (b) FZ Si:P ($n=7.0 \times 10^{15} \text{ cm}^{-3}$), — cooling at zero bias, ---- cooling at 2.5 V reverse bias, and (c) Cz Si:P ($n=1.2 \times 10^{15} \text{ cm}^{-3}$).

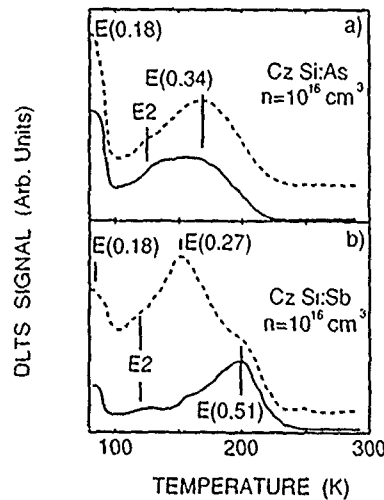


Fig.2: DLTS spectra recorded in Si:As and Si:Sb at a rate window of 3.125 s^{-1} — directly after irradiation, ---- after annealing at 200°C .

EXPERIMENTAL RESULTS

The DLTS spectra obtained in irradiated Si:P are displayed in Fig.1(a)-(c). Fig.1(a) and (b) show spectra obtained in FZ samples in which the phosphorus concentration is varied over one order of magnitude, whereas the spectrum shown in Fig.1(c) is recorded in the Cz material. The electron traps E(0.18), E(0.23), E(0.30), and E(0.42) are seen (the quantity between brackets denotes the energy level position in eV below E_C). The energy level of the broad signal E1 could not be accurately determined. The DLTS signal E(0.18) dominates the spectra in the Cz and low P-content FZ materials. In FZ material of high P-concentration only E(0.30) and E(0.42) are seen. These two states arise from configurationally multistable defect(s) as their intensities are dependent on the method of cooling to 78K (Fig.1(b)). Noticeably, the concentrations of E(0.30) and E(0.42) become remarkably high as the concentration of phosphorus in the samples is increased or the concentration of oxygen is decreased. E(0.30) and E(0.42) are found to anneal out below 200°C , whereas E(0.18) and E(0.23) persisted to exist after 60 minutes annealing at 300°C . No metastability is observed in any of the two latter electron traps.

The spectra recorded in irradiated Si:As and Si:Sb are shown in Fig.2(a) and (b), respectively. In both materials E(0.18) is observed. An electron trap E(0.34) produced upon irradiation of Si:As is stable up to $\approx 200^\circ\text{C}$. Similarly in Si:Sb an electron trap E(0.51) produced directly after irradiation is stable up to 200°C . After annealing at 200°C the Si:Sb defect spectrum is dominated by an electron trap E(0.27) which anneals out at 300°C . The exact position of E2 is uncertain, however, its position in temperature suggests that it may be the same as E(0.23). No change in the DLTS signal intensities is observed as the cooling procedure is varied indicating that the associated defects are configurationally stable.

DISCUSSION AND CONCLUSIONS

The following is a brief account of the observed defect states, including discussions of the possible defect identities :

E(0.42) {P-V} and E(0.30) {P- and V-related}:

E(0.42) is only measured in P-doped samples. This strongly suggests that the P-atom is a defect constituent. Its concentration in FZ material is significantly higher than in Cz material. This may suggest the involvement of a vacancy in the defect structure, and the low concentration of E(0.42) in Cz material is, presumably, due to the vacancies being predominantly trapped next to the abundant interstitial oxygen [9]. Similar arguments hold in the case of E(0.30). However, the energy level position of E(0.42) coincides with that estimated for the P-V centre from EPR [1]. We therefore associate E(0.42) with the P-V centre. As for E(0.30) our results indicate the involvement of the P-atom and the vacancy in the defect complex, however, the lack of correlation with results from other informative techniques such as EPR does not allow a definitive conclusion on the defect identity.

E(0.34) {As-V}, E(0.51) {Sb-V} and E(0.27) {Sb-related}:

In early EPR work [3] spectra labelled as Si-G23 and Si-G24 have been identified as arising from As-V and Sb-V centres, respectively. The electrical properties of these defects are similar, each introduces a single net acceptor level, estimated to be at $E_C - 0.4$ eV. However, differences of up to ≈ 0.1 eV in the exact level position for these defects have been reported [3,10]. The production and annealing characteristics of these traps lead us to the associations of E(0.34) to the As-V centre, and E(0.51) to the Sb-V centre. The occurrence of the E(0.27) only in Sb-doped material indicates that it is Sb-related.

E(0.18) {A centre} and E(0.23) {V-V}:

The production of E(0.18) dominates that of other centres in Cz material where the concentration of oxygen is large (Fig.1(c)). The growth of E(0.18) with annealing and its stability up to 300 °C conform with previously published data on O-V [9]. It is also observed that in FZ material of low P-content, O-V production is still significant. The configurational stability of E(0.18) excludes its probable association with the multistable carbon interstitial-carbon substitutional pair [11]. The association of E(0.23) to the divacancy is based on its introduction and annealing properties [4,11]. E(0.23) corresponds to the (=/-) charge transition in V-V. A (-/0) charge transition in V-V reported at $E_C - 0.4$ eV [12] is not seen, due to overlap with the more intense signals E(0.42), E(0.52) and E(0.34).

The metastable properties of E(0.42) and E(0.30):

It is revealed in this study that only the P-related states E(0.42) and E(0.30) are metastable as shown in Fig.1(b). However, it is as yet unclear whether E(0.30) and E(0.42) arise from the multistability of the same centre or two different centres. This is apparent from Fig.3 in which the intensity of both E(0.30) and E(0.42) change in the same manner as the cooling conditions are varied. It is inferred from these results that changes in the concentrations of other possible undetected defect configurations may account for the constancy of the total defect concentration(s). It is, nonetheless, interesting to note that E(0.42), associated here with the prominent P-V defect, is metastable. This

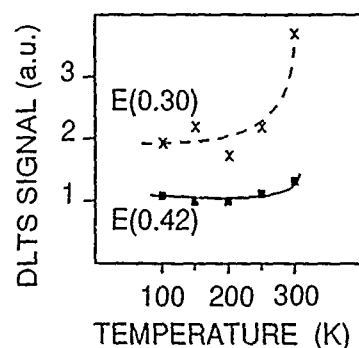


Fig. 3: The DLTS signal intensities for E(0.42) (solid line) and E(0.30) (dashed line) as a function of the temperature at which a reverse bias of 5V is applied to the diode before it is rapidly cooled to 77K.

larger lattice relaxation occurs in the case of defects involving smaller radius and mass P-atom. This is not entirely unexpected since there are evidences for strong relaxation effects in defects comprising smaller or lighter atoms such as in H-related complexes in silicon [17].

result supports earlier suggestions that the P-V pair is a potentially configurationally multistable defect [13]. Energy levels corresponding to other configurations of this centre are still to be experimentally observed. Although other group V-vacancy centres are very similar in the electronic and structural properties to the P-V centre [1,2], it is rather surprising that only the P-V centre exhibits configurational multistability. Previously reported carbon-related metastable states observed in Si:Sb [14] are not seen in this study. This is, presumably, due to the low carbon content ($\leq 10^{16} \text{ cm}^{-3}$ as measured by infra-red) in the samples. The P-atom has a smaller covalent radius of 1.10 \AA compared to 1.18 \AA for As and 1.36 \AA for Sb. This fact introduces noticeable differences in the annealing temperatures of group V-vacancy centres [15] as well as in their electronic level structures [16], and may also be related to the observed defect multistability. The multistability observed in the P-related defects suggests that a

References.

1. G.D. Watkins and J.W. Corbett, Phys. Rev. **138**, A1359 (1964).
2. E.L. Elkin and G.D. Watkins, Phys. Rev. **174**, 881 (1968).
3. E. Sonder and L.C. Templeton, J. Appl. Phys. **34**, 3295 (1963).
4. L.C. Kimerling in *Radiation Effects in Semiconductors*, edited by N.B. Urli and G.D. Watkins (Inst. Phys. Conf. Ser. **21**, London, 1977), pp.221-230.
5. L.W. Song, P.W. Benson and G.D. Watkins, Phys. Rev. B **33**, 1452 (1986).
6. O.O. Awadelkarim and B. Monemar, Phys. Rev. B **38**, 10116 (1988).
7. D.V. Lang, J. Appl. Phys. **45**, 3023 (1974).
8. J.L. Benton and M. Levinson in *Defects in Semiconductors II*, edited by S. Mahajan and J.W. Corbett (Mater. Res. Soc. Proc. **14**, North Holland, New York, 1983), pp.95-100.
9. G.D. Watkins and J.W. Corbett, Phys. Rev. **121**, 1001 (1961).
10. M. Hirata, M. Hirata and H. Saito, J. Phys. Soc. Jpn. **27**, 405 (1969).
11. L.W. Song, B.W. Benson and G.D. Watkins, Appl. Phys. Lett. **51**, 1155 (1987).
12. G.D. Watkins and J.W. Corbett, Phys. Rev. A **138**, 543 (1965).
13. A. Chantre in *Defects in Electronic Materials*, edited by M. Stavola, S.J. Pearton and G. Davies (Mater. Res. Soc. Proc. **104**, Pittsburgh, Pennsylvania 1988) pp.37-46.
14. B.W. Benson, E. Gurer and G.D. Watkins in *Defects in Semiconductors 15*, edited by G. Ferenczi (Mater. Sci. Forum **38-41**, Trans. Tech. Publications, 1989) pp.391-395.
15. M. Hirata, M. Hirata and H. Saito, J. Appl. Phys. **38**, 2433 (1967).
16. O.L. Curtis, Jr. and J.H. Crawford, Jr., Phys. Rev. **124**, 1731 (1961).
17. S.J. Pearton, J.W. Corbett and T.S. Shi, Appl. Phys. A **43**, 153 (1987) and references therein.

ELECTRONIC STRUCTURE OF VACANCY-PHOSPHORUS IMPURITY COMPLEXES IN SILICON

HONGQI XU* AND U. LINDEFELT**

*Department of Theoretical Physics, University of Lund, Sölvegatan 14A, S-223 62 Lund, Sweden

**Asea Brown Boveri Corporate Research, S-721 78 Västerås, Sweden

ABSTRACT

We present a systematic theoretical investigation on four vacancy-phosphorus impurity complexes in silicon, i.e., a vacancy with one through four phosphorus impurities on the nearest neighbour sites of the vacancy, using a semi-empirical self-consistent tight-binding theory. The calculations are based on the Lanczos-Haydock recursion Green's function method. The predicted energy levels in the band gap for the five cases, the isolated Si vacancy and the four complexes, show a remarkable regularity. We shed light on this regularity by relating it to the localization of the wavefunctions on the Si and P atoms surrounding the vacancy. We compare our results with experimental work.

Introduction

In many semiconductor compounds, especially in high power components like thyristors, charge carrier lifetime is controlled by vacancy- and divacancy-related defects created by electron irradiation. It is strongly suspected that the carrier lifetime is controlled to a large extent by an interplay between doping (for instance with phosphorus atoms) and vacancies / divacancies created by the electron irradiation. Therefore, there is an interest from manufacturers of power components to understand better the interaction between a vacancy and phosphorus atoms.

Experimentally, some vacancy-phosphorus impurity complexes in Si were identified. Watkins and Corbett [1] thoroughly investigated the phosphorus-vacancy complex ($V-P_1$ or E-center) with EPR and ENDOR in 1964. The electronic structure of the defect in its neutral charge state was derived. The defect in its negative charge state was studied by Kimerling and his co-workers in 1975 [2]. More recently, positron-annihilation spectroscopy [3] and the hydrostatic pressure technique [4] have also been used to study the defect. The phosphorus-vacancy-phosphorus complex ($V-P_2$) in its positive charge state was identified by Sieverts and Ammerlaan [5] using the EPR technique. The defect complexes involving more than two phosphorus atoms have not been identified so far. However, a very recent work [6] shows that there may exist such a complex in heavily P-doped Si.

In this paper, we report a theoretical investigation on the electronic structure of four neutral vacancy (V)-phosphorus impurity complexes, $V-P_1$, $V-P_2$, $V-P_3$, and $V-P_4$, in Si. The effect of lattice distortion is discussed. Comparison of our results with experimental work is presented.

Theory

The calculations are based on a semi-empirical self-consistent tight-binding method. The perfect crystal is described by an sp^3 first and second nearest neighbour tight-binding Hamiltonian [7] in a supercell containing 2662 Si atoms [8]. A vacancy is simply created

by removing a Si atom from the supercell. The defect potential on the neighbouring Si atoms of the vacancy is determined by a charge-neutrality condition [9]. When phosphorus atoms are introduced into the solid to form the vacancy-phosphorus complexes, the defect potential is determined self-consistently using a semi-empirical model [10]. The resulting defect Hamiltonian is processed with the recursion (a real space Green's function) method [11], which is very well suited for studying defect complexes. For further details in the computational aspects, see Ref. [9].

Results and Discussion

The calculated energy levels of major interest around the band gap for the four vacancy-P complexes and for an isolated ideal vacancy ($V-Si_4$) are shown in Fig. 1. The corresponding energy values and symmetries of the defect levels are listed in Table 1, where the localizations of each level on all nearest neighbour Si atoms and on all nearest neighbour P atoms of the vacancy are also included. It is very well known that the ideal isolated Si vacancy introduces a deep t_2 level into the band gap. Our calculated energy value for the defect level is 0.72 eV above the top of the valence band. The defect complex $V-P_1$ is found to lower the t_2 localized state of $V-Si_4$ to the top of the valence band. When neutral, this level is fully occupied by six electrons. Thus, the neutral complex $V-P_4$ is electrically inactive. The neutral complex $V-P_1$ introduces a fully occupied a_1 gap level at 0.10 eV and a one-quarter occupied e gap level at 0.72 eV above the top of the valence band. Jahn-Teller distortion can occur for the neutral $V-P_1$. The neutral complex $V-P_3$ introduces a fully occupied e level at the top of the valence band and a half occupied a_1 gap level at 0.59 eV. We note that the ordering of the two levels of the complex $V-P_3$ is inverted compared to the ordering of the gap levels of the complex $V-P_1$. We note

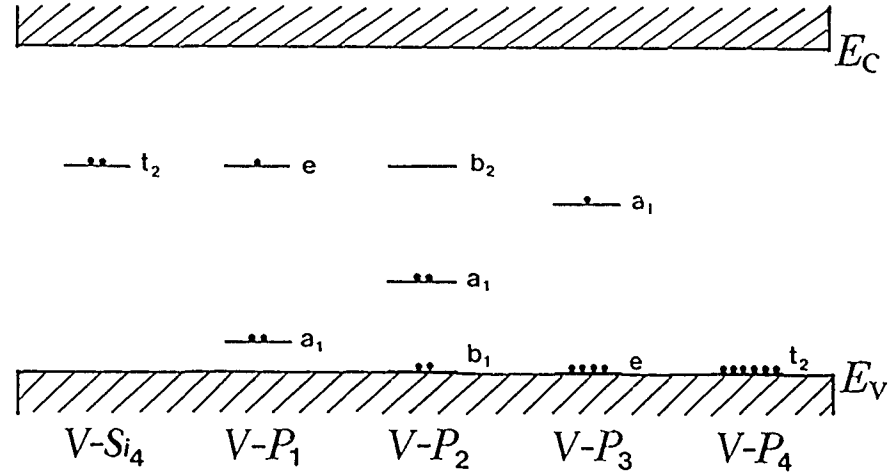


Figure 1: Calculated defect energy levels of major interest around the band gap for the isolated Si vacancy (point-symmetry group T_d) and for the vacancy-phosphorus impurity complexes $V-P_1$ (point-symmetry group C_{3v}), $V-P_2$ (point-symmetry group C_{2v}), $V-P_3$ (point-symmetry group C_{3v}), and $V-P_4$ (point-symmetry group T_d) in Si. E_v and E_c denote the valence band and the conduction band edges. Solid circles indicated the occupancy of the gap levels in the neutral states of the defects.

also that the lattice distortion for the defect complex $V-P_3$ in its neutral state is not of Jahn-Teller type. Finally, the complex $V-P_2$ is found to give three non-degenerate levels around the gap, a b_1 level at the top of the valence band, an a_1 level at 0.31 eV, and a b_2 level at 0.72 eV. In the neutral state, the b_1 and a_1 levels of the complex are fully occupied and the b_2 level is completely empty. No Jahn-Teller distortion can thus occur for the defect complex $V-P_2$.

The ordering of the defect levels for the neutral complexes $V-P_1$, $V-P_2$, and $V-P_3$, can be understood through the localizations of the corresponding defect wavefunctions on the nearest neighbour Si and P atoms around the vacancy (see Table 1). The t_2 gap state for an ideal isolated vacancy is very localized. About 63.7% of its wavefunction is located at the four nearest neighbour Si atoms of the vacancy, whereas the t_2 state for the complex $V-P_4$ is very delocalized in consistence with our findings that the corresponding level in this case becomes shallow. It can be seen in Table 1 that both the ϵ state of the complex $V-P_1$ and the b_2 state of the complex $V-P_2$ are as localized on the neighbouring Si atoms of the vacancy as the t_2 state of the isolated vacancy ($V-Si_4$) and do not have contributions from the neighbouring P atoms. Thus, these two levels are mainly Si vacancy-like and, therefore, stay at the same energy as the t_2 vacancy level. On the other hand, the contributions to the b_1 level of the complex $V-P_2$ and to the ϵ level of the complex $V-P_3$ from the nearest neighbour Si atoms of the vacancy are very small. These level are essentially complex $V-P_4$ like and thus stay at the same energy as the t_2 level of the complex $V-P_4$. The remaining three a_1 levels, i.e., the a_1 levels of $V-P_1$, $V-P_2$, and $V-P_3$, contain character of both the nearest neighbour Si atomic orbitals and the nearest

Table 1: Calculated defect energy levels produced by four vacancy-phosphorus impurity complexes $V-P_1$, $V-P_2$, $V-P_3$, and $V-P_4$ in silicon. All energies are measured relative to the top of the valence-band. The calculated width of the band gap E_g is 1.14 eV. Level localization on Si (P) is the total localization of the defect wavefunction on all first nearest neighbour Si (P) atoms of the vacancy. Level occupancy means the number of electrons in the corresponding gap level for a neutral defect. The calculated gap level for the ideal isolated vacancy $V-Si_4$ is also included for comparison.

Defect	Point group	Level symmetry	Level Energy (eV)	Level Localization on Si on P		Level Occupancy
$V-Si_4$	T_d	t_2	0.72	63.7%	—	2
$V-P_1$	C_{3v}	ϵ	0.72	63.8%	0.0%	1
		a_1	0.10	21.4%	21.6%	2
$V-P_2$	C_{2v}	b_2	0.72	63.9%	0.0%	0
		a_1	0.31	41.6%	10.8%	2
		b_1	0.00	0.9%	2.4%	2
$V-P_3$	C_{3v}	a_1	0.59	55.1%	6.3%	1
		ϵ	0.00	2.7%	1.9%	4
$V-P_4$	T_d	t_2	0.00	—	2.0%	6

neighbour P atomic orbitals. The localizations of the three a_1 levels on the nearest neighbour Si (P) atoms of the vacancy increase (decrease) as the number of P atoms involved in the complex is increased. Therefore, the energies of the three a_1 levels for V-P₁, V-P₂, and V-P₃ are in ascending order and all three levels remain in a region of energy bounded by the energies of the t_2 level of the ideal isolated vacancy (V-Si₁) and the t_2 level of the complex V-P₄.

The defect complex V-P₁ was studied in some detail by Watkins and Corbett with EPR and ENDOR techniques [1]. It has also been found that the complex produces an acceptor level at $E_c - 0.44$ eV [2]. Our calculation shows that the ideal defect complex V-P₁ produces a doubly degenerate ϵ level at $E_c - 0.42$ eV. The Jahn-Teller distortion will lift the degeneracy and the ϵ level will be split into two levels. Since the wavefunction for the ϵ level is mainly localized on the nearest neighbour Si atoms (Table 1) we can regard it as mainly vacancy-like. Furthermore, P is not very different from Si. Thus, we expect the Jahn-Teller distortion for neutral V-P₁ to be very similar to that for V⁻-Si₁. Therefore, the experimentally detected acceptor level mentioned above should bear a close resemblance to a vacancy level. The energy levels for the defect complexes involving more than one P atom have not been reported so far. However, a new configurationally bistable defect in heavily phosphorus-doped silicon has been detected recently with the deep-level transient spectroscopy technique [6]. The defect is tentatively considered as a complex involving a vacancy and more than one phosphorus atom. The present results could help the experimentalists to further identify the bistable defect.

References

- [1] G. D. Watkins and J. W. Corbett, *Phys. Rev.* **143**, A1359, (1964).
- [2] L. C. Kimerling, H. M. DeAngelis and J. W. Diebold, *Solid State Commun.* **16**, 171 (1975). See also L. C. Kimerling, *Inst. Phys. Conf. Ser. No. 31*, 221 (1977).
- [3] J. Mäkinen, C. Corbel, P. Hautojärvi, P. Moser, and F. Pierre, *Phys. Rev.* **B39**, 10162 (1989).
- [4] G. A. Samara, *Phys. Rev.* **B39**, 11001 (1989); **B39**, 12764 (1989).
- [5] E. G. Sieverts and C. A. J. Ammerlaan, *Inst. Phys. Conf. Ser. No. 31*, 213 (1977).
- [6] O. O. Awadelkarim and B. Monemar, *Phys. Rev.* **B38**, 10116 (1988).
- [7] J. van Rest and P. Pêcheur, *J. Phys. Chem. Solids* **45** 563 (1984).
- [8] U. Lindefelt, *J. Phys. C* **11** 3651 (1978). See also U. Lindefelt and A. Zunger, *Phys. Rev.* **B26** 846 (1982).
- [9] Hongqi Xu and U. Lindefelt, unpublished.
- [10] O. F. Sankey and J. D. Dow, *Phys. Rev.* **B27** 7641 (1983).
- [11] R. Haydock, in *Solid State Phys. Vol. 35*, edited by H. Ehrenreich, F. Seitz, and D. Turnbull (Academic Press, New York, 1980) p. 215.

NEW DLTS PEAKS ASSOCIATED WITH NEW DONORS AND RODLIKE DEFECTS IN CZOCHRALSKI SILICON

YOICHI KAMIURA, FUMIO HASHIMOTO, AND MINORU YONETA
Faculty of Engineering, Okayama University, Okayama 700, Japan

ABSTRACT

We have studied the effects of low-temperature preannealing and carbon on new donor formation at 650°C in phosphorus-doped Czochralski (CZ) silicon by deep-level transient spectroscopy (DLTS). In not preannealed carbon-lean samples, only a weak continuous DLTS spectrum often reported so far was observed. The intensity of this broad feature became significantly stronger in not preannealed carbon-rich samples. On the contrary, preannealed samples showed no such continuous spectra but two new DLTS peaks arising from shallow donor levels. Carbon enhanced the low-temperature peak, but retarded the high-temperature one. The latter peak is in strong correlation with the rodlike defect.

INTRODUCTION

Oxygen-related donors, called new donors (NDs), have been recognized to be created by annealing CZ silicon at 600 to 800°C [1-9]. However, little has been known about their electronic properties. Hall experiments indicated that the activation energy of ND level varied from 30 to 120 meV depending upon annealing temperature and duration [10]. DLTS experiments showed no discrete electronic levels but only continuous spectra explained by interface states at the surface of SiO_x precipitates [11, 12]. On the contrary, admittance spectroscopy experiments revealed a discrete peak at $E_c - 19$ meV ascribed to a level localized within the quantum well surrounding small positively charged oxide precipitates [13, 14]. On the other hand, two kinds of structural defects, oxide platelet precipitates and $\langle 011 \rangle$ elongated rodlike defects (RLDs) have been observed by transmission electron microscopy (TEM) [15-18]. However, connections between these defects and NDs have not been clear yet. In this paper, we present results of DLTS experiments on the effects of low-temperature preannealing and carbon atoms involved in crystals on ND formation at 650°C, and discuss the correlations of observed DLTS peaks with NDs and the above structural defects.

EXPERIMENTAL

We used two kinds of n-type CZ crystals with comparable phosphorus densities ($4-7 \times 10^{14} \text{ cm}^{-3}$) and oxygen densities ($8-10 \times 10^{17} \text{ cm}^{-3}$) but different carbon densities; one is a normal crystal (C-lean) with a low carbon density less than $1 \times 10^{16} \text{ cm}^{-3}$, and the other (C-rich) is a carbon-doped one ($1.5 \times 10^{17} \text{ cm}^{-3}$). Experimental details of heat treatments of samples and measurement procedure of resistivity and DLTS were the same as described in our previous paper [19]. Wright etching [20] was applied to reveal defects. TEM observations were done in the bright field under an accelerating voltage

of 200kV.

RESULTS AND DISCUSSION

Figure 1 shows the effects of low-temperature preannealing and carbon on DLTS spectra due to NDs generated at 650°C. In a carbon-lean sample annealed directly at 650°C for 1.5×10^4 min (dotted curve), there is no discrete peak but only a weak continuous spectrum as reported previously [11, 12]. This broad band (ND3) grows considerably in a not preannealed carbon-rich sample (dashed curve), where an additional peak (ND2) is visible as a shoulder in the low-temperature tail of ND3 band. In a carbon-lean sample preannealed at 450°C for 3×10^4 min and then annealed at 650°C for 1×10^4 min (solid curve), the broad band and continuous background decays in magnitude, and two peaks, ND1 and ND2, dominate in the spectrum. In a preannealed carbon-rich sample (dashed-dotted curve), the formation of ND1 peak is enhanced, but that of ND2 peak is retarded. Our resistivity measurements indicated that, among the above four cases, the only one case ("not preannealed" and "carbon-lean") produced a low ND density less than 10^{14} cm^{-3} , while the other three did comparable high ND densities, $2\text{--}3 \times 10^{15} \text{ cm}^{-3}$. The above DLTS results clearly show that under these three conditions totally different kinds of NDs were generated in spite of their comparable densities. This point has been completely omitted from consideration in the past investigations of NDs, and will provide a new insight in understanding the nature of NDs.

We have investigated correlations between the above DLTS spectra and structural defects. In carbon-lean samples annealed only at 650°C (without preannealing), only oxide precipitates were observed by TEM. When preannealing was done at 450°C for 1×10^3 min, sizes of oxide precipitates became smaller with their densities becoming higher. At the same time, RLDs became observable. RLDs were also observed as etch pits by Wright etching as previously reported [6]. As the preannealing time increased, the densities of RLDs and etch pits became higher. The density of etch pits showed a strong and quantitative correlation with that of NDs formed at 650°C in carbon-lean preannealed samples. On the other hand, sufficiently long annealing for more than 3×10^4 min at 650°C annihilated ND1 peak, leaving only ND2 peak. Thus, it becomes evident that ND2 peak corresponds to the stable kind of ND at 650°C in carbon-lean preannealed samples and this kind of ND probably arises from RLDs. It was reported that RLDs and etch pits were

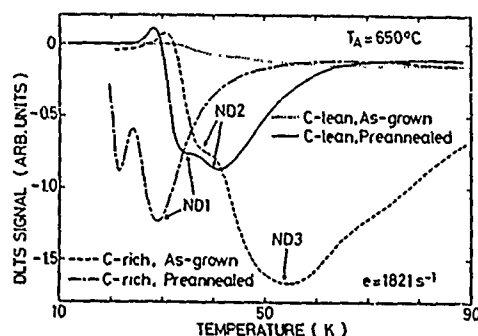


Fig. 1. Effects of low-temperature preannealing and carbon on DLTS spectra of NDs generated at 650°C. The emission rate was 1821 s^{-1} . Annealing temperatures and times (min) are listed below.

Curve	Carbon	450°C →	650°C
.....	lean	0	1.5×10^4
————	lean	3×10^4	1×10^4
-----	rich	0	6×10^4
- - - - -	rich	3×10^4	6×10^4

hardly observed in preannealed carbon-rich crystals [6, 15, 18]. We also have found that the density of etch pits was very low in carbon-rich samples. These support our conclusion that the origin of ND2 peak is RLD.

We have recently discovered that four kinds of oxygen-related thermal donors were generated at 520°C in carbon-lean crystals [21]. This result is shown as open triangles in Fig. 2, where four stages of thermal donor generation clearly appear. In each stage, a particular DLTS peak was generated [21]. TD1 has been identified as a family of so-called thermal donors, which are dominant below 500°C. TD2 is a new kind of thermal donor generated by prolonged annealing around 450°C [19]. TD3 and TD4 were donors formed by very long annealing at 520°C, and can, in fact, be identified as ND1 and ND2, respectively, from the coincidence of their DLTS peaks. In Fig. 2, the change in etch pit density for carbon-lean samples is also plotted as filled triangles, and are in strong correlation with the generation of TD4. Moreover, we observed RLDs by TEM in carbon-lean samples annealed for more than 1×10^5 min at 520°C. It is interesting to note that the final densities of TD4 donors and etch pits at 520°C are the same as those for the two-step annealing (450 → 650°C). In carbon-rich samples, as shown by open circles, TD1 and TD4 donors were not formed, while the formation of TD2 and TD3 donors was greatly enhanced. In addition, we have never observed any etch pits even after extremely long annealing at 520°C. All the above results again lead to the conclusion that ND1 is a kind of carbon-related new donor and ND2 is a RLD-related one.

Carbon has been recognized to provide nucleation sites for oxygen precipitation around 650°C [6]. The above DLTS results have indicated that ND1 peak and ND3 band are both carbon-related. However, the conditions of their formation are quite different. ND1 needs an incubation period, but ND3 does not. We tentatively attribute ND3 band to the superposition of several unresolved peaks, which are due to several kinds of oxygen clusters nucleated at carbon atoms. On the other hand, ND1 peak may arise from a certain oxygen cluster which grows at 650°C around a nucleus involving a carbon atom. This nucleus may not be formed at 650°C but effectively done below this temperature. At 520°C, the nucleation may occur at the initial stage of annealing. We presume that this cluster has a special defect structure. This hypothesis is now under investigation by TEM. The generation of ND2 peak also needs a nucleus which, however, does not contain any carbon atoms. If carbon atoms are present, oxygen atoms preferentially aggregate at carbon sites, forming the nuclei of ND1. As a result, ND2 donors are not generated.

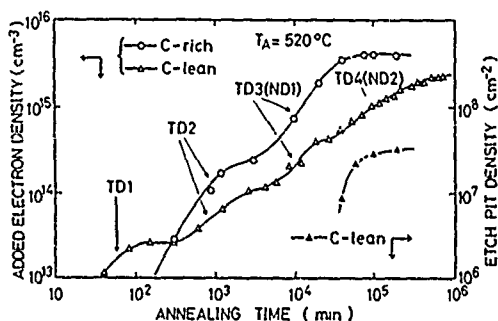


Fig. 2. Generation of several kinds of oxygen-related thermal donors, TD1 - TD4, at 520°C [21]. The ordinate represents the increase in carrier density at room temperature. TD3 and TD4 are identified as ND1 and ND2, respectively. The change in etch pit density is also shown.

CONCLUSIONS

We have found two discrete peaks and a broad band related to new donors in DLTS spectra. The broad band dominated the spectra of not preannealed crystals annealed directly at 650°C. Its intensity became stronger in carbon-rich crystals. This band is attributable to various oxygen clusters nucleated carbon atoms. In crystals preannealed at 450°C, this band was diminished, and two peaks appeared. The low-temperature peak was enhanced in carbon-rich crystals, and is tentatively ascribed to a special oxygen precipitate growing around a nucleus containing carbon atoms. The high temperature peak was retarded in carbon-rich crystals, and was in strong correlation with the rodlike defect, indicating that this peak arises from the rodlike defect.

ACKNOWLEDGMENTS

We would like to thank Mr. M. Yamada to whom we entirely owed our TEM observations, and also wish to thank Mr. K. Endo of Japan. Silicon Co., Ltd. for the offer of silicon crystals.

REFERENCES

1. A. Kanamori and M. Kanamori, *J. Appl. Phys.* 50, 8095 (1979).
2. V. Cazcarra and P. Zunino, *J. Appl. Phys.* 51, 4206 (1980).
3. M. Tajima, A. Kanamori, S. Kishino, and T. Iizuka, *Jpn. J. Appl. Phys.* 19, L755 (1980).
4. J. Lerouelle, *Phys. Status Solidi A* 67, 177 (1981).
5. A. Ohsawa, R. Tanizawa, K. Honda, A. Shibatomi, and S. Ohkawa, *J. Appl. Phys.* 53, 5733 (1982).
6. K. Yasutake, M. Umeno, H. Kawabe, H. Nakayama, T. Nishino, and Y. Hamakawa, *Jpn. J. Appl. Phys.* 21, 28 (1982).
7. P. Gaworzewski and K. Schmalz, *Phys. Status Solidi A* 77, 571 (1983).
8. N. Fukuoka, *Jpn. J. Appl. Phys.* 24, 1450 (1985).
9. C.Y. Kung, *J. Appl. Phys.* 61, 2817 (1987).
10. K. Schmalz and P. Gaworzewski, *Phys. Status Solidi A* 64, 151 (1981).
11. K. Holzlein, G. Pensl, and M. Schulz, *Appl. Phys. A* 34, 155 (1984).
12. K. Holzlein, G. Pensl, M. Schulz, and N.M. Johnson, *Appl. Phys. Lett.* 48, 916 (1986).
13. A. Henry, J.L. Pautrat, and K. Saminadayer, *J. Appl. Phys.* 60, 3192 (1986).
14. A. Henry, J.L. Pautrat, P. Vendange, and K. Saminadayer, *Appl. Phys. Lett.* 49, 1266 (1986).
15. A. Bourret, J. Thibault-Desseaux, and D.N. Seidman, *J. Appl. Phys.* 55, 825 (1984).
16. M. Reiche and O. Breitenstein, *Phys. Status Solidi A* 101, K97 (1987).
17. A. Bourret, *Microscopy of Semiconducting Materials 1987*, edited by A.G. Cullis and P.D. Augustus, (*Inst. Phys. Conf. Ser.* 87, The Institute of Physics, London, 1987) pp. 39-48.
18. M. Reiche, J. Reichel, and W. Nitzsche, *Phys. Status Solidi A* 107, 851 (1988).
19. Y. Kamiura, F. Hashimoto, and M. Yoneta, *J. Appl. Phys.* 65, 600 (1989).
20. M. Wright-Jenkins, *J. Electrochem. Soc.* 124, 757 (1977).
21. Y. Kamiura, F. Hashimoto, and M. Yoneta, *J. Appl. Phys.* 66, 3926 (1989).

MULTICONFIGURATIONAL CARBON-GROUP V PAIR DEFECTS IN SILICON

E. GÜRER and B. W. BENSON
Department of physics, Lehigh University
Bethlehem, Pennsylvania, 18015

Abstract

In addition to a new configuration of the previously reported multistable carbon-phosphorus pair, we report on two new multiconfigurational defects in electron irradiated silicon doped, with arsenic and antimony. These defects are also identified as interstitial carbon-substitutional group V pairs, ($C_i-D_V^V$). We identified two different types of metastability for $C_i-D_V^V$. Type I is similar to the bistable carbon-carbon pair defect for which a bond switching mechanism has been reported [1]. Type II is similar to donor-acceptor pairs in silicon which show electrostatically driven metastability [2,3]. The three $C_i-D_V^V$ pairs have many similar features, but also show surprising donor related differences. In this paper we will discuss the general features of these defects.

Introduction

Carbon interstitial is a major irradiation product in electron irradiated silicon. C_i has a single acceptor state at $E_c-0.1$ eV [4,5] and it migrates above 300K, forming bistable carbon-carbon pairs [1] and multistable carbon-phosphorus pairs [6,7] in phosphorus doped silicon. Recently, we discovered two new multistable defects, one in arsenic [8] and another one in antimony [9] doped, carbon rich silicon. These two defects are also observed after C_i anneals, and they anneal themselves into C_i-C_i pairs at higher temperatures. This new finding supports the tentative identification of the multistable defect in P doped Si. We therefore identify these defects as $C_i-D_V^V$ pairs, formed when migrating interstitial carbon is trapped by a substitutional group V atom.

Transformations among the configurations can be induced by manipulating the charge state and the temperature of the sample. Six, five, and six energy levels have been observed for C_i-P_i , C_i-As_i , and C_i-Sb_i , respectively using DLTS and TSCAP. Arranging the conditions under which various levels are observed, we identify four configurations for both C_i-As_i and C_i-Sb_i , and five configurations for C_i-P_i pairs as shown in fig. 1. The numbers in each box represent energy level positions corresponding to the particular configuration of C_i-P_i , C_i-As_i , and C_i-Sb_i pairs. The DLTS emission energies have been corrected by $2kT$ for the temperature dependence of electron density of states in the conduction band and the temperature dependence of the thermal velocity of electrons, except for the 0.27 eV level of IIA. None of the levels have been corrected for the temperature dependence of the electron capture cross section. Also included in fig. 1 are the energy barriers for transformations among various configurations. All of the $C_i-D_V^V$ pairs have a stable configuration (I) with a level around $E_c-0.4$ eV to which the defect returns upon thermal annealing. In the case of C_i-P_i , we discovered a new configuration (IV) which has two energy levels at 0.07 and 0.39 eV (first and second ionization levels) after injecting minority carriers at 140K [10]. Reverse conversion to I takes place around 180K. The 240K injection converts I (0.38 eV) to III (0.23 eV). The rest of the conversions of C_i-P_i can be induced by thermally annealing the sample. The 0.26 and 0.32 eV levels of IIA

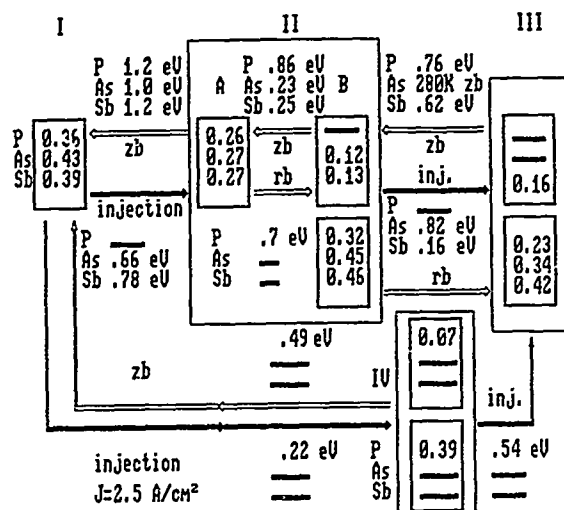


Figure 1: Interconversion diagram for $C_i-D_V^+$ pairs. Energy level positions in the boxes are in eV, as are conversion barriers listed beside the arrows.

and IIB form a bistable pair. The IIA is stable under zero bias and converts to IIB at 250K under reverse bias. Conversion back to I takes place around 340K.

In the case of C_i-As , and C_i-Sb , 270K and 300K injection of minority carriers induce I to II conversion. IIA and IIB form a bistable pair with close similarity to the bistable C_i-C_s pair. A configuration coordinate diagram consistent with the experimental observations is shown in fig. 2. Configuration A (0.27 eV) is stable for the negative charge state and B (0.12/0.13 eV) is stable for the neutral charge state. The temperature dependence of the conversion rates between B^- and A^- have yielded energy barriers of 0.23 eV for C_i-As , and 0.25 eV for C_i-Sb . Pre-exponential factors are consistent with one jump conversion. A close similarity to the C_i-C_s pair suggests that the bond switching mechanism is responsible for the bistability observed. We should note that this low barrier bistability (type I) is different than the type of bistability observed in C_i-P , (0.26 and 0.32 eV) and C_i-As , (0.12/0.27 and 0.34 eV). Detailed kinetics results show that the barriers involved in the type II bistability are higher than that of the type I bistability and comparable to the migration barrier of C_i (0.8 eV), as shown in fig. 1. This suggests that the type II bistability actually involves motion of C_i from one site to another whereas the type I bistability is result of a bond switching and the subsequent relaxation of atoms. The 0.45 and 0.46 eV levels are the second ionization levels of C_i-As , and C_i-Sb , respectively. A second injection at 140K converts II to III for C_i-Sb . Reverse transformation takes place at 185K.

Enhancement Processes

Low barrier bistability of C_i-As , and C_i-Sb , is charge state controlled. By changing the Fermi level position, different configurations can be populated. In addition, these two bistable pairs undergo ionization or recombination enhanced conversion. This is induced by electrical minority carrier injection, which is consistent with the CC diagram shown

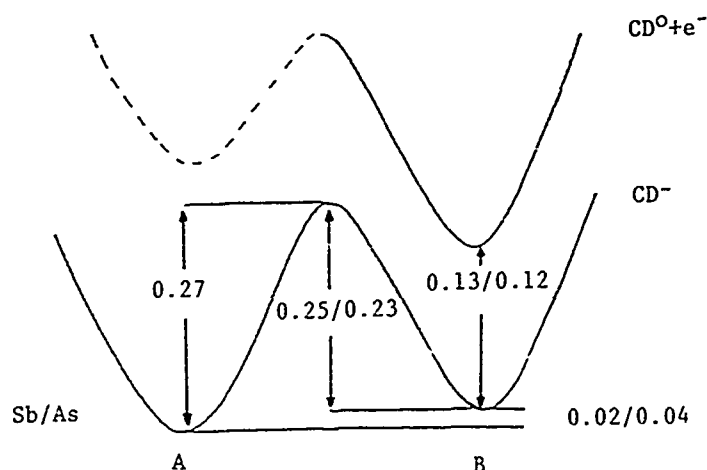


Figure 2: CC diagram for bistable $C_i\text{-As}_s$ and $C_i\text{-Sb}_s$ pairs.

in fig. 2. In both cases, DLTS energy levels corresponding to B configuration can be observed after 40K electrical injection regardless of the cooldown conditions. This is another similarity between the bistable pairs of $C_i\text{-D}_s^V$ and $C_i\text{-C}_s$. It was shown in EPR experiments that, by changing the Fermi level position with electron irradiation and by using photoionization, conversion from the stable to the metastable configuration of $C_i\text{-C}_s$ pair could be induced.

Detailed kinetics have shown barrier heights of 0.54 eV, 0.66 eV and 0.78 eV for $C_i\text{-P}_s$ (I to III), $C_i\text{-As}_s$ (I to II) and $C_i\text{-Sb}_s$ (I to II) respectively, under saturated injection conditions. The migration barrier of isolated C_i is measured to be 0.55 eV under the same conditions. This suggests size dependent, short range, attractive interaction between C and group V atom. A small reduction of the migration barrier of C, under injection conditions (from 0.8 to 0.55 eV) may suggest a recombination enhanced migration mechanism. This is consistent with the fact that minority carrier injection above 300K regenerates C_i , dissociating $C_i\text{-D}_s^V$ pairs.

Structure

Pairing of $(D_s^V)^+$ with negatively charged C_i involves Coulomb interaction as a major source of binding between them. In the simple model of a uniform medium of dielectric constant ϵ , the level position for the $C_i\text{-D}_s^V$ pair is lowered from that of C_i by $e^2/\epsilon \cdot r$. This predicts $r=2A$ for the stable configuration (I) of $C_i\text{-D}_s^V$ pairs, which is very close to typical carbon-group V molecular bond length⁹. One structure consistent with this information is shown in fig. 3a. It is a 3 coordinated carbon-group V molecule occupying a single lattice site, similar to the C_i structure [11]. The observed succession of shallower energy levels could be the result of C_i moving to a more distant sites, as discussed above with reduced Coulomb interaction. A possible structure for IIA and IIB of $C_i\text{-As}_s$ and $C_i\text{-Sb}_s$ is shown in fig. 3b. This structure is similar to that observed for the $C_i\text{-C}_s$ pair which is also bistable, and it would have a smaller Coulomb interaction than I due to the increased carbon donor distance. Structures of the other observed configurations may also be determined by the combination of bond configurations and Coulomb interaction

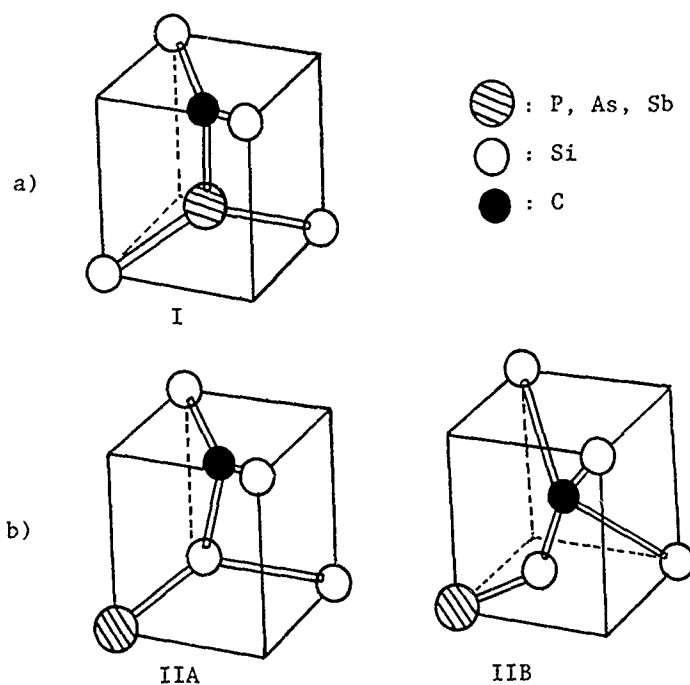


Figure 3: Possible structure for a) I of $C_i-D_V^V$ b) IIA and IIB of C_i-As_V and C_i-Sb_V .

between C and group V atom at different lattice sites. A proper structural determination requires EPR or other spectroscopic results.

In summary, we have identified three $C_i-D_V^V$ pair defects in silicon. The remarkable multiplicity of configurations apparently results from a unique combination of electrostatically driven metastability and bond switching bistability.

This work was made possible by support from the Office of Naval Research Contract No. N00014-84-K-0025.

References

- 1) L.W. Song, B.W. Benson and G.D. Watkins, Appl. Phys. Lett. **51**, 1155 (1987).
- 2) J.J. Van Kooten, G.A. Weller and C.A.J. Ammerlaan
Phys. Rev. B, **30**, 4564 (1984).
- 3) A. Chantre and D. Bois, Phys. Rev. B, **31**, 7979 (1985).
- 4) L.C. Kimerling, P. Blood and W.M. Gibson, in Defects and Radiation Effects in Semiconductors, 1978 (IOP Conf. Ser. No. 46, London 1979) p. 273.
- 5) L.W. Song, PhD dissertation thesis, unpublished 1988.
- 6) L.W. Song, B.W. Benson and G.D. Watkins, Phys. Rev. B **33**, 1452 (1986).
- 7) A. Chantre, J.L. Benton, M.T. Asom and L.C. Kimerling
Mat. Sci. For. Vol. **10-12** (1986) p. 1111.
- 8) B.W. Benson and E. Güler, B. Am. Phys. Soc. **34**, 834 (1989).
- 9) B.W. Benson and E. Güler, Mat. Sci. For. Vol. **38-41**, (1989) p. 391.
- 10) E. Güler and B.W. Benson, B. Am. Phys. Soc. **34**, 834 (1989).
- 11) G.D. Watkins and K.L. Brower, Phys. Rev. Lett. **36**, 1329 (1976).

EXCITONIC RECOMBINATION AT A TRANSITION-METAL RELATED DEFECT IN SILICON

K.G. MCGUIGAN*, M.O. HENRY*, E.C. LIGHTOWLERS**, M.H. NAZARE#

* School of Physical Sciences, Dublin City University, Collins Avenue, Dublin 9, Ireland

** Physics Department, King's College London, Strand, London, WC2R 2LS, UK

Departamento e Centro de Física, Universidade de Aveiro, 3800 Aveiro, Portugal

ABSTRACT

A new photoluminescence system is reported for copper-doped silicon. The luminescence system consists of two doublet zero phonon lines at 1033.51 ± 0.05 meV, 1033.62 ± 0.05 meV, 1040.05 ± 0.05 meV and 1040.17 ± 0.05 meV. We establish from Zeeman studies that the lower energy lines are isotropic magnetic triplets, and the upper energy lines are singlets. From temperature dependence measurements the energy separation between triplet and singlet states is determined to be approximately 6 meV, in agreement with the spectroscopic separation. Also from temperature dependence PL we show that the transition probability ratio for the higher and lower states is 210. We conclude that the main features of the luminescence agree with radiative recombination of excitons bound to an axial isoelectronic defect. The chemical identity of the constituent(s) involved is uncertain although the participation of copper is likely.

INTRODUCTION

Transition metal elements, even in very low concentrations, are feared contaminants in most semiconductor fabrication processes since they can drastically influence the free-carrier lifetimes and electrical conductivity of the host material [1]. Transition metals are fast diffusers in silicon, in particular copper has a diffusion coefficient of 10^{-4} cm² sec at 1100° C [2]. Copper contamination is therefore a frequent occurrence especially after furnace anneals since it is given off by the furnace windings at high temperatures [3]. Over the last ten years several copper related defects have been reported [4,5].

In this paper we report a new band present in the photoluminescence spectrum of copper doped silicon (Figures 1, 2). This luminescence system, labelled SK, has doublet zero phonon lines at 1033.51 meV and 1033.62 meV (SK⁰ and SK¹ respectively) and at 1040.05 meV and 1040.17 meV (SK³ and SK⁴ respectively). We identify this system with the decay of bound excitons at an isoelectronic defect. From Zeeman measurements the higher energy lines are identified as transitions from singlet states ($S = 0$) and the lower energy lines as transitions from isotropic ($S = 1$) triplet states. From the temperature dependent behaviour of the zero phonon lines, the transition probability ratio of the triplet and singlet states is found to be about 210, and the energy separation between each triplet-singlet about 6.5 meV in agreement with the spectroscopically observed line separations.

EXPERIMENTAL

The starting material was an as-received ingot of silicon of 4500Ω cm resistivity and with a copper concentration of 10^{13} atoms cm⁻² measured by atomic absorption. Samples of dimensions $9 \times 4 \times 2$ mm were cut from this ingot, etched to remove any surface damage, and rinsed thoroughly in de-ionized water. These were then placed in a vertical furnace pre-heated to 1100° C, for two minutes, after which time they were quenched by dropping

them directly from the furnace into rotary pump oil. In this manner an average quench rate of approximately 1000°C/sec was achieved.

As previously reported [5,6] the quench rate was found to be the most critical factor in determining the PL centres created in the samples. If the sample dimensions were reduced to $7 \times 3 \times 1.5\text{ mm}$ the reduced surface area facilitated a faster quench rate with the result that the 943 meV [5,6] band was found to dominate the luminescence spectrum. Samples cut to the larger dimensions favoured the formation of the SK and the 1014 meV copper-related [2] defect systems (Figure 1).

The experiments were conducted with the sample immersed in a helium-flow cryostat or attached to the primary heat station of a helium-cryogen closed-cycle refrigerator. A temperature controller enabled temperatures of between 4.2 K and 300 K to be maintained. The excitation source was a 150 W Xenon arc lamp filtered through a 0.25 m focal length Spex monochromator with an output wavelength in the 900 nm spectral region. The luminescence was dispersed by a 1 m focal length Spex monochromator and detected by a North Coast EO-817 germanium detector cooled to liquid nitrogen temperatures.

The excitation source for the Zeeman spectra was the 514.8 nm line of an argon ion laser. Typically the incident power on the samples was $\approx 500\text{ mW}$. These spectra were recorded with a Nicolet 60SX Fourier transform (FT) spectrometer in conjunction with a Spectro Mag 4 helium bath cryostat with a superconducting magnet in a split pair arrangement to produce fields of up to 5 Tesla. All Zeeman measurements were made in Faraday configuration.

RESULTS AND DISCUSSION

Figure 1 shows a low resolution luminescence spectrum of a copper doped sample. Although the spectrum is dominated by the 1014 meV band, the two ZPLs of the SK system can be clearly seen in the 1040 meV region. A high resolution spectrum of this region is shown in figure 2, and reveals the doublet nature of each zero phonon line. The lowest energy no-phonon feature consists of two transitions at $1033.51 \pm 0.05\text{ meV}$ and $1033.62 \pm 0.05\text{ meV}$ labelled SK^0 and SK^1 , respectively. The higher energy no-phonon feature also consists of two ZPLs labelled SK^2 and SK^3 for which the energies are $1040.05 \pm 0.05\text{ meV}$ and $1040.17 \pm 0.05\text{ meV}$ respectively.

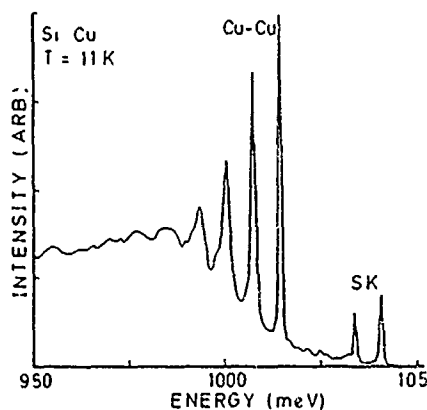


Fig. 1 - An 11 K PL spectrum of copper-doped silicon showing the new SK system and the well documented 1014 meV Cu-Cu system

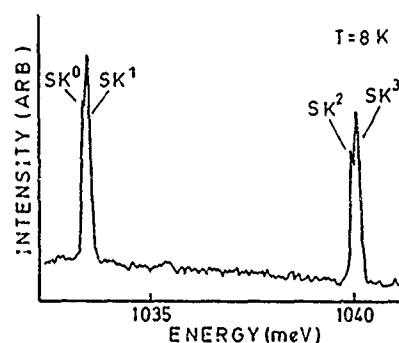


Fig. 2 - A high resolution, low temperature spectrum of the SK system showing the doublet nature of both PL features, recorded using a FT spectrometer

Figure 3 shows the changes in the PL spectrum as the temperature is raised from 11 K to 31 K. Below 5 K the $SK^{2,3}$ line is not observed; however above this temperature it is seen to grow rapidly in intensity at the expense of the $SK^{0,1}$ line, above 35 K this latter line has almost completely disappeared. The variation of the $SK^{2,3}$ to $SK^{0,1}$ intensity ratio with inverse temperature is shown in figure 4. The straight line is a least square fit to the data points of

$$I_1(T)/I_2(T) = (g_1 f_1 / g_2 f_2) e^{-E/kT} \quad (1)$$

where $g_1 f_1$ are the degeneracies and transition probabilities respectively, and E the energy separation. Best fit values for the energy and infinite temperature ratio are 5.71 meV and 71 respectively.

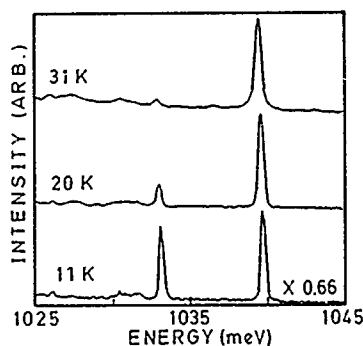


Fig. 3 - PL spectra of the SK system recorded (using a dispersive spectrometer), at 11 K, 20 K and 31 K. The doublet nature of the no-phonon lines is not resolved

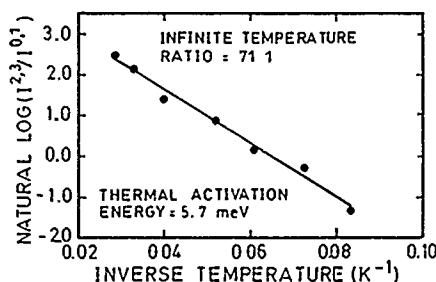


Fig. 4 - Plot of the ratio of the singlet and triplet lines ($SK^{2,3}/SK^{0,1}$) against inverse temperature

Zeeman data is shown in figure 5. The $SK^{0,1}$ lines are seen to split isotropically into three thermalising components, giving an effective g -value of 2. Each split component retains its doublet nature and the splitting is found to be equal to the zero field value. Figure 5 shows the isotropic triplet splittings of the $SK^{0,1}$ transitions. Magnetic fields were applied parallel to the crystallographic directions, $\langle 001 \rangle$, $\langle 111 \rangle$, $\langle 110 \rangle$, but no discernable differences in the splitting patterns were observed.

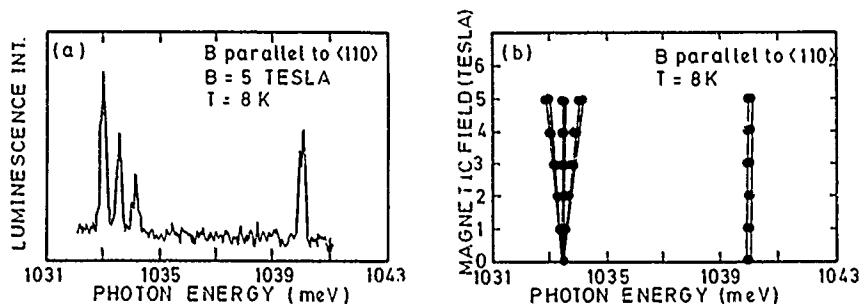


Fig. 5 - (a) A representative Zeeman spectrum recorded in Faraday configuration for a field of 5 T parallel to the $\langle 110 \rangle$ direction taken at 8 K. (b) A fan diagram showing the splitting of the SK features in magnetic fields from 0 to 5 Tesla

The ZPLs SK^{2,3} exhibited no splitting or shift for magnetic fields of up to 5 T. This indicates that these transitions are spin singlets ($S = 0$), and the SK^{0,1} are spin triplets ($S = 1$).

If the fine structure in the lines is ignored, the spectrum is typical of recombination of excitons bound at an axial isoelectronic defect. According to Davies (1984) [7] the axial nature of the defect can be represented by a uniaxial stress, that lowers the energy of the free exciton states of the perfect crystal, producing the bound states. These can be described in terms of a built in stress and the electron-hole exchange energy. In the case of the SK system, and using published results (figure 8 in ref. 7), the exciton axial binding energy of 114 meV corresponds to an internal stress of about -3.65 GPa along a $\langle 001 \rangle$ axis. This gives a value of .0086 for the transition probability from the triplet relative to the transition probability from the singlet state, this value is close to the experimental value of .0141, found from the infinite temperature ratio, equal to $g_1 f_1 / g_2 f_2$ with $g_1 = 1$, $g_2 = 3$.

The occurrence of the fine structure within each line can perhaps be explained by invoking local strain to lift the degeneracy of the band extrema. This would give rise to excitonic states of different energy. However in silicon the experimental and theoretical values known for the splitting due to internal strain of valley-orbit states are at least on order of magnitude greater than the ones found in this case [8]. Another possible explanation for the existence of the fine structure is isotope splitting, this is being currently investigated.

SUMMARY

We have reported a new PL centre in copper-doped silicon, consisting of four zero phonon lines. High resolution spectroscopy and Zeeman studies show the lines to split into two isotropic singlet-triplet pairs suggesting that the luminescence originates from the recombination of excitons formed at a hole attractive central cell combined with a strong compressive strain. The chemical identity of the constituents involved is uncertain although the participation of copper is likely.

ACKNOWLEDGEMENTS

We are grateful to A. Brinklow (Plessey Caswell) for carrying out the atomic absorption measurement.

This work was supported by the Irish Science and Technology Agency (EOLAS), the INIC and JNICT of Portugal, the SERC of the UK and EEC (Commission contract n° SC1*0187-C (SMA)).

REFERENCES

1. R.H. Hopkins, R.G. Seidensticker, J.R. Davies, P. Rai Chondhury, P.D. Blais, J.R. McCornick, J. Crystl. Growth 42, 493 (1977)
2. E.R. Weber, Appl. Phys. A30, 1 (1983)
3. L.C. Canham, M.R. Dyball, K.G. Barraclough, J. Appl. Phys. 66 (2), 920 (1989) and references therein
4. J. Weber, H. Bauch, R. Sauer, Phys. Rev. 25 (12), 7688 (1982)
5. K.G. McGuigan, M.O. Henry, E.C. Lightowers, A.G. Steele, M.L.W. Thewalt, Sol. Stat. Commun. 68 (1), 7 (1988)
6. K.G. McGuigan, M.O. Henry, M.C. Carmo, G. Davies, E.C. Lightowers, Mat. Sci. Eng. B-255-1 (1989)
7. G. Davies, J. Phys. C: Solid State Phys. 17, 6331 (1984)
8. K. Thonke, A. Hangleiter, J. Wagner, R. Sauer, J. Phys. C: Solid State Phys. 18, 1795 (1985)

ELECTRONIC STRUCTURE OF TWO SULPHUR-RELATED BOUND EXCITONS IN SILICON STUDIED BY OPTICAL DETECTION OF MAGNETIC RESONANCE

W.M. CHEN*, A. HENRY*, E. JANZÉN*, B. MONEMAR*,** AND M.L.W. THEWALT***

* Department of Physics and Measurement Technology, Linköping University, S-581 83 Linköping, SWEDEN

** Present address: Max-Planck-Institut für Festkörperforschung, Heisenbergstrasse 1, D-7000 Stuttgart 80, FRG

*** Department of Physics, Simon Fraser University, Burnaby, BC, CANADA V5A 1S6

ABSTRACT

We report an investigation on the electronic structure of two bound exciton (BE) systems from a complex defect in S-doped Si, by optical detection of magnetic resonance (ODMR). A spin-triplet ($S=1$) is identified to be the lowest electronic state of the BE's, which gives rise to deep photoluminescence (PL) emissions when recombining. A weak anisotropy of the magnetic interaction of the BE's (not possible to resolve in Zeeman data) is revealed, which leads directly to the determination of the symmetry for the excited state of the defect. A S-related complex model is suggested as the identity of the defect. A critical test of two possible metastable configurations of the constituents of a single defect is undertaken.

INTRODUCTION

Two recently reported luminescent systems in thermally quenched sulphur-doped silicon have received great attention [1-5]. This is mainly due to the possible presence of interesting configurational metastability of the associated defect [4,5] as well as the rather high external quantum efficiency [1-3]. Previous studies by steady-state [1-5] and time-resolved [1] PL spectroscopy, electroluminescence (EL) [3], PL excitation (PLE), far-infrared exciton absorption spectroscopy (FIEAS) [4] and Zeeman measurements [5] have yielded useful information on the optical and electronic properties of the BE systems and their associated deep level defect center.

In this paper we report on an investigation of these two S-related BE systems by the ODMR technique, with hopes of revealing the detailed electronic as well as geometric structure of the defect and particularly to provide a critical test on the configurational metastability.

EXPERIMENTAL

The preparation of the S-diffused silicon single crystals used in this work was described elsewhere [4].

The ODMR experiments were performed with the aid of a modified Bruker 200D-SRC electron spin resonance (ESR) 9-GHz spectrometer, equipped with a TE₀₁₁ microwave (MW) cavity with optical access from all directions. MW power up to 200 mW was available. The sample temperature could be continuously varied down to 2 K during experiments with an Oxford Instruments ESR 10 liquid-He continuous-flow cryostat. The ODMR spectra were taken with a liquid-nitrogen

cooled North Coast Ge-detector, lock-in detected in phase with the amplitude-modulated MW field. A Jobin-Yvon 0.25-m grating monochromator or a set of infrared band-pass filters were used to obtain the spectral dependence of the ODMR signals. To avoid strong background signals arising from the heating effect of free carriers by the MW electric field [6], which obscured any possible detection of ODMR signals from the S-related defect under study, we employed a newly developed delayed-ODMR (D-ODMR) technique. A detailed description of the D-ODMR technique can be found elsewhere [7].

RESULTS AND DISCUSSION

In Fig.1 we show PL spectra from the Si:S sample studied in this work at two different temperatures. The spectra are dominated by the two S-related PL emissions (namely S_A and S_B) [1-5], characterised by the sharp no-phonon electronic transition lines, S_A^0 at 968.24 meV and S_A^1 at 977.05 meV for the S_A , and S_B^0 at 811.96 meV and S_B^1 at 821.91 meV for the S_B [4]. Here we follow the notation used in Ref.4. S_A^0 and S_B^0 are the lowest electronic transition lines corresponding to the two BE's, which are spin forbidden [5]. S_A^1 and S_B^1 exhibit, however, much higher transition probability (by about three orders of magnitude [5]) compared to the S_A^0 and S_B^0 . This results in a characteristic temperature dependence of the PL transitions, i.e. S_A^0 and S_B^0 dominate at very low temperature while S_A^1 and S_B^1 prevail at elevated temperatures, as shown in Fig.1.

In the previous studies by Zeeman measurements, S_A^1 and S_B^1 were observed to have singlet character while S_A^0 and S_B^0 split into three components [5]. This led to the conclusion that the S_A^0 and S_B^0 arise from the transition between the lowest spin-triplet states and the diamagnetic ground state of the binding center. S_A^1 and S_B^1 correspond to the BE singlet excited states, which separate from the triplet by the electron-hole (e-h) exchange interaction of the BE's. Such an assignment is, however, not as straightforward as it seems, since a transition between two doublets may give rise to a similar experimental appearance in Zeeman measurements as has been noticed earlier [8]. Special caution must therefore be taken in this case.

It has been shown in many ODMR studies of defect systems in semiconductors [9] that a distinction between electronic transitions such as triplet-

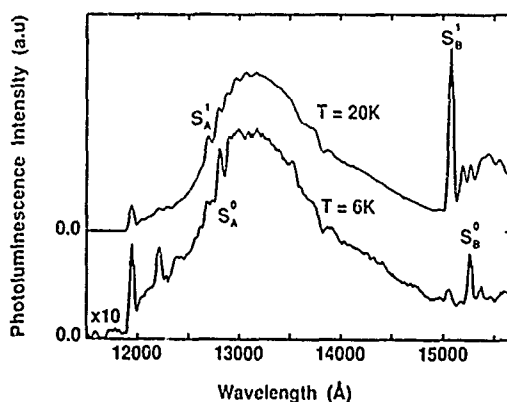


Fig.1
PL spectra from the S-diffused silicon at two different temperatures. The no-phonon electronic transition lines from the two S-related BE's are indicated, following the notation given in Ref.4.

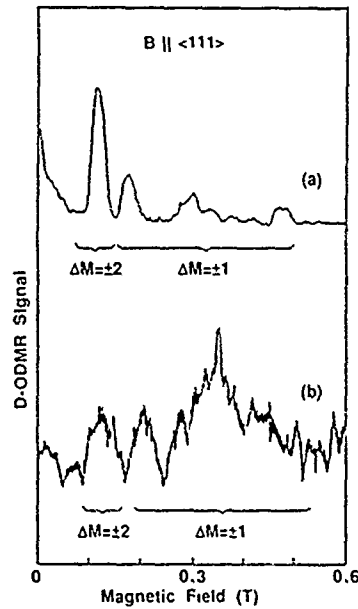


Fig.2 D-ODMR spectra from (a) the S_A BE at 4K and (b) the S_B BE at 6K, taken at 9.16 GHz.

to-singlet and doublet-to-doublet is quite obvious, since only the initial electronic state participates in the magnetic resonances. In the former case a spin-triplet ODMR is observed, characterized by the lower-field $\Delta M=\pm 2$ and the higher-field $\Delta M=\pm 1$ electronic transitions. In the latter case, however, only a donor-like ODMR signal corresponding to the $\Delta M=\pm 1$ electronic transitions within the doublet is observed. Therefore the ODMR technique is believed to be particularly useful here, to unambiguously determine the electronic structure of the BE's and the symmetry of the defect.

A conventional ODMR spectrum of the crystal shows a predominant background signal, which obscures any possible detection of the ODMR signal from the S-related BE's. However, an application of a new D-ODMR technique [7] is successful. In Fig. 2 we show two D-ODMR spectra when the detection wavelength is taken at around 1.3 μm and 1.6 μm , respectively, with the aid of optical band-pass filters. They are both identified to arise from a spin-triplet, characterized by the lower-field $\Delta M=\pm 2$ and the higher-field $\Delta M=\pm 1$ microwave-induced electronic transitions. A spectral dependence study reveals that the D-ODMR spectra in Fig.2(a) and 2(b) originate from the S_A and S_B BE's, respectively.

An angular dependence of the D-ODMR spectra was carried out with the external magnetic field B rotated in the $(1\bar{1}0)$ crystallographic plane, and was analysed by using a spin Hamiltonian

$$H_S = \mu_B B \cdot g \cdot S + S \cdot D \cdot S. \quad (1)$$

Here S denotes the effective spin of the BE, with $S=1$ for the spin-triplet. μ_B is the Bohr magneton. The first term in Eq.(1) represents the electronic Zeeman interaction, and the second term is the so-called fine-structure term, describing the residual symmetry-breaking interactions of the BE-defect system. The preliminary spin Hamiltonian parameters for the S_A BE were obtained, by fitting the spin Hamiltonian to the experimental data with a computer program, as follows: $g_x \approx g_y \approx g_z \approx 2.0$, $D_x \approx -1.4 \times 10^{-5}$ eV, $D_y \approx 0.2 \times 10^{-5}$ eV, $D_z \approx 1.2 \times 10^{-5}$ eV, where $x=[1\bar{1}2]$, $y=[1\bar{1}0]$ and $z=[111]$ are the principal axes of the g - and D -tensor. A spin-1 basis set of wavefunctions was employed in the diagonalization of the spin Hamiltonian in Eq.(1). A distorted trigonal symmetry, distorted in the $(1\bar{1}0)$ plane for the S_A BE and its associated binding center in the corresponding configuration has been deduced, i.e. C_{1h} , containing the reflection plane $(1\bar{1}0)$. The corresponding parameters and symmetry information for the S_B BE (except $g \approx 2$) could so far not be obtained, unfortunately, due to very weak D-ODMR signals. However, we believe that the

S_A and S_B BE configurations are distinctly different as evidenced from their different D-ODMR spectra.

The electronic structure of both the S_A and S_B BE can be understood as derived from a spin-like electron-hole pair. The quenching of the hole orbital angular momentum of a BE is commonly observed in cases of a deep neutral complex defect center with an overall hole-attractive low-symmetry defect potential [10]. The e-h exchange interaction leaves the spin-triplet in the lowest energy, separated from the higher-lying spin-singlet by about 9 meV in this case [4].

It was noticed that the D-ODMR signal from the S_B BE was much weaker (by at least a factor of 10) than that from the S_A BE, though the PL intensity of the S_B BE was optimised to be comparable to that of the S_A BE, by cooling the sample in an intensive laser light and measuring at a somewhat elevated temperature (6K). Moreover, the formally forbidden $\Delta M = \pm 2$ transitions were comparably weaker for the S_B BE than for the S_A BE, which indicated that the symmetry of the defect configuration related to the S_B BE might be higher, i.e. higher than C_{1h} . If this is true, the S_A and S_B BE's are the electronic excitations localized at two different bistable configurations of the same defect constituents.

No hyperfine structure from the S defect atoms was expected to be observed in the D-ODMR spectra, due to the vanishing nuclear spins $I=0$ for the naturally abundant ^{32}S (95.0%) and ^{34}S (4.22%). Therefore no definite atomic structure of the defect could be revealed in the present stage. We tentatively suggest a distorted trigonal complex as the identity of the defect system studied in this work, such as a sulphur pair. A detailed description of the models for the electronic and geometric structure of the defect will be presented shortly. More detailed D-ODMR and ENDOR (electron nuclear double resonance) studies in combination with $^{33}\text{S}(I=3/2)$ -rich isotope doping for this defect system is now in progress.

In summary we have carried out a D-ODMR study of the two S-related BE systems. We have confirmed that the lowest electronic state of both BE's is a spin-triplet. The presence of two metastable configurations of a single S-related complex is shown to be plausible. This work provides the first case where ODMR of an electronic state can be observed directly from its radiative transitions in Si.

REFERENCES

1. T.G. Brown and D.G. Hall, Appl. Phys. Lett. **49**, 245 (1986).
2. T.G. Brown, P.L. Bradfield and D.G. Hall, Appl. Phys. Lett. **51**, 1585 (1987).
3. P.L. Bradfield, T.G. Brown and D.G. Hall, Appl. Phys. Lett. **55**, 100 (1989).
4. M.L.W. Thewalt, M. Nissen, D.J.S. Beckett and S. Charbonneau, in Shallow Impurities in Semiconductors, edited by B. Monemar (Inst. of Phys. Conf. Series **95**, Bristol, 1989) pp. 505-514.
5. M. Singh, E.C. Lightowers and G. Davies, presented in the E-MRS Spring Meeting, Strasbourg, France, 1989 (unpublished).
6. M. Godlewski, H. Weman, F.P. Wang, B. Monemar, W.M. Chen and Q.X. Zhao, in Defects in Electronic Materials, edited by M. Stavola, S.J. Pearton and G. Davies (Mat. Res. Soc. Symp. Proc. **104**, Pittsburgh, PA, 1988) pp.117-120.
7. W.M. Chen and B. Monemar, these proceedings.
8. P.J. Dean, in Deep Centers in Semiconductors, ed. S.T. Pantelides (Gordon and Breach, New York, 1986) Chap.4.
9. B.C. Cavenett, Adv. in Physics **30**, 475 (1981).
10. B. Monemar, U. Lindefelt and W.M. Chen, Physica **146B**, 256 (1987).

AN ELECTRON PARAMAGNETIC RESONANCE INVESTIGATION OF IRON-INDIUM PAIRS IN SILICON

P. EMANUELSSON*, W. GEHLHOFF**, P. OMLING* AND H. G. GRIMMEISS*

*Department of Solid State Physics, University of Lund, Box 118, S-221 00 Lund, Sweden

**Academy of Sciences of the GDR, Centre for Scientific Instruments, Rudower Chaussee 6, Berlin 1199, GDR

ABSTRACT

Three different Electron Paramagnetic Resonance (EPR) signals, one trigonal and two orthorhombic, which originates from iron-indium pairs in silicon are investigated. It is shown that the two orthorhombic spectra can be explained as transitions within the two doublets of a $S=3/2$ system with a large zero-field splitting. The temperature dependence of the intensities reveals that the newly discovered spectrum corresponds to the lower doublet and that the zero-field splitting is $9.8 \pm 2.0 \text{ cm}^{-1}$.

INTRODUCTION

Pairs of a substitutional group III acceptor and an interstitial iron atom in silicon have been extensively studied in recent years [1-7], partly due to the fact that these defects can exist in two different configurations [1]. The two structural arrangements are the nearest neighbour configuration (nn) where the interstitial iron atom is situated along a $\langle 111 \rangle$ direction from the acceptor (trigonal symmetry) and the next nearest neighbour configuration (nnn) where the iron atom is situated along a $\langle 100 \rangle$ direction (orthorhombic I symmetry).

The Electron Paramagnetic Resonance (EPR) investigations of iron-acceptor pairs [2-4] have revealed that the FeAl and FeGa centres exist in both the nn and the nnn configuration. For the orthorhombic pairs an additional spectrum, belonging to an excited state, has been detected. FeB is only found in the nn configuration and FeIn in the nnn. The spectra can be described as transitions within the two doublets of a $S=3/2$ system with a large zero-field splitting. The ground state spectrum then corresponds to transitions within the lower doublet and the excited state spectrum to transitions within the upper doublet. The sign of the axial fine structure parameter is found positive for FeB, negative for FeAl and FeGa and positive for FeIn. This surprising chemical trend and the missing trigonal FeIn pair is an unsolved problem.

However, recently a new spectrum was found that could be identified as an FeIn pair with trigonal symmetry [5]. Later a new orthorhombic spectrum was detected in addition to the old orthorhombic FeIn signal [6]. It was concluded that the new spectrum belongs to the ground state and that the previously reported one corresponds to the excited state. The aim of this paper is to summarise these new findings and to present new measurements of the temperature dependencies of the two orthorhombic EPR spectra

EXPERIMENTAL DETAILS

The samples were prepared from Czochralski grown silicon

crystals doped with indium (2 Ωcm). Iron was evaporated onto the samples and diffused at 1200 °C for two hours. The ^{57}Fe isotope doping took place in a closed ampoule where a piece of ^{57}Fe was placed close to the silicon crystal. After the heat treatment the samples were quenched in diffusion pump oil and then etched. The EPR measurements were performed at temperatures between 4 and 30 K with a $\langle 110 \rangle$ axis perpendicular to the magnetic field in a Bruker ESP 300 spectrometer, working in the X-band and equipped with an Air Products helium gas flow cryostat.

EXPERIMENTAL RESULTS AND DISCUSSION

After the iron diffusion three different EPR spectra were detected. One of them shows trigonal symmetry and can only be observed when the sample is illuminated. The other two exhibit orthorhombic I symmetry and they appear both under illumination and in darkness. The spectra can be described with an effective spin $S'=1/2$ and the following spin Hamiltonian:

$$H = \mu_B \cdot B \cdot g' \cdot S' \quad (1)$$

where the symbols have their usual meaning. Using Eq. 1, a computer fit of the angular dependence of the spectrum showing trigonal symmetry gives $g_{||}'=6.38$ and $g_{\perp}'=1.08$. We will hereafter call this spectrum Lu2. One of the spectra with orthorhombic symmetry has g' -values which are in good agreement with those for the FeIn pair reported by Ludwig and Woodbury [2], i. e. $g_x'=3.78$, $g_y'=4.40$ and $g_z'=2.07$ ($z//\langle 100 \rangle$ and $x,y//\langle 110 \rangle$). We will call this spectrum LW. The other one has a very anisotropic resonance pattern and a computer fit gives $g_x'=0.36$, $g_y'=0.35$ and $g_z'=6.26$. It should be noted, however, that the g_x' - and g_y' -values for this spectrum are not determined in the main directions since we only could measure the part of the spectrum which is below 1.4 T [6]. This EPR signal is labelled Lu4.

In order to chemically identify the centres, we studied the hyperfine structure. Natural indium consists of 95.7% ^{115}In and 4.3% ^{113}In , which both have $I=9/2$. Since the two isotopes have almost identical g_N values, they give rise to only one set of ten lines. All three spectra (Lu2, Lu4 and LW) show a very clear splitting in ten lines, i. e. one indium atom is part of each defect. The presence of iron is more difficult to prove, since natural iron to 97.8% consists of isotopes with $I=0$. We therefore performed isotope doping experiments using iron enriched to 96% of ^{57}Fe ($I=1/2$). For the Lu2 and LW spectra an additional twofold splitting of each line was observed. It was thereby proved that the centres that give rise to the Lu2 and LW spectra consist of one indium and one iron atom. For the Lu4 spectrum the signal to noise ratio in the isotope doped samples was not sufficient to resolve the iron splitting. However, since we only observe the Lu4 spectrum in samples doped with iron, it is not unreasonable to suggest that also this signal is caused by an FeIn pair.

In order to further support the identification of Lu4 as being an FeIn pair and, if this is the case, to give an answer to the question whether or not this orthorhombic defect is the same as the one that gives rise to the LW spectrum, we have compared our experimental g' -values with those from a model calculation. The spectra can be analysed with a $S=3/2$ system and the following spin Hamiltonian [6]:

$$H = D \cdot \left(S_z^2 - \frac{1}{3} S \cdot (S+1) \right) + E \cdot (S_x^2 - S_y^2) + g_x \cdot \mu_B \cdot B_x \cdot S_x + g_y \cdot \mu_B \cdot B_y \cdot S_y + g_z \cdot \mu_B \cdot B_z \cdot S_z \quad (2)$$

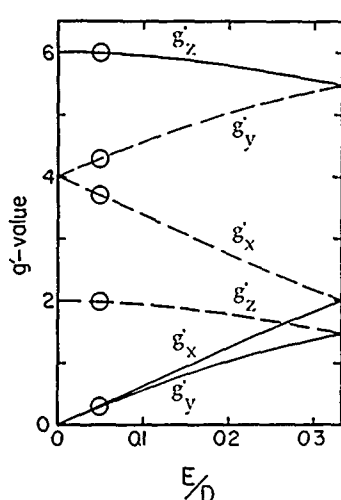


Fig. 1: Calculated g' -values versus E/D . The values consistent with the experimental situation are indicated.

where the symbols have their conventional meaning. If we assume that the zero-field splitting $\Delta = 2(D^2 + 3E^2)^{1/2}$ is much larger than the microwave photon energy, then the $S=3/2$ system will split into two Kramers doublets and we will get transitions within these two doublets. The g' -values can for each doublet be calculated as a function of E/D . This relation is plotted in Fig. 1, assuming that the orbital contributions to the true g -values can be neglected. Since we have proved that the LW spectrum is caused by an FeIn pair, it is possible to use its g' -values to determine the value of E/D . We can see in Fig. 1 that for $E/D=0.05$ the g' -values for one of the two doublets are close to those of the LW spectrum. The g' -values for the other doublet are then predicted to be: $g'_x=0.31$, $g'_y=0.29$ and $g'_z=5.99$, very close to those observed for the LW spectrum. An even better agreement is obtained for the true g -values: $g_x=2.094$, $g_y=2.016$ and $g_z=2.095$ and $E/D=0.06335$. In this case, we get $g'_x=3.78$, $g'_y=4.40$ and $g'_z=2.07$ for the LW spectrum and $g'_x=0.41$, $g'_y=0.37$ and $g'_z=6.26$ for Lu4, almost exactly equal to the experimentally observed ones. From this result, together with the previously mentioned hyperfine structure and doping experiments, we conclude that Lu4 originates from the same FeIn pair as the LW spectrum.

The next task is to determine which one of the two EPR signals corresponds to the ground state (i. e. the lower doublet). To answer this question, we measured the temperature dependence of the intensities for the two spectra. The result is plotted in Fig. 2. For the LW spectrum, the intensity increases

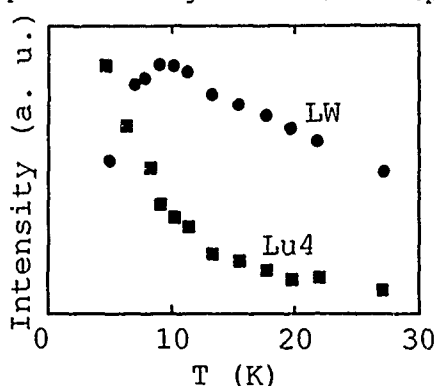


Fig. 2: Temperature dependence of the intensities for the LW and Lu4 spectra.

with increasing temperature up to approximately 10 K and starts then to decrease. For the Lu4 spectrum, the intensity decreases monotonously with increasing temperature. This means that Lu4 belongs to the ground state and that LW, in contrary to what has been believed, originates from the excited state. It also implies that the sign of D is negative, thereby removing the discontinuity in the chemical trend for the iron-acceptor pairs. Furthermore, in Fig. 3 we have plotted the logarithmic of the ratio between the two intensities versus $1/T$ and from

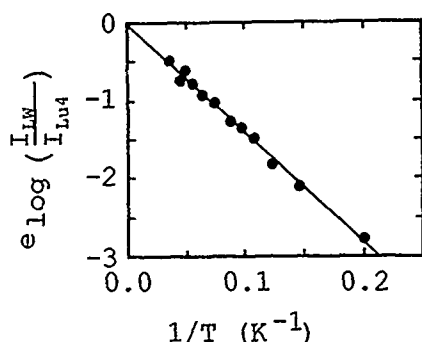


Fig. 3: The logarithm of the ratio of the intensities for the LW and Lu4 spectra as a function of $1/T$.

the slope of the straight line the zero-field splitting can be calculated to $\Delta = 2(D^2 + 3E^2)^{1/2} = 9.8 (\pm 2.0) \text{ cm}^{-1}$. This, together with the relation $|E/D| = 0.06335$, makes it possible to calculate the values of D and $|E|$: $D = -4.9 (\pm 1.0) \text{ cm}^{-1}$, $|E| = 0.31 (\pm 0.06) \text{ cm}^{-1}$.

If we now focus our attention again on Lu2, we have identified this spectrum as originating from a trigonal FeIn pair. To be able to observe this spectrum it was necessary to illuminate the sample. This means that we have to photo-ionise the defect to be able to achieve the paramagnetic (neutral) charge state. This

photoionisation was effective for photon energies all the way from 0.5 eV (the spectral limit of our setup) up to above the bandgap, indicating that the energy level of the defect is located in the forbidden energy gap not more than 0.5 eV from the top of the valence band. This is consistent with the activation energy of 0.27 eV for emission of holes, obtained from electrical measurements of a level which is believed to correspond to the trigonal FeIn pair [7].

A new picture of the iron-indium pair in silicon emerges. This defect seems to be very much like the FeAl and FeGa pairs. They can all exist in two different configurations, one with trigonal and one with orthorhombic symmetry. The electronic structure can be explained as a $S=3/2$ system with a large zero-field splitting and all three defects have the same sign of the axial fine structure parameter.

The authors are grateful to the Swedish Natural Science Research Council and to the Wallenberg foundation for financial support.

REFERENCES

- 1) A. Chantre and D. Bois, *Phys. Rev. B* **31**, 7979 (1985).
- 2) G. W. Ludwig and H. H. Woodbury, *Solid State Phys.* **13**, 223 (1962).
- 3) J. J. van Kooten, G. A. Weller and C. A. J. Ammerlaan, *Phys. Rev. B* **30**, 4564 (1984).
- 4) W. Gehlhoff, K. Irmischer and J. Kreissl, *Proc. 2nd Int. autumn meeting, Garzau 1987*, 262 (1987).
- 5) P. Omling, P. Emanuelsson, W. Gehlhoff and H. G. Grimmeiss, *Solid State Commun.* **70**, 807 (1989).
- 6) W. Gehlhoff, P. Emanuelsson, P. Omling and H. G. Grimmeiss, to be published in *Phys. Rev. B*.
- 7) A. Chantre and L. C. Kimerling, in Defects in Semiconductors, Material Science Forum Vol. 10-12, edited by H. J. von Bardeleben (Trans Tech Publ. Ltd, Switzerland, 1986), p. 387.

PART V

Electronic Structure -
Superlattices

LIGHT- AND HEAVY-HOLE BOUND EXCITON TRANSITIONS AND FREE TO BOUND
TRANSITIONS IN $\text{Ga}_{1-x}\text{Al}_x\text{As}/\text{GaAs}$ QUANTUM WELLS

DONALD C. REYNOLDS* AND K.K. BAJAJ*

*Electronic Technology Laboratory, Wright Research and Development Center,
Wright-Patterson Air Force Base, OH 45433

* Arizona State University, Tempe, AZ 86443

ABSTRACT

Excitons bound to neutral donors in $\text{Al}_x\text{Ga}_{1-x}\text{As}/\text{GaAs}$ quantum wells were observed by high resolution resonant excitation photoluminescence, and temperature dependent photoluminescence measurements. Changes in the binding energy of excitons are observed when the donors are located in the center of the well, at the edge of the well, or in the center of the barrier. The variations in these binding energies are reported as a function of well size from 75-350Å. The binding energies increased as the well size was reduced to about 100Å, with further reductions in well size they decreased.

Light-hole free excitons bound to neutral donors were observed in $\text{Al}_x\text{Ga}_{1-x}\text{As}/\text{GaAs}$ quantum wells. The transitions were observed, using selective excitation photoluminescence spectroscopy, in the energy region between the light-hole and heavy-hole free exciton transitions where no other intrinsic transitions exist. The neutral donor-bound heavy-hole free-exciton transitions were also observed when the light-hole bound exciton transitions were observed. Quantum well structures which showed no evidence of a heavy-hole donor bound exciton also showed no evidence of a light-hole donor bound exciton.

Free to bound transitions, free hole to bound electron, have also been observed in the $\text{Al}_x\text{Ga}_{1-x}\text{As}/\text{GaAs}$ quantum wells. The diamagnetic shift of these transitions was used to distinguish them from excitonic transitions.

Introduction

There have been few measurements of the binding energy of excitons to neutral donors (D^0, X) or ionized donors (D^+, X) in quantum wells (QWs). The original report of donor related complexes in quantum wells was by Shanabrook and Comas [1]. Reynolds et al [2] reported sharp lines observed in photoluminescence (PL) associated with D^0, X transitions in $\text{GaAs-Al}_x\text{Ga}_{1-x}\text{As}$ multiple-quantum wells (MQWs). D^0, X transitions were also reported by Nomura et al [3] in Si-doped $\text{GaAs-Al}_x\text{Ga}_{1-x}\text{As}$ single QWs (SQWs). Recently, Liu et al [4] have also observed transitions in PL associated with excitons bound to neutral and ionized donors located at the center of the quantum wells. An impurity-bound exciton (probably D^0, X) transition was reported by Charbonneau et al [5] in a 180Å SQW where interrupted growth was used.

We report a systematic study of the binding energy of D^0, X in several QWs of varying sizes and as altered by the physical location of the neutral donors. The $\text{GaAs-Al}_x\text{Ga}_{1-x}\text{As}$ QW samples investigated were either nominally undoped, Si-doped in the center of the well (CW), the edges of the well

(EW), or doped in the center of the $\text{Al}_x\text{Ga}_{1-x}\text{As}$ barrier (CB). We also speculate on the binding energy of D^+X by tentatively identifying some transitions with this feature. The experimental techniques used in this study include high resolution PL, resonant excitation (RE), as well as temperature dependent PL.

An estimate of the energetic ordering of excitonic transitions in semiconductors has been made. An empirical relationship between the binding energy of the exciton (E_1) to the neutral donor and the donor binding energy (E_D) was first postulated by Haynes [6] from experiments performed on Si. This relation can be expressed as follows:

$$E_1 = BE_D \quad (1)$$

where B is a constant of proportionality having a value of 0.1 for Si. It was shown by Hopfield [7] that the binding energy of D^0X could be obtained by subtracting the free exciton energy (E_{ex}) from the energy required for removing an electron and a hole from a neutral donor (E_L). Furthermore, the binding energy of an exciton to an ionized donor can be approximately obtained [7] by subtracting E_{ex} from E_D , since the binding energy of the hole to a neutral donor is small. The relationship between E_{ex} and E_D can then be expressed as follows:

$$E_{\text{ex}} = E_D/(1+\sigma) \quad (2)$$

where σ is the ratio of the electron mass to the hole mass. It was also shown [7] that E_L varied from $1.33 E_D$ for $\sigma = 0$ to $0.055 E_D$ for $\sigma = \infty$ which crosses E_D for a value of σ somewhere between 0.2 and 0.25. Thus for σ -values less than the crossover value, the D^+X transition will fall on the high energy side of D^0X and for values greater than the crossover value, on the lower energy side of D^0X transition.

In addition to the usual heavy-hole free exciton (HHFE) transition, very clear D^0X transitions were observed in all samples regardless of the position of the dopant in the QW. Interpretation of the other transitions observed in the $\text{GaAs-Al}_x\text{Ga}_{1-x}\text{As}$ quantum wells is assisted by an extension of the above arguments. The calculated value of σ , obtained from Eq. 2 using calculated values of E_{ex} [8] and E_D of CW donors [9] for all of the well dimensions investigated, is approximately 0.5, which is higher than the crossover value of 0.25, thereby predicting that the D^+X transition will occur at lower energy than the D^0X transition. However, no transitions were observed in CW-doped samples on the low energy side of D^0X that could be attributed to D^+X .

For EW or CB donors, one cannot use the above-mentioned arguments, which are applicable only to bulk-like donors. Prominent transitions on the high energy side of D^0X were observed in both EW- and CB-doped samples which may be D^+X transitions since the ordering is unknown. It is the detailed comparison of the relative transition energies of D^0X associated

with donors located at CW, EW, or CB versus well size that is the primary object of this study.

Although several groups have observed (HHFE's) bound to neutral donors (D^0, X) in $\text{Al}_x\text{Ga}_{1-x}\text{As-GaAs}$ (QW's), to our knowledge, a similar transition associated with the light-hole free-exciton (LHFE) (D^0, X) has not been reported. Here we report on the observation of the light-hole free-exciton bound to neutral donors in $\text{Al}_x\text{Ga}_{1-x}\text{As-GaAs}$ quantum wells, using the technique of photoluminescence excitation spectroscopy (PLE).

The LHFE D^0, X transitions appear as peaks in PLE in the energy range between the HHFE and LHFE transitions, where it is well known that no intrinsic transitions occur in $\text{Al}_x\text{Ga}_{1-x}\text{As-GaAs}$ QW structures. The energies of the peak positions relative to the LHFE transition further identifies them as the LHFE D^0, X transition. The LHFE D^0, X transitions were observed from two nominally 350Å (MQW) structures, both of which were doped with Be; sample A was doped center of the barrier, and sample B in the center of the well. In sample B, besides the LHFE D^0, X transitions, free to bound transitions, free hole to donor (D^0, h), and light hole excitons bound to acceptors, LHFE (A^0, X) were also observed. The behavior of these transitions in a magnetic field applied perpendicular to the growth direction aided in their identification.

Experimental Method

The samples used to determine the binding energy of excitons to donors as a function of donor location were (MQWs) grown by molecular beam epitaxy (MBE). The wells varied in size from 75Å-350Å and the barriers of $\text{Al}_{0.25}\text{Ga}_{0.75}\text{As}$ were 100Å wide. The single donor dopant used was Si. The CW-doped samples were doped over the central 50Å at a concentration of $1 \times 10^{16}/\text{cm}^3$. However, samples for the narrowest well widths studied ($\leq 100\text{Å}$) were doped only in the central 25Å at $2 \times 10^{16}/\text{cm}^3$, so that the net dopant level was the same as for other samples. The EW-doped samples were doped 25Å at each interface within the well, also at a concentration of $1 \times 10^{16}/\text{cm}^3$. The EW-doped samples of $\leq 100\text{Å}$ well width were doped 12.5Å at each interface at $2 \times 10^{16}/\text{cm}^3$. The CB-doped samples were doped the central 25Å of the barrier at a concentration of $2 \times 10^{16}/\text{cm}^3$. All the samples were grown at a temperature of 580°C using dimeric arsenic.

The PL was excited either with an Ar^+ ion laser or with a tunable dye laser using styryl 9 dye which was pumped by an Ar^+ ion laser. The RE differs from conventional PL in that it was excited by the dye laser tuned to a particular excited state of the transition of interest. For the spectra reported, the samples having well widths $\geq 100\text{Å}$ were resonantly excited either from the LHFE or the $n=2$ state of the HHFE. However, for narrower well widths, RE could not be excited due to tuning limitations of the Styryl 9 dye. The pump power used in all RE experiments in this study was approximately $50 \text{ mW}/\text{cm}^2$. The above power was measured at the exit of the laser, the intensity at the sample was reduced by at least a factor of two.

In straight PL measurements using the Ar^+ ion laser, a pump power of 200 mW/cm² was found to produce satisfactory results and was used throughout this study except for Fig. 7, where a pump power of 600 mW/cm² was used. The samples used for studying light- and heavy-hole bound exciton transitions and free to bound transitions were $Al_{1-x}Ga_xAs$ -GaAs MQW structures with a nominal width of 350Å. The high resolution PL, RE and PLE measurements were made at 2K with the sample immersed in liquid He. To aid in the identification of transitions a magnetic field was applied, and the diamagnetic shifts were observed. In the intrinsic region of GaAs a dispersion of 0.54Å/nm was achieved using a 4m spectrometer equipped with an RCA C31034A photomultiplier tube for detection.

Experimental Results

Prior to beginning the comparison of the various doping schemes, some observations common to all will be noted. It is not possible to control the exact well size sufficiently so that the excitonic features align exactly. To remove this effect, we artificially align the D^0X transitions due to CW donors in spectra of nominally the same well size. The indicated energy scale corresponds to the solid curve in each figure. The displacement of dashed or dot-dashed curves with respect to this scale is indicated in the figure caption. Thus, the absolute transition energies observed may be recovered by subtracting the indicated shift from the displayed spectrum. The binding energy of D^0X is a function of well size. Consequently, if the correction is small, alignment of D^0X also has the effect of aligning the HHFE included in the figures. It should be pointed out that the intensities for different transitions within a given spectrum for a MQW are relative, but the intensities between spectra from different MQWs are arbitrary. The emission spectra from a CW-doped (solid curve) and undoped (dashed curve) nominal 350Å MQWs are shown in Fig. 1. The transition intensity for the D^0X transition in the undoped sample is weak as would be expected since both the well and the barrier are probably p-type; therefore, in the dark the residual donors will be ionized. In the light, as photo-excited electrons are added to the system, the donors at the center of the well will be preferentially neutralized since they have the greatest binding energy. These donors can then form D^0X complexes in the presence of light and recombine producing this D^0X transition. We shall now speculate on the identity of the peak at 1.51690eV. Since the D^+X for CW donors is expected to occur at lower energy than CW D^0X , the

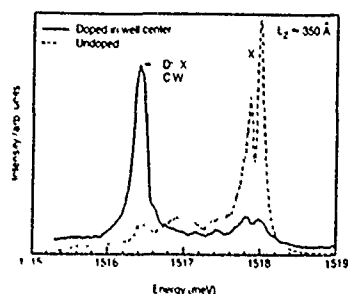


Fig. 1. RE emission spectra from an undoped (dashed curve) and a center of the well doped (solid curve) nominal 350Å MQWs resonantly excited from the $n=2$ state of the HHFE. To account for well width variation, the undoped sample (dashed) has been displaced by 0.1 meV which aligns the CW D^0X .

remaining possibilities are either D^0, X or D^+, X complexes involving either EW or CB donors. In the controlled doping location studies which follow, the D^0, X transition associated with either EW or CB donors are observed to have a smaller shift to higher energy above CW D^0, X than the feature at 1.51690eV. This leaves the possibility of it being D^+, X for either EW or CB donors. This is plausible since these EW and CB donors will be the last to be photo-neutralized and are thus available for D^+, X formation. However, it is also possible that this feature arises from some other unknown origin. The peaks at 1.51791eV and 1.51778eV in the undoped sample are the HHFE transitions corresponding to a one monolayer variation in well width. The correspondingly weaker transitions in the doped sample are also the HHFE transitions. Similar observations may be made about the spectra from samples containing narrower wells.

The PL emission spectra resulting from 350Å MQWs doped at the CW, EW, and CB are shown in Fig. 2. The CW D^0, X transition for the sample doped at the center of the well is dominant over all transitions including HHFE. The EW and CB D^0, X transitions are observed in EW- and CB-doped samples, respectively, and are accompanied by the CW D^0, X transition. They are absent in the CW-doped sample. This is expected since electrons will tend to preferentially relax to the lowest energy state available, which would be the CW-donor, which also has the highest density of states. Theoretical calculations of Greene and Bajaj [10] show that for samples spike-doped at the edge of the well, there is still a transition associated with CW donors. Similarly, there are two well defined peaks expected for the CB-doped sample. The theory of Lane and Greene [11] predicts that for a uniform distribution of donors in samples where the barrier width equals the well width that two peaks should be observed in PL, one associated with the CW donors and the other with CB donors. It is clear from Ref. 11 that the CW donor binding energy is appreciably greater than that of the EW or CB donor. Therefore, since the CW donor binding energy is greater than that of the EW or CB donor, it would be expected that the exciton would also have a greater binding energy to CW donors than to either EW or CB donors. This is clearly the case as shown in Fig. 2. Furthermore, Ref. 11 indicates that EW donors have a greater binding energy than CB donors which is also consistent with the results in Fig. 2.

A complementary set of data to that shown in Fig. 2 is shown in Figs. 3, 4, and 5 for nominal 250Å, 200Å, and 150Å MQWs, respectively for CW-, EW-, and CB-doping. The spectra in these figures are very similar to the analogous spectra in Fig. 2 with the energy shift taken into account due to the change in well size. There are some features that should be noted however in samples with narrower well widths. For the 200Å well shown in Fig. 4, the CW D^0, X transition appears to contain some contribution from donors nearer the edge of the well. As the wells get narrower, the effects of diffusion of donors away from the position at which they were intended may be magnified. The segregation of donors away from the intended doping location in the direction of growth by as much as 70Å has been reported [13,14]. This effect is enhanced in the 150Å wells in Fig. 5 where the CW-doped sample shows a well defined CW D^0, X transition and, in addition, shows a well defined but less intense EW D^0, X transition. The CB-doped

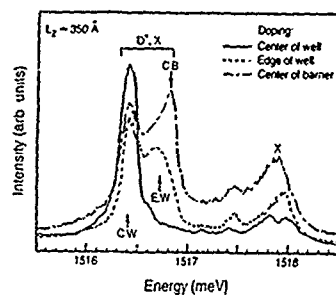


Fig. 2. RE emission spectra from CW-doped (solid curve), EW-doped (dashed curve) and CB-doped (dot dashed curve) for nominal 350Å MQWs. The CW D^0, X transitions have been aligned to account for well width variation. The energy scale on the abscissa relates to the solid curve. The EW-doped (CB-doped) spectra represented by the dashed (dot-dashed) curves have been displaced by 0.35 meV (0.30 meV) which must be subtracted to recover actual energies.

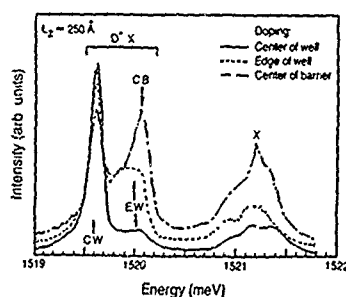


Fig. 3. RE emission spectra from CW-doped (solid curve), EW-doped (dashed curve), and CB-doped (dot dashed curve) for nominal 250Å MQWs. The CW D^0, X transitions have been aligned to account for well width variation. The energy scale on the abscissa relates to the solid curve. The EW-doped (CB-doped) spectra represented by the dashed (dot-dashed) curves have been displaced by 0.62 meV (0.51 meV) which must be subtracted to recover actual energies.

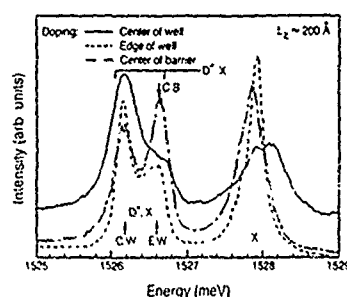


Fig. 4. RE emission spectra from CW-doped (solid curve), EW-doped (dashed curve), and CB-doped (dot dashed curve) for nominal 200Å MQWs. The CW D^0, X transitions have been aligned to account for well width variation. The energy scale on the abscissa relates to the solid curve. The EW-doped (CB-doped) spectra represented by the dashed (dot-dashed) curves have been displaced by 3.86 meV (3.57 meV) which must be subtracted to recover actual energies.

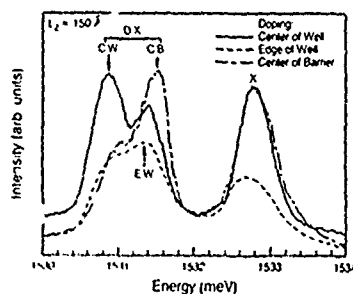


Fig. 5. RE emission spectra from center of the well doped (solid curve), edge of the well doped (dashed curve), and center of the barrier doped (dot-dashed curve), nominal 150Å MQWs. The CW D^0, X transitions have been aligned to account for well width variation. The energy scale on the abscissa relates to the solid curve. The EW-doped spectrum represented by the dashed curve has been displaced by 2.53 meV which must be subtracted to recover actual energies. The CB-doped spectrum represented by the dot-dashed curve has been displaced by 0.17 meV which must be added to recover actual energies.

sample shows a well defined CB D^0, X transition and also shows contributions from CW D^0, X transitions. The CW D^0, X transitions most likely result from the CW donors becoming neutralized since they have the greatest binding energy. The neutral donors can then trap excitons with the resulting CW D^0, X transition being observed. It is clear from Figs. 2-5 that the donor doping positions can be clearly tracked as the well size changes from 350Å to 150Å. As one proceeds in doping to still narrower wells, the transition lines broaden and resolution of the D^0, X transitions from the three doping positions in the sample decreases. Only one emission peak is resolved for each doping position. The accuracy in determining the energy of the transitions therefore, is not as precise as it is for the wider wells.

It is furthermore noted that both the CW and CB D^0, X transitions are generally narrower than the EW D^0, X transitions. CW D^0, X complexes have emission lines as narrow as 0.15 meV full width at half maximum. This would be expected from the shape of the curve shown in Fig. 1 of Ref. 11 which describes the binding energy of the donor as a function of the donor position in the sample. It is seen that the slope of the curve flattens for both doping positions (CW and CB) producing a degenerate contribution for a range of these positions. This would predict narrower emission lines. On the contrary, EW donors would produce an energy spread given the same range of positions with respect to the interface thereby producing a broader emission line.

The temperature dependence of PL emission from EW-doped MQW sample of nominal 350Å, 250Å, and 200Å well widths is shown in Fig. 6. This is a single sample containing the three different well widths. The CW D^0, X transitions have greater intensity than the EW D^0, X transitions as was observed in Figs. 2-4. In Fig. 6a the relative intensities of the labelled transitions at 2K are shown. At 10K shown in Fig. 6b and 30K in Fig. 6c, it is noted that intensities of the various D^0, X transitions fall off much faster with temperature than the intensities of the HHFE transitions. In Fig. 6c, the D^0, X transition intensities have almost vanished while the HHFE transitions are still plainly visible, demonstrating that the D^0, X transitions are properly identified.

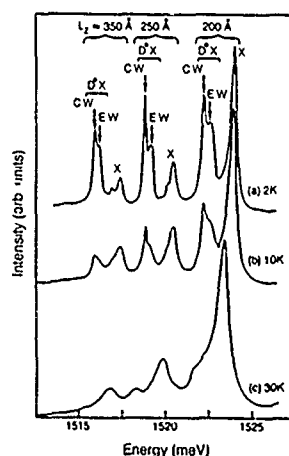


Fig. 6. Temperature dependent PL excited with an Ar^+ ion laser from three edge MQWs samples of nominal 350Å, 250Å, and 200Å well widths. Curves a, b and c are for temperatures of 2K, 10K, and 30K respectively.

In Fig. 7, we display the variations of the binding energies of excitons to neutral donors located at the center and edges of the wells and at the center of the barriers as a function of the HHFE emission energy and the well size. The well sizes are calculated from the measured HHFE emission energies using the theoretical results of Greene et al [8].

Included in Fig. 7 (indicated by \oplus) is also the CW D^0X transition energy for a single QW of 300Å as reported by Nomura et al [3]. The solid lines drawn through the experimental points are merely aids to the eye and are not the result of any calculation. It is clear from Fig. 7 that the

binding energies of D^0X complexes increase as the well size is reduced for all three doping situations. However, for well width of about 100Å, they tend to reach their respective maximum values and then decrease as the well widths are further reduced. The binding energies of HHFE [8] and of isolated donors [9] are known to increase as the well size is reduced and reach their respective maximum values in basic quantum well systems at values less than about 50Å. It is not clear why the binding energy of excitons to neutral donors reaches a maximum at well sizes of about 100Å. We observe that our measured values of the binding energies of excitons to neutral donors located at the center of the wells as a function of well size are consistently larger than those calculated by Kleinman [12]. For well sizes larger than about 230Å, calculated [12] values of the binding energies are smaller than the experimentally determined value (1.2 meV) for bulk GaAs, a result contrary to physical expectations. However, for the range of the well sizes studied, our values of the binding energies are always larger than the bulk value. The calculations include an assumption of potential barriers which predicts a monotonic increase in the binding energy of excitons to neutral donors as the well size is reduced. This disagrees with the observations summarized in Fig. 7 which do not monotonically increase as the well size decreases. The binding energy of excitons in quantum wells does not monotonically increase as the well size decreases, nor does the binding energy of donors increase monotonically as the well size decreases. It is not surprising, therefore, that the binding energy of excitons to donors in quantum wells does not monotonically increase as the well size decreases.

Two different samples (A and B) are used to study HHFE (D^0X), HHFE (A^0X), and D^0h transitions. Sample A was doped with $3 \times 10^{10} \text{ cm}^{-2}$ Be's in the center of each barrier; sample B was delta doped at the center of the well width $3 \times 10^9 \text{ cm}^{-2}$ Be's. The PL spectra from sample A are shown in Fig. 8. No clear evidence of an HHFE A^0X peak is observed; however, structure in the HHFE D^0X region is observed with peak separations suggesting monolayer variations in well size. Three HHFE D^0X peaks are resolved at 1.5186 eV, 1.5184 eV, and 1.5182 eV. PLE spectra for this sample are shown in Fig. 9. The solid curve is obtained with the detector holding on the 1.5186 eV HHFE (D^0X) transition; the dashed curve is obtained with the detector holding on the 1.5184 eV HHFE (D^0X) transition; and the dot-dashed curve is obtained with the detector holding on the 1.5182 eV HHFE (D^0X) transition. The lowest energy transition shown for each curve in Fig. 9 is due to the specific HHFE transition which is coupled to the particular HHFE (D^0X) transition being monitored. These HHFE transitions occur at 1.5193, 1.5190, and 1.5188 eV, respectively, and their peak separations correspond to monolayer variations in well size (which was not resolved in the PL spectra of Fig. 8). Two rather broad peaks are seen on the high energy side of the HHFE structure. The higher

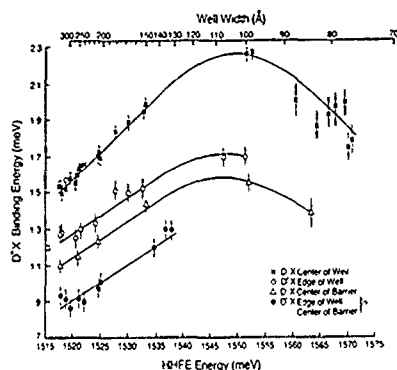


Fig. 7. Binding energies of excitons to neutral donors located at CW (indicated by x's), EW (o's), and CB (Δ 's) as a function of the HHFE energy. A scale containing the calculated well sizes corresponding to HHFE energies is included at the top of the figure. Included are data (indicated by •'s) speculated to be the D^+,X binding energy of excitons to EW and/or CB ionized donors as a function of HHFE energy. The binding energy of D^+,X in bulk GaAs is indicated by \square and the 300Å well data of Nomura et al [3] by \oplus .

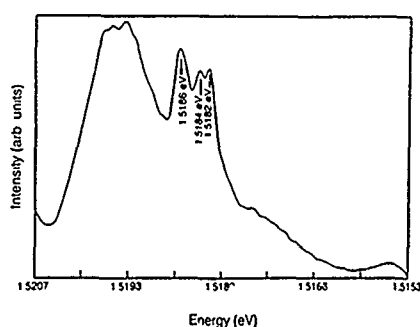


Fig. 8. PL spectra from sample A, resonantly pumped at the LHFE transition at 1.5222 eV.

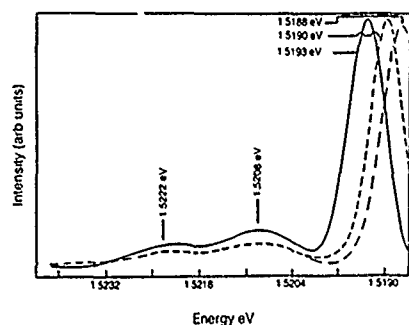


Fig. 9. PLE spectra from sample A. Detector hold positions monitor HHFE D^0,X emission at 1.5186 eV (solid), 1.5184 eV (dashed), and 1.5182 eV dot-dashed).

energy peak at 1.5222 eV is due to the LHFE, and the peak at 1.5208 is attributed to the LHFE (D^0,X). This gives a value of 1.4 meV for the binding energy of the LHFE to the neutral donor. The LHFE is 2.9 meV higher in energy than the HHFE which is in close agreement with the calculated value of 2.8 meV. The peak at 1.5208 eV is clearly extrinsic since there are no intrinsic transitions in the energy region between the LHFE and the HHFE transitions.

The PL spectra for sample B were obtained using an excitation energy of 1.5230 eV and are displayed in Fig. 10. The solid curve shows the

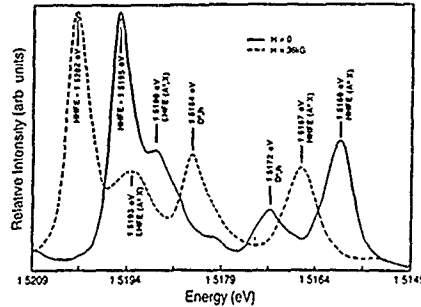


Fig. 10. PL spectra showing the optical transitions from a 350Å MQW in zero magnetic field (solid line), and in a field of 35 KG (dashed line).

spectra in zero magnetic field and the dashed curve in a magnetic field of 36 kG which was applied perpendicular to the growth direction. At zero magnetic field the transition at 1.5160 eV is ascribed to the collapse of a heavy-hole exciton bound to a neutral acceptor HHFE (A^0, X). This transition has been observed previously [13]. The transition at 1.5172 eV is tentatively assigned to the recombination of a free heavy-hole with a neutral donor located at the well center (D^0, h). The small peak at 1.5180 eV is due to the collapse of a heavy-hole exciton bound to a neutral donor at the well center [14]. It is suggested that the transition at 1.5190 eV is due to the radiative collapse of a light-hole exciton bound to a neutral acceptor. And finally, the transition at 1.5195 eV is the HHFE transition.

The behavior of these transitions in the presence of a magnetic field is consistent with the foregoing assignments. For example, the shift in energy with magnetic field of the HHFE (A^0, X) transition at 36 kG is observed to be 0.7 meV, which is about the same as that of the HHFE. This is not unexpected since the binding energy of the heavy-hole exciton to a neutral acceptor is rather small (3.5 meV). Similarly, the diamagnetic shift of the LHFE (A^0, X) transition at 36 kG is found to be 0.3 meV, which is about the same as that of the light-hole free exciton [15]. This and the fact that this peak is located at about 3.3 meV below the LHFE transition suggests that this transition is associated with a light-hole exciton bound to a neutral acceptor. It should be noted that this complex is a rather complicated system. The wave function of the neutral acceptor consists of a linear combination of light- and heavy-hole wave functions. Similarly the wave function of the light-hole exciton consists of a somewhat different linear combination of light- and heavy-hole wave functions with emphasis on the light-hole character. When a light-hole exciton combines with a neutral acceptor to form a LHFE (A^0, X) complex, the two holes are indistinguishable and the complex is associated predominately with the light-hole subband. A similar situation exists for the HHFE (A^0, X) complex. Calculations of the dissociation energies for such complexes represents a rather formidable task.

As mentioned earlier, the transition at 1.5172 eV observed at zero magnetic field is tentatively assigned to the recombination of a free heavy-hole with a neutral donor located at the well center (D^0, h). This assignment is based on two criteria. First, the observed transition energy agrees very well with the calculated value obtained from the binding energy of a donor located at the well center [16] and the heavy-hole subband energy in a 350Å well. Second, the observed diamagnetic shift of this

transition at 36 kG is 1.2 meV, which is considerably larger than that observed for excitonic transitions.

The diamagnetic shift observed for the (D^0, X) transition can be separated into two contributions - one associated with the heavy-hole and one with the neutral donor. Recently Greene and Bajaj [17] calculated the diamagnetic shift of a neutral donor in a quantum well as a function of well size and magnetic field applied perpendicular to the growth direction. For a 350Å well at 36 kG they find a diamagnetic shift of 0.70 meV. The difference between the observed diamagnetic shift for (D^0, h) and the calculated shift of the donor level is 0.50 meV and is due to the Landau level energy of the free hole; i.e., $e\hbar B/2m^*c$, where m^* is the average hole mass in the z and y directions (with z the growth direction). The measured value of m^* thus obtained is $0.41 \pm .05 m_0$. The value of m^* defined as $m^* = (m_y m_z)^{1/2}$, using values obtained from cyclotron resonance measurements [18] of $m_z = 0.45 m_0$ and $m_y = 0.51 m_0$, is found to be $0.48 m_0$. The value of the heavy-hole mass used in the calculations of Chang and Schulman [19] is $0.45 m_0$, while the value obtained from the $k \cdot p$ theory of Lawaetz [20] is $0.35 m_0$. Bangert and Landwehr's Hartree approach [21] predicts a heavy-hole mass of $0.61 m_0$, while Broido and Sham calculate [22] a value of $0.43 m_0$. All of these heavy-hole mass values are based on bulk GaAs parameters. The value we obtain in this experiment for the effective mass of a heavy-hole in a 350Å quantum well agrees quite well with the values used by other investigators.

Conclusions

We have determined the binding energy of excitons to neutral donors in quantum wells and have observed changes when the dopant was located in the center of the well, at the edge of the well, or in the center of the barrier. This was investigated as a function of well size from 75-350Å, which yielded an increase in binding energy as the well size was reduced to about 100Å, after which the binding energy decreased. This behavior was compared to existing theoretical descriptions. The increase in binding energy as well size is reduced is due to the increase in donor as well as exciton binding energy and consequently that of D^0, X . Below 100Å the binding energy decreases. An additional transition is tentatively identified as due to excitons bound to EW and/or CB ionized donors (D^+, X); these transitions are marked by •'s in Fig. 9. These transitions occur in undoped samples where the donors are expected to be ionized. CW D^+, X may be eliminated as a candidate since it is expected to fall on the low energy side of CW D^0, X . Likewise, EW and CB D^0, X have been shown to have greater binding energies. We may thus speculate on the remaining possibilities. A peak CW D^0, X transition is observed in undoped samples as shown in Fig. 1, indicating that some CW donors are photo-neutralized at this pump power. The EW and CB donors are less likely to be neutralized than the CW donors due to their respective reduced binding energies. Therefore, this transition is consistent with the ionized donor bound exciton transitions D^+, X associated with donors at the center of the barrier and/or edge of the well. Temperature dependence measurements of these transitions confirm

that they result from bound excitons. There, of course, remain other complexes which are possible alternatives.

The neutral donor-bound light-hole free-exciton has been observed in a nominally 350Å wide $\text{Al}_{1-x}\text{Ga}_x\text{As}$ -GaAs MQW structure using PLE. The LHFE D^0, X transition occurs in the energy region between the LHFE and HHFE transitions, where no other intrinsic transitions exist. The binding energies of the LHFE to the neutral donor are consistent with expected values based on the known HHFE D^0, X values. In the same sample HHFE D^0, X transitions were also observed.

The recombination of a free heavy-hole with a neutral donor located at the center of the well has been confirmed. Light-hole excitons bound to neutral acceptors have been identified based on energy considerations and diamagnetic shifts.

References

1. B.V. Shanabrook and J. Comas, *Surf. Sci.*, **142**, 504 (1984).
2. D.C. Reynolds, K.K. Bajaj, C.W. Litton, P.W. Yu, W.T. Masselink, R. Fischer, and H. Morkoc, *Phys. Rev. B* **29**, 7038 (1984).
3. Y. Nomura, K. Shinozaki, and M. Ishii, *J. Appl. Phys.* **58**, 1864 (1985).
4. X. Liu, A. Petrou, B.D. McCombe, J. Ralston and G. Wicks, *Phys. Rev. B* **38**, 8522 (1988).
5. S. Charbonneau, T. Steiner, M.L.W. Thewalt, Emils S. Koteles, J.Y. Chi, and B. Elman, *Phys. Rev. B* **38**, 3583 (1988).
6. J.R. Haynes, *Phys. Rev. Lett.* **4**, 361 (1960).
7. J.J. Hopfield, *Proc. Int. Conf. Phys. Semicond.*, 7th, Paris (M. Hulin, ed.) pp. 729-735, Donod, Paris (1964).
8. R.L. Greene, K.K. Bajaj, and D.E. Phelps, *Phys. Rev. B* **29**, 1807 (1984).
9. R.L. Greene, and K.K. Bajaj, *Solid State Comm.* **53**, 1103 (1985).
10. R.L. Greene, and K.K. Bajaj, *Phys. Rev. B* **34**, 951 (1986).
11. P. Lane, and R.L. Greene, *Phys. Rev. B* **33**, 5871 (1986).
12. D.A. Kleinman, *Phys. Rev. B* **28**, 871 (1983).
13. R.C. Miller, A.C. Gossard, W.T. Tsang and O. Munteanu, *Solid State Commun.* **43**, 519 (1982).
14. D.C. Reynolds, K.K. Bajaj, C.E. Leak, C.E. Stutz, R.L. Jones, K.R. Evans, P.W. Yu, and W.M. Theis, *Phys. Rev. B* (in press).
15. K.K. Bajaj, D.C. Reynolds, C.W. Litton, R.L. Greene, P.W. Yu, C.K. Peng and H. Morkoc, "Gallium Arsenide and Related Compounds", *Inst. Phys. Conf. Series No. 83*, editor W.T. Londley. (Institute of Physics, Bristol, 1987), p. 325.
16. R.L. Greene and K.K. Bajaj, *Solid State Commun.* **45**, 825 (1983).
17. R.L. Greene and K.K. Bajaj, *Phys. Rev. B* **37**, 4604 (1988).
18. M.S. Skolnick, A.K. Jain, R.A. Stradling, J.C. Ousset, and S. Askenasy, *J. Phys. C* **9**, 2809 (1976).
19. Y.C. Chang and J.M. Schulman, *Appl. Phys. Lett.* **43**, 536 (1983).
20. P. Lawaetz, *Phys. Rev. B* **4**, 3460 (1971).
21. E. Bangert and G. Landwehr, *Superlattices and Microstructures* **1**, 363 (1985).
22. D.A. Broido and L.J. Sham, *Phys. Rev. B* **31**, (1985).

DECAY MEASUREMENTS OF FREE AND BOUND EXCITON RECOMBINATION IN DOPED GaAs/GaAlAs QUANTUM WELLS

J.P. BERGMAN*, P.O. HOLTZ*, B. MONEMAR*, M. SUNDARAM**, J.L. MERZ**
AND A.C. GOSSARD**.

*Department of Physics and Measurement Technology
Linköping University, S-581 83 Linköping, SWEDEN

**Department of Electrical and Computer Engineering,
and Materials Department
University of California, Santa Barbara, California 93106, USA.

ABSTRACT

In this study we present photoluminescence decay measurements of free exciton (FE) and bound exciton (BE) recombination in doped GaAs/AlGaAs quantum wells (QW). It is found that the FE decay time is reduced in the doped QW's compared to similar undoped samples. The low temperature decay time of the BE is slightly longer than for the FE, with BE decay times from 300 to 600 ps for well widths of 50 to 150 Å, respectively. It is also found that the observed decay of the BE is strongly influenced by the decay time of the FE. This is especially observed in the similarity of the temperature dependence for the FE and BE decay time.

INTRODUCTION

The radiative kinetics of the free exciton (FE) in GaAs/GaAlAs MQW has in recent years been studied both experimentally [1-7] and theoretically [8,9] by a number of authors. It is concluded that potential fluctuations due to variations in the QW width play an important role in the capture and kinetic behaviour of the exciton [4-7]. Some controversy exist, however, whether the observed FE recombination originates from laterally localized excitons or from free excitons with mobility in areas larger than the exciton Bohr radius [4,7]. A linear decrease of the exciton decay time with decreasing QW width is predicted by theoretical calculations [3]. This predicted linear dependence has recently been experimentally verified [1,3]. FE decay times in high quality samples in the range of 300 to 500 ps were reported for QW widths close to 5.0 nm. Furthermore, the FE decay times are found to rapidly increase with increasing temperature. This is explained in terms of a thermal redistribution of the exciton momentum, decreasing the number of excitons obeying the $K=0$ conservation rule for radiative recombination [3]. The same effect is observed in bulk GaAs [10], although the effect is

more pronounced in the QW due to less competing non radiative recombination channels.

The defect energy levels in QW's are mainly observed through the recombination of an exciton bound to the neutral defect. The pioneer study of the BE associated with the acceptor level caused by Be doping was performed by Miller et.al. [11]. After this initial work, a number of reports have followed showing that e.g. the binding energy of this acceptor BE (ABE) is in the range of 4 to 6 meV, for QW widths appropriate in this study. To our knowledge no studies have been performed on the kinetics of these acceptor BE's (ABE), and its influence on the kinetics of the FE. In this paper we present the first measurements of the FE and BE decay in doped multi QW's.

EXPERIMENTAL PROCEDURE

The samples used in this study are grown by molecular beam epitaxy (MBE) and consist of 50 periods of GaAs/AlGaAs QW's. Each period has a GaAs well with a width L_z varying in the range 50 to 150 Å, followed by a 150 Å wide $\text{Al}_{0.7}\text{Ga}_{0.3}\text{As}$ barrier. For all samples, the QW width L_z is determined from the energy position of the FE transition. The different layers were grown at non-interrupted growth conditions. The GaAs wells are Be doped in the central 20% of the wells to a concentration of 10^{17} cm^{-3} .

The measurements were performed using a standard photoluminescence (PL) setup, where the samples were excited by 5 ps pulses from a dye laser synchronously pumped by a modelocked argon laser. The excitation energy could be selected both below and above the bandgap of AlGaAs, but no difference in either the spectral or the time decay measurements was observed for these two cases. The luminescence was detected with a microchannel plate photomultiplier (with S1 response). The decay signal was measured with a time correlated photon counting technique. The time resolution of the system is about 200 ps.

EXPERIMENTAL RESULTS

The PL spectra for all samples with $L_z > 70 \text{ Å}$ are dominated by two well resolved peaks corresponding to the recombination of the FE and of the BE associated with the Be-acceptor, located in the center of the well. Other emissions, such as the BE and free to bound (FB) recombination in bulk GaAs and FB recombination and two hole transitions in the QW, are also observed but at about two order of magnitude lower intensity. At QW widths $L_z < 70 \text{ Å}$, the FE is the dominating recombination in PL and the BE is only present as a shoulder on the low energy side of this peak.

The measured decay times of the FE and BE recombinations are shown in Fig.1 for samples with different well width. The linear relationship between the decay time of the FE and the QW width, which have been

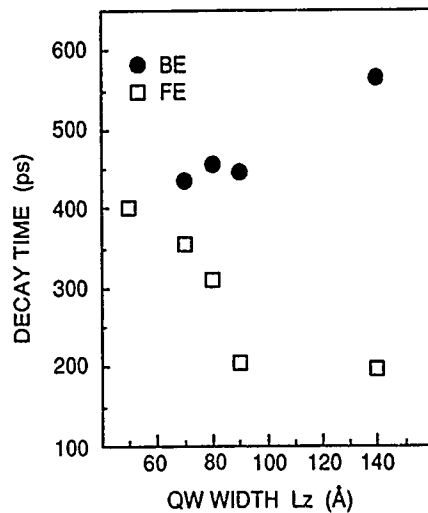


Fig.1 Measured decay time of the FE and BE, as a function of QW width, L_z .

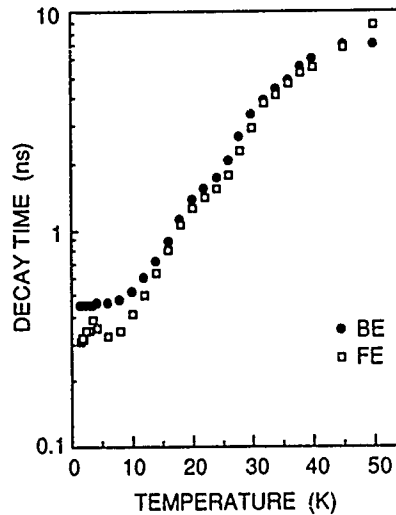


Fig.2 Measured decay time of the FE and BE recombination, as a function of temperature. $L_z=90$ Å.

reported earlier [1,3], is not observed in our measurements. One possible explanation for this can be that the observed FE decay time is influenced by recombination mechanisms other than the radiative transition, induced by the relatively high doping in our samples. Such recombinations can be either non radiative, reducing the total PL efficiency in the QW, or due to capture of FE states into BE's. A comparison between two similar QW's, both 90 Å wide but one intentionally undoped and the other doped ($p=10^{17}$ cm $^{-3}$), shows a decrease of the FE decay time at low temperatures from 450 ps to 250 ps in the doped QW, supporting the assumption of parallel recombination channels in the doped samples. The observed decrease of the FE decay time with increased well width, is assumed to be a consequence of the wider dopant layer in the wider wells.

The decay time of the BE is slightly longer than the corresponding decay time of the FE, except for small QW widths. The values should in the latter case not be taken too literally, since the BE is not clearly resolved and the BE decay measurement is made in the high energy tail of the FE. For wider wells the BE decay time exhibits a weak but significant correlation with the QW width.

The temperature dependence of the FE and BE for the 90Å QW sample is shown in Fig.2. The increase of the decay time of the FE with temperature is expected as due to a change in the momentum distribution of the FE's, reducing the fraction of FE's involved in the radiative recombination [3]. The corresponding increase of the BE decay time is not possible to directly explain with the same model, since localized states should exhibit no distribution of its momentum. A similar temperature

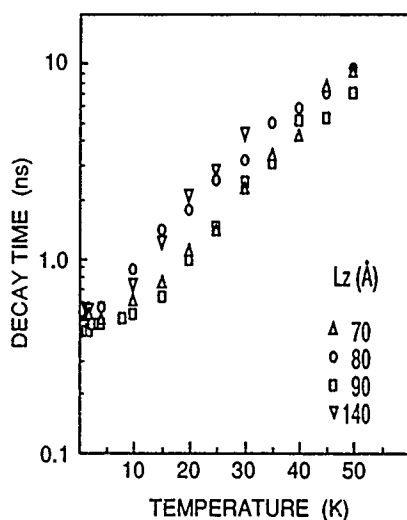


Fig.3 Measured BE decay time as a function of temperature, for samples with different QW width L_z .

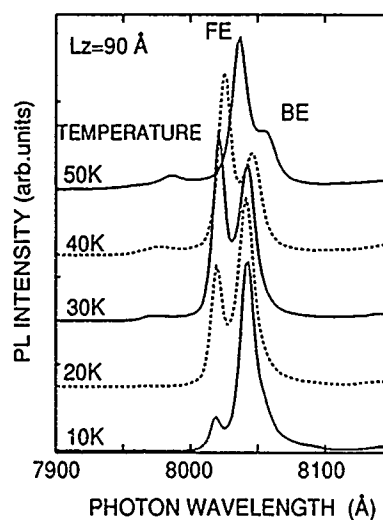


Fig.4 PL spectra at different temperatures for a sample with well width, $L_z=90$ Å.

dependence for the FE and BE is found in samples with different QW widths. Some differences are however observed, as can be seen in fig.3. Since no relation with QW width is observed, we conclude that these differences are due to sample dependent properties other than the QW width. It seems however reasonable to assume that the BE decay time is strongly influenced by the FE decay time, and a possible model for this will be discussed in the next chapter.

The PL spectra of the FE and BE recombination at different temperatures are shown in Fig.4, for a sample with QW width of 100Å . At low temperatures the BE emission dominates, but it is rapidly quenched as the temperature is increased. At the same time the FE recombination increases in intensity so the total luminescence intensity remains constant up to about 100 K. This indicates that no other recombination mechanisms other than the radiative transition from the FE and the BE, respectively, are important in this temperature range.

DISCUSSION

It is reasonable to assume that the BE's are created by trapping of FE's to the acceptor. The observed BE decay curve is then influenced by the FE population at a certain time after the excitation, i.e. the decay time of the FE. To obtain the radiative decay time of the BE, it is necessary to deconvolute the observed BE decay curve with the observed decay of the FE according to

$$I_{BE}(t) = \int_0^t e^{-t'W_{FE}} e^{-(t-t')W_{BE}} dt' \quad (1)$$

where W_{FE} and W_{BE} are the transition rates for the FE and BE, defined as the inverse of the respective decay times. The results of the deconvolution gives a reduction of the BE radiative decay time compared to the observed value, as shown in Fig.1. We obtain a decrease from 458 to 325 ps, and from 566 to 529 ps for samples with $L_z=80$ and 140 Å, respectively.

To our knowledge no theoretical calculations have been performed on the ABE in QW's, predicting its transition probability. Calculations have however been done for donor bound excitons (DBE) [8] and a comparison with our results seems appropriate, since the quantization should influence the ABE and the DBE in a similar way. In contrast to our experimental results these calculations predicted a decrease of the oscillator strength, corresponding to an increased decay time, for the DBE confined in a QW, compared to bulk GaAs. The decay time was also predicted to be almost independent of QW width for narrow wells ($L_z < 145 \text{ Å}$), but for wider wells a width dependence must be included to be able to continuously approach the value 0.75 ns, which is reported for the DBE in bulk GaAs [12]. The corresponding value for the ABE in GaAs is 1.0 ns [12]. It is obvious that detailed theoretical calculations of the transition probabilities will be of great importance in further studies.

The increase of the FE decay time with temperature was recently reported, and was explained as due to a thermal redistribution of the FE momentum, decreasing the number of excitons obeying the $K=0$ conservation rule for radiative recombination. If only excitons within the spectral width $\Delta(T)$ contribute to the radiative transition, we can write the decay time of the two dimensional FE as [3]

$$\tau(T) = \tau(0) \frac{\Delta(T)}{1 - e^{-\Delta(T)/kT}} \quad (2)$$

where $\tau(0)$ is the low temperature decay time, and $\Delta(T)$ is assumed to have a form of $\Delta(T)=a+bT$ [13]. It should be noticed that we observe a faster increase of the FE decay time than expected from Eq.1. This model for the FE is not valid for a localized state, and can not be used to explain the temperature dependence of the BE recombination.

From the experimental results it is however obvious that the BE decay is strongly influenced by the decay of the FE, particularly at elevated temperatures. One possible way to explain the observed temperature behaviour is to assume that the trapping probability of a FE into a BE, W_{τ} , has a strong temperature dependence, to ensure that the radiative transition is the dominating transition for the FE's. If this is not the case, the trapping rate will dominate over the radiative recombination rate for the FE, and an increasing number of FE's will

recombine via the BE when the temperature is increased. An increase of the BE PL intensity and a decrease of the observed FE decay time should then be expected, which is in contrast to our experimental results.

We have in this paper presented decay measurements on FE and BE recombinations in doped QW's. We have found that the FE decay time is reduced in the doped QW's compared to similar undoped samples. The decay of the BE is, at all temperatures, strongly influenced by the decay of the FE. From deconvolution of the decay curve at low temperatures, we have obtained values in the range of 300 to 600 ps, for the radiative decay time of the BE. To explain the observed temperature dependence of the PL intensity and decay time, we suggest that the trapping rate of a FE into a BE has a strong temperature dependence. However, the details of the FE and BE kinetics is at the moment not fully understood, and further studies are in progress.

ACKNOWLEDGEMENTS

This work was partially supported by the NSF Science and Technology Center for Quantized Electronic Structures (QUEST).

REFERENCES

- 1 E.O. Göbel, H. Jung, J. Kuhl and K. Ploog, *Phys. Rev. Lett.* **51**, 1588 (1983).
- 2 J. Christen, D. Bimberg, A. Steckenborn, G. Weimann and W. Schlapp, *Superlattices and Microstructures* **2**, 251 (1986).
- 3 J. Feldmann, G. Peter, E.O. Göbel, P. Dawson, K. Moore, C. Foxon and R.J. Elliott, *Phys. Rev. Lett.* **59**, 2337 (1987).
- 4 H. Stolz, D. Schwarz, W. von der Osten and G. Weimann, *Superlattices and Microstructures* **6**, 271 (1989).
- 5 G. Bastard, C. Delalande, M.H. Meynadier, P.M. Frijlink and M. Voos, *Phys. Rev. B* **29**, 7042 (1984).
- 6 T. Amand, F. Lefhaye, S. Valloggia, F. Voillot, M. Brousseau and A. Regreny, *Superlattices and Microstructures* **6**, 323 (1989).
- 7 B. Deveaud, T.C. Damen, J. Shah, and C.W. Tu, *Appl. Phys. Lett.* **51**, 828 (1987).
- 8 J.M. Rorison and D.C. Herbert, *Superlattices and Microstruct.* **1**, 423 (1985).
- 9 T. Takagahara and E. Hanamura, *Phys. Rev. Lett.* **56**, 2533 (1986).
- 10 G.W. 't Hooft, W.A.J.A. van der Poel, L.W. Molenkamp, and C.T. Foxon, *Phys. Rev. B* **35**, 8281 (1987).
- 11 R.C. Miller, A.C. Gossard, W.T. Tsang, and O. Munteanu, *Phys. Rev. B* **25**, 3871 (1984).
- 12 E. Finkman, M.D. Sturge, and R. Bhat, *J. Luminescence* **35**, 235 (1986).
- 13 L. Schultheis, A. Honold, J. Kuhl, K. Köhler, and C.W. Tu, *Phys. Rev. B* **34**, 9027 (1986).

EFFECTS OF CONFINEMENT ON THE OPTICAL PROPERTIES OF A SHALLOW ACCEPTOR AND ITS BOUND EXCITON IN NARROW GaAs/AlGaAs QUANTUM WELLS

P.O. HOLTZ^{*,**}, M. SUNDARAM^{**}, G.C. RUNE^{*}, B. MONEMAR^{*}, J.L. MERZ^{**}, AND A.C. GOSSARD^{**}

^{*} Department of Physics and Measurement Technology, Linköping University, S-581 83 Linköping, Sweden

^{**} Department of Electrical and Computer Engineering and Materials Department, University of California at Santa Barbara, Santa Barbara, CA 93106

ABSTRACT

Transitions from the 1s ground state to 2s excited states of the Be-acceptor confined in GaAs/AlGaAs quantum wells (QWs) have been observed via two independent spectroscopic techniques: Two-hole transitions of the bound exciton (BE) measured in selective photoluminescence and Resonant Raman Scattering. The dependence of the 1s - 2s transition energy on the QW thickness ($50 \text{ \AA} < L_z < 140 \text{ \AA}$) has been studied for the case of acceptors in the center of the QW. The experimentally determined 1s - 2s transition energies have then been added to recently calculated binding energies for the 2s excited state in order to obtain the total binding energies for the acceptor at different confinements. The derived binding energies are finally compared with theoretical predictions. The same kind of measurements have been performed for a QW with a given thickness, but in which the position of the acceptor has been varied from the center to the edge of the QW.

The dependencies of the binding energies of the exciton bound to the investigated acceptor on the QW thickness and the position of the acceptor in the QW have also been studied. For the case of varying QW thickness, an almost linear relationship between the binding energies of the BE and the acceptor binding the exciton is found. This fact implies that a correspondence to Haynes' rule in bulk material could be applied to these QW systems, but in this case for the same acceptor at different binding energies due to the effect of varying confinement.

INTRODUCTION

The knowledge of the electronic properties of impurities confined in QWs is much more limited than the corresponding level for bulk defects. The situation is expected to be more complicated in a QW due to the reduced symmetry from T_d for a point defect in bulk to D_{2d} for an acceptor at the center of a QW and to C_{2v} for an off-center acceptor [1-3]. Electronic properties such as the binding energy of the ground state and the excited states of acceptors confined in quantum wells (QWs)

have been predicted in several theoretical papers. In the original calculation by G. Bastard [4] hydrogenic impurity potentials and infinite barrier heights were used, which resulted in continuously increasing binding energies with decreasing QW width. When more realistic finite heights for the barriers were used in the calculations by W.T. Masselink *et al.* [1, 2], it was shown that the binding energy goes through a maximum at a non-zero QW width. The acceptor energies were calculated for varying positions in the QW and thicknesses of the QW. A. Pasquarello *et al.* [3] have recently presented a variational calculation, which is particularly suited for the binding energies of the excited states of the acceptor, with the acceptor position and the QW thickness as the variable parameters.

The aim of this study has been to experimentally investigate the above described dependencies of the acceptor binding energies. We have used selective photoluminescence (SPL) in order to observe the two-hole-transitions (THTs) of the acceptor bound exciton (BE) in the QWs. By this technique it has been possible to observe the transitions from the ground state to excited states of the Be-acceptor confined in GaAs/Al_{0.3}Ga_{0.7}As QWs. We have also observed the same acceptor transitions in Resonant Raman Scattering (RRS). The derived dependencies of the acceptor energy on the QW width and the acceptor position in the QW are finally compared with theoretical predictions by W.T. Masselink *et al.* [1, 2] and A. Pasquarello *et al.* [3].

EXPERIMENT

The samples used in this study were grown by MBE in a Varian Gen II system on semi-insulating GaAs substrates. Six samples with identical structure except for the QW width ($50 < L_z < 140 \text{ \AA}$) were used in the first part of this study. These samples were multiple QW (MQW) structures with 50 periods of alternating layers of GaAs wells and 150 \AA wide Al_{0.30}Ga_{0.70}As barriers. The QWs were δ -doped with Be in the central 20% of the wells at a level of $1 \times 10^{17} \text{ cm}^{-3}$. In the second part of this study, five δ -doped QWs with the same width ($L_z = 96 \text{ \AA}$), but with different positions for the dopant layer within the QW, were investigated. The dopant layers consisted of typically three Be-doped monolayers centered at $z_0 = 0, 13, 27, 37$, and 45 \AA in the QW.

A cw Kr-ion laser pumping a dye-laser with LD 700 was used as the excitation source for the SPL and RRS experiments. The dye-laser could be continuously tuned for PL excitation (PLE) measurements. The luminescence signal was detected with a cooled GaAs photomultiplier tube. All measurements presented in this study were performed at 1.7 K.

RESULTS

The PL spectra measured with excitation above the AlGaAs bandgap

shows only the free exciton (FE) and the BE for the samples investigated. However, if instead selective excitation close to the FE states is used, several new features will appear in the SPL spectra below the excitons. This fact is illustrated in Fig. 1 for the case of a center-doped 94 Å wide QW at different excitation energies. The SPL spectra measured with the excitation resonant with either the heavy hole (hh) or the light hole (lh) state of the FE as observed in the PLE spectrum are very similar (Fig. 1). The strongest peak originates from the free-to-bound (FB) transition due to the recombination between free electrons and holes bound to the confined Be-acceptor. The position of the FB band yields a rough estimate of the acceptor binding energy ($E_A \approx 34$ meV). The second peak

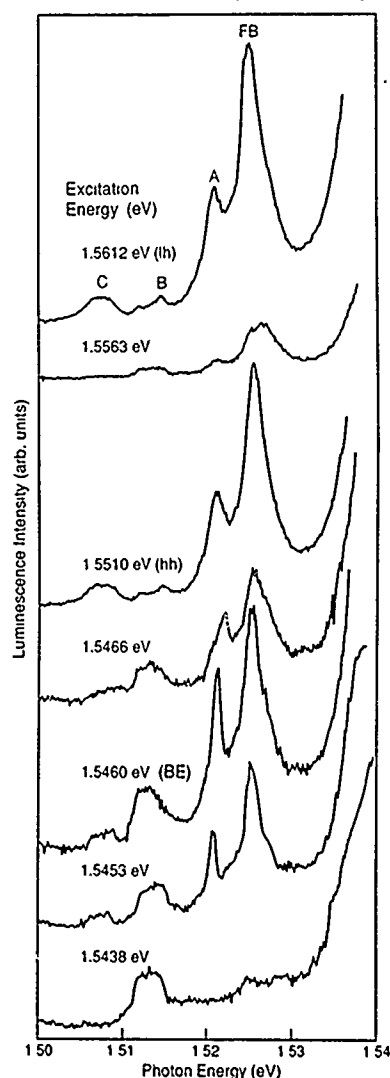
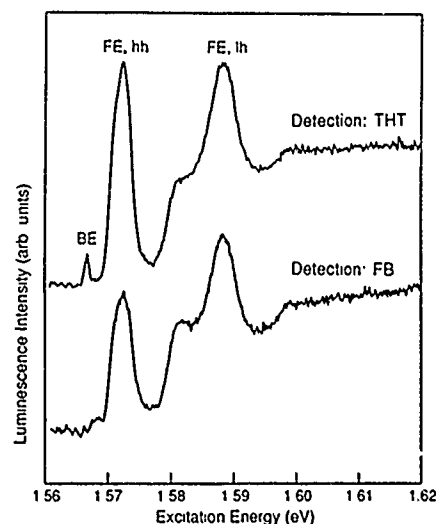


Fig. 1 A synopsis of SPL spectra for a center doped 94 Å wide QW with the excitation in the range 1.544 - 1.561 eV. Several new features appear in these spectra compared with the case of above bandgap excitation: The FB transition and the THT (or RRS) peaks (denoted A and B in the figure). When the excitation is resonant with the FE states (the hh- or lh-state) as observed in PLE or the BE as observed in PL, these features are strikingly enhanced.

Fig. 2 PLE spectra of a center doped 71 Å wide QW, when a) the THT peak and b) the FB peak is detected.



(denoted A in Fig. 1) is interpreted as the first THT. The Be-acceptor is left in the excited $2s(\Gamma_6)$ state instead of in the $1s(\Gamma_6)$ ground state as is the case for the principal BE recombination. The separation between the THT peak and the principal BE is $E(A^{1s} - 2s) = 24.6$ meV. The intensity of the THT peak is strikingly reduced, when the excitation is shifted off the resonant position (as shown in the second spectrum from top in Fig. 1) with a $\Delta_{FWHM} \approx 2$ meV corresponding to the halfwidth of the $F\bar{E}$ states. A third peak (denoted B in Fig. 1) is tentatively interpreted as the second THT corresponding to the acceptor transition $1s(\Gamma_6) - 2s(\Gamma_7)$ [5].

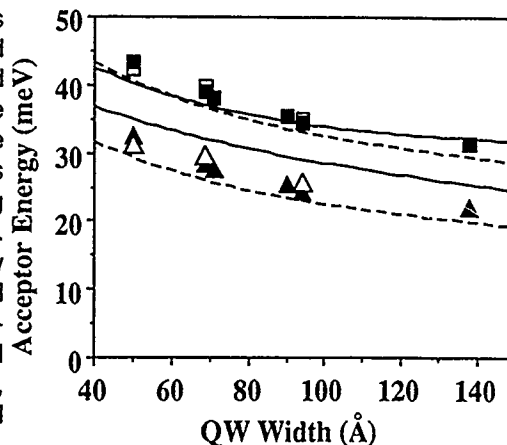
When the excitation is shifted further towards lower energies below the FE hh-state, the same peaks are still observed, but at a lower intensity level. However, one important difference should be noted: The main component of peak A is shifting with the excitation energy in such a way that the energy separation between this component and the excitation energy, 24.8 meV, is constant, which is a characteristic behavior for RRS. The transition energy for the RRS is thus very close to the observed THT energy. Further, the intensity of the RRS component has a maximum, when the excitation is resonant with the BE. The RRS line is thus assumed to originate from the same acceptor transition as observed for the THTs.

A common way to verify the interpretation of the THT peaks in bulk is to look for the enhancement of the BE in the PLE spectrum, when the THT peak is detected. Such an enhancement is expected, since the THT can be considered as a generalized form of BE recombination. The problem to perform the same procedure in QWs is that the PLE spectra are normally totally dominated by the intrinsic FE states. This fact is illustrated in the lower PLE spectrum in Fig. 2, in which the FB band in a 71 Å wide QW is detected. However, if instead the THT peak for the same QW is detected, a novel weak feature appears about 4 meV below the FE , i.e. with the same separation as between the FE and the BE in PL. The observation of the BE in the PLE spectrum, when the THT is detected, thus supports our interpretation of peak A (Fig. 1) as the THT peak.

A synopsis of the THT and RRS results for the center-doped QWs with thicknesses in the range 50 - 138 Å is shown in Fig. 3. The solid and dashed lines correspond to the theoretical predictions by A. Pasquarello *et al.* [3] and W.T. Masselink *et al.* [1, 2], respectively, for the Be-acceptor transition $1s(\Gamma_6) - 2s(\Gamma_6)$, where the same central-cell correction as in bulk (1 meV) has been used. We have also added the theoretically predicted binding energies of the $2s(\Gamma_6)$ states to the experimental values on the $1s(\Gamma_6) - 2s(\Gamma_6)$ acceptor energies in order to estimate the total acceptor binding energies (the upper data points in Fig. 3). The derived binding energies are also compared with two different theoretical predictions [1-3] in the same figure.

The binding energies of the acceptor as well as its BE are dependent on the QW width. The BE binding energies, determined from the separation between the FE and the BE, are plotted in Fig. 4, but instead of plotting the QW width on the x-axis, we have chosen to plot the acceptor

Fig. 3 The triangles correspond to the experimental 1s-2s transition energies derived from THT (filled triangles) and RRS (unfilled triangles). The squares correspond to the experimental 1s-2s energies added to the predicted binding energies of the 2s states (ref. 3). The two sets of lines show the theoretically predicted acceptor energies for the 1s-2s transition and the total binding energy, respectively, given in ref 1 (solid line) and ref 3 (dashed line).



binding energy (estimated from Fig. 3) on this axis. The point at the lowest energy corresponds to bulk GaAs and the BE binding energies for the points at highest energy are derived from PLE measurements, since the BE is barely resolved in PL for the narrow QWs [6]. An approximately linear relationship is found between the binding energies of the BE and the acceptor binding the exciton from Fig. 4. Such a linear relationship, usually referred to as Haynes' rule [7], is found to be valid for many impurities in bulk semiconductors, but notably not for acceptors in GaAs. However, we are in this case dealing with the same acceptor, whose binding energy is varied by different degree of confinement.

The dependence of the binding energy of the acceptor on its position in the QW has been investigated via THT and RRS measurements on δ -doped QWs in a similar way as described above. The obtained results are summarized in Fig. 5. The transition energies corresponding to the $1s(\Gamma_6) - 2s(\Gamma_6)$ transitions derived from both THT and RRS are shown together with the theoretical prediction for the same transitions [3]. In order to provide the total acceptor binding energy, the calculated $2s(\Gamma_6)$ binding energy [3] is added to the experimental $1s(\Gamma_6) - 2s(\Gamma_6)$ transition energy in the same way as described above. The derived binding energies

Fig. 4 The dependence of the BE binding energies on the Be acceptor binding energy (deduced from the results in Fig. 3). The point at lowest energy corresponds to bulk GaAs.

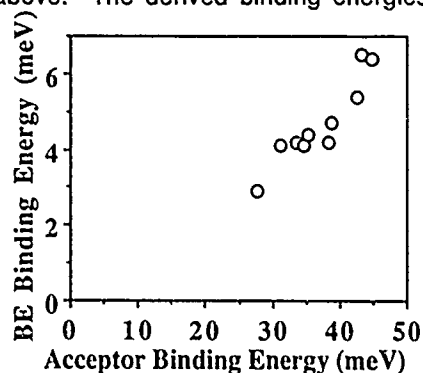
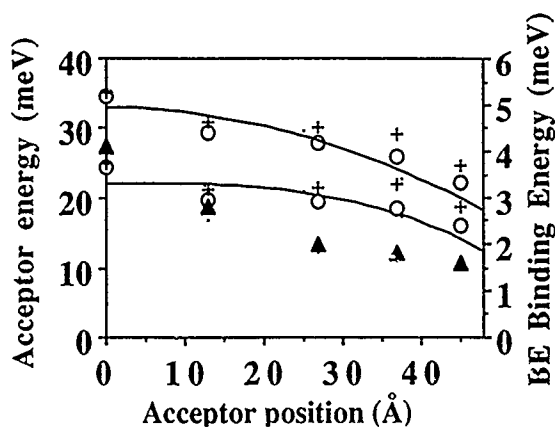


Fig. 5 The dependence of the 1s-2s transition energy and the total binding energy of the acceptor on its position in a 96 Å QW estimated from THT (crosses) and RRS (circles). The upper set of data points are obtained by adding the calculated 2s binding energies to the experimental 1s-2s energies. The solid lines are the theoretically predicted energies [3]. The triangles correspond to the BE binding energies (righthand scale).



are shown in Fig. 5 together with the theoretically predicted energies by Masselink *et al.* [1, 2]. Furthermore, the dependence of the BE binding energy on the the acceptor position is shown in the same figure. In this case there is no simple relationship between the binding energies of the BE and the acceptor.

ACKNOWLEDGEMENTS

This work was partially supported by National Science Foundation (NSF) Science and Technology Center for Quantized Electronic Structures (QUEST).

REFERENCES

1. W.T. Masselink, Y.-C. Chang, and H. Morkoç, Phys. Rev. B32, 5190 (1985)
2. W.T. Masselink, Y.-C. Chang, H. Morkoç, D.C. Reynolds, C.W. Litton, K.K. Bajaj, and P.W. Yu, Solid State Electr. 29, 205 (1986)
3. A. Pasquarello, L.C. Andreani, and R. Buczko, to be published, Phys. Rev. B
4. G. Bastard, Phys. Rev. B24, 4714 (1982)
5. P.O. Holtz, M. Sundaram, R. Simes, J.L. Merz, A.C. Gossard, and J.H. English, Phys. Rev. B39, 13293 (1989)
6. P.O. Holtz, M. Sundaram, J.L. Merz, and A.C. Gossard, to be published, Phys. Rev. B
7. J.R. Haynes, Phys. Rev. Lett. 4, 361 (1960)

INTRINSIC LUMINESCENCE OF GaAs/AlGaAs HETEROJUNCTIONS IN A TRANSVERSE ELECTRIC FIELD

Q.X. ZHAO, J.P. BERGMAN, P.O. HOLTZ, B. MONEMAR, and C. HALLIN
Department of Physics and Measurement Technology, Linköping
University, S-581 83 Linköping, Sweden

M. SUNDARAM, J. L. MERZ and A.C. GOSSARD
Department of Electrical and Computer Engineering and Materials
Department, University of California, Santa Barbara, California 93106,
USA

ABSTRACT

Radiative recombination of the two dimensional electron gas (2DEG) in a modulation doped GaAs/AlGaAs heterojunction (the so called H-band luminescence) has been studied under transverse electric field perturbation (i.e. perpendicular to the layers) in special structures prepared by molecular beam epitaxy. Both positive and negative gate voltages have been applied to the GaAs/AlGaAs interface, and shifts of the H-band energy position depending on the gate voltage are induced by the corresponding changes in the notch potential and the potential across the GaAs layer. It is demonstrated that a transverse electric field allows a simple way to modify the width and shape of the potential, so that detailed spectroscopy can be done on the recombination of carriers localized in a interface potential.

INTRODUCTION

During the last decade there has been a considerable interest in the electronic properties of two-dimensional (2D) systems [1]. With the recent developments of epitaxial growth techniques a good quality 2D interface between GaAs and AlGaAs can be achieved. A large number of experimental studies have been carried out on GaAs/AlGaAs heterostructures using various electrical techniques, while our knowledge about the optical properties is much more limited. Photoluminescence (PL) studies of the so called H-band, which is due to radiative recombination involving carriers confined in the GaAs/AlGaAs interface potential, have been presented for samples grown by different techniques, such as liquid phase epitaxy (LPE) [2], molecular beam epitaxy (MBE) [3,4,5,6], and metalorganic chemical vapor deposition (MOCVD) [7]. To our knowledge, no detailed work has previously been published on the electronic properties of carriers localized at the GaAs/AlGaAs hetero-interface, where electrical and optical methods have been combined.

In this presentation, we report the first results on the optical properties of the PL H-band with an electric field as a perturbation. The experimental results show that the energy position of the H-band depends on the external applied gate voltage. For positive and negative gate voltages the energy position of the H-band shifts in opposite directions, which has to be explained by the change of the potential at and close to the interface caused by a electric field. The dependence of the H-band on the excitation power and the temperature has also been studied for different gate voltages. The results of this work are consistent with a model of the H-band as due to the radiative recombination of the 2DEG confined at the hetero-interface. The decay time of the H-band has also been measured and is found to increase with decreasing energy of the H-band.

EXPERIMENTAL

The samples used for this study were grown by the MBE method. Semi-insulating undoped GaAs was used as substrate, and a 10-period GaAs-AlAs (2.0nm) superlattice was grown directly on the substrate. The modulation doped hetero-junction studied was part of a structure consisting of a 50nm thick undoped GaAs layer, an undoped 8nm thick $\text{Al}_{0.35}\text{Ga}_{0.65}\text{As}$ spacer layer, a Si-doped n-type 76nm thick $\text{Al}_{0.35}\text{Ga}_{0.65}\text{As}$ layer, and finally an 18 nm thick undoped GaAs cap layer. The samples were cut in a 2x3 mm rectangular shape. A semi-transparent metal gate consisting of 1nm Cr and 5nm Au was evaporated on the top GaAs cap layer. To apply the electric field perpendicular to the hetero-interface between the GaAs and the $\text{Al}_{0.35}\text{Ga}_{0.65}\text{As}$ layer, thin electrical wires were contacted on both the gate metal and the back side of the GaAs substrate. In order to get a good bonding contact, 40 nm Au was used at the contact point on top of the semitransparent metal gate. The sample was mounted on the sample holder, and put into a liquid-He cryostat. The sample temperature could be continuously regulated down to 2.0 K. To eliminate heating effects of the electric current, the electric field was pulsed, typically at 100Hz with a 10 percent duty cycle. The laser beam was also pulsed synchronously with the electrical bias pulse, by using an acousto-optical modulator (Intra Action AOM-125). In this way current heating effects can be eliminated by adjusting the length of the pulses. For the decay time measurements a cavity dumped dye laser synchronously pumped with a mode-locked Ar⁺ laser together with a photon counting system was employed.

RESULTS AND DISCUSSION

A schematic band diagram for the region near the GaAs/AlGaAs interface without external bias is shown in Fig. 1(a). A notch at the interface between the GaAs and AlGaAs is formed, in which the electrons

can be confined to form the 2DEG. Fig. 1(b) and Fig. 1(c) show schematically the cases, where a positive and a negative gate voltage has been applied, respectively. A positive gate voltage will deepen the notch, while a negative gate voltage, on the other hand, will make the notch more shallow. In this way the notch potential and its confined electron levels can be changed by the gate voltage.

A typical PL spectrum for the heterojunction structure without external bias is shown in Fig. 2. Two bands can be seen. The low energy band is due to bulk GaAs luminescence, while the high energy band, the so called H-band [2], originates from the 2DEG recombination with 3D-holes.

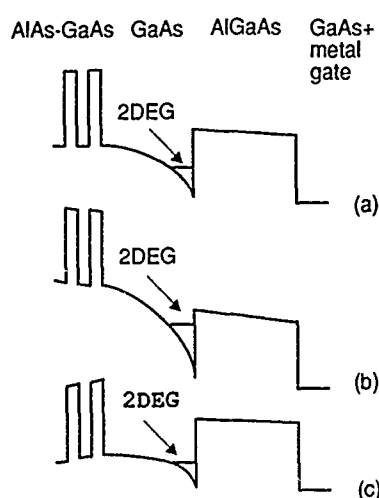


Fig.1 Schematic band diagram near the GaAs/AlGaAs interface for a) zero, b) positive and c) negative gate voltage.

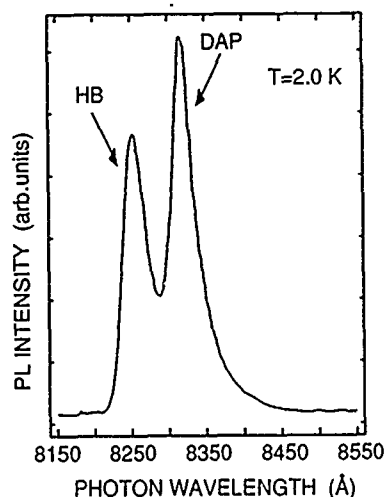


Fig.2 PL spectrum for a GaAs/AlGaAs heterojunction measured at 2.0K, with the 5145Å line from a cw Ar⁺ laser as the excitation source.

Fig. 3 shows the dependence of the H-band peak position on the applied gate voltage. Since the electric field drop across the studied interface is difficult to estimate exactly in this case, due to the presence of a semiinsulating substrate [8], the indicated fields in the figure refer to the total applied electric fields. During these electric field dependence measurements the excitation power is kept constant. Fig. 3 indicates that the shift of the H-band luminescence has a threshold for both signs of the bias polarity, and the energy position of the H-band is constant for a certain range of gate voltages close to zero.

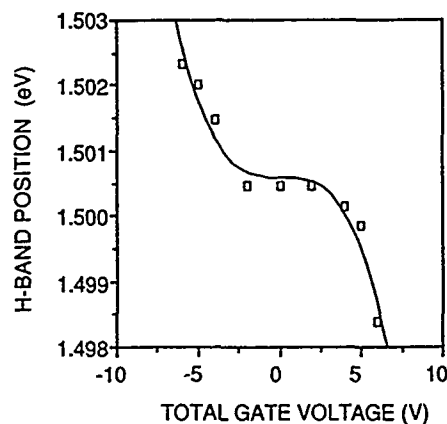


Fig.3 The electric field dependence of the H-band energy position. The values indicated in the figure denoted the total voltage across the structure.

The observed H-band shift with an applied electric field can be understood by considering the change of the interface potential between GaAs and AlGaAs with an external electric field. Since Schottky contacts have been used on both sides, and there are several layers between the two external contacts and the studied interface, most of voltage drop occurs at the Schottky barrier and inside each layer [8]. Thus for small applied voltages, the interface potential will not change very much. Consequently the confined 2D electron sublevels remain almost unchanged, and the H-band shows no significant shift with gate voltage. This is in agreement with the observed threshold in the electric field dependence of the H-band (Fig. 3). But at a certain total field, the potential of the studied interface changes significantly, and a shift of the H-band can be observed.

The H-band has been suggested to be due to the recombination between the confined 2D electrons at the interface and the 3D holes (holes in the valence band or holes bound to acceptors) [2-6]. Since the active 3D holes are mainly accumulated near the opposite interface of the active GaAs layer, their energy position is almost unchanged with the applied electric field. The confined 2D electron levels at the interface, on the other hand, will change as the external electric field changes the potential at the interface. When a positive gate voltage is applied, the interface potential notch becomes deeper, causing the H-band to shift towards lower energy. In the case of a negative gate voltage the situation is opposite, the notch becomes more shallow to give a shift of the H-band towards higher photon energies (Fig. 3).

One interesting phenomenon is that at fairly high negative gate voltages, the H-band recombination is quenched, and instead another emission (denoted F in Fig. 4) appears. For a positive gate voltage, on the other hand, only a shift and a quenching of the H-band have been seen, no new recombination appears. This is shown in Fig. 4. Obviously the two polarities of electric field have different effects on the different recombination channels in the active GaAs layer. One possible explanation is that the shallow notch potential obtained with negative

bias (Fig. 1(c)) will introduce a flat band region in the active GaAs layer, thus making the 3D recombination (including free excitons) more dominant. A positive gate voltage, on the other hand, will give rise to a deeper notch potential and accordingly an increasing band bending across the active GaAs layer, thus reducing the 3D recombination. An alternative explanation is that for the case of a shallow notch potential (negative gate bias) the higher 2D sublevel can easily be populated, thus making the recombination involving a higher 2D sublevel becomes possible. For a positive gate voltage, on the other hand, the notch potential becomes deeper, the higher 2D sublevel is accordingly not populated, and no recombination involving the higher 2D subband is observed. From our measurements it is at the present stage difficult to exclude any of the possibilities. For a detailed explanation of the F line more experiments are needed. Further work in order to definitely determine the origin of the F line is in progress.

Fig. 5 shows the measured decay times of the H-band without gate bias. The decay times are found to increase with decreasing energy of the H-band from few ns up to 100 ns. This fact is consistent with the proposed model [6] for the H-band recombination, in which it is assumed that the spatial separation between the electrons and holes increases

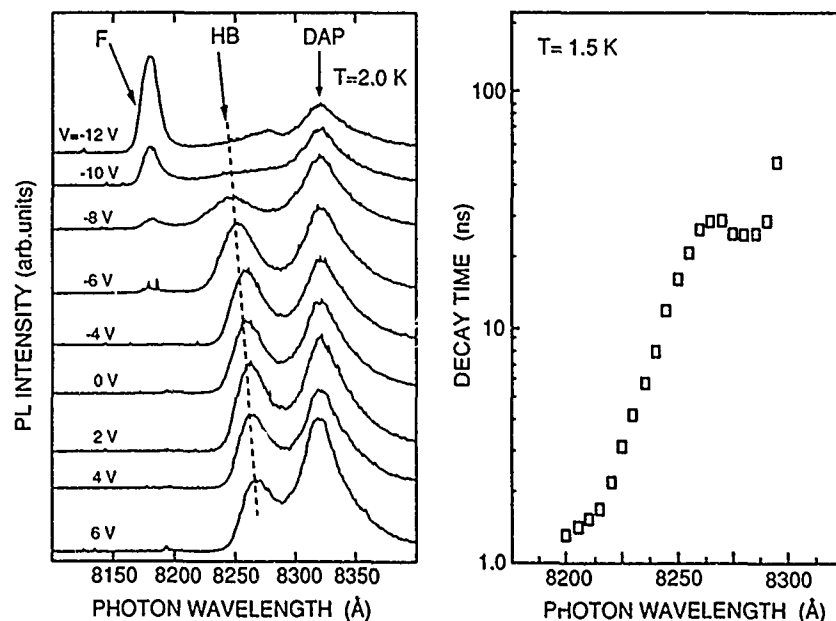


Fig.4 PL spectra for different gate voltages measured at 2.0 K, with pulsed excitation (5145Å) from an Ar⁺ laser.

Fig.5 The spectral dependence of the H-band decay time, measured with constant laser excitation intensity at 1.5 K.

with decreasing H-band energy. The decay time is expected to increase with increasing electron-hole separation, and the observed trend in decay times is in agreement with this model.

CONCLUSIONS

In summary we have studied the recombination between the confined 2D electron gas and 3D holes under an external electric field perturbation. Positive and negative gate voltages give rise to shifts of the H-band in opposite directions. This can be explained in terms of a change of the interface potential with the electric field. The decay time of the H-band are found to depend on the detection energy of the H-band. PL studies with external electric field as a perturbation proves that the H-band is directly related to the recombination of the 2DEG at the interface. It is demonstrated that in a special structure as used in this work, an external bias can be used to modify the shape of the notch potential at the interface, and thereby change the conditions for the 2D and 3D recombination in the active GaAs layer. This opens up the possibility of a more detailed optical spectroscopy of recombination at interfaces than hitherto has been presented.

ACKNOWLEDGEMENT

This work was partially supported by the NSF Science and Technology Center for Quantized Electronic Structures (QUEST).

REFERENCES

1. T. Ando, A. B. Fowler and F. Stern, *Reviews of Modern Physics* **54** (1982).
2. Y. R. Yuan, K. Mohammed, M.A.A. Pudensi and J. L. Merz, *Appl. Phys. Lett.* **45** 739 (1984).
3. A. M. Vasil'ev, P.S. Kop'ev, V.P. Kochereshko, N.N. Ledentsov, B. Ya. Mel'tser, I.N. Ural'tsev, V.M. Ustinov, and D.R. Yakovlev, *Sov. Phys. Semicond.* **20** 220 (1986).
4. W. Ossau, E. Bangert, and G. Weimann, *Solid State Communications* **64** 711 (1987).
5. I.V. Kukushkin, K.V. Klitzing and K. Ploog, *Phys. Rev.* **B37** 8509 (1988).
6. Q.X. Zhao, J.P. Bergman, P.O. Holtz, B. Monemar, C. Hallin, M. Sundaram, J.L. Merz and A.C. Gossard, submitted to *Phys. Rev. B*.
7. W.M. Chen, Q.X. Zhao, M. Ahlström and B. Monemar, *Proc 19th Int Conf on the Physics of Semiconductors*, Ed. W. Zawadzki (Institute of Physics, Polish Academy of Sciences, Warsaw, 1988), p 279.
8. T. W. Hickmott, *Phys. Rev.* **B32** 6532 (1985).

DEFECT INDUCED LUMINESCENCE FROM MBE PREPARED Si/Si_{1-x}Ge_x SUPERLATTICES†

G.A. Northrop, S.S. Iyer, and D.J. Wolford
IBM Thomas J. Watson Research Center, Yorktown Heights, NY 10598.

ABSTRACT

We report the first definitive observation of photoluminescence from Si/Si_{1-x}Ge_x superlattice heterostructures. Excitons bound to a deep-level radiation damage center (I_1) are observed in a series of low Ge content ($x = 0.05$) unrelaxed structures. We also present preliminary results on photoluminescence from as-grown narrow period (Si₆Ge₄) superlattices.

INTRODUCTION

Epitaxially grown Si and Si_{1-x}Ge_x alloys have received substantial attention in recent years. While considerable success has been achieved in their use in purely electronic devices, such as heterojunction bipolar transistors [1], even the most basic exploration of their optical properties has met with significant difficulties, particularly in the case of optical emission. To date there have been no clearly documented reports of photoluminescence from epitaxially grown Si_{1-x}Ge_x superlattices. This is particularly troubling in the light of a recent work showing that both intrinsic and dopant bound exciton luminescence are readily observable in bulk grown Si_{1-x}Ge_x alloys over the entire alloy range [2]. The only definitive observations of photoluminescence in epitaxially grown single layer alloys have been for recombination at deep levels, particularly through their intentional introduction by radiation damage [3].

In addition to the question of whether epitaxially grown Si_{1-x}Ge_x has the luminescence efficiency equivalent to bulk material, is the possibility of radiative recombination rates being significantly enhanced by the careful growth of symmetrically strained narrow period Si_nGe_m superlattices. Much theoretical work has concentrated on the possibility that the combination of strain and zone folding in these structures might overcome the indirect gap nature of the two constituents and create optical transitions with large oscillator strengths [4-6]. One report of luminescence between 750 and 850 meV has received considerable attention as possibly being of this nature [7]. This paper will also present results on this system and address the difficulty of establishing the true nature of this type of luminescence.

I_1 IN DILUTE ALLOY SUPERLATTICES

We have attempted to observe photoluminescence from a number of epitaxially grown layers, including unrelaxed Si_{1-x}Ge_x alloy single layers and Si/Si_{1-x}Ge_x superlattices, and Si_nGe_m symmetrically strained superlattices. All failed to show any feature that could clearly be identified with the epitaxial layers. However, a method for inducing luminescence through the introduction of a deep level, I_1 , was quite successful for low Ge content single alloy layers [3]. In the present work we have extended this method to the case of Si/Si_{0.95}Ge_{0.05} superlattices, grown lattice matched to (001) silicon. Three samples, shown schematically in Fig. 1, were grown with three different periods to an approximate total thickness of 2200 Å, well below the critical thickness for relaxation. Introduction of I_1 , a well known radiation damage center in silicon [8,9], was achieved

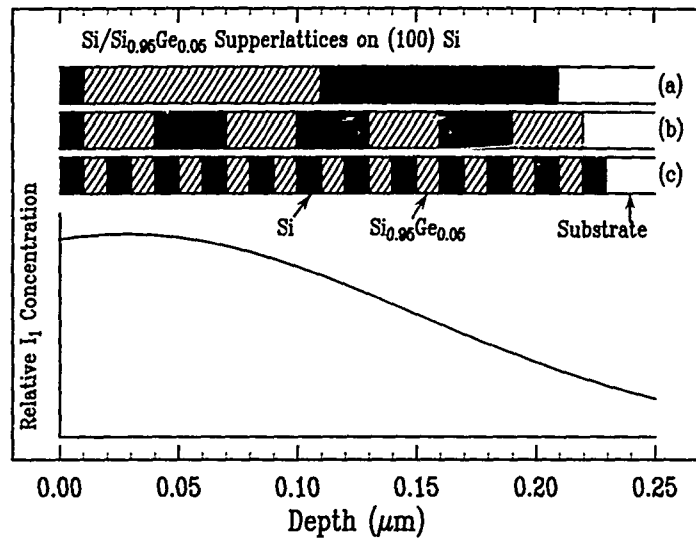


Figure 1. Schematic of three symmetric superlattices with periods of (a) 2000Å, (b) 600Å, (c) 200Å. All were grown below the critical thickness, thus the alloy layers are strained and the silicon layers are not. The plot below shows the expected Gaussian distribution of I₁ centers, based upon etch profiling of similar silicon samples.

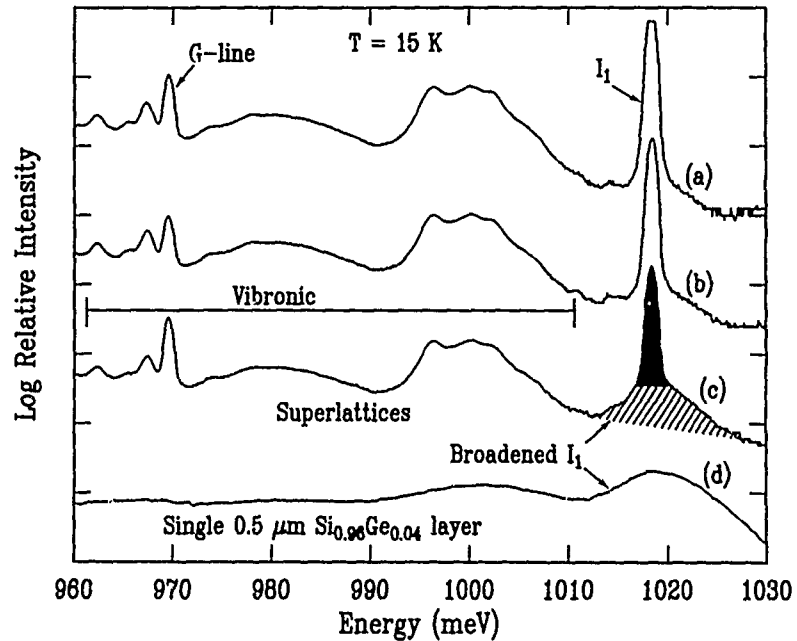


Figure 2. Spectra (a-c) for the respective samples in Figure 1, plotted on a logarithmic scale. The hatched area in (c) is no-phonon recombination at I₁ centers in the alloy layers, while the filled area is the same for the pure silicon layers. Spectrum (d) is for a similarly treated thick single alloy layer, and shows only the alloy component.

by ion implantation (Si^+ at 50 keV, $3 \times 10^{12} \text{ cm}^{-2}$), followed by annealing at 200°C for 30 minutes. Although the ion range under these conditions is only about 900 Å, the distribution of I_1 centers penetrates somewhat deeper, as shown in Fig. 1. This distribution was obtained from a fit to PL intensity data from a series of similarly prepared silicon samples which had been chemically etched to various depths. This depth profiling method will be described in detail below. From this profile it is estimated that better than 95% of the I_1 centers should be contained in the epitaxial layers.

The first 3 spectra (a-c) in Fig. 2 are the photoluminescence detected for the three superlattice samples in Fig. 1. The principal feature is the I_1 no-phonon line at 1018 meV. The G-line is the no-phonon line of another radiation damage center, similar to I_1 , but associated with carbon impurities [10]. With the exception of the G-line, all of additional structure in these spectra is the vibronic side band associated with emission of a phonon and a photon from the I_1 center. This data is plotted on a logarithmic intensity scale, in order to make the multi-component nature of the I_1 line observable. The I_1 no-phonon line appears as the superposition of a sharp line on a broadened background. This is interpreted as independent recombination at I_1 centers in the unperturbed Si layers (sharp component) and in or near the alloy layers (broad component). Support for this assertion is found in a comparison of the broad component to the broadened I_1 line observed for a single thick alloy layer, Fig 2(d). The observation of the broadened component, combined with the selective and controllable introduction of the luminescing defect, provides clear evidence that the luminescence is coming primarily from the superlattices.

Although the additional I_1 luminescence shows no dramatic influence from the superlattices, some information can be inferred from the data in Fig. 2. The sharp component of I_1 shows no shift, from either confinement in the narrowest layer, or from any unintended strain in the silicon layers. Unfortunately, I_1 is not highly sensitive to uniaxial strain [11]; the 0.2% strain in this case would only be expected to produce a 0.1 meV shift. Of greater significance is the fact that the overall luminescence intensity is not reduced as one proceeds to the narrower layers. This indicates that, at least for this relatively low strain system, non-radiative recombination at interfaces is not a significant problem, when compared to capture at these I_1 centers.

PHOTOLUMINESCENCE IN NARROW PERIOD SUPERLATTICES

Of all reports of the observation of photoluminescence in the Si/Ge materials system the one that has attracted the most attention is due to Abstreiter [7]. These authors reported luminescence for symmetrically strained (100) structures at energies between 750 and 900 meV. The strongest luminescence came for a symmetrically strained Si_xGe_x structure, which produced a 50 meV wide line at 840 meV. The only evidence given to support the assertion that this was a superlattice induced transition was that similarly prepared samples, including the strain symmetrizing alloy buffer layer, but with the superlattice omitted, did not exhibit this line.

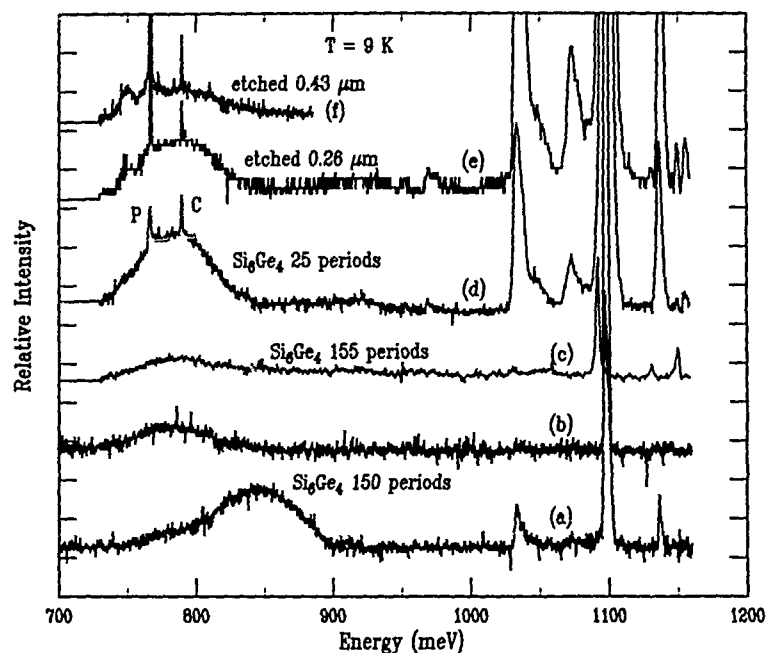


Figure 3. Comparison of weak luminescence from symmetrically strained (100) Si_6Ge_4 superlattices, all measured on the same system and plotted on the same scale. None have been corrected for the spectral response of the detector, which is near maximum at 800 meV, and zero at 700 meV. Spectra (a) and (b) are from two nominally identical samples grown by E. Kasper and H. Kibbel, each of which contains 150 periods. The 850 meV feature in (a) is identical to that reported by Abstreiter [7]. The samples for (c) and (d) were grown by the authors, and consisted of 155 and 25 periods, respectively. Spectra (e) and (f) show the material from (d) etched to the indicated depths. The two sharp lines (P and C) are point defects, probably in the substrate.

We report here photoluminescence from similar Si_6Ge_4 superlattices, and compare them with, among others, a sample from the same growth reported in reference [7] by Abstreiter et al. The spectrum obtained from that sample, along with one from one of 10 similarly grown samples, is shown in Fig. 3. Spectrum (a) reproduces the 840 meV feature reported in reference [7], however (b), a nominally similar sample grown on the same system, has only a weak feature at 780 meV. Only one sample showed the 840 meV feature. We also prepared two similar Si_6Ge_4 structures, one of 150 periods and one of 25 periods. The spectra for these, shown in Fig. 3 (c) and (d), show a feature at 780 meV which is quite similar to (b). These signals are quite weak, as indicated by comparison to the signals above 1000 meV, which come from the substrate. Even in (d) these band edge processes are only residual excitation of the substrate though the epitaxial layer, yet are quite strong compared to the deep emission. Although these results are intriguing, there is no evidence that the observed luminescence is intrinsic to the superlattice. The other explanation which must be eliminated is recombination at defects. The primary candidate in this case would be dislocations, which are known to produce substantial and varied luminescence spectra in pure silicon [12]. Several dislocation bands, commonly known as D_1 through D_6 , occur at energies between 0.8 and 1.0 eV. They have been associated with dislocations created in a wide variety of ways, including misfit dislocations intentionally introduced through poor epitaxial growth

conditions [13]. These superlattices are grown on relaxed buffer layers which by their nature contain high densities of dislocations. Although there has been no work demonstrating what this luminescence would look like in $\text{Si}_{1-x}\text{Ge}_x$, the low energy luminescence in Fig. 3 is highly suggestive of dislocations. Independent of this it remains to be demonstrated conclusively that these luminescence signals are coming from the superlattice rather than the buffer layer. The following results attempt to make that distinction.

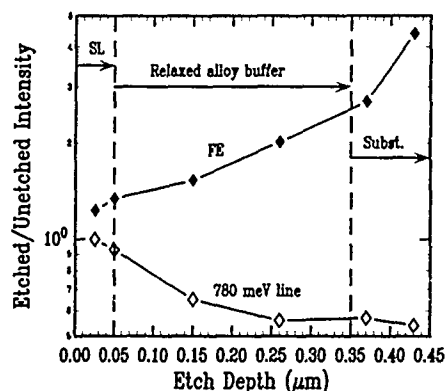


Figure 4. PL depth profile for the 780 meV line in the 25 period Si_6Ge_4 superlattice. The increase in the free exciton (FE) results from a greater transmission through the epi and subsequent increased excitation of the substrate.

most of its reduction upon removal of the buffer layer. We conclude that in this case the low energy luminescence is not due directly to the superlattice. This depth profiling technique is the type of experiment which can successfully attest to the origin of luminescence observed in this system.

CONCLUSIONS

We have provided the first conclusive evidence of photoluminescence from $\text{Si}/\text{Si}_{1-x}\text{Ge}_x$ superlattices by the controlled introduction of a strongly luminescing defect. These results demonstrate that the material can luminesce, and indicate that the interfaces do not significantly interfere with the emission process. This approach may be continued toward shorter periods, but its use with Ge contents higher than the 5% used here presumes that I_1 forms and luminesces in such material. To pursue higher Ge content samples, we intend to switch to growing on relaxed buffer layers and symmetrically strained structures, as the I_1 penetration depth exceeds the critical thickness for unrelaxed growth at around 10% Ge. If the I_1 center can be traced well into the SiGe alloy system, it may prove to be a useful probe of recombination, strain effects, and perhaps even the quantum structure of the narrow period superlattices.

We have applied stepwise chemical etching to the sample in Fig. 3(b) to try to understand the origin of the low energy photoluminescence. A number of adjacent samples from that growth were partially masked and etched to various depths in 70:1:25 $\text{HNO}_3\text{:HF:H}_2\text{O}$, and each etch depth measured by surface profiling. Spectra (e) and (f) in Fig. 3 show the luminescence from the etched position of two of these samples. In both cases the superlattice has been completely removed, yet a significant amount of the low energy luminescence remains. This is made more quantitative in Fig. 4, which plots the ratio of etched to unetched photoluminescence intensity for these samples. The 780 meV line is reduced only a small amount, upon removal of the superlattice, and sees

ACKNOWLEDGEMENTS

We gratefully acknowledge E. Kasper and H. Kibbel for access to of a number of their Si₆Ge₄ growths.

† Supported in part by the U.S. Office of Naval Research under contract N00014-85-C-0868.

REFERENCES

1. See for example G.L. Patton, S.S. Iyer, S.L. Delage, S. Tiwari, and J.M.C. Stork, IEEE Elect. Dev. Lett. 9, 165 (1988).
2. J. Weber and M.I. Alonso, Phys. Rev. B40, 5683 (1989).
3. G.A. Northrop, S.S. Iyer, D.J. Wolford, and S.L. Delage, Proceedings of the 19th International Conference on the Physics of Semiconductors (DHN Ltd., Warsaw 1988).
4. I. Morrison and M. Jaros, Phys. Rev. B37, 916 (1988).
5. S. Satpathy, R.M. Martin, and C.G. Van de Walle, Phys. Rev. B38, 13237 (1988).
6. S. Froyen, D.M. Wood, and A. Zunger, Phys. Rev. B37, 6893 (1988).
7. G. Abstreiter, K. Eberl, E. Friess, W. Wegscheider, and R. Zachai, J. Cryst. Growth 95, 431 (1989).
8. Gordon Davies, E.C. Lightowers, and Zofia E. Ciechanowska, J. Phys. C20, 191 (1987).
9. For a recent review of luminescing deep levels in silicon see: Gordon Davies, Physics Reports 176, 84 (1989).
10. G. Davies, A.S. Oates, R.C. Newman, R. Woolley, E.C. Lightowers, M.J. Binns, and J.G. Wilkes, J. Phys. C176, 841 (1986).
11. N. Burger, E. Irion, A. Teschner K. Thonke, and R. Sauer, Phys. Rev. B35, 3804 (1987).
12. R. Sauer, J. Weber, J. Stolz, E.R. Weber, K.-H. Küsters, and H. Alexander, Appl. Phys. A 36, 1 (1985).
13. B. Hamilton, E.C. Sidebotham, A.R. Peaker, E.H.C. Parker, G. Patel and T.E. Whall, Proceedings of the Second International Symposium on MBE Si, ed. by J.C. Bean and L.J. Schowalter, (Electrochemical Society), p. 355, (1988).

DEEP LEVELS IN SUPERLATTICES

JOHN D. DOW, SHANG YUAN REN, JUN SHEN, AND MIN-HSIUNG TSAI

Department of Physics, University of Notre Dame, Notre Dame, Indiana 46556 U.S.A.

ABSTRACT

The physics of deep levels in semiconductors is reviewed, with emphasis on the fact that all substitutional impurities produce deep levels – some of which may not lie within the fundamental band gap. The character of a dopant changes when one of the deep levels moves into or out of the fundamental gap in response to a perturbation such as pressure or change of host composition. For example, Si on a Ga site in GaAs is a shallow donor, but becomes a deep trap for $x > 0.3$ in $\text{Al}_x\text{Ga}_{1-x}\text{As}$. Such shallow-deep transitions can be induced in superlattices by changing the period-widths and quantum confinement. A good rule of thumb for deep levels in superlattices is that the energy levels with respect to vacuum are relatively insensitive (on a >0.1 eV scale) to superlattice period-widths, but that the band edges of the superlattices are sensitive to changes of period. Hence the deep level positions *relative to the band edges* are sensitive to the period-widths, and shallow-deep transitions can be induced by band-gap engineering the superlattice periods.

DOPING AND DEEP LEVELS IN BULK SEMICONDUCTORS

In recent years, the theory of doping has been revised from the old effective-mass theory [1] which explained the behavior of substitutional P in Si and Se on an As site (Se_{As}) in GaAs so well. In the effective-mass model, one simply assumed that an impurity such as Se substituting for As would have a singly-ionized stable ground state Se^+ were it not for the long-ranged screened Coulomb potential $-e^2/\epsilon r$ which binds the "extra" electron of Se in a hydrogenic shallow-donor orbital with radius $a \approx \frac{1}{2} \epsilon / m^* e^2$ much larger than a typical lattice constant. (Here m^* is the effective mass of the electron, ϵ is the dielectric constant of the host, and we have, for simplicity of presentation, overlooked the anisotropy of m^* .) Hydrogenic effective-mass theory has a significant weakness, however: it does not *predict* that a particular impurity such as Se in GaAs should be a shallow donor, but rather *assumes* that all atoms coming from Columns to the right of As (Column-V) in the Periodic Table are donors, when they substitute for As. Therefore effective-mass theory offers no criterion for determining when the extra electron of an impurity such as Se in GaAs should occupy a delocalized "shallow" hydrogenic orbital rather than a localized "deep" orbital, but rather assumes that all impurity levels are shallow.

Because there was no accepted theory of deep impurity levels in semiconductors several years ago, an unfortunate semantic problem has arisen in the literature: Shallow energy levels were defined as levels within ≈ 0.1 eV of a band edge and hence thermally ionizable with significant probability at room temperature. Deep levels were levels in *the fundamental band gap* by more than 0.1 eV. With the advent of the theory of deep levels [2], this energy definition has been supplanted by one that relies more on the localization of the state than its energy with respect to a nearby band edge: Shallow levels arise from the long-ranged Coulomb potential of the defect, and have extended, hydrogenic wavefunctions described by effective-mass theory. Deep levels originate from the central-cell potential of the defect. As a result, all levels that were shallow by the previous definition are shallow by the new one, except those few deep levels (by the new definition) that accidentally lie

within 0.1 eV of a band edge. All levels that were deep by the old definition are also deep by the new one, but now there are previously unanticipated deep levels that may lie in the bands or in the gap within 0.1 eV of a band edge. In this paper, we always adopt the following modern definitions: A shallow donor (acceptor) is a defect whose only energy levels in the fundamental band gap are shallow effective-mass theory levels. A deep trap is a defect that has one or more deep levels in the gap. An isoelectronic trap is a deep trap associated with an isoelectronic substitutional impurity. An isoelectronic resonant scattering center is an isoelectronic impurity whose deep levels lie energetically within the host bands and hence resonantly scatter carriers.

The character of a substitutional impurity, namely whether it is a shallow donor, a shallow acceptor, a deep trap, an isoelectronic trap, or an isoelectronic resonant scattering center is now known to be determined not solely by the position of an impurity in the Periodic Table relative to the host atom it replaces, but also by the strength of the central-cell defect potential and the energies of the "deep" levels produced by that potential relative to the band edges of the fundamental gap. Missing from the effective-mass model are the local bonds that are perturbed by the defect (and their bonding and antibonding states), and a symptom of this short-coming is the fact that the *s*-atomic energies of Se and As differ by ≈ 4 eV, indicating that the central-cell potential which models the difference must be larger yet. Clearly one cannot introduce a ≈ 4 eV attractive potential into a solid and have its *sole* effect be the formation of shallow donor states with binding energies of less than 10 meV; something must also happen to the electronic structure on the 4 eV scale. What happens is the formation of the hyperdeep and deep levels.

Fig. {1} [3,4] illustrates the case of N substituting for P in GaP, but (for simplicity) considers only a single directed orbital of each atom. The Ga and P atoms, when brought together into a molecule, form bonding and antibonding orbitals, with a bonding-antibonding splitting inversely proportional to the atomic energy difference $\epsilon_{\text{Ga}} - \epsilon_{\text{P}}$. In the solid, these molecular levels broaden into bands. When N substitutes for P, its energy ϵ_{N} is ≈ 7 eV lower than that of P; hence the energy denominator $\epsilon_{\text{Ga}} - \epsilon_{\text{N}}$ is ≈ 7 eV larger than $\epsilon_{\text{Ga}} - \epsilon_{\text{P}}$ and the impurity bonding-antibonding splitting is correspondingly smaller, causing the antibonding deep level to lie in the gap. The N-like impurity level is the unobserved hyperdeep level below the valence band maximum, whereas the deep level that lies in the gap has a wavefunction that is Ga-dangling-bond-like (almost independent of the N impurity). If the conduction band were somewhat broader in energy, the deep level would be covered up (as happens for N in GaAs).

N, being isoelectronic to P, simply produces a deep level in GaP that lies in the fundamental band gap, slightly below the conduction band edge. For Se in GaAs and P in Si, the bonding-antibonding physics is the same, but there is an extra electron (the "donor" electron) that will occupy this deep state if it is within the gap, or alternatively, if the deep level lies above the conduction band edge, the extra electron will fall to the conduction band edge, produce Se^+ or P^+ , and be bound to the ionized impurity in the hydrogenic effective-mass donor state.

For Se in GaAs (or for P in Si) the hyperdeep or bonding levels have *s*-like and *p*-like symmetry, are fully occupied by electrons, and lie well below the valence band maximum and are unobserved and normally uninteresting. The antibonding or deep levels of Se in GaAs are also *s*-like and *p*-like, and lie *above* the conduction band minimum. These deep levels in particular are missing from the effective-mass model, and *their energies with respect to the conduction band edge determine the doping character of the impurity.*

In the effective-mass model, the anion-substitutional dopants oxygen, sulfur, selenium, and tellurium should all be shallow donors in GaAs, GaP, and $\text{GaAs}_{1-x}\text{P}_x$. Yet oxygen has been observed to be a deep trap in GaP, and is thought to be deep in GaAs as well

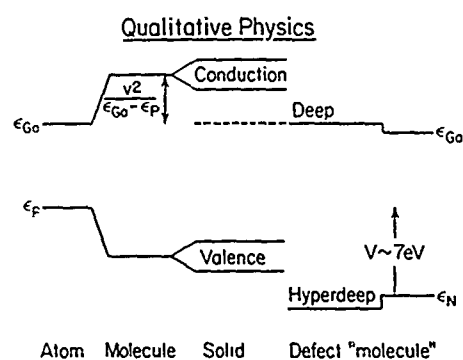


Fig. {1}. Schematic energy levels of Ga, P, molecular GaP, and solid GaP, together with the energy levels of a N anion-substitutional impurity "defect molecule" in GaP, after Refs. [3] and [4].

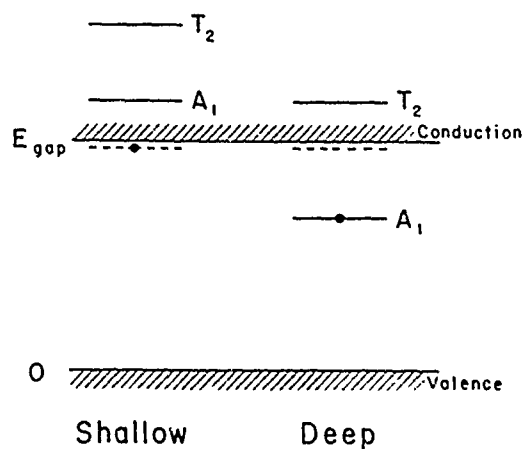


Fig. {2}. Energy level diagram illustrating the difference between shallow impurities such as S and Se in GaAs, which have their deep levels (of A_1 and T_2 symmetry for substitutional defects in zincblende hosts) outside the fundamental band gap and deep impurities such as O in GaAs or GaP, which have at least one deep level in the gap.

[5]. In contrast to oxygen, S and Se are shallow donors. The reason for the different doping character in GaAs of S and Se on the one hand and oxygen on the other is that the s-like (A_1 -symmetric) antibonding deep level of oxygen lies *below* the conduction band minimum, but the corresponding deep levels of S and Se lie *above* the conduction band edge. (See Fig. {2}.) As a result, the ground state of the neutral oxygen impurity in GaAs has the deep level in the gap occupied by one electron. This level lies about 0.4 eV [5] below the conduction band edge, and so is not thermally ionizable – and does not contribute to the semiconductivity of GaAs. Moreover, the neutral oxygen impurity can trap another electron of opposite spin, and so rather than donating an electron and making GaAs n-type, it can remove one and make the host semi-insulating.

In contrast to oxygen, S and Se are shallow donor impurities that make GaAs n-type, because their A_1 -symmetric antibonding deep levels lie *above* the conduction band minimum. As a result, their extra electrons are autoionized, fall to the conduction band edge, and are then bound (at zero temperature) in the hydrogenic shallow donor levels produced by the ionized S^+ or Se^+ . These shallow levels lie within 0.1 eV of the conduction band edge and so can be thermally ionized rather easily at room temperatures. Since the A_1 deep level lies well above the Fermi energy and the Coulombic potential of S^+ or Se^+ is screened by the donor electron, each of these impurities is incapable of binding a second electron [6]. Thus the shallow donor impurities S and Se are thermally ionized and contribute to the n-type semiconductivity of GaAs. In contrast, the deep impurity oxygen traps electrons and detracts from conductivity.

A central notion of the modern theory of doping is that *the character of a dopant is determined by the relative positions of its deep levels and the band edges (and Fermi energy)*.

Fig. {3} shows how the doping character of an impurity such as Se_{As} in GaAs could be changed from a shallow donor to a deep trap to a false valence shallow acceptor, provided one could perturb the band edges of the host GaAs relative to the deep level so that first the conduction band edge and then the valence band maximum passed through the A_1 -symmetric deep level. In the cases considered in Fig. {3}, the bonding s-like and p-like levels are fully occupied by electrons, lie well below the valence band maximum, and are electrically inactive and uninteresting. The anti-bonding p-like levels lie well above the conduction band minimum, and are unoccupied and also uninteresting. Thus, for Se_{As} in GaAs, the interesting deep level is the s-like or A_1 -symmetric deep level and it lies above the conduction band edge. But we could imagine applying a very large pressure, which would cause the GaAs conduction band edge to pass above the Se deep level – changing the doping character of this impurity from a shallow donor to a deep-trap, and causing the conductivity to drop precipitously. One could also imagine applying a uniaxial stress so strong that the Se deep level would pass into the valence band. (The magnitude of the stress would actually exceed the breaking point of GaAs.) In this case Se_{As} would become a shallow acceptor because the hole in the deep level would bubble up to the valence band maximum or Fermi energy, leaving the stable ion of Se to be Se^- . A hole could then orbit the negative ion in a hydrogenic effective-mass state. We call this case the case of false valence. It does not occur often, because it generally requires a small band-gap host, whose vacancy has no deep level in the gap. Nevertheless when the conditions for false valence are met, an impurity such as Se_{As} from Column-VI can appear to act as if it were from Column-IV (from the viewpoint of someone familiar only with effective-mass theory). In general the false valence will differ from the true valence by two or six, depending on whether the deep level that has crossed the fundamental band gap is an s-state or a p-state.

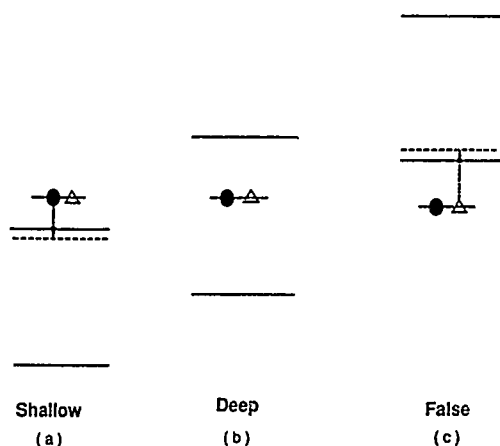


Fig. {3}. Energy level diagram illustrating how the relative positions of a deep level and the band edges could affect the character of a dopant. Band edges are long solid lines; shallow levels are dashed, and the deep level is a short solid line. The relevant deep level is assumed to be s-like and capable of holding two electrons of opposite spin. This impurity is assumed to come from one Column to the right in the Periodic Table of the atom it replaces (such as Se_{As} in GaAs). If the relevant deep level is in the gap (b), it is occupied by an electron (solid circle) and a hole (open triangle), and the neutral impurity is a deep trap for an electron or a hole. If the level is in the conduction band (a), the electron is autoionized, falls to the conduction band edge, and is trapped in the shallow donor level (dashed). If the level is in the valence band (c), the hole will bubble up into the shallow acceptor level.

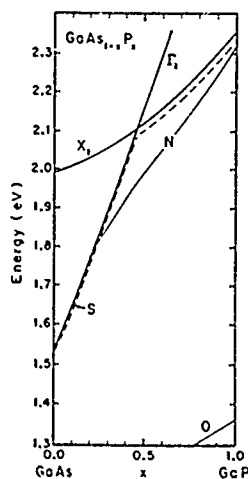


Fig. {4}. The band edges at the X-point and the Γ -point of the Brillouin zone, the N deep level, the O deep level, and the S and Se shallow levels in $\text{GaAs}_{1-x}\text{P}_x$ versus alloy composition x , after Refs. [5] and [3].

ALTERING THE CHARACTER OF A DOPANT

Interesting physics occurs when a band edge passes through a deep level, because the character of a dopant changes. This effect was first explicitly recognized by Wolford et al. [5], who studied anion-site N, O, S, and Se in $\text{GaAs}_{1-x}\text{P}_x$. These impurity-host combinations were especially interesting because O, S, and Se are all Column-VI impurities and were naively expected to have the same doping character as shallow donors, but N is a Column-V isoelectronic defect and should not have produced any level according to the then-conventional thinking. Instead, only S and Se produced shallow donors. N produced an "isoelectronic trap" in GaP that actually lies closer to the conduction band edge than the shallow donor states. We now know that this isoelectronic trap state is in fact a deep level that by accident lies only slightly below the conduction band edge, but when it was first discovered in GaP, the isoelectronic trap concept was novel and no one considered the possibility that the trap level was in fact a deep level (with "deep" defined in a localization sense) although it was energetically shallower than the shallow levels. Oxygen in GaP produced a level energetically deep in the gap, ≈ 1 eV below the conduction band edge.

The key to the difference between S and Se on the one hand and oxygen on the other is provided by the data for N in the alloy $\text{GaAs}_{1-x}\text{P}_x$ [5]. In the alloy the N and O energy levels behave similarly, being roughly linear functions of alloy composition x , while the S and Se levels are rather obviously "attached" to the band edges and so vary quadratically (Fig. 4). This fact indicated that the physics responsible for the N and O levels is the same, and, since N is isoelectronic to As and P and hence has no long-ranged defect potential, that the long-ranged or Coulombic parts of the defect potential are not responsible for the O level. This was an important fact because it showed that the O level was not a shallow level that somehow appeared energetically lower in the gap - lower due to some extra physics that is unimportant in most shallow donor problems. The data demonstrated that the O deep level originated instead from the central-cell potential of the defect. This meant that there were two separate limits to the impurity problem: (1) ordinary shallow-donor, one-band, effective-mass theory in which the long-ranged Coulomb potential of the impurity created hydrogenic states localized in \vec{k} -space near a band extremum and delocalized in \vec{r} -space, and (2) deep-level theory which relied upon the localized central-cell potential, created bonding and antibonding states, and had sp^3 -character wavefunctions involving at least eight energy bands - the wavefunctions of such levels are delocalized in \vec{k} -space.

A direct consequence of this way of thinking about impurities was the notion that every s- and p-bonded impurity produces four localized bonding and four antibonding deep levels associated with the impurity's perturbed bonds. Typically the antibonding levels of an electronegative defect are near the band gap, while the bonding levels are in or below the valence band, are termed hyperdeep levels [2], and normally are neither electrically active nor interesting. Therefore, there must be both an s-like and a three-fold degenerate p-like deep level of S (or Se) in GaP that lies *above* the conduction band edge and varies approximately linearly with x in $\text{GaAs}_{1-x}\text{P}_x$ - as the N and O (s-like) levels do.

The data for N in $\text{GaAs}_{1-x}\text{P}_x$ indicate that a deep level, namely an antibonding (s-like, in this case) level can be either in the gap or in the band (for $x < 0.2$). Indeed the level passes rather readily into the conduction band near $x \approx 0.2$, without a large Fano resonance effect, indicating that its wavefunction has rather different character from the shallow levels or the $\text{GaAs}_{1-x}\text{P}_x$ conduction band minimum. (Recall that GaP has an indirect band gap at the X point of the Brillouin zone, in the [001] direction, while GaAs has a direct gap at Γ or $\vec{k} = \vec{0}$.)

DEEP LEVELS IN SUPERLATTICES

Shallow-deep transitions

Since the relative positions of the substitutional impurity's deep levels and the band edges of the host determine the character of a dopant, the physics of deep levels in superlattices is particularly interesting [7-14]. The energy of a deep level with respect to vacuum is relatively insensitive (on a scale of >0.1 eV) to the structure of the superlattice, because the spatial extent of the deep level wavefunction is only of order ≈ 10 Å and only infrequently comes into contact with the interfaces of all but the smallest-period superlattices. *Therefore the wavefunction and energies of a deep impurity in a superlattice do not change much when the period of the superlattice changes.* In contrast to the deep levels themselves, *the superlattice band edges are readily perturbed* by changes of the superlattice periods, exhibiting the well-known effects of quantum confinement: for example, reducing the width of the GaAs layers in a $\text{GaAs}/\text{Al}_x\text{Ga}_{1-x}\text{As}$ superlattice causes a quantum-well effect, which results in the conduction band edge of the superlattice moving up in energy while the valence band maximum descends to lower energy. (See Fig. {5}.) Hence it is possible to "band-gap engineer" the period sizes of a superlattice so that, for example, the small-period superlattice's conduction band maximum lies *above* the deep level of a dopant – although the corresponding large-period superlattice's conduction band edge lies *below* the deep level. This means that the doping character of the impurity changes with period size [7].

To be specific, consider $N_1 \times N_2$ $\text{GaAs}/\text{Al}_{0.7}\text{Ga}_{0.3}\text{As}$ superlattices grown in the [001] direction and doped with Ga-site Si near the center of the GaAs quantum wells (Fig. {6}). Here N_1 is the number of GaAs layers in the superlattice period, and N_2 is the number of $\text{Al}_{0.7}\text{Ga}_{0.3}$ layers. For the 18×18 large-period superlattice, the Si deep level lies above the conduction band edge, resonant with the conduction band, so that the "extra" Si electron is autoionized, making Si^+ – and the Coulombic potential of Si^+ binds the electron (at low temperature) in a shallow donor level. However, for the small-period 2×34 superlattice, the conduction band minimum lies at higher energy than the Si deep level (according to theory [7,8,15]) and so the Si deep level lies in the gap, where it can trap an additional electron of opposite spin to its own electron, becoming Si^- . In the thick-period superlattice, Si_{Ga} near the center of a GaAs well is a shallow donor, making the quantum well n-type, but in the thin-period 2×34 structure, Si_{Ga} is a deep trap which tends to make the GaAs well semi-insulating. This transition from shallow donor to deep trap behavior of the Si substitutional impurity, as a function of GaAs layer thickness (Fig. {7}), is one of many examples of shallow-to-deep transitions of substitutional impurities in semiconductor superlattices. The fact that the most common donor in the most widely studied superlattice exhibits this behavior should be disturbing to people who have assumed that impurities do not change their doping character in superlattices.

Indeed, one can show theoretically that in *two-dimensional semiconductor hosts* every substitutional impurity has at least one deep level in the fundamental band gap. That is, in two-dimensions all impurities are deep traps with levels in the gap. This behavior is to be contrasted with the situation for three dimensions: most impurities do not produce deep levels in the gap. Thus *with increasing quantum confinement, many shallow donors or acceptors can be expected to become deep traps and to cease providing free carriers.* In other words, thin quantum well structures will have a greater tendency to exhibit semi-insulating behavior rather than doping behavior.

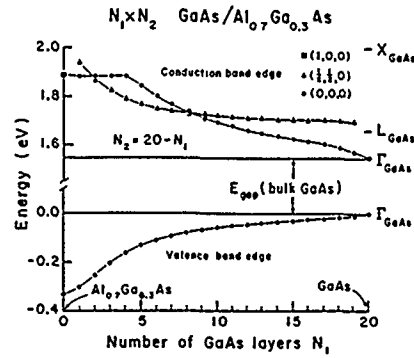


Fig. {5}. Predicted energies (in eV) of the superlattice conduction band minimum and valence band maximum with respect to the valence band maximum of bulk GaAs for a GaAs/ $\text{Al}_x\text{Ga}_{1-x}\text{As}$ [001] superlattice versus reduced layer thicknesses N_1 and N_2 for various $N_1 \times N_2$ [001] GaAs/ $\text{Al}_x\text{Ga}_{1-x}\text{As}$ superlattices, with $x=0.7$ and N_1+N_2 fixed to be 20, after Ref. [7]. Note the broken scale on the ordinate. The positions of the band extrema of bulk GaAs at Γ , L, and X are shown on the right of the figure, at $N_1=20$.

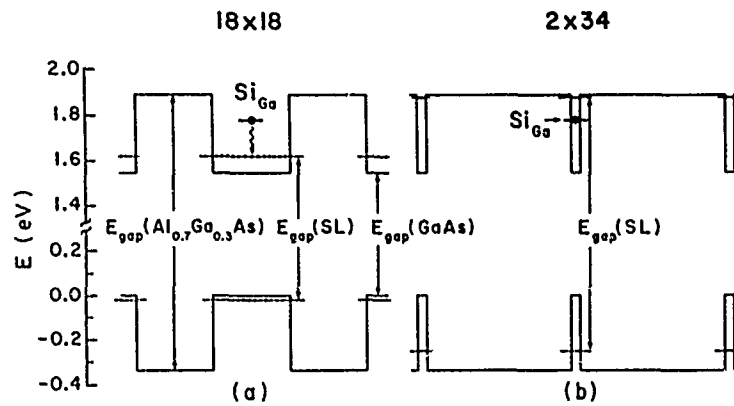


Fig. {6}. Illustrating the quantum-well effect on the band gap $E_{\text{gap}}^{\text{SL}}$ of a $N_1 \times N_2$ GaAs/ $\text{Al}_{0.7}\text{Ga}_{0.3}\text{As}$ superlattice, after Ref. [7]: (a) $N_1=N_2=18$; and (b) $N_1=2$, $N_2=34$. The band edges of the superlattice are denoted by chained lines. For this alloy composition the superlattice gap is indirect for case (b), with the conduction band edge at $\vec{k}=(2\pi/a_L)(1/2, 1/2, 0)$. Note the broken energy scale. The zero of energy is the valence band maximum of GaAs.

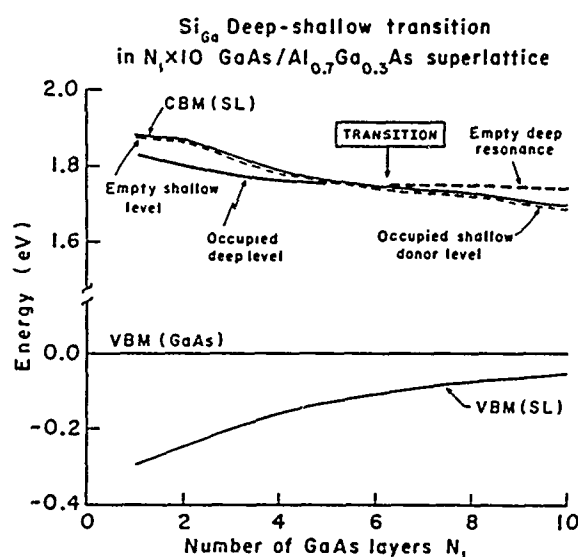


Fig. {7}. Illustrating the deep-to-shallow transition as a function of GaAs layer thickness N_1 in a GaAs/Al_xGa_{1-x}As $N_1 \times 10$ superlattice (SL) with $x=0.7$ for a Si impurity on a Column-III site in the center of a GaAs layer of the superlattice host, after Ref. [7]. The conduction band edge (CBM) and valence band maximum (VBM) are indicated by light solid lines. The Si deep level is denoted by a heavy line, which is solid when the level is in the gap but dashed when the level is resonant with the conduction band. The deep level in the band gap for $N_1 < 6$ is covered up by the conduction band as a result of changes in the host for $N_1 > 6$. The impurity's deep level lies in the gap for $N_1 < 6$ and is occupied by the extra Si electron; the Si, in this case, is thus a "deep impurity." For $N_1 > 6$, the deep level lies above the conduction band edge as a resonance. The daughter electron from the Si impurity which was destined for this deep level is autoionized, spills out of the deep resonance level, and falls to the conduction band edge (light solid line) where it is subsequently bound (at low temperature) in a shallow level associated with the long-ranged Coulomb potential of the donor (indicated by the short dashed line). It is important to realize that *both* the deep level and the shallow levels coexist and are distinct levels with qualitatively different wavefunctions. The issue of whether an *impurity* is "deep" or "shallow" is determined by whether or not a deep level associated with the impurity lies in the band gap. The computed deep-shallow transition occurs for $N_1 \approx 6$ layers. While the qualitative physics is completely reliable, it is possible that the transition layer thickness may differ somewhat from $N_1=6$ in real superlattices. The predicted fundamental band gap of the superlattice is indirect for $1 < N_1 \leq 8$. All energies are with respect to the valence band maximum of GaAs.

Dependence of deep levels on location

Although shallow-deep transitions that occur when a quantum-confined band edge passes through a deep level are the most dramatic superlattice effect, the interfaces between layers in superlattices have the effect of shifting and splitting deep levels on a scale of order 0.1 eV. Fig. {8} shows the predicted [8] dependence on site of an As vacancy's deep levels in a 10×10 GaAs/ $\text{Al}_{0.7}\text{Ga}_{0.3}\text{As}$ superlattice grown in the [111] direction. Note that the valence band edges of GaAs, $\text{Al}_{0.7}\text{Ga}_{0.3}\text{As}$, and the superlattice are aligned according to the measured band offset [16], and that once this is done, the deep levels are relatively independent of site, except for a variation on the scale of 0.1 eV. The bulk p-like valence band maximum is split into an upper π -like and lower σ -like band edge due to the reduced symmetry of the superlattice. This splitting is reflected in different energies for π -like and σ -like deep levels, even if the parent impurity is distant from an interface. The T_2 or p-like deep levels split the most at an interface into one or two levels corresponding to hybrid orbitals directed primarily into GaAs (which orbitals have energies near the bulk GaAs vacancy energy) and hybrids directed primarily into $\text{Al}_{0.7}\text{Ga}_{0.3}\text{As}$ with corresponding energies [7,8]. In addition to this effect, the band offset between the two materials is reflected in both the p-like deep level and the s-like level.

The s-like deep levels of cation-site Si in a 3×10 GaAs/ $\text{Al}_{0.7}\text{Ga}_{0.3}\text{As}$ superlattice are given in Fig. {9}, and show (i) how undramatic the effects of the superlattice are on the level itself and (ii) how an impurity can produce a shallow donor and n-type doping in bulk GaAs but yield a deep trap and semi-insulating behavior in the superlattice. Si (or a defect involving Si) is thought to be the DX center in $\text{Al}_x\text{Ga}_{1-x}\text{As}$ [15].

These shifts and splittings of the deep levels as a function of position in the superlattice will manifest themselves experimentally as inhomogeneously broadened deep level energies.

Formalism

The formalism employed here is rather simple, and has been discussed in Refs. [7] and [8] in detail. Basically, one solves the secular equation

$$\det \{ 1 - GV \} = 0,$$

where $G=(E-H)^{-1}$ is the Green's function operator associated with the host Hamiltonian H and E is the deep level energy. The defect potential operator is V , and we have obtained solutions to this equation using the tight-binding model of Vogl et al. [17]. The basic approach is the same as that used by Hjalmarson et al. [2] for substitutional impurities in bulk semiconductors.

SUMMARY

Deep impurity levels in semiconductor superlattices will, on an absolute energy scale, be shifted only slightly and split (or inhomogeneously broadened) from their bulk semiconductor energies. This relative insensitivity of the levels to superlattice geometry, combined with the superlattice's property of being sensitive to quantum confinement effects on its band edges should lead to shallow-deep transitions and novel doping properties of impurities in thin quantum wells. The inhomogeneous broadening of deep levels will be a less dramatic effect on the electronic structure, but will nonetheless have important consequences in areas such as exciton transport and resonant energy transfer of excitons bound to deep impurities.

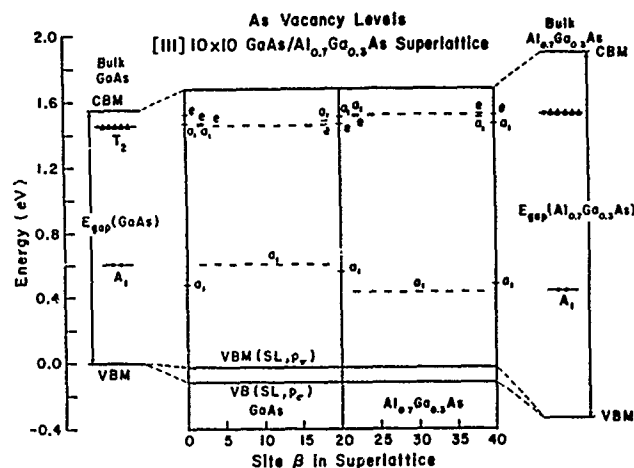


Fig. {8}. Predicted energy levels of an As-vacancy in a $(\text{GaAs})_{10}(\text{Al}_{0.7}\text{Ga}_{0.3}\text{As})_{10}$ [111] superlattice, as a function of β , the position of the vacancy (even values of β correspond to As-sites), after Ref. [8]. Note the splitting of the T_2 levels at and near the interfaces ($\beta = 0, 20$, and 40), and that the T_2 -derived vacancy levels lie at higher energy in an $\text{Al}_{0.7}\text{Ga}_{0.3}\text{As}$ layer than in a GaAs layer. The a_1 and e ordering changes at successive interfaces. The zero of energy is the valence band maximum of bulk GaAs, and the corresponding valence band (VBM) and conduction band (CBM) edges and deep levels in bulk GaAs and bulk $\text{Al}_{0.7}\text{Ga}_{0.3}\text{As}$ are given to the left and right of the central figure, respectively. The top of the central figure is the conduction band edge of the superlattice, and the bottom corresponds to the split valence band in the superlattice – the valence band maximum of the superlattice being of e symmetry (p_π) and the split-off a_1 (p_σ) band maximum lying 0.087 eV lower in energy. The A_1 level in the $\text{Al}_x\text{Ga}_{1-x}\text{As}$ layer of the superlattice is lower than the corresponding level in the GaAs layer because of the band offset of 0.334 eV. The electron (hole) occupancies of the deep levels in bulk GaAs and bulk $\text{Al}_{0.7}\text{Ga}_{0.3}\text{As}$ are denoted by solid circles (open triangles).

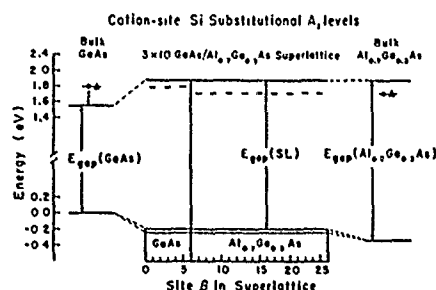


Fig. {9}. Predicted A_1 -derived deep levels of Si in GaAs, In a 3×10 GaAs/ $Al_{0.7}Ga_{0.3}As$ superlattice, after J. D. Dow, S. Y. Ren, and J. Shen, Ref. [10], as a function of the position β of the Si in the superlattice, and in the bulk materials. Interfaces correspond to sites $\beta = 0, 6$, and 26. Note that in bulk GaAs Si is a shallow donor, but that it is a deep trap in this superlattice, according to the theory.

ACKNOWLEDGMENT

We are grateful to the U. S. Office of Naval Research and the Air Force Office of Scientific Research (Contract Nos. N00014-89-J-1136 and AF-AFOSR-89-0063) for their generous support.

REFERENCES

- [1] W. Kohn, in *Solid State Physics*, edited by F. Seitz and D. Turnbull, (Academic Press, New York, 1957), Vol. 5, P. 258-321.
- [2] H. P. Hjalmarson, P. Vogl, D. J. Wolford, and J. D. Dow, Phys. Rev. Letters 44, 810 (1980); H. P. Hjalmarson, Ph.D. thesis, University of Illinois at Urbana-Champaign, 1979, unpublished. See also W. Y. Hsu, J. D. Dow, D. J. Wolford, and B. G. Streetman, Phys. Rev. B 16, 1597 (1977) for the concepts that form the foundation of this work.
- [3] J. D. Dow, Mater. Res. Soc. Symp. Proc. 46, 71 (1985).
- [4] J. D. Dow, in *Highlights of Condensed Matter Theory* (Proc. Intl. School of Phys. "Enrico Fermi" Course 89, Varenna, 1983) ed. by F. Bassani, F. Fumi, and M. P. Tosi (Societa Italiana di Fisica, Bologna, Italy, and North Holland, Amsterdam, 1985), pp. 465 et seq.
- [5] D. J. Wolford, W. Y. Hsu, J. D. Dow, and B. G. Streetman, J. Lumin. 18/19, 863 (1979).
- [6] The hydrogenic potential, strictly speaking, can bind a second electron, since the ion H^+ is stable. However, this second-electron binding energy is so small compared with typical thermal energies that we neglect it.
- [7] S. Y. Ren, J. D. Dow, and J. Shen, Phys. Rev. B 38, 10677 (1988).
- [8] S. Y. Ren and J. D. Dow, J. Appl. Phys. 65, 1987 (1989).
- [9] R.-D. Hong, D. W. Jenkins, S. Y. Ren, and J. D. Dow, Proc. Materials Research Soc. 77, 545 (1987), *Interfaces, Superlattices, and Thin Films*, ed. J. D. Dow and I. K. Schuller.
- [10] For a review of the physics of impurities in superlattices, see *Properties of impurity states in superlattice semiconductors*, ed. by C. Y. Fong, I. P. Batra, and S. Ciraci (Plenum Publishing Corporation, 1988). See also Refs. [7], [8], [11], [12], [13], and [14].
- [11] S. Das Sarma and A. Madhukar, J. Vac. Sci. Technol. 19, 447 (1981).
- [12] D. K. Maude, J. C. Portal, L. Dmowski, T. Foster, L. Eaves, M. Nathan, M. Heiblum, J. J. Harris, and R. B. Beall, Phys. Rev. Letters 59, 815 (1987).
- [13] J. S. Nelson, C. Y. Fong, I. P. Batra, W. E. Pickett, and B. M. Klein, unpublished.
- [14] M. Lannoo and J. Bourgoin, to be published.
- [15] H. P. Hjalmarson and T. J. Drummond, Appl. Phys. Letters 48, 657 (1986). A preliminary account was given by H. P. Hjalmarson, Bull. Amer. Phys. Soc. 32, 814 (1987).
- [16] D. J. Wolford, T. F. Kuech, J. A. Bradley, M. A. Grell, D. Ninno, and M. Jaros, J. Vac. Sci. Technol. B4, 1043 (1986).
- [17] P. Vogl, H. P. Hjalmarson, and J. D. Dow, J. Phys. Chem. Solids 44, 365 (1983).

QUALITATIVE PHYSICS OF DEFECTS IN QUANTUM WELLS: INTERFACE ROUGHNESS

HAROLD P. HJALMARSON

Sandia National Laboratories, Albuquerque, New Mexico 87185.

ABSTRACT

The electronic properties of interface roughness in a quantum well are described. Interface roughness is shown to always produce localized bound states. Thus intrinsic roughness can explain the giant oscillator strength observed for "free" excitons in quantum wells.

INTRODUCTION

Interface roughness can affect both the optical and electrical properties of semiconductor quantum wells. Typically such roughness has a height of 3-10 Å (1-3 monolayers) and a lateral size of 50 - 250 Å. This roughness causes local fluctuation in the quantum sub-band energy which leads to photoluminescence line broadening [1,2] and increased carrier scattering [3,4]. In earlier work, Gaussian type wavefunctions were used to compute exciton binding energies; no binding occurred if the lateral size of the roughness was smaller than a critical size of approximately 40 Å [1]. In other work, the Born approximation was used to compute carrier mobility in quantum wells [3].

In this paper the qualitative properties of interface roughness are described. In an idealized model, interface roughness consists of islands with a distribution of radii a and thicknesses b . A multi-band variational calculation and a single band two-dimensional (2D) square well approximation are used to compute the electronic properties.

By analogy to bulk defect problems, the wavefunction is expressed in terms of quantum well eigenfunctions $\chi(\rho, z)$. Assuming a single quantum well of depth Δ for $0 \leq z \leq d$, the wavefunction can be written as

$$\Psi(r) = \sum_{kn} c_{kn} \chi_{kn}(\rho, z) \quad (1)$$

$$\text{with } \chi_{kn}(\rho, z) = \psi_k(\rho) \phi_n(z). \quad (2)$$

In the limit of an infinitely deep well ($\Delta \rightarrow \infty$),

$$\phi(z) \rightarrow d^{-1/2} \sin(\pi n/d); \quad (3)$$

for an isotropic effective mass, $\psi(\rho)$ is a Bloch function of the form

$$\psi(\rho) \rightarrow A^{-1/2} \exp(ik\rho) \quad (4)$$

in which A is the unit cell area.

For this defect problem with cylindrical symmetry, it is convenient to replace the plane waves with Bessel functions. Thus we use

$$\chi(r) = N_{mi} J_m(k_i \rho) \phi_n(z) T_m(\theta) \quad (5)$$

as an orthonormal complete set of states in which $J_m(k\rho)$ is a Bessel function of the first kind and $T_m(\theta) = \pi^{-1/2} \exp(im\theta)$ [5,6]. Boundary conditions on a cylinder of radius R ($R \gg a$) quantize the radial wavevector; assuming that the wavefunction vanishes at $\rho = R$ defines $k_i = Z_{mi}/R$ in which Z_{mi} is the i^{th} zero of the Bessel function [5,6].

The energies are obtained by diagonalizing the matrix

$$[(E_n + \epsilon_i - E) \delta_{n',n} \delta_{i',i} + \langle n'i' | V(\rho, z) | ni \rangle] C_{ni} = 0 \quad (6)$$

in which $\epsilon_i = \hbar^2/2m k_i^2$ is the Bessel function "kinetic energy" and $E_n \approx \hbar^2/2m (n\pi/d)^2$ are the bound state energies of the quantum well. The potential $V(\rho, z) = -\Delta$ iff $d \leq z \leq d+b$ and $0 \leq \rho \leq a$. The matrix elements are separable; $\langle n'i' | V(\rho, z) | ni \rangle = V(n', n) S(i', i)$ with

$$V(n', n) = -\Delta \int_d^{d+b} \phi_{n'}(z)^* \phi_n(z) dz \quad (7)$$

and

$$S(i', i) = N_{mi} N_{mi} \int_0^a \rho J_m(k_{i'} \rho) J_m(k_i \rho) d\rho, \quad (8)$$

an overlap function. It is important to use accurate bound state wavefunctions. For example, $V(n', n) = 0$ if infinite depth quantum well wavefunctions are used because they vanish on the wall.

The radius a and the thickness b of the defect determine the size of the matrix needed for numerical convergence. The size is directly controlled by the number of bound states; free states have smaller effect. The size is indirectly controlled by the radius a .

In the limit of weak potentials, the binding energy becomes small and the wavefunction becomes very large. Therefore, the brute force variational technique fails. However, in this limit a one-mini-band approximation becomes adequate.

This approximation is equivalent to the effective mass treatment of donors and acceptors which leads to a hydrogenic Schrodinger equation. In this approximation, the calculation simplifies to solving the problem of a two-dimensional (2D) square well. The radial Schrodinger equation for the n^{th} sub-band becomes

$$[1/\rho \partial/\partial \rho (\rho \partial/\partial \rho) + k^2 - v(\rho)] B(\rho) = 0 \quad (9)$$

$$\text{with } v(\rho) = \begin{cases} v_n & \rho \leq a \\ 0 & \rho > a \end{cases} \quad (10)$$

The square well potential depends sensitively on the penetration of the quantum well eigenfunctions into the barrier:

$$v_n = \langle n | V(\rho, z) | n \rangle \approx -\Delta |(d)|^2 b. \quad (11)$$

Bessel's equation is satisfied either inside ($k=k^i$) or outside ($k=k^o$) the cylinder. The wavevectors are

$$k^i a = (\epsilon_i)^{1/2} \quad (12)$$

$$k^o a = (\epsilon_i - v_n)^{1/2} \quad (13)$$

The bound state solutions are determined by the solutions to the continuity equation for the wavefunction and its first derivative. By analogy to the 3D problem,

$$k^i a J'_0(k^i a)/J_0(k^i a) = k^o a K'_0(k^o a)/K_0(k^o a) \quad (14)$$

In the limit of very small potentials $k_i a, k_o a \ll 1$, and one can use a small argument expansion to find

$$\frac{E + |v_n|}{T} \approx -1/2 \ln(E/T) \quad (15)$$

which yields

$$E = T \exp(-2T/|v_0|) \quad (16)$$

This equation has a nonzero solution E for any attractive potential v . Thus it states that all states are localized for these defects in a 2D system. Further, a reduction of the radius a corresponds to an increase of T . As T increases, this equation always has a nonzero energy solution. In actuality, a cannot be smaller than a_L , the lattice constant. In this limit such a defect corresponds to a substitutional defect. As described below, the qualitative physics of a substitutional impurity in a quantum well corresponds closely to that of interface roughness [7].

DISCUSSION

Both techniques yield nearly identical energies and wavefunctions for moderate potentials with $b \ll d, a$. As a representative case, consider a GaAs quantum well with AlAs barriers. For this case, $\Delta \approx 200$ meV. For $d = 100$ Å, $a = 100$ Å, and $b = 3$ Å, the variational binding energy $E_b = 5$ meV. The one-band approximation yields $E_b = 4.5$ meV.

The fact that any potential will localize a state in a quantum well contrasts with the behavior of a defect in a 3D system. It is well known that a critical strength 3D square well potential is necessary to bind a state [8]; however, in 2D an arbitrary potential will localize a state [9]. Earlier work on the qualitative physics of 3D deep levels showed that if one uses a multi-band approximation, the threshold potential in a semiconductor is of "atomic-like" magnitude representing the central-cell which is a difference of atomic orbital energies [10]. However, in later work, a substitutional defect in a superlattice was found to localize a 2D like state if it was not strong enough to produce an bulk-like deep level [7]. In particular, the binding energy relative to each sub-band is

$$E = E_0 \exp(-sE_0/|V|) \quad (17)$$

in which E_0 is the bandwidth and s is an overlap function [7].

Interface roughness scattering has been found important for thin quantum wells [3]. The presence of a bound state has implications for carrier scattering by the interface roughness; this corresponds to neutral impurity scattering in the limit that $a \rightarrow a_L$. The scattering length, equivalent to the 3D cross-section, can be defined in terms of scattering phase shifts [11]. For the 2D square well, I find these phase shifts are generally nonzero at very low energies and thus the scattering length diverges as $1/k$ at low energies [12].

The model also applies to excitons. For a system in which the electron and hole quantum wells overlap, the model predicts that arbitrarily weak defect will bind or localize an exciton. Such an exciton will generally have a large oscillator strength [13]. If the electron and hole masses are similar, the oscillator strength will be approximately one. Thus

this work can qualitatively explain the "giant" oscillator strength observed in quantum wells [14,15].

ACKNOWLEDGMENTS

I acknowledge useful discussions with C. S. Lent and L. A. Romero. This work was supported by the U. S. Department of Energy under contract number DE-AC04-756DP00789.

REFERENCES

1. G. Bastard, C. Delalande, M. H. Meynadier, P. M. Frijlink, and M. Voos, Phys. Rev. B 29, 7042 (1984).
2. J. Singh and K. K. Bajaj, J. Appl. Phys. 57, 5433 (1985).
3. H. Sakaki, T. Noda, K. Hirakawa, M. Tanaka, T. Matsusue, Appl. Phys. Lett. 51, 1934 (1987).
4. H. P. Hjalmarson, I. J. Fritz, and L. R. Dawson, Proceedings of the International Conference on Hot Carriers in Semiconductors, 1989.
5. J. D. Jackson, "Classical Electrodynamics", (John Wiley, New York, 1962).
6. M. Abramowitz and I. A. Stegun, "Handbook of Mathematical Functions", (Dover Publications, New York, 1972).
7. H. P. Hjalmarson, Bull. Am. Phys. Soc. 32, 814 (1987).
8. L. I. Schiff, "Quantum Mechanics", (McGraw-Hill, New York, 1968).
9. H. P. Hjalmarson, P. Vogl, D. J. Welford, and J. D. Dow, Phys. Rev. Lett. 44, 810 (1980).
10. B. Simon, Ann. Phys. 97, 279 (1976).
11. I. R. Lapidus, Am. J. Phys. 50, 45 (1982).
12. H. P. Hjalmarson, unpublished.
13. J. M. Rorison and D. C. Herbert, Superlattices and Microstructures 1, 425 (1985).
14. G. W. 't Hooft, W. A. J. A. van der Poel, L. W. Molenkamp, and C. T. Foxon, Phys. Rev. B 35, 8281 (1987).
15. J. Feldmann, G. Peter, E. O. Gobel, P. Dawson, K. Moore, C. Foxon, and R. J. Elliott, Phys. Rev. Lett. 59, 2337 (1987).

PART VI

Hydrogen in Silicon

FERMI RESONANCE EFFECTS ON THE VIBRATION MODES OF HYDROGEN-PASSIVATED BORON IN SILICON

G.D. WATKINS*, W.B. FOWLER*, G.G. DELEO*, M. STAVOLA*, D.M. KOZUCH*,
S.J. PEARTON** AND J. LOPATA**

* Department of Physics, Lehigh University, Bethlehem, PA, 18015

** AT&T Bell Laboratories, Murray Hill, NJ, 07974

ABSTRACT

^{10}B - ^{11}B isotope shifts have been reported recently for the vibrational frequencies of hydrogen (H) and its isotope deuterium (D) in the H-B complex in silicon. The D- ^{10}B - D- ^{11}B shift was found to be anomalously large. We show that this effect finds a natural explanation in a phenomenon called "Fermi resonance", arising from a weak anharmonic coupling between the second harmonic of the transverse B vibration and the longitudinal D vibration. We first present a simple classical explanation of the effect in terms of a "parametric oscillator", or a child pumping a swing. We then outline a simple quantum mechanical treatment that provides a satisfactory quantitative explanation of the results. Our calculations also predict infrared absorption at the boron second harmonic frequencies. These are observed for both ^{10}B and ^{11}B with intensities and polarization as predicted, providing direct confirmation of the interpretation. The Pankove Si-H-B model, therefore, remains intact.

INTRODUCTION

The disruption of a crystalline solid by the presence of impurities has, for decades, presented scientists with an opportunity to probe the physics of many body atomic systems. Occasionally, rather basic principles have been distilled from observations and interpretations of such systems. We believe that the work described here can be considered as such an example. It has to do with an "anomalous" isotope shift reported recently [1] for a localized vibrational mode of deuterium in the deuterium-boron pair defect in silicon. As originally interpreted, the results served to challenge the generally accepted Pankove model [2] for the defect.

In this paper, we conclude instead that the unexpectedly large isotope effect can be explained simply as arising from a small anharmonic coupling between the vibration of the deuterium atom and the nearly degenerate second harmonic of a perpendicular boron vibration. Classically, this corresponds to the parametric oscillator problem, or that of a child pumping a swing. Quantum mechanically, this is known as a Fermi resonance [3], a phenomenon well established for molecules [4] but not previously identified, we believe, for a defect in a solid. This interpretation, and the experimental confirmation that we present here, explains the isotope effect quite naturally in terms of the accepted model of the defect and, in fact, actually further strengthens it by confirming essential features not previously established.

THE PANKOVE MODEL

The generally accepted model of the H-B pair, first presented by Pankove [2], has an interstitial hydrogen atom occupying a bond centered (BC) site directly between substitutional boron and one of its neighboring silicon atoms. In this model, as shown in Fig. 1, the hydrogen bonds primarily to the silicon, while the boron moves away from the hydrogen almost into the plane of its three other silicon neighbors. All dangling

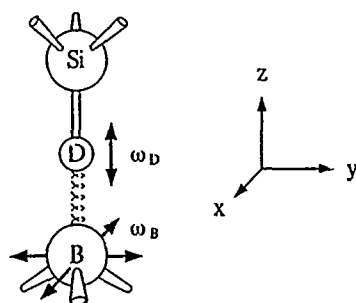


Fig. 1. Pankove model for the D-B (H-B) pair in silicon, showing the longitudinal D (H) and transverse B vibrational modes.

bonds are satisfied. Therefore, the boron acceptor is "passivated", and there is no electrical activity. This proposed structure has found support in infrared [5-7], Raman [8], and channeling experiments [9,10], and electronic structure calculations [11].

In particular, sharp infrared vibrational bands of hydrogen (H) and deuterium (D) have been reported for the complex at 1903cm^{-1} and 1390cm^{-1} , respectively [5]. Combined with uniaxial stress, these studies revealed the bands to arise from longitudinal vibrations of each of the two hydrogen isotopes in the complex [6,7] (z axis, Fig. 1). Boron vibrational modes, presumed, but not experimentally confirmed, to be transverse (x,y axis, Fig. 1), have been found by Raman studies for ^{10}B and ^{11}B at 680cm^{-1} and 652cm^{-1} , respectively [8]. Finally, Pajot et al. [1] in a recent careful examination of the hydrogen and deuterium modes detected small shifts with ^{10}B , ^{11}B substitutions. In this study, the H (D) longitudinal vibrations were found to lie at 1904.4cm^{-1} (1390.6cm^{-1}) for the H- ^{11}B (D- ^{11}B) complex and at 1905.2cm^{-1} (1393.9cm^{-1}) for the H- ^{10}B (D- ^{10}B) complex. These small boron-induced isotope shifts confirm the weak but nonzero coupling between boron and hydrogen inherent in the Pankove model, as depicted in Fig. 1 by the dashed spring.

The surprising feature of the Pajot et al. results, however, is the large magnitude of the shift for the D vibration ($3.3 \pm 0.4\text{cm}^{-1}$) compared to that for H ($0.8 \pm 0.4\text{cm}^{-1}$). As pointed out by these workers, harmonic coupling of the boron atom should produce less than a factor of two difference in the ^{10}B - ^{11}B shift for the two isotopes of hydrogen. They were led to conclude, therefore, that the equilibrium position of D must be different from that for H, and suggested an alternative double potential well model for hydrogen in the defect. Hence, although the observation of Pajot et al. provided the clearest demonstration that hydrogen and boron are both part of the same defect and also that the coupling between them is weak, as predicted in the Pankove model, the detailed result proved to be anomalous and therefore a challenge to the model.

MODEL FOR THE EFFECT

The key to our explanation is to note the near degeneracy between the longitudinal vibration frequency of D (1390cm^{-1}) and twice the transverse vibration frequency (i.e. second harmonic) of ^{10}B ($2 \times 680\text{cm}^{-1} = 1360\text{cm}^{-1}$). Under such conditions, even a weak interaction of the correct form between the two modes can serve to couple them significantly. Classically, this is the analogue of the parametric oscillator. We will first explore this briefly for the physical insight it provides. We will then treat it quantum mechanically, which turns out to be a simpler way to solve the problem.

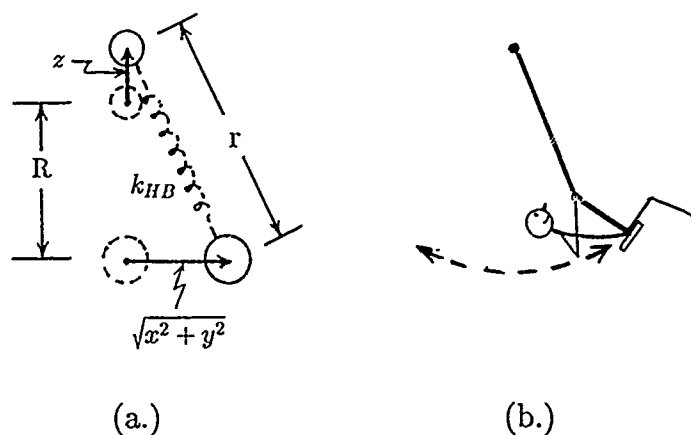


Fig. 2. (a) Simple single spring model for the anharmonic coupling between the longitudinal H-atom (z) and transverse B-atom (x, y) displacements. (b) Analogue of a child pumping a swing.

Classical Model

The nature of the coupling between the two modes is made clear in Fig. 2(a), where we consider the effect of a weak spring between the B and H atoms. As the boron atom moves to either the left or the right in its vibration, it exerts a downward tug via the spring to the hydrogen atom. It therefore serves to drive the hydrogen longitudinal motion at twice the frequency of the boron vibration. Conversely, the hydrogen upward motion gives a tug to the boron atom assisting its return from either left or right. Vibration of the hydrogen therefore drives the boron vibration at half the hydrogen frequency. This is the principle of the parametric oscillator. It should be familiar to us also in another context. When, as children, we pumped ourselves on a swing, we were giving ourselves a vertical tug at each half period of our transverse swinging motion, see Fig. 2(b). In the case of the D- ^{10}B defect, with the deuterium longitudinal vibration frequency approximately twice the transverse ^{10}B frequency, this paramagnetic coupling is nearly resonant and can serve effectively to mix and shift the modes.

We could solve for the effect classically as two independent vibrating particles perturbed by the coupling as shown in Fig. 2(a). Expanding the energy stored in the weak spring as a power series of the displacements gives

$$\begin{aligned} \frac{1}{2} k_{HB} (r-R)^2 &= \frac{1}{2} k_{HB} (\sqrt{x^2 + y^2 + (R+z)^2} - R)^2 \\ &\approx \frac{1}{2} k_{HB} z^2 + \frac{1}{2} \frac{k_{HB}}{R} z (x^2 + y^2) + \dots \end{aligned} \quad (1)$$

The second term, the first anharmonic term in the expansion, contains the essence of the effect. For example, this term represents a spring for the transverse B vibration with spring constant proportional to z and therefore oscillating at the frequency of the longitudinal hydrogen motion.

As mentioned earlier, it turns out, however, that it is simpler to

treat the system quantum mechanically. Eq. (1) is still helpful because it reveals the form of the perturbation associated with the coupling, which we abbreviate

$$H' = k_3(x^2 + y^2)z, \quad (2)$$

In so doing, we avoid the specific form of k_3 given by Eq. (1) because its origin is probably more complex than that given by the simple single spring model of Fig. 2(a).

Fermi Resonance

The problem of two orthogonal vibrational modes coupled by an anharmonic perturbation of the form given by Eq. (2) was first considered by Fermi to describe the similar situation of coupling between transverse (x,y) and longitudinal (z) vibrations of the CO_2 molecule which are also accidentally approximately 1:2 in frequency [3]. This effect, subsequently found also in several other molecules, has become known as a Fermi resonance [4].

We label the vibrational states before they are coupled by the quantum numbers of the independent oscillators, $|n_x^B, n_y^B, n_z^D\rangle$. The corresponding unperturbed energies are

$$E^{(0)} = \hbar\omega_B(n_x^B + n_y^B + 1) + \hbar\omega_D(n_z^D + 1/2). \quad (3)$$

Selected vibrational states are shown schematically on the left side of Fig. 3. We need consider only the nearly degenerate states which are coupled by the perturbation of Eq. (2), which has selection rules $\Delta n_x^B, \Delta n_y^B = 0, \pm 2$ and $\Delta n_z^D = \pm 1$. There are thus only two states, the symmetric combination of $|200\rangle$ and $|020\rangle$ (the two phonon levels for B) and $|001\rangle$ (the one phonon level for D). The perturbation matrix is constructed therefore from the basis states

$$|B\rangle = (1/\sqrt{2}) (|200\rangle + |020\rangle), \quad (4)$$

$$|D\rangle = |001\rangle, \quad (5)$$

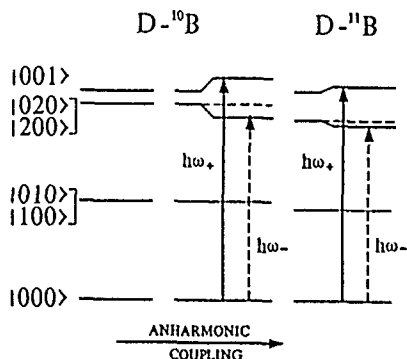


Fig. 3. Vibrational states, labeled $|n_x^B, n_y^B, n_z^D\rangle$, corresponding to axial D-atom vibrations and perpendicular B-atom vibrations in the absence and presence of anharmonic coupling.

where the perturbed wave functions have the form

$$|\psi\rangle \approx c_B|B\rangle + c_D|D\rangle. \quad (6)$$

The eigen value matrix equation becomes

$$\begin{pmatrix} 2\hbar\omega_B - E & \eta \\ \eta & \hbar\omega_D - E \end{pmatrix} \begin{pmatrix} c_B \\ c_D \end{pmatrix} = 0, \quad (7)$$

where

$$\eta = \hbar^{3/2} k_3 (2\omega_B^2 m_B^2 \omega_D m_D)^{-1/2}, \quad (8)$$

as determined from the well known harmonic oscillator matrix elements. Here the zero of energy has been taken as that of the $|000\rangle$ ground state.

Solving the secular determinant, the vibrational energies ($E_{\pm} = \hbar\omega_{\pm}$) become

$$\hbar\omega_{\pm} = \frac{\hbar\omega_D + 2\hbar\omega_B}{2} \pm \frac{1}{2} \sqrt{(\hbar^2(\omega_D - 2\omega_B)^2 + 4\eta^2)}, \quad (9)$$

where ω_+ refers to the higher-frequency mode (primarily a one-phonon longitudinal D excitation at $\sim\omega_D$) and ω_- refers to the lower-frequency mode (primarily a two-phonon B excitation at $\sim 2\omega_B$). The frequency shifts expected for the ^{10}B and ^{11}B cases in the presence of the anharmonic coupling are illustrated schematically in Fig. 3. One can see from the figure that the frequency shifts are in the direction consistent with experiment. The frequency, ω_+ , decreases in going from ^{10}B to ^{11}B as a consequence of the reduced "level repulsion" as $|\omega_D - 2\omega_B|$, the degree of parametric resonance, increases.

The intensities of the expected electric-dipole transitions can also be extracted from the matrix solution since the ω_+ transition will have intensity proportional to $|c_D|^2$ (~ 1), and that for ω_- will be $|c_B|^2$ (~ 0), (see Fig. 3). In the absence of the anharmonic coupling, the ω_- transition is electric-dipole forbidden (i.e., c_D is zero). However, in the presence of the anharmonic coupling, this two-phonon transition "steals" oscillator strength from the deuterium longitudinal vibration. Our model therefore predicts that there should be a weak but allowed two-phonon transition for the boron which is stronger in the ^{10}B case than in the ^{11}B case (ω_- in Fig. 3).

The results of an infrared study are shown in Fig. 4. The strong bands are due to the D stretching vibration; the large isotope effect originally observed by Pajot et al.[1] is evident. Additionally, there are new, previously unreported weak features at close to twice the frequencies of the ^{10}B and ^{11}B modes reported by Herrero and Stutzmann[8] for the D-B complex. The new feature in the ^{10}B spectrum is more intense relative to the D fundamental than the ^{11}B feature, consistent with the greater coupling of the overtone with the fundamental modes that is expected in our model. The

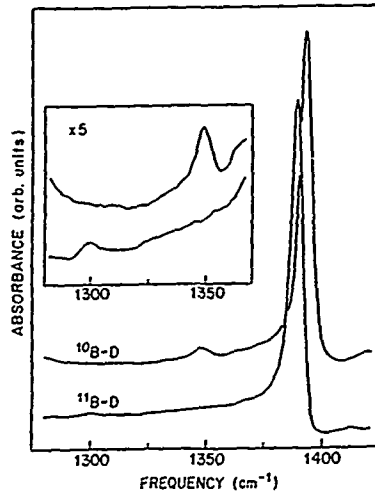


Fig. 4. Infrared vibrational spectra of the D- ^{10}B and D- ^{11}B pairs in silicon showing the one-phonon deuterium spectra (strong signals) and the two-phonon boron spectra (weak signals).

new, weak bands appear only for the appropriate B isotope; i.e., there is no ^{11}B feature in the ^{10}B spectrum and vice versa, establishing that this is a B-related feature.

Using Eq. (9) with ω_D , $2\omega_B$ and η as adjustable parameters, a very close fit can be obtained to the four measured frequencies (ω_+ and ω_- for both D- ^{10}B and D- ^{11}B) as shown in Table I. (In the fit, it has been assumed that 1.2cm^{-1} of the shift for the D vibration with boron isotope substitution results from the normal, i.e., linear harmonic coupling by scaling according to the isotopic masses from the 0.8cm^{-1} shift observed in the hydrogen

TABLE I: Measured and predicted vibrational frequencies (ω_{\pm}) and relative intensities (I_-/I_+) appropriate to the D- ^{10}B and D- ^{11}B pairs in silicon. The "one-phonon deuterium mode" results are denoted ω_+ and I_+ , and the "two-phonon boron mode" results are denoted ω_- and I_- (see text). The frequency units are cm^{-1} .

Parameter	Experiment	Model
$\omega_+ (^{10}\text{B})$	1393.9 ± 0.2^b	1393.9
$\omega_+ (^{11}\text{B})$	1390.6 ± 0.2^b	1390.7
$\omega_- (^{10}\text{B})$	1347.8 ± 1.0^a	1347.9
$\omega_- (^{11}\text{B})$	1298.0 ± 1.0^a	1297.9
$I_-/I_+ (^{10}\text{B})$	0.03^a	0.080
$I_-/I_+ (^{11}\text{B})$	0.01^a	0.015

^aPresent work

^bB. Pajot, A. Chari, A. Aucouturier, M. Astier, and A. Chantre, Solid State Commun. **67**, 855 (1988).

vibration, for which the Fermi resonance contribution should be negligible. The remaining 2.1cm^{-1} shift is treated therefore as arising from the Fermi resonance. η was scaled according to the boron isotopic masses in Eq. (8) and the values $2\omega_B$ for the two boron isotopes were restricted to have the same ratio as observed experimentally for ω_B in the Raman studies). The fitting parameters for ω_D and $2\omega_B$ were 1389.8cm^{-1} and 1351.4cm^{-1} (for ^{10}B), respectively. This value for $2\omega_B$ is slightly smaller than twice the quoted value from the Raman studies [8] for the ^{10}B frequency ($2 \times 680\text{cm}^{-1}$) but probably well within the error bars of those measurements. On the other hand, we expect $2\omega_B$ to be somewhat smaller due to normal anharmonicity in the uncoupled boron mode. The coupling constant η is found to equal 12cm^{-1} (0.0015eV) for $^{10}\text{B-D}$, which corresponds to $k_3 = 3.9\text{eV/\AA}^3$. Values for molecules are often larger (eg., for CO_2 , $\eta = 50\text{cm}^{-1}$).

The close agreement in Table I, with reasonable values for the coupling and unperturbed eigen frequencies, clearly demonstrates that the Fermi resonance model fully explains the "anomalous" isotope shifts. A strong further confirmation comes from the effect of uniaxial stress on the ω_+ and ω_- transitions. In Fig. 5, we show dichroism quenched into the bands of the $\text{D-}^{10}\text{B}$ pair after applying uniaxial compressional stress at $T=80\text{K}$ and cooling with stress on to the measurement temperature, $T=15\text{K}$. The stress was then removed and the spectrum taken. As previously established for the stronger longitudinal D vibration (ω_+) [7], this arises from quenched-in alignment of the $\langle 111 \rangle$ pair axis induced by the stress at $\sim 80\text{K}$ where the defect is free to reorient. The identical dichroism for both the strong and weak bands seen in the figure confirms again that the two bands arise from the same defect. More importantly, it establishes that the polarization for exciting the weak two phonon transverse B vibration (ω_-) is the same as that for the one-phonon longitudinal D vibration (ω_+) from which it borrows its oscillator strength. This is a feature unique to the Fermi resonance model.

Finally, in the table we also list the predicted intensity ratios ($|C_D^-|^2/|C_D^+|^2$) for the ω_- and ω_+ transitions with the above fitting parameters. In this case, the predictions are somewhat greater than the experimentally estimated values, although they are clearly of the correct magnitude. Considering the simplicity of our limited 2×2 matrix model on the one hand, and uncertainty in the experimental estimates on the other,

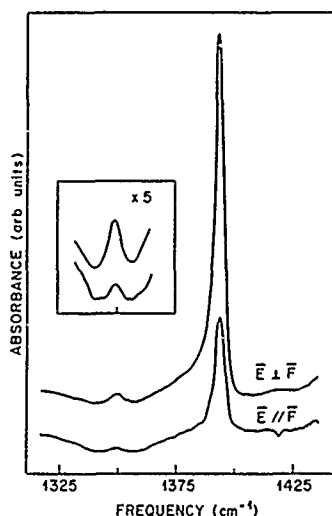


Fig. 5. Dichroism quenched into the $\text{D-}^{10}\text{B}$ spectrum after cooling from $T=80\text{K}$ with 39.5 kg/mm^2 compressional stress \vec{F} applied. The spectra were taken at $T=15\text{K}$ with stress removed. Here $\vec{F} \parallel [110]$, with the propagation of the light vector $\vec{k} \parallel [001]$.

this agreement must also be considered very good. In particular, there are often considerable uncertainties in estimating intensities of localized transitions on the background of strong free carrier absorption as is always the case in these experiments. The characteristic asymmetric Fano character of the lines [12] is evident in the figure and might affect the ω_+ and ω_- intensities differently due to different phonon-continuum coupling constants for the different modes involved. For example, it has been speculated that strong Fano coupling for the ω_B first harmonic is what prevents direct detection of this band in infrared absorption studies [13]. Strong coupling is evident also in the very broad lines ($\sim 20\text{cm}^{-1}$) for this band in the Raman studies [8]. Some of this may also be translated to its two phonon band.

The value that we have estimated for the anharmonic coupling coefficient k_3 ($3.9\text{eV}/\text{\AA}^3$) provides important new experimental information regarding the interactions among the constituent atoms of the defect. It is too large to arise simply through a single spring model as in Fig. 2(a), since it would predict a substantially larger value for the k_{HB} spring constant ($\sim 7\text{eV}/\text{\AA}^2$) than is consistent with the Pankove model. (The small 0.8 cm^{-1} ^{10}B - ^{11}B shift of the hydrogen vibration confirms that it is small.) Instead it probably arises from longer range coupling through the silicon matrix. As such it offers an important point for contact with computational theory. We have begun preliminary calculations using the MNDO cluster method to simulate the effect. So far, our estimates give $k_3 \sim 1\text{eV}/\text{\AA}^3$, too small but at least of the correct order of magnitude [14].

SUMMARY

The anomalous ^{10}B - ^{11}B isotope shift observed for the D vibration of the D-B pairs in silicon has been explained successfully in terms of a Fermi resonance arising from anharmonic coupling between the transverse B vibration and the longitudinal D vibration of the pair. The model predicts the appearance of otherwise forbidden two-phonon boron vibrational transitions which we have detected and found to have the appropriate intensities and polarization properties. In so doing, we have preserved the Pankove model of the H-B pair in silicon, and, in fact, strengthened it by supporting the identification of the boron vibrational modes, first detected by Raman studies, as transverse modes.

ACKNOWLEDGEMENTS

This work was supported by the U. S. Navy Office of Naval Research (Electronics and Solid State Sciences Program) under contract numbers N00014-84-K-0025 and N00014-89-J-1223. We gratefully acknowledge AT&T Bell Laboratories and L.C. Kimerling for the use of the Nicolet FTIR spectrometer, and A.X. Chu and K.J. O'Brien for computational contributions.

References

1. B. Pajot, A. Chari, A. Aucouturier, M. Astier, and A. Chantre, Solid State Commun. **67**, 855 (1988).
2. J.I. Pankove, P.J. Zanzucchi, C.W. Magee, and G. Lucovsky, Appl. Phys. Lett. **46**, 421 (1985).
3. E. Fermi, Z. Phys. **71**, 250 (1931).

4. See, for example, G. Herzberg, "Molecular Spectra and Molecular Structure II. Infrared and Raman Spectra of Polyatomic Molecules" (Van Nostrand, 1945), pp. 215-218, 266; L. Halonen, J. Phys. Chem. 93, 3386 (1989).
5. M. Stavola, S.J. Pearton, J. Lopata, and W.C. Dautremont-Smith, Phys. Rev. B 37, 8313 (1988).
6. K. Bergmann, M. Stavola, S.J. Pearton, and T. Hayes, Phys. Rev. B 38, 9643 (1988).
7. M. Stavola, K. Bergmann, S.J. Pearton, and J. Lopata, Phys. Rev. Lett. 61, 2786 (1988).
8. C.P. Herrero and M. Stutzmann, Phys. Rev. B 38, 12668 (1988).
9. B. Bech Nielsen, J.V. Andersen, and S.J. Pearton, Phys. Rev. Lett. 60, 321 (1988).
10. A.D. Marwick, G.S. Oehrlein, and N.M. Johnson, Phys. Rev. B 36, 4539 (1987).
11. For a recent review, see G.G. DeLeo and W.B. Fowler, in Hydrogen in Semiconductors, ed. by J.I. Pankove and N.M. Johnson, to appear as a volume in the Semiconductors and Semimetals series, ed. by R.K. Willardson and A.C. Beer (Academic Press, Boston).
12. U. Fano, Phys. Rev. 124, 1866 (1961).
13. R.C. Newman, private communication
14. G.G. DeLeo, K.J. O'Brien, and W.B. Fowler, unpublished.

OPTICALLY DETECTED MAGNETIC RESONANCE OF A HYDROGEN-RELATED COMPLEX DEFECT IN SILICON

W.M. CHEN*, O.O. AWADELKARIM*, B. MONEMAR**, J.L. LINDSTRÖM***, AND G.S. OEHRLEIN****

* Department of Physics and Measurement Technology, Linköping University, S-581 83 Linköping, SWEDEN

** Present address: Max-Planck-Institut für Festkörperforschung, Heisenbergstrasse 1, D-7000 Stuttgart 80, FRG

*** Swedish Defence Research Establishment, P.O. Box 1165, S-581 11 Linköping, SWEDEN

**** IBM Research Division, T.J. Watson Research Center, Yorktown Heights, N.Y. 10598 USA

ABSTRACT

We present for the first time an optically detected magnetic resonance (ODMR) study of a hydrogen-related defect in silicon. The defect is present in hydrogenated boron-doped silicon single crystals, after room-temperature electron-irradiation. A spin-triplet ($S=1$) is shown to be the electronic state responsible for the observed ODMR spectrum. An angular dependence study of the ODMR spectrum reveals a C_{2v} defect symmetry. The defect model is discussed in terms of a di-hydrogen-vacancy complex. The role of this defect as an efficient recombination channel (presumably non-radiative) for the non-equilibrium free carriers is also demonstrated.

INTRODUCTION

Hydrogen in semiconductors has recently received great attention, not only because of its fascinating physical properties, but also due to its technological importance [1]. The prevalence of hydrogen incorporation in silicon and the ability of hydrogen to passivate the electrical properties of shallow acceptors, donors and point defects are now well established [1-14], both from experimental investigations by a variety of techniques [2-10] and from extensive theoretical efforts [11-14]. Such studies by magnetic resonance techniques, which are particularly useful for a better understanding of the detailed electronic structure and direct microscopic identification of hydrogen-related defects, have been very limited so far [15].

In this paper, we report on microscopic identification and electronic structure of a hydrogen-related complex defect in silicon (denoted as HX below) by ODMR. Recombination processes of free carriers via this complex will also be discussed.

EXPERIMENTAL

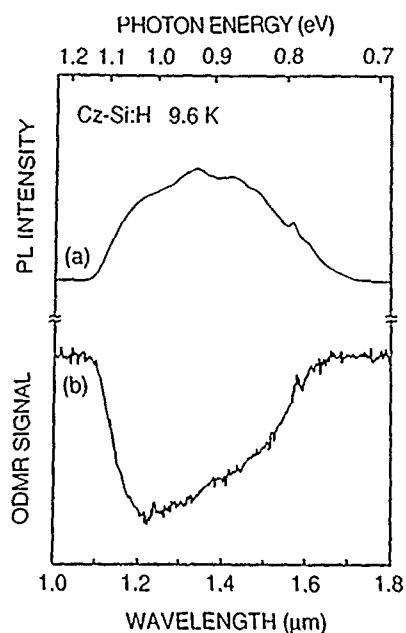
The ODMR experiments in this work were performed on a modified Bruker 200 D-SRC X-band spectrometer, equipped with an Oxford ESR 10 liquid helium continuous flow cryostat and a cylindrical TE_{011} microwave (MW) cavity with optical access from all directions. The sample temperature could be varied continuously down to about 2 K, with the aid of a second pump line. An Ar⁺-laser (5145 Å line) was employed for above bandgap optical excitation. The ODMR signal was collected by a North-Coast EO-817 Ge detector, sometimes via a Jobin-Yvon 0.25 m grating monochromator for spectral studies, and was lock-in detected in phase with the amplitude-modulated microwave radiation.

Boron-doped single crystalline silicon wafers (10-20 $\Omega\cdot\text{cm}$), grown by the Czochralski (Cz) method, were used in this work. Hydrogenation was performed by exposing the wafers to an H₂ plasma. The wafers were placed on the bottom electrode of a diode reactor where the top and the bottom electrode can be independently powered, as is commonly used for reactive ion and plasma etching [16]. The conditions during H₂ treatment were: (i) a 13.56 MHz rf power of 200 W applied to the bottom electrode, (ii) the H₂ pressure maintained at 400 mT, (iii) the sample temperature kept at 250°C, and (iv) the maximum ion energy reached was less than 200 eV. The treatment time for the wafers was 35 minutes. The samples cut from these wafers were then irradiated with 2.0 MeV monoenergetic electrons to a total fluence of $5.0 \times 10^{17} \text{ e}^-/\text{cm}^2$ at room temperature.

RESULTS AND DISCUSSION

A low temperature PL spectrum from such a sample is usually dominated by a number of

Fig.1 (a) PL spectrum from the Cz-Si:H samples after e⁻ irradiation, taken at 9.6 K. (b) Spectral dependence of the HX ODMR signal (as shown in Fig.2) taken at 9.6 K, showing that the ODMR signal can be detected via the entire spectral region shown in (a). The same spectral resolution was employed in both cases for easy comparison. The spectral response of the Ge-detector and the optical setup was not calibrated.



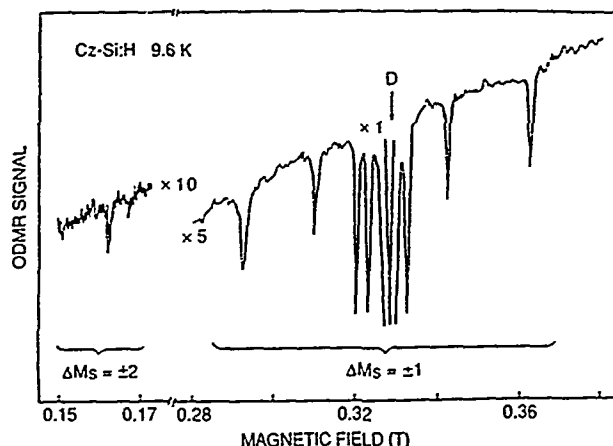


Fig.2 ODMR spectrum from the HX complex taken at 9.6 K. The central ODMR line, denoted as "D", is not related to the HX complex under study.

broad bands, as shown in Fig.1(a). The origin of these PL bands is not

completely understood yet and is currently under investigation. At least some of these PL bands have been argued to be related to electronic excitations localized at some extended defects such as hydrogen platelets [10]. The near band edge shallow boron-acceptor related bound exciton (BE) PL lines are observed to be very weak, indicating a passivation of the boron-acceptor by hydrogenation [8].

When placed in a MW cavity, the sample gave rise to a strong negative ODMR signal, which corresponds to a decrease in the PL emission. In Fig.2 we show such an ODMR spectrum, when the external static magnetic field B is close to the $[110]$ crystallographic axis.

To investigate the electronic structure and magnetic interactions of the HX complex, we have performed an angular dependence study of the ODMR spectrum when B is rotated in the (110) crystallographic plane. The experimental data have been analysed with the aid of a spin Hamiltonian given by [17],

$$H_S = \mu_B B \cdot g \cdot S + S \cdot D \cdot S + \sum_j I_j \cdot A_j \cdot S \quad \dots(1)$$

S is the effective electronic spin of the paramagnetic state of the HX complex where ODMR occurs. The first term in Eq. (1) describes the electronic Zeeman interaction in the presence of the external magnetic field B . The second term is terminologically denoted as the fine-structure term, representing the residual electronic and magnetic interactions of the defect (spin-orbit or magnetic dipole-dipole interactions) [17]. The last term is the so-called hyperfine (HF) structure term, describing the mutual interactions between the electronic spin and nuclear spins of the defect and ligand atoms. The higher order terms have not been included in Eq.(1) for simplicity. (They should be considered if e.g. $S > 1$ [17].) A satisfactory agreement between the theoretical expectations from Eq.(1) and the experimental results could be obtained only if a spin-triplet ($S=1$) state was assumed. The evaluated spin Hamiltonian parameters are given in Table I. (A spin-1 basis set of wavefunctions, $|S, M_S\rangle$ (where $S = 1$, $M_S = -1, 0, +1$) was

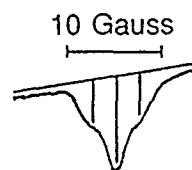
Table I. Spin Hamiltonian parameters for the HX complex of C_{2v} symmetry studied in this work. x, y and z denote the principal axes of the g- and D-tensor.

Principal axes of the HX complex	g-tensor	D-tensor (10^{-6} eV)	$A_j(^1\text{H})$ -tensor (10^{-6} eV)
x \equiv [001]	2.002 ± 0.001	-1.44 ± 0.02	~ 0.026
y \equiv [$\bar{1}\bar{1}0$]	2.005 ± 0.001	-1.25 ± 0.02	~ 0.024
z \equiv [110]	2.002 ± 0.001	2.69 ± 0.02	~ 0.029

employed in the diagonalization of Eq.(1) with the aid of a computer program.) The high-field ODMR lines shown in Fig.2 around $g \approx 2$ can be explained as arising from the $\Delta M_s = \pm 1$ MW-induced electronic transitions. However, the spectrum is complicated by many inequivalent sites of the same anisotropic HX complex of low symmetry at this specific magnetic field direction. The weak and nearly isotropic low-field ODMR lines are attributed to the formally forbidden $\Delta M_s = \pm 2$ electronic transitions, which is a signature of ODMR from a spin-triplet. This is the first case to our knowledge where the $\Delta M_s = \pm 2$ ODMR lines have been observed for a defect in silicon, which leads unambiguously to the electronic structure of a spin-triplet for the defect. This is not a surprising observation, however, such transitions are common e.g. for defects in GaP [18].

A partially resolved HF structure has been consistently observed in the HX ODMR spectrum, which displays a 1-2-1 HF intensity pattern when B is along the defect principal axes (Fig. 3 when $B \parallel z$). There are two possibilities to account for this observation. First, this may be contributed by HF interactions of ligand ^{29}Si atoms ($I=1/2$, 4.7% naturally abundant) from a number (10-12) of equivalent sites in the vicinity of the defect. Secondly, the HF structure may originate from two equivalent nuclear spins of $I=1/2$ with about 100% natural abundance. The only possible candidate for such species with appreciable concentration in the sample is then the ^1H atom ($I=1/2$ and 99.985% natural abundance). Previous electron paramagnetic resonance (EPR) studies have shown the HF interaction from distant ^{29}Si ligand atoms than the nearest neighbours is mostly isotropic [19]. This fact when contrasted to a slight but clear anisotropic HF structure in the HX ODMR spectrum (Table I), the second argument that two H atoms are incorporated in the HX complex seems to be more plausible. However, a definite distinction between the two models requires a future study in deuterium treated crystals. The need for e-irradiation in creating the

Fig.3 The HF structure from two ^1H atoms when $B \parallel z$. The stick diagram for the 1-2-1 HF structure pattern of two ^1H atoms is also shown as a guide for the eyes.



HX complex, on the other hand, strongly suggests that irradiation-induced defect(s) may also be involved as defect constituent(s). It is known that the primary damage products after electron-irradiation include vacancies (V), divacancies (V_2) and self-interstitials (Si_i) [20]. The HX complex we suggest is quite likely to be vacancy-related, based on the following reasons. First, at least 30% of the total wavefunction was estimated to be localized within the nearest neighbour shell as deduced from the experimentally observed ^{29}Si HF interaction ($A_j \sim 0.8 \times 10^{-6}$ eV), by using a one-electron linear-combination-of-atomic-orbitals (LCAO) method [19]. This is similar to previous observations in a vacancy-associated defect, possessing a very localized wavefunction [19]. Secondly, the g-value obtained for the HX center is within the category of vacancy-related defects [21]. A di-hydrogen-vacancy complex of a C_{2v} symmetry is, therefore, suggested to be the model of the HX defect, where the H atoms passivate two of the four dangling bonds of the monovacancy. The ODMR-active spin-triplet will, hence, arise from an excited state of the two-electron state in the neutral HX complex.

A spectral dependence study, as shown in Fig. 1(b), indicates that the negative ODMR signal (Fig. 2) corresponds to a decrease in the entire PL emission spectrum of various origins shown in Fig. 1(a) [10]. This suggests that the HX complex does not relate to any of these PL emissions, as further supported by the fact that no polarizations could be detected via these PL emissions in ODMR. Possible mechanisms responsible for the observation of the HX ODMR spectrum can be better understood by considering an indirect recombination process, such as inter-center energy transfer and competition between the HX complex and the PL centers in recombination or capture of free carriers [22]. The competition in capture of free carriers is presumably dominant in this case, since it requires no strong overlap between the wavefunctions of the ODMR center and the PL centers [22]. This recombination mechanism explains why the ODMR center can link to a number of the PL centers with various origin (Fig.1), which is otherwise difficult to be explained by other spin-dependent processes.

We are grateful to J.H. Svensson, J. Weber and J.W. Corbett for valuable discussions.

REFERENCES

1. S.J. Pearton, J.W. Corbett and T.S. Shi, Appl. Phys. **A43**, 153 (1987).
2. J.I. Pankove, D.E. Carlson, J.E. Berkeyheiser and R.O. Wance, Phys. Rev. Lett. **51**, 2224 (1983); S.J. Pearton, *ibid.*, **53**, 855 (1984); J.I. Pankove, D.E. Carlson, J.E. Berkeyheiser and R.O. Wance, *ibid.*, **53**, 856 (1984).
3. N.M. Johnson, Phys. Rev. **B31**, 5525 (1985).
4. K. Irmscher, H. Klose and K. Maass, J. Phys. **C17**, 6317 (1984).
5. S.T. Picraux and F.L. Vook, Phys. Rev. **B18**, 2066 (1978).

6. M. Stavola, S.J. Pearton, J. Lopata and W.C. Dautremont-Smith, Appl. Phys. Lett. 50, 1086 (1987); M. Stavola, K. Bergman, S.J. Pearton and J. Lopata, Phys. Rev. Lett. 61, 2786 (1988).
7. J.C. Mikkelsen, Jr., Appl. Phys. Lett. 46, 882 (1985).
8. M.L.W. Thewalt, E.C. Lightowers and J.I. Pankove, Appl. Phys. Lett. 46, 689 (1985).
9. M. Singh, J. Weber, T. Zundel, M. Konuma and H. Cerva, Mat. Sci. Forum 38-41, 1033 (1989).
10. H. Weman, J.L. Lindström and G.S. Oehrlein, presented at the E-MRS Spring Meeting, Strasbourg, France, 1989 (unpublished).
11. G.G. DeLeo, W.B. Fowler and G.D. Watkins, Phys. Rev. B29, 1819 (1984).
12. C.G. Van de Walle, Y. Bar-Yam and S.T. Pantelides, Phys. Rev. Lett. 60, 2761 (1988).
13. K.J. Chang and D.J. Chadi, Phys. Rev. Lett. 62, 937 (1989).
14. P.J.H. Denteneer, C.G. Van de Walle and S.T. Pantelides, Phys. Rev. Lett. 62, 1884 (1989).
15. Yu.V. Gorelkinskii and N.N. Nevinnyi, Sov. Tech. Phys. Lett. 13, 45 (1987).
16. J.W. Coburn, Plasma Etching and Reactive Ion Etching (American Vacuum Society Monograph Series, New York, 1982).
17. A. Abragam and B. Bleaney, Electronic Paramagnetic Resonance of Transition Ions (Clarendon Press, Oxford, 1970).
18. W.M. Chen, B. Monemar and M. Godlewski, in Defect and Diffusion Forum, Vol. 62/63, edited by H.J. von Bardeleben (Trans. Tech. Publications, Aedermannsdorf, 1989) p. 133.
19. G.D. Watkins and J.W. Corbett, Phys. Rev. 121, 1001 (1961).
20. G.D. Watkins, in Deep Centers in Semiconductors, edited by S.T. Pantelides (Gordon and Breach Science Publishers, New York, 1986) p. 147.
21. E.G. Sieverts, Phys. Stat. Sol. (b) 120, 11 (1983).
22. W.M. Chen, O.O. Awadelkarim, H. Weman and B. Monemar, Phys. Rev. B40, 10013 (1989).

HYDROGEN IN CRYSTALLINE AND AMORPHOUS SILICON

Guido L. Chiarotti^(a), F. Buda^(a), R. Car^(a), M. Parrinello^(a,b)

(a) - International School for Advanced Studies, Trieste, Italy

(b) - IBM Research Division, Zurich Research Laboratory, Rüschlikon, Switzerland

Abstract

We investigate static and dynamic properties of hydrogen in crystalline and amorphous silicon by means of *ab initio* molecular dynamics simulations. In the crystalline case we focus mainly on the diffusion process of an isolated positively charged hydrogen impurity at high temperature. In the amorphous case we analyze the local order and the dynamical properties corresponding to an atomic hydrogen concentration of $\sim 11\%$, typical of a device quality material. In both crystalline and amorphous cases, our results are in good agreement with available experimental data and give unique insight into the microscopic details of hydrogen incorporation in silicon.

INTRODUCTION

Hydrogen (H) can be incorporated in crystalline silicon (c-Si) up to equilibrium atomic concentrations of $\sim 10^{-7}$. Much larger concentrations are possible in amorphous silicon (a-Si) due to the presence of a disordered network. In this case the typical H concentration in the so called device quality materials is in the range $\sim 2 \div 15\%$. Despite the large difference in concentrations, H plays an equally important role in both c- and a-Si, due to its ability to passivate impurity-related states in c-Si [1], and to eliminate gap-states, thus making doping practical, in a-Si [2]. It is therefore no surprise that H incorporation in Si has been the object of extensive investigations in the last decade. In spite of that, our understanding of the phenomena associated to the presence of H in Si is far from being complete, particularly at the microscopic level. Some of the crucial questions that one would like to answer are the following: (i) what are the equilibrium locations of H, (ii) how do they correlate with the modifications induced by H in optical and vibrational spectra, and (iii) how can H diffusion be characterized microscopically.

We have investigated the above questions with *ab initio* molecular dynamics (MD) simulations [3]. In this method one computes numerically the atomic trajectories resulting from interatomic forces derived directly from the instantaneous electronic ground-state, which is treated with accurate density-functional techniques. The scheme is parameter-free and is particularly suited to describe systems, like covalent semiconductors, where chemical bonds may break and form as a consequence of the atomic motion. As usual in MD simulations, trajectories appropriate to different temperatures can be generated by changing the initial conditions for particle motion. In this way one can simulate thermal treatments, such as heating and cooling, or one can investigate processes occurring at finite temperature, such as atomic diffusion.

In this paper we report on recent progress made in simulations of H in both c- and a-Si. In the case of c-Si we have studied an isolated positively charged H impurity (H^+), for which we have calculated the $T = 0$ energetics at different lattice sites, the vibrational frequencies and the diffusion properties at high temperature ($T > 1000$ K).

Our calculated adiabatic total energy surface at $T = 0$ is in very good agreement with previous pseudopotential-density-functional calculations, showing that the energetically favoured site for H^+ is the bond-center (BC) site located midway between two neighbouring Si atoms in the region of high valence charge density. Similarly, the energetically favoured migration path for H^+ lies entirely in the high density region and is characterized by a very small activation energy, suggesting a fast diffusing character. However, static total energy calculations do not always allow an unambiguous determination of the diffusion path, due to the neglect of dynamical effects. These are fully taken into account in our MD simulations, where diffusion of H^+ at high T occurs spontaneously as a consequence of thermal motion. This allowed us to determine the migration path and to compute the diffusion coefficient, which turned out to be in excellent agreement with experimental data in the same temperature range. Interestingly, substantial differences compared to the $T = 0$ calculations were observed in the diffusion path as a consequence of dynamical effects.

The situation concerning H in a-Si is much less clear, due to the difficulty in a microscopic characterization of the disordered structure. As a consequence, accurate first-principles approaches could not be applied to a-Si until very recently, and one had largely to rely on phenomenological models. For instance, it has been suggested that H diffusion in a-Si is mediated by coordination defects [4], in a way similar to how vacancies and self-interstitials mediate impurity diffusion in c-Si. This and other qualitative predictions are still lacking a quantitative theoretical confirmation based on first-principles calculations. Clearly an accurate structural model for a-Si:H is a prerequisite for a microscopic theoretical investigation of the diffusion processes in this material. For this reason we have generated, with *ab initio* MD, a structural model of a-Si:H corresponding to an atomic H concentration of $\sim 11\%$, typical of a device quality material. The amorphous system was generated by quenching to room temperature a liquid Si sample containing an appropriate amount of H atoms. Average structural and dynamical properties of the computer generated system are in excellent agreement with experimental data. While in c-Si an H atom, sitting at a BC site forms a three-center bond with two neighbouring Si atoms, in a-Si H binds preferentially to a single Si atom that is otherwise threefold coordinated in the amorphous network. These so-called monohydride groups (SiH) are not uniformly distributed but show interesting clustering effects.

Some of the results presented here for H in c-Si were already reported in a previous publication, while most of the results referring to a-Si:H are new and are published here for the first time: they constitute a detailed structural model for H incorporation in a-Si. This can be considered as a first step toward a study of the diffusion process in the disordered amorphous network.

HYDROGEN DIFFUSION IN CRYSTALLINE SILICON

A controversial picture emerges from the available experimental data on the equilibrium sites and diffusivity of H in c-Si. Recently, however, some important advances were made by combined theoretical and experimental effort.

Equilibrium sites have been investigated by means of channeling experiments on implanted deuterium [5,6]. These results show a dependence on deuterium preferred sites from temperature of implantation and/or annealing treatment. In addition, the large amount of damage induced by the high energy implantation ($10 \div 13\text{KeV}$)

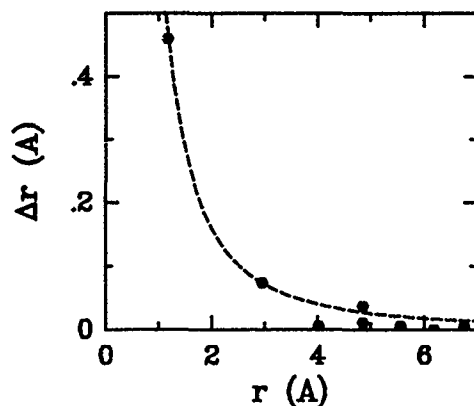


Figure 1:
Ionic displacements of Silicon atoms for H^+ located in the BC site vs. shell radius. All the reported shells are complete within our supercell. Dashed Line: $\frac{1}{r}$.

makes data interpretation difficult. Nevertheless, at low temperature in as-implanted samples, H appears to be mainly located at the Bond Center (BC) site [6]. Indirect support to the BC configuration comes from the Muon Spin Rotational Spectra for anomalous muonium recently presented by Kiefl et al. [7].

H diffusion coefficients have been measured with various techniques. At high temperatures ($T > 1000$ K), Van Wieringen and Warmoltz (VW) [8] found by direct permeability measurements that the diffusing species consisted mainly of atomic hydrogen, either neutral or positively charged. This was characterized by a very high mobility ($D \approx 2 \times 10^{-4} \text{ cm}^2/\text{sec}$ at $T \approx 1470$ K) and a thermal activation barrier of 0.48 eV within a 10% error. At lower temperatures, DLTS spectra [9] of H passivation of deep levels led to estimates of the diffusion coefficient that were orders of magnitude lower than the Arrhenius extrapolation of the VW data. Recently, however, diffusivity data at low T have been presented [10,11] that agree with the Arrhenius extrapolation of the VW results. These measurements confirm the high mobility of H in Si and suggest that a single Arrhenius behaviour can be roughly traced from room up to high temperature ($T > 1200$ K).

Theoretically, much of the effort has been devoted to study the energetically favoured sites for H at zero temperature on the basis of total energy calculations. In the most notable of these investigations [12] the fully relaxed adiabatic total energy surface for an isolated H impurity was parametrized for all H locations in the unit cell. One of the important results of this study is that H^+ (H^0) prefers to sit in regions of high valence charge density (HD) rather than in interstitial low density regions (LD). All the HD configurations are characterized by a large relaxation of the neighbouring Si atoms, in contrast to the LD configurations where only small distortions are induced. The BC site is the lowest energy configuration. A low energy path connecting adjacent BC sites through the intermediate C [13] site can be traced, lying entirely in the HD region: this was indicated in Ref. [12] as the most likely diffusion path for H in the neutral or the positively charged state.

It should be noticed that the above picture considers the H atom as a classical particle, whereas, in view of its small mass, possible quantum effects cannot be *a priori* neglected [14]. At high temperature the classical model is more justified. In this case, however, dynamical effects can substantially modify the picture resulting from $T=0$ calculations. All possible dynamical effects are included in MD simulations, where the main limitations are the assumption of classical dynamics and the finite simulation time (typically of the order of a few picoseconds). During such a short time, at high temperature, an H impurity in Si can travel distances of the order of several bond lengths and the diffusion process can be studied with sufficient accuracy using MD techniques.

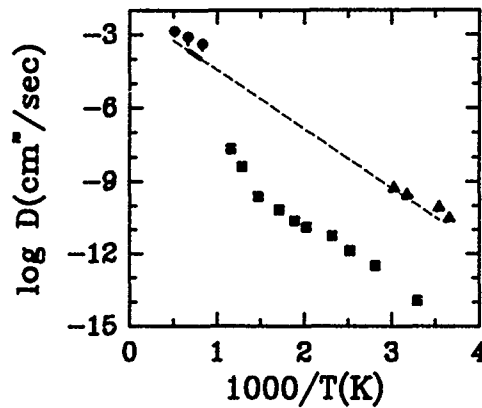


Figure 2:

Diffusion coefficient for hydrogen in c-Si as a function of inverse temperature. Solid circles: present calculation for H^+ . Error bars are indicated by vertical bars. Solid line: $D = 9.41 \times 10^{-3} \exp(-0.48 \text{ eV}/k_B T) \text{ cm}^2 \text{ sec}^{-1}$ as obtained by VW (see text) in the temperature range $1240 \div 1480 \text{ K}$; extrapolation outside this range is given by the dashed line. Squares: experimental data from ref. [9]. Triangles: experimental diffusivity values in Au Schottky barrier sample [10].

In our *ab initio* MD simulation of H in c-Si we focused on H^+ [15]. The H^+ charge state has been argued to be the dominant one, at least in p-doped material, both experimentally [10,11] and theoretically [12]. In our calculation we used a periodically repeated FCC supercell containing 128 Si atoms and one proton. The lattice constant was fixed at $a=5.43 \text{ \AA}$. Si was treated with norm-conserving pseudopotentials retaining s-nonlocality only, while H was treated as purely local. The electronic orbitals were expanded in plane waves with a cutoff of 6 Ry and the $k = 0$ point only was used for Brillouin zone sampling. As explained in Ref. [15] this choice of parameters gives a sufficiently accurate description of the H^+ energy surface, which is overall very similar to the one of Ref. [12] (the largest differences are of the order of $\sim 0.1 \text{ eV}$). In particular, we recover the distinction between HD and LD regions in the $T = 0$ total energy surface. The importance of lattice relaxation in the HD region is exemplified in Fig. 1 where we plot the relaxation of the various shells of Si atoms around an H^+ impurity located at the BC site.

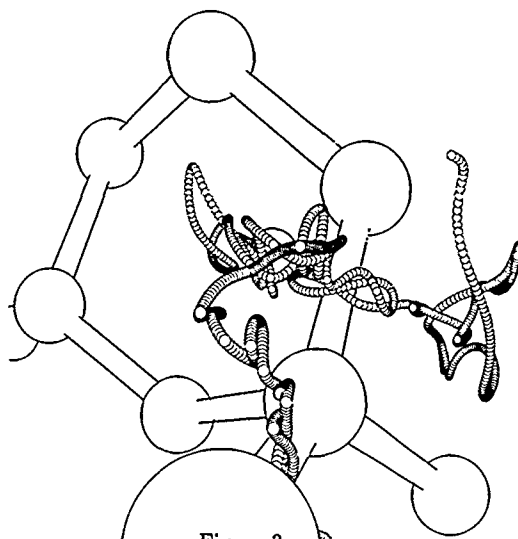


Figure 3:

H^+ trajectory at 1200K for about 0.7 psec. The large balls represent the silicon atoms in the perfect crystalline positions. The small balls correspond to the hydrogen position reported every $5 \Delta t$ ($\Delta t \approx 1.2 \times 10^{-16}$ sec). This represents the so called twofold-coordinated path (see text).

We have performed several MD runs at different temperatures higher than 1000 K. The proton diffusion coefficient D was obtained by measuring the mean square displacement. In Fig. 2 we report our results for D at three different temperatures, one of which would correspond to an overheated crystal. The agreement with the experimental VW data is remarkable, considering the uncertainties of both theory and experiment in addition to the fact that theory does not take into account presence of defects, possible molecular formation or other factors that could hinder the diffusion process.

An analysis of the diffusive path of the proton in the various MD runs reveals several interesting characteristics. In particular we find that the diffusion process proceeds via jumps between sites of high symmetry. Both high- and low-density regions are visited by the migrating particle, at variance with the predictions based on zero temperature calculations. More specifically we have detected, as the most likely, a path in which the proton jumps from a two-fold (BC, M [13]) coordinated site in the HD region to another one, using sites close to hexagonal (Hex) and/or tetrahedral (Td) in the LD region as intermediate ones (see Fig. 3).

We call this path the two-fold coordinated path indicating with this the fact that the proton spends most of its time in two-fold coordinated sites in the HD region. In other segments of the trajectory, the proton has been observed to follow a path lying completely in the LD region (see Fig. 4). This path proceeds via jumps from a near antibonding (AB) site (about 1.6 Å from a Si atom) to another one, going through Td or Hex sites. We call this the one-fold coordinated path since the proton spends most of its time in one-fold coordinated sites (AB). These two paths can alternate

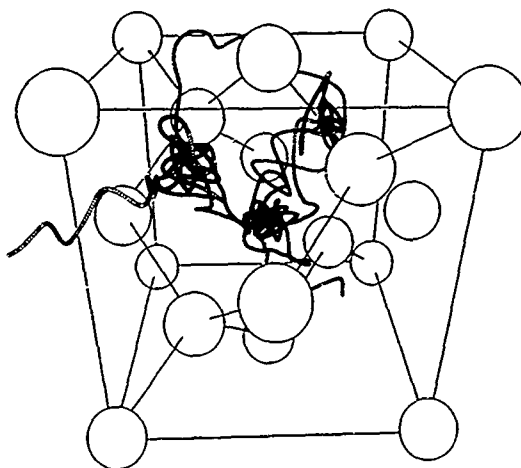


Figure 4:

H^+ trajectory at 1100K for about 1.9 psec. The large balls represent the silicon atoms in the perfect crystalline positions; only few bonds are shown. The small balls correspond to the hydrogen position reported every $5 \Delta t$ ($\Delta t \simeq 1.2 \times 10^{-16}$ sec). This represents the so called onefold-coordinated path (see text).

during the same simulation run. We are not able at this stage to give a precise estimate of the relative occurrence frequency of the two paths, although on the base of the statistics accumulated in about ten MD runs, we can state that the two-fold path occurs more frequently. Interestingly, the diffusion coefficient calculated along segments of the trajectory belonging to the one-fold path is, within the error bars, essentially the same as the one corresponding to the two-fold path.

The reason why the proton does not follow the strictly HD path resulting from $T=0$ calculations, can be traced to the large difference in mass between H and Si. When the H^+ motion is fast, as it is the case at these high temperatures, the heavy Si ions cannot follow adiabatically the proton. Thus the lattice may not have the time to undergo the large relaxation needed for the HD sites to become energetically favourable. When this happens the proton prefers to move through regions of low energy for the undistorted lattice. This explains the observation of the one-fold coordinated path.

The two paths are characterized by a significant difference in the vibrational frequencies associated to the proton. These can be extracted from the velocity autocorrelation function $Z(t)$ of the proton. We report in Fig. 5 the power spectra of $Z(t)$ for H^+ diffusing in the one-fold and in the two-fold paths respectively. In the same picture we also show the spectrum computed for silicon which closely reproduces the measured phonon density of states of the pure system [16]: in particular the transverse acoustical (TA) and transverse optical (TO) bands are well described. In the spectrum corresponding to the one-fold path there are three prominent peaks: the first two are resonances with TA and TO modes of the host lattice, the third one could be associated to the motion of a proton in the AB site. Similar frequencies, identified as bending modes, are observed in a-Si:H [17] ($\omega \simeq 78$ meV $\simeq 630$ cm $^{-1}$).

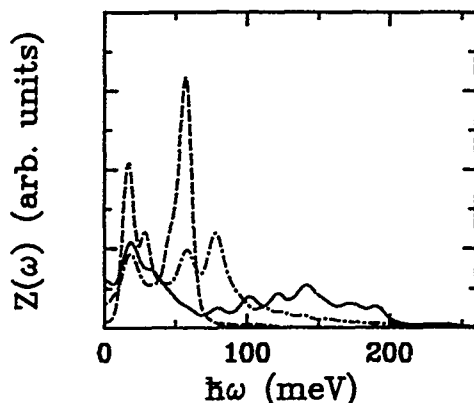


Figure 5:
Phonon density of states at ≈ 1000 K. Dashed line: silicon. Dash-dotted line: H^+ in the "one-fold" path (see text). Solid line: H^+ in the "two-fold" path (see text).

In the case of the two-fold path, higher frequency components appear. At the same time the resonance with the TO peak disappears, which is not unreasonable, since an H^+ at a BC site breaks a Si-Si bond and strongly modifies its stretching vibration. The highest frequencies ($\omega \approx 200 \text{ meV} \approx 1600 \text{ cm}^{-1}$) are most likely due to stretching modes of hydrogen in the HD region. The frequency $\omega \approx 1600 \text{ cm}^{-1}$ is lower than the value $\omega \approx 2200 \text{ cm}^{-1}$ obtained in Ref. [18] for H^+ in the BC site with a frozen phonon calculation. The difference can be explained partly with anharmonic effects, that are present at finite T , and partly because in our simulation we measure an average frequency corresponding to several HD configurations and not only to the BC site. The remarkable differences in the vibrational spectra associated to the one-fold and the two-fold path led us to suggest that scattering experiments could distinguish between the two situations.

THE STRUCTURE OF HYDROGENATED AMORPHOUS SILICON

A review of experimental results on the structure of a-Si:H, has been recently presented by Elliott [19]. Here we just mention a few results that will be used in the following in connection with our calculations. Since a-Si:H is a binary system, three partial pair correlation functions (Si-Si, H-Si, H-H) are needed to describe the average short-range order (SRO). These partial correlation functions have been extracted from elastic neutron scattering experiments performed on sputtered a-Si:(H,D) [20,21]. Inelastic neutron scattering experiments have also been performed to study the vibrational density of states (VDOS) of pure [22,23] and hydrogenated a-Si [22]. Due to the very large and primarily incoherent neutron scattering cross-section of H, Si-related VDOS could be observed only in pure and not in hydrogenated a-Si samples. Vibrational frequencies associated to H have been identified by means of infrared-spectroscopy (see, e.g. the review by Lucovsky and Pollard in ref. [2]). In particular peaks of the infrared spectrum have been associated to several Si-H structural groups,

namely monohydride (Si-H), dihydride (Si-H₂) and even "polysilane" groups (Si-H₂)_n.

Previous studies have demonstrated that the *ab initio* MD method allows to generate very accurate structural models of disordered semiconductors. In particular, pure Si both in the liquid and in the amorphous state has already been extensively investigated [24]. In the present simulation of a-Si:H, we considered a SC supercell containing 64 silicon atoms initially arranged in the perfect crystalline positions, and 8 (neutral) hydrogen atoms located at different interstitial sites. This corresponds to about 11% at. H concentration. The volume of the box was fixed at the experimental value of c-Si. We used the same parameters adopted for c-Si:H except that the plane wave cutoff was now taken to be 12 Ry. This value is necessary for an accurate description of liquid Si [25]. The box used in our simulation allows to describe correlations up to distances of $\approx 5.4\text{\AA}$, enough to describe SRO in the system.

The amorphous structure was generated with the following procedure. We heated up the system to a temperature of about 2000K at which it reached the liquid state. We let the liquid equilibrate for more than 1psec and then we quenched the system to 300K using a cooling rate of about $2. \div 5. \times 10^{14}\text{K/sec}$. After equilibration for about 1.5 psec, we performed an additional annealing cycle in which the temperature was raised up to $\approx 1100\text{K}$. Finally, we performed a new quench to 300K with the same cooling rate as before. The entire annealing cycle took about 3 psec. The final structure was equilibrated for ≈ 2 psec.

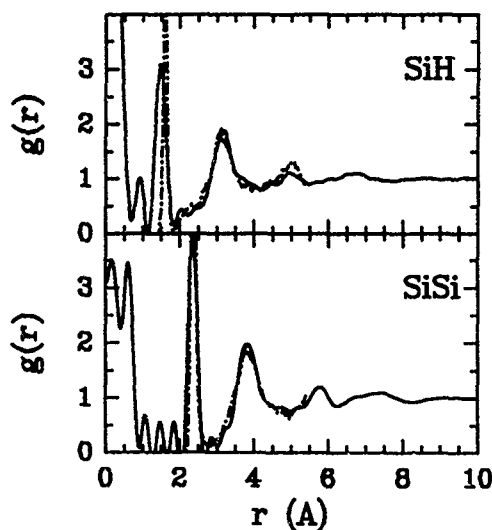


Figure 6:
Partial Pair Correlation Functions in a-Si:H. Full lines: Experimental data from ref. [21].
Dash-dotted lines: Present calculation.

The agreement of the computer generated structure with experiment is rather remarkable, as can be seen in Fig. 6, where we report the two partial pair correlation functions g_{SiSi} and g_{SiH} . The theoretical correlation functions are plotted up to the

maximum correlation length allowed by the simulation box. The experimental data correspond to a sample with an H content very close to the one of the simulation. The Si-Si partial correlation function reflects the local tetrahedral order characteristic of the material. It has a well defined first peak at a distance $r_1 \simeq 2.35 \text{ \AA}$, with a coordination number $N_1 \simeq 3.9$. In agreement with experiment [20], this is slightly smaller than the value of 4 corresponding to a perfect tetrahedral network. The Si-H partial correlation function is also characterized by a sharp first peak occurring at $r_1 \simeq 1.59 \text{ \AA}$ and corresponding to singly bonded Si-H units with a well defined bond length. Notice that the position of the theoretical peak is slightly shifted outward compared to experiment: the difference is of the same order and sign of the error resulting in the equilibrium bond length of the SiH molecule when using the same plane-wave and pseudopotential parameters of the present simulation. Only monohydride (Si-H) and no dihydride (Si-H₂) groups are found in the simulation, in agreement with experiment, according to which the occurrence of dihydride groups should be quite rare, in this regime of H concentrations [21]. In almost all the cases the Si atom close to H is bonded to three other Si atoms only, confirming that H saturates dangling bonds.

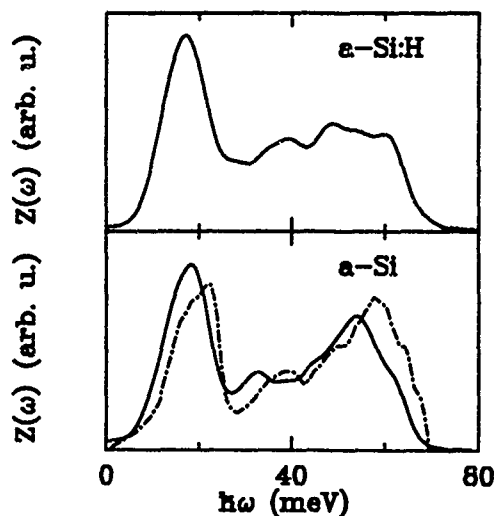


Figure 7:

Lower panel: Vibrational Density of States in a-Si. Full line: *Ab initio* Molecular Dynamics simulation [24]. Dash-dotted line: Experimental data from ref [23]. Upper panel: Calculated Silicon-related Vibrational Density of States in a-Si:H.

We do not report a plot of the H-H pair correlation function, which shows a large statistical noise due to the rather small number (8) of H atoms in our sample. The most notable feature of the computed g_{HH} is a rather broad first peak around $2-3 \text{ \AA}$, in qualitative agreement with neutron scattering results. This constitutes evidence for H clustering. A more detailed analysis of the clusters present in our sample reveals that there are two small clusters, each containing four H atoms. In one of them

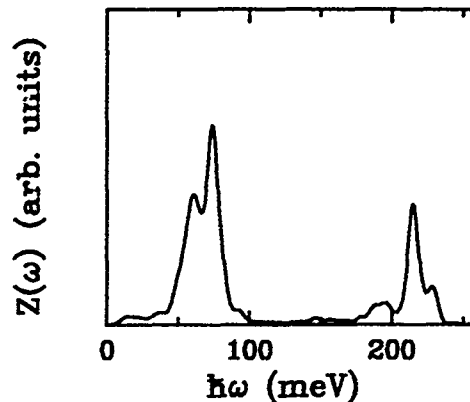


Figure 8:
Calculated Hydrogen-related Vibrational Density of States in a-Si:H.

the atoms occupy the edges of a distorted square in a quasi-planar configuration, in the other one three atoms form an almost equilateral triangle with the fourth atom lying on the extension of one side of the triangle. H clustering is seen in many experiments on a-Si:H. In particular, recent multiple-quantum NMR studies [26] have suggested the existence of clusters consisting mainly of a number of H atoms ranging from four to seven. We note that H clustering may be induced from the underlying disordered network, since some of its characteristic features have similarities with defect clustering in pure a-Si. This point deserves further investigation.

The vibrational properties of a-Si:H are very interesting. In our simulation we compute the VDOS from the Fourier spectrum of the particle velocity autocorrelation function. By treating separately Si and H atoms, we obtain the relative contributions to the VDOS due to Si and H respectively.

We report in Fig. 7, in the upper panel, the Si-related VDOS. In the same figure, in the lower panel, we report the recent experimental data of Ref. [23], together with the results of an *ab initio* MD simulation of pure a-Si [24], showing very good agreement with the experimental data. The VDOS displays four main features that correspond to the four major peaks in the phonon density of states of c-Si at 20, 40, 50 and 60 meV, conventionally referred to as TA, LA, LO, and TO modes [23] respectively. Compared to pure a-Si, the main characteristics of the hydrogenated sample appears to be a strongly reduced intensity in the TO peak. This is probably an effect induced by H whose presence affects the stretching vibrations of the neighbouring Si atoms. Indeed, by calculating the VDOS corresponding only to the Si atoms not belonging to Si-H units, we observe an enhancement of the TO peak. Unfortunately, as mentioned before, the Si-related VDOS in a-Si:H cannot be measured directly with neutron scattering. However, far-infrared absorption spectra of pure and hydrogenated a-Si with different H concentrations [27] show a reduction of the intensity in the TO peak with increasing H concentration, consistent with our findings.

H-related frequencies in a-Si:H have been extensively studied with infrared spectroscopy [2]. The infrared bands around 630 cm^{-1} (78 meV) and 2000 cm^{-1} (248 meV)

have been unambiguously identified with the bond-bending and the bond-stretching modes of the monohydride groups. The band around 900 cm^{-1} (111 meV) has been assigned to the scissor bending mode of (Si-H₂) units. In Fig. 8 we report the H-related VDOS in our sample. Bending and stretching modes of the Si-H units are evident. Consistently with the absence of (Si-H₂) units in our sample, the band around 900 cm^{-1} is absent from the VDOS. Compared to experiment, the stretching frequencies are underestimated by about 10%, while the bending frequencies are only underestimated by about 5%. We notice that, using the same parameters of the MD simulation, we also get an error of about 10% toward lower frequencies in the vibrational mode of the SiH molecule. The width of the stretching band in the simulation is a consequence of the spread in the bond lengths of the Si-H units. In particular, we have found that there is a linear correlation between Si-H distances and stretching frequencies.

In conclusion, for all the properties considered so far, the agreement between theory and experiment is rather encouraging. Further work to better characterize the microscopic structure of a-Si:H is currently underway. The study reported here constitutes also a first step toward the investigation of the H diffusion processes in a-Si.

This work has been supported by the collaborative project SISSA-CINECA, under the sponsorship of the Italian Ministry for Public Education, and by the European Research Office of the U.S. Army.

References

- [1] See, for instance, S. J. Pearton, J. W. Corbett and T. S. Shi, *Appl. Phys. A* **43**, 153 (1987)
- [2] See, for instance, *The Physics of Hydrogenated Amorphous Silicon*, edited by J. D. Joannopoulos and G. Lucovsky, Springer-Verlag, 1984
- [3] R. Car and M. Parrinello, *Phys. Rev. Lett.* **55**, 2471 (1985)
- [4] S. T. Pantelides, *Phys. Rev. Lett.* **58**, 1344 (1987)
- [5] S. T. Picraux and F. L. Vook, *Phys. Rev. B* **18**, 2066 (1978)
- [6] B. Bech Nielsen, *Phys. Rev. B* **37**, 6353 (1988)
- [7] R. F. Kiefl, M. Celio, T. L. Estle, S. R. Kreitzman, G. M. Luke, T. M. Riseman and E. J. Ansaldo, *Phys. Rev. Lett.* **60**, 224 (1988)
- [8] A. Van Wieringen and N. Warmoltz, *Physica* **22**, 849 (1956)
- [9] S. J. Pearton, *J. Electron. Mater.* **14a**, 737 (1985)
- [10] C. H. Seager and R. A. Anderson, *Appl. Phys. Lett.* **53**, 1181 (1988)
- [11] A. E. Jaworowski, *Radiation Effects and Defects in Solids*, to appear
- [12] C. G. Van de Walle, Y. Bar-Yam and S. T. Pantelides, *Phys. Rev. Lett.* **60**, 2761 (1988)

- [13] M individuates a two-fold coordinated site located midway of the axis connecting the bond-center with the nearest hexagonal site; C individuates a site located midway of the axis connecting two adjacent M sites.
- [14] H. R. Schober, and A. M. Stoneham, *Phys. Rev. Lett.* **60**, 2307 (1988)
- [15] F. Buda, G. L. Chiarotti, R. Car and M. Parrinello, *Phys. Rev. Lett.* **63**, 294 (1989)
- [16] W. Weber, *Phys. Rev. B* **15**, 4789 (1977)
- [17] G. Lucovsky, R. J. Nemanich, J. C. Knights, *Phys. Rev. B* **19**, 2064 (1979)
- [18] C. G. Van de Walle, P. J. H. Denteneer, Y. Bar-Yam and S. T. Pantelides, *Phys. Rev. B* **39**, 10791 (1989)
- [19] S. R. Elliott, *Advances in Physics* **38**, 1 (1989)
- [20] R. Bellisent, A. Chenevas-Paul, P. Chieux and A. Menelle, *J. Non-Crystalline Solids* **77-78**, 213 (1985)
- [21] A. Menelle, Ph.D. thesis, Paris (1987)
- [22] W. A. Kamitakahara, H. R. Shanks, J. F. McClelland, U. Buchenau, F. Gompf, and L. Pintchovious, *Phys. Rev. Lett.* **52**, 644 (1984)
- [23] W. A. Kamitakahara, C. M. Soukoulis, H. R. Shanks, U. Buchenau, G. S. Grest, *Phys. Rev. B* **36**, 6539 (1987)
- [24] F. Buda, G. L. Chiarotti, I. Stich, R. Car and M. Parrinello, *J. Non-Crystalline Solids*, to appear
- [25] I. Stich, R. Car and M. Parrinello, *Phys. Rev. Lett.* **63**, 2240 (1989)
- [26] J. Baum *et al.*, *Phys. Rev. Lett.* **56**, 1377 (1986)
- [27] S. C. Shen, C. J. Fang, M. Cardona, and L. Genzel, *Phys. Rev. B* **22**, 2913 (1980)

HYDROGEN DIFFUSION IN BORON-DOPED SILICON

C.P. HERRERO*, M. STUTZMANN**, AND A. BREITSCHWERDT**

* Instituto de Ciencia de Materiales, Serrano 115 dpdo, 28006 Madrid, Spain

** Max-Planck-Institut für Festkörperforschung, Heisenbergstrasse 1, D-7000 Stuttgart 80, Federal Republic of Germany

ABSTRACT

Infrared reflectance spectroscopy is employed to obtain hydrogen depth profiles in boron-doped silicon, hydrogenated under various plasma conditions. From the obtained profiles, H-diffusion coefficients are calculated for different temperatures and dopant concentrations. Our results are interpreted by assuming that diffusion in the bulk is limited by trapping at the acceptor sites. A binding energy of 0.6 eV is deduced for B-H pairs. We also analyze the influence of a bias applied to the sample on the hydrogenation process. This sample bias can favor or completely hinder the diffusion of hydrogen into the silicon bulk. Also, a surface oxide layer can drastically inhibit the hydrogen in-diffusion.

INTRODUCTION

The diffusion of hydrogen in crystalline silicon has been studied in the last years in several experimental and theoretical investigations.^{1,2} In particular, experimental work has provided evidence for an influence of doping on the diffusion of hydrogen, notably in p-type silicon.^{3,4,5} This dependence may be due to a Fermi-level effect, as discussed by Capizzi and Mittiga,⁶ who proposed that H in B-doped silicon is present in two charge states (H^0 and H^+) with rather different diffusion coefficients. A second possibility is the influence of complex-formation, namely B-H pairs, on the diffusivity of hydrogen in boron-doped Si. This effect is investigated in the present paper.

In addition to the bulk conductivity, surface conditions play also an important role for the hydrogen diffusion into a silicon sample. Thus, a good knowledge of the surface barrier created by different oxide layer thicknesses is crucial for a characterization of the hydrogenation process. External plasma conditions can also favor or hinder the hydrogen in-diffusion.

EXPERIMENT

In our experiments, we have used B-doped Si specimens with dopant concentrations between 1×10^{19} and $1.2 \times 10^{20} \text{ cm}^{-3}$. Samples were hydrogenated via a remote H_2 glow discharge plasma (see Fig. 1) at temperatures in the range 90-210°C and at a gas pressure of 1.5 mbar. Our passivation apparatus contains three electrodes (A, B, and C). Electrodes A and B are located at one end of the tube, where dissociation of the incoming H_2 molecules is achieved by applying a voltage U_P of 800-1000 V across these two electrodes. Crystalline silicon samples are situated ~ 10 cm downstream from the DC plasma on a heatable sample-holder, which acts also as a third electrode, C. A variable voltage U_B , called hereafter "sample bias", can be applied between electrodes B and C.

Hydrogen depth profiles were obtained from reflectance spectra of the treated Si specimens. This is a well established method to obtain depth profiles of hydrogen in semiconductors.⁷ The reflectance spectra were recorded at room temperature in the far-infrared region between 200 and 4000 cm^{-1} . A mirror was used as reference for the reflexion, and a sample region of about 0.5 cm^2 was probed by the infrared beam.

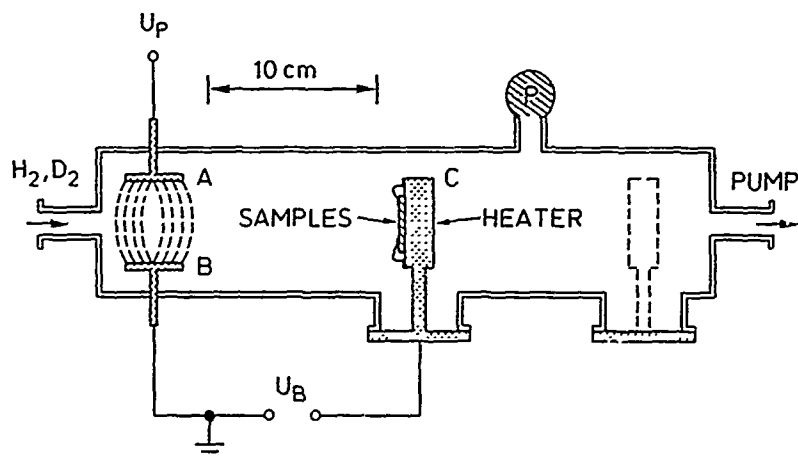


Fig. 1. Schematic diagram of the apparatus used for the hydrogenation of the silicon samples studied in this work.

RESULTS AND DISCUSSION

Hydrogen profiles

For the B-doped samples, the free carrier plasma edge is observed in the infrared reflectance spectra at a frequency ω_p proportional to the square root of the free hole density. After hydrogenation, a shift of the plasma edge to lower wavenumbers is observed, corresponding to a decrease of the free hole concentration, as expected for a hydrogen-passivation of the boron acceptors.⁸ Also, an interference pattern appears in the IR spectra of the

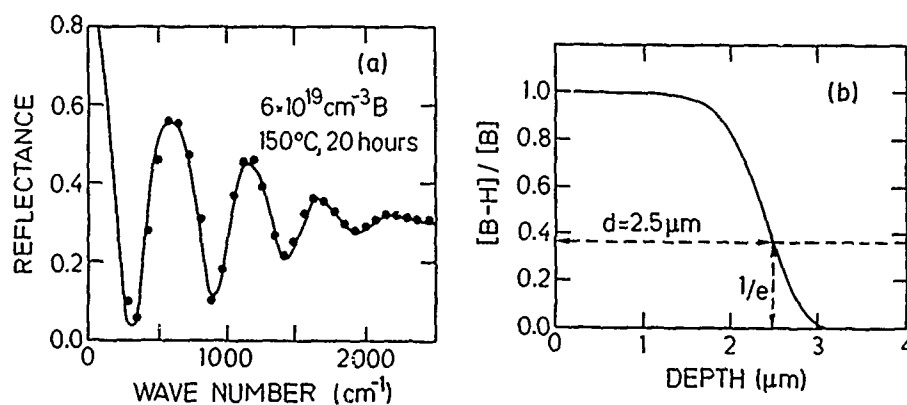


Fig. 2. (a) Experimental (points) and calculated (continuous line) infrared reflectance spectra of hydrogenated boron-doped silicon. (b) Boron-hydrogen complex depth profile used to obtain the calculated spectrum in (a).

hydrogenated specimens (see Fig. 2.a), which allows us to calculate the thickness of the passivated surface region. From a fit to the experimental spectra, one can obtain the passivation depth for silicon samples hydrogenated under different conditions. A typical fit along with the corresponding B-H complex profile is shown in Fig. 2. More details about the fitting method are given elsewhere.^{7,9}

The obtained H-profiles show a well defined plateau at the acceptor concentration followed by a rapid drop of the H concentration in all cases. These profiles are in agreement with those deduced for deuterium by Secondary Ion Mass Spectroscopy (SIMS), with the exception of a peak that appears near the surface in the SIMS profiles.¹⁰ It is currently believed that this peak is due to H (or D) atoms present at extended defects in the material or as molecular H₂.¹¹ In the highly doped specimens used in this study, we know from Raman scattering that the concentration of other forms of bound hydrogen is much lower than that of B-H complexes in the near surface region of the samples studied here.

Bias dependence of the penetration depth

In Fig. 3, we show the influence of sample bias and oxide layer thickness on the efficiency of the passivation process as measured by the achieved passivation depth. All samples ($[B] = 2 \times 10^{19} \text{ cm}^{-3}$) were hydrogenated during 15 hours at constant temperature and gas pressure. The oxide layer thicknesses were determined prior to hydrogenation by means of spectroscopic ellipsometry.¹² The two curves in Fig. 3 were obtained for two different oxide layer thicknesses: a "natural" layer thickness of about 20 Å (curve (a), solid points), and an enhanced thickness of about 100 Å obtained after a 500°C anneal (curve (b), open circles). From this picture, it is clear that positive voltages of $U_B \sim +100 \text{ V}$ are sufficient to suppress the acceptor passivation. For negative bias voltages applied to samples with the thin oxide layer, one finds a saturation of the passivation depth at $\sim 3 \mu\text{m}$ for $U_B > -50 \text{ V}$. The curve (b), obtained for the thicker oxide layer, is similar to curve (a), but shifted towards negative bias voltages by $\sim 150 \text{ V}$, and still covers the same range of attainable passivation depths.

These results indicate that hydrogen passivation occurs mainly not via a neutral atomic H, but via a positively charged plasma species, which can be H_2^+ , since at gas pressures of about 1 mbar pure protons are likely to react with neutral H or H₂ molecules (for example: $\text{H}^+ + \text{H}_2 \rightarrow \text{H}^0 + \text{H}_2^+$) along their way between the plasma region and the Si sample. The pronounced effect of thin oxide layers on the bias voltage dependencies is not understood at present. One possible explanation is that the passivating species must have a minimum kinetic energy in order to cross the oxide layer.

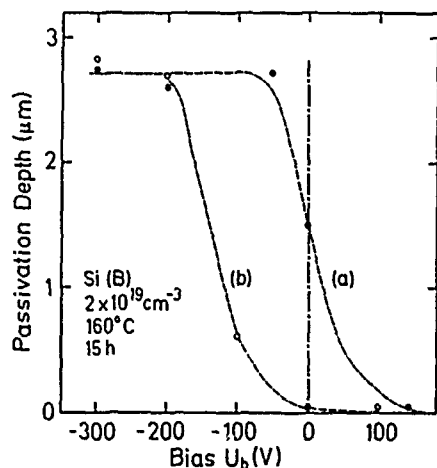


Fig. 3. Dependence of the hydrogen penetration depth in boron-doped silicon on the bias applied to the sample during hydrogenation. Black points (curve a) correspond to samples with a surface oxide-layer thickness of 20 Å, and open circles (curve b) to samples with an oxide thickness of 100 Å.

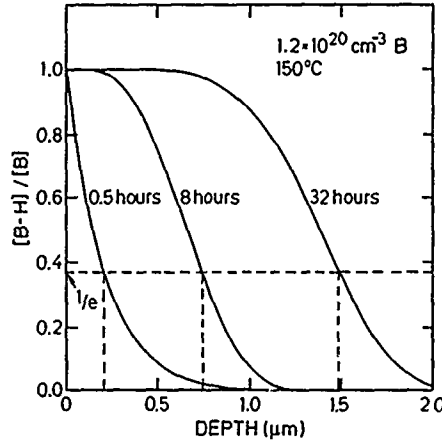


Fig. 4. Depth profiles of boron-hydrogen pairs obtained from infrared reflectance spectra for silicon samples hydrogenated during different exposure times.

Trap-limited hydrogen diffusion

In Fig. 4, we present the B-H pair profiles obtained for silicon specimens with the same boron concentrations, passivated under the same plasma conditions (150°C, 1.5 mbar, zero sample bias) for different hydrogenation times (All samples considered in this section contain a "natural" oxide layer of about 20 Å). One finds that the penetration depth of hydrogen increases as the square root of the exposure time, as expected for a diffusion process. Thus, one can obtain effective diffusion coefficients D_{eff} for hydrogen by using the expression $d = \sqrt{D_{eff}t}$, (t , hydrogenation time). To the extent that stable B-H complexes are formed, the hydrogen diffusion has to be affected by the presence of the acceptors in the bulk. The effective diffusion coefficient D_{eff} can then be obtained from the diffusion coefficient D in a pure silicon crystal by means of the equation^{9,13}

$$D_{eff} = D \left[1 + r[B] \exp \left(\frac{E_B}{kT} \right) \right]^{-1}, \quad (1)$$

where E_B is the binding energy of the B-H complex, and the coefficient D is given by an Arrhenius expression

$$D = D_0 \exp \left(-\frac{E_M}{kT} \right). \quad (2)$$

E_M is an activation energy for hydrogen migration in pure silicon. The parameter r plays the role of an effective pre-exponential factor in Eq. (1), and is considered here as a fitting parameter. More details are published elsewhere.⁹

We have measured the dependence of D_{eff} on boron concentration and on temperature. The experimental results are summarized in Fig. 5 along with a fitting to Eq. (1). This equation gives the correct dependence for D_{eff} as a function of both, dopant concentration and temperature. The extrapolated diffusion coefficient for hydrogen in pure silicon, $D(150^\circ\text{C}) = 1.9 \times 10^{-12} \text{ cm}^2 \text{ s}^{-1}$, is in agreement with experimental measurements on low defect density silicon at this temperature.¹ For the binding energy of B-H complexes we obtain a value $E_B = 0.6 (\pm 0.1) \text{ eV}$.

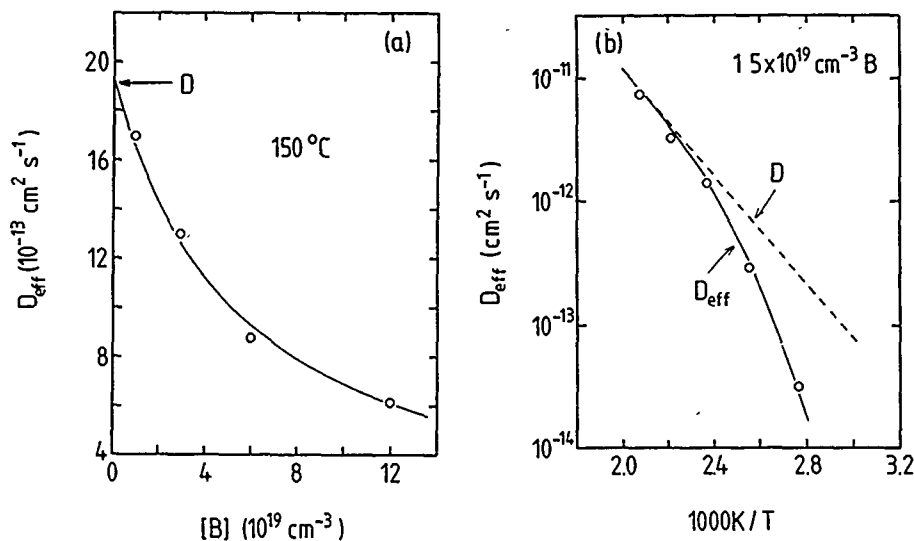


Fig. 5. (a) Boron-concentration dependence of the effective hydrogen diffusion coefficient D_{eff} at 150°C . (b) Temperature dependence of D_{eff} for 1.5×10^{19} boron atoms cm^{-3} . Continuous lines are fits to Eq. (1), with $E_B = 0.6 \text{ eV}$ and $r = 7 \times 10^{-5}$. D is the H-diffusion coefficient in undoped silicon. The dashed line in (b) corresponds to Eq. (2) with $D_0 = 2.4 \times 10^{-7} \text{ cm}^2 \text{ s}^{-1}$, $E_M = 0.43 \text{ eV}$.

REFERENCES

1. S.J. Pearton, in *Proc. 13th Int. Conf. Defects in Semicond.*, edited by L.C. Kimerling, and J.M. Parsey, Jr. (Metallurgical Soc. AIME, Warrendale, PA, 1985) 14a, 737.
2. C.G. Van de Walle, P.J.H. Denteneer, Y. Bar-Yam, and S.T. Pantelides, *Phys. Rev. B* 39, 10791 (1989).
3. J.I. Pankove, D.E. Carlson, J.E. Berkeyheiser, and R.O. Wance, *Phys. Rev. Lett.* 51, 2224 (1983).
4. J.C. Mikkelsen, Jr., *Appl. Phys. Lett.* 46, 882 (1985).
5. J.W. Corbett, J.L. Lindström, and S.J. Pearton, in *Defects in Electronic Materials*, edited by M. Stavola, S.J. Pearton, and G.A. Davis (Mater. Res. Soc. Proc. 104, Pittsburgh, PA 1988) pp. 229-239.
6. M. Capizzi and A. Mittiga, *Appl. Phys. Lett.* 50, 918 (1987).
7. L.L. Liou, W.G. Spitzer, J.M. Zavada, and H.A. Jenkinson, *J. Appl. Phys.* 59, 1936 (1986).
8. M. Stutzmann, *Phys. Rev. B* 35, 5921 (1987).
9. C.P. Herrero, M. Stutzmann, A. Breitschwerdt, and P.V. Santos, *Phys. Rev. B*, in press.
10. N.M. Johnson, *Phys. Rev. B* 31, 5525 (1985).

11. N.M. Johnson, F.A. Ponce, R.A. Street, and R.J. Nemanich, *Phys. Rev. B* **35**, 4166 (1987).
12. D.E. Aspnes and A. Studna, *Phys. Rev B* **27**, 985 (1983).
13. P.A. Fedders, *Phys. Rev. B* **16**, 4769 (1977).

MODELING OF THE DIFFUSION OF HYDROGEN IN SILICON

D. MATHIOT*, D. BALLUTAUD**, P. DE MIERRY**, and M. AUCOUTURIER**

* CNET-CNS, BP. 98, 38243 Meylan Cédex, France

** Laboratoire Physique des Solides, CNRS, 1, place A. Briand, 92135 Meudon Principal, France

ABSTRACT

A model is proposed to describe hydrogen motion in silicon near 150°C. This model leads to a consistent view of H^0 behaviour in low doped n and p-type Si, with a diffusivity in agreement with the high temperature data. On the other hand, a systematic variation of D_{H^+} with the boron concentration forces us to conclude that some still unknown interactions take place and contribute to hydrogen trapping in highly doped p-Si.

INTRODUCTION

One of the major questions concerning the behaviour of hydrogen in Si is the determination of its microscopic mechanisms of motion. The pioneer permeation results of Van Wieringen and Warmoltz (VWW) lead to a migration enthalpy of about 0.48 eV [1]. Extrapolation of these high-temperature data in the 100-200°C temperature range leads to values of hydrogen diffusivity of the order of 10^{-9} - 10^{-7} cm²s⁻¹. However, direct measurements of deuterium profiles indicate penetration depths of only a few micrometers for plasma hydrogenation at 150°C, corresponding to effective diffusivities several orders of magnitude lower than the values extrapolated from VWW data, and which depend on both dopant type and concentration [2,3].

Recently, one of us proposed a diffusion model which takes into account all the interactions, reported in the literature, between the hydrogen species (in its various charge states) and the dopant atoms [4]. It was shown that reliable fits are obtained in both n- and p-type silicon. The main result was that deuterium diffusion profiles in low doped silicon can be simulated with a diffusivity of neutral hydrogen in agreement with the extrapolated high temperature data. On the other hand the situation in highly doped p-type silicon was more confusing. Good simulations on the existing experimental data were possible only with very low H^+ diffusivity. Moreover the fits were not unique, and as a consequence it was not possible to extract definitive values for the various parameters of the model. The aim of this paper is thus to present new experimental deuterium diffusion profiles and their analysis with an improved version of the model of Ref.4.

THEORY

In this analysis it is considered that hydrogen has both an acceptor (E_a) and a donor (E_d) level in the band gap, and thus can exist in the three charge states H^+ , H^0 and H^- . The relative concentrations of these species depend only on the local Fermi level position and follow the usual deep impurity statistics. In the following we will focus only on the reactions in p-type Si where the relevant species are H^0 and H^+ (analogous reactions occur in n-type Si).

H^+ can react with the ionized B^- dopant atoms to form neutral complexes, following the reaction



The forward rate coefficient is given by

$$k_{BH} = 4 \pi r_c D_{H^+} \quad (2)$$

where D_{H^+} is the diffusivity of H^+ , and r_c is the coulombic capture radius, i.e. $r_c = 30 \text{ \AA}$ at 150°C [4]. In addition to this neutralization reaction (dopant passivation) it is considered that H_2 molecules can be formed following the reaction



with

$$k_{H_2} = 8 \pi r_{H_2} D_{H^0} \quad (4)$$

In contrast with the analysis of Ref.4, we consider here that H_2 molecules can also be formed by reaction between H^+ and H^0 according to :



with

$$k^+_{H_2} = 4 \pi r_{H_2} (D_{H^0} + D_{H^+}) \quad (6)$$

This interaction between H^0 and H^+ was first proposed by Johnson and Herring to explain deuterium accumulation in reversed biased diodes [5]. Moreover the fact that this interaction was neglected in Ref.4 could explain, at least partially, the low reported value of D_{H^+} . For the fitting procedure we considered that the capture radius was the same for reactions (3) and (5), and we fixed it to $r_{H_2} = 5 \text{ \AA}$.

Finally, as explained in Ref. [4], the deuterium high concentration region, at the surface of the sample, is interpreted as due to hydrogen trapping on plasma induced micro-defects, and is empirically modeled by trapping reactions between free hydrogen (H^0 and H^+) and immobile traps having an initial Gaussian profile.

Among the various species, only H^0 and H^+ are assumed to be mobile and actually contribute to H diffusion. The individual fluxes are given by the first Fick's law, modified by a drift term to take into account the influence of the built-in electric field in the case of H^+ :

$$J_{H^0} = - D_{H^0} \frac{\partial [H^0]}{\partial x} \quad (7a)$$

$$J_{H^+} = -D_H + \frac{\partial[H^+]}{\partial x} - D_H + [H^+] \frac{1}{n} \frac{\partial n}{\partial x} \quad (7b)$$

The local density of free carriers is obtained by the resolution of Poisson's equation.

The evolution of the various concentrations can then be calculated by the following system of equations :

$$\frac{\partial[H]^{tot}}{\partial t} = - \frac{\partial[J_{H^0} + J_{H^+}]}{\partial x} \quad (8a)$$

$$\frac{\partial[H_2]}{\partial t} = K_{H_2} [H^0]^2 + K_{H_2}^+ [H^0] [H^+] - k'_{H_2} [H_2] \quad (8b)$$

$$\frac{\partial[BH]}{\partial t} = k_{BH} [B^-] [H^+] - k'_{H_2} [BH] \quad (8c)$$

where $[H]^{tot}$ is the total concentration of hydrogen.

FITS ON EXPERIMENTAL PROFILES

In order to be able to determine the various physical parameters governing H diffusion in Si, it is necessary to simulate diffusion profiles covering the widest possible range of experimental conditions. In Ref.4 it was pointed out that the main problem which remains to be solved is the behaviour of H^+ in p-type Si. Thus for this study we focused on this type of samples. Our main objective was to enlarge the existing set of experimental data.

Deuteration experiments were performed in p-type silicon substrates of various resistivities. For this purpose we used a R.F. deuterium plasma free of residual oxygen or water contamination. The working pressure was 1 mbar, with a constant power of 30 W. During the deuteration the sample temperature was controlled with an accuracy better than 1°C.

The deuterium diffusion profiles was then analysed by Secondary Ion Mass Spectroscopy (SIMS), using a Cameca IMS 4f apparatus. The primary ion was C_s^+ , and the absolute concentrations were determined by calibration with deuterium implanted reference samples. The corresponding deuterium profiles, for deuteration near 150°C, are shown on Figures 1-2.

Although not shown here, we have also determined deuterium profiles in low-doped n- and p-type silicon (dopant concentrations of a few 10^{14} cm^{-3}), at a slightly higher temperature of 163°C. These profiles are similar to the existing data of the literature [3,6], and confirm the observation that, in low doped silicon, the profiles are independent of the dopant type. As a consequence we started our fitting procedure for deuterium diffusion at 150°C by the simulation of the experimental result of Ref.3, i.e. deuteration of n-Si ($n = 2 \times 10^{14} \text{ cm}^{-3}$) at 150°C for 10 minutes. As explained in Ref.4, accurate simulations (see Fig.1 of Ref.4) are obtained if one assumes that, in these low doped samples, the hydrogen penetration is mainly governed by H_2 formation, through reaction (3) (reaction (5)

can be neglected because of the low H^+ concentration). The value found for D_{H^0} ($1.5 \times 10^{-8} \text{ cm}^2 \text{ s}^{-1}$) is in agreement with the extrapolated high temperature data, leading to a consistent view of the behaviour of neutral hydrogen in the whole temperature range. Thus, in the following, we will focus only on the simulation on more doped p-type Si.

The calculated diffusion profiles for various experimental conditions at 150°C are shown as full lines on Figures 1-3. Accurate simulations are possible for each doping level, between a few 10^{16} cm^{-3} to a few 10^{18} cm^{-3} . The only exception occurs for boron concentration of the order of a few 10^{17} cm^{-3} (Fig.2). In this case the experimental profiles exhibit a transition region with a small plateau between about 0.1 and 0.2 μm , at a deuterium level of $3-4 \times 10^{18} \text{ cm}^{-3}$. It is worth to notice that this plateau is reproducible from an experiment to another and is not an artefact (the same observation is also found in an analogous profile in Ref.2). Although the calculated profile describes nicely the overall behaviour (penetration depth, hydrogen plateau near the dopant level), we were not able to

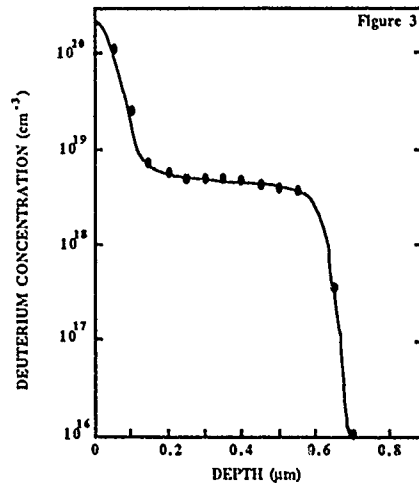
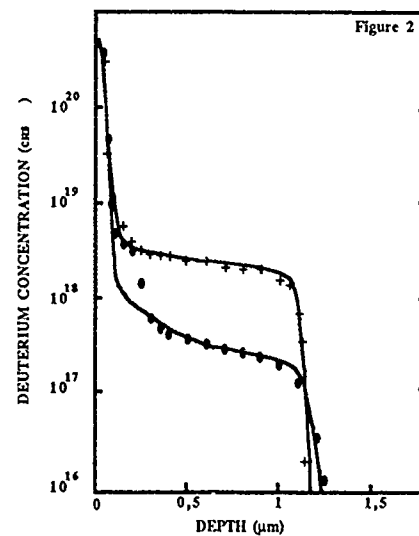
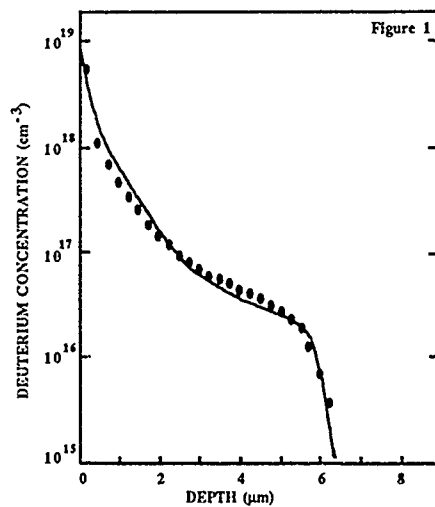


Fig.1 : Deuterium profile in p-type Si ($[B] = 3 \times 10^{16} \text{ cm}^{-3}$) after deuteration at 150°C for 3hrs. The solid line is the calculated profile.

Fig.2 : Deuterium profiles in p-type Si
 • : $[B] = 3 \times 10^{17} \text{ cm}^{-3}$ - 153°C , 27 min.
 + : $[B] = 2.5 \times 10^{18} \text{ cm}^{-3}$ - 151°C , 2hrs
 solid lines are calculated profiles.

Fig.3 : Comparison between calculated and experimental profiles in p-type Si ($[B] = 5 \times 10^{18} \text{ cm}^{-3}$), 150°C , 30 min. The experimental profile is from Ref.2.

simulate the transition region on the basis of the theoretical model described above. Thus we have to conclude that hydrogen probably encounters some other interactions which remain to be determined.

DISCUSSION

The parameters used for the simulations shown on Fig.1-3 are summarized in Table I. In this table E_D is the dissociation energy of the BH pair, calculated by $k'_{BH} = v_0 \exp(-E_D/kT)$ and assuming $v_0 = 10^{13} \text{ s}^{-1}$. T is the exact temperature as given in the figure captions. All the simulations are obtained with $D_H^0 = 1.5 \times 10^{-8} \text{ cm}^2 \text{ s}^{-1}$ as obtained from the result on the low doped sample, and with $k'_{H_2} = 5 \times 10^{-4} \text{ s}^{-1}$. In contrast with Ref.4, a rather good estimation of k'_{H_2} was possible here, by the fit of the model on diffusion profiles corresponding to rather large deuteration times, for which the dissociation of H_2 becomes significant. This value of k'_{H_2} corresponds to a dissociation energy of the order of 1.4 eV, in agreement with theoretical predictions [7,8].

More surprising is the fact that it is not possible to obtain good simulations with a constant value of D_H^+ and k'_{BH} (the values given in Table I are obtained by assuming the hydrogen donor level at $E_c - 0.52 \text{ eV}$ [4]. In the case of k'_{BH} this can be easily explained by taking into account small temperature variations between the various experiments. Indeed, as shown in Table I, the dissociation energy calculated with the actual sample temperature is found to be nearly constant, at a value of about 1.2 eV (in these conditions, a 1 percent variation of T near 150°C , corresponds to a 32 percent variation for k'_{BH}). Moreover the value of k'_{BH} determines essentially the calculated slope of the sharp hydrogen profiles in the bulk of the sample, and thus depends drastically on the experimental accuracy.

On the other hand the systematic variation of D_H^+ with the boron concentration cannot be explained by experimental uncertainties. The observation that the (effective) H^+ diffusivity decreases when the boron concentration increases is probably the indication that some interactions between H^+ and boron are not well described by the model and become significant at high dopant level.

Nevertheless, even at the lowest boron concentration of $3 \times 10^{16} \text{ cm}^{-3}$, the value of D_H^+ is still about two orders of magnitude lower than D_H^0 , corresponding to a difference of migration energies of about 0.15 eV. Such a difference is relatively small and cannot be ruled out a priori. In fact the only experimental indication that D_H^+ should be consistent with the extrapolated high

TABLE I : Fitting parameters for H diffusion

[B] (cm^{-3})	[H ⁰] s (cm^{-3})	D_H^+ ($\text{cm}^2 \text{s}^{-1}$)	k'_{BH} (s^{-1})	E_D (eV)
3×10^{16}	8×10^{13}	2×10^{-10}	3×10^{-2}	1.22
3×10^{17}	2×10^{13}	8×10^{-11}	1.1×10^{-1}	1.18
2.5×10^{18}	4×10^{12}	4×10^{-11}	9×10^{-2}	1.18
5×10^{18}	4×10^{12}	4×10^{-11}	4×10^{-1}	1.13

temperature data comes from the so-called "drift" experiments, monitoring hydrogen motion in reverse biased n+p diodes [9]. However, assuming as usual that the hydrogen donor level is fixed with respect to the valence band, this level will cross the Fermi level in reverse biased junctions, because of the band bending. As a consequence the level is empty of hole in the depletion region and H is then in its neutral charge state. Within this model, the "drift" experiments can be explained in the following way.

At temperatures above about 80°C, BH pairs can dissociate, leading to the generation of free hydrogen atoms. Since, as explained previously, these atoms are neutral in the space charge region, there is no Coulombic interaction with the B⁻ atoms, and the formation rate of BH is strongly reduced. Thus, in the space charge region, H⁰ can freely diffuse, up to the edge of the depletion layer where the equilibrium charge state is H⁺ and favours trapping on B⁻. In other words the diffusing species in these experiments is H⁰ and not H⁺, and thus numerical analysis of these experiments [12] leads to a determination of D_{H⁰}.

CONCLUSION

We have shown that the behaviour of hydrogen in low doped silicon can be accurately described by assuming that H is mainly neutral and that its diffusion is slowed down by H₂ pairing. The corresponding fitted D_{H⁰} value is in agreement with the extrapolated high temperature data. It is also shown by fitting on an extended set of experimental profiles that some still unknown hydrogen interactions probably exist in addition to H₂ and BH pairing. And finally we have proposed a new interpretation of the "drift" experiments, which suggest that H⁰ is the diffusing species.

ACKNOWLEDGEMENTS

Preliminary experiments used in this work (Fig. 1) was part of the thesis dissertation of A. Chari (Paris Orsay, 1988). The authors wish to thank A. Boutry-Forveille who performed the SIMS analysis. Thanks are also due to J.C. Pfister for helpful discussions and critical reading of the manuscript.

REFERENCES

1. A. Van Wieringen and N. Warmoltz, *Physica* **22**, 849 (1956)
2. N.M. Johnson and M.D. Moyer, *Appl. Phys. Lett.* **46**, 787 (1985)
3. N.M. Johnson, C. Herring and D.J. Chadi, *Phys. Rev. Lett.* **56**, 769 (1986)
4. D. Mathiot, *Phys. Rev. B* **40**, 5867 (1989)
5. N.M. Johnson and C. Herring, in *Shallow Impurities in Semiconductors 1988*, edited by B. Monemar (Inst. Phys. Conf. Ser. **95**, Bristol, 1989), p. 415
6. J.W. Corbett, J.L. Lindström and S.J. Pearton, in *Defects in Electronic Materials*, edited by M. Stavola, S.J. Pearton and G. Davies (Mater. Res. Soc. Proc. **104**, Pittsburgh, 1988), p. 229
7. S.J. Pearton, J.W. Corbett and T.S. Shi, *Appl. Phys.* **A43**, 153 (1987)
8. C.G. Van de Walle, Y. Bar-Yam and S.T. Pantelides, *Phys. Rev. Lett.* **60**, 2761 (1988)
9. See, e.g., C.H. Seager and R.A. Anderson, *Appl. Phys. Lett.* **53**, 1181 (1988)

STRUCTURE AND METASTABILITY OF MUONIUM CENTERS IN SEMICONDUCTORS AND THEIR SIMULATION OF ISOLATED HYDROGEN CENTERS

T.L. ESTLE*, R.F. KIEFL†, J.W. SCHNEIDER‡, AND C. SCHWAB**

* Physics Department, Rice University, Houston, TX 77251

† TRIUMF, Vancouver, B.C., Canada V6T 2A3

‡ Physics Institute, University of Zurich, CH8001 Zurich, Switzerland

** Centre de Recherches Nucléaires, Université Louis Pasteur, 67037 Strasbourg Cedex, France

ABSTRACT

The study of isolated hydrogen in semiconductors is difficult because of the tendency for hydrogen to form complexes. An alternative to direct studies of hydrogen is the study of muonium in semiconductors. In such experiments the muon is essentially an isotope of hydrogen with $\frac{1}{9}$ th the mass of the proton. Twenty isolated muonium centers have been observed in tetrahedrally-coordinated crystals ranging from Si to the cuprous halides. Muon level-crossing resonance has provided detailed information on neutral interstitial muonium located at a bond center in Si (the analog of the hydrogen center seen by EPR) and very near a bond center in GaP and GaAs. This paper reviews these measurements and discusses the structures and their metastabilities. Comparison is made to EPR for Si and to theoretical studies. Recent results on the metastable and stable muonium centers in CuCl are discussed.

INTRODUCTION

Since the discovery that hydrogen passivates or neutralizes electrically-active centers in semiconductors, hydrogen and the mechanisms for passivation have been studied extensively in Si, GaAs, and several other semiconductors[1,2]. The centers formed during passivation are complexes of hydrogen and other impurities or defects. Quite a bit is known about these associated centers but until very recently there has been little direct information about the nature of isolated hydrogen centers. These centers are of interest in their own right and also because they are the precursors of the associates formed during passivation. Part of the reason that so little was known about hydrogen centers was that no electron paramagnetic resonance (EPR) or electron nuclear double resonance (ENDOR) studies had been reported. A very important recent development is the first and still the only observation of EPR from isolated hydrogen in a semiconductor[3]. The major difficulty with studying *isolated* hydrogen is that its high diffusivity results in hydrogen forming complexes rather than remaining isolated.

An alternative to the study of hydrogen is the study of muonium (an electron bound to a positive muon), which may be regarded as a very light pseudoisotope of hydrogen ($m_\mu \sim \frac{1}{9}m_p$)[4,5]. The structures of muonium centers should be very close to those of hydrogen. This is illustrated dramatically by the one direct comparison that can be made: an isolated hydrogen center observed in Si by EPR[3] which has the same structure as that of a muonium center in Si, as evidenced by the almost identical hyperfine parameters[6]. Although to date this is the only EPR of isolated hydrogen in a semiconductor, the fact that the hydrogen and muonium adiabatic potential energy surfaces are identical suggests that differences in structure will usually be small.

As a way of inferring the behavior of isolated hydrogen, the study of muonium has many advantages. Muonium centers have been studied in a large number of semiconductors (11 total)[4] and in several cases nuclear hyperfine structure has been resolved leading to structural models of the centers[5]. In many of the crystals studied (8 of the 11) more than one type of muonium center is known to exist. In several of these cases a thermal conversion of one type of muonium center to another has been observed. Consequently

the studies of muonium yield information about the structural metastability of defects. The metastability of muonium centers involves relatively simple isolated defects whose atomic-scale structures can be or have been obtained.

The techniques employed to study muonium are muon spin rotation (μ SR) and muon level-crossing resonance (μ LCR). They have many similarities to the magnetic resonance methods of EPR and ENDOR, respectively. With μ SR one can determine the muon hyperfine parameter(s) and sometimes the nuclear hyperfine parameters for the surrounding nuclei with the largest interaction. The recent development of μ LCR has yielded precise nuclear hyperfine parameters for several inequivalent nuclei in some crystals. In principle hyperfine interactions exceeding 1 MHz may be studied with μ LCR although for low values of the hyperfine interaction the resolution may be poor.

The muonium centers in semiconductors all appear to be isolated interstitial neutral muonium[4,5]. Two types of muonium centers or structures have been observed. One is called anomalous muonium or Mu^* and is muonium at the center of a covalent bond. It has been seen in diamond, Si, Ge, GaP, and GaAs. Of more common occurrence is normal muonium or Mu which is almost certainly muonium at a tetrahedral interstice. It is seen in both the highly covalent crystals in which Mu^* is seen and in much more ionic ones, such as the cuprous halides.

In diamond it has been established that Mu is metastable and that it is converted into Mu^* thermally[7]. Similar behavior is inferred for Si[8]. This represents one of the simplest and best understood examples of metastability yet studied. Recent investigation of the two normal muonium centers in CuCl indicates a surprisingly different type of metastability in which the muon site does not change[9].

There has been considerable interest in the metastability of defects in semiconductors in recent years[10]. A number of fascinating metastable systems have been studied, including the EL2 center in GaAs and the DX centers in $Al_xGa_{1-x}As$. Many of these have generated considerable controversy, in part because direct measurements yielding the structure of the metastable and stable configurations have been lacking. In those metastable systems in which the structures were determined with confidence one was usually dealing with a defect complex, such as a donor-acceptor pair or a vacancy-impurity associate, in which the two simple defects could exist with different discrete separations. By contrast the metastabilities observed for muonium centers involve *isolated* muonium, as simple an impurity as one can imagine, and much is known about the structures in detail.

In the next section we will describe very briefly the experimental techniques of μ SR and μ LCR. Then we will present the μ SR data on normal muonium centers and discuss their structures. This will be followed by a discussion of the structure of Mu^* deduced from μ SR and μ LCR. A brief discussion of the results of recent theoretical calculations will be followed by the current results concerning metastability of muonium centers.

For more detail on the studies of muonium in semiconductors the reader is directed to the reviews by Patterson[4] and by Kiell and Estle[5].

THE EXPERIMENTAL TECHNIQUES

The positive muon is an unstable elementary particle which decays into a positron and two neutrinos. Since parity is not conserved in this weak decay, the emitted positron is more likely to come out in the direction of the muon spin. Thus detection of the angular distribution of decay positrons tells the direction of the muon spins at any given time after arrival in the sample. Because a muon is produced by the parity-nonconserving decay of a pion, muon beams are naturally highly spin polarized. Intense beams of low-energy spin-polarized muons are now available at several medium-energy particle accelerators around the world¹. The muons have low energy (~ 4 MeV) by accelerator standards but are extremely energetic from the perspective of solid-state physics.

The time evolution of the muon spin polarization can be determined by monitoring

¹TRIUMF in Canada, PSI in Switzerland, LAMPF and BNL in the United States, RAL in England, and KEK in Japan.

the decay positrons. It is possible to observe the Larmor precession of the muon spin after obtaining 10^6 muon decay events. To determine the more complicated frequency spectra of muonium in semiconductors about 10^7 muon decay events are needed. In the case of μ SR the magnetic field is transverse to the direction of the muon spin in the beam. By determining the direction of positron emission and the time interval between the muon entering the sample and its decay² one obtains the direction of the muon spin polarization as a function of time. From this the muon spin precessional frequency spectrum can be obtained by Fourier analysis. The decay lifetime of the muon is $2.2\mu\text{s}$ so muon stopping rates of up to $\sim 10^6\text{s}^{-1}$ will result in acceptably few events being rejected because of two or more muons entering too close together.

Since in time-differential transverse-field μ SR one is obtaining information about the precession of the muon spin, the frequency spectra of muonium centers yield directly the muon hyperfine parameters. However at high field they give no information about nuclear hyperfine interactions since the muon spin and those of the nuclei are decoupled. At lower fields there may be resolved nuclear hyperfine structure in the μ SR frequency spectra but more commonly for muonium centers one simply obtains a significantly increased linewidth from unresolved nuclear hyperfine structure³.

For μ LCR one monitors the muon spin polarization in the direction of the magnetic field. Normally there is an appreciable polarization which changes little with time. However near an avoided crossing of two levels corresponding to two different muon spin states (assuming high field), the muon spin will oscillate between being along the field and opposite to it so that the normal asymmetry is reduced. This field-dependent reduction of the positron asymmetry is the signature of a μ LCR. Since it is not necessary to know when the muon decay occurs, arbitrarily high muon stopping rates can be used. However the largest current rates are about 10^7s^{-1} so that even in this case only a few muons are in the sample at any one time. Consequently one studies muonium at the extreme limit of low concentrations where two muoniums are never close to each other.

The muon level-crossing method was proposed by Abragam[11] and first applied to μ^+ in copper[12]. An avoided level crossing is analogous to cross relaxation and in the case of copper corresponded to the resonance between the muon Zeeman splitting and the nuclear electric quadrupole splitting of the Cu nuclei arising from the electric-field gradient created by the μ^+ . The corresponding resonances for muonium may be viewed approximately as occurring at those fields at which the muon spin splitting is equal to the nuclear spin splittings. The latter are dominated by the nuclear hyperfine and electric quadrupolar interactions so that analysis of the fields at which μ LCR lines occur yields the nuclear hyperfine and quadrupole parameters. The typical μ LCR is strong and fairly narrow ($\sim 10\text{ mT}$ wide). The fields at which μ LCR lines occur are usually above 0.5 T and can be as high as 15 T , the latter being beyond the fields available with magnets suitable for these experiments⁴.

STRUCTURE

A typical μ SR spectrum for muonium in semiconductors is that of GaAs shown in Figure 1. This frequency spectrum was obtained at high field in order to avoid the line broadening from the gallium and arsenic nuclear hyperfine interactions[13]. It consists of two lines at high frequency, which arise from normal muonium (Mu), and several at lower frequencies arising from anomalous muonium (Mu^*) and muons in electronically diamagnetic environments (labeled μ^+). Normal muonium has been assumed to arise from muonium at tetrahedral interstices. The only direct verification has occurred for the two normal muonium centers in CuCl [9,14]. There is a growing realization that many normal muonium centers are not localized at a single interstice but in fact diffuse rapidly among these sites. In contrast, for a long time there was no consensus on what

²The muon typically thermalizes in a time less than 10^{-10}s .

³This will occur only if the abundance of isotopes with nonzero nuclear spin is high and the muonium is stationary so that motional narrowing does not occur.

⁴Fields of the order of 15 T are required for muonium with a hyperfine interaction comparable to that for free muonium, 4463.302 MHz .

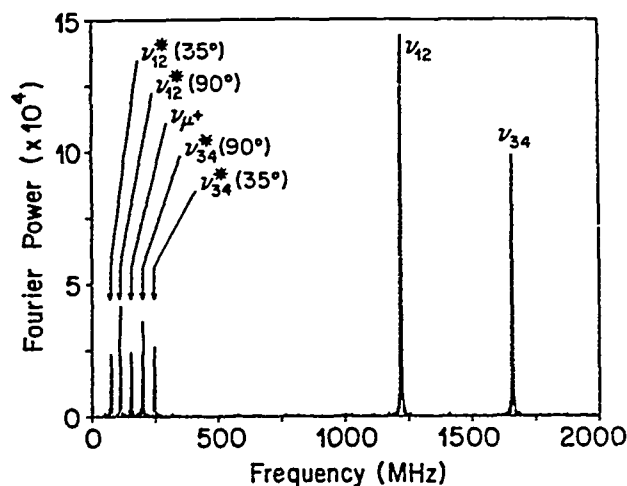


Figure 1: The high-field μ SR frequency spectrum of GaAs with the field parallel to a $\langle 110 \rangle$ direction[13].

anomalous muonium was. Several explanations were proposed for its structure and its coexistence with normal muonium. It is only within the last two years that a consistent and unambiguous model of this controversial center has appeared[6,15] showing that Mu^* is muonium at the center of a covalent bond.

Normal Muonium

A muonium center is categorized as normal muonium if it has an isotropic muon hyperfine interaction. The 15 normal muonium centers observed in semiconductors are listed in Table I along with their muon hyperfine parameters A^μ . The low-temperature muon hyperfine parameters vary from 0.27 times that for free muonium to 0.83 times A^{free} . The muon hyperfine parameters have been measured either in zero field, where the singlet-triplet splitting gives directly the value of A^μ , or in very high fields where the sum of the two precessional frequencies gives A^μ . If one plots $\eta_\mu^2 = A^\mu / A^{\text{free}}$ versus ionicity [16] for crystals from a given row of the periodic table, one gets approximately a straight line (η_μ^2 increases with ionicity) with the notable exception of the cuprous halides which lie at about $\frac{1}{3}$ the value of η_μ^2 inferred from the other crystals. Also note that the hyperfine values are nearly independent of the anion ⁵.

The isotropy of the muon hyperfine parameter implies that the normal muonium center occupies a site with tetrahedral symmetry or is moving so rapidly among lower symmetry sites that any anisotropy is motionally averaged to zero⁶. For Si and Ge there is evidence that Mu is moving rapidly at all temperatures[4], a result consistent with theoretical calculations showing a small barrier between adjacent tetrahedral interstices in Si[17]. If Mu moves rapidly, the low-field nuclear hyperfine broadening of the μ SR lines would be absent because of motional narrowing. Even if the nuclear hyperfine broadening were present, as it is for Mu in GaAs and GaP[13], motional effects can reduce the width and change its dependence on field. In this way it can be concluded that normal muonium in GaP and GaAs is moving slower than in Si and Ge. The most convincing evidence

⁵The values for Ga or Zn or Cu compounds all are close to each other.

⁶All crystals studied were cubic except SiC which was a hexagonal polytype (6H). An effort to observe anisotropy of Mu in SiC was negative[18].

Table I: The isotropic muon hyperfine parameter for Mu in semiconductors. The 1s spin density on the muon is given by $\eta_s^2 = A^\mu/A^{\text{free}}$ with $A^{\text{free}} = 4463.302$ MHz.

Center	A^μ (MHz)	η_s^2	Temperature (K)	Reference
Mu C	3711(21)	0.831	T \rightarrow 0	[20]
Mu Si	2006(2)	0.449	T \rightarrow 0	[20]
Mu Ge	2359.5(2)	0.529	T \rightarrow 0	[20]
Mu ^{AI} SiC	2767.8(2)	0.620	20	[18]
Mu ^{AI} SiC	2797.3(4)	0.627	20	[18]
Mu ^B SiC	3005.7(2)	0.673	20	[18]
Mu GaAs	2883.6(3)	0.646	10	[13]
Mu GaP	2914(5)	0.653	10	[13]
Mu ZnS	3547.8(3)	0.795	10	[16]
Mu ZnSe	3456.7(3)	0.774	13	[16]
Mu ^I CuCl	1334.23(8)	0.299	T \rightarrow 0	[16]
Mu ^{II} CuCl	1212.3(1)	0.272	T \rightarrow 0	[16]
Mu ^I CuBr	1403.67(6)	0.314	T \rightarrow 0	[16]
Mu ^{II} CuBr	1250.9(2)	0.280	T \rightarrow 0	[16]
Mu CuI	1670.9(2)	0.374	T \rightarrow 0	[16]

that it is moving comes from measurements of motion-induced spin relaxation similar to what has been seen in the alkali halides [19].

The occurrence of two tetrahedral interstitial sites in binary compounds with the cubic zinc blende structure raises the possibility that two different normal muonium centers will occur corresponding to muonium in the two inequivalent interstices. No evidence for this exists for GaP, GaAs, ZnS, or ZnSe. However two muonium centers are seen in both CuCl and CuBr and three have been resolved in 6H SiC [18]. As was shown by μ LCR and discussed below, the two centers in CuCl are both located at the same tetrahedral interstice, the one surrounded by four Cu atoms [9,14]. Thus in the cuprous halides there is no evidence for muonium at two inequivalent interstices. However in SiC we suspect that at least two inequivalent interstices are involved.

Any uncertainty concerning the structure of normal muonium could be reduced and probably eliminated if μ LCR could be performed on these centers. However because the muon hyperfine interaction for Mu is fairly large, the fields required to reach μ LCR lines are beyond the limit of current magnets for all Mu centers except those in the cuprous halides. There is also a more fundamental limit imposed by the fact that μ LCR can only be performed on centers which are stationary on the time scale of the muon lifetime.

More is known about the structure of the two muonium centers in CuCl than about any other normal muonium center [9,14]. Both Mu^I and Mu^{II} have been observed with μ LCR (see Figure 2) and the hyperfine parameters obtained by fitting the spectra are shown in Table II. The striking similarity of the Mu^I and Mu^{II} μ LCR spectra for the field parallel to (100) shown in Figure 2 demonstrates that the two centers are very similar⁷. This is quantified by noting that the fitted hyperfine parameters differ by less than 10% for the two centers, with the exception of the Cu contact interaction, which corresponds to a relatively small fraction of the unpaired spin density. The Cu nuclear hyperfine structures of the two centers are the low- and high-field clusters of lines. The structure in the center consist of the zero-crossing resonance (ZCR)⁸, which yields the value of A^μ in Table II, and lines from the next-nearest neighbor (NNN) Cl atoms. Although the Cl lines

⁷The spectra for fields along (110) and (111) are also very similar.

⁸The ZCR is the strongest line and occurs where one muon spin transition frequency is zero.

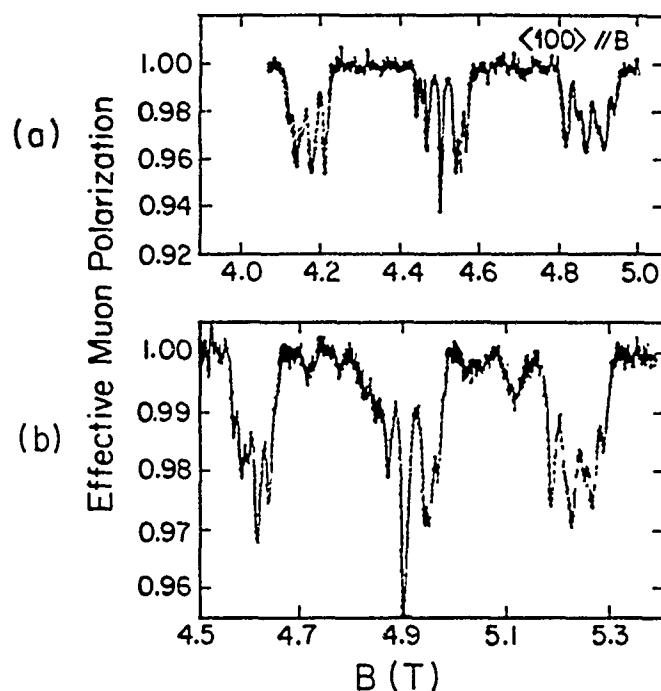


Figure 2: The μ LCR spectra of (a) Mu^{II} and (b) Mu^{I} in CuCl for the field along a $\langle 100 \rangle$ axis. The temperatures were 100 K and 8 K respectively.

have not been fit with the correct orthorhombic-symmetry terms in the spin Hamiltonian, it is clear that the nuclear hyperfine parameters for the NNN are comparable for Mu^{I} and Mu^{II} also. The μ LCR spectra can be unambiguously related to the Mu centers seen with μ SR[16] by their temperature dependence and by the values of A^{μ} . No spin density beyond the first two shells of nuclei was detected by μ LCR.

The facts that the Cu hyperfine and quadrupole interactions are axial, the common axis of symmetry is a $\langle 111 \rangle$ axis (all four orientations being seen in general), and the spin density on the coppers is large argue that these centers correspond to muonium at the tetrahedral interstice with four nearest-neighbor (NN) coppers. The Cl substitutional site can be ruled out by the approximate fit of the NNN structure with six Cl having axial symmetry about the $\langle 100 \rangle$ axes. The Cu spin density has far more d character than the sd^3 which would be associated with bonding orbitals formed from s and d atomic valence orbitals for tetrahedral coordination. This suggests that the coppers have relaxed away from the interstitial muon[21].

There are thermally driven transitions of Mu^{I} to Mu^{II} in both CuCl and CuBr[16]. These will be discussed later in the METASTABILITY section.

Anomalous Muonium

In all of the more covalent semiconductors in which muonium has been seen a center called anomalous muonium and denoted Mu^* was seen as well, with the single

Table II: Hyperfine parameters and spin densities for Mu^I and Mu^{II} in CuCl. The contact (A_s^i) and dipolar (A_p^i) hyperfine parameters are given by $A_s^i = \frac{1}{3}(A_{\parallel}^i + 2A_{\perp}^i)$ and $A_p^i = \frac{1}{3}(A_{\parallel}^i - A_{\perp}^i)$. Estimates of the spin densities are obtained from $(\eta_s^2)^i = A_s^i/A_s^{free}$ and $(\eta_d^2)^i = A_p^i/A_d^{free}$ and similarly for p orbitals. The parameters for Cu are for ^{65}Cu and those for Cl are for ^{35}Cl .

Parameter	Mu^I	Mu^{II}	Units
A^μ	1334.50(3)	1226.69(1)	MHz
A_s^{Cu}	60.07	39.33(3)	MHz
A_p^{Cu}	45.41	48.48(3)	MHz
Q^{Cu}	6.21(3)	6.75(3)	MHz
A_s^{Cl}	—	32(1)	MHz
A_p^{Cl}	—	7(1)	MHz
Q^{Cl}	—	1.7(2)	MHz
$(\eta_s^2)^\mu$	0.298994(7)	0.274839(2)	—
$(\eta_s^2)^{Cu}$	0.010020	0.00656(1)	—
$(\eta_d^2)^{Cu}$	0.13278	0.1418(1)	—
$(\eta_s^2)^{Cl}$	—	0.0055	—
$(\eta_p^2)^{Cl}$	—	0.041	—
Reference	[9]	[14]	—

exception of SiCl^0 . Anomalous muonium is characterized by a small (less than 5% of A^{free}) highly-anisotropic muon hyperfine interaction with axial symmetry about a $\langle 111 \rangle$ axis. In Table III we list the muon hyperfine parameters of Mu^* in diamond, Si, Ge, GaP, and GaAs together with NN nuclear hyperfine parameters determined from μLCR . The small values of A_{\parallel}^μ and A_{\perp}^μ mean that in μSR the Mu^* frequency spectra will be much lower than those for Mu . In Figure 1 four of the five low-frequency lines from GaAs arise from Mu^* centers whose symmetry axes make angles of 35.3° and 90° with respect to the field, which is applied along a $\langle 110 \rangle$ direction. Analysis of the μSR spectra for several orientations determined the muon hyperfine parameters and the symmetry of the interaction.

At low fields the μSR lines of Mu^* are broadened by unresolved nuclear hyperfine structure. This varies considerably from GaAs and GaP, which are broadened excessively below about 0.3 T because all nuclei have magnetic dipole moments[13], to diamond for which no broadening is noticeable. For Ge[22] the broadening begins below about 50 mT and for Si[23] it occurs below about 5 mT. In GaAs resolved nuclear hyperfine structure can be observed in μSR with the best resolution occurring near 0.3 T with the field along a $\langle 110 \rangle$ direction[15]. The GaAs data gave approximate nuclear hyperfine parameters and agreed in detail with calculated spectra using the parameters obtained from μLCR .

Even more information was obtained from the observation of weak satellite lines to the previously-observed strong μSR lines in Si[6]. Because ^{29}Si has a natural abundance of 4.7% and it is the only isotope with a nuclear spin, the amplitudes of these satellite lines relative to the main lines was used to determine the number of equivalent Si sites at which the ^{29}Si could reside and give the observed satellites. It was concluded that there were two equivalent silicons on the $\langle 111 \rangle$ axis of symmetry of the Mu^* and estimates of the nuclear hyperfine parameters were obtained.

The μLCR measurements on Si have determined unambiguously that there is a nuclear hyperfine interaction with two equivalent silicons which is large 10 and with considerably more p character than sp^3 . The μLCR from a second shell of six equivalent silicons was measured but nothing else was detected. The picture that emerges is that of

¹⁰The μSR measurements were made on a small 6H sample mosaic which gave weak signals.

¹¹It corresponds to about 21% of the electron spin density on each Si.

Table III: Hyperfine parameters of the muon ($i = \mu$) and nearest-neighbor nuclei ($i = n$) for Mu^+ in semiconductors. The "proton" hyperfine parameters are multiplied by the ratio of the muonium and hydrogen atomic hyperfine parameters (3.1423). Estimates of the spin densities are obtained as described in the caption of Table II.

Center	Nucleus	A_{\parallel}^i (MHz)	A_{\perp}^i (MHz)	Q (MHz)	η_s^i	η_p^i	Refer.
Mu^+ Si	muon	-16.82(1)	-92.59(5)	—	-0.0151	—	[24]
	^{29}Si	-137.5(1)	-73.96(5)	—	+0.0207	+0.185	[6]
AA9 Si	"proton"	19.5(30)	98.7(30)	—	—	—	[3]
	^{29}Si	128.9(10)	72.9(10)	—	—	—	[3]
Mu^+ GaAs	muon	+218.54(3)	+87.87(5)	—	+0.0294	—	[15]
	^{75}As	+563.1(4)	+128.4(2)	+18.8(2)	+0.0186	+0.434	[15]
	^{69}Ga	+1052(2)	+867.9(3)	+1.08(3)	+0.0761	+0.301	[15]
Mu^+ GaP	muon	+219.0(2)	+79.48(7)	—	+0.0282	—	[13]
	^{31}P	+620.2(4)	+249.7(1)	—	+0.0280	+0.337	[5]
Mu^+ C	muon	+167.98(6)	-392.59(6)	—	-0.0461	—	[24]
Mu^+ Ge	muon	-27.27(1)	-131.04(3)	—	-0.0216	—	[24]

a muon at the center of a covalent bond between two silicons. These two silicons relax away from the muon by about 30% and the unpaired electron is localized primarily on these two silicons. There is a smaller spin density associated with the six NNN silicons but that from still further neighbors is negligible[25].

This model of Mu^+ in Si is in good agreement with theory (see next section) and also is the same as that for the isolated hydrogen center seen by EPR in Si[3] (labelled AA9). The parameters for the AA9 center are also given in Table III where instead of the proton hyperfine parameters the values in the table are the proton values multiplied by 3.1423, the ratio of the muonium to the hydrogen hyperfine splitting for free atoms.

The μLCR results for GaAs give a comparable picture of Mu^+ in that crystal[15]. The muon is located on the bond axis near the center of the covalent bond and the majority of the electron spin density is on the arsenic and gallium atoms whose bond the muon has entered. These two atoms relax away from the muon as was the case in Si but the arsenic relaxes appreciably more than the gallium as evidenced by the much larger p to s spin density ratio for arsenic. There is a very complicated poorly resolved spectrum near 0.5 T associated with nuclei other than the As and Ga NN. This has not yet been analyzed but it would be consistent with localization comparable to that for Mu^+ in Si.

GaP μLCR spectra have also been obtained for the NN P atom but not yet for Ga. The P spin density in GaP is less than that of As in GaAs and the p to s spin density ratio is less as well, suggesting a smaller relaxation than for As in GaAs (but still larger than for Ga in GaAs).

Comparison to Theory

During the last few years there has been extensive theoretical work on hydrogen centers, which for adiabatic calculations neglecting vibrations are identical to those for muonium. Much of this concerns the complexes which form during passivation but there are many references on isolated hydrogen and muonium. This section is brief because of the recent review on this subject by Van de Walle[17].

In order to make a detailed comparison of experiment and theory it is necessary to have many experimentally determined hyperfine parameters and calculations of these. Although many muonium hyperfine parameters have been measured, there is only one extensive comparison that can be made with theory because of the lack of calculated

hyperfine values. This one is for muonium and the AA9 EPR H center in Si. Van de Walle has calculated nuclear hyperfine parameters using density-functional methods and the agreement with experiment is very good[26]. Isolated hydrogen in Si is the best understood of any hydrogen center. The close similarity to Mu^+ means that detailed information which has not been obtained yet on hydrogen can be inferred from the Mu^+ studies. Theory is more advanced for Si with impressive agreement with observation. The lowest energy for hydrogen in Si occurs when it is at the bond center with the two closest Si atoms relaxed away from the muon by about 30%. The spin density is primarily on these two silicons and falls off rapidly on further neighbors.

The current bond-centered model of Mu^+ grew out of the arguments of Cox and Symons[27]. Prior to that the principle theoretical activity was on normal muonium in diamond and Si[28,29]. The primary conclusion was that Mu was in a tetrahedral interstice and that the barrier between adjacent interstices was low enough for easy diffusion of Mu , especially in Si. The suggestion of the bond-centered model of Mu^+ [27] led to calculations which confirmed that in diamond there was a large outward relaxation of the two NN and that the energy of the *relaxed* bond-centered muonium was lower than that of the tetrahedral center even though without relaxation it was much higher[30,31,32]. Calculations by many theorists have reached similar conclusions for Si [30,33,34].

The theoretical work has been primarily on Si and diamond. In addition there have been some recent results for Ge[34,35] and GaAs[36]. Only in the case of Si have detailed hyperfine calculations been carried out. These parameters are of most value in comparisons with experiment, μ lCR especially. For other muonium centers there are no detailed calculations. It would be especially valuable to extend calculations to the cuprous halides since they are probably the system which currently has the most unexplained experimental observations.

METASTABILITY

Defects may exist with more than one structure or geometrical configuration[10]. When the different configurations occur as a consequence of changes in the charge state of the defect, one speaks of bistability and numerous examples of this kind of behavior exist. It is also possible that for a single charge state there may exist more than one structure, only one of which can be stable. One can learn a great deal about these metastable structures if they live for a sufficient length of time. In some cases the metastable configuration is persistent and one must use some external excitation to change the system back to the stable configuration. This is usually done optically, electrically, or thermally. It is also possible to create excited electronic states that are metastable, although their lifetimes for defects are normally very short compared to configurational metastabilities.

Configurational or structural metastabilities arise because of an energy barrier between the two configurations. In order for there to be such a barrier the configurational coordinate leading from one to the other must change significantly, often called large lattice relaxation. The defect metastabilities which have been studied by EPR, DLTS, optical, and electrical measurements have often involved defect complexes such as donor-acceptor pairs which can exist with an essentially unlimited number of discrete separations. Only one of these can be stable. Two of the metastable defects which have attracted the most attention are EL2 in GaAs and the DX centers in $Al_xGa_{1-x}As$. They have recently been proposed to be isolated defects (an As antisite defect and a substitutional donor, respectively) in which a large displacement of one of the atoms occurs; between a substitutional position and one which is nearly interstitial. This represents a different type of configurational metastability from those for complexes. Muonium and presumably hydrogen in the more covalent semiconductors have a type of metastability which also arises because a single isolated defect undergoes large atomic displacements. In this case the defect is an isolated interstitial and the displacements include an actual movement of the muonium impurity from one interstitial site to another (tetrahedral interstice and bond center). In addition there is a substantial displacement of the two atoms whose bond the muonium enters. The two features of muonium metastability that make these studies so different from the more usual ones are that both stable and metastable

structures are created by stopping very energetic muons (~ 4 MeV) and that metastable in the case of muonium means that it lives longer than 10^{-8} s (the muon radiative lifetime is 2.2×10^{-6} s).

Muonium in Diamond and Silicon

In diamond two muonium centers, Mu and Mu^{*}, are seen by μ SR[7] (no μ LGR studies have been done yet). At low temperatures both Mu and Mu^{*} occur but at a temperature of 600 K only Mu^{*} is seen and its amplitude is increased to about the sum of the low temperature amplitudes of the two centers. The μ SR lines of Mu broaden near 400 K as a consequence of its shortened lifetime. These observations support the model that Mu is being converted to Mu^{*} thermally. This explanation is made unambiguous by the observation of coherent transfer of the muon spin polarization from Mu to Mu^{*}[37]. Thus from the experimental point-of-view there is no doubt that Mu is metastable and that there is a large barrier separating it from the stable configuration, Mu^{*}. Although direct μ LGR evidence of the structure of these centers is lacking, the proof that Mu^{*} in Si is bond centered, the general agreement that Mu is always in a tetrahedral interstice, and the support for these structures by theory argue strongly that in diamond muonium at a tetrahedral interstice is metastable and muonium at the bond center is stable.

Studies of the coherent polarization transfer[37] revealed the sign of the muon hyperfine parameters of Mu^{*} relative to that of Mu which is certainly positive. This led to a negative value of the muon contact hyperfine interaction, a result which implies spin polarization of the paired spin orbitals in Mu^{*} and which is consistent with theory.

In high purity Si there is no indication of a thermal conversion of Mu to Mu^{*} or vice-versa but in electron-irradiated Si coherent transfer of the muon spin polarization from Mu to Mu^{*} was observed at a temperature of 15 K[8]. Thus in Si as in diamond there is a thermal conversion of the metastable normal muonium center to the stable anomalous muonium. It would appear that a reasonably high barrier exists but that in damaged material the rapidly diffusing Mu^{*} converts in regions where the damage has resulted in a lowered barrier. In Si we know the stable structure because of the detailed μ LGR studies of Mu^{*} described above.

Cuprous Halides

In both CuCl and CuBr two muonium centers with very similar muon hyperfine parameters were seen with μ SR[16]. Both centers are formed at low temperatures but the one with the larger low-temperature amplitude, Mu^I, is thermally converted to the other, Mu^{II}, at temperatures of roughly 200 K. The structures of these centers in CuCl have recently been determined by μ LGR[9,14]. Both the stable Mu^{II} center and the metastable Mu^I center correspond to muonium at the tetrahedral interstice which is surrounded by four coppers. In addition, as stated above the spin density on the muon and the closest two shells of nuclei are remarkably alike for the two. If this is an example of configurational metastability, then there is a surprisingly small effect on the spin-density distribution of the different configurations. The other alternative is that, because we only know that the Mu^I lifetime exceeds about 10 μ s, we are dealing with a metastable excited electronic state and that the thermally induced decay results from excitation to another slightly higher electronic state which decays rapidly to the ground state. Here we face problems as well. Why are the two electronic states so similar in their spin densities and why is there such a close excited state? This interesting result is not understood!

Other Materials

In the remaining three crystals in which both Mu and Mu^{*} have been seen, Ge, GaP, and GaAs, there is as yet no evidence of a transition between Mu and Mu^{*}. Because the accumulated evidence argues that both Mu and Mu^{*} are isolated interstitials, one of

the two must be metastable. However there is no direct determination of which of the two has the lower energy and hence is stable in these crystals.

There is some evidence for metastability of other muonium centers than those mentioned above, such as the observation of three Mu centers in 6H SiC at low temperatures but only two at room temperature[18]. It seems that for interstitial muonium centers metastability is the rule rather than the exception. It is not confined to just the tetrahedrally-coordinated semiconductors as is evidenced by the observation of two muonium centers in KBr and the thermal conversion of one to the other at temperatures near 50 K[38].

SUMMARY

The techniques of muon spin rotation and muon level-crossing resonance have yielded much information about the structure and the metastability of muonium centers in semiconductors. Much of this should be directly applicable to hydrogen. All of the muonium centers are isolated interstitials either in the center of a covalent bond or at a tetrahedral interstice. At least two types of metastable systems have been documented. In one the configurations are the bond center and the tetrahedral interstice while in the other we find both the metastable and stable forms are located at the same interstice and have very similar spin-density distributions.

ACKNOWLEDGEMENTS

The authors acknowledge the extremely important role of our many collaborators in the experiments which form the basis of this review. Their names appear in the many references listed here and in others referenced in these publications. This work was supported by the National Research and Natural Sciences and Engineering Research Councils of Canada. One of us (T.L.E.) would like to acknowledge support from Robert A. Welch Foundation grant C-1048.

REFERENCES

- [1] S.J. Pearton, J.W. Corbett, and T.S. Shi, *Appl. Phys. A* **43**, 153 (1987).
- [2] J. I. Pankove and N. M. Johnson, editors, *Hydrogen in Semiconductors*, (Academic Press, 1990), in press.
- [3] Yu.V. Gorelkinskii and N.N. Nevinsky, *Pis'ma Zh. Tekh. Fiz.* **13**, 105 (1987)[*Sov. Tech. Phys. Lett.* **13**, 45 (1987)].
- [4] B.D. Patterson, *Rev. Mod. Phys.* **60**, 69 (1988).
- [5] R.F. Kiehl and T.L. Estle, In *Hydrogen in Semiconductors*, ed. by J.I. Pankove and N.M. Johnson, (Academic Press, 1990), in press.
- [6] R.F. Kiehl, M. Celio, T.L. Estle, S.R. Kretziman, G.M. Luke, T.M. Riseman, and E.J. Ansaldo, *Phys. Rev. Lett.* **60**, 224 (1988).
- [7] E. Holzschuh, W. Kündig, P.F. Meier, B.D. Patterson, J.P.F. Sellschop, M.C. Stenmet, and H. Appel, *Phys. Rev. A* **25**, 1272 (1982).
- [8] E. Westhauser, E. Albert, M. Hamma, E. Recknagel, A. Weidinger, and P. Moser, *Hyperfine Int.* **32**, 589 (1986).
- [9] T. L. Estle, S. A. Dodds, R. G. DuVarney, R. Kadono, R. F. Kiehl, R. Lichti, J. W. Schneider, and C. Schwab, to be published.
- [10] G.D. Watkins, In *Proceedings of the 15th International Conference on Defects in Semiconductors*, in press.
- [11] A. Abragam, *C.R. Acad. Sci. Paris, Ser. II* **200**, 95 (1984).
- [12] S.R. Kretziman, J.H. Brewer, D.R. Harshman, R. Keitel, D.L. Williams, K.M. Crowe, and E.J. Ansaldo, *Phys. Rev. Lett.* **50**, 181 (1986).

- [13] R.F. Kiefl, J.W. Schneider, H. Keller, W. Kündig, W. Odermatt, B.D. Patterson, K.W. Blazey, T.L. Estle, and S.L. Rudaz, *Phys. Rev. B* **32**, 530 (1985).
- [14] J.W. Schneider, M. Celio, H. Keller, W. Kündig, W. Odermatt, B.D. Patterson, B. Pümpin, I.M. Savić, H. Simmler, T.L. Estle, C. Schwab, R.F. Kiefl, and D. Renker, to be published.
- [15] R.F. Kiefl, M. Celio, T.L. Estle, G.M. Luke, S.R. Kreitzman, J.H. Brewer, D.R. Noakes, E.J. Ansaldo, and K. Nishiyama, *Phys. Rev. Lett.* **58**, 1780 (1987).
- [16] R.F. Kiefl, W. Odermatt, H. Baumeier, J. Felber, H. Keller, W. Kündig, K.W. Blazey, T.L. Estle, and C. Schwab, *Phys. Rev. B* **34**, 1474 (1986).
- [17] C.G. Van de Walle, In *Hydrogen in Semiconductors*, ed. by J.I. Pankove and N.M. Johnson, (Academic Press, 1990), in press.
- [18] B.D. Patterson, H. Baumeier, H. Keller, R.F. Kiefl, W. Kündig, W. Odermatt, J.W. Schneider, W.J. Choyke, T.L. Estle, D.P. Spencer, K.W. Blazey, and I.M. Savić, *Hyperfine Int.* **32**, 625 (1986).
- [19] R.F. Kiefl, R. Kadono, J.H. Brewer, G.M. Luke, H.K. Yen, M. Celio, and E.J. Ansaldo, *Phys. Rev. Lett.* **62**, 792 (1989).
- [20] E. Holzschuh, *Phys. Rev. B* **27**, 102 (1983).
- [21] R. C. DuVarney, private communication.
- [22] G. Balzer, H. Graf, E. Recknagel, A. Weidinger, and Th. Wichert, *Hyperfine Int.* **9**, 603 (1981).
- [23] K.W. Blazey, T.L. Estle, S.L. Rudaz, E. Holzschuh, W. Kündig, and B.D. Patterson, *Phys. Rev. B* **34**, 1422 (1986).
- [24] K.W. Blazey, T.L. Estle, E. Holzschuh, W. Odermatt, and B.D. Patterson, *Phys. Rev. B* **27**, 15 (1983).
- [25] R.F. Kiefl, J.H. Brewer, S.R. Kreitzman, G.M. Luke, T.M. Riseman, T.L. Estle, M. Celio, and E.J. Ansaldo, In *Proceedings of the 15th International Conference on Defects in Semiconductors*, in press.
- [26] C. G. Van de Walle, see paper in these Proceedings and to be published.
- [27] S.F.J. Cox and M.C.R. Symons, *Chem. Phys. Lett.* **120**, 516 (1986).
- [28] A. Mainwood, and A.M. Stoneham, *J. Phys. C* **17**, 2513 (1984).
- [29] H. Katayama-Yoshida and K. Shiido, *Phys. Rev. Lett.* **51**, 207 (1983).
- [30] T.L. Estle, S. Estreicher, and D.S. Marynick, *Hyperfine Int.* **32**, 637 (1986).
- [31] T.A. Claxton, A. Evans, and M.C.R. Symons, *J. Chem. Soc., Faraday Trans. 2* **82**, 2031 (1986).
- [32] T.L. Estle, S. Estreicher, and D.S. Marynick, *Phys. Rev. Lett.* **58**, 1547 (1987).
- [33] S. Estreicher, *Phys. Rev. B* **30**, 9122 (1987); G.L. Bendazzoli and O. Donzelli, submitted to *J. Phys. C*; A.A. Bonapasta, A. Lapicciarella, N. Tomassini, and M. Capizzi, *Europhys. Lett.* **7**, 145 (1988); P. Deák, L.C. Snyder, and J.W. Corbett, *Phys. Rev. B* **37**, 6887 (1988); G.G. DeLeo, M.J. Dorogi, and W.B. Fowler, *Phys. Rev. B* **38**, 7520 (1988); S.A. Kuten, V.I. Rapoport, A.V. Mudry, R.B. Gelfand, A.L. Pushkarchuk, and A.G. Ulyashin, *Hyperfine Int.* **30**, 379 (1988); G.S. Mjakenkaya, G.L. Gutsev, Yu.V. Obukhov, and V.M. Smoylov, to be published; C.G. Van de Walle, Y. Bar-Yam, and S.T. Pantelides, *Phys. Rev. Lett.* **60**, 2761 (1988); W.B. Fowler, G.G. DeLeo, and M.J. Dorogi, In *Proceedings of the 15th International Conference on Defects in Semiconductors*, in press; C.G. Van de Walle, P.J.H. Denteneer, Y. Bar-Yam, and S.T. Pantelides, *Phys. Rev. B* **30**, 10791 (1989).
- [34] S. Vogel, M. Celio, Dj.M. Maric, and P.F. Meier, *J. Phys.:Condens. Matter* **1**, 4729 (1989).
- [35] P.J.H. Denteneer, C.G. Van de Walle, and S.T. Pantelides, *Phys. Rev. Lett.*, in press.
- [36] Dj.M. Maric, S. Vogel, P.F. Meier, and S.K. Estreicher, *Phys. Rev. B*, in press.
- [37] W. Odermatt, H. Baumeier, H. Keller, W. Kündig, B.D. Patterson, J.W. Schneider, J.P.F. Sellschop, M.C. Stemmet, S. Connell, and D.P. Spencer, *Phys. Rev. B* **38**, 4388 (1988).
- [38] H. Baumeier, R.F. Kiefl, H. Keller, W. Kündig, W. Odermatt, B.D. Patterson, J.W. Schneider, T.L. Estle, S.P. Rudaz, D.P. Spencer, K.W. Blazey, and I.M. Savić, *Hyperfine Int.* **32**, 659 (1986).

ELECTRONIC STRUCTURE AND HYPERFINE PARAMETERS FOR HYDROGEN AND MUONIUM IN SILICON

CHRIS G. VAN DE WALLE

Philips Laboratories, North American Philips Corporation, Briarcliff Manor, NY 10510

ABSTRACT

First-principles spin-density-functional calculations are used to evaluate hyperfine and superhyperfine parameters for hydrogen and muonium at various sites in the Si lattice. The results can be directly compared with values from muon-spin-rotation experiments, leading to an unambiguous identification of "anomalous muonium" with the bond-center site. The agreement found in this case instills confidence in the general use of spin-density-functional calculations for predicting hyperfine parameters of defects.

INTRODUCTION

The behavior of hydrogen in semiconductors has been the focus of intense experimental and theoretical interest in recent years. The observation that hydrogen can passivate shallow impurities¹ illustrated the technological importance of the subject; it also emphasized the need for a more profound understanding of hydrogen as an impurity in a semiconductor lattice. Theory²⁻⁸ has been able to significantly enhance insight in the interactions between hydrogen (H) and the semiconductor host atoms, and with other impurities. In the case of isolated interstitial hydrogen, an unambiguous identification of the proposed structures with the experimentally observed defects was still missing, however. Experimental information about defect configurations can be obtained from electron paramagnetic resonance (EPR) or muon spin rotation (μ SR),⁹ which probe the interaction between electronic wavefunctions and nuclear spins. A conclusive structural identification of the defect is possible if reliable theoretical calculations of the hyperfine parameters for various configurations are available. Comparison of theory and experiment then determines whether a proposed structure is consistent with experimental observations.

In this paper I present theoretical results for hyperfine parameters calculated for H at various sites in the Si lattice. Apart from the parameters for the impurity itself, I also give values for the so-called superhyperfine parameters which describe the interaction of the defect wavefunctions with neighboring host atoms. The electronic-structure calculations, based on pseudopotential-spin-density-functional theory, are shown to yield values in good agreement with experiment, allowing an unambiguous identification of "normal muonium" with the tetrahedral interstitial site, and "anomalous muonium" with the bond-center site.

Experimentally, it has proved very difficult to obtain results for an isolated hydrogen atom. Fortunately, a vast amount of information is available about muonium.⁹ Muonium is a pseudo-isotope of hydrogen; it consists of an electron bound to a positive muon (μ^+). The mass of μ^+ is 1/9 of that of the proton, and its lifetime is 2.2 μ s. Muon spin rotation and muon level-crossing resonance are the experimental techniques that have provided a wealth of information about muonium in solid-state materials.^{9,10} Two distinct types of paramagnetic centers have been observed; they are labeled Mu ("normal muonium") and Mu* ("anomalous muonium"). The muon-electron hyperfine coupling is isotropic for Mu; its value is reduced from the vacuum value, indicating a delocalization of the spin density. Because of its isotropic character, Mu has usually been associated with the tetrahedral interstitial (T) site. Anomalous muonium exhibits very different properties. Its isotropic hyperfine coupling is much smaller than for Mu, and significant anisotropic coupling is

present, showing a $\langle 111 \rangle$ symmetric hyperfine interaction (C_{3v} symmetry). The spin density is strongly p-like, indicating large lattice relaxation and a substantial increase in the bond length. These features were considered to be indicative of a bond-center position.^{10,12} Only one observation has been reported of a paramagnetic center associated with interstitial hydrogen in silicon: the so-called AA9 center has been shown to have characteristics very similar to anomalous muonium.^{11,12}

For most practical purposes, the theoretical results for hydrogen and muonium are equivalent, since both the proton and muon are point particles with identical charge. The terms hydrogen and muonium can therefore be used interchangeably in our discussion; only when dynamics are important can the difference in mass and lifetime lead to differences in behavior. The similarity of the experimental hyperfine results for muonium^{10,12} and hydrogen¹¹ indicates that such effects are minor for the problem at hand.

Using pseudopotential-density-functional theory, we previously mapped out the complete total energy surfaces for various charge states of H in Si.^{7,8} Since the present study concentrates on paramagnetic centers, we only consider the neutral charge state here. It was found that neutral H is most stable in the bond-center (BC) position. Large relaxations of the neighboring Si atoms (over 0.45 Å for the nearest neighbors) are required to accommodate the H atom. The electronic structure of this defect can, to a first approximation, be understood as arising from only three states⁵: the semiconductor bonding and antibonding states, and the H 1s orbital. The symmetric H orbital only couples to the bonding state, leading to a lowering of this state (which still contains two electrons), and the occurrence of a state at higher energy. The original antibonding state has a node midway between the Si atoms, and is therefore now labeled as a non-bonding state of the defect complex. In the neutral charge state, this state contains one electron. A contour plot of the spin density is shown in Fig. 1a; it corresponds to an antibonding combination of Si orbitals, with mainly p-like character.

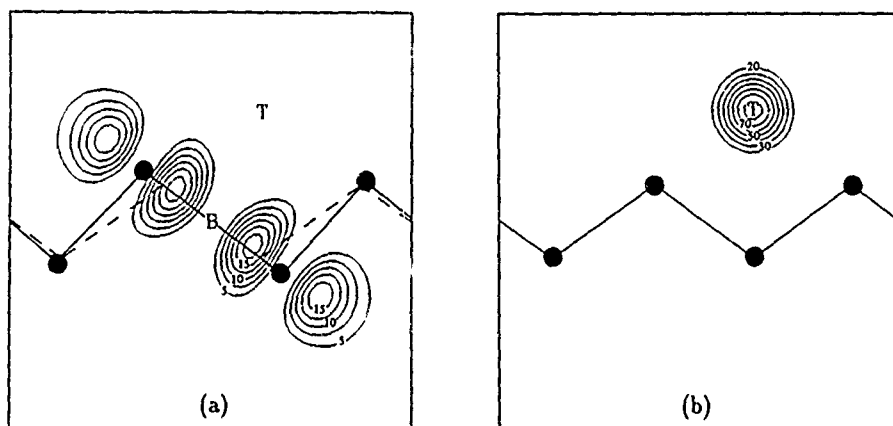


FIG. 1: (a) Contour plot of the spin density in the (110) plane through the atoms for neutral H at the bond center. The Si atoms in their relaxed positions are indicated with black dots and connected with solid lines. Dashed lines connect the unrelaxed atomic positions. The contour interval is 2.5 electrons/(unit cell) (for a supercell containing 1 H and 32 Si atoms). (b) Contour plot of the spin density in the (110) plane through the atoms for neutral H at T. The Si atoms are indicated with black dots; no relaxation occurs. The contour interval is 10 electrons/(unit cell).

The energy at the T site is ~ 0.3 eV higher than at the BC site; T is not a local minimum, but the energy surface in that region is quite flat. Negligible relaxation of the surrounding lattice takes place here. The electronic structure for hydrogen (or muonium) at T corresponds to that of an s-like state centered on the impurity, as illustrated in Fig. 1b. Even though BC is the global minimum, muonium may also be found in positions close to the T site which do not require the large lattice relaxation necessary at the bond center.¹³ In the non-equilibrium situation of the muonium experiments, a significant fraction of muonium atoms may be inhibited from reaching the lowest-energy BC site, and stay in the interstitial channels. If Mu tunnels between equivalent sites in the neighborhood of T, the effective isotropy of the center would be preserved.

THEORETICAL BACKGROUND

The interaction between an electron and a nuclear spin in general includes an isotropic (contact interaction) and an anisotropic (dipole-dipole) part.¹⁴ The paramagnetic muonium states observed to date in semiconductors have either an isotropic hyperfine interaction (for which the hyperfine tensor \tilde{A} is simply proportional to the unit matrix) or one with axial symmetry. In the latter case, \tilde{A} is diagonal with elements A_{\parallel} and A_{\perp} , which are usually written as $A_{\perp} = a - b$ and $A_{\parallel} = a + 2b$. a and b are given by:

$$a = \frac{2\mu_0}{3} g_e \mu^e g_I \mu^I |\psi(\mathbf{R})|^2; \quad b = \frac{\mu_0}{8\pi} g_e \mu^e g_I \mu^I \int d^3r |\psi(\mathbf{s})|^2 \frac{3\cos^2\tau - 1}{r^3}. \quad (1)$$

\mathbf{R} is the coordinate of the nucleus, \mathbf{s} is the coordinate of the electron, and r is the distance between the electron and the nucleus. a and b have units of energy; often they are expressed as a frequency (in MHz), using $E = h\nu$. The notation $|\psi(\mathbf{s})|^2$ is used here to represent a spin density, which corresponds to the difference between the charge densities of the spin-up and the spin-down electrons, i.e. $\rho_{\uparrow} - \rho_{\downarrow}$. These equations describe the interaction of the muonium (or hydrogen) electron with any nucleus that has a non-vanishing magnetic moment. If this nucleus is the muon (or proton) itself, the Hamiltonian describes the regular hyperfine or Fermi contact interaction. In free space, this leads to a value of the hyperfine constant a of 4463 MHz for muonium, or 1420 MHz for hydrogen (see Ref. 9).

The calculations were carried out using spin-density-functional theory¹⁵, with an *ab initio* norm-conserving pseudopotential¹⁶ for Si, and the Coulomb potential for H. A supercell geometry was used, in which the impurity is surrounded by a sufficiently large number of Si atoms, and this whole structure is periodically repeated. Calculations were performed for supercells containing 8, 16, and 32 atoms to make sure the supercells are large enough to include all relevant details of the spin density, and ensure sufficient separation of impurities in neighboring supercells. The basis set in the calculations consists of plane waves with kinetic energy below a cutoff (E_1 ; E_2).¹⁷ Test calculations were carried out up to (15;30) Ry. Additional details about the theoretical techniques can be found in Ref. 8. The results presented below were obtained in 32-atom supercells at a cutoff of (7.5;15) Ry.

RESULTS AND COMPARISON WITH EXPERIMENT

Normal muonium

For reasons of numerical accuracy, and to facilitate presentation, it is appropriate to compare the calculated hyperfine parameters to reference quantities in the free atom. For instance, the isotropic hyperfine parameter is often expressed as a ratio of the spin density at the muon inside the semiconductor to the spin density at the muon in free muonium, i.e. $|\psi(0)|^2/|\psi(0)|_{\text{vac}}^2$. The value I obtain for this quantity is 0.515. I carried

out a number of calculations in which the muon was moved away from the T site. The maximum spin density occurs when the muon is at T itself, and falls off when the muon is moved away from T. When the muon is moved by 0.27 \AA in either the $\langle 111 \rangle$ or the $\langle 001 \rangle$ direction, the spin density is reduced by $\sim 12\%$. Most of the change is due to polarization effects: if the unpaired electron is contributing to the spin-up density, then this density decreases only slightly when the muon is moved away from T. The spin-down density, however, increases more significantly, leading to a net reduction of the spin density $\rho_{\uparrow} - \rho_{\downarrow}$. This illustrates the importance of polarization of the valence states, which is only included if the calculations are performed in a spin-unrestricted scheme. Indeed, if the contact interaction were calculated based solely on the charge density of the defect state, its value would be off by a factor of two.

Muon spin rotation experiments (see Ref. 9) show a reduction of the spin density in normal muonium (compared to the free atom) by 0.45 in Si, to be compared with the calculated value of 0.515. The fact that the experimental value is lower is consistent with the notion that the muon does not sit exactly at T itself, but rather moves in a region around it, where the spin density is somewhat lower than at T itself.

Anomalous muonium

Results for muonium at BC are displayed in Table 1. First- and second-neighbor relaxations were included, and the impurity was placed symmetrically between two Si atoms, in accord with the results from first-principles total-energy calculations.⁸ The calculated spin density (and isotropic hyperfine parameter) for muonium at BC is small and negative. This is in agreement with the electronic structure discussed above, and illustrated in Fig. 1a: the muon sits at a node of the wavefunction of the unpaired electron, and spin-polarization of bonding electrons is present. The sign of the spin density is in agreement with experiment,^{10,12} but its magnitude is underestimated. In view of the small value of this parameter (more than an order of magnitude smaller than at T), the agreement can still be considered reasonable.

The dependence of the hyperfine constants on the position of the muon and the Si atoms was also examined. When the muon is moved by 0.1 \AA along the Si-Si bond direction (as in a stretching mode displacement), with the Si atoms fixed, $|a|$ decreases by $\sim 11\%$ and b by only 2% . For displacements perpendicular to the Si-Si bond, $|a|$ decreases by 6% for a 0.33 \AA displacement, if the Si atoms are kept fixed. If the Si atoms are allowed to relax, to keep the Si-muon distance constant, the same perpendicular displacement of the muon reduces $|a|$ by 12% . Finally, when the relaxation of the Si neighbors was reduced from 0.45 \AA to 0.38 \AA , keeping the muon at bond center, $|a|$ decreased by 17% , while b increased by 2% . The effect on the isotropic hyperfine constant is thus seen to always be a decrease in magnitude, indicating that the larger experimental value of $|a|$, as compared to our theoretical prediction, can not be explained by vibrations or a static displacement of the muon from the exact BC site.

Table 1: Theoretical and experimental (Ref. 10) values of $\eta_s^2 = |\psi(0)|_{BC}^2/|\psi(0)|_{vac}^2$ and of the anisotropic hyperfine parameter b for muonium at the bond-center site in Si.

η_s^2		b (MHz)	
theoretical	experimental	theoretical	experimental
-0.006	-0.015	18.1	25.3

Table 2: Theoretical and experimental (Refs. 10, 19) values of $\eta_s^2 = a/A_p^{frec} = |\psi(0)|_{Si}^2/|\psi(0)|_{vac}^2$ and $\eta_p^2 = b/A_p^{frec}$ for the first and second ^{29}Si neighbors of muonium at the bond-center site in Si.

	η_s^2		η_p^2	
	theoretical	experimental	theoretical	experimental
1st neighbors	0.020	0.021	0.214	0.186
2nd neighbors	0.0055	0.0049	0.017	0.0083

Superhyperfine parameters

Superhyperfine parameters describe the interaction of the defect wavefunction with surrounding host atoms, in this case with nearest-neighbor and second-nearest neighbor ^{29}Si atoms (spin 1/2). These values have been accurately measured^{12,18} for the case of anomalous muonium. Even though the Si atoms are represented by a pseudopotential, and therefore the wave functions in the core region differ from the full wave functions, values for the hyperfine parameters can still be obtained by comparing the spin density with an appropriate reference quantity. This assumption can be justified *a posteriori* by the good agreement of the results with experiment. The reference is determined from calculations on a single (pseudo-)atom in vacuum. For the isotropic hyperfine parameter, the value of $|\psi(0)|^2/|\psi(0)|_{vac}^2$ is calculated. For the anisotropic parameters, it is customary to compare b with A_p^{frec} , which is an average of r^{-3} determined for the valence p-orbital.¹⁹ The results are shown in Table 2.

Measurement of superhyperfine parameters played an important role in the experimental identification of anomalous muonium, which became possible thanks to the development of a novel level-crossing-resonance technique.^{10,12} Comparing experimental and theoretical values in Table 2 we conclude that both the reduction in the hyperfine parameters in going from first to second neighbors, as well as the actual values themselves, are in satisfactory agreement with experiment.

The evidence in favor of identification of anomalous muonium with the bond-center position is convincing. The so-called vacancy-associated model,⁶ which had been proposed on the basis of hyperfine calculations for clusters, shows distinct disagreement with the experimental results,¹⁰ which clearly establish that there are two equivalent Si neighbors along $\langle 111 \rangle$. The same cluster calculations⁶ on which the vacancy-associated model was based produce hyperfine parameters for the bond center which deviate by more than an order of magnitude from the present results (which agree with experiment for Mu^*).

CONCLUSION

Using the example of muonium (or hydrogen) paramagnetic centers in silicon, I have shown that pseudopotential-spin-density-functional calculations can yield values for hyperfine parameters that are in good agreement with experiment. Combined with the ability to produce accurate total energy surfaces (including all relaxations), this method emerges as a powerful and versatile tool for the study and identification of defects in semiconductors.

ACKNOWLEDGMENTS

Thanks are due to R. Kiefl for encouraging me to investigate this problem, and to T. L. Estle and S. T. Pantelides for helpful suggestions.

REFERENCES

- ¹ S. J. Pearton, J. W. Corbett, and T. S. Shi, *Appl. Phys. A* **43**, 153 (1987) and references therein.
- ² S. F. J. Cox and M. C. R. Symons, *Chem. Phys. Lett.* **126**, 516 (1986).
- ³ S. Estreicher, *Phys. Rev. B* **36**, 9122 (1987).
- ⁴ P. Deák, L. C. Snyder, and J. W. Corbett, *Phys. Rev. B* **37**, 6887 (1988).
- ⁵ G. G. DeLeo, M. J. Dorogi, and W. B. Fowler, *Phys. Rev. B* **38**, 7520 (1988).
- ⁶ N. Sahoo, K. C. Mishra, and T. P. Das, *Phys. Rev. Lett.* **55**, 1506 (1985); N. Sahoo, S. B. Sulaiman, K. C. Mishra, and T. P. Das, *Phys. Rev. B* **39**, 13389 (1989).
- ⁷ C. G. Van de Walle, Y. Bar-Yam, and S. T. Pantelides, *Phys. Rev. Lett.* **60**, 2761 (1988).
- ⁸ C. G. Van de Walle, P. J. H. Denteneer, Y. Bar-Yam, and S. T. Pantelides, *Phys. Rev. B* **39**, 10791 (1989).
- ⁹ B. D. Patterson, *Rev. Mod. Phys.* **60**, 69 (1988).
- ¹⁰ R. F. Kiefl, M. Celio, T. L. Estle, S. R. Kreitzman, G. M. Luke, T. M. Riseman, and E. J. Ansaldo, *Phys. Rev. Lett.* **60**, 224 (1988).
- ¹¹ V. A. Gordeev, Yu. V. Gorelinskii, R. F. Konopleva, N. N. Nevinnii, Yu. V. Obukhov, and V. G. Firsov (unpublished); Yu. V. Gorelinskii and N. N. Nevinnii, *Pis'ma Zh. Tekh. Fiz.* **13**, 105 (1987) [*Sov. Tech. Phys. Lett.* **13**, 45 (1987)].
- ¹² R. F. Kiefl, J. H. Brewer, S. R. Kreitzmann, G. M. Luke, T. M. Riseman, T. L. Estle, M. Celio, and E. J. Ansaldo, in *Proceedings of the 15th International Conference on Defects in Semiconductors*, Budapest, Hungary, 22-26 August 1988 (Trans Tech Publications, Switzerland).
- ¹³ G. Watkins, in *Proceedings of the 15th International Conference on Defects in Semiconductors*, Budapest, Hungary, 1988 (Trans Tech Publications, Switzerland).
- ¹⁴ R. Beck, P. F. Meier, and A. Schenck, *Z. Physik B* **22**, 109 (1975); the formulas were taken from this reference, except that SI units are used here (instead of atomic units, where $\mu_0/4\pi=1$).
- ¹⁵ P. Hohenberg and W. Kohn, *Phys. Rev.* **136**, B864 (1964); W. Kohn and L. J. Sham, *ibid.* **140**, A1133 (1965); L. Hedin and B. I. Lundqvist, *J. Phys. C* **4**, 2064 (1971); U. von Barth and L. Hedin, *J. Phys. C* **5**, 1629 (1972).
- ¹⁶ D. R. Hamann, M. Schlüter, and C. Chiang, *Phys. Rev. Lett.* **43**, 1494 (1979).
- ¹⁷ The notation $(E_1; E_2)$ means that plane waves with kinetic energy up to E_2 Ry are included in the expansions of wave functions and potentials; waves with kinetic energy up to E_1 Ry are included in an exact diagonalization of the Hamiltonian matrix, while those with kinetic energy between E_1 and E_2 Ry are included in second-order Löwdin perturbation theory [P. O. Löwdin, *J. Chem. Phys.* **19**, 1396 (1951)]. I consistently choose $E_2 = 2E_1$.
- ¹⁸ R. F. Kiefl and T. L. Estle, to be published in *Hydrogen in Semiconductors*, edited by J. I. Pankove and N. M. Johnson, (Academic Press).
- ¹⁹ J. R. Morton and K. F. Preston, *J. Magn. Reson.* **30**, 577 (1978).

HYDROGEN IN CRYSTALLINE SILICON UNDER COMPRESSION AND TENSION

C.S. NICHOLS and D.R. CLARKE, IBM Research Division, T. J. Watson Research Center, Yorktown Heights, NY 10598

ABSTRACT

The behavior of hydrogen in crystalline silicon (c-Si) containing regions of compressive or tensile stress is important for understanding the solute's interaction with dislocations, grain boundaries, and crack tips. A series of first-principles total-energy calculations probing the stable site for hydrogen as a function of its charge state, the Fermi level position, and the crystalline lattice constant has been performed. We find that the stable site for hydrogen depends critically on both pressure and on the hydrogen charge state. Furthermore, hydrogen is predicted to undergo a transition from an interstitial site to the bond-center site as a function of pressure.

INTRODUCTION

Because of its ubiquitous presence, hydrogen (H) in crystalline silicon (c-Si) has been of great theoretical and experimental interest. Attention has focused primarily, although not exclusively, on the diffusion of atomic hydrogen, its molecule formation, and its complexing with and passivation of dopant impurities. A rather comprehensive understanding of hydrogen in silicon under ambient pressures has been obtained through complementary experimental¹ and theoretical² work. The behavior of hydrogen in compressional or tensional stress fields in c-Si has, however, received little systematic attention. Such information is relevant for understanding the behavior of H in Si which contains, for example, dislocations, grain boundaries, and cracks, as well as in Si devices and multilayers.

We present the results of first-principles total-energy calculations exploring the behavior of H in c-Si as a function of its charge state, the Fermi level position, and the lattice constant. We examine strains for which many physical properties are expected to vary linearly although no linearity is assumed *a priori*. For ambient pressures, our results agree with previously reported findings for the stable charge state, minimum-energy position, and energy difference between selected locations for the H atom.² However, under compression and tension, we find that the energy difference between the bond-center (BC) position and the tetrahedral (T) site changes rapidly, indicating a transition to a different minimum-energy position.³

METHODOLOGY

Our calculations are based on density-functional theory,⁴ within the local-density approximation, and norm-conserving pseudopotentials⁵ with a plane-wave basis. A momentum-space formalism is used to solve the relevant Schrödinger equation⁶ for a supercell geometry.⁷ *Ab initio* pseudopotentials, constructed according to the scheme of Hamann, Schlüter, and Chiang,⁵ were used for the host Si atoms, while a Coulomb potential was used for the H atom. Careful convergence studies have been performed with respect to supercell size, plane wave cut-off energy, and special points sampling in the irreducible wedge of the Brillouin zone. In particular, it was necessary to use supercells of 32 atoms such that the distance between H atoms in neighboring cells is 9.4 Å. Indeed, convergence of the final results could not be obtained with smaller cells under tension. Plane waves with a kinetic energy cut-off of 16 Ry were used in the expansions for the wave functions and potentials (plane waves up to 8 Ry were included in the exact diagonalization of the Hamiltonian while plane waves between 8 and 16 Ry were used in second-order Löwdin perturbation theory⁸). Convergence tests of the basis-set size show that for this particular basis, the energy differences are converged to less than 0.3 eV of the fully converged result. In addition, we have included symmetry-preserving relaxations of all first and second neighbors of the H atom in all the calculations. The different charge states of the H are treated following Van de Walle *et al.*⁸ Spin polarization effects have not been included because such effects are small.⁹

RESULTS AND DISCUSSION

Before investigating the properties of H in c-Si (c-Si:H) under compression and tension, both the bulk properties of c-Si and the previously reported results for c-Si:H under ambient pressure were reproduced. The total energy of the pure c-Si supercell was calculated at five different lattice constants, (5.13 Å, 5.28 Å, 5.43 Å, 5.58 Å, and 5.73 Å), representing maximum strains of $\pm 5.5\%$. These particular values were chosen so as to avoid lattice constants corresponding to "jumps" in the energy versus volume curve¹⁰ which arise because of discrete changes in the size of the basis set as the lattice constant is varied. All calculations were performed at a constant plane-wave cut-off and the results were fitted to a Murnaghan equation of state¹¹ to determine the equilibrium lattice constant, a_0 , and the bulk modulus, B_0 (Table I). The agreement with the corresponding experimental properties is quite good for the lattice constant ($\sim 0.5\%$ deviation from experiment) and, as is well known for such LDA calculations, somewhat poorer for the bulk modulus ($\sim 6\%$ deviation from experiment).

Table I. Tabulation of the calculated bulk moduli, B_0 , and lattice constants, a_0 , for the various charge states and positions of the H solute. The experimental values for pure crystalline Si are also included.

System	B_0 (GPa)	a_0 (Å)
Experiment	99.0	5.429
c-Si	93.0	5.404
H ⁰ (BC)	88.9	5.427
H ⁰ (T)	90.6	5.405
H ⁺ (BC)	92.5	5.401
H ⁺ (T)	94.3	5.377
H ⁻ (BC)	85.8	5.453
H ⁻ (T)	87.2	5.431

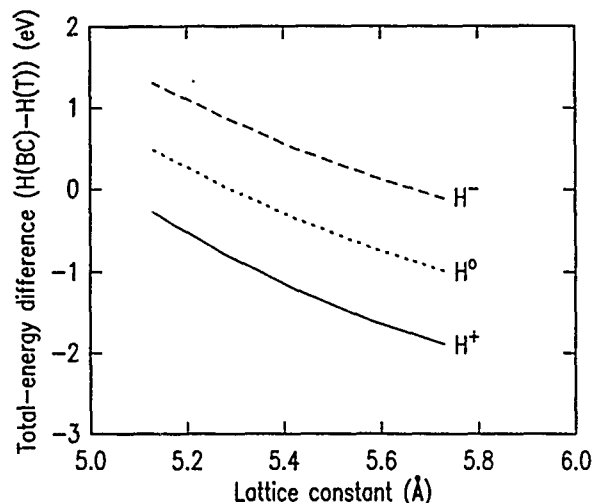
We next introduced a single H atom into the host matrix at two representative sites. From previous studies,² it was determined that the global minimum, at the equilibrium lattice constant, is at the BC site (positive and neutral charge states) or at the T site (negative charge state). Furthermore, in order to ascertain the behavior of H in the vicinity of a crack tip, we wanted to probe whether H would disrupt the Si network by inserting itself in a bond-center position, thus reducing the fracture resistance, or whether H preferred "inert" interstitial positions. Hence the choice of bond-center and tetrahedral interstitial sites.

The total energy of H in the positive, neutral, and negative charge states at the two sites was calculated for the same five lattice constants used in the bulk Si calculation. Equilibrium lattice constants and bulk moduli were obtained from a fit to a Murnaghan equation and the results are also reproduced in Table I. For all the configurations studied (with the exception of H⁺(T)), a softening is observed, as evidenced by a decrease in the bulk modulus. In addition, the electronic structure of c-Si:H was found to vary strongly as a function of the lattice constant. For the present purposes, we focus on the change with pressure in the energy difference between the H-induced level and the top of the valence band. For H at the T site, the defect level is slightly below the top of the valence band maximum at ambient pressure in the negative charge state. In all charge states, the level shifts to lower energy at the rate 1.5 eV/Å for increasing lattice constant.¹² For H at the BC site, the H-induced level is in the upper part of the band gap and shifts to lower energy at the rate 0.4 eV/Å for increasing lattice constant.

For each given charge state, a plot of the total-energy difference between hydrogen at the T site and at the BC site as a function of lattice constant was calculated. These curves are reproduced in Fig. 1. The total-energy difference is nearly linear with a negative slope over the entire range of strains investigated ($\pm 5.5\%$). This linear dependence arises because of the similarities of the bulk moduli calculated for H at the two different sites. Fig. 1 indicates that under large enough compression, the T site is energetically preferred, while the negative slope of the total-energy difference indicates that the BC site becomes more favored under smaller compression or under tension. (For H⁺, extrapolation of the calculations to slightly smaller lattice constants is required before this transition is observed.) Using the calculated bulk moduli and the lattice constant at which the crossover occurs, we can determine an upper limit for the pressure region in which the ambient-pressure global energy minimum can remain stable. These

upper limits are 19.7 GPa (positive charge state), -12.0 GPa (negative charge state), and 6.9 GPa (neutral charge state), where we use the convention that positive pressure corresponds to compression, and negative pressure corresponds to tension. It should be noted that the extrapolated value for the positive charge state lies at a pressure which is beyond the phase transition from the diamond to the β -tin structure. These pressures are not modest, but are accessible in some laboratories. (The case of tension is discussed below).

Fig. 1 Total-energy difference between H at the T and BC sites as a function of lattice constant for H in its different charge states.



These observations are intuitively reasonable and arise from the competition between two effects: size and electronic structure. For the smallest lattice constant studied (5.13 Å), the Si-H distance for H at the T site is 2.22 Å, while the Si-H distance for H at the BC site was calculated to be 1.52 Å. The latter value is substantially reduced from the value 1.63 Å for H⁰ at ambient pressure, indicating the more severe constraints imposed on the H solute by the surrounding lattice at the BC site. The T site poses less severe spatial constraints, explaining in part why it becomes increasingly favorable with respect to the BC site under pressure.

The effects of electronic structure on the transition from the T to the BC site are most conveniently demonstrated by defining a heat of solution for the single H concentration (3%) of interest in the present study:

$$E_{\text{soln}} \equiv E(\text{H}) - E_{\text{bulk}} - E_{\text{atom}} \quad (1)$$

$E(\text{H})$ is the total energy per supercell containing a H atom ($N+1$ atoms), E_{bulk} is the total energy of a bulk crystalline Si supercell (N atoms), and E_{atom} is the total energy of an isolated H pseudo-atom. Because the total energy of the pseudo-atom is a constant for each H atom location inside the crystal, an effective heat of solution may be defined as:

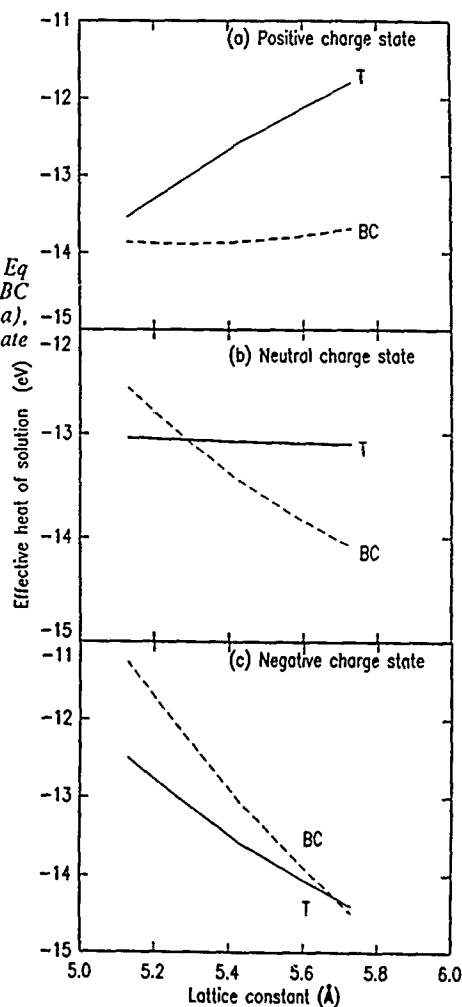
$$E_{\text{soln}}^{\text{eff}} \equiv E_{\text{soln}} + E_{\text{atom}} \quad (1a)$$

The heats of solution defined in Eqs. (1) and (1a) are valid for neutral species. For singly charged species, the heat of solution depends linearly on the Fermi level position.⁹ Note that the effective heat of solution defined in Eq. (1a) is negative and that the more negative it is, the greater the H solubility.

The effective heats of solution for H at the T site (solid line) and at the BC site (dashed line) for the positive, neutral, and negative charge states are plotted in Figs. 2a, 2b, and 2c, respectively. Different charge states are obtained by taking or removing electrons to or from the Fermi level. For Figs. 2a and 2c, it has been assumed that the Fermi level is at the bottom of the forbidden energy gap, making the material p-like. n-type material is simulated by placing the Fermi level at the top of the calculated energy gap (0.6 eV). Thus, the heat of solution for the positive charge state in n-type material is obtained by adding the calculated band gap to the p-type material value, while that for the negative charge state is obtained by subtracting the calculated band gap. Note that the heats of solution for the neutral charge state are independent of the Fermi level position. The different pressure dependences of the two heats of

solution can be traced to differences in the electronic structure induced by H at the two locations.

Fig. 2 Effective heat of solution as defined by Eq (1a) for H at the T site (solid line) and at the BC site (dashed line) in the positive charge state (a), neutral charge state (b), and negative charge state (c).



H at the BC site interacts strongly with the two neighboring Si atoms and produces three levels.¹³ The lowest energy level is completely bonding in nature and lies in the bulk of the valence band. There is also a corresponding anti-bonding level which lies in the conduction band. The third level has been identified as non-bonding by examining its charge density; it is this level which lies in the forbidden gap. On the other hand, for H at the T site, there is only a weak overlap with the neighboring Si atoms; a hydrogen-induced level is identified below the valence band edge.

For positively-charged H, it is clearly favorable to produce the BC bonding level, which is fully occupied, and to leave the non-bonding level empty. This conclusion is valid for all strains investigated and is consistent with the heats of solution plotted in Fig. 2a. For neutral H, the non-bonding level contains one electron, but its occupation is still favorable. However, the BC site energy rises rapidly as a function of pressure, and ultimately this site will become unstable. Finally, for negatively-charged H, the BC non-bonding level must accommodate two electrons which imposes too high an energy cost and hence the T site is preferred. Additionally, because

the T-site level drops in energy for larger lattice constants, as discussed above, it becomes increasingly favorable to occupy this level.

The calculated heats of solution also provide an understanding of the solubility of H in c-Si under various conditions. For p-type material, H is stable in the positive charge state (H^+). This can be seen by a direct comparison of Figs. 2a, 2b, and 2c. For ambient pressure and under compression, H^+ is stable at the BC site. Application of hydrostatic pressure to p-type c-Si:H should have little effect on the H solubility because the BC heat of solution in Fig. 2a is relatively insensitive to pressure. On the other hand, for n-type material, H is stable in the negative charge state (H^-). Thus, for ambient pressure and under compression, H^- is stable at the T site. For increasing pressure, H^- becomes less soluble in the crystal because of the decreasing magnitude of the heat of solution, Fig. 2c. H in c-Si is believed to be a negative-U system,⁹ so that the neutral charge state is never stable for any position of the Fermi level. This conclusion is indeed borne out by our results not only at ambient pressure but also under compression and tension. However, comparisons between different charge states are subject to larger error bars to the extent that they are limited by the LDA uncertainty. To the best of our knowledge, experimental data relevant to our theoretical findings regarding H solubility under pressure are lacking.

Application of hydrostatic compression is easily achieved by external means in diamond anvil cells. Crystalline regions under tension may be realized in samples which contain extended defects such as, for example, dislocations, grain boundaries (which may be envisioned as arrays of dislocation cores), and crack tips. Consider first an isolated dislocation. In p-type Si, H^+ is stable at the BC site and the heat of solution depends only weakly on strain (Fig. 2a). In n-type Si, H^- is stable at the T site for tensile strains up to $\approx 4\%$ but at the BC site for larger strains. The magnitude of the heat of solution for H^- is a strongly increasing function of lattice parameter, Fig. 2c. From these findings, we predict that H in n-type Si will prefer the tensile strain field in the vicinity of a dislocation core over unstrained crystalline regions with the concomitant formation of a Cottrell atmosphere around the dislocation. No such effect is expected in p-type Si. There is also the possibility, not calculated here, of charge transfer between the H solute and the bonds at the dislocation core that could lead to compensation of the charge levels and also a difference in dislocation mobility under shear stress (akin to the Patel effect).

There exists a wealth of experimental data¹⁴ concerning H passivation of grain boundaries in polycrystalline Si. Although the microscopic mechanism of such passivation is not clear and it is not known whether dopants are involved, we predict from the considerations of the previous paragraph that H will passivate grain boundaries in n-type Si more effectively than in p-type Si.

Finally, our findings may well have some relevance to the fracture of silicon in the presence of hydrogen. In the vicinity of a crack-tip there is a volume of material under tensile stress, the value of which decreases as $1/\sqrt{r}$ away from the crack tip. In p-type Si, we would therefore expect that H^+ would preferably adopt a BC position in a region about the crack-tip, possibly affecting the energy of cleavage and thereby altering the fracture resistance. Since in n-type Si, H remains in an interstitial position independent of pressure, no such effect is expected. We thus conjecture that p-type and n-type Si should exhibit a difference in fracture resistance, and if the rate of hydrogen diffusion to the tip region is kinetically limited, a difference in crack propagation rate at a given, constant driving force. Little experimental data appears to exist. An investigation of the fracture resistance of n-type Si in the presence of hydrogen has shown no difference from that in the absence of hydrogen.¹⁵ The fracture resistance of p-type silicon in hydrogen does not appear to have yet been performed, although there are occasional cryptic remarks in the literature regarding the greater "brittleness" of p-type Si in the presence of hydrogen.^{1,16}

In conclusion, we have examined the behavior of hydrogen in crystalline silicon under compression and tension and specific predictions have been put forward. It has been conjectured that H should preferentially form a Cottrell atmosphere around isolated dislocations in n-type Si while no such effect should be observed in p-type Si. Furthermore, we posit that the fracture resistance of p-type c-Si:H should be less than that of n-type c-Si:H because of the tendency of H to insert itself in the BC position in the former material.

ACKNOWLEDGMENTS

We acknowledge many helpful conversations with C.G. Van de Walle and R.F. Cook. This work was supported in part by ONR under Contract No. N00014-88-C-0176.

REFERENCES

1. S. J. Pearton, J. W. Corbett, and T. S. Shi, *Appl. Phys. A* **43**, 153 (1987).
2. C. G. Van de Walle, Y. Bar-Yam, and S. T. Pantelides, *Phys. Rev. Lett.*, **60**, 2761 (1988), K. J. Chang and D. J. Chadi, *Phys. Rev. Lett.*, **62**, 937 (1989), P. Deák, L. C. Snyder, and J. W. Corbett, *Phys. Rev. B*, **37**, 6887 (1988), G. G. DeLeo, M. J. Dorogi, and W. B. Fowler, *Phys. Rev. B*, **38**, 7520 (1988), and S. Estreicher, *Phys. Rev. B*, **36**, 9122 (1987).
3. C.S. Nichols, D.R. Clarke, and C.G. Van de Walle, *Phys. Rev. Lett.* **63**, 1090 (1989).
4. P. Hohenberg and W. Kohn, *Phys. Rev.* **136**, B864 (1964); W. Kohn and L. J. Sham, *Phys. Rev.* **140**, A1133 (1965). The exchange and correlation potentials are based on work by D. M. Ceperley and B. J. Alder, *Phys. Rev. Lett.* **45**, 566 (1980), as parametrized by J. Perdew and A. Zunger, *Phys. Rev. B* **23**, 5048 (1981).
5. D. R. Hamann, M. Schlüter, and C. Chiang, *Phys. Rev. Lett.*, **43**, 1494 (1979).
6. J. Ihm, A. Zunger, and M. L. Cohen, *J. Phys. C* **12**, 4409 (1979).
7. Y. Bar-Yam and J. D. Joannopoulos, *Phys. Rev. B* **30**, 1844 (1984).
8. P. O. Löwdin, *J. Chem. Phys.* **19**, 1396 (1951).
9. C. G. Van de Walle, P. J. H. Denteneer, Y. Bar-Yam, and S. T. Pantelides, *Phys. Rev. B*, in publication.
10. P. J. H. Denteneer and W. van Haeringen, *Phys. Rev. B*, **33**, 2831 (1986).
11. F. D. Murnaghan, *Proc. Nat. Acad. Sci. U.S.A.* **30**, 244 (1944).
12. The position of the defect level relative to the top of the valence band is calculated by finding the weighted average of the level over the special points.
13. C. G. Van de Walle, in *Hydrogen in Semiconductors*, edited by J. I. Pankove and N. M. Johnson (Academic Press), to be published.
14. See, for example, P. C. Srivastava and J. C. Bourgoin, *Grain Boundaries in Semiconductors*, edited by Pike, Seager, and Leamy (Elsevier, 1982), p. 137 and V. J. Rao, W. A. Anderson, and F. Kai, *ibid*, p. 227 and references therein.
15. T-Y. Zhang and P. Haasen, *Phil. Mag.*, **60**, 15 (1989).
16. A. Schnegg, M. Grundner, and H. Jacob, in *Semiconductor Silicon 1986*, edited by H. R. Huff (Electrochem. Soc., Pennington, NJ, 1986), p. 198.

ANALYSIS OF REAL-TIME HYDROGENATION DATA FROM P AND N-TYPE SILICON

CARLETON H. SEAGER AND ROBERT A. ANDERSON
Sandia National Laboratories, Albuquerque, NM 87185

ABSTRACT

Hydrogenation of metal/thin oxide/p-type silicon and metal/n-type silicon diodes has been studied using high frequency capacitance profiling. In situ observations of acceptor and donor passivation were made while H⁺ ions were implanted through thin gate metallizations. Direct measurement of ion transits at a variety of electric fields establish that a unique mobility can be assigned to positive H ions, and modeling of low and high field data in both n and p-type samples is consistent with the notion that the positive charge state is occupied ~1/10 of the time. The time dependence of hydrogen penetration for both p and n-type diodes indicates that hydrogen is, in addition to being trapped at unpassivated shallow donors or acceptors, becoming immobilized at other sites in silicon. The density of these secondary trapping sites correlates well with the shallow dopant population suggesting that additional hydrogen atoms may become trapped near already-passivated dopant atoms.

INTRODUCTION

The motion and trapping of hydrogen in silicon can be studied on a "real time" basis by implanting low energy protons through the thin metal gates of Schottky or thin oxide MIS structures while monitoring changes in the depletion layer charge density with capacitance techniques [1,2]. In a companion paper [3] presented at this symposium, we discuss the modelling of this implantation process and conclude that it results in the rapid establishment of a nearly time independent H density near the end of range in the semiconductor. This end of range depth is 50-250 Å for the ion energies used in the present studies. In this work, we shall primarily concern ourselves with two additional features of the problem. The first is a direct estimate of ion mobilities obtained by measuring arrival times of H⁺ crossing trap depleted regions. The second is a full exposition of the field and time dependence of hydrogenation profiles in numerous p and n-type samples at various shallow doping concentrations.

Sample preparation and measurement techniques have been discussed elsewhere in full detail [1,2]. All plots of charge density versus depth were obtained by 1 MHz capacitance profiling of Schottky and MIS depletion regions during H introduction. Most of the samples discussed here were fabricated on <100> or <111> CZ silicon and had 400 Å thick evaporated Al gates; however, a few were made from Edge Fed Growth (EFG), ribbon silicon, which has high concentrations of dissolved carbon and low interstitial oxygen content, and several others were fabricated from FZ silicon, which has 50-100 times less O than typical CZ material. Data obtained from these capacitors will be useful in assessing the importance of C or O in trapping H.

ION TRANSIT EXPERIMENTS

If hydrogen is introduced into a sample at time $t=0$ and drifts into the bulk in the presence of an electric field E , the ion flux is given by:

$$J = \frac{eDEH_s}{kT}, \quad (1)$$

where H_s is the near surface H concentration. If this hydrogen is primarily trapped at acceptors, the demarcation distance, d , separating passivated from unpassivated acceptors will advance in time according to:

$$J = N_A \frac{\partial d}{\partial t} \quad (2)$$

Combining (1) and (2), we find:

$$d(t) = \left[\frac{2eH_s}{N_A kT} (V+V_b)Dt \right]^{1/2}, \quad (3)$$

where V is the applied (reverse) diode bias and V_b is the zero bias band bending. In this equation, we have assumed that $E \approx (V+V_b)/d$, since $\partial E/\partial x (=p/ee_0)$ is low in the passivated region. This equation, while containing many simplifications, is borne out by the more involved H transport code calculations discussed below. It immediately illustrates one important feature of the problem; measurement of charge density profiles gives direct information only about the product of H_s and D . In earlier work [1], we attempted a separation of these two quantities by measuring the additional amount of H bonding which occurred after our ion beam was shut off. We expect that the extra charge neutralization will be given by the spatial integral of the H concentration profile at the moment of beam extinction. This assumption is subject to a number of caveats; in addition the amount of H present is generally much less than the acceptor density, and measurement of this quantity entails considerable error.

A more straightforward approach to this problem is to create conditions in the sample which allow the observation of the field driven H wave as it moves toward a well defined "marker". The conditions chosen are a previous hydrogenation cycle which removes most of the active acceptors up to some depth d , followed by a no-beam time interval long enough to let all mobile H leave the sample. The "marker" is the edge of the region of active acceptors. Movements of this "edge" after H is reintroduced at some later time define the arrival of H ions in a relatively clean fashion. Figure 1 illustrates this for a sample which has a single hydrogenation cycle performed at 5V and three later rehydrogenation drive-in cycles, each at a different bias. A 200°C anneal was performed on the sample after each transit time experiment to restore the sample to its "virgin" state. While the time where the "penetration edge" starts to move deeper is perhaps uncertain by $\pm 40\%$, the figure shows clearly that the lower parts of the three curves are separated in time by factors of two, in accordance with the applied diode bias. We have independently verified that the electric fields in the hydrogenated zone scale linearly with the applied bias to within $\sim 15\%$. It is thus possible to use the onset of hydrogenation defined by the arrows in Figure 1 to define an ion mobility. In making this calculation, it is important to take account of the diffusive broadening of moving ion front. Our transport code simulations indicate that, at these fields, this effect causes the transit time to be about a factor of 1.75 longer than the arrow positions in Figure 1.

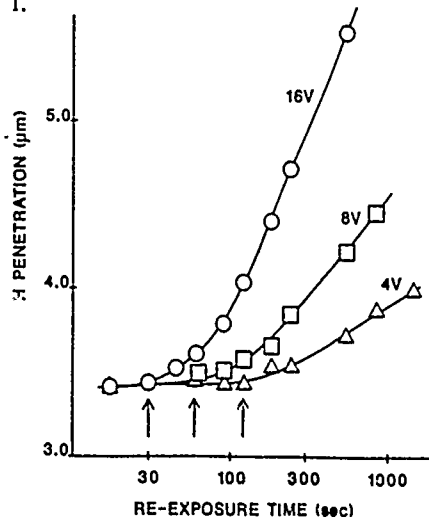
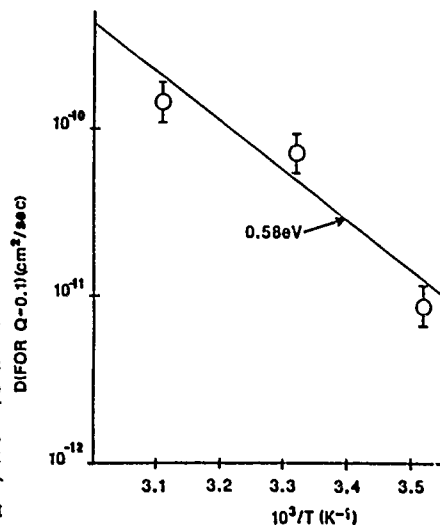


Figure 1. H penetration (measured at a charge density of $7 \times 10^{14} \text{ cm}^{-3}$) versus re-exposure time at three different diode biases for a p-type diode. The initial exposure of 16 minutes at +5 V diode bias at an ion energy of 1000 eV was followed by an 1/2 hr. waiting time at 298 K. The sample was annealed at 200°C for 10 minutes after each pair of hydrogenation runs. Arrows mark the point where significant penetration enhancement begins.

Figure 2. H diffusivity versus inverse temperature deduced from transit experiments on a p-type diode with $N_A = 1.35 \times 10^{15} \text{ cm}^{-3}$. D is computed using the Einstein relation and an effective charge, Q , of 0.1.



These transit measurements have been repeated at samples doped from $2.2 \times 10^{14} \text{ cm}^{-3}$ to $8 \times 10^{15} \text{ cm}^{-3}$ with similar results for the diffusivity. A summary of measurements done at other temperatures is shown in Figure 2. These data are more steeply varying with temperature than our prior results (Fig. 3 of Reference 1) largely because the previous assumption that the surface hydrogen concentration is temperature independent is not completely correct [3].

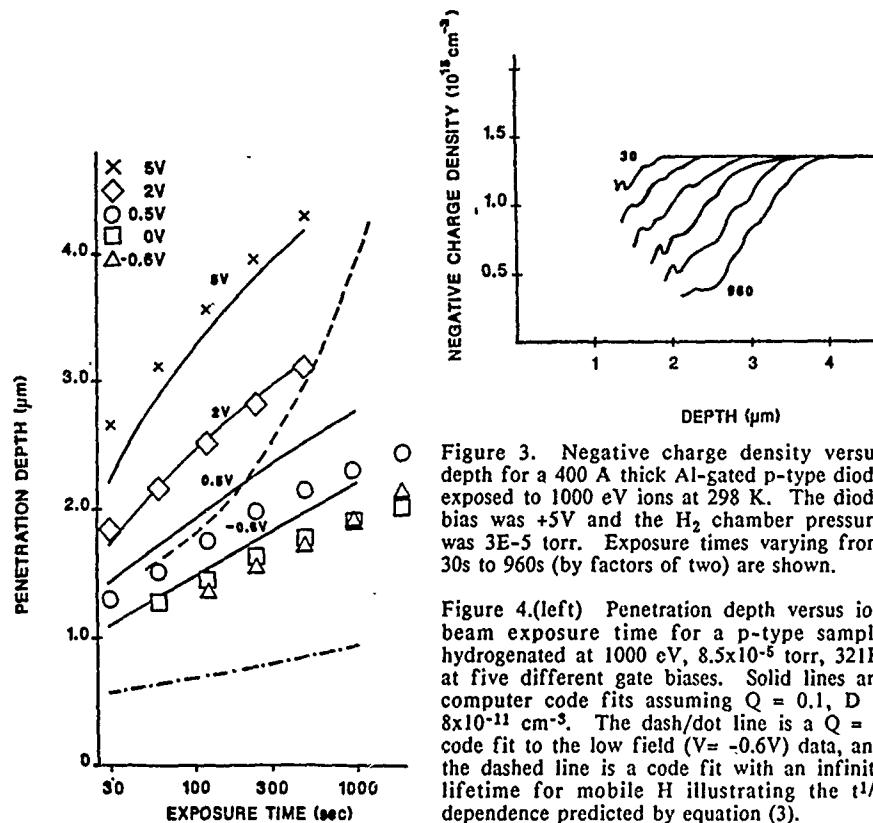


Figure 3. Negative charge density versus depth for a 400 Å thick Al-gated p-type diode exposed to 1000 eV ions at 298 K. The diode bias was +5V and the H_2 chamber pressure was 3×10^{-5} torr. Exposure times varying from 30s to 960s (by factors of two) are shown.

Figure 4.(left) Penetration depth versus ion beam exposure time for a p-type sample hydrogenated at 1000 eV, 8.5×10^{-5} torr, 321K at five different gate biases. Solid lines are computer code fits assuming $Q = 0.1$, $D = 8 \times 10^{-11} \text{ cm}^2/\text{s}$. The dash/dot line is a $Q = 1$ code fit to the low field ($V = -0.6\text{V}$) data, and the dashed line is a code fit with an infinite lifetime for mobile H illustrating the $t^{1/2}$ dependence predicted by equation (3).

THE TIME AND ELECTRIC FIELD DEPENDENCE OF HYDROGEN PENETRATION

p-Type Samples

Figure 3 shows a series of charge density profiles obtained during hydrogenation with 1000 eV H ions incident on a 5 volt biased p-type CZ MIS diode (oxide thickness 20-25 Å). Each successive curve is taken at a factor of two longer beam exposure. By arbitrarily choosing a fixed charge density ($7 \times 10^{14} \text{ cm}^{-3}$, in this case) we can define a penetration depth, d , from these plots. This depth can then be compared to the prediction of equation (3). $d(t)$ values measured on one sample at various diode biases are plotted in Figure 4. While there is indeed a strong bias dependence of d , the observed time dependence is much weaker than the $t^{1/2}$ dependence of equation (3); it is, in fact, even slower than $\log t$. Two explanations can be offered for this behavior. The first one would be to suppose that the surface hydrogen concentration is dropping at longer exposure times, perhaps due to ion-damage-induced H trapping. However, the H penetration data taken at a variety of ion energies [3] (discussed in our companion paper) suggest that ion damage plays little role in these experiments. Other non-implantation-damage-related mechanisms for near surface trapping, such as the build up of H platelets, [4] could be offered to explain a drop in H_2 . However, a number of experiments, including those where we have measured the amount of H trapped after beam shut-off [5], favor a second explanation for this very slow time dependence. It is likely that hydrogen is being 'lost' to other traps in the silicon bulk besides unpassivated shallow

acceptors; these trapping events do not appreciably change the local charge density and are therefore "invisible" in our capacitance measurements. This can be simulated by postulating that mobile H has a finite lifetime, τ . We have used a computer code to solve the coupled equations for ion diffusion, drift, and trapping, including a term which describes disappearance of hydrogen by trapping at "unsaturable" sites in the lattice. This latter term could, in principal, account for H trapping at interstitial O, C, or perhaps even conversion of mobile tetrahedral interstitials to an immobile bond-centered species. We have also derived a simple analytic approximation for the penetration depths which agrees reasonably well with the transport code calculations [5]. In the case where charge density traces are measured at time intervals differing by factors of two, we obtain [5] for the difference in trace spacings, Δd :

$$\Delta d = \frac{\ln 2 (V+V_b)e Dr}{2kT d_{avg}} \quad (4)$$

where d_{avg} is the average of the two penetration depths. Output from the full transport code calculations is shown fitted to p-type sample data at several biases in Figure 4. It is clear that the theory comes much closer to predicting the time dependence of H penetration than equation (3).

We also find, as in our previous work, [1,3] that neutral H must be playing an important role in H transport as well. The forward biased (low field) diode data displays much more penetration than is predicted if all hydrogens are in a charged state (see Figure 4). As before, we have made the assumption that we can treat this situation by assigning a charge fraction, Q , to all hydrogens irregardless of spatial location. The limitations and possible improvements on this assumption are discussed elsewhere [5]. The value of Q which best fits the data is $0.1 \pm 50\%$. In the case of partial charging, Q should appear as a multiplier to D in eqns (3) and (4).

In the case where a finite lifetime of mobile hydrogen is due to trapping at a background species having density N_t , τ can be expressed as:

$$\tau = \frac{1}{4\pi r_c D N_t} \quad (5)$$

where r_c is the capture radius for H at the unknown defect. In this case, $\Delta d \cdot d_{avg}$, the product of the penetration spacing and the average depth, can be seen (from equations (4) and (5)) to be proportional to inverse absolute temperature. Measurements of $\Delta d \cdot d_{avg}$ from 270-320 K indeed are consistent with this dependence (not shown).

A compilation of $\Delta d \cdot d_{avg}$ values measured on a variety of boron doped samples is shown in Figure 5. All samples had 400 Å Al gates and were hydrogenated at 1000 eV (at a gun pressure of 3×10^{-6} torr) with 5V applied bias [6]. The solid line drawn through these values has a slope of ≈ -0.9 . The high carbon content (EFG) and low oxygen (FZ) diodes yield data similar to the CZ samples, and $1/r$ (hence N_t) is roughly proportional to the shallow dopant density [7]. This suggests that passivated acceptors are capable of further reactions with mobile hydrogen, and other common impurities are not a major factor.

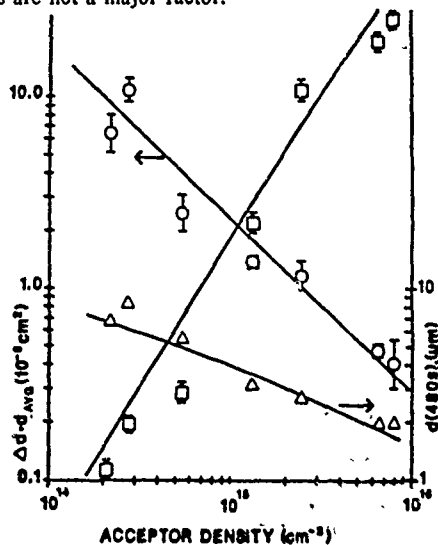


Figure 5. Hydrogen penetration, d , (triangles), $\Delta d \cdot d_{avg}$, (circles), and charge density slopes (squares), plotted versus acceptor density. The sample at $6.5 \times 10^{16} \text{ cm}^{-3}$ is from EFG silicon, the sample at $2.8 \times 10^{14} \text{ cm}^{-3}$ is FZ silicon; all others are CZ silicon. The solid line fits to the penetration and charge slope data (arb. units) are computed by choosing r values necessary to generate the "eyeball fit" line to the $\Delta d \cdot d_{avg}$ data.

Figure 5 also shows the values of d (480 seconds) and the slopes of the charge density plots versus depth; these parameters are sensitive to the values of the surface hydrogen density and the capture cross section for the initial H-B bonding process. The solid lines drawn through both sets of data were obtained from the transport code predictions using the r values necessary to reproduce the "eyeball fit" line drawn through the $\Delta d \cdot d_{avg}$ data. A value of $Q \cdot D = 4 \times 10^{-12} \text{ cm}^2/\text{sec}$ at 298K was used consistent with the ion transit measurements; a boron/hydrogen capture radius of 40 Å was employed and H_2 was fixed at $1.5 \times 10^{15} \text{ cm}^{-3}$ for all doping densities. This latter value is within 50% of the H_2 density calculated from ion flux measurements [3] and ion penetration code simulations (see our companion paper).

While the data show quite a bit of scatter, the transport code does a creditable job of reproducing the functional trends that are observed. Variations in the metallization and oxide thicknesses as well as thin-oxide-induced corrections to the charge density and depth are probably responsible for some of this scatter.

n-Type Samples

We have previously reported that a shallow layer of positive charge builds up near the gate metallization in hydrogenated n-type diodes. This layer causes 0.1-0.5 volt shifts of the Mott-Schottky capacitance plots and large increases in diode conductance. We have recently reviewed this data [5] and concluded that, while the origin of this charge is still uncertain, it is possible to experimentally separate this effect from H passivation of donors in the silicon bulk. It is the time and field dependence of this latter process that we shall discuss here.

Figure 6 shows the time dependence of the depletion layer charge density for an n-type (phosphorus doped) Schottky diode hydrogenated in forward bias (low field). If reverse bias is applied during hydrogenation, less hydrogenation is observed, (not shown), suggesting that some positively charged hydrogen is present. We have modelled n-type data taken at several biases and find that, as in the p-type case, it is consistent with an effective charge fraction of ~ 0.1 . The weak time dependence seen in Figure 6 is similar to that for p-type samples and is again consistent with the loss of mobile H to sites other than unpassivated donors. Only two phosphorus doping levels have been measured as of the present, but the trend for the H lifetime to vary inversely with doping is also seen. r values are typically 1/2 of those seen at equivalent acceptor concentrations suggesting that further trapping of H at passivated phosphorus is somewhat more efficient than at H-B sites.

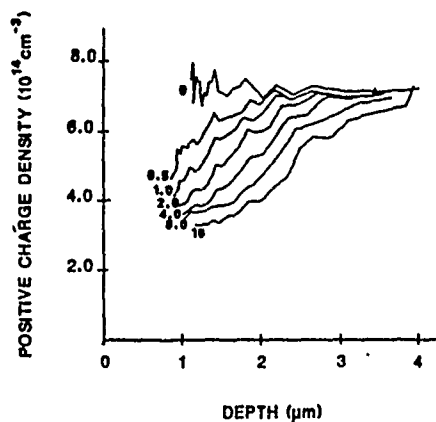


Figure 6. Charge density versus depth for an n-type diode hydrogenated with 1200 eV ions at an H_2 pressure of 3×10^{-5} torr at 297 K. The diode bias was +0.4 V during the experiment. Exposure times (in minutes) are indicated next to each curve.

SUMMARY

Well defined transit times for protons have been measured in p-type MIS diodes. The deduced H diffusivity varies with temperature with an activation energy of $\sim 0.6 \text{ eV}$ and has a 300 K value of $\sim 4 \times 10^{-11} \text{ cm}^2/\text{sec}$. This behavior of D is close to the extrapolation of the high temperature permeation data of Van Wieringen and Warmoltz [8]. Modelling of the electric field dependence of hydrogenation in both n and p-type capacitors indicates that H is positively charged $\sim 10\%$ of the time, so that hydrogenation with zero or small negative gate biases is dominated by the diffusion of neutral species.

Major deviations of the data from the models assuming only H capture at unpassivated shallow dopants lead us to suggest that H is becoming immobilized at other sites in the lattice. As was stressed [3] in our companion paper direct H-H interactions cannot be responsible for this behavior, and the observed doping dependence of this effect is consistent with H capture at already passivated dopants. Recent SIMS data by Corbett, et. al. [9] have shown evidence for H trapped in amounts well in excess of shallow dopant concentrations at depths larger than those normally associated with H platelet formation. Their suggestion that passivated dopants can act as further trapping sites for mobile H is consistent with our finding. The nature of these "post-passivation" reactions remains a subject for further study.

ACKNOWLEDGEMENTS

The authors would like to thank W. R. Bayless for help in fabricating several of the samples used in this experiment and C. Herring, H. Stein, and S. Estreicher for useful discussions about the properties of H in silicon. This work was performed at Sandia National Laboratories, supported by the U. S. Department of Energy, under contract DE-AC04-76DP00789.

REFERENCES

1. C. H. Seager and R. A. Anderson, Appl. Phys. Lett. **53**, 1181 (1988).
2. C. H. Seager and R. A. Anderson, Proc. 1988 Mat. Res. Soc. Mtg., Vol. 138, p. 197 (1989).
3. R. A. Anderson and C. H. Seager, in this symposium.
4. N. M. Johnson, F. A. Ponce, R. A. Street, and R. J. Nemanich, Phys. Rev. **B35**, 4166 (1987).
5. C. H. Seager, R. A. Anderson, and D. K. Brice, submitted to Journal of Applied Physics.
6. Except for the sample at $N_A = 2.5 \times 10^{15} \text{ cm}^{-3}$, which had values of $d(480\text{s})$ extrapolated from hydrogenation experiments at 1200 eV.
7. The actual dependence of the r values used to fit the Δd_{avg} line in Figure 5 is $\sim N_A^{-0.75}$.
8. A. Van Weiringen and N. Warmoltz, Physics **22**, 849 (1956).
9. J. W. Corbett, S. J. Pearton, and M. Stavola, Proceedings of the International conference on the Science and Technology of Defect Control in Semiconductors, 1989, p1.

HYDROGEN SEGREGATION AT THE Al/Si INTERFACE STUDIED USING A NUCLEAR RESONANT REACTION

JOYCE C. LIU, A.D. MARWICK AND F.K. LEGOUES
IBM, T.J. Watson Research Center, Yorktown Heights, NY 10598

ABSTRACT

Hydrogen segregation at the interface between an epitaxial Al film and a Si (111) substrate is studied using the $^1\text{H}(^{15}\text{N}, \alpha\gamma)^{12}\text{C}$ nuclear resonant reaction. Hydrogen depth profiles show that H atoms diffuse through the 1600 Å thick Al layer during 500 eV H implantation and are trapped at the Al/Si interface. The total amount of interface H is about 2×10^{15} /cm² after a 1.4×10^{18} H/cm² implantation, and the H atoms are narrowly distributed in the direction normal to the interface. During an isothermal anneal at 360 K, the amount of interface H decreases exponentially with annealing time; and during ramp annealing from 110 to 500 K, an abrupt release of the interface H is observed at temperature around 380 K. The release rates in both cases are controlled by a first order thermally activated de-trapping process with a binding energy of 0.86 eV/atom.

INTRODUCTION

Hydrogen segregation at grain boundaries and interfaces has a substantial effect on their mechanical and electrical properties. However, only a limited number of direct measurements of hydrogen at grain boundaries or interfaces have been made. For example, the segregation of deuterium at grain boundaries in Ni has been observed by using secondary ion mass spectroscopy (SIMS) [3] and the distribution of hydrogen in Al/SiO₂/Si (MOS) structures has been investigated by SIMS [4] and by using the $^1\text{H}(^{15}\text{N}, \alpha\gamma)^{12}\text{C}$ resonant nuclear reaction [7].

In the present paper, we study the H distribution at an interface between an epitaxial Al layer and a Si (111) substrate by using the $^1\text{H}(^{15}\text{N}, \alpha\gamma)^{12}\text{C}$ resonant nuclear reaction, and determine the H-interface binding energy from de-trapping kinetics.

EXPERIMENTAL PROCEDURE

The samples were prepared by electron beam evaporation of 1600 Å thick Al layers onto 10 Ω·cm P-type Si (111) substrates at room temperature and a base pressure of 1×10^{-7} Torr. The as-deposited samples were annealed in forming gas at 673 K for 2 hours and then implanted with H at room temperature using a Kaufman ion source. The energy of the H ions was 500 eV and the current density was 0.068 mA/cm². During the implantation, the sample was held in contact with a water-cooled block. After 30 and 60-min implantations, which correspond to doses of approximately 7×10^{17} and 1.4×10^{18} /cm², the samples were stored in liquid nitrogen to prevent hydrogen out-diffusion. The microstructure of the Al/Si interface was examined by high-resolution cross-section transmission electron microscopy (TEM) in a JEOL 4000 microscope. Auger depth profiling was used to check for possible contaminants at the interface.

The hydrogen depth profile in the samples was measured using the 6.4 MeV $^1\text{H}(^{15}\text{N}, \alpha\gamma)^{12}\text{C}$ nuclear resonant reaction. A hydrogen-implanted silicon standard was used for calibration of the amount of hydrogen detected. During the measurement the samples were mounted on a heating/cooling manipulator in a UHV chamber, so that several differ-

ent spots on each sample could be measured. Both isothermal and ramp anneals were carried out *in situ*, at temperatures between 110 K and 500 K.

RESULTS AND DISCUSSION

The Al/Si interface

A high resolution cross section TEM micrograph of an annealed Al/Si sample (before hydrogenation) is shown in Fig. 1. This lattice image shows the epitaxy of the Al layer on the Si substrate, as previously studied in detail [6]. The epitaxial relationship is such that $\text{Al } (111) \parallel \text{Si } (111)$ and $\text{Al } \langle 110 \rangle \parallel \text{Si } \langle 110 \rangle$. The ratio of the lattice constants of Al and Si is almost exactly 3:4, so that at the interface four Al (111) planes are matched to three Si (111) planes. Consequently, broken bonds and discontinuous planes exist at the interfaces. Fig. 1 shows that the structure of the interface resembles a dense array of edge dislocations.

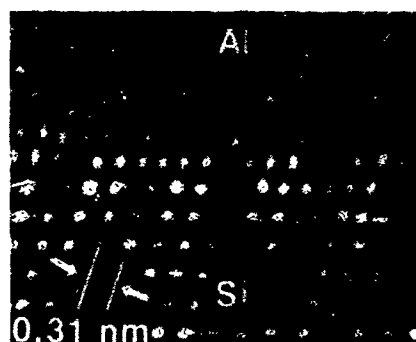


Fig. 1 Cross-sectional lattice image of the Al/Si interface showing how four Al (111) planes are matched to three Si (111) planes.

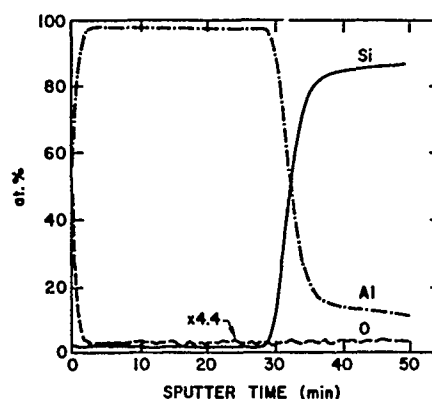


Fig. 2 Auger depth profile of an unimplanted Al/Si sample. The Al signal in the Si substrate is probably due to the interference of the Al_{LVV} and Si_{LVV} signals.

An Auger depth profile of the unimplanted sample, shown in Fig. 2, shows no evidence of any oxygen peak in the neighborhood of the Al/Si interface. A full Auger spectrum taken at the interface did not show any other contaminant signals. Further, an Auger depth profile of the H implanted sample shows similar results, indicating that no impurities were introduced during the implantation. Hence, in our study of hydrogen segregation, the structural defects at the interface should be the predominant traps, with chemical impurities playing a negligible role.

Hydrogen segregation

Typical depth profiles of hydrogen in an unimplanted sample and one implanted for 60 min are shown in Fig. 3. Compared to the unimplanted sample, the implanted one has a large peak of hydrogen concentration close to the surface, an increased level of hydrogen concentration within the Al film, and a peak of hydrogen concentration at the Al/Si interface.

The near-surface hydrogen concentration peak in the implanted sample, containing about 1×10^{16} H/cm², is located within approximately 100 Å from the surface, which is approximately the near-surface depth resolution. The near-surface peak in the unimplanted sample is smaller, and is presumably due to surface contamination with water. The width of the implant peak can be compared to the projected range and straggling of the 500 eV H implant, which are 85 Å and 94 Å respectively, as calculated by the TRIM code [1]. We conclude that this peak is caused by retained implanted hydrogen, probably associated with implant damage. The hydrogen signal within the unimplanted Al layer corresponds within statistical error to the cosmic-ray background in the gamma-ray detector. The higher signal measured from the H-implanted sample, $1 - 2 \times 10^{19}$ /cm³, may be associated with hydrogen at traps in the bulk of the aluminum.

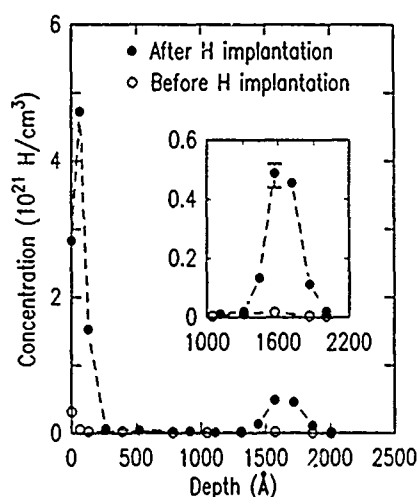


Fig. 3 Hydrogen profiles of unimplanted and 60-min-implanted samples. The insert shows hydrogen concentration at the Al/Si interface with a larger scale.

A significant feature of our results is the finding that a small portion of the implanted hydrogen segregates to the vicinity of the Al/Si interface, as shown by the peak in concentration in Fig. 3 at a depth of 1600 Å. The area under this peak depends on the implantation time, as further outlined below. In Fig. 3 it is 1.6×10^{15} /cm². This is larger than the number of plane-edge Si atoms in the interface (i.e. Si atoms along the edge of Si (111) planes which terminate at the interface), a rough estimate for which would be one-third of the (111) plane atomic density, or $\sim 4 \times 10^{14}$ atom/cm². Thus, the interface can accommodate at least four H atoms per Si plane-edge atom. Annealing data, presented later, show that most of this hydrogen anneals with a single binding energy, implying that only one site is involved.

Only limited information about the spatial extent of the hydrogen associated with the interface can be deduced from the data to date. The measured FWHM of the segregated hydrogen peak, 300 Å, is close to the calculated depth resolution of the H profile at the Al/Si interface, 320 Å. This depth resolution is determined by the width of the the 6.4 MeV $^1\text{H}(^1\text{N}, \alpha\gamma)^{12}\text{C}$ resonance [2], beam energy straggling (measured by Rud *et al* [9]), and Doppler broadening of 12 keV FWHM due to the thermal vibration of the H atoms [11]. Thus, our measurements show no appreciable extra broadening due to any finite extent of the H distribution, but can put only an upper limit of ~ 200 Å FWHM on the true width

of the distribution. This spatial extent of the hydrogen is much less than that measured by SIMS lateral profiling of deuterium segregated at the grain boundaries in Ni [3]. This may be a consequence of the very low residual strain in vicinity of the Al/Si interface.

Isothermal anneal

The change of H concentration at the Al/Si interface during 360 K isothermal anneal was monitored by recording the peak hydrogen concentration as a function of time from the sample implanted for 60 min. This data is shown in Fig. 4, expressed as a total hydrogen concentration in the interface, deduced from the peak height and the measured FWHM already quoted.

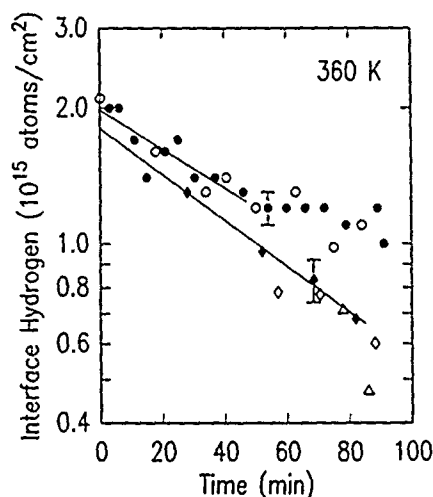


Fig. 4 The interface hydrogen concentration of a sample implanted for 60 min vs. time during a 360 K *in situ* anneal.

Different symbols shown in Fig. 4 represent data collected from different areas on the sample. The figure shows that the amount of H decreases with annealing time in each area, but the areas exposed to the analyzing ion beam for longer times, *i.e.* where more measurement points have been taken, tend to have slower release rates. Furthermore, the H release rate in these areas decreases with time. This beam effect is presumably due to an increase of H traps generated by the ^{15}N ions. Thus, the most reliable data is obtained from the most lightly-irradiated areas. However, as the figure shows, the initial rate of H release is the same, within the errors, in all the areas investigated.

Data from areas least affected by the ion beam show an exponential dependence of the interface H concentration on the annealing time, which implies that the release rate of H from the interface is controlled by a thermally activated first order de-trapping process. Thus, diffusion terms in the annealing equation can be neglected and the release rate of the hydrogen from the interfacial traps, dn/dt , can be given by

$$dn/dt = -nA \exp(-E_b/kT),$$

where E_b is the binding energy, T the annealing temperature, k Boltzmann's constant and A a constant equal to $4\pi R_T D N$ [8, 10]. The parameter R_T is the effective trap radius, D is the diffusivity of H, and N is the atomic density of Al. In the calculation, the parameters used are: R_T equal to 4.05×10^{-8} cm, and D equal to 8.6×10^{-9} cm²/sec [5]. It should be

noted that the diffusivity is sufficiently high to allow H to diffuse through the 1600 Å thick Al layer in a few seconds. By a least square fit of the experimental data shown in Fig. 4, the binding energy is found to be 0.86 eV/atom.

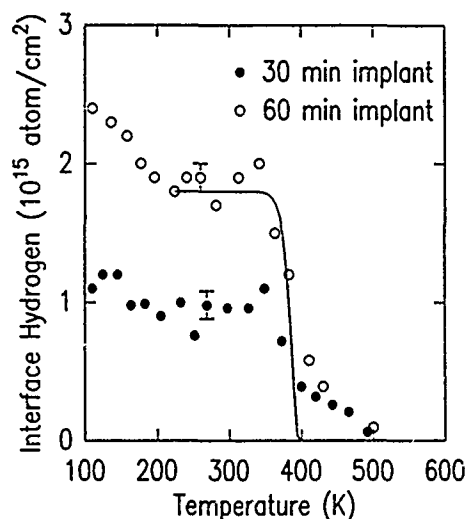


Fig. 5 The interface hydrogen concentration vs. temperature during annealing from 110 to 500 K at a ramping rate of 3 K/min, for samples implanted for 30 and 60 min.

Ramp anneal

During ramp annealing from 110 to 500 K at 3 K/min, the change of interface H in two samples (30-min and 60-min implanted) was monitored by the same method described in the isothermal annealing case. In Fig 5, the amount of interface H is plotted against the temperature. At 110 K, the interface H in the 60-min implanted sample is about 2 times higher than it in the 30-min implanted one ($2.4 \times 10^{15}/\text{cm}^2$ vs $1.1 \times 10^{15}/\text{cm}^2$), suggesting that the interface is not yet saturated with hydrogen, though the data is not sufficiently complete to be definite on this point. The anneal reveals two major annealing stages. The first, around 150 K, is more prominent in the 60-min implanted sample, where it caused a noticeable reduction of H from 2.4×10^{15} to $1.9 \times 10^{15}/\text{cm}^2$. In the sample implanted for only 30 min, this stage is almost absent, implying that these shallower traps only begin to fill at higher hydrogen concentrations.

The most prominent annealing stage shown in Fig. 5 occurs near 380 K, and causes the abrupt release of the interface H from $\sim 1.9 \times 10^{15}$ to $\sim 5 \times 10^{14}/\text{cm}^2$ and from $\sim 9.5 \times 10^{14}$ to $\sim 3.9 \times 10^{14}/\text{cm}^2$ for the 60-min and 30-min implanted samples, respectively. In order to quantitatively interpret this stage, we calculated the value of interface H as a function of temperature in the ramp anneal by using the kinetic equation given in the isothermal annealing analysis and the same binding energy of 0.86 eV/atom. The calculated release curve, shown by the solid line in Fig. 5 agrees well with the experimental data, suggesting that a single binding energy represents a fair description of the data. However, the gradual H release at temperatures above 400 K shows that some deeper traps may also be present.

CONCLUSIONS

We have shown that H segregation to the epitaxial Al/Si interface occurs during 500 eV implantation at room temperature. The amount of segregated H increases with implantation time, up to 2.4×10^{15} /cm². By comparing the width of the H peak to the calculated depth resolution, we conclude that the H distribution is at most 200 Å wide. Ramp anneals show a minor release stage around 150 K, more prominent in samples implanted for longer times, and a major stage at ~ 380 K in which most of the trapped H is released. Isothermal annealing at 360 K shows that the release kinetics in this stage are predominantly first order, with a binding energy of 0.86 eV/atom.

ACKNOWLEDGMENTS

We thank T.H. Zabel for his management of the Tandem accelerator facility, and P. Saunders for assistance with the experiment. We also thank J.P. Doyle for the hydrogen implantations, R.G. Schad for the Auger profiling, and members of the CSS Materials Laboratory for the sample depositions.

REFERENCES

- [1] J. Biersack and L. Haggmark, Nucl. Instr. Methods 174, 257 (1980).
- [2] H. Damjantschitsch, M. Weiser, G. Heusser, S. Kalbitzer, and H. Mannsperger, Nucl. Instr. Meth. 218, 129 (1983).
- [3] H. Fukushima and H. Birnbaum, Acta Metall. 32, 851 (1984).
- [4] R. Gale, F. Feigl, C. Magee, and D. Young, J. Appl. Phys. 54, 6938 (1983).
- [5] T. Ishikawa and R. McLellan, Acta Metall. 34, 1091 (1986).
- [6] F. LeGoues, W. Krakow, and R. Ho, Phil. Mag. A 53, 833 (1986).
- [7] A. Marwick and D. Young, J. Appl. Phys. 63, 2291 (1988).
- [8] S. Myers and S. Picraux, J. Appl. Phys. 50, 5710 (1979).
- [9] N. Rud, J. Bottiger, and P. Jensen, Nucl. Instr. Meth. 151, 247 (1978).
- [10] P. Shewmon, Y. Shen, C. Shen, and M. Meshi, Acta Metall. 37, 1913 (1989).
- [11] M. Zinke-Allmang, S. Kalbitzer, and M. Weiser, Z. Phys. A 320, 697 (1985).

DISSOCIATION KINETICS OF SHALLOW-ACCEPTOR-HYDROGEN PAIRS IN SILICON

ZUNDEL T. and WEBER J.

Max-Planck-Institut für Festkörperforschung, Heisenbergstr.1,
D-7000 Stuttgart 80, Federal Republic of Germany

ABSTRACT

Annealing of hydrogenated p-type silicon with a reverse bias applied to a Schottky diode allows us to precisely determine the dissociation frequency ν_A of shallow acceptor-hydrogen pairs (AH with A = B, Al, Ga, and In). The temperature dependent values of ν_A satisfy the relation $\nu_A = \nu_{oA} \exp(-E_A/kT)$, with $\nu_{oB} = 2.8 \cdot 10^{14} \text{ s}^{-1}$, $\nu_{oAl} = 3.1 \cdot 10^{13} \text{ s}^{-1}$, $\nu_{oGa} = 6.9 \cdot 10^{13} \text{ s}^{-1}$, and $\nu_{oIn} = 8.4 \cdot 10^{13} \text{ s}^{-1}$. The dissociation energies E_A depend only weakly on the acceptors: $E_B = (1.28 \pm 0.03) \text{ eV}$, $E_{Al} = (1.44 \pm 0.02) \text{ eV}$, $E_{Ga} = (1.40 \pm 0.03) \text{ eV}$, and $E_{In} = (1.42 \pm 0.05) \text{ eV}$. The dissociation frequency of BH pairs shifts to a lower value when H is replaced by the deuterium isotope.

INTRODUCTION

Atomic hydrogen forms electrically neutral complexes with group-III shallow acceptors (B, Al, Ga, In, and Tl) in silicon. [1,2] Despite many studies on the thermal stability of the acceptor neutralization [1,3,4,5,6], there are no reliable data on the dissociation energies E_A of these pairs. Capizzi *et al.* [6] tried to fit deuterium diffusion profiles in boron-doped Si by taking into account the D-diffusion and the formation and dissociation of BD pairs. The fit requires many unknown parameters and is poor in the near surface region. In the *isochronal* annealing experiments of Ref. [1] and [3], a first-order kinetic is implicitly assumed to derive E_A from a plot of the AH complex concentration versus annealing temperature. However, *isothermal* anneals [4,5,7] give evidence of much more complex reactivation kinetics of the acceptor, which makes the determination of E_A inaccurate [4,5] or even impossible [7]. The reversibility of the reaction $AH \leftrightarrow A + H$ is the main reason for the departure from first-order kinetics.

In our experiment, the drift property of positively charged hydrogen under an electric field [8] is used to remove the atomic hydrogen released by the dissociation of the AH complexes. We anneal hydrogenated samples with a *reverse bias* applied to a Schottky diode, and observe a reactivation of the acceptor which rigorously follows first-order kinetics in the high-field space-charge region.

EXPERIMENTAL DETAILS AND RESULTS

We use B-doped (100) float-zone silicon, Al-, or Ga-doped (111) Czochralski silicon, and In-doped (111) float zone silicon of 10 Ωcm resistivity. The samples are exposed to a radio-frequency (13 MHz) hydrogen plasma for 2h at temperatures in the range of 120°C - 250°C. A layer of thickness d ($d = 2\text{-}4 \mu\text{m}$) below the irradiated surface is then chemically removed, and titanium Schottky contacts (1 mm diameter) are evaporated. The ohmic

contact consists of an indium-gallium alloy scratched onto the back surface. Anneals at a temperature T_a in the range 40°C to 220°C with a reverse-bias V_R applied to the Schottky diode are performed in a cryostat under ambient atmosphere. After annealing for a time t_a , the temperature is rapidly decreased by immersing the sample holder in liquid nitrogen with the bias on. Capacitance versus voltage $[C(V)]$ measurements at 1 MHz and room temperature provide the profile $N_A(x, t_a)$ of the electrically active acceptor concentration.

A gallium-doped hydrogenated sample is annealed at a temperature $T_a=120^\circ\text{C}$ with a reverse bias $V_R=60\text{ V}$. The active acceptor profiles are shown in Fig. 1 for various annealing times t_a . As t_a increases, the dopant is progressively reactivated in the region $x \leq 10\text{ }\mu\text{m}$ while the neutralization becomes more pronounced in the region $10\text{ }\mu\text{m} < x < 19\text{ }\mu\text{m}$, in qualitative agreement with similar experiments reported in the literature. [7,8] In order to quantitatively analyse the acceptor reactivation in the high electric field

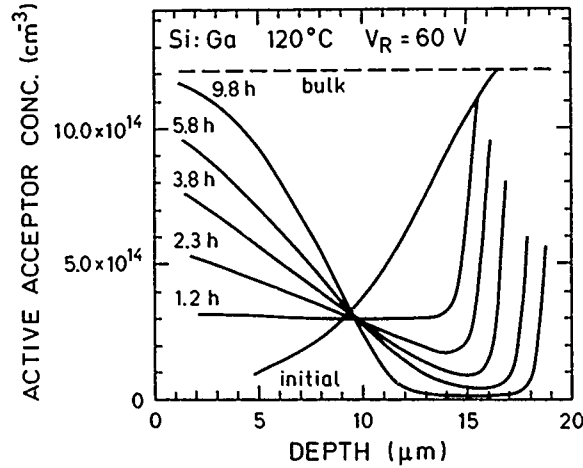


Figure 1: Evolution of the active gallium concentration profile as a function of the reverse-bias annealing time ($V_R = 60\text{ V}$, $T_a = 120^\circ\text{C}$) in a hydrogen plasma treated sample.

region $x < 3\text{ }\mu\text{m}$, we plot the electrically inactive acceptor concentration $A(t_a) = N_{A0} - N_A(2\text{ }\mu\text{m}, t_a)$ versus t_a . (See Fig. 2, stars.) The symbol N_{A0} represents the uniform acceptor concentration in the non-hydrogenated control sample. The reactivation of the acceptor follows first-order kinetics, characterized by $A(t_a) = A(t_a = 0) \exp[-\nu_{Ga}(T_a)t_a]$ with $\nu_{Ga}(120^\circ\text{C}) = 7.0 \cdot 10^{-5}\text{ s}^{-1}$.

We explain the changes in the active gallium profile after annealing under reverse-bias (see Fig. 1) in the following way. The dopant neutralization results from the formation of a neutral GaH complex [1] $\text{Ga} + \text{H} \rightleftharpoons \text{GaH}$. The formation and dissociation of the GaH complex is described by equation

$$\frac{\partial[\text{GaH}]}{\partial t} = \sigma[\text{H}](N_{A0} - [\text{GaH}]) - \nu_{Ga}[\text{GaH}] \quad (1)$$

where $[\text{H}]$ and $[\text{GaH}]$ are the concentrations of free atomic hydrogen and GaH complexes,

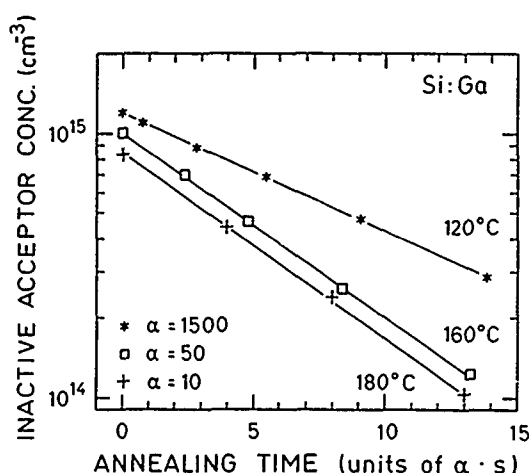


Figure 2: Inactive gallium concentration vs reduced annealing time, measured in the high-field region ($x = 2\mu\text{m}$) of a reverse-biased diode. A reduced time scale is used to clearly reveal the first-order kinetics in the entire annealing temperature range.

respectively, and σ is the capture rate of the atomic hydrogen at the acceptor gallium. The atomic hydrogen released by the thermal dissociation of the GaH complex is positively charged, and drifts toward the interior under the electric field present in the space charge region. New GaH complexes are formed in the neutral or low-field region ($x \geq 10\mu\text{m}$). The local concentration of H is low in the high-field region, due to the drift, and the term $\nu_{Ga}[GaH]$ dominates the righthand side of Eq. 1, leading to the experimentally observed first-order dissociation of the complex. In Ref. [9] we have performed a computer simulation of the drift process in a hydrogenated B-doped sample, which confirm this interpretation.

The first-order reactivation of the acceptors in the high-field region is observed in samples isochronally annealed under reverse bias at various temperatures in the range of 100°C to 200°C . For the sake of clarity, we show only the data corresponding to $T_a = 120^\circ\text{C}$, 160°C , 180°C in Fig. 2. The dissociation frequencies $\nu_{Ga}(T_a)$ follow the Arrhenius equation $\nu_{Ga}(T_a) = \nu_{oGa} \exp(-E_{Ga}/kT)$ with $E_{Ga} = (1.40 \pm 0.03) \text{ eV}$, and $\nu_{oGa} = 6.9 \cdot 10^{13} \text{ s}^{-1}$.

Similar anneals under reverse bias are performed on hydrogenated samples doped with either B, Al, or In, and B-doped samples treated in a deuterium plasma. The Arrhenius plots of the dissociation frequencies $\nu_A(T_a)$ corresponding to the various AH complexes ($A = \text{B, Al, In}$), and BD pairs are shown in Fig. 3. The solid lines represent a least-squares fit of the experimental values $\nu_A(T_a)$ to the relation $\nu_A(T_a) = \nu_{oA} \exp(-E_A/kT)$. The adjusted parameters E_A , and ν_{oA} are listed in Table I.

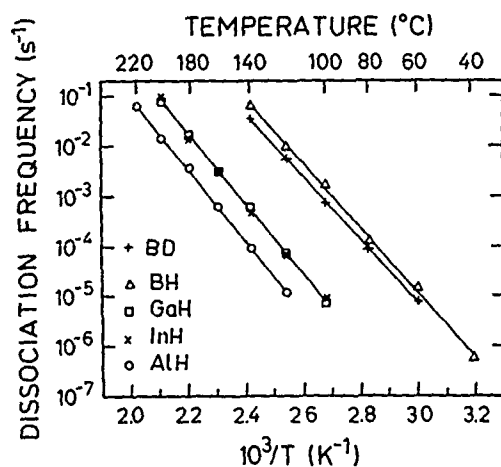


Figure 3: Arrhenius plot of the dissociation frequency of various acceptor-hydrogen pairs, and the boron-deuterium pair.

Table I Dissociation energies E_A and attempt frequencies ν_{oA} of AH, and BD pairs

	BH	BD	AlH	GaH	InH
E_A (eV)	1.28 ± 0.03	1.24 ± 0.02	1.44 ± 0.02	1.40 ± 0.03	1.42 ± 0.05
ν_{oA} (s ⁻¹)	$2.8 \cdot 10^{14}$	$3.4 \cdot 10^{13}$	$3.1 \cdot 10^{13}$	$6.9 \cdot 10^{13}$	$8.4 \cdot 10^{13}$

DISCUSSION

The BH pair is the most weakly bound, no difference is detected between GaH and InH, and AlH is the most stable pair. (See Fig. 3.) The prefactors ν_{oA} of the dissociation frequencies ν_A are in the same order of magnitude as the lattice phonon vibration frequencies ($\sim 10^{13}$ s⁻¹). Within the experimental uncertainty ($\approx 90\%$), the values of ν_{oA} show no clear dependence on the acceptor species. The weak dependence of the dissociation energy on the acceptor species supports the "bonding configuration" proposed by Pankove *et al.* [10] where the H-atom lies between the acceptor and one of its silicon neighbors, forming a Si-H bond. [10] In this model, the H-atom interacts weakly with the acceptor, in agreement with an acceptor-independent dissociation energy. In contrast, the alternative anti-bonding configuration proposed by Assali and Leite [11] predicts a strong H-acceptor interaction. On closer observation, the binding energy of the BH pair (1.28 ± 0.03) eV is slightly, but significantly smaller than the value corresponding to Ga, Al, In (1.42 ± 0.02) eV. Raman [12] and infrared [13] data also suggest that the structure of the BH complex differs from the structure of the other AH complexes. Stavola *et al.* [13] proposed an off $\langle 111 \rangle$ -axis position for H in the complexes involving large acceptor species (Al, Ga, In).

The ratio $r = \nu_B^H / \nu_B^D$ of the dissociation frequency of the BH pair to the dissociation frequency of the BD complex is shown versus T_a in Fig. 4. Due to the large experimental

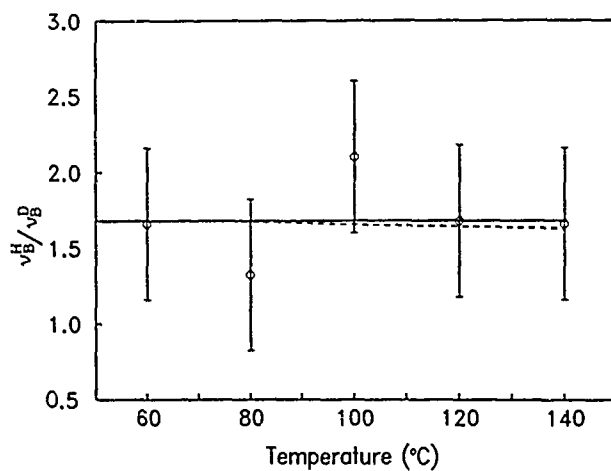


Figure 4: Ratio $r = \nu_B^H / \nu_B^D$ of the dissociation frequency of the BH pair to the dissociation frequency of the BD complex versus temperature. The lines represent $r = r_o \exp(\Delta E / kT_a)$ with $\Delta E = 0$, $r_o = 1.69$ (solid line), and $\Delta E = 6$ meV, $r_o = 1.39$ (dashed line).

error on r , it makes no sense to determine both $r_o = \nu_{oB}^H / \nu_{oB}^D$, and $\Delta E = E_B^D - E_B^H$ by fitting the data of Fig. 4 to the relation $r = r_o \exp(\Delta E / kT_a)$. We perform the fit, assuming that one parameter is constant. If $\Delta E = 0$, we find $r_o \simeq 1.7$ (Fig. 4, solid line). This ratio is significantly larger than the square root of the reduced mass ratio of 1.39 expected for Si-H relative to Si-D vibrations in a simple diatomic molecule. However, if r_o is set equal to 1.39, if we find $\Delta E \simeq 6$ meV, which is within the experimental error on E_B^H , and E_B^D (Fig. 4, dashed line). The infrared measurements of Pajot *et al.* [14] suggest slightly different configurations for the BH, and BD complexes. The corresponding dissociation energies might also be different.

The dissociation energy determined in our experiments corresponds to the energy required to fully separate the hydrogen atom from the acceptor. It is equal to the sum of the H-migration energy and the binding energy of the AH pair. The experimental dissociation energy of the BH pair (1.28 eV) is in good agreement with the value calculated by DeLeo and Fowler (1.46 eV) [15], and Denteneer *et al.* (1.1 eV) [16]. In the recent investigations by Denteneer *et al.* [17] the binding energy corresponding to the reaction $(BH)^o \rightarrow B^- + H^+$ is 0.59 eV, which is consistent with our value, if we assume a migration energy of $1.28 \text{ eV} - 0.59 \text{ eV} = 0.69 \text{ eV}$.

We hope that our data will provide a sensitive criterion to check future theoretical work. Moreover, our simple method can be used to identify hydrogen at low concentrations ($\simeq 10^{12} \text{ cm}^{-3}$), which are not detectable by infrared, Raman, or Secondary Ion Mass Spectroscopy measurements.

Acknowledgments The Si samples were kindly supplied by Wacker Chemitronic. We are grateful to H.J. Queisser for his interest and support throughout this work. We acknowledge stimulating discussions with M. Stutzmann, C.P. Herrero, and Th. Prescha, and appreciate the technical assistance of W. Krause and W. Heinz.

References

- [1] S.J. Pearton, J.W. Corbett, and T.S. Shi, *Appl. Phys.* **A43**, 153 (1987)
- [2] S.J. Pearton, M. Stavola, and J.W. Corbett, 15th Int. Conf. Defects. Semicond. Proc., "Mat. Sci. Forum", ed. by G. Ferenczi (Trans. Tech. Publications, CH-Aedermannsdorf, 1989) Vol. 38-41, p. 25
- [3] M. Deicher, G. Grübel, R. Keller, E. Recknagel, N. Schulz, H. Skudlik, and Th. Wichert, in Ref. 2, p. 1045
- [4] C.T. Sah, S.C.S. Pan, and C.C.H. Hsu, *J. Appl. Phys.* **57**, 5148 (1985)
- [5] S.C.S. Pan and C.T. Sah, *J. Appl. Phys.* **60**, 156 (1986)
- [6] M. Capizzi, A. Mittiga, and A. Frova: 18th Int. Conf. Defects. Semicond., Proc. ed. by O. Engström (World Scientific, Singapore 1987) Vol. 2, p. 995
- [7] T. Zundel, A. Mesli, J.C. Muller, and P. Siffert, *Appl. Phys.* **A48**, 31 (1989)
- [8] A.J. Tavendale, D. Alexiev, and A.A. Williams, *Appl. Phys. Lett.* **47**, 316 (1985) **A40**, 67 (1986)
- [9] T. Zundel and J. Weber, *Phys. Rev.* **B39**, 13549 (1989)
- [10] J.I. Pankove, P.J. Zanzucchi, C.W. Magee, and G. Lucovsky, *Appl. Phys. Lett.* **46**, 421 (1985)
- [11] L.V.C. Assali, and J.R. Leite, *Phys. Rev. Lett.* **55**, 980 (1985)
- [12] M. Stutzmann and C.P. Herrero, *Physica Scripta* **T25**, 276 (1989)
- [13] M. Stavola, S.J. Pearton, J. Lopata, and W.C. Dautremont-Smith, *Phys. Rev.* **B37**, 8313 (1988)
- [14] B. Pajot, A. Chari, M. Aucouturier, M. Astier, and A. Chantre, *Solid State Commun.*, **67**, 855 (1988)
- [15] G. DeLeo and W.B. Fowler, 13th Int. Conf. Defects Semicond. Proc., ed. by L.C. Kimerling and J.M. Parsey, Jr. (The Metallurgical Society of AIME, Warrendale, PA, 1985) Vol. 14a, p. 745
- [16] P.J.H. Denteneer, C.G. Van de Walle, Y. Bar-Yam, and S.T. Pantelides, in Ref. 2, p. 979
- [17] P. J. H. Denteneer, C. G. Van de Walle, and S. T. Pantelides, *Phys. Rev.* **B39**, 10809 (1989)

HYDROGEN INDUCED DEFECTS AT SILICON SURFACES AND BURIED EPITAXIAL MISFIT DISLOCATION INTERFACES

Tian-Qun Zhou, Zbigniew Radzimski, Zhigang Xiao, Bhushan Sopori*, and
George A. Rozgonyi

Dept. of Materials Science and Engineering, North Carolina State University,
Raleigh, NC 27695-7916

*Solar Energy Research Institute, 1617 Cole Boulevard, Golden, CO 80401

ABSTRACT

A silicon epitaxial structure containing spatially confined arrays of misfit dislocations has been used in order to investigate the interaction between hydrogen and individual extended defects. Hydrogen was introduced using a Kaufman plasma ion beam source. A characteristic Si-H peak at 2100 cm^{-1} was obtained using multiple internal reflection infrared spectrophotometry. Microdefects such as gas bubbles and $\{111\}$ planar defects were found near the surface, as well as at the misfit dislocation interfaces, using transmission electron microscopy. A heavily damaged region was obtained on the top Si surface and an extended area SEM/EBIC contrast was obtained due to a surface electrical field.

INTRODUCTION

The effect of hydrogen on the electrical properties of silicon has become an important issue due to its ability to passivate, at moderate temperatures, both shallow impurities and deep-level defects^[1]. Hydrogen can tie up silicon dangling bonds or distorted silicon bonds at dislocations and grain boundaries, thereby making them electrical inactive^[2,3]. Controlled hydrogenation is usually done by exposure of the silicon surface to a hydrogen plasma source; however, the chemically active and energetic hydrogen ions can also induce surface degradation by introducing extended defects during the plasma process^[4-6]. In this paper, we present chemical, structural and electrical data on hydrogen plasma treated silicon wafers containing buried sheets of interfacial misfit dislocations.

EXPERIMENTAL

In this study, two types of silicon crystal were used. One was a virgin (111) oriented silicon wafer, while the other was a (100) epitaxial silicon wafer with a buried Si(Ge) layer. The epitaxial Si(Ge) layer contained two buried interfaces with misfit dislocations which act as gettering sites for metal impurities or hydrogen^[7,8]. The silicon layers were grown by adding approximately 2% GeH_4 to a SiCl_2H_2 CVD reactor. The misfit dislocation node density is easily adjusted from 10^6 to 10^8 by varying the gas phase ratio of GeH_4 to SiCl_2H_2 from 1% to 4%, or adjusting the Si(Ge) epitaxial layer thickness. The samples were anisotropically etched with $\text{KOH}:\text{H}_2\text{O}$ ^[9] following growth of 70 nm thermal oxide and opening $10\text{ }\mu\text{m}$

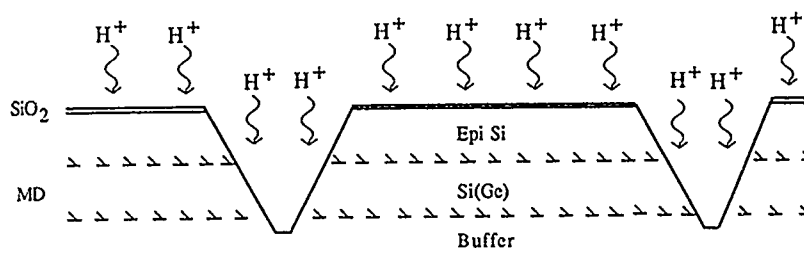


Fig.1 Schematic Diagram of Anisotropically Etched Grooves in Oxidized Epitaxial silicon with Misfit Dislocations

wide windows on 500 μm wide centers, as schematically shown in Fig.1. In this way, misfit dislocation end points could be exposed along the (111) side walls of an etched trench, while the 70 nm capping oxide was designed to reduce the hydrogen exposure damage to the top surface.

Hydrogenation was carried out in a Kaufman Ion Beam System at the Solar Energy Research Institute. The Kaufman ion source produced a beam of 0.4 keV hydrogen ions. The samples were exposed to the plasma for 60 m and reached a maximum substrate temperature of 350°C. Transmission electron microscopy (TEM), secondary ion mass spectroscopy (SIMS), multiple internal reflection infrared spectrophotometry (MIR), and scanning electron microscopy in the electron beam induced current mode (EBIC/SEM) were used for characterization. TEM was used to reveal the hydrogen induced defects and surface radiation damage, SIMS gave a hydrogen depth profile, MIR examined the states of surface hydrogen and impurities, while EBIC/SEM gave an indication of the electrical activities as a function of location.

RESULTS AND DISCUSSION

Both cross-section and plan-view bright field TEM images of the near surface region of the $\langle 111 \rangle$ silicon wafer after hydrogenation are shown in Fig.2. The micrographs indicate a very heavy band of surface damage up to 100 nm deep. Individual planar defects lying on {111} habit planes, which extended up to 500 nm deep, are also evident. They are similar to defects identified by Ponce[5] and Jeng[6] as H-stabilized platelets, induced by the hydrogen plasma process. The {111} planar defects exhibit fringe contrast as shown in the plan-view TEM of Fig.2(b). A defect density as high as 10^8 to 10^{10} cm^{-2} is evident in Fig.2(b). Chemical bonding at the surface of this sample was studied using a MIR spectrophotometer, which has a higher sensitivity than conventional transmission infrared method for sampling surface regions[10]. The spectra were taken at room temperature and multiple scanned to reduce instrument background noise. An absorption peak was obtained at 2100 cm^{-1} which corresponds to the stretching vibration of Si-H bonds in crystalline silicon. A hydrogen concentration depth profile obtained by SIMS showed that most of the hydrogen was accumulated at the surface damaged by the plasma, and a small, but

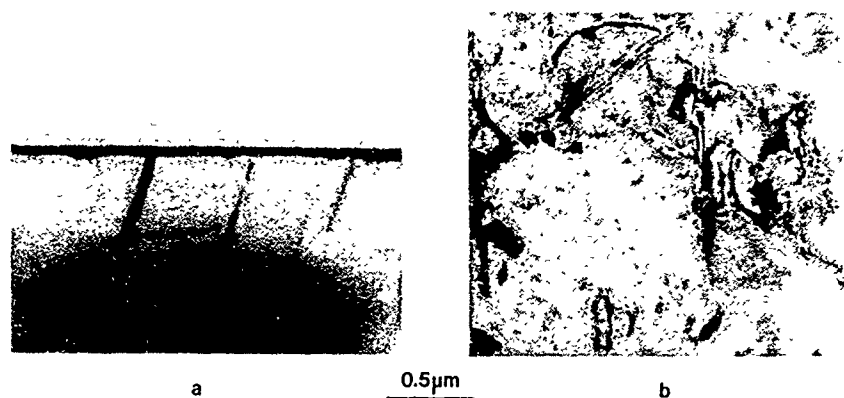


Fig.2 Bright filed TEM images of hydrogenated (111) silicon wafer (a) cross-section and (b) plan-view

significant concentration increase occurred at a depth coinciding with the upper MD interface.

The effect of hydrogenation on the electrical properties of the (100) Si surface structured as in Fig.1 was investigated using EBIC/SEM. Al Schottky diodes were fabricated on samples for charge collection and Au was deposited on the backside for ohmic contact. Typical EBIC contrast for a non-hydrogenated sample is shown in Fig. 3(a). Notice that only those areas physically connected to the Schottky contact show contrast in this EBIC image; whereas the EBIC image of the hydrogenated sample shown in Fig. 3(b) shows a very large lateral extension of electrically active region beyond the circular Schottky contact on the top surface, while only the Schottky diode area is in contrast on the bevel surface. Note also, that those neighboring regions which are cut off by trenches do not contribute to the EBIC signal. The trench isolation and shallow image on the beveled sample indicates that the hydrogenated surface is exhibiting a surface electrical field effect.

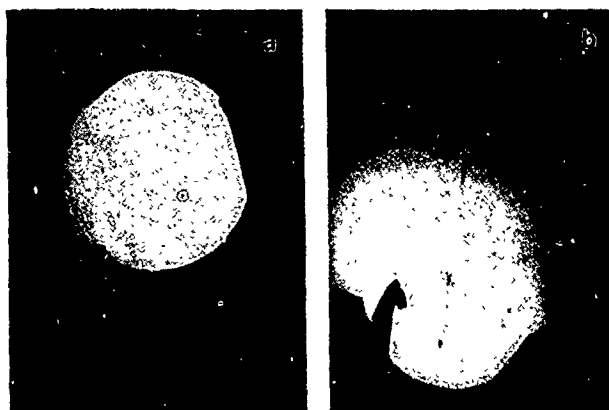


Fig.3 EBIC/SEM images of epitaxial silicon (a) reference and (b) hydrogenated sample with beveled surface

From SIMS we know that hydrogen was concentrated in the near surface region and its density decreased gradually with distance into the bulk. In this hydrogen concentrated region, the surface was heavily damaged and many microdefects were formed. Hydrogen which diffuses into the crystal can form Si-H bonds to stabilize these microdefects, as mentioned by Ponce[8,9]. Therefore, this surface layer containing hydrogen decorated defects or hydrogen stabilized defects will have a different energy state than the bulk crystal. The difference of the energy state between surface and bulk can form a junction and results in the extended area of the EBIC/SEM image. On the other hand, hydrogen can neutralize the dopant[11], effectively reducing the concentration of acceptors on the hydrogen-rich surface. The surface compensation, or even inversion to n-type silicon, can form a junction between the surface layer and the p-type bulk. Because of both these reasons, the hydrogen plasma process can produce an internal electrical field on the surface which gives rise to the EBIC image in the SEM outside the Schottky contact area.

Extended defects and bubbles were found all along the buried misfit dislocation interfaces after hydrogenation, as shown in Fig.4, indicating the expected strong interaction between hydrogen and misfit dislocations. Fig.4(a) shows two orthogonal dislocation networks at each buried interface of the non-hydrogenated reference sample. The horizontal lines are dislocations parallel to the image plane while end points correspond to the dislocations perpendicular to the plane. After hydrogenation, see Fig.4(b), the two interfaces were decorated with gas bubbles (white contrast) whose stress fields (black contrast) extended up to $0.5\ \mu\text{m}$. Also, the $\{111\}$ planar defects in Fig.4(b), are more dense at the upper interface, which was closer to the surface source of hydrogen. The SIMS profile showed an increase in concentration at the upper misfit dislocation interface. An unexpected result was the absence of a dependence on distance to the dislocation emergence site at the $\{111\}$ side wall of the etched trenches. These observations indicate that hydrogen atoms mainly diffused through the top silicon layer and not, as desired with the special structure, from the trenches via pipe diffusion.

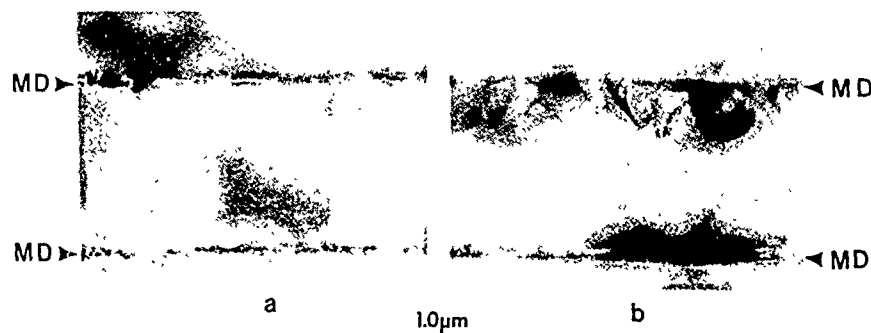


Fig.4 Bright field cross-section TEM images of epitaxial silicon
(a) before hydrogenation and (b) after hydrogenation

We conclude that hydrogen atoms diffuse into silicon and are gettered at dislocation stress fields creating damaged layers in the form of gas bubbles and (111) platelet defects. The high dose plasma process produced a hydrogen-rich damaged layer which results in a surface electrical field effect.

ACKNOWLEDGEMENT

The authors would like to acknowledge the technical assistance and useful discussion provided by Jack Olsen with MIR measurements, Ratnaji Kola for sample fabrication and Dieter Griffis with SIMS measurement. The support of the Solar Energy Research Institute under grant DOE/SERI XL-8-18097-2 is also gratefully acknowledged.

REFERENCE

1. N. M. Johnson and M. D. Moyer, Appl. Phys. Lett. 46, 787 (1985); 48, 709 (1986); R. Singh and S. Fonash, 49, 800 (1986); M. Stutzman, 52, 1667 (1988)
2. J. Hanoka et al. Appl. Phys. Lett. 42, 618 (1983); A. Rohatgi et al., 59, 4167 (1986)
3. J. Hanoka, Hydrogen in Disordered and Amorphous Solid, edited by G. Bambakidis, (1986) pp.81
4. J. Muller et al., Rev. Phys. Appl. 22, 649 (1987)
5. F. A. Ponce et al., Inst. Phys. Conf. Ser. 87, 49 (1987)
6. S.J. Jeng, G. Oehrleih and G. Scilla, Appl. Phys. Lett. 53, 1735 (1988)
7. G. A. Rozgonyi, et al. J. Cryst. Growth, 85, 300 (1987)
8. A. Salih et al. Appl. Phys. Lett. 46, 419 (1985); D.M. Lee, J. Posthill and G. Rozgonyi, 53, 370 (1988)
9. Kenneth Bean, IEEE Trans. on Electron Devices, ED-25, 70 (1978)
10. J. Olsen and F. Shimura. Appl. Phys. Lett. 53, 1934 (1988)

SURFACE AND BULK PROPERTIES WHICH INFLUENCE ION-BEAM HYDROGENATION OF SILICON

ROBERT A. ANDERSON AND CARLETON H. SEAGER
Sandia National Laboratories, Albuquerque, NM 87185

ABSTRACT

The time evolution of dopant passivation in p and n-type silicon Schottky and MIS barriers has been investigated for low-energy H ions implanted directly into the silicon through a 400-Å front-electrode metallization. Knowledge of the dependence of the near-surface hydrogen concentration on time and experimental parameters is crucial to the analysis of these experiments. Hydrogenation effects are observed to vanish at ion energies below 800 eV, which suggests that the front electrode, rather than being a source of H, will behave as a sink for H diffusing in the silicon. Accordingly, we show that a steady-state H concentration proportional to the ion-deposition flux and deposition depth is established in a time interval less than a second near the electrode. Although some of the mobile H appears to be in a positively charged state, we calculate that the bias voltage applied to samples has only a small influence on the near-surface H concentration. An extensive study of the effects of sample temperature, beam flux, and ion energy supports these concepts and has revealed no evidence of ion-damage induced H trapping. The possible importance of H-H recombination is suggested by data obtained at the higher H concentrations.

INTRODUCTION

We are studying hydrogen motion and bonding in silicon by means of rapid 1 MHz capacitance-voltage profiling of Schottky and MIS barriers [1]. Our results display the time evolution of charge density (dopant passivation) when low-energy H ions are implanted directly into the silicon through the front-electrode metallization. These data can be compared with numerical transport simulations and simple analytic approximations to deduce the charge state, diffusivity, and trapping parameters appropriate to the hydrogenation process in p and n-type material [2]. Such an analysis, however, relies on a knowledge of the surface boundary condition and bulk processes which affect the H concentration at the implantation depth; this hydrogen concentration is the source of mobile H that transports into the silicon bulk. Therefore, we have performed an extensive study of the effects of varying the sample temperature and the beam current and energy from our ion source, in order to deduce the simplest physical models which are consistent with observed behavior. Results from this study support our approach and, furthermore, give important insight into the role of implantation-induced damage and direct H-H interactions.

SURFACE BOUNDARY CONDITION

Previously postulated that H implanted into the front metallization of our Schottky-barrier diodes was diffusing into the silicon [1]. High-resolution TEM and SEM examinations of these early samples have revealed numerous small pinholes in the metallizations, so that some H was being implanted directly into the silicon even at low ion energies. The hydrogenation of these samples is likely to have been spatially inhomogeneous and the boundary conditions applicable to H transport nearly intractable. Procedural improvements now result in uniform, 400-Å aluminum metallizations which appear to be free of pinholes. Hydrogenation effects are now strongly dependent on ion energy and essentially vanish at energies below 800 eV, in accordance with numerical calculations of proton penetration [3].

Based on these observations, it is reasonable to assume that the front electrode is behaving as a sink for H that diffuses back to the metal-silicon interface from the implantation depth in the silicon. If, for the moment, we presume that all of the H is deposited at a single depth, h , the steady-state near-surface H concentration (evaluated at depth h) can be approximated by

$$H_s = \phi h / D, \quad (1)$$

where ϕ is the flux of deposited H. With H diffusivities, D , of the order of $10^{-10} \text{ cm}^2 \text{ sec}^{-1}$ [1,2] and implantation depths of the order of 100 \AA [3], steady state is attained in less than a second, a time interval short compared to our experiments.

Some fraction Q , roughly 10%, of the diffusing H appears to be positively charged [1,2]. Thus, the internal field of a reverse-biased p-type sample impels H ions into the silicon bulk. With an internal field, E , Eq. (1) becomes modified by the factor $[1 - \exp(-x)]/x$, where $x = QeEh/kT$ and e and kT are the electronic charge and the Boltzmann thermal energy. This factor remains close to unity under typical conditions in our experiments, and the corrections to Eq. (1) are small. To a good approximation, then, the depth h can be evaluated as the first moment of the H-deposition distribution and H_s can be presumed to be independent of E .

EXPERIMENTAL RESULTS AND DISCUSSION

Ion-Flux Dependence

Hydrogen penetration depths (defined at a fixed fraction of the depletion space-charge density) have been measured at several temperatures over a wide range of ion flux. Room-temperature results for one p-type sample are shown in Fig. 1. The abscissa is proportional to the product of ion flux (controlled by the H pressure in the vacuum system) and the duration of beam exposure. Hydrogenation is dependent on the total dose but independent, except at the highest pressure, of the flux. At 321 K, data at all pressures

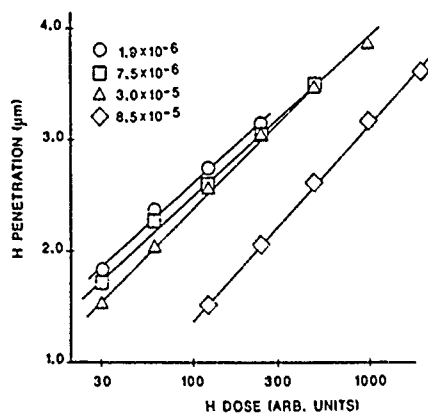


FIG. 1 - H penetration vs. H dose (proportional to flux \cdot exposure time) for a boron-doped Schottky diode (acceptor density $1.3 \times 10^{15} \text{ cm}^{-3}$) which was hydrogenated, at 297 K and under 5 V reverse bias, with 1000 eV ions. Vacuum system H pressures (torr) are indicated; each successively higher pressure gives a measured fourfold increase in ion flux.

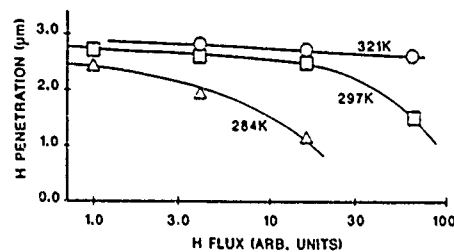


FIG. 2 - H penetration at a fixed dose (120, in the units of Fig. 1) vs. H flux, for the p-type diode of Fig. 1. Data obtained at three different temperatures are shown. The low-flux results are roughly temperature independent as expected from Eq. (1).

investigated nearly coincides with the flux-independent room-temperature curves; however, at temperatures below room there is a consistent reduction in penetration with increased flux. These data are summarized in Fig. 2, where the penetration at fixed H dose is plotted as a function of ion flux. The H penetration at low flux is nearly equal at all three temperatures, despite the strong dependence of diffusivity on temperature that is experimentally deduced [2]. This result clearly is consistent with the prediction from Eq. (1) that the product of H_s and D is independent of T (H_s varies inversely with D) and the conclusion from our hydrogenation modeling, reported elsewhere [1,2], that H penetration depends on the product of these two quantities. In this regime, direct H-H interactions must be negligible, but may become important at the higher H concentrations which are found at higher flux and lower temperature.

Ion-Energy Dependence

A clearly indicated dependence of hydrogen penetration on ion energy is apparent in Fig. 3, where data from both p and n-type samples are displayed. As in Fig. 1, the abscissa is determined by the beam current and exposure duration. These data all appear to be characterized by a roughly logarithmic dependence of penetration on dose despite the fact that field-implemented drift dominates in the p-type material while diffusion is mainly responsible for H penetration in the n-type material. (Reference 2 discusses the origin of this slow time dependence.) Furthermore, the influence of ion energy is similar for both dopant types. Such simple and consistent behavior over the range of ion energies argues against the significance of ion-damage induced H trapping, since the amount of damage would depend strongly on ion energy and would accumulate with increasing dose.

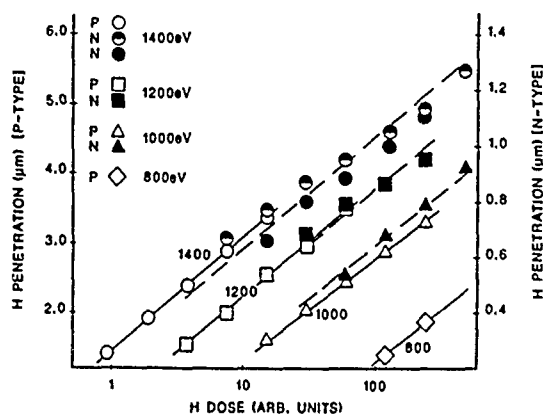


FIG. 3 - H penetration vs. H dose for room-temperature hydrogenations of reverse biased p-type (boron doped) and forward biased n-type (phosphorus doped) diodes at various ion energies. Note that different vertical scales have been chosen for these two sample types to illustrate the similarity of the dose and ion-energy dependences that were observed. Solid (p-type) and dashed (n-type) lines are manual fits to the data.

Data from Fig. 3 may be compared with calculated proton-deposition distributions at various energies. In Fig. 4, measured values of H concentration were inferred from the Fig. 3 data, and the theoretical values were obtained by integrating Eq. (1) over the calculated deposition distributions in the silicon [3] which are shown in the Fig. 4 inset. Not only is there good agreement between the normalized H concentrations in Fig. 4, but the actual values are also consistent. In order to calculate H_s , we measured the ion-beam current density and, from gas-fragmentation data applicable to a quadrupole mass analyzer [4], assumed that the beam contained about 3% protons. H_2^+ ions, which constitute the main part of the beam, are stopped within the metallization at the ion energies we used. This calculation

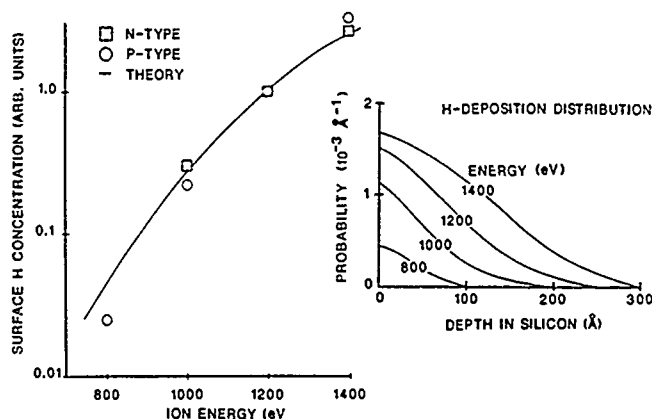


FIG. 4 - Comparison of the near-surface H concentrations determined by inverting the dose required for a fixed penetration depth in Fig. 3 and (solid line) by applying Eq. (1) to the calculated H-deposition distributions [3] shown in the inset. Both data and theory are normalized to unity at 1200 eV.

yielded a H density of $1.5 \times 10^{15} \text{ cm}^{-3}$ with the ion gun operating at 1000 eV in 3×10^{-5} torr hydrogen, a value that is in remarkably good agreement (in view of the uncertainties which enter the calculation) with experimentally deduced values [2].

CONCLUSIONS

A variety of experimental results support the hypothesis that the front electrode behaves as a sink for H, and the calculated values of H_2 agree with experimental determinations. Accordingly, the near surface H concentration is expected to reach steady state in less than a second and to be nearly independent of the applied bias. Temperature independence of H penetration, another consequence of this boundary condition, is observed at low H concentrations where the results are independent of ion flux as well. Recombination to H_2 molecules may be important at higher H concentrations. We find no evidence of ion-damage induced H trapping at the energies investigated.

ACKNOWLEDGEMENTS

The authors would like to thank D. K. Brice for performing numerical calculations of proton penetration into our samples, and W. Bayless for technical aid with sample preparation. This work was performed at Sandia National Laboratories, supported by the U. S. Department of Energy under contract DE-AC04-76DP00789.

REFERENCES

1. C. H. Seager and R. A. Anderson, Appl. Phys. Lett. **53**, 1181 (1988).
2. C. H. Seager and R. A. Anderson, in this symposium.
3. C. H. Seager, R. A. Anderson, and D. K. Brice, to be published.
4. UTI 100C Quadrupole Mass Analyzer Operating Manual (Uthe Technology International, Sunnyvale, CA, 1977), Appendix C.

HYDROGEN PASSIVATION STUDIES IN DISLOCATED CZ AND FZ SILICON

C. Dubé, J. P. Kalejs and S. Rajendran
 Mobil Solar Energy Corporation, 4 Suburban Park Drive,
 Billerica, Mass 01821

ABSTRACT

Hydrogen passivation using a Kaufmann ion source at 400°C has been carried out on FZ and CZ silicon dislocated by four-point bending at high temperatures. The results differ from those reported for dislocations passivated in silicon sheet grown by the EFG technique. A model for hydrogen diffusion and trapping is presented to argue that the differences observed are not produced by hydrogen transport effects in the bulk.

INTRODUCTION

Passivation of dislocations by hydrogen has been shown to lead to increases in the bulk lifetime of silicon sheet grown by the Edge-defined Film-fed Growth (EFG) technique [1]. Passivation mechanisms are not yet well understood, however, because there remain major areas of confusion regarding hydrogen diffusion and trapping behavior in silicon [2].

In this report we examine Kaufmann ion source passivation of dislocations introduced in initially dislocation-free single crystal FZ and CZ silicon. Four point bending at temperatures above 800°C is used to provide dislocated samples with reduced minority carrier diffusion lengths for the passivation studies at 400°C. A model for hydrogen diffusion and trapping [3] is used to obtain a consistent interpretation for the passivation response observed in the single crystal materials and in the EFG sheet.

EXPERIMENTAL DETAILS

The samples used in the present study were (111) and (100) orientation single crystal FZ and CZ silicon wafers, 1-2 ohm-cm p-type. Interstitial oxygen in the FZ material was below about $1 \times 10^{16}/\text{cm}^3$, and in the range of $5-10 \times 10^{17}/\text{cm}^3$ for the CZ silicon. Some CZ material with comparable carbon oxygen levels (both about $5 \times 10^{17}/\text{cm}^3$) was also examined. Samples $5 \times 10 \text{ cm}^2$ were stressed at temperatures between 600 and 1400°C using a four-point bending apparatus constructed from graphite according to the specifications of ASTM E 328-78 [4]. The bending axis was $\langle 110 \rangle$ for the (111) and $\langle 100 \rangle$ for the (100) samples. Here we discuss only the results obtained above 800°C where the dislocation arrays were clearly defined in the uniform stress central region of the sample. The experimental procedure consisted of a temperature ramp of about a half to one hour up to the operating temperature without a load on the sample, a load application time of a few seconds to one hour (depending on the operating temperature and stress used), and a cooling time to 400°C of about one half hour with the load removed. The experiments were carried out in a resistance heated furnace used for growth of EFG silicon ribbon. All graphite parts were purified with a high temperature halogen treatment used to prepare graphite for EFG furnaces.

The hydrogen passivation was performed with a Kaufmann ion source operated at 2 keV. The substrate temperature was kept at 400°C and the passivation time was 2 min, identical to conditions used for passivation of EFG material reported previously [1].

RESULTS

Cross sectional EBIC was performed on material prepared from both the end of a sample, which was not under stress, and from the center, which had the maximum level of dislocations. Typical EBIC scans through the center and end regions of a 400 μm thick FZ sample stressed at 1370°C are shown in Fig. 1. Cross sectional micrographs taken perpendicular to the $\langle 110 \rangle$ bending axis in the region of the traces show the dislocation configurations. Abrupt changes in signal near the sample edge are due to spurious EBIC response at the surface. The reason for the internal structure observed in the EBIC line scans is not known. Similar results were qualitatively reproduced in both FZ and CZ silicon, i.e., regardless of the material oxygen and carbon level. The CZ samples tended to be more inhomogeneous in their degradation. To check if impurities specifically connected to the graphite were involved in the degradation, companion samples were furnace annealed in a closed quartz tube. These exhibited lifetime degradation to levels similar to those of Fig 1.

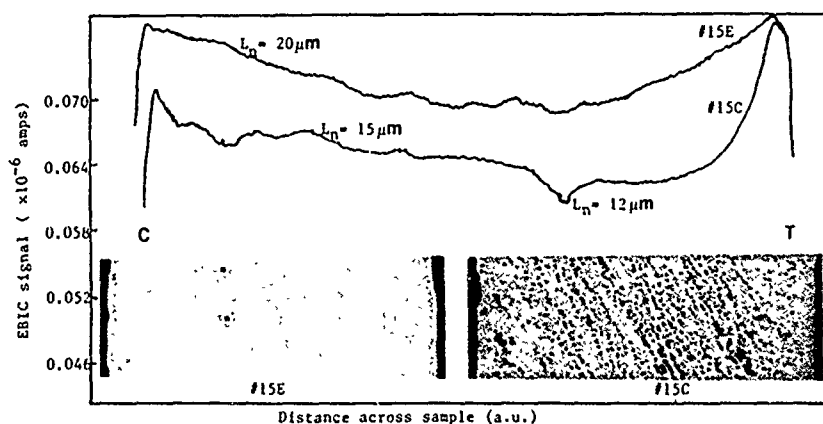


Fig. 1. EBIC line scans and photomicrographs of stressed FZ silicon for edge region (15E) with $N_D = 1 \times 10^{16}/\text{cm}^2$, and center region (15C) with $N_D = 1 \times 10^{16}/\text{cm}^2$. Tension surface (T) in each case is on right, compression (C) surface is on left.

EBIC line scans across the sample thickness before and after hydrogen passivation are shown in Figs. 2 and 3. Each pair of traces does not have a one-to-one correspondence of EBIC features because they were taken on adjacent regions of passivated and unpassivated material. The hydrogen source was located on the right hand surface in all cases.

The important results from this data may be summarized as follows. Essentially dislocation-free material (Fig. 2) and highly dislocated material (Fig. 3) do not show clear differences in response to passivation. There is no consistent appearance of a gradient in the diffusion length improvement through the thickness. This implies that the hydrogen has penetrated through the entire sample during the time of the passivation. A distinct passivation front, as seen in the case of passivation of dislocations in EFG material [1], or in boron deactivation [2,3], is not found for all dislocation densities up to $10^7/\text{cm}^2$. The results for a CZ silicon sample with comparable carbon and oxygen levels indicate such impurities do not introduce new features in the passivation.

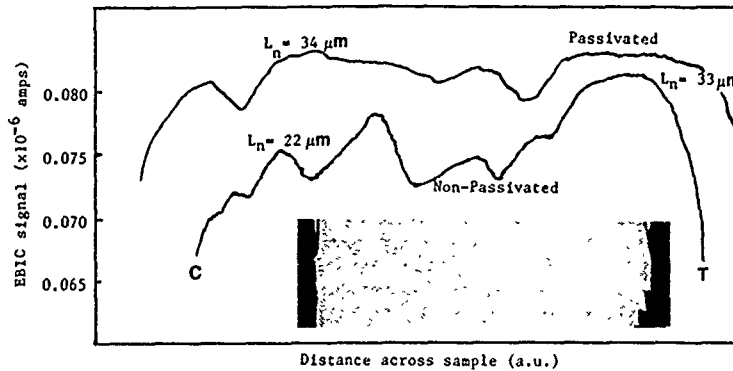


Fig. 2. EBIC line scans for very low dislocation density ($N_D \leq 10^4/\text{cm}^2$) FZ sample before and after hydrogen passivation.

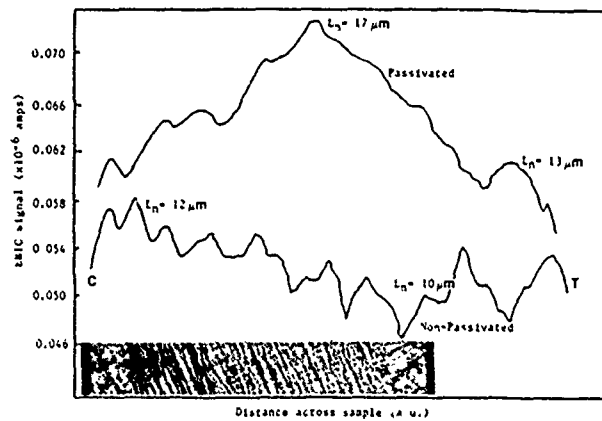


Fig. 3. EBIC line scans for high dislocation density FZ ($N_D \sim 10^7/\text{cm}^2$) sample before and after hydrogen passivation.

DISCUSSION

The simplest formulation of our model for diffusion and trapping of hydrogen [3] predicts that the hydrogen passivation depth, X , is a function only of the density of trapping sites for the hydrogen, N_T , given that the surface concentration, C_0 , defining the diffusing hydrogen flux is maintained constant. The calculations also relate N_T to an effective diffusivity, D_T , for the advance of the passivation front. D_T may vary with N_T between $(N_T)^{-1}$ and $(N_T)^{-0.5}$. Here we identify N_T with the density of recombination centers responsible for limiting the minority carrier diffusion length L_n . Changes in L_n occurring during passivation may be used to estimate N_T through the relationship $N_T = D_n / \sigma V L_n^2$. For dislocated silicon we use an electron diffusivity $D_n = 15 \text{ cm}^2/\text{s}$, a thermal velocity $V = 10^7 \text{ cm/s}$ and $\sigma = 10^{-15} \text{ cm}^2$ for the recombination cross section of the defects limiting the diffusion length, giving $N_T = 1.5 \times 10^9 / L_n^2$. For unpassivated material with $L_n = 20 \text{ μm}$, $N_T = 3 \times 10^{14}/\text{cm}^3$ recombination sites. An increase in L_n by a factor of two after passivation indicates that 75%, or of the order of $10^{14}/\text{cm}^3$, of the active traps are passivated.

The passivation depths in EFG material are correctly predicted with the use of N_T values within this estimated range. For example, modeling with $N_T=1 \times 10^{14}/\text{cm}^3$ and $C_0=2 \times 10^{13}/\text{cm}^3$ gives $X=100 \mu\text{m}$ to reproduce the passivation depth reported for dislocation arrays (1), with $D_T=7 \times 10^{-7} \text{cm}^2/\text{s}$. Reduced passivation depths below $30 \mu\text{m}$ along grain boundaries clearly require higher values of N_T , of the order of $10^{15}/\text{cm}^3$, and correspondingly lower effective diffusivities D_T . In these cases, since we are in a regime of $C_0 < N_T$, D_T is considerably smaller than the diffusivity for hydrogen in the absence of traps, D_H , used in the model. We previously established [3] that the diffusivity data of Van Wieringen and Warmoltz [5], extrapolated to lower temperatures, must be used for D_H , which give $D_H=2.4 \times 10^{-6} \text{cm}^2/\text{s}$ at 400°C . The assignment of higher trap densities with grain boundaries having the reduced X is in agreement with experimental work. Estimates of the surface recombination velocity S at some grain boundaries show that the boundaries with lower S have higher effective diffusivities [1].

The evidence that the passivation front in the FZ and CZ silicon has moved through the entire $400 \mu\text{m}$ thickness in the 2 min passivation provides a lower bound of $D_T > 1.3 \times 10^{-5} \text{cm}^2/\text{s}$. Now D_T is considerably greater than D_H and they are in the reverse relationship to that observed for EFG passivation. $D_T > D_H$ only if $C_0 \gg N_T$. This leads to the conclusion that the defect density effective in trapping hydrogen in the dislocated FZ and CZ silicon is significantly lower than that in EFG material, and remains so in the former regardless of the dislocation density. Since EFG and dislocated FZ and CZ all have comparable starting L_n , the lower N_T in the dislocated single crystal silicon requires either that these traps have proportionately greater recombination cross sections, or there exists another set of lifetime limiting traps, which are not dislocations, and that are not as easily passivated as the traps in EFG material.

ACKNOWLEDGEMENTS

The authors would like to thank A. Menna for performing the four-point bending and D. Sandstrom for the EBIC analysis.

REFERENCES

1. C. Dubé J.I. Hanoka and D.B. Sandstrom. Appl. Phys. Lett. 44, 425(1984); C. Dube and J.I. Hanoka, *ibid.*, 45, 1135(1984).
2. S.J. Pearton, J.W. Corbett and T.S. Shi, Appl. Phys. A 43, 153(1987).
3. J.P. Kalejs and S. Rajendran, to be published in Applied Physics Letters, Dec. 1989.
4. Annual Book of ASTM Standards (McGraw Hill, Philadelphia, 1978).
5. A. Van Wieringen and N. Warmoltz, Physica 22, 849(1956).

PART VII

Hydrogen in III-Vs

HYDROGEN COMPLEXES IN III-V SEMICONDUCTORS

BERNARD PAJOT

Groupe de Physique des Solides de l'Ecole Normale Supérieure,
 Tour 23, Université Paris 7, 2 place Jussieu, F-75251 Paris Cedex
 05, France

ABSTRACT

A review of the occurrence, nature, structure and stability of the H complexes in III-V compounds is presented, mainly based on electrical and spectroscopical data. The importance of the problem of formation and dissociation of the complexes is pointed out and the use of H complexes in actual III-V devices is described.

INTRODUCTION

The importance of H complexes in semiconductors stems from the fact that some of these complexes are directly related to the electrical neutralization of the dopants and to the passivation of the recombination properties of deep centres [1,2]. Isolated hydrogen has been the model for the electronic behavior of shallow dopants (the so-called hydrogen-like centers) in group IV semiconductors. In intrinsic or n-type silicon, its closest equivalent is interstitial lithium, acting as a shallow donor with an ionization energy of 33 meV and a rather high diffusion coefficient; in p-type B-doped silicon, lithium diffuses as a positively charged ion and it can form electrically neutral pairs with negative boron ions [3]. These pairs are stabilized by electrostatic interaction and their bonding should have merely an ionic character. The bonds involving hydrogen are however stronger than those involving lithium and infrared absorption related to the stretching motion of Si-H bands in crystalline silicon [4] indicates a bonding comparable to the ones found for molecular species containing Si-H bonds.

First evidence for H complexes in GaAs and GaP was obtained spectroscopically after proton and deuteron implantation [5]. Later on, it was rightly guessed that sharp IR lines observed in as-grown GaAs and InP materials between 2000 and 2300 cm⁻¹ were related to the presence of H complexes [6]. It was also shown that deliberate exposure of n-type GaAs:Si to H or D plasmas producing electrical neutralization of the dopant [7] gave rise to H- or D-related lines [8]. In that case, the control of the doping of the samples and the choice of the hydrogen isotope led to an unambiguous assignment and to a proposal of the hydrogen neutralization mechanism [9]. Since then, the interest for the role of hydrogen in III-V has grown considerably and many investigations have been undertaken on the physics of hydrogen in these semiconductors. This is partly due to the fact that in silicon as well as in III-V compounds, the H complexes are directly related to the neutralization of dopant atoms and to the passivation of defects as this property can be used in the fabrication of some electronic and opto electronic devices whose stability depend on dissociation kinetics of the H complexes. In this review, I will first discuss of the occurrence of the H complexes. This point is directly linked to their structure and I will try to show how this structure, at least for some of them,

can be inferred from optical spectroscopy and piezo-spectroscopy. The structure, in turn, can help to understand the thermal stability of the H complexes which will be discussed in view of possible technological uses of hydrogenation of III-V compounds.

OCCURENCE OF H COMPLEXES

Vibrational infrared (IR) and Raman spectroscopy can detect the presence of H bonds in molecules; hence, a similar observation in semiconductors is an indication of the presence of H complexes. IR absorption of modes associated with such bonds have been observed in amorphous hydrogenated GaAs and in crystalline GaP, GaAs and InP implanted with protons or deuterons [5, 10-13]. The attribution of the modes to hydrogen is relatively straightforward as hydrogen-related frequencies should decrease by a factor of about $\sqrt{2}$ when deuterons are used instead of protons. The frequencies of these modes and correlations between different compounds with a common constituent (e.g. GaAs and GaP or GaP and InP) indicate binding of hydrogen with Ga, As and P atoms. H or D implantation in n-type GaAs:Si and in GaAs:Zn reveals the additional presence of H complexes not observed with semi-insulating (si) material [14,15].

The features observed depend on the implantation doses and on the energy of the ions, which determine the defect concentration and the penetration depth, but also on the current intensity which can produce, if too high, *in situ* annealing of defect centers stable at room temperature. The minimum dose required to observe H complexes decreases for measurements performed near LHeT: In GaAs; for instance, H complexes can be observed for 190 keV protons doses of $5 \times 10^{15} \text{ cm}^{-2}$ [14], but measurements at ambient can require doses one order of magnitude larger.

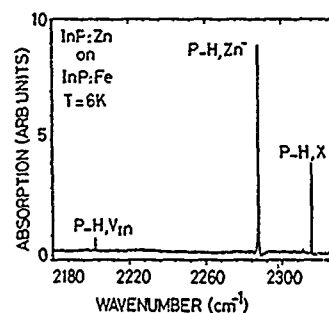
In III-V compounds grown by the LEC technique, the observation at LHeT of sharp absorption lines between 2000 and 2320 cm^{-1} has been reported [6,16] and other lines at still higher frequencies have also been observed. Their attribution to H complexes present in the bulk has been made on the ground that they have a vibrational origin and that the only element which could produce such high frequencies is hydrogen. Some of these lines are impurity-independent but some others are not. It has been shown that two seemingly impurity-independent lines observed at 2204 and 2315 cm^{-1} in LEC InP could also be produced by proton implantation and that they had a deuteron counterpart [13]; similarly, a line observed in p-type LEC InP at 2288 cm^{-1} was observed later on in H plasma-treated InP:Zn, with a counterpart at 1665 cm^{-1} in a D plasma-treated sample [17]. These are experimental confirmations that hydrogen is present in as-grown LEC III-V compounds. Hydrogen very probably comes from the dissociation of water of the wet encapsulant, but hydrogen has also been detected in InP after its synthesis and there, it could originate from a small amount of water present in phosphorus [16]. The concentration of the H-Zn complexes in as-grown p-type LEC InP can be estimated to be in the $10^{15} \text{ atoms/cm}^3$ range. From this value, the H concentration associated with the whole H complexes series in the LEC III-V compounds could be in the $5 \times 10^{15} - 1 \times 10^{16} \text{ atoms/cm}^3$ range.

H and D complexes are produced in doped III-V compounds by exposure to RF or microwave pure H or D plasmas while no complexes are seen in si material besides the ones already present in the as-grown material [18]. Reactive ion etching with H-containing gases also produces H complexes responsible for the dopant

neutralization reported [19,20]. The conditions for the formation of the complexes depend on the type of plasma and also on the chemical nature of the dopant.

In InP:Zn epilayers with undoped or p-type InGaAs cap, the electrical activity of zinc is reduced and the same IR line as the one observed in H plasma treated InP:Zn samples is detected, indicating again the presence of H complexes (Fig. 1). The source of hydrogen in this case is H atoms formed by the dissociation of AsH₃ gas used in the system during the cooling down step.

Figure 1. Absorption of P-H, Zn complexes in as-grown MOVPE InP:Zn epilayer with InGaAs:Zn cap. The true absorption of the native P-H, V_{In} and P-H, X complexes in the InP substrate is 200 times less than shown.



The amount of hydrogen introduced in InP:Zn increases with the doping level of GaInAs but no neutralization of InP:Zn is observed with n-type GaInAs [21]. The presence of H complexes in GaAs:Sn grown by MBE in the presence of atomic hydrogen can also be inferred from the properties of this material [22].

Secondary ion mass spectroscopy (SIMS) of D-plasma treated si GaAs shows the presence of deuterium in the material at a level comparable to the one in n-type GaAs:Si while no D-related IR bands are observed in the former material [23]. This could be considered as indirect evidence of the existence in this material of complexes between hydrogen or deuterium and native defects, whose existence has been deduced from the comparison of DLTS results before and after hydrogenation [2], but the concentration of these complexes should account only for a small fraction of the total hydrogen concentration and we are then led to conclude that hydrogen is also present as a molecule in this material.

IDENTIFICATION OF THE COMPLEXES

Chemical identification

The identification of the H complexes starts with the identification of the atom bonded to the H atom. The stretching frequency of the X-H bond depends on the strength of the bond. The trend is that the highest the mass of atom X, the lowest the frequency and that for all but the light atoms (B, C, N and O), the frequencies lie in the 1800 - 2200 cm⁻¹ region. This frequency is not too sensitive to the nature of the other atoms of the molecule and to the phase where the molecule is observed. Hence the value of the frequency is already an indication which can help ruling out some possibilities and strengthening others.

A second indication is given by the r-factor defined here as the ratio of the frequencies of the X-H and X-D bonds. In the one-dimensional harmonic oscillator approximation, the stretching

frequency of an X-Y oscillator is inversely proportional to the square root of the reduced mass of the oscillator, namely:

$$r = \sqrt{(2(M_X + 1)/(M_X + 2))} \quad (1)$$

for X, H and D atoms of respective masses M_X , 1 and 2. The experimental r-factor shows, as expected, a steady increase with the mass of atom X, but it is systematically lower than the one calculated from (1). Moreover, it can depend on the molecule where the X-H bond is located: for Si-H in SiH_4 , r is 1.372 but it increases to 1.383 in SiH_2Cl_2 . However, its value in a material containing unknown X-H bond with comparable frequencies can help to choose between two atoms with very different masses.

More direct information on the chemical nature of the X atom comes from the observation of an isotope effect when the X atom is light and has several isotopes with reasonable relative abundances. If the X-H mode is sharp, it is then possible to detect as many lines as there are different isotopes. The line width condition is met for a line observed at 1717.25 cm^{-1} (LHeT) in hydrogenated n-type GaAs:Si. This line, related to hydrogen (it has an equivalent at 1247.61 cm^{-1} in deuterated material), has two low-frequency side-bands whose relative intensities match the relative abundance of the Si isotopes and the spacings are compatible with the expected isotope shift. This is an evidence of a strong interaction between H and Si atoms in this material, and it can be explained by the formation of a Si-H bond [9].

Another evidence is related to the observation of localized modes of light dopant atoms in semiconductors. When these atoms interact with a light atom like hydrogen, the frequency of the localized mode of the isolated atom is modified by the presence of the H atom and a new mode can appear in the same frequency domain. The correlation with the presence of hydrogen is clear as the frequency of the new mode decreases when a H atom is replaced by a D atom. Conversely, the intensity of the mode of the isolated atom is reduced by the decrease of its concentration. Such effects have been observed for H plasma treated GaAs:Si and GaAs:Be [9,24,25].

When no direct identification of atom X is possible, one must rely on indirect evidence. One is the dependence of the X-H frequency on the nature of the dopant atom: for hydrogenated GaAs:Be and GaAs:Zn, two distinct H-related lines are observed and this is also true for p-type GaAs:Si and GaAs:Ge where Si and Ge predominantly occupy As sites. This does not necessarily mean that a bond is formed between the dopant atom and hydrogen, but this is an indication that the dopant atom takes part to the H complex.

Structural identification

Information on the symmetry and structure of the H complexes in silicon has been obtained from piezo-spectroscopy, from channeling of ^4He ions and from perturbed $\gamma\gamma$ angular correlation [26-29]. For III-V compounds, however, the results come only from piezo-spectroscopic data. The basic idea is that when simple defects or complexes are formed in a crystal with diamond or zinc blende structure, they are mostly oriented along directions of high symmetry ($\langle 111 \rangle$, $\langle 110 \rangle$ and less often $\langle 100 \rangle$) and this results in an orientational degeneracy of the levels. Now, an X-H stretching mode is singly degenerate so that if a compressive force is applied to the sample, the splitting of the mode will be related to the removing of the orientational degeneracy by the uniaxial

stress. For simple defects, the splitting pattern and the optical polarization of the split components enable to determine the orientation of the complex [30].

The structure and vibrational modes of GaAs:Si_{Ga} and GaAs:Be H complexes have been calculated using *ab initio* local density functional pseudopotential theory [31]. This method, which is very useful to predict or confirm the microscopic structure of the H complexes also gives indications on the relaxation of the atoms of the complex.

Complexes with donor atoms

The existence of H complexes after H plasma neutralization of n-type GaAs:Si is inferred from the presence of two lines attributed to the wagging and stretching modes of the Si_{Ga}-H bond and similar structures have also been reported in H neutralized Ga_{1-x}Al_xAs:Si alloys [32]. Two lines are also observed in H plasma neutralized n-type GaAs:Sn; the similarity with the GaAs:Si:H case and the frequency shift suggests the presence of a Sn_{Ga}-H bond [33]. The observation of a wagging mode of the Si_{Ga}-H bond favors an antibonding (AB) site for the H atom rather than a bond centered (BC) location as in this latter case the interaction between the H and As atoms would certainly lower substantially the wagging frequency. *Ab initio* calculations have shown indeed that the minimum energy is for a Si_{Ga} atom bonded to three As atoms and to one H atom in the configuration shown in Fig. 2. The dangling bond of the fourth As atom turns into a lone pair by coupling with the extra electron, achieving the neutralization of the donor. The trigonal symmetry of the center along a <111> axis is confirmed by piezo-absorption studies of GaAs:Si:H (Fig.3).

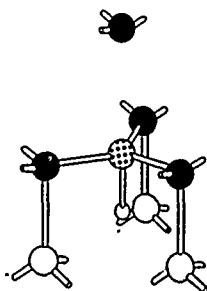


Figure 2. Structure of the Si_{Ga}-H complex in n-type GaAs:Si. Black balls: As atoms.

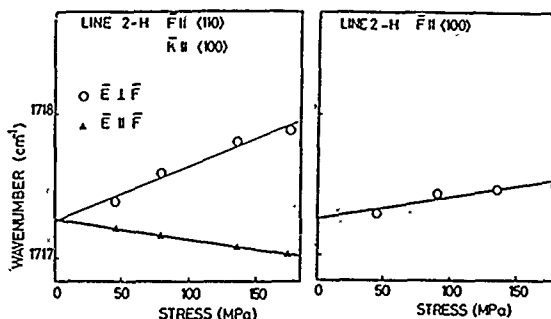


Figure 3. Stress-induced splitting of the stretching mode of Si_{Ga}-H in n-type GaAs near 10K.

Under a <110> stress, the stretching mode, labelled 2-H, splits into two components corresponding to the two classes of <111> complexes with respect to stress. For a <100> stress, all the complexes are equivalent and no splitting is observed, but only a shift due to the hydrostatic component of the stress. Neutralization of the group VI donors on As sites by H plasma has been reported [7], but not the observation of lines related to the

bonding of a group VI atom to hydrogen. Neutralization of Si donors seems to be far less efficient in InP than in GaAs and no direct evidence of Si-H bonding exists in this material.

Complexes with acceptor atoms

Acceptors on group III atoms sublattice. The hydrogen neutralization of an acceptor (Zn) in GaAs was first reported in ref. 34. For GaAs doped with Zn, Be and Mg and InP doped with Zn, the r-factors and the frequencies of the H lines are consistent with the bonding of hydrogen to the group V atom. Moreover, in the case of GaAs:Mg and InP:Zn where the lines are sharp (about 0.1 cm^{-1} for the D complex), there is no indication of an isotope effect and this is in agreement with the fact that ^{31}P and ^{75}As are both 100% abundant.

In GaAs:Zn:H, two H-related lines are observed [35], the most intense one at 2147 cm^{-1} and a weaker one at 2144 cm^{-1} . The strong line is related to a As-H, Zn^- complex whose structure is shown in Fig. 4. In this structure, the Zn^- ion facing the BC H atom is threefold co-ordinated and electrically inactive. The weak line is not related to the same center as the strong one since 1) the relative intensities of the two lines can change in proton-irradiated GaAs:Zn [15] and 2) the 2144 cm^{-1} line is the only line observed in hydrogenated GaAs:Mg (Fig.5).

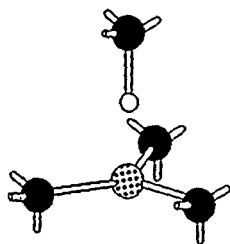


Figure 4. Structure of the complexes between H and acceptors on group III site in III-V compounds. White ball: H atom in BC location.

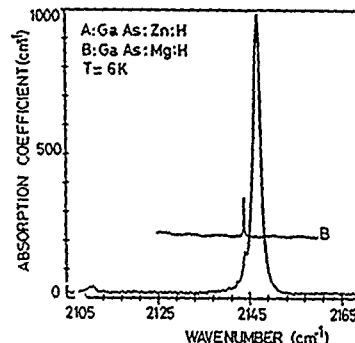


Figure 5. Absorption of GaAs:Zn:H (A) and GaAs:Mg:H (B). Note the shoulder of the strong As-H, Zn line in (A).

This line, which is not related to Mg either is about one order of magnitude sharper than the one ascribed to the Zn complex. Its frequency and r-factor indicate that it can be also due to an As-H bond. Its sharpness seems to rule out an As-H, Ga structure similar to the As-H, Zn^- complex which produces a much broader line. Another possibility is the presence of interstitial As atoms resulting from the H plasma treatment, known to produce a damaged layer at the surface of the sample: these As atoms could diffuse and trap H species to form interstitial AsH molecules. This attribution is further substantiated by the line width increase of this mode from 0.2 cm^{-1} at LHeT to only 2.5 cm^{-1} at room temperature, in agreement with an interstitial molecule decoupled from the GaAs lattice, and by the observation of an increase of the intensity of this mode during annealing steps of proton-implanted GaAs:Zn where As interstitials are also produced

[15]. The structure of the H complexes produced in GaAs:Be has been calculated: the frequency obtained (2083 cm^{-1}) compares fairly with experiment (2037 cm^{-1}) and a large relaxation of the Be atom is found [31]. A confirmation of the trigonal symmetry of the As-H, Be^- complex comes from piezo-spectroscopy [36]. The As-H, Be^- complex can also be partially aligned by stress above 120 K (Fig.6). A study of the temperature recovery from this stress-induced dichroism shows that the motion of the H atom from one BC site to another about the Be atom is thermally activated with an energy of 0.37 eV [36].

Group IV acceptors on group V atoms sublattice. H-related IR lines were observed in hydrogenated p-type GaAs doped with Si or Ge. The frequency scaling with the Si-H and Ge-H frequencies in light molecules and the r-factors of 1.383 in GaAs:Si compared to 1.389 in GaAs:Ge indicate that the H atom is bonded directly to the group IV acceptor in the BC configuration and the structure of the complexes is shown in Fig.7. Additional evidence for interaction between H and acceptor atoms comes also from the reduction of the localized mode of isolated Si_{As} in hydrogenated GaAs: Si_{As} indicating a reduction of the concentration of this center. A H-related line at 972 cm^{-1} with $r=1.382$ observed in some p-type GaAs:Si samples is attributed to the wagging mode of the Si_{Ga} -H mode of a $\text{Si}_{\text{As}}, \text{Si}_{\text{Ga}}$ -H complex produced by hydrogenation of Si pairs known to exist in this material [24].

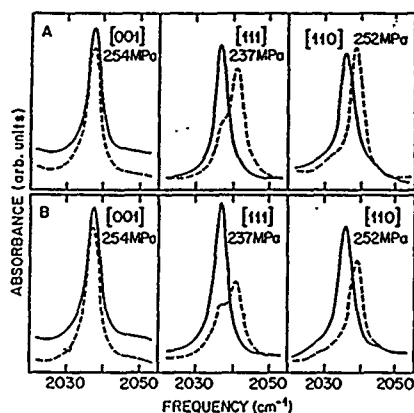


Figure 6. Stress-induced splitting of the As-H mode in GaAs:Be at 15 K. E//F —, E⊥F ----. A: Stress applied at 15 K. B: Sample cooled from ambient to 15 K under indicated stress. The traces for [001] stress are displaced vertically for clarity.

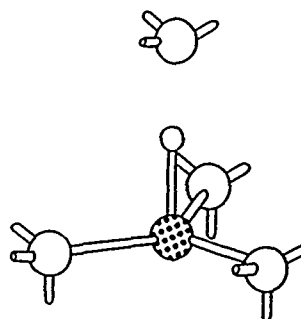


Figure 7. Structure of the complexes between H and acceptors on group V site in III-V compounds. White balls: group III atoms, dotted ball: acceptor atom.

Complexes in bulk as-grown materials

The H complexes in bulk as grown LEC are difficult to identify as the D-related lines are not observed in this material. Some of

the IR lines observed are related to residual impurities like carbon [37] or to transition metals [16]; other are related to native defects. From piezo-spectroscopic results, it has been proposed that the complexes producing the 2001 and 2202 cm^{-1} lines in si GaAs and InP were the trigonal As-H, V_{Ga} and P-H, V_{In} centers [38]. In si GaP, the line at 2204 cm^{-1} should be similarly related to P-H, V_{Ga} . In Table I is summarized some information on the H complexes in III-V compounds derived from IR spectroscopy.

Table I. LHeT frequencies (cm^{-1}) of IR lines associated with some H complexes in hydrogenated III-V compounds. When a D-related line is observed, the r-factor is given.

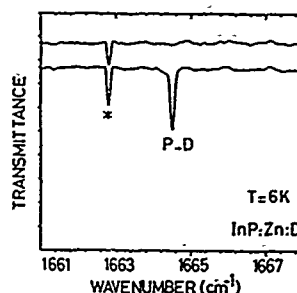
Material	Frequency	r-factor	Complex	Reference
n-GaAs:Sn	747			33
n-GaAs:Si	896,8	1.3980	$\text{Si}_{\text{Ga}}\text{-H}$	9
p-GaAs:Si	972,2	1.3820	$\text{Si}_{\text{As}}\text{-Si}_{\text{Ga}}\text{-H}$	24
n-GaAs:Sn	1328	1.3719	$\text{Sn}_{\text{Ga}}\text{-H}$	33
n-GaAs:Si	1717.3	1.3764	$\text{Si}_{\text{Ga}}\text{-H}$	9
si GaAs	1838 *	1.3914	Ga-H, V_{As}	12
"	1998 *	1.3856	As-H, V_{Ga}	12
"	2001.0 +		"	6
p-GaAs:Be	2037	1.3845	As-H, Be	25
p-GaAs:Si	2095	1.3832	$\text{Si}_{\text{As}}\text{-H}$, Ga	24
p-GaAs:Ge	2010	1.3889	$\text{Ge}_{\text{As}}\text{-H}$, Ga	18
p-GaAs:Mg or Zn	2144.0	1.3859	(As-H) _i ?	18
p-GaAs:Zn	2147	1.3860	As-H, Zn	35
<hr/>				
si GaP	1849 * †	1.3867	Ga-H, V_{P}	5
"	2204 *	1.3775	P-H, Ga	11
"	2204.3 +		"	6
<hr/>				
si InP	2202 *	1.3728	P-H, V_{In}	13
"	2202.4 + ¶		"	13
p-InP:Mn	2272		P-H, Mn	6
p-InP:Zn	2287.7	1.3744	P-H, Zn	17
si InP	2300.0 +		P-H, Ti	6
"	2315 *	1.3755	P-H, ?	13
"	2315.6 +		"	5
<hr/>				
* Proton implanted		† 77 K		
+ As-grown		¶ Room temperature		

FORMATION AND DISSOCIATION OF THE H COMPLEXES

The H complexes have each a definite domain of stability and their formation depends also on the availability of a hydrogen species in the vicinity of the dopant atom, i.e. on the diffusion coefficient and on the charge state of hydrogen. In highly doped p-type material, hydrogen seems to diffuse as a proton. The

following the dissociation of H complexes in all the cases and the

Figure 8. Absorption of the P-D, Zn complex in InP:Zn:D. A: After 10 minutes annealing at 375°C under argon. B: 10 minutes annealing under molecular hydrogen. * denotes a water vapor line.



formation of H₂ molecules should certainly be considered; it also shows the need to reconsider in some cases the assumption of a first order kinetics to interpret the data on the dissociation of the complexes or the re-activation of the dopants [42].

TECHNOLOGICAL PERSPECTIVES AND CONCLUSION

Proton implantation is currently used for electrical insulation of active parts of III-V devices where compensation of the carriers is produced by deep traps, some probably including H-related defects. More recently, H neutralization of the dopant has also been used for the fabrication of gain-guided GaAs-Al_xGa_{1-x}As quantum well laser arrays or buried ridge structure lasers [43,44]. When the requirement is a reduced well-controlled carrier concentration, neutralization is superior to compensation because of the higher carrier mobility in the neutralized material due to the reduction by a factor of two of the concentration of scatterers and to the lower scattering efficiency of the H complexes; a GaAs FET using partial hydrogenation of the gate has been realized which shows good performance [45]. Competing again with proton implantation, a potential use of hydrogenation is the fabrication of high resistivity waveguides in p⁺ GaAs or InP based on the increase of the refractive index and small absorption coefficient of the high resistivity material [46]. The initial properties of the III-V devices hydrogenated during the processing are comparable to those for classical ones, but their time and temperature stabilities have also to prove to be the same before using routinely hydrogenation in technological processes.

Most of the H complexes investigated in III-V compounds show a trigonal symmetry with the H atom on the C₃ axis either in a BC or an AB location. At a difference with the Si-H, Al and Si-H, Ga complexes in silicon [47], no temperature-dependent satellite structure is observed for the H-Acceptor complexes, indicating that in the III-V compounds, the H bond is along the <111> axis. However, the structure of many complexes still needs to be elucidated, specially in as-grown materials, and interstitial H complexes could display non trigonal symmetries. More serious, we still do not fully realize the reason for the formation of a hydrogen-dopant complex. The spectral width of the absorption lines related to H complexes vary by more than two orders of magnitude at LHeT and if properly understood, the differences could bring information on the coupling between the complex and

ionization comes from the compensation of the acceptors and it confers to isolated hydrogen a deep donor character as well as a high mobility, hence the possibility of attraction of H^+ by the negative acceptor ion. For hydrogen, the energy balance, including relaxation, seems in many cases favorable to binding to the acceptor atom or to its nearest neighbor. This seems to hold for p-type GaAs:Si and InP:Zn where a close correlation is found between the dopant and the D profiles so that the latter can be thought to represent the D complex profile at least for plasma treatments below 300°C [17]. When other energetically favorable situations exist, they can compete with or even overcome the formation of acceptor hydrogen related complexes.

If hydrogen diffuses in n-type semiconductors as H^- , the first step of the building of H complexes would be also Coulomb interaction, but if it diffuses as H^0 , a H complex will result from statistical close encounter and from an energetically favorable situation. Whatever the charge state of the diffusing species in hydrogenated n-type GaAs:Si, it remains that the D profile in this material is closer to a normal diffusion profile than in p-type material.

GaAs:Zn and InP:Zn epilayers can be fully H- or D-neutralized on the whole thickness of the sample (typically a few micrometers) so that the IR lines related to the complexes correspond in this case to the zinc concentration measured by SIMS or to the free hole concentration which can be measured when the dopant has been fully reactivated. Hence, a calibration of the integrated absorption A_i of the H complexes can be obtained. For GaAs:Zn, $N_{(Zn-H)} (cm^{-3}) = 4 \times 10^{16} \cdot A_i(As-H) (cm^{-2})$. For InP:Zn, $N_{(Zn-H)} (cm^{-3}) = 2 \times 10^{16} \cdot A_i(P-H) (cm^{-2})$. The detection limit of the H complexes in InP:Zn is $\approx 2 \times 10^{13}$ centers/cm² and the calibration factor allows to determine spectroscopically the free hole concentration in a sample with unknown neutralization.

The dissociation energy of the H complexes with donors in GaAs was measured to be near 2 eV compared to 1.6 eV for the As-H, Zn⁻ complex [7,39]. This can be explained by the dissociation energies, greater for the bonds between H and group VI and group IV atoms than for the As-H bond, but other considerations like the site of the bonded H atom and its charge state when dissociated should also be considered. An activation energy of 3.1 eV for H diffusion has been measured in as-grown InP:Zn MOVPE layers with a p⁺ GaInAs:Zn cap, where the neutralization efficiency is ≈ 0.8 [40]; it must be compared with an overall dissociation energy of 2.0 eV measured on deliberately deuterated samples with the GaInAs cap removed [41]. The effective dissociation of the H-acceptors complexes results from a dissociation-recombination equilibrium and what is actually measured is the combination of the dissociation energy of the complex and of the activation energy for the out-diffusion of protons. On this ground, the dissociation should be considered as complete only after the out diffusion of most of hydrogen from the sample. This is shown (Fig.8) when comparing the dissociation of the H-Zn complexes after annealing in an Ar or H₂ atmosphere: with the H₂ atmosphere, the equilibrium for out-diffusion is displaced and the energy required is higher than with an Ar atmosphere so that the H complexes can still be observed after annealing in H₂ atmosphere at temperatures where full dissociation would be achieved with Ar. This does not mean that out-diffusion of atomic hydrogen is the only mechanism

the host crystal. Studies of the dissociation kinetics of the H complexes would be also beneficial to the understanding of the hydrogen diffusion in III-V compounds and to the optimization of the hydrogenated devices. Last, the microscopic structure of hydrogenated native defects like EL2 or the DX centers is still poorly understood and possible correlations with the H-related lines in as grown LEC material should be welcome.

ACKNOWLEDGMENTS

Part of the original work described here has been performed in co-operation with J. Chevallier and his group at CNRS-Bellevue, with R. Azoulay, B. Rose B. Descouts and M. Gauneau from CNET and Laboratoire OMC from University Paris 6. I wish to thank B. Clerjaud for stimulating discussions and M. Stavola for letting me use material published or to be published for this review. The help of C.Y. Song, visiting scientist from the Beijing Institute of Semiconductors is gratefully acknowledged.

REFERENCES

1. J. I. Pankove, P. J. Zanzucchi, C. W. Magee and G. Lucovsky, *Appl. Phys. Lett.* **46**, 421 (1985).
2. J. Lagowski, M. Kaminska, J. M. Parsey, Jr., H. C. Gatos and M. Lichtensteiger, *Appl. Phys. Lett.* **41**, 1078 (1982).
3. R. M. Chrenko, R. S. McDonald and E. M. Pell, *Phys. Rev.* **138**, A1775 (1965).
4. S. J. Pearton, J. W. Corbett and T. S. Shi, *Appl. Phys.* **A43**, 153 (1987).
5. R. C. Newman and J. Woodhead, *Radiation effects* **53**, 41 (1980).
6. B. Clerjaud, D. Côte and C. Naud, *Phys. Rev. Lett.* **58**, 1755 (1987).
7. S. J. Pearton, W. C. Dautremont-Smith, J. Chevallier, C. W. Tu and K. D. Cummings, *J. Appl. Phys.* **59**, 2821 (1986).
8. A. Jalil, J. Chevallier, J. C. Pesant, R. Mostefaoui, B. Pajot, P. Murawala and R. Azoulay, *Appl. Phys. Lett.* **50**, 439 (1987).
9. B. Pajot, R. C. Newman, R. Murray, A. Jalil, J. Chevallier and R. Azoulay, *Phys. Rev. B* **37**, 4188 (1988).
10. Z. P. Wang, L. Ley and M. Cardona, *Phys. Rev. B* **26**, 3249 (1982).
11. G. Ascheron, C. Bauer, H. Sobotta and V. Riede, *Phys. Stat. Sol. (a)* **89**, 549 (1985).
12. J. Tatarkiewicz, A. Krol, A. Breitschwerdt and M. Cardona, *Phys. Stat. Sol. (b)* **140**, 369 (1987).
13. J. Tatarkiewicz, B. Clerjaud, D. Côte, F. Gendron and A. M. Hennel, *Appl. Phys. Lett.* **53**, 382 (1988).
14. B. Pajot, J. Chevallier, J. Chaumont and R. Azoulay, *Mat. Res. Symp. Proc.* **104**, 345 (1988).
15. Ph. Roduit, B. Pajot, C. H. Song, unpublished.
16. B. Clerjaud, D. Côte, M. Krause and C. Naud, *Mat. Res. Symp. Proc.* **104**, 341 (1988).
17. B. Pajot, J. Chevallier, A. Jalil and B. Rose, *Semicond. Sci. Technol.* **4**, 91 (1989).
18. J. Chevallier, B. Clerjaud and B. Pajot, in *Hydrogen in Semiconductors*, edited by J. I. Pankove and N. M. Johnson (Academic Press, San Diego) to be published.

19. S. M. Shin, H. K. Chung, C. H. Chen and K. Tan, *J. Appl. Phys.* **62**, 1729 (1987).
20. T. R. Hayes, W. C. Dautremont-Smith, H. S. Luftman and J. W. Lee, *Appl. Phys. Lett.* **55**, 56 (1989).
21. G. R. Antell, A. T. R. Briggs, B. R. Butler, S. A. Kitching, J. P. Stagg, A. Chew and D. E. Sykes, *Appl. Phys. Lett.* **53**, 758 (1988).
22. A. Bossachi, S. Franchi, E. Gombia, R. Mosca, P. Allegri, V. Avanzini and C. Ghezzi, *Mat. Sci. Forum* **38-41**, 1027 (1989).
23. A. Jalil, Doctoral dissertation, Paris, 1987, unpublished.
24. J. Chevallier, B. Pajot, A. Jalil, R. Mostefaoui, R. Rahbi and M. C. Boissy, *Mat. Res. Symp. Proc.* **104**, 337 (1988).
25. P. S. Nandhra, R. C. Newman, R. Murray, B. Pajot, J. Chevallier, R. B. Beall, and J. J. Harris, *Semicond. Sci. Technol.* **3**, 356 (1988).
26. K. Bergman, M. Stavola, S. J. Pearton, J. Lopata, T. Hayes and H. G. Grimmeiss, *Mat. Sci. Forum* **38-41**, 1015 (1989).
27. C. Herrero and M. Stutzmann, *Phys. Rev. B* **38**, 12668 (1988).
28. B. Bech Nielsen, J. U. Anderson and S. J. Pearton, *Phys. Rev. Lett.* **60**, 321 (1988).
29. Th. Wichert, H. Skudlik, M. Deicher, G. Gröbel, R. Keller, E. Recknagel and L. Song, *Phys. Rev. Lett.* **59**, 2087 (1987).
30. A. A. Kaplyanskii, *Optics and Spectroscopy* **16**, 329 and 557 (1964).
31. P. Briddon and R. Jones, *Inst. Phys. Conf. Ser. No 95*, 459 (1989).
32. B. Pajot, *Inst. Phys. Conf. Ser. No 95*, 437 (1989).
33. D. M. Kozuch, M. Stavola, S. J. Pearton, C. R. Abernathy and J. Lopata, this volume.
34. N. M. Johnson, R. D. Burnham, R. A. Street and R. L. Thornton, *Phys. Rev. B* **33**, 1102 (1986).
35. B. Pajot, A. Jalil, J. Chevallier and R. Azoulay, *Semicond. Sci. Technol.* **2**, 305 (1987).
36. M. Stavola, S. J. Pearton, J. Lopata, C. R. Abernathy and K. Bergman, *Phys. Rev. B* **39**, 8051 (1989).
37. B. Clerjaud, private communication.
38. B. Clerjaud, M. Krause, C. Porte and W. Ulrici, *Proc. 19th ICPS, Warsaw 15-19 Aug. 89*, edited by W. Zawadzki, *Inst. Phys. Polish Acad. Sci.*, 1989, p. 1175.
39. J. C. Nabity, M. Stavola, J. Lopata, W. C. Dautremont-Smith, W. C. Tu and S. J. Pearton, *Appl. Phys. Lett.* **50**, 921 (1987).
40. M. Glade, D. Grützmacher, R. Meyer, E. G. Woelk and P. Balk, *Appl. Phys. Lett.* **54**, 2411 (1989).
41. B. Theys, B. Pajot, B. Rose, A. Jalil and J. Chevallier, to be published.
42. R. A. Morrow, *J. Appl. Phys.* **66**, 2973 (1989).
43. G. S. Jackson, D. C. Hall, L. J. Guido, W. E. Plano, N. Pan, N. Holonyak, Jr. and G. E. Stillman, *Appl. Phys. Lett.* **52**, 691 (1988).
44. C. Kazmierski, B. Theys, B. Rose, A. Mircea, A. Jalil and J. Chevallier, *Electron. Lett.* **25**, 1433 (1989).
45. E. Constant, N. Caglio, J. Chevallier and J. C. Pesant, *Electron. Lett.* **23**, 841 (1987).
46. J. M. Zavada, H. A. Jenkinson, R. G. Sarkis and R. G. Wilson, *J. Appl. Lett.* **58**, 3731 (1985).
47. M. Stavola, S. J. Pearton, J. Lopata and W. C. Dautremont-Smith, *Phys. Rev.* **37**, 8313 (1988).

Sn-H COMPLEX IN HYDROGEN PASSIVATED GaAs

D. M. KOZUCH*, MICHAEL STAVOLA*, S. J. PEARTON**, C. R. ABERNATHY**,
AND J. LOPATA**

*Department of Physics and Sherman Fairchild Center, Lehigh University,
Bethlehem, Pennsylvania 18015

**AT&T Bell Laboratories, Murray Hill, New Jersey 07974

ABSTRACT

It is confirmed that Sn donors in GaAs are passivated by exposure to a hydrogen plasma. The Sn-H complexes give rise to vibrational absorption bands at 1327.8 cm^{-1} and 967.7 cm^{-1} that are assigned to H-stretching and H-wagging modes respectively. A study of the thermal stability of the Sn-H complexes shows that they dissociate for annealing temperatures above $\sim 150^\circ\text{C}$. The properties of the Sn-H complexes are compared to those of other donor-H complexes. Our results suggest a configuration for the complex with H at the antibonding site adjacent to the Sn.

Introduction

Recently, there have been discovered several defect complexes in semiconductors that include a substitutional dopant and a nearby hydrogen atom [1-3]. In such complexes the attached hydrogen eliminates or modifies the electrical activity of the dopant. Here we report the results of an infrared (IR) absorption study of hydrogen passivated Sn donors in GaAs. Our results for the vibrational characteristics and thermal stability are compared to the well studied complexes with H near group V donors in Si [4-10] and the Si₆₅ donor in GaAs [11,12].

There are several examples of acceptor-H complexes in Ge, Si, GaAs, and InP [1-3] that appear to have similar structures (i.e. with the H at the bond centered site between the acceptor and one of its nearest neighbors) and similar properties although there are some fascinating exceptions [13]. For the donor impurities in semiconductors, there are fewer examples of donor-H complexes. Further, the structures of the donor-H complexes in the Si and GaAs hosts appear to be different. (H has not been observed to interact with donors in InP at all [14,15].)

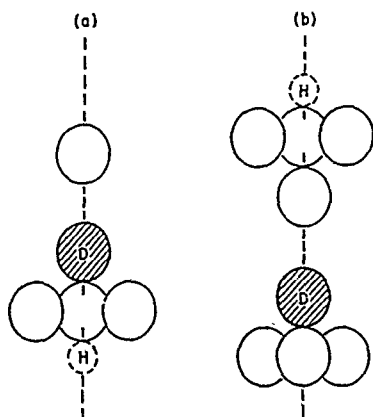


FIG. 1. Schematic diagrams of donor-H complexes with the H at (a) the antibonding site adjacent to the donor (labeled D) and (b) the antibonding site adjacent to the donor's nearest neighbor.

The only IR absorption study of a hydrogen passivated donor in GaAs until now has been for the Si_{Ga} donor [11]. In this case, H stretching and wagging vibrations as well as the vibrations of the Si in the complex have been studied. Further, features in the H-stretching spectrum associated with H attached to ^{28}Si , ^{29}Si , and ^{30}Si were identified. These results [11], with the support of theory [12], provide a convincing picture of the $\text{Si}_{\text{Ga}}\text{-H}$ complex in which H is attached directly to the Si_{Ga} donor and lies along the [111] axis in an antibonding direction (Fig. 1a). For other donors in GaAs, the different reports in the literature disagree about whether Sn_{Ga} donors can be passivated by hydrogen at all [15,16]. Vibrational bands have not been reported for complexes of H with the group VI donors (on the As sublattice). This study confirms the passivation of Sn by H and provides IR data for another donor-H complex in GaAs.

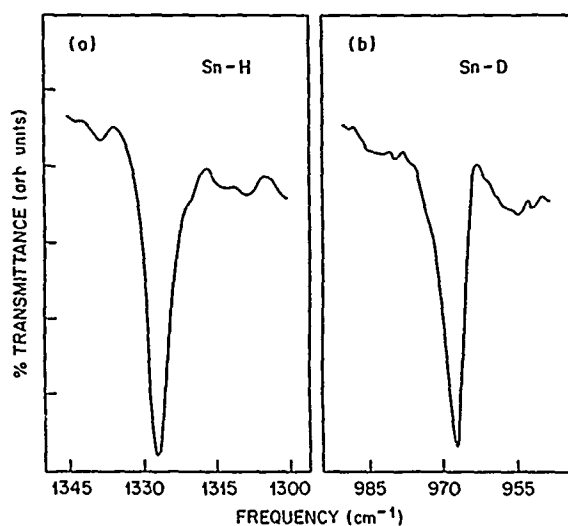


FIG. 2. Transmittance spectra of the (a) H-stretching and (b) D-stretching modes of the Sn-H and Sn-D complexes in GaAs.

Experimental Results

The samples for our experiments were Sn-doped epitaxial layers grown by molecular beam epitaxy on semiinsulating GaAs substrates. One set of samples had $N_{\text{D}} - N_{\text{A}} = 1.1 \times 10^{19} \text{ cm}^{-3}$ with an n⁺-layer thickness of $2.2 \mu\text{m}$. A second set of samples had $N_{\text{D}} - N_{\text{A}} = 1.0 \times 10^{19} \text{ cm}^{-3}$ and an epilayer thickness of $0.3 \mu\text{m}$. The samples were exposed to an H_2 (or D_2) plasma in a Technics Planar Etch II parallel plate reactor for 2 hrs. at 150°C . The IR absorption was measured with a Nicolet 60 SX Fourier transform spectrometer equipped with a broad band HgCdTe detector. Spectra were measured with 2 cm^{-1} resolution. Samples were cooled to near liquid He temperature by mounting them on the cold finger of an Air Products Helitran dewar. Annealing experiments were performed in a rapid thermal annealing furnace.

The H-stretching spectra of the Sn-H and Sn-D complexes are shown in Figs. 2a and 2b. The H-wagging band of the Sn-H complex is shown in Fig. 3. A table of the frequencies of these bands as well as the bands for $\text{GaAs}:\text{Si}_{\text{Ga}}\text{-H}$ (or D) are given in Table I for comparison. No D-wagging mode is reported for the Sn-D complex. An estimate of the Sn-D wagging frequency from the position of the Sn-H wagging band shows that the D-wagging band should appear near 530 cm^{-1} and would be obscured by strong, intrinsic GaAs absorption.

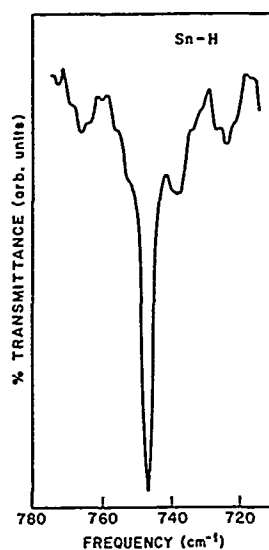


FIG. 3. Transmittance spectrum of the H-wagging mode of the Sn-H complex in GaAs.

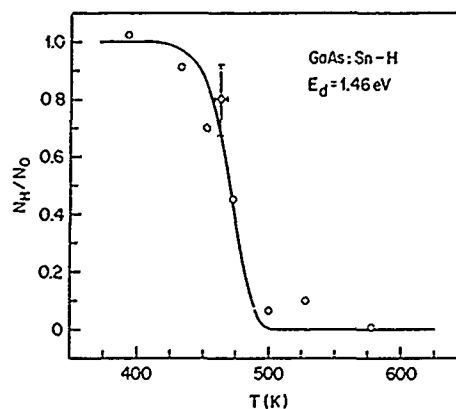


FIG. 4. Isochronal (5 min.) annealing data for the Sn-H complex. The solid line corresponds to Eq. (1) with $E_d = 1.46$ eV and $\nu = 10^{13}$ s $^{-1}$.

TABLE I. Characteristics of donor-H complexes in GaAs.

	H ₂ plasma		D ₂ plasma		E_d (eV)
	frequency (cm $^{-1}$)	relative strength	frequency (cm $^{-1}$)	relative strength	
GaAs: ²⁸ Si (a)	1717.3	1	1247.6	1	2.1 ^(b)
	896.8	2.9	641.5	3	
GaAs:Sn	1327.8	1	967.7	1	1.46
	746.6	2.1	-----	-	

(a) Pajot et al., ref. 11

(b) Pearton et al. ref. 16

It was confirmed that these new vibrational bands are due to H passivated Sn by making Hall measurements (by the Van der Pauw method with HgIn alloyed contacts) and IR measurements on the same samples. The 0.3 μ m thick layers were used because the thinner layers could be more fully passivated for our plasma conditions than the thicker ones. Following plasma treatment, the new bands appear while the carrier density decreases and the Hall mobility increases. An annealing treatment which caused the vibrational bands to disappear also lead to partial recovery of the donor concentration. The residual donor loss following passivation and annealing is attributed to compensation that results from plasma damage in the thin layers; the carrier concentration could not be restored by further annealing at 400°C and was accompanied by a decrease in the Hall mobility as compared to the measurements made before H passivation. These electrical and optical measurements confirm that the new vibrational bands are well correlated to the donor passivation.

Data are shown in Fig. 4 for a series of isochronal anneals in which the intensity of the H-stretching band was monitored. The samples with $N_D - N_A = 1.1 \times 10^{19} \text{ cm}^{-3}$ and a layer thickness of $2.2 \mu\text{m}$ were used. The data have been fit by the expression [17],

$$N_H/N_0 = \exp[-t\nu \exp(-E_d/kT)]. \quad (1)$$

The ratio N_H/N_0 is the concentration of hydrogenated complexes following annealing normalized to the concentration measured before annealing. The solid line corresponds to a dissociation energy of $E_d = 1.46 \text{ eV}$ and an assumed attempt frequency of $\nu = 10^{13} \text{ s}^{-1}$.

It has been discovered recently by Johnson and Herring [18] for n-type Si that hydrogen is in the charge state H^- and that the H^- can hop from donor to donor before finding a sink or diffusing away in dissociation kinetics measurements. Effects such as these can lead to departures from first order dissociation kinetics [and our Eq. (1)], as is now well known for acceptor-H complexes in Si [19]. Similar considerations are likely to apply to donor-H complexes in GaAs also. Our E_d should be considered to be an upper limit until further experiments are completed. In spite of the uncertainty in the value of E_d , the Sn-H complexes are less stable than was reported previously [16] and explains why other groups have had difficulty passivating Sn.

Discussion

From our data it is difficult to arrive at a definitive structure for the Sn-H complex although a reasonable case can be made for the trigonal configuration shown in Fig. 1a with H attached directly to the Sn atom. (i) The wagging band has $\sim 2\times$ the intensity of the H-stretching band which is evidence for the wag being a doubly degenerate mode as would be expected for a complex with trigonal symmetry. (ii) The presence of a wagging mode is characteristic of configurations that are believed to have H in an antibonding configuration; complexes with H in a bond centered configuration in several dopant-H complexes show no wagging mode [20]. (iii) The H-stretching and wagging frequencies of the Sn-H complex are substantially less than those of the $\text{Si}_{\text{Ga}}\text{-H}$ complex [11] (Table I). This is probably because Sn is larger than Si thereby leading to a crowded configuration, and hence, weaker bonds to the H and smaller stretching force constants. The weaker bonding is also reflected in the lowered stability for Sn-H. (iv) The Sn-H and Sn-D stretching bands are surprisingly broad ($\sim 4 \text{ cm}^{-1}$). Other donor-H complexes in Si and GaAs give rise to narrower absorption lines [5,11]. Sn has 6 isotopes with natural abundances $> 5\%$. If the H is attached directly to Sn then the linewidth might be explained by the effect of the Sn isotopes on the H-stretching frequency.

It is interesting to compare the H-passivated donors in GaAs to those in Si. Superficially, the donor-H complexes with P, As, and Sb donors in the Si host [5] have vibrational characteristics similar to H complexes with Si_{Ga} [11] and Sn_{Ga} in GaAs (i.e. all have stretching modes at frequencies lower than is typically observed for the acceptor-H complexes and wagging modes in the $700\text{-}900 \text{ cm}^{-1}$ range). However, the vibrational frequencies for the H attached to the different group V donor species in Si are nearly identical whereas the frequencies for H attached to the group IV donors in GaAs are strongly donor dependent. This difference in the donor dependence of the vibrational frequencies reflects the different structures of the complexes. For the Si host it was argued that the H is attached to a neighboring Si atom rather than to the donor (Fig. 1b) because of the lack of donor dependence of the vibrations [5]. For the GaAs host the H is attached directly to the donor at least for Si_{Ga} [11] and probably for Sn also (Fig. 1a). Theoretical calculations support these structures for $\text{GaAs:Si}_{\text{Ga}}\text{-H}$ and Si:P-H although

There has been controversy about the sizes of the various relaxations for the donors in the P-H complex [6-10]. Our observation that the vibrational frequencies of the donor-H complexes in GaAs are strongly dependent on the group IV donor provides further experimental support for the earlier argument [5] against direct H attachment to donors in Si.

The calculations made by several groups for P-H in Si [7-10] provide a possible reason for why the donor-H configurations are different for Si and GaAs while the acceptor-H configurations are similar. For P-H it has been found that the configurations shown in Figs. 1a and 1b have similar total energies. Configuration 1b is favored by only a few tenths of an eV for P-H. (A configuration with H bond-centered is also close in total energy. DeLeo et al. [10] have tabulated recent theoretical results.) It is easy to imagine that in a different host the relative stabilities of the configurations that are close in total energy might be changed.

Conclusion

In conclusion, we have confirmed that the Sn donor in GaAs can be passivated by H₂ plasma exposure. The vibrational frequencies for H stretching and wagging modes for the Sn-H complex are much smaller (a few 100 cm⁻¹) than for GaAs:Si_{0.25}-H [11] in marked contrast to the different donor-H complexes in Si [5] which have nearly identical vibrational frequencies. This is because in GaAs the H is attached to the donor atom directly [11,12] while in Si the H is attached to one of the donor's nearest neighbors [4-10]. The stability of the Sn-H complex is substantially less than was previously reported [16], explaining why some groups have found Sn difficult to passivate [15].

References

1. S. J. Pearton, J. W. Corbett, and T. S. Shi, Appl. Phys. A **43**, 153 (1987).
2. Hydrogen in Semiconductors, edited by J. I. Pankove and N. M. Johnson (Academic Press, San Diego) to be published.
3. B. Pajot, this volume.
4. N. M. Johnson, C. Herring, and D. J. Chadi, Phys. Rev. Lett. **56**, 769 (1986).
5. K. Bergman, M. Stavola, S. J. Pearton, and J. Lopata, Phys. Rev. B **37**, 2770 (1988).
6. K. J. Chang and D. J. Chadi, Phys. Rev. Lett. **60**, 1422 (1988).
7. A. Amore-Bonapasta, A. Lapicciarella, N. Tamassini, and M. Capizzi, Defects in Semiconductors 15, edited by G. Ferenczi, (Trans Tech, Switzerland, 1989) p. 1051.
8. S. K. Estreicher, S. K. Throckmorton, D. S. Marynick, Phys. Rev. B **39**, 13241 (1989).
9. P. J. H. Denteneer, C. G. Van de Walle, S. T. Pantelides, Phys. Rev. B, to be published.
10. G. G. DeLeo, W. Beall Fowler, T. M. Sudol, and K. J. O'Brien, Phys. Rev. B, to be published.

11. B. Pajot, R. C. Newman, R. Murray, A. Jalil, J. Chevallier, and R. Azoulay, Phys. Rev. B37, 4188 (1988).
12. P. Briddon and R. Jones, in Shallow Impurities in Semiconductors 1988, edited by B. Monemar (Inst. of Phys., Bristol, 1989) p. 459.
13. K. Muro and A. J. Sievers, Phys. Rev. Lett. 57, 897 (1986).
14. W. C. Dautremont-Smith, J. Lopata, S. J. Pearton, L. A. Koszi, M. Stavola, and V. Swaminathan, J. Appl. Phys. 66, 1993 (1989).
15. J. Chevallier, B. Clerjaud, and B. Pajot, in Ref. 2.
16. S. J. Pearton, W. C. Dautremont-Smith, J. Chevallier, C. W. Tu, and K. D. Cummings, J. Appl. Phys. 59, 2821 (1986).
17. W. L. Hansen, E. E. Haller, and P. N. Luke, IEEE Trans. on Nuclear Science NS-29, 738 (1982).
18. N. M. Johnson, in the closing summary of the Workshop on Hydrogen Effects in InP and Related Compounds, Oct., 1989, Lannion, France.
19. T. Zundel and J. Weber, Phys. Rev. B; to be published.
20. This appears to be true for many of the dopant-H complexes studied. See M. Stavola and S. J. Pearton, in Ref. 2 and also the data in refs. 3 and 15.

REASSESSMENT OF ACCEPTOR PASSIVATION MODELS IN p-TYPE HYDROGENATED GaAs

I. SZAFRANEK AND G.E. STILLMAN

Center for Compound Semiconductor Microelectronics, Materials Research Laboratory and
Coordinated Science Laboratory, University of Illinois at Urbana-Champaign, IL 61801

ABSTRACT

The existing microscopic models of acceptor passivation in p-type hydrogenated GaAs are reviewed in light of new experimental results concerning the relative thermodynamic stability of the passivating complexes. In particular, the present model for neutralization of Group II acceptors, Be, Mg and Zn, on Ga sites is shown to be inadequate to account for the observed trends, which imply existence of a strong interaction between the hydrogen and acceptor. It is proposed that a direct acceptor-hydrogen bond is formed due to attractive Coulomb interaction between the ionized species. The relative stability of the pair complex can be then explained based on electronegativity of the acceptor species. Passivation at intermediate pair separations up to about twice the Bohr radius of the nearest acceptor, is also discussed.

INTRODUCTION

It is a well established fact that the electrical and optical activity of shallow substitutional acceptors in p-type GaAs can be neutralized by exposure to hydrogen plasma.^{1,2} By analogy with silicon it is assumed that interstitial hydrogen atoms form a deep donor level in GaAs.² Thus, in p-type material, in the extrinsic temperature regime compensation takes place, and this effect is sufficient to explain the observed reduction in carrier concentration upon hydrogenation. However, in order to account for phenomena such as mobility enhancement³ or changes in photoluminescence (PL)⁴ and infrared local vibrational mode (IR LVM)⁵⁻⁸ spectra after hydrogenation, the concept of passivation is used to imply formation of neutral acceptor-hydrogen complexes (Acc-H).⁹ In GaAs two types of acceptors are distinguished: Group II elements Be, Mg, Zn and Cd on Ga sites, and Group IV elements C, Si and Ge on As sites. Accordingly, models have been proposed for the two possible passivating configurations.^{1,7} The underlying mechanism, invariant with the acceptor type, is assumed to be Coulomb-field enhanced diffusion of protons toward the ionized acceptor sites.

Any proposal for the microscopic structure of the passivating complexes should be consistent with the experimentally established relative extent and thermodynamic stability of passivation of different acceptor species. However, no such data has been available so far. Recently, we have reported the first results on this aspect of hydrogenation,¹⁰ based on PL investigation of passivation efficiency and susceptibility to light-induced reactivation (LIR)⁴ of different acceptors in high-purity p-type GaAs. The observed stability trends do not fully comply with predictions of the existing model for passivation of Group [II]Ga acceptors.¹ In this paper the experimental results are reviewed and the discrepancies with the model predictions analyzed. A modified passivation mechanism is then proposed, which is in general agreement with our measurements and is inherently compatible with the athermal, electronically stimulated acceptor reactivation effect previously reported.⁴ Although PL does not provide a direct structural information, it allows for characterization of very high-purity materials (10^{13} - 10^{15} cm⁻³) compared to other techniques (SIMS, IR, Raman). We shall demonstrate that impurity concentration is an important factor to be considered, because it may affect the passivation process itself.

EXPERIMENTAL

Experimental procedures of hydrogenation, LIR and PL characterization are similar to those described in Ref. 4. High-purity epitaxial GaAs layers grown by molecular beam epitaxy (MBE), metal-organic chemical vapor deposition (MOCVD) and AsH₃-vapor phase epitaxy (VPE) were analyzed. They were either intentionally doped or nominally undoped, with total impurity concentrations of the order of 10^{14} - 10^{15} cm⁻³.

RESULTS

Two independent experiments were performed to investigate Acc-H complexes. Detailed results will be reported elsewhere.¹¹ Here only a brief summary is presented.

First, the effects of passivation were studied by PL on freshly hydrogenated samples. Very low excitation levels were employed in order to minimize possible modifications of the spectra due to exposure to light.⁴ The extent of neutralization of different acceptors present in the analyzed layers was then established by comparing intensities of PL peaks induced by these acceptors in the as-grown and the hydrogenated samples. It is assumed that the extent of passivation of various acceptors is directly related to the binding energies of the corresponding Acc-H complexes. A typical example is shown in Fig. 1, where the passivation efficiency of Zn_{Ga} and C_{As} acceptors is compared. The various peaks are due to recombination of free and donor-bound electrons, $(e-A^0)$ and (D^0-A^0) , respectively, with Zn and C neutral acceptor species.¹² In the as grown epitaxial layer C_{As} was the dominant residual impurity, rendering the sample p-type. A shoulder due to $\text{Zn}(D^0-A^0)$ peak is discernible. After hydrogenation the relative intensities of these two transitions changed, indicating increased concentration of optically active Zn acceptors compared to C, that was more extensively passivated.

It is interesting to note that a similar behavior has been also observed in residually *n*-type GaAs layers, even under hydrogenation conditions which are known to be ineffective for passivation of donors. The implication of this is that neither large concentrations of free holes nor the mobile proton species, presumably present in p-type material, are instrumental in the passivation mechanism. This observation contradicts a recent conclusion by Pajot⁸ that compensated impurities should not be passivated. Our result suggests that in high purity materials, where the mean inter-impurity distance is much greater than the Bohr radii of the impurities, the mobile H atoms become the preferred compensating donor species of shallow acceptors that they encounter via field-enhanced diffusion in p-type, or random walk in n-type semiconductors. The electrostatic interaction between an ionized acceptor and H atom reduces the binding energy of the latter,¹³ thus increasing its ionization probability and inducing subsequent neutralization of the nearest acceptor in a way similar to that discussed later for p-type materials. The conclusion of Pajot⁸ mentioned above may be valid for heavily doped samples (10^{18} - 10^{19} cm^{-3}), where the Fermi energy is always much higher than whatever the H donor energy level may be, there are no isolated dopants, and the screening effects may significantly affect the passivation mechanism.

In another experiment the relative susceptibility of different passivated acceptor species to LIR has been monitored with PL.⁴ It is assumed that both the rate and the extent of the LIR process are inversely related to the dissociation energy of various passivating complexes. In the case of the sample discussed previously (Fig. 1) no changes in the PL spectra could be detected after 30 min. illumination with 360 mW/cm^2 power density of above bandgap radiation from argon ion laser, and therefore it may be concluded that neither C_{As} nor Zn_{Ga} are reactivated under these excitation conditions.

A different case is demonstrated in Fig. 2. A new piece of the Si-doped p-type GaAs sample described in Ref. 4 was hydrogenated and carefully analyzed. The PL spectra of the as-grown and the freshly hydrogenated material are shown in the upper part of Fig. 2, while the bottom spectrum is of the hydrogenated sample after 60 min. of illumination with 4 mW/cm^2 argon laser light. The most prominent feature of this spectrum is the appearance of the peak at

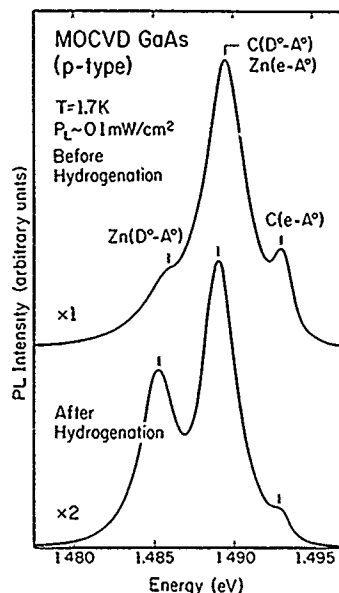


FIG. 1: PL assessment of relative passivation efficiency of Zn_{Ga} and C_{As} acceptors in high-purity hydrogenated GaAs.

1.49061 eV, labeled $\text{Mg}(\text{e-A}^0)$. In the original, unhydrogenated material this peak was not detected; the energetically nearest transition is at 1.49146 eV and it is identified as a conduction band-to-Be acceptor recombination $\text{Be}(\text{e-A}^0)$ and, possibly, also $\text{Mg}(\text{e-A}^0)$ because it is usually difficult to mutually resolve these two transitions in GaAs.^{4,12} In the PL spectrum taken after LIR, the peak at 1.49146 eV is discernible as a shoulder on the high energy side of the 1.49061 eV transition, which grew to be more intense. Based on the temperature and excitation intensity dependence of these two transitions, as well as on the excellent agreement of their positions with those determined by Ashen *et al.*¹² it can be inferred that the peak at 1.49146 eV represents $\text{Be}(\text{e-A}^0)$ recombination, whereas the lower energy, LIR-generated transition at 1.49061 eV corresponds to $\text{Mg}(\text{e-A}^0)$. It follows that Mg_{Ga} acceptors, present in this sample in a trace amount, are weakly neutralized by the hydrogenation process, and they undergo much more extensive LIR than other acceptor impurities also shown in Fig. 2, namely Be_{Ga} , Si_{As} , C_{As} and Ge_{As} . The LIR of Si_{As} has been discussed in Ref. 4.

Based on the experiments described above and combining all the available data, the following general trend in the passivation efficiency and the stability of hydrogen-acceptor complexes as a function of the acceptor's chemical identity has been found:



DISCUSSION

The currently accepted bonding configurations of the hydrogen-acceptor passivating complexes in p-type GaAs^{1,7} are schematically represented in Fig. 3. In the case of the Group II acceptors on Ga sites it has been proposed¹ that the hydrogen atom occupies a bond centered position along $\langle 111 \rangle$ crystallographic direction, and forms a strong covalent bond with one of the As atoms adjacent to a Group II acceptor, thus terminating the dangling bond on As. In this process the acceptor-As bond is broken, followed by the acceptor relaxation to a threefold coordinated configuration of covalent bonds with the remaining As atoms.^{5,6,8} In the case of the Group IV acceptors on As sites, it has been proposed⁷ that the H atom binds directly with the acceptor atom, leaving one of the nearest neighbour Ga atoms tri-coordinated.

The major deficiency of these models is their inability to correctly account for the following aspects of passivation and reactivation, that were discussed above:

1. The efficiency and stability of passivation of Group [II]_{Ga} acceptors is expected to be only weakly dependent on the chemical identity of the acceptor species. In contrast, we have observed a large variation, with Mg forming very unstable complex compared to Be and Zn. An equivalent result has been reported recently by Singh and Weber,¹⁴ who observed extremely weak neutralization of Mg_{Ga} relative to Zn_{Ga} and Cd_{Ga} in GaP.

2. Since the two configurations in Fig. 3 imply formation of a covalent bond with the passivating hydrogen atom, one might expect existence of a direct correspondence between the dissociation energy of the complex and the bond strength of the similar isolated diatomic bond. Such relationship was found to be obeyed in a simple linear form for the passivating donor-

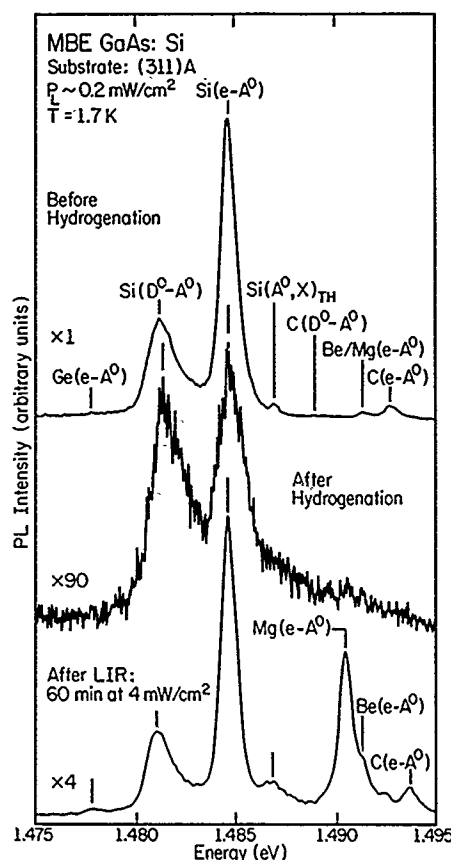


FIG. 2: PL assessment of passivation and light-induced reactivation of Mg_{Ga} , Be_{Ga} and Si_{As} acceptors in hydrogenated GaAs.

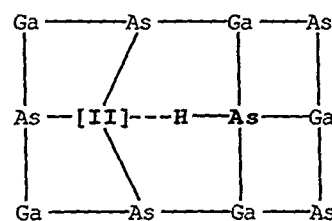
hydrogen complexes in GaAs.¹⁵ If this trend was assumed to exist also for shallow acceptors, one would be led to the wrong prediction that the As-H bond in Fig. 3-a should be more stable than any other acceptor-H or host atom-H bonds possible, including the C_{As} -H complex in Fig. 3-b.¹⁶ Contradictory to this, we have established that C_{As} is by far the most extensively passivated shallow substitutional acceptor, whereas Mg_{Ga} is both less efficiently neutralized and more prone to be light-reactivated than any Group [IV]_{As} impurity.

Dautremont-Smith¹⁷ predicted that the thermal stability of passivation should be greater for Group [IV]_{As} acceptors than for Group [II]_{Ga}. Again, our results show a different trend, because Zn does not undergo LIR under illumination conditions that stimulate a partial reactivation of Si and Ge in a fraction of a second. Although no direct comparison of the hydrogenation efficiency of Zn with Si or Ge is available, the LIR studies indicate a more stable passivation of Zn relative to both Si and Ge.

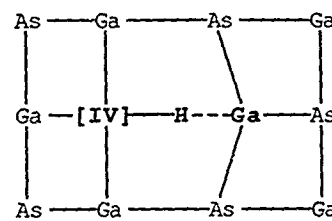
The most obvious conclusion from the discussion above is that the substitution of different Group II acceptor species on Ga sites in the configuration shown in Fig. 3-a causes very significant variations in the physical and chemical properties of the resulting hydrogenated complexes. This conclusion is supported by the IR LVM data, which show that the shift in the stretching mode frequency of the postulated As-H bond for Zn vs. Be-decorated acceptor site in Fig. 3-a is larger than between any of these two cases and the Si_{As} -H bond in Fig. 3-b.⁵⁻⁸ To account for these facts, a strong interaction between hydrogen and acceptor species must be, in general, assumed, even though the IR LVM data suggest that there is no strong bond between Be and H in the specific case of hydrogenated GaAs:Be.⁶ However, no such definitive work as yet exists for other Group [II] acceptors, and a simple extrapolation may be not valid in view of a large size difference between those elements and Be. The only other reported IR LVM study on hydrogenated GaAs:[II]_{Ga} systems is for [II]=Zn.⁵ Although the conclusions were similar to those for Be, it has been pointed out⁶ that these measurements are not as reliable, because the masses of Zn and the host lattice atoms in GaAs are practically indistinguishable.

To improve the agreement with the experimentally found strongly acceptor-dependent passivation trends, as well as to account for other observations, including the occurrence of the LIR effect itself, we propose a modified model for acceptor passivation in GaAs. Considering again the hydrogen atom to be a deep donor, the electrical neutralization of acceptors in p-type materials is simply a result of compensation, which also leads to field-assisted diffusion of protons toward the ionized acceptor sites. The compensation becomes effectively passivation for $Acc-H^+$ pair separations, R , smaller than about twice the Bohr radius of an acceptor, a_A .¹³ Since for shallow substitutional impurities in GaAs a_A may be assumed to be much greater than the Bohr radius of the deeper H donor, it follows that when $R < \sim 2a_A$ holes cannot be independently trapped to neutralize the hydrogen-passivated acceptors.¹³ Only if the ionization energy of the H donor is greater than the proton-ionized acceptor Coulomb interaction at a specific $R < \sim 2a_A$, can a free electron be captured first, followed by a hole binding to the acceptor. In addition, an exciton or an electron and a hole (simultaneously) can be trapped at the $Acc-H$ complex, although the probability for these multi-particle events is much lower at low temperature, doping, injection or excitation levels,¹³ and therefore the acceptor becomes passivated.

A proton presumably occupies an interstitial site when it is more than the nearest neighbor distance away from an acceptor atom. In the immediate vicinity of an acceptor the proton will occupy any energetically favorable position at the defect site. From the IR LVM spectroscopy it has been inferred that for Be_{Ga} -H complex this should be a bond-centered position.⁶ It can be



(a)



(b)

FIG. 3: Schematic representation of the currently accepted passivation models in p-type hydrogenated GaAs: (a)- passivation of Group [II]_{Ga} and (b)- of Group [IV]_{As} acceptors.

speculated that the relaxation of the much larger Mg and Zn atoms from the tetrahedral site should be less feasible and therefore a distortion of H from the $\langle 111 \rangle$ bond axis may occur. Also, as asserted above, a strong interaction between H and an acceptor must be considered. One possibility is a tri-center bond $[\text{III}]_{\text{Ga}}\text{-H-As}$ suggested by the dashed line in Fig. 3-a, and by symmetry, also in the configuration (b). In this context it is instructive to invoke the analogy with the classic system of hydrogenated c-Si:B. It is now clear that the original form of the passivation model,⁹ which also inspired the presently accepted Acc-H configuration in p-type GaAs,¹ is inaccurate and H binds to both the host Si and to the B acceptor atoms.¹⁸ Furthermore, it has been theoretically predicted¹⁹ and experimentally confirmed²⁰ that the H atom can easily redistribute among $\langle 111 \rangle$ axes around B, which would be difficult to understand if the H atom were energetically confined to the bond-centered position and strongly bound to the Si atom. Similarly, a rapid reorientation of the Acc-H bond can be envisioned in GaAs, provided that a strong interaction exists between hydrogen and acceptor, as proposed in our model. This motion could possibly explain the observed larger line width of the stretching mode absorption band in hydrogenated relative to deuterated p-type GaAs.^{5,6,8}

Thus, we propose that for both the Group $[\text{III}]_{\text{Ga}}$ and the Group $[\text{IV}]_{\text{As}}$ acceptors there is a direct, strong Acc-H interaction, which is ionic in nature and therefore its strength is expected to be dependent on the electronegativity of the acceptor species. Since the nearest neighbour atoms, Ga for $[\text{IV}]_{\text{As}}$ and As for $[\text{III}]_{\text{Ga}}$ acceptors, affect the electronic charge distribution at the acceptor, we consider these two configurations separately. Using Pauling's electronegativity values²¹ a general trend of the passivation effectiveness and stability for the most abundant acceptor impurities in p-type GaAs can be predicted as follows:

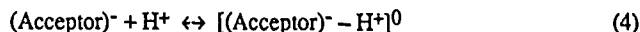
$$\text{Group II on Ga sites: } \text{Mg} < \text{Be} \leq \text{Zn} \quad (2)$$

$$\text{Group IV on As sites: } \text{Si} \leq \text{Ge} < \text{C} \quad (3)$$

Comparison with Eq. (1) indicates consistency within each group of acceptors. Clearly, more direct and quantitative experimental data concerning the thermal stability of passivation are necessary in order to further refine this or any other model of acceptor passivation in GaAs.

An important attribute of the modified binding model is its inherent ability to account for the LIR phenomenon. We have proposed that the LIR process is brought about by a recombination-enhanced mechanism of nonradiative capture of an electron or hole or both at a deep defect center.^{4,22} In the existing model there is no simple provision for such an effect, because passivation is interpreted as a removal of states from the forbidden gap via rearrangement of the defect structure and formation of stable bonds.²³ In the model proposed here the pairs form neutral complexes, but those can still induce dipolar scattering giving rise to mobility increase. The constraint on formation of neutral acceptors renders them inefficient as radiative recombination centers, thus explaining the decay of acceptor-related luminescence after hydrogenation. However, the pairs continue to act as electron and hole traps or as exciton binding center.¹³ In all these cases an energy equal to about material's bandgap may be locally deposited at the defect sites via multiphonon recombination and Auger processes, stimulating the observed athermal reactivation.⁴

In our model passivation results from the reaction:



Any reactivation process, LIR included, is basically the reverse of the reaction (4). Since the stability of the complex is reduced by capture of carriers, carrier concentration should have a dominant effect on the reactivation rate. In this context even the reported recovery of electrical activity of acceptors upon high temperature treatment at 300-500 °C^{2,23} can be regarded, to some extent, as a recombination-enhanced process. Although the high thermal energy heats the lattice, providing for the simple, phonon-generated bond dissociation and hydrogen diffusion, the large intrinsic concentration of electron-hole pairs pushes the reaction (4) to the left via recombination-assisted weakening of the Acc-H complex. The observed trend of increasing passivation stability of acceptors with bandgap for Ge, Si and GaAs²³ supports the above argument, assuming that the passivation mechanism is similar in these materials.

CONCLUSIONS

The first experimental results of relative passivation efficiency and stability for different substitutional shallow acceptors in GaAs have been presented. Major discrepancies have been found between these data and the predictions of the currently accepted model for passivation of Group III_{Ga} acceptors. A modified passivation mechanism has been proposed, based on compensation followed by a close pairing of ionized acceptors and protons according to the overall reaction in Eq. (4). Passivation is effective for pair separations as large as about twice the Bohr radius of the acceptor. We also propose that when a proton diffuses to the immediate vicinity of an acceptor, a direct bond between the two is formed due to the ionic interaction. The strength of this interaction may be qualitatively estimated, based on Pauling's electronegativity values for the different acceptors species. This structure of the passivating complex can account for a variety of effects related to hydrogenation and reactivation of acceptor impurities in GaAs.

Technical assistance of M.C. Day, R. MacFarlane and R.T. Gladin in preparation of this manuscript is appreciated. This work was supported by the Joint Services Electronics Program, under contract N00015-84-C-0149, by the National Science Foundation, under grants DMR 86-12860 and CDR 85-22666 and by SDIO/IST under contract No. DAAL 03-89-K-0080 administered by the Army Research Office.

REFERENCES

1. N.M. Johnson, R.D. Burnham, R.A. Street and R.L. Thornton, *Phys. Rev.* **B33**, 1102 (1986).
2. S.J. Pearton, W.C. Dautremont-Smith, J. Lopata, C.W. Tu and C.R. Abernathy, *Phys. Rev.* **B36**, 4260 (1987).
3. A. Jalil, J. Chevallier, R. Azoulay and A. Mircea, *J. Appl. Phys.* **59**, 3774 (1986).
4. I. Szafrank, S.S. Bose and G.E. Stillman, *Appl. Phys. Lett.* **55**, 1205 (1989).
5. B. Pajot, A. Jalil, J. Chevallier and R. Azoulay, *Semicond. Sci. Technol.* **2**, 305 (1987).
6. P.S. Nandhra, R.C. Newman, R. Murray, B. Pajot, J. Chevallier, R.B. Beall and J.J. Harris, *Semicond. Sci. Technol.* **3**, 356 (1988).
7. J. Chevallier, B. Pajot, A. Jalil, R. Mostefaoui, R. Rahbi and M.C. Boissy, *Mater. Res. Soc. Symp. Proc.*, **104**, 337 (1988).
8. B. Pajot, in *Proc. Int. Conf. Shallow Impurities in Semiconductors*, Linköping, Sweden, 1988, edited by B. Monemar (Inst. Phys. Conf. Ser. **95**, Bristol, UK, 1989), p. 437.
9. J.I. Pankove, P.J. Zanzucchi, C.W. Magee and G. Lucovski, *Appl. Phys. Lett.* **46**, 421 (1985).
10. I. Szafrank, S.S. Bose and G.E. Stillman, presented at 1989 Electron. Mater. Conf., Cambridge, MA (unpublished).
11. I. Szafrank and G.E. Stillman, (unpublished).
12. D.J. Ashen, P.J. Dean, D.T.J. Hurle, J.B. Mullin, A.M. White and P.D. Greene, *J. Phys. Chem. Solids*, **36**, 1041 (1975).
13. J.J. Hopfield, in *Physics of Semiconductors* (Proc. 7th Int. Conf., Dunod, Paris and Academic Press, New York, 1964), p. 725.
14. M. Singh and J. Weber, *Appl. Phys. Lett.* **54**, 424 (1989).
15. S.J. Pearton, W.C. Dautremont-Smith, J. Chevallier, C.W. Tu and K.D. Cummings, *J. Appl. Phys.* **59**, 2821 (1986).
16. K.P. Huber and G. Herzberg, *Molecular Spectra and Molecular Structure: IV: Constants of Diatomic Molecules* (Van Nostrand Reinhold, New York, 1979).
17. W.C. Dautremont-Smith, *Mat. Res. Soc. Symp. Proc.* **104**, 313, (1988).
18. E.E. Haller, in *Proc. Int. Conf. Shallow Impurities in Semiconductors*, Linköping, Sweden, 1988, edited by B. Monemar (Inst. Phys. Conf. Ser. **95**, Bristol, UK, 1989), p. 425.
19. C.G. Van de Walle, P.J.H. Denteneer, Y. Bar-Yam and S.T. Pantelides, *ibid.*, p. 405.
20. M. Stavola, K. Bergman, S.J. Pearton, J. Lopata and T. Hayes, *ibid.*, p.447.
21. *Encyclopedia of Science and Technology*, 6th ed. (McGraw-Hill, New York, 1987), vol. 6, p.211.
22. J.D. Weeks, J.C. Tully and L.C. Kimerling, *Phys. Rev.* **B12**, 3286 (1975).
23. S.J. Pearton, J.W. Corbett and T.S. Shi, *Appl. Phys.* **A43**, 153 (1987).

HYDROGEN PASSIVATION OF INTERFACIAL DEFECTS IN MOCVD GROWN GaAs/InP

V. SWAMINATHAN*, U. K. CHAKRABARTI**, W. S. HOBSON**, R. CARUSO**,
J. LOPATA**, AND S. J. PEARTON**

*AT&T Bell Laboratories, Solid State Technology Center, Breinigsville, PA 18103

**AT&T Bell Laboratories, Murray Hill, New Jersey 07974

ABSTRACT

The results of a low temperature (5K) photoluminescence study of hydrogenation of GaAs on InP grown by metal organic chemical vapor deposition are presented. An emission band at ~1.4 eV originating from the GaAs/InP interfacial region shows a 30 fold increase in intensity relative to the GaAs band edge emission after exposure to hydrogen plasma for 30 min at 250°C. This improvement in intensity is attributed to hydrogen passivation of defects at the heterointerface caused by the large (~4%) lattice mismatch between GaAs and InP. The passivation effect recovers on annealing the hydrogenated sample at 350°C. Excitation dependence of the ~1.4 eV band suggests that the interfacial region consists of a compositionally graded layer. Further, this band shifts to higher energy on annealing the sample in the temperature range 150-450°C with the hydrogenated sample exhibiting a larger shift than the untreated sample. It is suggested that the annealing induced peak shift arises due to intermixing of the compositionally graded interface and that the degree of intermixing is greater in the hydrogenated sample compared to the untreated sample.

INTRODUCTION

Recently there has been considerable interest in the GaAs on InP heteroepitaxial system.¹⁻¹⁰ This interest arises because of the potential application for opto-electronic integration of GaAs electronic devices with InP based photonic devices on the same wafer.⁶⁻⁸ A major deterrent for this application is the high density of defects caused by the large lattice mismatch (3.7%) between GaAs and InP. Cross-sectional transmission electron microscopic investigation has revealed a dislocation density of $\sim 10^{10}/\text{cm}^2$ near the heterointerface and of $8 \times 10^9/\text{cm}^2$ near the surface.⁹ Several schemes such as growth on misoriented substrates^{1,2} growing AlGaAs/GaAs multiple quantum well buffer layer³ or GaInAs/GaAs strained-layer superlattice⁴ prior to GaAs growth, have been adopted to reduce the dislocation density.

One method to mitigate the deleterious effect of defects in heteroepitaxial samples is to subject the samples to post-growth hydrogenation. It is well documented that atomic hydrogen passivates both shallow and deep energy levels in III-V semiconductors.¹¹⁻¹³ In addition, it has been shown in Si that hydrogen passivates dislocations, grain boundaries and Si/SiO₂ interfacial defects.¹¹ Pearton et al.¹⁴ have reported that in GaAs/Si diodes the reverse breakdown voltage increases significantly following hydrogenation and attributed the improvement to passivation by hydrogen of dangling bonds associated with threading dislocations.

In this paper we present the results of a photoluminescence (PL) study of the effects of plasma hydrogenation of GaAs on InP grown by metal organic chemical vapor deposition (MOCVD). We find that a luminescence band in the low temperature (5K) PL spectrum arising from the interfacial region increases ~30 fold relative to the band edge emission following hydrogenation. The improvement in PL intensity is consistent with the passivation of interfacial defects by atomic hydrogen and further shows that post-growth hydrogenation can be a viable process for passivating interfacial defects in GaAs/InP heterostructure.

EXPERIMENTAL

The GaAs layers were grown on (100) oriented n-type InP substrates in a barrel-type atmospheric pressure MOCVD reactor. Trimethylgallium and arsine were used as the sources and high purity helium was used as the carrier gas. A thin prelayer (<100Å) was first deposited at 425°C followed by another at 525°C before the final growth of the GaAs layer at 650°C at a growth

rate of 1.5 $\mu\text{m/hr}$.

The 1-3 μm thick layers had high resistivity ($>10^6 \Omega\text{cm}$) and the surface morphology was specular except for a slight texture. The as-grown samples were hydrogenated by exposure to a low frequency 30 kHz, 0.08 W cm^{-2} hydrogen plasma at 250°C and 0.75 torr for 30 min. Under these conditions hydrogen diffuses to a depth of 4-6 μm in semi-insulating GaAs.¹⁵ We expect that for the undoped high resistive GaAs on InP samples hydrogen penetrates the entire thickness of the layer. To determine the thermal stability of the hydrogenation effects, hydrogenated as well as as-grown samples were annealed in the temperature range 150-450°C for 30 min in forming gas. Photoluminescence (PL) measurements were made at 5K by exciting the samples with the 5145Å line from an Ar⁺ ion laser.

RESULTS AND DISCUSSION

Figure 1 compares the PL spectrum of a GaAs/InP sample before and after hydrogenation. The near band edge emission consists of three peaks at 1.5109, 1.5042 and 1.486 eV. These three bands originate from the GaAs layer. The two high energy peaks are, respectively, due to e-h recombinations associated with the conduction band electron and hole from the heavy hole and light hole valence bands, whose degeneracy is lifted by the biaxial tensile stress in the film.⁹ The 1.486 peak is associated with a donor-to-acceptor pair transition involving carbon.

The as-grown sample also shows a weak and broad band at 1.424 eV. If the luminescence from the InP substrate was also excited it would occur in this spectral region. Figure 1 shows the luminescence from the substrate after the epitaxial layer is chemically etched away. The peak of the emission occurs at 1.417 eV and is much narrower compared to the 1.424 eV band indicating that the latter originates from the GaAs epitaxial layer and not from the substrate. An emission band around 1.4 eV is usually observed in bulk Si-doped GaAs after heat treatment at high temperatures in the range 600-800°C.¹⁶⁻²¹ This band has been shown to involve the Si_{As} acceptor and perhaps a non-stoichiometric defect such as arsenic vacancy or gallium interstitial due to Ga-rich GaAs.

In the present GaAs/InP sample the 1.42 eV band cannot be ascribed to the same radiative centers as in the case of the bulk crystals. This band is seen only in the GaAs layer grown on InP substrate but not in the GaAs layer grown on GaAs substrate in the same reactor. Further, the response of the 1.42 eV band to varying excitation intensity, to hydrogenation and annealing (as discussed later), suggests that it arises from the interfacial region between the epitaxial layer and the substrate. The interfacial luminescence can occur either because the photoexcited carriers diffuse to the interfacial region and recombine there or because of secondary excitation of this region by the higher energy luminescence originating from the near surface regions of GaAs.

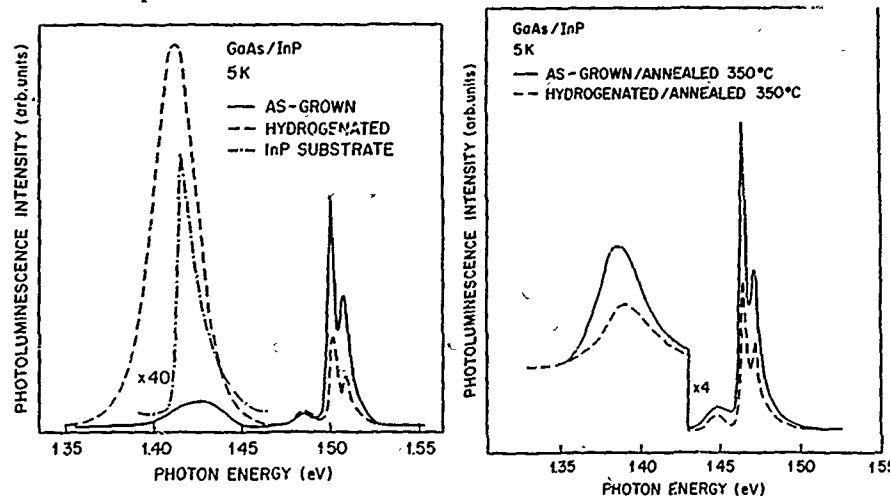
Figure 1 also shows the spectrum observed after hydrogenation. In the spectral range investigated, no new emission band is observed in the hydrogenated sample. The intensity of the higher energy bands due to band-to-band transitions at 1.5109 and 1.5042 eV decrease in intensity by a factor of 2. In contrast, the broad 1.424 eV luminescence shows a significant increase in intensity and also shifts to lower energy, viz., 1.414 eV.[†] Normalized to the near band edge emission the increase in the intensity is a factor of 30 relative to the as-grown sample.

The improvement in the luminescence efficiency following hydrogenation is consistent with the passivation of non-radiative centers by atomic hydrogen as observed previously in GaAs,²² AlGaAs,^{22,23} GaP²⁴ and InP.²⁵ In the present GaAs/InP sample only the deep emission at ~1.4 eV shows an improvement while the near band edge luminescence shows actually a decrease after hydrogenation. If non-radiative defects in the bulk of the epitaxial layer are passivated by hydrogen, one should have observed an improvement in the near band edge luminescence as well. The improvement of only the ~1.4 eV band is further evidence that it originates from the epitaxial-substrate interface. The high density of defects existing at this interface are likely to trap the atomic hydrogen and be passivated.

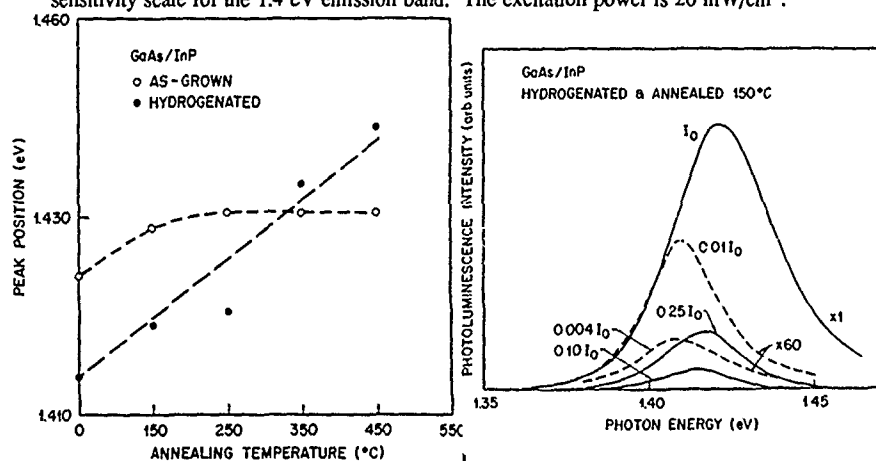
The passivation of shallow or deep impurities by hydrogen is unstable upon heating the sample. In GaAs, passivation of shallow impurities is thermally stable up to 400°C while that of deep impurities up to 600°C.²² In InP both shallow and deep impurity passivation are lost upon heating in the temperature range 300-400°C.²⁵ In GaAs/InP the thermal stability of the passivation of non-radiative centers and the consequent improvement in the intensity of the 1.4 eV band is

[†] Hereafter we refer to this broad emission band as 1.4 eV band even though its spectral position varies following hydrogenation, annealing and with excitation intensity.

found to be $\sim 350^\circ\text{C}$. This is illustrated in Fig. 2 in the PL spectra from the as-grown and hydrogenated samples after annealing at 350°C . The intensity of the 1.4 eV band normalized to the near band edge emission is the same for the as-grown and hydrogenated samples, indicating that the passivation effect is completely nullified. In other words, for device application the maximum processing temperature of hydrogenated GaAs/InP has to be below 350°C in order to avail the benefits of the passivation of non-radiative centers in the interfacial region by hydrogen.



1. 5K photoluminescence spectra from as-grown (solid line) and hydrogenated (dashed line) GaAs/InP. The luminescence from the InP substrate after chemically removing the GaAs layer is also shown (dot dashed line). Note the increased sensitivity scale for the substrate luminescence. The excitation power is 20 mW/cm^2 .
2. 5K photoluminescence spectra from GaAs/InP samples annealed at 350°C for 30 min: as-grown sample (solid line), hydrogenated sample (dashed line). Note the change in the sensitivity scale for the 1.4 eV emission band. The excitation power is 20 mW/cm^2 .



3. Peak position of the 1.4 eV band versus annealing temperature for the as-grown (open circles) and hydrogenated (solid circles) GaAs/InP.
4. Photoluminescence spectra in the 1.35-1.45 eV spectral range at several excitation intensities showing the shift of the peak position towards higher energy with increasing excitation intensity. I_0 denotes the maximum excitation power of 80 W/cm^2 .

As noted earlier, the 1.42 eV band in the as-grown sample shifts by 10 meV to lower energy coinciding with the peak position of the InP substrate luminescence after hydrogenation (Fig. 1). On the other hand, after annealing at 350°C the band occurs at 1.43 eV in both as-grown and hydrogenated samples as shown in Fig. 2. The shift of the 1.4 eV band towards higher energy with increasing temperature is illustrated in Fig. 3. In both the as-grown and hydrogenated samples the band shows a shift to higher energy with increasing temperature. In the as-grown sample the peak position shifts from 1.424 eV to 1.4305 eV at 250°C with no further shift above 250°C. This saturation is not observed in the hydrogenated sample in which the 1.4 eV band shifts from 1.414 eV in the as-hydrogenated condition to 1.439 eV after annealing at 450°C.

The 1.4 eV band also shifts towards higher energy with increasing excitation intensity. This is illustrated by the spectra shown in Fig. 4 taken at several excitation powers from a hydrogenated sample after annealing at 150°C.^{††} The magnitude of the peak shift is ~6 meV per decade change in excitation intensity. It should be noted that for the same excitation range as in Fig. 4, the band-to-band transitions do not show any shift. The donor-to-acceptor pair transition at 1.486 eV shifts to higher energy by 1 meV per decade change in excitation intensity consistent with the general behavior of pair recombination bands in GaAs.²⁶

The peak shift of the 1.4 eV band after hydrogenation, with excitation intensity and after annealing are all consistent with the hypothesis that the band originates from the substrate-epitaxial layer interface. In heteroepitaxial growth the transition region between the substrate and the epitaxial layer would be expected to consist of a graded composition whose band gap varies from the band gap of the substrate to that of the epitaxial layer. In GaAs grown on InP, the band gap at the transition region will vary continuously from 1.41 eV (InP) to 1.51 eV (GaAs). In the as-hydrogenated condition the 1.4 eV band appears at 1.414 eV close to InP band gap (Fig. 1) compared to 1.42 eV in the as-grown sample. If the diffusion length of photoexcited carriers had increased with hydrogen passivation of defects then the carriers diffuse farther and recombine at the

transition region closer to the InP substrate. Correspondingly the emission peak is InP-like.

In a compositionally graded region with varying band gap, at low excitation powers photoexcited carriers would recombine in the region of lowest band gap. However, with increasing excitation intensity, due to band filling effects recombination occurs at regions of higher band gap resulting in the shift of emission band towards higher energy in agreement with the behavior of the 1.4 eV band with excitation intensity. The shift of the 1.4 eV band to higher energy on heat-treatment in both the as-grown and hydrogenated samples suggests that compositional change of the graded substrate-epi interfacial region occurs. The larger shift in the case of the hydrogenated sample indicates that the extent of the compositional change is greater compared to the as-grown sample. Hydrogen induced compositional change has been observed previously by Hsieh et al. in GaAs/Si.²⁷ These authors noted that in GaAs/Si dark patches, which exhibited strong strain contrast in transmission electron microscopy, developed along the defects after hydrogenation. These patches extended up to the passivation depth (~1.5 μm) observed in C-V profiles. Hsieh et al. suggested that the dark patches are the result of compositional change that occur due to chemical reactions between GaAs and atomic hydrogen.

SUMMARY

We have presented the results of a low temperature (5K) photoluminescence study of the effects of plasma hydrogenation of GaAs on InP substrate grown by metal organic chemical vapor deposition. Besides the near band edge emission bands, a deep luminescence band at ~1.4 eV was observed in the as-grown sample. Upon hydrogenation the band showed a ~30 fold increase in intensity relative to the band edge emission. The band is attributed to radiative recombination occurring at the substrate - epitaxial layer interface and the increase in its intensity after hydrogenation is the result of hydrogen passivation of non-radiative defects at the heterointerface. The improvement in luminescence was nullified after a 350°C anneal of the hydrogenated sample. Excitation dependence of the 1.4 eV band indicated that the substrate-epi interfacial region is compositionally graded. The peak of the band shifted to higher energy upon annealing with the magnitude of the shift being greater in the hydrogenated sample than in the as-grown sample. The peak shift with annealing suggested that some intermixing of the compositionally graded interfacial region and that the intermixing is enhanced in the hydrogenated sample.

^{††} Since the 1.4 eV band is weak in the as-grown sample the peak could not be measured at low excitation levels.

ACKNOWLEDGEMENT

The authors thank A. Kinsella for her excellent assistance with the photoluminescence measurement.

References

- [1] Y. H. Lo, R. Bhat and T. P. Lee, *Electron. Lett.* **24**, 865 (1988).
- [2] Y. H. Lo, J. Harbison, J. H. Abeles, T. P. Lee and R. E. Nahory, *IEEE Electron Device Lett.*, **9**, 383 (1988).
- [3] K. Asano, K. Kasahara and T. Itoh, *IEEE Electron Device Lett.*, **8**, 289 (1987).
- [4] D. Huang, S. Agrawala and H. Morkoc, *Appl. Phys. Lett.*, **54**, 51 (1989).
- [5] C. J. Chang-Hasnain, Y. H. Lo, R. Bhat, N. G. Stoffel and T. P. Lee, *Appl. Phys. Lett.*, **54**, 156 (1989).
- [6] A. Suzuki, T. Itoh, T. Terakado, K. Kasahara, K. Asano, Y. Inomoto, H. Ishihara, T. Torikai and S. Fujita, *Electron. Lett.*, **27**, 954 (1987).
- [7] A. Suzuki, T. Itoh, T. Terakado, K. Kasahara, K. Asano, H. Ishihara, S. Fujita and T. Torikai, *European Conference on Optical Communication Proceedings*, 1987.
- [8] T. Suzuki, S. Fujita, Y. Inomoto, T. Terakado, K. Kasahara, K. Asano, T. Torikai, T. Itoh, M. Shikada and A. Suzuki, *Electron Lett.*, **24**, 1283 (1988).
- [9] U. K. Chakrabarti, W. S. Hobson, V. Swaminathan, S. J. Pearton, S. Nakahara, M. Lemont Schnoes, and P. M. Thomas, *1st International Conf. on InP and related materials*, Oklahoma, USA, 1989.
- [10] F. Ren, W. S. Hobson, S. J. Pearton, L. J. Oster and P. R. Smith, *IEEE Electron Dev. Lett.*, EDL-10, 389 (1989).
- [11] S. J. Pearton, J. W. Corbett and T. S. Shi, *Appl. Phys.* **A43**, 153 (1987).
- [12] W. C. Dautremont-Smith, *Mat. Res. Soc. Symp. Proc.* **104**, 313 (1988).
- [13] J. Chevallier and M. Aucouturier, *Ann. Rev. Mat. Sci.* **18**, 219 (1988).
- [14] S. J. Pearton, C. S. Wu, M. Stavola, F. Ren, J. Lopata, W. C. Dautremont-Smith, S. M. Vernon and V. E. Haven, *Appl. Phys. Lett.*, **51**, 496 (1987).
- [15] S. J. Pearton, W. C. Dautremont-Smith, C. W. Tu, and C. R. Abernathy, *Phys. Rev. B.* **36**, 4260 (1987).
- [16] H. Iwasaki and K. Sugibuchi, *Appl. Phys. Lett.*, **18**, 420 (1971).
- [17] R. Romano-Meran and K. L. Ashley, *J. Phys. Chem. Solids* **34**, 427 (1973).
- [18] W. Y. Lum and H. H. Weider, *J. Appl. Phys.* **49**, 6187 (1978).
- [19] E. V. K. Rao and N. Duhamel, *J. Appl. Phys.* **49**, 3457 (1978).
- [20] H. Birey and J. Sites, *J. Appl. Phys.* **51**, 619 (1980).
- [21] V. Swaminathan, N. E. Schumaker and J. L. Zilko, *J. Luminescence*, **22**, 153 (1981).
- [22] W. C. Dautremont-Smith, J. C. Nabity, V. Swaminathan, M. Stavola, J. Chevallier, C. W. Tu, and S. J. Pearton, *Appl. Phys. Lett.*, **49**, 1098 (1986).
- [23] L. Pavesi, F. Martelli, D. Martin, and F. K. Reinhart, *Appl. Phys. Lett.*, **54**, 1522 (1989).
- [24] J. Weber and M. Singh, *Mat. Res. Soc. Symp. Proc.* **104**, 325 (1988).

- [25] V. Swaminathan, J. Lopata, S. E. G. Slusky, W. C. Dautremont-Smith, and S. J. Pearton, unpublished.
- [26] R. Dingle, *Phys. Rev.* **184**, 788 (1969).
- [27] K. Hsieh, M. S. Feng, G. E. Stillman, N. Holonyak, Jr., C. R. Ito and M. Feng, *Appl. Phys. Lett.*, **54**, 341 (1989).

PASSIVATION OF Zn-ACCEPTORS IN InGaAs DURING RIE WITH CHF_3/H_2 AND CH_4/H_2

MARTIN MOHRLE

Heinrich-Hertz-Institut für Nachrichtentechnik Berlin GmbH, Einsteinufer 37,
D-1000 Berlin, Federal Republic of Germany

ABSTRACT

Reactive ion etching of highly Zn-doped InGaAs with hydrogen-containing gases such as CHF_3/H_2 , CH_4/H_2 and CH_4/He leads to a drastical reduction of the concentration of electrically active acceptors in a near-surface layer. Ti/Pt/Au contacts applied on as-treated p⁺-InGaAs layers show non-ohmic I/V-characteristics due to this passivation effect. Annealing at moderate temperatures (330°C, 20 minutes) was found to restore full electrical activity.

Introduction

Passivation of shallow acceptor impurities by atomic hydrogen is known as a general effect in elemental and compound semiconductors. Passivation of acceptors has been observed in Zn-doped GaAs [1] and InP [2]. In both cases samples were treated in a pure hydrogen plasma. De-activation of acceptors in Zn-doped InP resulting from reactive ion etching with CH_4/H_2 has recently been reported [3]. However, no similar effects in InGaAs have been published up to now.

In this paper clear evidence is presented of the occurrence of acceptor passivation also in this ternary material during reactive ion etching using a variety of hydrogen containing gases. The impact of this passivation effect on the formation of non-alloyed ohmic contacts to p-InGaAs will be pointed out.

Experimental

InGaAs layers (LPE) either epitaxially doped with Zn to $1 \cdot 10^{19} \text{ cm}^{-3}$ or doped by Zn-diffusion to $\approx 10^{20} \text{ cm}^{-3}$ were used in this study. The samples were subjected to reactive ion etching in a parallel-plate reactive ion etching (RIE) system operating at 13.56 MHz. Various etching gases such as CHF_3/H_2 (95%/5%), CHF_3 , CF_4 , CF_4/O_2 (95%/5%), CF_4/Ar (95%/5%) which are commonly used for the etching of dielectric films such as SiO_2 but which inevitably attack the exposed semiconductor layer underneath when ensuring complete etching, were investigated. In addition, the gas mixtures CH_4/H_2 (7%/93%) and CH_4/He (7%/93%) were tested which are employed in the well-established methane RIE-process for the etching of InP, InGaAs and InGaAsP. In the case of the former gases the experiments were carried out at a fixed gas pressure of 1.2 Pa and a RF power density of 0.16 Wcm^{-2} . The respective values of the methane-based RIE processes were 10 Pa and 0.41 Wcm^{-2} . The cathode involved was water-cooled and good thermal contact to the etched samples was ensured. To measure the electrically active acceptor concentration conventional electrochemical C-V-profiling was used.

Results on Passivation

In fig. 1 the hole concentration profiles measured on a diffused InGaAs layer before and after a 3 min exposure to a CHF_3/H_2 plasma (etching rate $< 1 \text{ nm/min}$) are depicted.

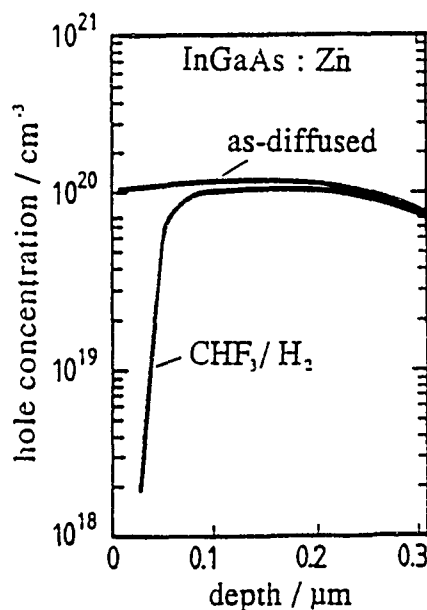


Fig. 1:

Hole concentration in highly doped p-InGaAs before and after RIE with CHF_3/H_2 (3 min)

Obviously the RIE treatment leads to a drastic decrease of the hole density by at least two orders of magnitude in a thin surface region which extends about 40-50 nm into the semiconductor layer. Longer etching times of up to 9 min hardly changed the depth of the passivated region. It is assumed that this passivation effect is due to atomic hydrogen which is generated in the RIE-plasma and which penetrates into the InGaAs-layer to form acceptor-hydrogen complexes [1], or other compensating defects. Comparative tests using hydrogen-free etching gases such as CF_4/O_2 , CF_4/Ar , CF_4 and pure Ar were made to verify this assumption. In all these cases the hole concentration profiles of the samples remained unchanged after the respective RIE treatments proving the absence of passivation when no hydrogen is involved.

To reveal whether the observed passivation is primarily due to the hydrogen admixture in the CHF_3/H_2 etching gas, a CHF_3 plasma and a H_2 plasma were tried separately. Fig. 2 shows the respective results for a plasma exposure time of 10 min in each case.

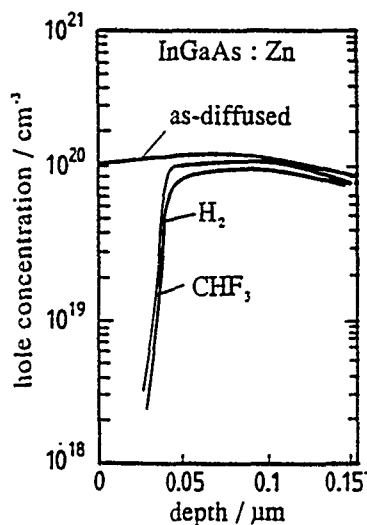


Fig. 2: Hole concentration in highly doped p-InGaAs before and after RIE with CHF_3 and H_2 , respectively (10 min)

As can clearly be seen from the profile plots, etching with merely CHF_3 again leads to passivation of acceptors implying that the hydrogen which is formed by dissociation from the CHF_3 molecules alone is sufficient to de-activate Zn-acceptors even in highly doped InGaAs. It should be noted that the observed depth of the passivated region of about 40 nm nearly coincides with that found with pure H_2 .

Similar results were obtained after reactive ion etching with CH_4/H_2 and CH_4/He . Fig. 3 shows the hole concentration profiles in an InGaAs layer after RIE with CH_4/H_2 and CH_4/He , respectively. In these experiments a thickness of 200 nm has been etched away from the ternary material.

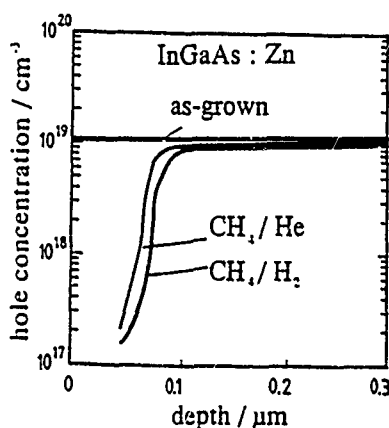


Fig. 3: Hole concentration in p-InGaAs after RIE with CH_4/H_2 and CH_4/He , respectively (200 nm etched)

In both cases the Zn-acceptors have been passivated to a depth of about 70-80 nm. Again it may be concluded that the hydrogen formed by dissociation from CH_4 is sufficient to yield strong passivation in a near-surface layer. However, a conclusive test is impossible since RIE using solely CH_4 leads to deposition of polymeric films rather than to an etching process [4].

To investigate the thermal stability of the passivated layers RIE treated samples were subsequently subjected to heating in a nitrogen ambient at 330°C for 20 min. In all cases a complete re-activation of the passivated acceptors could be achieved. For illustration the hole concentration profiles after CH_4/H_2 -RIE and after subsequent annealing are shown in fig. 4. It should be mentioned that no other annealing conditions were tried so far.

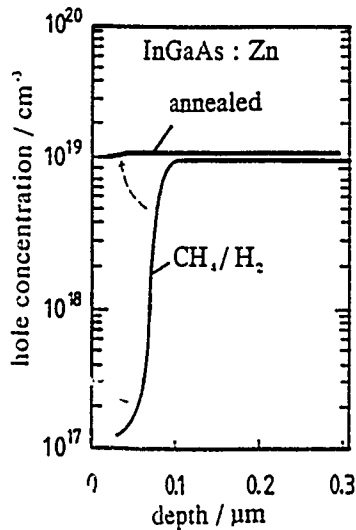


Fig. 4: Hole concentration in CH_4/H_2 etched InGaAs (200 nm etched away) before and after annealing (330°C ; 20 min)

Impact on Contacts

The obtained results are of particular importance to the fabrication of non-alloyed ohmic contacts, such as Ti/Pt/Au, on highly doped p-InGaAs which require a hole concentration of more than $5 \cdot 10^{17} \text{ cm}^{-3}$ in order to achieve a low contact resistance [5]. Consequently, due to the observed passivation effect, Ti/Pt/Au contacts deposited on a p^{++} -InGaAs layer directly after exposure to a CHF_3/H_2 RIE plasma showed strong non-ohmic behaviour. However, upon post-etch annealing (330°C , 20 min) to re-activate the passivated acceptors prior to the deposition of the metal contacts perfectly ohmic contact behaviour characterized by specific resistivities of less than $10^{-6} \Omega\text{cm}^2$ has again been achieved.

Summary

In conclusion, the influence of reactive ion etching on the electrically active Zn-acceptor concentration in InGaAs was investigated. It was found that hydrogen containing etching gases lead to a passivation of the Zn-acceptors in a thin region near the surface. In table I the effect of the various investigated gases on acceptor activity is summarized. Complete re-activation of the passivated acceptors could be obtained by thermal annealing at relatively low temperatures of the order of 300°C.

Table I Influence of RIE using different gas mixtures on the hole concentration in p-InGaAs

<u>RIE plasma</u>	<u>Zn-acceptor passivation</u>
CHF ₃ /H ₂	yes
CHF ₃	yes
H ₂	yes
CF ₄	no
CF ₄ /O ₂	no
CF ₄ /Ar	no
Ar	no
CH ₄ /H ₂	yes
CH ₄ /He	yes

Acknowledgments

This work was funded by the ESPRIT-programme (project 263).

References

- [1] N.M. Johnson, R.D. Burnham, R.A. Street, R.L. Thornton, Phys. Rev. B 33, 1102 (1986)
- [2] W.C. Dautremont-Smith, J. Lopata, S.J. Pearton, L.A. Koszi, M. Stavola, J. Appl. Phys. 66, 1993 (1989)
- [3] T.R. Hayes, W.C. Dautremont-Smith, H.S. Luftman, J.W. Lee, Appl. Phys. Lett. 55, 56 (1989)
- [4] U. Niggebrügge, M. Klug, G. Garus, Inst. Phys. Conf. Ser. 79, 367 (1986)
- [5] R. Kaumanns, N. Grote, H.G. Bach, F. Fidorra, Inst. Phys. Conf. Ser. 91, 501 (1988)

SURFACE PROTECTION DURING PLASMA HYDROGENATION FOR ACCEPTOR PASSIVATION IN InP

J. LOPATA, W. C. DAUTREMONT-SMITH, S. J. PEARTON, J. W. LEE, N. T. HA,
AND H. S. LUFTMAN
AT&T Bell Laboratories, Murray Hill, NJ 07974

ABSTRACT

Various dielectric and metallic films were examined as H-permeable surface protection layers on InP during H₂ or D₂ plasma exposure for passivation of acceptors in the InP. Plasma deposited SiN_x, SiO₂, and a-Si(H) films ranging in thickness from 85 to 225 Å were used to protect *p*-InP during D₂ plasma exposure at 250°C. Optimum protective layer thicknesses were determined by a trade-off between the effectiveness of the layer to prevent P loss from the wafer surface and the ability to diffuse atomic H or D at a rate greater than or equal to that in the underlying InP. SIMS and capacitance-voltage depth profiling were used to determine the extent of D in-diffusion and acceptor passivation respectively. Sputter deposited W and e-beam evaporated Ti films ~100 Å thick were also evaluated. The W coated sample yielded similar results to those with dielectric films in that acceptors in *p*-InP were passivated to a similar depth for the same plasma exposure. The 100 Å Ti film, however, did not allow the D to diffuse into the InP substrate. It is surmised that the Ti film trapped the D, thus preventing diffusion into the substrate.

INTRODUCTION

Hydrogen passivation of shallow dopants and deep levels in semiconductors has been widely reported and reviewed^(1,2) but until recently little has been reported on the effects in InP. The use of a hydrogen plasma is the most commonly used technique to introduce hydrogen into crystalline semiconductors. Attempts to hydrogenate InP by this method however result in preferential P loss from the surface as PH₃ and therefore In droplet formation.^(3,4) In order to successfully diffuse hydrogen into single crystal InP without degradation a surface protection layer which is H permeable but PH₃ impermeable must be employed.

In recent reports on the passivation of acceptors in *p*-InP various hydrogen permeable capping layers have been used to protect the InP surface from degradation during the hydrogen in-diffusion process. Chevallier et al.⁽⁵⁾ used 0.55 µm InGaAs to protect InP during plasma hydrogenation for acceptor passivation and Omeljanovsky et al.⁽⁶⁾ used a Schottky Au layer to act as a surface protectant. In an earlier paper we reported the use of SiN_x cap layers to protect InP during plasma hydrogenation.⁽⁷⁾ A thin layer of ~85 Å PECVD SiN_x was found to be adequate to protect a *p*-InP surface during a 0.5h, 250°C hydrogen or deuterium plasma exposure to achieve a depth of acceptor passivation of ~1.0 µm.

In this paper we investigate the useful range of SiN_x cap layer thickness to provide surface protection and yet allow acceptor passivation to occur during a typical 0.5h plasma exposure. In addition to SiN_x, thin PECVD films of SiO₂ and a-Si(H) and metallic films of e-beam evaporated Ti and RF sputtered W were also evaluated as H-permeable protective layers.

EXPERIMENTAL PROCEDURE

Polished LEC-grown *p*-type InP (100) wafers Zn doped to $\sim 5 \times 10^{18} \text{ cm}^{-3}$ were used for this hydrogenation study. GaAs (100) *n*-type Si doped to $1 \times 10^{17} \text{ cm}^{-3}$ and (100) *p*-

type Zn doped to $8 \times 10^{18} \text{ cm}^{-3}$ wafers were also used. Before coating with protective cap layers all wafers were cleaned with organic solvents and dilute HF solution to remove any hydrocarbon contamination and the native oxide. Thin films of SiN_x , SiO_2 and a-Si(H) were deposited in a 13.56 MHz PECVD parallel plate reactor from $\text{NH}_3/\text{SiH}_4/\text{Ar}$, $\text{N}_2\text{O}/\text{SiH}_4/\text{Ar}$, or SiH_4/Ar plasmas respectively. Thin $\sim 100 \text{ \AA}$ W films were deposited by RF sputtering and 100 \AA Ti films were deposited by e-beam evaporation. The capped wafers were subsequently exposed to a 30 kHz, 0.08 Wcm^{-2} D_2 plasma at 0.75 Torr pressure for 0.5h at 250°C substrate temperature. Following D_2 plasma exposure the SiN_x , SiO_2 , a-Si(H), and Ti cap layers were removed by etching in a dilute HF solution. The W film was removed by $\text{CF}_4:\text{O}_2$ plasma etching. Complete removal of the cap layers was verified by ellipsometry.

Carrier concentrations were measured by Polaron electrochemical capacitance-voltage (C-V) depth profiling. Deuterium concentration depth profiles were obtained by Cs^+ negative secondary ion mass spectrometry (SIMS) in a Cameca IMS 3f spectrometer. Typically absolute concentrations reported are accurate to a factor 2 whereas depth measurements are accurate to $\pm 7\%$. Wafer surfaces were examined for evidence of degradation by optical microscopy and ellipsometry.

RESULTS AND DISCUSSION

The effectiveness of a thin 85 \AA SiN_x cap layer in protecting InP from surface degradation during a 0.5h, 250°C D_2 plasma exposure is shown in Figure 1.^[7] The uncapped region of the wafer was severely degraded with extensive In droplet formation unlike the SiN_x capped region which showed no apparent degradation in the form of In droplets. The capped InP surface showed no damage by ellipsometry as the InP substrate optical constants (n and k values of the refractive index) measured both before SiN_x cap layer deposition and after D_2 plasma exposure and cap layer removal were identical. Close examination of another wafer (Figure 2) also capped with 85 \AA SiN_x and exposed to 0.5h, 250°C D_2 plasma showed the initiation of surface damage occurring at the wafer corners. This was caused by the partial etching of the SiN_x cap layer in the D_2 plasma, and resulted in holes in the SiN_x cap layer where direct plasma exposure of InP could occur leading to In droplet formation. Measurement of the SiN_x film thickness after D_2 plasma exposure for 0.5h at 250°C showed a decrease in the apparent film thickness to $\sim 65 \text{ \AA}$. Chang et al.^[3] reported an H_2 plasma etch rate of SiN_x of $\sim 10\text{--}15 \text{ \AA min}^{-1}$ but for a much higher RF plasma power. The slight decrease in SiN_x thickness we observed was expected for the D_2 plasma conditions used for acceptor passivation in InP. In order to protect the InP from degradation at wafer corners the SiN_x layer must be thick enough to withstand the plasma etching which occurs during the D_2 plasma exposure but yet be thin enough to allow atomic D to penetrate into the semiconductor.

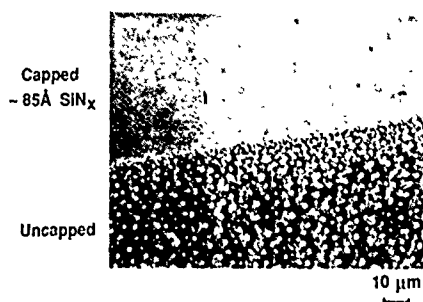


Figure 1. D_2 plasma exposed $p\text{-InP}$ partially capped with $\sim 85 \text{ \AA}$ SiN_x .

Extensive In droplet formation resulted on the uncapped region of the InP wafer during the 0.5h, 250°C plasma exposure.

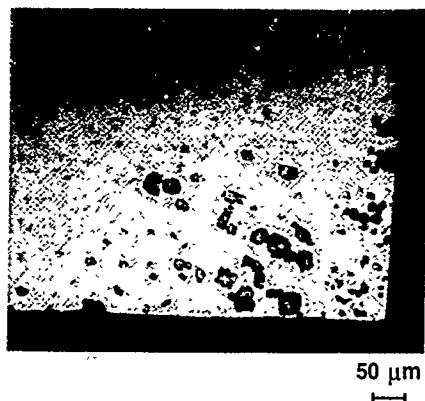


Figure 2. Initiation of surface damage on 85 Å SiN_x capped p -InP during D_2 plasma exposure for 0.5h at 250°C. In droplets formed at regions in the corners of the wafer due to D_2 etching of the SiN_x layer, allowing exposure of bare InP to the D_2 plasma.

To demonstrate the effect of an 85 Å SiN_x cap layer on the atomic D in-diffusion both SiN_x capped and uncapped GaAs wafers were exposed to a D_2 plasma for 0.5h at 250°C. Note that this experiment could not be duplicated with InP because of the severe degradation which would result for bare InP exposed to D_2 plasma. The atomic D concentration depth profiles in n and p -type GaAs with and without 85 Å SiN_x protective cap layers are shown in Figures 3 and 4 respectively. In both cases the D concentration is decreased for the SiN_x capped samples by ~30% but the in-diffusion depths appear similar. Summarized in Table 1, the depth of D in-diffusion is ~3 μm for n -GaAs and about ~4 μm for p -GaAs for the same 0.5h, 250°C D_2 plasma exposure regardless of the use of the SiN_x protective cap layer. Thus the 85 Å SiN_x layer provides very little impedance to D in-diffusion, even on a semiconductor as here which permits both rapid in-diffusion and a high concentration of diffused D. Once in the material the atomic D would passivate the Si donors in n -GaAs and Zn acceptors in p -GaAs as was previously shown by Chevallier et al.^[8] and Johnson et al.^[9] respectively.

Similarly to GaAs the D in-diffusion into InP through an 85 Å SiN_x layer would also result in a slight decrease in the atomic D concentration but the D diffusion depth would

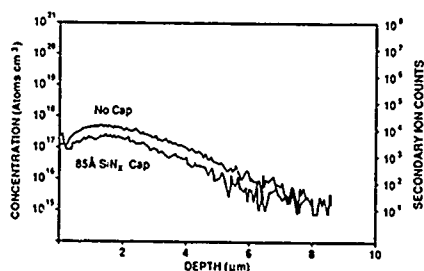


Figure 3. SIMS depth profiles of deuterium in D_2 plasma exposed n -GaAs ($\text{Si}, 1 \times 10^{17} \text{ cm}^{-3}$) with an 85 Å SiN_x cap layer and also without. The use of SiN_x cap layer resulted in an overall decrease in the D concentration but had no effect on the depth of D in-diffusion.

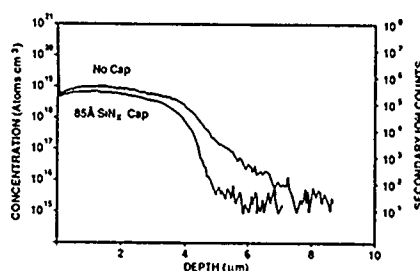


Figure 4. SiN_x capped and uncapped D_2 plasma exposed p -GaAs ($\text{Zn}, 8 \times 10^{18} \text{ cm}^{-3}$) SIMS depth profiles show a similar D concentration decrease for the sample with an 85 Å SiN_x cap as did the n -type GaAs of Figure 3.

Table 1: Depth of Deuterium In-diffusion into Both Capped and Uncapped GaAs During Plasma Exposure

Material	Cap Layer	Concentration (atom cm ⁻³)	Depth (Peak) (μ m)	Depth ($\frac{1}{e}$ of peak) (μ m)
<i>n</i> -GaAs	None	4.3×10^{17}	1.4	3.1
(Si, 1×10^{17} cm ⁻³)	~85 Å SiN _x	2.6×10^{17}	1.4	2.8
<i>p</i> -GaAs	None	8.8×10^{18}	1.5	3.7
(Zn, 8×10^{18} cm ⁻³)	~85 Å SiN _x	6.2×10^{18}	1.3	3.7

be unaffected. Shown in Figure 5 the D concentration profile of a D₂ plasma treated SiN_x capped *p*-InP (Zn, 5×10^{18} cm⁻³) sample matches closely the Zn dopant level to ~1.0 μm. This SIMS depth profile was taken on the same sample shown in Figure 2 indicating that 85 Å SiN_x is the minimum thickness to achieve 1.0 μm D in-diffusion into *p*⁺ InP while maintaining good surface protection. As we previously reported^[7] the depth of D matches the reduction in the acceptor level shown in Figure 6.

Increasing the thickness of the SiN_x cap layer to 225 Å reduced the depth of D in-diffusion into the *p*-InP substrate by about a factor 6. Shown in Figure 7, this reduction in depth resulted from the SiN_x layer restricting the supply of D into the InP during the D₂ plasma exposure. Although no plasma damage of the 225 Å SiN_x capped sample was observed either by optical microscopy or ellipsometry, this was only accomplished at the expense of the D in-diffusion depth. Thus increasing the cap layer thickness allows for better surface protection but significantly reduces the amount of D diffusing through during D₂ plasma exposure, and consequently the control of the D diffusion depth into the underlying *p*-InP would require tight control of the SiN_x cap layer thickness. In order to achieve adequate surface protection during longer plasma exposures for deeper D in-diffusion, the cap layer thickness must be increased by an amount which would be etched away during D₂ plasma exposure or another cap layer material which exhibits a slower D₂ plasma etch rate must be used.

PECVD films of SiN_x, SiO₂, and a-Si(H) can be deposited at reasonably controlled deposition rates for thicknesses of ~ 100 Å. These PECVD films contain substantial amounts of H which is known to be mobile at deposition temperatures as a result of the PECVD process; thus it is unlikely that the films would absorb more H or D during plasma exposure and would be good candidates as surface protection layers. The films are easily

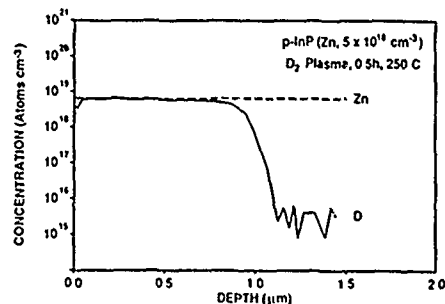


Figure 5. SIMS depth profile of deuterium in *p*-InP (Zn, 5×10^{18} cm⁻³) capped with 85 Å SiN_x during D₂ plasma exposure for 0.5h at 250°C.

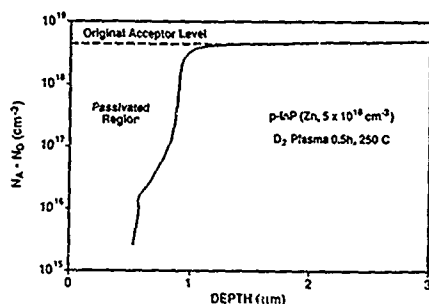


Figure 6. Electrochemical capacitance-voltage (C-V) depth profile of the acceptor concentration in D_2 plasma exposed p -InP sample indicates a depth of acceptor passivation in agreement with the SIMS depth of D in-diffusion.

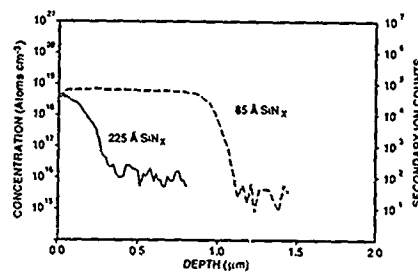


Figure 7. The effect on D in-diffusion for increasing SiN_x cap layer thickness is shown by SIMS deuterium depth profiles of D_2 plasma exposed p -InP capped with 225 Å SiN_x and the 85 Å SiN_x capped sample of Figure 5. The D in-diffusion depth decreased by about a factor 6.

removed by wet etching in dilute HF solution without etching the underlying InP substrate.

The depth of D in-diffusion into p -InP wafers capped with ~ 150 Å SiO_2 or ~ 75 Å a -Si(H) are shown in Figure 8 while the acceptor passivation depths are shown in Figure 9. Both samples showed acceptor passivation depths to ~ 0.5 μm or roughly half the depth observed for the 85 Å SiN_x capped sample. Neither sample showed any surface damage to the InP substrate in the form of In droplets although the a -Si(H) capped sample did show damage along scratches in the a -Si(H) film which must have occurred prior to D_2 plasma exposure. The 150 Å SiO_2 film did show a 25 Å decrease in thickness as a result of 0.5h D_2 plasma exposure, which was similar to the decrease in film thickness observed for SiN_x films. The factor 2 decrease in D depth of diffusion for the SiO_2 capped sample compared to SiN_x probably is due to the greater thickness of the SiO_2 layer. The similar factor 2 decrease in D depth of diffusion for the a -Si(H) sample resulted from the a -Si(H) layer being less permeable to atomic D than was the SiN_x . The a -Si(H) layer was expected to show a similar thickness decrease also due to D_2 plasma etching but was not measured directly. The generation of a volatile reaction product such as SiH_4 due to the reaction of atomic D with the Si containing films could account for the decrease in film thickness for all 3 samples.

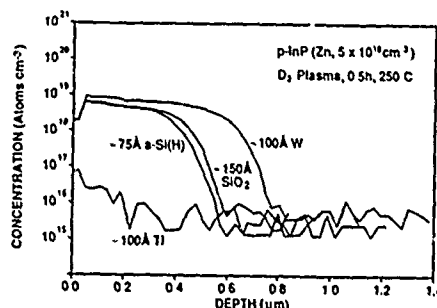


Figure 8. SIMS depth profiles of deuterium in p -InP capped with ~ 150 Å SiO_2 , 75 Å a -Si(H), ~ 100 Å W, or ~ 100 Å Ti during D_2 plasma exposure for 0.5h at 250°C.

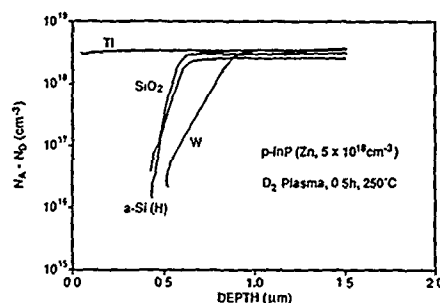


Figure 9. Electrochemical capacitance-voltage (C-V) depth profiles of the D_2 plasma treated samples of Figure 8. Similar agreement of the depth of acceptor passivation to the SIMS depth of D in-diffusion is observed as occurred for the 85 Å SiN_x capped p -InP of Figure 5.

Thin films of H-permeable materials which would not react to form volatile hydrides were next considered as surface protection layers for longer plasma exposures. The metal films of Ti and W were used because of the ease of deposition by e-beam evaporation and sputtering and subsequent removal by dilute HF wet etching and CF_4/O_2 plasma etching respectively. The D in-diffusion and acceptor passivation depths for p -InP substrates capped with 100 Å Ti and 100 Å W are shown in Figures 8 and 9. In both cases the film thicknesses were determined from known deposition rates and not measured directly. The 100 Å W capped sample showed D in-diffusion and acceptor passivation depths similar to the SiN_x results with no damage in the form of In droplets anywhere on the wafer. Ellipsometric measurements of the InP refractive index before cap layer deposition and following D_2 plasma exposure and cap layer removal were similar indicating very good surface protection. On the other hand the 100 Å Ti capped sample showed only a slight amount of D in-diffusion and acceptor passivation as shown in Figures 8 and 9. The atomic D generated in the D_2 plasma did not penetrate through the Ti cap layer to diffuse into the p -InP but most likely instead preferentially reacted with the Ti to form a stable hydride such as TiD_2 or remained in solid solution with the Ti. The Ti film also became blistered in spots and the InP surface was damaged due to In droplet formation where blisters had broken during the D_2 plasma exposure. The W film clearly showed superior performance as a protective cap layer during D_2 plasma exposure over the PECVD or Ti films in that an acceptor passivation depth of nearly 1 μm was achieved while no surface damage or cap layer etching was observed.

CONCLUSIONS

1. InP surfaces must be protected in some fashion during plasma hydrogenation for acceptor passivation to prevent surface degradation due to loss of P.
2. ~85 Å SiN_x layers adequately protect the wafer surface but are etched during plasma hydrogenation leading to damage at wafer edges.
3. Increasing SiN_x cap layer thickness to 225 Å provides better surface protection but with strongly decreased depth of atomic deuterium in-diffusion and acceptor passivation by about a factor 6 in p -InP ($Zn, 5 \times 10^{18} \text{ cm}^{-3}$).
4. SiO_2 and $a\text{-Si(H)}$ cap layers protect InP surfaces equally as well as SiN_x with similar permeability to H or D, but also etch during plasma hydrogenation.

5. W cap layers provide the best surface protection in that no etching at wafer corners was observed, and slightly better H or D permeability was shown by SIMS.
6. Ti cap layers protect the surface adequately but did not allow any significant amount of atomic deuterium to penetrate into the InP to passivate the acceptors, presumably due to the D remaining in solid solution in the Ti in preference to the InP or due to the formation of a stable hydride TiD_2 .

ACKNOWLEDGMENTS

The authors gratefully acknowledge A. Katz and A. Lahav for the deposition of Ti and W thin films respectively.

REFERENCES

- [1] S. J. Pearton, J. W. Corbett, and T. S. Shi, *Appl. Phys.* **A43**, 153 (1987).
- [2] W. C. Dautremont-Smith, *Mater. Res. Soc. Symp. Proc.* **104**, 313 (1988).
- [3] R. P. H. Chang, C. C. Chang, and S. Darack, *J. Vac. Sci. Technol.*, **20**, 45 (1982).
- [4] D. T. Clark and T. Fok, *Thin Solid Films* **78**, 271 (1981).
- [5] J. Chevallier, A. Jalil, B. Theys, J. C. Pesant, M. Aucouturier, B. Rose, and A. Mircea, *Semicond. Sci. Technol.* **4**, 87 (1989).
- [6] E. M. Omeljanovsky, A. V. Pakhomov, and A. Y. Polyakov, *Materials Science Forum Vols. 38-41*, 1063 (1989).
- [7] W. C. Dautremont-Smith, J. Lopata, S. J. Pearton, L. A. Koszi, M. Stavola, and V. Swaminathan, *J. Appl. Phys.* **66**, 1993 (1989).
- [8] J. Chevallier, W. C. Dautremont-Smith, C. W. Tu, and S. J. Pearton, *Appl. Phys. Lett.* **47** (2), 108 (1985).
- [9] N. M. Johnson, R. D. Burnham, R. A. Street, and R. L. Thornton, *Phys. Rev. B*, **33** (2), 1102 (1986).

PART VIII

Diffusion in
Silicon and Germanium

ATOMIC DIFFUSION PROCESSES IN SILICON

SOKRATES T. PANTELIDES
IBM Research Division
Thomas J. Watson Research Center
Yorktown Heights, NY 10598

ABSTRACT

The mechanisms of self-diffusion and dopant impurity diffusion in silicon have been the subject of intense debate since the 1960's. Until the mid-1980's, there was only limited experimental information and virtually no theory. In the last five years, however, first-principles calculations of many key quantities and new experimental data have led to significant progress. This paper traces the major theoretical advances and the key experimental data that have resolved many controversies and have provided a fairly comprehensive picture of diffusion processes. Theory has also recently provided detailed microscopic information about the diffusion of interstitial hydrogen.

INTRODUCTION

Questions of atomic diffusion in Si have been quite controversial largely because experimental data are incomplete and theory for the underlying key quantities was, until recently, lacking. In this paper, we will first trace briefly a number of key theoretical developments that happened in recent years. We will then describe the impact of these developments on our understanding of self-diffusion, dopant impurity diffusion and hydrogen diffusion. In each of these cases, we will discuss the historical background and key experimental advances that also contributed to unraveling many puzzles. The prospects for future developments to elucidate remaining questions are assessed as very promising.

THEORETICAL DEVELOPMENTS

In order to obtain a complete theoretical description of atomic diffusion processes in a crystal, one must first be capable of calculating the properties of point defects. Until about the end of the 1970's, the theory of point defects was quite primitive. Though a number of formalisms had been developed, actual calculations were limited to simple techniques that entailed drastic approximations whose consequences could not be assessed.¹ Beginning in 1978, there has been an explosion in theoretical developments for describing point defects in semiconductors. Two seminal papers by Baraff and Schluter² and by Bernholc, Lipari and Pantelides³ reported practical Green's-function approaches that allowed first-principles calculations of the charge density and energy levels of point defects at the same level of sophistication and accuracy as was already possible for perfect bulk crystals and surfaces. The Schroedinger equation for a point defect in an oth-

erwise perfect crystal was solved self-consistently without free parameters. The Green's-function approach was used widely by many authors over the next several years.⁴ In 1984, Car, Kelly, Oshiyama and Pantelides⁵ implemented a modified Green's-function approach and reported *total energies*, which are key quantities in diffusion questions as formation and migration energies. Independently, Bar-Yam and Joannopoulos⁶ showed that a supercell approach, which employs a periodic array of defects to simulate isolated defects, can be practically implemented to yield total energies. Both Green's-function and supercell techniques were used to obtain activation energies for diffusion.⁵⁻⁸ More recently, Van de Walle, Bar-Yam and Pantelides⁹ showed that one could exploit the symmetry of the lattice and get global total-energy surfaces for a diffusing impurity. Buda, Chiarotti, Car and Parrinello,¹⁰ on the other hand, showed that a full dynamical first-principles calculation is possible for a diffusing hydrogen ion. This calculation yielded a first-principles diffusion coefficient for the first time. In a more recent development, Bloechl, Van de Walle, and Pantelides¹¹ showed that an approximate calculation of the diffusion coefficient using the static total-energy surfaces as an effective potential yields very satisfactory results.

SELF-DIFFUSION

Self-diffusion is the process by which substitutional host atoms move through the lattice to other substitutional sites. Experimentally, the coefficient of diffusion is measured by using radioactive Si atoms and monitoring their movement through the Si lattice. For Si, the coefficient of self-diffusion has been measured by several experimental groups.¹² It has been found to have an Arrhenius behavior over several overlapping temperature ranges (different techniques are usually limited to somewhat different temperature ranges). The activation energy is typically found to be between 4 and 5 eV. It is often argued that this variation in measured activation energies suggests a curvature or kink in the Arrhenius plot. In fact, however, no single experiment has reported anything but a straight line. In view of the difficulties inherent in the experiments, it is, therefore, best to view the range 4-5 eV as reflecting an experimental uncertainty which may hide a curvature or kink.

The self-diffusion activation energy does not by itself give even a hint about the underlying mechanism. Textbooks for many years recognized the fact that self-diffusion can proceed without defects (direct exchange between neighboring atoms or motion of atoms around a ring, etc.) or with the assistance of native defects such as vacancies and self-interstitials.¹³ Elementary diffusion theory finds that, in the latter case, the self-diffusion activation energy is equal to the sum of the relevant defect's formation and migration energies.¹³ Thus, independent measurements of these quantities for vacancies and self-interstitials can provide an important test for determining the mechanism.

Until the mid-1980's, defect-less mechanisms were assumed to require too much energy and the debate focussed on vacancies and self-interstitials. A number of authors came out strongly in favor of one or the other, typically with largely circumstantial arguments to back their position. The evidence invoked was usually indirect and depended crucially on assumptions and data interpretations whose validity was in turn not strongly

documented. In some cases, the same experimental data were invoked by the opposite camps as supporting their case, by merely injecting different undocumented assumptions.¹⁴

In addition to the vacancy-versus-interstitial debate, another debate raged about the nature of the intrinsic defect. The notion of a simple vacancy (a nominal atomic site without an atom) or a simple self-interstitial (an extra atom at an interstitial site) were not viewed as adequate. A number of authors, some advocating vacancies¹⁵ and some advocating interstitials,¹² argued that the relevant defect must be "extended". These notions, which were generally imprecise, had two distinct sources.

One source was the experimentally observed large pre-exponential of the coefficient of self-diffusion as compared with corresponding values in simple metals. The argument was that pre-exponentials depend on entropies and "extended" configurations (e.g. an extended region containing $N-1$ atoms instead of the normal N would be an extended vacancy) are likely to have large configurations and/or vibrational entropies.

The second source was the experimentally observed migration energies of the vacancy and self-interstitial at cryogenic temperatures (~ 4 K). In the 1960's, Watkins created vacancies and self-interstitials by electron bombardment and monitored their migration. He found that the vacancy has a migration energy of 0.2-0.4 eV depending on its charge state. The interstitial, on the other hand, was inferred to move athermally. Athermal motion implies either negligible barrier or a finite barrier that can be overcome by electron-hole recombination at the defect (a high concentration of electrons and holes is present in the crystal during high-energy electron bombardment). In the latter case, the barrier is likely to be equal to or smaller than one band gap, i.e. less than 1 eV or so. Thus, whether one believed in vacancies or interstitials, the cryogenic data suggested that the bulk of the self-diffusion activation energy (4-5 eV) is due to the defect's formation energy, which would have to be of order 4 eV. There was, however, significant reluctance among many to accept such a conclusion. Experience from diffusion in metals suggested that the formation and migration energies are comparable. Furthermore, a number of available estimates from simple calculations or indirect data found that the vacancy formation energy is about 2.5 eV. If so, and the cryogenic migration energies are used, the resulting self-diffusion activation energy would be just under 3 eV, nowhere near the experimental 4-5 eV! The way out of this dilemma was to postulate that the cryogenic migration energies are not relevant at high temperatures. Somehow the vacancy or interstitial was a different beast at the high temperatures of self-diffusion, perhaps an extended object that faced a higher migration barrier. Such assertions were consistent with the entropy arguments invoked to account for the large pre-exponential of the self-diffusion coefficient.

In 1984 and 1985, Car, Kelly and Oshiyama and Pantelides⁵ reported first-principles calculations of formation energies for vacancies and self-interstitials. Similar calculations were performed independently by Bar-Yam and Joannopoulos⁶ with virtually identical results. The key result was that simple forms of the vacancy and interstitial have comparable formation energies, both of order 4 eV. Migration energies were small for both, in agreement with experimental data. The self-interstitial indeed was capable

of athermal migration by the successive capture of electrons and holes which change the charge state and, in turn the stable site. The picture that emerged was rather simple: Both intrinsic defects have large formation energies and small migration energies. Both defects contribute to self-diffusion with an activation energy in the range between 4 and 5 eV that is observed experimentally.

In 1986, Pandey⁷ calculated the total energy variation accompanying the exchange of two neighboring atoms. He found the maximum barrier to be again of order 4 eV! This surprising result means that all three mechanisms contribute to self-diffusion with comparable activation energies. Thus, it is not possible to tell which, if any, is dominant. One must look at pre-exponentials. One of these mechanisms may have a larger pre-exponential than the others, or all of them may be comparable *and* large. Reliable calculations are not yet available. We will see later on, however, that first-principles calculations of the full diffusion coefficient, not just the activation energy, are now becoming possible.

Also in 1986, Dannefaer, Mascher and Kerr¹⁶ reported positron annihilation experiments from which they extracted a vacancy formation energy of 3.6 ± 0.2 eV, which is in excellent agreement with the theoretical value (3.8 ± 0.2 eV). In addition, experiments using buried layers of Ge have concluded that both vacancies and self-interstitials mediate the diffusion of substitutional Ge.¹⁷ Because of the similarities between Si and Ge atoms, it is tempting to view these results as evidence that both vacancies and self-interstitials play a role in self-diffusion. The same experiments suggest that the role of exchange may be minimal. We will discuss these experiments further in the context of dopant impurity diffusion in the next section.

DOPANT IMPURITY DIFFUSION

Substitutional impurities (e.g. phosphorus, arsenic, boron, etc.) can in principle diffuse by the same mechanisms as self-diffusion: exchange, vacancies and self-interstitials. As in the case of self-diffusion, a strong debate went on for years regarding the relative role of the two intrinsic defects without strong evidence that could truly distinguish between the two.^{11,18}

One of the points that was not explicitly discussed in most of the literature on dopant diffusion is the more complex role that vacancies and self-interstitials play.⁵ For example, when a vacancy becomes a nearest neighbor to a substitutional impurity, a bound vacancy-impurity pair can form (in contrast, a vacancy does not form a bound pair with a radioactive Si atom). The pair can then migrate as a single entity. In such a case, the diffusion coefficient is determined by the concentration and migration of these pairs. The corresponding activation energy is the formation plus migration energy of the pair. Since the formation energy of the pair is by definition smaller than the formation energy of a free vacancy (the difference is called the binding energy of the pair), the resulting impurity diffusion activation energy can be smaller than the self-diffusion activation energy. Similarly, a self-interstitial can form a bound pair with a substitutional impurity and the pair can migrate as an entity. Alternatively, the self-interstitial may kick the

substitutional impurity into an interstitial site while taking its place at the nominal atomic site. In either case, the resulting diffusion coefficient can have an activation energy that is smaller than the corresponding activation energy of self-diffusion.

First-principles calculations for aluminum and phosphorus in Si in 1985 by Car, Kelly, Oshiyama and Pantelides⁵ showed that both vacancies and self-interstitials yield diffusion activation energies that are smaller than the corresponding self-diffusion activation energies, as indeed found by experiment. A more extensive set of calculations in 1989 by Nichols, Van de Walle and Pantelides⁸ (see Fig. 1) found the following: The activation energies for vacancy-mediated and interstitial-mediated diffusion are comparable for all impurities with the exception of antimony. In the latter case, the interstitials yield an activation energy that is substantially larger than that of vacancies. One can then safely conclude that vacancies dominate antimony diffusion. This conclusion was reached earlier by several authors on the basis of experimental data.¹⁸ The role of exchange is unclear in all cases because, again, the corresponding activation energy is in the same range as the activation energies of the defect-mediated mechanisms.

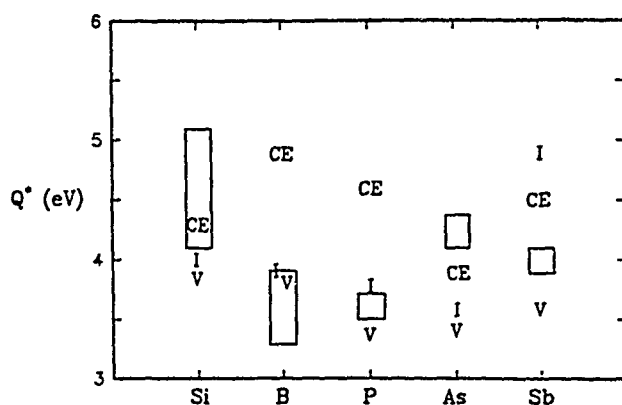


Fig. 1. Calculated activation energies under equilibrium conditions for vacancy-mediated (V), interstitial-mediated (I) and concerted-exchange (CE) mechanisms for Si self-diffusion and several dopant impurities. The boxed areas are ranges of experimental data. Figure from Ref. 8.

A set of ingenious experiments, however, provide information that allow fairly strong conclusions regarding the relative roles of the three mechanisms.¹⁸ In these experiments, thin doped layers are buried in high-resistivity material. The spreading of these layers at high temperatures allows one to determine the impurity diffusion coefficient at those temperatures. The measurements can be repeated, however, under conditions that cause a surface reaction to occur (e.g. oxidation or nitridation). It has been found that the resulting diffusion coefficients are drastically different. Independent evidence has led to the conclusion that oxidation injects excess self-interstitials into the subsurface region whereas nitridation injects vacancies. The changes in the diffusion coefficient can, therefore, be attributed to the injection of non-equilibrium defect concentrations.

Perhaps the most dramatic inference from these experiments is on the role of the exchange mechanism. Since this mechanism does not depend on defects, the injection of non-equilibrium defects should not affect it at all. The fact that the diffusion of all impurities is either retarded or enhanced by defect injection provides strong evidence that the exchange mechanism is not dominant.⁸

In the case of antimony, it has been found that its diffusion is retarded by interstitial injection and enhanced by vacancy injection. The obvious conclusion is that antimony diffusion is predominantly mediated by vacancies. Thus, when interstitials are injected, they recombine with vacancies and retard vacancy-mediated diffusion. Inversely, when vacancies are injected, the vacancy-mediated-diffusion is enhanced. A careful analysis is actually more complex. The details have been given by Nichols et al.⁸ Fahey et al.¹⁸ have pursued a different approach, but their conclusions are in agreement.

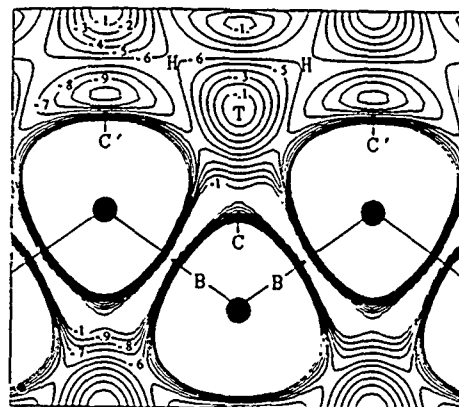
Buried-layer experiments have also been carried out with Ge impurities. It has been found that injection of either vacancies or interstitials enhances the diffusion coefficient. The result suggests that both defects play a role in mediating the equilibrium diffusion of Ge. Because of the similarities between Si and Ge, the conclusion can be extended to self-diffusion.

HYDROGEN DIFFUSION

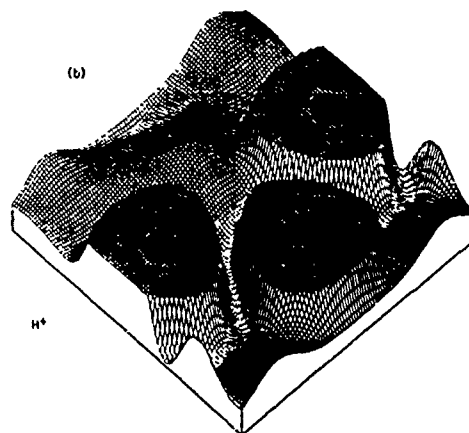
The primary role of hydrogen in crystalline Si has long been believed to be the passivation of dangling bonds at defects. In 1983, a study of MOS devices under avalanche electron injection led Sah, Sun and Tzou¹⁹ to suggest that hydrogen entering p-type Si can deactivate the dopant by forming acceptor-hydrogen pairs. This observation triggered extensive experimental and theoretical studies of the properties of H and its reactions with impurities. A recent volume contains a number of comprehensive reviews.²⁰ Here we will only summarize recent advances in the theoretical description of hydrogen diffusion. These developments are very promising for further work that will elucidate the remaining questions in self-diffusion and dopant impurity diffusion that we discussed earlier in this paper.

There have been two very distinct approaches, one "static" and one "dynamic" that have complemented each other rather nicely. The static approach has been pursued by the present author with several collaborators. The dynamic approach has been pursued by Car and Parrinello and their collaborators. The developments occurred within the last year or so and are at a stage of rapid evolution. It is still too early to stand back and objectively assess their full impact. We will, therefore, summarize these developments in a chronological sequence.

The first step was taken in the static approach by Van de Walle, Bar-Yam, and Pantelides.⁹ They showed that first-principles calculations can be used to generate a set of hypersurfaces that represent the total energy of the system as a function of the position of a hydrogen atom in the lattice. At each such position of H, all Si atoms are allowed to relax. By utilizing the symmetry of the crystal, one actually has to carry out the



(a)



(b)

Fig. 2. Contour plot (a) and perspective plot (b) of the total-energy surface for H^+ in a (110) plane through Si atoms. The zero of energy is arbitrarily chosen at the tetrahedral interstitial site T. The black dots represent Si atoms at their unrelaxed positions, shown merely to establish a coordinate system. Relaxations of the Si atoms cannot be displayed because they are different for different H^+ positions, but are of course included in the calculations. In (a), the contour interval is 0.1 eV. In (b), the energy surface is cut off at 0.3 eV (hence the flat mountain tops) for clarity. Figure from Ref. 9.

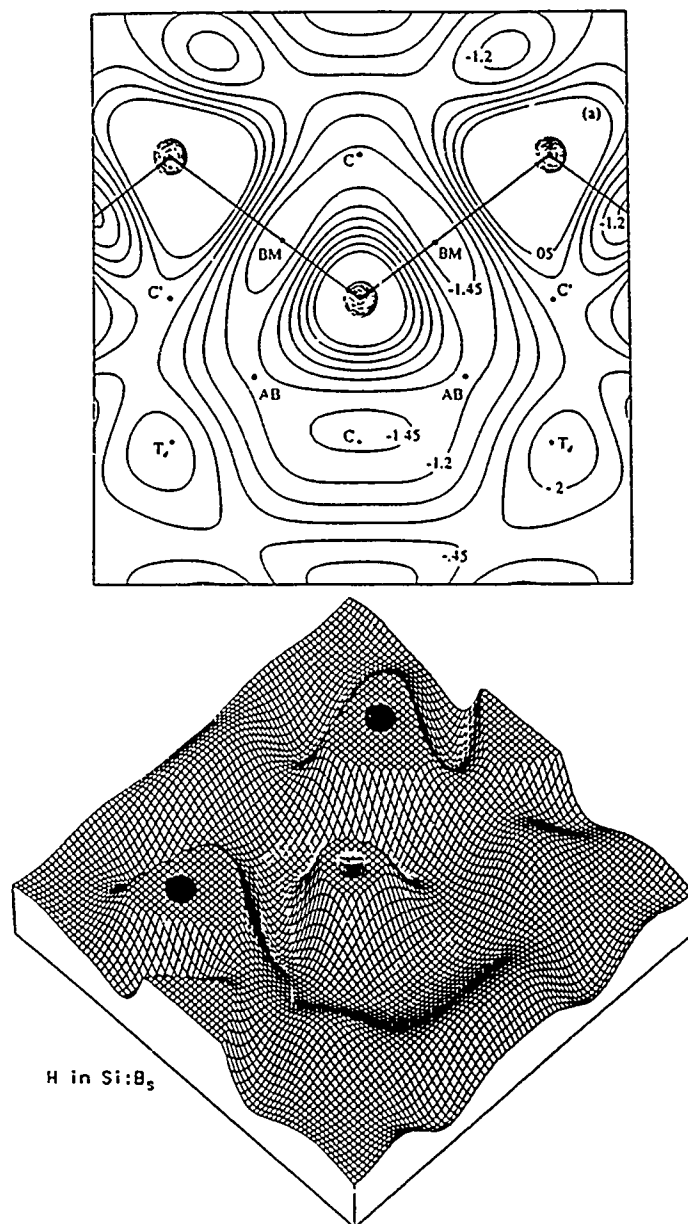


Fig. 3. Contour plot (a) and perspective plot (b) of the total-energy surface for a hydrogen atom in the vicinity of a substitutional boron impurity in Si. A (110) plane containing a chain of atoms is shown. In (a), the central black dot is the boron, the others are Si positions. In (b), the large black dots designate Si positions, the smaller black dot designates the boron position. The energy surface is cut off (hence the flat regions) for clarity. Figure from Ref. 21.

full relaxation calculations for only a few positions. An example of the resulting total-energy surfaces is shown in Fig. 2 for the positively charged state of H. The surfaces shown correspond to H being restricted in the (110) plane. Such total-energy surfaces can also be constructed when an impurity atom occupies a substitutional site. Fig. 3 (from Denteneer, Van de Walle and Pantelides²¹) shows an example for H around a boron impurity in Si.

Global total-energy surfaces such as those of Figs. 2 and 3 constitute a powerful tool in qualitatively understanding the diffusion pathways of H and the structure of H-impurity pairs. For example, for H diffusion in an otherwise perfect Si crystal, the total-energy surfaces revealed clearly that H^+ migrates primarily through the high-electron-density bond regions. In contrast, H^- migrates primarily in the low-electron-density channels. In the case of the pairs, controversies about the site occupied by H were resolved with the conclusion that, in the B-H pair, the bond site is the stable site but H can actually move around B with a very small activation energy (~ 0.2 eV). This result was independently obtained from experimental data.²² Furthermore, examination of the global surfaces for several H-impurity pairs has made it possible to understand when the H atom is capable of tunneling around the impurity. The reader can find the details of that fascinating story in Ref. 21.

Soon after the static total-energy surfaces were reported, Buda, Chiarotti, Car and Parrinello¹⁰ reported dynamical first-principles calculations of H^+ in a Si crystal. Their calculations treat the proton and Si ions as classical particles acted upon by the full quantum-mechanical forces of the self-consistently adjusting electron density at finite temperatures. The motion of the proton is monitored over a period of time which allows the determination of the diffusion coefficient. These calculations are the first to yield a diffusion coefficient (entropies and pre-exponential and all) completely from first-principles. The only limitation of the method is that it is practical only at fairly high temperatures at which the diffusing impurity can cover sufficient ground in a period of time that is practical on today's computers. For the same reason, the energy barriers need to be quite small. The results of Buda et al. at three temperatures are shown in Fig. 4. They are in good agreement with old data by van Wieringen and Warmoltz.²³

The next step was very recently taken in the static approach. Bloechl, Van de Walle and Pantelides¹² recognized that the total-energy surfaces of Fig. 2 can be viewed as rigid potential surfaces in which H diffuses. It is then straightforward to adopt a formalism that allows one to calculate the corresponding diffusion coefficient at any temperature. This technique is not limited to small barriers and high temperatures, but it entails some approximations. The resulting diffusion coefficient contains only part of the entropy contributions. It leaves out the part arising from changes in the vibrational frequencies of the *host* atoms as the impurity moves about. For H, these terms can be estimated to be small and, indeed, the final diffusion coefficients are in astounding agreement with the dynamical calculations of Buda et al. as shown in Fig. 4.

Both the dynamical and the static approaches are promising. Their application to the problem of self-diffusion and substitutional impurity diffusion is likely to provide answers to the remaining outstanding questions.

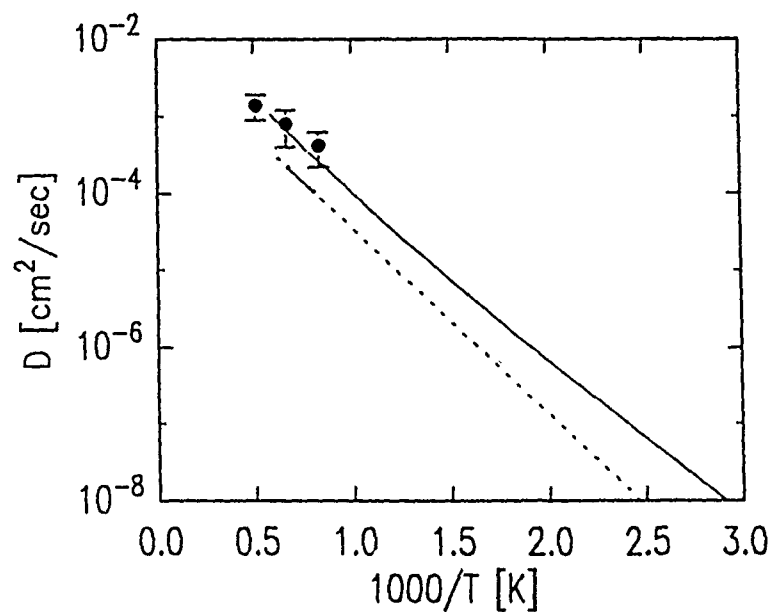


Fig. 4. Diffusion coefficient of H^+ in crystalline Si as function of the inverse absolute temperature. Large dots are the dynamical results of Buda et al. (Ref. 10). The dotted line is the experimental result from Ref. 23 (only the region of the short solid line was actually measured, the rest is extrapolated). The solid line are the "static" results of Ref. 12. Figure from Ref. 12.

CONCLUSIONS

Theory has made big strides in the last ten years. First-principles calculations of point defects can now be carried out with high sophistication and accuracy. Techniques for calculating diffusion coefficients entirely from first-principles are maturing fast. Though many controversies have been resolved, a number of important questions still remain. There is great promise, however, that many more answers will soon be possible.

Acknowledgments: This work was supported in part by the Office of Naval Research under Contract No. N00014-84-0396. The author is greatly indebted to many collaborators who played key roles in different aspects of the work reviewed in this paper, in particular Y. Bar-Yam, P. Bloechl, R. Car, P. J. H. Denteneer, P. J. Kelly, C. S. Nichols, A. Oshiyama, and C. G. Van de Walle.

REFERENCES

1. For a review of work prior to 1978, see S. T. Pantelides, *Rev. Mod. Phys.* **50**, 797 (1978).
2. G. A. Baraff and M. Schluter, *Phys. Rev. Lett.* **41**, 892 (1978).
3. J. Bernholc, N. O. Lipari, and S. T. Pantelides, *Phys. Rev. Lett.* **41**, 895 (1978).
4. For reviews of some of this work, see S. T. Pantelides, in *Deep Centers in Semiconductors* edited by S. T. Pantelides, (Gordon and Breach, New York, 1986), p. 1.
5. R. Car, P. J. Kelly, A. Oshiyama, and S. T. Pantelides, *Phys. Rev. Lett.* **52**, 1814 (1984); *ibid.* **54**, 360 (1985).
6. Y. Bar-Yam and J. Joannopoulos, *Phys. Rev. Lett.* **52**, 1129 (1984); *J. Electron. Mater.* **14a**, 261 (1985).
7. K. C. Pandey, *Phys. Rev. Lett.* **57**, 2287 (1986).
8. C. S. Nichols, C. G. Van de Walle, and S. T. Pantelides, *Phys. Rev. Lett.* **62**, 1049 (1989); *Phys. Rev. B* **40**, 5484 (1989).
9. C. G. Van de Walle, Y. Bar-Yam, and S. T. Pantelides, *Phys. Rev. Lett.* **60**, 2761 (1988); C. G. Van de Walle, P. J. H. Denteneer, Y. Bar-Yam, and S. T. Pantelides, *Phys. Rev. B* **39**, 10791 (1989).
10. F. Buda, G. L. Chiarotti, R. Car, and M. Parrinello, *Phys. Rev. Lett.* **63**, 294 (1989).
11. For a review of experimental data and theoretical understanding of diffusion in Si as it evolved in the 1970's and early 1980's, see W. Frank, U. Goesele, H. Mehrer, and A. Seeger, in *Diffusion in Crystalline Solids*, edited by G. E. Murch and A. S. Nowick, (Academic, Orlando, 1984), p. 63.
12. P. Blochl, C. G. Van de Walle, and S. T. Pantelides, to be published.
13. See, e.g., review articles in *Atomic Diffusion in Semiconductors*, edited by D. Shaw, (Plenum, London, 1973).
14. See S. T. Pantelides, in *Materials Issues in Silicon Integrated Circuit Processing*, edited by M. Wittmer, J. Stimmel, and M. Strathman, Materials Research Society Symposia Proceedings Volume 71, p 147.
15. J. A. Van Vechten, *J. Electron. Mater.* **14a**, 293 (1985).
16. S. Dannefaer, P. Mascher and D. Kerr, *Phys. Rev. Lett.* **56**, 2195 (1986).
17. P. M. Fahey, private communication
18. P. M. Fahey, P. B. Griffin, and J. D. Plummer, *Rev. Mod. Phys.* **61**, 289 (1989).
19. C. T. Sah, J. Y. C. Sun, and J. J. T. Tzou, *Appl. Phys. Lett.* **43**, 204 (1983).
20. *Hydrogen in Silicon*, edited by J. I. Pankove and N. M. Johnson, to be published.
21. P. J. H. Denteneer, C. G. Van de Walle, and S. T. Pantelides, *Phys. Rev. Lett.* **62**, 1884 (1989); *Phys. Rev. B* **39**, 10809 (1989).
22. M. Stavola, K. Bergman, S. J. Pearton, and J. Lopata, *Phys. Rev. Lett.* **61**, 2786 (1988).
23. A. van Wieringen and N. Warmoltz, *Physica* **22**, 849 (1956).

PRESSURE AND STRAIN EFFECTS ON DIFFUSION

A. Antonelli and J. Bernholc
Department of Physics, North Carolina State University, Raleigh, NC 27695

ABSTRACT

We have investigated, via parameter-free calculations, the effects of hydrostatic and nonhydrostatic strains on the energetics of defect formation and self-diffusion in silicon. The three microscopic mechanisms, vacancy, interstitial, and concerted exchange, have very similar activation enthalpies at zero pressure but exhibit different behavior with hydrostatic pressure. Our results suggest that experiments performed at different pressures can determine the relative contributions of each of these mechanisms. The calculations also show that the neutral Si vacancy has a negative relaxation volume, with the nearest neighbors of the vacancy relaxing inwards, in contrast to the Si (111) surface. Large nonhydrostatic strains, which are present in e.g. Si/Ge_xSi_{1-x} pseudomorphic heterostructures, substantially reduce the formation energy of the tetrahedral interstitial, but do not affect the formation energy of the vacancy. These findings suggest that, aside from being another useful tool for the investigation of self-diffusion in Si, nonhydrostatic strain may significantly affect annealing and impurity diffusion in strained heterostructures. In particular, the interstitial-assisted impurity diffusion may proceed more rapidly in Si lattice-matched to Ge_xSi_{1-x}, but be slowed down in Ge_xSi_{1-x} lattice-matched to Si. The compressed Ge_xSi_{1-x} layers may thus act as diffusion barriers for impurities diffusing with help of native interstitials, such as B or P.

INTRODUCTION

The microscopic understanding of self-diffusion in silicon remains a controversial issue, despite extensive experimental and theoretical efforts. Various microscopic mechanisms have been proposed, but their relative importance has not yet been determined. Experimental measurements using different techniques have shown that the self-diffusion activation energy varies from 4.1 to 5.1 eV in the temperature range of 1100 to 1500 K [1]. Native defects are the natural candidates to mediate self-diffusion. Since it is known experimentally that the concentration of complex defects in Si is negligible [2] only simple defects need to be considered. Theoretical studies [3,4] have shown that the vacancy and interstitial mechanisms have very similar activation energies, both within the experimentally measured range. More recently, Pandey [5] proposed the concerted exchange mechanism, which has an activation energy similar to the ones of the defect mechanisms. Until now, however, both theoretical approximations and experimental uncertainties have precluded the determination of the relative contributions of each of these mechanisms to the self-diffusion process.

Hydrostatic pressure has long been used to investigate diffusive processes in metals and ionic compounds. Several experimental results can be found in the literature from over twenty years ago [6]. Due to experimental difficulties, however, the first studies of pressure effects on self-diffusion in germanium [1] and silicon [7], and on diffusion of As in silicon [8], have been reported only recently.

In recent years there has been an increasing interest in the study and development of Si/Ge heterostructures, which can be integrated directly with the existing Si devices. The presence of large nonhydrostatic strains, due to the lattice parameter mismatch between Si and Ge, poses important questions concerning its effects on diffusive processes in such heterostructures. On the other hand, Manda et al [9] studied nonhydrostatic strain effects on the diffusion of As and B in silicon and found no measurable effects up to the yield point of silicon. However, the yield point of Si corresponds to a stress of 10 bars, which is three orders of magnitude smaller than those found in Si/Ge heterostructures.

At high temperatures, the self-diffusion coefficient is given by the Arrhenius rate law

$$D_{sd} = D_0 \exp(-\Delta H_{sd}/kT), \quad (1)$$

where ΔH_{sd} is the activation enthalpy and the prefactor D_0 depends on the activation entropy. For mechanisms involving defects, the activation enthalpy is the sum of the formation enthalpy ΔH_f and the migration enthalpy ΔH_m . For the concerted exchange mechanism, the activation enthalpy is given by the difference between the energy of the atomic configuration corresponding to the saddle point and the energy of the perfect crystal.

CALCULATIONS

The results were obtained by parameter-free total energy calculations using the local density approximation. They were carried out in supercells corresponding to 16 and 32 atoms in the perfect crystal. A comparison between the results of 16- and 32-atom calculations showed that the 32-atom results were converged with respect to supercell size. All the results presented here have been obtained with the 32-atom supercell. Nonlocal norm-conserving pseudopotentials [10] were employed in the calculations, and the electronic wave functions were expanded in plane waves with kinetic energies up to 6 Ry. Plane waves with kinetic energies up to 12 Ry were included via Löwdin's perturbation theory. Convergence tests concerning the basis set were carried out by enlarging the cutoffs to 8 Ry and 16 Ry, respectively. Only negligible changes in the pressure and strain effects were observed.

HYDROSTATIC PRESSURE

We discuss first the process of formation of a native defect in a crystal and the effects of external pressure on its formation enthalpy. In a dislocation-free crystal, when a vacancy is created an atom leaves its site on the crystalline lattice and migrates to the surface. Therefore, the volume of the crystal increases by one atomic volume. When an interstitial is created one atom leaves the surface and migrates to an interstitial site. In this case, the volume of the crystal decreases by one atomic volume. When external pressure is applied, the work associated with the change in volume must be considered in order to determine the formation enthalpy of the defect. In order to obtain the formation enthalpy, we first calculate the formation energy of the defect at a constant lattice parameter. The formation enthalpy is obtained from [11]

$$\Delta H_f = \Delta E_f + P\Delta V_0 + T(\alpha/\kappa_T)\Delta V_P, \quad (2)$$

where ΔE_f is the internal formation energy at a given pressure P and ΔV_0 is plus or minus one atomic volume, for the vacancy and the interstitial formation, respectively. The last term in (2) is due to the difference in the formation entropy at constant volume and the formation entropy at constant pressure, where T is the absolute temperature, α is the coefficient of thermal expansion, κ_T is the isothermal compressibility, and ΔV_P is the variation in volume of the crystal upon the formation of the defect at constant pressure. For Si, this term is of the order of 10^{-2} eV at high temperatures and therefore negligible when compared to the first two terms.

Since in the concerted exchange mechanism there is no migration of atoms to or from the surface of the crystal, the pressure dependence of the activation enthalpy is given by that of the activation energy only.

In Figs. 1(a) and 1(b) we show the pressure dependence of the formation energy ΔE_f and the formation enthalpy ΔH_f of the neutral interstitial in the tetrahedral (I_T) and in the bond-centered (I_{BC}) configurations, respectively. These two configurations participate in a very important path for interstitial diffusion at high temperatures. The importance of this path stems

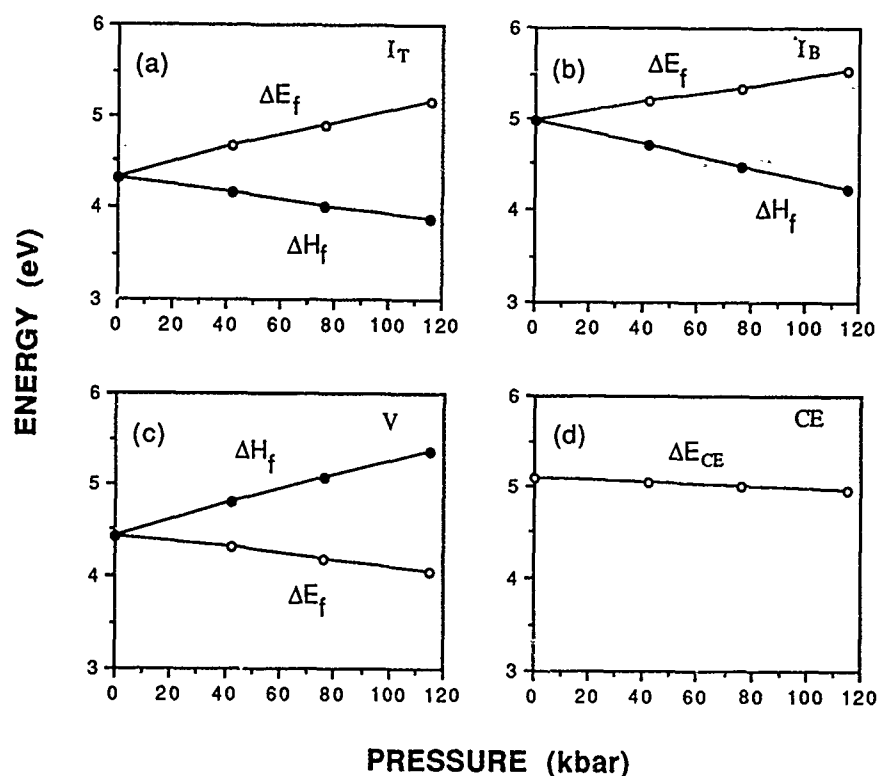


Figure 1. Pressure effects on the formation energy (ΔE_f) and formation enthalpy (ΔH_f) of (a) the neutral tetrahedral interstitial; (b) the neutral bond-centered interstitial; (c) the neutral vacancy; and (d) the energy of the saddle point of the concerted exchange mechanism relative to the ground state of the system.

from the fact that it involves exchange with atoms at lattice sites and therefore contributes to self-diffusion [3]. For both I_T and I_B the formation energy increases with pressure. The formation enthalpy, however, decreases with pressure because the volume term $P\Delta V_0$, which is negative in this case, overcomes the increase in the formation energy. Since the neutral interstitial in the bond-centered configuration is the saddle point of this path [3,4], the activation enthalpy for self-diffusion via interstitials decreases substantially with pressure. Fig 1(c) shows the variation of the formation energy and the formation enthalpy with pressure for the neutral vacancy (V). For the vacancy, the formation energy decreases with an increasing pressure. However, the volume term (positive in this case) is again dominant, and the formation enthalpy increases with pressure. Since the measured migration barrier for vacancy diffusion in Si is 0.45 eV [12], which is small when compared to its formation energy, the pressure dependence of this mechanism is mainly determined by the variation of its formation enthalpy with pressure. Fig 1(d) depicts the pressure dependence of the activation enthalpy of the concerted exchange mechanism (CE). It shows a very weak dependence on pressure, decreasing by only 0.12 eV in the range of pressure from 0 to 115 kbar. We have also carried out calculations of the pressure effects on charged defects. We found trends similar to those of the neutral defects [13].

In the experimental studies by Aziz et al [7] on the pressure dependence of self-diffusion in Si, a tenfold increase in the self-diffusion coefficient was observed when the pressure was increased to 35 kbar. However, since these experiments were carried out at only one temperature (1000° C) it is not possible to extract the variation of the activation enthalpy with pressure from the

experimental data, because the prefactor D_0 may also change with pressure. For example, the experiments studying the pressure effects on the diffusion of As in silicon [8] found a sizable variation of D_0 with pressure. Thus we cannot compare the present results to those of Ref. [7].

The defect formation volume, i.e. the change in the volume of the crystal due to the formation of a defect, is given by $(\partial \Delta G_f / \partial P)_T$, where ΔG_f is the Gibbs formation energy at constant pressure. Since the Helmholtz free energy of a process at constant volume (constant lattice parameter) is equal to its Gibbs free energy at constant pressure [11], the formation volume at the low-pressure limit and zero temperature can be written as

$$\Delta V_f = (\partial \Delta E_f / \partial P)_T + \Delta V_0. \quad (3)$$

The first term in (3) is due to the volume relaxation of the crystal following the creation of the defect. As in (2), ΔV_0 accounts for the atom that is placed at (removed from) the surface. In the case of the neutral vacancy, the calculated relaxation volume is -5 \AA^3 . The negative sign occurs because the formation energy of the vacancy decreases with pressure (see Fig. 1c). In a Si crystal, the volume occupied by a Si atom is 20 \AA^3 . Therefore, the calculated formation volume of the neutral vacancy is 15 \AA^3 .

It is well known from the elasticity theory that the volume relaxation of the crystal due to the formation of a point defect is mainly determined by the local changes in the volume of the region surrounding the defect. In fact, the present calculations show that the nearest neighbors of the neutral vacancy relax radially inwards by 3% of a bond length, which is equivalent to a reduction of 4.9 \AA^3 in the region surrounding the vacancy. This inwards relaxation is counter-intuitive, since by analogy with the Si (111) surface one would expect an outwards relaxation [14]. It is the result of the interaction of the dangling bonds across the vacancy cavity. A more recent calculation also found an inwards relaxation [15]. To our knowledge, no experimental studies of the formation volume of the vacancy in Si have yet been reported. An experimental study of the activation volume for the annealing of E centers (vacancy-phosphorus pairs) [16] suggests a volume of formation of 10 \AA^3 for these centers. Since the isolated vacancy and the E center are expected to have formation volumes of similar magnitude, our result is in qualitative agreement with the experimental data.

The present results show that experimental studies of pressure effects carried out at various pressure and temperature ranges can determine the nature and predominance of microscopic mechanisms that mediate self-diffusion in silicon. If several mechanisms are simultaneously operative in the same temperature range, which can only occur if their activation enthalpies differ by a few kTs, an increasing non-linearity in the Arrhenius plot should be observed, because the three mechanisms have distinct pressure dependencies.

NONHYDROSTATIC STRAIN

We have investigated the effects of nonhydrostatic strain in Si pseudomorphically grown on a $\text{Ge}_x\text{Si}_{1-x}$ alloy in the (001) direction. The lattice parameter of the strained Si in the plane parallel to the interface, a_{\parallel} , is constrained, by pseudomorphic growth, to be equal to the a_{\parallel} of the $\text{Ge}_x\text{Si}_{1-x}$ alloy. It has been shown [17] that the lattice parameter of the strained Si in the direction perpendicular to the interface is given by the elasticity theory as

$$a_{\perp} = a_{\text{Si}} [1 - D_{001} (a_{\parallel} / a_{\text{Si}} - 1)] \quad (3a)$$

$$D_{001} = 2(c_{12} / c_{11}), \quad (3b)$$

where a_{Si} is the Si equilibrium lattice parameter and c_{11} and c_{12} are Si elastic constants. The supercell calculations were carried out for strained bulk Si with a_{\parallel} determined by Ge content and Vegard's law and a_{\perp} determined by eq. (3a).

Since the components of the strain depend linearly on the lattice parameters, we plot the

formation energies as functions of lattice parameter $a_{||}$, which depends linearly on the fraction x of Ge present in the alloy. Fig. 2(a) shows the strain dependence of the formation energy of the neutral tetrahedral interstitial. Its formation energy decreases significantly with an increasing strain or an increasing percentage of Ge in the alloy. Fig 2(b) shows that the formation energy of the neutral vacancy is not affected by the strain. It remains practically constant in the entire range of variation of $a_{||}$, from pure Si ($x=0$) to pure Ge ($x=1$).

The results reveal that nonhydrostatic strain in Si strongly affects self-diffusion via interstitials, but not via vacancies. Nonhydrostatic strain can thus also be used as a probe to investigate self-diffusion mechanisms in Si.

The results also suggest that the properties of Si which depend on the diffusion of interstitials may change when the material is in a strained heterostructure, due to the sizable decrease in the formation energy of interstitials. Annealing is likely to be enhanced by the tensile strain. It is currently believed that the diffusion of B, P, and As in Si is mediated by interstitials [18,19]. Therefore, it is possible that the higher concentration of interstitials in the strained Si may enhance the diffusion of B, P, and As. This would be desirable for in-diffusion of these impurities, but it may require a lower temperature processing of the strained structures. Since the formation energy of the tetrahedral interstitial varies linearly with strain (cf. fig 2a), one can expect that the compressive strain occurring in the pseudomorphic growth of $\text{Ge}_x\text{Si}_{1-x}$ on Si will result in a significant increase in the formation energies of interstitials and lead to a decrease in the diffusion of B, P, and As. Strained $\text{Ge}_x\text{Si}_{1-x}$ layers could thus act as a diffusion barriers during high temperature processing of devices.

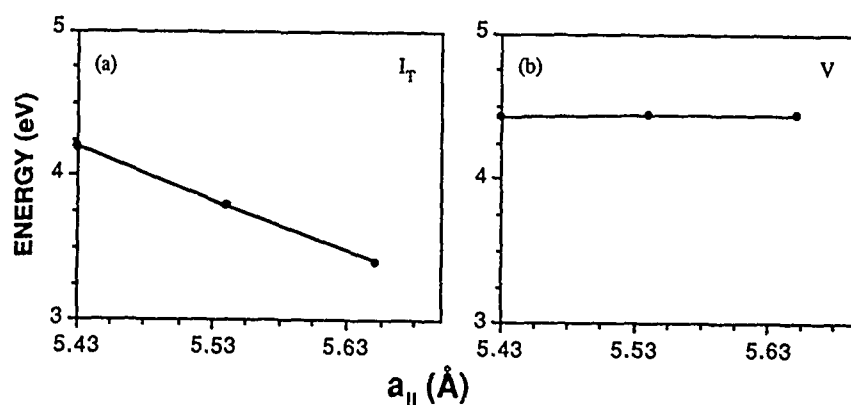


Figure 2. The effects of strain in pseudomorphic $\text{Si}/\text{Ge}_x\text{Si}_{1-x}$ on the formation energy of (a) the neutral tetrahedral interstitial; and (b) the neutral vacancy.

SUMMARY AND CONCLUSIONS

We have found, via first-principles calculations, that the various self-diffusion mechanisms respond differently to hydrostatic pressure and/or nonhydrostatic strain. When a hydrostatic pressure is applied to the crystal, the activation enthalpy for the interstitial mechanism decreases with pressure, while it increases for the vacancy mechanism and remains approximately constant for the concerted exchange. These results can be understood qualitatively by noting that the pressure-induced changes in the formation energies of native defects and in the saddle point energy of the concerted exchange are relatively small. The pressure-induced changes in the activation enthalpy are thus dominated by the changes in the volume of the crystal resulting from the formation of native defects. Since the formation of an interstitial decreases the volume of the crystal by one atomic volume, the formation of the vacancy increases it by one atomic volume, and the concerted exchange does not affect the volume of the crystal, the above trends follow. As a by-product of the calculations it has also been shown that although the isolated vacancy has a positive formation vol-

ume, the nearest neighbors to the vacancy relax inwards.

Considering non-hydrostatic stresses present in lattice-matched strained heterostructures, we have shown that a lattice expansion in the lateral direction of 1-4% substantially decreases the formation energy of a tetrahedral interstitial in Si, while the formation energy of a vacancy remains practically the same. These results suggest that the annealing of Si pseudomorphically deposited on $\text{Ge}_x\text{Si}_{1-x}$ may proceed at lower temperature. The interstitial-assisted diffusion of impurities may also be enhanced, while the diffusion of these impurities in $\text{Ge}_x\text{Si}_{1-x}$ lattice-matched to Si may be retarded. The compressed $\text{Ge}_x\text{Si}_{1-x}$ layers may thus act as diffusion barriers for impurities diffusing with the help of interstitials, such as B or P.

REFERENCES

1. W. Frank, U. Gösele, H. Mehrer, and A. Seeger, in Diffusion in Crystalline Solids, edited by G. E. Murch and A. S. Nowick (Academic, Orlando, FL, 1985), p. 64.
2. W. Frank and N. A. Stolwijk, in Vacancies and Interstitials in Metals and Alloys, edited by C. Abromeit and H. Wollenberger, Materials Science Forum 15-18 (Trans. Tech. Publications, Aedermannsdorf, Switzerland, 1987), p. 369.
3. R. Car, P. J. Kelly, A. Oshiyama, and S. T. Pantelides, *Phys. Rev. Lett.* **52**, 1814 (1984).
4. Y. Bar-Yam and J. D. Joannopoulos, in Proceedings of the Thirteenth International Conference on Defects in Semiconductors, edited by L. C. Kimerling and J. M. Parsey (The Metallurgical Society, American Institute of Mining, Metallurgical and Petroleum Engineers, New York, 1985), p. 261.
5. K. C. Pandey, *Phys. Rev. Lett.* **57**, 2287 (1986).
6. D. Lazarus and N. H. Nachtrieb, in Solids Under Pressure, edited by W. Paul and D. M. Warschauer (McGraw-Hill, New York, 1963), p. 43.
7. M. J. Aziz, E. Nygren, W. H. Christie, C. W. White, and D. Turnbull, in Impurity Diffusion and Gettering in Silicon, edited by R. B. Fair, C. W. Pearce, and J. Washburn, Materials Research Symposia Proceedings, vol. 36 (Materials Research Society, Pittsburgh, PA, 1985), p. 101.
8. E. Nygren, M. J. Aziz, D. Turnbull, J. M. Poate, D. C. Jacobson, and R. Hull, *Appl. Phys. Lett.* **47**, 105 (1985).
9. M. L. Manda, M. L. Shepard, R. B. Fair, and H. Z. Massoud, in Impurity Diffusion and Gettering in Silicon, edited by R. B. Fair, C. W. Pearce, and J. Washburn, Materials Research Symposia Proceedings, vol. 36 (Materials Research Society, Pittsburgh, PA, 1985), p. 71.
10. D. R. Hamann, M. Schluter, and C. Chiang, *Phys. Rev. Lett.* **43**, 1494 (1979).
11. A. V. Chadwick and H. R. Glyde, in Rare Gas Solids, edited by M. L. Klein and J. A. Venables (Academic, London, 1977), Vol II, p. 1151; G. Jacucci and R. Taylor, *J. Phys. F* **9**, 1489 (1979).
12. G. D. Watkins, J. T. Troxell, and A. P. Chatterjee, in Proceedings of the International Conference on Defects and Radiation Effects in Semiconductors, edited by J. H. Albany, Institute of Physics Conference Series, Vol. 46 (Institute of Physics, London, 1979), p. 16.
13. A. Antonelli and J. Bernholc, *Phys. Rev. B* **40**, 10463 (1989).
14. G. A. Baraff, E. O. Kane, and M. Schluter, *Phys. Rev. B* **21**, 5662 (1980); U. Lindfelt, *Phys. Rev. B* **28**, 4150 (1983); M. Scheffler, J. P. Vigneron, and G. B. Bachelet, *Phys. Rev. B* **31**, 6541 (1985).
15. P. J. Kelly, R. Car, and S. T. Pantelides, in Defects in Semiconductors, edited by H. J. Bardeleben, Materials Science Forum 10-12 (Trans. Tech. Publications, Aedermannsdorf, Switzerland, 1986), p. 115.
16. C. E. Barnes and G. Samara, in Microscopic Identification of Electronic Defects in Semiconductors, edited by N. M. Johnson, S. G. Bishop, G. D. Watkins, Materials Research Society Symposia Proceedings, Vol. 46 (Materials Research Society, Pittsburgh, PA 1985), p. 471.
17. C. G. Van de Walle and R. M. Martin, *Phys. Rev. B* **34**, 5621 (1986).
18. P. Fahey, G. Barbuscia, M. Moslehi, and R. W. Dutton, *Appl. Phys. Lett.* **46**, 784 (1985).
19. C. S. Nichols, C. G. Van de Walle, and S. T. Pantelides, *Phys. Rev. B* **40**, 5484 (1989).

LOW-TEMPERATURE DIFFUSION OF DOPANTS IN SILICON

P. FAHEY AND M. WITTMER

IBM T. J. Watson Research Center, Yorktown Heights, New York 10598

ABSTRACT

It has been reported that diffusion of substitutional dopant atoms in silicon occurs during the formation of transition-metal silicides at temperatures below 300°C. By observing the diffusion enhancements of buried marker layers of Sb-, Ga-, Ge-, and B-doped silicon layers, we provide solid experimental evidence that the diffusion enhancement induced by Pd₂Si formation at low temperatures is due to point defects generated by the silicide reactions. Diffusion enhancement is observed at temperatures as low as 200°C. We have found the surprising result that diffusion is asymmetric: diffusion occurs preferentially towards the siliciding interface.

1. INTRODUCTION

Silicides are being used at an increasing rate in modern integrated circuit technologies, primarily as contacts, gate materials and interconnect lines. A number of reports in the literature have indicated that silicide reactions generate point defects which are injected into the silicon, inducing dopant diffusion and sometimes shrinking of dislocation loops. Wittmer and Tu [1] showed that dopant diffusion is induced at the surprisingly low temperature of 300°C. In their experiment, dopants implanted at the Si surface are pushed ahead into the substrate by the advancing Pd₂Si interface; this has been termed the "snowplow" effect. Ohdomari et al. [2] have also demonstrated the snowplow effect with Pd₂Si — see [2] for a summary of systems exhibiting the snowplow effect — and in addition found that this silicide reaction resulted in the shrinkage of extrinsic dislocation loops. The shrinkage of extrinsic loops implies the injection of vacancies from the silicide reaction. More recently, Wen et al. [3] demonstrated that formation of TiSi₂ also eliminates extrinsic dislocation loops. Hu [4] has shown that formation of TaSi₂ can enhance the diffusion of buried marker layers of B- and Sb-doped Si and proposed vacancy injection by the silicide reactions as the explanation.

In this study, we have prepared special structures of thin ($\approx 200\text{\AA}$) lightly doped buried marker layers grown at temperatures of about 500°C. These structures are much more sensitive to point-defect changes than conventional structures formed by ion implantation and high-temperature epitaxy. Since the buried marker layers are physically separated from the silicide interface, they are ideally suited to studies of surface point-defect injection phenomena. We have chosen to study the effect of Pd₂Si formation on dopant diffusion. Our specialized structures have allowed us to observe new diffusion phenomena not seen in previous studies.

2. SAMPLE PREPARATION

The special sample structures used in this work consisted of narrow buried marker layers of different dopants formed in silicon by either molecular beam epitaxy or an ultra-high vacuum low temperature epitaxy (LTE) technique [5]. The starting material were oxygen-denuded Czochralski-grown silicon wafers of $\langle 100 \rangle$ orientation, p type, 50 Ωcm resistivity. Buffer layers of about 1000 Å undoped Si were grown first, then a thin layer of typically 200 Å silicon doped with either Sb, Ga, Ge (MBE technique) or B (LTE technique), followed by a thick layer of typically 5000 Å of undoped silicon. After a standard RCA clean the wafers were loaded into an electron gun evaporator and a 2500 Å thick layer of palladium was blanket deposited at room temperature. Subsequently, the wafers were cleaved into small samples which were then annealed in a furnace flushed with Ar of 99.999% purity. The thickness and composition of the silicide layer formed were investigated with Rutherford backscattering spectroscopy (RBS). Transmission electron microscopy was performed on selected samples and electron diffraction confirmed the silicide formed as Pd_2Si . Unreacted Pd as well as Pd_2Si were etched off with aqua regia ($\text{HCl}:\text{HNO}_3 = 3:1$), which does not attack the silicon, prior to profile measurements of the buried dopant profiles by secondary ion mass spectroscopy (SIMS) analysis.

3. RESULTS AND DISCUSSION

Figures 1(a) and 1(b) show typical results for dopant diffusion induced by silicidation of Pd to form Pd_2Si . The initial concentration profiles of Ga- and Sb-doped buried marker layers are indicated by dashed lines. Solid lines show profiles measured after reacting the Pd layer for 1 hr at 300°C. The profiles after silicide formation have been shifted to the right by an amount equal to the thickness of silicon consumed by the silicide reaction in order to demonstrate the magnitude of the asymmetric broadening. The uncertainty in the exact amount of shifting is given by the resolution of the RBS (≈ 50 Å in our case) and the accuracy of the SIMS depth profile. There are two striking features of these results. First, the diffusion of dopants at such low temperatures. (Diffusion has been observed at temperatures as low as 200°C, the lowest temperature studied in these experiments.) Second, the asymmetric diffusion of the buried layers.

Before discussing possible explanations for this highly unusual diffusion behavior, we first summarize other salient results of our study:

1. Diffusion of buried marker layers occurs for Ga-, Ge- and Sb-doped samples grown by MBE and for B-doped samples grown by LTE.
2. The amount of broadening due to diffusion does not correlate directly with the amount of silicide formed. For example, after 15 min at 250°C only 45% of the Pd layer has reacted to form Pd_2Si and yet the amount of broadening is the same as that found after reacting the entire film. Evidently, the reactions responsible for dopant diffusion occur in the beginning of the silicide formation and do not continue for the entire time of silicidation. We have found that at 200°C the silicon reaction rate is slow enough that increased broadening with time can be observed.

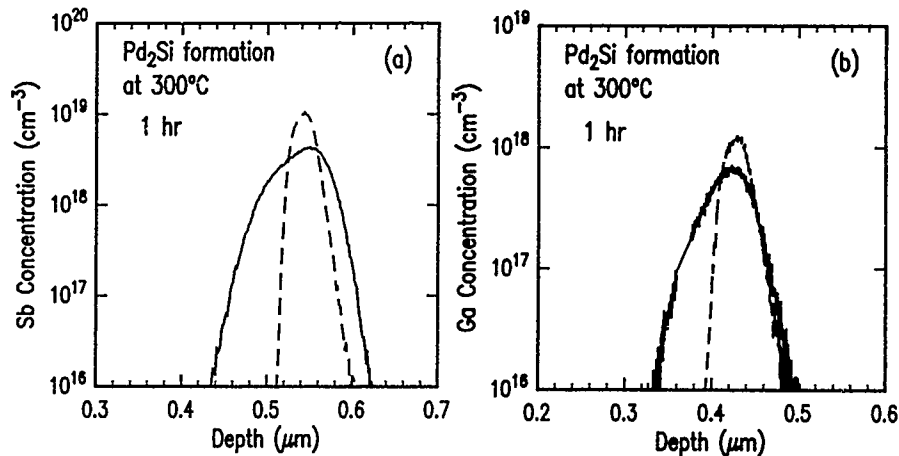


FIG. 1: Pd_2Si formation at 300°C for 1 hr. Asymmetric diffusion is induced in (a) Sb-doped and (b) Ga-doped buried marker layers. Profiles after Pd reaction are shifted to the right by an amount corresponding to the thickness of Si consumed by the silicide formation.

3. Diffusion of the marker layers is not strongly dependent on temperature. Between 250°C and 500°C , profiles measured after reacting the entire Pd film are roughly the same.
4. Some wafers were first annealed at 700°C for 4.5 hr before deposition of Pd; this made no difference in the diffusion effect observed.
5. The material used in this study is the same as that used in separate higher temperature diffusion studies where simple Fickian diffusion was observed to take place [6]. In these studies, symmetric broadening of profiles was observed under equilibrium conditions between 850°C and 1100°C . Symmetric broadening was also observed at 950°C and 1050°C under nonequilibrium conditions in which silicon vacancies or interstitials were injected from the surface by nitridation or oxidation reactions.

Diffusion enhancement of the buried marker layers is strong evidence that point defects are generated at the surface and diffuse into the substrate. The relevant questions are: What type of defects (vacancy or interstitial) are generated? By what mechanism are they generated? How does point-defect generation at the surface lead to asymmetric diffusion of the marker layers? Are these findings consistent with previous high temperature experiments?

The finding by Ohdomari et al. [2] that extrinsic dislocation loops shrink after Pd_2Si formation is evidence that vacancies are generated by this silicide reaction. In this paper we do not address the question of the process by which vacancies might be generated. To provide a sound explanation for asymmetric profile broadening, we should first examine why asymmetric diffusion did not occur in previous studies that used the same material and where point defects are also generated at the surface (see point 5. above). The most obvious difference between this and previous buried marker studies is the low temper-

ature of diffusion in this study. At these low temperatures, the marker layers are extrinsically doped (i.e., carrier concentrations exceed the intrinsic carrier concentration) whereas for the higher temperatures in previous studies, diffusion always occurs under intrinsic doping conditions. The presence of internal electric fields brought about by extrinsically doped layers can greatly affect the diffusion of charged point defects. Aside from extrinsic doping effects, there is also the increased tendency of point defects to be trapped by dopant atoms at low temperatures (a point discussed in more detail below). Also, the levels of supersaturation of point defects are orders of magnitude higher in the present experiments compared to previous higher temperature studies.

Asymmetric diffusion such as that shown in Fig. 1 has never been observed before in Si. Perhaps the most obvious explanation for this diffusion behavior is one involving a "vacancy wind" effect. In this picture, a net flux of vacancies away from the siliciding surface results in a net flux of substitutional dopant atoms (and silicon atoms as well) in the opposite direction. For these situations, diffusion is not modeled by a simple Fick's Law description of diffusion but instead is usually treated by a linear transport approach using the Onsager relations (see for example the article by Anthony [7]). There is, however, a serious problem with the vacancy wind explanation. In order for dopant diffusion to be induced in a direction opposite to the vacancy flux, there must be only weak binding between dopants and vacancies. In the case of strong binding, the dopants and vacancies will diffuse in the same direction. Experimental results and theoretical predictions agree that there is strong binding between dopants and vacancies. Hirata et al. [8] monitored the annealing behavior for dopant vacancy pairs formed by low temperature irradiation. In the temperature range 100 - 230°C it was found that the binding energies, E^b , for PV, AsV, SbV and BiV were greater than 1.04 eV, 1.23 eV, 1.44 eV and 1.64 eV, respectively. Total energy calculations by Car et al. [9] put the binding energy for PV at 2.25 eV.

We have attempted to simulate asymmetric diffusion with a model that assumes no wind effect but does include strong binding between dopants and vacancies. The basis for the model is the fact that under a strong binding assumption, it is predicted that at any instant of time there are substantially more vacancies associated with dopant atoms than there are vacancies freely diffusing through the lattice, even for low dopant concentrations [10]. For a given dopant A, this condition can be stated as

$$C_{AV} \gg C_V, \quad [1]$$

where C_{AV} is the concentration of dopant vacancy pairs and C_V is the concentration of free vacancies. In a kinetic picture, Eq. [1] implies that a vacancy diffusing through the bulk spends most of its time next to a dopant atom. It can be shown in general [10] that the effective vacancy diffusivity obeys the inequality

$$D_V \frac{C_V}{C_V + C_{AV}} \leq D_V^{\text{eff}} \leq D_V, \quad [2]$$

where D_V is the diffusivity of free vacancies.

In this model, vacancies generated at the surface quickly move to the buried layer where their diffusion is substantially reduced by trapping at dopant atoms. As the diffusion front of the vacancies moves through the doped marker layer, diffusion is first induced in the part of the profile closest to the surface and eventually progresses through the layer. It is possible with this model to simulate asymmetric diffusion and still assume a

simple Fick's Law behavior for diffusion flux. (It should also be mentioned that the model results are exactly the same if it is assumed that interstitial-type defects are involved instead of vacancies.) As mentioned previously, the real situation is considerably more complicated because of the effects of internal electric fields on charged point defects. One problem with our model is that strong binding is an essential feature, and yet for the case of Ge, which exhibits enhanced diffusion, no strong binding is expected between Ge and V. A valid test for our model centers on its prediction that for a structure with two doped layers, one grown above the other, the deeper layer will initially experience less diffusion because of the trapping of point defects in the layer closer to the surface. We are in the process of studying diffusion in such structures.

As a final note, we comment briefly on the results of previous experiments [6] that have shown under vacancy injection conditions diffusion of B and Ga is retarded while diffusion of Ge and Sb is enhanced. In comparison, we find enhanced diffusion for all these elements. There are several explanations for our results that are consistent with previous experiments. One could always make the ad hoc hypothesis that both interstitials and vacancies are injected by Pd_2Si formation. Alternatively, assuming that the Pd_2Si reaction generates only vacancies, one could suppose that B and Ga diffusion are dominated by a vacancy mechanism at low temperature and an interstitial-type mechanism at higher temperatures. It should also be realized that even for a dopant with a very small vacancy component of diffusion, enhanced diffusion will occur under vacancy injection if the supersaturation level is high enough; in this experiment the supersaturation levels are obviously extraordinarily high.

4. CONCLUSIONS

We have discovered that reaction of Pd to form Pd_2Si induces diffusion of buried marker layers of doped Si at temperatures as low as 200°C . It is found that diffusion is asymmetric, with diffusion occurring preferentially towards the siliciding interface. This diffusion effect was observed for Sb-, Ga-, Ge-, and B-doped layers. Silicide-induced diffusion occurs at the beginning of the silicide formation process and does not always continue for the entire time of silicidation. Explanations of the asymmetric diffusion broadening in terms of a vacancy wind effect suffer from the fact that such an explanation requires only weak binding between dopants and vacancies, a requirement contrary to previous experimental studies and theoretical predictions. We have provided a simple model that can predict asymmetrical broadening based on trapping of point defects at low temperatures; however, this model does not explain diffusion of Ge-doped layers well since Ge is expected to have much weaker interactions with point defects compared to dopants. The results of these experiments are not easily explained by standard theories. The Pd_2Si reactions offer the opportunity to study dopant/point-defect reactions in a new temperature regime.

ACKNOWLEDGMENT

We are grateful to S.S. Iyer for providing the MBE grown wafers, B. Meyerson for the LTE grown wafers, and J. Scilla for SIMS analysis.

REFERENCES

1. M. Wittmer and K.N. Tu, *Phys. Rev. B* **29**, 2010 (1984) and references therein.
2. I. Ohdomari, K. Konuma, M. Takano, T. Chikyow, H. Kwarada, J. Nakanishi, and T. Ueno, *Mat. Res. Soc. Symp. Proc.*, Vol. 54, p. 63 (1986).
3. D. S. Wen, P. L. Smith, C. M. Osburn, and G. A. Rozgonyi, *Appl. Phys. Lett.*, **51**, 1182 (1987).
4. S. M. Hu, *Appl. Phys. Lett.*, **51**, 308 (1987).
5. B. S. Meyerson, F. K. LeGoues, T. N. Nguyen, and D. L. Harnae, *Appl. Phys. Lett.*, **50**, 113 (1987).
6. P. Fahey, S. S. Iyer, and G. J. Scilla, *Appl. Phys. Lett.*, **54**, 843 (1989); and unpublished results.
7. T. R. Anthony in "Diffusion in Solids," edited by A. S. Nowick and J. J. Burton (Academic, New York, 1975), p. 353.
8. M. Hirata, M. Hirata, and H. Saito, *J. Phys. Soc. Jpn.*, **27**, 405 (1969).
9. R. Car, P. J. Kelly, A. Oshiyama, and S. Pantelides, *Phys. Rev. Lett.*, **54**, 360 (1985).
10. P. M. Fahey, P. B. Griffin, and J. D. Plummer, *Rev. Mod. Phys.*, **61**, 289 (1989).

DETERMINATION OF DIFFUSION PARAMETERS FOR ARSENIC

MICHAEL HEINRICH, MATTHIAS BUDIL AND HANS W. PÖTZL
 TU-Wien, E3598, Gußhausstraße 27-29, A-1040 Wien, Austria

ABSTRACT

This paper deals with an analysis of the oxynitridation and direct nitridation experiments of Fahey et al. (1984[1]). The inconsistencies in the evaluation of the fractional component of diffusion for arsenic are discussed. Using a recently developed diffusion model an explanation for the diffusion data for arsenic is given. The standard equation $\frac{\langle C_{As(I,V)} \rangle}{C_{As(I,V)}} = \frac{\langle C_{(I,V)} \rangle}{C_{(I,V)}}$ for analyzing diffusion under nonequilibrium conditions is shown to lead to erroneous results. A consistent treatment must account for the concentrations of arsenic, point defects and arsenic point defect pairs. Pair formation kinetics must be included. Values are presented for the diffusion constants D_{IAs} , D_{VAs} and the reaction constants k_{IAs} , k_{VAs} depending on the fractional interstitial component of diffusion f_I^{As} .

INTRODUCTION

Modeling the redistribution of impurities in silicon is still a major task. Diffusion modeling has advanced due to the implementation of point defect and pair formation kinetics (Budil[2], Orlowski[3], Mulvaney[4], Morehead[5]) putting the models on a sound physical basis, but increasing the number of parameters at the same time. Budil[2] introduced separate treatments of dopant, dopant point defect pairs and point defects. The model needs three equations to be solved for the dopant and dopant point defect pairs, and two equations for the point defects. Compared with earlier models diffusion and reaction constants have been introduced for dopant point defect pairs, which are not defined a priori. This paper deals with the analysis of the oxynitridation and nitridation experiments of Fahey[1] and the evaluation of the diffusion and reaction constants for arsenic at 1100°C.

NITRIDATION AND OXYNITRIDATION EXPERIMENTS

It was found by Fahey[1] that nitridation of a SiO_2 layer enhances diffusion of interstitial-mediated diffusion type dopants like P and As, while direct nitridation of the Si surface enhances Sb-diffusion. Diffusion of As is enhanced in both cases - significantly during interstitial injection and slightly during vacancy injection. Generally, those data are explained by an excess generation of interstitials at the surface during the oxynitridation process and an excess generation of vacancies during direct surface nitridation. Both kinds of point defects diffuse into the bulk, where they enhance or retard the diffusivity of the dopants. Fahey used FZ (100) oriented, n-type (p-doped), silicon. Arsenic, Phosphorus, Boron and Antimony were implanted to a dose of $5 \cdot 10^{13} \text{ cm}^{-2}$. Wafers were annealed, a thin thermal oxide was grown, and 600Å of Si_3N_4 was deposited on the sample surface. Lithographic patterning produced three different regions on the same wafer corresponding to three different surface conditions during nitridation: an area in which the SiO_2/Si_3N_4 films remain, which act as a blocking layer to nitridation reactions at the surface, an area in which only an SiO_2

layer remains to obtain conditions of oxynitridation and an area in which all layers were removed to allow direct nitridation of the surface. Nitridations were performed at 1100°C in 100% NH_3 . Spreading resistance measurements were used and diffusivity enhancement was calculated (see Figs. (5,6) for experimental data).

An analysis was added to the experiments. The diffusivity under inert conditions can be expressed as

$$D_{As}^* = D_{AsI}^* + D_{AsV}^* \quad (1)$$

with D_{AsI}^* being the interstitial part of the diffusivity and D_{AsV}^* being the vacancy part. Diffusivity under nonequilibrium conditions can be written as (2). The value of f_I^{As} can be extracted (3).

$$\frac{\langle D_{As} \rangle}{D_{As}^*} = (1 - f_I^{As}) \frac{\langle C_{AsV} \rangle}{C_{AsV}^*} + f_I^{As} \frac{\langle C_{AsI} \rangle}{C_{AsI}^*} \quad (2)$$

$$f_I^{As} = \left[\frac{\langle D_{As} \rangle}{D_{As}^*} - \frac{\langle C_{AsV} \rangle}{C_{AsV}^*} \right] \div \left[\frac{\langle C_{AsI} \rangle}{C_{AsI}^*} - \frac{\langle C_{AsV} \rangle}{C_{AsV}^*} \right] \quad (3)$$

$\langle C_{As(I,V)} \rangle$ denotes the time-averaged pair concentration during the nonequilibrium process such as nitridation and oxynitridation and $C_{As(I,V)}^*$ denotes pair concentration during equilibrium conditions, hence $\frac{\langle C_{As(I,V)} \rangle}{C_{As(I,V)}^*}$ denotes the pair supersaturation. Because of the impossibility of gaining any information on the behaviour of the dopant-point defect pair concentrations after the diffusion process has finished, the assumption

$$\frac{\langle C_{As(I,V)} \rangle}{C_{As(I,V)}^*} = \frac{\langle C_{(I,V)} \rangle}{C_{(I,V)}^*} \quad (4)$$

was introduced. Using this assumption the nonequilibrium enhancement becomes

$$\frac{\langle D_{As} \rangle}{D_{As}^*} = (1 - f_I^{As}) \frac{\langle C_V \rangle}{C_V^*} + f_I^{As} \frac{\langle C_I \rangle}{C_I^*} \quad (5)$$

This equation can be used to express f_I^{As}

$$f_I^{As} = \left[\frac{\langle D_{As} \rangle}{D_{As}^*} - \frac{\langle C_V \rangle}{C_V^*} \right] \div \left[\frac{\langle C_I \rangle}{C_I^*} - \frac{\langle C_V \rangle}{C_V^*} \right] \quad (6)$$

As phosphorus is believed to diffuse almost entirely by interstitials, the phosphorus enhancement can be used to set a lower boundary for the interstitial supersaturation. This lower boundary in turn can be used to determine an upper boundary for f_I^{As} . Changing the role of interstitials and vacancies, a lower boundary for f_I^{As} can be derived, too. Fahey concluded from his data

$$0.41, 0.44, 0.40 \leq f_I^{As} \leq 0.29, 0.38, 0.43 \quad (7)$$

that selfconsistence cannot be achieved.

SIMULATION

We simulated both nitridation and oxynitridation by using the pair diffusion model developed by Budil[2], which accounts for the concentration of the dopant, the dopant-interstitial and dopant-vacancy pairs and the interstitials and vacancies. The dopant resides on substitutional sites and is not allowed to diffuse. Diffusion takes place solely via dopant-point

defect pairs. The equations are solved with the program package ZOMBIE [6], a one dimensional solver for general diffusion equations. The model of Budil[2] defines a reaction between impurities (*As*) and defects (*D*) (interstitials and vacancies).



Different charge states are allowed for impurity, point defects and pairs. Formation of *As-D* pairs is controlled by a generation term G_{AsD}

$$\frac{\partial c_{AsD}}{\partial t} + \frac{\partial J_{AsD}}{\partial x} = G_{AsD} \quad (9)$$

$$\frac{\partial c_{As}}{\partial t} = \sum_D -G_{AsD} \quad (10)$$

$$\frac{\partial c_D}{\partial t} + \frac{\partial J_D}{\partial x} = -G_{AsD} \quad (11)$$

$$G_{AsD} = k_{generation}^D c_{As} c_D \sum_i k_{AsD}^i \left(\frac{n}{n_i}\right)^{-i} - k_{decay}^D c_{AsD} \sum_i k_D^i \left(\frac{n}{n_i}\right)^{-i} \quad (12)$$

For analysis we set

$$k_{generation}^D = k_{AsD} \cdot A \quad (13)$$

$$k_{decay}^D = A \quad (14)$$

as only the ratio $k_{generation}^D \div k_{decay}^D$ is responsible for the final concentration the reaction will tend to. Transient effects of the pair formation process have been excluded by taking a high value for the coupling constant *A*, thus resulting in a fast (compared to diffusion phenomena) buildup of the pair concentration without changing the equilibrium concentration of the dopant point defect pairs.

Values for interstitial diffusivity and equilibrium concentration are taken from Tani-guchi[8], values for vacancy diffusivity and equilibrium concentration are taken from Tan[7]. The formation of *As* point defect pairs is described by reaction constants k_{AsI} and k_{AsV} . Concerning diffusion under equilibrium conditions, it is neither necessary nor possible to extract exact values for both D_{AsD} and k_{AsD} , as over a wide range only the product $D_{AsD} \cdot k_{AsD}$ determines the material transported via the corresponding diffusion mechanism.

For a given diffusion length it is possible to fit the data by either adjusting the value of $D_{AsI} \cdot k_{AsI} (f_I^{As} = 100\%)$ leaving the other small, or by adjusting $D_{AsV} \cdot k_{AsV} (f_I^{As} = 0\%)$ or by using both of them with f_I^{As} being a freely chooseable parameter.

Simulating oxynitridation was done by changing the interstitial surface concentration by a factor determined by the enhancement of the phosphorus diffusion during oxynitridation. Phosphorus is believed to diffuse by interstitials and therefore can be used as a monitor for interstitial supersaturation. Similarly the enhancement of Sb diffusion was taken for the determination of the vacancy supersaturation. During the diffusion of a typical intermediate dopant like *As* ($f_I^{As} \sim 40\%$) under point defect surface supersaturation it can be seen that the supersaturation of point defect dopant pairs is not the same as the point defect supersaturation as assumed in (4). Pair supersaturation tends to be significantly lower than point defect supersaturation. This can be understood by considering the fact that the pair concentration can only be increased if both point defect concentration and dopant concentration

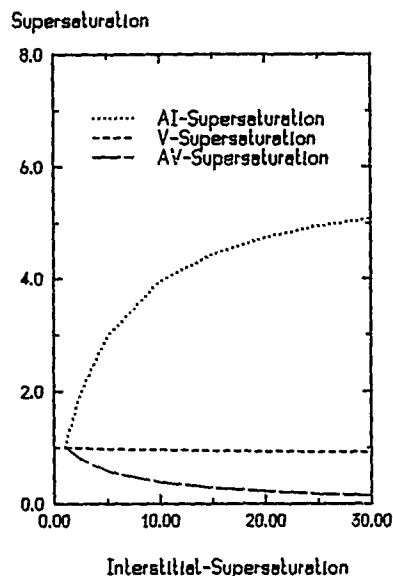


Figure 1: Behaviour of point defects and vacancies under interstitial injection for a typical intermediate dopant with $f_I = 40\%$ at 1100°C .

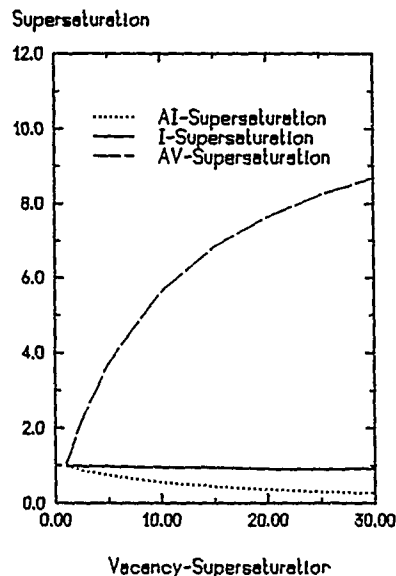


Figure 2: Behaviour of point defects and interstitials under vacancy injection for a typical intermediate dopant with $f_I = 40\%$ at 1100°C .

are increased. As the number of dopant atoms is limited, pair supersaturation naturally tends to reach a limit. A direct consequence of this is the fact that pair concentration and diffusion enhancement cannot be pushed to infinite levels by merely injecting more point defects (Fig.1). During interstitial injection and subsequent pair supersaturation a decrease of dopant vacancy supersaturation can be observed. This decrease results from the lack of free dopants, as due to the higher interstitial concentration more dopants tend to form pairs with interstitials and therefore less are free to form vacancy pairs. Results during vacancy injection are quite similar (Fig.2). This result shows clearly that the assumption made in equation (4) is not justified and leads to erroneous results if used for analysis of experimental results (in equation 6). A completely consistent treatment therefore has to include diffusion via pairs and cannot rely on the assumption (4).

It must be stated definitely that the analysis uses only three known parameters as input, namely D_{As} - the overall intrinsic diffusion coefficient for arsenic at 1100°C , the enhancement $\frac{D_{AI}}{D_{As}}$ of the arsenic diffusion during interstitial injection, and the enhancement $\frac{D_{AV}}{D_{As}}$ during vacancy injection. Not all of the free parameters D_{IA} , D_{VA} and k_{IA} , k_{VA} can be determined. We therefore evaluated them in dependence on the fractional interstitial coefficient f_I^{As} , a value used to describe the portion of diffusion taking place due to interstitials. f_I^{As} was computed by equation (3). Using the plausible value for f_I^{As} from Antoniadis[9] ($f_I^{As} = 44\%$), the model parameters can be determined (Fig.3, Fig.4). Simulating the time dependence of the diffusion enhancement, it appears that the values for the lower diffusion time (7 min) cannot be represented accurately (Fig.5, Fig.6). This effect might be due to time transients in the surface kinetics and is not included in this treatment. It can be seen from Fig.4 that the diffusivity of As point defect pairs is not very high above the overall diffusivity of arsenic at 1100°C . A direct consequence of this is the fact that the part of

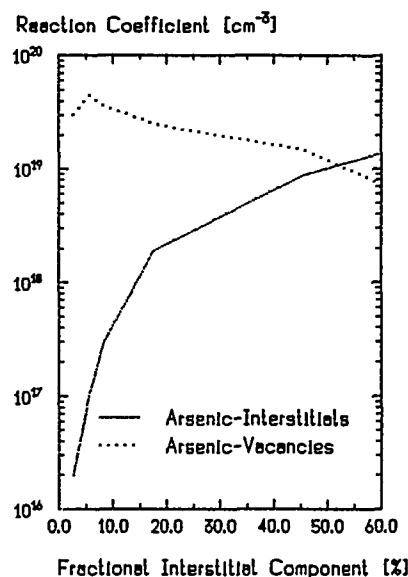


Figure 3: Reaction constants for As-point defect pairs at 1100°C

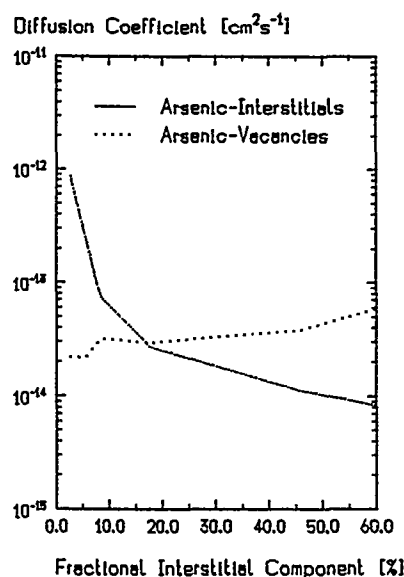


Figure 4: Diffusion constants for As-point defect pairs at 1100°C

$As(I,V)$ pairs is rather high under normal diffusion conditions (up to 40% of the arsenic concentration). The values used for C_I^{eq} [8] and for C_V^{eq} [7] are relatively high. No simulations with lower equilibrium point defect concentrations have been carried out in this work. The low diffusivities $D_{As(I,V)}$ and the high percentage of $As(I,V)$ pairs supports the observation that no significant transient diffusion effect has been reported so far for As (Hoyt[10], Michel[11], Seidel[12]) although different authors report on transient enhanced diffusion for arsenic (Kalish[13], Narayan[14]). It is believed that transient diffusion occurs due to an anomalously high dopant point defect pair concentration after ion-implantation. A high equilibrium As point defect pair concentration will obviously diminish any transient effect.

SUMMARY

In the present work the oxynitridation and nitridation experiments of Fahey et al.[1] have been reexamined with a recently developed diffusion model. The inconsistencies during the evaluation of the fractional component of diffusion for arsenic (f_I^{As}) have been discussed. The assumption $\frac{C_{As(I,V)}}{C_{As(I,V)}} = \frac{C_{(I,V)}}{C_{(I,V)}}$ used for the analysis of nonequilibrium diffusion phenomena is shown to be not adequate. A consistent treatment must account for the concentration of arsenic, point defects and arsenic point defect pairs. Pair formation kinetics must be included. It is shown that it is possible to explain the experimental data in a single theoretical framework by using a diffusion model based on pair diffusion. Transient effects have been excluded from this treatment. Calculations lead to a high percentage of arsenic point defect pairs. Diffusion parameters for arsenic point defect pairs have been extracted and implications on transient enhanced diffusion have been pointed out.

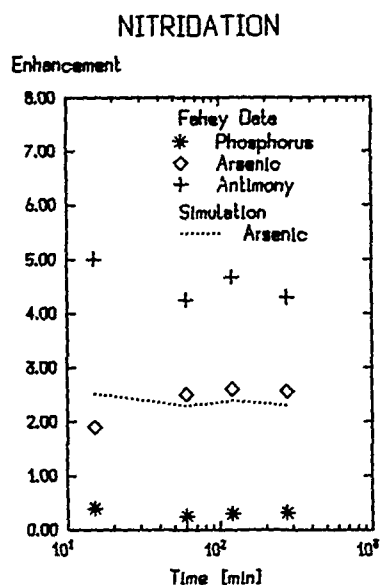


Figure 5: Simulation of the nitridation process of ref.[1]

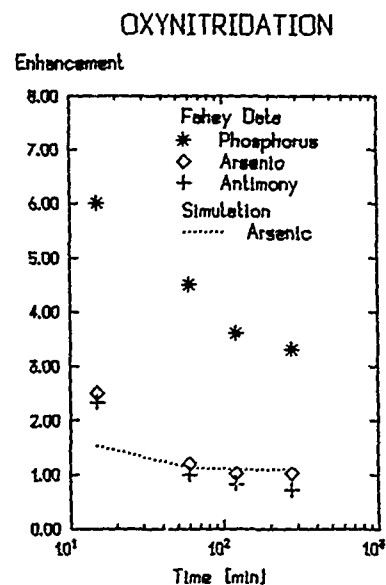


Figure 6: Simulation of the oxynitridation process of ref.[1]

ACKNOWLEDGMENTS

This work has been supported by the Fonds zur Förderung der wissenschaftlichen Forschung and by the research laboratories of Siemens AG in Munich, FRG. Helpfull discussions with N.E.B. Cowern are thankfully acknowledged. Furthermore we wish to acknowledge Prof.Dr.S. Selberherr for free computer access.

References

- [1] P. Fahey, G. Barbuscia, M. Moslehi, R.W. Dutton, *Appl. Phys. Lett.* 46(8), 1984, p. 784
- [2] M. Budil, H. Pötzl, G. Stingeder, M. Grasserbauer, K. Goser, *Materials Science Forum (Proc. 15. ICDS)*, Vol. 38-41, Part 2, pp. 719-724, 1989
- [3] M. Orlowski, *Appl. Phys. Lett.* 53(14), 1988, p. 1439
- [4] B.O. Mulvaney, W.B. Richardson, *Appl. Phys. Lett.* 51(18), 1987, p.1439
- [5] F.F. Morehead, R.F. Lever, *Appl. Phys. Lett.* 48(2), 1986, p. 151
- [6] W. Jüngling, *IEEE Trans ED-32*, 1985, p. 156
- [7] T.Y. Tan, U. Gösele, *Appl. Phys. A* 37(1-17), 1985, p. 1
- [8] K. Taniguchi, D.A. Antoniadis, Y. Matsushita, *Appl. Phys. Lett.* 42(11), 1983, p.961
- [9] D.A. Antoniadis, I. Moskovitz, *J. Appl. Phys.* 53(10), 1982, p. 6788
- [10] J.L. Hoyt, J.F. Gibbons *Mat. Res. Soc. Symp. Proc. Vol. 52*, 1986, p. 15
- [11] A.E. Michel *Mat. Res. Soc. Symp. Proc. Vol. 52*, 1986, p. 3

- [12] T.E. Seidel, D.J. Lischner, C.S. Pai, R.V. Knoell, D.M. Mahrer, D.C. Jacobson *Nuclear Instruments and Methods in Physics Research B* 7/8, 1985, p.
- [13] R. Kalish, T.O. Sedgwick, S. Mader *Appl. Phys. Lett.* 44(1), 1984, p. 107
- [14] J. Narayan, O.W. Holland, R.E. Eby, J.J. Wortman, V. Oguz, G.A. Rozgonyi *Appl. Phys. Lett.* 43(10), 1983, p. 957

MEASUREMENTS OF ENHANCED DIFFUSION OF BURIED LAYERS IN SILICON MEMBRANE STRUCTURES DURING OXIDATION

SCOTT T. DUNHAM, ANURADHA M. AGARWAL AND NANSENG JENG
Boston University, Electrical, Computer and Systems Engineering Department,
44 Cummings Street, Boston, MA 02215.

ABSTRACT

Reported calculations of the diffusion coefficient of silicon self interstitials vary over several orders of magnitude at temperatures of interest for integrated circuit fabrication. In this work, we measure the enhanced diffusion of phosphorus buried layers while interstitials are injected at a wafer surface via thermal oxidation. The starting substrates were either float-zone silicon or Czochralski silicon with a pre-treatment to precipitate excess oxygen. The samples were prepared by implantation of phosphorus followed by the growth of a 40-60 μm epitaxial layer. They were then etched anisotropically from the frontside or backside to yield membrane structures. Local oxidation was performed at 1100°C on either the frontside or backside of each wafer and buried layer diffusion was monitored, yielding information about interstitial diffusion in silicon and its dependence on bulk properties.

INTRODUCTION

There exists considerable disagreement over the correct value of interstitial diffusivity in silicon. Reported values have varied over 2 to 5 orders of magnitude at temperatures of interest for integrated circuit fabrication. The calculated values of interstitial diffusivity appear to fall into two major groups, depending on the type of experiment conducted. Determination of the point defect concentrations at the frontside of a wafer via monitoring of dopant diffusion [1,2] or stacking fault growth [3] during backside oxidation, or by measuring the lateral extent of enhanced diffusion due to frontside oxidation [4,5] gives relatively low diffusivity values ($\sim 10^{-9}\text{cm}^2/\text{sec}$ at 1100°C). Much larger values ($\sim 10^{-7}\text{cm}^2/\text{sec}$ at 1100°C) have been reported when monitoring the gettering of gold during interstitial injection from backside damage [6,7] and also when monitoring the diffusion of buried layers during oxidation [8]. Despite the huge range of reported values, individual experiments or types of experiments generally give consistent and repeatable results.

Previously, these differences have been explained by invoking a bulk trapping phenomenon [9]. This theory assumes that the diffusion front of interstitials is slowed down by the need to first fill up bulk trapping sites. The net result is that it takes longer for interstitial supersaturations to propagate, producing a reduced effective diffusion coefficient. The fast diffusion noted in the buried layer experiments is explained by assuming that epitaxial material has a much smaller density of these traps, while the gettering results are accounted for by assuming that the large supersaturation resulting from backside damage quickly fills the traps.

An alternative explanation for the observed discrepancy is suggested by the observation that lower values of interstitial diffusivity are calculated from experiments in which interstitial concentration is monitored near non-oxidizing SiO_2 interfaces and higher values are calculated when monitored in the bulk. Thus, point defect interactions at the Si- SiO_2 interface may affect calculations of the effective interstitial diffusivity. In this work, in order to distinguish between bulk and interface interactions we measure the enhanced diffusion of phosphorus buried layers while interstitials are injected at a wafer surface via thermal

oxidation.

EXPERIMENTAL PROCEDURES

The starting substrates were lightly phosphorus-doped (100) float-zone ($>500 \Omega\text{-cm}$) and Czochralski ($10\text{-}20 \Omega\text{-cm}$) silicon. In the Czochralski material, excess oxygen precipitates out during thermal processing, generating excess interstitials [10]. In order to avoid changes in interstitial concentration due to this phenomena, the Czochralski wafers were subjected to a pre-treatment to precipitate the excess oxygen. The process included an initial low temperature diffusion in argon (4 hours at 750°C) to facilitate nucleation of oxygen precipitates, followed by a long high temperature anneal (1050°C) to grow the precipitates, first in dry O_2 to grow a protective oxide (4 hours) and then in argon (50 hours).

These treated Czochralski wafers and the as-purchased float-zone wafers were implanted with phosphorus at 150keV with a dose of $2 \times 10^{13} \text{cm}^{-2}$. The dose was kept small enough that the material remained intrinsic at processing temperatures. After annealing, epitaxial silicon (40 or $60 \mu\text{m}$) was then grown on the implanted substrates. The $60 \mu\text{m}$ films were grown at 1000°C for 200 minutes, while the $40 \mu\text{m}$ films were grown at 1040°C for 80 minutes.

A multilayer structure consisting of a thermal oxide covered with a deposited nitride was used as an oxidation barrier in all the experiments. The oxide was 1500\AA thick and grown using a dry/wet/dry oxidation cycle at 900°C . The 1500\AA of LPCVD nitride was deposited at 800°C . The wafers were patterned either on the frontside or the backside to yield 1cm^2 openings in the oxide/nitride multilayer. Each wafer was cleaved such that every sample piece had one window. The exposed silicon areas in these windows were etched anisotropically in KOH to obtain the final test structures with membranes of varying thicknesses (L). The resulting test structures are shown in Figure 1.

The final processing step was a diffusion in dry oxygen at 1100°C , the frontside oxidation samples for 1 hour and the backside oxidation samples for 4 hours. By measuring the broadening of the buried layer profile as it varied with the distance of the buried layer away from the oxidizing and nonoxidizing Si-SiO₂ interfaces, it was possible to calculate the effective interstitial diffusivity.

ANALYSIS

The dopant profiles were measured by spreading resistance and compared to simulated diffusion profiles generated by the process simulator SUPREM IV [11]. A pre-diffusion sample was measured to use as a starting profile for the simulations. Diffusion of the initial profile was simulated using a number of different constant dopant diffusion coefficients. The amount of enhanced diffusion was determined by finding the diffusion coefficient for which the simulation best fit the spreading resistance data. The intrinsic diffusion coefficient was determined by measuring the profile in a region where both front and back were protected from oxidation. To account for the differences between dopant concentration and carrier concentration (as measured by spreading resistance), the simulated concentration profiles were sent to a Poisson-Boltzmann solver which calculated electron concentrations and those results were compared to the spreading resistance measurements.

The results of the measurements and comparisons to simulated profiles is an average diffusion coefficient for the dopant as a function of the distance from the oxidizing interface. Low concentration dopant diffusivity can be written in terms of interstitial and vacancy

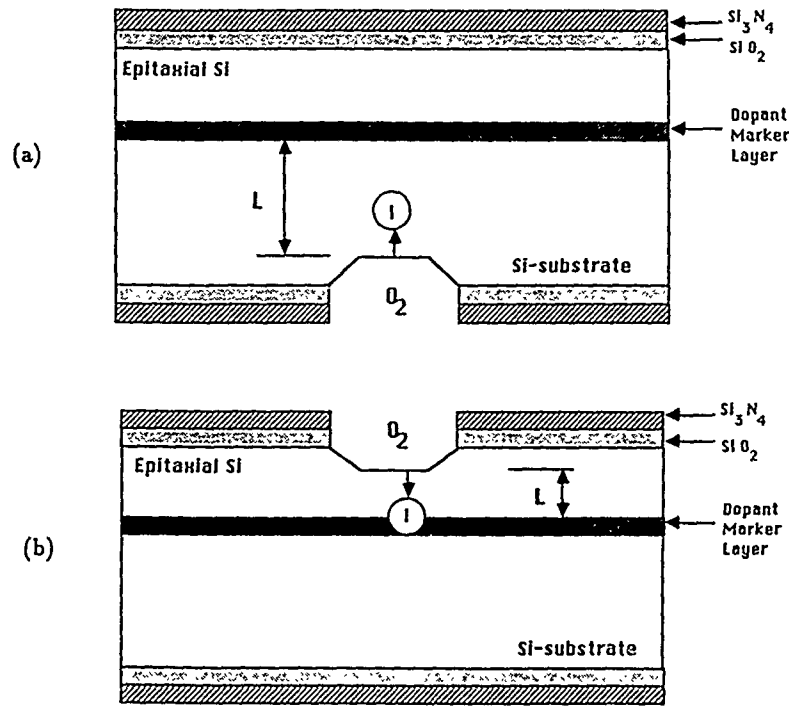


Figure 1: Test structures prior to oxidation for (a) backside oxidation and (b) frontside oxidation.

components:

$$\frac{D_P}{D_P^*} = f_I^P \frac{C_I}{C_I^*} + (1 - f_I^P) \frac{C_V}{C_V^*}, \quad (1)$$

where the * represents equilibrium or intrinsic values. We have chosen phosphorus as the marker layers because it diffuses predominantly with interstitials [12]. In order to simplify the analysis, we will assume that $f_I^P \cong 1$. Thus, the diffusivity enhancement is directly proportional to the interstitial supersaturation.

Once the phosphorus diffusivity enhancements are determined as a function of buried layer position and substrate material, SUPREM IV was again used, this time to simulate the diffusion of interstitials during the oxidation process. The concentration of interstitials at the oxidizing interface was considered a function of oxidation rate, with the injection rate chosen to match measurements of layers near the oxidizing interface. Recombination at the nonoxidizing interface was assumed to be zero, but using the SUPREM IV defaults gave no perceptible difference for the experimental conditions. Bulk interstitial recombination was also assumed to be zero. A series of simulations was done in which the interstitial diffusivity was varied. For each of these simulations, the time-averaged interstitial concentration for each of the experimental membrane thicknesses was calculated and compared to the average enhancement in phosphorus diffusivity previously calculated assuming $f_I^P \cong 1.0$. Thus,

$$\frac{\langle D_P \rangle}{D_P^*} \cong \frac{\langle C_I \rangle}{C_I^*}, \quad (2)$$

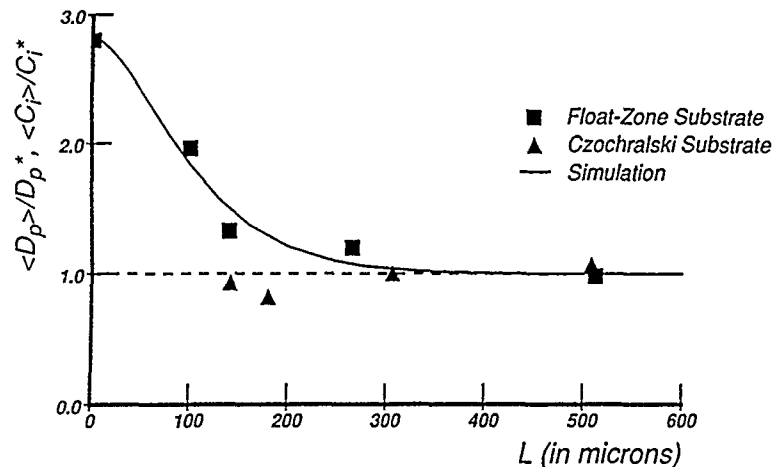


Figure 2: Measured values of time-averaged phosphorus diffusion enhancement compared to simulation of time-averaged interstitial supersaturation as functions of distance of buried layer from oxidizing interface during backside oxidation.

where the brackets represent time-averaged values.

RESULTS AND DISCUSSION

In Figures 2 and 3, we show comparisons between the time-averaged diffusivity enhancement for phosphorus ($\langle D_p \rangle / D_p^*$) as a function of the distance of the buried layer from the oxidizing interface (L) and simulations of time-averaged interstitial supersaturation ($\langle C_i \rangle / C_i^*$). Figure 2 is for backside oxidation, where the distance between the nonoxidizing oxide surface and the buried layer is fixed at $44\mu\text{m}$ (see Figure 1a). The simulation shown is for the interstitial diffusivity which gives the best fit to the data ($D_I = 1.7 \times 10^{-9}\text{cm}^2/\text{sec}$). Figure 3 is for front side oxidation, where the distance to the nonoxidizing film on the backside is fixed at $510\mu\text{m}$ (see Figure 1b). The simulation, once again, uses the best fit interstitial diffusivity, which for this data was calculated to be $D_I = 0.7 \times 10^{-9}\text{cm}^2/\text{sec}$.

The diffusivities calculated for epitaxial material (frontside oxidation) and float zone material (backside oxidation) are similar and consistent with previous measurements using membranes and 2D enhanced diffusion [1-5]. A single interstitial diffusivity of $D_I = 10^{-9}\text{cm}^2/\text{sec}$ for both the frontside and backside oxidation experiments would only slightly reduce the accuracy of the fits between simulation and measurements.

These results contradict previous measurements of buried layer diffusion during frontside oxidation. A previous report by Griffin *et al.* [8] found that interstitial diffusion in epitaxial material was orders of magnitude larger ($\sim 10^{-7}\text{cm}^2/\text{sec}$) than that found here. There are several possible explanations for the differences. First, it is possible that the properties of the epilayers used in the two experiments are very different. To address this issue, more experiments are underway using epi from a different source. In addition, Griffin *et al.* used thinner epitaxial layers ($40\mu\text{m}$) and longer diffusion times (200 minutes), both of which would reduce the observed differences between the deepest and shallowest buried layers, and

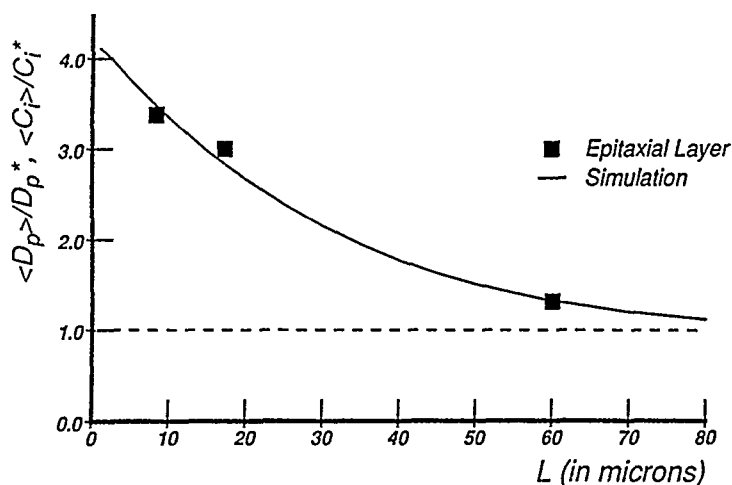


Figure 3: Measured values of time-averaged diffusivity enhancement ratio for phosphorus and simulation of time-averaged interstitial supersaturation as functions of distance of buried layer from oxidizing interface during frontside oxidation.

determined their lower limit for interstitial diffusivity based on the lack of any significant differences between the measured profiles. They also used wet rather than dry oxidation, which increases the interstitial supersaturation and may give a larger effective diffusivity as noted in the next paragraph. The source of the differences may actually be a combination of these effects.

If we assume that the diffusivity values for epi calculated here are correct, there still remains a conflict with measurements from metal gettering [6,7]. There is, however, a possible explanation for those differences. During gettering, the interstitial supersaturation is much larger than during oxidation (sometimes more than 1000). If there is trapping or recombination occurring in the bulk, the much larger supersaturation would quickly fill up or annihilate the trapping species. This would result in a much larger effective recombination as noted by Griffin *et al.* [9]. One of the problems with the trapping model previously is the lack of a plausible trap candidate that was present in float zone material, but not in epitaxial layers. If the effective diffusivity through epi is similar to that in float zone material, however, then the effective diffusivity could be reduced simply by recombination with vacancies. The recombination process would not allow the interstitial concentration to increase until the vacancy concentration was reduced, slowing the diffusion front.

Measurements were also made on the Czochralski material and that data is included in Figure 2. For Czochralski substrates, no apparent diffusivity enhancement is observed. A possible explanation for these results is that the oxygen precipitates may stabilize the interstitial concentrations. During the pretreatment, the excess oxygen was precipitated in a process that generates excess interstitials. Because of the long inert anneal, the final concentrations of interstitial and precipitated oxygen should be near equilibrium with the interstitial concentration. Upon interstitial injection, those precipitates may either provide sites for annihilating the excess interstitials or may partially dissolve, reversing the precipitation process and using up interstitials or generating vacancies. Thus, the precipitated

oxygen may significantly reduce the distance over which the supersaturation extends from the oxidizing interface.

CONCLUSIONS

In summary, we have measured the diffusion of phosphorus buried layers during both front and backside oxidation at 1100°C. From the dependence of the diffusivity enhancement on the distance of the buried layer from the oxidizing interface, we have calculated effective diffusion coefficients for silicon interstitials in epitaxial and float zone material. In both cases, we have found the effective diffusivity to be about 10^{-9} cm²/sec. This value is consistent with a number of backside OED or OISF growth experiments, but is much less than that calculated from metal gettering experiments and previous measurements for epitaxial silicon. The effective diffusivity in the pre-treated Czochralski material was found to be much smaller than in the float-zone or epitaxial material. These results are consistent with slowing of the interstitial diffusion front due to recombination with vacancies and dissolution of oxygen precipitates.

ACKNOWLEDGEMENTS

This work was supported by a SEMATECH Center of Excellence #88-MC-503. We would like to thank Professors Dimitri Antoniadis and Rafael Reif at MIT for allowing use of some of their fabrication and characterization facilities and Walter Metz at Digital Equipment Corporation for growth of some of the epitaxial layers.

REFERENCES

- [1] S. T. Ahn, J. D. Shott and W. A. Tiller, *Proceedings of the Electrochemical Society Meeting*, San Diego, CA, October 1986.
- [2] E. Scheid and P. Chenevier, *Phys. Stat. Solidi* **93**, 523 (1986).
- [3] K. Taniguchi, D. A. Antoniadis and Y. Matsushita, *Appl. Phys. Lett.* **42**, 961 (1983).
- [4] P. B. Griffin and J. D. Plummer, *Proceedings of the Electrochemical Society Meeting*, San Diego, CA, October 1986.
- [5] K. Taniguchi and D. A. Antoniadis, *Appl. Phys. Lett.* **46**, 944 (1985).
- [6] G. B. Bronner and J. D. Plummer, *Mat. Res. Soc. Symp. Proc.* **36**, 49 (1985).
- [7] T. Y. Tan and U. Gösele, *Appl. Phys. A* **37**, 1 (1985).
- [8] P. B. Griffin, P. M. Fahey, J. D. Plummer and R. W. Dutton, *Appl. Phys. Lett.* **47**, 319 (1985).
- [9] P. B. Griffin, S. T. Ahn, W. A. Tiller and J. D. Plummer, *Appl. Phys. Lett.* **51**, 115 (1987).
- [10] S. Mizuo and H. Higuchi, *Jap. J. Appl. Phys.* **20**, 791 (1981).
- [11] M. E. Law and R. W. Dutton, *IEEE Trans. Comp. Aid. Des.*, 181 (1987).
- [12] P. Fahey, G. Barbuscia, M. Moslehi and R. W. Dutton, *Appl. Phys. Lett.* **43**, 683 (1983).

MIGRATIONS OF INTERSTITIAL ATOMS IN SEMICONDUCTORS (SURFACE DIFFUSION AND KICK-OUT MECHANISM)

TAKAO WADA*, AKIHIRO TAKEDA*, MASAYA ICHIMURA*, and MICHIIHIKO TAKEDA**

*Nagoya Institute of Technology, Showa, Nagoya, 466, Japan

**Government Industrial Research Institute, Nagoya, 462, Japan

ABSTRACT

Ge and Zn atoms were introduced into the unirradiated regions of Si at 150°C and GaAs wafers at 50°C, respectively by using the electron-beam doping method. The surfaces of Si and GaAs substrates were covered partially by the overlayers of Ge and Zn sheets, respectively. The only surfaces of the Ge and Zn sheets were irradiated locally with high-energy electrons at 7MeV with the fluences of 5×10^{17} - 1×10^{18} electrons cm^{-2} . Even at a distance of 10mm from the irradiated overlayers in the Si and GaAs substrates, Ge and Zn atoms respectively, whose interstitials may migrate the unirradiated regions, were detected by SIMS measurements. PL signal due to band-to-acceptor (Zn_{Ga}) transition at 1.48eV becomes observable after annealing at 800°C for 20min in the unirradiated GaAs region, which is separated from Zn sheet by nearly 10mm.

I. INTRODUCTION

When a crystal is irradiated with energetic electrons and the transmitted energy to a knocked atom is larger than a threshold energy T_d , the atom is displaced from its regular site into an interstitial position and a Frenkel (vacancy-interstitial) pair is created [1].

We do have some firm information about the interstitial, but it has not yet been firmly identified. Watkins has observed the formation of aluminium interstitials in Al-doped Si irradiated at 4.2K. The production rate of these Al interstitials was considerably larger than the production rate expected if these interstitials were produced by direct encounters with energetic electrons. Watkins [2] has indicated that the presence of these Al interstitials can only be the result of long-range migration of Si interstitials with subsequent exchange with substitutional Al, giving Al interstitials. Nagata et al. [3] have estimated gallium surface diffusion distances in the molecular-beam epitaxial (MBE) growth of (001) oriented GaAs films under both Ga- and As-stable conditions. And the surface diffusion length of Ga on GaAs (111) B has been obtained [4] as a function of reciprocal growth temperature by taking account of the supersaturation ratio of adatoms on the terrace for MBE growth. Electron beam doping (EBD) [5-8], oxidation [9] and epitaxy [10-11], which utilize high-energy electron-irradiation, have recently reported by the authors and others. For EBD, U-shaped diffusion profiles of impurities in substrates have been explained by considering the "kick-out" mechanism and the surface diffusion [6].

In the present paper, we study the introduction of Ge and Zn atoms into the unirradiated regions of Si at 150°C and GaAs wafers at 50°C, respectively by using the EBD method.

Table I Impurity sheets and substrates used in the experiments.

	Material	Purity, conduction type, resistivity, orientation, thickness
Impurity sheet	Zn	99.9%, $t=0.5\text{mm}$
	Ge	Sb doped, n type, $\rho=0.01\Omega\text{cm}$, (111), $t=0.5\text{mm}$
Substrate	GaAs	undoped, semi insulating, $\rho=6.8 \times 10^4\Omega\text{cm}$, (100), $t=0.5\text{mm}$
	Si	N doped, n type, $\rho=20-45\Omega\text{cm}$, (111), $t=0.25\text{mm}$

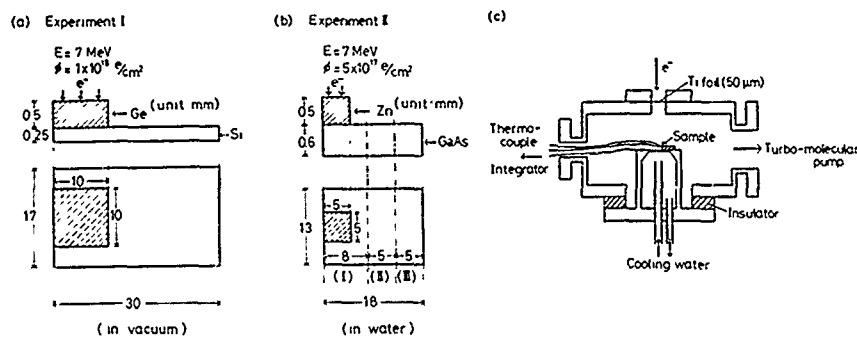


Fig.1 Schematic diagram of electron beam doping in vacuum (experiment I) (a), in running water (experiment II)(b), and schematic diagram of electron irradiation at 150°C in vacuum (c).

II. EXPERIMENTAL PROCEDURE

The samples used in the experiments are summarized in Table I. As shown in Figs.1 (a) and (b), the surfaces of Si wafer and GaAs substrate were covered partially by the overlayers of Ge and Zn sheets, respectively. Only the surfaces of the Ge and Zn sheets were irradiated locally with the fluences of 1×10^{18} in vacuum (experiment I) and 5×10^{17} electrons cm^{-2} in water bath (experiment II) respectively, at 7 MeV from an electron linear accelerator with a pulse width of $3.5 \mu\text{s}$, a 200 Hz duty cycle and an average electron-beam current of $40 \mu\text{A}$. In the case of experiment I, the scheme of the sample mount (at 150°C irradiation) in vacuum is illustrated in Fig.1 (c). And for experiment II, the sample was put in a circulating water bath, which was kept at a constant temperature of 50°C by using a thermoregulator. After irradiation, the concentration profiles of impurity atoms in Si and GaAs were measured utilizing secondary-ion-mass spectrometry (SIMS) (CAMECA IMS-3f). A focused oxygen-ion beam (diameter $\sim 40 \mu\text{m}$) with an ion energy of 8 keV was used in a $\sim 5 \times 10^{-9}$ Torr vacuum. Then, the irradiated GaAs sample was cleaved in three regions (see Fig.1 (b)) and each of them was annealed at the same condition (800°C, 20 min) with a SiO_2 cap in a conventional furnace. After stripping off the SiO_2 films, photoluminescence (PL) measurements were performed at 77 K for each annealed region. A focused 80 mW 5145 Å argon laser beam was used as the excitation source.

III. EXPERIMENTAL RESULTS

When the surface of the Si substrate is covered partially by an overlayer of Ge sheet and irradiated locally, the Ge impurities diffuse into the unirradiated regions of Si. The concentration profiles of Ge atoms, which were introduced into Si substrate in vacuum are shown in Fig.2 (a). Here, signal intensity of Ge was plotted in arbitrary units as a function of lateral position in the unirradiated regions at different depths of 50, 100 and 200 Å from the Si surface. The resultant plot is mainly composed of two curves. It is suggested that two kinds of species diffuse at the surface. Ge atoms are detected even at a distance of more than 10 mm from the edge of the overlayer. Values of diffusivity D_s (for surface diffusion) of the lateral direction estimated using the analysis of Boltzmann [12] and Matano [13] are indicated in the figure. They suggest that there is a surface diffusion having a very large diffusivity during irradiation.

The concentration profiles of Zn atoms which were introduced into GaAs substrate in running water are shown in Fig.2 (b). The results of SIMS

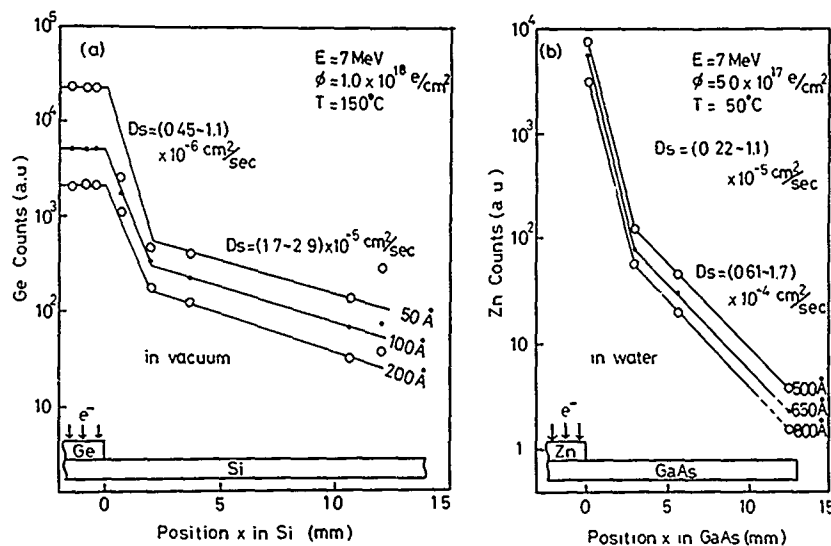


Fig.2 Concentration profiles of Ge (a) and Zn (b) atoms which were introduced into Si and GaAs substrates, respectively as a function of lateral position in the unirradiated regions

measurements were all plotted in arbitrary units as a function of lateral position in the unirradiated regions at different depths of 500, 650, and 800 Å from the GaAs surface. It is very similar to the profile of Ge atoms introduced in vacuum shown in Fig.2 (a). Therefore, the surface diffusion may not be strongly affected by water or oxide layer formed by a reaction with water.

Figure 3 indicates the depth profiles of Zn atom concentration under the Zn impurity sheet ($x=0$) and at different distances of $x=3$, 5.6 and 12.5 mm from the edge of overlayer. The values of D_v (for volume diffusion) are also indicated in the figure. The diffusion profiles do not follow complementary error-function distribution. This suggests that the diffusivity is concentration dependent. This figure indicates that there is a volume diffusion having the smaller diffusivities D_v ($D_v \ll D_s$) of impurity atoms in the unirradiated regions.

Figures 4 (a) and (b) show typical PL spectra at 77K after annealing at 800°C for 20 min for the GaAs samples of region I and III, respectively (see inset of the figure). From region I, the luminescence attributed to Ga antisite defect (Ga_{As}) at 1.45 eV were observed. The solid line indicates the experimental result, and the broken line shows Lorentzian curve computed to show the most suitable agreement for the spectrum. For region II, no PL spectrum appeared after annealing.

The PL spectrum for region III is represented in Fig.4 (b). It should be emphasized here that PL signal due to band-to-acceptor (Zn_{Ga}) transition at 1.48 eV becomes observable in the unirradiated region, which is separated from Zn sheet by nearly 10 mm.

IV. DISCUSSION

The extrapolated ranges of electrons at 7 MeV in Si, GaAs, Ge and Zn are about 15, 5.65, 5.6, and 4.3 mm, respectively. Thus, the irradiating electrons penetrate through the sample without a significant loss in kinetic energy.

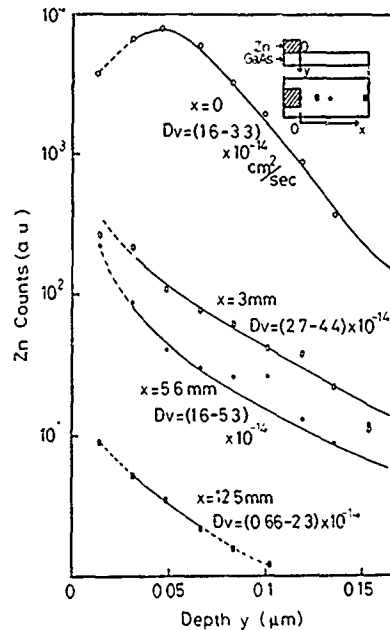


Fig.3 Depth profiles of Zn atom concentration under the Zn impurity sheet ($x=0$) and at different distances of $x=3$, 5.6 and 12.5mm from the edge of overlayer.

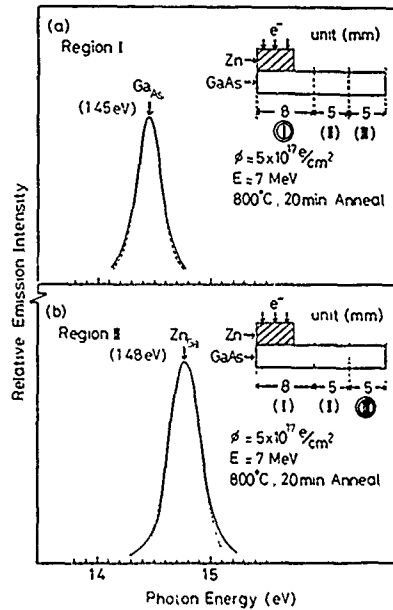


Fig.4 Typical PL spectra at 77K after annealing at 800°C for 20min for the GaAs samples. (a): region I. (b): region III.

Surface and volume diffusion

It has been reported that the free valencies which exist at the surface of metals becomes saturated or partly saturated during the act of adsorption and there are two quite distinct types of adsorption [14]. In the first type, termed physical adsorption or van der Waals adsorption, the adsorbed molecule (in the present case, e.g. nearly free atoms) is held to the surface by weak van der Waals or dispersion forces. In the second type, termed chemical adsorption or chemisorption, there is a chemical reaction between the molecule (free atoms) being adsorbed and the metal surface. The potential energy curve for physical adsorption shows a broad and shallow minimum at a distance from the surface.

The Ge and Zn impurity profiles as a function of lateral position at the surface of the unirradiated regions (see Figs.2 (a) and (b)) may be mainly due to the surface diffusion of impurity atoms in the states of nearly free Ge and Zn, respectively, because of D (10^{-4} - 10^{-6} cm²/sec) (Fig.2 (b)) $\gg D_v$ (10^{-13} - 10^{-15} cm²/sec) (Fig.3). The impurity concentrations of Ge at Si surface and Zn at GaAs surface vary as $\exp(-x/L_D)$, where L_D is the surface diffusion length of free Ge and Zn. Their profiles are mainly composed of two curves. It is suggested that two kinds of species diffuse at the surfaces. From the straight line fitted to the curves, $L_{D1} \approx 0.6$ mm and $L_{D2} \approx 8$ mm for Ge/Si system, $L_{D1} \approx 0.7$ mm and $L_{D2} \approx 3.6$ mm for Zn/GaAs system. In the case of MBE growth, the surface diffusion lengths L_D of free Ga atoms have been obtained to be $L_D \approx 0.19$ μm (at 550°C) [3] and $L_D \approx 700$ Å (in 580-600°C) [4]. But, in the present experiments of EBD at 150°C and 50°C, there may be no desorption or no chemisorption in the states of free atoms for surface diffusion, because of very low temperatures. Then, much longer

surface diffusion lengths are expected in the present. If we assumed that the relationship of L_D versus T for MBE growth [4] is established even at room temperature, L_D may be estimated as 0.34mm at 50°C. This value is in roughly agreement with the experimental values. As secondary steps of impurity atom migration after the surface diffusion, there may be the "direct" diffusion (volume diffusion) of foreign interstitial atoms (i.e. their jumping from interstice to interstice), since here the only defect involved are the foreign interstitials themselves. In the case of normal direct diffusion, the diffusivities D_α refer to different states α of the defect species involved, e.g., to the different electric charge states in which a given foreign interstitial in a semiconductor may occur. Thus the resultant concentration profiles of impurity atoms by surface and volume diffusions, as shown in Fig.5 (a), may be qualitatively given by

$$\begin{aligned} C(x,y,t) &\approx C_{so} f_s(x,t) f_v(y,t) \\ &\approx C_{so} \exp[-(x^2/4D_s t + y^2/4D_v t)] \end{aligned} \quad (1)$$

where f_s and f_v are the atom distribution functions by surface and volume (e.g. interstitial) diffusion respectively, x a distance from the edge ($x=0$, see Fig.2) of an irradiated region in the substrate surface, y a depth from the surface at a position of x (unirradiated region), and C_{so} the atom concentration at $x=y=0$. Figure 5 (b) may indicate tentatively a schematic view for the free energy G distribution near to a substrate surface. It is important to note that the parameter ΔG is the difference between free energies in the interstitials and the free atom from which the interstitials are introduced. Thus there is a spatial separation (λ) between the atoms considered. ΔG_i represents the barrier to attaching an atom to the interstitials. ΔG_s is the free energy barriers to movement in the interstitials. Actually attaching the atoms which can reduce the free energy may involve surmounting a barrier as shown in Fig.5 (b).

Defect reaction

Near the surface of region III of substrates, Zn concentrations are

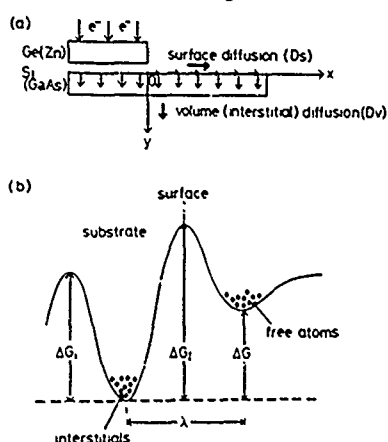
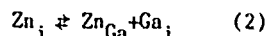


Fig.5 Schematic representations of surface and volume diffusions (a) and schematic view for the free energy G distribution near to a substrate surface (b).

very high and the diffusivities D are relatively small (Fig.3). Since Zn substitutionals have larger solubility and smaller D than Zn interstitials, it is expected that most Zn atoms are in the substitutional state there. This may be interpreted by considering the kick-out mechanism, originally proposed for Au in Si [15]. According to the mechanism, the following reaction occurs



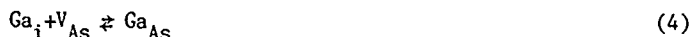
where Zn_i , (Ga_i) and Zn_{Ga} represent interstitial and substitutional states, respectively. In the unirradiated region III, there is no vacancy, and a number of Zn interstitials may exist by a volume diffusion. Such a condition is just favor-

able for the kick-out mechanism. Ga_i concentration is reduced near the surfaces since a surface acts as a sink of interstitials. Hence, Zn_{Ga} concentrations can be high near the surfaces. Then the PL signals at 1.48eV (Fig.4) attributed to Zn_{Ga} were observed after furnace annealing at 800°C for 20min.

It has been demonstrated that the defects created in GaAs by electron irradiations are caused by displacements of As atoms and not of Ga atoms [16]. A mechanism that produces the As vacancies is the creation of As Frenkel defects:



this process can take place throughout the irradiated region of the substrates. In the region I of the Zn-covered and irradiated substrate, the reaction of Eq.(2) also occurs. Then, the basic defect interaction between the two types of atoms is given by



Thus, in the region I (Fig.4), the PL signals at 1.45eV attributed to Ga antisite defects Ga_{As} were observed after furnace annealing at 800°C for 20min.

In the region II of substrates, as a number of complex defects are probably produced by some reactions between simple defects of Zn_i , V_{As} , Ga_{As} and As_i et al, a PL signal disappears. A study on PL signals of defects is now in progressive.

ACKNOWLEDGEMENTS

We are grateful to H.Morikawa of the Government Industrial Research Institute of Nagoya for his help in connection with SIMS measurement of the samples.

REFERENCES

1. for example, J.W. Corbett and J.C. Bourgoin, in Point Defects in Solids, edited by J.H. Crawford and L.M. Slifkin (Plenum, New York, 1975), Vol.2, Chap.1.
2. G.D. Watkins, Radiation Damage in Semiconductors, edited by P. Baruch (Paris; Dunod, 1955), p.97.
3. S. Nagata and T. Tanaka, J. Appl. Phys. **48**, 940 (1977).
4. T. Shibata, E. Kondo and T. Nishinaga, 8th Record of Alloy Semiconductor Physics and Electronics Symposium, Kyoto, 1989, p.19.
5. T. Wada, Nucl. Instr. and Meth. **182/183**, 131 (1981).
6. T. Wada and H. Hada, Phys. Rev. B **30**, 3384 (1984).
7. T. Wada and A. Takeda, Nucl. Instr. and Meth. B **37/38**, 348 (1989).
8. T. Wada and A. Takeda, Nucl. Instr. and Meth. B **37/38**, 352 (1989).
9. T. Wada, Appl. Phys. Lett. **52**, 1056 (1988).
10. T. Wada and Y. Maeda, Appl. Phys. Lett. **51**, 2130 (1987).
11. T. Wada and Y. Maeda, Appl. Phys. Lett. **52**, 60 (1988).
12. L. Boltzmann, Ann. Phys. **53**, 948 (1894).
13. J.H. Crawford, Jr. and L.M. Slifkin, Point Defects in Solids (Plenum, New York, 1975), Vol.2, p.177; C. Matano, Jpn. J. Phys. **8**, 109 (1933).
14. G.C. Bond, Catalysis by Metals (Academic Press, London, 1962).
15. W. Frank, A. Seeger and U. Gosele, in Defects in Semiconductors (North-Holland, Amsterdam, 1981), p.31.
16. D. Pons and J. Bourgoin, Phys. Rev. Lett. **47**, 1293 (1981).

MEASUREMENTS OF ENHANCED OXYGEN DIFFUSION IN SILICON DURING THERMAL DONOR FORMATION: NEW EVIDENCE FOR POSSIBLE MECHANISMS

A.R. BROWN, R. MURRAY, R.C. NEWMAN AND J.H. TUCKER
Interdisciplinary Research Centre for Semiconductor Materials, The Blackett Laboratory, Imperial College of Science, Prince Consort Road, London, SW7 2BZ, U.K.

ABSTRACT

Czochralski silicon has been heated in a H-plasma at temperatures in the range 300-450°C, and compared with furnace annealed material. Plasma treatments produce enhanced rates of oxygen diffusion jumps, loss of oxygen from solution and formation of thermal donor centres. The available evidence indicates that atomic hydrogen catalyses the enhancements via the oxygen diffusion rate. Donor concentrations greater than 10^{17}cm^{-3} have been observed in samples heated in a plasma at 350°C. Doubts have been raised about dimer formation being the primary mechanism for oxygen loss in furnace anneals at 350°C, but invoking enhanced diffusion leads to a conflict with stress dichroism data.

INTRODUCTION

Heat treatment of Czochralski silicon at 450°C leads to the formation of a sequence of at least nine helium-like double donors, designated thermal donors TDN which have progressively smaller ionisation energies as N is increased [1]. EPR [2] and ENDOR [3] studies imply that the core of a TD centre incorporates at least four oxygen atoms. A commonly accepted model is that a TD(N+1) centre is produced when a TDN centre captures a mobile atom, which is usually presumed to be another oxygen impurity. Symmetry arguments which suggested that two atoms had to be captured at each stage can be discounted in the light of new evidence [4] but the possibility that the captured atom is a self-interstitial cannot be ruled out. Even if TD-centres incorporate only four oxygen atoms, it is necessary that the oxygen diffusion coefficient, D, be enhanced by a factor of about ten compared with the normal value, to account for the rate of TD-formation [5,6]. If TD-centres are larger oxygen agglomerates, the required enhancement factor is close to 10^4 [7].

Studies of the conversion of TD1 to TD2 by electrical measurements have suggested that there is indeed a fast diffusing species with an activation energy of $1.8 \pm 0.2\text{eV}$ [8]. It was proposed that the species was interstitial oxygen, O_i , itself which always transferred to an 'excited metastable state' at low temperatures. However measurements of the rate of relaxation of stress-induced dichroism carried out with sample temperatures in the range 330-400°C show that normal oxygen diffusion can occur with an activation energy of 2.5eV [9-11]. Nevertheless, this latter technique has shown that enhanced diffusion jumps can also occur with an activation energy of 1.8eV in samples given a pre-heat treatment for 2h at 900°C [10]. These results have been confirmed [11], but the mechanism of the enhancement has still not been determined. It has been speculated that it might be due to the interaction of O_i atoms with either self-interstitials (I-atoms) [12], or vacancies [13]. Other models to explain TD-formation have invoked rapidly diffusing O_2 molecules [14]. However, if the formation of dimers occurs by the diffusion of O_i atoms this will be the rate limiting process with an activation energy of 2.5eV.

Recently we have shown that heat treatment of low-carbon Cz silicon in a hydrogen plasma, rather than a conventional furnace, leads to enhanced rates of formation of TD-centres and the loss of O_i atoms from solution [12, 15, 16]. These enhancements were attributed to enhancements of D but this step must now be justified. If the plasma treatment produced a large non-equilibrium concentration of precursor defects, which were subsequently converted to TD-centres by the capture of diffusing O_i atoms, they would have shorter average distances to diffuse than in

furnace treated samples. A correlation of $d[O_i]/dt$ and $d\Sigma[TDN]/dt$ could then occur, but D may not be changed. Such a possibility was rejected since the maximum concentrations of TD-centres formed at 450°C were the same for furnace and plasma treated material [15]. New data discussed below have now shown that $[TD]_{max}$ can also be enhanced in plasma treated samples heated for long times.

The purpose of this paper is to demonstrate directly from measurements of the rates of relaxation of stress-induced dichroism that enhanced oxygen diffusion does occur in samples annealed in a hydrogen plasma. A range of new data is then given to explain how enhancement factors are determined. It is concluded that the effects are due to the interaction of O_i atoms with hydrogen.

DIRECT EVIDENCE FOR ENHANCED INTERSTITIAL OXYGEN DIFFUSION

Samples 12mm long (parallel to a crystallographic [111]-axis) with a cross-section of 2mm x 2mm were cut from two different as-grown Si boules and subjected to a stress of 9.8×10^7 Pa at a temperature of 420°C for 15 min. They were cooled at a rate of 1000deg/h to room temperature after which the load was removed. Spectra were recorded on a Perkin-Elmer double beam dispersive spectrometer (Model 983G) fitted with a polarizer. Values of the dichroism, $R = (a_{\perp} - a_{\parallel})/a_{\perp}$ were obtained from the 9μm oxygen band spectra recorded at room temperature. a_{\perp} and a_{\parallel} are the absorption coefficients with the incident electric vector perpendicular and parallel to the [111] axis respectively. The samples were then annealed at 300°C, either in a furnace or in an inductively coupled RF plasma (13.56 MHz) operated at 50W power in flowing hydrogen at a pressure of about 1 Torr.

Values of R as a function of anneal time for an undoped low-carbon sample and a carbon doped sample ($8 \times 10^{16} \text{ cm}^{-3}$) heated in the plasma are shown in Figure 1. These samples contained a grown-in oxygen concentration $[O_i] = 10^{18} \text{ cm}^{-3}$. The time constants obtained from these data were converted to values of the diffusion coefficient by means of the relation $D = a_0^2/8\tau$, where $a_0 = 5.42 \text{ \AA}$ is the lattice spacing of silicon [10,11]. This value of $D = 4.1 \times 10^{-21} \text{ cm}^2/\text{s}$ is a factor of 400 times greater than extrapolated from the relationship for normal diffusion $D = 0.11 \exp(-2.51 \text{ eV}/kT) \text{ cm}^2/\text{s}$. No loss of dichroism could be detected within experimental error for a furnace annealed undoped control sample (Figure 1). Diffusion jumps with the

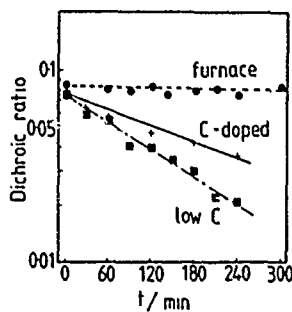


Fig 1. The loss of dichroism in the 9μm oxygen band as a function of heating time at 300°C in a H-plasma for undoped Si and carbon doped Si. Other points refer to a furnace annealed control sample.

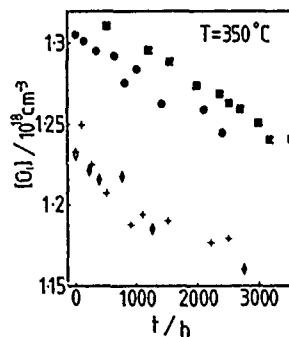


Fig 2. The decrease in $[O_i]$ as a function of time for four samples heated in a furnace at 350°C.

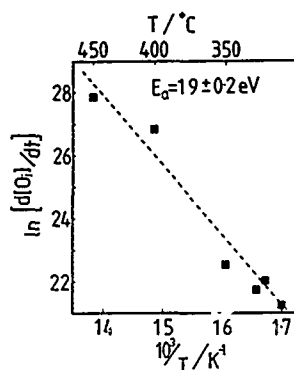


Fig 3. Arrhenius plot of the loss of oxygen from solution for undoped CZ samples cut from a common boule.

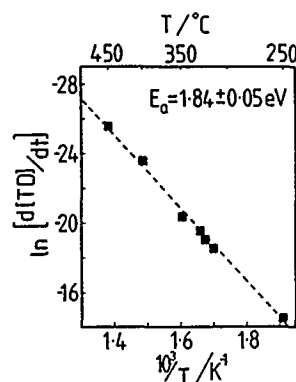


Fig 4. Arrhenius plot of the rate of formation of TD centres for the same samples giving the data in Figure 3.

normal value of D would not have been detected for the heating times used, consistent with these observations.

In summary, it is deduced that the plasma treatment enhances the value of D by a factor of 400 at a temperature of 300°C, in agreement with preliminary data outlined elsewhere [17] and must be primarily responsible for the enhanced values of $d[O_i]/dt$.

RATES OF OXYGEN LOSS FROM SOLUTION AND TD FORMATION

Furnace annealed samples

Measurements of the loss of oxygen from solution $d[O_i]/dt$ for undoped Cz Si have been reported for various heating temperatures including 350°C [12]. Later, it became evident that the data for the lower temperatures were likely to have been underestimates as new measurements have revealed an initial increase in the oxygen concentration after low temperature treatment [16]. As a consequence we now report a new set of data for furnace annealed samples cut from a common boule and annealed at 315, 325, 330, 350, 400 and 450°C. Values of $d[O_i]/dt$ for four different samples heated at 350°C (Figure 2) are seen to be in reasonable agreement. An Arrhenius plot over the range 315 to 450°C for the whole set of samples (Figure 3) yields an activation energy of 1.9 ± 0.2 eV, which is substantially lower than the value of 2.4 ± 0.13 eV quoted by us previously [12]. The reasons are partly due to those outlined above but also because samples cut from several different boules were used in the earlier work.

Resistivity measurements were made on the same set of samples at each stage of the heat treatment when the value of $[O_i]$ was determined. The added total donor concentration $\Sigma[TDN]$ found from our calibration [18], led to experimental values of $d\Sigma[TDN]/dt$. An Arrhenius plot of this quantity (Figure 4) for the temperature range 250–450°C gives an activation energy of 1.84 ± 0.05 eV.

As the activation energies of the oxygen loss and the donor formation are equal within experimental error and lead to a ratio of $\Delta[O_i]/\Delta\Sigma[TDN] = 11 \pm 2$ for the

set of samples under discussion, irrespective of the temperature of heating. For other samples with different thermal histories different ratios have been found.

Plasma annealed samples

A similar set of samples was annealed in a hydrogen plasma and values of $[O_i]$ and $\Sigma[TDN]$ were likewise determined. Correlated values of the rates of change were again found with the same ratio of $\Delta[O_i]/\Delta\Sigma[TDN]$. However, both $d[O_i]/dt$ and $d\Sigma[TDN]/dt$ were enhanced by factors close to 5, 30 and 300 at temperatures of 450, 400 and 350°C respectively. In addition to these measurements the rate of oxygen loss was measured for a similar sample heated at 300°C in a H plasma and a value of $d[O_i]/dt=2.6 \times 10^{11} \text{cm}^{-3}/\text{s}$ was obtained.

CARBON DOPED MAGNETIC CZ SILICON

Material containing $[C_s]=1.3 \times 10^{18} \text{cm}^{-3}$ and $[O_i]=9 \times 10^{17} \text{cm}^{-3}$ was heated at 450°C (a) in a furnace and (b) in a plasma. The values of $d[O_i]/dt$ were $2.4 \times 10^{11} \text{cm}^{-3}/\text{s}$ and $1.0 \times 10^{12} \text{cm}^{-3}/\text{s}$ respectively, showing a plasma enhancement factor of 4 for the rate of the oxygen loss. The value of $d[O_i]/dt$ for the furnace heated sample may be compared with that of $1.7 \times 10^{11} \text{cm}^{-3}/\text{s}$ for a low carbon sample with an initial value of $[O_i]=7.5 \times 10^{17} \text{cm}^{-3}$. An immediate conclusion is that the presence of the carbon has only a minor effect on this rate.

The values of $d\Sigma[TDN]/dt$ for the furnace and plasma treated MCZ material were $1.9 \times 10^8 \text{cm}^{-3}/\text{s}$ and $1.9 \times 10^9 \text{cm}^{-3}/\text{s}$ respectively. The enhancement factor for donor formation is 10, but the absolute rates are lower than those for low carbon silicon by about two orders of magnitude [19]. Thus values of the ratio $\Delta[O_i]/\Delta\Sigma[TDN]$ only have meaning for low carbon material. It follows that previously reported variations in this ratio may be due in part to variations in the carbon content of samples.

MECHANISM OF ENHANCED OXYGEN DIFFUSION

It has been established that plasma treatment of samples leads to enhanced values of D and $d[O_i]/dt$ and it appears that the whole TD-formation sequence is controlled by the diffusion coefficient of $[O_i]$ atoms. The depths of the induced enhancements are typically 1mm. Samples heated at 400°C in He, Ar, Ar/O₂ or N₂ plasmas showed enhancement effects which were very much smaller than those for H₂ or D₂ plasmas. Various experiments with N₂ plasmas indicated that these residual effects were due to the presence of water vapour which would have dissociated to produce H atoms. It follows that there must have been injection of H-atoms, vacancies or I-atoms at the surface, since H-plasma treatments produce surface damage [20]. We sought spectroscopic evidence for I-atom or vacancy injection. Float zone carbon doped samples were treated but there was no evidence for a loss of carbon from substitutional sites which would be expected if there were a flux of I-atoms. Corresponding measurements made on Cz material are not meaningful since C_s atoms are removed by the formation of O₂C_i defects [19]. In plasma treated Cz material no IR absorption at 894cm^{-1} , or other frequencies, was detected from vibrational modes of defects attributed to O₂-V [21], or other O_i-V complexes, although such absorption was present in material following 2MeV electron irradiation while it was held at 400°C. There is therefore no evidence for the injection of vacancies.

The conclusion is that H-atoms must be responsible for the enhancement effects, although SIMS data show that the concentration was no greater than 10^{16}cm^{-3} [16]. A similar conclusion, but only for TD enhancement, was reached independently by exposing Si samples with buried SiO₂ or Si₃N₄ layers to a H-plasma [22]. The buried layers would block the diffusion of vacancies and I-atoms. Si₃N₄ blocks H-

diffusion, whereas SiO_2 does not, consistent with observations of enhanced TD-formation only in samples with the latter type of buried layer.

MAXIMUM TD CONCENTRATION

The maximum value of $\Sigma[\text{TDN}]$ is usually no greater than $2 \times 10^{16} \text{cm}^{-3}$ in samples containing $[\text{O}_i] = 10^{18} \text{cm}^{-3}$ after extended heat treatments (200h at 450°C): longer heating times then lead to a reduction in $\Sigma[\text{TDN}]$. Two samples with $[\text{O}_i] = 12.4 \times 10^{17}$ and $7.3 \times 10^{17} \text{cm}^{-3}$ respectively have now been treated in a H_2 -plasma for up to 600h at $T = 350^\circ\text{C}$. The values of $\Sigma[\text{TDN}]_{\text{max}}$ were 10^{17} and $7 \times 10^{16} \text{cm}^{-3}$, while the loss of oxygen $\Delta[\text{O}_i]$ was 7.6×10^{17} and $4.5 \times 10^{17} \text{cm}^{-3}$ respectively. Thus, there was an enhancement in $\Sigma[\text{TDN}]_{\text{max}}$ by a factor of at least five and the ratios of $\Delta[\text{O}_i]/\Delta\Sigma[\text{TDN}]$ were 7 for both samples. IR electronic spectra of these samples showed broad absorption in the region (450cm^{-1}) expected for TD^0 centres at 4.2K , while there was other absorption in the region of 200cm^{-1} . Further work is required to determine the evolution of this absorption.

CONCLUSIONS

The injection of hydrogen into Cz silicon from a plasma leads to enhanced oxygen diffusion which has been measured directly as single diffusion jumps. Details of the O-H interaction still have to be established. There is also enhanced loss of O_i atoms from solution, presumably due to the formation of oxygen agglomerates. It appears that the latter process controls the rate of TD-formation. The presence of a high concentration of carbon inhibits TD-formation in either furnace or plasma treated samples.

The new results, for furnace annealed samples (Figures 3 and 4), enable the correlation between the loss of oxygen and the formation of TD-centres at different temperatures to be understood. It is clearly necessary that the temperature dependence of each process should be the same. However, there are outstanding problems. We may write $d[\text{O}_i]/dt = -4\pi r_c (D(X) + D(\text{O}_i)) [X][\text{O}_i]$, where $[X]$ is the concentration of traps to which O_i atoms diffuse, $r_c = 5\text{\AA}$ is their capture radius, and $D(X)$ and $D(\text{O}_i)$ are the diffusion coefficients of X and O_i centres respectively. Previously we assumed that X was also an O_i atom and found $D(\text{O}_i)$ equal to the normal value at 450°C . The same model now leads to a value of D an order of magnitude too large at $T = 350^\circ\text{C}$. This result appears to be inconsistent with the dimer model as the predominant process leading to the loss of oxygen unless $D(\text{O}_i)$ is enhanced for furnace anneals.

Instead, it could be assumed that X is some other immobile precursor defect for TD-centres with a concentration equal to $\Sigma[\text{TDN}]_{\text{max}} = 10^{16} \text{cm}^{-3}$. $D(\text{O}_i)$ would then have to be enhanced by a factor of 10^2 to produce the measured loss of O_i atoms at 450°C : the corresponding enhancement factor would be 10^3 at 350°C . This difference cannot be explained by a change in $\Sigma[\text{TDN}]_{\text{max}}$ which was comparable in samples heated at 450°C and 350°C . It is therefore incorrect to identify $[X]$ with $\Sigma[\text{TDN}]_{\text{max}}$, which is clearly evident for carbon doped material.

Any model in which $D(\text{O}_i)$ is enhanced in furnace annealed samples in the range 330 – 400°C is in direct conflict with published stress-dichroism data [9–11] which show a normal value of $D(\text{O}_i)$, unless samples are given special pretreatments. However it could be speculated that $D(\text{O}_i)$ is normal for the relatively short heating times of days, used for the stress dichroism measurements, and that it is enhanced only for longer treatments of months (350°C) necessary to measure the oxygen loss. It might be further speculated that hydrogen diffuses into samples from the surface (from H_2O) during this extended period to account for the difference. Such a proposal might also explain early work which showed that TD formation at 450°C was more rapid in Cz samples grown in H_2 gas rather than He [23]. Clearly, further work is required to resolve these difficulties.

In this paper the ASTM calibration of the 9 μ m band has been used to determine values of [O_i]. A recent new calibration [24] would require these values to be increased by a factor of 3.14/2.45=1.28.

ACKNOWLEDGMENTS

We wish to thank the Science and Engineering Research Council for financial support on grant no. GR/E 95392. ARB also thanks the SERC for a research studentship. Wackerchemitronic, Monsanto and Philips Components (Southampton) are thanked for the provision of the silicon.

REFERENCES

1. R. Oeder and P. Wagner, in *Defects in Semicond II*, edited by S. Mahajan and J.W. Corbett (North Holland, New York, 1983) p. 71.
2. K.M. Lee, J.M. Trombetta and G.D. Watkins, *Proc. Mater Res, Symp.* **46**, 263 (1986).
3. J. Michel, N. Heilwes, J.R. Niklas and J-M. Spaeth, *Inst. Phys. Conf. Ser.* **95**, 201 (1989).
4. T. Gregorkiewicz, H.H.P. Th. Bekman and C.A.J. Ammerlaan, *Acta Physica Polonica*, **A75**, 89 (1989).
5. D. Helmreich and E. Sirtl, *Semicond Silicon Mat. Res. and Devices*, edited by H.R. Huff and E. Sirtl (Electrochem Soc: New York: 1977) p. 626.
6. T.Y. Tan, R. Kleinhenz and C.P. Schneider, *Proc. Mater. Res. Soc. Symp.* **59**, 195 (1986).
7. A. Ourmazd, W. Schroter and A. Bourret, *J. Appl. Phys.* **56**, 1670 (1984).
8. V.P. Markevich, L.F. Makarenko and L.I. Murin, *Phys. Stat. Sol.*, (a) **92**, K173, (1986).
9. G.D. Watkins and J.W. Corbett, *Phys. Rev.*, **121**, 1001 (1961).
10. M. Stavola, J.R. Patel, L.C. Kimerling and P.E. Freeland, *Appl. Phys. Lett.*, **42**, 73 (1983).
11. A.K. Tipping, R.C. Newman, D.C. Newton and J.H. Tucker, *Defects in Semicond.*, edited by H.J. von Bardeleben, *Mat. Sci. Forum* **10-12**, 887 (1986).
12. R.C. Newman and M. Claybourn, *Inst. Phys. Conf. Ser.* **95**, 211, (1989).
13. A.S. Oates and R.C. Newman, *Appl. Phys. Lett.* **49**, 262 (1986).
14. U. Gosele and H.Y. Tan, *Appl. Phys.* **A28**, 79 (1982).
15. A.R. Brown, M. Claybourn, R. Murray, P.S. Nandhra, R.C. Newman and J.H. Tucker, *Semicond. Sci. and Technol.* **3**, 591 (1988).
16. R. Murray, A.R. Brown and R.C. Newman, *E-MRS Conf.*, edited by C.A.J. Ammerlaan, A. Chantre and P. Wagner, Strasbourg 1989, in the press.
17. S. Messoloras, R.C. Newman, R.J. Stewart, A.R. Brown, M. Claybourn, R. Murray and J.G. Wilkes, *IEE UK IT88 Conf. Swansea 1988*, p. 529.
18. M. Claybourn and R.C. Newman, *Appl. Phys. Lett.* **52**, 2159 (1988).
19. A.R. Bean and R.C. Newman, *J. Phys. Chem. Solids* **33**, 255 (1972).
20. F.A. Ponce, N.M. Johnson, J.C. Tramontana and J. Walker, *Inst. Phys. Conf. Ser.* **87**, 49 (1987).
21. J.L. Lindstrom and B.G. Svensson, *Proc. Mater. Res. Soc. Symp.* **59**, 45 (1986).
22. H.J. Stein and S. Hahn, *Int. Conf. on Defect Control in Semicond*, Yokohama, Japan 1989, in the press.
23. C.S. Fuller and R.A. Logan, *J. Appl. Phys.* **28**, 1427 (1957).
24. A. Baghdadi, W.M. Bullis, M.C. Croarkin, Yue-Zhen Li, R.I. Scace, R.W. Series, P. Stallhofer, M. Watanabe, *J. Electrochem. Soc.*, **136**, 2015 (1989).

A STEADY-STATE MODEL FOR COUPLED DEFECT IMPURITY DIFFUSION IN SILICON

F. F. MOREHEAD AND R. F. LEVER

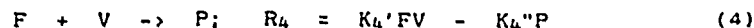
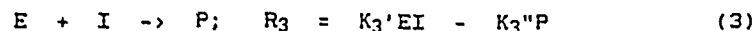
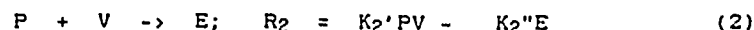
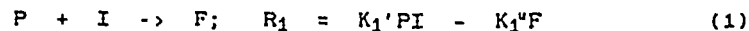
IBM East Fishkill Facility, Hopewell Junction, New York 12533

ABSTRACT

We extend our earlier model which was proposed to explain tails in the diffusion profiles of high concentration boron and phosphorus in silicon. Our quasi-steady-state approach is generalized here to include both vacancies (V) and interstitials (I) at equivalent levels. I-V recombination is regarded as near local equilibrium, occurring through reactions of the defects with defect-impurity pairs. This approach leads to the well-known plateau, kink and tail in high surface concentration P diffusions in Si and to the less well recognized tails in B as well. Our extended model, in its simplest form, allows a more complete and less restrictive treatment of Au diffusion in Si. An important advantage is the direct inclusion of these defect-impurity interactions and the resulting gradients in the defect concentrations.

Recently models for impurity diffusion in silicon have been proposed, by us [1] and subsequently by others [2,3], which attempt directly to include the effects of counter-fluxes of impurity-defect pairs and the unpaired defects, such as tails in high concentrations of boron and phosphorus. In Ref. (1), we used the equality of the oppositely directed fluxes of interstitials (e.g., I and I^{*}) and the interstitial-boron pairs [(BI) and (BI)^{*}] to yield a quasi-steady-state distribution of I's in the bulk Si crystal, rising from an equilibrium value I₀ at the surface to a higher level in the interior. The V's were determined from IV = I₀V₀. Here we write a complete set of coupled diffusion equations for B, I, V, BI- and BV-pairs and find a steady-state solution by setting to 0 a particular sum containing the time derivatives of all these entities except B (in comparison with which they are all very small). The sum is formed so that all of the kinetic terms for interactions of these diffusing species cancel out.

To illustrate, consider a simple system with no concentration enhanced diffusion, no clustering, no field effect for a substitutional dopant P (not necessarily phosphorus) which diffuses via E-centers (PV) and F-centers (PI) with four reactions:



Here K_i' is the kinetic constant for the forward ith reaction, K_i'' its reverse. For simplicity (following closely the con-

ventions of Ref.[4]), we have used the same symbol both for the entity and its concentration, e.g., I is the symbol both for the interstitial Si and its concentration. The complete set of coupled differential equations is

$$dP/dt = -R_1 - R_2 + R_3 + R_4 \quad (5)$$

$$dF/dt = (d/dx)D_F(dF/dx) + R_1 - R_4, \quad (6)$$

$$dE/dt = (d/dx)D_E(dE/dx) + R_2 - R_3, \quad (7)$$

$$dI/dt = (d/dx)D_I(dI/dx) - R_1 - R_3, \quad (8)$$

$$dV/dt = (d/dx)D_V(dV/dx) - R_2 - R_4. \quad (9)$$

Here D_F is the diffusivity of the F-center (PI); D_E is that of the E-center (PV); D_I is that of the I's; D_V , that of the V's.

We now aim for a simple analysis of Eqs.(5-9) to obtain a steady-state solution for the defect concentrations I and V (radically changed from their equilibrium values by the diffusion) which are a function of P alone. This in turn enables the computation of an effective diffusivity of the dopant which also will be a function of P alone. We first assume that the concentrations of the defects and the defect-dopant pairs, I, V, F, and E, are all negligible compared to that of the dopant, P. We next assume local equilibrium for all the reactions in Eqs.(1-4). We can then set the sum $dF/dt + dI/dt - dE/dt - dV/dt = 0$ for the quasi-steady-state. Then

$$(d/dx)[D_F(dF/dx) + D_I(dI/dx) - D_E(dE/dx) - D_V(dV/dx)] = 0 \quad (10)$$

where the kinetic R-terms all drop out. Even without assuming local equilibrium, one can integrate Eq.(10) twice to give

$$D_F F + D_I I - D_E E - D_V V = A, \quad (11)$$

or

$$S_F + \mu S_I - \xi S_E - R \mu S_V = a, \quad (12)$$

where we define the following supersaturation ratios: $S_F = F/F_0$; $S_I = I/I_0$; $S_E = E/E_0$; $S_V = V/V_0$; and the concentration diffusivity ratios: $\mu = (D_I I_0)/(D_F F_0)$; $\xi = (D_E E_0)/(D_F F_0)$; $R = (D_V V_0)/(D_I I_0)$. The integration constant $a = 1 + \mu - \xi - R\mu$. Here the subscript 0 indicates the equilibrium, s the surface value. The first integration constant is taken as 0, since that is the value of the sum of fluxes deep within the crystal. For local equilibrium for reactions (1-4), we have

$$S_F = S S_I; \quad S_E = S S_V; \quad S_I S_V = 1 \quad (13)$$

(where $S = P/P_0$). By substituting these relations into Eq.(12)

we obtain

$$(S + \nu)S_I^2 - aS_I - (\xi S + R\nu) = 0, \quad (14)$$

where ν , ξ , R and a are known quantities. The solution of Eq. (14), giving $S_I(S)$, allows us to write an effective diffusivity for P , the impurity. From Eqs.(5-7),

$$(dP/dt) + (dF/dt) + (dE/dt) = (d/dx)[D_F(dF/dx) + D_E(dE/dx)], \quad (15)$$

or, since $P \gg E$ or F , from Eqs.(13)

$$P_S(dS/dt) = (d/dx)D_F F_S[(dS_F/dx) + \xi(dS_E/dx)]. \quad (16)$$

The effective diffusivity for P or $S = P/P_S$ from

$$dP/dt = (d/dx)D_P^{\text{eff}}(dP/dx) \quad (17)$$

is then

$$D_P^{\text{eff}} = (D_F F_S / P_S)[(dS_F/dS) + \xi(dS_E/dS)], \quad (18)$$

which yields $D_P^{\text{eff}}(S)$ from Eqs. (13,14). Eq.(17) can be solved numerically to give $P(x,t)$ for a given diffusion.

Figure 1 illustrates this simple system of Eqs.(1-4) with some specific numbers from which $\nu = .00833$, $\xi = .9$ and $R = .6$. For I and V the numbers are taken from analyses of Au and Pt diffusion [5]. For E and F the numbers are such to assure that everywhere $F, E, I, V \ll P$ so that Eq.(16) and Eq.(18) are good approximations. For a ten minute diffusion we see a phosphorus-like profile with "plateau," "kink," and "tail." In the "plateau," where I and V approximate their equilibrium values I_0 and V_0 , the P profile is roughly a complementary error function with an effective diffusivity of about 4×10^{-14} cm²/s. Concentration enhanced diffusion would tend to flatten it. Here nearly half the P is carried by the E 's (PV pairs) since ξ (see Eq.(12) and ff.) is 0.9. Almost all of the P in the tail is carried by the F 's (PI pairs or interstitial P 's). An extended plateau region does require a lot of E 's to force the I 's flowing to the surface to their equilibrium value I_0 via the reaction in Eq.(3). Note that a small change in ξ from .9 to 1.1 would reverse the roles of I and V . An even smaller change, from .9 to 1.0, would eliminate the tail altogether. However, lowering ξ to a value of .1 [our f_V for phosphorus in Ref.(1)] greatly enhances the tail and eliminates the plateau, suggesting that the (PV) 's dominate the (PI) 's in the high concentration surface regime for a real phosphorus simulation [6]. I - V recombination occurs through Eqs.(1,4) and Eqs.(2,3). Direct recombination is slow [7]. A similar, simplified simulation is described in Ref.(4) where the set of coupled equations like our Eqs.(5-9) is solved numerically directly.

Mathiot and Pfister [8], among others, have described a much more elaborate system of coupled equations, but invoked an

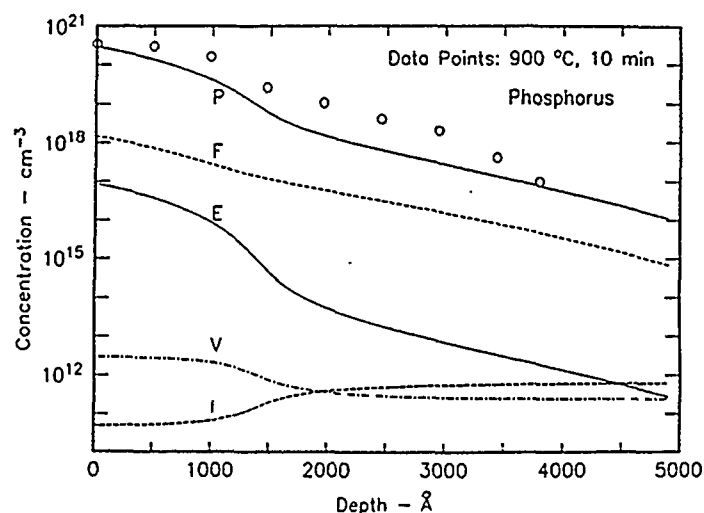


Fig. 1. The profiles resulting from a 10 minute diffusion simulation using Eqs.(17,18). The surface values of the phosphorus-like dopant P, interstitial I, vacancy V, P-I pair F, P-V pair E are given in the text and indicated on the figure. The diffusion constants in cm^2/s are for I, 10^{-6} ; for V, 10^{-8} ; for F, 4×10^{-12} ; for E, 6×10^{-11} . For comparison, data points are shown for a 10 minute 900 °C phosphorus diffusion, after M. Yoshida, Jap.J.Appl.Phys. 18, 479 (1979).

ad hoc assumption (percolation) to explain the phosphorus plateau (the I-V recombination which they invoke is too weak). The results of Ref.(4), despite the close similarity, cannot be quite duplicated with Eqs.(14,18) since these authors [4] have chosen kinetic constants such that F is substantially equal to P for $x > .2 \mu\text{m}$ so that Eq.(10) is no longer accurate. This choice of constants [4] makes the numeric solution of the coupled differential equations faster (D_F is lower for a given $D_F F_0$) but it is not realistic since it is almost certain that $I, V, E, F \ll P$ for all x to the end of the profile. If the constants of these authors [4] are adjusted for lower E_0 and F_0 but with the values of the products $D_F E_0$ and $D_F F_0$ still the same, the "complete" solution and our steady-state approximation converge nicely, with a higher value of I in the tail (~ 20). Our approach computes a million times faster.

In an earlier paper [2] Mulvaney and Richardson and in a later work Orlowski [3] use variations of the following equations (we have used our present notation, eliminated any field effect or concentration enhanced diffusivity):

$$dP/dt = (d/dx)D_F(dF/dx) + (d/dx)D_E(dE/dx), \quad (19a)$$

$$dI/dt = (d/dx)D_I(dI/dx) + (d/dx)D_F(dF/dx) + K_r(I_0 V_0 - IV), \quad (19b)$$

$$dV/dt = (d/dx)D_V(dV/dx) + (d/dx)D_E(dE/dx) + K_r(I_0 V_0 - IV). \quad (19c)$$

But from our Eqs.(5-9), Eqs.(19b,19c) should include dF/dt and dE/dt in their respective left members. Solving Eqs.(19) will yield P , I , and V , if the recombination rate k_r is large (as described above it is proportional to P) but only because this is another, more costly approach to the steady-state solution of our model, since, compared to dP/dt , $dI/dt \sim dV/dt \sim 0$. Eqs. (19) do offer a reasonable route to 2- and 3-dimensional diffusions [9], as well as including the effects of dislocations, traps, clustering, etc.

Eqs.(1-4) do represent completely a real system, Au diffusion in Si, in which, for $T < 1100^\circ\text{C}$, $\bar{E} \sim 0$, i.e., there is no contribution to the diffusion from a gold-vacancy pair. The usual approach to modeling Au diffusion in undischarged Si [11] is to assume that interstitial Au is constant (F_S) everywhere because its diffusivity D_F is so large. Eqs.(5,8,9) give

$$\begin{aligned} dP/dt [1 + (dV/dP) - (dI/dP)] = \\ (d/dx) [D_V(dV/dP) - D_I(dI/dP)] (dP/dx), \end{aligned} \quad (20)$$

which for $S_F = 1$ ($F = F_S$) gives

$$\begin{aligned} (dP/dt) [1 + (V_0/P_S) + I_0/(P_S S^2)] = \\ (d/dx) (D_I I_0 / P_S) [(1/S^2) + R] (dP/dx), \end{aligned} \quad (21)$$

since $S_I S = S_I S_V = 1$, where $S = P/P_S$, $S_I = I/I_0$, $S_V = V/V_0$. If without assuming $F = F_S$ we use Eqs.(14,15) with $\bar{E} = E = D_F = 0$ and make appropriate approximations we obtain the same right-hand side of Eq.(21) but the second and third terms of the factor multiplying dP/dt in the left-hand side are multiplied by D_V/D_F and D_I/D_F , respectively. If we apply Eq.(14) to Eq.(20), again with appropriate approximations, we get Eq.(21) exactly. These results are consistent only for V_0/P_S and $I_0/(P_S S^2)$ much less than 1. Otherwise in a given diffusion of gold into silicon, I , V , and F are not functions of P only, but of x and t as well [12]. With previously determined constants [13], Eqs.(14,15) without approximations reproduce the Au indiffused profiles perfectly for $T < 1100^\circ\text{C}$, (Fig. 2, curve A, for example) but not for a thick sample indiffused at 1200°C [12], even though the assumption $F = F_S$ is no longer made. Here an E contribution (Au-V pair) to the diffusion, with $\bar{E} \sim 0.14$ appears to be required (Fig.2, curve B).

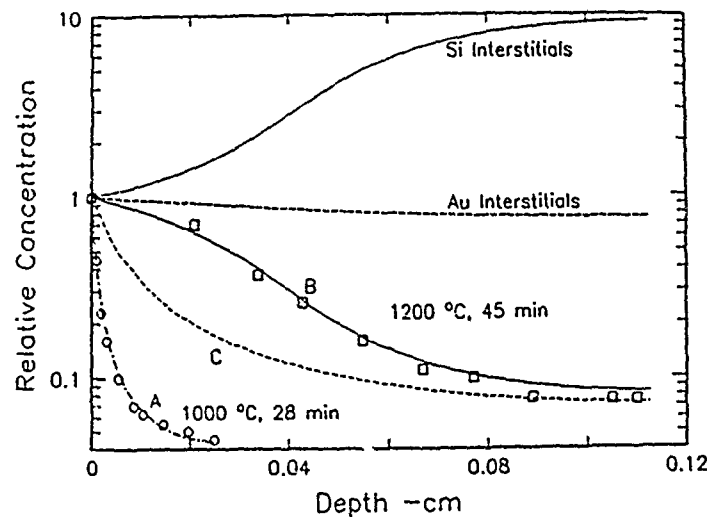


Fig. 2. Curve A: Gold diffusion at 1000 °C for 28 minutes into a 500 μ m Si wafer with no Au-V contribution. Curve B: Au-V contribution is required ($\xi = .14$) for a 1200 °C, 45 minute diffusion into a 2.25 mm wafer. Curve C: same as B, but $\xi = 0$. The lines are from our model, points are data [13]. Also shown for B are the relative concentrations of the Si and Au interstitials.

References

1. F.F. Morehead and R.F. Lever, Appl. Phys. Lett., **51** (1986).
2. B.J. Mulvaney and W.B. Richardson, Appl. Phys. Lett. **51**, 1917 (1987).
3. M. Orlowski, Appl. Phys. Lett. **53**, 1323 (1988).
4. W. B. Richardson and B. J. Mulvaney, Appl. Phys. Lett. **53**, 1917 (1988).
5. F. Morehead, Mater. Res. Soc. Proc. **104**, 99 (1988).
6. F.F. Morehead and R.F. Lever, unpublished.
7. S.M. Hu, J. Appl. Phys. **57**, 1069 (1985).
8. D. Mathiot and J.C. Pfister, J. Appl. Phys. **55**, 3518 (1984).
9. E. Morris, R.R. O'Brien, F.F. Morehead, R.F. Lever, J.P. Peng and G.R. Srinivasan, unpublished.
10. R.F. Lever and F.F. Morehead, unpublished.
11. U. Gösele, F.F. Morehead, W. Frank and A. Seeger, Appl. Phys. Lett. **38**, 157 (1981).
12. Since Eq(19c) was used to analyze Au and Pt in-diffusion profiles in Ref. (5) to obtain an estimate of D_i while an alternate expression (see text) may be equally valid (or invalid), the estimate given in Ref. (5) for the diffusivity of interstitial Si may equally well be that of the interstitial Au.
13. N.A. Stolwijk, J. Hölzel, W. Frank, E.R. Weber and H. Mehrer, Appl. Phys. A **39**, 37 (1986).
14. W.A. Orr Arienzo, R. Glang, R.F. Lever, R.K. Lewis and F.F. Morehead, J. Appl. Phys. **63**, 116 (1988).
15. M. Orlowski, IEDM 1988 Technical Digest, (Proceedings of the Dec. 1988 meeting, International Electron Devices, San Francisco), p. 632.

HIGH AND LOW TEMPERATURE MEASUREMENTS OF THE CHROMIUM DIFFUSIVITY IN SILICON

J. ZHU AND D. BARBIER

Laboratoire de Physique de la Matière, Institut National des Sciences Appliquées de Lyon, 20
Avenue Albert Einstein, F69621, Villeurbanne cedex, FRANCE

ABSTRACT

By grouping high and low temperature diffusivity measurements in boron-doped silicon, a new diffusivity law for chromium in the 20-1050 °C temperature range has been established. High temperature diffusivities were deduced from erfc fits of chromium-boron pair profiles measured by means of Deep Level Transient Spectroscopy in chromium-plated substrates, after annealing for a short time in a lamp furnace. Low temperature diffusivities were derived from the association time constants of the chromium-boron pairing reaction in chromium-contaminated specimens. The whole data points were well fitted using the following expression for the diffusion coefficient: $D = 2.6 \times 10^{-3} \exp(-0.81 \pm 0.02 \text{ eV}/kT)$. Because of the wide $1/T$ interval available, the migration enthalpy value is more accurate than the previous determinations using only high temperature diffusivity results.

INTRODUCTION

Transition metals are known as fast diffusers in silicon and therefore constitute a major source of electrically active defects in bulk or layered structures during microelectronic device processing. A detailed analysis of the chemical trends and properties of transition metals in silicon can be found in a review paper by E.R. Weber [1]. The 3d elements preferentially reside in the tetrahedral interstitial sites of the silicon lattice, with very low solid solubilities, and diffusivities at high temperature in the range of those measured for substitutional impurities in liquid silicon. Going from Cu to Ti in the 3d row, the solubility and the diffusivity decreases by several orders of magnitude. This trend is likely to be related to the increasing atomic size with the decreasing nucleus charge. The diffusivity of most of the 3d metals in silicon have already been assessed in the high temperature range, using sensitive methods such as Neutron Activation Analysis (NAA) [2], the radiotracer method or Deep Level Transient Spectroscopy (DLTS) [3,4,5]. However the scattering observed in the diffusivity values together with the shrinkage of the $1/T$ interval at high temperature yield only rough estimates for preexponential factors and migration enthalpies. The diffusivity of Cr was first investigated in the 900-1250 °C temperature range by Bendik et al. [6], with the p-n junction method. These authors derived the diffusivity law: $D = 10^{-2} \exp(-1.0 \text{ eV}/kT)$, which was afterwards confirmed by Würker et al. [7] using the same experimental technique. The migration enthalpy value of 1.0 eV suggests a gradual increase from Mn (0.63 eV) [3] to Ti (1.8 eV) [5]. However, as pointed out by Gilles et al. [3], there is only a small change in the migration enthalpy from Cu to Mn, so that the question of a sharp or a gradual increase from Mn to Ti still remains unanswered. In this work we have combined high and low temperature diffusivity measurements to re-assess the migration enthalpy of Cr in B-doped silicon. Diffusion experiments were carried out on Cr-plated samples between 850 °C and 1050 °C. In the 20-100 °C temperature range the Cr diffusivity was studied by monitoring the diffusion-limited Cr-B pairing reaction.

EXPERIMENTS

The Cr diffusivity experiments were carried out on commercial Czochralski-grown (100) P-type Si, with a B concentration of $6-7 \times 10^{14} \text{ cm}^{-3}$. A 60-100 nm thick Cr film was sputtered on one side of $1 \times 1.5 \text{ cm}^2$ samples cut in the wafers. In-diffusion of the Cr atoms was achieved in a low thermal inertia rapid thermal processor of JIPELEC specially designed for laboratory specimens of $1-10 \text{ cm}^2$ areas. The specimen under study was placed in a cold wall chamber under an Ar gas flow and illuminated by a bank of 7 tungsten halogen lamps through a water-cooled quartz window. This arrangement allows contactless temperature measurements using a Ge diode pyrometer, combined with a convenient optical filtering around $1.4 \mu\text{m}$ that eliminates the lamp contribution in the diode response. For low temperature diffusion studies flat Cr profiles were

realized by annealing the samples at 950 °C for 30 min. For high temperature diffusivity measurements slowly decreasing Cr profiles were obtained by annealing the Cr-plated specimens between 850 °C and 1050 °C for a time varying from a few seconds to a few minutes. These short time annealed samples were submitted to a pre-annealing at 600 °C for 10 min before the high temperature diffusion step, in order to ensure the formation of the Si-rich silicide CrSi_2 as a well-defined boundary phase for Cr diffusion. Moreover, the high temperature plateau was terminated by a fast cooling in the process chamber of the lamp furnace at about 140 °C/s down to 600 °C. The samples were cooled from this temperature down to room temperature within a few minutes by the Ar gas flow. This procedure was effective to avoid any early precipitation of the interstitial Cr atoms (Cr_i) during cooling down.

In solid solution, the Cr atoms occupies the tetrahedral interstitial sites of the Si lattice, and give rise to a donor level ($0/+$) located at 0.22 eV from the conduction band [8]. After rapid cooling down from the plateau temperature of the diffusion annealing, the Cr_i solution is strongly supersaturated, and thus evolves toward more stable lattice configurations. In B-doped silicon Cr_i is positively charged and combines with the negatively-charged substitutional B (B_s) to form the Cr_iB_s pair defect which is stable at room temperature. This pairing reaction produces the appearance of the Cr_iB_s donor level at 0.28 eV from the valence band [9,10], which was used as a probe for Cr profiling in high temperature diffusivity investigations. The Cr-contaminated surface of the samples annealed for high temperature diffusivity measurements was bevelled with a 1° angle and chemically etched. A pattern of Al Schottky contacts was then photolithographically delimited on the bevelled surface. This pattern allowed to probe the Cr concentration down to 150 μm from the initial surface, with a depth accuracy of 10 μm . A boxcar DLTS equipment with a sensitivity $\Delta C/C$ of 10^{-5} was used in this study. The DLTS analysis was performed two weeks after the diffusion treatment. In addition to this period, the samples were stored at least for 3 days at 60 °C before the DLTS measurements in order to accelerate the pairing reaction. According to H. Conzelmann [10], the equilibrium fraction of paired Cr should be about 80 % at this temperature for the doping level used in this work. Thus, as long as the acceptor concentration is higher than the Cr_i solubility at 1050 °C, the Cr_iB_s profile must reflect the Cr_i profile resulting from any of the diffusion treatments performed in this work. For low temperature diffusivity investigations the samples with a flat Cr profile were not bevelled before Schottky diode evaporation. They were annealed at 200 °C for 30 min in order to produce the total Cr_iB_s pair dissociation and rapidly mounted in the cryostat of the DLTS equipment, where the temperature was kept constant in the 20-100 °C interval. The repetitive measurement of the growing Cr_iB_s donor level concentration during the course of the pairing reaction allowed to monitor the diffusion-limited association kinetics of Cr_i with B_s , at a fixed temperature.

RESULTS

Diffusivity measurements from 850 °C to 1050 °C

Fig. 1 shows the Cr_iB_s profiles measured by DLTS after pair formation in Cr-diffused samples. The experimental points are well fitted by an erfc function (solid line) including the diffusivity D and the surface concentration C_0 as adjustable parameters. The erfc shape of the experimental profiles indicates that diffusion occurred from a steady concentration Cr source at the interface. Moreover, a good agreement was found between the C_0 values and the Cr solubilities in Si in equilibrium with CrSi_2 reported by E.R. Weber [1] for the same temperature range. These results are consistent with the formation of a sufficiently thick CrSi_2 layer during the pre-annealing treatment at 600 °C. The best Arrhenius fit of the data points, plotted on a logarithmic scale as a function of the reciprocal temperature (see Fig. 3), yielded the following diffusivity law, which is very close to the expression derived by N.T. Bendik et al. [6]:

$$D = 0.04 \exp(-1.1 \text{ eV}/kT) \quad (1)$$

The error margin concerning the migration enthalpy ΔH_m was estimated by introducing maximum ordinate variations for the end points of the fitting straight line at 850 °C and 1050 °C. These variations were taken equal to the scattering in the D values measured at 900 °C, that is 25 %. The large error margin obtained ($\Delta(\Delta H_m) = 0.3 \text{ eV}$) is mostly related to the narrow $1/T$ interval available for fitting the high temperature diffusivity data.

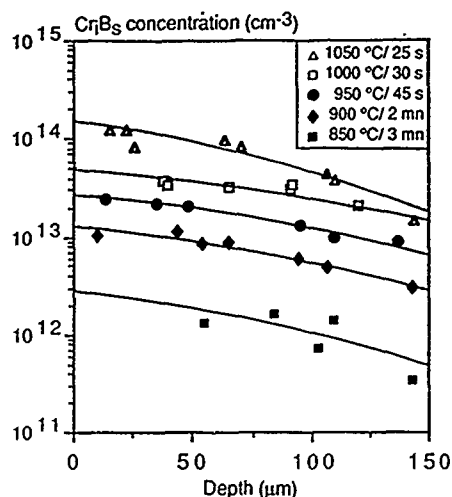


Fig. 1: Cr_iB_5 profiles in B-doped and Cr-plated CZ Si, measured by DLTS on bevelled samples after Cr diffusion in a rapid thermal processor. The solid lines represent the best erfc fits of the experimental points.

Low temperature diffusivity measurements

Reiss et al. [9] have developed a model for diffusion-limited impurity reactions in semiconductors, which have been applied in this work for the system formed by an initial number n of mobile Cr_i^+ ions and a concentration N_A of immobile B_s^- ions. In this model the diffusion medium is seen as an equivalent spherical volume $1/N_A$ at the center of which the B_s^- ions are superimposed and constitute an infinite capture shell for all the metal ions initially gathered around the edge of the sphere. This representation of the diffusion medium implies the following assumptions: i) the acceptor concentration is much higher than the metal ion concentration, and ii) the dissociation reaction is considered negligible. The first condition allows to consider a first order kinetics for the capture reaction:

$$-dn/dt = \tau^{-1}n \quad (2)$$

The second condition is only valid in the first stage of the reaction kinetics. Before being captured, the Cr_i^+ ions must diffuse over a distance equal to the equivalent sphere radius, and approach the capture shell by less than a certain capture radius R . Assuming a steady state flux of Cr_i^+ ions through the capture sphere surface at the beginning of the association reaction, the following expression of the time constant τ , including the diffusion coefficient D of the mobile species, have been derived:

$$\tau = (4\pi R N_A D)^{-1} \quad (3)$$

The capture radius R of a B_s^- ion is the distance over which the thermal energy kT of the mobile ion is exceeded by the Coulomb interaction energy $q^2/4\pi\epsilon R$. Now, substituting the expression of the capture radius, $R = q^2/4\pi\epsilon kT$, in equation (3) we obtain:

$$\tau = \epsilon kT / q^2 N_A D \quad (4)$$

Equation (4) has been used to calculate the diffusion coefficients of Cr in Si at four temperatures of the 20-100 °C interval starting from the time constant τ of the Cr_iB_5 pairing reaction. The τ values have been determined by plotting the percentage of unpaired Cr_i^+ ions $f(t)$ in a logarithmic scale as a function of time during the first stage of the association kinetics. The two examples of association kinetics presented in Fig. 2 show that $f(t)$ exhibited a straight line shape, as expected for a first order kinetics. From the scattering of the results obtained on several Schottky diodes at a given temperature, we deduced a maximum error margin of 20 % in the determination of D .

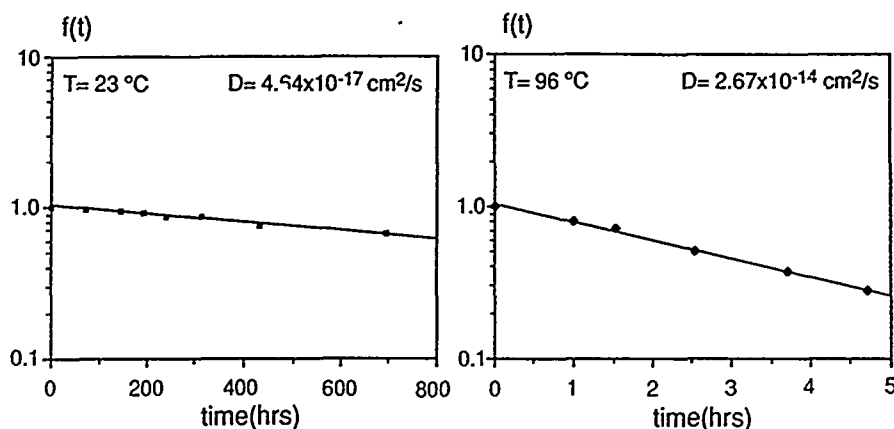


Fig. 2: Examples of Cr_iB_s pair formation kinetics in B-doped CZ Si ($N_A = 6.7 \times 10^{14} \text{ cm}^{-3}$), after Cr contamination ($950^\circ\text{C}/30 \text{ mn}$) and total pair dissociation ($200^\circ\text{C}/30 \text{ mn}$).

Cr DIFFUSIVITY IN Si FROM 20°C TO 1050°C

A logarithmic plot of both high and low temperature diffusivity values as a function of $1/T$ is shown in Fig. 3. Note the very good alignment of the low temperature points. The Arrhenius fit was performed either including or excluding the high temperature D values. In both cases, we found the same activation energy of 0.81 eV, and only a slight difference appeared in the preexponential factor D_0 . This clearly illustrates the dominant contribution of the low temperature measurements, and also the good correlation between the high temperature D values with the low temperature Arrhenius fit. Moreover, considering the large scattering of the data points, we obtained an error margin of only 0.02 eV for the migration enthalpy ΔH_m . The wide $1/T$ interval available allowed to derive a precise diffusivity law for Cr in Si:

$$D = 2.6 \times 10^{-3} \exp(-0.81 \pm 0.02 \text{ eV}/kT) \quad (5)$$

In Fig. 3 one can observe the significant discrepancy between our low temperature results and the values calculated using either the diffusivity law determined by Bendik et al. [6] or expression (1). This discrepancy certainly comes from the poor accuracy of the fit when using only high temperature diffusivity data.

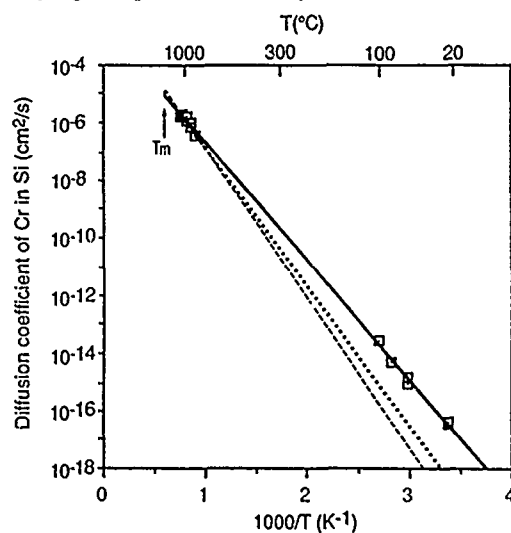


Fig. 3: Logarithmic plot of the high and low temperature Cr diffusivity data obtained in this work, as a function of $1/T$. The best Arrhenius fits of the high temperature points alone (dashed line), and of both high and low temperature points (solid line) are shown, together with the previously determined diffusivity law of N.T. Bendik (dotted line).

DISCUSSION

The diffusion coefficients of 3d metals are strongly correlated to their atomic radii, and may be consequently to their charge state, but this later trend has not been experimentally verified. Indeed, as long as the charge state of a metal ion depends on the Fermi level position in the bandgap, the migration enthalpy of a given metal might be temperature dependent. In the case of Cr the single donor level ($0/+$) is located in the upper midgap, so that Cr is always positively charged in p-type Si whatever the temperature value. It follows that the objection of two different charge states of the diffusing species in the high and low temperature range do not hold in the case of Cr. So, assuming no significant lattice effects, it is reasonable to consider expression (5) as a unique diffusivity law valid from room temperature to high temperatures. The migration enthalpy of 0.81 eV is coherent with interstitial diffusion of Cr in Si. Moreover the low value of the preexponential factor 2.6×10^{-3} is typical of a low migration entropy, which is a further indication of an interstitial diffusion mechanism.

The migration enthalpy of Cr in Si obtained in this work is close to the values of ΔH_m determined for other metals on the right side of Cr in the 3d row (Mn: 0.63 eV [3], Fe: 0.65 eV [1]). Then, the question of the unique behaviour of Ti compared to other 3d metals is furthermore pointed out by our low temperature results. Indeed Mathiot et al. confirmed that Ti diffuses in interstitial site with a migration enthalpy of 1.8 eV [5], which is more than twice the value of ΔH_m for Mn and Fe. An attractive explanation of the sharp increase of ΔH_m from Cr to Ti has been given by Utzig in a recent paper [12]. These authors proposed that the migration enthalpy of 3d metals could be assessed by the change in elastic energy ΔU_{el} of the compressively strained Si lattice, when an interstitial metal atom passes from the tetrahedral interstitial position to the saddle hexagonal position during a diffusion jump. The essential parameter of this model is the metallic radius of the metal atom, which increases significantly from Cr to Ti. The migration enthalpy of 0.81 eV obtained in this work is in fairly good agreement with the mean value of ΔU_{el} calculated by Utzig for Cr, using two extreme values of the metallic radius. So, the low temperature diffusivity results of this work support the prediction of a sharp increase of the migration enthalpy from Cr to Ti.

CONCLUSION

The diffusivity of Cr in Si was studied for the first time in the 20-100 °C temperature range, by monitoring the Cr_2B_3 pairing reaction. The low temperature data points yielded a significant improvement in the accuracy of the diffusivity law, compared to that given by only high temperature measurements. A migration enthalpy of only 0.81 eV was found with a 0.02 eV error margin. We consider this value more reliable than the previous estimates around 1.0 eV derived from high temperature measurements. Moreover, this result is consistent with the elastic approach of the migration enthalpy for 3d metals in Si proposed by Utzig, according to which a sharp increase from Cr to Ti can be predicted.

ACKNOWLEDGEMENT

The authors wish to thank D. Mathiot for encouragement and interesting discussions, and the CNET for financial support of this work.

REFERENCES

1. E. R. Weber, Appl. Phys. A, 30, 1-22 (1983).
2. E.R. Weber and N. Wiehl in *Defects in Semiconductors II*, edited by S. Mahajan and J.W. Corbett (Mater. res. Soc. proc. 14, North Holland, New York, 1983) pp 19-32.
3. D. Gilles, W. Bergholz and W. Schröter, J. Appl. Phys. 59 (10), 3590 (1986).
4. J. Utzig and D. Gilles in *Defects in Semiconductors 15*, edited by G. Ferenczi (Materials Science Forum, 38-41, Trans. Tech. Publications, Aldermansdorf, Switzerland, 1989) p. 729.

5. S. Hocine and D. Mathiot, Appl. Phys. Lett., 53, 1269 (1988).
6. N.T. Bendik, V.S. Garnyk and L.S. Milevskii, Soviet Physics-Solid State, 12 (1), 150 (1970).
7. W. Würker, K. Roy and J. Hesse, Mat. Res. Bull., 9, 971 (1974).
8. H.H. Woodbury and G.W. Ludwig, Phys. Rev., 117, 102 (1960).
9. K. Graff and H. Pieper in Semiconductor Silicon, edited by H.R. Huff, R.J. Kriegler, and Y. Takeishi (The Electrochemical Society, Pennington, 1981) p. 331.
10. H. Conzelmann, K. Graff and E.R. Weber, Appl. Phys. A, 30, 169 (1983).
11. H. Reiss, C.S. Fuller and F.J. Morin in Chemical Interactions among Defects in Germanium and Silicon, Bell Syst. Tech. J., 35, pp. 535-635 (1956).
12. J. Utzig, J. Appl. Phys., 65 (10), 3868 (1989).

THE FORMATION OF SILICON-RICH SILICIDES

MARIA RONAY and R.G. SCHAD

IBM Research Division, Thomas J. Watson Research Center, Yorktown Heights, New York, 10598

ABSTRACT

Diffusion studies of mono and bilayers of transition-metal films on silicon showed that the formation of η' - Cu_3Si lowers the formation temperature of subsequently forming ReSi_2 by 400°C. This is due to the creation of a large amount of silicon self-interstitials accompanying the formation of the copper silicide, which lowers the activation energy for silicon diffusion. The generalization of this result - stating that the formation of all silicides, in which the volume density of silicon is much larger than in elementary silicon injects silicon self-interstitials into the silicon lattice - gives new insight into silicide formation, silicide-enhanced dopant diffusion and the self-diffusion of silicon itself⁶.

INTRODUCTION

The most important goal in silicon integrated circuit technology today is to increase the density of circuits per unit silicon area in order to enhance their performance. High density multi-level metal interconnects and self-aligned silicide contacts between the first metal layer and silicon are key areas of development. Currently the most favored silicides are the two disilicides TiSi_2 and CoSi_2 . Among the most important questions concerning silicide contacts is their formation temperature and the nature of the moving species. While it is known that transition-metal disilicides form by silicon diffusion¹ in a temperature range between 450°C and 750°C, such relatively low formation temperatures are difficult to reconcile with the large activation energy for the self-diffusion² of silicon (4.1-5.1 eV).

We observed that the formation temperature of disilicides correlates with the size of the transition metal atom, suggesting that transition-metal diffusion may be a precursor to silicon diffusion, and may lower the formation enthalpy of mobile defects in silicon. Transition metals diffuse interstitially in silicon with an activation energy as low as 0.43 eV for the small copper ion and as high as 1.5 eV for the large titanium atom³. If a fast-diffusing transition-metal lowers the formation enthalpy of a silicon defect, then this should decrease the formation temperature of a subsequently forming silicide of a slow-diffusing transition-metal.

In order to investigate this suggestion we chose copper for a fast-diffusing transition-metal, which in thin film reactions forms only Cu_3Si . For a slow-diffusing transition-metal we chose rhenium, which in thin film reactions forms only ReSi_2 (ref.4). What we want to find out is whether the formation of Cu_3Si will introduce mobile silicon defects in silicon and thereby lower the formation temperature of ReSi_2 .

EXPERIMENTAL

We used silicon [100] n-type wafers of 8-12 Ωcm resistivity. Following standard cleaning the wafers were dipped for 30 seconds in buffered HF to remove any oxide layer prior to metal film deposition. Thin films of rhenium and copper were evaporated onto the wafers with an electron gun at pressures in the low 10^{-7} Torr range. The annealings of the samples took place in 99.999% pure argon gettered with copper and titanium; the samples were heated at $10^\circ\text{C}/\text{min}$, held at temperature for 30 minutes and cooled in a few minutes out of the diffusion range.

The elemental composition of the samples was determined with Auger Electron Spectroscopy (AES) combined with Ar ion etching for depth profiling. The measurements were performed using a Perkin-Elmer PHI-600 scanning Auger microprobe. The spectra were recorded using a 5 keV primary electron beam at $1\mu\text{A}$ current which was rastered over a $80\times 80\mu$ area. The sputter etching was done using 2 keV Ar^+ ions. The sputter etch rate was $60\text{\AA}/\text{min}$ for an SiO_2 standard. Peak to peak Auger signals were recorded as a function of depth, with standard sensitivity factors applied to obtain a semi-quantitative analysis of the spectra. Due to preferential sputtering Auger sputter profiles are not suitable to determine stoichiometry. The silicide phases formed were identified by x-ray diffraction.

RESULTS

First we studied the formation of ReSi_2 without any copper being present. A 2000\AA thick rhenium film was deposited on a silicon wafer at 250°C substrate temperature.

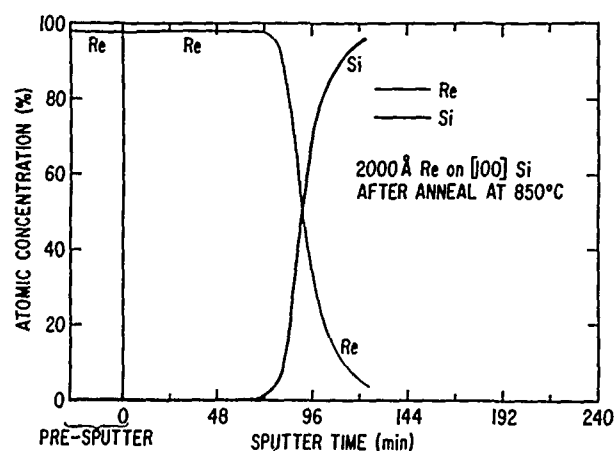


Figure 1 shows the composition profile of the rhenium film on silicon after an anneal at 850°C . We see no interdiffusion and no silicide formation. The profile looks the same

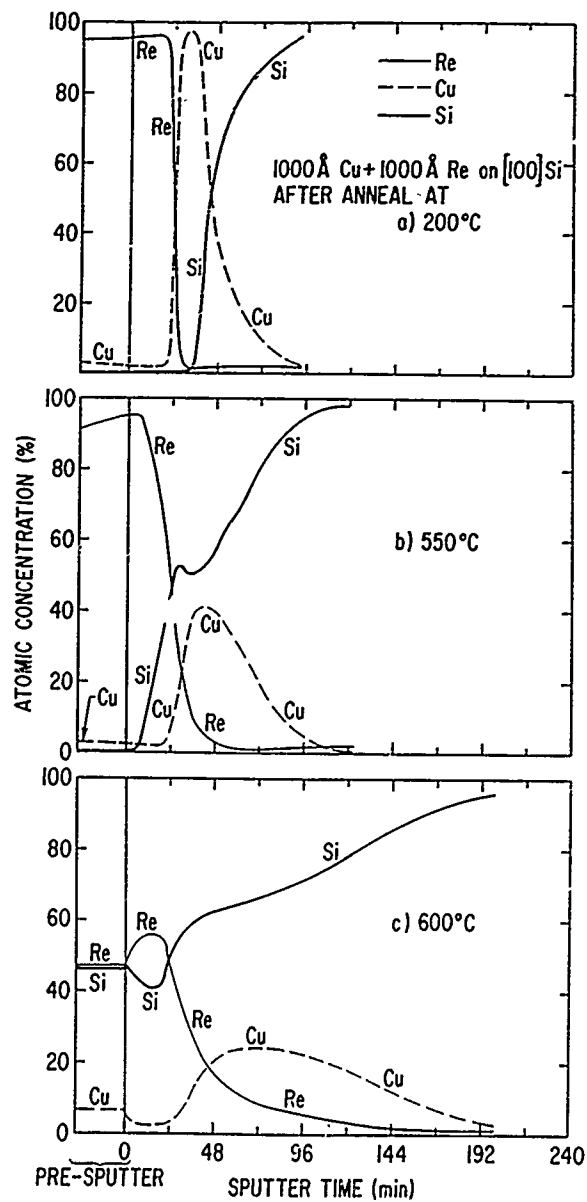


Figure 2. The composition profile of copper, and, on top of it, rhenium films on silicon after an anneal at a. 200°C, b. 550°C, and c. 600°C.

after an anneal at 900°C and no silicide formation is indicated by x-ray diffraction. After an anneal at 950°C almost all of the rhenium transformed into ReSi_2 , as evidenced by x-ray diffraction. This is the highest formation temperature for a disilicide reported to date.

Next we deposited, at room temperature, on silicon substrates, 1000Å copper, and on top of it, 1000Å rhenium. After an anneal at 260°C the composition profile in figure 2a shows that copper diffuses into silicon but according to x-ray analysis no new phases are formed. There is a dramatic change after an anneal at 550°C as shown in figure 2b. The copper film diffused completely into the silicon while seemingly no copper diffused into the rhenium. As evidenced by x-ray analysis, large amounts of η' - Cu_3Si phase forms⁵, and, most importantly, *silicon diffuses into the rhenium*, way beyond the original interface, (compare with figure 2a), and way beyond the copper front characterizing the η' - Cu_3Si phase. The composition profile after an anneal at 600°C is shown in figure 2c. We see that the copper diffuses further into the silicon, while the silicon diffusion front reaches the surface. Both silicon and rhenium have a nearly constant concentration in the better part of the original rhenium layer indicating the formation of substantial amounts of ReSi_2 in agreement with x-ray analysis. There is an increased amount of rhenium diffusion into the silicon as compared to figure 2b.

Some may argue that the formation temperature of ReSi_2 in our first experiment was found to be high because rhenium or silicon oxides form at the interface, which present a large barrier to silicon diffusion, but when there is copper between silicon and rhenium, the copper oxidizes, and copper oxide with its open structure does not present a large barrier to silicon diffusion. To prove that this is not the case, we deposited at 250°C substrate temperature 1000Å rhenium and, on top of it, at room temperature, 1000Å copper, so as to preserve the Re-Si interface and found that in this case too silicon diffused out of the copper silicide and ReSi_2 started to form at 550°C (reference 6). It seems then, that the copper silicide-induced silicon diffusion into rhenium is independent of the sequence of the copper and rhenium films and is not governed by an interface phenomenon. What we found is, that the formation temperature of ReSi_2 , which is over 900°C, got reduced to 550°C when ReSi_2 formation was preceded by η' - Cu_3Si .

How does this happen? Silicon atoms in pure crystalline silicon occupy 20 Å³ volume. This we call the volume density of silicon in silicon. The volume density of silicon in a metal-rich silicide is much larger. We estimated⁶ the volume density of silicon in Cu_3Si and found it to be 46 Å³. This dramatic increase in volume density can take place either by the metal-rich silicide absorbing vacancies or by the metal-rich silicide ejecting silicon. Since vacancy absorption by the silicide and a consequent vacancy undersaturation in the remaining silicon cannot lead to enhanced silicon diffusion, we rather conclude that the increase of the volume density of silicon takes place by the emission of silicon self-interstitials. Our experiments clearly show the out-diffusion of silicon from the Cu_3Si demonstrated in figure 2. The silicide formation lowers the formation enthalpy of silicon self-interstitials⁶ and thereby lowers the activation energy for silicon diffusion lowering the formation temperature of ReSi_2 by about 400°C.

This phenomenon is quite general. In reference 6 we tabulated the volume density of silicon atoms in a variety of metal-rich silicides, monosilicides and disilicides. The table shows that in all the metal-rich silicides the volume density of silicon is considerably larger (46-32.1 Å³) than in silicon; thus we expect that their formation always cre-

ates silicon self-interstitials. In the family of monosilicides, silicon has an intermediate volume density ($33.4\text{--}21.7 \text{ \AA}^3$), which overlaps on the high end with the density of metal-rich silicides and at the low end with the volume density in disilicides ($21.7\text{--}18.9 \text{ \AA}^3$.) The volume density of silicon in disilicides is quite low, as low as, or even lower than in silicon itself. Our examples of η' - Cu_3Si and ReSi_2 represent the highest (46 \AA^3) and the lowest (18.9 \AA^3) volume density of silicon in all known silicides. We believe that the phenomenon of metal-rich silicide formation injecting silicon self-interstitials into the silicon lattice is quite general, and may also take place during the formation of some of the larger volume density monosilicides.

It is customary to infer the creation of silicon self-interstitials in a certain process from the presence of interstitial-type dislocation loops. When very small amounts of metal-rich silicides are precipitated from silicon by quenching from very high temperatures, the precipitates are surrounded by interstitial-type dislocation loops containing extra silicon planes. This was found for Cu_3Si and Pd_2Si by Seibt and Graff⁷ and for α - Fe_3Si by Nes and Washburn⁸ using transmission electron microscopy. These results are in agreement with our results if we assume that the interstitial-type dislocation loops are formed by clustering of interstitial point defects⁹.

Wittmer and Seidel reported an enhancement of dopant diffusion brought about by silicide formation¹⁰. More recent experiments by Wittmer and Tu¹¹ showed that the diffusivity of arsenic in silicon was greatly enhanced by the formation of near-noble-metal silicides and not affected by the formation of refractory-metal silicides.

Table: Redistribution of arsenic during silicide formation

Metal	Silicide	Volume/Si atom \AA^3	Redistribution
Ni	Ni_2Si	32.14	yes
	NiSi	24.00	yes
Pd	Pd_2Si	42.26	yes
Pt	Pt_2Si	45.71	yes
	PtSi	29.89	yes
Ti	TiSi	29.74	no
	TiSi_2	21.21	no
Ta	TaSi_2	21.68	no
V	VSi_2	19.22	no

The authors explain the enhancement by the formation of point defects such as vacancies and/or self-interstitials, however their experiments and the current theoretical understanding of the relevant mechanisms did not allow them to determine the nature of point defects responsible for dopant redistribution.

We suggest that silicides, in which the volume density of silicon is considerably larger than in elementary silicon, inject silicon self-interstitials into the lattice and the self-interstitial exchanges place with the substitutional arsenic atoms by the well-known kick-out mechanism¹² by which the arsenic becomes interstitial and fast-diffusing and the silicon substitutional. In fact Wittmer and Tu deduced that part of the redistributed As is interstitial¹¹. In the table we reproduce table I. from their work and add to it the volume density of silicon for the various silicides. We see that the formation of silicides, in which the volume-density of silicon is large, enhance arsenic diffusion, while the formation of silicides, in which the volume density of silicon is low, do not affect arsenic diffusion. A single exception to the rule is NiSi, where the volume density of silicon is low, yet arsenic diffusion is enhanced. We can however not rule out the possibility that during heating to the formation temperature of NiSi (400°C) some Ni₂Si formed (formation temperature 200°C) temporarily and created silicon self-interstitials enhancing arsenic diffusion. Only those cases of silicide formation are straightforward examples where the formation of the small volume-density silicide is not preceded by the formation of a large volume-density silicide.

REFERENCES

1. K.N. Tu and J.W. Mayer in *Thin Films-Interdiffusion and Reactions* edited by J.M. Poate, K.N. Tu and J.W. Mayer (Wiley, New York, 1978), p. 359.
2. W. Frank, U. Gösele, H. Mehrer and A. Seeger in *Diffusion in Crystalline Solids* edited by G.E. Murch and A.S. Nowick, Materials Science Series (Academic, New York, 1984), p. 63.
3. Eicke R. Weber, Appl. Phys. A 30, 1 (1983).
4. J.J. Chu, L.J. Chen, and K.N. Tu, J. Appl. Phys. 62, 461 (1987).
5. K.P. Mukherjee, J. Bandyopadhyaya, and K.P. Gupta, AIME Trans. 245, 2335 (1969).
6. Maria Ronay and R.G. Schad, 'A new insight into silicide formation: the creation of silicon self-interstitials' submitted to Phys.Rev.Lett. on November 13, 1989.
7. M. Seibt and K. Graff, J. Appl. Phys. 63, 4444 (1988).
8. E. Nes and J. Washburn, J. Appl. Phys. 42, 3562 (1971).
9. H. Föll and B.O. Kolbesen, Appl. Phys. 8, 319 (1975).
10. M. Wittmer and T.E. Seidel, J. Appl. Phys. 49, 5827 (1978).
11. M. Wittmer and K.N. Tu, Phys. Rev. B 29, 2010 (1984).
12. U. Gösele, W. Frank and A. Seeger, Appl. Phys. 23, 361 (1980).

PRECIPITATION OF COPPER AND COBALT AT GRAIN BOUNDARIES IN SILICON

U. JENDRICH, H. J. MÖLLER,

Department of Materials Science and Engineering, Case Western Reserve University, Cleveland, OH 44106

ABSTRACT

The precipitation of copper and (radioactive) cobalt at low energy grain boundaries in polycrystalline silicon and bicrystals is investigated. The metals are diffused in from a surface source between 800 - 1000 °C and the precipitation after cooling down is studied by TEM (for Cu) and Mößbauer spectroscopy (for Co). The precipitates are metal silicides. For copper it is shown that they appear in form of colonies containing hundreds of precipitates with a particle size between 5 - 60 nm. In the grain boundary they nucleate preferentially at dislocations and steps. The distribution and size of the precipitates depend on the cooling rate after the diffusion. In the vicinity of the grain boundary the volume is depleted from the impurities.

INTRODUCTION

The atomic structure of a grain boundary and the reconstruction of the covalent bonds has been related to their electrical activity [1]. Recent experimental investigations for instance by combined Auger/EBIC [2] and TEM/DLTS [3] measurements have shown, however, that the electronic properties of grain boundaries can also be changed by the presence of impurities. These results raise the question to what extent the electrical properties in general are determined by impurities. In view of the importance of these lattice defects for the electronic properties of polycrystalline semiconductors it seems necessary to investigate the problem further.

The transition metals are of particular interest since they are very mobile even at low temperatures and introduce deep levels themselves. However, there is little information available on their interaction with grain boundaries and the influence on their electrical activity. It is therefore the purpose of this study to investigate the behavior of some of the 3d transition elements quantitatively. Copper, nickel and cobalt are the elements with the highest diffusion coefficients and solubilities in silicon among the 3d transition elements and it has been shown that even after quenching they cannot be kept in solution. Their tendency to accumulate at grain boundaries and other lattice defects is therefore expected to be high. In this study results on cobalt and copper will be given.

It is well known that copper in silicon precipitates at dislocations ("decoration") during cooling when the solubility is exceeded. The behavior in dislocation free, single crystalline silicon is more complicated [4-12]. Without favorable nucleation sites it precipitates in planar arrangements mostly on {110} planes in form of colonies. They extend over 0.5 to 100 µm often exhibiting a dendritic shape. The whole colony is usually surrounded by an extrinsic dislocation loop and consists of ten to hundreds of small precipitates, 5 to 30 nm in size. It has been assumed that the first growing particles punch out dislocation loops during precipitation to release the misfit strain [11] which again serve as nucleation sites for further precipitates. From an investigation of diffraction patterns of particles in the TEM, Solberg [10] suggested the orthorhombic Cu_3Si (η'') - phase for the precipitates which is the equilibrium phase with silicon at room temperatures [13].

The behavior of cobalt has been thoroughly studied by Mößbauer spectroscopy and TEM [14,15]. It precipitates as CoSi_2 which has the cubic CaF_2 structure. The precipitates form platelets on {111} planes and are either prismatic or circular in shape. The platelets are only a few atomic layers thick and the {111} planes match those of the silicon matrix almost perfectly (mismatch 1%). Since a large fraction of the cobalt atoms then occupies sites at the interface between the silicon and the precipitate the Mößbauer spectrum is not completely identical to that of bulk CoSi_2 . The precipitation can be partly prevented in silicon which is doped with shallow acceptors because cobalt on interstitial sites can form pairs with the acceptor impurity. The formation of the pairs strongly depends on the cooling rate: fast cooling hampers the precipitation and promotes the complex formation. A similar complex has not been reported for copper probably because it is even more difficult to keep it in the interstitial lattice.

EXPERIMENTAL PROCEDURE

Czochralski grown bicrystals with a low energy Σ 13 [001] tilt grain boundary have been used for the cobalt and polycrystalline silicon (with grain sizes of a few mm) for the copper experiments. Both materials were p-doped: the bicrystals with boron ($9 \times 10^{14} \text{ cm}^{-3}$) and the polycrystalline silicon mainly with aluminium ($\approx 10^{17} \text{ cm}^{-3}$). The specimens were cut, polished and chemically etched. The grain boundaries in the bicrystals were oriented approximately parallel to two surfaces. The metal was applied to opposite surfaces either by scraping it on the surface from a wire of high purity copper or from a solution of CoCl_2 containing radioactive ^{57}Co , respectively. The CoCl_2 dissociates at about 550°C and releases the cobalt. The specimens were annealed then in a quartz tube at 1000°C (Cu) or between $800 - 1000^\circ\text{C}$ (Co) under flowing Argon gas and then quenched or cooled down slowly. The annealing times were chosen so that the metal could saturate the whole specimen. From previous experiments one could expect a homogeneous bulk concentration of about 1/30 of the equilibrium concentration at the annealing temperature: about $3 \cdot 10^{16} \text{ cm}^{-3}$ for copper and $10^{12} - 10^{13} \text{ cm}^{-3}$ for cobalt [16].

The preparation of the bicrystals with radioactive cobalt for tracer and Mößbauer measurements has been described in a previous paper [14]. The polycrystals used for the copper diffusion were investigated in the TEM. Specimens were ground and polished down manually to a thickness of about $20 \mu\text{m}$ and finally thinned in an ion thinner. This procedure yields large transparent areas that can be analyzed in the microscope. The TEM was performed using a Philips 400 T operating at 120 KV with an EDX facility and a JEOL 200 CX operating at 200 KV.

EXPERIMENTAL RESULTS

Cobalt

The distribution of the radioactive cobalt in the bulk of the bicrystal and near the grain boundary has been studied by measuring the intensity of the 6 keV and 14.4 keV radiation after each step of a successive removal of thin layers parallel to the grain boundary. Mößbauer spectra were recorded at different positions along the concentration profile. Two different spectra were found representing the position of cobalt in the bulk and near the grain boundary. They were analyzed by fitting Lorentz lines which have been previously [17] associated with different positions of cobalt in boron doped silicon. It was possible to describe the spectra completely with lines that are related to cobalt-boron pairs (B1, B2, B3 for three different cobalt interstitial sites) and cobalt silicide precipitates (lines P1, P2 for cobalt at the interface of the precipitate or inside, respectively). The results on the fraction of cobalt in the particular position are given in the table below. They show that after quenching the cobalt in the volume is mostly present as cobalt-boron pairs, whereas the precipitated cobalt is located at or near the grain boundary. The large fraction of cobalt in the interface position (P1) indicates a plate-like shape of the precipitates. Since the Mößbauer spectra show the same properties as they have been found for plate-like cobalt precipitates in the bulk one can exclude here the possibility that atomic cobalt occupies sites in the disturbed grain boundary structure which would possibly give rise to new lines in the spectra.

The previously reported results [14] have also shown that in the vicinity of the grain boundary the volume is depleted from cobalt and the amount of missing cobalt corresponds approximately to the cobalt enriched at the grain boundary. Qualitatively it has been found that slow cooling increases the accumulation. Assuming a simple model for the interaction of the cobalt with the grain boundary, the concentration profile in the bulk could be simulated by solving the diffusion equation numerically and fitting it to the experimental results. The main fitting parameters (given in the table) are the cobalt concentration at the grain boundary and the mean density of the nucleation sites for the precipitates.

	B1	B2	B3	P1	P2		970 °C	870 °C	
Bulk	31	32	11	16	10	[%]	$2 \cdot 10^{13}$	$3 \cdot 10^{12}$	$[\text{cm}^{-3}]$
Grain boundary	2	8	1	89	0	[%]	$4 \cdot 10^{10}$	$1 \cdot 10^{10}$	$[\text{cm}^{-2}]$
Precipitate density							$7 \cdot 10^9$	$1 \cdot 10^9$	$[\text{cm}^{-2}]$

Copper

The precipitation process at grain boundaries was further studied in polycrystalline silicon which offers a greater variety of different grain boundary structures. The material that was used for the experiments showed a preferential orientation of the grains and a large number of low energy grain boundaries. The orientation was determined from the diffraction patterns in the TEM. The majority of the investigated grain boundaries were either twins ($\Sigma 3$, 70.59° tilt around $\langle 110 \rangle$ axis) or near second order twins ($\Sigma 9$, 38.94° around $\langle 110 \rangle$), sometimes with dislocation arrays in the boundary plane. The bulk dislocation density was estimated to be $\leq 10^4 \text{ cm}^{-2}$.

The results which have been obtained so far indicate that the distribution and the size of the precipitates depend on the cooling rate after the diffusion. After slow cooling ($\approx 0.1 \text{ K/s}$) no precipitates have been observed so far. However, it cannot be excluded that precipitates still occur at large distances ($\gg 200 \mu\text{m}$) so that it may be difficult to find them in the TEM specimens.

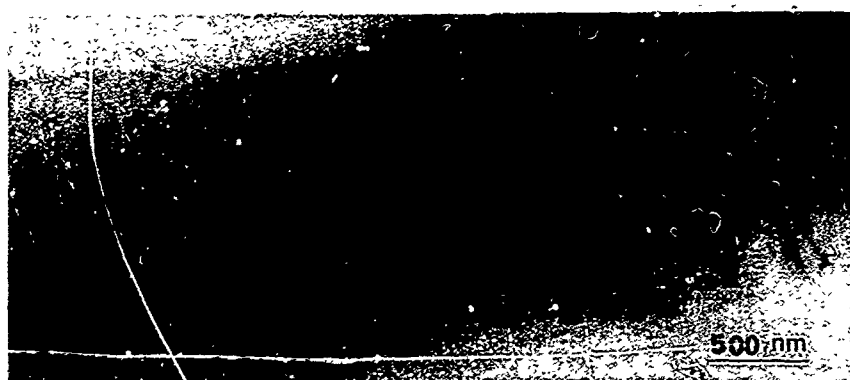


Fig. 1 A colony of copper precipitates in a grain boundary showing the alignment of precipitates along dislocations. (Intermediate cooling rate 5 K/s).

In specimens cooled down at an intermediate rate ($\approx 5 \text{ K/s}$) precipitation occurs at grain boundaries (Fig. 1) and dislocations. The distribution of the precipitates in the grain boundaries is inhomogeneous in form of colonies which contain hundreds of precipitates. They have a mean distance of about $100 \mu\text{m}$ and a mean diameter of about $1 - 3 \mu\text{m}$. The size of the particles in the colonies is largest in the center (up to 60 nm) and decreases toward the ends. In some cases very small particles ($5 - 10 \text{ nm}$) could be found adjacent to the colony as well as far away from it, however, basically the precipitation is localized in the colonies. The average density of precipitates is about $10^9 - 10^{10} \text{ cm}^{-2}$. In general the precipitates grow on either side of the grain boundary and show no preferential growth into one of the grains. In TEM specimens which have been prepared from the near surface region of the diffused samples (within about 50 to $100 \mu\text{m}$) where the copper concentration increases up to the equilibrium concentration, more and larger colonies of precipitates were observed.

An EDX analysis was performed on a colony and, for comparison, on sites in the grains. The spectrum revealed only silicon and copper, with the copper intensity in the colony being about 100 times larger than the background. Therefore one can assume that a copper-silicide has precipitated. Furthermore the precipitates showed the same features as those described by other authors for copper-silicides [4-11] which have precipitated in the bulk: almost spherical or ellipsoidal shape with the long axis in the $\langle 110 \rangle$ direction and a mean size between $5 - 35 \text{ nm}$. A special orientation relationship to the matrix was indicated by Moiré fringes with a spacing of 3.5 nm when viewed under a $\langle 220 \rangle$ type g -vector of a $\langle 110 \rangle$ or $\langle 111 \rangle$ zone axis. Occasionally the fringes deviate from the general direction or have a different spacing. This has also been reported for bulk precipitates, however, the effect is more pronounced in the grain boundaries here and needs further investigation. The observed faceting of the precipitates also shows the occurrence of a preferential orientation of the interface planes between the copper-silicide and the silicon matrix.

Another typical feature is that the precipitates within a colony are aligned along dislocations or steps in the grain boundary plane, whereas most of the dislocations and steps outside a colony are undecorated. In addition to this result it could also be observed that the type of the grain boundary has an influence on the distribution of the precipitates:

- No particles were found in twin boundaries ($\Sigma 3$).
- In $\Sigma 9$ or near- $\Sigma 9$ grain boundaries the particles are larger (up to 30 nm) compared to those which have precipitated at dislocations in the bulk.
- In a near- $\Sigma 49$ (a 35° tilt around $\langle 210 \rangle$) the density is much higher and the particles on average larger (in the range 30 to 60 nm).

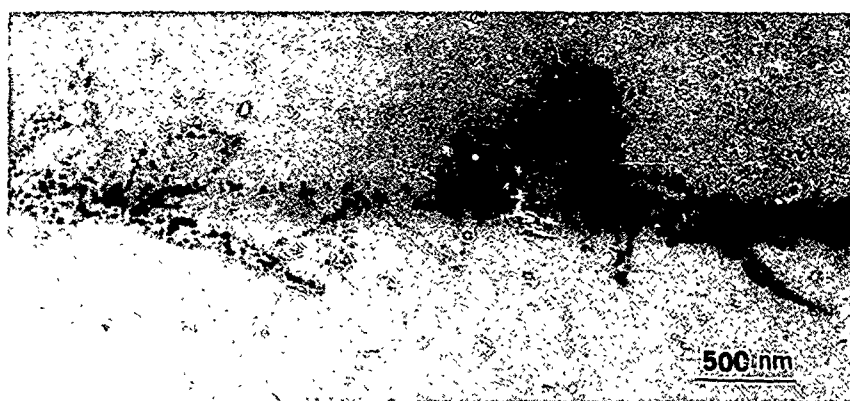


Fig. 2 Copper precipitates at a twin boundary in a quenched specimen (500 K/s). The colonies extend into the bulk and are surrounded by dislocations.

In quenched specimens (≈ 500 K/s) the distribution of precipitates is different again: in general the precipitates are smaller and more distributed. A larger fraction of copper precipitates now at bulk dislocations and in form of colonies in the bulk. These colonies are frequently surrounded by dislocations which are also decorated. This behavior is very similar to the observations of the copper precipitation in bulk single crystals [4-11] where it has been concluded that the surrounding dislocations are punched out during the precipitation.

A similar behavior can also be observed for precipitates at incoherent twin boundaries (Fig. 2). The copper precipitates form colonies which extend into the bulk and are surrounded by dislocations. The mean size of the particles is about 10 nm. The distribution for a more general type of grain boundary is different. Fig. 3 shows the distribution for a near- $\Sigma 19$ boundary: the colonies lie in the grain boundary plane and have an oval shape with a high density of precipitates inside. No dislocations are punched out into the adjacent grains. In addition there are more individual precipitates between the colonies compared to the specimens cooled down at intermediate rates. The mean distance of the colonies is about $1 \mu\text{m}$, the precipitate size in the colonies about 20 nm, and on average the density of the precipitates $10^{11} - 10^{12} \text{ cm}^{-2}$. One can also observe that there are more precipitates distributed between colonies as compared to the specimens cooled down at an intermediate cooling rate.

DISCUSSION

The investigation of the cobalt and copper interaction with grain boundaries has shown several common features. The impurities precipitate as metal silicides probably forming the equilibrium phase with silicon at room temperature. In the case of cobalt the Mößbauer spectra obtained from the grain boundary region could be completely described with the Lorentz lines of the cubic CoSi_2 phase and assuming mainly plate-like precipitates. There was no indication of another phase or of atomic cobalt on grain boundary sites.

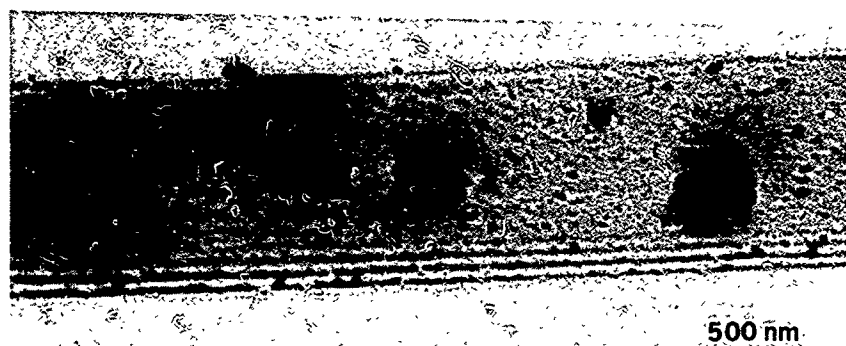


Fig. 3 Colonies and individual copper precipitates in a near- $\Sigma 19$ grain boundary in a quenched specimen. The precipitate size in the colonies is about 20 nm.

From the appearance of the Moiré fringes in the case of copper it can be concluded, that there is an orientation relationship between a lattice plane of the precipitates and a {011} plane of the silicon matrix. The difference in the lattice spacings was calculated to be 0.203 nm for a larger spacing in the precipitate (or 1.82 nm in case of a smaller spacing), corresponding to the distance of the fringes of 3.5 nm. This is consistent with the orthorhombic η'' structure proposed by Solberg [10], who obtained a value of 0.202 nm for the distance of the {001} planes of the precipitates, which are parallel to the {011} matrix planes. This spacing is also in agreement with the value of 0.203 nm found by Das [4] who proposed the cubic CuSi structure for the precipitates. Since both structures are consistent with the Moiré fringes found in this work no conclusion can be drawn here, however the η'' phase is more likely since it is the equilibrium phase at low temperatures. From the Moiré fringes for precipitates in the grain boundaries it can be concluded here that they have a special orientation relationship to either one of the adjacent grains.

Although the distribution of the cobalt precipitates has not been studied yet in the TEM it is assumed that the density of nucleation sites that could be derived corresponds to the average densities of precipitates. It is comparable to the densities obtained for copper. In both cases a dependence on the cooling rate is observed. The cobalt enrichment is enhanced for a slowly cooled (0.2 K/s) specimen, though it could not be determined whether the density or only the particle size has increased. The results for copper show that with slower cooling rates the distribution of the precipitates becomes more inhomogeneous in form of colonies and the precipitates larger. However, for the same slow cooling rate as for cobalt no copper precipitations could be observed any more. A possible explanation may be that the colonies are so far apart already that they are difficult to detect in the TEM. This behavior may indicate that during cooling smaller precipitates disappear on the expense of larger similar to Oswald ripening. Since the diffusion coefficient of cobalt is smaller compared to copper this process should be slower then. That may explain the different behavior of the two elements.

In quenched specimens the diffusion times are so short that only a fraction of the atoms can diffuse to the grain boundary and precipitate there. Far away either the formation of Co-B pairs occurs or in the case of copper the precipitation at bulk dislocations or dislocations that have formed during the precipitation. This behavior is similar then to the processes that have been studied earlier in single crystals. It is interesting to note that for copper the dislocation generation during precipitation also occurs at precipitates that have nucleated at twin boundaries. If one assumes that the supersaturation of self-interstitials as a result of the lattice strain from the precipitates generates the dislocations one can conclude that the rather perfect twin boundary is not an effective sink for the self-interstitials as compared to grain boundaries with a less perfect atomic structure where no dislocations are punched out.

Another important result from the copper investigation is the observation that the particles seem to nucleate preferentially at dislocations or steps in the grain boundaries. In addition there are also differences between the grain boundaries: Steps/dislocations in the $\Sigma 49$ grain boundary

are apparently energetically more favorable sinks compared to the same defects in the $\Sigma 9$ and twin grain boundary. The different interaction of copper with twins, $\Sigma 9$ and $\Sigma 49$ corresponds to differences in the grain boundary energies [18,19]. Although the energy of a $\Sigma 49$ tilt grain boundary has not been calculated yet, one can assume that it has a higher energy because of the low density of coincidence points, compared to the $\Sigma 9$ grain boundaries, which again has a higher energy than the twin. If it is allowed to generalize this observation, one has the result that with increasing grain boundary energy the gettering efficiency increases.

An explanation for this result may be given by the following consideration. Grain boundaries with low energies have a rather well reconstructed atomic structure, as has been shown by a number of TEM investigations. Steps and dislocations occur if the orientation of the two adjacent grains or of the grain boundary plane deviates from the low energy coincidence orientation. Although only in a few cases the energy of such defects has been calculated [20] the following conclusions seem reasonable:

- the atomic structure of steps and dislocations in the grain boundary is less perfect and they have a higher energy if the grain boundary itself has a high energy;
- a less perfectly reconstructed defect is a better nucleation site for a precipitate.

It is important to note, however, that by far the largest part of the grain boundary area does not show any precipitates, although they often contain structural defects like dislocations and steps. Therefore the presence of these defects in the grain boundary alone is not sufficient to render the nucleation. Summarizing the observations so far one can conclude that a complete understanding of the precipitation behavior has to take into account not only the structural aspect but also the kinetic of the process.

ACKNOWLEDGEMENTS

This work was supported in part by Du Pont de Nemours & Company Inc. and one of us (U. J.) was granted a fellowship by the Alexander von Humboldt Foundation. This is gratefully acknowledged.

REFERENCES

- 1) X.J. Wu, W. Szkielko, and P. Haasen; J.Phys. **43**, C1 - 135 (1982)
- 2) L.L. Kazmerski and P.E. Russell: J. de Phys. **C1**, 43, p. 171, 1983
- 3) M. Aucouturier, A. Broniatowski, A. Chari, J.L. Maurice, in Polycrystalline Semiconductors, ed. by H.J. Möller et al., Springer Proc. in Physics **35**, 64 (1989)
- 4) G. Das: J. Appl. Phys. **44**, p. 4459, 1973
- 5) E. Nes and J. Washburn: J. Appl. Phys. **42**, p. 3562, 1971
- 6) E. Nes and J. Washburn: J. Appl. Phys. **44**, p. 3682, 1973
- 7) E. Nes and J. K. Solberg: J. Appl. Phys. **44**, p. 486, 1973
- 8) K. Ryoo, R. Drosd, and W. Wood: J. Appl. Phys. **63**, p. 4440, 1988
- 9) M. Seibt and K. Graff: J. Appl. Phys. **63**, 4444, 1988
- 10) J.K. Solberg: Acta Cryst. **34**, 684, 1978
- 11) J.K. Solberg, E. Nes: Phil. Mag. **A37**, p. 465, 1978
- 12) H. Cerva and H. Wendt, Mater. Res. Soc. Proc. **99**, 99 (1988)
- 13) Binary alloy phase diagrams, ed. by T.B. Massalski, Amer. Soc. of Metals, Ohio 1986
- 14) T. Tütken, W. Schröter and H.J. Möller, in Polycrystalline Semiconductors, ed. by H.J. Möller et al., Springer Proc. in Physics **35**, 108 (1989)
- 15) M. Pasemann, W. Bergholz, and W. Schröter; Phys. Stat. Sol. (a) **81**, 273 (1984)
- 16) E. Weber; Appl. Phys. **A30**, 1 (1983)
- 17) W. Bergholz, Physica **116B**, 312 (1983); and J. Utzig; unpublished results
- 18) H.J. Möller: Phil. Mag. **A43**, p. 1045, 1981
- 19) H.J. Möller: Cryst. Res. and Technol. **16**, p. 259, 1981
- 20) H.H. Singer and H.J. Möller; Suppl. to Trans. Jap. Inst. of Metals **27**, 987 (1986)

ANNEALING OF ION IMPLANTED TIN IN SILICON: A RBS/ CHANNELING, MÖSSBAUER SPECTROSCOPY AND TEM INVESTIGATION OF SOLUBILITY AND RESIDUAL DEFECTS.

P. KRINGHØJ, A. NYLANDSTED LARSEN, and J. W. PETERSEN, Institute of Physics, University of Aarhus, DK-8000 Aarhus C, Denmark

ABSTRACT.

By combining RBS/channeling, Mössbauer spectroscopy, and TEM measurements on implanted Sn in Silicon, the solid solubility has been determined at 1025°C, 1075°C, and 1188°C to be respectively, 6.1 , 4.8 , $3.1 \cdot 10^{20} \text{ cm}^{-3}$.

INTRODUCTION.

There has been several reports on implantations of Sn in Si in which no precipitation and full substitutionality were observed[1-3] although the solid solubility limit given by Trumbore[4] was exceeded. Even in-diffusion from the surface has led to Sn concentrations exceeding this limit[5]. There could be two reasons for that: Either, a supersaturated solution far away from equilibrium has been formed, or Trumbore's data are not correct.

The aim of this work was to try to resolve this controversy. Electrical measurements (Hall, C-V) have been successfully applied to studies of the solubility of electrically active impurities[6]. This does not work, however, for the isoelectronic impurity Sn. Instead, by using the ^{119}Sn isotope as a micro probe one can obtain information about the substitutional and precipitated impurities from Mössbauer spectroscopy. Thus, by combining this method with RBS/channeling and TEM a detailed picture of the Si-Sn system can be obtained.

EXPERIMENTAL PROCEDURES.

The silicon samples were float-zone material, n-type (phosphor-doped $0.8 \Omega\text{cm}$). All implantations were performed at room temperature at three different energies, 80, 200, and 400 keV with relative doses of 20:35:84 resulting in impurity profiles which were homogeneous to a depth of 200 nm (see fig. 1). Distributions of four different concentrations were made in this way ($3.0, 6.5, 9.0$, and $15.0 \times 10^{20} \text{ cm}^{-3}$). Prior to annealing the profiles were measured with RBS. The annealing was performed in a temperature range from 600°C to 1200°C in a RTA system or/and a furnace. After annealing, channeling and TEM measurements were performed to investigate the recrystallization. Substitutional fractions were deduced from channeling and Mössbauer measurements.

There are two main reasons for using a box-profile: Firstly, almost all the impurity atoms are situated in the same surroundings.

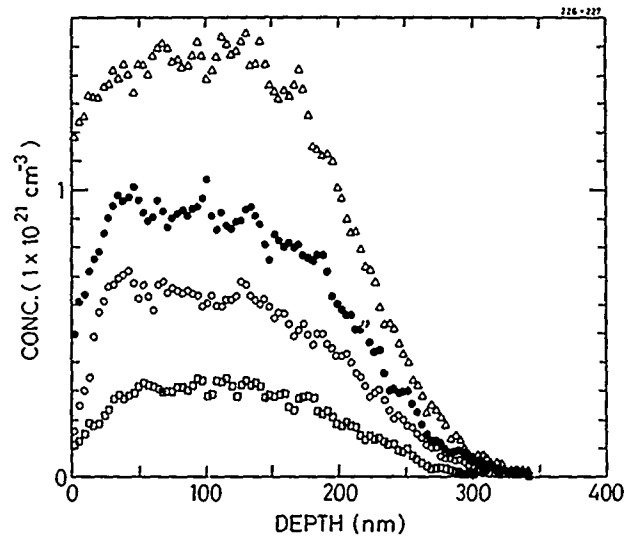


Fig. 1: As-implanted Sn profiles from RBS for the four different implanted concentration.

Secondly, when diffusion takes place the profiles are almost unchanged due to the lack of an impurity gradient in the central part of the profile. This is demonstrated in fig. 2 which shows profiles after annealing at 1025°C, 1075°C, and 1188°C for one hour. The corresponding diffusion lengths are approximately 20, 40, and 1600 nm, respectively[5].

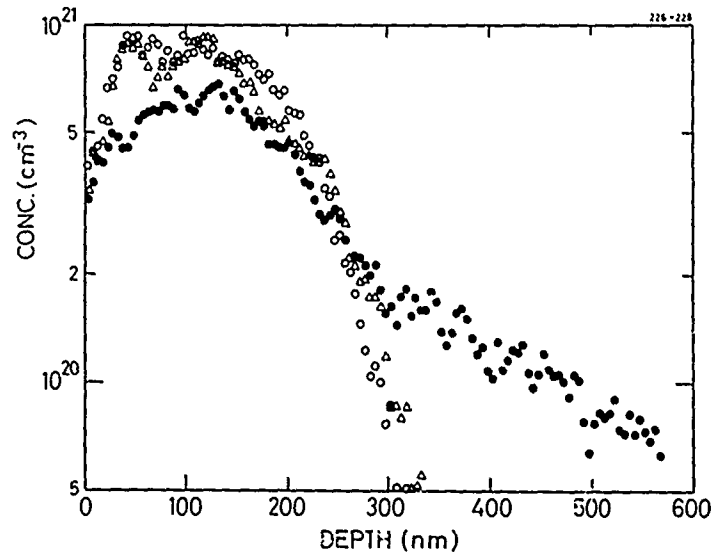


Fig. 2: Sn profiles measured by RBS of the second highest concentration ($9 \cdot 10^{20} \text{ cm}^{-3}$) after annealing for one hour at 1025°C (o), 1075°C (Δ), 1188°C (\bullet).

RESULTS AND DISCUSSIONS.

At low annealing temperatures ($< 1000^{\circ}\text{C}$) and concentrations ($\leq 9 \cdot 10^{20} \text{ cm}^{-3}$) recrystallization was always achieved, but a defect region was present at the a/c interface (at a depth of about 250 nm). These defects were mainly dislocation loops and their location in depth and their structure were easily discernable with channeling and TEM. At the high concentrations ($> 9 \cdot 10^{20} \text{ cm}^{-3}$) recrystallization was not possible and a polycrystalline layer was formed with the grain size depending on the annealing temperature and time. At high temperatures ($\geq 1000^{\circ}\text{C}$) recrystallization was obtained for all concentrations. Under conditions where no Sn precipitation occurred the dislocation loops disappeared, otherwise the precipitates stabilized the dislocation loops as seen with TEM. Below a certain critical concentration – depending on temperature – the channeling measurements gave low normalized minimum yields, $\chi_{\min}(\text{Sn})$, and the Mössbauer spectrum consisted of only one line demonstrating that all the Sn atoms were on substitutional sites. Above this concentration, the $\chi_{\min}(\text{Sn})$ value was higher whereas $\chi_{\min}(\text{Si})$ was constant indicating that a fraction of the Sn atoms were nonsubstitutional. The Mössbauer spectrum contained now two components: one from substitutional Sn in Si and one from β -Sn precipitates[7].

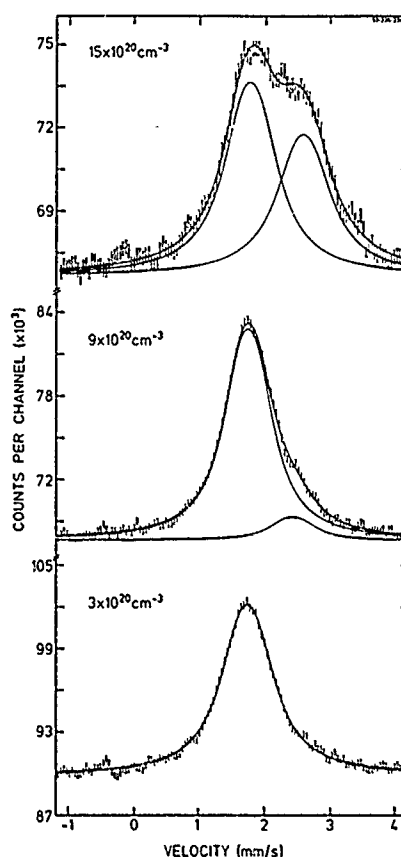


Fig. 3: Mössbauer spectra from samples with three different Sn concentrations ($3 \cdot 10^{20}$, $9 \cdot 10^{20}$, $15 \cdot 10^{20} \text{ cm}^{-3}$), annealed at 1075°C in one hour.

By comparing the relative intensities and taking into account the Debye-Waller factor of each component, the substitutional fraction, f_{ms} , could be deduced:

$$f_{ms} = [1 + A_{rel}]^{-1} \quad (1)$$

where A_{rel} is the relative area of the β -Sn component multiplied with the relative Debye-Waller factor. This can be compared to the corresponding equivalent fraction, f_{ch} , derived from channeling measurements:

$$f_{ch} = \frac{1 + \chi_{min}(Sn)}{1 + \chi_{min}(Si)} \quad (2)$$

In fig. 3 the Mössbauer spectra measured from samples with three different concentrations after annealing at 1075°C are shown. The appearance of the β -Sn component around 2.5 $\frac{mm}{s}$ can be seen. Due to the fact that the Debye-Waller factor of the β -Sn component[8] is a factor of 5 lower than that of the substitutional component[9], the small relative intensity of the β -Sn component in the second spectrum in fig. 3 corresponds to ~50% of the Sn atoms being situated in precipitates.

In figures 4 and 5 the channeling spectra and the Mössbauer spectrum for a sample with the second highest dose ($9 \cdot 10^{20} \text{ cm}^{-3}$), annealed at $T=1188^\circ\text{C}$ are shown. The random and aligned spectra show that precipitation takes place in the main region of the box-profile. The substitutional fraction deduced from the two measurements are $f_{ms}=0.22$ and $f_{ch}=0.26$. From this and using the concentration deduced from RBS, the substitutional concentration is determined. Under the assumption that the Sn-Si system is in thermodynamic equilibrium this concentration corresponds to the solubility limit. The deduced limit should be independent of the implanted dose provided that it is high enough to provoke precipitation. The interaction between substitutional and precipitated Sn ensures that equilibrium can be established. This was observed experimentally. In addition no precipitation was observed for concentrations below this limit. The achievement of equilibrium was checked at 1025°C by comparing annealing times of 10 sec., one hour and 4 hour annealing and the results derived from those experiments are the same within uncertainties. Annealing at 1025°C for 4 hours leads to the same diffusion length as a one hour annealing at 1075°C so if the precipitation was only governed by diffusion the substitutional fractions in the two cases should be the same, which they are not. Therefore we conclude that equilibrium is reached after one hour.

Also two step annealing was investigated. Selected samples were recrystallized at ~800°C for 10 sec., before the high temperature annealing. This alternative procedure did not lead to any differences in the channeling and Mössbauer spectra. The recrystallization process can therefore be excluded as the origin of the diffusion/precipitation phenomena.

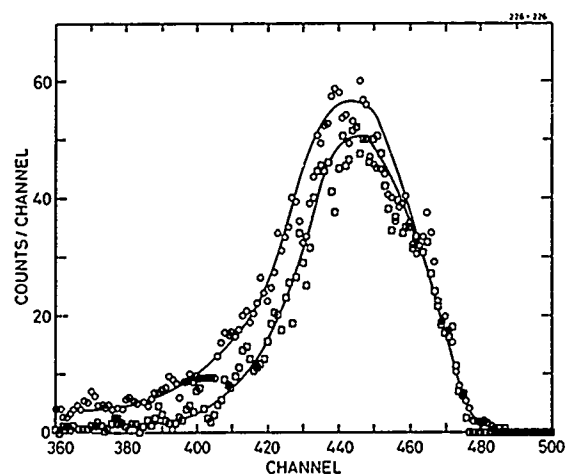


Fig. 4: Random (○) and aligned (□) RBS spectra of a sample with concentration $= 9 \cdot 10^{20} \text{ cm}^{-3}$ annealed at 1188°C one hour. The surface is in channel = 470.

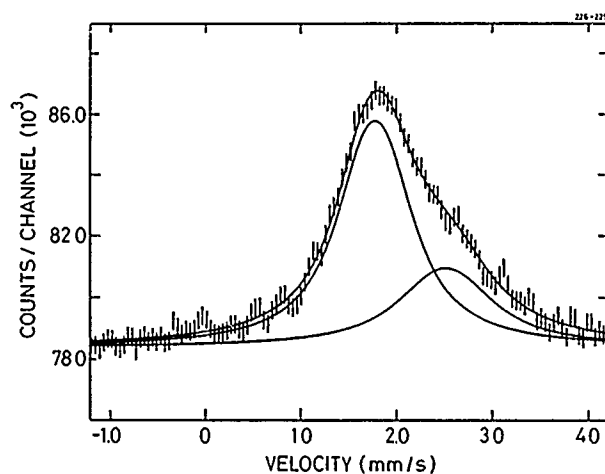


Fig. 5: The Mössbauer spectrum of the same sample as in fig. 4 showing the two components.

In fig. 6 the deduced solubility limits are shown. At each temperature several values from measurements on different concentrations are plotted. Results from experiments with the highest implanted dose are not shown because at the two lowest temperatures (1025°C and 1075°C) the box-profiles were completely destroyed and all the Sn had moved to the surface and at 1188°C almost all the Sn had evaporated from the sample.

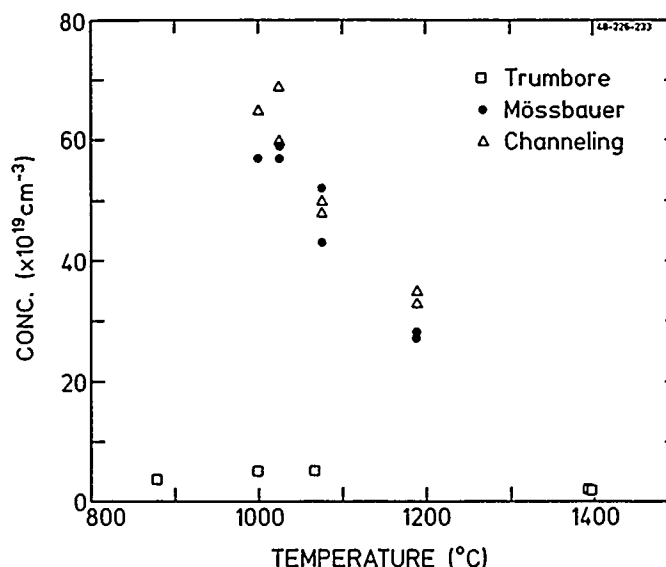


Fig. 6: The solubility limit deduced from the channeling and Mössbauer measurements. Also shown are the values from Trumbore[1].

CONCLUSION.

We have derived the solubility limit at three temperatures (1025°C, 1075°C, and 1188°C) by comparing equivalents fractions from Mössbauer spectroscopy and channeling measurements. The data are shown in fig. 6. The mean values are 6.1(4), 4.8(3), and 3.1(3) $\cdot 10^{20} \text{ cm}^{-3}$, respectively. The uncertainties are one sigma values and represent only the statistical uncertainty. At lower temperatures no limits could be obtained because of the formation of a polycrystalline layer. The solubility limits are higher than those given by Trumbore[4]. A decreasing tendency as a function of temperature is observed which could be an indication of lack of equilibrium. This is in disagreement, however, with the observed constancy of the solubility as a function of time. Further experiments are needed to clarify this problem.

REFERENCES.

- [1] M. Delfino, A. E. Morgan, and D. K. Sadana, Nucl. Instr. Meth. B **19/20**, 363 (1987).
- [2] G. Weyer, A. Nylandsted Larsen and F. T. Pedersen, Mat. Soc. Forum **10-12**, 1135 (1986)
- [3] E. M. Scherer, J. P. de Souza, C. M. Hasenack and I. J. R. Baumvol, Semicond. Sci. Technol. **1**, 211 (1986)
- [4] F. A. Trumbore, C. R. Isenberg and E. M. Porbansky, J. Phys. Chem. Solids, **9**, 60 (1958).
- [5] T. H. Yeh, S. M. Hu, and R. H. Kastl, J. Appl. Phys. **39**, 4266 (1968).
- [6] R. Angelucci, A. Armigliato, E. Landi, D. Nobili and S. Solmi, ESSDERC, 461 (1987).
- [7] Stevens J. G. & Stevens V. E., "Mössbauer Effect Data Index", Plenum, New York 1978
- [8] K. P. Mitrofanov, V. P. Gor'kov, M. V. Plotnikova, S. I. Reiman, Nucl. Instr. Meth. **155**, 539 (1978)
- [9] J. W. Petersen, O. H. Nielsen, G. Weyer, E. Antoncik, and S. Damgaard, Physical Review B **21**, 1292 (1980)

EXTREME SUPERSATURATION OF OXYGEN IN LOW TEMPERATURE EPITAXIAL SILICON AND SILICON-GERMANIUM ALLOYS

P.V. SCHWARTZ*, J.C. STURM*, P.M. GARONE*, AND S.A. SCHWARZ**

*Department of Electrical Engineering, Princeton University, Princeton, New Jersey 08544

**Bell Communications Research, Inc., Red Bank, New Jersey 07701

Abstract

We report the low temperature growth (625 - 700 °C) of epitaxial silicon and silicon-germanium alloy films by vapor phase techniques with oxygen concentrations approximately 10^{20} cm^{-3} . These concentrations are well above the accepted solid solubility for oxygen in silicon. The films, however, have excellent structural and electrical properties with virtually no stacking faults or "haze". Infrared transmission analysis suggests the possible presence of OH, but the exact nature of the oxygen is not known.

Introduction

Generally, oxygen is a harmful contaminant in epitaxial films. The presence of oxygen precipitates may give rise to stacking faults in the epitaxial film and in extreme cases cause haze on the surface of the wafer. Here we report the low temperature growth of crystalline epitaxial films with oxygen concentrations reaching 10^{20} cm^{-3} .

Growth

The samples were grown by Limited Reaction Processing (LRP) [1], a combination of Chemical Vapor Deposition (CVD) and Rapid Thermal Processing (RTP). The reactor is a lamp heated system which utilizes no susceptor. Each sample is suspended on quartz pins in a quartz wall chamber above a bank of twelve tungsten halogen lamps. The radiation from the lamps heats the wafer directly while leaving the chamber wall cool. Another feature of the system is that it has no load lock. During each loading process, the chamber must be vented to atmosphere. This is a possible source of contamination to the system.

The epitaxial films are grown at a pressure of 6 torr. Dichlorosilane and germane are used as the source gases and hydrogen is used as the carrier gas. Before growth, each sample undergoes a high temperature clean (1200 °C). The clean is done in a hydrogen atmosphere and removes impurities from the wafer surface. The growth process begins with the growth of a silicon buffer layer (1000 °C), followed by a temperature drop to 700 °C for growth of Si epitaxial layers or to 625 °C for growth of $\text{Si}_{1-x}\text{Ge}_x$ epitaxial layers. Typical sample structures are

shown in Figure 1.

The epitaxial films grown at low temperature have excellent structural characteristics. They are all single crystals and

exhibit no observable haze on the surface of the wafer in either the visible or the ultra-violet regions. In plan view TEM, we notice misfit dislocations in some $\text{Si}_{1-x}\text{Ge}_x$ strained layer samples, but stacking faults are seldom observed. Stacking faults are virtually absent from our silicon samples as well.

Characterization

In order to characterize our system, we performed Secondary Ion Mass Spectroscopy (SIMS), calibrated against implant standards, on our epitaxial samples. In Figure 2, it can be seen that the oxygen concentration in the silicon (grown at 700 °C) is nearly $5 \times 10^{20} \text{ cm}^{-3}$. This is an extreme case, and it is more typical to see oxygen concentrations of $1 \times 10^{20} \text{ cm}^{-3}$ in these silicon films. The interface between the high temperature buffer and the low temperature epitaxial layers is clearly defined by the oxygen profile. The buffer layer has an oxygen concentration less than 10^{17} cm^{-3} while the layer grown at 700 °C has an oxygen concentration of approximately $5 \times 10^{20} \text{ cm}^{-3}$ throughout the film. This is two orders of magnitude above the accepted peak level solubility of oxygen in silicon of $2 \times 10^{18} \text{ cm}^{-3}$.

We have also performed SIMS on a Heterojunction Bipolar Transistor (HBT) structure (shown in Figure 1B). The silicon-germanium layer defines the narrow bandgap base region. The alloy base is sandwiched between two silicon layers which were grown at 850 °C and serve as the transistor's collector and emitter. As seen in Figure 3, an oxygen concentration of approximately 10^{20} cm^{-3} is found in the alloy layer grown at 625 °C. Since this is found in the base of the HBT, one might expect the electrical characteristics of the device to be degraded. As we will see in the next section, the electrical properties of the devices are not adversely affected.

The source of the oxygen is thought to be water vapor or oxygen that adsorbs on the walls of the sample chamber during the loading process. Careful loading procedures can reduce the oxygen levels somewhat, but they generally remain well above $2 \times 10^{18} \text{ cm}^{-3}$. To establish the form taken by the oxygen, Fourier Transform Infrared Spectroscopy (FTIR) was performed at room temperature (Figure 4). Notice the large peak centered at approximately 1000 cm^{-1} with a Full Width at Half Maximum (FWHM) of 100 cm^{-1} . This FWHM is much larger than the accepted FWHM ($\sim 32 \text{ cm}^{-1}$) for interstitial oxygen and is removed from the interstitial peak location (1107 cm^{-1}) [2] by more than 100 wavenumbers. Furthermore, the interstitial peak should be easily resolved on this scale yet there is no hint of this peak. The peak at 1000 cm^{-1} is also not characteristic of the formation of precipitates since precipitates are typically associated with a peak which is displaced toward an energy higher than that of the 1107 cm^{-1} peak [3].

The peak at 3400 cm^{-1} suggests the possible presence of an OH molecule. The OH bond has been studied extensively in fused

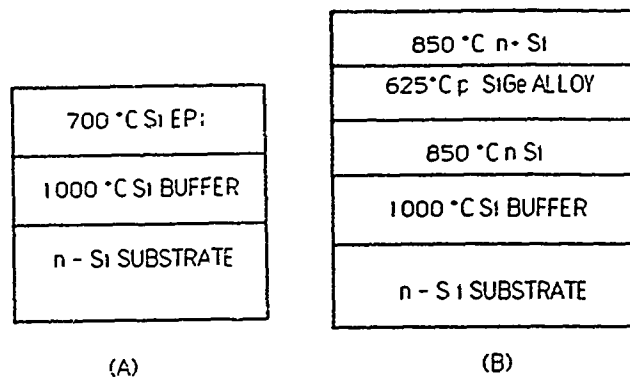


Figure 1: Typical Structures. A) Silicon epitaxial growth at the temperature of 700 °C. B) Silicon-germanium epitaxial growth at 625 °C for a Heterojunction Bipolar Transistor (HBT).

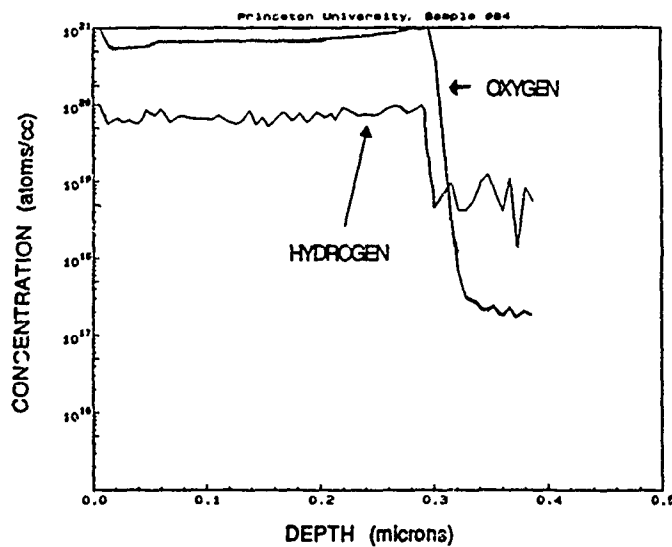


Figure 2: SIMS Profile. The top layer is 3000 Å of silicon grown at 700 °C with an oxygen concentration of approximately $5 \times 10^{20} \text{ cm}^{-3}$. The 1000 °C buffer has an oxygen concentration less than 10^{17} cm^{-3} .

silica and the O-H vibrational mode at 3690 wavenumbers is well documented. The fact that we see a peak at 3400 wavenumbers may be attributed to the difference between the two host materials. Stolen and Walrafen reported a Si-(OH) vibrational mode at 970 cm^{-1} [4] (in a Raman spectrum) when studying wet optical fibers. The peak seen at 970 cm^{-1} was noticed in fibers containing large amounts of OH as determined by the presence of the 3690 cm^{-1} peak. They also calculated a vibrational mode for this bond at 988 cm^{-1} using a modified model of an anchored SiO_4 tetrahedron. This theoretical oscillation corresponds well to their observed peak. We also performed a Raman analysis of our silicon layer and noticed a small peak at 970 cm^{-1} . However, we attribute this peak to a second order Raman mode for a Si-Si bond.

A second SIMS profile on the silicon layer (seen as Figure 2) confirms the presence of hydrogen. The hydrogen profile follows that of the oxygen ($5 \times 10^{20} \text{ cm}^{-3}$) but at a concentration of $7 \times 10^{19} \text{ cm}^{-3}$. With these concentrations, one cannot account for every oxygen atom as an OH molecule since there is less than one hydrogen atom for each oxygen atom. However, the presence of hydrogen may explain the presence of the 1000 cm^{-1} peak in the FTIR. The shift of the peak toward a lower energy can be due to the effect of hydrogen weakening the strength of the Si-O bond.

Electrical Properties

As seen in Figure 3, the oxygen concentration reaches 10^{20} cm^{-3} in the base of the HBT structure. We have fabricated transistors in films with oxygen concentrations of approximately 10^{19} cm^{-3} and obtained gains on the order of twenty even with base dopings two orders of magnitude above the collector dopings (10^{19} cm^{-3} vs. 10^{17} cm^{-3} , respectively). A Gummel plot (log of the collector and base currents vs. the base-emitter voltage) in our previous work [5] shows the ideal collector current (60 mV/dec) in the transistor and a base current with an ideality factor of 1.3. King et al., at Stanford, have fabricated HBTs with gains near 400 which exhibit ideal collector and base currents [6]. The base regions of their transistors also contain large amounts of oxygen. Even though the oxygen concentration is large in the base region, it does not seem to degrade device performance.

Conclusion

We have grown epitaxial silicon and silicon-germanium layers with oxygen concentrations of approximately 10^{20} cm^{-3} . Even though there is a large amount of oxygen in the epitaxial films grown at low temperatures (625 - 700 °C), the films are still single crystals virtually free of stacking faults. There are also large amounts of hydrogen in the films, and there is evidence that some of it exists as OH. However, the exact form of most of the oxygen is not known. The transistors fabricated in these films also

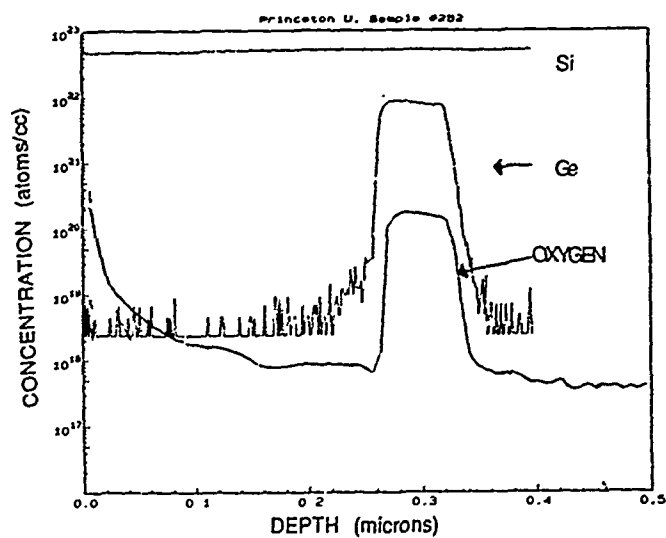


Figure 3: SIMS Profile. SIMS profile for a typical Heterojunction Bipolar Transistor structure. The base is defined by the $\text{Si}_{80}\text{Ge}_{20}$ layer.

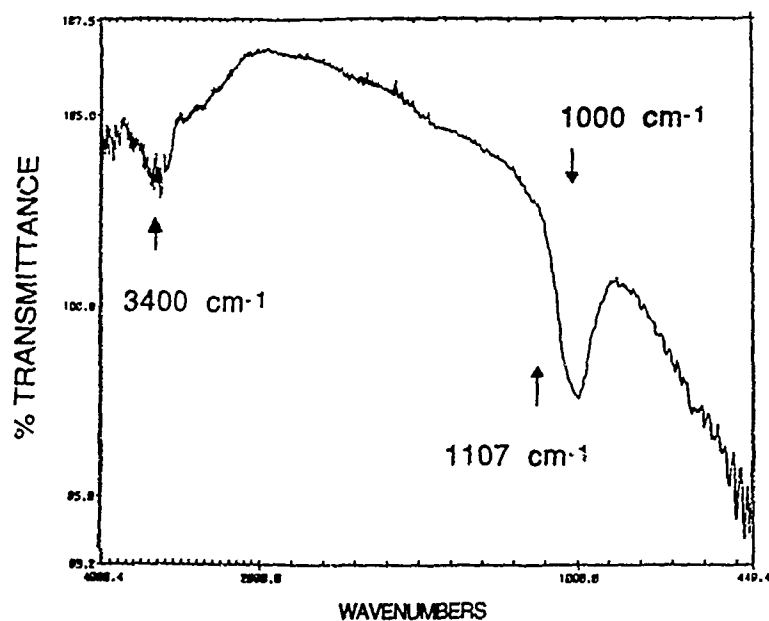


Figure 4: FTIR. Transmission spectrum for a typical silicon epitaxial layer grown at 700 °C. This sample was referenced to its substrate.

exhibit excellent electrical characteristics showing that the oxygen does not seem to adversely effect device performance.

The authors would like to acknowledge the assistance of Dr. C. Magee of Evans East for his SIMS analysis, Dr. P. Zanzucchi of SRI for his FTIR work and J. Yee for his Raman work. This work was funded by the Office of Naval Research and the National Science Foundation.

References

1. J.F. Gibbons, C.M. Gronet and K.E. Williams, Appl. Phys. Lett. 47, 721-723 (1985)
2. W. Kaiser and P.H. Keck, J. Appl. Phys. 28, 882 (1957)
3. S.M. Hu, J. Appl. Phys. 51 (11), 5945-5948 (1980)
4. R.H. Stolen and G.E. Walrafen, J. Chem. Phys. 64, (6), 2623-2631 (1976)
5. J.C. Sturm, E.J. Prinz, P.M. Garone, P.V. Schwartz, Appl. Phys. Lett., 54 (26), 2707-2709 (1989)
6. C.A. King, J. L. Hoyt, C.M. Gronet, J.F. Gibbons, M.P. Scott, and J. Turner, Elect. Dev. Lett., 10 (2), 52-54 (1989)

AN ANOMALOUS VACANCY DIFFUSION IN SILICON DURING THE ANTIMONY DRIVE-IN DIFFUSION

W. WIJARANAKULA AND J.H. MATLOCK

Materials Characterization Laboratory, SEH America, Incorporated
4111 Northeast 112th Avenue, Vancouver, Washington 98682-6776, USA

ABSTRACT

In the substrate region underneath the antimony buried layer, an enhanced oxygen donor generation and a retardation of the oxygen precipitation were observed. Both phenomena can be explained by the vacancy mechanism in which the charged vacancies dominate at high temperatures. Based upon this hypothetical model, it is suggested that the intrinsic vacancy concentration could play a significant role in both oxygen thermal donor generation and oxygen precipitation in silicon.

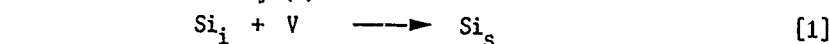
INTRODUCTION

In the junction-isolated bipolar integrated circuit device fabrication, a high temperature processing sequence consisting of an Sb buried layer diffusion followed by epitaxial deposition is commonly used. In the usage of a high temperature process, a retarded oxygen precipitation and reduction in internal gettering efficiency could be anticipated. A retardation of oxygen precipitation can occur as a result of a dissolution of "grown-in" nuclei. It can also be caused by a reduction in the vacancy concentration, e.g. via a complex formation between doping impurities and vacancies. The latter mechanism has been used to explain a retardation of oxygen precipitation in silicon heavily doped with Sb (1). Thus far, no direct evidence of the SbV^- complex formation has been presented. If it is assumed that this mechanism is to prevail in the case of Sb buried layer diffusion, a localized reduction in the vacancy concentration could occur, particularly underneath the buried layer. Charged vacancies could be attracted by indiffusing Sb and form the SbV^- complexes. This is a hypothetical model that requires an experimental verification.

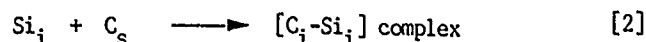
In this work, the 450°C oxygen thermal donors (TDs) were used as a point defect monitor in silicon after an Sb drive-in diffusion. Based upon the results for TD generation and oxygen precipitation, a hypothetical model for charged vacancy diffusion is developed.

MICROSCOPIC MODEL FOR THE 450°C OXYGEN DONORS

The generation mechanism of TDs formed in the temperature range between 400°C and 500°C has been a subject of study for the past thirty years. The exact microscopic model of these donors is still being debated, but the most plausible one is the model in which the donor activity arises from the two broken bonds of a silicon interstitial (Si_i) located at the core of the donor (2). In this model, the donor activity is terminated when the double-positively charged Si_i is annihilated. In the bulk silicon, an annihilation of Si_i occurs via a recombination process involving vacancies. Substitutional impurities having a tetrahedral covalent radius much smaller than silicon (1.17Å), e.g. carbon (0.77 Å), act also as a Si_i trap. Both reactions are described by (3):



and



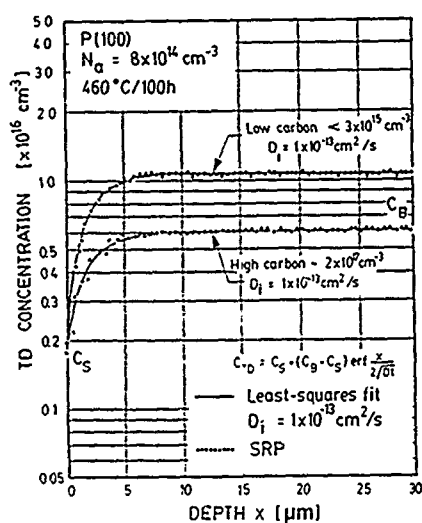


FIG. 1: TD concentration profiles in low and high carbon samples after 100h anneal at 460°C (5).

Therefore, it is plausible that the concentration of vacancies and interstitial traps can have a significant impact on the TD generation. There is sufficient evidence to support this model. First, the TD generation is enhanced by excess Si_i generated during pre-oxidation prior to the 450°C TD anneal (4). Another evidence is a retardation of TD generation by carbon (5). In Fig. 1., both profiles are not likely to be related to oxygen because the diffusivity of oxygen, out-diffused from high carbon silicon, is much higher than low carbon silicon (6). Considering the above TD model, the observed high $1 \times 10^{-13} \text{ cm}^2/\text{s}$ diffusivity of Si_i at low temperatures.

EXPERIMENTAL PROCEDURES

The starting materials were p-type Czochralski-grown 100 mm silicon wafers having a $[100]$ orientation. The boron doping concentration was $8 \times 10^{14} \text{ atoms/cm}^3$. Dissolved interstitial oxygen O_i concentration was measured by a Nicolet MX-ECO FTIR spectrometer and calibrated to the ASTM F121-80. The O_i concentration was $6.5 \times 10^{17} \text{ atoms/cm}^3$. The wafers were divided into two groups with the following processing conditions; Group I: etched surface and Group II: a 1.5- μm low pressure polysilicon deposition at 660°C. Prior to the Sb drive-in diffusion, the wafer backsurface was encapsulated with a thin CVD oxide layer to prevent an autodoping. The front surface was then polished. The 6h drive-in diffusion was performed at 1200°C. This resulted in a buried layer thickness of 4.5- μm .

The TDs were generated by annealing the samples at 450°C for 100h in N_2 ambient. The TD concentration profiles were obtained by subtracting the carrier concentration measured by the spreading resistance probe (SRP) before and after the TD anneal. A 16h oxygen precipitation test at 1050°C in dry O_2 was also performed on Sb diffused samples without TD anneal. The precipitation test was necessary because no bulk defects were observed after the Sb diffusion. The bulk defects were revealed by Wright etch.

RESULTS AND DISCUSSION

Fig. 2 shows the TD concentration-depth profiles in the Group I sample. In comparison to the backsurface region, the TD generation in the front surface region is enhanced. Several SRP measurements were repeated to ensure that the observed phenomenon is not related to the SRP measurement error. Fig. 3 shows the subsurface regions after the oxygen precipitation test. In Fig. 3a, the front surface region is relatively free from bulk microdefects. In the bulk surface region, a high density of bulk microdefects is observed. The difference in precipitation behaviors between the front and backsurface cannot be explained by the oxygen outdiffusion

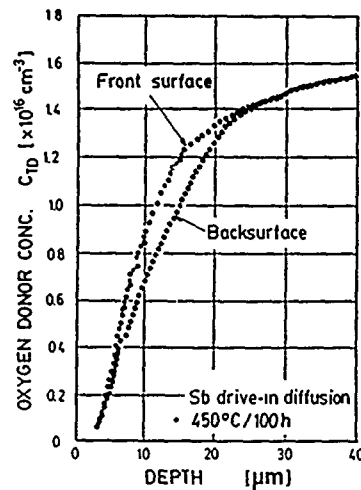


FIG. 2: TD concentration profiles from Group I sample

microprecipitates were detected in the backsurface region after the Sb diffusion. Therefore, the above observation is interpreted as a result of vacancy saturation where TDs are annihilated via a recombination process, according to Eq. [1]. During the drive-in diffusion, the backsurface region could be saturated with vacancies because Si_i are absorbed by the polysilicon layer on the backsurface (8).

phenomenon because the oxygen diffusion is not affected by the Sb doping concentration (7). If it is assumed that the vacancy mechanism was to prevail, the observed retardation of oxygen precipitation in the front surface can be interpreted as a result of a vacancy undersaturation. This implies that an anomalous depletion of vacancies underneath the buried layer could occur during the Sb diffusion. The above explanation seems to be the most plausible one because it agrees with the observed enhancement of TD generation in the front surface.

Fig. 4 shows the TD concentration-depth profiles in a sample from Group II. In the Group II sample, the TD generation in the backsurface region is retarded. Based upon the growth kinetic of TDs (2), the retardation could be due to a reduction in the oxygen content in the backsurface region as a result of an enhanced oxygen precipitation. This hypothesis is in contrast to the result from the cross section examination in which no bulk

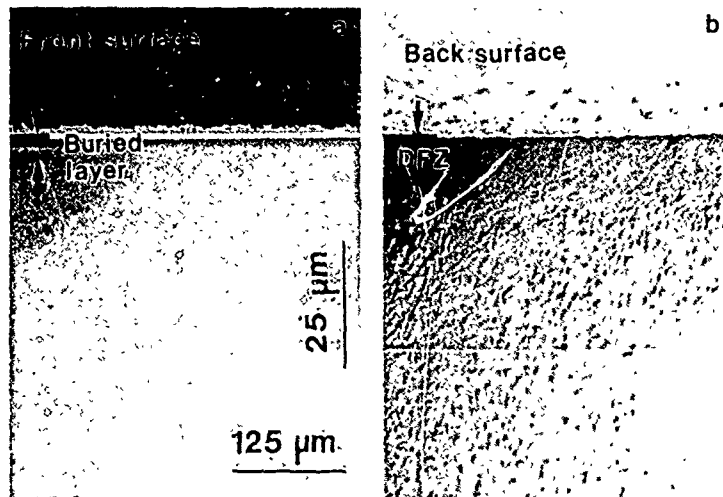


FIG. 3: The subsurface regions from a Group I sample after the precipitation test (DFZ - Defect-Free Zone)

From the above results, it is suggested that a vacancy depletion in the region underneath the buried layer could occur during the Sb diffusion. The built-in electric field originating from the buried layer could facilitate the vacancy diffusion. The negatively charged vacancies are attracted by Sb^+ whereas the positively charged vacancies are repelled. In the buried

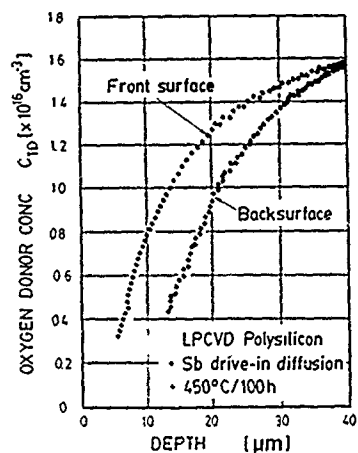


FIG. 4: TD concentration profiles from a Group II sample

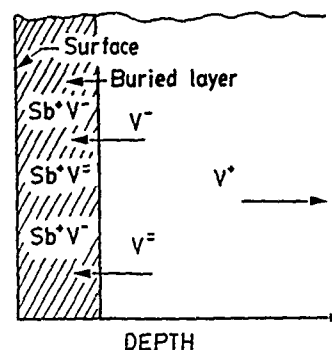


FIG. 5: Hypothetical model for a vacancy diffusion

layer, a Sb^+V^- complex formation is hypothesized. The model for the vacancy diffusion is summarized in Fig. 5. It should be pointed out that a similar argument can also be made for the case of boron drive-in diffusion. In this case, a formation of B Si_i^+ complexes and a saturation of Si_i in the front surface region are anticipated. An evidence of Si_i saturation during a boron diffusion has already been observed and reported (9).

SUMMARY

In the subsurface region underneath the Sb buried layer, an enhanced TD generation and a retardation of the oxygen precipitation are observed. Both phenomena can be explained by the vacancy mechanism in which the charged vacancies dominate at high temperatures. In this work, evidence which supports the absorption mechanism of Si_i by the polysilicon layer is also observed. Based upon these observations, it is suggested that the intrinsic vacancy concentration could play a significant role in both TD generation and oxygen precipitation in silicon.

REFERENCES

1. F. Shimura, W. Dyson, J.W. Moody, and R.S. Hockett, in *VLSI Science and Technology 1985*, edited by W.M. Bullis and S. Broydo, (The Electrochemical Society, Pennington, NJ, 1985)pp.507.
2. A. Ourmard, W. Schroter, and A. Borret, *J.Appl.Phys.*, **56**, 1967(1984).
3. G.D. Watkins, in *Defects and Their Structure in Nonmetallic Solids*, edited by B. Hendersen and A.E. Hughes, (Plenum Press, New York, 1975), pp.203.
4. J.O. Borland, in *Semiconductor Processing*, edited by D.C. Gupta, (ASIM, Philadelphia, PA, 1988), pp.201.
5. W. Wijaranakula, submitted to *J.Appl.Phys.*
6. F. Shimura, T. Higuchi, and R.S. Hockett, *Appl.Phys.Lett.*, **53**, 69(1988).
7. W. Wijaranakula, J.H. Matlock, and H. Mollenkopf, *Appl.Phys.Lett.*, **54**, 1068(1988).
8. H. Shirai, A. Yamaguchi, and F. Shimura, *Appl.Phys.Lett.*, **54**, 1748(1989).
9. C.L. Claeys, G.J. Declerck, and R.J. Van Overstraeten, *Rev.Phys.Appl.*, **13**, 797(1978).

A COMPARISON OF THE DIFFUSIVITY OF As and Ge in Si AT HIGH DONOR CONCENTRATIONS

K. KYLLESBECH LARSEN, P. GAIDUK, and A. NYLANDSTED LARSEN
Institute of Physics, University of Aarhus, DK-8000, Aarhus C,
Denmark

ABSTRACT

The effect of high background doping (8×10^{19} - 5×10^{20} cm⁻³) on the diffusion of Ge and As in Si has been studied. A strong enhancement is found for As for donor concentrations higher than $\sim 2 \times 10^{20}$ cm⁻³, but not for Ge. These experimental findings are discussed within the percolation model.

INTRODUCTION

It has been previously demonstrated by us that the diffusion of ion implanted Sn, Sb, and As in Si single crystals show an anomalous behaviour at high donor concentrations during rapid thermal annealing at temperatures of 1000 - 1050°C [1-5]. For donor concentrations higher than approximately 2×10^{20} cm⁻³ the effective diffusion coefficient D_{eff} is found to be proportional to $(n/n_i)^S$, where n and n_i are the actual and intrinsic carrier concentrations at the diffusion temperature, respectively, and where S has a value between ~ 3 and ~ 5 depending on the diffusing specie, i.e., significantly higher than the value of one expected for diffusion via singly charged negative vacancies or of two expected for diffusion via doubly charged negative vacancies. Moreover, in the case of Sb where Mössbauer spectroscopy has been possible, the diffusivity enhancement has been found to correlate with the appearance of a new defect complex containing Sb: For the highest donor concentration ($\sim 5 \times 10^{20}$ cm⁻³) about 70% of the implanted Sb was found in these complexes. The diffusion enhancement observed for Sb has been modelled within the percolation model by Mathiot and Pfister [6], and by Antoncik [7] using a system of reaction-diffusion equations in which the reaction constants depend on temperature and donor background concentration.

The purpose of this paper is to compare the diffusivities of As and Ge at high donor concentrations and to try to model the results within the percolation model. A comparison between As and Ge is interesting because they have approximately the same covalent radii (1.18 Å and 1.22 Å) and the same fractional interstitial component of diffusion at high temperatures (0.3 and 0.3-0.4, respectively) [8,9] but are differently charged as substitutional impurities.

EXPERIMENTAL

The silicon samples were p-type (boron doped) 150 Ωcm, float-zone refined monocrystals. The background donor concentration was formed by implantation of P to different doses followed by rapid thermal annealing (RTA) at 1050°C. In this way flat carrier density profiles extending to depths of more than 3000 Å with carrier concentrations between 9×10^{19} and 5×10^{20} cm⁻³ could be obtained [3]. Arsenic or germanium were subsequently implanted at an energy of 80 keV to doses of either 4×10^{14} or

$6 \times 10^{14} \text{ cm}^{-2}$. Annealing and diffusion were then achieved by RTA in an argon ambient at a temperature of 1050°C for a duration of 15s (including the temperature rise time of about 5s). Carrier density profiles (from the P-background doping) and chemical profiles of As and Ge were measured by respectively Hall effect/resistivity measurements combined with anodic oxidation and stripping in steps of 100Å, and Rutherford backscattering spectrometry (RBS) with 2-MeV He^+ ions.

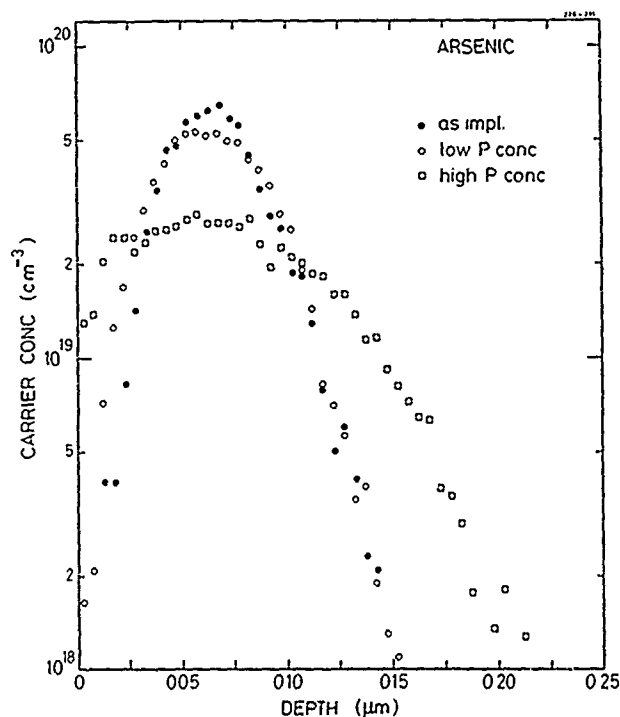


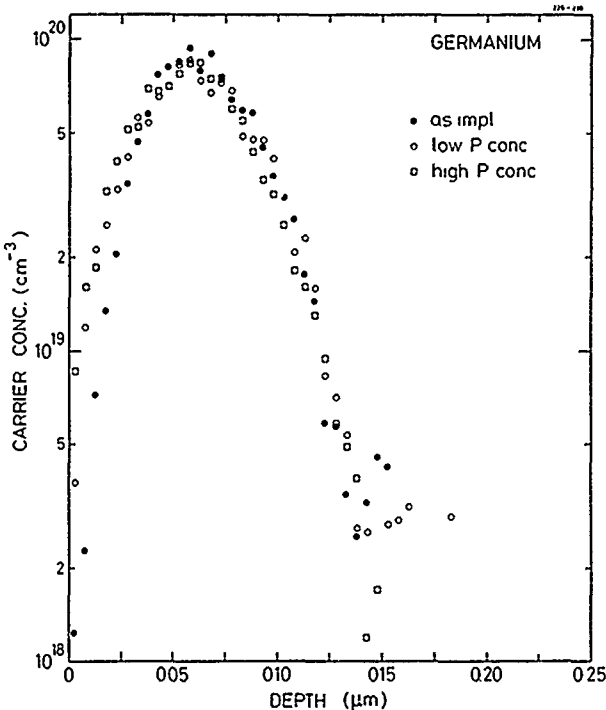
Fig.1 Chemical profiles of As measured by RBS after RTA at 1050°C for 15s (o, □). The P background concentrations were (o): $9 \times 10^{19} \text{ cm}^{-3}$ and (□): $4 \times 10^{20} \text{ cm}^{-3}$.

RESULTS AND DISCUSSION

Figures 1 and 2 show chemical profiles of As and Ge before and after RTA at 1050°C in 15 sec for two different P background concentrations ($9 \times 10^{19} \text{ cm}^{-3}$ and $4 \times 10^{20} \text{ cm}^{-3}$). A very strong redistribution is observed for As for the highest P concentration, an effect which is not observed for Ge. Effective diffusion coefficients for As were extracted from the As profiles by a fitting procedure described elsewhere [1]. For Ge this was not possible as the diffusion is too small to be analyzed by the techniques at our disposal (we can only determine diffusion coefficients $> 2 \times 10^{-14} \text{ cm}^2/\text{sec}$).

The effective diffusion coefficients of arsenic as a function of donor concentration normalized to the intrinsic carrier concentration n_i is shown in Fig.3. Also shown in the figure are results by Fair et al. [10] obtained by furnace annealing and

Fig.2 Chemical profiles of Ge measured by RBS after RTA at 1050°C for 15s (○, □). The P background concentrations were (○): $9 \times 10^{19} \text{ cm}^{-3}$ and (□): $4 \times 10^{20} \text{ cm}^{-3}$.



without a constant background carrier concentration. Two regions can be identified: one for $n/n_i < 20$ where $D_{\text{eff}} \sim (n/n_i)^1$ and one for $n/n_i > 20$ where $D_{\text{eff}} \sim (n/n_i)^3$. The former dependence can be interpreted as diffusion via singly charged negative vacancies whereas the latter dependence is significantly higher than the $(n/n_i)^2$ dependence which would be expected for diffusion via doubly charged negative vacancies. The transition occurs at $n/n_i = 20$ corresponding to a carrier concentration (or donor concentration) of $\sim 2 \times 10^{20} \text{ cm}^{-3}$.

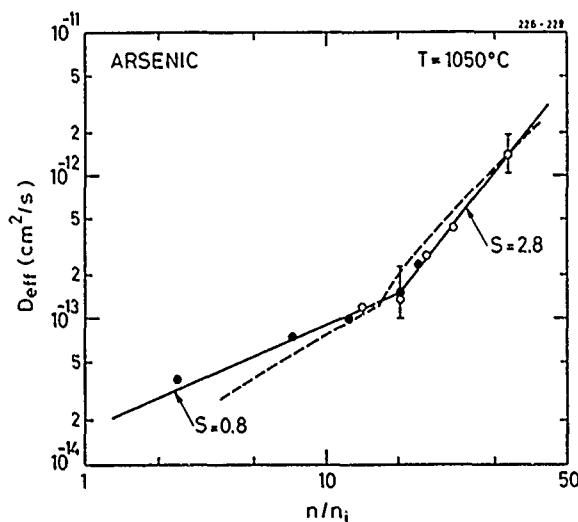


Fig.3 Effective diffusion coefficients as a function of donor concentration. The open symbols are from present investigation and the closed from Fair et al. [10]. The broken curve shows diffusion coefficients calculated within the vacancy-percolation model.

Values of the effective arsenic diffusivity calculated within the vacancy-percolation model are also given in Fig.3 (a detailed description of the vacancy-percolation is given in ref. [11]). The values have been calculated by using the parameters determined by Mathiot and Pfister in ref. [11]. It appears that the model-percolation-threshold of $1.3 \times 10^{20} \text{ cm}^{-3}$ is slightly lower than the threshold of $2 \times 10^{20} \text{ cm}^{-3}$ observed by us (the percolation threshold of $1.3 \times 10^{20} \text{ cm}^{-3}$ was already in [4] considered to be surprisingly low) and that the non-percolated diffusivities at low concentration is lower than the experimental ones. Apart from that, however, the overall agreement is very good. Thus, the enhanced diffusivity of As in Si for donor concentrations higher than $\sim 2 \times 10^{20} \text{ cm}^{-3}$ can be accounted for by the percolation model in the same way as could the enhanced diffusivity of Sb in Si [6].

The enhancement in the As diffusivity at the highest n/n_i -value compared to the intrinsic diffusivity at 1050°C ($D_i(\text{As}) = 5 \times 10^{-15} \text{ cm}^2/\text{s}$ [12]) is about a factor of 300. A similar enhancement for Ge ($D_i(\text{Ge}) = 5.3 \times 10^{-16} \text{ cm}^2/\text{s}$ [9]) would result in a diffusivity of about $1.6 \times 10^{-13} \text{ cm}^2/\text{s}$ at the highest n/n_i -value. Such a diffusivity could be easily determined and, thus, we are led to the conclusion that the enhancement of Ge, if any, is at least a factor of 10 smaller than the one for As. These observations are in qualitative agreement with the percolation model. From isothermal annealing studies of irradiation induced vacancy-Ge and vacancy-As pairs it can be concluded that the binding between a vacancy and a Ge impurity is much smaller than the binding between a vacancy and an As impurity [13]. This effect can result in a much weaker percolation in the case of Ge than in the case of As and thereby in a much smaller diffusivity enhancement.

REFERENCES

- [1] A.Nylandsted Larsen, S.Yu.Shiryaev, E.Schwartz Sørensen, and P. Tidemand-Petersson, Appl.Phys.Lett. **48** (1986) 1805
- [2] S.Yu.Shiryaev, A.Nylandsted Larsen, E.Schwartz Sørensen, and P. Tidemand-Petersson, Nucl.Instrum.Methods B **19-20** (1987) 507
- [3] P.E. Andersen, A.Nylandsted Larsen, P.Tidemand-Petersson and G.Weyer, Appl.Phys.Lett. **53** (1988) 755
- [4] A. Nylandsted Larsen, P.Tidemand-Petersson, P.E.Andersen and G.Weyer, Inst.Phys.Conf.Ser. **95** (1989) 499
- [5] A.Nylandsted Larsen, P.E.Andersen, P.Gaiduk and K.Kyllenbech Larsen, Mat.Sci.Eng.to be publ.1989
- [6] D.Mathiot and J.C.Pfister, J.Appl.Phys., **66** (1989) 970
- [7] A.Antoncik, paper presented at the Int.Conf.on the Science and Technology of Defect Control in Semiconductors, Yokohama, Japan 1989
- [8] P.M.Fahey, P.B.Griffin and J.D.Plummer, Rev.Mod.Phys., **61** (1989) 289
- [9] P.M.Fahey, S.S. Iyer and G.J. Scilla, Appl.Phys.Lett., **54** (1989) 843
- [10] R.B. Fair and J.C.C. Tsai, J.Electrochem. Soc., **122** (1975) 1689
- [11] D.Mathiot and J.C.Pfister, J.Appl.Phys., **55** (1984) 3518
- [12] J.L.Hoyt and J.F.Gibbons, MRS Symp.Proc., **52** (1986) 15
- [13] G.D.Watkins, Inst.Phys.Conf.Ser., **23** (1975) 1

ANOMALOUS TRANSIENT TAIL DIFFUSION OF BORON IN SILICON: KINETIC MODELING OF DIFFUSION AND CLUSTER FORMATION

N.E.B. COWERH*, H.F.F. JOS**, K.T.F. JANSSEN*** AND A.J.H. WACHTERS*

* Philips Centre for Manufacturing Technology, P.O. Box 218, 5600 MD Eindhoven, The Netherlands

** Philips Components, Gerstweg 2, 6534 AE Nijmegen, The Netherlands

*** Philips Research Laboratories, P.O. Box 80000, 5600 JA Eindhoven, The Netherlands

ABSTRACT

A kinetic modeling approach is used together with experimental studies to gain insight into the processes taking place during anomalous transient diffusion. A physical process analogous to B clustering is found to play an important role, even at B concentrations well below the solid solubility limit.

INTRODUCTION

The mechanisms of implantation-induced transient diffusion have been the subject of study and speculation for more than 15 years, but considerable uncertainty still remains. From the technological point of view, this limits the effectiveness of computer-aided process design tools, as the vertical dimensions of the simulated devices shrink to the same order as the transient diffusion length. From a scientific perspective, the challenge is to identify relationships between the complex diffusion behaviour that is observed and basic interactions that might control this behaviour, such as kickout of dopant atoms and nucleation and growth of precipitates.

Transient diffusion after B implantation into silicon provides a typical example of the problem. Over a rather wide range of implantation doses one observes a rapid diffusion in the tail of the implant profile during annealing. At the same time, relatively little diffusion occurs near the peak of the B profile. Several ideas [1-4] have been put forward to account for this anomalous diffusion behaviour, which is also seen in other dopants such as P [2] and Ga [5].

A number of workers have pointed out that anomalous diffusion profiles can arise when only part of the implanted dopant is assumed to be mobile. Hofker *et al* [1] were able to account for observed B diffusion profiles with peak concentrations above the solid solubility limit in terms of a 2-component model where a large fraction of the implanted dopant was assumed to be immobile. This fraction was attributed to B precipitates. Morehead and Hodgson [2] analysed anomalous P transient diffusion with a 2-component model and suggested that their mobile component should be associated with dopant-defect pairs. Finally, Michel [3] proposed a 2-component model in which the B is initially immobile and electrically inactive, and decays exponentially with time into a mobile, electrically active component.

The model of Ref. 2 closely resembles the physical mechanism responsible for normal, steady-state dopant diffusion, if we identify the static component as substitutional atoms. In this case, the only difference between transient and normal diffusion is the extreme supersaturation of the mobile species during transient diffusion. In the models of Refs. 1 and 3, electrically inactive dopant trapped in clusters or precipitates is assumed to be responsible for the static component of the anomalous profile. However the proposed mechanisms apparently apply to different concentration ranges, one (Ref.1) above the solid solubility limit, and the other (Ref. 3) at lower concentrations.

In this paper we present an analysis of these alternative models, and propose a synthesis between the ideas presented in Ref. 1 and Ref. 3. This is done by considering the interactions during transient diffusion at a more basic level, with the help of a kinetic model for the dopant species and intrinsic point defects involved. The model is embedded in an efficient solver for strongly coupled, stiff systems of diffusion equations.

SUBSTITUTIONAL-MOBILE SPECIES DIFFUSION

A detailed treatment of the mechanism outlined in Ref. 2 requires consideration of four coupled diffusion equations. Under intrinsic diffusion conditions these can be written as

$$\partial C_s / \partial t = \nabla \cdot (D_s \nabla C_s) + G_I - G_V \quad (1)$$

$$\partial C_t / \partial t = \nabla \cdot (D_t \nabla C_t) - G_I + G_V \quad (2)$$

$$\partial C_I / \partial t = \nabla \cdot (D_I \nabla C_I) + G_I - R_{IV} \quad (3)$$

$$\partial C_V / \partial t = \nabla \cdot (D_V \nabla C_V) + G_V - R_{IV} \quad (4)$$

where C , D and G refer to concentrations, diffusivities and net generation rates via dopant reactions, the

subscripts s, t, I, V refer to substitutional dopant, mobile dopant, self interstitials and vacancies, respectively, and R_{IV} refers to bimolecular I-V recombination. The diffusivity D_s is assumed to be zero. The sign of the terms G_I and G_V in equations (1) and (2) is based on the generally-accepted view [6] that B diffuses predominantly by an interstitial-mediated mechanism. The terms G_I and G_V are given in this case by

$$G_I = -g(C_I/C_I^*)C_s + rC_t \quad (5)$$

$$G_V = k[gC_s - r(C_V/C_V^*)C_t] \quad (6)$$

where g is the equilibrium knockout rate of substitutional dopant atoms by self interstitials, r is the rate for the inverse process, kg is the equilibrium formation rate for species V and t by dissociation of the substitutional dopant, s, and asterisks denote equilibrium values. The ratio g/r determines the mobile dopant fraction under equilibrium point-defect conditions, so that $g/r = D_X/D_t$ where D_X is the experimentally determined intrinsic dopant diffusivity. The value of g is controlled by the rate of encounters between the species I and s, and by the energy barrier ΔE for the knockout process, according to the relation $g = 4\pi a_0 D_I C_I^* \exp(-\Delta E/kT)$ where a_0 is an interaction radius of order one lattice constant. Similar formulas exist for R_{IV} and kg . For present purposes we treat R_{IV} and k as negligible, although a non-zero k may play a significant role in dopant-assisted I-V recombination [7,8].

To fit anomalous diffusion profiles following the approach of Ref. 2, the equations must be solved starting from initial conditions where species t constitutes a sizeable fraction of the dopant. The values of ΔE and D_t have to be adjusted so that the diffusion profile of the mobile species t is approximately Gaussian and the majority of the substitutional dopant atoms, s, remain undisturbed by knockout reactions. It is possible to obtain fits to individual transient diffusion profiles of both P and B in this way. However, fits can only be obtained by using very small values of g to suppress transformation reactions between species t and s. This is the only way to prevent broadening in the peak of the profile. Such small values of g , however, also produce anomalous profile shapes for diffusion under equilibrium point-defect conditions [9], in disagreement with observations. This is because only a small fraction of species s is allowed to be displaced into the mobile form t during the diffusion. We may conclude that the immobile species giving rise to the anomalous diffusion profile cannot simply be the substitutional dopant atom. In the next section, we consider the possible role of clusters or precipitates containing dopant atoms.

CLUSTERING

In the present discussion we substitute a simple dynamic clustering model for the relatively complex processes of B precipitate nucleation and growth which are known to occur at high B doping concentrations in silicon. Some justification for this approach can be claimed when a very high supersaturation of interstitial dopant atoms is present, leading to homogeneous nucleation. Our simplified model provides the opportunity to assess the transient diffusion kinetics in the presence of an electrically inactive, immobile species that is coupled to the dopant and the intrinsic point defects. We assume that during cluster formation, m interstitial B atoms are incorporated, $n-j$ vacancies are absorbed and j self interstitials are emitted, where m and n are fixed and $0 \leq j \leq n$. In the present discussion we take $m = 2$, $n = 1$ which approximately satisfies the volume requirement for B precipitation without generation of residual stress.

The dynamic clustering model is included in our mathematical description by adding a new equation for the concentration C_c of clustered B atoms and including corresponding generation/recombination terms in equations 2-4. The new equation is given by

$$r_c^{-1} \partial C_c / \partial t = (r/g)^m (C_t/C_{s,d}^*)^{m-1} (1 + k_c C_V/C_V^*)^n C_t - (k_c + C_I/C_I^*)^n C_c \quad (7)$$

where $(1 + k_c)r_c$ is the equilibrium rate coefficient for a B atom of species c to be released as a mobile atom of species t, and k_c is the relative probability of V emission relative to I absorption during this process. The quantity $C_{s,d}^*$ represents the solid solubility for B in silicon, the asterisk emphasizing the fact that this solubility is defined under equilibrium point-defect conditions. In the simulations which follow, we show that the effective solubility of B may be considerably reduced as a result of the large values of C_t present during transient diffusion. The clustering process may therefore play a role in transient diffusion at concentrations significantly below the equilibrium solubility limit. Our present model is qualitatively in agreement with a recently proposed steady-state B clustering model [10], but now allows a more realistic time-dependent treatment of the problem.

A qualitative view of the transient diffusion and clustering kinetics in the present model can be obtained by using the simple 2-component initial conditions discussed in the previous section. The dopant is partitioned between species s and t at time zero, while all other species are allowed to evolve from small values in response to the initial supersaturation in species t. The evolution of the concentrations through time is tracked by the kinetic model, using standard literature values for the model parameters as far as

possible. For example, the point defect diffusivities and equilibrium concentrations are taken from Ref 11, the effective B diffusivity from Ref. 12, and we assume $D_i = D_I$, $\Delta E = 0$ and $k_c = 0$. The main fitting parameters are the clustering coefficient r_c and the initial fraction of dopant atoms in species t .

Some simulation results for the case of a $2 \times 10^{14}/\text{cm}^2$, 25 keV ^{11}B implant, annealed at 800°C in inert ambient with an overlying oxide, are presented in Fig. 1. An implanted B distribution measured by SIMS is used as the starting profile, partitioned between C_s and C_t with $C_t/(C_s + C_t) = 0.25$. After 10^{-6} sec,

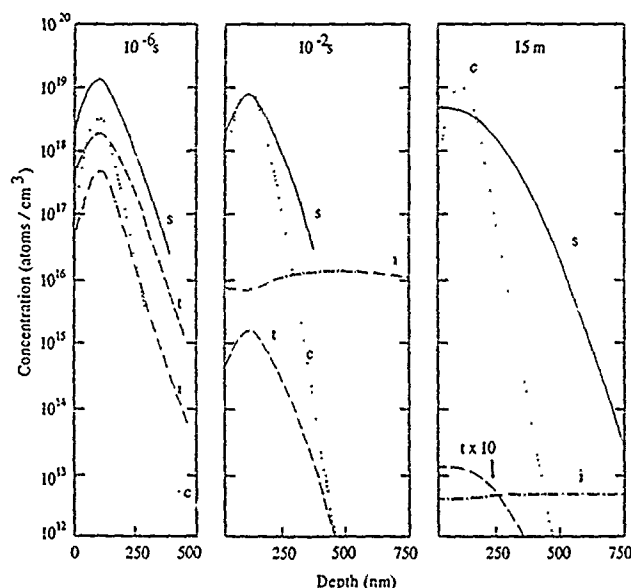


Figure 1: Transient evolution of the substitutional (s), interstitial (t) and clustered (c) dopant concentrations and the self interstitial (I) concentration simulated with the kinetic model. Simulated process conditions are a $2 \times 10^{14}/\text{cm}^2$ B implant annealed in inert ambient at 800°C .

this fraction has declined slightly at the peak of the doping profile (curve t) and has been overtaken by the clustered B (curve c). A large supersaturation of self interstitials (curve I) has also developed due to kickout of Si atoms by interstitial B. For reference, the value of C_i^* in this simulation is $\sim 10^{10}/\text{cm}^2$. At 10^{-2} sec, the clustering is complete and species I has propagated several microns into the silicon. The fluxes of t and I are now approximately equal and opposite in the near-surface region up to 500 nm depth, leading to the dip in curve I corresponding to the peak in curve t . This is essentially the quasi steady-state behaviour originally pointed out by Morehead and Lever in their analysis of high-concentration B and P diffusion [13]. After 15 min, a large redistribution of species s is evident. There is still a substantial I supersaturation, but the diffusion transient is now almost over. Most of the clustered B remains trapped in its location at the peak of the implant profile, forming an electrically inactive component of the dopant distribution. The existence of such a component even after quite low implant doses was pointed out by Michel [3] and we have obtained experimental data from SIMS and spreading-resistance measurements indicating that it survives a 30 min furnace anneal even at the higher temperature of 900°C .

Results from the above simulations are compared with experimental SIMS data in Fig. 2. Solid lines show the simulated total B concentration ($C_s + C_c + C_t$) and dashed lines the electrically active component C_s . Clearly the agreement is excellent: the simulation reproduces both the static peak and the magnitude and time dependence of the tail diffusion. Nevertheless, the present model is still at an early stage of development. An important feature to be included in addition to the extrinsic defect (dopant) clusters described here, is the role of clusters of intrinsic defects formed during ion implantation [14]. We believe this will remove the need for an arbitrary choice of initial point-defect conditions, because the defect clusters are an important source of the point-defect supersaturation during transient diffusion.

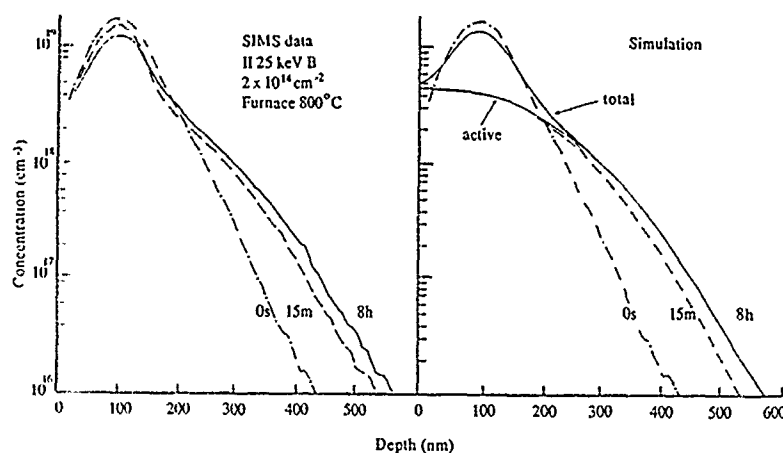


Figure 2: Comparison of experimental data and simulations for two typical furnace anneal times. Simulation parameters are the same as for Fig. 1. Simulations of the total B concentration (the quantity measured by SIMS) and the electrically active B concentration are shown for anneal times of 15 min and 8 hr.

CONCLUSIONS

Detailed kinetic modeling of anomalous B transient diffusion leads to the conclusion that the anomaly arises from a non-equilibrium clustering (or precipitation) process. The B solubility is reduced below the equilibrium solubility limit as a result of a large supersaturation of the mobile B component. This conclusion is consistent with experimental observations of electrically inactive dopant in the static part of the diffusion profile. Our model is qualitatively similar to the semi-empirical model of Michel [3], but also allows a connection to be made with basic quantities that can be measured in independent experiments. The present approach can be developed in future to produce a more predictive model for transient diffusion over the parameter space of implant dose and energy, anneal temperature and time.

ACKNOWLEDGEMENTS

The authors thank W.P.M. van der Linden for assistance with the package generator used to create the kinetic modeling code, and J. Ottenheim and M. Pawlik for spreading-resistance measurements.

REFERENCES

1. W.K. Hofker, H.W. Werner, D.P. Oosthoek and H.A.M. de Grefte, *Appl. Phys.* **2**, 265 (1973); W.K. Hofker, H.W. Werner, D.P. Oosthoek and N.J. Koeman, *Appl. Phys.* **4**, 125 (1974).
2. F.F. Morehead and R.T. Hodgson, *Mat. Res. Soc. Symp. Proc.* **35**, 341 (1985).
3. A.E. Michel, *Mat. Res. Soc. Symp. Proc.* **52**, 3 (1986).
4. R.B. Fair, J.J. Wortman and J. Liu, *J. Electrochem. Soc.* **131**, 2387 (1984).
5. P. Woerlee and A.J. Walker (unpublished).
6. P.M. Fahey, P.B. Griffin and J.D. Plummer, *Rev. Mod. Phys.* **61**, 289 (1989).
7. U. Goesele, in *Semiconductor Silicon*, edited by H.R. Huff, T. Abe and B. Kolbesen (Electrochem. Soc., Pennington, NJ, 1986).
8. T.L. Crandle, W.B. Richardson and B.G. Mulvaney, *IEDM Tech. Dig.* 1988.
9. N.E.B. Cowern, to be published.
10. N.E.B. Cowern, H.F.F. Jos and K.T.F. Janssen, *Mat. Sci. and Eng.* **B4**, 1989 (in press).
11. U. Goesele and T.Y. Tan, *Mat. Res. Soc. Symp. Proc.* **36**, 105 (1985).
12. R.B. Fair, in *Impurity Doping Processes in Silicon*, edited by F.F.Y. Wang (North-Holland, Amsterdam, 1981), page 315.
13. F.F. Morehead and R.F. Lever, *Appl. Phys. Lett.* **48**, 151 (1986).
14. A.E. Michel, *Nucl. Instrum. Meth. Phys. Res.* **B37/38**, 379 (1989).

FAILURE OF THE "KICK-OUT" MODEL FOR THE DIFFUSION OF Au INTO Si WHEN TESTED BY MONTE CARLO SIMULATION

U. Schmid*, J. A. Van Vechten†, N. C. Myers†‡, and U. Koch†§

* Max-Planck-Institut für Festkörperforschung, Heisenbergstr. 1, D-7000 Stuttgart 80, Federal Republic of Germany.

† Center for Advanced Materials Research, Department of Electrical and Computer Engineering, Oregon State University, Corvallis, OR 97331-3211, USA.

ABSTRACT

We have performed large scale computer simulations on the controversial issue of Au diffusion into Si at $T = 1095^\circ \text{C}$. Using a Monte Carlo algorithm and a conveniently parametrized set of parameters, our computer program is capable of working out the macroscopic consequences of a variety of models, i.e. atom level assumptions, in an unbiased way and without the approximations introduced in analytic calculations.

When applied to the "kick-out" hypothesis, our results are dramatically at odds with the properties claimed by its proponents. Neither the profile of the Au substitutionals, nor the Au-interstitial profiles are in agreement with the analytically obtained results. The discrepancy becomes most pronounced when comparing the variation with time of the Au concentration in the center of the sample, which we find to be linear at all times, in contrast to the alleged $t^{1/2}$ behavior. Moreover, the Au profile of a one-sided diffusion never becomes U-shaped, as experimentally observed.

1. INTRODUCTION

The understanding and control of diffusion in semiconductors is crucial to the progress in semiconductor electronics, and yet this is one of the least understood subjects in modern materials research. Major controversies rage about almost every aspect in this field, such as the role of self-interstitials and vacancies in atomic diffusion. For one part, this sad situation is due to the fact that atomic diffusion is a very complex subject, and thus the interpretation of experimental data can lead to contradictory reports. On the other hand, it can be attributed to the introduction of more and more models with an increasing number of parameters, which added confusion rather than clarification to the subject. Even the simpler models suffer from one major deficiency: the relationship between the atom level assumptions and its macroscopic consequences are extremely complex and not easy to establish. The connection between these two classes should be made in terms of thermodynamic reasoning. This task has been attempted in the case of vacancy hopping processes for Si and impurities by a few authors [1-5], but still all such work relies on intuition, contains approximations and passages to limits and is based on thermodynamic equilibrium assumptions for processes, which do not take place in equilibrium.

For this reason we conclude that only a computer program that takes into account the complex interaction of a diffusing particle with its vicinity can establish an exact and unbiased relation between microscopic assumptions and macroscopic consequences. Therefore we have developed the computer program VIDSIM (Vacancy and Interstitial Diffusion Simulator) [6, 7], that models the evolution of an initial set of particles in space and time for any of the chosen models the user wants to simulate. This is possible with the help of a "brute force" Monte Carlo algorithm, which involves an enormous amount of computational effort, if statistically significant results are to be obtained. Nonetheless, this effort can be achieved in a rather inexpensive way with the use of several ordinary PCs, which can work simultaneously on the same problem in the background while they are used for other purposes,

such as word processing. Of course, VIDSIM can also run on other computers, such as UNIX workstations and superminis.

We have designed VIDSIM in such a way, that virtually anyone who wants to test his model and parameters, such as activation energies, can use it, even if he or she is no computer expert. Its documentation is published in Ref. [8], and it is available from the Computer Physics Communications Library, catalogue number ABRF, or, for the cost of the medium, from the authors.

Monte Carlo simulations are not the only useful computational method for the investigation of diffusion processes in semiconductors. Some workers try to make progress with ab initio methods on supercomputers, with the help of calculations which are based on the local density approximation (LDA) [9]. While this method is well adapted to bulk ground state properties, it gives band gaps that are much smaller than the experimental excitation energies [10]. For this reason it is common practice to adjust the calculated band gaps to experiments by shifting the conduction bands with the so-called "scissors-operator", or by other "ad hoc" corrections [11, 12]. Whereas these corrections give extremely satisfactory results for band-structure calculations, it has been argued that the corrections needed for diffusion processes might be entirely different [13]. These calculations should be regarded with some care, as their uncertainty is typically more than 1.0 eV. In addition, such calculations can only be carried out by specialists on state of the art supercomputers, which makes them quite expensive and inaccessible to the experimentalist. This is especially true when the LDA is combined with molecular dynamics [14], which restricts calculations to just a couple of atoms during extremely short periods of time [15]. Some workers try to circumvent these restrictions by developing new theories and combine them with LDA calculations and available experimental data [16], or empirical tight-binding force models [15].

Such new techniques are very impressive and interesting and can be complementary to Monte Carlo methods, but with the problems mentioned above and the computer resources available today they have to be regarded as beyond the state of art. Practical progress is more likely to be made with semi-empirical theories.

2. VIDSIM ALGORITHM

VIDSIM performs a computer experiment on the theory which is to be tested. Our approach is simple brute force - the computer calculates the hopping probabilities for each mobile defect, based on the total free energy for the relevant process, which again depends on the assumptions and parameters the user inputs into the program. In addition to these parameters, the user has to supply the diffusion temperature T and an initial defect configuration, which can consist of both native point defects (vacancies and three different types of interstitials), and impurity related defects. The computer then adds up all partial probabilities of any process that can happen, and calculates the mean time for something to happen somewhere as the inverse of the total probability, in units of phonon cycles. According to the Mean Value Theorem, VIDSIM assumes that one diffusion process ("event") occurs after the calculated mean time, and chooses the event to occur with the help of a random number in the 0 to 1 interval from the set of possible events, which are weighted according to their normalized, individual hop probabilities. After the hop is completed, all possible events which are effected by this hop are reconsidered and the mean time for the next hop is re-evaluated. This process is repeated as many times as desired, or until a certain diffusion time is exceeded.

We prefer to run the same kind of simulation on various PCs and minicomputers simultaneously in order to obtain reliable statistics. We have also shown [13], that with this method even small university departments can obtain rates of computation which are equivalent to the speed of the order of one CRAY XMP or similar supercomputers all the time and as a single user! In fact, we have performed a "multi Giga-event" simulation (several 10^9 discrete events) in a sample of 6.4×10^8 sites exclusively on PCs. This striking effect can be traced

down to the scalar nature of Monte Carlo algorithms, which do not allow vectorization or parallelization, and thus perform rather unfavorably on expensive vector-(super)computers.

An excellent example for the difficulties which arise when trying to deduce macroscopic properties from atom level assumptions is the diffusion of Au in Si.

3. THE DIFFUSION OF Au INTO Si CONTROVERSY

It has been known for a long time that, under thermal equilibrium conditions, Au is dissolved both on substitutional (Au_S) and interstitial sites (Au_i), and that during diffusion processes there is an exchange between them [17]. With the help of VIDSIM we now want to clarify the controversy about this mechanism. The first model, the "Frank-Turnbull mechanism" (FT) [18] involves vacancies (V) and gold interstitials (Au_i), which diffuse separately in the bulk and finally annihilate to form a substitutional site (Au_S):



Willoughby and co-workers concluded [19], that the FT was consistent with empirical observations that: a) the Au_S profile from a two-sided diffusion is more U-shaped than the result predicted by simple Fickian assumptions; b) the concentration of Au_S in the middle of this U-shaped profile, C_s^m , increases with time t roughly as $t^{1/2}$; and c) that an asymmetric U-shaped profile is obtained from one-sided diffusion.

The alternative model, the "kick-out mechanism" (KO), was proposed by Seeger and co-workers [20, 21] after analytical calculations, which seemed to indicate that the FT behaves more or less like a Fickian diffusion process, which is not in accordance with a) to c). The KO assumes that it is not the vacancies, but self-interstitials (Si_i), which determine the diffusion process. The Si_i is formed when an Au_i displaces a host Si atom:



and then migrates to the free surface, which is the only available sink in a highly perfect wafer. It is argued that it is the out-diffusion of Si_i that limits the increase of the central gold concentration C_s^m , and thus yields a $t^{1/2}$ behavior in agreement with b).

As the controversy about the two competing mechanisms has raged for many years, with different authors deriving contradictory conclusions from basically the same data, we decided to examine carefully the microscopic and macroscopic implications of the kick-out model without the approximations introduced in the analytic calculations [21], i. e. with a Monte Carlo computer experiment.

We also want to point out that neither the analytic calculations nor our computer simulation take into account any charge state effects of Si_i or Au_i , any Fermi level or recombination enhancements effects, and any elastic effects, and therefore still represents a great simplification of the real problem.

4. THE KICK-OUT SIMULATION

The simulation temperature was fixed at $T = 1095^\circ \text{C}$, a value which is typically used in experiments and for which some combined models (a sum of FT and KO models) claim a predominant KO character of the diffusion process. For the injection conditions of the Au_i , we examined two extreme cases: a) the stimulated KO, in which an Au_i is injected into the surface at a random position every time an Au_S is formed in the bulk via reaction (2), this keeps the total number of Au_i in the sample constant; and b) the spontaneous case, in which the rate of injection occurs randomly, at a constant average rate. We have found no major qualitative difference between the two [6], and suppose that the true situation lies somewhere in the middle of these two. As it does not make much difference, we restrict ourselves to case b). We took the bond-centered interstitial for our simulation.

The necessary parameters for our simulation, enthalpies of formation and migration, were taken from the literature [22, 23], and we calculated the single bond enthalpy of Si and Au from their enthalpy of melting [2].

For practical reasons [6, 13], we increased the enthalpy of migration to 2.2 eV, compared to Weber's 0.39 eV. This is a concession to economy of simulation and examined in Ref. [6]. For the same reason, we had to choose the size of the simulated crystal smaller than what VIDSIM allows. We took the x-direction to be 1000 lattice constants, a , i. e. 543 nm, a value, which is expanded to about 1.2 mm by the increase of the enthalpy of migration [13]. To check that our sample is adequately thick, we repeated the simulation in "thick" samples, which are $z = 2000 a$. As we use cyclic boundary conditions for the other two directions, we can keep the y and z dimensions rather small (200 a).

Having examined our early results, which turned out to be totally at odds with claims by its proponents, we sought the advice of Prof. U. Gösele how he evaluates our choice of parameters. He argued [24] that our simulation did not achieve the supersaturation of Si; necessary to reproduce the claimed behavior, as the Si_i is too mobile. He also stated that the critical ratio of the product of the diffusivity and concentration of Au versus that of Si, R , is much too low. Following his advice [24], we increased the enthalpy of migration of Si_i from 0.39 eV to 0.94 eV. Thus, our simulation parameters are now in accordance with the recommendations of the KO advocates.

5. RESULTS

Our earlier results on that issue have been presented elsewhere [13]. They have clearly shown that:

- the profile of the Au_i is steeply sloped (approximately exponential) for all t even up to the point that the sample would be basically melted. This feature is not affected by t , nor by choice of R , nor the thickness of the sample, and contradicts a KO boundary condition, that $[Au_i]$ should be flat and near equilibrium with the eutectic layer for all t .
- the variation with time of the Au_i concentration in the center of the sample, C_m^s , is linear for all t , which extends the order of 2 sec., and never becomes $t^{1/2}$.
- the Au_i profile itself, which we find to be much more exponential and less U-shaped than claimed.

These results have been obtained under the assumption that there is except for reaction (2) no annihilation process (sink) for the Au_i, so that the concentration of Au_i grows steadily on the surface. This results in the progressive melting of the crystal from the surface

on. We note that none of the above results change qualitatively, if we assume that the Au_i annihilate at the surface, so that the surface acts as a sink for both the Si_i and Au_i.

Experiment shows, that a one-sided diffusion of Au into Si produces an asymmetric U-shaped profile. The simulation of the kick-out mechanism for a source on one side only with annihilation of all interstitials leads to the results and Figs. 1 - 3.

In Fig. 1 we present the time evolution of the number of Au_i for 4 different layers, each 100 a thick. The layer which is closest to the surface (0-100 a) contains the

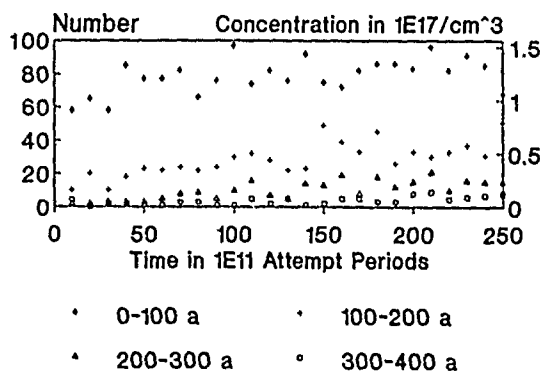


Fig. 1: One sided diffusion: $[Au_i]$ versus time for 4 different layers. The injection takes place at $x = 0 a$. At greater depths all numbers are zero.

highest concentration of Au_i , of course. We see from this plot that the number of interstitials per layer increases perceptively. Initially, the $[Au_i]$ is determined by the balance between injection of Au_i from the source and their annihilation at the surfaces or displacement

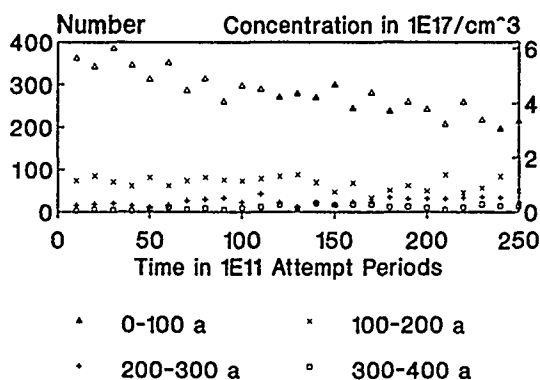


Fig. 2: One sided diffusion: $\Delta[Au_i](t)$ for 4 different layers.

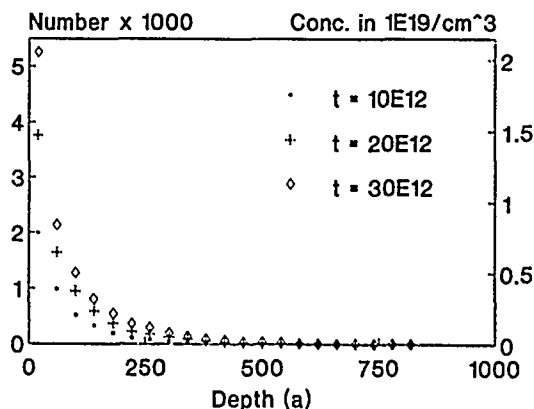


Fig. 3: $[Au_i]$ from a one-sided diffusion for different times.

of Si. As time increases, Au_i are also created by the back reaction (2). We see that the total number of Au_i has increased a factor of two in the course of the simulation.

In Fig. 2 we depict the increment of $[Au_i]$ for various layers. For the surface region (0-100 a) one can clearly see the saturation of $[Au_i]$. The two-sided diffusion again failed to find any evidence for the $t^{1/2}$ behavior of the central gold concentration.

Fig. 3 shows a Au_i profile for 4 different diffusion times, in units of attempt periods. The diffusion started from the left side at $x = 0$ a. Our simulation does not reproduce the experimental U-shaped profile. Although further investigation has to be done on that issue (the simulation has to run a little longer), we are convinced that the basic features of this profile will not change, when the simulation is based on the KO assumptions, no matter how parameters are varied. We think the rise in $[Au_i]$ at the far side of the sample can only occur if Au_i pass through the center of the sample without creating Si_i , to find V coming from the far side. This occurs only if $\Delta H^f(Si_i)$ is too high for Si_i to play a role.

6. CONCLUSIONS

We have performed a multi Giga-event simulation of the kick-out theory on PCs. Even with the parameters as suggested by the proponents of that theory, we could not reproduce any of the features claimed by them. We have shown that the exponential decay of the Au_i profile is neither affected by the thickness of the sample, nor by t , nor R . Based on our latest results, we think the fact that the surface acts as a sink for the Au_i has little effect on the simulation. One major problem of the KO theory and the parameters we tested can be traced down to the high probability with which an Au_i can displace a Si. Its "scattering cross section" is simply too high. Thus it can not penetrate deeply into the sample, and its profile decays exponentially. Another major point we have elucidated is the one-sided diffusion issue. It is impossible to obtain an asymmetric U-shaped profile with the KO hypothesis.

Based on our results, we think it is appropriate to exclude the KO as one of the possible mechanisms which mediate the Au in Si diffusion.

ACKNOWLEDGEMENTS

Supported in part by A.F.O.S.R. under contract No. 89-0309. Presentation at this conference made possible by "Stifterverband für die Deutsche Wissenschaft", for which U. S. is especially grateful. Two of us (U.S. and U.K.) thank the Fulbright commission and the Land Baden-Württemberg for a scholarship. Valuable discussions with U. Gösele (Duke University), P. Reineker and H. Jex (Universität Ulm) are acknowledged.

REFERENCES

- ‡ Present address: Mentor Graphics, Inc., Beaverton, OR, USA.
- § Present address: Institut für Informationsverarbeitung der Universität Tübingen, D-7400 Tübingen, FRG.
- [1] J.A. Van Vechten, Phys. Rev. B 33, 2674 (1986).
- [2] J.A. Van Vechten, in *Handbook on Semiconductors*, Vol. 3, edited by S. P. Keller (North Holland, Amsterdam, 1980), pp. 1 and therein.
- [3] D. Mathiot and J. C. Pfister, J. Appl. Phys. 55, 3518 (1984).
- [4] J. A. Van Vechten, Phys. Rev. B 38, 9913 (1988).
- [5] M. Yoshida, Jpn. J. Appl. Phys. 27, 967 (1988).
- [6] U. Schmid, Thesis, Dept. of Physics, Oregon State University (1988); Diplomarbeit, Abt. Theoretische Physik, Universität Ulm (1989).
- [7] J. A. Van Vechten and U. Schmid, J. Vac. Sci. Technol B 7, 827 (1989).
- [8] U. Schmid, N. C. Myers, and J. A. Van Vechten, Comp. Phys. Commun., in press.
- [9] W. Kohn and L. J. Sham, Phys. Rev. 140, A1133 (1965).
- [10] G. B. Bachelet and N. E. Christensen, Phys. Rev. B 31, 879 (1985).
- [11] N. E. Christensen, Phys. Rev. B 30, 5753 (1984).
- [12] U. Schmid, N. E. Christensen, and M. Cardona, Phys. Rev. B submitted.
- [13] J. A. Van Vechten, U. Schmid, and N. C. Myers, in *Proceedings of the International Conference on the Science and Technology of Defect Control in Semiconductors*, edited by K. Sumino (North Holland, 1989), and therein.
- [14] R. Car and M. Parrinello, Phys. Rev. Lett. 55, 2471 (1985).
- [15] C. Z. Wang, C. T. Chan, and K. M. Ho, Phys. Rev. B 39, 8586 (1989).
- [16] C. S. Nichols, C. G. Van de Walle, and S. T. Pantelides, Phys. Rev. Lett. 62, 1049 (1989); Phys. Rev. B 40, 5484 (1989).
- [17] W. R. Wilcox and T. J. LaChapelle, J. Appl. Phys. 35, 240 (1964).
- [18] F. C. Frank and D. Turnbull, Phys. Rev. 104, 617 (1956).
- [19] F. A. Huntley and A. F. W. Willoughby, J. Electrochem. Soc. 120, 414 (1973); Solid-State Electron. 13, 1231 (1970).
- [20] A. Seeger, Phys. Stat. Solidi (a) 61, 521 (1980).
- [21] U. Gösele, W. Frank, A. Seeger, Appl. Phys. 23, 361 (1980).
- [22] T. Y. Tan and U. Gösele, Appl. Phys. A 37, 1 (1985).
- [23] E. R. Weber in: *Properties of Silicon*, EMIS Datareview (INSPEC, IIE London, 1988).
- [24] U. Gösele, private communication, Jan. 1989.

DIFFUSION OF POINT DEFECTS IN A STRESSED SIMPLE CUBIC LATTICE

DIMITRIOS MAROUDAS AND ROBERT A. BROWN

Massachusetts Institute of Technology, Department of Chemical Engineering, Cambridge, MA 02139

ABSTRACT

A systematic theoretical and computational study is presented for the diffusion of point defects in a stressed cubic lattice. The study combines an atomistic description of point defect migration with a continuum model for point defect transport. Moment analysis of the macroscale transport equation gives expressions for the drift velocity and the diffusivity tensor of the point defects, which are calculated by a dynamic Monte Carlo simulation of the defect migration process. Results are presented for the case of diffusion under a constant force of interaction between the applied stress on the crystal and the defects. The continuum model gives the general constitutive model for stress-assisted point defect diffusion.

1. INTRODUCTION

Quantitative analysis of the influence of processing conditions on the number and type of defects in crystalline semiconductors requires the development of macroscale constitutive equations that relate the number, creation and motion of defects in the lattice to the mechanical stress and temperature history of the material. The first step in such a development is an analysis of the diffusion of point defects, either vacancies or interstitial atoms, in the presence of applied or internal mechanical stresses.

Migration of point defects in a crystal takes place in a stress field. The distribution of point defects is characterized by its number density $n(\mathbf{r}, t)$. A force $\mathbf{F}(\mathbf{r})$ is exerted on each of the point defects in the distribution through the interaction potential $U(\mathbf{r})$ between the stress field and the point defect; $\mathbf{F}(\mathbf{r}) = -\nabla U(\mathbf{r})$. Quantitative modelling of the point defect dynamics in the lattice is based on the solution of the macroscopic transport equation of point defect migration

$$\frac{\partial n}{\partial t} = -\nabla \cdot (\mathbf{u}_d n) + \nabla \cdot (\mathbf{D} \cdot \nabla n), \quad (1)$$

where \mathbf{D} is the diffusivity tensor and \mathbf{u}_d is the drift velocity of the point defect distribution due to the potential U that is superimposed on the perfect lattice potential. A constitutive model for the dependence of \mathbf{D} and \mathbf{u}_d on the force \mathbf{F} and the temperature field $T(\mathbf{r}, t)$ in the crystal is necessary to solve eq. (1). Such a constitutive model is obtained by analysis of the diffusion process in the crystalline lattice.

2. ANALYSIS OF THE POINT DEFECT DIFFUSION PROCESS

Point defect migration is modelled on the lattice scale as a thermally activated jump process between nearest neighbor equilibrium lattice sites. If a particle occupies an equi-

librium position i , at either a substitutional or an interstitial site, it can move from this site to Z nearest neighbor sites labelled j , where Z is the coordination number of the lattice. Each $i-j$ jump is characterized by a jump frequency w_{ij} , that is proportional to the Boltzmann factor $\exp(-Q_{ij}/kT)$, where Q_{ij} is the potential energy barrier given by the difference between the saddle point energy and the original equilibrium point energy.

In the unstressed lattice, the potential energy surface is spatially periodic. The atomic jump process is described by a random walk model and leads to an isotropic diffusion coefficient in a cubic lattice given by the well known result

$$D = a^2 w_0 \exp\left(-\frac{Q^0}{kT}\right), \quad (2)$$

where a is the nearest neighbor distance equal to the lattice parameter for the simple cubic structure, w_0 is the attempt frequency, and Q^0 is the constant energy barrier for all the $i-j$ jumps. In the stressed lattice the force F acts on the diffusing point defect, which develops a slope in the potential energy surface and creates preferred directions for diffusion. Homogeneous and inhomogeneous forces develop constant and spatially dependent slopes respectively. This effect leads to anisotropic diffusion expressed by an anisotropic tensor D that may be either homogeneous or inhomogeneous. In both cases, D is diagonal, because its principal axes coincide with the crystallographic axes of the cubic lattice.

Our modelling begins with the moment analysis of the transport equation (1), which is a continuum representation of the master equation [1]. The point defect distribution moment analysis is an extension in three dimensions of the procedure used by Jacoboni et al. [2] for the study of charge carrier transport in semiconductors. The first two moments of the number density distribution are given by

$$M_1 = \frac{1}{N} \int_V r n(r, t) d^3 r = \langle r \rangle, \quad (3)$$

$$M_2 = \frac{1}{N} \int_V r r n(r, t) d^3 r = \langle r r \rangle, \quad (4)$$

where N is the total number of point defects in the lattice and r is the displacement vector of the defect from its initial position.

Time differentiation of (3) and (4) and incorporation of equation (1) for the time derivative of $n(r, t)$ gives expressions for u_d and D as functions of the moments. For the random walk diffusion process, the results are

$$\frac{d\langle r \rangle}{dt} = 0, \quad D = \frac{1}{2} \frac{d}{dt} \langle r r \rangle, \quad (5)$$

and for diffusion under a constant force F , the constant values of u_d and D are given by

$$\frac{d\langle r \rangle}{dt} = u_d, \quad D = \frac{1}{2} \frac{d}{dt} (\langle r r \rangle - \langle r \rangle \langle r \rangle). \quad (6)$$

Equations (5) and (6) give no statement on the isotropy of diffusion, because the lattice structure is not taken into account by the continuum model. For the general case of

spatially inhomogeneous forces $F(r)$, moment analysis does not give explicit relations for the drift velocity and the diffusivity.

3. DIFFUSION WITH CONSTANT FORCE: ANALYTICAL RESULTS

The problem of diffusion under a homogeneous force has been solved in closed form [1]. The jump frequency w_{ij} is proportional to a Boltzmann factor that contains the effect of the component of the force in the $i-j$ direction

$$w_{ij} = c \exp\left(-\frac{Q^0}{kT}\right) \exp\left(\frac{F_j a}{2kT}\right). \quad (7)$$

The frequency c is proportional to the attempt frequency w_0 with a proportionality factor that depends on the magnitudes of the force components and expresses that jumps are easier over the lower energy barriers. For a two-dimensional square lattice

$$c = \frac{2 \exp\left[\max\left\{\frac{F_x a}{2kT}, \frac{F_y a}{2kT}\right\}\right]}{\cosh\left(\frac{F_x a}{2kT}\right) + \cosh\left(\frac{F_y a}{2kT}\right)} w_0. \quad (8)$$

The probability for successful $i-j$ jump, which is necessary for the calculation of the first and second moments, is

$$p_j = \frac{w_{ij}}{\sum_{j=1}^Z w_{ij}} = \frac{\exp\left(\frac{F_j a}{2kT}\right)}{\cosh\left(\frac{F_x a}{2kT}\right) + \cosh\left(\frac{F_y a}{2kT}\right)}. \quad (9)$$

Application of equation (6) leads to closed form expressions for the components of u_d and D :

$$u_{d,j} = 2ac \exp\left(-\frac{Q^0}{kT}\right) \sinh\left(\frac{F_j a}{2kT}\right), \quad (10)$$

$$D_{jj} = a^2 c \exp\left(-\frac{Q^0}{kT}\right) \cosh\left(\frac{F_j a}{2kT}\right). \quad (11)$$

Equations (10) and (11) imply that Einstein's equation $u_d = \frac{D \cdot F}{kT}$ is valid only in the asymptotic limit of high temperatures and low forces.

4. DIFFUSION WITH CONSTANT FORCE: COMPUTATIONAL RESULTS

Dynamic Monte Carlo simulations, with the appropriate transition probability [3] and the correct introduction of the time variable [4], have been used for the calculation of the time dependence of the moments over the temperature range 300 K - 1000 K. The random walk problem has been used as a test to check the accuracy of the simulation and the definition of the time unit. Both a two-dimensional square lattice and a three-dimensional cubic lattice have been used. For the constant interaction force, a linear potential is superimposed on the perfect lattice potential; the value of $Q^0=10$ kJ/mol is used as typical of light interstitial diffusion in metals [5]. The algorithm is a modification

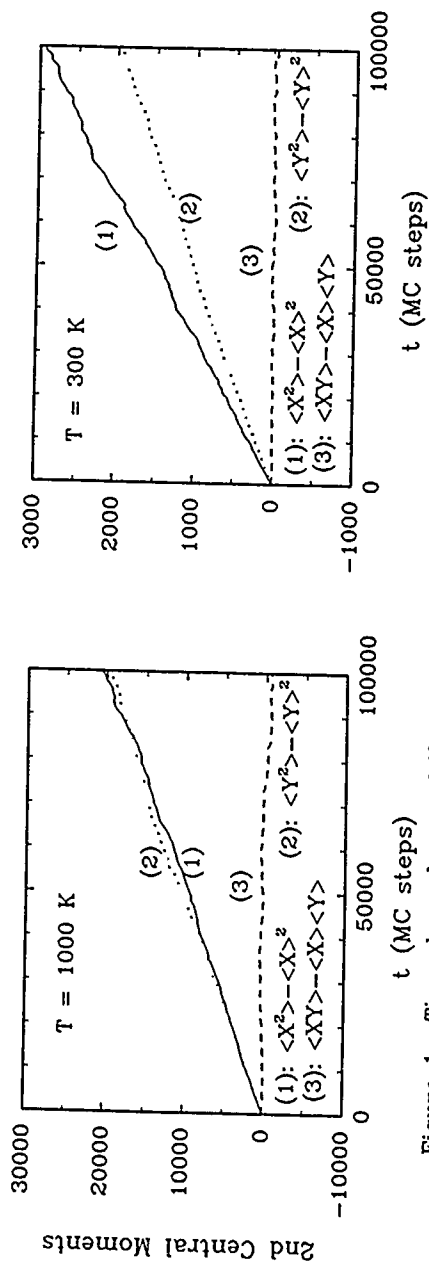


Figure 1. Time dependence of the components of the second central moment tensor for the case: $U = -0.5(Q^0/a)x - 0.2(Q^0/a)y$

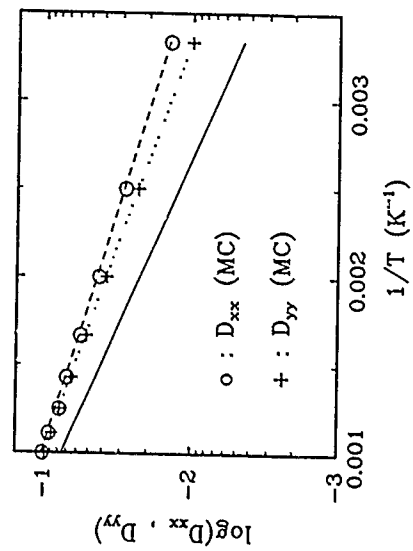


Figure 2. Temperature dependence of the diffusivity components. Dashed and dotted lines are the analytical results for D_{xx} and D_{yy} respectively for the same potential U as in Fig. 1 and the solid line represents the random walk result.

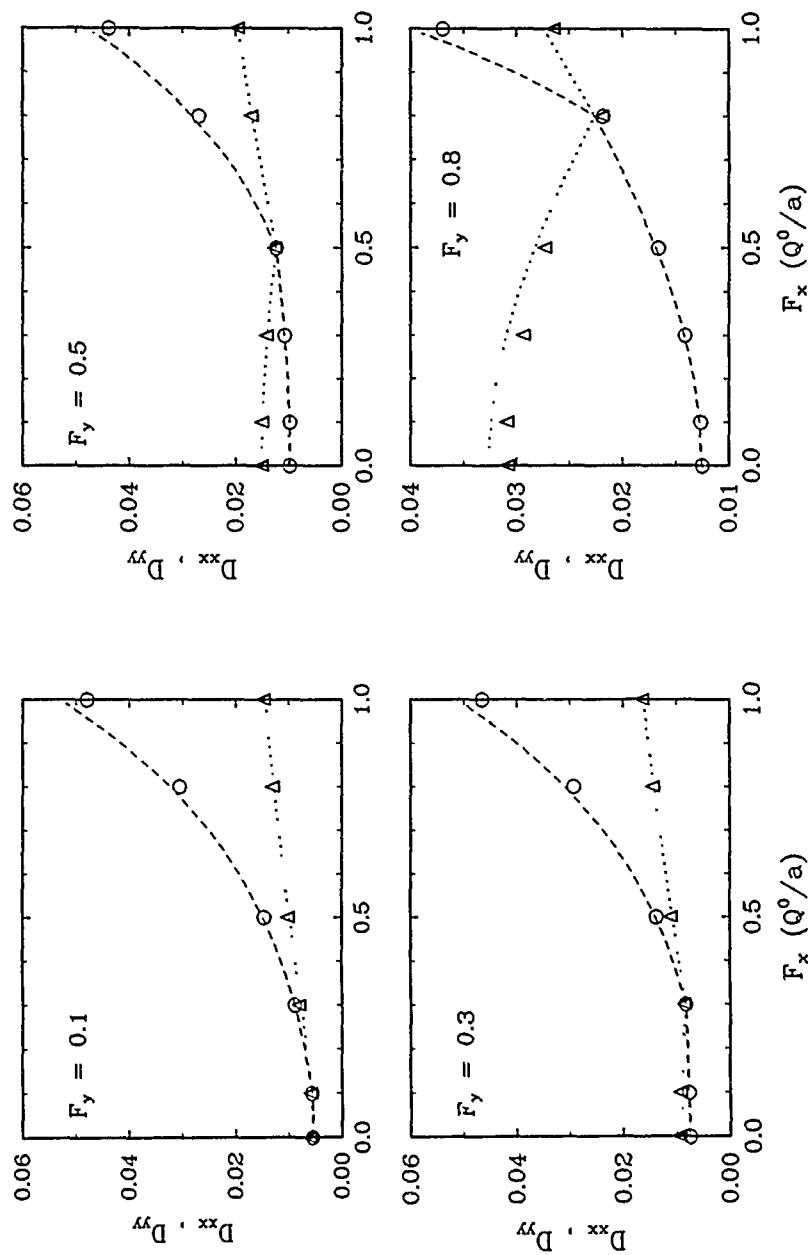


Figure 3. Dependence of the diffusivity components on the magnitude of the component F_x . Circles and triangles give the Monte Carlo results, while dashed and dotted lines are the analytical results for D_{xx} and D_{yy} respectively. Calculations are shown for F_y equal to 0.1, 0.3, 0.5 and 0.8 of Q^0/a .

of the one developed by Lancon et al. [6] and Limoge and Bocquet [4] for interstitial random walk diffusion in periodic disordered media. The success of a jump is determined by the energy fluctuation using a random number generator and Boltzmann statistics. The direction of the jump is set by the relative magnitudes of the jump frequencies in the Z possible directions. We have used $M = 1000$ particle trajectories for ensemble averaging and $m = 100$ subtrajectories of equal duration to reduce growing fluctuations about straight lines; the simulation time is equal to 10^5 jump attempts. The statistical uncertainty of the calculated components of \mathbf{u}_d and \mathbf{D} is proportional to $(Mm)^{-1/2}$.

The time dependence of the second central moments is presented in Fig. 1 for a two dimensional square lattice with an added potential $U = -F_x x - F_y y$, where $F_x = 0.5Q^0/a$ and $F_y = 0.2Q^0/a$; $T = 1000$ K and $T = 300$ K. The anisotropy introduced by the force \mathbf{F} is not significant at high temperatures, but becomes large at lower temperatures. The temperature dependence of the diffusivity components is presented in an Arrhenius plot in Fig. 2 for the same values of the force components. Finally, the dependence of the diffusivity components on the magnitude of the applied force is presented in Fig. 3, for $T = 300$ K. The diffusivity components are plotted as functions of F_x for constant F_y . Anisotropy becomes more important as the magnitudes of F_x , F_y are increased; for $F_x = F_y$ the diffusivity is isotropic. The agreement between the Monte Carlo results and the analytical solution is very good, as it is demonstrated in both Figs. 2 and 3.

5. EXTENSIONS

For the general case of diffusion under the action of spatially inhomogeneous forces, the constitutive expressions (10) and (11), which are valid throughout the infinite lattice for the constant force case, can be used as local results at the appropriate values of the force. In addition, our calculations can be easily extended in other cubic structures, by changing only geometrical details. The closed-form expressions and the continuum model (1) are the starting point of analysis of point defect diffusion in crystals.

References

1. D. Maroudas, and R. A. Brown, in preparation (1989)
2. C. Jacoboni, and L. Reggiani, *Rev. Mod. Phys.*, **55**, 545 (1983)
3. H. C. Kang, and W. H. Weinberg, *J. Chem. Phys.*, **90**, 2824 (1989)
4. Y. Limoge, and L. Bocquet, *Acta Metallurgica*, **36**, 1717 (1988)
5. R. Kirchheim, and U. Stolz, *Acta Metallurgica*, **35**, 281 (1987)
6. F. Lancon, L. Billard, W. Chambon, and A. Chamberod, *J. Phys. F : Met. Phys.*, **15**, 1485 (1985)

THE ENHANCEMENT OF THE INTERDIFFUSION IN Si/Ge AMORPHOUS ARTIFICIAL MULTILAYERS BY ADDITIONS OF B AND Au

B. Park^{*} and F. Spaepen
Division of Applied Sciences, Harvard University, Cambridge, MA 02138
J.M. Poate and D.C. Jacobson
AT&T Bell Laboratories, 600 Mountain Avenue, Murray Hill, NJ 07974

ABSTRACT

Amorphous Si/ amorphous Ge artificial multilayers were prepared by ion beam sputtering. Boron or gold impurities were introduced into the Si/Ge multilayers by ion implantation or during the sputtering deposition. Diffusion coefficients were determined by measuring the decrease in the intensity of the first order X-ray diffraction peak resulting from the composition modulation. It was found that the interdiffusion of Si and Ge in their amorphous phase can be enhanced by doping. The enhancement factor is independent of the degree of structural relaxation, as observed by the decrease of diffusivity with annealing time, of the amorphous phase. A model is proposed that describes this behavior in terms of electronic effects, introduced by the dopants, on the pre-existing structural defects governing diffusion.

INTRODUCTION

Atomic diffusion in amorphous covalent network formers, such as Si and Ge, is most easily thought of as governed by the presence and motion of structural defects like broken bonds, vacancies or interstitials. These non-equilibrium structural defects, which are present as a result of the growth (deposition) or implantation processes, have been used to interpret, respectively, the results of thermal diffusion [1] or ion beam-enhanced diffusion [1-3] measurements in amorphous Si/ amorphous Ge artificial multilayers. The artificial multilayer technique is known to be the most sensitive method for diffusivity measurements [4], and has been used to study the relatively slow diffusion [1,5] of the covalent network formers themselves, i.e., the Si and Ge atoms, without the risk of crystallization. Because the measurement is non-destructive, it is also suitable for the observation of the possible transients or effects of structural relaxation in the amorphous phase.

The presence of dopant atoms in the amorphous phase may affect the concentration or character of the structural defects that control the diffusivity of the host atoms. Enhancement of the self-diffusivity by doping has been observed in crystalline Si and Ge, and has been explained by changes in equilibrium concentrations of defects due to a shift of the Fermi level [6,7]. It is also known that incorporation of dopants causes enhancement of the solid phase epitaxial (SPE) regrowth rate [8-12]. This is interpreted by electrically-induced generation of structural defects [13-15]. One of the problems is to understand whether these defects originate from the crystal-amorphous interface or from the bulk amorphous phase. In this paper, the effect of dopants on the interdiffusion in Si/Ge amorphous artificial multilayers are investigated. Although the atomic mechanisms for diffusion and SPE are not identical, they may be similar, since they both require bond breaking processes [16]. Therefore a better understanding of the effect of dopants on the interdiffusion in the amorphous phase can elucidate their effect in SPE as well.

EXPERIMENTAL METHODS

The artificial multilayers were prepared by ion beam sputtering onto oxidized Si (100) substrates. The sputtering Ar gas was cleaned in a Ti gettering furnace, and the actual deposition was started after sputtering for one hour. The repeat lengths of the multilayers, obtained from the position of the X-ray diffraction peaks resulting from the composition

^{*} Present Address: IBM T.J. Watson Research Center, Yorktown Heights, NY 10598

modulation, corrected for the index of refraction of the material [17], were around 60 Å. The total film thickness was around 2000 Å, and the average composition of the multilayers was equiatomic. Cross-sectional transmission electron microscopy investigation of ion-implanted or annealed samples with impurities confirmed that the planar layer structures were preserved, and no crystallization or precipitation had occurred at any stage of experiments [1,2].

Some multilayers were implanted at a substrate temperature of 77 K with ^{11}B (a dose Φ at 20 keV, and 2Φ at 50 keV), in the range from $\Phi = 2 \times 10^{14}$ to 1.6×10^{15} ions/cm². These implantation energies were chosen to give reasonably uniform impurity distributions throughout the 2000 Å multilayer films [18]. Gold impurities were incorporated into the Si/Ge amorphous multilayers during the ion beam sputtering deposition by mounting small pieces of Au foil on the Si and Ge elemental targets. The size and position of the foils on these two targets were adjusted to have equal concentrations of Au at 0.4 at. % in the Si and Ge layers, and the composition was checked by Rutherford backscattering spectrometry.

The diffusion coefficients were determined by X-ray diffraction in a $\theta - 2\theta$ scan on a GE horizontal diffractometer, using Cr $K\alpha$ radiation. The diffusivity is calculated from $D(t) = -d^2/8\pi^2 [d \ln I(t)/dt]$, where d is the repeat length, $I(t)$ is the intensity of the first order X-ray diffraction peak, and t is the annealing time [4].

Each doped sample was simultaneously annealed with a control sample to reduce any experimental errors. For samples with B impurities, the control samples were unimplanted multilayers. For samples with Au impurities, the control samples were prepared immediately after each sample deposition in the ion beam sputtering chamber.

THE EFFECT OF BORON IMPLANTATION

Figures 1, 2 and 3 show diffusivities during thermal annealing of three implanted samples (peak concentrations 0.05, 0.2 and 0.4 at. % B, respectively) and their unimplanted controls. The square of the mixing length resulting from ion implantation of ^{11}B at 77 K is 5.3, 57.8 and 124.9 Å², respectively. As shown in Figures 1 and 2, the diffusion in the implanted samples were somewhat faster than in their controls during the first anneal at 650 K. This result is similar to what has been observed for ^{29}Si self-implantation [2], and has been explained by the presence of implantation-induced structural defects [1]. For the second anneal at a higher temperature (670 K), no difference is observed between the 0.05 at. % B sample and the control (Figure 1). This is also similar to the case of the ^{29}Si implantation [2].

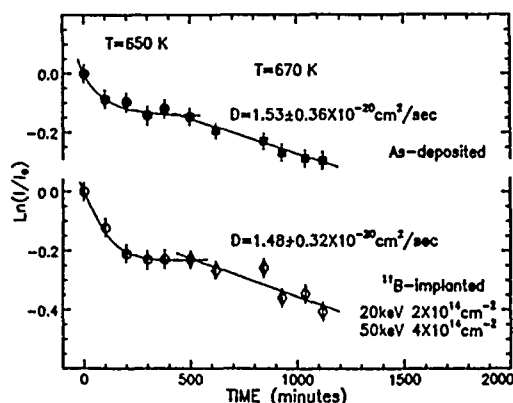


FIG. 1. Intensity of the first order X-ray diffraction peak resulting from the composition modulation as a function of annealing time at 650 K and 670 K. Open symbols: ^{11}B -implanted sample (0.05 at. %); closed symbols: control sample.

In the 0.2 at. % B sample, the diffusivity at 690 K (see Figure 2) is enhanced by factors 1.54 and 1.63 over the control, while the decrease in diffusivity with annealing time is about a factor of 2 in both the sample and control. Figure 3 shows that the diffusivity at 700 K in the 0.4 at. % B sample is enhanced by factors 2.33 and 2.49 over the control, while the de-

crease in diffusivity with annealing time is about a factor of 7. These data show that atomic diffusion is enhanced by boron addition, and that the enhancement factor of the diffusivity is independent of the degree of structural relaxation, as measured by the decrease in diffusivity with annealing time, of the amorphous phase.

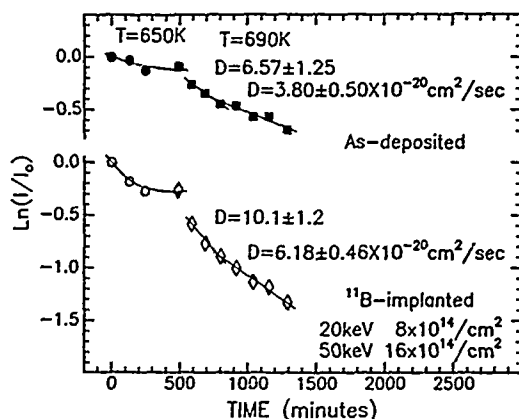


FIG. 2. Decay of the first order X-ray diffraction peak resulting from the composition modulation as a function of annealing time at 650 K and 690 K. Open symbols: ^{11}B -implanted sample (0.2 at. %); closed symbols: control sample. At 690 K, the diffusivity in the ^{11}B -implanted sample is enhanced by factors 1.54 and 1.63 over the control. The size of symbols corresponds to the error bar for the X-ray intensity measurements (same for the following figures).

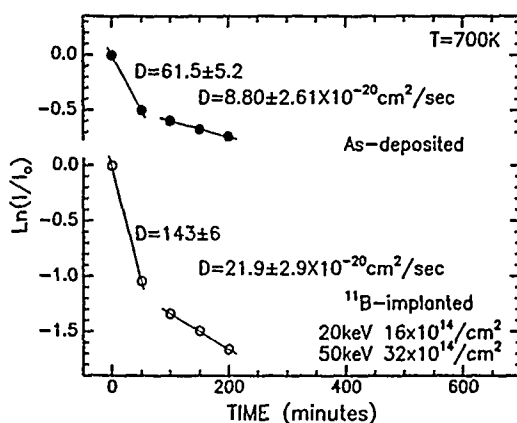


FIG. 3. Decay of the first order X-ray diffraction peak resulting from the composition modulation as a function of annealing time at 700 K. Open symbols: ^{11}B -implanted sample (0.4 at. %); closed symbols: control sample. The diffusivity in the 0.4 at. % B sample is enhanced by factors 2.33 and 2.49 over the control.

THE EFFECT OF Au IMPURITIES

Figures 4 and 5 show diffusivities for two multilayer films with 0.4 at. % Au at annealing temperatures of 680 K and 700 K, respectively. The diffusivity in a 0.4 at. % Au sample at 680 K is enhanced by factors 1.77 and 1.57 over the control, while the decrease in diffusivity with annealing time is about a factor of 7 (Figure 4). At 700 K, the diffusivity is enhanced by factors 1.74, 1.74 and 1.71 over the control, while the decrease in diffusivity with annealing time is about a factor of 11, as shown in Figure 5. Again, the interdiffusion of Si and Ge in the amorphous phase is enhanced by Au dopants, and the enhancement factor does not depend on the degree of structural relaxation, as measured by the decrease in the diffusivity.

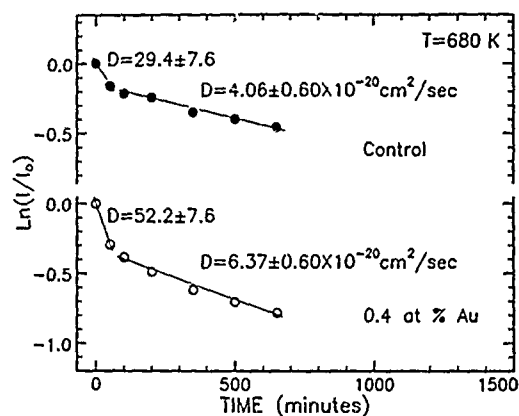


FIG. 4. Decay of the first order X-ray diffraction peak resulting from the composition modulation as a function of annealing time at 680 K. Open symbols: multilayer film with 0.4 at. % Au; closed symbols: control sample. The diffusivity is enhanced by factors 1.77 and 1.57 over the control.

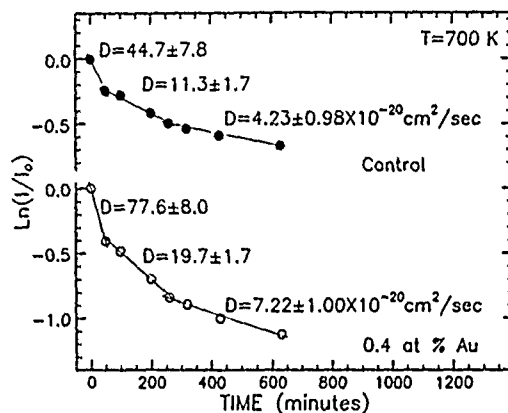


FIG. 5. Decay of the first order X-ray diffraction peak resulting from the composition modulation as a function of annealing time at 700 K. Open symbols: multilayer film with 0.4 at. % Au; closed symbols: control sample. The diffusivity is enhanced by factors 1.74, 1.74 and 1.71 over the control.

DISCUSSION

A comparison of the SPE and interdiffusion data suggests that a fraction of the dopant-induced defects contributing to SPE growth is contributing to the diffusion process as well. For 0.4 at. % B, the SPE rate is enhanced by a factor of 10 in Si [11]. At 0.2 at. % B, it is enhanced by a factor of 5 and 2.5 in Si [11] and Ge [10], respectively. At 0.05 at. % B in Si, the enhancement factor is almost negligible [11]. For 0.4 at. % Au, the SPE rate is enhanced by a factor of 6 in Si [12].

Still, it is somewhat surprising that atomic diffusion can be enhanced by dopants in the amorphous phase, for the following reasons:

- (1) In these fully amorphous Si/Ge multilayers, structural defects cannot be supplied from the crystalline phase, as in the proposed mechanism for the SPE rate enhancement [13-15].
- (2) The doping efficiency of impurity atoms in amorphous Si and Ge is low. In other words, only a fraction of impurities becomes electrically active [19].

(3) Amorphous Si and Ge have a high concentration of neutral dangling bonds, and each neutral dangling bond can trap either an electron or a hole, which comes from the ionized dopants [19-22].

The following is a possible model for the enhancement of interdiffusion by B or Au in the amorphous Si/Ge multilayers. Atomic diffusion in the amorphous phase is controlled by non-equilibrium structural defects. Electrons or holes, from the B or Au atoms, affect the structural defects and help the bond breaking process. That the enhancement factor is independent of the degree of structural relaxation can be explained if the *fraction* of the pre-existing structural defects affected by electrons or holes in the deposited Si/Ge amorphous multilayers is constant in time. More detailed analysis can be found in the later publication [23].

That the relaxation rate is not affected by the presence of impurity atoms, even though these impurity atoms can enhance the diffusivity of Si and Ge host atoms (Figures 2, 3, 4 and 5), implies that the relaxation processes are not controlled by the same processes that control the interdiffusion. One possible explanation is that the annihilation of structural defects is a two-step process: diffusion to a sink, followed by a rearrangement at the sink leading to a more stable network. That the relaxation rate does not scale with the diffusivity implies that the final rearrangement at the sink is the rate-limiting step.

CONCLUSIONS

The atomic diffusion of Si and Ge in the amorphous phase is enhanced by the presence of dopants such as boron and gold. The enhancement can be described by a constant factor, independent of time, and is explained by trapping of electrons or holes from the dopant elements at the pre-existing structural defects. A comparison of this experiment and the SPE growth rate enhancement suggests that a mechanism of the dopant-induced diffusion enhancement can also operate in the SPE process, which requires bond breaking for the crystallization rearrangements [16].

ACKNOWLEDGEMENTS

We thank Michael Aziz, Ken MacKenzie and Choochun Lee for useful discussions, and C.S. Pai for the boron implantation. The work at Harvard has been supported by the National Science Foundation through the Materials Research Laboratory under contract number DMR-86-14003.

REFERENCES

1. B. Park, Ph.D. Thesis (Harvard University, 1989).
2. B. Park, F. Spaepen, J.M. Poate, F. Priolo, D.C. Jacobson, C.S. Pai, A.E. White and K.T. Short, *Mat. Res. Soc. Symp. Proc.* 103, 173 (1988).
3. B. Park, F. Spaepen, J.M. Poate, F. Priolo and D.C. Jacobson, *Mat. Res. Soc. Symp. Proc.* 128, 243 (1989).
4. A.L. Greer and F. Spaepen, in *Synthetic Modulated Structures*, edited by L.L. Chang and B.C. Giessen (Academic Press, New York, 1985) p.419.
5. R.G. Elliman, J.M. Gibson, D.C. Jacobson, J.M. Poate and J.S. Williams, *Appl. Phys. Lett.* 46, 478 (1985).
6. A. Seeger and K.P. Chik, *Phys. Status Solidi* 29, 455 (1968).
7. W. Frank, U. Gösele, H. Mehrer and A. Seeger, in *Diffusion in Crystalline Solids*, edited by G.E. Murch and A.S. Norwick (Academic Press, Orlando, 1984) p. 63.
8. L. Csepregi, E.F. Kennedy, T.J. Gallagher, J.W. Mayer and T.W. Sigmon, *J. Appl. Phys.* 48, 4234 (1977).
9. A. Lietoila, A. Wakita, T.W. Sigmon and J.F. Gibbons, *J. Appl. Phys.* 53, 4399 (1982).

10. I. Suni, G. Göltz, M.-A. Nicolet and S.S. Lau, *Thin Solid Films* 93, 171 (1982).
11. G.L. Olson and J.A. Roth, *Materials Science Report* 3, 1 (1988).
12. D.C. Jacobson, J.M. Poate and G.L. Olson, *Appl. Phys. Lett.* 48, 118 (1986).
13. L.E. Mosley and M.A. Paesler, *Appl. Phys. Lett.* 45, 86 (1984).
14. C. Licoppe and Y.I. Nissim, *J. Appl. Phys.* 59, 15 (1986).
15. B. Park (unpublished).
16. F. Spaepen and D. Turnbull, in *Laser-Solid Interactions and Laser Processing*, edited by S.D. Ferris, H.J. Leamy and J.M. Poate, Am. Inst. Phys., New York (1979), p.73.
17. A.M. Kadin and J.E. Keem, *Scripta Metall.* 20, 440 (1986).
18. J.F. Ziegler, J.P. Biersack and U. Littmark, *The Stopping and Range of Ions in Solids*, Pergamon Press, New York (1985).
19. R.A. Street, *J. Non-Cryst. Solids* 77&78, 1 (1985).
20. R.A. Street, D.K. Biegelsen and J.C. Knights, *Phys. Rev. B* 24, 969 (1981).
21. S. Hasegawa, T. Kasajima and T. Shimizu, *Philos. Mag. B* 43, 149 (1981).
22. W.E. Spear and P.G. Le Comber, *Solid State Commun.* 17, 1193, (1975).
23. B. Park, F. Spaepen, J.M. Poate and D.C. Jacobson, to be published.

Diffusion of Au in Amorphous Si Measured by the Artificial Multilayer Technique

E. Nygren^{a)}, B. Park^{b)}, L.M. Goldman, D.T. Wu, A.V. Wagner and F. Spaepen
Division of Applied Sciences, Harvard University, Cambridge, MA 02138

ABSTRACT

The diffusivity of Au in amorphous Si (a-Si) has been determined in the temperature range 200-260°C using Ar-ion sputter deposited artificial multilayered films of a-Si and a-Si(0.7at%Au) with repeat lengths between 44 and 48 Å. Diffusion on lengths scales of the order of interatomic spacings have been investigated. The Au diffusivity exhibits an Arrhenius temperature dependence with an activation enthalpy of 1.2eV and shows good agreement with extrapolations of higher temperature Au diffusion data obtained by Rutherford backscattering spectrometry (RBS) in ion-implanted, CVD, and sputter deposited a-Si. The measured Au diffusivity also shows a significant time dependence.

INTRODUCTION

Atomic diffusion in crystalline silicon has been studied extensively for decades, and can be understood in detail by the concentration and motion of structural defects in thermal equilibrium [1,2]. Experimental investigations are usually restricted to high temperatures because limited solubilities and low diffusivities hamper detection. By contrast, there have been relatively few studies of atomic transport in the amorphous phase of silicon [3-8], in which non-equilibrium defects, introduced by the growth or implantation processes, can play an important role. Difficulties with these investigations arise due to the metastabilities of the material. Measurements must be made at temperatures sufficiently low or for times sufficiently short to prevent crystallization and/or precipitation. These restrictions necessitate the use of very sensitive techniques.

Au is a so-called 'fast diffuser' in crystalline silicon (c-Si). It also diffuses fast enough in amorphous silicon (a-Si) to permit study by conventional techniques, such as Rutherford backscattering spectrometry (RBS), without complications from phase transformations [4,5]. Diffusion of Cu and Ag in a-Si have also been studied this way [4]. However, c-Si 'slow diffusers', such as In, As, Sb and Bi, show no detectable diffusion in RBS measurements on a-Si.

The artificial multilayer technique is the most sensitive technique available for the measurement of diffusion. In the technique, the intensity of radiation (x-ray) diffracted from the composition modulation of a multilayer film with repeat length of a few nanometers is monitored as a function of annealing time. The multilayer film functions as a collection of parallel diffusion couples and the change in diffracted x-ray intensity can be related to the amount of interdiffusion. By this method, diffusivities as low as 10^{-23} cm²/sec and diffusion or mixing lengths smaller than an interatomic distance can be routinely measured [9-11]. The technique is non-destructive so diffusivity can be measured as a function of time.

In this paper we report the first measurements of diffusion, on a length scale on the order of an interatomic spacing, of an impurity, Au, in a-Si. We also demonstrate the use of the multilayer technique for diffusion studies of small concentrations of impurities.

EXPERIMENTAL METHODS

The a-Si/a-Si(0.7at%Au) multilayer films used in this study were deposited by Ar ion sputtering from alternating targets [12] on polished (100) Si wafers at room temperature. Two targets were used, a Si target and a composite target made up of Si and pieces of Au foil. The make-up of the composite target was adjusted to give 0.7at% Au in homogeneous films as determined by RBS. The base vacuum in the chamber was 3×10^{-7} torr and the Ar was cleaned in a Ti gettering furnace. Multilayer films

^{a)} Present Address: Department of Materials Science and Engineering, The Ohio State University, Columbus, OH 43210

^{b)} Present Address: IBM T.J. Watson Research Center, Yorktown Heights, NY 10598

consisted of ~300 bilayers with repeat lengths ranging between 44 and 48 Å. The repeat lengths were determined from the position of the first order x-ray diffraction peak, resulting from the composition modulation, corrected for the average index of refraction of the material [13,14]. The amorphous nature of the films was confirmed by glancing angle x-ray diffraction.

X-ray measurements of multilayer diffraction were performed in θ -2 θ scans on a Huber 424 two-circle goniometer with tilt and sample translation stages. A single crystal Ge monochromator was used to provide a well-collimated beam of MoK α_1 from a fixed anode source operated at 45 KeV and 15 ma. Mo radiation was selected over the longer wavelengths of Cu and Cr because optical multilayer calculations [15] showed that greater diffracted intensities were possible [16]. Detection was by a NaI scintillation counter. A second NaI detector was used for continuous monitoring of incident beam through a Kapton beamsplitter. Integrated peak intensities were calculated by subtracting from the data a smooth curve fit to the background. The intensity of multilayer reflections in this system is intrinsically weak due to small electron concentration contrast provided by the small concentration of Au. Best results were achieved by using small samples, approximately 0.125" \times 1", aligned with their long dimension parallel to the long dimension of the beam spot. Such a sample represents a compromise between the conflicting demands for increased intensity through increased sample size and decreased sensitivity to position in the beam through decreased sample size. The exposed cross-section of such a sample oriented at the Bragg angle ($\theta=0.46^\circ$) was approximately four times smaller than the lateral dimension of the beam. Repeated measurements established that, with careful alignment, the integrated normalized peak intensities could be reproduced to within $\pm 5\%$.

Samples were annealed in a lamp heated, silica tube furnace to minimize heating and cooling times. The tube was first evacuated with a cryogenic pump to 10^{-7} torr and then backfilled with flowing He. All anneals were carried out under flowing He gas that had been cleaned in a Ti gettering furnace.

RESULTS

The rate of interdiffusion of the modulated film was determined from the changes in intensity of the first order x-ray peak resulting from the composition modulation as shown in Figure 1. Higher order peaks were not detectable. In the kinematic diffraction approximation, which is valid in this case because the reflectivity is small [14], the integrated intensity of each reflection is proportional to the square of the corresponding coefficient in the Fourier expansion of the composition profile. The effective interdiffusion coefficient, D , is given by:

$$\frac{d \ln I(t)}{dt} = -\frac{8\pi^2}{d^2} D(t)$$

where I is the intensity of the first order peak, t is the annealing time and d is the repeat length [11]. The integrated intensity after background subtraction was measured as a function of annealing time. Figure 2 shows plots of $\ln[I(t)/I(0)]$ versus annealing time for six different multilayer samples annealed at five different temperatures.

The changing slope of the plots in Figure 2 indicates a decrease in interdiffusivity with continued annealing. Such behavior is often observed in diffusion studies in the amorphous state [11]. Studies of potassium diffusion in a-Si by high resolution RBS showed a similar decrease of diffusivity with time [3]. Interdiffusivities were determined by piece-wise, linear least-squares fits to approximately linear portions of the plots in Figure 2 and are shown on the Arrhenius plot of Figure 3. Since d is fairly large compared to typical critical wavelengths [11,17,18] the calculated values of D are probably close to the bulk interdiffusivities.

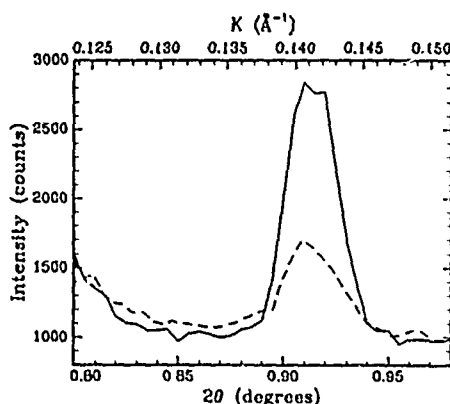


Figure 1. Typical 0-20 scan of the first order X-ray diffraction peak from an a-Si/a-Si(0.7at%Au) multilayer film using MoK α_1 radiation. Solid line: sample #6 as-deposited. Dashed line: after 390 minutes at 460°C.

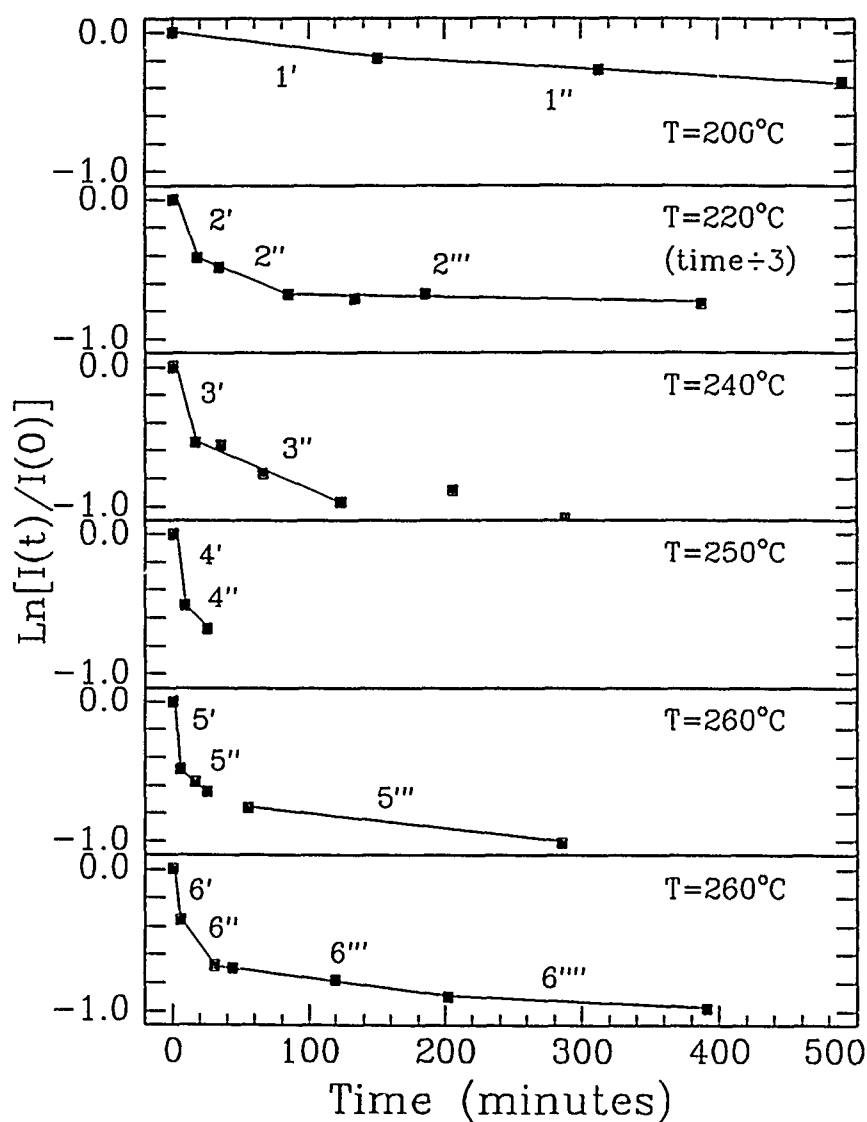


Figure 2. The decrease in the intensity of the first order X-ray diffraction peaks as a function of annealing time for six different multilayer films (labeled 1 thru 6) at various temperatures. See Table 1 for diffusivities corresponding to the indicated slopes.

DISCUSSION

Estimates of the self-diffusivity in a-Si, based on studies of interdiffusion in a-Si/a-Ge multilayers [8], fall far below the interdiffusivities measured in these experiments. This, combined with the low concentration of Au in the films, permits the identification of interdiffusivity, in the

Table 1. Diffusion coefficients in a-Si/a-Si(0.7at%Au) modulated films, obtained from linear least-square fits on the data shown in figure 2.

Sample	Repeat Length (Å)	T (°C)	Sequence	Total Annealing Time (minutes)	Diffusivity (cm ² /sec)	Total Diffusion Length (Å)
#1	48	200	1'	150	$6.04 \pm 2.29 \times 10^{-20}$	2.3
			1''	490	$2.48 \pm 1.01 \times 10^{-20}$	3.2
#2	47	220	2'	50	$3.92 \pm 0.66 \times 10^{-19}$	3.4
			2''	250	$6.26 \pm 1.58 \times 10^{-20}$	4.4
			2'''	1150	$3.26 \pm 3.41 \times 10^{-21}$	4.6
#3	47	240	3'	15	$1.72 \pm 0.22 \times 10^{-18}$	3.9
			3''	125	$1.84 \pm 0.28 \times 10^{-19}$	5.2
#4	45	250	4'	10	$2.25 \pm 0.30 \times 10^{-18}$	3.7
			4''	25	$4.52 \pm 2.02 \times 10^{-19}$	4.2
#5	44	260	5'	5	$4.02 \pm 0.58 \times 10^{-18}$	3.5
			5''	25	$2.82 \pm 1.44 \times 10^{-19}$	3.9
			5'''	285	$4.59 \pm 1.26 \times 10^{-20}$	5.0
#6	46	260	6'	5	$3.18 \pm 0.63 \times 10^{-18}$	3.1
			6''	30	$5.95 \pm 1.26 \times 10^{-19}$	4.3
			6'''	200	$5.69 \pm 1.65 \times 10^{-20}$	4.9
			6''''	390	$1.69 \pm 1.66 \times 10^{-20}$	5.1

present context, with diffusivity of Au in a-Si. Included on the Arrhenius plot of Figure 3 are Au diffusivities determined at higher temperatures by RBS for ion-implanted [5], CVD [20] and ion sputtered deposited [19] a-Si. The method of preparation of a-Si is known to affect the structure and some properties [21] but is not manifest in the diffusion behavior of Au. There is also good agreement between extrapolations of the high temperature RBS measurements and the diffusivities determined in the present study despite very large differences in diffusion distances. Diffusion distances for RBS measurements are typically in the range 100-1000 Å while the smallest diffusion distance measured in the present study was 2.3 Å, occurring for the first anneal at 200°C. The largest cumulative diffusion distance in the study is under 10 Å or less than the resolution limit of RBS.

The determination of a meaningful activation enthalpy for a time-dependent diffusivity requires special care. Ideally, the so-called iso-configurational activation enthalpy [22] is determined from diffusivities that are shown by temperature cycling to be relatively stationary at a given temperature. The system being investigated did not lend itself to such a study because the weak x-ray signal allowed only a small number of annealing treatments. Under these circumstances the most meaningful activation enthalpy that can be derived is the one corresponding to the earliest available observations since in those cases at least the initial configuration is the same. A least squares fit to those data gives an activation enthalpy, Q , of 1.32 ± 0.10 eV and a pre-exponential factor, D_0 , 1×10^5 cm²/sec. Another configuration is suggested by the fairly abrupt change in the slope of $\ln I(t)$ following the initial anneals. A least squares fit of the second set of diffusivities for each sample gives $Q = 1.18 \pm 0.14$ eV and $D_0 = 7 \times 10^8$ cm²/sec. The agreement between these two activation energies and the similarity with those measured at higher temperatures [5,19,20] gives us some confidence that they are reasonably close to the iso-configurational value.

RBS studies in the higher temperature regime [5,19] have shown the Au diffusivity to be composition dependent (see Figure 3). Although the composition dependence contributes to the time dependence observed in the present study, it is much too weak to account for the strong decrease [11,23]. The continuous decrease in $D(t)$ must therefore be attributed to transient effects in the atomic mechanism for diffusion, or to structural relaxation of the amorphous phase.

The transport of Au in crystalline semiconductors is understood to occur by the motion of Au interstitials. The solubility of substitutional Au is, however, much greater than that of interstitial Au, and equilibrium is established between the two components through interaction with vacancies or matrix interstitials. The mechanism was first used to explain the diffusion of Au in c-Ge [24] appealing to vacancies for equilibration, and later to explain high temperature ($T > 800^\circ\text{C}$) Au diffusion in c-Si [25] using Si interstitials.

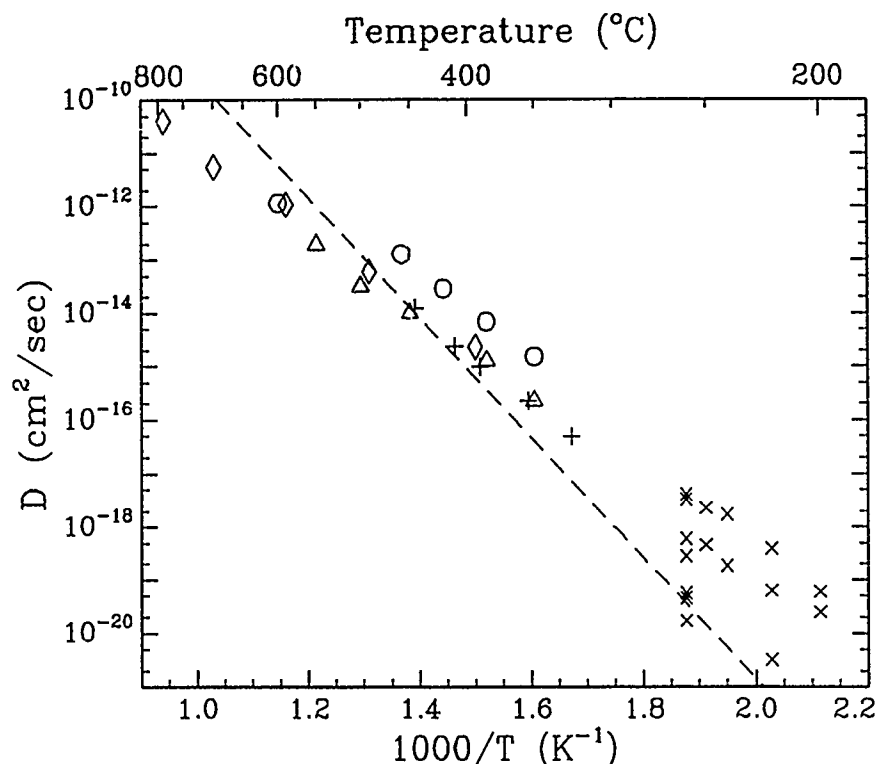


Figure 3. Arrhenius plot of Au diffusion data. \diamond [20] CVD a-Si, 0.06% Au; \circ , Δ [5] ion-implanted a-Si, 1.7% and 0.08% Au; + [19] ion beam-sputter deposited, 0.8% Au; \times this work. Line is extrapolation of Au diffusivity in highly dislocated c-Si [29].

The microscopic mechanism for Au diffusion in covalent random networks such as a-Si has not been unambiguously identified. An extrapolation of the effective diffusion coefficient for Au in highly dislocated c-Si [26], measured between 906 and 1154°C, shows remarkable agreement with the a-Si data (see Figure 3). Dislocations in c-Si act as sources and sinks for vacancies and Si interstitials. In highly dislocated Si, these lattice defects should exist in thermal equilibrium concentrations. Under such conditions, Au transport is controlled by the diffusion of the interstitial component. The effective Au diffusivity will be the same independent of whether equilibration between the interstitial and substitutional components is controlled by interaction with vacancies or Si interstitials [25]. The same general conditions may hold true for the diffusion of Au in a-Si with the random network, in this case, acting as a source and sink for defects. The efficiency of the network for this purpose may be evident in the similarity of diffusion behavior for a-Si prepared by different means.

Recent investigations into the relaxation phenomenon in a-Si suggest that the annealing of point defects [27] is responsible for the enthalpic relaxation observed in calorimetric studies [28]. The isothermal rate of enthalpic relaxation over a wide temperature range is well described by an exponential decay with characteristic time of the order of 100 seconds. By contrast, the characteristic time exhibited by the Au diffusion decay is approximately 70 minutes at 260°C and increases sharply with decreasing temperature. This can not be explained simply by point defect annealing if the point defect population that mirrors the changing enthalpy. Defect complexes may play a role.

ACKNOWLEDGEMENTS

We thank John M. Poate and Michael Aziz for useful discussions and Eric Chason for the initial design of the diffractometer. This work has been supported by the National Science Foundation through the Materials Research Laboratory under contract number DMR-86-14003.

REFERENCES

1. W. Frank, U. Gösele, H. Mehrer and A. Seeger, in *Diffusion in Crystalline Solids*, edited by G.E. Murch and A.S. Nowick (Academic Press, Orlando, 1984) p. 63.
2. A. Seeger and K.P. Chik, *Phys. Status Solidi* **29**, 455 (1968).
3. M. Reinelt and S. Kalbitzer, *Journal De Physique*, **C-4**, C4-843 (1981).
4. R.G. Elliman, J.M. Gibson, D.C. Jacobson, J.M. Poate and J.S. Williams, *Appl. Phys. Lett.* **46**, 478 (1985).
5. J.M. Poate, D.C. Jacobson, J.S. Williams, R.G. Elliman and D.O. Boerma, *Nucl. Instr. and Meth.* **B19/20**, 480 (1987).
6. B. Park, F. Spaepen, J.M. Poate, F. Priolo, D.C. Jacobson, C.S. Pai, A.E. White and K.T. Short, *Mater. Res. Soc. Proc.* **103**, 173 (1988).
7. B. Park, F. Spaepen, J.M. Poate, F. Priolo and D.C. Jacobson, *Mater. Res. Soc. Proc.* **128**, 243 (1989).
8. B. Park, Ph.D. Thesis (Harvard University, 1989).
9. H.E. Cook and J.E. Hilliard, *J. Appl. Phys.* **40**, 2191 (1969).
10. M.P. Rosenblum, F. Spaepen and D. Turnbull, *Appl. Phys. Lett.* **37**, 184 (1980).
11. A.L. Greer and F. Spaepen, in *Synthetic Modulated Structures*, edited by L.L. Chang and B.C. Giessen (Academic Press, New York, 1985) p. 419.
12. F. Spaepen, A.L. Greer, K.F. Kelton and J.L. Bell, *Rev. Sci. Instrum.* **56**, 1340 (1985).
13. M. Sugawara, M. Kondo, S. Yamazaki and K. Nakajima, *Appl. Phys. Lett.* **52**, 742 (1988). The index of refraction of pure c-Si was used and the correction was approximately 1 Å.
14. A.M. Kadin and J.E. Krcm, *Scripta Metall.* **20**, 440 (1986).
15. J.H. Underwood and T.W. Barbee, Jr., *Applied Optics* **20**, 3027 (1981).
16. The effect is due to decreased absorption and will result in increased intensity provided the film has a corresponding increase in the number of layers.
17. W.M. Paulson and J.E. Hilliard, *J. Appl. Phys.* **48**, 2117 (1977).
18. M. Atzmon and F. Spaepen, *Mater. Res. Soc. Proc.* **80**, 55 (1987).
19. D.T. Wu, A.V. Wagner, E. Nygren and F. Spaepen, unpublished results.
20. L. Calcagno, S.U. Campisano and S. Coffa, *J. Appl. Phys.* **66**, 1874 (1989).
21. J. Fortner and J.S. Lannin, *Phys. Rev. B* **37**, 10154 (1988).
22. A.I. Taub and F. Spaepen, *Acta Metall.* **28**, 1781 (1980).
23. R.M. Fleming, D.B. McWhan, A.C. Gossard, W. Wiegmann and R.A. Logan, *J. Appl. Phys.* **51**, 357 (1980).
24. F.C. Frank and D. Turnbull, *Phys. Rev.* **104**, 617 (1956).
25. U. Gösele, W. Frank and A. Seeger, *Appl. Phys.* **23**, 361 (1980).
26. N.A. Stolwijk, J. Hölzl, W. Frank, E.R. Weber and H. Mehrer, *Appl. Phys. A* **39**, 37 (1986).
27. S. Roorda, W.C. Sinke, J.M. Poate, D.C. Jacobson, S. Dierker, B.S. Dennis, D.J. Eaglesham and F. Spaepen, to be published, *Mater. Res. Soc. Proc.* **157**, (1990).
28. E.P. Donovan, F. Spaepen, J.M. Poate and D.C. Jacobson, *Appl. Phys. Lett.* **55**, 1516 (1989).
29. The effective Au diffusivity in highly dislocated Si from [26], $D=44\exp(-2.23/kT)$ cm²/sec.

HYDROGEN DIFFUSION AND COMPLEX FORMATION IN SILICON

J.T. BORENSTEIN*, D. TULCHINSKI** AND J.W. CORBETT**

* Mobil Solar Energy Corporation, 4 Suburban Park Drive,
Billerica, MA 01821

** Physics Department, SUNY at Albany, Albany, NY 12222.

ABSTRACT

The kinetics of hydrogen diffusion and complex formation in crystalline silicon are investigated using a model previously developed to explain the influence of dopant type and concentration on observed deuterium profiles in silicon. The predictions of the model have been shown to be in close agreement with recent SIMS profiles of deuterated FZ-Si crystals, with the in-diffusion process dominated by trapping at impurity sites and by the formation of immobile hydrogen molecules.

Previous studies have treated the surface concentration of hydrogen and the capture radii of hydrogen at complexes as free kinetic parameters. We present an analytic relationship between the diffusion coefficient D of neutral hydrogen and both the hydrogen surface concentration and the capture radius for molecule formation. The consequences of fixing D at the known high-temperature value for the diffusion coefficient in the model are determined. The existence of this analytic relation reduces the number of free parameters in the kinetic model and leads to an improved understanding of hydrogen reactions in silicon.

INTRODUCTION

The interaction of hydrogen with crystalline silicon has attracted considerable interest over the last several years, both from a fundamental standpoint and because of important technological applications. Despite its small size and simple atomic structure, hydrogen is associated with a wide array of complex phenomena in the silicon lattice, including passivation of deep levels, dopant deactivation, and structural changes [1]. Several theoretical calculations [2-4] have resulted in important predictions regarding the state and motion of hydrogen in the silicon lattice. Several of these calculations have obtained close agreement with the early high-temperature diffusion measurements of van Wierengen and Warmoltz (VWV) [5], providing evidence that unencumbered hydrogen diffusion does in fact proceed at the rapid VWV rate.

Recent kinetic models [6-10] have been proposed in order to explain observed low-temperature H passivation data, including the strong differences between H profiles in n- and p-type silicon. These models have attempted to describe various effects, including hydrogen molecule formation, hydrogen-dopant trapping and charge-state effects, electric field drift of charged species, and thermal dissociation of the hydrogen complexes. In order to account for all of these effects, the models typically contain a large number of free parameters, and the results and conclusions differ widely. The large number of parameters, as well as the multitude of best-fit models capable of describing the process, preclude the opportunity for new physical insight.

In the present work we have attempted to explain observed hydrogen diffusion profiles with a simplified model, so that we may draw conclusions based on the physical properties of the system. We find that the observed data can be fitted by numerous combinations of the free parameters, and we have established relationships between these parameters. These

relationships allow the number of free parameters to be reduced, leading to an improved understanding of the system.

KINETIC MODEL

The kinetic model we employ here is a simple reaction-diffusion system [6], comprised of a set of coupled partial differential equations. These equations are typically solved numerically, but can also be simplified in order to obtain analytic solutions. A complete treatment of hydrogen diffusion-reaction phenomena includes: a) An assumed hydrogen surface concentration, b) Diffusion coefficients for each charge state of H, c) Electric field drift of charged H species, d) The formation of hydrogen molecules, e) Capture radii for each species of hydrogen with the acceptors, donors, and H atoms, and f) Dissociation of the hydrogen-dopant complexes. In the present, simplified system, we find that good fits can be obtained for several of the observed hydrogen profiles without accounting for field drift and dissociation of complexes. These simplifications do not imply that other effects are not significant, but rather argue that their inclusion is not necessary to explain the data.

The simplified set of equations for the model are:

$$\frac{\delta H}{\delta t} = D \frac{\delta^2 [H]}{\delta x^2} - k_1 [H]^2 - k_2 [H][X], \quad (1)$$

$$\frac{\delta [H_2]}{\delta t} = (1/2) k_1 [H]^2, \quad (2)$$

$$\frac{\delta [H^*X]}{\delta t} = k_2 [H][X]. \quad (3)$$

Here D is the diffusion coefficient for hydrogen, $[H]$, $[H_2]$ and $[X]$ represent the concentrations of hydrogen atoms, hydrogen molecules, and unpassivated donors or acceptors, and k_1 and k_2 are the rate constants for molecule formation and H-dopant complexes, respectively. The boundary conditions for this system include the assumption of a constant surface concentration:

$$[H(x=0, t \geq 0)] = [H_0]. \quad (4)$$

The rate constants k are given by the product

$$k = 4\pi R D, \quad (5)$$

with R equal to the capture radius for the reaction. These equations have been solved numerically, using a finite differencing scheme, for various experimental conditions.

RESULTS AND DISCUSSION

The simplest system for investigation is the case where hydrogen is incorporated into low-doped float-zone silicon (FZ-Si) at low temperatures. Since there are no defects in the near-surface, hydrogen might be expected to diffuse freely into the lattice. If this were the case SINS profiles would exhibit the classic error function (erfc) profile. The erfc profile has not been observed in crystalline silicon, a result largely attributed

to the formation of hydrogen molecules near the surface. This situation can be modeled by solving equations (1) and (2) above, with $[X] = 0$. Using this simple scheme we have attempted to fit a SIMS profile of 100 Ω -cm p-type FZ-Si passivated by a deuterium plasma at 125 $^{\circ}\text{C}$ for 1 h [11]. The best-fit we obtain is shown in Figure 1, with the diffusion coefficient D set at the VWW value corrected for deuterium ($5 \times 10^{-9} \text{ cm}^2/\text{sec}$), the surface concentration $H_0 = 9 \times 10^{13} \text{ cm}^{-3}$ and the capture radius for molecule formation $R = 4$ Angstroms.

We have found that the best-fit obtained using this simplified model does not represent a unique set of experimental parameters. Using several different values of D , we were able to obtain equivalent best-fits by correcting the values of H_0 and R . The combinations of these three parameters which are capable of yielding a best-fit comprise a system which obeys the following two paradigms:

$$R D H_0^2 = \text{Constant}, \text{ and } R H_0 = \text{Constant}'. \quad (6)$$

The significance of the relationships shown in equation (6) lies in the ability to tie experimental parameters together. If we accept the experimentally-determined VWW value of D , then the set of relationships (6) isolates values of H_0 and R which are capable of fitting the observed data.

The relationships (6) are a result of the time-independent behavior of the in-diffusion process. We have found that the in-diffusion can be approximated as a steady-state process for the passivation time and depth scale of interest. Therefore the SIMS profile in low-doped silicon can be described by an analytic solution, (Eqn. 7), with x and t equal to the depth and time of passivation, respectively:

$$[H_2] = [36\pi D R H_0^2 t] / [4(4\pi R H_0)x + \sqrt{3}]^4. \quad (7)$$

The relation (7), which is obtained by solving Eqn. (1) by setting $k_2 = 0$ and by using the steady-state approximation, obviates the need for trial-and-error fitting of the profiles. This analytic solution is in excellent agreement with available experimental data, and will be discussed in a future paper.

We have applied similar analysis to SIMS data for low resistivity silicon, solving equations (1)-(3). In heavily-doped p-type material, the hydrogen is believed to be positively charged [6-9], and therefore molecule formation would not occur because of ionic repulsion. We find that sets of parameters capable of describing the data are not unique, as in the earlier case. The sets of data appear to hold to the relationship

$$D \times H_0 = \text{Constant}, \quad (8)$$

with a fixed capture radius R_1 . One such best-fit, with D set to $5 \times 10^{-10} \text{ cm}^2/\text{sec}$, (about an order of magnitude lower than the VWW value), is shown in Figure 2, for 1 Ω -cm p-type FZ-Si [11]. The plateau region is well-described by this simple approach, but other phenomena are clearly occurring near the surface.

The product of D and H_0 capable of fitting the 1 Ω -cm data appears to be about an order of magnitude lower than the corresponding quantity for the 100 Ω -cm data of Figure 1. Earlier work [6] suggested that hydrogen is positively charged in 1 Ω -cm p-type material, and neutral in 100 Ω -cm material; therefore the observed difference in the $D \times H_0$ product might be attributed to a difference in diffusion coefficient between the neutral (D^0) and ionized (D^+) deuterium. Mathiot [9] predicted a large difference between D^0 and D^+ , corresponding to a substantial difference in migration barriers. The small difference implied by the present model is in closer agreement with theoretical calculations [2,12].

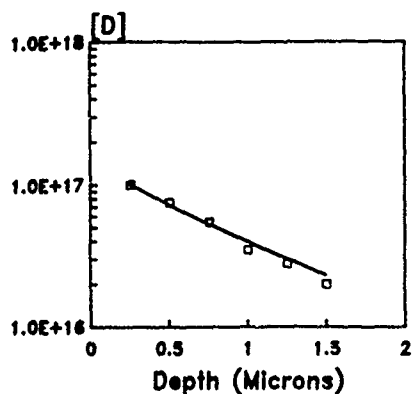


Figure 1. Best-fit (Solid Line) to SIMS profile of deuterium [D] (squares) vs. depth for 100 Ω -cm n-type FZ-Si passivated by a D_2 plasma at 125 $^{\circ}$ C for 1 h.

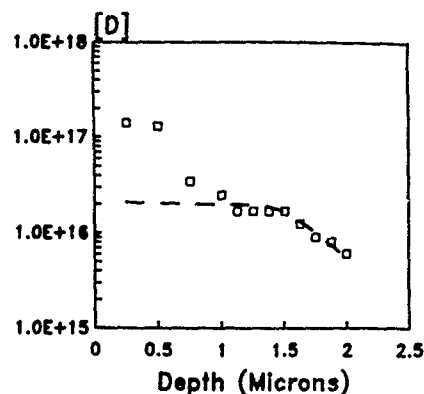


Figure 2. Best-fit (Dashed Line) to SIMS profile of deuterium [D] (squares) vs. depth for 1 Ω -cm p-type FZ-Si passivated by a D_2 plasma at 125 $^{\circ}$ C for 1 h.

CONCLUSION

We have found that physical descriptions of the hydrogen diffusion process in silicon are not unique, but that under some conditions, simple relationships exist between the parameters. The molecule formation process, which dominates hydrogen in-diffusion in low-doped FZ-Si, approximates steady-state behavior. This observation leads to an analytic description of the system, which allows relationships between previously freely-varying parameters to be established. Analysis of dopant trapping profiles in more heavily-doped material yields similar relationships between parameters, leading to new insight into the diffusion kinetics.

REFERENCES

1. S.J. Pearton, J.W. Corbett and T.S. Shi, Appl. Phys. A 43, 153 (1987).
2. P. Deak, L.C. Snyder and J.W. Corbett, Phys. Rev. B 37, 6887 (1988).
3. S.J. Pearton, M. Stavola and J.W. Corbett, Rad. Eff. and Defects in Solids 111-112 [1-2], 323 (1989).
4. F. Buda, G.L. Chiarotti, R. Car and M. Parrinello, Phys. Rev. Lett. 63, 294 (1989).
5. A. Van Wieringen and N. Warmoltz, Physica 22, 849 (1956).
6. J.T. Borenstein, D. Angell and J.W. Corbett, Mat. Res. Soc. Proc. 138, 209 (1989).
7. C.H. Seager and R.A. Anderson, in Ref. 6, p. 197.
8. M. Capizzi and A. Mittiga, Appl. Phys. Lett. 50, 918 (1987).
9. D. Mathiot, Phys. Rev. B 40, 5867 (1989).
10. J.P. Kalejs and S. Rajendran, Appl. Phys. Lett., in press.
11. J.W. Corbett, J.L. Lindstrom, S.J. Pearton and A.J. Tavendale, Solar Cells 24, 127 (1988).
12. C.G. Van de Walle, Y. Bar-Yam, and S.T. Pantelides, Phys. Rev. Lett. 60 2761 (1988).

PART IX

Diffusion in Compounds

DIFFUSION AND INTERDIFFUSION IN MULTILAYERED SEMICONDUCTOR SYSTEMS

A. OURMAZD, Y. KIM, and M. BODE

AT&T Bell Laboratories, Holmdel, NJ 07733, USA.

ABSTRACT

We apply quantitative chemical mapping techniques to study thermal interdiffusion and ion-implantation induced intermixing at single heterointerfaces at the atomic level. Our results show thermal interdiffusion to be strongly depth dependent. This is related to the need for the presence of native point defects (interstitials and vacancies) to bring about interdiffusion. Since their initial concentration in the bulk is negligible, the point defects must be injected at the surface and transported to the interface for interdiffusion to occur. In the case of ion-implanted samples, we find the passage of a single energetic ion through a sample at 77 K causes significant intermixing, even when the sample receives no subsequent thermal treatment.

INTRODUCTION

The formation of chemically different (doped) layers has long been the basis of solid state technology. Of more recent importance is the ability to tailor the properties of materials by the growth of heterostructure multilayers, with individual layer thicknesses approaching the lattice constant.

Such structures are far from equilibrium; the sophistication required for their growth bears testimony to this fact. It is thus important to investigate the stability of modern multilayers and the ways in which they can relax. Here, we are concerned with the relaxation of lattice matched, pseudomorphic systems such as GaAs/AlGaAs, which relax by interdiffusion. Since these materials are isostructural, interdiffusion causes only chemical changes. We use modern chemical lattice imaging and pattern recognition techniques [1,2,3] to investigate interdiffusion in GaAs/AlGaAs multilayers after annealing, or ion-implantation. Since we can measure interdiffusion coefficients as small as $10^{-21} \text{ cm}^2/\text{s}$ in volumes as small as 10^{-19} cm^3 , we are able to investigate the chemical relaxation of solids at the atomic level.

Our results show thermally-induced interdiffusion to depend strongly on the depth of the interface from the surface. This is a general effect, which is related to the injection and arrival of native point defects (interstitials and vacancies) from the surface during the anneal. Several important consequences follow. (a) The layer and hence device stability depend critically on the depth of the layer. Thus the layer depth must be regarded as an important design parameter in device technology. (b) Measurements of interdiffusion are meaningful only if they refer to a known and well-defined depth. (c) Since chemical interdiffusion is assisted by the native point defects injected from the surface, it is a sensitive means of detecting the arrival and passage of such defects.

In the case of ion-implantation, we find the passage of a single energetic ion to cause intermixing, which can be detected and quantified. This allows us to investigate the fundamental atomic processes involved in the transfer of energy from an energetic ion to an inhomogeneous solid [4].

Our experiments essentially use a stack of interfaces to detect the passage of "particles", be they low energy native point defects, or relatively high energy damage cascades produced by ion-implantation. In other words, we use a series of interfaces

as a stack of photographic plates to record the diffusion and drift of point defects, thus investigating their fundamental properties.

EXPERIMENTAL

Chemical lattice imaging has been described in detail elsewhere [1,2,3]. Here we present only a brief outline.

The passage of an electron wave through a crystalline sample produces a large number of diffracted beams (reflections), some of which are transmitted by the objective lens to form a lattice image. A chemical lattice image is obtained, when the sample thickness is chosen so as to enhance the chemical information in the diffraction pattern, and the lens is used as a bandpass filter to select the chemically sensitive reflections. The chemical information in the sample is thus encoded into the patterns that combine in a mosaic to form the image. Fig. 1 shows a chemical lattice image of a GaAs/AlGaAs interface.

Quantitative analysis of such images can be achieved by means of a vector pattern recognition algorithm [3]. This procedure compares a given $2.8 \times 2.8 \text{ \AA}^2$ image unit cell with a corresponding template obtained by averaging over a large area of known composition. Thus the algorithm determines the Al (or Ga) content of each atomic column quantitatively, and yields a confidence level for this determination. By averaging the data on each plane parallel to the interface a composition profile across the interface can be obtained (Fig. 2).

To obtain the diffusion coefficient, the composition profile across a given interface is measured in two pieces of the same sample, one of which has been annealed in bulk form. Starting with the initial profile and using the diffusion coefficient D as free parameter, we solve the diffusion equation to fit the final (annealed) profile, thus deducing D as a function of temperature and interface depth [5]. In the case of ion-implanted samples, the composition profiles are characterized by fitting an erf-profile to the data, with the profile width L as the free parameter. Interdiffusion due to implantation is thus quantified in terms of changes in the interfacial width L [4].

The samples used for thermal annealing consisted of 20 periods of 50 Å C-doped GaAs / 50 Å undoped GaAs / 50 Å $\text{Al}_{0.4}\text{Ga}_{0.6}\text{As}$, grown on GaAs (100) by Molecular Beam Epitaxy (MBE) at 600°C. The carbon doping level was 10^{19} cm^{-3} . Bulk samples were annealed in the temperature range 650°C to 750°C in an evacuated ampule under As poor conditions, to induce enhanced interdiffusion in the p-type layers [6]. The annealing time at each temperature was chosen to produce the same small amount of carbon diffusion.

The samples used for ion-implantation were MBE grown, consisting of 20 periods of 50 Å GaAs / 50 Å AlAs and a 250 Å cap layer, with a doping level below 10^{15} cm^{-3} . Ga^+ implantation was carried out at 77 K in order to reduce dynamic annealing, with a specimen tilt of 7° to eliminate channeling effects. The energy of the implanted Ga was 320 keV (projected range $R_p = 1600 \text{ \AA}$). No thermal annealing was carried out after implantation other than necessary for the specimen preparation ($T_{\text{max}} \approx 150^\circ \text{C}$). Specimens were prepared for the TEM investigations by mechanical thinning and subsequent chemical etching to perforation. No ion milling was employed.

RESULTS AND DISCUSSION

(a) Thermal Annealing

The analysis of chemical images, such as the one shown in Fig. 1, by the procedure described above yields quantitative composition profiles across single interfaces. Note that the profiles shown in Fig. 2 quantify, with atomic plane resolution, the compositional change across a single interface at a depth of 300 Å, before and after

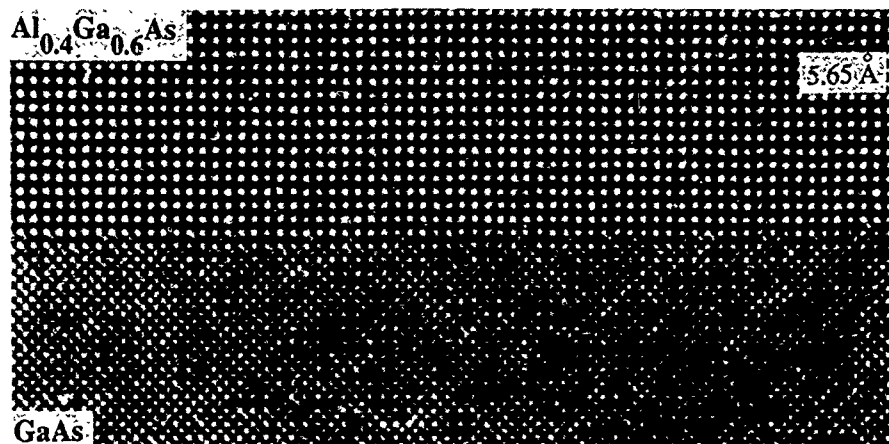


Fig. 1 Chemical lattice image of a GaAs/AlGaAs interface at a depth of 2500 Å from the surface, annealed at 650°C for 2.5 hrs.

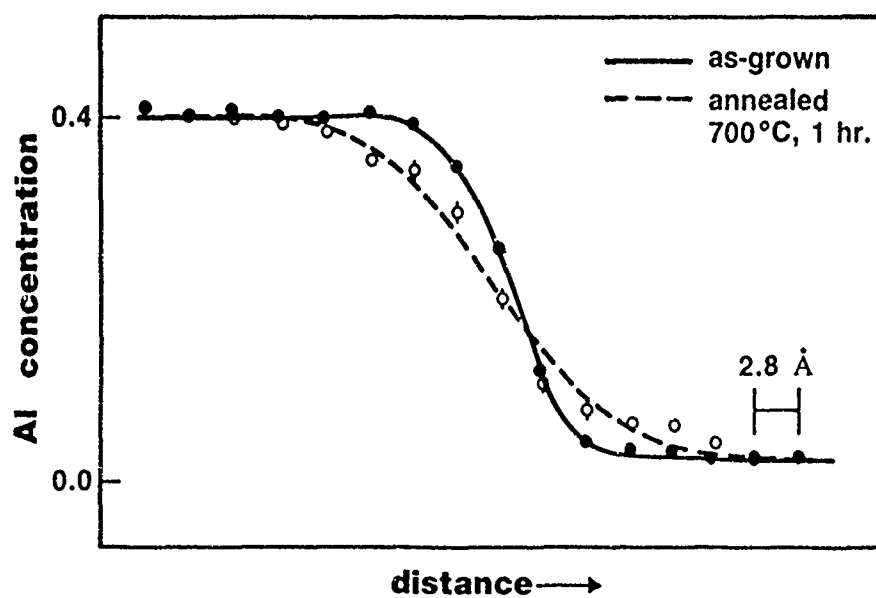


Fig. 2 Composition profiles of a C:GaAs/AlGaAs interface at a depth ~ 300 Å, as-grown (solid line), and after 700°C, one hour anneal (dotted line). One standard deviation error bars are shown. Each measurement refers to a 100 Å segment of a single atomic plane.

annealing at 700 C for one hour. Starting with the initial composition profile for a given interface, we solve the linear diffusion equation to fit the profile after the anneal, using the interdiffusion coefficient D as the adjustable parameter. This is carried out by a Marquardt procedure, which also yields the uncertainty in the deduced value of the fitting parameter D [7].

Fig. 3 is an Arrhenius plot of D vs $1/kT$ for C-doped interfaces at three different depths beneath the surface. Remarkably, the magnitude of the interdiffusion coefficient, as well as the activation energy for intermixing change strongly with depth. Since this behavior is also observed in the HgCdTe/CdTe system [5], we conclude that the depth-dependence of the interdiffusion coefficient is a general effect. This depth-dependence is more clearly displayed in Fig. 4, where $\ln D$ is plotted as a function of the interface depth. At the lower temperatures (700C and particularly at 650C), $\ln D$ initially decreases linearly with increasing distance from the surface, but drops exponentially beyond a certain critical depth.

Our analysis, to be reported elsewhere, shows this effect to be related to the injection of point defects from the sample surface. In particular, interdiffusion in these systems is assisted by the presence of native point defects (interstitials and vacancies), whose concentration is negligible in our as-grown samples. For interdiffusion to occur, such native defects must be injected from the sample surface during the anneal. The interdiffusion coefficient is a sensitive function of the concentration of these defects at the particular interface studied, and thus can be used to investigate the microscopics of native point defect diffusion in multilayered systems. Indeed, it should be possible to measure the formation energy and migration energy of a given native defect (interstitial or vacancy) as a function of its charge state.

Returning to interdiffusion, two important points emerge. First that the interdiffusion coefficient varies strongly with depth. Thus a measurement of this parameter is meaningful only if it refers to a single interface at a known depth. Second, it follows that the interface stability is also depth-dependent. Thus the layer depth must be regarded as an important design parameter in the fabrication of modern devices. This effect assumes additional importance when interdiffusion is also concentration dependent, leading to strong intermixing at very low temperatures [8].

(b) Ion-implantation

Fig. 5 shows a chemical lattice image of an as-grown 50 Å GaAs layer between its two adjacent AlAs layers, together with the composition profiles for each interface. The GaAs layer is situated 1400 Å beneath the surface and is thus close to the depth where the maximum damage during implantation is expected to occur. (All the data presented in this section stem from a depth between 1000 Å and 1700 Å.) The growth direction is from bottom to top, the (later) implantation direction from top to bottom. Each point on the profiles of Fig. 5 represents the average composition of a 1 μm segment of a given atomic plane before implantation. Both top and bottom interfaces (A and B) display excellent lateral uniformity and can be characterized by similar characteristic widths L ($L_A = 2.4 \pm 0.1$ Å, $L_B = 2.67 \pm 0.11$ Å).

After implantation to a dose of $5 \times 10^{12} \text{ cm}^{-2}$, chemical analysis of individual interfaces located at depths between 1000 Å and 1700 Å beneath the surface reveals significant intermixing across the top interfaces, although (on average) only one Ga^+ ion has passed through each 2000 Å^2 of the specimen. The intermixing is not uniform along the top interfaces, but shows large fluctuations. In Fig. 6 three concentration profiles for adjacent 50 Å segments of an interface are shown. Profiles a and c display about the same degree of intermixing, characterized by a width L of $\approx 6.2 \pm 0.2$ Å, while profile b is characterized by $L = 4.6 \pm 0.17$ Å.

Kinematic implantation simulations using the TRIM program [9] show, that under our experimental conditions, a single implanted Ga^+ ion creates a damage track ~ 50 Å

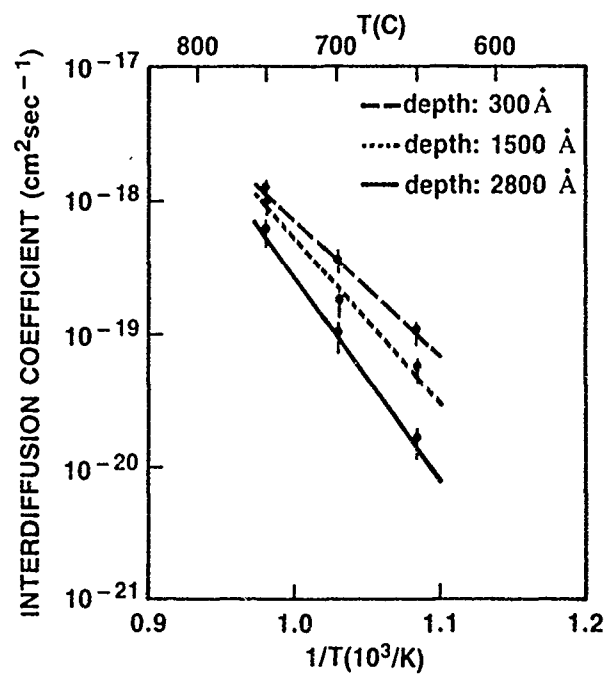


Fig. 3 Arrhenius plot of the interdiffusion coefficient at C:GaAs/AlGaAs interfaces at three different depths.

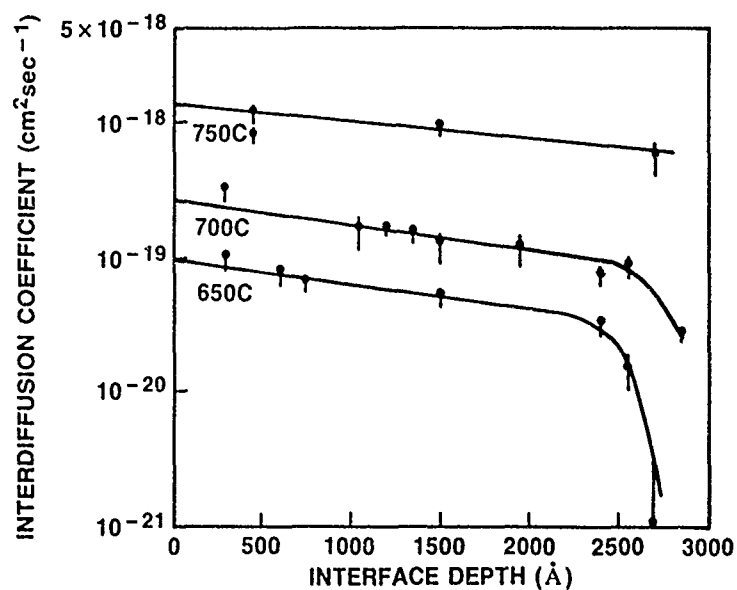


Fig. 4 Plot of the $\ln D$ vs interface depth (z) at three different temperatures, for C:GaAs/AlGaAs interfaces.

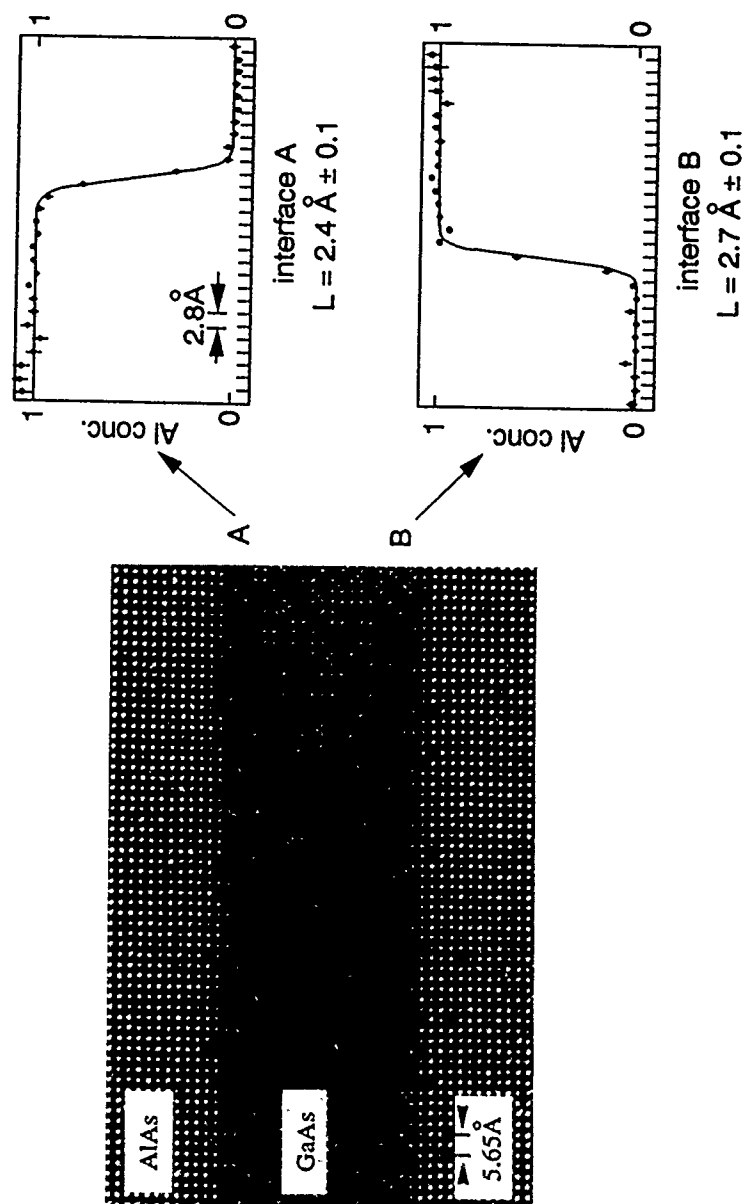


Fig. 5

Chemical lattice image of GaAs layer between two AlAs layers, with composition profiles across the interfaces. Growth direction is from bottom to top. One standard deviation error bars are shown. Each measurement refer to a $1 \mu\text{m}$ segment of an individual atomic plane.

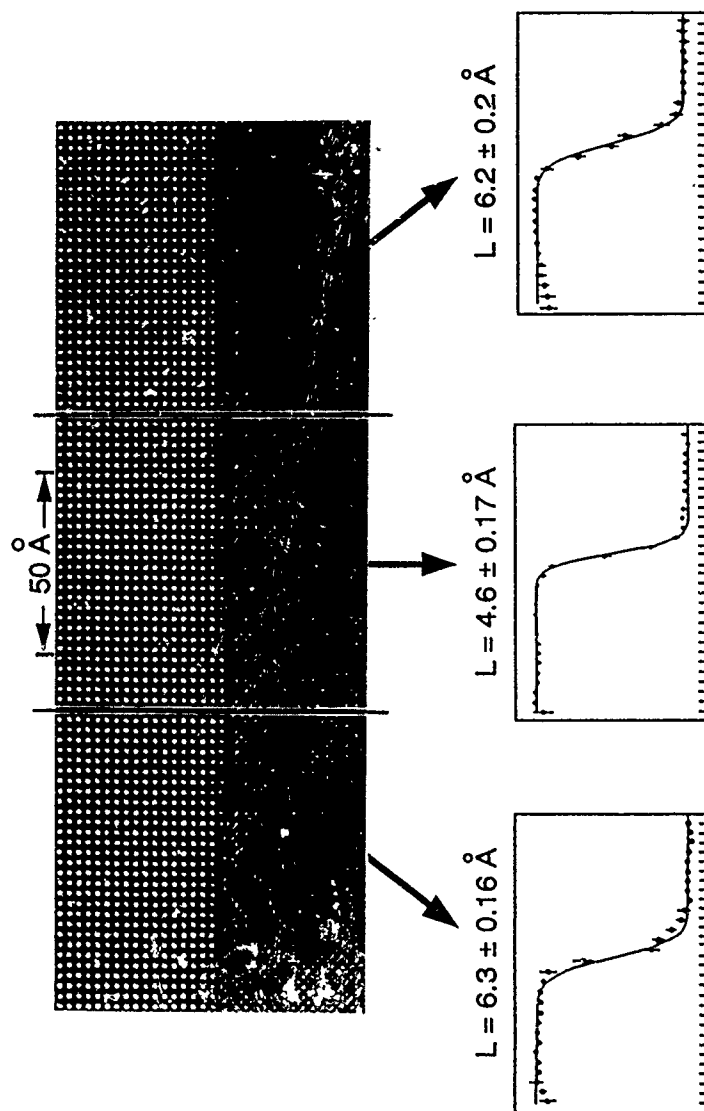


Fig. 6 Chemical lattice image of GaAs/AlAs sample implanted with 320 keV Ga^+ ions to a dose of $5 \times 10^{12} \text{ cm}^{-2}$. This dose corresponds to the implantation of \sim one ion per 45 Å length of the interface. The composition profiles refer to adjacent \sim 50 Å segments of the top interface. Note the large local variations in intermixing on the 50 Å lateral scale. This corresponds to the width of the damage track expected from the passage of a single ion.

wide. This agrees closely with the width of the observed fluctuations in the degree of intermixing along the interface. After implantation at a higher dose ($1 \times 10^{13} \text{ cm}^{-2}$), the intermixing along the interface is more uniform. It is thus likely that we are directly imaging the intermixing caused by the passage of single energetic ions.

SUMMARY

The combination of chemical lattice imaging and vector pattern recognition allows the quantitative study of interdiffusion and intermixing at very high spatial resolution and sensitivity, thus revealing a spectrum of new effects. In the case of thermal annealing, the diffusion coefficient is shown to be strongly depth dependent. This stems from the need for the presence of native point defects for low temperature interdiffusion. Since the concentration of such defects in our as-grown samples is negligible, they must be injected at the surface and transported to the interface during the anneal. A stack of interfaces can therefore be used to track the arrival and passage of native point defects, and thus measure their formation and migration energies separately. In the case of ion-implantation, the intermixing caused by the passage of a single energetic ion can be detected and quantified. The techniques we have outlined here thus promise to help elucidate the microscopics of diffusion and ion-implantation at the atomic level.

We acknowledge valuable discussion with A. Bourret, and are grateful to R. Malik and M. Hong for supplying the crystals used in this study.

REFERENCES

1. A. Ourmazd, W.T. Tsang, J.A. Rentschler, and D.W. Taylor, *Appl. Phys. Lett.* **50**, 1417 (1987).
2. A. Ourmazd, D.W. Taylor, J. Cunningham and C.W. Tu, *Phys. Rev. Lett.* **62**, 933 (1989).
3. A. Ourmazd, D.W. Taylor, M. Bode, and Y. Kim, *Science* **246**, 1571 (1989).
4. M. Bode, A. Ourmazd, J.A. Rentschler, M. Hong, L.C. Feldman and J.P. Mannaerts, *Proc. MRS Fall Meeting, Symposium A* (1989), in press.
5. Y. Kim, A. Ourmazd, M. Bode and R.D. Feldman, *Phys. Rev. Lett.* **63**, 636 (1989).
6. D.G. Deppe and N. Holonyak, Jr., *J. Appl. Phys.* **64**, R93 (1988).
7. W.H. Press, B.P. Flannery, S.A. Teukolsky and W.T. Vetterling, *Numerical Recipes* (Cambridge University Press, Cambridge, 1986), chapter 14.
8. Y. Kim, A. Ourmazd and R.D. Feldman, *J. Vac. Sci. Technol. A*, in press.
9. J.P. Biersack, *Nucl. Instr. Methods B*, **19**, 32 (1987).

ATOMIC LAYER EPITAXY OF GaAs ON Ge SUBSTRATES

J. RAMDANI, B.T. MCDERMOTT AND S.M. BEDAIR

Department of Electrical and Computer Engineering, North Carolina State University,
Raleigh, North Carolina 27695-7911

ABSTRACT

We report on the low temperature growth of GaAs on Ge substrates using Atomic Layer Epitaxy. Low temperature deposition has resulted in substantial reduction of the outdiffusion of Ge into the GaAs epilayer as being indicated from SIMS. The I-V characteristics of the GaAs/Ge heterojunction were thyristor like or near abrupt depending on the growth temperature. We also report on the use of the Atomic Layer Epitaxy self-limiting adsorption process of TMGa to control the diffusion of Ga into Ge substrates at the monolayer level.

INTRODUCTION

For over two decades, there has been great interest in the growth of GaAs on Ge. Ge has only .07% lattice and 2% thermal expansion mismatch to GaAs and has the highest hole mobility of Group IV and III-V semiconductor materials. Several growth techniques have investigated this system, such as Chemical Vapor Deposition (CVD) and Molecular Beam Epitaxy (MBE) techniques. The GaAs/Ge heterojunction has potential applications such as: heterojunction bipolar transistors [1], high efficiency solar cells [2], and the possibility of monolithically integrating III-V devices with those of Si by using Ge as a buffer layer [3]. However, this combination (GaAs/Ge) suffers from autodoping which leads to the modification of the interfacial electronic structure, especially when a n-GaAs/p-Ge junction is desired. Atomic layer epitaxy (ALE) is a growth technique that can potentially address this current GaAs/Ge interdiffusion problem. For III-V semiconductor compounds, ALE growth proceeds by alternating deposition of group III and group V molecules, resulting in a well controlled stoichiometric growth [4]. In the present work, the growth of GaAs on Ge has been carried out by ALE as an alternative low temperature growth techniques, to minimize the interdiffusion of different atomic species. In addition we report on the feasibility of in-situ Ga doping of Ge by taking advantage of the self-limiting mechanism inherent in the ALE process.

EXPERIMENTAL

Both n-type and p-type Ge substrates were used. They had 0.1 Ω -cm resistivity and were oriented 6° off toward $\langle 111 \rangle$ for the n-type and 9° off toward $\langle 111 \rangle$ for the p-type. The Ge substrates were first solvent cleaned successively in 1,1,1 Trichloroethane, Acetone and methanol. Surface etching was a two-step procedure; first exposure to HCl: H₂O₂: H₂O (1:1:10) then D.I. water rinsed, and finished with

$\text{NH}_4\text{OH}:\text{H}_2\text{O}_2:\text{H}_2\text{O}$ (1:1:10), D.I. rinsed and dried with N_2 gas flow. The substrates were annealed at 650°C for 10 minutes in H_2 prior to initiating growth at the desired temperature (400°C - 500°C) for these samples. Details concerning the ALE growth process have been reported elsewhere [5-6]. TMGa [$[\text{Ga}(\text{CH}_3)_3]$] (-10%) and AsH_3 (10% in H_2) were used as the sources for Ga and As respectively. The substrate was exposed to the TMGa flux (4 cc/min.) and the AsH_3 flux (25 cc/min.) for ~ 0.3 seconds each during a total 2.5 second rotation for the deposition of one monolayer of GaAs. Approximately $0.5 \mu\text{m}$ of GaAs was deposited on the Ge substrate in about one hour. All the GaAs epilayers grown on Ge by ALE showed a smooth mirror surface. Transmission electron microscopy (TEM) studies revealed a considerable reduction in antiphase domains and other interfacial defects when comparing ALE grown material to metal-organic chemical vapor deposition (MOCVD) grown material at the same temperature [7].

Diffusion near the GaAs/Ge heterojunction interfaces were examined by Secondary Ion Mass Spectroscopy (SIMS) and Current-Voltage (I-V) method.

SIMS (Cesium source) was performed to determine the extent that the various atomic species diffused during growth. Both Ge diffusion into GaAs epilayer and Ga diffusion into the Ge substrate were studied versus growth temperature as shown in figures 1a and 1b, respectively. Results showed a dramatic reduction in interdiffusion due to ALE's capability of GaAs epitaxy at reduced temperature. For samples grown at typical MBE and MOCVD temperatures (i.e. 550°C - 600°C) the Ge diffused from 3500 \AA to as much as 6000 \AA away from the GaAs/Ge interface. Ga diffused on the order of 1000 \AA into the Ge substrate. Reducing the growth temperature to 450°C the cracking efficiency of TMGa and AsH_3 is reduced, so the growth rate is less than the ideal one monolayer/cycle that ALE produces. With these reactants, GaAs deposition still occurs at temperatures as low as 400°C , with reduction of the Ga diffusion to 450 \AA and Ge diffusion as low as 300 \AA .

It should also be mentioned that As diffuses into Ge along with Ga. In general, since As has a higher diffusion coefficient than Ga yet a lower solid solubility, one could get separate Ge layers with n and p dominate doping, respectively if these two species diffuse sufficiently. This would be a factor at higher growth temperature in determining junction properties.

The I-V characteristics were performed on samples grown on p-type Ge substrates. Samples grown at temperatures higher than 480°C showed a "thyristor-like" behavior in forward bias. Similar results were reported using MBE to grow n-type GaAs on p-type Ge substrates [8], except in our work the thyristor-like behavior indicates that an n GaAs - pnp Ge structure exists. This behavior can be readily understood as a result of the interdiffusion processes. As diffuses faster than Ga in Ge, but has a lower solid solubility. Thus the As-diffused region creates an n-type layer in the p-Ge substrate; while the Ga diffused region creates a compensated p-type layer near the metallurgical interface. Additionally the Ge autodoping of the GaAs epilayers can result in changing the background p-type ALE GaAs to n-type. For structures grown at temperatures equal or less than 480°C the I-V characteristic indicates that we are dealing with n GaAs-p Ge heterojunction. This can be due to either As diffusion being insignificant or it is compensated by the Ga. SIMS results indicated that both Ga and Ge are still diffusing at this low temperature. Thus we believe that a compensated p-type Ge layer due to Ga diffusion is masking any diffusion of As. The junction has low breakdown voltage and is essentially due to higher carrier concentration in both sides of the metallurgical junction which may increase tunneling currents at this

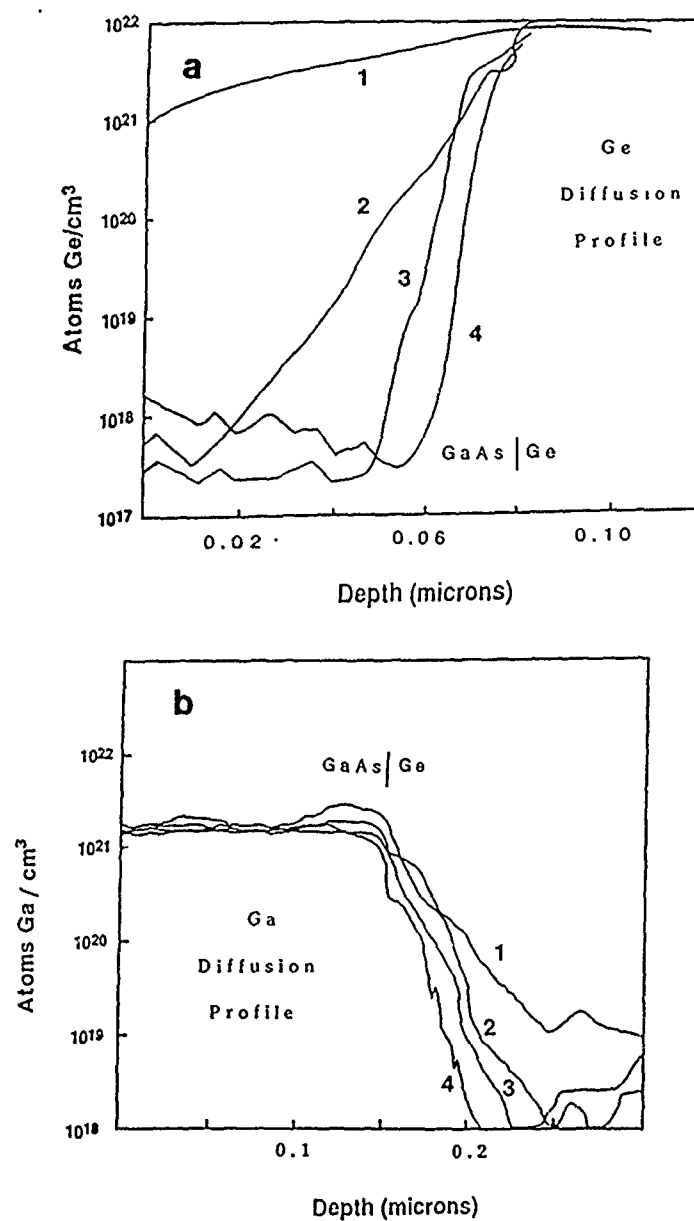


Fig. 1 SIMS depth profiles of GaAs on Ge. (a) Ge diffusion into GaAs, (b) Ga diffusion into Ge. (1) Conventional MOCVD at 580°C. (2) ALE at 500°C. (3) ALE at 480°C. (4) ALE at 400°C.

heterojunction. The structure is then $nn^+ \text{GaAs-p}^+ \text{p Ge}$.

Another approach, based on the previous results and the ALE self-limiting mechanism, is to grow GaAs on a diffused Ga (p-type layer) into n-type Ge substrate. Such structure, for instance, can be used in heterojunction bipolar transistor, or phototransistor ($n \text{ GaAs-p-n Ge}$), or ($p \text{ GaAs-nGaAs-pGe-nGe}$) tandem solar cells. The Ge (n-type) substrate was exposed to TMGa flux in the same manner as growing ALE GaAs (i.e., by rotating the sample under TMGa flux). This should result in monolayer deposition of Ga on the Ge surface, which was followed by a 15 minute anneal at 650°C to allow the Ga to diffuse into the Ge substrate thus forming a p-type layer. Typically this cycle was performed three times and the temperature was then lowered to 480°C for the ALE growth of GaAs. Such approach allows the selective diffusion of only Ga into the Ge substrate. The initial (I-V) results with (base open) shown in figure 2 indicate an ($nn^+ \text{GaAs-p}^+ \text{n Ge}$). These results are encouraging in improvement to device applications of this material combination.

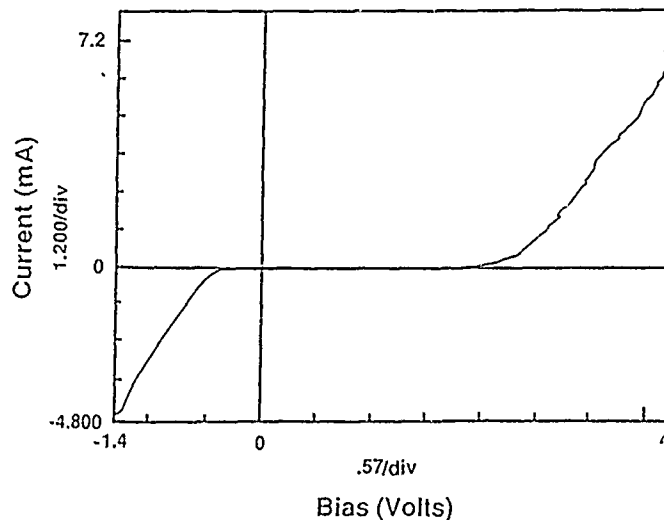


Fig. 2 Current-voltage characteristics of GaAs on n-type Ge substrate that has been pre-diffused with Ga.

CONCLUSION

GaAs has been successfully grown on Ge substrate by ALE. The resulting material has a reduced number of interfacial defects in comparison to materials grown by conventional MOCVD. Due to ALE's ability to grow GaAs at low temperatures, the interdiffusion of Ga, Ge and probably also As is considerably reduced as well as their effects on electrical properties. Above 480°C , the heterointerface produces a npnp thyristor-like behavior, while at temperatures less than 480°C , normal n-p heterojunction I-V readings are measured. Initial electrical results of GaAs grown on Ge that has been pre-diffused from a TMGa source, are promising in the development of devices in this material combination.

ACKNOWLEDGMENTS

The authors would like to thank Dr. N.H. Karam and Y. Huang for their many helpful discussions. This work is supported by office of Naval Research SDIO contract number N-00014-88-K-0527.

REFERENCES

1. D.K. Jadus and D.L. Feucht, IEEE Transaction on Electron Devices, vol. ED-16, No. 1, 102 (1960).
2. S.P. Tobin, S.H. Vernon, C. Bojgar, V.E. Haven, L.M. Geoffroy and D.R. Lillington, IEEE Electron Device Letters, vol. 9, No. 5, 256 (1988).
3. M. Abdul Awal, El Hang Lee, and Eric Y. Chan, Mat. Res. Soc. Symp. Proceedings, Vol. 91, 241 (1987).
4. S.M. Bedair, M.A. Tischler, T. Katsuyama and N.A. El-Masry, Appl. Phys. Lett., 47, 51 (1985).
5. M.A. Tischler and S.M. Bedair, Appl. Phys. Lett., 48, 1681 (1986).
6. M.A. Tischler and S.M. Bedair, J. Crystal Growth, 77, 89 (1986).
7. S.M. Bedair, B.T. McDermott, Y. Ide, N.H. Karam, M. Hashemi, M.A. Tischler, M. Timmons, J.L.L. Tarn and N.A. El-Masry, J. Crystal Growth, 93, 182 (1988).
8. N. Chand, J. Klem, T. Henderson and H. Morkoc, J. App. Phys., 59, 3601 (1986).

DIFFUSION OF ION IMPLANTED Mg AND Be IN GaAs

H. G. ROBINSON,* M. D. DEAL,** and D. A. STEVENSON*

*Department of Materials Science and Engineering, Stanford University, Stanford CA 94305

**Center for Integrated Systems, Stanford University, Stanford CA, 94305

ABSTRACT

Annealed Mg implants into GaAs show three diffusion regions: 1) rapid uphill diffusion in the peak of the implant; 2) rapid concentration-independent diffusion in the tail; and 3) slow concentration-dependent diffusion in between. Implanted Be, in contrast, exhibits only concentration-dependent diffusion. Constant Fermi level experiments show that this diffusion is actually hole-dependent. Uphill diffusion can be induced in Be implants by co-implanting with a heavier element such as Ar. Paradoxically, this retards the concentration-dependent diffusion. This behavior can be explained with the Substitutional-Interstitial-Diffusion (SID) mechanism and an understanding of the defect chemistry after implantation. In the region of uphill diffusion, the dopants are seen to getter from areas of excess Ga interstitials toward areas of excess Ga vacancies. The magnitude of the Ga interstitial gradient with respect to the dopant concentration is shown to be critical for the uphill diffusion. The reduction in concentration-dependent diffusion with co-implants is thought to be caused by implant damage allowing dopant atoms to shift from interstitial to substitutional sites.

INTRODUCTION

Ion implantation has long been a popular technique for introducing dopants into semiconductors. It can be used to implant virtually any dopant into any substrate. Dopants can be implanted precisely over a wide range of concentrations and depths and can often be introduced at concentrations greater than their thermodynamic solid solubility. The most frequently implanted p-type dopants in GaAs are Be and Mg. They are used instead of the traditional GaAs p-type dopant, Zn, due to their lower mass and concomitant deeper penetration into the substrate. They are used in the fabrication of both JFETS and buried p layers in MESFETS. However, like Zn, they both exhibit rapid diffusivity under certain conditions [1-11]. This diffusivity is a severe limitation on their use and consequently on the types of devices that can be fabricated with them. Understanding the basic mechanisms that cause this diffusion is a requisite first step in possibly controlling it. The damage caused during the implant complicates the diffusion behavior and damage effects must be separated from non damage effects. It is no longer adequate to speak simply of implant damage. The various types of damage produced during an implant, their spatial distribution, and their annealing properties must all be considered.

Mg and Be are nearly ideal candidates for studying implanted dopant diffusion. Their annealed profiles show many similarities but also significant differences that give clues as to the underlying mechanisms of the diffusion. Mg exhibits two annealing phases, one in which rapid uphill diffusion creates "humps" in the implanted profile, and another slower, concentration-dependent phase. Be only exhibits a single concentration-dependent phase, leading to "box" shaped profiles. Their masses are both smaller than Ga or As so that the induced damage is not too great to obscure subtle features. The mass of Mg is over twice as large as that of Be, however, so that distinctly contrasting damage distributions are obtained. Finally, the damage distribution in a Be implant can be made to mimic that of Mg by co-implanting with a heavier element such as Ar, to study whether "Mg like" diffusion can be induced in Be implants. In this paper, the annealing behavior of Mg and Be implants and the types of damage produced by each

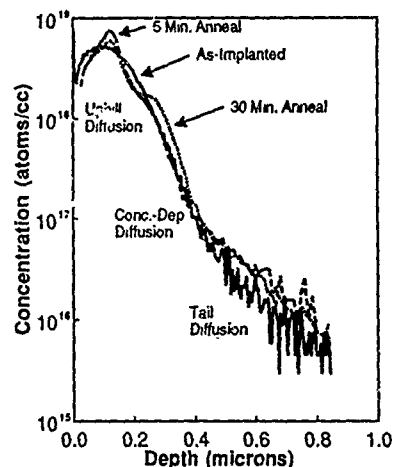


FIG 1. SIMS profiles of a $1 \times 10^{14} \text{ cm}^{-2}$, 120 keV Mg implant into GaAs before and after annealing. Three diffusion regions are identified. The implant was done through a 1000Å Si_3N_4 cap which was stripped prior to SIMS analysis.

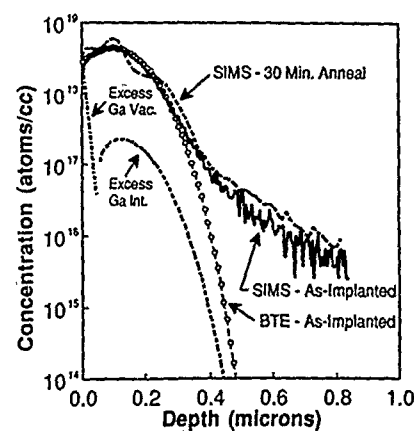


FIG 2. SIMS profile and BTE simulation for a $1 \times 10^{14} \text{ cm}^{-2}$, 120 keV Mg implant into GaAs through 1000Å Si_3N_4 . The electronic stopping powers of the program were adjusted to overlay the non-channeling parts of the profiles. Regions of excess matrix interstitials and vacancies are identified in the figure.

are compared. This comparison is used to consider the mechanisms underlying p-type dopant diffusion in GaAs.

EXPERIMENTAL

Undoped, semi-insulating liquid encapsulated Czochralski (LEC) GaAs wafers were cleaned and wet etched to remove approximately 2000 Å of material. ^{24}Mg was implanted into the substrates at energies ranging from 40 to 200 keV and doses between $1 \times 10^{13} \text{ cm}^{-2}$ and $1 \times 10^{15} \text{ cm}^{-2}$. ^9Be was implanted at energies between 50 and 150 keV at doses from $1 \times 10^{13} \text{ cm}^{-2}$ to $1 \times 10^{15} \text{ cm}^{-2}$. Some samples were implanted through 1000 Å plasma-enhanced chemical-vapor deposited (PECVD) Si_3N_4 caps. PECVD Si_3N_4 was also used as an annealing cap. Constant Fermi level experiments were performed by implanting Be into substrates that were uniformly doped with either Zn ($3 \times 10^{19} \text{ cm}^{-3}$) or Si ($5 \times 10^{18} \text{ cm}^{-3}$). All samples were furnace annealed in flowing forming gas between 700 and 900 °C for times ranging from 5 to 30 minutes. The caps were stripped in concentrated HF after the anneal. SIMS was performed at Charles Evans and Associates to determine the concentration-depth profiles.

RESULTS AND DISCUSSION

Implanted Mg and Be show markedly contrasting behavior upon annealing. Mg exhibits two phases in its anneal (Figure 1). A rapid, transient phase occurs first, in which the dopant diffuses uphill in the peak of the implant leading to humps in the profile. This diffusion is seen in the first few seconds of the anneal. A second, slower phase occurs at longer times (30 minutes). It is characterized by a "shoulder" in the profile, suggesting concentration-dependent diffusion. Be, in contrast, shows only the concentration-dependent phase, although to a much larger extent than Mg. Be diffusion can be easily modeled with SUPREM 3.5, a GaAs process simulator,

using a concentration-dependent or hole-dependent diffusivity [11,12]. To understand this diffusion, the mechanism by which Mg and Be diffuse in GaAs must first be considered.

P-type dopant atoms in GaAs can diffuse via two paths: interstitially or substitutionally. The interstitial diffusivity is very fast but the interstitial solubility is very low, and the mechanism is known as the Substitutional-Interstitial-Diffusion (SID) mechanism [13,14,15]. These paths are in parallel and the jumps are assumed to be independent. The governing differential equation is an extension of Fick's second law

$$\frac{\partial C_s}{\partial t} + \frac{\partial C_i}{\partial t} = \frac{\partial}{\partial x} \left(D_s \frac{\partial C_s}{\partial x} + D_i \frac{\partial C_i}{\partial x} \right) \quad (1)$$

where C_s and C_i are the dopant substitutional and interstitial concentrations and D_s and D_i are the dopant substitutional and interstitial diffusivities, respectively. The equation is often simplified since $C_s \gg C_i$ and $D_i \gg D_s$ giving an effective diffusivity [13]

$$D \equiv D_i \frac{\partial C_i}{\partial C_s} \quad (2)$$

$\partial C_i / \partial C_s$ can be found by considering the equilibrium between substitutional and interstitial atoms. This is given by either the Frank-Turnbull mechanism or the kick-out mechanism, depending on whether the reaction proceeds via Ga vacancies or Ga interstitials. The analysis below is given for the kick-out model. The dissociation is given by the reaction



where Mg_i and Mg_{Ga} are the interstitial and substitutional impurities, respectively, I_{Ga} is the Ga interstitial concentration and p is the hole concentration. Applying the law of mass action to this reaction gives

$$K = \frac{C_s I p^2}{C_i} \quad (4)$$

Rearranging and differentiating with respect to C_s leads to

$$\frac{\partial C_i}{\partial C_s} = \frac{p}{K} \left(pI + 2IC_s \frac{\partial p}{\partial C_s} + pC_s \frac{\partial I}{\partial C_s} \right) \quad (5)$$

If p is assumed equal to C_s , this reduces to

$$\frac{\partial C_i}{\partial C_s} = \frac{p^2}{K} \left(3I + p \frac{\partial I}{\partial p} \right) \quad (6)$$

The corresponding equation for the Frank-Turnbull mechanism is

$$\frac{\partial C_i}{\partial C_s} = \frac{p^2}{KV^2} \left(3V - p \frac{\partial V}{\partial p} \right) \quad (7)$$

where V is the Ga vacancy concentration. Local equilibrium between the Ga vacancies and interstitials is assumed so that an excess of one would result in a corresponding deficit in the other. Thus, in accord with equations 6 and 7, the diffusivity depends on the Ga interstitial or vacancy concentration and the *gradient* of Ga interstitials or vacancies with respect to the doping. This gradient term can play a significant role in the diffusion process, as discussed below.

Ion implantation causes regions of excess matrix (Ga and As) vacancies and interstitials in the substrate. The magnitude and distribution of these defects can be predicted with a Boltzmann transport equation (BTE) simulation. Figure 2 shows a $1 \times 10^{14} \text{ cm}^{-2}$, 120 keV BTE Mg implant simulation overlaid with the SIMS data. The region of excess Ga vacancies is near the surface and the region of excess Ga interstitials is deeper, near R_p . (Only Ga vacancies and interstitials are shown since the diffusion takes place on the Ga sublattice; the profiles for the As point defects would be similar.) During the transient phase of the anneal, Mg atoms diffuse from the region of excess interstitials toward the region of excess vacancies. No diffusion occurs from the peak region *into* the material during this phase. This behavior can be explained by examination of $\partial I / \partial C_s$ in Figure 2. Near the peak of the implant, the gradient ($\partial I / \partial C_s$) is large and *negative*, while deeper in the profile, it is small and positive. This negative gradient will cause the diffusivity (from equations 2 and 6) to be negative in the peak region and the Mg atoms will diffuse toward the surface. When the atoms move into the region of excess vacancies, they will become substitutional, creating a hump in the profile.

This diffusion is "uphill" since the Mg atoms are moving up the gradient in their concentration. However, as discussed above, the dopant atoms are moving down the Ga interstitial gradient. The transient nature of the diffusion is consistent with this mechanism since the excess Ga interstitials, due to their high strain energy [16], will have short lifetimes. They will either recombine with vacancies or coalesce into dislocation loops during the first moments of the anneal and thus cease to drive the diffusion.

Be implants, in contrast to Mg, exhibit only concentration-dependent diffusion upon annealing [2,10] except when the implants are very shallow [9]. As seen in equation 6, however, the dependence is actually on the hole concentration (or the square of the hole concentration, depending on the charge of the dopant interstitial in equation 3). This can be tested experimentally by implanting into substrates uniformly doped n- or p-type to a concentration above the peak implant concentration so that constant Fermi level conditions apply [11]. The results for the Zn doped case are shown in Figure 3. The penetration of Be into the GaAs is much larger than for the undoped substrate case. This diffusion can be simulated in SUPREM 3.5 using a constant diffusivity of $1 \times 10^{11} \text{ cm}^2/\text{sec}$. When the experiment was repeated, but with the substrate uniformly doped n-type, no diffusion occurred [11]. This is again consistent with equation 6 since $p = n/n_i^2$ and the effective diffusivity would be small. These experiments confirm that the diffusion is indeed dependent on the position of the Fermi level and only on the implanted dopant concentration when it determines the Fermi level.

As mentioned above, uphill diffusion is not normally seen in annealed Be implants. This implies that the gradient in the excess Ga interstitial concentration created during the implant is not great enough to initiate uphill diffusion. BTE simulations of Be implants show that the excess Ga interstitial distribution is 5 to 6 times lower than that for Mg [17]. Uphill diffusion can be induced in I profiles by co-implanting with a heavier element such as Ar, as seen in Figure 4. The Ar has a slightly larger mass than Mg and consequently will be expected to produce enough damage to initiate uphill diffusion. This may also explain the uphill diffusion seen by Baratte, et. al. [9]. In their experiments that showed uphill diffusion, Be was implanted very shallow (20 keV) and at a high dose ($1 \times 10^{15} \text{ cm}^{-2}$). This high concentration of implant damage at the surface could have created the necessary Ga interstitial concentration to induce uphill diffusion.

Another significant feature seen in the co-implanted profile in Figure 4 is the reduction in the concentration-dependent diffusion. The extra damage from the Ar has evidently slowed down this diffusion. This phenomenon has also been observed for Be implanted into GaAs with a B co-implant [10]. A possible explanation is given in [10] and summarized here. After the dopant

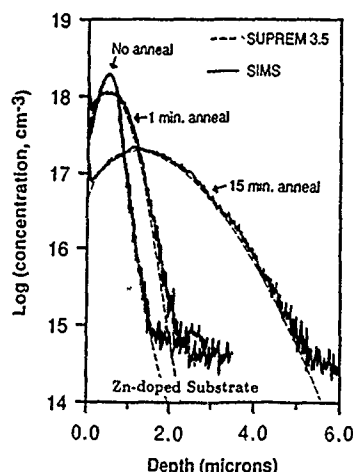


FIG 3. Concentration-depth profiles of Be implanted into Zn-doped GaAs ($p = 3 \times 10^{19} \text{ cm}^{-3}$) and annealed for 1 and 15 minutes at 800°C . The dose was 1×10^{14} and the energy was 150 keV. Also shown are SUPREM 3.5 simulations using a constant D value of $1 \times 10^{-11} \text{ cm}^2/\text{s}$.

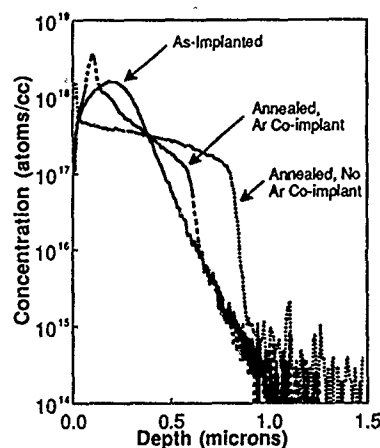


FIG 4. SIMS profile of an as-implanted and annealed (700°C , 15 Min.) Be implant ($5 \times 10^{13} \text{ cm}^{-2}$, 50 keV) with and without an Ar co-implant. The damage created by the Ar is seen to induce uphill diffusion the Be profile while retarding the normal concentration-dependent diffusion.

atoms are implanted, most are interstitial. This results in a high value for D effective. The implant damage helps to mediate any under- or over-saturation of point defects and bring them toward equilibrium or quasi-equilibrium. The damage may be in the form of dislocations, for instance, which act as sources and sinks for vacancies and interstitials. The greater the damage, the more quickly a steady state will be achieved. The damage thus allows the dopant atoms to shift from relatively mobile interstitial sites to relatively stationary substitutional sites, thereby reducing D effective.

One feature that has yet to be explained in Mg profiles is the rapid diffusion that occurs in the implant tail during the transient phase of the anneal. This diffusion may simply be an extension of the channeling during the first moments of the anneal [18]. The implant damage in this region is minimal. If the channeled atoms remained in their channels (an interstitial site) after the implant, they could move easily into the crystal during the anneal. Those dopant atoms that did become substitutional by reacting with a vacancy would leave the region undersaturated in vacancies. This would decrease the probability of other interstitial dopant atoms encountering a vacancy and consequently would increase the diffusion.

SUMMARY

Mg and Be implants both show considerable redistribution upon annealing. Uphill diffusion is observed in Mg implants but not generally in Be implants. This behavior can be understood by including the effect of Ga interstitials and vacancies on the effective diffusivity. The gradient in the Ga interstitial distribution relative to the dopant distribution is shown to drive the observed uphill diffusion. BTE simulations can be used to predict the magnitude and distribution of excess point defects created during implantation. Mg implants are predicted to create five to six times the number of excess point defects as Be implants. This explains why uphill diffusion is not normally seen in Be profiles. When Ar is co-implanted with Be, or when the implant is made at a very low energy and high dose, uphill diffusion does occur in Be

profiles. In these cases, the requisite damage has been created and there are sufficient Ga interstitials to cause uphill diffusion.

The concentration-dependent diffusion of Be is shown to actually be hole-dependent diffusion. This was done with constant Fermi level experiments whereby Be was implanted into uniformly doped n- and p-type GaAs. Fast, concentration-independent diffusion was observed. This is consistent with the SID mechanism, which predicts a hole dependent diffusivity.

The concentration-dependent diffusion of Be was retarded by increasing implant damage. This is thought to be caused by the damage allowing Be atoms to shift from relatively mobile interstitial sites to relatively stationary substitutional sites. This is not in conflict with damage enhancement of uphill diffusion, since uphill diffusion is a transient phenomenon, caused by a momentary, non uniform excess of point defects, while concentration-dependent diffusion is a slower, steady state process that can be mitigated by residual damage.

ACKNOWLEDGEMENTS

The authors would like to acknowledge helpful discussions with T.W. Sigmon, E.L. Allen, J.J. Murray and L.S. Vanasupa of Stanford University and U.M. Gösele of Duke University. This work was funded by DARPA.

REFERENCES

1. R. Zolch, H. Rysell, H. Kranz, H. Reich and I. Ruge, in Ion Implantation in Semiconductors, edited by F. Chemow, J. A. Borders and D. K. Brice (Plenum, New York, 1977), p. 593.
2. W. V. McLevige, K. V. Vaidyanathan, B. G. Streetman, J. Comas and L. Plew, *Sol. State Comm.* **25**, 1003 (1978).
3. M. B. Small, R. M. Potemski, W. Reuter and R. Ghez, *Appl. Phys. Lett.* **41**, 1608 (1982).
4. Y. K. Yeo, Y. S. Park, F. L. Pedrotti and B. D. Choe, *J. Appl. Phys.* **53**, 6148 (1982).
5. H. Kanber, M. Feng and J. M. Whelan, *SPIE* **463**, 67 (1984).
6. N. Duhamel, K. Daoud-Ketata, B. Descouts, P. Krauz, M. Gauneau and S. Godefroy, *J. Elect. Mats.* **15**, 377 (1986).
7. I. A. Naik, *J. Electrochem Soc.* **134**, 1270 (1987).
8. T. Humer-Hager and P. Zwicknagl, *Jap. J. Appl. Phys.* **27**, 428 (1988).
9. H. Baratte, T. N. Jackson, D. K. Sadana, J. F. Degelormo, G. J. Scilla and F. Cordone, presented at MRS fall meeting, symposium W, Advances in Materials, Processing and Devices in III-V Compound Semiconductors (1988).
10. M. D. Deal and H. G. Robinson, *Appl. Phys. Lett.* **55**, 996 (1989).
11. M. D. Deal and H. G. Robinson, *Appl. Phys. Lett.* **55**, 1990 (1989).
12. M. D. Deal, S. E. Hansen and T. W. Sigmon, *IEEE Trans. Computer-Aided Design* **8**, 939 (1989).
13. S. K. Ghandhi, VLSI Fabrication Principles, (John Wiley & Sons, New York, 1983).
14. B. Tuck, Introduction to Diffusion in Semiconductors, (Peregrinus, Stevenage, 1974).
15. U. M. Gösele, *Ann. Rev. Mater. Sci.* **18**, 257 (1988).
16. W. D. Nix (private communication).
17. H. G. Robinson, M. D. Deal and D. A. Stevenson, accepted for publication in *Appl. Phys. Lett.* (1989).
18. T. W. Sigmon (private communication).

DEFECT FORMATION DURING Zn DIFFUSION INTO GaAs

MARTINA LUYSEBERG, W. JÄGER, K. URBAN, M. PERRET*, N.A. STOLWIJK*,
and H. MEHRER*

Institut für Festkörperforschung, KFA Jülich, D-5170 Jülich, F.R. Germany

* Institut für Metallforschung, Universität Münster, F.R. Germany

ABSTRACT

The microstructure induced by the Zn diffusion at 1170 K into doped and undoped semi-insulating GaAs single crystals was characterized for various diffusion times $t < 1740$ min by analytical electron microscopy. The results were compared with Zn concentration profiles obtained by spreading resistance measurements (SRM) on the same samples. At the diffusion front the formation of prismatic interstitial dislocation loops, dislocation networks, and of cavities partly filled with Ga was observed. Closer to the surface faceted voids and, for the undoped samples, vacancy-type dislocation loops formed. The near surface region of highest Zn-concentration showed a high density of Zn-rich precipitates. A model is presented which accounts for these observations. It is based on fast interstitial Zn diffusion and the kick-out mechanism for interstitial-substitutional exchange.

INTRODUCTION

Galliumarsenide as compound semiconductor is besides Si the most important material in solid-state microelectronics and optoelectronics. The fabrication of p-n junctions and heterojunctions requires the diffusion of dopants at elevated temperatures. An example is the production of laser diodes by diffusion of Zn from the vapor phase into n-type GaAs. The anomalously fast diffusion and the large solubility of Zn in GaAs lead to step like diffusion profiles with high Zn concentrations at the surface and an anomalously steep decrease towards smaller concentrations at the diffusion front [1-5].

It is generally accepted that diffusion of Zn into GaAs is governed by an interstitial-substitutional exchange mechanism. Two mechanisms are suggested to account for the interchange between interstitial Zn_i and substitutional Zn_s : (i) The dissociative mechanism [6,7] involves Gallium vacancies V_{Ga} . Interstitial Zn_i is incorporated as substitutional Zn_s on vacant Ga lattice sites. Interstitial Zn is generally considered to be a donor whereas Zn atoms occupy sites on the Ga sublattice as shallow acceptors. (ii) In the "kick-out" mechanism [8] the interstitial Zn-atoms take substitutional Ga sites by pushing Ga-atoms into the interstitial lattice. Experiments in which the concentration dependence of the Zn diffusion coefficient and its variation with As vapour pressure was measured could not differentiate between the two models. Also it was found that the dislocation density of the starting material has essentially no influence on Zn diffusion [4]. From recent experiments of diffusion-induced superlattice disordering in GaAs/AlAs it has been concluded that Zn-diffusion is governed by the kick-out mechanism [9].

On the other hand, Zn diffusion itself induces a high density of extended crystal defects into GaAs. This has been concluded first from the

results of surface etching of diffused samples [1,4]. Microstructural investigations by transmission electron microscopy (TEM) were performed for material heavily doped with Te [10] and with Si [11], respectively. Under these conditions the formation of interstitial-type dislocation loops and dislocation networks was observed.

This paper summarizes results of TEM investigations of the microstructural evolution during Zn diffusion into undoped and In-doped semi-insulating GaAs at 1170 K for various diffusion conditions. The results are compared to Zn concentration profiles obtained by SRM.

EXPERIMENTAL PROCEDURES

Diffusion of Zn was performed from the vapor phase into semi-insulating GaAs wafers (dislocation density of typically $2 \times 10^4 \text{ cm}^{-2}$) as well as into In-doped wafers with an extremely low dislocation density ($< 10^3 \text{ cm}^{-2}$). The dislocation densities correspond to average distances between dislocations which are larger or comparable to the maximum penetration depth of Zn. Therefore both types of wafers may be considered as effectively free of dislocations.

The diffusion anneals were performed at 1170 K in Ar-flushed and sealed quartz ampoules employing elemental Zn as vapor diffusion source. The effect of the annealing time t was studied for $t = 15 \text{ min}$ (short term anneal) and $t = 1740 \text{ min}$ (long term anneal). In this case, an elemental As source was added in order to prevent As loss from the crystal. The effect of the absence of such an As source was investigated for $t = 90 \text{ min}$.

Zn concentration depth profiles $C_{\text{Zn}}(x)$ were measured on the same samples by the spreading-resistance technique whereby the electrical resistance $R(x)$ between two probes is recorded and converted into the Zn-concentration. This procedure permits to measure Zn concentrations down to 10^{17} cm^{-3} [4].

Microstructural characterization by TEM was performed on cross-sectional specimens in a Philips EM 430 at 300 kV and in a JEOL 2000 EX at 200 kV. The diffusion-induced precipitates were analyzed by energy-dispersive X-ray spectroscopy and by electron diffraction.

RESULTS

In all cases investigated the diffusion of Zn into GaAs led to the typical step-like concentration profiles and to the formation of a high density of dislocation loops, dislocation networks, and various types of precipitates. Diffusion-induced crystal defects were observed only within the Zn diffused region ($C_{\text{Zn}} > 10^{17} \text{ cm}^{-3}$). The crystals were free of defects at depths larger than the maximum penetration depth of Zn. Within the diffusion zone three depth regions with characteristically different defect structures could be distinguished: diffusion front, transition region, and near-surface region. The widths of these depth regions depended on the diffusion conditions.

Fig. 1 shows as an example the concentration profile $C_{\text{Zn}}(x)$ after the long-term anneal as obtained by the spreading-resistance technique. The profile is characterized by two pronounced steps, one at the diffusion front at about $180 \mu\text{m}$ and a second at $100 \mu\text{m}$. The concentration close to the surface is about $2 \cdot 10^{20} \text{ cm}^{-3}$, that at $100 \mu\text{m}$ is about $8 \cdot 10^{18} \text{ cm}^{-3}$. A qualitatively similar behaviour was found for the short-term anneal and the anneal without As source. Within experimental error, the near-surface con-

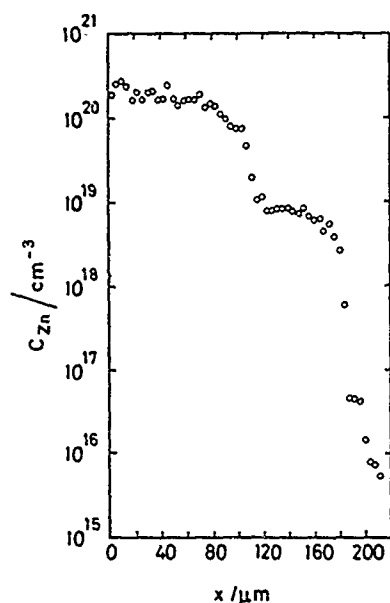


Fig. 1: Concentration profile of Zn in GaAs diffused for 1740 min at 1170 K

diffusion front (Fig. 3). Quantitative analysis of the type of dislocation loops [12] were performed for all diffusion conditions investigated. The loops were found to be of interstitial type with $\{111\}$ and $\{110\}$ habit planes and Burgers vectors parallel to $\langle 110 \rangle$. No stacking fault contrast could be observed. This implies that the loops consist of an extra layer containing both Ga and As. Typical loop diameters are of the order of 0.5 μm . The precipitates formed at the diffusion front were found to be enriched in Ga. Frequently contrast fluctuations could be observed by focussing the electron beam on the precipitates (Fig. 3). This could result from the agitation of liquid gallium due to beam heating effects. The precipitates have typical diameters of about 30 nm at an estimated volume density of 10^{13} cm^{-3} .

The defect structure found in the transition region ($10^{19} \text{ cm}^{-3} < C_{\text{Zn}} < 10^{20} \text{ cm}^{-3}$) consists of dislocation loops of vacancy type, of faceted cavities with low or no Ga content, and of dislocation segments (Fig. 5). The vacancy loops have $\{111\}$ and $\{110\}$ habit planes and Burgers vectors parallel to $\langle 110 \rangle$. They do not comprise a stacking-fault and therefore must contain both Ga and As vacancies. In the In-doped sample only interstitial-type and no vacancy-type loops were observed. This indicates that the defect structure in this region depends on the starting material.

The microstructure in the near-surface region (plateau at $C_{\text{Zn}} = 10^{20} \text{ cm}^{-3}$, Fig. 1) is strongly dependent on the diffusion condition. Crystalline precipitates with typical Moiré fringe contrast are characteristic of this region (Fig. 6). Generally they are found to be enriched in Zn and in As. For the long-term and short-term anneal the precipitates are homogeneously arranged. Diffusion without an As source

concentrations in these experiments were found to be the same as in Fig. 1. The diffusion fronts were found to lie at about 12 μm and 60 μm , respectively. The defect structure at and behind the diffusion front ($C_{\text{Zn}} < 10^{19} \text{ cm}^{-3}$, Fig. 1) is qualitatively similar in all samples independent on the diffusion conditions employed. Figs. 2-6 show examples of the long-term anneal corresponding to the depth range between 100 μm and 180 μm . Dislocation loops and precipitates which partly decorate the loops, as well as dislocation segments are present at the diffusion front (Fig. 2). The precipitates are faceted and decorated by small voids (Fig. 4). Comparison with the short-term anneal indicates that the network observed behind the diffusion front results from growth and entanglement of interstitial dislocation loops. There exists a clear spatial correlation between the precipitate arrangement and the dislocation structure at and behind the



Fig. 2: Diffusion-induced dislocation loops and precipitates at the diffusion front.



Fig. 3: Spatial correlation of precipitates and dislocation structure close to the diffusion front.

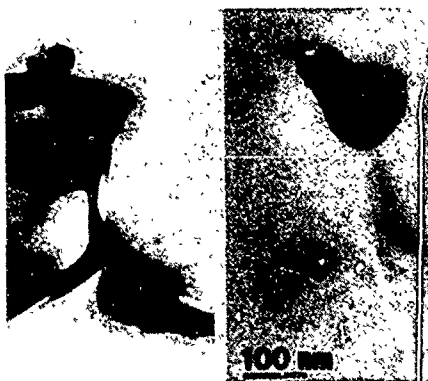


Fig. 4: Gallium-enriched precipitate at the diffusion front. Note change in void contrast during observation

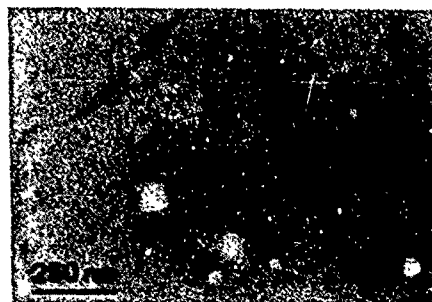


Fig. 5: Cavities with low or no Ga content and vacancy loop in the transition region.

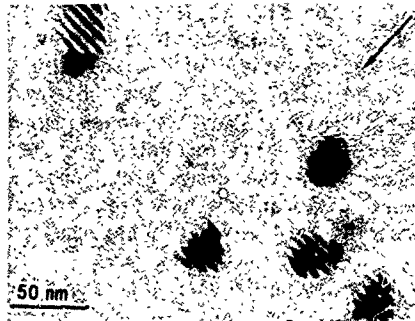


Fig. 6 Precipitates with Moiré contrasts in the surface region of the long-term anneal.



Fig.7 Precipitates with Moiré contrasts in the surface region of the anneal without As source

results in a more complex precipitate and dislocation structure (Fig. 7). Defects that were formed during the earlier stages of the diffusion are no longer observed in the near-surface region.

DISCUSSION

The experimental results show that diffusion-induced defects are observed only in depth regions of detectable Zn concentrations whereas the crystals are free of defects beyond these regions. In the diffusion zone we can distinguish individual depth regions with characteristic types and arrangements of defects. Since the defect structure close to the diffusion front is independent of the diffusion conditions the microstructure observed in different depths regions after the long-term anneal directly reflects the stages in the temporal evolution.

In the following we briefly discuss a model for the diffusion induced defect formation at the diffusion front. It is based on fast interstitial Zn diffusion (Zn_i) and the substitutional incorporation of Zn on the Ga sublattice (Zn_s). The formation of interstitial loops without stacking faults in the present investigations of undoped and doped GaAs can be explained in a direct way by the supersaturation of Ga interstitials during the diffusion and their condensation into dislocation loops. In the description of the kick-out mechanism [8] a supersaturation of Ga interstitials is the direct consequence of the Zn_i - Zn_s interchange. Simultaneously As interstitials must be provided for loop growth in order to avoid a loop stacking fault and to maintain stoichiometry. Similar to a mechanism suggested for the climb of dislocations [13] the required As interstitials can be produced at the loop periphery by emitting As vacancies. These As vacancies agglomerate and form cavities partially filled with Ga which can act as further sinks for Ga interstitials produced by the Zn_i - Zn_s interchange.

In the dissociative mechanism the Zn_i - Zn_s transition would occur by occupation of Ga vacancies. Creation of new Ga vacancies in defect-free GaAs would require the diffusion of vacancies from the surface. Since, compared to the anomalously large diffusion velocity of the Zn atoms, this

supply of vacancies from the surface would be too slow at larger depths it was postulated in the literature that vacancies could be produced by a spontaneous Frenkel pair creation. The agglomeration of interstitials created by this process in principle could also explain the observed interstitial loops at the diffusion front. However, there is no evidence that spontaneous Frenkel pair production for which high formation energies of 4-6 eV are predicted [14] actually occurs. On the other hand, once a higher density of defects such as network dislocations has been formed these defects can act as sources for vacancies [15] which can be occupied by interstitial Zn.

The temporal evolution of the defect structure is characterized by a transition region where perfect vacancy loops and the Ga-depletion of cavities were observed. The existence of these loops indicates a local supersaturation of vacancies of both sublattices. The creation of vacancies is no direct consequence of the diffusion models proposed above. A possible explanation could be vacancy injection during evaporation at the surface.

The establishment of the thermodynamical equilibrium in the region of constant Zn concentration close to the surface implies the dissolution of the defects observed at the diffusion front. The formation of precipitates enriched in As and Zn in the surface region can result from a supersaturation of Zn, probably created during quenching.

REFERENCES

1. H.R. Winteler, *Helv. Phys. Acta* **44**, 451 (1971)
2. C.H. Ting and G.L. Pearson, *J. Electrochem. Soc.* **118**, 1455 (1971)
3. H.C. Casey, in *Atomic Diffusion in Semiconductors* edited by Shaw (Plenum Press, 1973)
4. N.A. Stolwijk, M. Perret and H. Mehrer, *Defect and Diffusion Forum* **59**, 79 (1988)
5. B. Tuck, *Atomic Diffusion in III - V Semiconductors* (Adam Hilger IOP Publishing Ltd, 1988)
6. F.C. Frank, D. Turnbull, *Phys. Rev.* **104**, 617 (1956)
7. P.L. Longini, *Solid State Electronics* **5**, 127 (1962)
8. U. Gösele and F. Morehead, *J. Appl. Phys.* **52**, 4617 (1981)
9. T.Y. Tan and U. Gösele, *Mat. Sci. En.* **B1**, 47 (1988)
10. R.K. Ball, P.W. Hutchinson and P.S. Dobson, *Phil. Mag* **43**, 1299 (1981)
11. P.W. Hutchinson and R.K. Ball, *J. Mat. Sci.* **17**, 406 (1982)
12. H. Föll and M. Wilkens, *phys. stat. sol (a)* **31**, 519 (1975)
13. P.M. Petroff and L.C. Kimerling, *Appl. Phys. Lett.* **29**, 461 (1976)
14. G.A. Baraff and M. Schlüter, *Phys. Rev. Lett.* **55**, 1327 (1985)
15. B.P.R. Marioton, T.Y. Tan and U. Gösele, *Appl. Phys. Lett.*, **54**, 849 (1989)

ROOM-TEMPERATURE DIFFUSION OF Mn IN CdTe
AND THE FORMATION OF $\text{Cd}_{1-x}\text{Mn}_x\text{Te}$

A. WALL, A. RAISANEN, G. HAUGSTAD, AND A. FRANCIOSI
Department of Chemical Engineering and Materials Science,
University of Minnesota, Minneapolis, MN 55455

ABSTRACT

Deposition of Mn at room temperature onto atomically clean CdTe(110) surfaces yields atomic interdiffusion for metal coverages <3 angstroms with Mn atoms occupying cation sites within the surface and near-surface layers of the semiconductor. Synchrotron radiation photoemission studies with variable photoelectron escape depth indicate the formation of a relatively homogeneous semiconductor surface alloy. The highest Mn concentration observed in the alloy exceeds those obtainable with bulk crystal growth methods.

INTRODUCTION

Semimagnetic ternary alloys involving Mn and a II-VI semiconductor matrix exist in a wide range of composition because of the propensity of Mn to occupy cation lattice sites in the matrix. $\text{Cd}_{1-x}\text{Mn}_x\text{Te}$ semiconductors, for example, can be produced in the form of high quality single phase, bulk single crystals for x up to 0.77 [1]. These materials have been attracting attention for their novel magneto-optical and magnetotransport properties, which derive from the spin-spin exchange interaction between the magnetic moments localized on the Mn sites and band and impurity states [2]. A substantial experimental and theoretical effort has been devoted to understanding the electronic properties of these materials [3-4], improving synthesis methods [1], and exploring the device potential of these materials in optoelectronics [5].

In this paper we examine the formation of $\text{Cd}_{1-x}\text{Mn}_x\text{Te}$ through surface reaction of Mn atoms with CdTe(110) surfaces. We performed synchrotron radiation photoemission studies of the effect of Mn deposition on CdTe surfaces cleaved in situ. We also obtained for comparison results for bulk $\text{Cd}_{1-x}\text{Mn}_x\text{Te}$ standards cleaved in situ. Resonant photoemission analysis of the valence band emission of the Mn-CdTe surface reaction products shows valence states compellingly similar to those of the bulk ternary standards. An investigation of the Cd 4d, Te 4d, and Mn 3d emission as a function of Mn coverage indicates that Mn diffuses in the II-VI matrix at room temperature partially replacing Cd. Results for different photoelectron escape depth indicate the formation of a ternary semiconductor surface layer of homogeneous composition. We used soft-X-ray core photoemission results for the bulk standards to calibrate the composition of the ternary layer. The results indicate that this simple interface reaction method can be used to obtain ternary phases with Mn concentration which exceed those obtainable with bulk crystal growth methods.

EXPERIMENT

Single crystals of CdTe were mounted in an analysis chamber and cleaved in situ to expose mirror-like (110) surfaces. Mn was deposited in situ by thermal deposition from a tungsten coil, with coverage measured by a quartz thickness monitor. Mn coverages are given in angstroms (0.83 angstroms=1 monolayer, in terms of the CdTe(110) surface atomic density of 6.73×10^{14} atoms/cm²). The operating pressure in the analysis chamber was $<5 \times 10^{-11}$ Torr, and even during metal deposition the pressure remained below 2×10^{-10} Torr. The bulk semimagnetic semiconductor standards were grown at Purdue University with a modified Bridgmann method, and characterized by X-ray diffraction and electron microprobe analysis. Samples with $x=0.20, 0.32, 0.45, 0.60$ and 0.68 were mounted on copper sample holders, introduced in the analysis chamber, and cleaved in situ to expose atomically clean surfaces.

The synchrotron radiation photoemission measurements were performed using the methodology described in Refs. [3-4]. Radiation from the 1 GeV electron storage ring Aladdin at the Synchrotron Radiation Center of the University of Wisconsin-Madison was monochromatized by means of a 3m toroidal grating monochromator. Angle-integrated photoelectron energy distribution curves (EDC's) were obtained with a commercial hemispherical electron energy analyzer. The overall measured energy resolution varied from 0.2 to 0.45 eV for photon energies from 40 to 130 eV.

RESULTS AND DISCUSSION

In Fig. 1 we compare EDC's for the valence band emission from bulk ternary standard (left) with $x=0.20$ and 0.68 , with those from the Mn-CdTe(110) system (right) for Mn coverages in the 0.2-3.0 angstroms range, at a photon energy of 50 eV. This photon energy corresponds to the Mn 3p-3d resonance [3-4], at which the Mn 3d cross section dominates the valence band emission of ternary semimagnetic semiconductors. The spectra have been approximately normalized to the main emission feature to emphasize lineshape changes, and the binding energy scale is referred to the linearly extrapolated position of the valence band maximum E_v . The results for the bulk ternaries in Fig. 1 show the characteristic dominant Mn 3d feature 3.5 eV below the valence band maximum E_v [4], a feature within 2-3 eV of the valence band maximum due to Mn 3d states hybridized with Te p states, and a broad 3d-related many-electron satellite in the 6-9 eV range [4].

The spectra for the Mn-CdTe(110) system in Fig. 1 cannot be obtained as a superposition of an elemental Mn valence band and a CdTe valence band [6], and exhibit, instead, a compelling similarity to the bulk ternary spectra. No metallic Fermi level is observed at Mn coverages <3 angstroms, and the dominant, hybrid, and many-body 3d features characteristic of $Cd_{1-x}Mn_xTe$ are clearly observed at all coverages in Fig. 1. Only at Mn coverages >10 angstroms such features progressively disappear, so that at a coverage of 50 angstroms the valence band EDC's become similar to those of elemental Mn films [6]. The results of Fig. 1 suggest that Mn deposition results in the formation of a $Cd_{1-x}Mn_xTe$ alloyed layer.

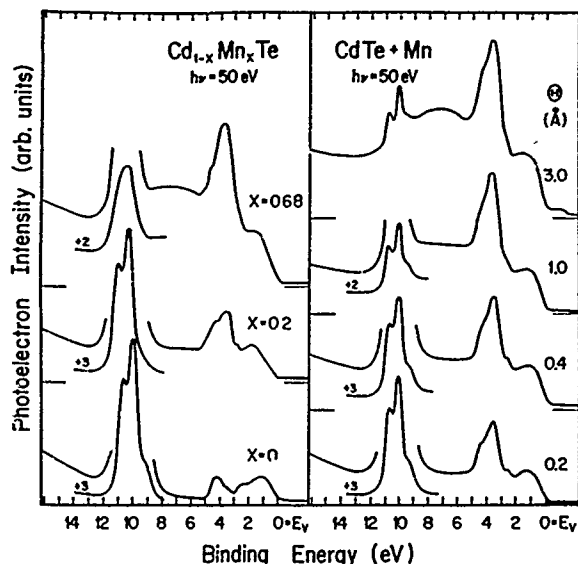


Figure 1. Valence band photoelectron energy distribution curves (EDC's) for bulk ternary $\text{Cd}_{1-x}\text{Mn}_x\text{Te}$ samples cleaved in situ (left), and $\text{Mn-CdTe}(110)$ interfaces (right) for several values of the Mn coverage θ . At a photon energy of 50 eV the valence band is dominated by resonant Mn 3d emission.

We have verified this through an analysis of the Cd 4d, Te 4d, Mn 3d integrated emission intensity as a function of Mn coverage. In the topmost section of Fig. 2 we show the integrated intensity of the Te 4d core levels at photon energies of 58 eV (open diamonds) and 110 eV (solid diamonds), together with the integrated intensity of the Cd 4d core levels at photon energies of 40 eV (open circles) and 95 eV (solid circles), normalized to the initial core emission intensity from the $\text{CdTe}(110)$ surface prior to Mn deposition. The solid symbols correspond to results obtained with a higher surface sensitivity (photoelectron escape depth 4-5 angstroms [6]) relative to the open symbols (escape depth 7-8 angstroms [6]) because of the kinetic energy dependence of the photoelectron escape depth. Yet, we see no detectable escape-depth dependence of the results within experimental uncertainty.

The shaded region in the topmost section of Fig. 2 marks the range of the coverage-dependence expected for Cd and Te features in the absence of interdiffusion and island formation, for an escape depth of 3-5 angstroms. The relatively low attenuation rate of the Te core levels, and the fast attenuation rate of the Cd core levels are consistent with Mn indiffusion to replace Cd in the matrix [7-8]. The lack of an escape-depth dependence of the results indicate a relatively homogeneous composition of the resulting reaction products, on the scale of the photoemission sampling depth.

In the lower section of Fig. 2 we show the coverage dependence of the Mn 3d integrated emission intensity (solid squares), calculated from the integrated intensity of resonance-antiresonance difference curves for the valence band emission, calculated following the methodology described in Ref. [4,6]. This is compared with the coverage dependence expected in the absence of interdiffusion and island formation (shaded area). The theoretical curve has been normalized to the experimental one at a coverage of 0.1 angstroms. The comparison shows that the growth rate of the Mn emission is only 50% of the growth rate

expected in the absence of interdiffusion, and supports the Mn-Cd exchange reaction discussed earlier.

Since the composition of the resulting ternary layer appears relatively homogeneous, it is possible to attempt an estimate of the average composition of the ternary layer. The crucial parameter to gauge the composition is the Mn/Cd concentration ratio. We used the Mn 3d integrated intensity and the Cd 4d

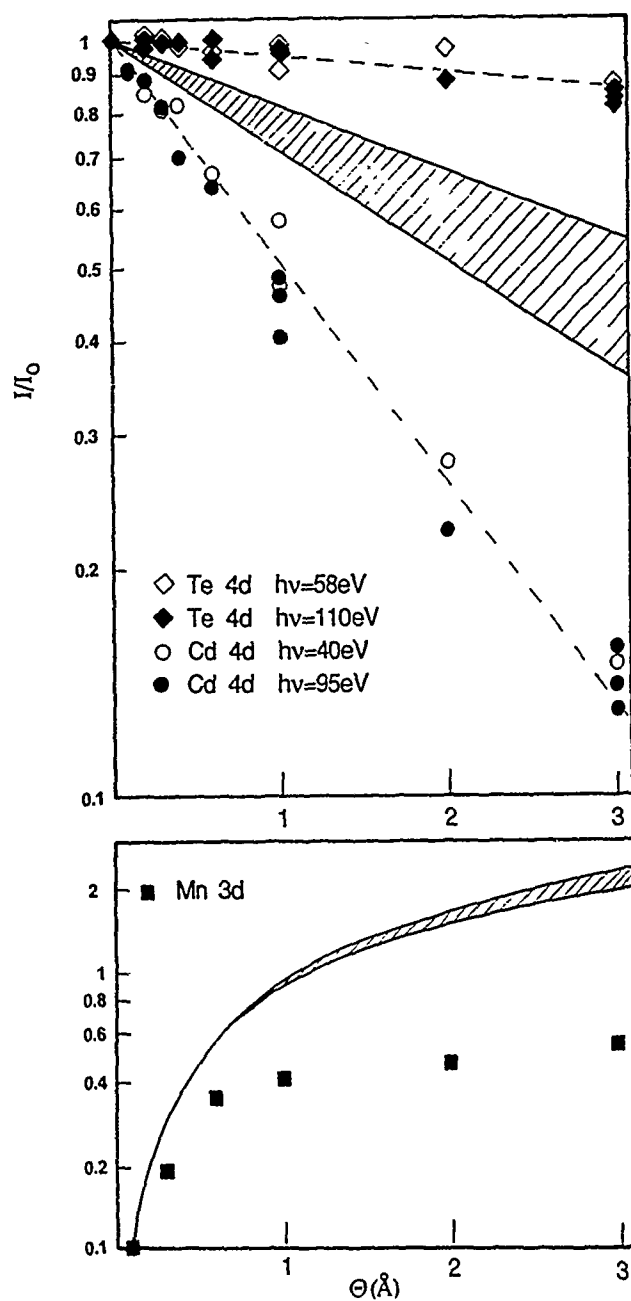


Figure 2. Top: Integrated photoemission intensity from the Te 4d and Cd 4d core levels from the Mn-CdTe(110) system, normalized to the initial core emission intensity from CdTe(110) prior to metal deposition, as a function of Mn coverage. The solid symbols correspond to results with increased surface sensitivity. The shaded area marks the range of the Te and Cd core emission coverage dependence in the absence of interdiffusion and island formation. Bottom: Integrated Mn 3d emission intensity from resonant-anti resonance valence band difference curves as a function of Mn coverage. The shaded area marks the range of behavior expected in the absence of interdiffusion or island formation.

integrated intensity from Fig. 2 to calculate a Mn/Cd intensity ratio as a function of coverage. We can use the results from the bulk ternary standards to translate the Mn/Cd intensity ratio in an average composition. In the inset of Fig. 3 we show (solid triangles) the Mn/Cd intensity ratio for the bulk samples as a function of the composition x as obtained from the electron microprobe analysis. The results are in perfect agreement with the expected $x/(1-x)$ coverage dependence (solid line).

The calibration curve in the inset of Fig. 3 was used to estimate average composition of the Mn-CdTe surface reaction products from the corresponding Mn/Cd photoemission intensity ratio. The results are plotted in Fig. 3 as a function of Mn coverage. The dashed line marks the composition of the bulk ternary sample with the highest Mn content ($x=0.77$) grown to date with bulk crystal growth methods. The surface reaction products exhibit an average composition richer in Mn at all coverages higher than 1.5 angstroms, suggesting that the surface free energy may play a role in determining the stability of the Mn-rich ternary interface phases relative to the bulk ternary alloys.

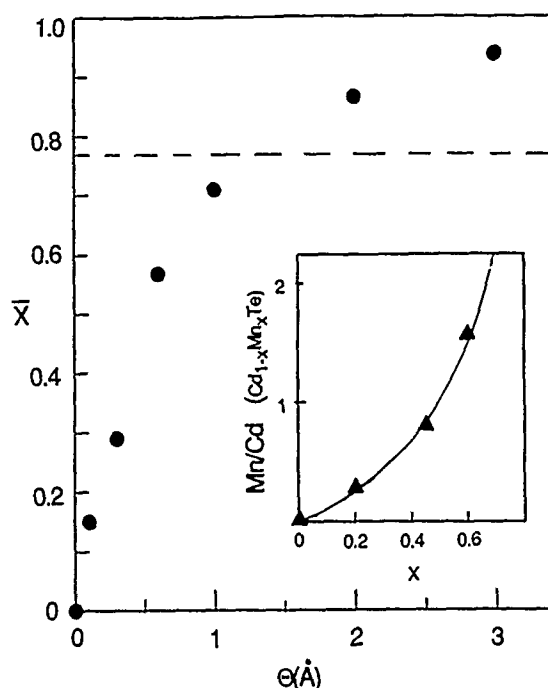


Figure 3. Average Mn concentration within the surface ternary semimagnetic alloy formed upon Mn deposition on CdTe, as a function of Mn coverage. This was derived from the experimental Mn/Cd photoemission intensity ratio. In the inset we show the Mn/Cd intensity ratio (solid triangles) for the bulk ternary standards as a function of the composition x as determined by electron microprobe analysis. The ratio follows the expected $x/(1-x)$ behavior (solid line).

CONCLUSION

We have demonstrated that room temperature deposition of Mn onto CdTe(110) surfaces yields Mn indiffusion and reaction and the formation of non-equilibrium $\text{Cd}_{1-x}\text{Mn}_x\text{Te}$ surface alloys, with composition which becomes increasingly Mn-rich with coverage. An estimate of the average composition of the reacted layer performed using data from bulk ternary samples as standards, indicates that Mn concentration exceeding the equilibrium bulk solubility limit can be obtained through Mn-CdTe(110) interface reaction at room temperature. This suggests that Mn deposition on II-VI semiconductors at moderate temperatures should be explored as a simplified atomic-layer-epitaxy method for the synthesis of a variety of ternary semimagnetic semiconductors.

ACKNOWLEDGMENTS

This work was supported in part by the Office of Naval Research under grant N00014-89-J-1407, and by the Center for Interfacial Engineering of the University of Minnesota. We thank J. Furdyna for providing us with the bulk samples used in the present study, R. Reifenberger, F. Pool, C. Balzarotti, and K. Prince for communicating their results to us prior to publication. Finally, we thank the whole staff of the Synchrotron Radiation Center of the University of Wisconsin-Madison, supported by the National Science Foundation, for their cheerful support.

REFERENCES

1. J.K. Furdyna, J. Vac. Sci. Technol. A4, 2002 (1986).
2. N.B. Brandt and V.V. Moshchalkov, Adv. Phys. 33, 193 (1984).
3. A. Franciosi, in Diluted Magnetic (Semimagnetic) Semiconductors, edited by R.L. Aggarwal, J.K. Furdyna, and S. von Molnar, Materials Research Society, Pittsburgh, 1987), p. 175, and references therein.
4. A. Franciosi, A. Wall, Y. Gao, J.H. Weaver, M.-H. Tsai, J.D. Dow, R.V. Kasowski, R. Reifenberger, and F. Pool, Phys. Rev. B Rapid Commun. 40, December 15 (1989), and A. Wall, A. Franciosi, Y. Gao, J.H. Weaver, M.-H. Tsai, J.D. Dow, and R.V. Kasowski, J. Vac. Sci. Technol. A7, 656 (1989).
5. M. von Ortenberg, Phys. Rev. Lett. 49, 1041 (1982).
6. A more extensive analysis will be presented in a longer forthcoming paper: A. Wall, A. Raisanen, G. Haugstad, and A. Franciosi (unpublished).
7. This characteristic behavior has been encountered for a number of metal-cation exchange reactions. See for example A. Raisanen, A. Wall, S. Chang, P. Philip, N. Troullier, A. Franciosi, and D.J. Peterman, J. Vac. Sci. Technol. A6, 2741 (1988), and references therein.
8. G. Margaritondo and A. Franciosi, Ann. Rev. Mater. Sci. 14, 67 (1984).

AN EXAMINATION OF THE MECHANISMS OF Si DIFFUSION IN GaAs

SHAOFENG YU, ULRICH M. GOSELE AND TEH Y. TAN
School of Engineering, Duke University
Durham, NC 27706

ABSTRACT

An examination of the three available quantitative models of Si diffusion in GaAs has led to the conclusion that the Fermi-level effect mechanism plays the most essential role. In some experimental results a point defect concentration transient is involved which should be incorporated in future models.

INTRODUCTION

Being the main n-type dopant used in device fabrications in GaAs based materials, one would think that a thorough understanding of the mechanisms governing Si diffusion has long been established. The contrary, however, is true. At low concentrations, Si atoms occupy the Ga sites to constitute shallow donors, Si_{Ga}^+ , and it is known that the Si diffusivity increases with an increase of the As pressure [1,2]. This means Si_{Ga}^+ diffuse via the Ga vacancy V_{Ga} . At high concentrations, Si does not produce an equal amount of electrons, because now some Si atoms occupy the As sites to constitute shallow acceptors, Si_{As}^- , which leads to a self-compensation [3,4]. Measured complete Si diffusion profiles were not available until quite recently [5-10]. Analyses of these profiles have led to the three quantitative Si diffusion models discussed in the following.

QUANTITATIVE Si DIFFUSION MODELS

With a high surface concentration, the measured Si diffusion profiles is concentration dependent. At the diffusion front, the profile declines steeply [5-10]. To explain this kind of feature, Greiner and Gibbons [5,6] proposed a $\text{Si}_{\text{Ga}}\text{-Si}_{\text{As}}$ pair diffusion model, the GG-model. In this model it is assumed that the concentration of the $\text{Si}_{\text{Ga}}\text{-Si}_{\text{As}}$ pairs increases as the Si concentration is increased, since there will then be more Si_{As}^- available. It is further assumed that the pairs diffuse fast by hopping alternately into V_{Ga} and V_{As} while Si_{Ga}^+ and Si_{As}^- do not move. The concentrations of V_{Ga} and V_{As} are assumed to be at their thermal equilibrium values. The GG-model has yielded satisfactory fits for the main concentration dependent part of some experimental Si profiles obtained under rapid thermal annealing (RTA) conditions [5-7].

For the RTA results, however, a gradient in the concentrations of the point defects, induced by the annealing process, may not be ignorable. Noting this point, Kavanagh et al. [8] proposed a point defect gradient model, the K-model, which fitted also satisfactorily the main concentration dependent part of some RTA results. In this model it is assumed that vacancies V , not distinguished between those of the Ga and those of the As sublattices, are injected from the surface into the GaAs interior starting at the onset of the RTA process. Invoking an increasing V surface concentration as the RTA time increases, which in principle can result from the transient V injection process, a V concentration gradient produces in the near-surface region of the GaAs interior which in turn yields a concentration dependence of the Si diffusion profile. Kavanagh et al. [8] recognized that, in any further possible development, the role of V_{Ga} and of V_{As} should be distinguished and that the role of the Fermi-level should be considered. Since Si atoms occupy two different sublattices, it seems only reasonable to consider that V_{Ga} and V_{As} contribute to Si diffusion independent of each other. The importance of the effect of the Fermi-level on Ga self-diffusion in GaAs or on Ga-Al inter-diffusion in GaAs/AlGaAs superlattices [11,12], and on Si diffusion in these materials [9,10] have been previously pointed out.

Independent of the work of Kavanagh et al. [8], two of the present authors [13] have outlined a steady state model for Si diffusion in GaAs. In this model, specifically, the roles of V_{Ga} and of V_{As} are distinguished and the effect of the Fermi-level considered. When further developed [14] by Yu et al. (the YGT-model), the model yielded quite satisfactory fits to the experimental data obtained by Deppe et al. [10] upon diffusing Si into Sn-doped GaAs under steady state conditions, as well as the Si diffusion data of Greiner and Gibbons [5] and of Kavanagh et al. [7] obtained under RTA conditions. However, the more recently available data of Kavanagh et al. [8] were not included and the K-model not examined in the work of Yu et al. [14]. Contrary to the assumption made in the $Si_{Ga}-Si_{As}$ diffusion model, in this model it is assumed that Si_{Ga}^+ and Si_{As}^- each diffuses via an appropriate point defect species and that the $Si_{Ga}-Si_{As}$ pair does not move. For Si_{Ga}^+ , this point defect species is V_{Ga} . For Si_{As}^- , there is a lack of experimental results for judging whether V_{As} or the As self-interstitial I_{As} should be the appropriate point defect species, but this is not a crucial point. For each appropriate point defect species, a few differently charged ones may be expected to make dominating contributions to the diffusion of the Si atoms residing on that sublattice. Under n-doping conditions, the Fermi-level effect increases the concentration of the k - charged point defect species in proportion to $\{n/n_i\}^k$, where n and n_i are respectively the actual and intrinsic carrier concentrations. This in turn affects the contribution of this defect species to the Si diffusivity according to

$$D^{k-}(n) = D^{k-}(n_i) \{n/n_i\}^k, \quad (1)$$

where $D^k(n_i)$ is that under intrinsic conditions. From the parameters used in obtaining the fits, we concluded that V_{Ga}^0 and V_{Ga}^{3-} are the dominant contributors to the Si_{Ga}^+ diffusion, while V_{As}^{3-} or I_{As}^{3-} is the dominant contributor to the Si_{As}^- diffusion. The contribution of V_{Ga}^0 to Si_{Ga}^+ diffusion is characterized by an activation enthalpy of ~ 2.4 eV, that of V_{Ga}^{3-} is ~ 5 eV, and that of V_{As}^{3-} (I_{As}^{3-}) to Si_{As}^- diffusion is ~ 2.5 eV. The finding that V_{Ga}^{3-} contributes to (in fact, in most cases dominates) the Si_{Ga}^+ diffusion is quite significant, as it is consistent with the earlier finding that this defect dominates the Ga self-diffusion (and Ga-Al inter-diffusion) under intrinsic and under n-doping conditions. According to the calculation of Baraff and Schluter [15], V_{Ga}^{3-} is the most abundant point defect species on the Ga sublattice under the same conditions.

VALIDITY AND IMPORTANCE OF THE INVOKED MECHANISMS

For the essential mechanisms invoked in the three models, the point defect concentration gradient mechanism of the K-model is in a sense complementary to the pair-diffusion mechanism of the GG-model and to the Fermi-level effect mechanism of the YGT-model. However, the two latter mechanisms are mutually exclusive. In Fig. 1 we show the concentration profiles of two cases of diffusing Si into Sn-doped GaAs which were obtained by Deppe et al. [10]. The fittings are per the YGT-model, which are satisfactory. The GG-model failed to fit the data D₂ [14] for which the substrate Sn-doping level is high and the profile is nearly a erfc function in shape. The GG-model is incapable to produce the erfc function shaped profiles. Similarly, in its present form, the K-model cannot fit the data D₁ which is obtained from a substrate that is essentially intrinsic. Even though the data is obtained by a long furnace annealing which assures that the steady state and constant point defect concentration conditions prevail, the steep profile at the diffusion front is the same as those obtained by RTA. Since for this case there is no V concentration gradient produced by the point defect injection transient, the K-model cannot produce a fit. Thus, the only valid mechanism for explaining this set of data is that of the Fermi-level effect invoked in the YGT-model. It should be noted, however, that the YGT-model is not applicable to the RTA cases if a point defect concentration transient is present, since it is a steady state model. In most RTA data, though, apparently the point defect concentrations have rapidly reached some steady state and constant values, as has been evidenced by the success of applying the YGT-model to analyse these data [14]. We note, however, the further incorporation of the point defect transient (but probably not a significant gradient) phenomenon into the model is essential. Some of the data of Kavanagh et al. [8] quite clearly demonstrated such a need. As a first step toward this goal, we mention that when treating the Si diffusion problem with a spatially changing point defect concentrations, the diffusion equation

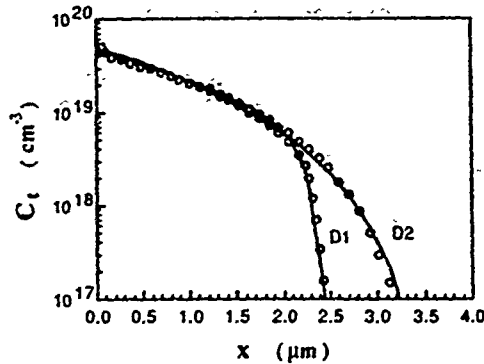


Fig. 1. Quantitatively Fitted profiles of diffusing Si into GaAs using furnace annealing at 815°C. Data from Deppe et al. [10] and fitting per the YGT-model. For data set D₁ the substrate is essentially intrinsic while for D₂ the substrate is Te-doped to $3 \times 10^{19} \text{ cm}^{-3}$.

$$\frac{\partial C}{\partial t} = \frac{\partial [D \frac{\partial C}{\partial x}]}{\partial x} \quad (2)$$

is not the correct one to use, although it is often cited in text books and in the literature for treating concentration dependent diffusion. A more fundamental consideration showed that one should use either

$$\frac{\partial C}{\partial t} = \frac{\partial [D \frac{\partial C}{\partial x} - C \frac{\partial D}{\partial x}]}{\partial x}, \quad (3)$$

if a simple Si-V exchange mechanism is assumed, or

$$\frac{\partial C}{\partial t} = \frac{\partial^2 (DC)}{\partial x^2}, \quad (4)$$

if a simple Si-I exchange mechanism is assumed. The latter expression is also approximately true if we assume that Si-V or Si-I pairs are the migrating species.

CONCLUSION

We mention in conclusion that the Fermi-level effect is playing the essential role in Si diffusion in GaAs. In a more complete model, however, the point defect transient should also be treated.

ACKNOWLEDGEMENT

We acknowledge support by Duke Endowment and by U. S. Army Research Office.

1. L. J. Viehand, J. Phys. Chem. Solids 21, 318 (1961).
2. G. R. Antell, Sol.-State Electr. 8, 943 (1965).

3. W. G. Spitzer and W. Allred, J. Appl. Phys 39, 4999 (1968).
4. C. J. Hwang, J. Appl. Phys. 39, 5347 (1968).
5. M. E. Greiner and J. F. Gibbons, Appl. Phys. Lett. 44, 740 (1984).
6. M. E. Greiner and J. F. Gibbons, J. Appl. Phys. 57, 5181 (1985).
7. K. L. Kavanagh, J. W. Mayer, J. W. Magee, J. Sheets, J. Tong, and J. M. Woodall, Appl. Phys. Lett. 47, 1208 (1985).
8. K. L. Kavanagh, C. W. Magee, J. Sheets, and J. W. Mayer, J. Appl. Phys. 64, 1845 (1988).
9. D. G. Deppe, N. Holonyak, Jr., F. A. Kish, and J. E. Baker, Appl. Phys. Lett. 50, 998 (1987).
10. D. G. Deppe, N. Holonyak, Jr., and J. E. Baker, Appl. Phys. Lett. 52, 129 (1988).
11. T. Y. Tan and U. Gosele, J. Appl. Phys. 61, 1841 (1987).
12. T. Y. Tan and U. Gosele, Appl. Phys. Lett. 52, 1242 (1988).
13. T. Y. Tan and U. Gosele, M at. Sci. Eng. B1, 47 (1988).
14. S. Yu, U. M. Gosele, and T. Y. Tan, J. Appl. Phys. 66,2952 (1989).
15. G. A. Baraff and M. Schluter, Phys. Rev. Lett. 55, 1327 (1985).

DIFFUSION OF Ga VACANCIES AND Si IN GaAs

K.B. KAHEN, D.J. LAWRENCE, D.L. PETERSON, and G. RAJESWARAN, Corporate Research Laboratories, Eastman Kodak Company, Rochester, NY 14650-2011

ABSTRACT

Using the Si-pair diffusion formalism of Greiner and Gibbons, a new Si diffusion model is developed based on the dominant diffusion species being $\text{Si}_{\text{Ga}}^+ - \text{V}_{\text{Ga}}^-$ pairs, where V_{Ga} is the Ga vacancy. In the model, the unknown parameters are the pair diffusion coefficient (D_p) and the equilibrium constant, which are fitted to the experimental data. D_p is also derived to be equal to one-half the Ga vacancy diffusivity. To verify this relation, an experiment to determine the V_{Ga} diffusivity, D_v , is performed. A relation for D_v of the form $0.962 \exp(-2.72 \text{ eV}/kT) \text{ cm}^2/\text{s}$ is obtained, and it is shown that the fitted D_p values are indeed approximately equal to $0.5 D_v$.

I. INTRODUCTION

For a number of years, the accepted model for the diffusion of Si in GaAs has been the Si-pair diffusion theory of Greiner and Gibbons [1]. Their proposal is that at high Si concentrations, the dominant diffusing species are $\text{Si}_{\text{Ga}}^+ - \text{Si}_{\text{As}}^-$ nearest-neighbor pairs. Using two adjustable parameters, the pair diffusion coefficient, D_p , and the pair equilibrium constant, K_p , their model can predict the available Si diffusion data [1,2]. In this paper, a model for Si diffusion will be presented based on combining the pair diffusion formalism of Greiner and Gibbons [1] with the notion of the dominant diffusion species being $\text{Si}_{\text{Ga}}^+ - \text{V}_{\text{Ga}}^-$ pairs. An advantage of our model is that the pair diffusion coefficient can be shown to be a simple function of the V_{Ga} diffusivity, D_v . Because of the lack of experimental values for D_v , an expression for D_v is also derived. The basis for the derivation is the observation that capping superlattice samples with SiO_2 enhances the rate of thermal interdiffusion [3]. Assuming this enhancement originates from an increased Ga vacancy distribution inside the sample and that the vacancies diffuse in from the surface, a procedure for determining D_v can be derived.

II. Si DIFFUSION MODEL

The pair diffusion model [1] is slightly modified when the dominant diffusing species are $\text{Si}_{\text{Ga}}^+ - \text{V}_{\text{Ga}}^-$ pairs. The major assumption of this model is that the high electrical compensation of Si in GaAs for large Si concentrations and high temperatures results mainly from the production of additional Ga-vacancy acceptors [4,5]. The starting point of the model is the following relation which defines the equilibrium pair concentration, P [6]:

$$([\text{Si}_{\text{Ga}}^+] - P)([\text{V}_{\text{Ga}}^-] - P) = K_p P \quad (1)$$

where $[]$ denotes concentration and K_p is given by

$$K_p = N/Z \exp(-E_B/kT). \quad (2)$$

In the above N is the molecular density of GaAs, Z is the number of configurations of the pair ($Z = 12$), and E_B is the binding energy of the pair, which is taken to be the Coulombic interac-

tion energy between the pair at the second nearest-neighbor distance, a_D . In terms of D_p , $[Si]$, and P , Greiner and Gibbons [1] derived a relation for the effective Si diffusivity, D_{eff} . Since P is difficult to determine experimentally, eq. (1) can be used to remove the dependence on P to obtain:

$$D_{eff} = D_p (1 - (1 + 4 [Si] / K_p)^{-1/2}). \quad (3)$$

To complete the formulation it is necessary to derive an expression for the pair diffusion coefficient, D_p . In the absence of Ga vacancies, an isolated Si atom is immobile. Therefore, the formalism of Reiss et al. [6] can be used to determine the reduction in the V_{Ga} diffusivity as a result of pairing with immobile Si atoms. Their results show that for the case of a high degree of pairing and $[Si_{Ga}^+] = [V_{Ga}^-]$ (assumed to occur for large Si concentrations), D_v is reduced by a factor of two. Under these conditions ($[Si] \gg K_p$), eq. (3) reduces to $D_{eff} = D_p$, i.e., the Si diffusivity equals D_p . However, Si_{Ga}^+ diffuses by exchanging positions with the Ga vacancies, which for the above diffusion conditions (a high degree of pairing) results in the Si diffusivity being equal to $D_v/2$. Consequently, this shows that $D_p = D_v/2$. Using this relation in eq. (3), the model has now one unknown, a_D , which is difficult to determine experimentally. a_D was adjusted to obtain the best fit to the data [1,2], within the constraint that $D_p \sim 0.5 D_v$. A value of 2.8 Å was obtained, which is a 30% decrease from the equilibrium separation. Greiner and Gibbons [1] obtained a best fit to their data by reducing a_D by ~18%. Additional details concerning the model can be found elsewhere [7].

Figure 1 compares the results of the model with the experimental Si diffusion data [1,2]. In both experiments, the diffusions were performed using rapid thermal annealing (RTA). The theoretical results were obtained by numerically solving the diffusion equation for Si with the diffusion coefficient set equal to D_{eff} (eq. (3)). The values for K_p were taken from eq. (2) with a_D set equal to 2.8 Å. Instead of using $D_p = D_v/2$ in eq. (3) for each of the diffusion temperatures, D_p was varied to obtain the best fit to the data and then compared with $D_v/2$ in Fig. 2, below. In this way it is simpler to determine if $D_p = D_v/2$, or whether D_p is some other function of D_v . Compared with profiles obtained using the Greiner-Gibbons model [1,2], Fig. 1 shows that the results from the $Si_{Ga}^+ - V_{Ga}^-$ pairs formalism are in comparable agreement with the diffusion data.

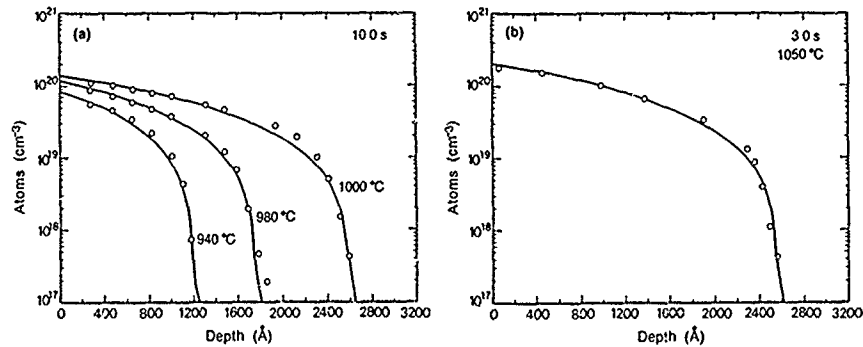


Fig. 1. Comparison between the theoretical Si diffusion profiles, solid lines, and the experimental results.

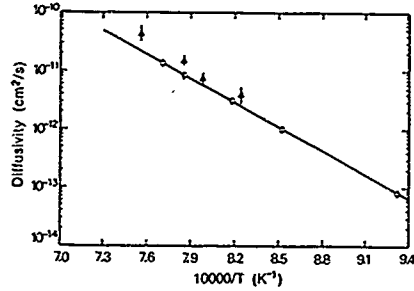


Fig. 2. Comparison between the derived D_p values, triangles, and one-half the Ga vacancy diffusivity values, circles. The solid line gives the best fit to one-half the Ga vacancy diffusivity values.

Figure 2 compares the fitted D_p values with one-half D_v . The determination of D_v is discussed in the next section. The D_p values have a calculated average uncertainty of ~26%. This error is due to the uncertainties involved in measuring the diffusion profiles and in heating, by RTA, for short periods of time [7]. Combining the uncertainties in the D_p and D_v values, Fig. 2 shows that for the 940 and 980°C profiles $D_p \sim 0.5 D_v$. For the 1000 and 1050°C profiles, D_p differs from $0.5 D_v$ by ~28%. The figure also shows that better agreement between the D_p and D_v values would be obtained if $D_p \sim 3/4 D_v$. This can be reconciled by the following argument. The relation between D_p and D_v was obtained using the formalism of Reiss et al. [6], in which it was assumed that one of the paired species was immobile. However, Si moves in the presence of Ga vacancies; thus, a more rigorous derivation of D_p would probably result in $D_p > 0.5 D_v$. Consequently, Fig. 2 shows that the $\text{Si}_{\text{Ga}}^+ - \text{V}_{\text{Ga}}^-$ pair formalism is able to account for the fitted pair diffusion coefficient values.

III. Ga VACANCY DIFFUSIVITY MEASUREMENT

The samples used in this measurement consisted of a 5000 Å barrier layer of $\text{Al}_{0.38}\text{Ga}_{0.62}\text{As}$, an 111-Å-thick GaAs quantum well (QW3), a 900-Å-thick barrier layer of $\text{Al}_{0.38}\text{Ga}_{0.62}\text{As}$, a 55-Å-thick GaAs quantum well (QW2), a 900-Å-thick barrier layer of $\text{Al}_{0.38}\text{Ga}_{0.62}\text{As}$, a 37-Å-thick GaAs quantum well (QW1), a 500-Å-thick barrier layer of $\text{Al}_{0.38}\text{Ga}_{0.62}\text{As}$, and a 250-Å-thick capping layer of GaAs. The samples were encapsulated with 3000 Å of SiO_2 , deposited by chemical vapor deposition at 400°C. Diffusions were performed at 900, 950, 1000, and 1025°C by RTA and at 800°C by conventional furnace annealing. At 900, 950, and 1000°C three diffusion times were employed, namely, 8, 40 and 80 s at 900°C; 8, 20 and 40 s at 950°C; and 6, 12, and 18 s at 1000°C. For 800 and 1025°C, two diffusion times were used: 20 and 30 minutes for 800°C and 10 and 18 s for 1025°C. Low temperature (5 K) photoluminescence was used to measure the $n = 1$ electron-heavy hole exciton transitions before and after RTA.

In order to extract the V_{Ga} diffusivities from the data, the following analysis was applied. The Al-Ga interdiffusion coefficient is proportional to the V_{Ga} concentration [8]. Thus, the following two equations describe the intermixing process:

$$\frac{\partial C_v'}{\partial t} = \frac{\partial}{\partial x} \left(D_v \frac{\partial C_v'}{\partial x} \right) \quad (4)$$

$$\frac{\partial C_{Al}}{\partial t} = \frac{\partial}{\partial x} \left(C_v' D_{Al,eq} \frac{\partial}{\partial x} C_{Al} \right) \quad (5)$$

where C_v' is the normalized V_{Ga} concentration and equals $[V_{Ga}]/C_{v,eq}$; $C_{v,eq}$ is the thermal equilibrium value of $[V_{Ga}]$; C_{Al} is the Al distribution; and $D_{Al,eq}$ is the thermal equilibrium interdiffusion coefficient. Values for $D_{Al,eq}$ were taken from the literature [9]. The solution to eqs. (4) and (5) yields the post-annealing Al distribution, which in turn can be converted to theoretical photoluminescence shifts for each of the wells [10]. By adjusting the value of D_v and the surface concentration of C_v' , $C_v's$ (a boundary condition for eq. (4)), which are unknown parameters in the above equation set, a best fit of the theoretical shifts to the experimental data was made for each temperature. For the fits at 900, 950, and 1000°C, there were nine data points to compare with, three transitions and three RTA times, while for 800 and 1025°C, there were six data points, three transitions and two annealing times. Implicit in this analysis is that the sole property of the SiO_2 capping layer is to increase the V_{Ga} surface concentration from $C_{v,eq}$ to $C_v's$, $C_{v,eq}$ and that its effect on D_v is minimal.

The results of performing fits at the five temperatures are given by the open circles in Fig. 2. Actually, Fig. 2 shows $0.5 D_v$, while $C_v's$ is given elsewhere [10]. The figure shows that the diffusivity data can be described well by a single activation energy of 2.72 eV (the solid line). Using this value, D_v can be written as $D_v = 0.962 \exp(-2.72/kT) \text{ cm}^2/\text{s}$, with an uncertainty of ~15%. Additional details concerning the derivation of D_v can be found elsewhere [10].

IV. CONCLUSIONS

In summary, the observation that SiO_2 capping enhances the thermal intermixing of Al-Ga interfaces has been used to determine the diffusivity of Ga vacancies. These results were then used as inputs for a Si diffusion model based on the dominant diffusion species being $Si_{Ga}^+ - V_{Ga}^-$ pairs. Using a formalism similar to that of Griener and Gibbons [1], good agreement with the experimental data was obtained.

REFERENCES

1. M.E. Greiner and J.F. Gibbons, J. Appl. Phys. **57**, 5181 (1985).
2. K.L. Kavanagh, J.W. Mayer, C.W. Magee, J. Sheets, J. Tong, J.M. Woodall, Appl. Phys. Lett. **47**, 1208 (1985).
3. L.J. Guido, N. Holonyak, Jr., K.C. Hsieh, R.W. Kaliski, W.E. Plano, R.D. Burnham, R.L. Thornton, J.E. Epler, T.L. Paoli, J. Appl. Phys. **61**, 1372 (1987).
4. R.T. Chen and W.G. Spitzer, J. Electron. Mater. **10**, 1085 (1981).
5. W. Walukiewicz, Appl. Phys. Lett. **54**, 2094 (1989).
6. H. Reiss, C.S. Fuller, F.J. Morin, Bell Syst. Tech. J. **25**, 535 (1956).
7. K.B. Kahen, J. Appl. Phys., December 1989.
8. K.B. Kahen, Appl. Phys. Lett. **53**, 2071 (1988).
9. T.E. Schlesinger and T. Kuech, Appl. Phys. Lett. **49**, 519 (1986).
10. K.B. Kahen, D.L. Peterson, G. Rajeswaran, D.J. Lawrence, Appl. Phys. Lett. **55**, 651 (1989).

MECHANISM FOR THE DIFFUSION OF ZINC IN GALLIUM ARSENIDE

K. B. KAHEN

Corporate Research Laboratory, Eastman Kodak Company, Rochester, NY 14650-2011

ABSTRACT

The anomalous shape of the Zn diffusion profile in GaAs has been quantitatively explained. The interchange between interstitial Zn and substitutional Zn is assumed to occur via the Ga vacancies. These vacancies are proposed to be either neutral or singly ionized, depending on the position of the Fermi level. In addition, two physical phenomena are proposed. Substitutional Zn thermally generates interstitial Zn-Ga vacancy pairs and there is pairing between the donor, interstitial Zn and the acceptor, substitutional Zn. This pairing leads to the interstitial Zn diffusivity being a decreasing function of the substitutional Zn concentration. The model is found to be in good agreement with the experimental data.

I. INTRODUCTION

Zn diffusion has been used for many years to form ohmic p-type contacts [1]. Recently, Zn diffusion has been employed in another processing capacity, namely, for interdiffusing multiple quantum-well layers to form laterally guided laser diodes [2]. In both of these processes, it is important that there be strict control over the depth and lateral extent of the Zn diffusion. Consequently, an understanding of the physical mechanisms which underlie the Zn diffusion process is important in order to be able to predict accurately the resulting Zn diffusion profiles. A typical kinked Zn profile is indicated by the circles in Fig. 1 (the error bars on the data and the theoretical results will be discussed below). The data were taken from the recent work of Tiwari et al. [1]. The zinc source was Zn_3As_2 and the diffusion was performed for five minutes using rapid thermal annealing (RTA).

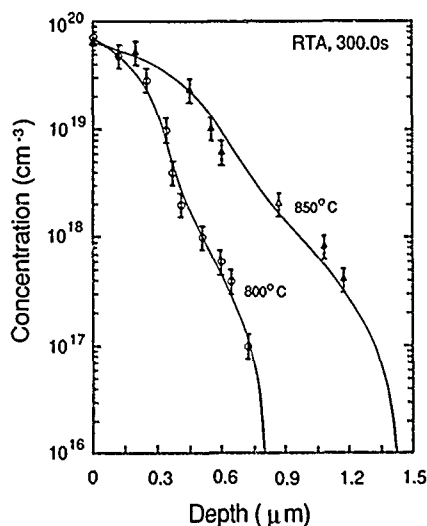
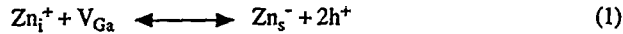


Fig. 1. Comparison of theoretical, solid lines, and experimental Zn profiles at 800°C and 850°C.

II. DIFFUSION MODEL

The starting basis for the model we propose is the Frank-Turnbull mechanism [3], which governs the interchange between interstitial Zn (Zn_i) and substitutional Zn (Zn_s) by means of the Ga vacancies (V_{Ga}),



where h^+ indicates holes. Because of the large electrical activation of Zn in GaAs [4], the hole concentration is approximately equal to the Zn_s concentration, C_s . Using eq. (1), it is simple to show that the effective Zn diffusivity, D_{eff} , is proportional to C_s^2 . As discussed by Reynolds et al. [4], the near surface-region structure of a kinked Zn profile (such as the 800°C profile in Fig. 1) can best be fit assuming $D_{eff} \propto C_s^2$, while the tail region can best be described by $D_{eff} \propto C_s$. Referring to eq. (1), the coefficient for holes can be reduced to one in a couple of ways (to obtain $D_{eff} \propto C_s$). In this work, eq. (1) is modified by the assumption that the Ga vacancies have multiple ionization states, where the dominant species are determined by the position of the Fermi level. For simplicity, only two states are considered, V_{Ga}^0 and V_{Ga}^- . Using Fermi-Dirac statistics, the fractional occupation of the V_{Ga}^- level is given by [5]

$$\Gamma = 1.0 / (1.0 + 2 \exp((E_a - E_f) / kT)) \quad (2)$$

where E_a is the temperature-dependent energy level of V_{Ga}^- and E_f is the Fermi level. Since E_a is unknown, it is treated as an adjustable parameter at one diffusion temperature (the 800°C profile of Fig. 1) and then varied as a function of temperature according to the model of Van Vechten and Thurmond [6], i.e., the temperature variation is the same as that of the direct energy gap.

To obtain a kink in the theoretical Zn profiles, it was found necessary to add two additional features to the model. The reaction described by eq. (1) can go both forward and backward (Zn_s dissociates thermally to give Zn_i and V_{Ga}) and the diffusivity of Zn_i , D_i , is a function of C_s . The first feature allows for the movement of the Zn profile in Zn-doped GaAs in the absence of a surface Zn source. It has been shown elsewhere that this phenomenon can occur under RTA conditions [7]. The second feature is based on the assumption of pairing between the donor, Zn_i^+ , and the acceptor, Zn_s^- , to form a neutral Coulomb pair. The formation of this species should be energetically favorable since it removes from the system unpaired point charges. The pairing would impede the diffusion of Zn_i^+ since Zn_s^- is relatively immobile. The modification of D_i as a result of pairing with the immobile species Zn_s^- , for conditions in which the Zn_i concentration $C_i \ll C_s$, is [8]

$$D_i(C_s) = D_{i,0} / (1 + C_s / K_p), \quad (3)$$

where $D_{i,0}$ is the diffusivity of free Zn_i (small Zn_s concentration) and K_p is the equilibrium pairing constant, which can be defined by an Arrhenius relation [9]. Since C_s/K_p can exceed unity by a large amount, the reduction in D_i can be significant.

The above model can be described by the following system of coupled diffusion equations for Zn_s and Zn_i . (For simplicity, it was assumed that C_v , the concentration of V_{Ga} , maintained its thermal equilibrium value, $C_{v,eq}$, during the diffusion process [9].)

$$\partial C_s / \partial t = k_f C_i C_v - k_r (\Gamma C_s^2 + (1 - \Gamma) C_s^3) \quad (4a)$$

$$k_r / k_f = K_{eq} = C_{i,eq} C_{v,eq} / (C_{s,eq})^3 \quad (4b)$$

$$\partial C_i / \partial t = \frac{\partial}{\partial x} (D_i (C_s) \partial C_i / \partial x) - \partial C_s / \partial t, \quad (4c)$$

where eq. (4b) is the law of mass action for eq. (1); K_{eq} depends only on temperature; and k_f and k_r are the forward and reverse reaction constants for eq. (1), respectively. The right-hand side of the mass action law for eq. (1) is proportional to either C_s^3 or C_s^2 , depending on whether the dominant Ga vacancy defect is V_{Ga}^0 or V_{Ga}^- , respectively. Equation (4a) does not include the Zn_s diffusivity since it is assumed to be many times smaller than D_i .

Equations (4a) and (4c) are solved numerically and the results are compared with experimental data of Tiwari et al. [1] at 700°C, 750°C, 800°C, and 850°C. For each profile $C_{s,eq}$ is constrained to produce the experimental surface concentration. E_a and K_p are adjusted to obtain a good theoretical fit to the profile at 800°C and then varied with temperature as discussed above. Zinc diffusion is found to proceed very rapidly [7]; therefore, k_f is set to an arbitrarily large number. A value of $10^{-3} \text{ cm}^3/\text{s}$ was chosen. $C_{v,eq}$ is given by the relation $1.25 \times 10^{31} \exp(-3.28 \text{ eV}/kT) \text{ cm}^{-3}$ [10]. The remaining unknown parameters are $D_{i,0}$ and $C_{i,eq}$. The sole effect of $D_{i,0}$ and $C_{i,eq}$ on the calculated profiles is to determine the overall diffusion depth. Guessing an enthalpy of formation of Zn_i is superfluous since $D_{i,0}$ is unknown. Thus, $C_{i,eq}$ is kept constant at an arbitrary value of $6.7 \times 10^{15} \text{ cm}^{-3}$ and $D_{i,0}$ is adjusted for each temperature to obtain the correct diffusion depth. Additional details about the model can be found elsewhere [9].

III. RESULTS AND DISCUSSION

Figures 1 and 2 compare the results of the theoretical model, eqs. (4a) and (4c), with the experimental RTA Zn-diffusion data of Tiwari et al. [1]. For the 800°C profile, the fitted

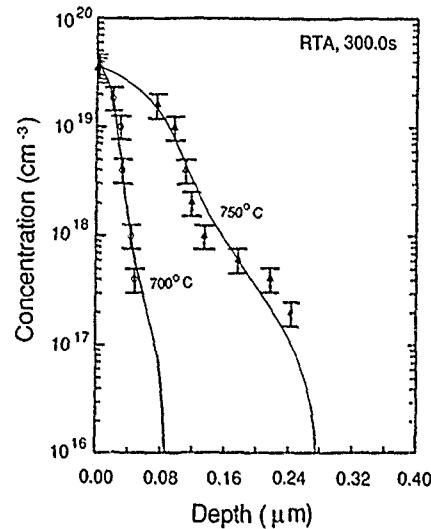


Fig. 2. Comparison of theoretical, solid lines, and experimental Zn profiles at 700°C and 750°C.

values for E_a , K_p , $C_{s,eq}$, and $D_{i,0}$ were 0.24 eV, $1.5 \times 10^{17} \text{ cm}^{-3}$, $1.0 \times 10^{20} \text{ cm}^{-3}$ and $1.1 \times 10^{-5} \text{ cm}^2/\text{s}$, respectively. Figure 1 shows that within the uncertainty in the experimental data, the theoretical results at 800°C agree well with the data. For the other diffusion temperatures, the only adjusted parameters were $D_{i,0}$ and $C_{s,eq}$. At 700°C, 750°C, and 850°C, the fitted values for $D_{i,0}$ were 4×10^{-7} , 1.08×10^{-6} , and $1.75 \times 10^{-5} \text{ cm}^2/\text{s}$, respectively, while for $C_{s,eq}$, the values were 1.2×10^{20} , 7.5×10^{19} , and $8.2 \times 10^{19} \text{ cm}^{-3}$, respectively. The lack of a trend in $C_{s,eq}$ is a reflection of the scatter in the experimental Zn surface concentration values [1]. Figure 1 shows that at 850°C, the calculated results are slightly outside of the established error bars. Figure 2 shows that at 700 and 750°C, both calculated profiles agree with the data within the experimental uncertainty. Overall, Figs. 1 and 2 demonstrate that with two adjustable parameters, the results of the model are in good agreement with the experimental data.

IV. CONCLUSIONS

In summary, a new model for the diffusion of Zn in GaAs has been proposed. Its basis is the interstitial-substitutional diffusion mechanism. To explain the anomalous shape of the Zn profile, three additional phenomena are suggested. The ionization state of the vacancies is a function of the Fermi level; there is thermal generation of interstitial Zn-vacancy pairs and interstitial Zn pairs with substitutional Zn.

ACKNOWLEDGEMENTS

We thank Jacqueline Nicoletti for technical assistance. This work was partially supported by the National Center for Supercomputing Applications under grant ECS890025N and utilized the Cray X-MP48 system at the University of Illinois.

REFERENCES

1. S. Tiwari, J. Hintzman, A. Callegari, Appl. Phys. Lett. **51**, 2118 (1987).
2. H. Nakashima, S. Semura, T. Ohta, Y. Uchida, H. Saito, T. Fukuzawa, T. Kuroda, K.L.I. Kobayashi, IEEE J. Quantum Electron. **21**, 629 (1985).
3. F.C. Frank and D. Turnbull, Phys. Rev. **104**, 617 (1956).
4. S. Reynolds, D.W. Vook, J.F. Gibbons, J. Appl. Phys. **63**, 1052 (1988).
5. H.C. Casey and M.B. Panish, Heterostructure Lasers, Part A (Academic, Orlando, 1978).
6. J.A. Van Vechten and C.D. Thurmond, Phys. Rev. **B14**, 3539 (1976).
7. G. Rajeswaran, D.J. Lawrence, S.-T. Lee, K.B. Kahen, to be published in the proceedings of the Fall 1988 Materials Research Society Meeting in Boston, MA.
8. H. Reiss, C.S. Fuller, F.J. Morin, Bell Syst. Tech. J. **35**, 535 (1956).
9. K.B. Kahen, Appl. Phys. Lett., November 1989.
10. K.B. Kahen, D.L. Peterson, G. Rajeswaran, D.J. Lawrence, Appl. Phys. Lett. **55**, 651 (1989).

DIFFUSION OF ION-IMPLANTED TIN IN GALLIUM ARSENIDE

E.L. Allen*, M.D. Deal** and J.D. Plummer**

*Department of Materials Science and Engineering, Stanford University

** Integrated Circuits Laboratory, Stanford University, Stanford, CA 94305.

ABSTRACT

The diffusion of ion-implanted tin in gallium arsenide was investigated as a function of temperature, dose and background doping. The chemical depth profiles were determined using SIMS and the carrier profiles were determined by CV Etch Profiling. The data was fit using a numerical process simulator, SUPREM 3.5. Sn diffusivity was found to depend on the square of the electron concentration. Sn and Ge were found to have relatively high diffusivities when implanted, while Si diffused very little.

INTRODUCTION

Tin has not assumed an important role as a dopant in digital GaAs technology primarily because of its high diffusivity. Silicon, another n-type Group IV dopant used extensively for channel implants, has a much lower diffusivity. However, its diffusion behavior is not well understood. Hopefully an understanding of Sn and Ge diffusion mechanisms will lead to a better understanding of Si diffusion behavior. In this work we studied the one-dimensional behavior of implanted Sn as a function of temperature, dose and background doping, and compared it to Si and Ge.

Implanted n-type dopants in GaAs usually have suppressed diffusivities compared to solid-source or grown-in dopants in GaAs [1]. This fact has generally been attributed to implant damage. The work presented here shows that high dose implants of Sn and Ge exhibit significant diffusion outside the implanted region, while Si diffuses very little. Both Sn and Ge diffusivities depend on the square of the electron concentration. Results of CV Etch Profiling suggest that the mechanism by which damage influences diffusion may be in the activation process.

EXPERIMENTAL PROCEDURE

Two sets of experiments were done. In the first set we determined the one-dimensional diffusivity of implanted Sn as a function of background doping. For these experiments, GaAs substrates with various background doping levels were solvent-cleaned, etched, and implanted with ^{118}Sn at 185 keV and a dose of either $1 \times 10^{13} \text{ cm}^{-2}$, $1 \times 10^{14} \text{ cm}^{-2}$ or $1 \times 10^{15} \text{ cm}^{-2}$. The semi-insulating wafers were undoped LEC(100), while the doped wafers were Horizontal Bridgman-grown(100), doped with either $3 \times 10^{18} \text{ cm}^{-3}$ Si for n-type or $1 \times 10^{19} \text{ cm}^{-3}$ Zn for p-type. The samples were then capped on both sides with 900 Å of SiN_x deposited by PECVD. The implanted specimens were annealed for various times and temperatures from 700 to 1000°C in an open tube furnace under flowing forming gas. The caps were then stripped and the dopant profiles analyzed using Secondary Ion Mass Spectrometry (SIMS). Some samples were also analyzed by Polaron CV Etch Profiling to obtain carrier profiles. The diffusion profiles were fit using the numerical process simulator SUPREM 3.5 to extract values of the tin diffusivity as a function of concentration.

In the second set of experiments we compared the diffusion behavior of Sn, Ge and Si under identical conditions. We used Te-doped substrates so that the background doping

could be controlled ($1 \times 10^{18} \text{ cm}^{-3}$ n-type) while allowing sufficient sensitivity in SIMS for the Si profiles. Each dopant was implanted at a dose of either $1 \times 10^{14} \text{ cm}^{-2}$ or $1 \times 10^{15} \text{ cm}^{-2}$, capped with 900 Å of SiN_x and annealed for various times and temperatures. We obtained CV Etch Profiles on similar implants into semi-insulating substrates.

RESULTS AND DISCUSSION

Figure 1 shows the SIMS profiles for a 1×10^{15} Sn implant into p-type, n-type and semi-insulating GaAs, annealed at 900°C for 30 minutes. Diffusion is clearly suppressed in the p-type background and enhanced in the n-type background. In the semi-insulating substrate the profile has the steep diffusion front typical of concentration-dependent diffusion. In the n-type substrate the profile is a complementary error function curve outside of the implanted region (i.e. beyond 0.3 μm). In both the semi-insulating and the n-type substrates, diffusion is suppressed in the implanted region but there is local dopant redistribution there, leading to a double peak. This may be due to precipitation of Sn [2] as well as to damage in the implanted region.

The shapes of the concentration profiles and their background dependence indicate that the Sn diffusivity depends on electron concentration. This dependence can be explained by assuming that Sn diffuses via negatively charged gallium vacancies [3]. It has been suggested that the dominant Ga vacancy in n-type GaAs is either singly [4], doubly [5] or triply charged [5,6]. Because the concentration of charged vacancies depends on the position of the Fermi level [7], the effective diffusivity can be expressed as:

$$D_{\text{eff}} = D_0 + D_1 \left(\frac{n}{n_i} \right) + D_2 \left(\frac{n}{n_i} \right)^2 + D_3 \left(\frac{n}{n_i} \right)^3 \quad (1)$$

where D_0 contains an exponential term for diffusion via neutral Ga vacancies, and the other terms correspond to diffusion via singly, doubly and triply negative charged Ga vacancies.

In heavily doped p-type substrates, where $n/n_i \ll 1$, then $D_{\text{eff}} = D_0$. Since the diffusivity of implanted Sn in p-type substrates appears to be zero, we conclude that D_0 is negligible. In heavily n-type substrates or semi-insulating substrates with high dose implants, the three charged vacancy terms in Equation 1 may all contribute. For the implant into an n-type substrate shown in Figure 1, n is determined by the background doping, making D_{eff} a constant. The resulting diffusion profile has the shape of a complementary error function for all implant doses. In the semi-insulating substrate shown in Figure 1, n varies with the Sn concentration, making D_{eff} dependent on concentration everywhere, which results in a box-like profile with a steep diffusion front.

The numerical process simulator SUPREM 3.5 uses a one term version of Equation 1 to simulate diffusion:

$$D_{\text{eff}} = D_0(T) \left(\frac{n}{n_i} \right)^m \quad (2)$$

To extract the effective Sn diffusivity from the SIMS profiles we assumed a constant tin source at the edge of the implanted region and then fit the SIMS profiles by varying D_0 and m . The best fit was found for $m = 2$, which corresponds to the doubly charged vacancy

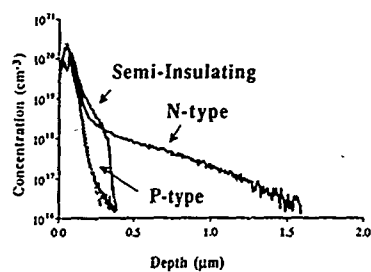


Figure 1. SIMS profiles for $1 \times 10^{15} \text{cm}^{-2}$ Sn implant in GaAs substrates with different doping levels. Annealed 30 min at 900°C .

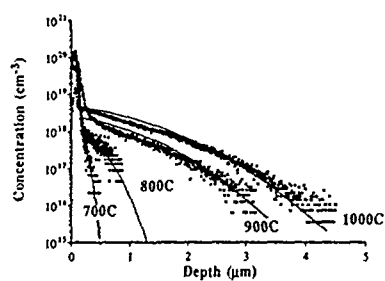


Figure 2. SIMS and calculated profiles for Sn diffusion in n-type substrate, annealed 45 min at 900°C .

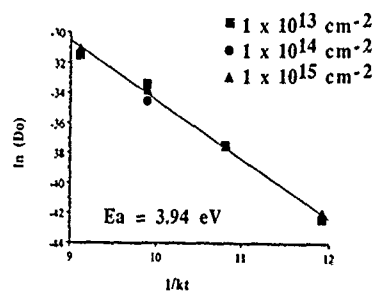


Figure 3. Arrhenius plot of $\ln(D_0)$ vs $1/kT$.

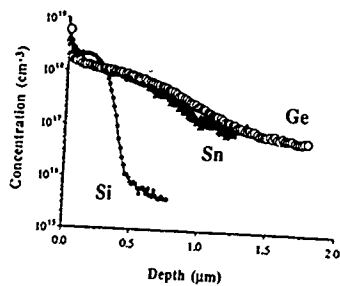


Figure 4. SIMS profiles of 1×10^{14} cm⁻² Si (40 keV), Ge (110 keV), and Sn (185 keV) in Te-doped substrates, annealed 45 min at 1000°C.

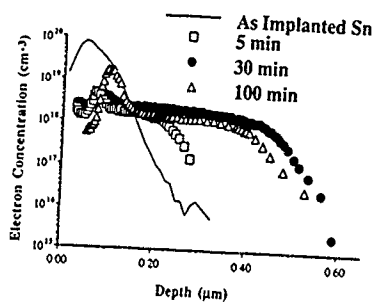


Figure 5. CV Etch profiles for Sn implants annealed at 900°C. 1×10^{15} cm⁻², 185 keV.

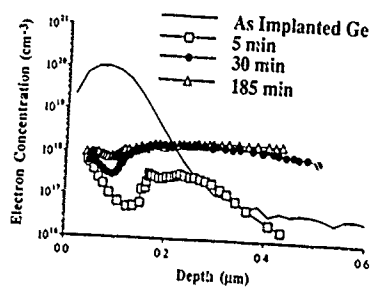


Figure 6. CV Etch profiles for Ge implants annealed at 900°C. 1×10^{15} cm⁻², 110 keV.

term in Equation 1. Figure 2 shows the SIMS and calculated profiles for the $1 \times 10^{15} \text{ cm}^{-2}$ Sn implant in an n-type substrate. Figure 3 is an Arrhenius plot of $\ln(D_0)$ vs $1/kT$. From this plot we extracted an activation energy for Sn diffusion of 3.9 eV, independent of implant dose. If we instead plotted $\ln(D_0/n_i^2)$ vs $1/kT$, the activation energy would be 1.98 eV, which is consistent with the values of 2-3 eV reported in the literature for Sn diffusion from solid sources [3,7]. In the literature the factor of n_i^2 (i.e. the Fermi level dependence) is not considered, resulting in a lower apparent activation energy.

Figure 4 shows SIMS profiles for Sn, Si and Ge implanted at a dose of $1 \times 10^{14} \text{ cm}^{-2}$ into a Te-doped substrate. The implant energies were 185, 40 and 110 keV, respectively, resulting in approximately the same R_p of 1000 Å. After a 45 minute furnace anneal at 1000°C, Sn and Ge have diffused the same distance, while Si has diffused very little. The Ge and Sn profiles are complementary error functions, indicating a constant diffusivity. Clearly the Si diffusivity is suppressed, even in the high n-type background.

Polaron CV Etch measurements were made for $1 \times 10^{15} \text{ cm}^{-2}$ Sn and Ge implants into LEC semi-insulating substrates, annealed for 5, 30 and 100 minutes at 900°C. The results are shown in Figures 5 and 6. In both cases the maximum carrier concentration outside the implanted region was about $1 \times 10^{18} \text{ cm}^{-3}$. However, significantly different profiles were found within the as-implanted region. The Sn CV profiles show a sharp peak in carrier concentration (about $7 \times 10^{18} \text{ cm}^{-3}$) just beyond R_p . The Ge profile shows a dip in the carrier concentration at the same depth. Apparently Sn exhibits excessive Ga-site occupation in the vicinity of R_p which increases with time, while Ge exhibits an initially decreased Ga-site occupation which increases with time. These two trends are consistent with each other, but we have not seen similar peaks or dips in carrier concentration for Si implants. Since Si is expected to cause the least damage on implantation, this finding is consistent with a damage-controlled activation mechanism in the region of the implant. This may be evidence that the diffusion of dopant into the bulk depends on its site distribution within the implanted region.

CONCLUSIONS

Both Sn and Ge diffuse extensively when implanted in GaAs, while Si does not. An activation energy of 3.9 eV was extracted from Sn diffusion profiles in n-type GaAs. Damage may be affecting activation of Sn and Ge in the implanted region as well as controlling diffusion deeper into the substrate.

REFERENCES

1. J.J.Murray, M.D.Deal and D.A.Stevenson, accepted for publication in Appl. Phys. Lett.
2. T.E.Shim, T.Itoh and Y.Yamamoto, J. Appl. Phys., **61**, 4635 (1987).
3. B. Tuck and M.H.Badawi, J.Phys. D, **11**, 2541 (1978).
4. S.Y.Chiang and G.L.Pearson, J. Appl. Phys. **46**, 2986 (1975).
5. G.A.Baraff and M.Schluter, Phys. Rev. Lett. **55**, 1327 (1985).
6. T.Y.Tan and U.Gosele, Mts. Sci. and Eng. **B1**, 47 (1988).
8. B.Goldstein and H.Keller, J. Appl. Phys **32**, 1180 (1961)

ACKNOWLEDGEMENTS

We thank R. Wilson at Hughes Research Laboratories for helpful discussions, as well as T. W. Sigmon at Stanford. This work was funded by DARPA.

THE ROLE OF CHARGED POINT DEFECTS ON THE DIFFUSION BEHAVIOR OF SILICON IN GaAs

Jeffrey J. Murray^{a)}, Michael D. Deal^{b)} and David A. Stevenson^{a)}

a) Department of Materials Science and Engineering

b) Center For Integrated Systems

Stanford University, Stanford CA 94305

ABSTRACT

A multilayered Si doped MBE structure was used to study the effective diffusivity of Si and the results are modeled with an $(n/n_i)^2$ dependence over the temperature range of 750°C - 950°C. An activation energy, E_a , of 4.0 eV is obtained which is higher than normally reported in the literature. This higher E_a value results from appropriate accounting of the temperature dependence of n_i , which is often neglected in the expression for D_{eff} . Si diffusion at a buried n^+/n^{++} junction of a MOCVD grown structure also follows an $(n/n_i)^2$ dependence. These results support a Fermi-level model of Si diffusion in GaAs and suggest that the local point defect chemistry of the GaAs, through Si doping, is responsible for this diffusion behavior, regardless of the proximity to the surface.

INTRODUCTION

Several models for Si diffusion in GaAs are proposed with recent papers focusing on a Fermi-level model to explain the Si diffusion behavior [1-4]. In this model, the point defect responsible for Si transport through the GaAs lattice is a charged gallium vacancy, V_{Ga}^{m+} , with m assigned a value of three by several authors [3, 5]. Following this assumption, an effective Si diffusivity from the Fermi-level model exhibits some form of $(n/n_i)^{m+}$ dependence [3]. This model can be confirmed and refined by obtaining more experimental information and modeling Si diffusion behavior at several well characterized electron concentrations. We have performed such a study using a novel MBE grown structure with well controlled plateaus of Si doping which range from 8×10^{16} Si/cm³ to 5×10^{19} Si/cm³ and known electron concentrations at each of these plateaus.

EXPERIMENTAL

In order to study the influence of doping level upon Si diffusion, we fabricated a novel MBE structure, grown at 580°C, consisting of a series of thin layers with different Si concentration levels on a semi-insulating substrate as shown in Fig. 1. This structure differs from most previous studies since Si is incorporated during homoepitaxial growth rather than from a surface source [6-8]. Each plateau has a constant Si doping concentration and all are approximately 380nm thick with the exception of the layer closest to the substrate, 8×10^{16} Si/cm³, which is approximately 760nm thick. The top ~70nm cap layer is undoped GaAs. A

photoelectrochemical C-V profile of this structure determined a constant carrier concentration of $4 \times 10^{18} \text{ cm}^{-3}$ over the first three layers (referenced from the surface). All the layers beyond the first three have the same carrier concentration as the Si atomic concentration.

The samples were encapsulated with a 50nm PECVD nitride prior to diffusion anneals, which were performed in a hot wall furnace with flowing forming gas. The nitride layer was subsequently removed and the resulting silicon concentration profile was measured using SIMS.

RESULTS AND DISCUSSION

Figures 1 and 2 show the Si concentration profiles from SIMS measurements for the as-grown structure and after annealing for 800°C and 950°C, respectively. Under extrinsic conditions and diffusion governed by gallium vacancies, the effective diffusivity of Si in GaAs is described by the following equation [3]:

$$D_{\text{eff}} = D_{\text{V}_{\text{Ga}}}^0 + \sum_m D_{\text{V}_{\text{Ga}}}^m \left(\frac{n}{n_i} \right)^{m-1} \quad (1)$$

where m represents the possible charge states of the gallium vacancy. The experimental diffusion profiles were fit with SUPREM 3.5, a GaAs process simulator, [9] and the best fit to the above expression was obtained with a single $(n/n_i)^2$ term. (In calculating n_i values, SUPREM 3.5 uses the temperature dependent expressions given by Blakemore [10].) The SUPREM 3.5 simulated profiles are superimposed with the SIMS data in the corresponding figures, Figs. 3 and 4. We also attempted to fit the data with both an (n/n_i) and an $(n/n_i)^3$ model but could not obtain a good fit over the entire temperature range of our experiment, 750°C - 950°C. Assuming that:

$$D_{\text{eff}} = D_0 \left(\frac{n}{n_i} \right)^2 \exp \left(-\frac{E_a}{kT} \right) \quad (2)$$

we have determined an activation energy for Si diffusion of 4.0 eV by plotting $[D_{\text{eff}} / (n/n_i)^2]$ against $1/T$; as shown in Fig. 5. If the temperature dependence of n_i is neglected, one obtains a net activation energy of 1.9 eV. This is close to values in the literature, which range from 2.4 - 2.65 eV [6,8,11]; these values normally do not account for the (n/n_i) dependence and as a result neglect the temperature dependence of n_i .

The $(n/n_i)^2$ dependence is most clearly shown in the 950°C anneal case. Significant diffusion is observed at high Si concentrations (large n/n_i values) while no diffusion is observed at the lower concentrations (i.e. at the $8 \times 10^{16} \text{ Si/cm}^3$ / semi-insulating GaAs junction). This is predicted from an $(n/n_i)^2$ dependence for these concentrations at this temperature.

We have applied the $(n/n_i)^2$ dependence to a reported D_{eff} of $7 \times 10^{-13} \text{ cm}^2/\text{sec}$. from previous work with a buried n^+/n^{++} junction grown by MOCVD and annealed at 850°C [12] with diffusion occurring far from the surface ($\sim 3.2 \mu\text{m}$). This data point has been added to our activation energy plot, Fig. 5 and fits well with the $(n/n_i)^2$ data from the MBE experiment. These results emphasize that the local point defect chemistry of the GaAs is the controlling factor for Si diffusion regardless of whether the high local Si concentration is near the surface (MBE sample) or deep within the sample (MOCVD results).

There may be an additional dependence of the effective Si diffusivity on n if the ratio of mobile Si to the total Si changes as a function of n [4,13]. For example if only Si on Ga sites

are mobile, but as n increases more Si resides on As sites, then the effective Si diffusivity will also include this n dependence. As a result, we can not conclude from a net effective diffusivity that follows an $(n/n_i)^2$ dependency that diffusion necessarily occurs via a doubly charged gallium vacancy, V_{Ga}^{2-} .

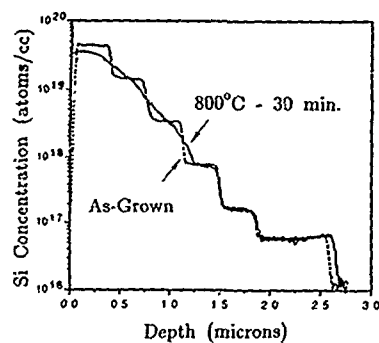


Fig. 1 SIMS depth profile of MBE sample, as-grown and after 800°C - 30' anneal.

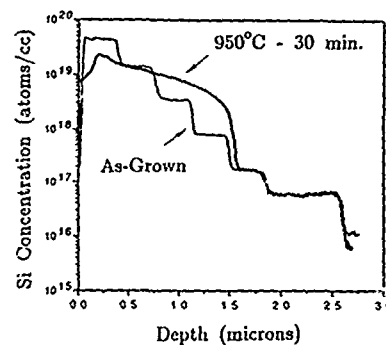


Fig. 2 SIMS depth profile of MBE sample, as-grown and after 950°C - 30' anneal.

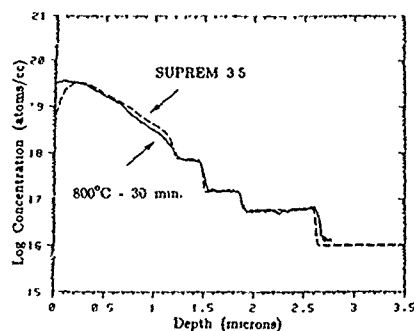


Fig. 3 Comparison of 800°C SIMS data with SUPREM 3.5 fit using an $(n/n_i)^2$ dependence.

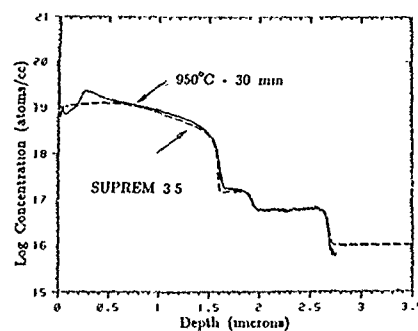


Fig. 4 Comparison of 950°C SIMS data with SUPREM 3.5 fit using an $(n/n_i)^2$ dependence.

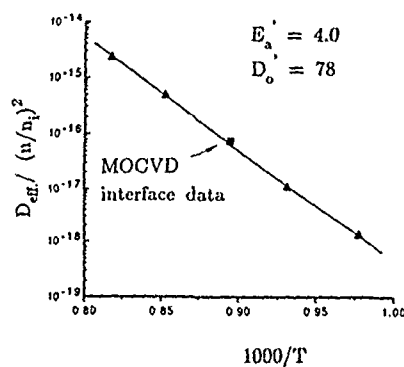


Fig. 5 Activation energy plot obtained by plotting $D_{eff}/(n/n_i)^2$ vs. $1000/T$.

SUMMARY

Experimental data from a Si doped homoepitaxially grown MBE structure with well defined Si and carrier concentrations was fit with SUPREM 3.5. These experiments establish the Fermi-level effect on Si diffusion in GaAs by fitting Si diffusion profiles with an $(n/n_i)^2$ model. Using this model an activation energy of 4.0 eV was calculated which includes the temperature dependence of n_i . An effective diffusivity proportional to $(n/n_i)^2$ fit the data better than either an (n/n_i) or $(n/n_i)^3$ model.

ACKNOWLEDGEMENTS

The authors wish to acknowledge S. Nozaki from Intel Corporation for providing the MBE grown sample as well as helpful discussions with E.L. Allen, H.G. Robinson and L.S. Vanasupa. This work has been supported through the Defense Advanced Research Projects Agency.

REFERENCES

- 1 D. G. Deppe, N. Holonyak, Jr., F. A. Kish, and J. E. Baker, Appl. Phys. Lett. **50**, 998 (1987).
- 2 D. G. Deppe, N. Holonyak, Jr., and J. E. Baker, Appl. Phys. Lett. **52**, 129 (1988).
- 3 T. Y. Tan and U. M. Gösele, Mater. Science and Eng. **B1**, 47, (1988).
- 4 S. Yu, U. M. Gösele and T. Y. Tan, J. Appl. Phys. **66**, 2952 (1989).
- 5 P. Mei, H.W. Yoon, T. Venkatesan, S. A. Schwarz, and J. P. Harbison, Appl. Phys. Lett. **50**, 1823 (1987).
- 6 M.E. Greiner and J.F. Gibbons, Appl. Phys. Lett. **44**, 705 (1984).
- 7 K. H. Lee, H.-H. Park, and D. A. Stevenson, J. Appl. Phys. **65**, 1048 (1989).
- 8 K. L. Kavanagh, J. W. Mayer, C. W. Magee, J. Sheets, J. Tong and J. M. Woodall, Appl. Phys. Lett. **47**, 1208 (1985).
- 9 M.D. Deal, S.E. Hansen and T.W. Sigmon, IEEE Trans. Computer-Aided Design **8**, 939 (1989).
- 10 J. S. Blakemore, J. Appl. Phys. **53**, 520 (1982).
- 11 E. F. Schubert, J. B. Stark, T.H. Chiu and B. Tell, Appl. Phys. Lett. **53**, 293 (1988).
- 12 J.J. Murray, D.A. Stevenson and M.D. Deal accepted for publication (Nov. 1989) in Appl. Phys. Lett.
- 13 B. Tuck, Introduction To Diffusion in Semiconductors, (Peregrinus, Stevenage, 1974), p. 140.

PART X

Diffusion in Superlattices

IMPURITY-INDUCED LAYER DISORDERING: CURRENT UNDERSTANDING AND AREAS FOR FUTURE INVESTIGATION

L.J. GUIDO* and NICK HOLONYAK, JR.**

*Yale University, Department of Electrical Engineering, Center for Microelectronic Materials and Structures, P O Box 2157 Yale Station, New Haven, CT 06520

**University of Illinois, Electrical Engineering Research Laboratory, Center for Compound Semiconductor Microelectronics, and Materials Research Laboratory, Urbana, IL 61801

ABSTRACT

The purpose of this work is to give an overview of the current phenomenological understanding of impurity-induced layer disordering (IILD). First, we identify key experimental findings such as the influence of the crystal surface-ambient interaction, the Fermi-level effect, and the impurity concentration on Al-Ga interdiffusion. Second, we review the strengths and weaknesses of existing IILD models in consideration of the above mentioned experimental data. Finally, we discuss the pitfalls involved in generalizing the results of individual Al-Ga interdiffusion experiments in order to explain a broader collection of IILD data.

INTRODUCTION

Because of the importance of high-temperature processes in semiconductor device fabrication the self-diffusion of host crystal atoms, e.g., in bulk Ge [1] and GaAs [2], has been studied previously to better understand the mechanisms of impurity diffusion. The recent interest in self-diffusion or interdiffusion phenomena in III-V semiconductors has been stimulated by advances in the epitaxial growth of quantum well heterostructure (QWH) crystals. Growth techniques such as metal organic chemical vapor deposition allow the device designer to replace homojunctions with heterojunctions and thick active layers with quantum wells to improve device performance. In many cases the key to realizing improved device performance is to maintain the as-grown heterointerface abruptness during subsequent high-temperature processing.

The first study of Al-Ga interdiffusion by Chang and Koma [3] focused on the effects of high-temperature As-rich annealing on heterointerface abruptness. The experiment involved a series of GaAs-AlGaAs-GaAs sandwich structures with relatively thick ($\geq 1000\text{\AA}$) undoped epitaxial layers. Post-annealing auger electron spectroscopy (AES) analysis showed that the Al-Ga interdiffusion coefficient ($D_{\text{Al-Ga}}$) is relatively small and

not strongly dependent upon Al mole fraction even at the high temperatures typically employed for impurity diffusion and implant annealing. These results suggested that Al-Ga interdiffusion would not limit QWH device performance.

However, a subsequent experiment by Holonyak and co-workers [4,5] on an AlAs-GaAs superlattice (SL) showed that D_{Al-Ga} is increased markedly by a low-temperature Zn diffusion; hence the phrase impurity-induced layer disordering (IILD). The significance of this discovery is that band-gap engineering can now be achieved selectively in the plane of the epitaxial layers by post-growth processing. In other words, a superlattice crystal with $Al_xGa_{1-x}As$ barriers and GaAs wells of thickness L_b and L_w , respectively, can be layer-averaged by selective masking and impurity diffusion into $Al_yGa_{1-y}As$ with $y \sim xL_b/(L_b + L_w)$. A demonstration of this form of band-gap engineering is given in Fig. 1 by the transmitted light image of an AlAs-GaAs SL that has been masked, Zn-diffused and layer-disordered, and removed from the GaAs substrate [5].

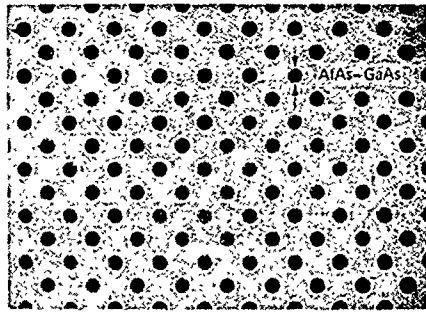


Figure 1: Black-white reproduction of a red-yellow color image showing light transmitted perpendicular to the layers of an AlAs-GaAs SL that has been removed from the GaAs substrate. The $38\mu m$ black (red) dots have been masked against Zn diffusion ($575^\circ C$, 0.5 h) by a patterned layer of Si_3N_4 . The white (yellow) region has been converted into higher-gap $Al_{0.77}Ga_{0.23}As$ by Zn-induced layer averaging. (From Holonyak et al. [5].)

Over the next few years most layer disordering experiments involved three issues: (1) the use of ion implantation for increased control of the impurity type, concentration, and depth profile [6]; (2) the demonstration of enhanced host atom interdiffusion in other III-V QWH crystals [7]; and (3) the use of IILD for device fabrication purposes. Much of the device work focused on employing IILD to define buried heterostructure QW laser diodes. By performing an acceptor (Zn) diffusion into a n-p QWH laser crystal [8] or a donor (Si) diffusion into a p-n crystal [9], good current confinement and real index guiding are provided for low threshold single-stripe lasers [10] or for high power multi-stripe laser arrays [11]. The scanning electron microscope (SEM) image of Fig. 2 shows a typical cleaved cross-section of such a Si-O diffusion-defined laser diode array [12]. For a more detailed accounting of the earlier work than is possible here, see the review by Deppe and Holonyak [13].

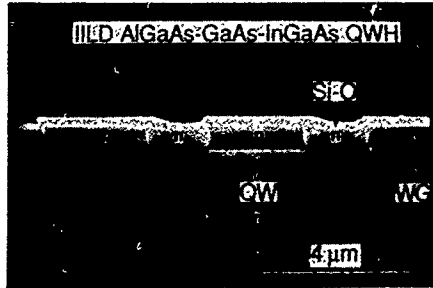


Figure 2: SEM image of a Si-O IILD patterned AlGaAs-GaAs-InGaAs QW laser diode array. Current injection is confined to $3\mu\text{m}$ vertical p-n junctions by Si_3N_4 masking. The Si-O diffusion (825°C , 12h) forms lateral higher-gap current blocking p-n junctions. The crystal adjacent to each laser stripe is of higher band-gap and lower refractive index. (From Major et al. [12].)

Al-Ga INTERDIFFUSION ENHANCEMENT

The earlier experiments have identified workable approaches for the study of IILD by post-growth impurity diffusion or implantation of undoped QWHs, and by dopant incorporation during crystal growth. Unfortunately, the first two methods tend to obscure the primary issue: to determine whether the impurity-enhancement of interdiffusion is caused by a global crystal Fermi-level effect, or a local perturbation of the Coulomb potential. For the case of ion implantation, it is difficult to quantify the effects of lattice damage and defect agglomeration. For impurity diffusion, a large atomic flux occurs simultaneously with electronic compensation. Consequently, the impurity concentration is typically much larger than the net carrier concentration. These factors complicate the interpretation of IILD data.

An example of this complexity is given by the secondary ion mass spectroscopy (SIMS) data shown in Fig. 3 for a p-type SL doped with carbon in the AlGaAs barriers. The superlattice heterointerfaces are stable against annealing (only) at 825°C for 24h. However, a much lower temperature Zn acceptor diffusion causes complete layer intermixing of the AlGaAs-GaAs heterointerfaces [14]. The key point here is that it is not appropriate to indiscriminately mix data from diffusion-, implantation-, and annealing-induced layer disordering experiments. In this work, we simplify matters by considering only high-temperature annealing experiments on nominally undoped AlGaAs-GaAs QWH crystals, or on crystals that have been intentionally doped during crystal growth.

Except for the unlikely case of direct host atom interchange, the Al-Ga interdiffusion mechanism must involve native defects. Therefore, the interdiffusion coefficient can be separated into two parts: (1) the jump probability, which depends on the native defect concentration; and (2) the jump activation energy, which is the potential energy barrier that a host crystal atom must overcome to exchange lattice sites [15]. For illustration purposes, we assume that Al-Ga interdiffusion is similar to Ga self-diffusion, and that self-diffusion occurs via a Column III vacancy (V_{III}) mechanism. In this case, the self-diffusion coefficient is enhanced by an impurity-induced increase in the V_{III} concentration ($[]$) or decrease in the activation energy barrier. The temperature dependence of D_{Ga} reflects both the vacancy formation enthalpy (H_f) and the jump activation enthalpy (H_j). These two terms combine to yield a single effective activation enthalpy (H_{eff}) for self-diffusion [16].

An example of this type of diffusion process is given by the work of Valenta and Ramasastri on self-diffusion in Ge [1]. The Arrhenius plots of D_{Ge} show that the magnitude

of self-diffusion is larger, and the slope smaller, for n-type versus p-type Ge crystals. Following the work of Reiss [17] they argued that the V_{Ge} acceptor is more soluble in an n-type crystal because of a lower free energy of formation (i.e., the Fermi-level effect). As a result the jump probability is increased, and H_{eff} is decreased, in agreement with the data.

The work of Kawabe et al. [18] provided the first evidence that a similar argument might also apply to Al-Ga interdiffusion. The AES profile of Fig. 4 demonstrates that D_{Al-Ga} is enhanced in the presence of Si-doping, except for layers in which the Be-doping density exceeds the Si-density. Tan and Gösele [19] proposed a model to explain these and other IILD data based on the premise that the above mentioned Fermi-level effect increases the concentration of V_{III} acceptor and donor defects in n- and p-type crystals, respectively.

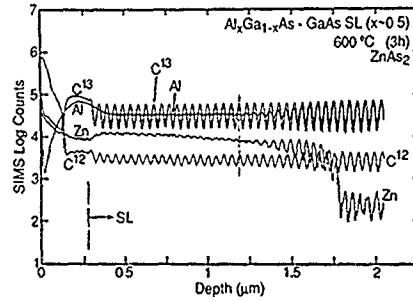


Figure 3: SIMS data for a ^{13}C -doped $\text{Al}_{0.50}\text{Ga}_{0.50}\text{As}$ -GaAs SL after Zn-IILD. Separate high temperature annealing experiments show that Al-Ga interdiffusion is not enhanced by carbon doping itself. Lower temperature Zn diffusion causes complete averaging of Column III sublattice atoms (From Guido et al. [14].)

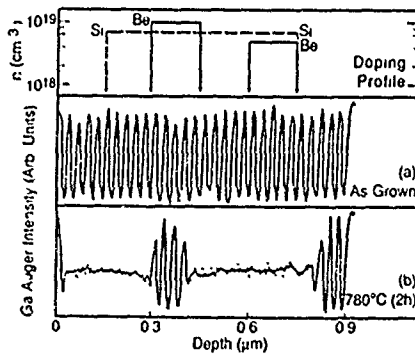


Figure 4: AES data for a Be and Si co-doped AlAs-GaAs SL annealed under the equilibrium GaAs vapor pressure. The Ga signal modulation is eliminated by Si-enhanced Al-Ga interdiffusion. (Redrawn from Kawabe et al. [18].)

Of course Al-Ga interdiffusion is complicated by the inequivalence of the cation and anion sublattices. The type and concentration of the dominant native defect for IILD is not only a function of temperature, but also depends on the deviation of the crystal from stoichiometry. This raises the question of whether the requisite native defects are incorporated during crystal growth, generated during annealing via bulk processes, or formed by the equilibration of the crystal surface with the anneal ambient. The transmission electron microscope (TEM) data shown in Figs. 5 and 6 demonstrate that Al-Ga interdiffusion is strongly influenced by the crystal surface encapsulant layer [20,21]. The Si_3N_4 -cap shown in Fig. 5 prevents Al and Ga out-diffusion and isolates the crystal from the anneal ambient. The SiO_2 -cap shown in Fig. 6 is porous to Al and Ga, and the As overpressure, causing an increase in $[V_{III}]$ for layer disordering.

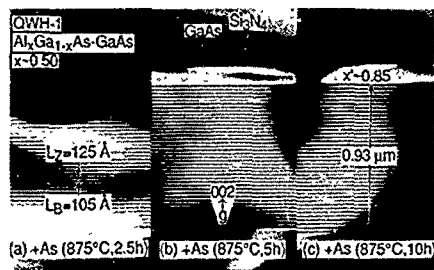


Figure 5: TEM images of an undoped $\text{Al}_{0.50}\text{Ga}_{0.50}\text{As} - \text{GaAs}$ SL after As-rich (+ As) annealing. The crystal surface is isolated from the anneal ambient by a Si_3N_4 - cap. There is no increase in Al-Ga interdiffusion with annealing time. (From Guido et al. [21].)

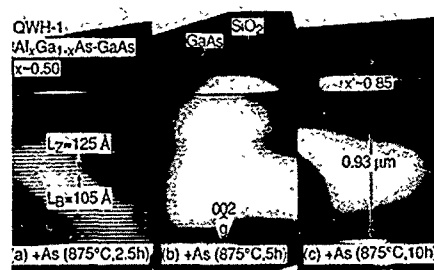


Figure 6: TEM images for the SL of Fig. 5, except with a SiO_2 cap layer. The superlattice is almost completely layer-averaged after a 10h As-rich (+ As) anneal. (From Guido et al. [21].)

The photoluminescence (PL) data shown in Fig. 7 suggest that two different native defects are responsible for IILD because the annealing-induced energy shift is not a simple increasing or decreasing function of the As overpressure [20,21]. The trend in PL energy shift versus annealing ambient has been independently confirmed by Furuya et al. [22]. This interpretation of the PL data is substantiated by the report of Hsieh et al. [23] on the temperature dependence of $D_{\text{Al-Ga}}$ under Ga-rich and As-rich annealing conditions. Both the magnitude and slope of $D_{\text{Al-Ga}}$ are reduced by annealing in a Ga-rich ambient. If the anneal ambient influenced only the neutral V_{III} concentration, one would expect H_{eff} to be identical for the Ga-rich and As-rich cases. The fact that the H_{eff} differs significantly supports our claim that two different native defects are involved in Al-Ga interdiffusion.

LAYER DISORDERING MODELS

The two most advanced models for IILD rely on the concept of Fermi-level control of the solubility of charged native defects [17]. The latest model proposed by Tan and Gösele [24] differs from their original model in that the triply ionized V_{III} acceptor and the

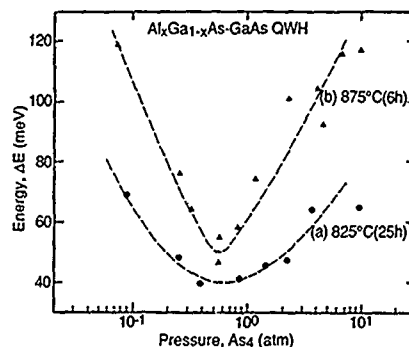


Figure 7: PL data (77K) for a Se-doped AlGaAs-GaAs QWH crystal showing the relationship between the Al-Ga interdiffusion-induced ΔE and the anneal ambient. (From Guido et al. [21].)

Column III self-interstitial (I_{III}) donor are identified as the dominant native defects. The assignment of the triple charge state for V_{III} is based on the data of Mei et al. [25] shown in Fig. 8. The original D_{Al-Ga} data for a Si-doped AlAs-GaAs superlattice has been normalized by Tan and Gösele using a fitted value for the intrinsic Al-Ga interdiffusion coefficient [24]. This treatment yields a third-order power law dependence for D_{Al-Ga} when plotted against the normalized electron concentration as shown in Fig. 9. To date there is no such quantitative data for p-type crystals to support the Column III self-interstitial assignment.

In an independent effort, Deppe et al. [26,27] reached a similar conclusion regarding the Fermi-level effect and the native defects responsible for IILD. However, their model differs from that of Tan and Gösele because it also considers the important contribution of the anneal ambient. The arguments of Deppe et al. are supported by the TEM cross-sections shown in Figs. 10 and 11. The data in Fig. 10 show a large increase in D_{Al-Ga} only for the combination of a Se-doped (n-type) crystal with an As-rich anneal ambient. In contrast, the Mg-doped (p-type) superlattice of Fig. 11 requires a Ga-rich anneal ambient for enhanced Al-Ga interdiffusion.

One shortcoming of these models is the implication that all acceptor and donor impurities have an identical effect on Al-Ga interdiffusion. Recent reports suggest that there is also a local enhancement of interdiffusion by the impurity atom itself (perhaps because of a reduced H_j). The latest work of Mei et al. [28] on a Te-doped AlAs-GaAs SL shows that H_{eff} is reduced from the $\sim 4\text{eV}$ reported previously for the Si-doped case [25] to $\sim 3\text{eV}$. In addition, D_{Al-Ga} exhibits a linear dependence on the electron concentration in sharp contrast to the data shown in Fig 9. A recent report for a p-type AlGaAs-GaAs SL doped with carbon demonstrates that Al-Ga interdiffusion is not enhanced by this combination of p-type dopant and Ga-rich anneal ambient [29]. The TEM cross-sections in Fig. 12 show that the superlattice heterointerfaces are stable against an even more rigorous anneal than for the Mg-doped SL case (Fig. 11).

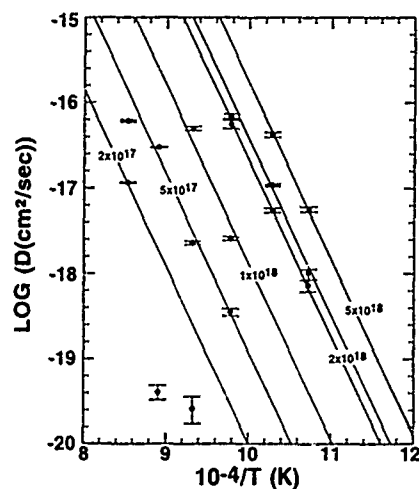


Figure 8: Arrhenius plots of D_{Al-Ga} for a Si-doped AlAs-GaAs SL annealed under the equilibrium GaAs vapor pressure. (From Mei et al. [25].)

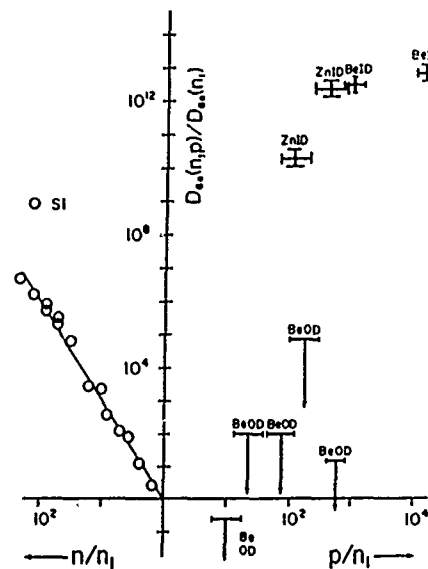


Figure 9: Plot of the normalized D_{Al-Ga} versus impurity concentration derived from various layer disordering experiments on n-type (left) and p-type (right) AlGaAs-GaAs QWH crystals. (From Tan and Gösele [24].)

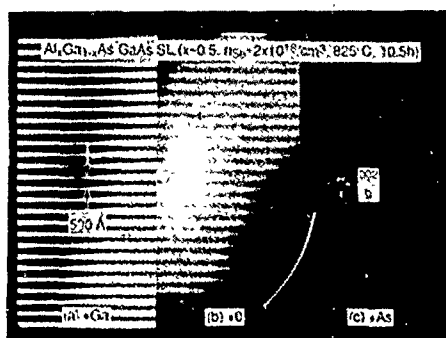


Figure 10: TEM images of a Se-doped $Al_{0.50}Ga_{0.50}As - GaAs$ SL after annealing under Ga-rich (+ Ga, + 0) and As-rich (+ As) conditions. (From Deppe et al. [27].)

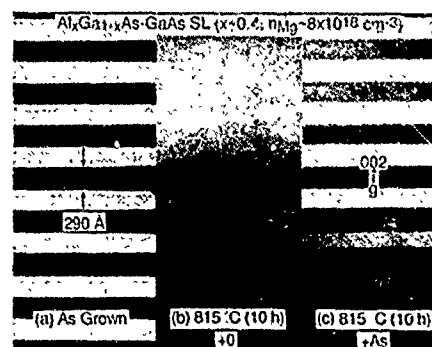


Figure 11: TEM images of a Mg-doped $Al_{0.40}Ga_{0.60}As - GaAs$ SL after Ga-rich (+ 0) and As-rich (+ As) annealing. (From Deppe et al. [26].)

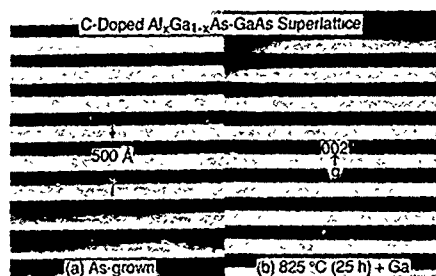


Figure 12: TEM images of a C-doped $Al_{0.60}Ga_{0.40}As - GaAs$ SL crystal ($p_C \sim 10^{18} cm^{-3}$) after Ga-rich (+ Ga) annealing. (From Guido et al. [29].)

For further illustration, let us reconsider the D_{Al-Ga} data of Mei et al. [25]. The measured value of H_{eff} ($\sim 4eV$) is considerably lower than the $\sim 6eV$ reported for undoped crystals [23,30]. The discrepancy could possibly be explained by invoking the Fermi-level argument. The formation enthalpy H_f is expected to be lower for a triply ionized V_{III} in n-type crystal than for a neutral V_{III} in undoped crystal. However, this approach fails to account for the constancy of H_{eff} with increasing Si concentration that conflicts with the report for Ge self-diffusion [1]. If we assume that the change in Fermi-level is negligible over the narrow Si doping range, the resulting change in H_{eff} may not be easily determined. The inconsistency here is that the Fermi-level models predict that impurity enhancement of D_{Al-Ga} is caused by a large increase in $[V_{III}]$. Following this argument, we expect a significant decrease in H_f (and in H_{eff}) which should be discernable in the Arrhenius plots of Fig. 8.

Another difficulty in interpreting IILD data is that experiments are typically performed under non-equilibrium conditions. The consequences of this fact have been demonstrated in a report on the depth-dependence of Al-Ga interdiffusion [31]. The interdiffusion-induced PL energy shift data shown in Fig. 13 indicate that D_{Al-Ga} is largest near the crystal surface. These PL data combined with the dependence of Al-Ga interdiffusion on surface encapsulation and anneal ambient [20,21] show that caution must be exercised when comparing data from different IILD experiments. To demonstrate the severity of this problem we show a series of Arrhenius plots for Ga self-diffusion and Al-Ga interdiffusion (Fig. 14). These data could easily be fitted by a single straight line, and yet the individual reports indicate a large variation in the measured values of H_{eff} [2,3,25,30,32]. The variation in H_{eff} is undoubtedly caused by real differences in QWH crystal design, doping, and annealing conditions.

SUMMARY

To summarize, we have shown that there is strong experimental evidence of the influence of the Fermi-level, and the crystal surface deviation from stoichiometry on Al-Ga interdiffusion. These trends are partially described by existing IILD models, but more consideration must be given to the local influence of impurity atoms on the potential energy barrier for Al-Ga interchange. Further understanding can be achieved by isolating the separate contributions to enhanced Al-Ga interdiffusion.

Figure 13: PL data for an undoped AlGaAs-GaAs QWH crystal showing the Al-Ga interdiffusion-induced energy shift after As-rich annealing at 825°C for 12h. (From Guido et al. [31].)

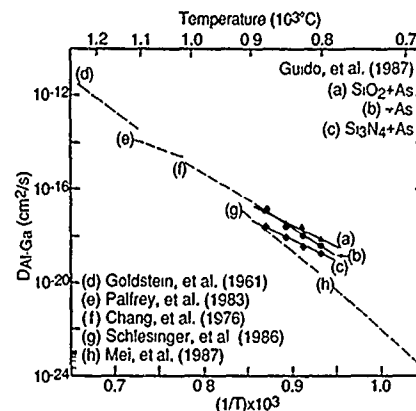
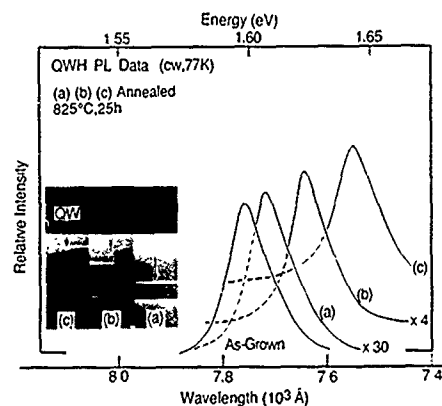


Figure 14: Arrhenius plots of Ga self-diffusion and Al-Ga interdiffusion coefficients for crystals annealed under various surface encapsulant and ambient conditions. (From Guido et al. [21].)

ACKNOWLEDGEMENTS

The authors are grateful to J.S. Major, Jr. (University of Illinois) for contributions to the experimental work; and to Arlene Ciociola and Bill Sacco (Yale University); and R.T. Gladin and B.L. Payne (University of Illinois) for assistance in manuscript preparation.

REFERENCES

1. M.W. Valenta and C. Ramasastry, Phys. Rev. **106**, 73 (1957).
2. B. Goldstein, Phys. Rev. **121**, 1305 (1961).
3. L.L. Chang and A. Koma, Appl. Phys. Lett. **29**, 138 (1976).
4. W.D. Laidig, N. Holonyak, Jr., M.D. Camras, K. Hess, J.J. Coleman, P.D. Dapkus, and J. Bardeen, Appl. Phys. Lett. **38**, 776 (1981).
5. N. Holonyak, Jr., W.D. Laidig, M.D. Camras, J.J. Coleman, and P.D. Dapkus, Appl. Phys. Lett. **39**, 102 (1981).
6. J.J. Coleman, P.D. Dapkus, C.G. Kirkpatrick, M.D. Camras, and N. Holonyak, Jr., Appl. Phys. Lett. **40**, 904 (1982).
7. M.D. Camras, N. Holonyak, Jr., K. Hess, M.J. Ludowise, W.T. Dietze, and C.R. Lewis, Appl. Phys. Lett. **42**, 185 (1983).
8. T. Fukuzawa, S. Semura, H. Saito, T. Ohta, Y. Uchida, and H. Nakashima, Appl. Phys. Lett. **45**, 1 (1984).

9. K. Meehan, N. Holonyak, Jr., J.M. Brown, M.A. Nixon, P. Gavrilovic, and R.D. Burnham, *Appl. Phys. Lett.* **45**, 549 (1984).
10. D.G. Deppe, K.C. Hsieh, N. Holonyak, Jr., R.D. Burnham, and R.L. Thornton, *J. Appl. Phys.* **58**, 4515 (1985).
11. P. Gavrilovic, K. Meehan, J.E. Epler, N. Holonyak, Jr., R.D. Burnham, R.L. Thornton, and W. Streifer, *Appl. Phys. Lett.* **46**, 857 (1985).
12. J.S. Major, Jr., D.C. Hall, L.J. Guido, N. Holonyak, Jr., P. Gavrilovic, K. Meehan, J.E. Williams, and W. Stutius, *Appl. Phys. Lett.* **55**, 271 (1989).
13. D.G. Deppe and N. Holonyak, Jr., *J. Appl. Phys.* **64**, R93 (1988).
14. L.J. Guido, J.S. Major, Jr., J.E. Baker, N. Holonyak, Jr., B.T. Cunningham, and G.E. Stillman, unpublished data.
15. C. Zener, *J. Appl. Phys.* **22**, 372 (1951).
16. R.P. Johnson, *Phys. Rev.* **56**, 814 (1939).
17. H. Reiss, *J. Chem. Phys.* **21**, 1209 (1953).
18. M. Kawabe, N. Shimizu, F. Hasegawa, and Y. Nannichi, *Appl. Phys. Lett.* **46**, 849 (1985).
19. T.Y. Tan and U. Gösele, *J. Appl. Phys.* **61**, 1841 (1987).
20. L.J. Guido, N. Holonyak, Jr., K.C. Hsieh, R.W. Kaliski, W.E. Plano, R.D. Burnham, R.L. Thornton, J.E. Epler, and T.L. Paoli, *J. Appl. Phys.* **61**, 1372 (1987).
21. L.J. Guido, N. Holonyak, Jr., and K.C. Hsieh, in *Proceedings of the 15th International Symposium on GaAs and Related Compounds*, edited by J.S. Harris (Inst. Phys. Conf. Ser. **96**, Bristol and Philadelphia, 1989), pp. 353-358.
22. A. Furuya, O. Wada, A. Takamori, and H. Hashimoto, *Jap. J. Appl. Phys.* **26**, L926 (1987).
23. K.Y. Hsieh, Y.C. Lo, J.H. Lee, and R.M. Kolbas, in *Proceedings of the 15th International Symposium on GaAs and Related Compounds*, edited by J.S. Harris (Inst. Phys. Conf. Ser. **96**, Bristol and Philadelphia, 1989), pp. 393-396.
24. T.Y. Tan and U. Gösele, *Appl. Phys. Lett.* **52**, 1240 (1988).
25. P. Mei, H.W. Yoon, T. Venkatesan, S.A. Schwarz, and J.P. Harbison, *Appl. Phys. Lett.* **50**, 1823 (1987).
26. D.G. Deppe, N. Holonyak, Jr., W.E. Plano, V.M. Robbins, J.M. Dallesasse, K.C. Hsieh, and J.E. Baker, *J. Appl. Phys.* **64**, 1838 (1988).
27. D.G. Deppe, N. Holonyak, Jr., K.C. Hsieh, P. Gavrilovic, W. Stutius, and J. Williams, *Appl. Phys. Lett.* **51**, 581 (1987).
28. P. Mei, S.A. Schwarz, T. Venkatesan, C.L. Schwartz, and E. Colas, *J. Appl. Phys.* **65**, 2165 (1989).

29. L.J. Guido, B.T. Cunningham, D.W. Nam, K.C. Hsieh, W.E. Plano, J.S. Major, Jr., E.J. Vesely, A.R. Sugg, N. Holonyak, Jr., and G.E. Stillman, unpublished data.
30. T.E. Schlesinger and T. Kuech, Appl. Phys. Lett. 49, 519 (1986).
31. L.J. Guido, N. Holonyak, Jr., K.C. Hsieh, and J.E. Baker, Appl. Phys. Lett. 54, 262 (1989).
32. H.D. Palfrey, M. Brown, and A.F.W. Willoughby, J. Electrochem. Soc. 128, 2224 (1981).

BEHAVIOR OF DOPANT-RELATED DEFECTS IN AlGaAs SUPERLATTICES

N.D. Theodore, P. Mei*, S.A. Schwarz**, C.B. Carter, C. Palmstrom**,
J.P. Harbison** and L.T. Florez**

Cornell University, Department of Materials Science and Engineering, Bard Hall,
Ithaca, NY 14853; * Columbia University, Department of Electrical Engineering,
500 W. 120th St., New York, NY 10027; **Bell Communications Research Inc.,
331 Newman Springs Rd., Redbank, NJ 07751.

ABSTRACT

During the course of investigation of the mixing of highly silicon-doped GaAs/AlAs superlattices, defects such as dislocation loops and Si-rich precipitates were found to form in the specimens. These defects formed at particular doping levels upon annealing of the samples. The presence of the defects can be related to changes in mixing behavior. In the present study, transmission electron microscopy has been used to characterize the defects. Superlattices with varying silicon doping levels were annealed at different temperatures for varying time-periods, to observe the temperature-time behavior of the dislocation loops. The defects aggregate preferentially in the GaAs as opposed to the AlAs in the superlattice. A number of the dislocation-loops were investigated using high-resolution TEM. All the loops observed were interstitial in nature.

INTRODUCTION

Superlattice mixing, induced by a variety of techniques in the AlGaAs system, has been studied extensively [1-15]. The objective has been to obtain regions of different bandgap and mobility integrated on one substrate. Methods used to obtain mixing have included ion-implantation followed by annealing [1-5], diffusion from the surface [6-12], and doping during growth [13-15]. In the AlGaAs system, silicon-induced mixing has been of interest because of the fact that mixing can be obtained at relatively modest doping levels and can be confined to well-defined regions. In a previous study, AlAs/GaAs superlattices doped with Si during molecular beam epitaxy (MBE) growth were characterized after annealing; doping levels ranged from 10^{18} to 10^{20} cm⁻³. The observation of defects related to doping levels in these superlattices has been reported. A correlation has also been reported between the presence of the defects (Si-rich precipitates or dislocation loops) and the inhibition of superlattice mixing [14,15]. In this study, the behavior of the dislocation loops related to doping levels is explored.

EXPERIMENTAL DETAILS

Cross-section TEM specimens were prepared to evaluate the behavior of defects present in these superlattice structures. The structures consisted of 20 periods of alternating AlAs (100Å) and GaAs (400Å) layers grown by MBE on a GaAs substrate. The samples contained three regions doped during growth to 10^{20} , 10^{19} and 10^{18} cm⁻³ Si; each region consisted of four of the AlAs/GaAs periods. Specimens were annealed at temperatures ranging from 650-750°C and for periods of 0.5-3 hours in a H₂:Ar atmosphere; the surface of the sample was maintained in contact with an undoped GaAs wafer. Cross-section TEM specimens were prepared by mechanical thinning and polishing followed by argon ion-milling at liquid-nitrogen temperatures. A JEOL JEM 1200EX transmission electron microscope was used to obtain bright- and dark-field images; (002) reflection were used in order to enhance contrast from the superlattices.

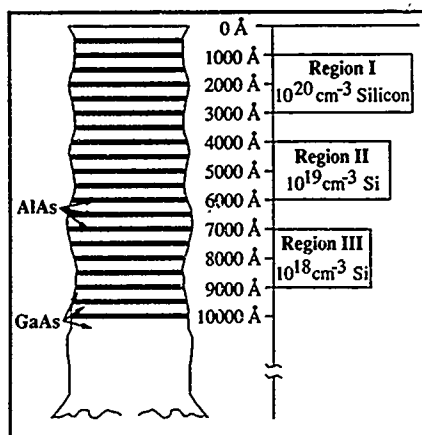


Fig. 1 Schematic of the as-grown superlattice. The left side of the figure shows the 20 periods of alternating AlAs and GaAs layers that comprise the superlattice. The surface of the specimen is at the top of the figure. The right side of the figure shows the corresponding doping levels of the superlattice. Regions I, II and III are doped at 10^{20} , 10^{19} and 10^{18} cm^{-3} Si respectively.

OBSERVATIONS AND DISCUSSION

Figure 1 shows a schematic of the as-grown superlattices. The left side of the figure shows the 20 periods of alternating AlAs and GaAs layers that comprise the superlattice. The surface of the specimen is at the top of the figure. The right side of the figure shows the corresponding doping levels of the superlattice. Note that region I, from 1000 Å to 3000 Å into the specimen is doped to 10^{20} cm^{-3} Si. Region II, from 4000 Å to 6000 Å into the sample, and region III, from 7000 Å to 9000 Å into the sample are doped to 10^{19} cm^{-3} Si and 10^{18} cm^{-3} Si respectively. Figure 2 shows a TEM micrograph of a specimen prior to annealing. Regions I and II are labelled on the micrograph. Notice the good quality of the GaAs and AlAs layers and the absence of extended defects.

Figure 3 presents a TEM micrograph of a specimen annealed at 750°C for 3 hours. Silicon-rich precipitates form in region I. These are discussed elsewhere [16]. Note the presence of dislocation loops in region II. Trace analysis indicates that these loops lie on {110} planes. The defects are induced by the presence of the 10^{19} cm^{-3} doping level of silicon in the superlattices; point defects associated with the doping coalesce during the post-growth anneal to form the dislocation loops. Figures 4 a-c show a series of images of the dislocation loops observed in specimens annealed at different temperatures. Note the increase in size of the loops with increasing temperatures of annealing. The increase in size of the loops is in conformity with the concept of point defects associated with the silicon doping-levels coalescing to form the defects; as annealing temperatures are raised, diffusion-lengths for the point defects (or complexes) increase, and therefore the dimensions of the dislocation loops increase. Observations of these defects in specimens annealed at lower temperatures indicate that the loops are preferentially nucleated at the AlAs/GaAs interfaces. The loops are also observed to form predominantly in GaAs rather than in AlAs. Figure 5 shows a TEM micrograph of a specimen annealed at 700°C for 3

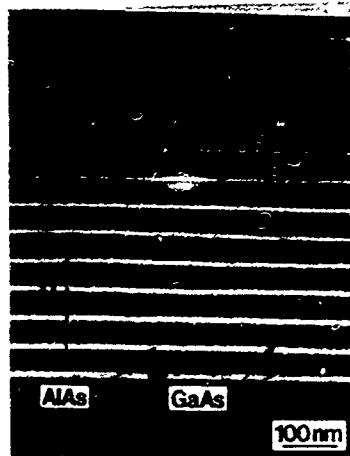


Fig. 2 Cross-section TEM micrograph of a specimen prior to annealing. Regions I and II are doped to 10^{20} and 10^{19} cm^{-3} Si respectively. Notice the good quality of the GaAs and AlAs layers and the absence of extended defects.

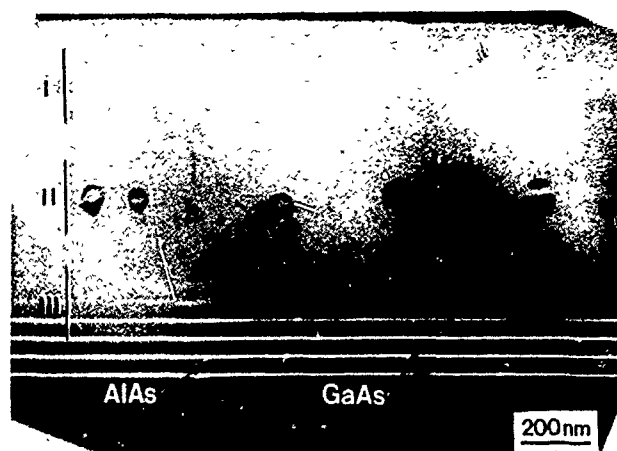


Fig. 3 Cross-section TEM micrograph of Si-doped AlGaAs superlattice specimen annealed at 750°C for 3 hours. Regions I, II and III are doped at 10^{20} , 10^{19} and 10^{18} cm^{-3} Si respectively. Notice the presence of dislocation loops in region II. Trace analysis indicates that these loops lie on $\{110\}$ planes.

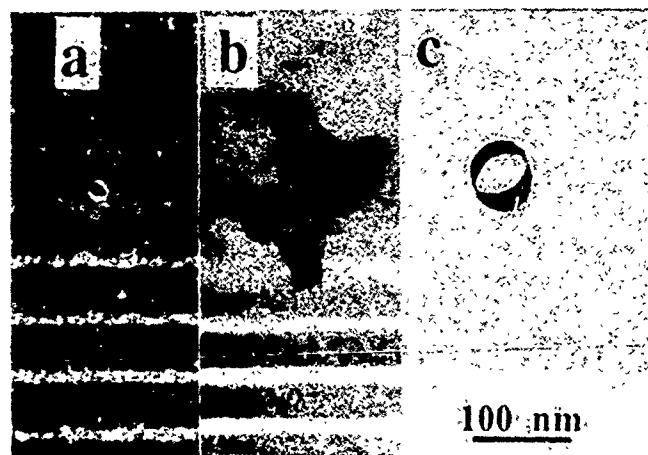


Fig. 4 Cross-section TEM micrographs of loops in specimens annealed for 3 hours at (a) 675°C, (b) 700°C, (c) 750°C. Notice increasing sizes of loops, moving from 675°C to 750°C.

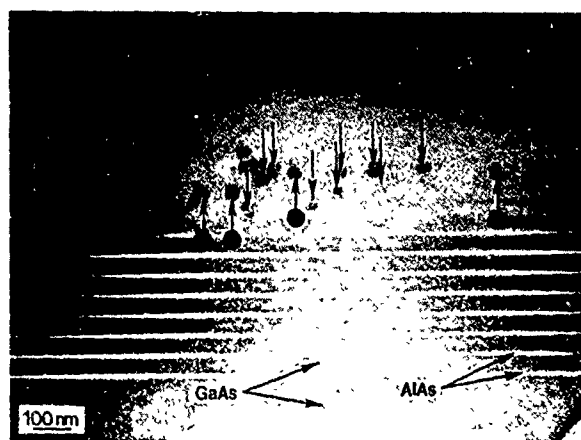


Fig. 5 TEM micrograph of a specimen annealed at 700°C for 3 hours. Arrows pointing downward indicate dislocation loops with their centers lying in GaAs; arrows pointing upward indicate defects centered on AlAs.

hours. Arrows pointing downward indicate defects with their centers lying in GaAs; arrows pointing upward indicate defects centered on AlAs. This preferential segregation of defects could be a result of the stronger bond strength of AlAs (as opposed to GaAs). Work is in progress to confirm this observation.

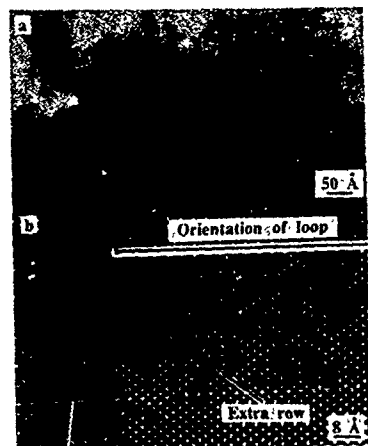


Fig 6 High-resolution TEM micrographs of dislocation-loop observed in doped superlattice. a) Low-magnification image showing the entire loop. b) Higher-magnification processed image of one end of the loop. The orientation of the loop is indicated at the top of the figure. An extra plane of atoms is observed to terminate at the dislocation. This can be seen by sighting down the photograph, in the direction of the arrow (bottom of figure 6). Similar behavior can be observed sighting from the top of the photograph.

In order to determine the vacancy or interstitial nature of the dislocation loops, several defects lying in the edge-on orientation (for 110 cross-section specimens), were investigated using high-resolution TEM. A JEOL JEM 4000EX microscope was used for this purpose, operating at 400 keV. Figure 6 shows micrographs of such a loop. Figure 6a is a low-magnification image showing the entire loop. Figure 6b is a higher-magnification image of one end of the loop. The orientation of the loop is indicated at the top of the figure. An extra plane of atoms is observed to terminate at the dislocation. This can be seen by sighting down the photograph, in the direction of the arrow (bottom of figure 6). Similar behavior can be observed sighting from the top of the photograph. All the loops investigated by high-resolution TEM were interstitial in nature. This is in conformity with the concept of the silicon dopant atoms coalescing to form the extended defects.

SUMMARY

Extended defects are observed to form upon annealing in highly silicon-doped AlGaAs superlattices. Specifically, dislocation loops are formed in specimen regions doped to 10^{19} cm^{-3} Si. The defects are found to nucleate at interfaces in the superlattice. The loops tend to form preferentially in GaAs (as opposed to AlAs). The defects are interstitial in nature. It is suggested that point defects, possibly silicon dopant atoms, introduced during growth and doping of the superlattices, coalesce upon annealing to form the dislocation loops. The defects increase in size with increasing temperatures of anneal as would be expected if loop-sizes were related to the diffusion lengths of the point defects.

ACKNOWLEDGEMENTS

The authors thank Mr. R. Coles for maintaining the electron microscopes and Ms. M. Fabrizio for photographic work. The microscope facility is supported, in part, by the NSF through the Material Science Center at Cornell. One of the authors, NDT, would like to thank YHWH for sustenance. NDT is indebted to the Semiconductor Research Corporation for support (Grant 89-DC-069).

REFERENCES

1. J.J. Coleman, P.D. Dapkus, C.G. Kirkpatrick, M.D. Camras, and N. Holonyak, Jr., Appl. Phys. Lett. 40, 904 (1982).
2. P. Mei, T. Venkatesan, S.A. Schwarz, N.G. Stoffel, J.P. Harbison, D.L. Hart, and L.A. Florez, Appl. Phys. Lett. 52, 1487 (1988).
3. P. Gavrilovic, D.G. Deppe, K. Meehan, N. Holonyak, Jr., J.J. Coleman, and R.D. Burnham, Appl. Phys. Lett. 47, 130 (1985).
4. J. Ralston, G.W. Wicks, L.F. Eastman, B.C. De Cooman, and C.B. Carter, J. Appl. Phys. 59, 120 (1986).
5. B.C. De Cooman, C.B. Carter, and J.R. Ralston, SPIE Vol. 797 Advanced Processing of Semiconductor Devices, 185 (1987); B.C. De Cooman, C.B. Carter, J. Ralston, G.W. Wicks, and L.F. Eastman, Mat. Res. Soc. Symp. Proc. 56, 333 (1986).
6. N. Holonyak, Jr., W.D. Laidig, J.J. Coleman, and P.D. Dapkus, Appl. Phys. Lett. 39, 102 (1981).
7. M. Kawabe, N. Matsura, N. Shimizu, F. Hasegawa, and Y. Nannichi, Jpn. J. Appl. Phys. Lett. 23, L623 (1984).
8. K. Meehan, P. Gavrilovic, N. Holonyak, Jr., R.D. Burnham, and R. Thornton, Appl. Phys. Lett. 46, 75 (1985).
9. T. Venkatesan, S.A. Schwarz, D.M. Hwang, R. Bhat, M. Koza, H.W. Yoon, P. Mei, Y. Arakawa, and A. Yariv, Appl. Phys. Lett. 49, 701 (1986).
10. T. Venkatesan, S.A. Schwarz, D.M. Hwang, R. Bhat, H.W. Yoon, Y. Arakawa, in Proceeding of Ion Beam Modification of Materials Conference, Catania, Italy, 1986, edited by E. Rimini (Elsevier, The Netherlands, 1987); also Nucl. Instrum. Methods B19/20, 777 (1987).
11. E.V.K. Rao, H. Thibierge, F. Brillouet, F. Alexandre, and R. Azoulay, Appl. Phys. Lett. 46, 869 (1985).
12. D.G. Deppe, N. Holonyak, Jr., K.C. Hsieh, P. Gavrilovic, W. Stutius, and J. Williams, Appl. Phys. Lett. 51, 581 (1987).
13. P. Mei, H.W. Yoon, T. Venkatesan, S.A. Schwarz, and J.P. Harbison, Appl. Phys. Lett. 50, 1823 (1987).
14. P. Mei, S.A. Schwarz, T. Venkatesan, C.L. Schwartz, J.P. Harbison, L. Florez, N.D. Theodore, and C.B. Carter, Appl. Phys. Lett. 53, 2650 (1988).
15. N.D. Theodore, C.B. Carter, P. Mei, S.A. Schwarz, T. Venkatesan, and J.P. Harbison, Mater. Res. Soc. Symp. Proc. (1988).
16. N.D. Theodore, S.A. Schwarz, C.B. Carter, P. Mei, C. Palmstrom, and J.P. Harbison, to be published.

DIFFUSION IN GALLIUM ARSENIDE AND GaAs-BASED LAYERED STRUCTURES

U. Gösele, T. Y. Tan and Shaofeng Yu
School of Engineering, Duke University, Durham, NC 27706, USA

ABSTRACT

The mechanisms of Ga self-diffusion can be derived from interdiffusion experiments in intrinsic and doped GaAs-based superlattices. These experiments allow to conclude that Ga self-diffusion in intrinsic and n-doped GaAs is carried by triply negatively charged gallium vacancies whereas in p-doped GaAs positively charged gallium self-interstitials dominate Ga self-diffusion. The diffusion mechanisms of Zn and Be are discussed with special emphasis on the difference between their in- and out-diffusion behavior which is due to diffusion-induced non-equilibrium point defects.

INTRODUCTION

Gallium arsenide and silicon are presently the most important semiconductors in the microelectronics and optoelectronics industry. Whereas diffusion processes and mechanisms are fairly well understood in silicon [1,2] such an understanding is just emerging in the case of GaAs. Interdiffusion experiments in intrinsic as well as in doped GaAs/AlAs superlattices have proven to be essential in determining self- and dopant diffusion mechanisms in GaAs [3,4]. This paper will mainly deal with developments over the last few years concerning gallium self-diffusion in GaAs and the diffusion of dopants predominantly dissolved on the gallium sublattice such as Si, Zn and Be. More general overviews covering the diffusion in GaAs and other III-V compound have been given by Kendall [5], Casey [6] and Tuck [7]. Before discussing superlattice interdiffusion results and their implications for diffusion mechanisms in GaAs we will first summarize some essential concepts underlying our present understanding of diffusion phenomena in silicon. Similar concepts also appear to govern diffusion processes in GaAs.

DIFFUSION IN Si AND GaAs - SIMILARITIES AND DIFFERENCES

Although it is certainly risky to extrapolate from the simple case of the elemental semiconductor silicon to the more complex case of the compound semiconductor GaAs with two sublattices, some basic concepts which play a role in diffusion processes in silicon can be applied in modified form to GaAs. We summarize these concepts and basic results in the following:

i) Both vacancies and self-interstitials are involved in self- and dopant diffusion processes in silicon [1,2,8,9]. Similarly, both gallium vacancies and gallium self-interstitials have to be taken into account to understand gallium self-diffusion and dopant diffusion in GaAs [3,4,10].

ii) Vacancies (V) and self-interstitials (I) may occur in various charge states. Their equilibrium concentrations depend on the position of the Fermi level, i.e., on the concentration of electrons (n) or holes (p) and are given for a charged species X^k ($X = V$ or I) with charge k ($0, \pm 1, \pm 2, \dots$) by

$$C_{X^k}^{eq}(n)/C_{X^k}^{eq}(n_i) = (n/n_i)^{-k}. \quad (1)$$

In eq. (1) n_i is the intrinsic electron concentration. In a different context this Fermi level effect had already been discussed by Shockley and Moll in 1960 [11]. This effect leads to a doping dependence of diffusion processes, since charged

point defects can serve as "diffusion vehicles" for substitutionally dissolved atoms. The Fermi level effect on diffusion appears to be more pronounced in GaAs [3,4,10,12] than in Si [1,2].

iii) Some elements such as Au and Pt are predominantly dissolved on substitutional sites in Si but diffuse very rapidly on interstitial sites. This substitutional-interstitial diffusion mechanism is characterized by a change-over of an interstitial atom (A_i) to a substitutional site (A_s) which involves either a vacancy V in the Frank-Turnbull mechanism [13]



or a silicon self-interstitial I in the "kick-out" mechanism [14]



Both mechanisms play a role in silicon although the kick-out mechanisms appears to dominate Au and Pt diffusion in silicon [1,14,15]. In GaAs impurities such as chromium, and also the p-type dopants dissolved on the Ga sublattice (e.g. Zn, Be and Mg) diffuse via a substitutional-interstitial mechanism [7,16-18].

iv) Non-equilibrium point defects induced by surface processes such as oxidation or nitridation) or by a high in-diffusion flux of substitutionally dissolved atoms (e.g., Au diffusion or high-concentration phosphorus diffusion) play an important role in silicon [1,2]. In GaAs, surface processes (e.g. associated with SiO_2 caps) can also induce non-equilibrium point defect concentrations [19]. Diffusion-induced non-equilibrium point defects play an essential role if the influx of substitutionally dissolved atoms is larger than the transport flux of intrinsic point defects described by the doping-dependent self-diffusion coefficient $D_{(n)}^{\text{SD}}$ i.e., if

$$D_s C_s \gg D_{(n)}^{\text{SD}}. \quad (4)$$

In eq. (4) D_s is the effective diffusivity and C_s is the surface concentration of the in-diffusing substitutional dopant. Diffusion-induced non-equilibrium point defects are essential for the diffusion of Zn and Be in GaAs [3,7,10] and for the effect of Zn and Be on superlattice disordering as discussed in later sections of this paper.

Obvious differences between Si and GaAs are the existence of two sublattices in GaAs with the corresponding increase in different possible intrinsic point defects such as gallium and arsenic self-interstitials and vacancies (I_{Ga} , I_{As} , V_{Ga} , V_{As}) and the dependence of their thermal equilibrium concentrations on the arsenic vapor pressure $P_{\text{As}q}$ via

$$C_{V_{\text{Ga}}}^{\text{eq}} \propto C_{I_{\text{As}}}^{\text{eq}} \propto 1/C_{V_{\text{As}}}^{\text{eq}} \propto 1/C_{I_{\text{Ga}}}^{\text{eq}} \propto P_{\text{As}q}^{1/q}. \quad (5)$$

In Eq. (5) $q = 4$ for high and $q = 2$ for very low arsenic vapor pressures [6]. This pressure dependence is not only a complicating feature but also helps to elucidate diffusion mechanisms in GaAs as will be mentioned several times in the following sections.

GALLIUM SELF-DIFFUSION IN INTRINSIC GaAs

The self-diffusion coefficient $D_{Ga}(n_i)$ of gallium in intrinsic gallium arsenide has been measured by a number of authors with radioactive gallium tracer atoms [20,21] (Fig. 1). This method allows measurements of $D_{Ga}(n_i)$ down to values of about 10^{-15} cm²/s. Measurements of the interdiffusion of Ga and Al in GaAs/AlAs superlattices with periods in the range of 100 Å extended the range of $D_{Ga}(n_i)$ to much lower values [22-25]. The various data points can roughly be fitted to [3]

$$D_{Ga}(n_i) \approx 2.9 \times 10^8 \exp(-6eV/kT) \text{ cm}^2/\text{s}. \quad (6)$$

Eq. (6) does not fit exactly since the arsenic pressure dependence has not been taken into account. Measurements of the As pressure dependence [4,27] show that the Ga/Al interdiffusion coefficient (assumed to be close to the Ga diffusion coefficient in GaAs itself) increases for high and for very low arsenic vapor pressures. This result indicates that $D_{Ga}(n_i)$ is governed by gallium vacancies for sufficiently high and by Ga self-interstitials for sufficiently low arsenic vapor pressures [4]. The role of both Ga vacancies and self-interstitials becomes clearer when Ga diffusion in doped GaAs is considered.

GALLIUM SELF-DIFFUSION IN DOPED GaAs

Dopant-Induced Superlattice Disordering

Whereas no studies of gallium self-diffusion in doped GaAs have been performed, a wealth of data on Ga/Al interdiffusion in both n-type and p-type doped GaAs/AlAs superlattices is available. Such interdiffusion studies had been triggered by the observation of Laidig et al. [28] in 1981 that high-concentration zinc diffusion in such a superlattice dramatically enhances the interdiffusion coefficients (by up to 12 orders of magnitude) and leads to intermixing or disordering of the superlattice in the zinc diffused region. It soon turned out that not only the p-type dopant zinc but also n-type dopants such as silicon, selenium or sulphur can lead to dopant-induced superlattice disordering [3,4]. Since this effect is of technological importance for the lateral patterning of superlattices for lasers and waveguides, it has been investigated in detail by dozens of groups and a number of disordering mechanisms have been proposed [10,12,28,29]. In this paper we will not discuss effects which are due to ion-implantation-induced point defects but only those related to the presence or diffusion of dopants. In the following we will concentrate on a proposal by two of the present authors [3,10,12] which is now widely accepted. Within this proposal the enhanced interdiffusion is due to two main effects:

i) The thermal equilibrium concentration of appropriately charged intrinsic point defects is enhanced by doping ("Fermi level effect"). In this case, which appears to hold e.g. for the n-dopant Si, only the presence of the dopant and not its movement is of importance.

ii) If one deals with a dopant with high diffusivity and solubility, so that the product $D_S C_S \gg D^{SD}(n)$ as discussed earlier, then non-equilibrium point defects are generated. Depending on whether a supersaturation or an undersaturation of point defects develops the disordering effect due to the Fermi level effect may be increased or decreased. Non-equilibrium point defects play an essential role in the diffusion of high-concentration Zn and Be in GaAs.

In the following sections we will shortly discuss the disordering results for n and p-dopants and the conclusions which can be drawn on the diffusion mechanisms and point defects involved.

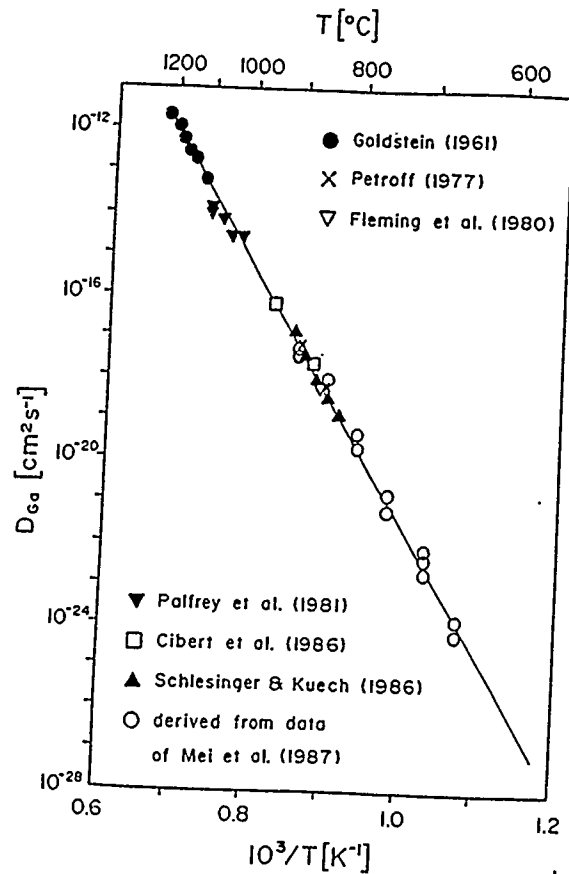
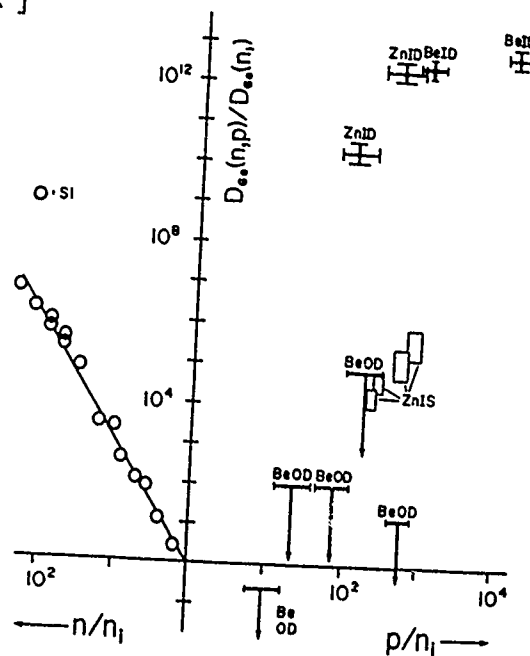


Fig. 1
Plots of available data for gallium self-diffusion in GaAs and data for Al-Ga interdiffusion in GaAs/AlGaAs superlattice under intrinsic conditions [20-25] together with the gallium diffusion data derived from the data of Mei et al. [26], according to ref. [3].

Fig. 2
Plot of $D_{Ga(n,p)}/D_{Ga(n_i)}$ versus the ratio of extrinsic to intrinsic carrier concentration. The silicon doping data on the left hand side are from Mei et al. [26]. On the right-hand side the data for zinc in-diffusion (ZnID), for Be in-diffusion (BeID), Be out-diffusion (BeOD), and for an implanted Zn source (ZnIS) are from ref. [34-40].



N-Type Dopant-Induced Disordering

On the left-hand side of Fig. 2 the enhanced Ga/Al interdiffusion coefficients as a function of Si induced n-doping level are plotted in a normalized form. These data obtained by Mei et al. [26] show a clear dependence

$$D_{Ga}(n) \propto (n/n_i)^3 \quad (7)$$

which indicates the involvement of a triply negatively charged intrinsic point defect. Based on the arsenic pressure dependence of the interdiffusion coefficient of n-doped superlattices [4,30] this defect has to be the gallium vacancy V_{Ga}^{3-} in accordance with an earlier theoretical prediction by Baraff and Schlüter [31]. Calculation of $D_{Ga}(n_i)$ based on the Mei et al. data leads to the values indicated in Fig. 1 which are in good accordance with the values extrapolated from higher temperature data [3]. Including the As pressure dependence, we may write the gallium self-diffusion coefficient in p-type GaAs as

$$D_{Ga}(n) = D_{V_{Ga}^{3-}} \left(n_i / P_{Asq}^\circ \right) (n/n_i)^3 \left(P_{Asq} / P_{Asq}^\circ \right)^{1/q}, \quad (8)$$

where P_{Asq}° is a suitably chosen reference arsenic vapor pressure. For sufficiently high arsenic vapor pressure $q=4$ and the expression can also be extended to intrinsic GaAs for which

$$D_{Ga}(n_i) = D_{V_{Ga}^{3-}} \left(n_i / P_{As4}^\circ \right) \left(P_{As4} / P_{As4}^\circ \right)^{1/4} \quad (9)$$

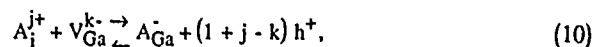
should hold. Eq. (9) should be close to eq. (6) which does not contain any specific arsenic pressure dependence.

Tellurium-doped GaAs based superlattices appear to show a weaker dependence of the Ga interdiffusion coefficient on n than found for the case of Si-doped superlattices [32]. These results have been discussed in detail elsewhere [33].

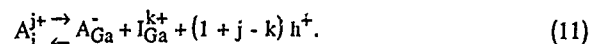
P-Type Dopant-Induced Disordering

On the right-hand side of Fig. 2 the enhanced Ga/Al interdiffusion coefficients as a function of Zn or Be induced p-doping levels are plotted in a normalized form. The data obtained by various groups [28,34-40] do not show a power law dependence as expected for the Fermi level effect but split in a group with an extremely high enhancement for experiments involving the presence of an outside source ("in-diffusion" conditions) and a group for which an enhancement could not be observed. These later experiments involved already grown-in dopants without an outside source ("out-diffusion" conditions). A measurable although considerable lower enhancement than under in-diffusion conditions have been found for implanted Zn ("implanted source") [40].

It is well established that p-type dopants dissolved on the Ga sublattice such as Zn, Be or Mg diffuse via a substitutional-interstitial mechanism involving either gallium vacancies (V_{Ga}) in the Frank-Turnbull [13] or Longini mechanism [41],



where h^+ denotes positively charged holes, or gallium self-interstitials (I_{Ga}) in the kick-out mechanism [42]



The arsenic pressure dependence of the disordering rate of Mg-doped GaAs/AlAs superlattices [43] indicates that an I_{Ga} species has to be involved, which favors the kick-out mechanism. As discussed in more detail in previous papers [3,10] the difference between the "in-diffusion" and the "out-diffusion" results is due to non-equilibrium point-defects generated or consumed by the fast diffusing p-type dopants. For in-diffusion conditions, provided the condition (4) is fulfilled, a supersaturation of I_{Ga} will develop within the framework of the kick-out mechanism:

$$s_{I_{Ga}} = (C_{I_{Ga}}^{k+} - C_{I_{Ga}}^{eq}) / C_{I_{Ga}}^{eq} > 0. \quad (12)$$

For out-diffusion-conditions an undersaturation of I_{Ga} will be generated ($-1 < s_{I_{Ga}} < 0$). If gallium self-interstitials carry gallium self-diffusion then during "in-diffusion" of the p-dopant the disordering rate due to the Fermi level effect for positively charged gallium self-interstitials is enhanced by the supersaturated Ga self-interstitials and retarded under "out-diffusion" conditions. This reflects the actually observed behavior. Since the Longini mechanism would just predict the opposite behavior we can rule out that V_{Ga} play a major role either in Ga self-diffusion or in the diffusion of Zn, Be or Mg.

In eq. (11) we have used charged Ga self-interstitials contrary to the neutral ones which have usually been assumed. There are two reasons which make positively charged (rather than neutral) gallium self-interstitials necessary:

a) The observable disordering effect is restricted to the diffused region, which requires an enhancement effect limited to the diffused region in addition to the diffusion-induced supersaturation which can spread beyond the profile. Positively charged point defects fulfill this requirement.

b) The observed enhancements of disordering rates are so extremely high (up to 10^{12} or more) that it is hard to imagine such a high diffusion-induced point defect supersaturation without immediate agglomeration of these point defects.

Presently, the most likely value for k in I_{Ga}^{k+} is 2 or 3 [3,40], in accordance with earlier conclusions arrived by Winteler [44] analyzing Zn diffusion profiles.

Combining the results for the p-type and the n-type dopant-induced disordering and allowing for a possible vacancy supersaturation s_v as well we may express the Ga self-diffusion coefficient approximately as

$$D_{Ga}(n, P_{Asq}) = D_{I_{Ga}}^{k+} \left(n_i, P_{Asq}^{\circ} \right) \left(p/n_i \right)^k \left(P_{Asq} / P_{Asq}^{\circ} \right)^{-1/q} (1 + s_I) \\ + D_{V_{Ga}}^3 \left(n_i, P_{Asq}^{\circ} \right) \left(n/n_i \right)^3 \left(P_{Asq} / P_{Asq}^{\circ} \right)^{1/q} (1 + s_v). \quad (13)$$

It cannot be excluded that eq. (13) should contain more than two terms, e.g., one for $k=2$, one for $k=3$ and possibly one for a neutral vacancy, but eq. (13) contains all presently known effects on GaAs/AlAs superlattice disordering. In the case of non-equilibrium gallium vacancies injected by an SiO_2 mask, $s_v > 0$ holds. In the case of ion-implantation, both $s_I > 0$ and $s_v > 0$ may hold and both s_I and s_v may be time-dependent. In the case of diffusion-induced non-equilibrium point defects

the presence of dislocations will allow local equilibrium between point defects in the two sublattices [45] such as

$$C_{\text{I}_{\text{Ga}}} C_{\text{I}_{\text{As}}} = C_{\text{I}_{\text{Ga}}}^{\text{eq}} C_{\text{I}_{\text{As}}}^{\text{eq}} \quad (14)$$

In this way a large supersaturation of I_{Ga} in the Ga sublattice (as e.g. induced by in-diffusing Zn) may lead to an undersaturation of I_{As} or a supersaturation of V_{As} in the As sublattice.

In the case of high concentration Zn or Be diffusion the Fermi level effect is generally combined with a supersaturation or undersaturation of point defects. A possibility to observe just the Fermi level effect appears to be to dope a GaAs/AlAs superlattice with the acceptor carbon [45], which is dissolved on the As sublattice and diffuses so slowly that no non-equilibrium effects are expected. In the case of low carbon doping or low concentration doping with grown-in Zn and Be the superlattice might be more stable than under intrinsic conditions [12,46], provided the arsenic pressure is sufficiently high so that $D_{\text{Ga}}(n_i)$ is dominated by gallium vacancies.

SILICON DIFFUSION IN GaAs

Silicon is the main n-type dopant for GaAs based devices. Silicon is an amphoteric dopant which is mainly dissolved on the gallium sublattice but shows a high degree of self-compensation at high concentrations due to an increasing solubility on the arsenic sublattice. The apparent concentration dependence of Si diffusion has been modeled by a variety of models. The Greiner-Gibbons model is based on the assumption that the silicon diffusion is carried predominantly by $\text{Si}_{\text{As}}\text{-Si}_{\text{Ga}}$ pairs [47,48]. Kavanagh et al. [49,50] assume that the concentration dependence of Si diffusion is a reflection of a depth-dependent vacancy concentration due to the in-diffusion of vacancies generated by a SiO_2 capping layer. More recently, it has been suggested that Si diffusion is associated with negatively charged Ga vacancies [3,4,51-54] and actually a Fermi level effect rather than a Si concentration dependence. Results on Si diffusion into n-doped GaAs [51,52] confirm the Fermi level effect and contradict the Greiner-Gibbons pair-diffusion model. The suggested charge state of the gallium vacancy ranges from -1 [4,51,52] to -3 [3,54]. The model involving triply negatively charged gallium vacancies is consistent with the Si-induced disordering results and can be used for quantitative fitting of Si diffusion in GaAs. For a detailed discussion see the contribution by Yu et al. in these proceedings [55]. Let us finally mention that even for high Si concentrations the condition (4) for the generation of non-equilibrium point defects is not fulfilled. Si diffusion in GaAs should therefore be essentially independent of specific in- and out-diffusion conditions. The faster moving Sn atoms [56] are closer to the condition for producing non-equilibrium point defects but are still not expected to show large (order of magnitude) differences between in- and out-diffusion cases which is in accordance with experimental results [57].

ZINC AND BERYLLIUM DIFFUSION IN GaAs

As discussed earlier in this paper zinc and beryllium diffuse via a substitutional-interstitial mechanism. Since only the kick-out mechanism (11) is consistent with the superlattice disordering results we will base our discussion on this mechanism. In terms of substitutional-interstitial mechanisms of p-type dopants the condition (4) for generating a non-equilibrium concentration of intrinsic point defects during indiffusion of Zn or Be may be expressed as

$$D_i C_i^{eq} \gg D^{SD}(p), \quad (15)$$

where D_i is the diffusivity and C_i^{eq} the solubility of the zinc (or beryllium) interstitials, respectively. C_i^{eq} will depend on the source conditions, such as e.g. the zinc vapor pressure if zinc is diffused from the vapor phase. For sufficiently low Zn or Be surface concentrations, condition (15) is not fulfilled and intrinsic point defects can be considered to be in equilibrium. Under these conditions the effective diffusivity of substitutional zinc is given by

$$D_{eff}^{(i)} \propto p^{j+1} \propto C_s^{j+1} \quad (16)$$

where $j=1$ for zinc [5,6,7] and $j=0$ for Be [17]. More specifically, in eq (18) we have assumed that the hole concentration p is determined by the concentration of substitutional zinc or beryllium, C_s . For higher surface concentrations when condition (15) becomes more and more valid, a supersaturation of I_{Ga} develops. The out-diffusion of I_{Ga} to the surface will then determine the shape of the Zn concentration profile. Typical examples are shown in Fig. 3 from the work of Winteler [44]. The effective substitutional zinc diffusivity near the surface is then given by [16]

$$D_{eff}^{(i)} \approx 2 [D_i C_i^{eq} (C_s^{eq}) / C_s^{eq}] (C_s / C_s^{eq})^{k-3} \quad (17)$$

where $C_i^{eq} (C_s^{eq})$ is the thermal equilibrium concentration of $(k+)$ charged Ga self-interstitials at the surface. Based on an analysis of such profiles Winteler [44], arrived at the conclusion that positively charged Ga interstitials with $k=2$ and 3 are involved in both zinc diffusion and gallium self-diffusion. For deeper parts of the profile condition (15) can no longer be applied. The profiles in the tail part

become dominated again by $D_{eff}^{(i)}$ from eq. (16) enhanced by a Ga self-interstitial supersaturation extending beyond the profile into the bulk [16]

$$D_{eff}^{tail} = D_{eff}^{(i)} (C_{I_{Ga}} / C_{I_{Ga}}^{eq}) \quad (18)$$

For even higher surface concentrations the profiles show typically a kink-and-tail structure [4,6,7,58] and are associated with a high density of dislocations [59,60] and other defects generated by the zinc diffusion-induced supersaturation of I_{Ga} [60].

For substitutional Zn (or Be) concentrations high enough to generate a supersaturation of I_{Ga} during in-diffusion, an undersaturation of I_{Ga} will develop for grown-in dopants or after taking away the outside dopant source; see schematic Figure 4. As a result, for these concentration conditions dopant "in-diffusion" will be much faster than dopant "out-diffusion", as has been frequently observed for Zn [5,6,62] and Be [63,64]. An example of slowed-down diffusion of Zn after the outside zinc source had been taken away is shown in Fig. 5. The simulation of the difference between in- and out-diffusion cases caused by non-equilibrium point defects requires to take into account the movement of intrinsic point defects, in addition to that of dopant atoms. We have just started developing such simulations. An example of such simulations, demonstrating the difference of the diffusion behavior with and without out-side source, is shown in Fig. 6.

Finally, let us shortly mention that the supersaturation of Ga self-interstitials generated by in-diffusion of Zn starting from a high surface concentration may enhance the diffusion of buried Zn or Be doped layers as

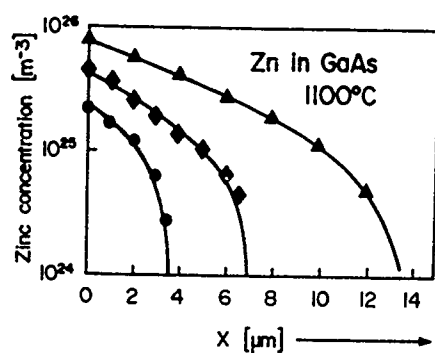


Fig. 3
Zinc concentration profiles in
GaAs for 15 minutes at 1100°C and
different zinc vapor pressures [44].

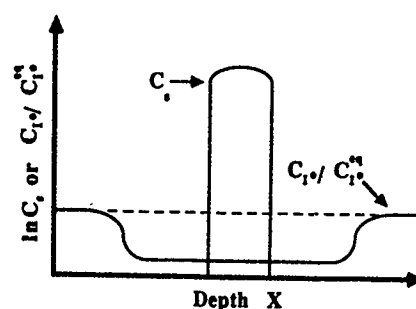


Fig. 4
Schematic of out-diffusion of buried
Be or Zn layer and its generation of
an undersaturation of self-interstitials.

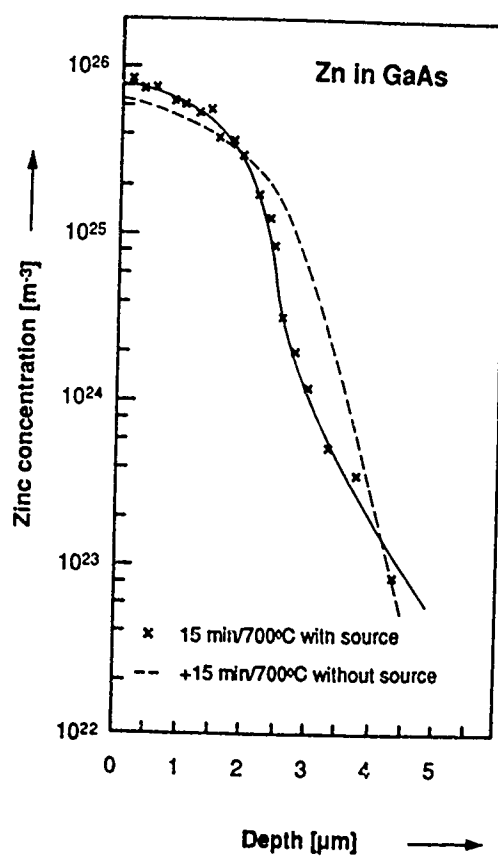


Fig. 5 Zinc concentration profile for a 15 min diffusion at 700°C and profile after
further 15 min anneal at 700°C in an empty ampoule [61].

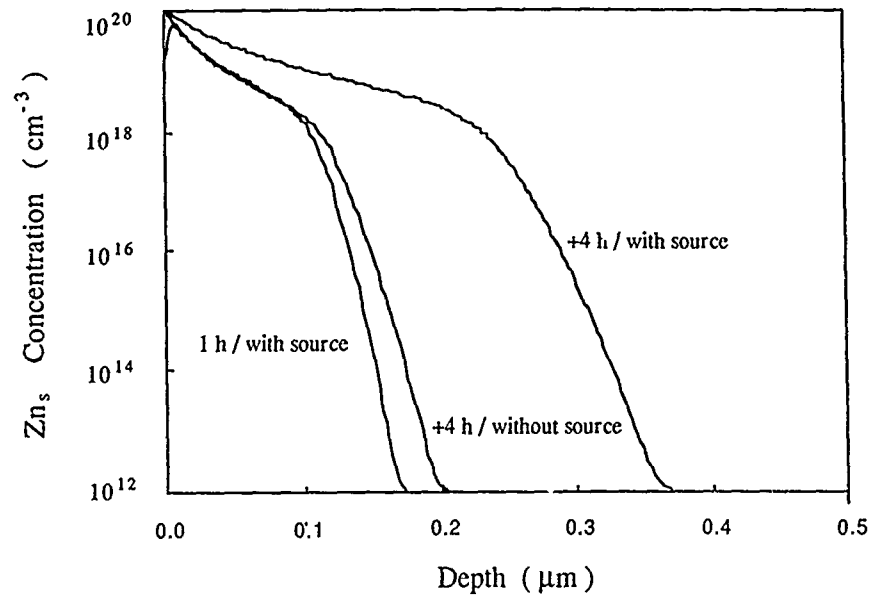


Fig. 6

Computer simulations of zinc diffusion showing the difference between in-diffusion (with source) and out-diffusion (without source) behavior due to non-equilibrium point defects.

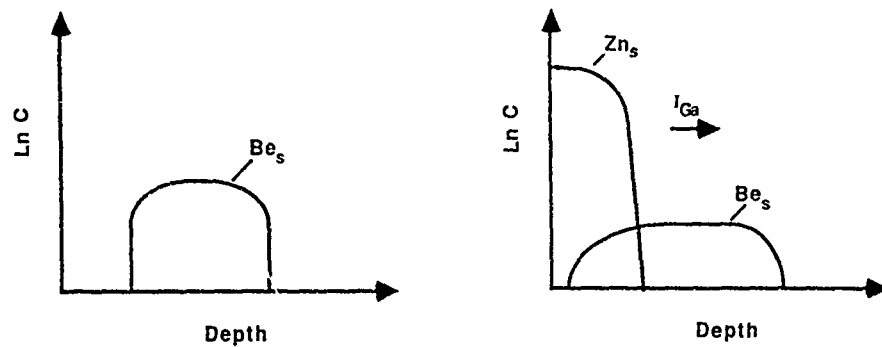


Fig. 7

Schematic of influence of supersaturation of I_{Ga} generated by in-diffusion of high-concentration zinc on buried Be (or also Zn) layer. Left: slow Be diffusion without Zn diffusion. Right: fast Be diffusion with Zn diffusion. This effect is analogous to the "emitter-push" effect in silicon involving high-concentration phosphorus diffusion [15].

schematically shown in Fig. 7. This effect is analogous to the "emitter-push" effect in silicon [15]. Although the effect is widely known in industrial labs concerned with high concentration Zn contact diffusion to p-doped layers in hetero-bipolar transistors or lasers, hardly any published reports exist [65]. Further systematic investigations in this area are certainly desirable.

Acknowledgement

We appreciate support by the Army Research Office.

References

1. T. Y. Tan and U. Gösele, Appl. Phys. **A37**, (1985).
2. P. M. Fahey, P. B. Griffin and J. D. Plummer, Rev. Mod. Phys. **61**, 289 (1989).
3. T. Y. Tan and U. Gösele, Mat. Science Eng. **31**, 47 (1988).
4. D. G. Deppe and N. Holonyak, Jr., J. Appl. Phys. **64**, R93 (1988).
5. D. L. Kendall, in Semiconductors and Semimetals, Vol. 4, (Academic Press, New York, 1968), p. 163.
6. H. C. Casey, in Atomic Diffusion in Semiconductors, Vol. 4, (Academic Press, New York, 1968), p. 163.
7. B. Tuck, Atomic Diffusion in III-V Semiconductors, (Hilger, Bristol, 1988).
8. A. Seeger and K. P. Chick, Phys. Stat. Sol. **22**, 455 (1968).
9. S. M. Hu, J. Appl. Phys. **45**, 1567 (1974).
10. T. Y. Tan and U. Gösele, Appl. Phys. Lett. **52**, 1240 (1988).
11. W. Shockley and J. L. Moll, Phys. Rev. **119**, 1480 (1960).
12. T. Y. Tan and U. Gösele, J. Appl. Phys. **61**, 1841 (1987).
13. F. C. Frank and D. Turnbull, Phys. Rev. **104**, 617 (1956).
14. U. Gösele, W. Frank and A. Seeger, Appl. Phys. A. **23**, 361 (1980).
15. W. Frank, U. Gösele, H. Mehrer and A. Seeger, in Diffusion in Crystalline Solids, G. E. Murch and A. S. Nowick, eds. (Academic Press, New York 1984) p. 64.
16. U. Gösele, Ann. Rev. Mater. Sci. **18**, 257 (1988).
17. M. D. Deal and H. G. Robinson, Appl. Phys. Lett. **55**, 1990 (1989).
18. H. G. Robinson, M. D. Deal and D. A. Stevenson, these proceedings.
19. K. L. Kavanagh, J. W. Mayer, J. W. Magee, J. Sheets, J. Tong and J. M. Woodall, Appl. Phys. Lett. **47**, 1208 (1985).
20. B. Goldstein, Phys. Rev. **121**, 1305 (1961).
21. H. D. Palfrey, M. Brown and A. F. W. Willoughby, J. Electrochem. Soc. **128**, 2224 (1981).
22. P. M. Petroff, J. Vac. Sci. Technol. **14**, 973 (1977).
23. R. M. Fleming, D. B. McWhan, A. C. Gossard, W. Wiegmann and R. A. Logan, J. Appl. Phys. **51**, 357 (1980).
24. J. Cibert, P. M. Petroff, D. J. Werder, S. J. Pearton, A. C. Gossard and J. H. English, Appl. Phys. Lett. **49**, 223 (1986).
25. T. E. Schlesinger and T. Kuech, Appl. Phys. Lett. **49**, 519 (1986).
26. P. Mei, H. W. Yoon, T. Venkatesan, S. A. Schwarz and J. P. Harbison, Appl. Phys. Lett. **50**, 1823 (1987).
27. L. J. Guido, N. Holonyak, Jr., K. C. Hsieh, R. W. Kaliski, W. E. Plano, R. D. Burnham, R. L. Thornton, J. E. Epler and T. L. Paoli, J. Appl. Phys. **61**, 1372 (1987).
28. W. D. Laidig, N. Holonyak, Jr., M. D. Camras, K. Hess, J. J. Coleman, P. D. Dapkus and J. Bardeen, Appl. Phys. Lett. **38**, 776 (1981).
29. J. A. Van Vechten, J. Appl. Phys. **53**, 7082 (1982); J. Vac. Sci. Technol. **B2**, 569 (1984).
30. D. G. Deppe, N. Holonyak, Jr., K. C. Hsieh, P. Gavrilovic, W. Stutius and L. Williams, Appl. Phys. Lett. **51**, 581 (1987).
31. G. A. Baraff and M. Schlüter, Phys. Rev. Lett. **55**, 1327 (1986).

32. P. Mei, S. A. Schwartz, T. Venkatesan, C. L. Schwartz, S. Bernsek, G. Stillman and H. Temkin, in *Mat. Res. Soc. Proc.* **126** (Pittsburgh, 1988) in press.
33. T. Y. Tan and U. Gösele, in *Mat. Res. Soc. Proc.* **144** (Pittsburgh, 1989) p.221.
34. J. W. Lee and W. D. Laidig, *J. Electron. Mater.* **13**, 147 (1984).
35. M. Kawabe, N. Shimizu, F. Hasegawa and Y. Nannidi, *Appl. Phys. Lett.* **46**, 849 (1985).
36. N. Kamata, K. Koboyashi, K. Eudo, T. Sasudi and A. Misu, *Jpn. J. Appl. Phys.* **26**, 1092 (1987).
37. D. R. Myers, R. M. Biefeld, I. J. Fritz, S. T. Piccaux and T. E. Zipperian, *Appl. Phys. Lett.* **44**, 1052 (1984).
38. Y. Hirayama, Y. Susuki and H. Okamoto, *Jpn. J. Appl. Phys.* **24**, 1498 (1985).
39. J. Ralston, G. W. Wicks, L. F. Eastman, B. C. Deooman and C. B. Carter, *J. Appl. Phys.* **59**, 120 (1986).
40. E. P. Zucker, A. Hasimoto, T. Fukunaga and N. Watanabe, *Appl. Phys. Lett.* **54**, 564 (1989).
41. R. L. Longini, *Solid-State Electronics* **5**, 127 (1962).
42. U. Gösele and F. Morehead, *J. Appl. Phys.* **52**, 4617 (1981).
43. D. G. Deppe, N. Holonyak, Jr., W. E. Plano, V. M. Robbins, J. M. Dallesasse, K. C. Hsieh and J. E. Baker, *J. Appl. Phys.* **64**, 2854 (1988).
44. H. R. Winteler, *Helv. Phys. Acta* **44**, 451 (1970).
45. B. R. P. Marioton, T. Y. Tan and U. Gösele, *Appl. Phys. Lett.* **54**, 849 (1989).
46. L. J. Guido, B. T. Cunningham, D. W. Nam, K. C. Hsieh, W. E. Plano, J. S. Major, Jr., E. J. Vesely, A. R. Sugg, N. Holonyak, Jr. and G. E. Stillman, *J. Appl. Phys.* **67** (1989), in press.
47. M. E. Greiner and J. F. Gibbons, *Appl. Phys. Lett.* **44**, 740 (1984).
48. M. E. Greiner and J. F. Gibbons, *J. Appl. Phys.* **57**, 5181 (1985).
49. K. L. Kavanagh, J. W. Mayer, J. W. Magee, J. Sheets, J. Tong and J. M. Woodall, *Appl. Phys. Lett.* **47**, 1208 (1985).
50. K. L. Kavanagh, C. W. Magee, J. Sheets, and J. W. Mayer, *J. Appl. Phys.* **64**, 1845 (1988).
51. D. G. Deppe, N. Holonyak, Jr., F. A. Kish and J. E. Baker, *Appl. Phys. Lett.* **50**, 998 (1987).
52. D. G. Deppe, N. Holonyak, Jr. and J. E. Baker, *Appl. Phys. Lett.* **52**, 129 (1988).
53. J. J. Murray, M. D. Deal and D. A. Stevenson, these proceedings.
54. S. Yu, U. Gösele and T. Y. Tan, *J. Appl. Phys.* **66**, 2952 (1989).
55. S. Yu, U. Gösele and T. Y. Tan, these proceedings.
56. E. L. Allen, M. D. Deal and J. D. Plummer, these proceedings.
57. T. F. Kuech, M. Goorsky, F. Cardone, G. Scilla and R. Potemski, these proceedings.
58. B. Tuck and M. A. Kadhim, *J. Mater. Science* **7**, 585 (1972).
59. R. K. Ball, P. W. Hutchinson and P. S. Dobson, *Phil. Mag.* **A43**, 1299 (1981).
60. M. Luysberg, W. Jäger, K. Urban, M. Perret, N. Stolwijk and H. Mehrer, these proceedings.
61. B. Tuck and A. J. N. Houghton, *J. Phys. D* **14**, 2147 (1981).
62. P. Enquist, J. H. Hutchby and T. J. Lyon, *J. Appl. Phys.* **63**, 4485 (1985).
63. K. Masu, M. Konagai and V. Takahashi, *Appl. Phys. Lett.* **37**, 183 (1980).
64. P. Enquist, G. W. Wicks, L. F. Eastman and C. Hitzman, *J. Appl. Phys.* **58**, 4130 (1985).
65. P. A. Houston, F. R. Shepherd, A. J. Springthorpe, P. Mandeville and A. Margittai, *Appl. Phys. Lett.* **52**, 49 (1981).

PART XI

DX Centers

THE DX CENTER: EVIDENCE FOR CHARGE CAPTURE VIA AN EXCITED INTERMEDIATE STATE

Thomas N. Theis and Patricia M. Mooney

IBM Research, T.J. Watson Research Center, P.O. Box 218, Yorktown Heights, NY 10598

ABSTRACT

We review three important experimental results which suggest that electron capture and emission by the DX center in $\text{Al}_x\text{Ga}_{1-x}\text{As}$ proceeds via an excited intermediate state: the very different dependencies of the thermal capture and emission rates on alloy composition, the exponential dependence of the thermal capture rate on the quasi-equilibrium Fermi energy, and the thermal activation of the hot electron capture rate. None of these results is readily explained by a conventional lattice relaxation model, in which an electron is captured directly from the lowest lying band edge, but each can be simply explained if the dominant channel for multiphonon capture is via a transition state which lies well above the band edge. This picture is consistent with recent pseudopotential calculations which predict that the lattice relaxed state (the DX state) is stabilized by capture of more than one electron, since such a model naturally admits the possibility of an intermediate one-electron state.

INTRODUCTION

Calculating the spectrum of electronic states of a substitutional donor is an old, but still unfinished problem in semiconductor physics. The hydrogenic states, bound by the long range Coulomb potential, are well predicted by effective mass theory. Highly localized or deep states, bound by the short range ion core potential, are predicted by tight binding theory.[1] The energy of such deep states relative to the spectrum of hydrogenic states depends sensitively on the balance between the long and short range potentials, and calculational techniques suitable for the hydrogenic spectrum are unsuitable for localized states, and *vice versa*.

Whether the ground state of the spectrum is hydrogenic or deep, the wave functions of deep and hydrogenic states will exhibit large spatial overlap. Excited states should therefore be relatively short-lived, decaying radiatively to the ground state. In contrast to this view, substitutional donors in some compound semiconductors are now believed to exhibit bistability. The most studied example is the DX center[2] in GaAs and $\text{Al}_x\text{Ga}_{1-x}\text{As}$, which captures electrons either to hydrogenic states,[3-5] or to a deep state[2] which we shall refer to as the DX state. Depending on the donor species, alloy composition, local alloy environment, and hydrostatic pressure, the ground state may be either hydrogenic or deep. The hydrogenic states are separated from the deep state by an energetic barrier, so that transitions between them are unobservably slow at low temperatures. This behavior implies a strong suppression of energetically allowed radiative transitions which is attributed to a large lattice relaxation associated with electron capture to the deep (DX) level.[2] A configuration coordinate diagram, appropriate for the DX center in direct gap $\text{Al}_x\text{Ga}_{1-x}\text{As}$ is shown in figure 1.

Because bistability was not expected of a substitutional donor, Lang *et al.* originally suggested that DX was a complex of a simple donor (D) and an unknown defect (X).[2] However, recent hydrostatic pressure studies,[6-8] especially when combined with infrared vibrational spectroscopy,[9,10] strongly suggest that DX is just the simple substitutional donor. The idea that the simple donor can participate in a large lattice relaxation has been difficult to accept, prompting repeated attempts to explain the DX level as either an unusu-

ally deep hydrogenic state,[11-14] or as a deep state[15-18] of the type proposed by Hjalmarson *et al.*[1] With only small lattice relaxation of the donor, all of these models lack a physical mechanism which can explain the immeasurably small radiative capture rate, and the corresponding immeasurably small photoionization cross section at energies on the order of the thermal binding energy.[2,19]

A large lattice relaxation of the simple donor is predicted by the pseudopotential calculations of Chadi and Chang.[20] The column IV substitutional donor breaks a bond with a nearest neighbor As and moves towards a threefold coordinated interstitial site. In the case of the group VI substitutional donor, a nearest neighbor Ga (or Al) atom moves away from the donor towards an interstitial site. For the column IV donor, the structural features of this model were independently deduced by Morgan[21] as an explanation of the family of DX centers associated with substitution of Al for Ga near neighbors in the dilute $\text{Al}_x\text{Ga}_{1-x}\text{As}$ alloy.[22] Perhaps the most interesting feature of Chadi and Chang's calculation is the prediction that the bond breaking distortion of the lattice is stable only if the donor localizes two electrons (becomes negatively charged). In other words, the donor exhibits a negative effective Hubbard correlation energy (negative effective U).[23] Several authors have analyzed various experiments and have concluded that this may indeed be the case.[24,25] Free electron mobility measurements, presented by one group as evidence against the model,[26] have been reinterpreted by others as being evidence for the model.[27-29] However, at least one experiment, the observation of a static paramagnetic susceptibility associated with the DX state, appears in contradiction,[30] and the issue of the charge state must be regarded as unsettled.

Here we review experimental evidence which, while not directly supporting the Chadi and Chang model, is entirely consistent with it. As pointed out by Theis,[5] the model quite naturally leads to the possibility that the dominant channel for electron capture involves an intermediate one-electron state. This is schematically illustrated by the configuration coordinate diagram of figure 2. The lattice relaxation of the one-electron state is assumed small, although this point is not essential to the argument. E_{DX} is defined as the average energy per electron of the negatively charged two electron state, following the notation of Theis *et al.*[24] Simultaneous multiphonon capture of two electrons from the lowest lying conduction valley to the deep level ground state ($2U_{\text{r}} \rightarrow 2U_{\text{DX}}$) is assumed improbable. The

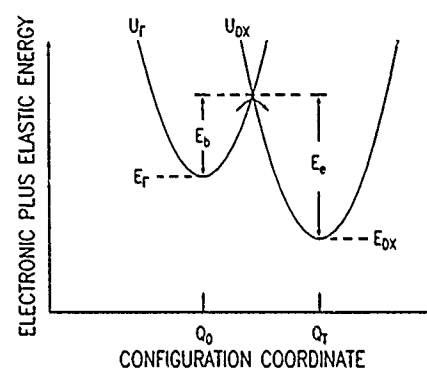


Fig. 1 Configuration coordinate diagram appropriate for a positive U model of the DX center in direct gap $\text{Al}_x\text{Ga}_{1-x}\text{As}$. E_b and E_e are the activation energies for thermal capture and thermal emission, respectively.

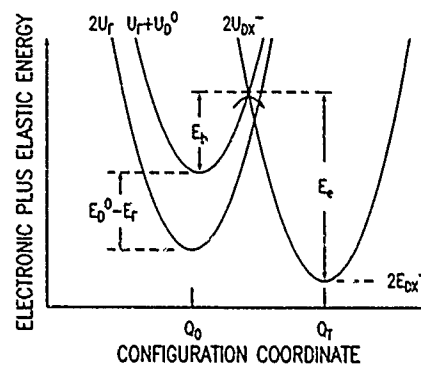


Fig. 2 Configuration coordinate diagram appropriate for a negative U model of the DX center in direct gap $\text{Al}_x\text{Ga}_{1-x}\text{As}$. E_{DX} is defined as the average energy per electron of the two-electron state.

dominant capture process ($2U_{\Gamma} \rightarrow U_{\Gamma} + U_{DX}^0 \rightarrow 2U_{DX}^0$) is assumed to be *via* the excited one-electron state. We shall argue below that our experimental results support a configuration coordinate diagram and capture mechanism of this general form.

That capture to DX must involve an excited state was first suggested by Mayerfeld and Bhattacharya,[31] who sought to show that electron capture and emission occurs *via* conduction states associated with the L valley. Their argument was based on the observation that the activation energy for emission (E_e in figure 1) referenced to the thermal depth of the DX level ($E_{\Gamma} - E_{DX}$) coincides with the L point. We now know that this is true only for the special case of the Sn-related DX center in $Al_xGa_{1-x}As$. The argument lacks general validity. Based on somewhat different arguments concerning the alloy dependence of the emission and capture barriers, other authors[32,33] have come to the conclusion that capture involves the L (or X) valleys. However, a physical explanation must then be provided to explain why this is the dominant capture channel. Most of the suggestions seem to be based on the idea of a selection rule; DX consists of basis states heavily weighted towards the L point, so that transitions to and from the Γ valley are suppressed. However, DX is highly spatially localized[22,34] and must therefore be extended in momentum space. Indeed, precision measurements of the hydrostatic pressure dependence of the DX level depth with respect to the band edges show that it does *not* precisely track the L valley.[35,36] The basis states of DX must be some weighted average of the entire Brillouin zone, as emphasized by Chadi and Chang.[20] In this case, basis states from the indirect L and X valleys will still be weighted heavily with respect to those from the low density of states Γ valley. One may then argue that this "density of states" effect might sufficiently enhance the transition rate via the indirect valleys, so that Γ valley transitions would not be observed in direct gap material.[37] Unfortunately this argument cannot explain the apparent suppression of X valley transitions in the indirect gap alloy.[37] Thus, all models involving symmetry or density of states arguments remain unsatisfactory. In reviewing the experimental evidence that charge capture and emission by the DX center proceeds *via* an excited intermediate state, we will not give much attention to these L-valley hypotheses. We will instead show that the data are consistent with a lattice relaxation associated with sequential capture of two electrons.

Chemical reactions often involve excited intermediates. (Indeed, the study of such transition states is essential to the theory of catalysis.) It should therefore be no surprise that defect reactions in semiconductor crystals should sometimes proceed in this manner. However, experimental data on defect reactions is almost universally interpreted in terms of models which ignore this possibility. Thus, in discussing three experiments concerning electron capture by the DX center in Si doped $Al_xGa_{1-x}As$, we shall emphasize how the results differ from those expected from conventional multiphonon capture models, and show how to reinterpret the results through a simple extension of the model to include a transition state.

DEPENDENCE OF THE CAPTURE AND EMISSION RATES ON ALLOY COMPOSITION

Figure 3 shows the alloy composition dependence of the activation energies for electron emission (E_e) and capture (E_c), as determined by Mooney *et al.*[38] The most striking thing about the emission energy is the lack of any measurable dependence on AlAs mole fraction, x , for $0.19 < x < 0.74$. The scatter in the data is related to alloy broadening of the transients. It is now known that the emission transients for each sample are composed of up to four distinguishable components,[22,39,40] presumably corresponding to the four distinguishable configurations of near neighbor Al and Ga atoms about the Si donor displaced towards an interstitial site.[21] Two of these components (DX levels) are now believed to be dominant over most of the alloy composition range sampled here. These exhibit, to within the accuracy of our experiment, identical activation energies for emission, E_e [38] but have been measured

to have slightly different values of E_c by Baba et al. [40]. The relative contribution of these two levels varies from sample to sample, presumably because the alloy is not perfectly random. These levels also lie at different positions with respect to the band edge [40,41] and each level is expected to move differently with temperature. Thus, in any given sample the relative occupation of these levels also changes as a function of temperature. Since the separate emission peaks tend to overlap (They have only recently been distinguished! [22,39,40]), this introduces some scatter in the activation energies determined from sets of transients in which emission from several DX levels is not separated.

In contrast to the behavior of the emission transients, note in figure 3b, on the same energy scale, the pronounced minimum in the activation energy for electron capture. At $T=115$ K this corresponds to a change in the time required to half-fill the available traps from 8×10^{-4} s at $x=0.35$ (near the composition, $x_c=0.37$, where the alloy changes from direct to indirect gap), to 1×10^4 s at $x=0.27$. We emphasize these experimentally observed changes in capture rates, because, as discussed in the next section, the precise values of E_c depend on how the capture transients are modeled. The gross trends with alloy composition are, however, unmistakable and model independent, allowing us to make the following point: A model in which multiphonon mediated capture occurs directly from the lowest conduction band edge would, in general, predict a dependence of both capture and emission energies on alloy composition. To illustrate, consider again the simple configuration coordinate diagram of figure 1, in which, for the sake of simplicity, we have assumed harmonic potential wells. If the center is highly localized, as indicated by the alloy perturbation experiments, the configuration coordinate must be a local coordinate, and the restoring force should depend very weakly on band structure (i.e. on the aggregate influence of all the surrounding atoms beyond the near neighbors). In this limit, changing the alloy composition corresponds to moving the DX parabola, U_{DX} , vertically, with respect to the conduction band parabola, U_T , without changing the shape of either parabola. Reflecting briefly, the reader will ascertain that both emission and capture energies, determined by the crossing point of the two parabolas, will change by *similar* amounts, contrary to experimental observation.

The above argument is not fully convincing, since arbitrary configuration coordinate diagrams can be constructed to explain the observations. For example, one might postulate a restoring force for the DX configuration which stiffens as x is increased. Of course, this would beg the question of what physics would be responsible for just the degree of stiffening

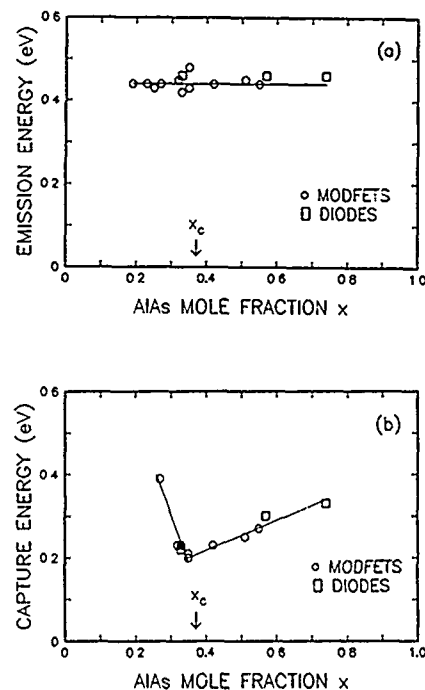


Fig. 3(a). The activation energy for thermal emission of an electron from the DX center, measured by constant capacitance DLTS, as a function of $\text{Al}_x\text{Ga}_{1-x}\text{As}$ alloy composition, x . The average value of the emission energy is 0.44 eV. (b). The activation energy for thermal capture as a function of x . The experimental uncertainty is about 20 meV in the energy and about 0.03 in x .

required to keep E_c nearly constant. A simple physical explanation for these trends is that capture occurs via an excited intermediate state which lies above the lowest lying band edge, and which roughly tracks DX as a function of x . The situation is illustrated by the configuration coordinate diagram of figure 2. As shown in the next section, the experimentally measured activation energy for capture, will be the sum of the activation energy to populate the excited state plus the activation energy to surmount the barrier separating this state from the DX state. That is, $E_c = (E_b^0 - E_F) + E_b$. Again in the limit that the restoring force is insensitive to x , changing x corresponds to translating the DX and excited state parabolas, U_{DX} and U_b^0 , vertically by similar amounts with respect to U_F . Both E_c and the multiphonon part, E_b , of the capture barrier will be independent of x , and the observed variation of E_c with x arises, in this model, from the variation of $E_b^0 - E_F$ with x .

The above argument does not depend on adopting the model of sequential capture of two electrons to the DX level illustrated by figure 2. As shown in the next section, similar conclusions will be reached for a wide variety of models involving capture through an intermediate excited state.

EXPONENTIAL DEPENDENCE OF THE CAPTURE RATE ON FERMI LEVEL

Although several authors have postulated the idea of capture via an intermediate state (i.e. L valley states) virtually none have considered how this would affect the capture kinetics. First, we recall the "standard" model by which virtually all multiphonon capture data is interpreted. We consider capture of a single electron from the lowest conduction valley, as schematically indicated by the configuration coordinate diagram of figure 1. Thus the donor has either neutral (with a deeply bound electron) or positive (ionized or with a shallowly bound electron) charge states present in concentrations of n_{DX}^0 and n_D^+ respectively, so that the total donor concentration is $N_D = n_{DX}^0 + n_D^+$. The concentrations of these charge states evolve in time according to

$$dn_D^+/dt = c_n n_{DX}^0 - c_n n_D^+, \quad (1)$$

where c_n is the electron emission rate for a neutral donor and c_n is the capture rate for an ionized donor. Ignoring acceptors and other possible donor species, the free electron concentration is $n = n_D^+$ and evolves in time as

$$dn/dt = c_n(N_D - n) - c_n n. \quad (2)$$

Typically, the electron capture cross section, σ , is defined by

$$c_n = \sigma \langle v \rangle n, \quad (3)$$

where n and $\langle v \rangle$ are the free electron concentration and mean free electron speed, respectively, and σ is taken from multiphonon capture theory to be of the form

$$\sigma = \sigma_\infty \exp(-E_b/kT). \quad (4)$$

Although σ_∞ is often assumed independent of temperature in the interpretation of experimental data, this cannot be generally correct. Depending on the physical assumptions of a particular multiphonon capture model and the statistics of population of the conduction states, σ_∞ will, in general, exhibit some weak (i.e. power law) dependence on kT . On the other hand, σ , as defined by equation 3 is not expected to depend strongly (i.e. exponentially) on the Fermi energy, even for a degenerate electron system. This is because the kinetic energy of an electron is not readily available to overcome the capture barrier. In order to be captured, the electron must coherently transfer this energy to phonon excitations of the defect. Since many phonons are involved, this is an extremely low probability process. Theoretical calculations support this intuitive view.[42]

Most capture rate experiments are done under conditions where emission from the defect is completely negligible except at the very end of the transient. Substituting equation 3 into equation 2, and ignoring emission gives

$$dn/dt = -\sigma <v> n^2. \quad (5)$$

This equation predicts non-exponential capture transients at constant temperature. In fitting the extremely non-exponential capture transients associated with the DX center, several authors have used equation 5 and found that a good fit could not be obtained without assuming some additional physical mechanism which broadens the transient. Usually a Gaussian distribution of capture barriers has been assumed.[43-45] Mooney *et al.*[38] tried such fits, and made an additional observation. In samples with identical alloy compositions, but different doping concentrations, neither a consistent average activation energy, nor a consistent broadening parameter could be found. This is illustrated by the data in figure 4, which shows capture transients (dots) obtained at various temperatures from two samples of nominally identical alloy composition, $x = 0.35$, with dopant concentrations differing by a factor of ten. Notice that in the lightly doped sample the transient extends over roughly 4 decades in time, compared to 6 decades in time in the heavily doped sample. At similar temperatures significant capture begins to occur two decades later in time in the lightly doped sample. Mooney *et al.* found that the n^2 dependence in equation 5 is not sufficient to explain these effects, unless they assumed that the distribution of capture barriers would broaden and decrease in energy with increasing doping. In contrast, they found they could consistently fit the data with a single distribution of capture barriers if they assumed kinetics appropriate for capture through an excited state. The fits are shown by the solid lines in figure 4.

The particular capture model developed by these authors is inconsistent with the hot electron capture results discussed in the next section, and thus differs from the model developed here. However, we will now demonstrate that a crucial feature of this model, the exponential dependence of capture rate on the quasi-equilibrium Fermi level, is shared by a broad class of models involving capture *via* an intermediate state. Consider the case where possible states of the donor include an intermediate state present in concentration n_D^0 , so that $N_D = n_D^0 + n_D^+ + n_{DX}$. If capture occurs *via* the excited state, the concentrations of these states must evolve in time according to

$$dn_D^0/dt = c_n n^0 - c_n n_D^+, \quad (6a)$$

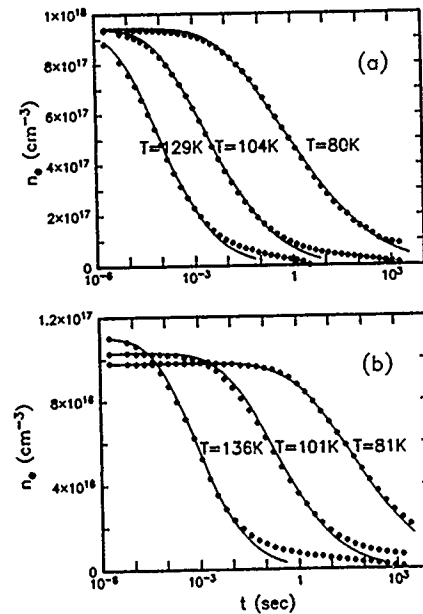


Fig. 4. The time dependence of the electron concentration in $Al_{0.35}Ga_{0.65}As$ at different temperatures for two samples with different silicon doping concentrations. (a) $N_{Si} = 1 \times 10^{18} \text{ cm}^{-3}$ and (b) $N_{Si} = 1 \times 10^{17} \text{ cm}^{-3}$. The points are experimental data and the solid lines are fits to the data.

and

$$dn_{DX}/dt = c_{n2}n_D^0 - c_{n1}n_{DX}, \quad (6b)$$

where c_{n1} and c_{n2} are the rates for transitions out of the excited and DX states, and c_{n1} and c_{n2} are the rates for transitions into the ionized and excited states, respectively. Note that we have not specified the charge of the DX state, and hence the transitions to and from this state may or may not involve a change of charge state. The physical assumption made by Mooney *et al.*[38] is that any donor which captures an electron in the excited state immediately (i.e. on a time scale short compared to the measurement) makes a transition to the DX state. This is equivalent to neglecting emission in equation 6a, and to neglecting the population of the excited state, which allows equation 6b to be replaced by $dn_{DX}/dt = -dn_D^0/dt$. Interpreted through this model, capture to the excited state was seen to be sufficiently slow as to leave the population of the conduction states essentially unperturbed, so that c_{n1} would be proportional to the conduction electron population at the energy of the transition state, or

$$c_{n1} = K \frac{1}{1 + \exp[(E_D^0 - E_F)/kT]}, \quad (7)$$

where K is a constant of proportionality, E_D^0 is the energy of the excited state, and E_F is the quasi-equilibrium Fermi energy, set by the total conduction electron population, conduction band density of states, and temperature without inclusion of the thermally disconnected DX state population. Neglecting the population of the excited state in the charge balance equation yields $n = n_D^0$. Combining this with equations 6a and 7 we obtain, in the limit that $E_D^0 - E_F > kT$,

$$dn/dt = -Kn \exp[-(E_D^0 - E_F)/kT], \quad (8)$$

which yields transients very different from those predicted by equation 5. According to equation 8, as the electron concentration drops while trapping proceeds, the quasi-Fermi level drops and the activation energy increases, stretching the capture transient in time. A heavily doped sample, with initially higher E_F must result in a capture process which starts sooner, but finishing at the nearly the same time as a more lightly doped sample, in agreement with the data of figure 4.

We regard the particular model which led to equation 8 as less important than the demonstration that the capture transients are well described by equation 8. As emphasized above, a conventional model, in which capture occurs from the lowest conduction valley will not yield an exponential dependence of dn/dt on the quasi-Fermi energy. However, in any model for capture via an intermediate state, dn/dt will be proportional to the population of the excited state, and if this state is in equilibrium with the conduction states, this population will depend exponentially on the quasi-Fermi level. Thus, models which invoke capture through the L valley will produce kinetics of this form, as previously pointed out by Theis.[33] The simultaneous assertions by Bourgoin *et al.*[14] that capture occurs through the L valley and that the capture transients can be described by equation 5, are thus seen to be mutually contradictory.

Very similar capture kinetics are found for a negative U model in the case of sequential capture of two electrons via an excited one-electron state. The donor then has a negatively charged ground state, present in concentration n_{DX} , so that $N_D = n_D^0 + n_D^+ + n_{DX}$. The concentrations of these states will evolve in time according to equations 6a and 6b, where we now set $n_{DX} = n_{DX}$. We assume, in accord with the configuration coordinate diagram of figure 2, that the one-electron state equilibrates relatively rapidly with the conduction states, and relatively slowly with the DX state. Thus, on the time scale of measurements of

the capture transients, it will always be in quasi-equilibrium with the conduction states, its population given by

$$n_D^0 = \frac{N_D - n_D^-}{1 + \exp(E_D^0 - E_F)/kT}, \quad (9)$$

where $E_D^0 - E_F$ is the energy difference between the excited state and the quasi-equilibrium Fermi level. The degeneracy of the excited state is included in equation 9 as an entropy term in E_D^0 . Substitution of equation 9 into the rate equation 6b, again ignoring emission which is negligible except at the very end of the capture transient under typical experimental conditions, gives

$$dn_D^-/dt = c_{n2} \frac{(N_D - n_D^-)}{1 + \exp(E_D^0 - E_F)/kT}. \quad (10)$$

c_{n2} is just the rate constant for multiphonon capture of a second electron from the conduction band to the DX level (the transition indicated by the curved arrow in figure 2). We may therefore follow convention and define a cross section for this capture process by writing $c_{n2} = \sigma <v> n$ just as in equation 3, where once again σ is of the form given by equation 4. From the charge balance equation, $n = N_D - n_D^0 - 2n_D^-$, we obtain $dn/dt = -dn_D^0/dt - 2dn_D^-/dt$ from which, with the aid of equations 9 and 10 we can easily obtain an equation for dn/dt . We shall not display the full result here. In the limit that $E_D^0 - E_F \gg kT$ we may simplify the Fermi factor in equation 10 and also neglect the population of the excited state as it enters the charge balance equation, yielding $dn/dt = -2dn_D^-/dt$, so that we finally obtain

$$dn/dt = -\sigma <v> n(N_D + n) \exp[-(E_D^0 - E_F)/kT]. \quad (11)$$

Once again we have obtained a capture rate which depends exponentially on the quasi-Fermi energy. The argument depends *only* on the assumptions that capture occurs through some intermediate excited state well above E_F and that this state equilibrates rapidly with the conduction states. Note that dn/dt is the product of two exponential factors. One is derived from the quasi-equilibrium population of the excited state, and is explicitly displayed in equation 10. The other factor is contained in $\sigma = \sigma_\infty \exp[-E_b/kT]$ and derives from the barrier, E_b , for a multiphonon transition to the DX state. Thus, as indicated in the previous section, the experimentally measured activation energy for capture will be the sum of the activation energy to populate the excited state plus the activation energy to surmount the barrier separating this state from the DX state. To extract an activation energy for capture from the bottom of the conduction band from a series of constant temperature capture transients fit with equation 11, one must account for the variation of E_F during each transient. The experimentally determined activation energy, referenced to the band edge, is given by $E_c = (E_D^0 - E_F) + E_b$.

THERMALLY ACTIVATED HOT ELECTRON CAPTURE

The measurements discussed above suggest the importance of an intermediate state in the capture process, but do not tell us much about this state. More information comes from the hot electron capture experiments of Theis *et al.* [46,47] Hot electron capture is observed in GaAs/Al_xGa_{1-x}As heterojunction field effect transistors when relatively high voltages are placed across the conducting channels of the devices. Theis *et al.* employed a pulse-probe technique in which brief (5 μ s - 5 ms) high voltage (0.5 - 3.0 V) square pulses, were applied across the channels of the devices. After each pulse the low field channel conductance was monitored. Care was taken to avoid significant lattice heating, and, in obtaining the results discussed here, to work under conditions where small changes in the channel conductance

are proportional to the amount of trapped charge in the Si-doped $\text{Al}_x\text{Ga}_{1-x}\text{As}$ layer. Relative capture rates were thus measured as a function of several variables by monitoring trapping induced transients in the low field conductance.

A sharp threshold voltage for hot electron capture was observed in each sample, and for samples of similar geometry and dimension, this threshold voltage increased with decreasing x . The threshold was found to be, at most, weakly dependent on sample temperature. Once the threshold was exceeded, the capture rate was found to increase rapidly with applied voltage. Important additional information is provided by the data of figure 5 showing relative capture rates at three different applied voltages,

as a function of reciprocal temperature for a sample with $x=0.35$. The relative rates were determined from the slopes of capture transients such as those found in Theis *et al.*[46], measured at the point where the channel conductance had decreased to 95 percent of its initial value. The data indicate two competing mechanisms for capture. At temperatures $\lesssim 80$ K, the dominant process is purely athermal, that is, independent of lattice temperature. Above this temperature the capture becomes thermally assisted, with an activation energy, $E_a \sim 0.1$ eV. Neither E_a nor the relative contributions of the thermally assisted and athermal processes to the total hot electron capture rate depended on the applied voltage (i.e. the average electric field). E_a was found to depend very weakly, if at all, on alloy composition ($0.2 < x < 0.35$). A value of $E_a = 0.08$ eV was obtained at $x=0.20$. This is in contrast to the strong dependence of the *thermal* capture rate on alloy composition over the same composition range as shown in figure 3b. Note also that E_a is an entirely new activation energy, much less than the smallest value observed in a thermal capture process.

This rather complex phenomenology can be summarized very simply with reference to our model of capture *via* an intermediate state. Once a threshold in the electric field is exceeded, capture begins and the capture rate is strongly dependent on field and alloy composition. In terms of our model, these parameters determine the non-thermal population of the intermediate state. On the other hand, the temperature dependence of the capture rate is not strongly dependent on field or alloy composition. In terms of our model, thermal excitation is required to overcome the barrier between the excited state and the DX state, and the electric field and alloy composition should have little effect on this barrier.

Thus we are led to picture of a two stage hot electron capture process. Referring to figure 2, the electric field drives the transfer of electrons from the Γ valley to the excited state, D^0 . Subsequent capture to the DX level is dominated either by a thermally assisted ($\gtrsim 80$ K) or by an athermal process ($\lesssim 80$ K). The thermally assisted channel is phonon mediated, and the activation energy, E_a , is a measure of E_b , the purely multiphonon part of the activation energy for thermal capture, $E_c = (E_b^0 - E_F) + E_b$. The athermal capture channel is probably direct or indirect tunneling from D^0 to DX. Such a tunneling process is expected in addition to the multiphonon process, but has not been observed in thermal capture experiments. It can now be understood that this is simply because radiative capture becomes the dominant capture channel only at temperatures $\lesssim 80$ K where the capture rate (in the

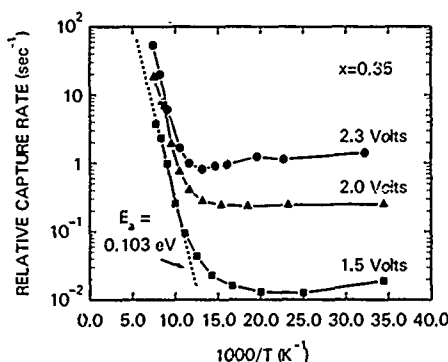


Fig. 5. Relative hot electron capture rates as a function of temperature for three source-drain voltages, showing thermally assisted ($T \gtrsim 80$ K) and athermal ($T \lesssim 80$ K) capture.

absence of an electric field) is unobservably slow. The effect of the field is to increase the population of the excited state, and hence the total capture rate, by orders of magnitude, so that the athermal process can be observed.

CONCLUSION

We have reviewed three experiments which suggest that the dominant channel for capture to the DX center is *via* an excited intermediate state. The weak dependence of the emission barrier on alloy composition, together with the pronounced minimum in the capture barrier near x_c suggest that this is the case. A stronger piece of evidence is the observation that the highly non-exponential capture transients are well described by a capture rate which depends exponentially on the quasi-Fermi level. To our knowledge, such a dependence is not predicted by any existing multiphonon capture model in which transitions occur to and from the lowest lying conduction valley. It is, however, a trivial consequence of capture *via* an excited state which equilibrates rapidly with the conduction states, and which lies well above the quasi-Fermi level. While these observations suggest the importance of an intermediate state in the capture process, we have emphasized that they do not tell us much about the state. Our best information in this regard comes from the hot electron capture experiments. These experiments are simply interpreted in terms of an intermediate state with a small lattice relaxation and a comparatively small thermal barrier for capture to the DX level.

Although all of these results are now several years old, and of importance in resolving the debate which still surrounds the DX center, the dependence of the capture transients on sample doping, and the existence of thermally activated hot electron capture have not yet been checked by other investigators. In particular, careful studies of the form of the capture transients in GaAs under hydrostatic pressure would be most interesting. When obtained under conditions of constant capacitance, the emission transients in GaAs are now known to be perfectly exponential.[48] Baba *et al.*[40] have also shown that emission transients for DX levels with no Al near neighbors are exponential. According to our model, the capture transients obtained at constant capacitance should still exhibit stretched exponential behavior which depends in a well defined way on the dopant concentration. Carrying the work reviewed here a step further would be a search for spectroscopic evidence of this state. Based on our interpretation of our experimental results, we expect that in Si-doped material this state will lie $E_c - E_b \sim 0.3$ eV above the DX level. This would place it above the lowest conduction band edge at all $\text{Al}_x\text{Ga}_{1-x}\text{As}$ alloy compositions, where it might be observed as a resonant peak in the photo-induced capture rate of the DX center. For dopants other than Si, E_c has smaller values and E_b (as defined in figure 2) remains unmeasured. The transition state might lie within the gap at alloy compositions near the direct to indirect crossing.

We have emphasized that these experimental results provide strong, if indirect, support for the idea that DX exhibits negative effective U. Only if DX captures more than one electron is there a physically plausible reason for the dominant capture channel to involve a transition state. We have said very little about the nature of this precursor to DX, except that it should roughly track the DX level as a function of alloy composition, it should be resonant with the conduction band in the Si-doped $\text{Al}_x\text{Ga}_{1-x}\text{As}$ alloy system, and it should have a relatively small lattice relaxation compared to the DX state. The hydrogenic states associated with the indirect valleys are obvious candidates. However, some explanation would then be required for the apparent suppression of X valley transitions in favor of L valley transitions in indirect gap $\text{Al}_x\text{Ga}_{1-x}\text{As}$. We therefore speculate that the transition state may be a deep level associated with the donor on its substitutional site, of the type predicted by Hjalmarson *et al.*[1]

ACKNOWLEDGEMENTS

We would like to thank F. Stern, T.N. Morgan and G.A. Baraff for extensive discussions which have helped to clarify the arguments presented here.

REFERENCES

1. H.P. Hjalmarson, P. Vogel, D.J. Wolford, and J.D. Dow, Phys. Rev. Lett. 44, 810 (1980).
2. D.V. Lang, R.A. Logan, and M. Jaros, Phys. Rev. B 19, 1015, (1979).
3. T.N. Theis, T.F. Kuech, L.F. Palmateer, and P.M. Mooney, Inst. Phys. Conf. Ser. 74, 241 (1985) (Proc. Int. Conf. on GaAs and Related Compounds, Biarritz, 1984); T.N. Theis in *Defects in Semiconductors*, edited by H.J. von Bardeleben, (Switzerland, Trans Tech, 1986) pp 393-8.
4. J.E. Dmochowski, J. Langer, J. Raczynska, and W. Jantsch, Phys. Rev. B 38, 3276 (1988).
5. T.N. Theis, Inst. Phys. Conf. Ser. 95, 307 (1989) (Proc. Int. Conf. Shallow Impurities in Semiconductors, Linköping, Sweden, 1988).
6. M. Mizuta, M. Tachikawa, H. Kukimoto, and S. Minomura, Jpn. J. Appl. Phys. 24, L143 (1985).
7. M. Tachikawa, T. Fujisawa, H. Kukimoto, A. Shibata, G. Oomi, and S. Minomura, Jpn. J. Appl. Phys. 24 L893 (1985).
8. D.K. Maude, J.C. Portal, L. Dmowski, T. Foster, L. Eaves, M. Nathan, M. Heiblum, J.J. Harris, and R.B. Beall, Phys. Rev. Lett. 59, 815 (1987).
9. J. Maguire, R. Murray, and R.C. Newman, Appl. Phys. Lett. 50, 516 (1987).
10. L. Eaves, T.J. Foster, D.K. Maude, G.A. Toombs, R. Murray, R.C. Newman, J.C. Portal, L. Dmowski, R.B. Beall, J.J. Harris, M.I. Nathan, and M. Heiblum, Inst. Phys. Conf. Ser. 91, 355 (1988) (Proc. Int. Symp. on Gallium Arsenide and Related Compounds, Heraklion, Greece, 1987).
11. J.C.M. Henning, and J.P.M. Ansems, Semicond. Sci. and Technol. 2, 1 (1987).
12. L. Resca, D.J. Lohrmann, and R.D. Graft, Phys. Rev. B 36, 2741 (1987).
13. J.C. Bourgoin and A. Mauger, Appl. Phys. Lett. 53, 749 (1988).
14. J.C. Bourgoin, S.L. Feng and H.J. von Bardeleben, Phys. Rev. B 40, 7663 (1989).
15. H.P. Hjalmarson and T.J. Drummond, Appl. Phys. Lett. 48, 656 (1986) and Phys. Rev. Lett. 60, 2410 (1988).
16. E. Yamagouchi, J. Phys. Soc. Japan 56, 2835 (1987).
17. A. Oshiyama, in *Defects in Semiconductors* 15 Ed. G. Ferenczi, Materials Science Forum vols. 38-41 (Trans Tech Publications, Switzerland, 1989) p. 287.
18. A. Oshiyama and S. Ohnishi, Phys. Rev. B 33 4320 (1986).
19. P.M. Mooney, G.A. Northrop, T.N. Morgan, and H.G. Grimmeiss, Phys. Rev. B 37, 8298 (1988).
20. D.J. Chadi and K.J. Chang, Phys. Rev. Lett. 61, 873 (1988) and Phys. Rev. B 49, 10366 (1989).
21. T.N. Morgan in *Defects in Semiconductors* 15, Ed. G. Ferenczi, Materials Science Forum 38-41 (Trans Tech Publications, Switzerland, 1989) p. 1079.
22. P.M. Mooney, T.N. Theis, and S.L. Wright, Appl. Phys. Lett. 53, 2546 (1988).
23. G.D. Watkins, in *Defects in Semiconductors*, Eds. J. Narayan and T.Y. Tan (North Holland, New York, 1981) p. 21.
24. T.N. Theis, T.N. Morgan, B.D. Parker, and S.L. Wright in *Defects in Semiconductors* 15, Ed. G. Ferenczi (Trans Tech Publications, Ltd., Switzerland, 1989) p. 1073.
25. J.M. Langer, J.E. Dmochowski and L. Dobaczewski, Ed. J. Bourgoin, Mat. Science Forum (Trans Tech Publications, Ltd., Switzerland, 1990) in press.
26. D.K. Maude, L. Eaves and J.C. Portal, Phys. Rev. Lett. 62, 1922 (1989).

27. D.J. Chadi, K.Y. Chang and W. Walukiewicz, *Phys. Rev. Lett.* **62**, 1923 (1989).
28. E.P. O'Reilly, *Appl. Phys. Lett.* **55**, 1409 (1989).
29. T. Dietle, J.E. Dmochowski, J. Kossut, J.M. Langer and K. Swiatek, *unpublished*.
30. K.A. Khachatryan, D.D. Awschalom, J.R. Rosen and E.R. Weber, *Phys. Rev. Lett.* **63**, 1311 (1989).
31. A. Majerfeld and P.K. Bhattacharya, *Appl. Phys. Lett.* **33**, 261 (1978) and P.K. Bhattacharya, A. Majerfeld and A.K. Saxena, *Inst. Phys. Conf. Ser.* **45**, 199 (1979).
32. E. Calleja, A. Gomez and E. Munoz, *Appl. Phys. Lett.* **52**, 383 (1988).
33. T.N. Theis, *Inst. Phys. Conf. Ser.* **91**, 1 (1988), *Proc. of Int. Symp. on GaAs and Related Compounds*, Heraklion, Greece, 1987. See also D.V. Lang in *Deep Centers in Semiconductors*, Ed. S.T. Pantelides (Gordon and Breach Science Publishers, New York, 1986), p. 527.
34. T.N. Theis, P.M. Mooney and S.L. Wright, *Phys. Rev. Lett.* **60**, 361 (1988).
35. T. Suski, E. Litwin-Staszewska, R. Piotrkowski, L. Dmowski, P. Wisniewski, L. Zanotti, X. Tang and L.J. Gilling, in *Proc. of the 19th Int. Conf. Phys. Semiconductors*, Ed. W. Zawadzki, (Inst. of Phys. of the Polish Acad. Sci., Warsaw 1988) p. 1047.
36. S. Azema, V. Mosser, J. Camassel, R. Piotrkowski, J.L. Robert, P. Gilbert, J.P. Contour, J. Massie and A. Marty, in *Defects in Semiconductors 15*, Ed. G. Ferenczi, Materials Science Forum Vols. 38-41, (Trans Tech Publications, Ltd., Switzerland, 1989) p. 857.
37. T.N. Theis in *Proc. of the 19th Int. Conf. on Phys. of Semiconductors*, Ed. W. Zawadzki (Inst. of Phys. of the Polish Acad. Sci., Warsaw, 1988) p. 1083.
38. P.M. Mooney, N.S. Caswell, and S.L. Wright, *J. Appl. Phys.* **62**, 4786 (1987).
39. E. Calleja, A. Gomez, E. Munoz and P. Camara, *Appl. Phys. Lett.* **52**, 1877 (1988).
40. T. Baba, M. Mizuta, T. Fujisawa, J. Yoshino, and H. Kukimoto, *Jpn. J. Appl. Phys.* **28**, L891 (1989).
41. E. Calleja, F. Garcia, A. Gomez, E. Munoz, P.M. Mooney, T.N. Morgan and S.L. Wright, *unpublished*.
42. A.S. Ioselevich and E.I. Rashba, *Sov. Phys. JETP* **64**, 1137 (1986). (*Zh. Eksp. Teor. Fiz.* **91**, 1917 (1986)).
43. M. Kaniewska and J. Kaniewski, *Solid State Comm.* **53**, 485 (1985) and *J. Appl. Phys.* **63**, 1086 (1988).
44. M. Takikawa and M. Ozeki, *Jpn. J. Appl. Phys.* **24**, 303 (1985).
45. L. Dobaczewski and J.M. Langer, in *Defects in Semiconductors*, Ed. H.J. von Bardeleben, Materials Science Forum Vols. 10-12 (Trans Tech Publications, Ltd., Switzerland, 1986) p. 399.
46. T.N. Theis, B.D. Parker, P.M. Solomon and S.L. Wright, *Appl. Phys. Lett.* **49**, 1542 (1986).
47. T.N. Theis and B.D. Parker, *Appl. Surf. Sci.* **30**, 52 (1987).
48. E. Calleja, P.M. Mooney, and S.L. Wright, *unpublished*.

EFFECT OF LOCAL ATOMIC CONFIGURATION ON DX ENERGY LEVEL

T. BABA*, M. MIZUTA*, T. FUJISAWA**, J. YOSHINO** and H. KUKIMOTO**

*Fundamental Research Laboratories, NEC Corporation, 34 Miyukigaoka, Tsukuba, Ibaraki 305, Japan

**Imaging Science and Engineering Laboratory, Tokyo Institute of Technology, 4259 Nagatsuda, Midori-ku, Yokohama, Kanagawa 227, Japan

ABSTRACT

The effects of specific local environments on DX centers were investigated for two different substitutional-site-donors of Si and Te in selectively-doped ordered-alloy samples. Capacitance transient technique under hydrostatic pressure was utilized for the determination of the DX energy-level structure. Downward movement of the energy levels for both Si- and Te-DX centers was observed when Al occupies the 2nd or 1st nearest neighbor site, respectively. A very large shift of the electron-emission activation-energy with pressure was found for the Te-DX centers surrounded by specific Al and Ga mixed-environments, whereas negligible shift for the Si-DX centers was observed regardless of the environment. These effects were discussed in relation to the lattice relaxation of the relevant DX centers.

INTRODUCTION

More than a decade has been passed since strange behaviors of n-type impurity, the DX center, in AlGaAs were discovered. In recent years, the origin of the DX center has been believed as a simple substitutional donor rather than the complex center consisting of a donor and a defect [1-5]. One of the important remaining issues is the lattice relaxation mechanism in real space. Recent findings of local-environment-specific energy level of the DX center together with theoretical prediction of multiplicity of the DLTS peak due to the large lattice relaxation scheme could make us possible to determine the relaxation mechanism by analyzing DLTS spectra of the DX center [6,7]. Local environment, especially the configuration of Al and Ga around a donor impurity, is apparently simpler for the group VI donors than for the group IV donors, if simple substitutional donor is assumed. In this regard, effect of local environment on the DX energy level of a Te donor was investigated and compared to that of the Si-DX center.

The main concern of this paper is to evaluate the effect of Al on the energy level of the Te (V-site) DX center and compare it for the case of Si (III-site). We have found that the neighboring of Al (the first nearest site) to Te donors decreases the DX energy level just like the Si donor case previously reported. However, two types of the DX centers are classified by the pressure dependence. One shows negligible shift of the DLTS peak-temperature upon pressure application, similar to the case for the Si DX centers. The other type shows very large shift on pressure change. This difference is discussed in relation to the lattice relaxation mechanism.

EXPERIMENTS

In order to clarify the effect of local atomic configuration around Si and Te donors, we fabricated samples of ordered alloy (OA) structure, which consist of 1 monolayer of AlAs and 14 monolayers of GaAs. Silicon or Te donors were doped with the average concentration of $1 \times 10^{18} \text{ cm}^{-3}$. These layers were repeatedly piled to make the total thickness of 3,000 Å. An undoped $\text{Al}_{0.5}\text{Ga}_{0.5}\text{As}$ or $\text{Al}_{0.2}\text{Ga}_{0.8}\text{As}$ layer (200 Å), for suppressing leak current of a Schottky diode, was successively grown on top of the OA structure by molecular beam epitaxy at 520°C. As shown in Fig.1 (a) and (b) for Si and Te donors,

respectively, only three or two local configurations around donors were allowed if the structure is ideally grown. From the lattice images of the transmission electron micrograph measurement, almost perfect and sharp interface between AlAs and GaAs was observed for the case of the Si-doped OA structure, although in some portion there are 2 monolayers of AlAs. On the other hand, rough AlAs/GaAs interface and up to 3 monolayers above AlAs layer was seen for the Te-doped OA structure despite the same growth temperature. The origin for such difference is presently unknown, but the unique behavior of Te diffusion and segregation may locally destroy the layer structure, which will be published in detail elsewhere. Due to this observation, we can expect much variety of local environment for Te as shown in Fig.1 (c) rather than the ideal layer structure of Fig.1 (b). As a reference, Te-doped GaAs ($n=1.5 \times 10^{17} \text{cm}^{-3}$) and Te-doped $\text{Al}_{0.1}\text{Ga}_{0.9}\text{As}$ ($n=1.0 \times 10^{17} \text{cm}^{-3}$) samples were also examined.

Bandgaps of the samples were determined by measuring photoluminescence at room temperature. Those are found to be 1.516eV, 1.527eV and 1.570eV for Si-OA, Te-OA structures and $\text{Al}_{0.1}\text{Ga}_{0.9}\text{As}:\text{Te}$. These values are equivalent to those of $\text{Al}_{0.07}\text{Ga}_{0.93}\text{As}$ and $\text{Al}_{0.08}\text{Ga}_{0.92}\text{As}$ for the Si- and Te-OA structures, respectively.

Gate metal of Ti/Au was deposited onto the surface of the samples to measure the capacitance-voltage characteristics and deep level transient spectroscopy (DLTS) under hydrostatic pressure, which was described in previous paper in detail [1].

RESULTS AND DISCUSSIONS

Figure 2 shows the DLTS spectra of the Te-OA structure under hydrostatic pressure from 6kbar to 29kbar. Five peaks labeled A, B, C, D and E can be seen in this figure, and their intensities change (increase or saturate) with increasing pressure. Similar DLTS spectra for GaAs:Te and $\text{Al}_{0.1}\text{Ga}_{0.9}\text{As}:\text{Te}$ are shown in Fig.3. The DX center due to the Te donor in pure GaAs appears around 110K at the critical pressure of 31kbar (Fig.3, peak A). In considering the similar critical pressure to appear, together with its peak position, the peak A in the Te-OA structure in Fig.2 can be attributed as the Te-DX center surrounded only by Ga (hereafter referred to as Te-OA1) (note the different

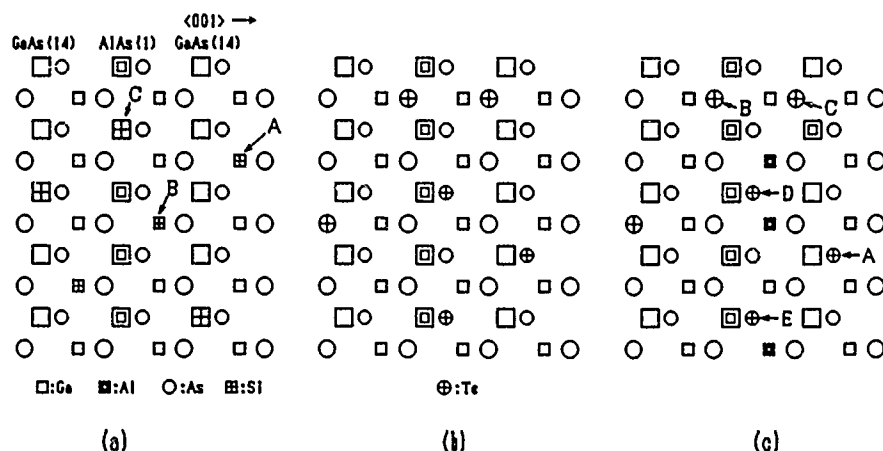


Fig. 1. Schematic diagram of the sample structures. (a) Ideal structure of Si-doped ordered alloy (OA). (b) Ideal structure of Te-OA. (c) Expected structure of Te-OA from TEM measurements. Labels from A to E are possible site for donors.

bandgaps of the OA structure in Fig.2 and GaAs in Fig.3, which results in the slight difference in the critical pressure). In $\text{Al}_{0.1}\text{Ga}_{0.9}\text{As}:\text{Te}$, two clear DLTS peaks appear from 21kbar to 25kbar. By simple calculation for the first nearest atoms (four group III sites) around Te in $\text{Al}_{0.1}\text{Ga}_{0.9}\text{As}$, the probability for one Al atom around Te (Te-1Al) is about 30% and 5% for two Al atoms (Te-2Al). Probability of more than 3 Al atoms is less than 1%. The concentration ratio of peak B and C in Fig.3 is almost 5 and is close to the predicted value for the ratio of Te-1Al and Te-2Al. Therefore, peak B and C in Fig.3 is reasonably assigned to be the DX centers of Te-2Al and Te-1Al, respectively. By comparing peaks B and C in Fig.2 with those in Fig.3, their peak temperatures and pressure dependence are almost identical. Therefore, it is concluded that peak B and C in Fig.2 are Te-2Al and Te-1Al in the Te-OA structure. Hence, the rest peaks of D and E in Fig.2 should be Te-4Al and Te-3Al (detailed assignment will be given below).

The energy levels of the distinct DX centers can be determined by curve-fitting for the pressure dependence of amplitude of each DLTS peak as was the case for the previous work [6]. This, unfortunately, was not possible for the present Te-doped samples, because the DLTS spectra are not so well separated, due to overlapping of B and C peaks upon pressure change. However, relative energy position of each peak can be known by comparing the critical pressure of each peak to appear in the DLTS spectra; the lowest lying energy level should appear at the lowest pressure and also the intensity of the peak should saturate first. We already determined the number of the first nearest neighbor Al associated with Te donor for peak A, B, and C as 0, 2, and 1, respectively. Within these three peaks, the peak B appears at the lowest pressure followed by peaks C and A in this order. Their saturation behavior is also consistent with this order; peak B tends to saturate around 21kbar in Fig.3, while peak C

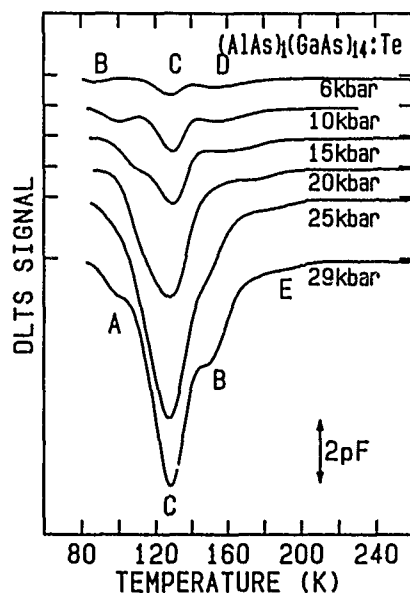


Fig. 2. DLTS signals from Te doped ordered alloy under various hydrostatic pressures. There are five apparent peaks, denoted as A, B, C, D, and E, which are corresponding to specific local environment as shown in Fig. 1 (c).

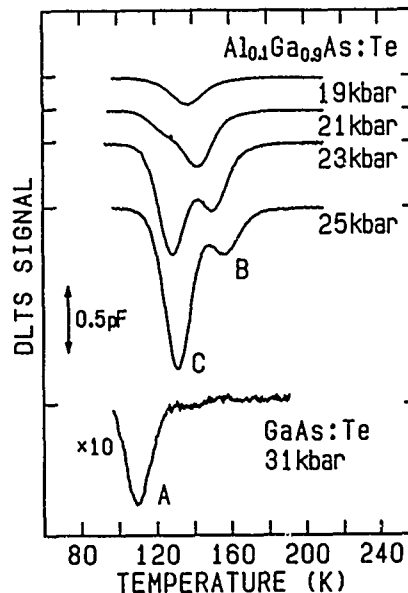


Fig. 3. DLTS signals from Te doped GaAs and $\text{Al}_{0.1}\text{Ga}_{0.9}\text{As}$ under various hydrostatic pressures. There are three apparent peaks, denoted as A, B and C, each of which is identical in Fig. 2.

does not saturate even at 25kbar. Therefore, the DX energy level of the peak B should be lower than C which should again be lower than A. We now know that the influence of Al-coordination to Te donor is to lower its energy level just like the case of Si donor. With this in mind, we can safely speculate the number of Al associated with peaks D and E as in the following. Since peak D saturates at lower pressure of 15kbar than the peak E does, peak D should have larger number of Al than peak E. In addition both peaks D and E have lower saturation pressure than those for peaks A, B, C, indicating peaks D, E should have more than 3Al around Te impurity in agreement with the previous assumption. It should be noted here that the energy level of peak A is obviously higher than the Si-DX center in GaAs with comparing their critical pressures. These are summarized in Table I with the results for the Si-OA structure. The Al atom influences both Si and Te DX centers, and lower their energy levels.

Figures 4 (a) and (b) show the pressure dependence of the DLTS peak temperature for the Si-OA structure and Te-doped samples. The inset in Fig. 4 (a) is typical DLTS spectrum under hydrostatic pressure for the Si-OA structure. In accordance with the previous study, the labels in this figure are corresponding to the specific local environments as shown in Fig.1 (a). The DLTS peak temperatures for Si case are almost constant in the pressure range investigated in this study. On the other hand, there are two classes of Te-DX centers which have vastly different pressure dependence as shown in Fig.4 (b). One type of the Te-DX centers corresponding to peaks A, C and D is pressure-insensitive just like the case for Si, while the other peaks B and E are quite sensitive. The peak B has large pressure coefficient of about 2.5K/kbar for DLTS peak temperature. The DLTS activation energy (electron emission barrier) also change from 0.25eV to 0.31eV under the pressure from 19kbar to 25kbar in $\text{Al}_{0.1}\text{Ga}_{0.9}\text{As}:\text{Te}$, resulting in the pressure coefficient of about 10meV/kbar. This large and similar pressure coefficient for the peak B in Fig.2 ($\text{Al}_{0.1}\text{Ga}_{0.9}\text{As}:\text{Te}$) and that in Fig.3 (Te-OA system) further confirms the identity of the two peak B's. The slight shift of peak temperature for the two peak B's is apparently caused by difference in their bandgaps. These results

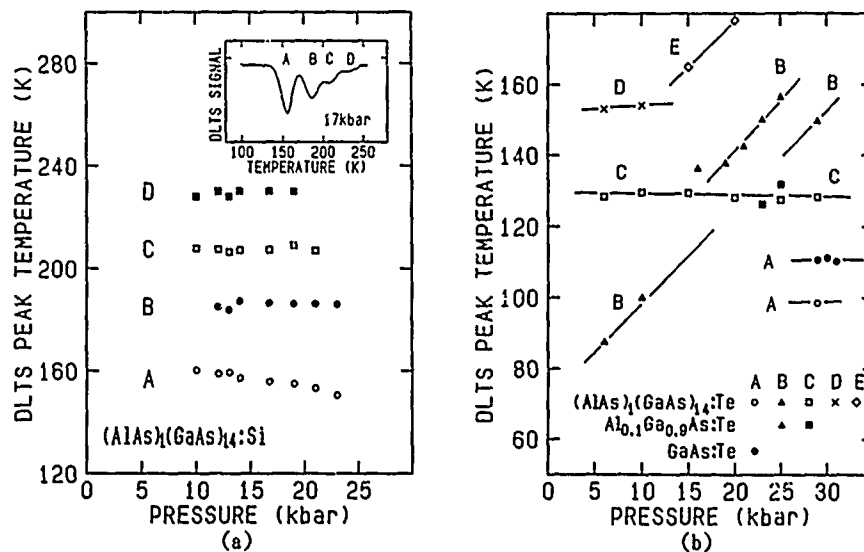


Fig. 4. Pressure dependence of peak temperature for various DLTS peaks. (a) For Si doped ordered alloy. Inset is a typical DLTS signal for Si-DX center in Si-OA structure under hydrostatic pressures. Label D is corresponding to Si-DX center in two monolayers of AlAs. (b) For Te doped OA structure, GaAs and $\text{Al}_{0.1}\text{Ga}_{0.9}\text{As}$.

Table I. DLTS results for Si- and Te-DX centers with different local environments. Numbers ①-⑤ indicate the descending order of DX energy level.

Donor Site	Al near donor	Number of	Peak temperature T _{DLTS} (K)	$\delta T_{DLTS}/\delta P$ (K/kbar)	Electron emission barrier E _e (meV)	DX energy level E _{DX} -E _C (GaAs) (meV)
Si	A	0	160	~0	320	295
	B	4	180	~0	400	245
	C	4	210	~0	430	225
	D	>4	230	~0	~470	175
Te	A	0	~100	~0	230	①
	C	1	130	~0	250	②
	B	2	90-150	~2.5	160-310	③
	E	3	160-190	~2.0		④
	D	4	150	~0	~300	⑤

are summarized in Table I. The value of electron emission barrier for the Te DX center in site B is listed with combining the results for the Te-0A and Al_{0.1}Ga_{0.9}As:Te samples. Although this energy was not determined successfully for the site E, similar dependence of the emission barrier upon pressure can be speculated, because of similar pressure dependence of the DLTS peak temperature for sites B and E. Why does the emission barrier change so much with pressure only for sites B and E? In the configuration coordinate diagram based on the large or small lattice relaxation model, the emission barrier is defined as the difference between the DX ground state and the crossing point of two adiabatic potentials. The energy movement of the emission barrier indicates the change in the relative positions or curvatures for two potentials by pressure. In this point of view, we can expect that the lattice relaxation of the DX center occurs with keeping the emission barrier constant for the Te-A, C, D sites and for all Si sites, but not for the Te-B, E sites. This means that different lattice relaxation proceeds depending upon the local environment around donor atoms.

The observation of different pressure-dependence for Te-DX centers is quite interesting, but the reason why this difference occurs is not easily understandable at present. To make it more clear, more precise experiments, e.g., determination of absolute energy level of Te-DX centers, and theoretical investigation should be necessary.

SUMMARY

Using samples consisting of a monolayer of AlAs and 14 monolayers of GaAs with Te as a dopant, DLTS measurements were conducted under various hydrostatic pressures. The energy level for the Te-DX center surrounded only by Ga was found to be higher than the energy of the Si-DX center in GaAs. Downward movement of Te-DX centers when associated with Al as the 1st nearest neighbor was also observed just like the case of Si. On the other hand, different from the Si-DX center, a very large shift of the activation energy for electron emission with pressure was found for the Te-DX center in the mixed-environments. These results strongly indicate that the local environments around donors affects their DX energy levels regardless of the group of donors.

ACKNOWLEDGMENT

The authors would like to thank N. Ikarashi and K. Ishida for TEM measurements of layer structures. Two of us (TB and MM) acknowledge Y. Mochizuki and A. Oshiyama for fruitful discussions.

REFERENCES

1. M. Mizuta, M. Tachikawa, H. Kukimoto and S. Minomura, Jpn. J. Appl. Phys. 24, L143 (1985).
2. T. Baba, T. Mizutani and M. Ogawa, Jpn. J. Appl. Phys. 22, L627 (1983).
3. T. Baba, M. Ogawa and T. Mizutani, Surf. Sci. 174, 408 (1986).
4. T. N. Theis, P. M. Mooney and S. L. Wright, Phys. Rev. Lett. 60, 361 (1988).
5. T. N. Theis, B. D. Parker, P. M. Solomon and S. L. Wright, Appl. Phys. Lett. 49, 1542 (1986).
6. T. Baba, M. Mizuta, T. Fujisawa, J. Yoshino and H. Kukimoto, Jpn. J. Appl. Phys. 28, L891 (1989).
7. T. N. Morgan, Material Science Forum 38-41, 1079 (1989).

ELECTRIC FIELD ENHANCEMENT OF ELECTRON EMISSION FROM DX CENTERS AND CONSEQUENCES

J.C. BOURGOIN*, M. ZAZOUI*, S.L. FENG*, H.J. von BARDELEBEN*, S. ALAYA** AND
H. MAAREF**

Groupe de Physique des Solides de l'École Normale Supérieure, Centre National de la Recherche Scientifique, Tour 23, 2 place Jussieu, 75251 Paris Cedex 05, France

**Faculté des Sciences, Université de Monastir, Monastir, Tunisie.

ABSTRACT

We present data which show that electron emission from the DX center is sensitive to the Poole-Frenkel effect. We demonstrate that this result implies that the DX center is an L effective-mass state of the donor impurity accompanied by a small lattice relaxation. We show that all the observations so far obtained on this center are in agreement with this model.

INTRODUCTION

Recent magnetic susceptibility experiments [1] demonstrate that the ground state of the DX center is occupied by a single electron. Here we show that the enhancement of the emission rate of this electron by an electric field, when studied in proper conditions, is caused by a purely Poole Frenkel effect. This result implies that the DX center corresponds to a single donor state. This donor state cannot be associated with either the Γ band or the X band since these states are well characterized in, respectively, direct and indirect band gap GaAlAs alloys. The DX center is therefore the effective-mass state associated with the L band : its level is 200 meV deep whatever the donor impurity [2] because it is submitted to a shallow-deep instability induced by intervalley mixing [3]. We shall therefore examine the main properties of the DX center and discuss how they can be understood in such a model.

ELECTRIC FIELD ENHANCEMENT OF ELECTRON EMISSION

The effect of the electric field on the emission rate of an electron from the DX center has already been studied [4,5] using Deep Level Transient Spectroscopy (DLTS). The data cannot be interpreted easily because the capacitance transients associated with electron emission from the DX center are usually non exponentials, and thus small changes such as those due to a perturbation by an electric field, even if they can be detected, cannot be mea-

*laboratoire associé à l'Université Paris VII.

sured correctly. The main reason for such non exponential behavior of the transient is that the concentration of the DX center is not small enough compared to the free carrier concentration [6], but there are several other causes such as strain effects, alloying effects, etc.

In order to perform quantitative measurements of this effect, we have used very short filling pulses so that the concentration of the filled center remains small compared to n . In addition we have used a liquid phase epitaxy material where the n-type doped layer is grown on a thick p-type layer whose alloy composition is continuously variable. We have selected Te as the n-type impurity for which the DLTS associated spectra have a shape identical to the theoretical one, i.e. for which the emission transients are purely exponentials.

Several values of the alloy composition ranging from $x = 0.25$ to 0.80 have been studied. For all of them a change in the emission rate e_n is

observed with the electric field. However, the associated ionization energy E_i , determined from the shape of the plot $\ln(e_n)$ versus T^{-1} , does not change significantly. Only in the case of an alloy composition $x = 0.25$ is the decrease ΔE_i in E_i significant. As shown in figure 1 ΔE_i varies with the electric field F demonstrating that this change is caused by a Poole-Frenkel effect. The slope of ΔE_i versus \sqrt{F} (i.e. assuming a Coulomb potential) indicates that electron emission corresponds to a $0/+$ transition of the DX center, i.e. that the center is a single donor.

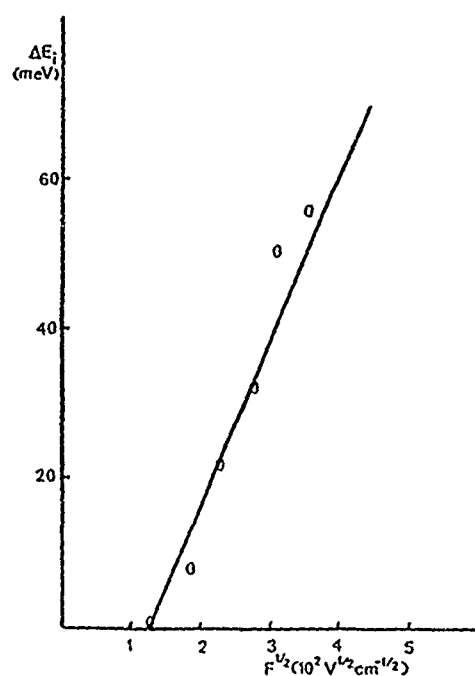


Fig. 1 : Decrease of the ionization energy of the DX center in a Te ($8 \times 10^{16} \text{ cm}^{-3}$) doped GaAlAs having an alloy composition of 0.25 (origin at the lowest field).

The reason why the Poole-Frenkel effect is only apparent in a small range of x values is described elsewhere [7]. Here we shall only show how the main properties of the DX center can be understood if this center is the effective-mass state associated with the L band that this result implies. Indeed, the

existence of this effect rules out the possibility that the DX center is a deep level (it is non negligible only for long range defect potentials) and above all a negative U defect ($-/0$ and $0/+$ transitions cannot be sensitive to it).

THE DX CENTER AS AN L EFFECTIVE-MASS STATE

The DX center behaves apparently [8] as a deep state because i) the thermal ionization energy (0.4 eV for Si) is small compared to the optical threshold (0.8 eV) for photoionization (thus implying a large Franck-Condon shift i.e. a large lattice relaxation); ii) the electron capture cross-section is thermally activated (thus implying a multiphonon emission process associated with the capture), the associated barrier B being a function of the alloy composition x.

However, such interpretation of the data is based on the assumption that the optical transition is a transition from the DX level to the bottom of the conduction band. This is in contradiction with two observations : first, recent electron paramagnetic resonance studies [9] show that in a direct gap material, the photoexcitation induces the filling of the X effective-mass state i.e. in which the X band is well above the bottom of the conduction band. Second, this optical threshold is not dependent on x i.e. on the band structure as it should be since the position of the DX level as compared to the bottom of the conduction band varies with x. This result directly obtained using photo-capacitance experiments [10] has been verified by photoluminescence. As shown in figure 2 the 0.8 eV photoluminescence band [11] which corresponds to the same energy as the threshold for optical absorption (this implying a negligible Franck-Condon shift) is independent on the alloy composition. This conclusion implies that the optical transition is an internal one [12], the photoionization into the bottom of the conduction band occurring at a considerably lower energy than

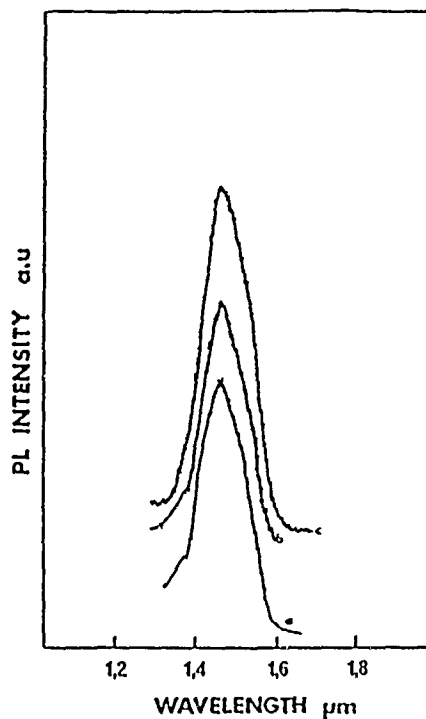
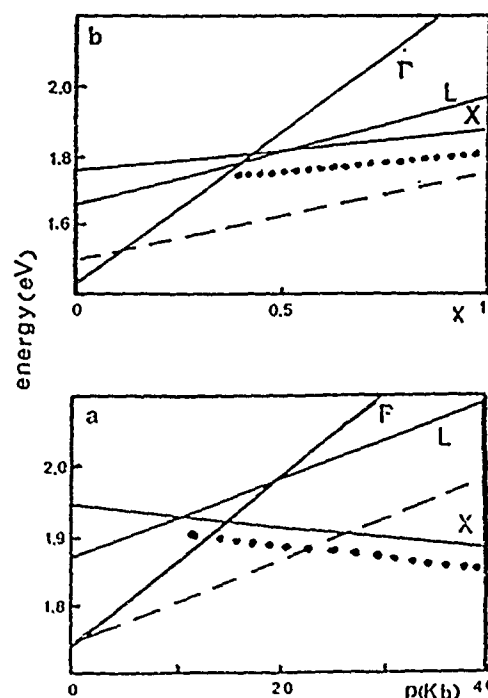


Fig. 2 : Dependence of the 0.8 eV photoluminescence band in Si doped GaAlAs with the alloy composition x = 0.27 (a), 0.29 (b) and 0.37 (c).

0.8 eV [13] with a low efficiency.

Moreover, a deep defect model for the DX center does not allow to understand the fact that the capture barrier B varies with x as the difference between the L band and the bottom of the conduction band [7,12]. But the effective-mass model does, because electron capture on an effective-mass state occurs via a cascade process which involves its excited states. These states lie close to the L band. Thus an electron must be first excited into the L band before it can recombine and the capture probability is proportional to $\exp(-B(x)/kT)$.

Deep state models, such as the one proposed by Chadi and Chang [14], cannot explain why the DX energy level remains at a constant energy (within the experimental accuracy) from the L band, a direct consequence of the effective-mass state nature of a level. Chadi and Chang argue [14] that the DX level follows the average conduction band energy, which is close to the L band variation. However, the state they derive for the DX center is an acceptor state which is built from valence band states and not at all from conduction band states. We note that, in addition, an effective-mass state predicts, as is observed, that the position of the associated level is independent of the chemical nature of the impurity and on its lattice site (As or Ga). This should not be so in a deep level model, the level being strongly dependent on the lattice distortion which is a function of both the nature of the impurity and of its lattice site.



Finally, we examine two final arguments used as evidences, one for the large lattice distortion model and the other against the effective-mass model.

Fig. 3 : Schematic variations of the Γ , L and X conduction band minima as a function of (a) hydrostatic pressure p (typically for an alloy composition of 0.25) and of (b) alloy composition x (at atmosphere pressure) showing the DX (L effective-mass) state (dashed line) and the X effective-mass state (point line). The state detected by DLTS is the deepest one i.e. the L state (DX) in cases b and a (direct gap) and the X state in case a (indirect gap).

The first one is so-called alloying effect which states that the existence of several components in the DX DLTS spectrum is a manifestation of the fact that there are several types of DX levels depending on the Al environment of the impurity [15]. Such interpretation can be ruled out easily since there are instances, such as the case of Te doped liquid phase epitaxial material, where the DLTS spectrum exhibits only one component whatever x , while there are other instances, the case of Si-doped GaAs under hydrostatic pressure, where the DLTS spectrum exhibits at least two components [16], although in the last case there is no Al i.e. no alloying effect possible. The second argument is that the fact that the pressure derivative of the DX level is not identical to the pressure derivative of the L band, at least in some pressure (or alloy composition) ranges, implies that the DX level cannot be an L effective-mass state. But, once again, if one looks in detail to this question one sees that this argument is not valid. As shown in a recent systematic study [17] the pressure coefficients of the L band and DX levels are equal in direct gap materials but differ in indirect gap materials. The reason is the following, based on the fact that the band structure modifications by varying the alloy composition and the hydrostatic pressure are not identical: alloying increases the energy of the X minima while hydrostatic pressure decreases it. The result is that, as illustrated on figure 3, the DX state (the L effective-mass donor state) remains the impurity ground state in indirect gap materials which result from a variation of the alloy composition. But, in indirect gap materials produced by hydrostatic pressure it is the X associated donor state which becomes the ground state, the DX state becoming resonant in the conduction band. The data of ref. [17] can be quantitatively accounted for using the X associated effective-mass state at ~ 30 meV below the X minimum. This explains why the DX ionization energy is found to change with pressure in the indirect region, while it does not with x .

CONCLUSION

We have shown that the properties of the DX center can reasonably be understood if this center is simply an L effective-mass state associated with the donor impurity, while a large lattice relaxation (LLR) model cannot. Actually, we have not discussed other observations which all are consistent with this model and not with a LLR models. They are: i) the absorption of localized vibrational modes on Si which does not detect any Si related centers exhibiting a lattice distortion; ii) the fine structure of extended X-ray absorption which is indicative of small, if any, relaxation at the donor impurity sites [18,19]; iii) the electric quadruple interaction provided by Mössbauer spectroscopy do not indicate a large lattice distortion at the Sn impurity [20]; and, finally, iv) the behavior of DX center in superlattices which shows that the DX level is linked to the L band [21,22].

REFERENCES

1. K.A. Khachaturyan, D.D. Awschalom, J.R. Rozen and E.R. Weber, Phys. Rev. Lett. 63, 1311 (1989).
2. M. Zazoui, S.L. Feng and J.C. Bourgoin (unpublished).
3. J.C. Bourgoin and A. Mauger, Appl. Phys. Lett. 53, 749 (1988).
4. J.R. Morante, J. Samitier, A. Cornet and A. Hems, Appl. Phys. Lett. 45, 1317 (1984).
5. H. Kunzel, A. Fischer, J. Knecht and K. Ploag, Appl. Phys. A 32, 69 (1983).
6. D. Stievenard, M. Lannoo and J.C. Bourgoin, Solid State Electron. 28, 485 (1985).
7. M. Zazoui and J.C. Bourgoin, unpublished.
8. D.V. Lang in Deep Centers in Semiconductors, edited by S.T. Pantelides (Gordon and Breach, New York, 1986), chap. 7.
9. H.J. von Bardeleben, J.C. Bourgoin, P. Basmaji and P. Gibart, Phys. Rev. B 40, 5892 (1989).
10. P.M. Mooney, G.A. Northrop, T.N. Morgan and H.G. Grimmeis, Phys. Rev. B 37, 8298 (1988).
11. S. Alaya, H. Maaref and J.C. Bourgoin, Appl. Phys. Lett. 55, 1406 (1989).
12. J.C. Bourgoin, S.L. Feng and H.J. von Bardeleben, Phys. Rev. B 40, 7663 (1989).
13. J.C.M. Henning and J.P.M. Ansems, Phys. Rev. B 38, 5772 (1988).
14. D.J. Chadi and K.J. Chang, Phys. Rev. Lett. 61, 873 (1988).
15. P.M. Mooney, T.N. Theis and S.L. Wright in Defects in Semiconductors, Material Sci. Forum 38-41, edited by H.J. von Bardeleben (Trans Tech Publ. Aedermannsdorf, Switzerland, 1989), p. 1109.
16. M. Mizuta, M. Tachikawa, H. Kukimoto and S. Minamura, Japan J. Appl. Phys. 24, L143 (1985).
17. W. Shan, P.Y. Yu, M.F. Li, W.L. Hansen and E. Bauser, Phys. Rev. B 40, 7831 (1982).
18. T. Kitano and M. Mizuta, Japan J. Appl. Phys. 28, L1806 (1987).
19. M. Mizuta and T. Kitano, Appl. Phys. Lett. 52, 126 (1988).
20. P. Gibart, D.L. Williamson, B. El Jani and P. Basmagi, Phys. Rev. B 38, 1885 (1988).
21. J.C. Bourgoin, S.L. Feng and F. Mollot, J. Appl. Phys. to be published.
22. S.L. Feng, J.C. Bourgoin, H.J. von Bardeleben, E. Barbier, J.P. Hirtz and F. Mollot, presented at the Proc. Mat. Res. Soc. Meeting, San Diego, USA, 1989, to be published.

OPTICALLY DETECTED MAGNETIC RESONANCE OF GROUP IV AND GROUP VI DONORS IN $\text{Al}_{0.4}\text{Ga}_{0.6}\text{As}/\text{GaAs}$ HETEROSTRUCTURES

E. GLASER*, T.A. KENNEDY*, B. MOLNAR*, AND M. MIZUTA**

*Naval Research Laboratory, Washington, D.C., 20375 U.S.A.

**Fundamental Research Laboratory, NEC Corporation, 34 Miyukigaoka, Tsukuba 305, Japan

ABSTRACT

The influence of chemically different donor species on the nature of shallow donor states in $\text{Al}_{0.4}\text{Ga}_{0.6}\text{As}/\text{GaAs}$ heterostructures has been investigated by optically detected magnetic resonance (ODMR). Previous theoretical work by Morgan predicts a triplet state for group IV donors and a singlet state for group VI donors. ODMR experiments were performed on as-grown and implanted Si-, Se-, and S-doped epitaxial layers of $\text{Al}_{0.4}\text{Ga}_{0.6}\text{As}$ grown on (001) GaAs substrates. The effective-mass states are modified by the heteroepitaxial strain in these layers. The Si donors are characterized as quasi-independent valley states. The Se and S donors have valley-orbit splitting energies (i.e. chemical shifts) of 19-20 meV. The results indicate that Si, Se, and S donors are on the lattice sites in the metastable state of DX.

I. INTRODUCTION

The doping of AlGaAs crystals with donor atoms from either group IV or group VI results in the formation of both shallow and deep levels [1]. In current models these levels are associated with the same defect, the DX center [2,3]. However, the microscopic structure of the DX center is a subject of considerable debate [4,5]. Magnetic resonance experiments performed on n-doped $\text{Al}_{0.35}\text{Ga}_{0.65}\text{As}/\text{GaAs}$ heterostructures with $x \geq 0.35$ have been most successful in elucidating the nature of the shallow, metastable state associated with the X-point conduction band minima. The symmetry of the shallow state was revealed recently by optically detected magnetic resonance (ODMR) experiments [6] on Si-doped epitaxial layers of AlAs and $\text{Al}_{0.35}\text{Ga}_{0.65}\text{As}$ ($x \geq 0.35$). The symmetry of the state was independently verified by electron paramagnetic resonance (EPR) experiments on similar samples [7].

Deep level transient spectroscopy (DLTS) experiments have been performed to study the influence of different chemical species on the nature of the deep state [8,9]. The thermal activation energies of the deep state in $\text{Al}_{0.35}\text{Ga}_{0.65}\text{As}$ ($0.30 \leq x \leq 0.43$) doped with group IV impurities (Si, Sn, Ge) were found to decrease with increasing mass number of the impurity. However, there is a constant thermal activation energy [9] for samples doped with a variety of group VI donor atoms (S, Se, Te).

The shallow and deep aspects of the DX problem must meet in the central cell. Chemical shifts have been observed in the ionization energies for various shallow donor and acceptor impurities in GaP [10]. An anomalous deepening of the ground state donor level was found for Ge in GaP [11,12]. Thus, we are motivated to study the chemical effects on the nature of the shallow donor states in AlGaAs/GaAs heterostructures.

II. EXPERIMENTAL ASPECTS

The ODMR experiments described in this work were performed on three epitaxial layers (1-1.5 μm) of $\text{Al}_{0.4}\text{Ga}_{0.6}\text{As}$ doped with group IV and group VI donor atoms on 350-500 μm thick (001) GaAs substrates. The aluminum mole fraction (x) of the sampler was determined by double crystal x-ray measurements. Two pieces from the same undoped LPE-grown wafer were subsequently ion-implanted with Si and S atoms. A multiple energy implantation procedure was employed to produce spatially uniform dopant profiles extending approxi-

mately 4000 Å from the $\text{Al}_{0.6}\text{Ga}_{0.4}\text{As}$ surfaces. The $\text{Al}_{0.6}\text{Ga}_{0.4}\text{As}$ sample grown by OMVPE was doped with Se atoms by the use of H_2Se during growth. The donor concentrations in these samples were between 1 and $5 \times 10^{17} \text{ cm}^{-3}$.

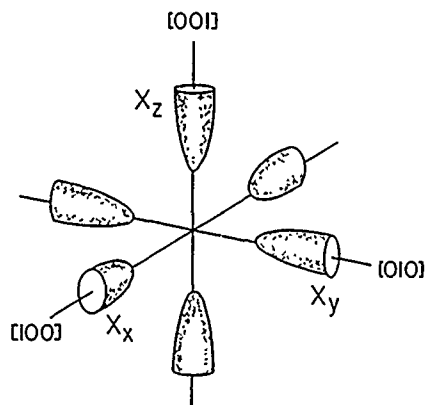
The magnetic resonance was detected synchronously as a change in the total intensity of donor-acceptor pair recombination which was coherent with the on/off switching (77-200 Hz) of 50 mW of microwave power in a conventional K-band (24 GHz) spectrometer. The photoluminescence was continuously excited with above bandgap radiation provided by a Ar^+ laser at 458 nm with power densities between 0.1 and 1 W/cm^2 . Deep photoluminescence from 1.0-1.8 μm was detected by a LN_2 -cooled Ge photodiode [13]. The immersed samples were studied under pumped-helium conditions (T-1.6K) in an optical cryostat.

Two sample geometries were employed in this work so that the applied magnetic field could be rotated in the $(1\bar{1}0)$ and (001) crystal planes. Details of how the excitation light was coupled to the samples in the two orientations are given elsewhere [6]. The measurements were carried out in the Voight geometry with the magnetic field supplied by a 9-inch pole face electromagnet.

III. SYMMETRY AND STRAIN EFFECTS ON DONORS IN III-V'S

The theory of the donor ground state in $\text{Al}_x\text{Ga}_{1-x}\text{As}$ with high (i.e. $x \geq 0.35$) AlAs mole fraction for group IV and group VI impurities substitutional on the III or V lattice sites, respectively, can be described following work by Morgan [14]. The conduction band constant energy surfaces are ellipsoidal in momentum space about the X-point minima with long axes along the $\langle 001 \rangle$ cube-edge directions (see Fig. 1). In the effective-mass approximation, the wavefunction of the donor ground state is derived from 1) Bloch functions for the X_x , X_y , and X_z valleys, and 2) 1s-like envelope functions that satisfy the effective-mass equation. In addition, the location of the donor atom in the lattice governs the degree to which the three hydrogenic effective-mass (HEM) states will interact. For group IV donors on the group III site, the central cell potential does not mix the three HEM states. Thus, the ground state of an electron bound to a group IV donor is an orbital (valley) triplet (T_2). However, the central cell potential for group VI donors on the group V site strongly mixes the three HEM states. As a result, an orbital singlet (A_1) ground state is formed (from the symmetric combination of the HEM states) with a binding energy greater than the energy level determined from effective-mass theory (~ 40 -50 meV). A two-fold degenerate excited state (E) remains near the effective-mass energy level. The difference in energy between the singlet ground state and the doublet excited state for a given donor species is commonly referred to as the valley-orbit splitting (E_{12}) or chemical shift.

Fig. 1 Schematic diagram of the conduction band constant energy ellipsoids about the X-point minima in momentum space for $\text{Al}_x\text{Ga}_{1-x}\text{As}$ crystals with high x. g-values for conduction electrons and donors depend on the orientation of B with respect to a valley axis.



The symmetry of the $\text{Al}_{0.4}\text{Ga}_{0.6}\text{As}$ crystal is altered and the degeneracy of the X-valleys is lifted in the presence of uniaxial strain. It has been shown [6] that the heteroepitaxial strain present in Si-doped AlAs/GaAs and AlGaAs/GaAs structures significantly modifies the donor ground state. It will be shown below that as a consequence of the heteroepitaxial strain in the (001) growth direction, the ground and excited states associated with the group VI donors in $\text{Al}_{0.4}\text{Ga}_{0.6}\text{As}$ /GaAs structures are also altered.

IV. RESULTS AND DISCUSSION

The spectra shown in Figs. 2 and 3 demonstrate the difference in character between group IV (Si) and group VI (Se, S) HEM ground states. In the (110) plane (Fig. 2), the strain-induced anisotropy is much larger for the Si-doped ($\Delta g=0.020$) sample than for the Se- and S-doped samples ($\Delta g=0.008$). With the field in the [100], the Si-donor line is split while the Se- and S-donor lines are unsplit (Fig. 3). In addition, the g-values associated with the group VI donors are found to be isotropic in the (001) plane. The ODMR linewidths for the Si- and Se-doped samples were similar, but the linewidth obtained for the S-implanted sample is larger. The resonance parameters are summarized in Table I. Because of the difference in HEM ground state character, further discussion is separated into group IV donors and group VI donors.

For the Si-implanted $\text{Al}_{0.4}\text{Ga}_{0.6}\text{As}$ /GaAs sample with the magnetic field rotated in the (110) plane (top half of Fig. 2), a single line is observed that shifts from $g=1.943$ for $B\parallel[110]$ to $g=1.962$ for $B\parallel[001]$. However, two, partially overlapped resonances with approximately equal amplitudes are observed with $g=1.928$ and $g=1.957$ for $B\parallel[100]$ (top spectrum in Fig. 3). No differences are observed in the linewidths or g-values of these two resonances with B along the third cube-edge direction (i.e. [010]).

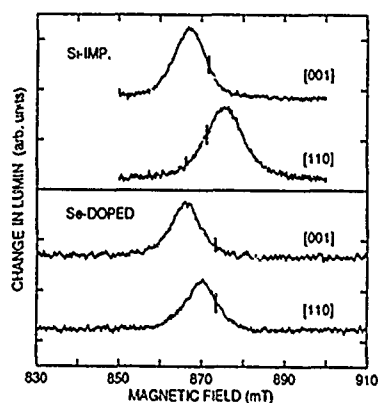


Fig. 2 ODMR spectra obtained for the Si- and Se-doped $\text{Al}_{0.4}\text{Ga}_{0.6}\text{As}$ /GaAs samples with B rotated in the (110) plane. Vertical bars indicate $g=1.95$.

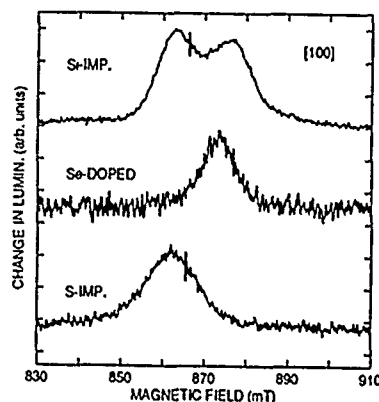


Fig. 3 ODMR spectra obtained for the Si-, Se-, and S-doped $\text{Al}_{0.4}\text{Ga}_{0.6}\text{As}$ /GaAs heterostructures with $B\parallel[100]$. Vertical bars indicate $g=1.95$.

Table I. Summary of the donor g-values and range of ODMR linewidths obtained from the n-doped $\text{Al}_{0.6}\text{Ga}_{0.4}\text{As}/\text{GaAs}$ heterostructures. The errors in the donor g-values and ODMR linewidths are ± 0.001 and ± 0.5 mT, respectively.

	Si	Se	S
N_D (cm^{-3})	1×10^{17}	5×10^{17}	3×10^{17}
$g_{\{001\}}$	1.962	1.961	1.963
$g_{\{110\}}$	1.943	1.953	1.954
$g_{\{100\}}$	1.928, 1.957	1.953	1.953
FWHM (mT)	8.4 - 9.5	7.9 - 8.2	12.6 - 14.5

The results can be understood with the discussion from Sect. III and the AlAs/GaAs results [6]. The heteroepitaxial stress along the (001) growth direction raises the X_z valley relative to the X_x and X_y valleys. The strain-induced splitting is given by [14]:

$$\Delta X = \Xi_u(e_{\perp} - e_{\parallel}), \quad (1)$$

where Ξ_u is the shear deformation potential and e_{\perp} and e_{\parallel} are the perpendicular and in-plane strains [16], respectively, in the $\text{Al}_{0.6}\text{Ga}_{0.4}\text{As}$ epitaxial layer. Since the deformation potentials do not differ much for III-V semiconductors, we use the AlAs deformation potential ($\Xi_u = 5.1 \pm 0.7$ eV) [17]. We estimate the valley splitting to be approximately 14 meV in the AlAs/GaAs heterostructure. Thus, the X_z valley at 1.6K is not populated. Two well-separated resonances were observed for the Si-doped AlAs/GaAs sample with the magnetic field along the [100] direction because the field is oriented parallel to the long axis of the X_z valley, but parallel to the short axis of the X_y valley [6]. A single resonance feature was observed as the field is rotated in the (110) plane since this plane mirrors the X_x and X_y valleys.

Similarly, the results for the Si-implanted $\text{Al}_{0.6}\text{Ga}_{0.4}\text{As}/\text{GaAs}$ sample can be understood using a quasi-independent valley model in the presence of strain (valley splitting = 14 meV \times 0.6 = 8.4 meV). The decrease of the anisotropy and splitting of the donor g-values compared to the results obtained for the Si-doped AlAs/GaAs heterostructure is attributed to a coupling interaction (probably spin-orbit) between the X_x and X_y valleys. In addition, the X_z valley may also begin to interact with the X_x/X_y valleys because the valley splitting energy decreases with decreasing Al mole fraction. However, the dominant effects that influence the nature of the ground state in this sample are the heteroepitaxial strain which effectively depopulates the X_z valley and the negligible valley-orbit interactions for group IV donors on the group III site. The ODMR results for the Si-doped $\text{Al}_{0.6}\text{Ga}_{0.4}\text{As}/\text{GaAs}$ structure provide evidence that the ground state can be described as a doublet with tetragonal symmetry about the [001] growth direction.

The behavior of the donor resonances for the Se- and S-doped $\text{Al}_{0.6}\text{Ga}_{0.4}\text{As}/\text{GaAs}$ samples can be understood by taking into account the heteroepitaxial strain and the strong valley-orbit interaction that couples the X_x , X_y , and X_z valleys for a group VI donor on the group V site. An isotropic g-value is expected for a pure singlet (A_1) ground state. However, a small g-value anisotropy is observed in the (110) plane because of the slight mixing between the ground (A_1) and excited (E) states. This interac-

tion is due to heteroepitaxial strain along the [001] growth axis. The observed g-value anisotropy of the resonance reflects the g-value anisotropy associated with the doublet state.

Similar admixing effects on the behavior of the donor g-values have been observed in EPR investigations of shallow donors in Si [18] under externally applied uniaxial stress. The valley-orbit splitting energies (E_{12}) between the ground (A_1) and excited (E) states in the absence of stress for the Se- and S-doped $\text{Al}_{0.6}\text{Ga}_{0.4}\text{As}$ samples can be deduced from the donor g-value anisotropies observed in the (110) plane. The expression for the g-shift due to the mixing between the ground and excited states with the strain along the [001] growth direction is:

$$g(\theta) - g_0 = (g_{\parallel} - g_{\perp}) [1 - (3 \sin^2 \theta) / 2] [1 - (1 + 3x'/2)(1 + x'/3 + x'^2/4)^{-1/2}], \quad (2)$$

where $g(\theta)$ is the donor g-value in the presence of strain, g_0 is the donor g-value in the absence of strain, θ is the angle between the [001] stress axis and the applied magnetic field, g_{\parallel} and g_{\perp} are the single-valley g-values associated with the X-conduction band minima, and x' is the ratio of the strain energy to the valley-orbit splitting (E_{12}). The values for g_{\parallel} and g_{\perp} are taken from the ODMR results [6] on the Si-doped AlAs/GaAs sample where the valleys are independent. Thus, the values of g_0 and E_{12} can be determined from the donor g-values obtained with the field parallel ($\theta = 0^\circ$) and perpendicular ($\theta = 90^\circ$) to the [001] growth axis (see, e.g., lower half of Fig. 2).

The values of g_0 and E_{12} deduced from the above analysis are summarized in Table II. The valley-orbit splitting energies (i.e. chemical shifts) are 19-20 meV. These results for the chemical shifts of shallow donor levels in $\text{Al}_{0.6}\text{Ga}_{0.4}\text{As}$ can be compared with earlier measurements [10] of the ionization energies of the same group IV and group VI substitutional donors in GaP, which has conduction band minima at the X-points. The difference in ionization energies between Si donors on the Ga site and either Se or S donors on the P site was also found to be 20 - 22 meV. The ODMR results for the Se- and S-doped $\text{Al}_{0.6}\text{Ga}_{0.4}\text{As/GaAs}$ heterostructures provide evidence that the ground singlet and excited doublet states are partially admixed due to the heteroepitaxial strain.

V. CONCLUSION

In the theory of donors in $\text{Al}_{0.6}\text{Ga}_{0.4}\text{As}$ [14], both the doublet excited state (E) associated with the group VI donors and the triplet ground state (T_2) associated with group IV donors are taken to lie very close to the effective-mass energy level. Thus, the finite valley-orbit splitting energies (E_{12} - 19-20 meV) found for Se and S donors necessarily imply a larger binding energy for these donors than for Si donors in $\text{Al}_{0.6}\text{Ga}_{0.4}\text{As}$. Recent Hall-effect measurements on similarly doped $\text{Al}_{0.6}\text{Ga}_{0.4}\text{As}$ samples yield binding

Table II. Symmetry of the unstrained shallow donor ground state and values of g_0 and E_{12} for the group VI donors determined from analysis of the ODMR results.

	Si	Se	S
Symmetry	T_2	A_1	A_1
g_0	---	1.955	1.957
Valley-orbit splitting (meV)	---	20	19

energies for the X-derived shallow donor state that contrast with the ODMR results. In particular, the binding energy of the lowest-lying hydrogenic level is reported to be larger for Si donors (~75 meV) [1] than for Te donors (~25 meV) [2] in $\text{Al}_{0.6}\text{Ga}_{0.4}\text{As}$. Note, however, that the binding energies may be in error by a factor of two due to compensation in the n-doped $\text{Al}_{0.6}\text{Ga}_{0.4}\text{As}$ samples. One approach to resolve this conflict may be direct determination of the HEM ground state energy for each species by luminescence spectroscopy. However, one would also need to know the binding energy of the acceptor involved in the donor-acceptor pair recombination to accurately determine the donor binding energy.

In summary, ODMR experiments performed on three n-doped $\text{Al}_{0.6}\text{Ga}_{0.4}\text{As}/\text{GaAs}$ heterostructures reveal features that can be attributed to the shallow donor states associated with the X-point conduction band minima which are modified by heteroepitaxial strain. In addition, the results show that central cell effects are negligible for a group IV donor (Si) and ~19-20 meV for group VI (Se, S) donor impurities in $\text{Al}_{0.6}\text{Ga}_{0.4}\text{As}$. The HEM ground state is the metastable state of DX at $x=0.6$. These symmetry-dependent results provide evidence that the metastable state corresponds to the impurity located precisely on the group III site for Si donor atoms or on the group V site for Se and S donor atoms.

We would like to thank J.M. Trombetta and M.G. Spencer for helpful contributions. This work was supported in part by the Office of Naval Research.

REFERENCES

1. For a review, see T.N. Theis, in Shallow Impurities in Semiconductors-1988, edited by B. Monemar, IOP Conf. Proc. No. 95 (Institute of Physics, Bristol, 1989), p.307.
2. J.E. Dmochowski, L. Dobaczewski, J.M. Langer, and W. Jantsch, Phys. Rev. B40, 9671 (1989).
3. M. Mizuta and K. Mori, Phys. Rev. B37, 1043 (1988).
4. J.C. Bourgoin, S.L. Feng, and H.J. von Bardeleben, Phys. Rev. B40, 7663 (1989).
5. D.J. Chadi and K.J. Chang, Phys. Rev. Lett. 61, 873 (1988).
6. E. Glaser, T.A. Kennedy, R. Sillmon, and M.G. Spencer, Phys. Rev. B40, 3447 (1989).
7. P.M. Mooney, W. Wilkening, U. Kaufmann, and T.F. Kuech, Phys. Rev. B39, 5554 (1989), and private communication.
8. D.V. Lang and R.A. Logan, Inst. Phys. Conf. Ser. No. 43, 433 (1979).
9. O. Kumagai, H. Kawai, Y. Mori, and K. Kaneko, Appl. Phys. Lett. 45, 1322 (1984).
10. See R.K. Watts, Point Defects in Crystals, (John Wiley and Sons, New York, 1977), p. 217.
11. M. Altarelli, J. Phys. Soc. Jpn. 49, Suppl. A, 169 (1980).
12. F. Mehran, T.N. Morgan, R.S. Title, and S.E. Blum, Solid State Comm. 11, 661 (1972).
13. T.A. Kennedy and E. Glaser, in The DX Center in III-V Ternary Compounds, edited by J.C. Bourgoin (Trans Tech Publications, Switzerland), in press.
14. T.N. Morgan, Phys. Rev. B34, 2664 (1986), and references therein.
15. H.W. van Kesteren, E.C. Cosman, P. Dawson, K.J. Moore, and C. T. Foxon, Phys. Rev. B39, 13426 (1989).
16. K. Kamigaki, H. Sakashita, H. Kato, M. Nakayama, N. Sano, and H. Terauchi, Appl. Phys. Lett. 49, 1071 (1986).
17. P. Lefebvre, B. Gil, H. Mathieu, and R. Planel, Phys. Rev. B40, 7802 (1989).
18. D.K. Wilson and G. Feher, Phys. Rev. 124, 1068 (1961).

PHOTOLUMINESCENCE AND BANDGAP NARROWING IN HEAVILY DOPED *n*-GaAs

H.D. Yao*

Center for Microelectronic and Optical Materials Research, and Department of Electrical Engineering, University of Nebraska-Lincoln, Lincoln, NE 68588-0511

A. Compaan

Department of Physics and Astronomy, University of Toledo, Toledo, Ohio 43606

ABSTRACT

Extremely heavily doped *n*-GaAs was produced by pulsed-laser annealing of Si implanted GaAs, achieving carrier concentrations exceeding $3.2 \times 10^{19}/\text{cm}^3$. Our photoluminescence (PL) spectra indicate a bandgap narrowing due to heavy *n*-type doping with a functional form of $\Delta E_g(\text{eV}) = -6.3 \times 10^{-8} [n(\text{cm}^{-3})]^{1/3}$. At the highest carrier concentration, the bandgap shrinkage reaches ~ 200 meV and the electron Fermi energy is ~ 410 meV. These large values indicate that there exists a considerable conduction band "stretch" between the Γ and L-valley of GaAs for very high *n*-type concentrations.

INTRODUCTION

In heavily doped *n*-type GaAs the valence and conduction bands are shifted in energy due to the presence of the ionized dopant ions and free carriers. Quantitative analysis of the bandgap shifts is an area of active investigation theoretically [1,2] and experimentally [3,4]. We report here the results of our photoluminescence (PL) measurements of bandgap narrowing due to heavy *n*-type doping. In this work we have taken advantage of the technique of ion implantation followed by pulsed laser annealing to extend the range of *n*-type dopant densities from the conventional limit of $\sim 7 \times 10^{18} \text{ cm}^{-3}$ to beyond $3.2 \times 10^{19} \text{ cm}^{-3}$. Pulsed-YAG-dye-laser annealing ($\lambda = 728 \text{ nm}$) of Si-implanted GaAs was used for sample preparation. The carrier concentrations were estimated from the positions of the Raman-plasmon mode (L^+) with inclusion of the effective mass changes due to the nonparabolic effects of the conduction band. The pulsed laser annealing procedure and the results of Raman scattering are reported separately [5].

* This work was performed while this author was at the University of Toledo, Toledo, Ohio 43606.

EXPERIMENTAL

PL spectra were obtained by a 514.5 nm probe beam with a power of ~200 mW. The samples were mounted in a cryogenic dewar and cooled by liquid N₂. Fig.1 shows a composite plot of the PL spectra from a series of GaAs samples with electron concentrations ranging from undoped to $\sim 3.2 \times 10^{19}/\text{cm}^3$. The top three spectra were prepared by pulsed dye-laser annealing of Si-implanted GaAs. These three upper spectra were obtained with a photomultiplier tube (PMT) of S1 response (Hamamatsu R632). The lower two spectra are from an undoped GaAs sample and from a sample conventionally doped with $5 \times 10^{17}/\text{cm}^3$ Si and were obtained with a GaAs PMT (Hamamatsu R943-02). Each spectrum has been corrected to remove the spectrometer-PMT efficiency effects.

The width of the PL band increases monotonically as the carrier concentration increases. This is a consequence of the increasing Fermi energy as electron concentration rises. In addition, the lower edge of the PL peak shifts towards lower energy as electron concentration increases. This is an indication of bandgap shrinkage at high carrier concentrations. The vertical dashed line indicates the bandgap position in undoped GaAs.

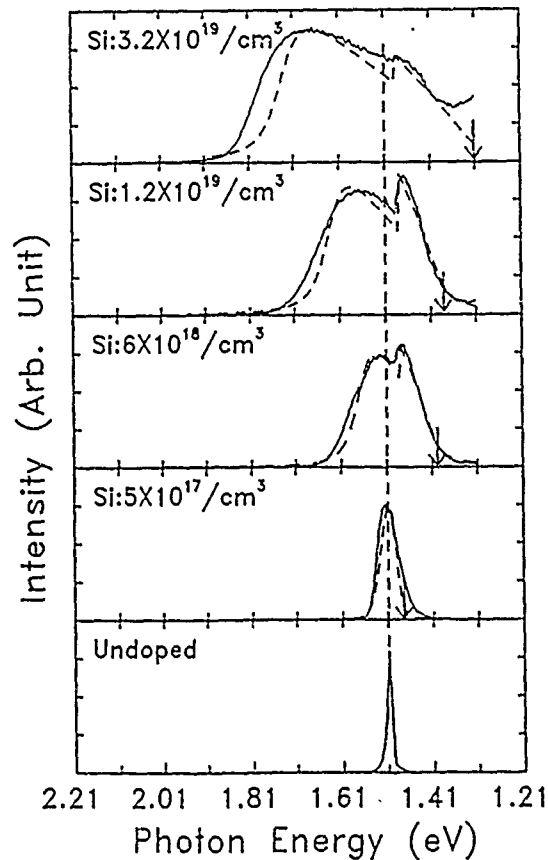


Fig.1.
PL spectra at 80 K for 514.5 nm excitation from five samples with different carrier concentrations. The dashed curves are line shape fits as described in the text. The vertical line indicates the bandgap position of undoped GaAs. The arrows indicate the positions of the shifted band edge used for the calculated curves.

ANALYSIS

For quantitative analysis, we calculated the PL spectral line-shape and compared the calculation with our data. The PL line shapes were calculated with two different models: 1) assuming momentum-conserving transitions and 2) assuming non-momentum-conserving transitions [6]. For momentum-conserving transitions,

$$I(\epsilon) = (\epsilon - \epsilon_g)^{1/2} \times \left[1 + \exp \left(\frac{m_h^*}{m_e^* + m_h^*} \times \frac{\epsilon - \epsilon_g}{kT} - \frac{\epsilon_F^e}{kT} \right) \right]^{-1} \times \left\{ 1 - \left[1 + \exp \left(\frac{-m_e^*}{m_e^* + m_h^*} \times \frac{\epsilon - \epsilon_g}{kT} - \frac{\epsilon_F^h}{kT} \right) \right]^{-1} \right\}, \quad (1)$$

where $\epsilon = \hbar \omega$ is the emitted photon energy, ϵ_g is the energy bandgap of GaAs.

the ϵ_F^e and ϵ_F^h are the quasi-Fermi levels for electrons and holes, respectively, and m_e^* and m_h^* are corresponding effective masses.

For non-momentum-conserving transitions,

$$I(\epsilon) \propto \int_0^{\epsilon - \epsilon_g} \mathcal{D}(\epsilon') (\epsilon - \epsilon_g - \epsilon')^{1/2} \times \left[1 + \exp \left(\frac{\epsilon' - \epsilon_F^e}{kT} \right) \right]^{-1} \times \left\{ 1 - \left[1 + \exp \left(\frac{-\epsilon + \epsilon_g + \epsilon'}{kT} - \frac{\epsilon_F^h}{kT} \right) \right]^{-1} \right\} d\epsilon', \quad (2)$$

where $\mathcal{D}(\epsilon)$ is the density of states of the conduction band. In heavily doped GaAs, electron energies reach large enough values that the conduction band can no longer be considered a simple parabola. Therefore, the density of states $\mathcal{D}(\epsilon)$ was calculated with the $k \cdot p$ expansion using the Rössler formulation, and the Fermi energy evaluated with this $\mathcal{D}(\epsilon)$. The valence band is considered parabolic since the low cw photon pumping rate will produce only a small steady state hole density within kT of the valence band extremum. Therefore, one may take $\epsilon_F^h \approx 0$.

By comparing the calculated PL line shape with our data, we find that k -conserving transitions in GaAs are negligible for doping above $5 \times 10^{17}/\text{cm}^3$ as also observed in Ref.6. This can be understood as originating in the high probability that momentum can be carried away by collisions between electrons and ionized or neutral impurities. For very heavily doped GaAs the collision rate of electrons with ionized impurities becomes large enough that collision broadening must also be folded into the calculation of the PL line shape. The collision rate was calculated by using the Brooks-Herring model [7,8] that assumes an electron collides with a single ionized impurity with a screened coulomb potential. Multiple scattering effects were not included.

Fig.2 shows the PL line shape fitting procedure for *n*-GaAs with a carrier concentration of $\sim 1.2 \times 10^{19}/\text{cm}^3$. It was calculated from Eq. (2) by convoluting a Lorentzian line shape function with each energy in the expression. Fig. 2 (a) shows the result if the bandgap is not shifted ($\epsilon_g = 1.51$ eV). The calculated PL-peak position is higher than the experimental data by an amount of ~ 0.13 eV. Good agreement for the entire line shape is obtained if the bandgap is adjusted downward by 0.13 eV as shown in Fig.2(b).

The experimental data exhibit a shoulder at ~ 1.48 eV and the fit shown in Fig 2(b) simulates this shoulder by a arbitrary multiplicative factor of 1.72 for all points below 1.48 eV. This shoulder has been identified recently by D.M. Szmyd et al [9] as a substrate-induced peak in the photoluminescence of heavily doped GaAs. That is, the low-energy, band-edge PL light emitted in the backward direction from the heavily doped surface layer passes through the substrate, reflects off the back surface, and is remitted through the front surface. Only photons with energies less than the bandgap of undoped GaAs will be able to do this. Therefore, this peak is supporting evidence for the bandgap shrinkage. It should be noted that the strength of this substrate-induced peak is quite sensitive to sample alignment and back surface conditions and varies from sample to sample.

Thus, by fitting each PL spectrum in both width and line shape as shown in Fig.1 by dashed curves, we obtained values of Fermi level and bandgap shrinkage at different electron concentrations. The values of the bandgap narrowing are plotted in Fig.3 along with the theoretical calculations for *n*-GaAs by Sernelius [1] and by Bennett and Lowney [2], and the results for *p*-type GaAs obtained by Casey and Stern and by Olego and Cardona [3,4]. Notice that our data indicate bandgap shifts greater than those of *p*-type material and agree nicely with calculations in ref.2 but are lower than the shifts calculated in ref.1. It is necessary to point out that Bennett and Lowney's calculation was done for GaAs at 300K, the band-edge shifts are general larger at lower temperature due to increasing degeneracy of the material [2]. However, for high electron densities, the degeneracy is very strong even at room temperature and should not affect the results substantially.

Our PL data indicate that at $n \sim 3.2 \times 10^{19}/\text{cm}^3$, the estimated Fermi energy exceeds 410 meV. This is indirect evidence of a conduction band "stretch" between the Γ and L-valley of GaAs since the Γ to L separation in undoped GaAs is only 300 meV. It should be pointed out that in heavily doped GaAs, our calculations do not fit our observed PL line shape exactly. Possible explanations include the following: (1) Our calculated density of states assumes the band parameters of the empty band, i.e., no distortion of the density of states due to the heavy doping. However, if the conduction band is distorted (stretched at the zone center) as our data appear to indicate, the density of states as well as the effective mass will be different from that of the empty band. (2) Some broadening may result from possible inhomogeneities in the impurity distribution and electron density after pulsed-laser annealing. However, Raman scattering studies of the plasmon peak with several wavelengths, having different penetration depths, indicate a quite uniform electron density in the implanted region.

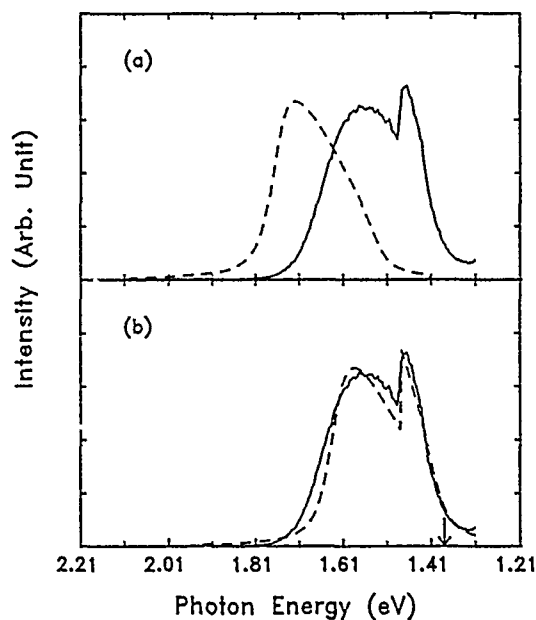


Fig.2.

(a) Comparison of PL data for GaAs: Si $\sim 1.2 \times 10^{19}/\text{cm}^3$ at 80K with calculated line shape for this concentration assuming a 1.51 eV bandgap.

(b) Comparison of the calculated PL spectrum using an adjusted bandgap value (~ 1.38 eV) with the experimental data.

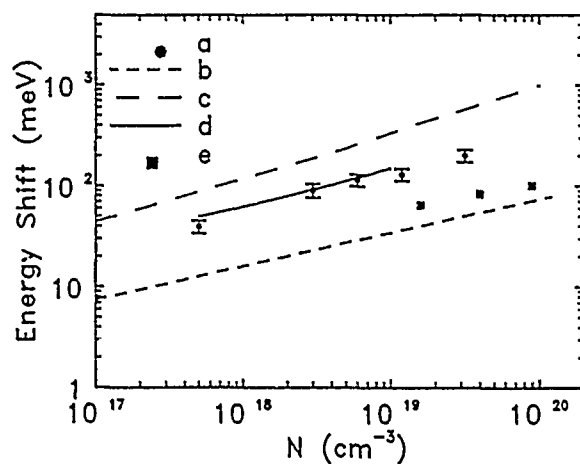


Fig.3.

Bandgap narrowing as a function of concentration for both n -type and p -type GaAs from the present work (a), from calculations of Bennett and Lowney [(d)-ref.2] and from Sernelius [(c)-ref. 1] as well as results for p -type GaAs from Casey and Stern [(b)-ref.3] and from Olego and Cardona [(e)-ref 4].

THE DX CENTER

Recent studies indicate that the DX center in GaAs and AlGaAs lies ~ 160 meV below the L-valley [10,11]. This defect is closely associated with donors and is produced at densities essentially equal to the donor density. Therefore, it has been suggested that the free carrier density in n -GaAs is limited to $\sim 2 \times 10^{19}/\text{cm}^3$. This limit assumes that there is little distortion of the conduction band at high dopant

densities [11]. However, the data presented in this paper indicate a bandgap narrowing of ~ 200 meV (at $n=3.2 \times 10^{19}/\text{cm}^3$). If the L-valley is assumed to be unchanged, and the DX center remains fixed relative to the L-valley during the course of the bandgap narrowing, the energy difference between the DX center and the Γ -band edge will increase by about 200 meV from its original value estimated at ~ 150 meV. In this case carrier concentrations significantly exceeding $\sim 2 \times 10^{19}/\text{cm}^3$ will be possible even in the presence of DX centers. Thus we conclude that the data presented here cannot definitively exclude the presence of DX centers in extremely heavily doped GaAs although the data suggest that the DX center may move closer to the L-valley as the doping density increases.

SUMMARY

We have presented photoluminescence data on bandgap shrinkage in extremely heavily doped n -GaAs. Our data show an energy gap shrinkage, $\Delta E_g(\text{eV}) = -6.3 \times 10^{-8} [n(\text{cm}^{-3})]^{1/3}$, where n is the electron concentration. For $n=3.2 \times 10^{19}/\text{cm}^3$, the bandgap shrinkage is ~ 200 meV. At this density the electron Fermi level is estimated as 410 meV, and significant distortion of the conduction band or "stretching" of the Γ -L separation is indicated.

ACKNOWLEDGMENTS

We wish to give our thanks to Professor N. O. Folland of Kansas State University for assistance with the numerical calculations of the Rössler model.

REFERENCES

1. Bo E. Sernelius, Phys. Rev. B **33**, 8582 (1986).
2. H.S. Bennett and J.R. Lowney, J. Appl. Phys. **62**, 521 (1987).
3. H.C. Casey Jr. and Frank Stern, J. Appl. Phys. **47**, 631 (1976).
4. D. Olego and M. Cardona, Phys. Rev. B **22**, 886 (1980); Phys. Rev. B **23**, 6592 (1981).
5. H.D. Yao and A. Compaan, Bull. Am. Phys. Soc. **33** 809 (1988), and **34** 917 (1989); A. Compaan, S.C. Abbi, H.D. Yao, A. Bhat, and D.W. Langer, J. Appl. Phys. **62**, 2561 (1987); H.D. Yao, A. Compaan and E.B. Hale, Solid State Commun. **56** 677 (1985); H.D. Yao and A. Compaan, unpublished.
6. Jiang De-Sheng, Y. Makita, K. Ploog, and H.J. Queisser, J. Appl. Phys. **53**, 999 (1982).
7. H. Brooks, Adv. Electronics & Electron Phys. **7**, 1508 (1955).
8. R.B. Dingle, Phil. Mag. **46**, 831 (1955).
9. D.M. Szmyd and A. Majerfeld, J. Appl. Phys. **65**, 1788 (1989).
10. D.J. Chadi and K.J. Chang, Phys. Rev. Lett. **61**, 873 (1988).
11. T.N. Theis, P.M. Mooney, and S.L. Wright, Phys. Rev. Lett. **60**, 361 (1988).

THEORY OF DX CENTERS IN $\text{Al}_x\text{Ga}_{1-x}\text{As}$ ALLOYS

D. J. Chadi and S. B. Zhang

Xerox Palo Alto Research Center, 3333 Coyote Hill Road, Palo Alto, California 94304

ABSTRACT

A theoretical model for DX centers which explains their unusual electronic properties in terms of two distinct bonding configurations for donor impurities in $\text{Al}_x\text{Ga}_{1-x}\text{As}$ alloys is examined. The results of our *ab initio* self-consistent pseudopotential calculations show that for $x > \approx 20\%$, the normal fourfold coordinated substitutional site becomes unstable with respect to a large lattice distortion. The model explains the large difference between the thermal and optical ionization energies of DX centers.

A successful theoretical model for the so called DX centers [1-2] in $\text{Al}_x\text{Ga}_{1-x}\text{As}$ alloys must explain the following key features of these defect centers: (1) The existence of two states for donors [3-6], the first a delocalized effective-mass type state whose energy follows the conduction band minimum as a function of alloying, the second a very localized state which does not exactly follow any of the conduction band minima [7]; (2) The metastability of the localized with respect to the delocalized state in GaAs and the reverse situation in $\text{Al}_x\text{Ga}_{1-x}\text{As}$ alloys with $x > 22\%$ [4]; (3) A repulsive energy barrier for the conversion of each state to the other [1-2]; (4) A large Stokes shift of about 1 eV between the optical and thermal ionization energies of the localized state [1-2,8]; and (5) The conversion of the localized state to the delocalized one at a temperature close to absolute zero through photo-excitation [9]. The theory must be able to give a proper account of other experimental observations such as the pressure, alloy, and impurity concentration dependence of the emission and capture barriers and of the thermal and optical excitation energies.

Over the past year we have developed such a theoretical model for the DX center [10] and we have now extended our previous first-principles approach for GaAs to $\text{Al}_x\text{Ga}_{1-x}\text{As}$ alloys [11]. Our theoretical results put our model for DX centers in the large-lattice-relaxation (LLR) category. We believe that such a LLR model is essential in explaining the large differences between the thermal and optical ionization energies of DX centers [1-2,8]. The primary result of our calculations is that donor impurities in $\text{Al}_x\text{Ga}_{1-x}\text{As}$ alloys possess two distinct bonding configurations and the

energy difference between these states changes sign as the Al concentration is increased. For a group IV dopant such as Si, the two structural states are shown in Fig. 1. Independent of x , the normal fourfold coordinated substitutional site in Fig. 1 (a) is found to be stable when the donor is in a neutral or positively charged state. The configuration in Fig. 1 (b) in which the Si atom has moved into an interstitial position (thereby breaking a bond with a nearest-neighbor As atom) is found to occur *only* when the donor is *negatively* charged. We have examined [10,11], therefore, the energetics of the following reaction via first-principles pseudopotential calculations:



where the superscripts denote the charge state of the center, d denotes a donor atom in the fourfold configuration shown in Fig. 1 (a), and DX^- represents the configuration in Fig. 1 (b).

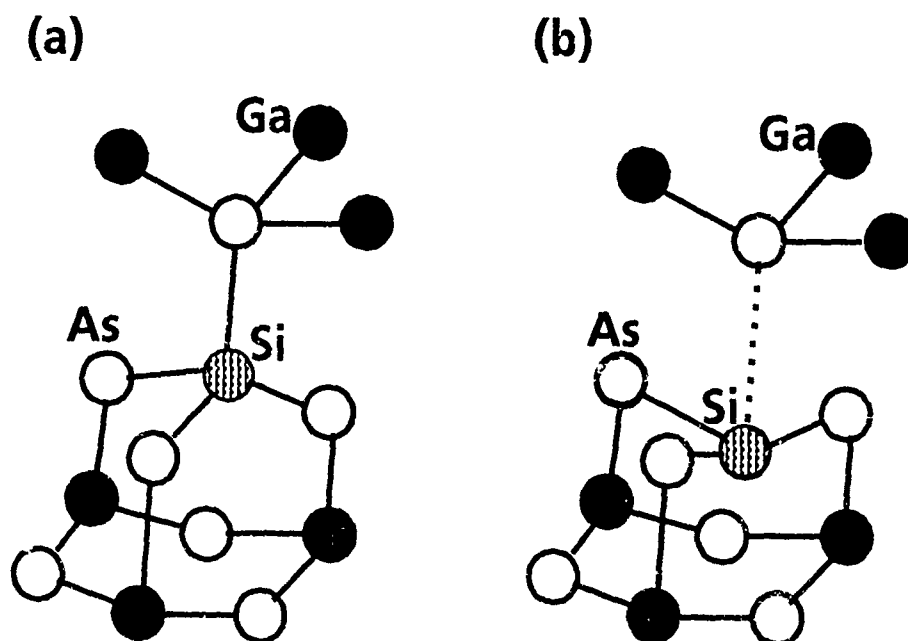


Figure 1. The two structural states of a Si donor atom in an AlGaAs alloy are shown. The structure shown in (a) is stable when the donor is in a positive or neutral charge state. The configuration in (b) occurs only for a *negatively* charged state. The relative stabilities of the two geometries is alloy dependent.

The primary results of our calculations are that:

- (1) The reaction specified by Eq. (1) is endothermic in GaAs but exothermic in $\text{Al}_x\text{Ga}_{1-x}\text{As}$ alloys with $x > \approx 20\%$. This means that DX becomes a "negative-U" center when the Al content is sufficiently high.
- (2) The optical ionization energy of a DX^- center is calculated to be significantly larger than its thermal ionization energy. The theoretical results for the optical excitation energy and its dependence on impurity type (e.g., Si vs. S donors) are in good agreement with experimental data.
- (3) The DX^- center with the large lattice relaxation shown in Fig. 1 (b) is unstable when it loses an electron through photoexcitation. The reaction



(or $DX^0 \rightarrow d^+ + e^-$) in which the distorted configuration goes back to the normal substitutional one is energetically extremely favorable [10] and there is no barrier to the conversion. This is consistent with the experimental observation that persistent photoconductivity can be induced at near absolute zero through photoexcitation of DX centers [9].

(4) There is a natural capture barrier since the transformation of the donor d [in Fig. 1 (a)] into DX [in Fig. 1 (b)] involves bond breaking. There is also an emission barrier for the DX center in our model. It arises from the energy needed to pass the interstitial atom through the plane of its three nearest neighbors atoms and back into the substitutional site. The barrier should be insensitive to the AlGaAs alloy composition since it involves primarily a lattice strain effect which is nearly the same whether the sample is Ga or Al rich. In addition the displacement does not lead to any significant change in the p_z character of the donor atom. A barrier of approximately $\frac{1}{2}$ eV, similar to the one calculated for the metastable to stable state transformation of the As-antisite defect in GaAs [12], is expected for the DX center. The experimental values [5,13-14] of the emission barrier are close to this energy. Calculations of the capture and emission barriers are currently in progress.

(5) If there are no extraneous donor or acceptor impurities in the sample and when all Si atoms are on the Ga sublattice, fully one half the Si atoms are in the LLR configuration when the reaction in Eq. (1) is exothermic. The experimental test of this result via extended X-ray absorption fine structure measurements have been hampered by the need for a large concentration of impurity centers and by the fact that at high concentrations the donors become amphoteric leading to a large compensation effect. In these samples, only the remaining uncompensated donor atoms would undergo the large lattice relaxation predicted for DX^- centers.

The negative-U property of the DX center suggested by Eq. (1) for $x > \approx 20\%$ is in very good agreement with the absence of an electron-spin-resonance (ESR) signal

from this center [15-16] and is consistent with experimental data on the temperature dependence of the free electron concentration [17]. The nature of the electronic state of DX has been opened for questioning, however, as a result of the recent magnetic susceptibility measurements of Khachatryan *et al.* [18] which show DX to be a paramagnetic center. The consequences of the ESR and magnetic susceptibility measurements for the spin and charge states of the DX center need to be examined in more detail. In particular, the possibility of a triplet $S=1$ ground state for DX^- has to be studied.

We have previously also examined [10] the case of a group VI dopant such as S substituting for an As atom in GaAs. The main difference with the results for Si doping is that the group VI atom does not move much from its substitutional site during DX^- formation. Instead, as shown in Fig. 2, it is a nearest-neighbor Ga or Al atom which moves into the interstitial position. The DX^- center resulting from S is also found to lead to a large Stokes shift between the optical and thermal ionization energies. The calculated optical excitation energies for S and Si-derived DX centers in

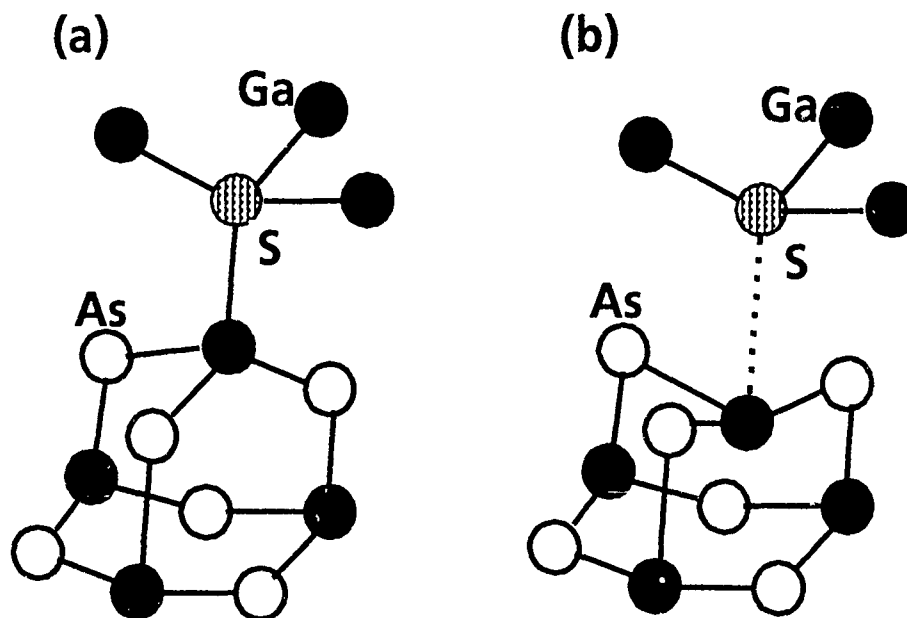


Figure 2. The structural states of a group VI donor in GaAs such as S are shown in (a) and (b). The fourfold substitutional site in (a) leads to a shallow donor state. The broken-bond configuration in (b) in which a nearest neighbor Ga atom has moved into an interstitial position leads to a localized state and occurs only for a negative charge state.

GaAs are 0.74 and 1.05 eV respectively. The 0.3 eV difference between the two is in very good agreement with the experimental data on the respective *DX* centers in AlGaAs alloys [19].

An alternate model for *DX* has been proposed by Bourgoin *et al.* [16]. They argue that *DX* is an effective-mass-like state which is derived from a mixture of the wave functions of the four conduction band minima at the L points of the Brillouin zone and that it involves a small lattice relaxation. The problem of the large Stokes shift between the thermal and optical excitation energies is resolved by the suggestion that it is an artifact, *i.e.*, the real optical excitation energy from *DX* to the conduction band minimum is argued to be small, with the large gap seen experimentally corresponding to an internal transition of the center. The most recent experimental results on the photoionization cross section [8,20] and pressure dependence [5,21] of the binding energy of *DX* centers are, however, in conflict with this picture. The measured photoionization cross sections of 10^{-24} – 10^{-22} cm² at photon energies of about 0.9 ± 0.1 eV are exceedingly small and cannot be satisfactorily explained by this model in which the *DX* level lies by only ≈ 0.1 eV below the conduction band minimum. In addition, the measured [20] pressure coefficient of 3 meV/kbar with respect to the conduction band minimum, for the case of a Si-derived *DX* center in GaAs, is substantially smaller than the corresponding experimental value of 5.5 meV/kbar for the L conduction band minimum. The pressure data of Shan *et al.* [5] for Te doped AlGaAs alloys are also in complete disagreement with the assumption of an L derived *DX* center. In the alloy regime where the X conduction band minima lies below Γ , the pressure dependence of the *DX* center is found to be only 0–1 meV/kbar which is significantly below that for the L band.

In conclusion, we have performed *ab initio* first-principles pseudopotential calculations to study the structural stability of donors in Si-doped AlGaAs alloys. The results of our calculations clearly show a bistability for this system. In GaAs, the normal fourfold coordinated configuration shown in Fig. 1 (a) leads to a shallow donor state and is the stable configuration. For $x < 0.4$, the addition of Al has the effect of increasing the energy of the conduction band minimum and, by extension, the energy of the shallow donor state which follows this minimum. In $\text{Al}_x\text{Ga}_{1-x}\text{As}$ alloys with $x > \approx 20\%$, the reaction given in Eq. (1) becomes exothermic and $\frac{1}{2}$ of the Si atoms undergo a large lattice distortion and become negatively charged. In addition, the magnitudes of the thermal and optical ionization energies of this system are in good agreement with experimental data on *DX* centers. For the case of GaAs, similar calculations for S-doping were done [10]. The main difference with Si is that here it is a nearest-neighbor Ga (or Al) atom of the donor that goes into an interstitial position when the donor becomes negatively charged. The thermal and optical ionization energies in this case are also consistent with experimental data. The results for *DX*[−] centers obtained here are very similar to those for the As-antisite

defect in GaAs [22]. In each case, the two electron perturbation caused by the defect leads to a low energy configuration with a large lattice relaxation. We have recently shown that similar types of lattice distortions can occur for single and double acceptors in ZnSe [23] and GaAs [24] respectively.

This work is supported in part by the Office of Naval Research Through Contract No. N00014-82-C-0244.

REFERENCES

1. D. V. Lang and R. A. Logan, Phys. Rev. Lett. 39, 635 (1971).
2. D. V. Lang, R. A. Logan, and M. Jaros, Phys. Rev. B 19, 1015 (1979).
3. M. Mizuta, M. Tachikawa, H. Kukimoto, and S. Minoura, Jpn. J. Appl. Phys. 24, L143 (1985); M. Tachikawa, T. Fujisawa, H. Kukimoto, A. Shibata, G. Oomi, and S. Minomura, *ibid.* 24, L893 (1985).
4. M. F. Li, P. Y. Yu, E. R. Weber, and W. Hansen, Appl. Phys. Lett. 51, 349 (1987); Phys. Rev. B 36, 4531 (1987).
5. W. Shan, P. Y. Yu, M. F. Li, W. L. Hansen, and E. Bause, Phys. Rev. B 40, 7831 (1989).
6. T. N. Theis, P. M. Mooney, and S. L. Wright, Phys. Rev. Lett. 60, 361 (1988).
7. N. Chand, T. Henderson, J. Klem, W. T. Masselink, R. Fischer, Y. C. Chang, and H. Morkoç, Phys. Rev. B 30, 4481 (1984).
8. P. M. Mooney, G. A. Northrop, T. N. Morgan, and H. G. Grimmeiss, Phys. Rev. B 37, 8258 (1988).
9. T. N. Theis, T. F. Kuech, L. F. Palmateer, and P. M. Mooney, in Gallium Arsenide and Related Compounds -1984, Inst. Phys. Conf. Ser. No. 74, edited by B. de Cremoux, (IOP, London, 1985) p. 241.
10. D. J. Chadi and K. J. Chang, Phys. Rev. Lett. 61, 873 (1988); Phys. Rev. B 39, 10063 (1989).
11. S. B. Zhang and D. J. Chadi (to be published).
12. D. J. Chadi and K. J. Chang, Phys. Rev. Lett. 60, 2187 (1988).
13. P. M. Mooney, N. S. Caswell, and S. L. Wright, J. Appl. Phys. 62, 4786 (1987).
14. E. Calleja, A. Gomez, and E. Muñoz, Appl. Phys. Lett. 52, 383 (1988).
15. P. M. Mooney, W. Wilkening, U. Kaufmann, and T. F. Kuech, Phys. Rev. B 39, 5554 (1989).
16. J. C. Bourgoin, S. L. Feng, and H. J. von Bardeleben, Phys. Rev. B 7663, (1989).
17. J. E. Dmochowski and L. Dobaczewski, Semicond. Sci. Technol. 4, 579 (1989).
18. K. A. Khachatryan, D. D. Awschalom, J. R. Rozen, and E. R. Weber, Phys. Rev. Lett. 63, 1311 (1989).

19. D. V. Lang, in Deep Centers in Semiconductors, edited by S. T. Pantelides (Gordon and Breach, New York, 1986) pp. 489-539.
20. G. Brunthaler, K. Ploog, and W. Jantsch, Phys. Rev. Lett. 63, 2276 (1989).
21. T. Baba, M. Mitzuta, T. Fujisawa, J. Yoshino, and H. Kukimoto, Jpn. J. Appl. Phys. 28, L891 (1989).
22. D. J. Chadi and K. J. Chang, Phys. Rev. Lett. 60, 2187 (1988); J. Dabrowski and M. Scheffler, *ibid.* 60, 2183; E. Kaziras and K. C. Pandey, Phys. Rev. B 40, 8020 (1989).
23. D. J. Chadi and K. J. Chang, Appl. Phys. Lett. 55, 575 (1989).
24. S. B. Zhang and D. J. Chadi (to be published).

A PHOTOCAPTURE TEST OF DX-CENTER MODELS

HAROLD P. HJALMARSON, S. R. KURTZ, AND T. M. BRENNAN
 Sandia National Laboratories, Albuquerque, New Mexico 87185.

ABSTRACT

The DX-center model is widely used to explain data for the persistent photoconductivity (PPC) effect. An analysis of the DX-center model suggests a new experiment to test its correctness. In this experiment, photons near the threshold energy of the photoionization cross-section for the DX-center induce transitions from the partially occupied conduction band to empty DX-centers. This mechanism, which we call photocapture, competes with the usual photoionization which empties the DX-centers. The photocapture cross-section is estimated and an experimental attempt is made to detect photocapture. The significance of the null result is discussed.

INTRODUCTION

The persistent photoconductivity (PPC) effect limits the usefulness of field effect transistors made from GaAlAs [1,2]. In this effect, photoconductivity at low temperatures remains after the light source is removed. The effect is caused by a deep level (called the DX-center) which has a barrier that prevents recapture of photoionized electrons [3,4]. However, the photoionization threshold E_{pi} is much greater than thermal depth E_t of the DX-center (typically, $E_{pi} \approx 0.1$ eV and $E_t \approx 1$ eV). These features are consistent with a phenomenological model in which lattice relaxation converts a conduction band resonant state to a deep level [4]. The energy difference between the thermal and optical depths represents lattice relaxation energy. An unusual feature of this class of models is that this lattice relaxation energy greatly exceeds the thermal energy; thus these models are called large lattice relaxation (LLR) models. In this paper, we theoretically and experimentally investigate another unusual feature of this model which we call photocapture (PC).

In photocapture, photon absorption causes a transition of free electrons in the conduction band to the resonant state which then becomes a bound state by undergoing large lattice relaxation. This mechanism is the reverse of the photoionization (PI) mechanism which creates the free electrons by emptying the DX-centers. In this paper, the photoionization and photocapture mechanisms are discussed, the cross-sections for both are estimated, and an experimental attempt to detect photocapture is also described. The null results suggest that more refined attempts should be made to measure this feature of the LLR class of models.

Several microscopic models have been proposed to explain the PPC effect. In the original DX-center model, a pair consisting of a donor (D) and an unknown impurity (X) underwent large lattice relaxation; the unknown defect was suggested to be a vacancy [4]. However, this model was disputed by an experiment on GaAs:Si in which pressure was used to induce the PPC effect [5]. These experiments suggesting that Si alone causes the DX-center have inspired new microscopic models. In one type of model, the substitutional donor itself undergoes large lattice relaxation [6,7]. Furthermore, in another class of models, a substitutional donor undergoes small lattice relaxation [8,9]. In this class of models, the photoionization cross-section is explained by transitions to energetically distant X- and L-point final states; however, this model has been disputed by recent photoionization experiments [10]. In yet another class of models, the trapped bipolaron models, substitutional Si undergoes large lattice relaxation and traps two electrons to form the stable charge state DX⁻ [11,12]. Regardless of the microscopic nature of the correct model, it clearly must preserve the essential features of the LLR class of models. Thus we turn to examination of the photoionization and photocapture cross-section of the phenomenological LLR model.

THEORY

The LLR model is illustrated by a configuration coordinate diagram, shown in Fig. 1, which shows the total energy $\Sigma_{DX}(Q)$ of the impurity state as a function of lattice distortion Q . This total energy can be written as a sum of electronic energy $E(Q) \approx E_0 - fQ$ together with lattice distortion energy $1/2 \kappa Q^2$:

$$\Sigma_{DX}(Q) = E(Q) + 1/2 \kappa Q^2 \quad (1)$$

in which f is a force constant, and κ is a spring constant. For comparison, the total energy $\Sigma_f(Q) = 1/2 \kappa Q^2$ of a Γ -point free electron state is also shown. The total energy of the impurity state is a minimum at $Q_0 = f/\kappa$. The distorted state lies at an energy $\Sigma_{DX}(Q_0) = E_0 - E_S$ in which the Stokes energy $E_S = 1/2 f^2/\kappa$ is the lattice relaxation energy. By inspection this state lies at an energy $E_t = E_0 - E_0$ below the band edge. For the case of Si donors in $\text{AlGa}_{1-x}\text{As}$, $E_t \approx 0.15$ eV and $E_S \approx 1.15$ eV for $x \approx 0.3$.

The non-radiative capture rate for this model is controlled by a capture cross-section which has the form $\sigma = \sigma_0 \exp(-E_b/KT)$ at high temperature [4]; the Arrhenius energy $E_b = E_0/4E_S$ is shown in Fig. 1.

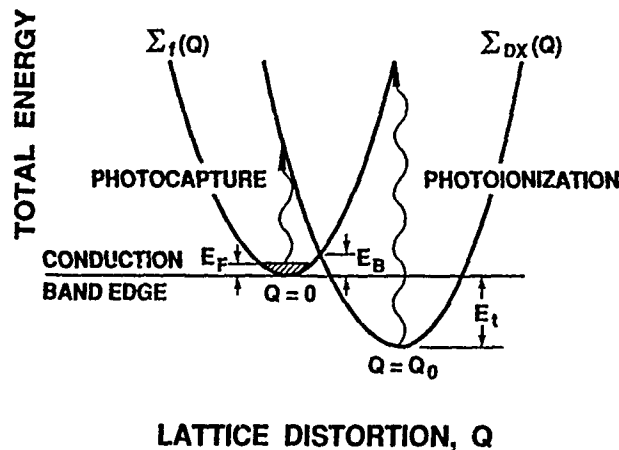


Fig. 1. The basic configuration coordinate model illustrating both photoionization and photocapture in the case of large lattice relaxation.

The DX-center can be emptied by photoionization. Such optical transitions are rapid compared with the time scale of the distortion Q , and thus they appear vertical on a configuration coordinate diagram. This transition is schematically indicated in Fig. 1 by the vertical wavy line originating at the minimum, $Q = Q_0$, of the distorted impurity state. The transition shown corresponds to the threshold energy,

$$\begin{aligned} E_{pi} &= \Sigma_{DX}(Q_0) - \Sigma_f(Q_0) \\ &= E_S + E_t. \end{aligned} \quad (2)$$

One unique and unusual aspect of LLR models in general is that radiative capture does not occur. Radiative capture would appear as vertical transition from the free to the deep state. By inspection, no transition involving emission of photons can be drawn on Fig. 1. The absence of radiative capture explains why photoconductivity persists for a long time in these systems at low temperature.

The price the LLR models pay for kinetically forbidden radiative capture is that photocapture can occur. In other words, capture cannot proceed by emission of a photon but it can by absorption of a photon. This mechanism can also be seen in Fig. 1. The photocapture transition originates at $Q = 0$ and terminates at the undistorted resonance state at energy E_0 . The threshold energy for this transition is

$$E_{pc} = E_0 = E_S + E_t. \quad (3)$$

Comparing Eqs. (2) and (3), the threshold for photocapture lies at an energy $2E_t \approx 0.30$ eV below the threshold for photoionization.

The photoionization spectrum can be readily calculated. Its cross-section $\sigma_e(E)$ can be written as

$$\sigma_e(E) = \int_{-\infty}^{\infty} dE' \sigma_e^0(E-E') G(E') \quad (4)$$

in which $\sigma_e^0(E)$ is the electronic portion and $G(E)$ is the electron-phonon lineshape function. For all the models,

$$G(E) \approx \frac{1}{\Delta \pi^{1/2}} e^{-(E-E_{pi})^2/\Delta^2} \quad (5)$$

in which $\Delta^2 = 4 E_S K T$. Using $E_S \approx 1$ eV for LLR, the width of the Gaussian $G(E)$ is $\Delta \approx 0.1$ eV for $T \approx 50$ K.

The electronic portion $\sigma_e^0(E)$ of the spectrum corresponds to a dipole forbidden radiative transition [4]. The deep level and conduction bandedge states are assumed to have s-like symmetry. Using the simplest model for this transition [13],

$$\sigma_e^0(E) \propto E^{3/2}/(E + E_{pi})^3 \quad (6)$$

which peaks at $E \approx 2E_{pi}$. In this model, the $E^{3/2}$ quantity is a product of a factor $E^{1/2}$ due to density of states and a factor E due to the dipole forbidden transition. For a dipole-allowed transition,

$$\sigma_e^0(E) \propto E^{1/2}/(E + E_{pi})^3. \quad (7)$$

The photocapture cross-section has a form very similar to the photoionization cross-section. It has the same magnitude, or prefactor, as the photoionization cross-section because of microscopic reversibility. However, conduction band states must be occupied for photocapture to occur. Because we compare with data taken at low temperature, we simply assume that all states below a Fermi energy E_F are occupied ($E_F = 50$ meV corresponding to $n \approx 10^{18} \text{ cm}^{-3}$). To reveal the structure of this spectrum, we do a calculation with minimal broadening ($\Delta = 5$ meV). To further illustrate the features, we plot $E^2 \sigma_e(E)^{2/3}$ in Fig. 2 for each cross-section. The photoionization cross-section becomes a straight line of slope one which asymptotically intercepts the axis at $E = E_{pi}$. The missing portion of this cross-section is due to electron-occupied final states. These states make the only contribution to the photocapture cross-section whose threshold lies lower by an energy $2E_t$. By comparison, we expect that photocapture should be observable if one can measure photoionization near the threshold.

These cross-sections for the LLR model differ from those predicted by the trapped bipolaron models [11,12]. In the interstitial donor model, the Si-donor undergoes a C_{2v} distortion [11]. For such a distortion, the photoionization transition of the A_1 ground state is dipole allowed. The resultant cross-section (see Eq. 7) is qualitatively different than that of the LLR model and should therefore be readily distinguishable. In addition, both trapped bipolaron models must contain a sub-threshold photoionization feature corresponding to transitions to the metastable DX^0 state [14].

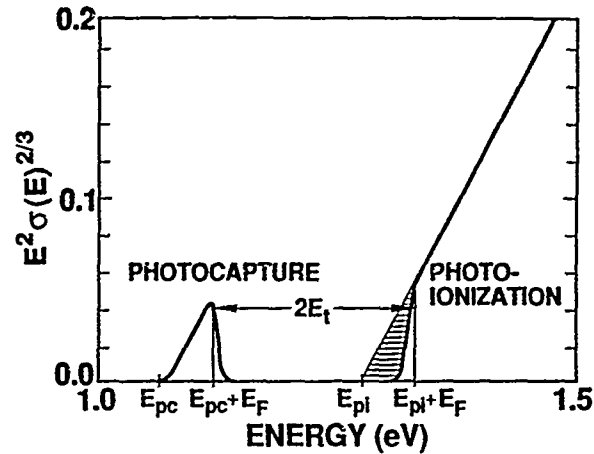


Fig. 2. The photoionization and the photocapture cross-sections. In each case, the quantity plotted is $E^2 \sigma(E)^{2/3}$.

EXPERIMENT

Having obtained the photocapture cross-section we consider the nature of an experiment. At low temperature in the presence of light, the only kinetic mechanisms which must be considered are photoionization and photocapture. Thus, one first uses short wavelength light to empty the DX-centers followed by longer wavelength light to fill them by photocapture. In the experiment to be described the occupancy of the DX-centers is monitored by measuring the capacitance.

The samples used for the photocapture and photoionization experiments consisted of a 2 μm thick layer of Al_{0.3}Ga_{0.7}As_{0.5} grown on p-type GaAs by molecular beam epitaxy. The samples were doped with $1 \times 10^{18} \text{ cm}^{-3}$ Si during growth. A semi-transparent Ti contact was deposited onto a 100 Å thick cap layer of undoped GaAs to form Schottky barrier diodes. All measurements were performed at low temperature, 15 K, to minimize drift in the capacitance and phonon-broadening of the photoionization and photocapture lineshapes so that small photocapture rates could be detected.

Photoionization cross sections were obtained using the constant capacitance technique of Lang and coworkers [3]. The data shown in Fig. 3 compare favorably with other photoionization results for Si donors obtained at higher temperatures [10]. The trapped electron population decayed exponentially with time during the photoionization experiment except in those measurements where the photoionization rate was smallest. Under those conditions a double exponential decay was observed indicating a small concentration of donors are present with lower photoionization energy than that of Si.

We attempted to observe photocapture by detecting a decrease in the capacitance of a photoionized sample illuminated with 0.7-1.4 eV photons. After completely photoionizing the defects with the diode in reverse bias, the sample was held at zero bias and illuminated with a tungsten-halogen lamp and monochromator for extended periods of time. Periodically, capacitance was measured in reverse bias, and the monochromator was stepped. Because the photocapture line predicted by a LLR model is narrow (50-100 meV) when compared with the broad photoionization line, scans lasting 24 hours were needed to obtain the required number of points. The drift in the reverse bias capacitance was $\leq 0.3\%$ during an experiment. Limited by the drift in capacitance occurring over a narrow energy range, photocapture was never detected in any experiment.

Based on the measured light intensity and experimental drift, we conservatively estimate that the maximum photocapture cross section for a specific energy is 1% of the photoionization cross section or 10^{-21} cm^2 ,

whichever is greater. Using capacitance to monitor photoionization, we can be certain that $< 1\%$ of the donors are populated prior to the photocapture experiment. Therefore, the minimum detectable photocapture rate is $< 1\%$ of the photoionization rate. Based on these photoionization measurements, our study limits the photocapture cross section to the region below the dashed line in Fig. 3.

In Fig. 4, the photocapacitance data $\sigma(E)$ are compared with the theoretical spectra for which $E_{\text{PI}} = 1.275$ eV and $\Delta = 90$ meV. In each case, the spectra are plotted as $E^2 \sigma(E)^{2/3}$. The PI portions of the theory and data are in good agreement. However, the data disagree with the dipole-allowed PI cross-section of the interstitial donor model (for which $E^2 \sigma(E)^{2/3} \propto E^{1/3}$). The threshold of our data agrees with earlier work but the width Δ is smaller due to the low temperature in our study [3]. By inspection, the PC cross-section should have been readily detected in our experiment. Thus the experiment does not agree with this feature of the LLR model.

DISCUSSION

Our experiments can be compared with recent studies in which long wavelength light was used to quench the PPC effect [15,16]. These studies had a motivation similar to ours but differed greatly in execution. The maximum photon energy was limited to 0.67 eV in one experiment [15] and 0.82 eV in the other [16]. Thus the resonant state was not probed in either experiment. Aside from intrinsic heterostructure artifacts, these experiments may have shown that the resonance state is much lower in energy

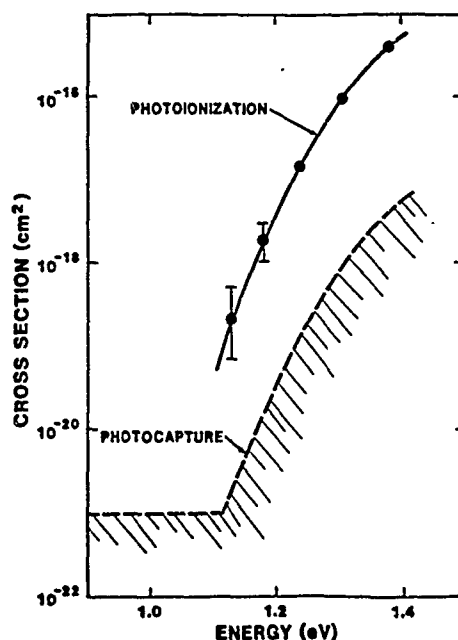


Fig. 3. The photocapacitance data for Si-doped $\text{Al}_{0.3}\text{Ga}_{0.7}\text{As}$. In no case was photocapture detected. The confidence limits on the experiment are also shown.

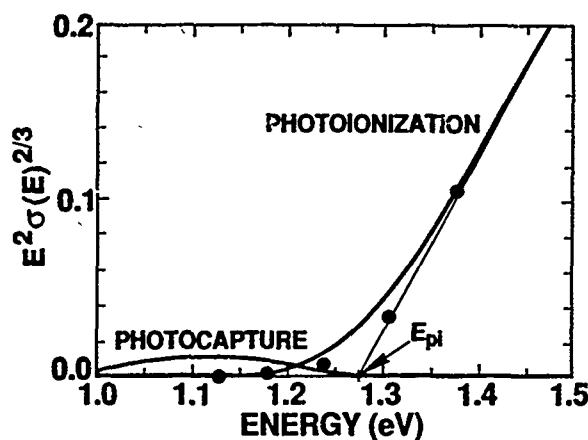


Fig. 4. The photocapitance data $\sigma(E)$ plotted as $E^2 \sigma(E)^{2/3}$ compared with the theoretical cross-section (solid lines) for both photoionization and photocapture.

than predicted by the LLR model. Thus the total energy state does not have the parabolic shape depicted in Fig. 1.

Another explanation for our failure to detect resonant photocapture is that electrons absorbed into the resonant state do not remain in this impurity state. They may be emitted as highly energetic free carriers. However, one can expect such emitted electrons to have a high probability for recapture. The complication introduced by this mechanism could be avoided by doing an experiment to detect absorption by the resonant state.

CONCLUSION

We have analyzed the photoionization cross-section for the phenomenological LLR model and also predicted the photocapture cross-section. This prediction relates the photocapture cross-section to the empirically observed photoionization cross-section. The absence of photocapture suggests that a more refined experiment such as measurement of optical absorption should be performed. The ultimate failure to detect photocapture would require modification of the the phenomenological LLR model of the DX-center.

ACKNOWLEDGMENTS

This work was supported by the U. S. Department of Energy under contract number DE-AC04-756DP00789.

REFERENCES

1. R. J. Nelson, J. App. Phys. **31**, 351 (1977).
2. T. J. Drummond, W. Kopp, R. E. Thorne, and A. Y. Cho, J. Appl. Phys. **20**, L913 (1981).
3. D. V. Lang and R. A. Logan, Phys. Rev. Lett. **39**, 635 (1977).
4. D. V. Lang, R. A. Logan, and M. Jaros, Phys. Rev. B **19**, 1015 (1979).

5. M. Mizuta, M. Tachikawa, H. Kukimota, and S. Minorua, Japan J. Appl. Phys. 24, L143 (1985).
6. A. Oshiyama and S. Ohnishi, Phys. Rev. B 33, 5320 (1986).
7. T. N. Morgan, Phys. Rev. B 34, 2664 (1986).
8. H. P. Hjalmarson and T. J. Drummond, Appl. Phys. Lett. 60, 2410 (1986).
9. J. C. M. Henning and J. P. M. Ansems, Semicond. Sci. Technol. 2, 1 (1987).
10. P. M. Mooney, G. A. Northrop, T. N. Morgan, and H. G. Grimmeiss, Phys. Rev. B 37, 8298 (1988).
11. D. J. Chadi and K. J. Chang, Phys. Rev. Lett. 61, 873 (1988).
12. K. Khacaturyan, E. R. Weber, and M. Kaminska, unpublished.
13. G. Lucovsky, Solid State Commun. 3, 299 (1965).
14. H. P. Hjalmarson and T. J. Drummond, Materials Science Forum 38-41, 1091 (1989).
15. M. I. Nathan, T. N. Jackson, P. D. Kirchner, E. E. Mendez, G. D. Pettit, and J. M. Woodall, J. Electron. Mater. 12, 719 (1983).
16. L. X. He, K. P. Martin, and R. J. Higgins, Phys. Rev. B 39, 1808 (1989).

DX-CENTER IN Se-DOPED $\text{Al}_x\text{Ga}_{1-x}\text{As}$

Thomas R. Hanak⁺, Assem M. Bakry^{**}, Richard K. Ahrenkiel^{**} and Michael L. Timmons^{***}

⁺ University of Denver, Department of Physics, University Park, Denver, CO 80210

^{**} Solar Energy Research Institute, 1617 Cole Blvd., Golden, CO 80401

^{***} Research Triangle Institute, Research Triangle Park, NC, 27709-2194

ABSTRACT

We report the measurement of the thermal activation energy for the DX-center in Se-doped $\text{Al}_x\text{Ga}_{1-x}\text{As}$ grown by metal-organic chemical vapor deposition (MOCVD) for different alloy compositions ($x=0.19, 0.23, 0.27, 0.31$). The peaks obtained from conventional DLTS are often broad or asymmetric with shoulders on one or both sides. These phenomena often arise from two or more traps which are active in the same temperature range.

The capacitive transients are recorded digitally and analyzed directly by applying a nonlinear double exponential fitting routine to the data. This fitting produces two Arrhenius plots and yields the densities of the defect states. From the Arrhenius plots, the capture cross sections at infinite temperature and the thermal activation energies are calculated. These results are then used to simulate the DLTS spectra. Excellent agreement between real and simulated spectra is shown.

INTRODUCTION

It is well known, that the conductivity in n-type $\text{Al}_x\text{Ga}_{1-x}\text{As}$ is controlled by a deep donor, namely the DX-center.¹ It is therefore of main importance to understand the optical and electrical properties of these traps. The energy levels of deep centers are closely connected to the band structure of the material which is in turn an important aspect in determining the properties of the material.

In this paper we present a study of the thermal ionization energies of the DX center for the alloy composition in the range between 0.19 and 0.31. The shapes of the DLTS peaks due to the DX center are often broad^{1,2,3} as it is in our spectrum as well. The possibility of nonexponential transients observed for deep levels has been discussed by Omeling⁴ et al. in terms of alloy broadening. The transient data in this study indicated a two trap model. All DLTS data were fit with the two level model. Thus, our data indicate DX center pairs with the two energy levels being nearly equal. A decrease of the activation energy values with increasing AlAs mole fraction was found. In addition, the capture cross-section of the DX-center-pairs strongly decreased with AlAs concentration.

EXPERIMENTAL

For the rate window spectra, we used the SULA Technologies Deep Level spectrometer. The details of the full transient acquisition apparatus are explained elsewhere^{5,6}. For all capacitance transient signals a pulse width of 100 ms and a pulse height of 2 V was used. The applied reverse bias was 2 V and the pulse frequency 3 s^{-1} .

⁺ Work performed at the Solar Energy Research Institute

THEORY

An important characteristic for the DX center is the temperature activated capture cross section

$$\sigma_e = \sigma_\infty \exp(-E_B/k_B T) \quad (1)$$

where σ_∞ is the capture cross section at infinite temperature and E_B is the capture barrier. With the well known equation for the emission rate

$$g_e = \sigma_e v_e N_c \exp(-(E_c - E_T)/k_B T) \quad (2)$$

and defining $E_0 = E_c - E_T$, the equation for the appropriate Arrhenius plot is given by

$$\ln \frac{g_e}{T^2} = \text{const.} - \frac{E_0 + E_B}{k_B T} \quad (3)$$

where the const. is equal to $\sigma_\infty \sqrt{3k_B/m^*} N_{CR}/(300)^{3/2}$. Here m^* is the effective electron mass [kg] and N_{CR} is the effective density of states in the conduction band at room temperature [cm⁻³]. One can see that the y-intercept of the Arrhenius plot determines the quantity σ_∞ which is the capture cross section at infinite temperature. In order to calculate σ_∞ one has to use an appropriate density of states effective mass⁷. This is given by $m_e = (0.067 + 0.083x)m_0$ where x is the AlAs mole fraction. It is important to note, that DLTS measurements determines the sum of energies $E_0 + E_B$ and not E_0 which is the activation energy determined by Hall measurements.

For slow pulse frequencies and sufficiently long pulse widths, it can be shown⁶ that the transient equation for two traps has the form

$$\frac{\Delta C}{C_0} = c_1 (e^{-c_2 t} + \frac{N_{T2}}{N_{T1}} e^{-c_3 t}) + c_4 \quad (4)$$

where c_1 is the ratio $N_{T1}/2N_D$ and c_2 and c_3 are the appropriate emission rates. This equation is used to analyse the data by determining the c_i 's with a nonlinear fitting routine⁸. This equation is used for the fitting routines. It is of crucial importance for this technique to keep the ratio N_{T1}/N_{T2} constant during the fitting procedure as this ratio is a quantity that physically cannot change. This means that one has to optimize its value until the best Arrhenius plots are obtained.

EXPERIMENTAL RESULTS AND DISCUSSION

A typical transient signal of the DX center is shown in Fig. 1 for $x=0.19$. The analysis determined two different emission-rates at that temperature. The same temperature intervall was used later for all the samples under consideration. The best ratio for the two traps found for $x=0.19$ was $N_{T2}/N_{T1} = 1.1$ and each fit determined the $N_{T1}/2N_D$ ratio according to equation (4). The average value was $N_{T1}/2N_D = 2.13 \times 10^{-3}$, constant within about 13%.

In Fig. 2 the emission rate values are plotted in an Arrhenius function (eqn.2). The two thermal ionization energy values determined nearly equal as will be found for all other trap pairs.

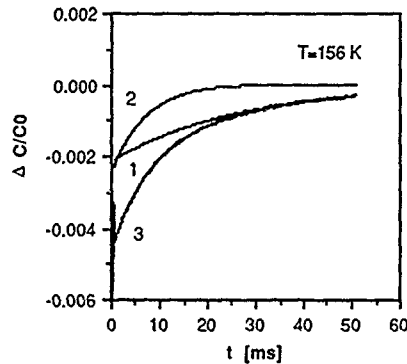


Fig. 1 Double exponential fit to the AlGaAs data with $x=0.19$. The curves marked with 1 and 2 are the single exponential functions found by the fitting routine. Curve 3 shows real data and fit. The two electron emission rates found were $g_{e1}=36.9 \text{ s}^{-1}$ and $g_{e2}=142.8 \text{ s}^{-1}$.

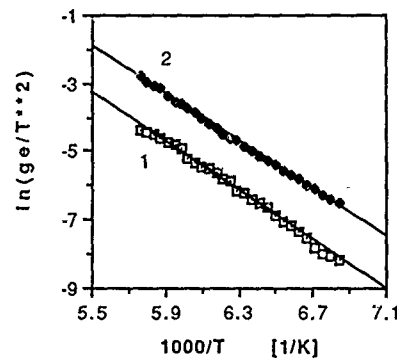


Fig. 2. Two Arrhenius plots for the DX-center in the AlGaAs with $x=0.19$ resulting from the double exponential fit. The energy levels determined were $\Delta E_1=316 \text{ meV}$ and $\Delta E_2=301 \text{ meV}$.

There is excellent agreement between the rate-window data (Fig. 3) and the simulation spectrum (Fig. 4). The upper half of the spectra are identical in shape and amplitude. This agreement also carries over to the ionization energy values determined from the single trap model applied to real and simulated spectrum i.e. 289 meV and 299 meV respectively.

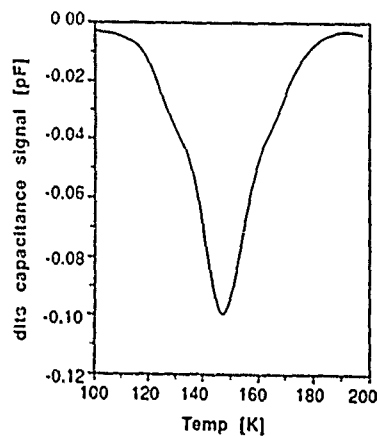


Fig. 3. Measured DLTS spectrum for AlGaAs sample with $x=0.19$. The rate-window used is $t_1=12.5 \text{ ms}$ and $t_2=2.6 \cdot t_1$. The pulse width is $d_n=20 \text{ ms}$.

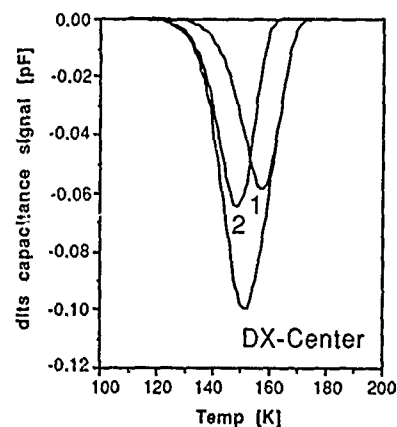


Fig. 4. Simulated DLTS spectrum for AlGaAs sample with $x=0.19$ using the results from Fig. 2. The single trap spectra are also shown.

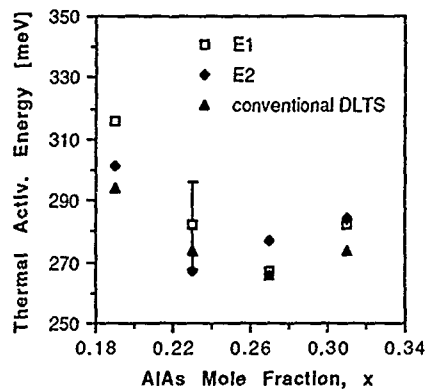


Fig. 5. The thermal activation energies of the DX center pairs and the rate-window data for different AlAs mole fractions. All energy values are about 5% uncertain.

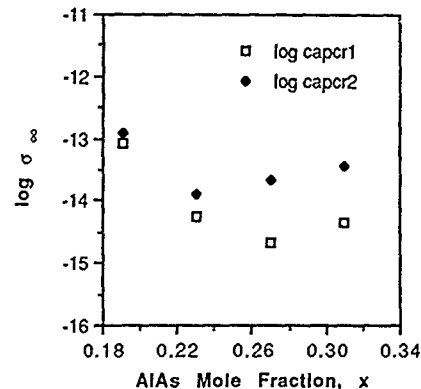


Fig. 6 The log of the capture cross section at infinite temperature of the DX center pairs as a function of AlAs mole fraction. The uncertainty is about 80 % for all σ_{∞} values given.

A plot of the thermal activation energies are shown in Fig. 5. These data overlap the published value⁹ of about 280 meV. The trend in activation energy as the AlAs mole fraction x is increased might be very closely connected to σ_{∞} values shown in Fig. 6. Here the same general trend is noticeable. All signals were measured in the same temperature range which indicates that the emission-rates are nearly equal for a particular temperature. With the σ_{∞} values decreasing drastically as x increases it would follow from equation (1) that E_B had to decrease as x increases. This trend that has been seen for Si-doped AlGaAs by Mooney et al.¹ This is of course only true if E_0 is not decreasing as the Al content is raised (see equ. (3)), which would be just the opposite trend from the one reported in the literature.¹⁰ The density of defect states was about equal for the 0.19, 0.23, and 0.27 samples. The high Al ($x=0.31$) sample indicated a factor of 25 higher trap level than the former.

CONCLUSIONS

It has been shown that DX center signal is due to a pair of values which are closely spaced in energy rather than a single level. Both levels may evolve from the same defect. For both traps, the data also indicates a decrease in the capture barrier E_B as the Al content is raised from $x=0.19$ to 0.27.

REFERENCES

- 1 P. M. Mooney, N. S. Caswell, and S. L. Wright, J. Appl. Phys. 62, 4786 (1987)
- 2 O. Kumagai, H. Kawai, Y. Mori, and K. Kaneko, Appl. Phys. Lett. 45, 12 (1984)
- 3 B. L. Zhou, K. Ploog, and E. Gmelin, Appl. Phys. A 28, 223 (1982)
- 4 P. Omeling, L. Samuelson, and H. G. Grimmeiss, J. Appl. Phys. 54, 5114 (1983)
- 5 R. K. Ahrenkiel, Solar Cells, 16, 549 (1986)
- 6 T. R. Hanak, submitted to J. Appl. Phys.
- 7 H. C. Casey JR. and M. B. Panish, Heterostructures Lasers, (Academic Press, 1978), p.194
- 8 P. R. Bevington, Data Reduction and Error Analysis for the Physical Sciences, (Mc Graw-Hill, 1969), p. 232.
- 9 D. V. Lang, in S. T. Pantelides (ed.), Deep Centers in Semiconductors, (Science Publisher, 1986), p.521.
- 10 J. J. Yang, L. A. Moudy, and W. I. Simpson Appl. Phys. Lett. 40, 244 (1982)

POOLE FRENKEL EFFECT ON THE DX CENTERS IN III-V
TERNARY ALLOYS

H. ALTELARREA, J. BOSCH, A. PEREZ, J. SAMITIER AND J.R. MORANTE.
Càtedra d'Electrònica. Fac.Física. Universitat de Barcelona.
Diagonal 645-647. Barcelona 08028. Spain.

ABSTRACT

The dependence of the DX centers thermal emission rates on the electric field has been measured by Isothermal Transient Spectroscopy (ITS) and differential ITS (DITS) techniques. These techniques allow us to achieve a more accurate analysis of these defects than the DLTS, which ability for the study of DX centers is discussed. This dependence has been found to be mainly due to a Poole-Frenkel effect and is the cause of the non-exponentiality of the thermal emission transients.

INTRODUCTION

In the last years there have been a lot of papers devoted to the DX centers in III-V ternary alloys, due to the detrimental influence of these traps on the performance of high electron mobility transistor (HEMT) devices. In these papers different techniques have been used to report values of parameters of great interest in order to explain the microscopic nature of donors with a DX type behaviour. However, their physical nature is still subject of controversy and the deduction of the parameters can depend on the physical model choosen, as for example the parameters related to the thermal emission and capture kinetics.

In this framework, the discussion reported by Lang et al. in early papers [1] shows that the application of the deep level transient spectroscopy (DLTS) for the characterization of these centers is not advisable. However, this technique has been extensively used and different authors have invoked several models, such as the broadening [2], local environment changes [3] and cross section distribution [4], to explain the DLTS spectra. Generally, a comparative study between these models and experimental single shot transients at different bias and temperatures has not been made. These models are not the only physical mechanisms which can explain the non exponential behaviour of the thermal emission and capture kinetics. So, the influence of the electric field on the microscopic parameters associated to the DX center has been reported [5] and even though the data from Calleja et al. [6] of the non-exponentiality factor do not show any dependence on the electric field, their experiments always correspond to transients carried out near edge region and, hence, at low field conditions.

We have to remark that, taking into account the characteristics of these centers, the DLTS spectra are obtained without complete filling of the centers. Bearing this in mind, this work has a double aim: i) to show that the use of the DLTS with non-saturated trap filling of the centers is not suitable, and ii) to characterize the center using other technique based on the time resolved analysis of the Isothermal Transients (ITS) and their differences (DITS). This characterization allows us to measure the dependence on the electric field of the DX emission kinetics.

EXPERIMENTAL DETAILS

For an ideal level with non-saturated trap filling the transient obtained after the filling pulses is given by

$$\Delta C(t) \approx \Delta C_0 (T, t_{\infty}, t_c) e^{-e_n t} \quad (1)$$

and, then, the emission rate of the DLTS maximum becomes

$$e_n = \frac{1}{t_2 - t_1} \ln \frac{t_2 - \frac{C_n n t_c E_B}{[\exp(C_n n t_c) - 1] E_T e_n}}{t_1 - \frac{C_n n t_c E_B}{[\exp(C_n n t_c) - 1] E_T e_n}} \quad (2)$$

where t_a and t_c are the emission and capture time, E_B is the thermal activation energy of the capture coefficient $C_n n$ and E_T is the energetic position of the trap level. Only when $C_n n t_c \gg 1$ this expression gives the standard DLTS emission rate. Otherwise, there would be an undervaluation of the emission coefficient which leads to incorrect Arrhenius plot, as it is shown in figure 1.

This error increases as the temperature decreases, obtaining higher activation energies. This is more significative when the capture activation energy is comparable to that of the emission process, as it seems to happen for the DX center, and could explain the differences in the values reported, for example, from 0.21 eV up to 0.38 eV for DX-Te related centers. Moreover, the non-exponential behaviour of the kinetics leads to complex DLTS spectra.

So, we have used an alternative technique, the ITS [7], based on the time logarithmic derivative of the measured signal. For a general non-exponential transient, the ITS signal obtained is given by the convolution product of the signal corresponding to a single exponential transient by the distribution function of time constants involved in the transient.

The samples studied have been GaAsP and AlGaAs light-emitting diodes and are similar to that described in previous papers [7,8]. Figure 2 shows the ITS spectra obtained maintaining constant the reverse polarization, $V_R = -9V$. The emission transient takes place after the application of bias pulses of different amplitude, $V_F - V_R$. As can be seen, the distribution function of time constants associated to the transient depends on the pulse amplitude. The signal shows the contribution of the different regions of the space charge

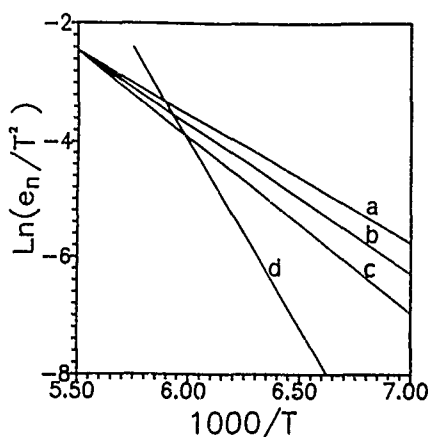


Figure 1. Theoretical Arrhenius plots for non-saturated trap-filling pulse DLTS. (a) Ideal DLTS in saturated case; (b) Non-saturated case for $t_2/t_1=2$; (c) Non-saturated case for $t_2/t_1=10$; (d) t_2/t_1 variable.

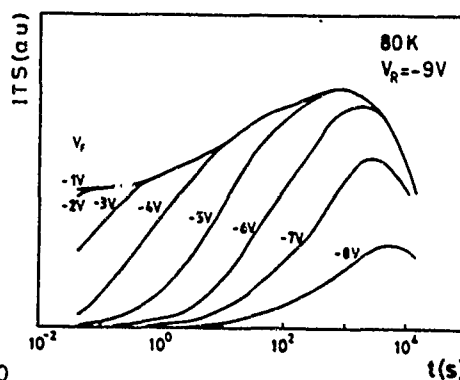


Figure 2. ITS spectra obtained from Capacitance emission transients in AlGaAs:Te samples at 80 K. For $V_R = -9V$ (emission bias) and different V_F values.

zone swept according to the pulse applied. Figure 3 presents the differential ITS (DITS) obtained subtracting every consecutive pair of ITS signals with a voltage window of 1 volt. The exponentiality of the differential spectra increases as the amplitude of the window decreases. The behaviour shown has been corroborated by constant capacitance transient experiments. All these results show the dependence of the emission coefficient on the electric field.

Likewise, the same technique has been used in order to determine the thermal cross section which, assuming that the capture process takes place through the L minima, has been found to be independent of the temperature in the measured interval, figure 4. So, the thermal activation of the capture time constant is attributed to the free carriers activation from the absolute minimum up to L minima.

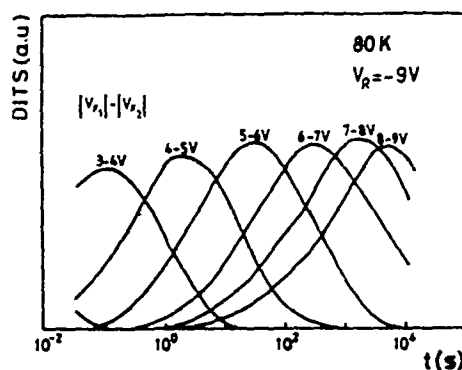


Figure 3. Emission DITS spectra in AlGaAs:Te samples at 80 K.

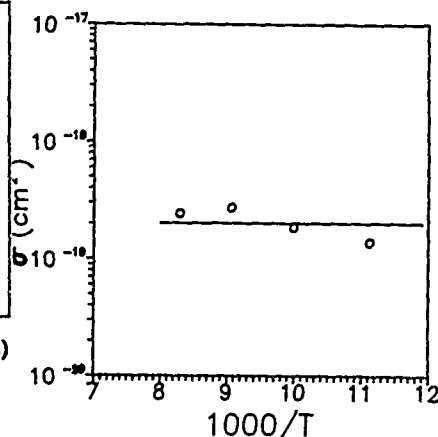


Figure 4. Evolution of the capture cross section with the temperature.

DISCUSSION AND CONCLUSIONS

Although the experimental results shown in figures 1 to 4 have been obtained on AlGaAs samples, the behaviour observed in GaAsP samples is completely similar to the discussed above. According to this behaviour, the Arrhenius plot depends on the chosen window, as it is shown in figure 5. The energy values are function of the electric field. They are not in agreement with the data measured by DLTS by others authors, but are closer to the data measured by Hall effect.

This dependence of the thermal emission rates on the field can be originated by several mechanisms: Poole-Frenkel [9], pure tunnel [10] and tunnel assisted by phonons [11]. Experimentally, all of them can be simultaneously present and their relative importance depends mainly on parameters such as the trap energy, electric field and effective mass. In our case, taking into account the parameters measured for the DX center and the theoretical analysis [12], we can claim on a predominant Poole-Frenkel effect. So, the measured dependence of the thermal activation energy decrease on the electric field is in agreement with the square root behaviour expected for a Poole-Frenkel mechanism, as it is shown in figure 6. To have an important contribution of the other effects we ought to have a field higher than the fields used (closer to 10^6 V/cm) [12].

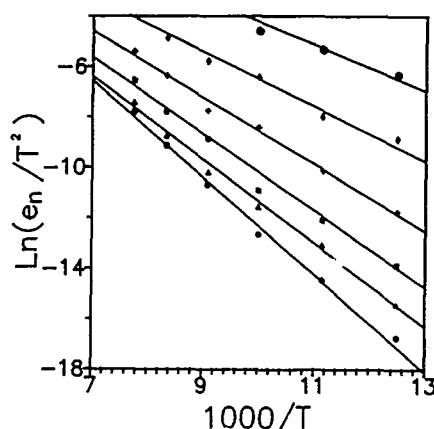


Figure 5. Arrhenius plots obtained from the DITS spectra of the samples of AlGaAs:Te at different bias window.

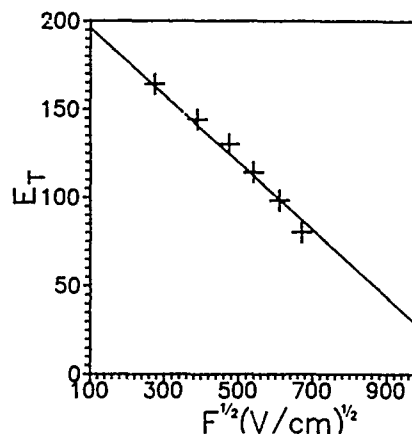


Figure 6. Evolution of the thermal activation energy with the electric field in samples of AlGaAs:Te

In summary, the emission and capture data measured corroborate the existence of a level originated by the shallow donors and associated to the L minima. The dependence of the thermal emission rates of this level on the electric field has been found to be mainly due to a Poole Frenkel effect and would be the cause of the non-exponential emission kinetics. On the other hand, the non-exponential capture kinetics has been explained assuming that the capture process takes place through the L minima. Moreover the non-dependence on the temperature of the cross section is incompatible with the existence of a strong relaxation unless high energy local vibration modes were associated with the DX center. In any case, measurement at high temperature, $kT \gg 15 \text{ meV}$ should be carried out in order to reject any possibility of relaxation.

REFERENCES

- [1] D.V. Lang and C.H. Henry, Phys. Rev. Lett. **35**, 1525 (1975)
- [2] P. Omling, L. Samuelson and H.G. Grimmeiss, J. Appl. Phys. **54**, 5117 (1983).
- [3] P.M. Mooney, T.N. Theis and S.L. Wright, Trans Tech Publ., Mat. Scien. For. **38-41**, 1109 (1989).
- [4] E. Calleja, A. Gómez, J. Criado and E. Muñoz, Trans Tech Publ., Mat. Scien. For. **38-41**, 1115 (1989).
- [5] J.R. Morante, J. Samitier, A. Cornet and A. Herms, Appl. Phys. Lett. **45**, 1317 (1984).
- [6] E. Calleja, P.M. Mooney, S.L. Wright, M. Heiblum, Appl. Phys. Lett. **49**, 657 (1986)
- [7] J.R. Morante, P. Roura, A. Pérez, J. Samitier, A. Cornet and A. Herms, Trans Tech Publ., Mat. Science. For. **10-12**, 533 (1986)
- [8] J.R. Morante, J. Samitier, A. Herms, A. Cornet and P. Cartujo, Solid St. Electron. **29**, 759 (1986).
- [9] J. Frenkel, Phys. Rev **54**, 647 (1938)
- [10] D. Pons, J. Appl. Phys. **55**, 3644 (1984)
- [11] S. Makram-Ebeid and M. Lannoo, Phys. Rev. **B25**, 6406 (1982)
- [12] G. Vincent, A. Chantre and D. Bois, J. Appl. Phys. **50**, 5484 (1979)

TRANSIENT CURRENT AND TRANSIENT CAPACITANCE MEASUREMENTS OF DEFECTS IN ALGAAAS HEMTS

R. Magno and R. Shelby, Naval Research Laboratory, Washington, DC 20375

ABSTRACT

The defects present in AlGaAs high electron mobility transistor (HEMT) devices subjected to accelerated lifetime tests have been studied by transient current, and when possible, by transient capacitance techniques. By measuring transient source-drain currents following the application of a voltage pulse to the gate it is possible to perform deep level transient spectroscopy (DLTS) experiments on HEMT devices which are too small for the conventional capacitance DLTS. The capacitance and current spectra for both stressed and unstressed HEMTs contain the AlGaAs DX defect. The current DLTS spectra for stressed devices contain an additional feature which is not found in capacitance DLTS measurements on the stressed HEMTs. This additional current DLTS feature is anomalous in that the transient has a sign which is opposite to that expected for a majority carrier trap. The absence of the new defect in the capacitance DLTS suggests that the defect is located in the channel between the gate and either the source or the drain. The current DLTS line shape of the stressed induced defect depends upon the polarity and size of the source-drain voltage.

INTRODUCTION

Deep level transient spectroscopy (DLTS) techniques are being investigated as a method for studying process induced or lifetime stress induced defects in high electron mobility transistor (HEMT) devices.[1] Because state of the art devices have gate lengths less than 0.3 μm their areas are too small for the usual capacitance DLTS techniques. An alternate approach is to monitor the transient source-drain current following the application of a defect filling bias pulse to the gate. The current transients are measured as the temperature of the device is swept over a range where the defects have a reasonable emission rate. These procedures are similar to those used in capacitance DLTS where a capacitance transient is monitored while sweeping the temperature.[2] Current DLTS is more difficult to interpret than capacitance DLTS because the source-drain current depends on the mobility and geometry of the conducting channel, as well as the carrier concentration. The source-drain voltage, V_{DS} , is an additional parameter which is not available in capacitance DLTS. The sensitivity of current DLTS line shapes to the size and polarity of V_{DS} , is the subject of this study. Because V_{DS} makes the potential under the gate nonuniform, it may be possible to profile the defects under the gate by varying the size and polarity of V_{DS} . Since a model for current DLTS line shapes is not available, the results presented here can only be discussed in a qualitative manner.

Current DLTS has been used by a number of research groups to study metal-semiconductor field-effect transistors (MESFET)[3,4], to examine the DX center[5] in AlGaAs HEMTs[5,6,7], and to study the results of accelerated lifetime stress tests in HEMTs[1]. In the current DLTS work on lifetime stress effects a "minority-trap feature" was reported in stressed devices in addition to the expected DX defect. Capacitance DLTS studies of the stressed HEMTs revealed the DX center but not the minority-trap feature. Similar minority-trap features have been reported for current DLTS of GaAs MESFETs where they are believed to be due to surface states[4]. Earlier reports on the MESFETs suggested that they were associated with traps at the substrate epilayer interface[3].

EXPERIMENT

The AlGaAs HEMTs reported here were prepared by molecular beam epitaxial growth with a 26% Al fraction and a 0.7 μm long gate. The DC lifetime stress tests were carried out by applying DC drain and gate biases at 225 °C for about 300 hours. The unstressed devices were measured as prepared.

The DLTS measurements were carried out by applying a quiescent reverse bias, V_{GS} ,

and a filling pulse between the gate and the source. Capacitance DLTS spectra were measured with 1 MHz Boonton capacitance meter connected between the gate and the source which was shorted to the drain. The current DLTS was carried out by applying a voltage, V_{DS} , between the source and drain and then recording the source-drain current. The polarity indicated for V_{DS} is that of the drain relative to the source. A dual channel boxcar was used to monitor either the current transient or the capacitance transient. The boxcar's output and the temperature were recorded by a computer controlled data acquisition system. Because the AlGaAs contains DX centers which can trap electrons, the samples were cooled to 100 K with V_{GS} and V_{DS} applied and the data were recorded on warming. The temperature dependence of both the source-drain conductivity and the gate capacitance were also measured in order to normalize the spectra by the background conductance or capacitance. A decade box was used to calibrate the current measurement system in order to present the current measurements as the conductance, G .

RESULTS

The effect of a DC lifetime stress test on a HEMT's source-drain conductance is illustrated in Fig. 1 where the results for an unstressed device are compared with those for a stressed one. The unstressed device measured with $V_{GS} = -0.3$ V has a higher conductivity and a different temperature dependence than the stressed one with $V_{GS} = -0.1$ V. The increasing conductivity on decreasing temperature for the unstressed device with $V_{DS} = -0.05$ V is consistent with what may be expected for conduction via the two dimensional electron gas (2 DEG) of a HEMT. The difference in the conductances for the two polarities of V_{DS} in Fig. 1a indicates that the potential under the gate is nonuniform. Qualitatively, the potential difference between the gate and channel is larger at the drain end of the gate for $V_{DS} = +0.05$ V than for $V_{DS} = -0.05$ V. Thus, for $V_{DS} = +0.05$ V the drain end of the gate is nearer to threshold than when $V_{DS} = -0.05$ V, and a lower conductivity is observed. The conductivity for the stressed device in Fig. 1b follows the same pattern.

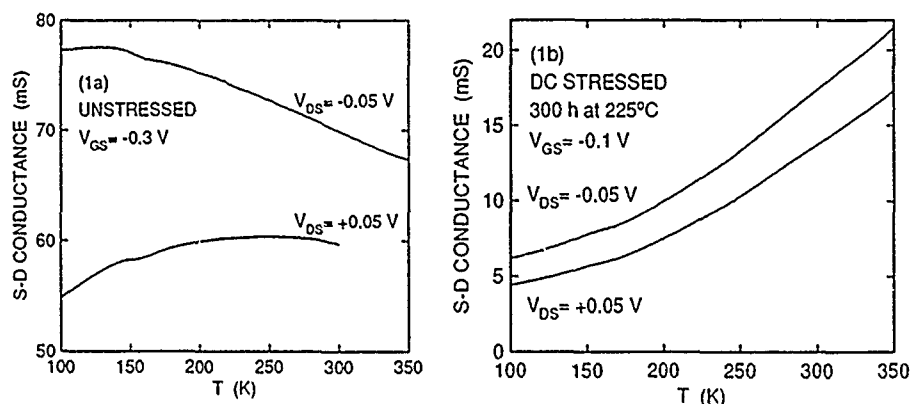


Fig. 1 Source-drain conductance versus temperature for (a) an unstressed and (b) a DC stressed HEMT.

The current DLTS spectra for these two HEMTs are presented in Fig. 2 for the same values of V_{GS} and V_{DS} used to acquire the conductance data in Fig. 1. The data are plotted using the convention that a majority carrier trap is represented by a downward pointing line like the DX line in Fig. 2a. The spectra in FIG. 2 have been normalized by the conductivity data in Fig. 1, which assumes that the conductivity changes during the emission process are small compared to the conductivity. The DX spectra in Fig. 2a for the two polarities of V_{DS} are almost identical in both shape and amplitude. Other DX spectra measured using -0.15 V $< V_{DS} < +0.05$ V have the line shape and amplitude shown in Fig. 2a. Assuming that the DX defect is uniformly distributed in the doped AlGaAs, these results indicate that it is possible to measure a spectrum which is independent of the size and polarity of V_{DS} . Care must be given to finding acceptable limits, as using $V_{DS} = +0.07$ V resulted in a DX line with a 10% larger amplitude.

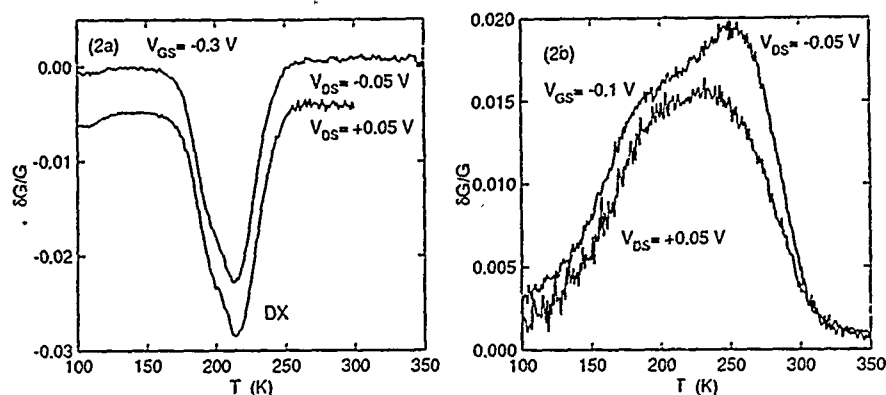


Fig. 2 Normalized current DLTS data for two polarities of V_{DS} for (a) an unstressed and (b) a DC stressed HEMT. The $V_{DS} = +0.05$ V data in (a) was offset downward by 0.005.

These results should be contrasted with those in Fig. 2b for a stressed device.

The DX peak in Fig. 2b for a stressed sample is barely visible as a depression on a large positive going line. The positive peak in Fig. 2b is broader than the DX defect, and much broader than expected for a point defect. In capacitance DLTS spectroscopy, a positive going peak is associated with a minority carrier trap, but since minority carriers are not injected in these measurements, minority carrier traps should not be detected. The positive peak for the stressed device will be referred to as a "minority-trap feature". This peak has been tentatively identified as being due to surface states located between the gate and either the source or drain because it is not observed in capacitance DLTS[1], and by analogy with studies on MES-FETs[4]. The data here for $V_{DS} = -0.05$ V differs noticeably in shape from that for $V_{DS} = +0.05$ V. Spectra recorded with -0.1 V $< V_{DS} < -0.02$ V gave the same line shape as that shown for $V_{DS} = -0.5$ V, and the line shape shown here for $V_{DS} = +0.05$ V was also measured for 0.02 V $< V_{DS} < 0.1$ V. Data were also measured for $V_{GS} = -0.3$ V and -0.15 V $< V_{DS} < 0.1$ V and similar results were found except the peak amplitudes were about four times larger than those shown here. The line shape's dependence upon the polarity of V_{DS} suggests that the defect distribution under the gate is nonuniform.

A further investigation of the distribution of the minority-trap feature was made by recording the spectra for $V_{GS} = -0.3$ V with filling pulse heights, PH, between 0.4 V and 0.2 V for both polarities of V_{DS} as shown in Fig. 3. The first point to note about the spectra in Fig. 3 is that the amplitude of the spectra decrease monotonically as the pulse height is reduced.

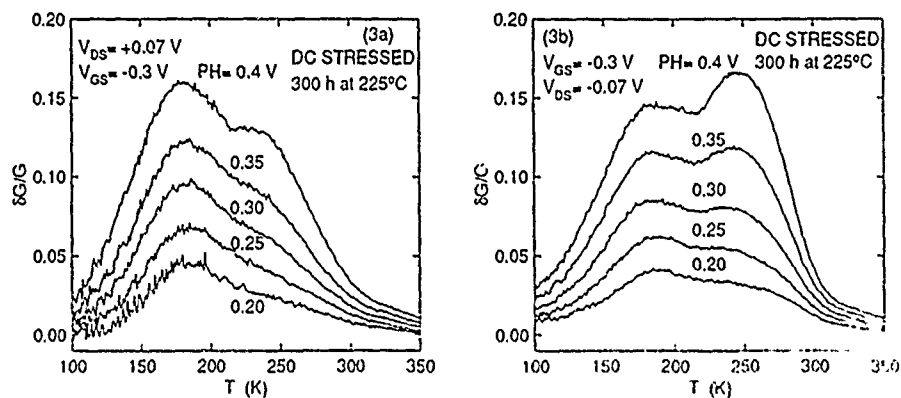


Fig. 3 Current DLTS for the stressed HEMT for several pulse heights for (a) $V_{DS} = +0.07$ V and (b) for $V_{DS} = -0.07$ V.

In a capacitance DLTS experiment on a diode, defect concentration profiles through the depletion region are measured by varying the pulse height, and if a similar intensity behavior was observed the conclusion would be that the defect was distributed throughout the depletion region. If the defect was concentrated near the surface the intensity would be expected to drop abruptly on reducing the pulse height. If a similar interpretation is given to the current DLTS spectra in Fig. 3 the conclusion would be that the minority-trap feature is due to a defect in the bulk, which is inconsistent with the earlier suggestion that the minority-trap feature is associated with a surface state between the gate and the source or drain. The data in Fig. 3 also show that the line shape depends upon the polarity of V_{DS} . The spectra have a low temperature peak for all positive values of V_{DS} , and for negative values of V_{DS} the peak is at high temperatures only for large values of the pulse height. Additional work is necessary to understand how V_{DS} and V_{GS} add to determine the portions of the samples contributing to the spectra.

DISCUSSION

Current DLTS has an advantage over capacitance DLTS in studying small HEMT like devices in that relatively simple hardware can give a much better signal to noise than conventional capacitance instruments. Since the HEMT device is a relatively complicated structure, it is difficult to devise simple models for analyzing the line shapes. The line shapes do depend upon the size and polarity of both V_{DS} , V_{GS} , and the pulse height. When capacitance and current DLTS are both possible on the same sample, they may prove to be complementary techniques because one is primarily sensitive to the region under the gate while the other is sensitive to the entire channel.

REFERENCES

1. R. Magno, R. Shelby, and W. T. Anderson, *J. Appl. Phys.* **66**, 5613 (1989).
2. D. V. Lang, *J. Appl. Phys.* **45**, 3023 (1974).
3. A. Zylbersztejn, G. Bert, and G. Nuzillat, *Inst. of Phys. Conf. Ser. No. 45*, edited by C. M. Wolfe (IOP, Bristol, 1979) p. 315.
4. S. R. Blight, R. H. Wallis, and H. Thomas, *IEEE Trans. Electron Devices* **Ed-33**, 1447 (1986).
5. For a recent review of DX see P. M. Mooney, *Defects in Electronic Materials*, edited by M. Stavola, S. J. Pearton, and G. Davies (Mater. Res. Soc., Pittsburgh, PA 1988), p.561.
6. A. J. Valois and G. Y. Robinson, *IEEE Electron Device Letters* **EDL-4**, 360 (1983).
7. G. N. Maracas, W. D. Laidig and H. R. Wittman, *J. Vac. Sci. Technol.* **B2**, 599 (1984).

ELECTRONIC AND OPTICAL PROPERTIES OF DEEP DONORS IN
HYDROGENATED $\text{Al}_x\text{Ga}_{1-x}\text{As}:\text{Si}$.

R.MOSTEFAOUI*, R.LEGROS*, J.CHEVALLIER*, C.W.TU**, R.F.KOPF**;
*Laboratoire de Physique des Solides, CNRS, 1 Place A.Briand,
92195 Meudon Cedex, FRANCE.
**A.T.T. Bell Laboratories, Murray Hill, New Jersey 07974, USA.

ABSTRACT:

Transient conductivity and photoconductivity experiments have been performed on hydrogenated $\text{Al}_{0.37}\text{Ga}_{0.63}\text{As}:\text{Si}$ epilayers. The recapture kinetics of free electrons on the remaining deep donors is significantly affected under hydrogenation. The energy barrier height for capture on the deep donors drops from 210 meV in the reference sample to 40 meV in the hydrogenated sample. We also note a shift toward higher energies of the photoionization cross section versus photon energy curve. Different models are proposed for explaining the data.

INTRODUCTION:

Many published papers have shown that the electrical properties of n type $\text{Al}_x\text{Ga}_{1-x}\text{As}:\text{Si}$ ($x > 0.2$) are controlled by deep centers (called D-X centers) directly related to donor impurities. They are characterized by a repulsive barrier for both electron emission and capture leading to persistent photoconductivity. The exact structural description of these centers is still a subject of controversy (1)(2)(3). The presence of these defects has a detrimental influence on the properties of devices (4). So the elimination or the neutralization of these centers would have a large impact in microelectronics. The passivation of deep centers by hydrogen have been demonstrated in GaAs. NABITY et al have shown that the D-X centers in n-AlGaAs:Si are passivated after exposure of the crystals to a hydrogen plasma (5). In a more recent paper, we have reported large mobility increase after hydrogenation of $\text{Al}_x\text{Ga}_{1-x}\text{As}:\text{Si}$. This effect has been related to the neutralization of shallow donors and D-X centers by hydrogen (6). For $x = 0.37$, the electrical properties after hydrogenation are governed by the ionization of remaining deep donors. In this work, we present the electronic and optical characteristics of these deep donors remaining after hydrogenation.

EXPERIMENTAL:

The AlGaAs samples were grown by molecular beam epitaxy on semi-insulating GaAs substrates. The sample structure consisted of a 0.5 μm undoped GaAs buffer layer, a 1000 Å undoped $\text{Al}_x\text{Ga}_{1-x}\text{As}$ layer with graded x ($0 < x < 0.37$) in order to avoid modulation doping effects and a 1.5 μm silicon doped $\text{Al}_x\text{Ga}_{1-x}\text{As}$ layer ($[\text{Si}] = 2 \times 10^{17} \text{ cm}^{-3}$, $n_H(300\text{K}) = 5 \times 10^{18} \text{ cm}^{-3}$). The Al fraction ($x=0.37$) was measured by electron microprobe and by photoluminescence at low temperature.

Hydrogenation of the samples was realized by exposure to a R.F. hydrogen plasma. The exposure conditions were: $T = 250^\circ\text{C}$, $t = 30 \text{ min.}$, R.F. power = 10W. In this study, we have determined the Hall energy, the optical ionization energy E_0

and the capture energy barrier E_c of the deep donors present in AlGaAs:Si before and after hydrogenation. The Hall energy has been deduced from conventional Hall effect and conductivity measurements. For optical ionization energy and capture energy barrier determinations, we essentially performed conductivity measurements with the sample fed by a constant current source (0.1mA). In optical ionization experiments the sample was first cooled down to 77K in the dark. Then the variation of its resistivity under monochromatic illumination was recorded versus time. Before recording any new transient, the sample was heated to 300K. To measure the recapture time of free electrons by the deep centers, the sample was first cooled to the desired temperature (± 1 K). Then the sample was illuminated by photons of energy 2.1eV, for a time long enough to empty the deep centers as completely as possible. Finally, we interrupt the illumination and measure the resistance as a function of time. Between two of these measurements, the sample was heated up to 300K.

RESULTS AND DISCUSSION:

Hall effect and conductivity experiments performed on $\text{Al}_{0.63}\text{Ga}_{0.37}\text{As:Si}$ ($x=0.37$) before exposure show the well known freeze out of free carriers on D-X centers as the temperature decreases. The corresponding activation energy is 160meV. After hydrogenation the free electron concentration at 300K decreases by a factor of 20 which means that the neutralization of D-X centers is partial. We find an activation energy of 160 meV (± 10 meV) for the remaining deep centers (6).

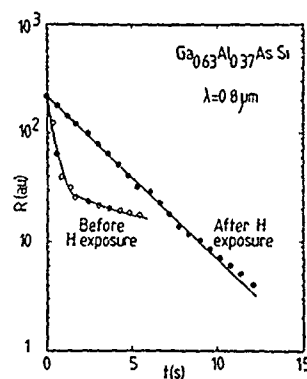


Fig. 1: Typical photoionization response of deep donors in the reference and the hydrogenated AlGaAs:Si samples under monochromatic illumination.

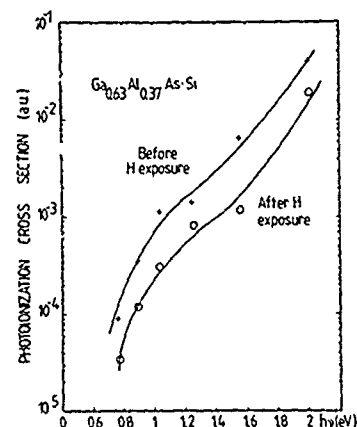


Fig. 2: Photon energy dependence of the deep donor photoionization cross section in the reference and the hydrogenated samples.

Figure 1 shows the typical variation of the sample resistance $R(t)$ after a duration t of monochromatic illumination (0.8 μm in the case of figure 1) before and after hydrogenation. For clarity, the $R(t)$ curves have been normalized. Assuming that the electron mobility remains constant, the $R(t)$

variation reflects the free electrons kinetics. Following the approach used by HENNING et al (7), we used the slope of the transient at $t=0$ in order to determine the photoionization cross section σ_n . In this approach, the rate of ionized deep donors at $t=0$, in low temperature conditions, is given by $(dN^+/dt)_{t=0} = \sigma_n \Phi N^+$, Φ being the light flux, since we can neglect the thermal emission and capture rates.

In figure 2 we present the photoionization cross section values at different photon energies before and after exposure. The main effect of hydrogenation is a shift towards higher energies of the cross section curves.

The recapture kinetics of free electrons on the D-X centers can be easily evaluated from the time dependence of the resistance after interruption of the illumination. The $R(t)$ dependence is quasi linear during the period which just follows the interruption. This can be understood assuming that the capture of electrons on D-X centers follows the bimolecular recombination model (8). Such a model is appropriate in our case because our samples are either only lightly (before exposure) or not (after exposure) degenerated. Writing the capture kinetics of free electrons as $dn/dt = -\gamma n^2$, with all the free electrons being provided by the D-X centers, the sample resistance at time t after interruption of illumination is $R(t) = Kt + R_0$ where R_0 is the sample resistance under illumination and K is a coefficient proportional to the capture cross section. Assuming that the electron mobility is constant, the temperature dependence of the rate of increase of the sample resistance provides the barrier energy for recapture. As we see on figure 3, the barrier energy calculated for

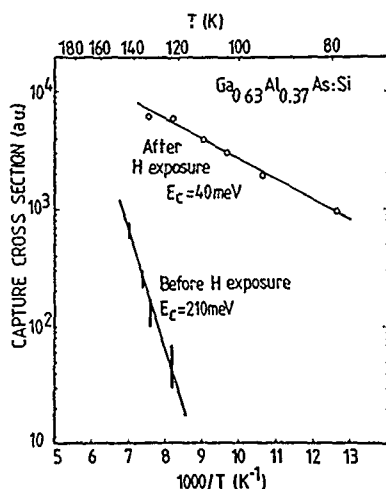


Fig. 3: Variation of the capture cross section for electrons on the deep donors as a function of temperature.

the reference sample is 210 ± 40 meV. This value is in good agreement with the capture barrier height found by MOONEY et al. in $\text{Al}_{0.37}\text{Ga}_{0.63}\text{As}$ alloys (9). After hydrogenation, we note a significant decrease of the capture barrier height down to $40 \text{ meV} \pm 5 \text{ meV}$. A change of the capture kinetics can be directly seen through the time necessary to fill half of the deep donors. A 79K for example, this time is $1.2 \times 10^3 \text{ s}$ for the reference sample and 8s for the hydrogenated sample.

Coming back to figure 2, it has to be noted that because of the low barrier energy after hydrogenation, it is likely that during photoionization experiments a fraction of the free electrons is recaptured by the deep centers. This will cause a reduction of the rate at which the free carrier concentration increases and consequently a smaller value of the photoionization cross section. Then, after hydrogenation the real photo-

toionization cross section curve is in fact less shifted than the experimental one.

At this point, we see two possible explanations for the modification of the electron capture kinetics. The amount of active donors after hydrogenation (a few 10^{15}cm^{-3}) is of the order of the residual sulphur donor concentration. In GaAs the hydrogen neutralization efficiency of donors on arsenic sites is rather low (10). Assuming that this holds true also in AlGaAs, one might think that the deep donors we studied in the hydrogenated sample are these residual donors. This is consistent with the fact that Te and Se donors in AlGaAs are known to give rise to D-X centers with a significantly lower barrier energy if compared to the case of Si donors (1). An argument against this explanation comes from the shift towards high energies of the photoionization cross section curve after hydrogenation: in AlGaAs:Se or Te, the corresponding curves are shifted towards low energies by $\approx 0.4\text{eV}$ with respect to the situation for AlGaAs:Si (1). For this reason, we propose another explanation in terms of a perturbation of the structural properties of the D-X centers by hydrogen atoms located in close proximity but not bonded to the silicon donor. We assume that the hydrogen atoms relax the local strains around these donors. This effect would reduce the barrier for electron capture. More experimental data are needed to confirm this view.

ACKNOWLEDGMENTS: We are very grateful to MM. J. BOURGOIN and H. J. VON BARDELEBEN (Groupe de Physique des Solides de l'E.N.S. Paris) for fruitful discussions. We also thank Mr. ROMMELUERE for electron microprobe analysis and M. J. C. PESANT for his assistance in plasma experiments.

REFERENCES:

- (1) D.V. LANG, R.A. LOGAN, Phys. Rev. Lett., 39, 635 (1977); Proceedings of the Institute Conference on Physics of Semiconductors, EDINBURGH (1978), edited by B.L.H. WILSON (Institute of Physics, LONDON, 1979), p.433
- (2) P.M. MOONEY, G.A. NORTHROP, T.N. MORGAN, H.G. GRIMMEISS, Phys. Rev. B, 37, 8298 (1988)
- (3) H.P. HJALMARSON, T.J. DRUMMOND, Phys. Rev. Lett., 60, 2410 (1988)
- (4) A. KASTALSKY, R.A. KIEHL, IEEE Trans. on Electron Devices ED-33, 3, 414 (1986)
- (5) J.C. NABITY, M. STAVOLA, J. LOPATA, W.C. DAUTREMONT-SMITH, C. W. TU, S.J. PEARTON, Appl. Phys. Lett., 50, 921 (1987)
- (6) R. MOSTEFAOUI, J. CHEVALLIER, A. JALIL, J.C. PESANT, C.W. TU, R.F. KOPF, J. Appl. Phys., 64, 207 (1988)
- (7) J.C.M. HENNING, J.P. ANSEMS, Appl. Phys., A44, 245 (1987)
- (8) J.C. BOURGOIN, S.L. FENG, H.J. VON BARDELEBEN, Appl. Phys. Lett., 53, 1841 (1988)
- (9) P.M. MOONEY, N.S. CASWELL, S.C. WRIGHT, J. Appl. Phys. 62, 4786 (1987).
- (10) A. JALIL, Private communication.

PART XII

EL2 Centers

THE METASTABILITY OF THE EL2 AND DX DEFECTS IN GaAs AND 3-5 ALLOYS

H.J. von BARDELEBEN AND J.C. BOURGOIN

Groupe de Physique des Solides de l'École Normale Supérieure, Centre National de la Recherche Scientifique*, Tour 23, 2 place Jussieu, 75251 Paris Cedex 05, France.

ABSTRACT

The metastability of the EL2 and DX defects in GaAs and $\text{Ga}_{1-x}\text{Al}_x\text{As}$ alloys is discussed in the context of recent hydrostatic pressure and photo-EPR results. A unified model is presented based on the metastable trapping of carriers in excited effective-mass (EM) states derived from secondary conduction band (CB) minima. The metastability is attributed to small lattice relaxation effects.

INTRODUCTION

The electronic properties of the native donor defect EL2 in GaAs and their relation with the atomic configuration have been extensively studied [1]. It has been shown that this defect can be transformed by low temperature optical excitation into a second configuration, which is separated from the ground state by a thermal barrier of ~ 0.3 eV [2]. Different models for this metastability have been proposed but the issue is still controversial [3-6]. Direct experimental verifications of the proposed metastable configurations are difficult in this case as no associated gap state has been detected.

Recently, it has been shown that the single substitutional donors, obtained by doping with group IV at VI ions, are equally metastable defects in GaAs [7] and the GaAlAs alloy system [8-12]. The related donor states have been studied as a function of alloy composition x and hydrostatic pressure, two perturbations which both lead to a modification of the lowest conduction band (CB) structure. Three different ground states of these single donors have been evidenced: the effective-mass state derived from the Γ CB minimum, which is the ground state for alloy composition $x \leq 0.2$, the X CB related EM state, which is the ground state for $x \geq 0.8$ as well as the "DX" level being the ground state for the intermediate composition $0.2 \leq x \leq 0.8$. The DX state follows the L CB minimum [13,14] and presents the characteristics of the L CB EM state [15]. By application of hydrostatic pressure or optical excitation at low temperature the DX center can be metastably transformed into an excited configuration, which contrary to the case of EL2 in GaAs is paramagnetic [11,12] and electrically [9] active. We have recently shown in the case of the Sn-DX center that the metastable state is the EM ground state derived from the secondary X CB minimum. We present in this paper new EPR results concerning the group VI related Te - DX center in $\text{Ga}_{0.67}\text{Al}_{0.33}\text{As}$, which confirm the existence of this metastable state. We further analyze very recent results on EL2 under hydrostatic pressure as well as previously reported variations of the EL2 metastability in the GaAsP alloy system. We conclude that the metastability of the double donor EL2 is equally related to the population of an excited resonant EM state derived from the secondary L CB minimum. This leads us to the proposal of a unified model for the metastability of the DX and EL2 defect. The long lifetime of these excited states resonant with the lowest CB is not predicted by the EM theory and indicates that the occupation of the states is accompanied by a lattice relaxation, leading to a self-trapping phenomena.

*Laboratoire associé à l'Université Paris VII.

THE METASTABILITY OF THE EL2 DEFECT

As the experimental results for the transformation of EL2 from the ground state into the metastable state as well as for the reverse reaction have been reviewed recently [1], we will just resume here the basic properties and analyze the very recent results concerning the hydrostatic pressure dependence of the zero phonon line at 1.04 eV, the internal transition at 1.2 eV as well as the pressure induced optical regeneration (PIOR) [16,17].

The ground state of the EL2 state is the antibonding state of A_1 symmetry at $E_c - 0.75$ eV. The transition into the metastable state proceeds from the neutral charge state, is charge state conserving, and is optically triggered by photons with energies $h\nu$ $1.0 \text{ eV} \leq h\nu \leq 1.4 \text{ eV}$. In this spectral range three EL2 related absorption processes have been identified: a zero phonon line at 1.04 eV accompanied by phonon replica, an internal transition centered at 1.2 eV with a width of $\sim 0.2 \text{ eV}$ [18] and the photoionization to the secondary L CB minimum with a threshold at $\sim 1 \text{ eV}$ [19]. The complication in the study of the EL2 metastable state is the fact that this state is not located in the gap. It has been shown by Baj *et al.* [17] from the pressure induced optical regeneration at 4 K that the associated level is resonant with the Γ conduction band in the absence of pressure and drops into the gap for pressures $P \geq 3 \text{ kbar}$. If this level is attributed to an EM state derived from the L CB, this implies that it lies $\sim 0.29 \text{ eV}$ below the L minimum. This attribution is justified by the hydrostatic pressure dependence of the ZPL at 1.04 eV. The interpretation of this line, and in particular its splitting under uniaxial stress being the main evidence for the isolated As_{Ga} model [20], are of high importance for the modelling of the atomic configuration of EL2; or it is generally but erroneously believed to be the zero-phonon line of the internal transition $A_1^{ab} - T_2^{ab}$ at 1.24 eV. In fact, Baj and Dreszer [16] have measured the hydrostatic pressure coefficients of these two transitions: $+ 24.4 \text{ meV/GPa}$ and $- 26.4 \text{ meV/GPa}$, respectively. Both transitions have the same initial A_1^{ab} state but as demonstrated by the different pressure coefficients different final states. In order to determine

	$\partial E/\partial P$ (meV/GPa)	References
CB minima :		
Γ	115	21, 22
L	55	
X	- 15	

ZPL	24.4	16
IT	- 26	16

E_f	38	24
E_c	- 49	23

$E(A_1^{ab})_\Gamma$	87	
$E(A_1^{ab})_{VB}$	27	

Table I : Pressure coefficients of the different CB minima, zero phonon line (ZPL) and internal transition (IT), thermal ionization, capture energy and A_1^{ab} EL2 ground state.

the final state of the zero-phonon transition, we compare its pressure dependence with that of the lowest Γ , L, X conduction bands minima [21]. If it is an effective-mass state derived from the L CB minima, as indicates its energy of $E_1 - 0.01$ eV, it should have the same pressure coefficients. In table I we have summarized these results : the A_1^{ab} ground state shifts with $(115 - 87)$ meV/GPa = 28 meV/GPa relative to the valence band (VB) and the final state of the ZPL thus $(28 + 24.4)$ meV/GPa = 52.4 meV/GPa. Within an estimated total error of ± 18 meV/GPa in the pressure coefficients, this is in very good agreement with the L CB minimum shift of 55 meV/GPa and in disagreement with that of the X CB minimum - 15 meV/GPa. We thus attribute the ZPL from its energy and pressure dependence to the transition $A_1^{ab} \rightarrow T_2^L(1s)$ and not to the $A_1^{ab} - T_2^{ab}$ as proposed by Kaminska *et al.* [20]. An important consequence of this new assignment is the different interpretation of its splitting under uniaxial stress, which reflects the symmetry of the L CB minimum and not the local point symmetry of the EL2 defect. The $T_2^L(1s)$ EM state is not the ground state derived from the L CB minimum; this is the $A_1^L(1s)$ state. As EL2 is a double donor the ground state $A_1^L(1s)$ will be expected to be about four times deeper than the single donor value, i.e. $\sim 4 \times 60$ meV ~ 240 meV not considering lattice relaxation effects, which will increase this energy further. This value is close to the one derived from the PIOR results ~ 290 meV (Fig. 1). The model for the EL2 metastability, which we thus propose is the following : optical excitation of an electron from the A_1^{ab} state into the L CB minimum or associated EM states leads to an efficient capture via a cascade process into the $A_1^L(1s)$ ground state (Fig. 2). This state is not as shallow as a usual EM state due to intervalley mixing introducing a central cell correction. The capture is

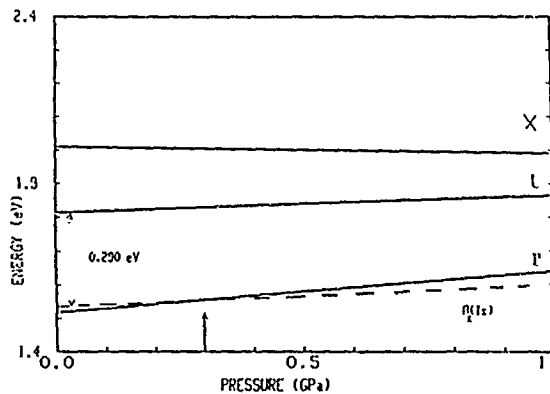
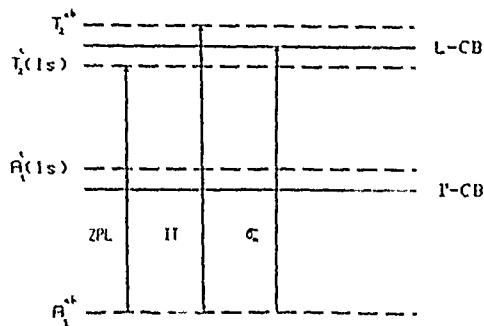


Fig. 1: Hydrostatic pressure dependence of the CB minima in GaAs and the $A_1(1s)$ EM state derived from the L CB.

Fig. 2 : Optical transitions of the EL2 defect in GaAs zero phonon line (ZPL), internal transition (IT) and photoionization to the L CB (σ_n).



associated with a lattice relaxation, creating a thermal barrier for the further relaxation of the electron into the lowest Γ CB minimum. The emission of the carrier and subsequent capture in the A_1^{ab} ground state is only possible via the L CB minimum, which implies the existence of a thermal barrier of at least ~ 0.3 eV. Application of hydrostatic pressure larger than $p \geq 0.3$ GPa drives the $A_1^{ab}(1s)$ state into the gap due to the difference in the pressure coefficients of the Γ and L CB minima and thus makes it optically and electrically active.

THE METASTABILITY OF THE DX CENTER IN $Ga_{1-x}Al_xAs$

The metastable occupation of excited resonant effective-mass states derived from secondary CB minima have been reported for the DX center in GaAs [7] as well as in $Ga_{1-x}Al_xAs$ [8-12].

In the case of GaAs [7] these states have been populated by cooling of the samples under hydrostatic pressure $P \geq 30$ kbar; after subsequent release of the pressure at low temperature ($T \lesssim 100$ K) the carrier remain trapped on this level even though it is now resonant with the lowest Γ CB minimum. In the alloy system $Ga_{1-x}Al_xAs$ in the composition range $0.15 \leq x \leq 0.35$ an excited EM state derived from either the L or the X CB minimum, depending on

Fig. 3 : EPR spectra of the X CB EM state of the DX center in GaAlAs :
Sn : $Ga_{0.69}Al_{0.31}As$ and
Te : $Ga_{0.67}Al_{0.33}As$.

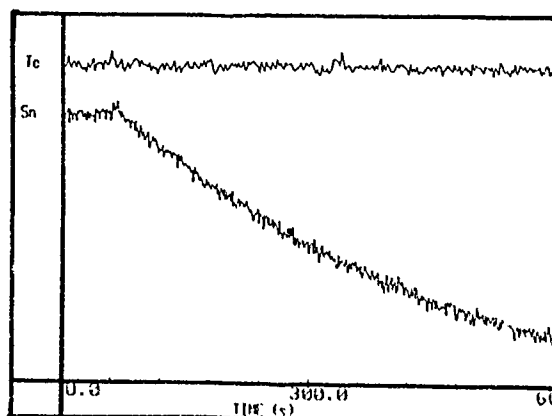
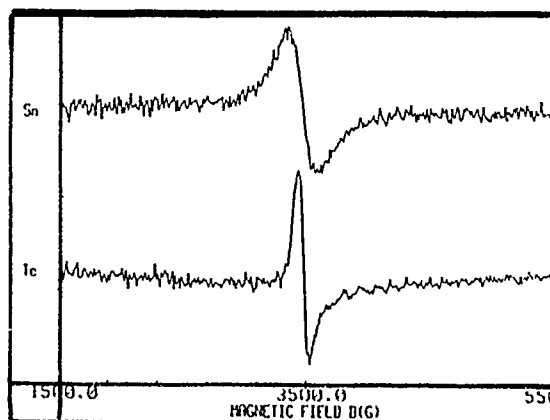


Fig. 4 : Decline of the DX EPR spectra after photo-excitation at 4 K.

the applied pressure, can equally be populated by the application of hydrostatic pressure. We have recently shown in the case of the Sn DX center that in the direct gap material with $x \approx 0.31$ the excited effective-mass state can also be metastably occupied by optical excitation with energies of 0.9 eV [11,12]. From its g -value the excited state has been assigned to the X associated EM ground state. We have confirmed these results by EPR spectroscopy for the group VI DX center Te in $\text{Ga}_{0.67}\text{Al}_{0.33}\text{As}$ (Fig. 3). The lifetime of this state is larger than several hours at 4 K and its occupation decreases thermally for $T \gtrsim 50$ K (Fig. 4). Our results are in close agreement with previous optical results concerning the $1s - 2p$ absorption of the Γ related EM donor and for infrared absorption attributed to the X CB derived EM donor [8,10].

CONCLUSION

The incorporation of a substitutional donor will give rise to a series of EM states (DX, EL2) - associated with each of the conduction band valleys ($\Gamma(1)$, L(4), X(3)) - resulting from the long range Coulomb potential as well as to deep states (EL2) connected with the short range central cell potential [25]. The EM states resonant with the lowest conduction band have generally very short lifetimes ($\sim 10^{-12}$ s). However, intervalley mixing can lead to a localization of the X and L CB derived ground states giving rise to lattice relaxation effects. The observation of metastable behavior of such resonant states implies the existence of lattice relaxation in the case of the EL2 and DX centers in GaAs and GaAlAs alloys, which lead to a persistent trapping of the carrier in the X or L CB valley derived EM ground state. If the associated thermal barrier for relaxation of the carrier to the lowest CB minimum is comparable to the thermal ionization energy of the donor state, emission of the trapped electron is only possible via the associated CB minimum. No direct experimental information on the type and amount of lattice relaxation involved are available up to now, which would allow a comparison with the models proposed for such states [26,27].

ACKNOWLEDGMENTS

Part of this work has been financially supported by the European Community Contract Basic 3168.

REFERENCES

1. "Recent Developments in the study of the EL2 defect in GaAs", edited by H.J. von Bardeleben and B. Pajot, Rev. Phys. Appl. **23**, 727 (1988).
2. G. Vincent, D. Bois and A. Chantre, J. Appl. Phys. **53**, 3643 (1982).
3. H.J. von Bardeleben, D. Stievenard, D. Deresmes, A. Huber and J.C. Bourgoin, Phys. Rev. B **34**, 7192 (1986).
4. D. Delerue, M. Lannoo, D. Stievenard, H.J. von Bardeleben and J.C. Bourgoin, Phys. Rev. Lett. **59**, 2875 (1987).
5. J. Dabrowski and M. Scheffier, Phys. Rev. Lett. **60**, 2183 (1988).
6. D.J. Chadi and K.J. Chang, Phys. Rev. Lett. **60**, 2187 (1988).
7. T. Fujisawa, J. Kristofik, J. Yoshino and H. Kukimoto, Japan J. Appl. Phys. **27**, L2373 (1988).
8. T.N. Theis, T.F. Kuech, L.F. Palmateer and P.M. Mooney, Inst. Phys. Conf. Ser. **74**, 241 (1985).
9. M. Mizuta and K. Mori, Phys. Rev. B **37**, 1043 (1988).
10. J.E. Dmochowski, J. Langer, J. Raczynska and W. Jantsch, Phys. Rev. B **38**, 3276 (1988).
11. H.J. von Bardeleben, J.C. Bourgoin, P. Basmaji and P. Gibart, Phys. Rev. B **40**, 5892 (1989).

12. H.J. von Bardeleben and J.C. Bourgoin, Proc. of the Int. Conf. on Science and Tech. of Defect Control in Semiconductors, edited by K. Sumino, Yokohama (1989), to be published.
13. N. Chand, T. Handerson, J. Klein, W.T. Masselink and R. Fischer, Phys. Rev. B 30, 4481 (1984).
14. J.C.M. Henning, J.P.M. Ansems and P.J. Roksnoer, Semicond. Sci. & Tech. 3, 361 (1988).
15. J.C. Bourgoin, S.L. Feng and H.J. von Bardeleben, Phys. Rev. B 40, 7663 (1989).
16. M. Baj and P. Dreszer, in Defects in Semiconductors, edited by G. Ferenczi, Mat. Sci. Forum 38 (Trans Tech Publ., Switzerland, 1989), p. 101.
17. M. Baj and P. Dreszer, Phys. Rev. B 39, 10470 (1989).
18. M. Kaminska, M. Skowronski, J. Lagowski, J.M. Parsey and H.C. Gatos, Appl. Phys. Lett. 43, 302 (1983).
19. A. Chantre, G. Vincent and D. Bois, Phys. Rev. B 23, 5335 (1981).
20. M. Kaminska, M. Skowronski and W. Kuszko, Phys. Rev. Lett. 55, 204 (1965).
21. D.E. Aspnes, Phys. Rev. B 14, 5331 (1976).
22. D.D. Nolte, W. Walukiewicz and E.E. Haller, Phys. Rev. B 30, 9374 (1987).
23. P. Dreszer and M. Baj, Acta Phys. Polon. A 73, 219 (1988).
24. A. Zylbersztejn, R.H. Wallis and J.M. Besson, Appl. Phys. Lett. 32, 765 (1978).
25. F. Bassani, G. Iadonisi and B. Preziosi, Rep. Prog. in Phys. 37, 1099 (1974).

PROGRESS IN UNDERSTANDING THE OPTICAL PROPERTIES OF EL2

G. A. BARAFF

A.T.&T. Bell Laboratories, Murray Hill, N.J., 07974

ABSTRACT

The material covered in the talk given under this title has already been published [1] or has been accepted for publication [2]. For this reason, the material to be presented below will consist only of a summary with references.

SUMMARY

Although there is still not universal agreement on the question of whether the EL2 defect consists of an isolated As_{Ga} antisite or whether, in addition, an As_i arsenic interstitial atom is an essential part of its structure, [3] the experimentally observed optical absorption gives no evidence of anything except the isolated antisite. The main features of the optical absorption spectrum can be broadly understood in terms of a combination of three processes, namely, transfer of an electron from the occupied midgap level to the conduction bands, transfer of an electron from the valence band to the midgap level when it is not occupied, and an internal transition in which an electron in the occupied midgap level is excited to a long lived resonance which, for most practical purposes, behaves as a truly localized state. In particular, this resonance has T_2 symmetry, is three-fold degenerate, and its occupation by an electron causes a symmetry lowering Jahn-Teller relaxation. Occupation of this resonant state is the trigger that, with finite but small probability, causes the defect to transfer to its metastable configuration. [4]

There are, however, problems with the detailed understanding of the internal optical transition. These have to do with aspects relating to lattice relaxation. In particular, although the broad shape of the absorption peak certainly seems to be indicative of lattice relaxation, and although there is what appears to be a zero-phonon line (ZPL) at its lower limit, the intensity of the ZPL and the energy of the observed multi-phonon replicas are not compatible with the width of the line. Furthermore, under hydrostatic pressure, the peak of the absorption and the ZPL move in opposite directions. [5] Although this is not impossible to rationalize, it is not what one would expect. Most difficult to explain is the fact that under hydrostatic pressure, the ZPL is observed to ride up over the onset of the broad absorption. [5] This by itself indicates that there is a component of the broad peak that has nothing to do with lattice relaxation, since the ZPL must lie at the very lower limit of any lattice relaxed absorption.

Motivated by these problems, we have undertaken a more detailed look at the information that can be obtained from these hydrostatic pressure experiments [5,6] and from the experiments in which uniaxial pressure was used to split the ZPL. [3a] We have found [2] that the observed lattice relaxation must be assigned to two different symmetries of lattice relaxation, with the Jahn-Teller relaxation contributing approximately 25% of the total and a breathing relaxation possibly accounting for the rest. The estimate of the breathing relaxation is crude, which is why we cannot be sure that breathing mode relaxation does indeed account for the rest. It is clear, however, that the problems in understanding the optical absorption will be eased

significantly if the actual breathing distortion is considerably less than the estimate we have obtained here. In such case, the most likely situation is that the internal transition takes place at an energy somewhat lower than the peak in the absorption, and is obscured by it. The more intense peak itself would be attributed to ionization of the electron from the same initial state as that of the internal transition.

We suggest an experiment by which this conjecture might be tested. The experiment is to study the optical cross section for transfer of EL2 into its metastable state, since this cross section serves as a measure of how many electrons have been transferred into the T_2 state. There are, we argue, two paths by which an electron from the midgap level can enter that T_2 state. One is directly via the internal transition. The other is via ionization to the conduction band followed by recapture at the ionized defect. The cross section for this latter process will be dominated by ionization into the L-band catch basin, by which is meant that portion of the lowest conduction band for which an electron will thermalize down into an L-point minimum.

The proposed experiment consists of a comparison of the optical cross section for transfer to the metastable state under two different conditions. The first condition is when there is no electric field present, as in a bulk sample. The transfer to the metastable would then be detected by optical bleaching, [7] or perhaps by optical quenching of photoluminescence. In the absence of an electric field, electrons could enter the T_2 level via both paths. The second measurement of the cross section should take place in the presence of a strong electric field, such as is present when photo-capacitance experiments are performed, namely, as in the experiment where the metastability of EL2 was first discovered. [8] In that case, electrons ionized to the conduction band are swept away by the field and transfer to the T_2 level can occur only via the direct internal transition.

The question now is whether the broad shapes of these two measured cross sections behave the same way under hydrostatic pressure. If the main peak in the optical absorption is really caused by ionization to the bands, and if subsequent recapture into the T_2 level really occurs, then one would expect the cross section as measured in the absence of fields to show the same behavior as does the main peak in optical absorption, namely, a shift to lower energies. On the other hand, if the vertical transition does track the ZPL in that it shifts to higher energies under hydrostatic pressure, then one would expect the cross section for transfer to the metastable in the presence of a strong electric field to do the same, namely shift to higher energy when hydrostatic pressure is applied, because now, the internal transition would be the only path into the T_2 state and from there, into the metastable.

References

1. G. A. Baraff, Phys. Rev. B40, 1030, 1989
2. G. A. Baraff, Phys. Rev. B41, 1990, (to be published)
3. a) M. Kaminska, W. Skowronski and W. Kuszko, Phys Rev. Lett., 55 220; (1985); b) M. Kaminska in Proc. 17th Int. Conf. on Phys. of Semiconductors, San Francisco (1984), Edited by D. J. Chadi and W. Harrison, Springer, New York, (1985) p.741; c) J. Dabrowski and M. Scheffler, Phys. Rev. Lett. 60, 2183, (1988); d) D.J. Chadi and K.J. Chang, Phys. Rev. Lett. 60, 2187, (1988); e) H.J. von Bardeleben, D. Stievenard, D. Desresmes, A. Huber and J.C. Bourgoin, Phys. Rev. B34, 7192 (1986); f) B.K. Meyer, D.M. Hofmann, J.R. Niklas, and J.-M. Spaeth, Phys. Rev. B36, 1332 (1987); g) G.A. Baraff, Phys. Rev. Lett. 62, 2156, (1989)
4. M. Kaminska, M. Skowronski, J Lagowski, J.M. Parsey, and H. C. Gatos, Appl. Phys. Lett. 43, 302 (1983)
5. M. Baj and P. Dreszer, in Proceedings of the 15th International Conference on Defects in Semiconductors. Edited by G. Ferenczi (Material Science Forum, Vol. 38-41, 1988, page 101. Trans Tech Publications, Switzerland)
6. P. Dreszer and M. Baj, Acta Physica Polonica, A73, 219, (1988)
7. G. M. Martin, Appl. Phys. Lett. 39, 747, (1981), P. Omling, L. Samuelson, and H. G. Grimmeiss, in Proc. 17 Intl. Conf. on Phys. of Semiconductors, San Francisco, Calif, 1984, Edited by J. D. Chadi and W. A. Harrison, (Springer Verlag, New York and Heidelberg, 1985) p.751
8. G. Vincent and D. Bois, Solid State Communications, 27, 431, (1978)

THE DOUBLE DONOR ISSUE OF THE EL2 DEFECT IN GaAs.

M. O. MANASREH* and G. J. BROWN**

*Electronic Technology laboratory (WRDC/ELRA), Wright Research and Development Center, Wright-Patterson Air Force Base, Ohio 45433-6543.

**Materials Laboratory (WRDC/MLPO), Wright Research and Development Center, Wright-Patterson Air Force Base, Ohio 45433-6533.

ABSTRACT

Photo-induced changes in the infrared (IR) absorption spectrum of the EL2 defect in undoped and lightly alloyed unannealed GaAs materials grown by the liquid-encapsulated Czochralski technique were observed under a monochromatic light irradiation. These changes were attributed to the change of the charge states of EL2. The spectrum which is believed to be due to the charged EL2 exhibits a complex structure with two peaks at 1.07 and 1.32 eV and a shoulder at 0.94 eV. The $EL2^{+/2+} \rightarrow EL2^{0/+}$ and $EL2^{0/+} \rightarrow EL2^{+/2+}$ transitions were obtained by illuminating the sample with $0.7 \leq h\nu \leq 0.95$ eV and $1.3 \leq h\nu \leq 1.5$ eV, respectively. The transformation $EL2^{+/2+} \leftrightarrow EL2^{0/+}$ can be achieved in less than 10 sec and can be repeatedly switched back and forth between the two states. Fourier-transform photoconductivity (FTPC) measurements were performed on a large number of samples both semi-insulating and n-type. Two broad peaks were observed in the FTPC spectra with thresholds at 0.80 and 0.95 eV. The photoquenching and thermal recovery properties of these two peaks are identical to those of EL2. Both IR and FTPC results suggest strongly that EL2 is a double donor.

INTRODUCTION

The EL2 defect in GaAs is believed to be a double donor with two energy levels in the band gap.^{1,2} It has also been argued that this defect is a single donor.^{3,4} A few attempts⁵⁻⁹ have been made to identify the second energy level of the EL2 defect. These attempts were limited to space-charge measurements performed on types of GaAs materials which are difficult to study by the infrared (IR) absorption technique. The EL2 IR absorption spectrum shows a threshold near 0.82 eV which is commonly identified with the first energy level of the double donor, but the spectrum shows no evidence of a second energy level. Part of the problem lies in the complex structure of the EL2 IR spectrum itself which creates difficulty in arriving at concrete interpretations and correlations for the various absorption components.

In this article, we report IR absorption and FTIR photoconductivity measurements of the second energy level of EL2. The spectrum of this energy level, i.e. $EL2^{+/2+}$, shows a complex structure. A large number of GaAs samples both lightly alloyed and undoped semi-insulating (SI) in both annealed and unannealed states were tested. In order to observe the $EL2^{+/2+}$ IR absorption spectrum, other defects (both acceptors and donors) must exist in the sample to trap electrons released from $EL2^0$ during monochromatic light ($1.3 \leq h\nu \leq 1.5$ eV) illumination. The $EL2^{0/+} \leftrightarrow EL2^{+/2+}$ transformations were achieved with illumination times of less than 10 sec.

EXPERIMENTAL TECHNIQUE

Several samples were cut from GaAs boules grown by the liquid-encapsulated Czochralski (LEC) technique. The samples were either undoped SI GaAs or lightly alloyed

with isovalent impurities (In, P, and Sb). Infrared absorption measurements were obtained with a CARY 2300 spectrophotometer. Photoconductivity measurements were performed by using a mid-infrared FTS-20CVX Digilab Spectrometer. A closed-cycle refrigerator was used to cool the samples in the dark to 9K. A Jarrell-Ash monochromator with a 590 grooves/mm grating and tungsten-halogen lamp provided monochromatic light in the energy range of 0.7 - 1.5 eV. EL2 was photoquenched either by 1.18 eV monochromatic light or by white light.

RESULTS AND DISCUSSIONS

The observed IR absorption effect is demonstrated in Fig. 1 in which GaAs:In is taken as an example. The solid line spectrum was obtained after cooling the sample in the dark to 9 K. When monochromatic light with an energy of 0.85 eV (or $0.7 \leq h\nu \leq 0.95$ eV) was used to illuminate the sample for 60 sec, the dotted dashed spectrum was obtained. The dashed spectrum, on the other hand, was obtained after the sample was illuminated for 10 sec with 1.45 eV monochromatic light (or $1.3 \leq h\nu \leq 1.5$ eV). For simplicity, we will refer to these spectra as A, B, and C, respectively. Switching between spectra B and C is achieved by illuminating the sample with either 0.85 or 1.45 eV light. This effect is reproducible as long as the illumination periods are less than 60 and 10 sec, respectively. Photoquenching of the normal EL2 state may occur if periods of time longer than those specified above are used. The photoquenching and photoinduced recovery effects of the unannealed samples used in the present study are different from those in the annealed SI GaAs samples.

The photo-induced changes of the spectra in Fig. 1 can be understood as follows. Spectrum A is due to both neutral ($EL2^{0/+}$) and charged ($EL2^{+/2+}$) EL2. Illuminating the samples with 0.85 eV light causes $EL2^{+/2+}$ to capture an electron (emit a hole) from either the valence band or shallow acceptors. We will refer to this as the first process or $EL2^{+/2+} + h\nu(\sim 0.85 \text{ eV}) \rightarrow EL2^{0/+} + h^+$. According to the first process, $[EL2^{0/+}]$ increases and $[EL2^{+/2+}]$ decreases under such illumination conditions. We believe this effect is actually observed in spectrum B where the upper energy ($h\nu > 1.1$ eV) portion of this spectrum increases while the lower portion ($h\nu < 1.1$ eV) decreases. The above process can be reversed according to $EL2^{0/+} + h\nu(\sim 1.45 \text{ eV}) \rightarrow EL2^{+/2+} + e^-$. We will refer to this as

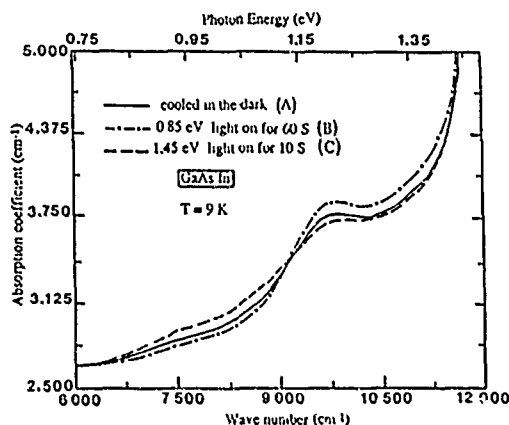


Fig. 1. The EL2 IR absorption spectra from GaAs:In sample. Spectrum A (—) was obtained after cooling to 9 K in the dark; spectrum B (— · —) was obtained after illuminating the sample with 0.85 eV light for 60 sec; and spectrum C (---) was obtained after illuminating the sample with 1.45 eV light for 10 sec.

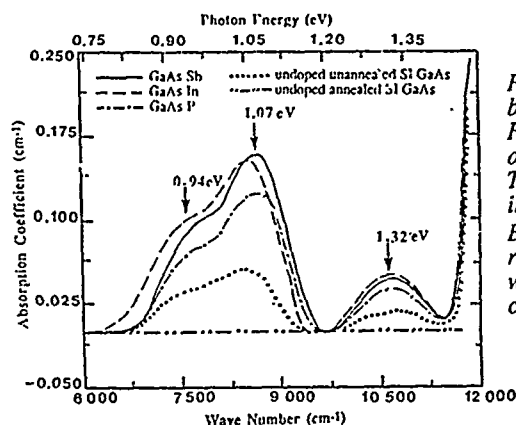


Fig. 2. The difference between spectra B and C in Fig. 1. Similar results were obtained for other samples. These spectra are interpreted as being due to EL 2 + 1 + +. Spectra representing 1.32 eV peak were shifted upward for clarity and comparison.

the second process. Spectrum C reflects the changes of both EL2^{0/+} and EL2^{+/2+} concentrations as expected from the second process. Based on these arguments, the difference between spectra B and C in the energy region $h\nu > 1.1$ eV therefore represents the change in the EL2^{0/+} concentration. Furthermore, the difference in the lower energy portion, $h\nu < 1.1$ eV, represents the change in the concentration of the second energy level of EL2, i.e. EL2^{+/2+}.

The difference between B and C is shown in Fig. 2 for GaAs:In and other samples that were cut from unannealed boules. The difference spectra in the higher energy region (>1.2 eV) were shifted upward for clarity and comparison. A shoulder at 0.94 eV and two peaks at 1.07 and 1.32 eV were observed in Fig. 2. It should be pointed out that the peak obtained at 1.32 eV was not observed in all samples that show photo-induced changes as described in Fig. 1. Samples that were cut from annealed boules do not exhibit any of the photo-induced changes shown in Fig. 2. We speculate that the spectra of the unannealed samples in Fig. 2 are due to the second energy level of the EL2 defect.

The observation of the second energy level of EL2 (EL2^{+/2+}) by the IR absorption technique (see Fig. 2) is dependent on the condition that other shallow defects (intrinsic, impurities, or combination of both) exist in high concentrations. This is because when an electron is emitted from EL2^{0/+} according to first process, it can be captured by these other defect(s) so that EL2^{+/2+} is long-lived and becomes observable. This process (Figs. 1 and 2) has also been demonstrated in the case of a GaAs:Sb sample by using EPR measurements concurrent with $h\nu = 1.46$ eV monochromatic light illumination¹¹. Baeumler *et al.*¹¹, in their attempt to identify the Sb_{Ga} hetero-antisite, have shown that the EL2 EPR spectrum appears and Sb_{Ga} EPR spectrum disappears after illuminating the sample with $h\nu = 1.46$ eV for 5 sec which is indicative of charge transfer processes between these defects. The GaAs:Sb sample tested by Baeumler *et al.* and the present GaAs:Sb sample were cut from the same boule.

The FTPC measurements show two broad peaks at 0.85 eV and 1.02 eV as indicated in Fig. 3. The photoionization thresholds of these two peaks are 0.80 and 0.95 eV. The ionization energy of the first peak is in good agreement with the 0.82 DLTS activation energy for EL2. In addition, these two peaks photoquench together and thermally recover together at about 120K, similar to the reported behavior of EL2. Therefore, we identify the two peaks in Fig. 3 with the two energy levels of the double donor EL2. It should be noted that the intensity of the spectrum in Fig. 3 after thermal recovery at 120K is larger than the initial intensity of the spectrum obtained after cooling the sample in the dark to 9K. This difference, mainly on the lower energy side of the first peak, is due to an increased

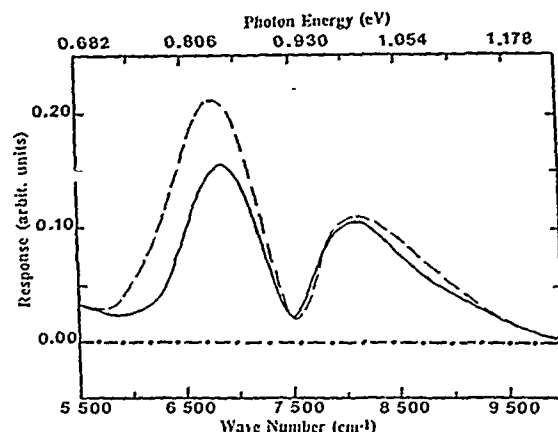


Fig. 3. The photoresponse spectra for semi-insulating GaAs: a) — initial spectrum at 9 K, b) --- 120 K spectrum after thermal recovery and c) - · - photoquenched spectrum at 9 K. The two peaks are interpreted as being due to photoionization of $EL2^{0+}$ and $EL2^{+/2+}$.

photoresponse from the $EL2^{2+} + h\nu \rightarrow EL2^{+} + h^{+}$ transition process. In good agreement with the IR absorption results discussed above, the hole cross section for this transition is found to extend from ~ 0.74 to 0.92 eV. We have also observed the corresponding hole cross section for the $EL2^{+} + h\nu \rightarrow EL2^{0} + h^{+}$ transition in other FTPEC spectra. A possible explanation for the increased probability of observing the hole transitions after photoquench and thermal recovery is that the neutral EL2 are transformed to the metastable state while the charged EL2 are ionized to the doubly charged state. If the hole transitions to convert the doubly charged state to neutral EL2 are somehow impeded when the $EL2^{0+}$ has become metastable, then an excess of $EL2^{+/2+}$ exists that was not present initially at 9K. The hole transitions are then recovered when the neutral EL2 state is thermally recovered. The photocapacitance studies of the second donor level of EL2 also found that the hole transitions were photoquenched and did not recover until the neutral EL2 state was recovered.⁵

Solidification and stress, in general, introduce many defects in materials grown by the LEC technique. Complexes of unidentified traps with acceptor-like properties¹²⁻¹⁶ and other defects such as EL3 and EL6 have been reported¹⁷. Isovalent impurities such as Sb, In, and P may also form electrically active complex defects (probably undergo non-radiative transitions). When these defects (acceptors and donors) are present in GaAs samples, they may play an important role in compensation mechanisms in a way that $EL2^{+/2+}$ can be turned on and off by monochromatic light [see first and second processes and Fig. 1] within short periods of time. Most of the defects other than EL2 and simple impurity defects can be annealed out. After annealing therefore, the effects shown in Fig. 1 should no longer be observed. In fact, all samples that were cut from annealed boules (typical annealing was at 850°C for 18 hours) do not show any photoinduced changes while all samples cut from unannealed boules (doped or undoped) exhibit the behavior shown in Fig. 1. This conclusion is tested in two samples that were cut from an annealed undoped LEC boule. These samples were irradiated by fast neutrons. The photo-induced changes were not observed prior to irradiation. However, it was observed that large photo-induced changes

were obtained after irradiation. These changes were found to be larger than those of Fig. 2 by a factor of three. This result clearly demonstrates that neutron irradiation introduces shallow defects that would trap electron and make the observation of $EL2^{+/2+}$ possible.

The hypothesis of relating the spectra in Fig. 2 to the second energy level of $EL2$ ($EL2^{+/2+}$) is based on the following arguments. First, the spectra in Fig. 2 represents an intrinsic defect which is independent of the dopants. Second, the photon energies 1.45 eV or $1.3 \leq h\nu \leq 1.5$ eV ($h\nu = 0.85$ eV or $0.7 \leq h\nu \leq 0.95$ eV) used are too high (low) to induce any quenching or recovery effects within short periods of time ($t \leq 60$ s). Third, switching between spectra B and C in Fig. 1 can be achieved in very short periods of time using monochromatic light according to the first and second processes. This effect cannot be attributed to photoquenching and photo-induced recovery effects of $EL2$, but rather to fast photoionization or neutralization processes. Fourth, when spectrum C, which we believe to be due to both $EL2^{0/+}$ and $EL2^{+/++}$ is photoquenched with 1.12 eV light and then thermally recovered at 150 K, it changes into spectrum A or B or somewhere in between them. Both the above results and the FTPEC results suggest the following. 1) The spectra in Fig. 2 are due only to $EL2$ and not to any other intrinsic defects; 2) The thermal recovery from the metastable back to the normal state proceeds primarily through the neutral ($EL2^{0/+}$) state rather than the charged state ($EL2^{+/2+}$). There has been previous speculation^{18,19} that the transformation of the normal to metastable state occurs through $EL2^{0/+}$. The present results provide additional and complementary data to support this view. This does not mean, however, that $EL2$ is the isolated As_{Ga} antisite. It should be pointed out that the identification of the $EL2$ atomic structure is outside the scope of the present study.

The situation in Si GaAs is more complicated because the Fermi level position is already near midgap. Adding defects (acceptors and donors) may not change the Fermi level position, but compensation mechanisms which involve $EL2$ are affected dramatically. Thermal annealing is the only physical parameter found so far that affects the $EL2^{+/2+}$ observation. In fact, the observation of $EL2^{+/2+}$ by the IR absorption technique can be taken as an effective criterion for the presence in high concentration of other defects (impurity related or intrinsic) in GaAs materials. The shoulder (0.94 eV) and the two peaks (1.07 and 1.32 eV) observed in the $EL2^{+/2+}$ spectra in Fig. 2 have not yet been discussed. This structure simply reflects the complex nature of the $EL2^{+/2+}$ defect. Further discussions and speculations regarding this matter will be presented elsewhere.

CONCLUSION

In conclusion, we have observed spectral features in both IR absorption and FTPEC data that are attributed to the first and second charge states of the $EL2$ double donor. The photoionization energy of the $EL2^{+/2+}$ state was found to be 0.95 eV. This level is 0.15 eV below the $EL2^{0/+}$ level in the FTPEC spectrum. By using the $E_v + 0.68$ photoluminescence position for $EL2$ and subtracting 0.15 eV, we calculate the $EL2^{+/2+}$ to be 0.53 eV above the valence band. This position matches the $E_v + 0.54$ position reported by photocapacitance techniques.^{5,7} The $EL2^{+/2+}$ IR absorption spectrum shows a complex structure suggesting that the atomic nature of $EL2^{+/2+}$ is more complex than a simple point defect. And in IR absorption, the observation of $EL2^{+/2+}$ is dependent on the presence of other defects which capture the electron released from $EL2^{0/+}$ and prevent them from decaying to $EL2^{+/2+}$.

ACKNOWLEDGMENT

The authors are grateful to T. White of Lawrence Livermore National Lab for providing the neutron irradiated samples and W. C. Mitchel for providing the transport measurements. This work was partially supported by the Air Force Office Of Scientific Research.

REFERENCES

1. J. Lagowski, H. C. Gatos, J. M. Parsey, K. Wada, M. Kaminska, and W. Walukiewicz, *Appl. Phys. Lett.* **40**, 342 (1982).
2. E. R. Weber, H. Ennon, U. Kaufmann, J. Windschief, J. Schneider, and T. Wosinski, *J. Appl. Phys.* **53**, 6140 (1982).
3. S. Makram-Ebeid and P. Boher, *Rev. Phys. Appl.* **23**, 847 (1988).
4. J. S. Blakemore, *J. Phys. Chem. Solids* **49**, 627 (1988).
5. P. Omling, P. Silverberg, and L. Samuelson, *Phys. Rev.* **B38**, 3606 (1988).
6. T. Wosinski, *Appl. Phys.* **A36**, 213 (1985).
7. J. Lagowski, D. G. Lin, T. P. Chen, M. Skowronski, and H. C. Gatos, *Appl. Phys. Lett.* **47**, 929 (1985).
8. J. Osaka, H. Okamoto, and K. Kobayashi, in *Semi-Insulating III-V Materials*, edited by H. Kukimoto and S. Miyazawa (Ohmsha, Tokyo, 1986), p.421.
9. B. K. Meyer, D. M. Hofmann, and J. -M. Spaeth, *J. Phys. C* **20**, 2445 (1987).
10. P. Silverberg, P. Omling, and L. Samuelson, *Appl. Phys. Lett.* **52**, 1689 (1988).
11. M. Bacumler, J. Schneider, U. Kaufmann, W. C. Mitchell, and P. W. Yu, *Phys. Rev. B* **39**, 6253 (1989).
12. U. Kaufmann, W. Wilkening, and M. Bacumler, *Phys. Rev.* **B36**, 7726 (1987); U. Kaufmann, M. Bacumler, J. Windschief, and W. Wilkening, *Appl. Phys. Lett.* **49**, 1254 (1986).
13. M. Tomozane and Y. Nannichi, *Jpn. J. Appl. Phys.* **25**, L273 (1986); *ibid.* **25**, L522 (1986).
14. W. R. Weber and P. Omling, in *Festkorpreprobleme, Advances in Solid State Physics*, edited by P. Grosse (Vieweg, Braunschweig, 1985), vol. 25, p. 623.
15. N. Tsukada, T. Kikuta, and K. Ishida, *Jpn. J. Appl. Phys.* **24**, L689 (1985).
16. A. Goltzené, B. Meyer, and C. Schwab, *J. Appl. Phys.* **59**, 2812 (1986).
17. A. Chantre, G. Vincent, and D. Bois, *Phys. Rev.* **B23**, 5335 (1981); For a review see J. C. Bourgoin, H. J. von Bardeleben, and D. Stiévenard, *J. Appl. Phys.* **64**, R65 (1988).
18. J. Dabrowski and M. Scheffler, *Phys. Rev. Lett.* **60**, 2183 (1988).
19. M. Skowronski, J. Lagowski, and H. C. Gatos, *Phys. Rev.* **B32**, 4264 (1985).

ABSOLUTE PRESSURE DEPENDENCE OF THE SECOND IONIZATION LEVEL OF EL2 IN GaAs

D.E. BLISS, W. WALUKIEWICZ, D.D. NOLTE*, AND E.E. HALLER

Dept. of Materials Science and Mineral Engineering, University of California at Berkeley,
and the Center for Advanced Materials, Materials and Chemical Sciences Division, Lawrence
Berkeley Laboratory, 1 Cyclotron Road, Berkeley, CA 94720

*Present Address: Dept. of Physics, Purdue University, West Lafayette, IN 47907

ABSTRACT

We report the results of DLTS experiments under uniaxial stress on the second ionization level of EL2(+/+) in p-type GaAs. We measured the shift in the hole emission rate as a function of stress applied in the [100] and [110] directions. By modeling the valence band with two independently displacing bands and appropriately derived effective masses, we obtain a small absolute hydrostatic pressure derivative for the defect, 39 ± 15 meV GPa⁻¹. The shear contribution is negligible. This result is very different than for the first ionization level, EL2(+o) with a emission energy pressure derivative of 90 ± 15 meV GPa⁻¹. The difference can be accounted for by the pressure dependence of the electron capture barrier of EL2(+o), 49 ± 15 meV GPa⁻¹. The absolute pressure derivatives of the two levels are then comparable and in good agreement with simple theory for Ga site point defects.

INTRODUCTION

The fundamentally interesting property of double donor EL2 in GaAs is the metastability of the defect. By illuminating a cooled crystal, $T < 100$ K, with $1.1 \mu\text{m}$ light the EL2 level in its neutral charge state can be removed from the bandgap. This photoquenching property of EL2 has been experimentally well documented, but despite extensive theoretical and experimental studies no commonly accepted microscopic model for EL2 in GaAs exists. Proposals range from very elaborate complexes involving arsenic antisite and vacancies [1] or antisite and interstitials [2] to simple arsenic antisite-like defects [3-6]. Common to all the various microscopic models, the defect metastability is interpreted in terms of a large lattice relaxation of the atoms forming the defect. To investigate the existence of a large lattice relaxation, applied stress can be used in conjunction with other experimental techniques to perturb the position of the atoms and measure the defect properties. The first ionization energy of EL2 is easily accessible by a variety of experimental techniques [7]. On the other hand, properties of the defect in the doubly ionized charge state have been investigated to a lesser extent [8,9]. The difficulty in studying this energy level results from the fact that EL2(+/+) is located in the lower half of the band-gap at $E_v + 0.52$ eV. This requires preparation of p-type GaAs with a sufficient concentration of EL2 so that it is not mistaken for Fe or Cu, which have energy levels close to EL2(+/+). We report on measurements of pressure dependence of the second ionization level of EL2. Using recently determined values of the valence band deformation potential we find the absolute pressure coefficient for this level.

EXPERIMENTAL

This study was carried out on a GaAs crystal grown by the liquid encapsulated Czochralski (LEC) technique. The crystal was doped p-type with Zn, $1.4 \times 10^{16} \text{ cm}^{-3}$ and with In, 0.01%, by weight, to reduce the dislocation density. To prepare samples for stress measurements, $1 \times 1 \times 6$ mm parallelepipeds were cut with the long axes in the [100] and [110] directions. The samples were lapped and lightly etched in 5:1:1 $\text{H}_2\text{SO}_4:\text{H}_2\text{O}_2:\text{H}_2\text{O}$ before evaporating Ni Schottky contacts on opposite faces for the DLTS measurements.

To measure the pressure derivative of the ionization energy, the experiment was performed in a DLTS uniaxial stress apparatus capable of applying pressures up to one GPa via a spring and lever arm [10]. The applied stress has been calibrated against the energy splitting of the oxygen thermal donor in Si [11,12] and a correction is made for the thermal dependence of the spring

constant. When stress is applied, endpads are used to cushion the brittle sample. The combination of a long slender sample and endpads produce a homogeneous stress field at the midpoint of the sample where the DLTS measurement is made. To further account for stress inhomogeneities across the sample, DLTS measurements are made on opposite sides of the sample. The sign of the bias is switched to probe under both contacts. The transient time constants of both contacts are then averaged or, if the difference is large, the sample is remounted.

The capacitance of the sample is measured by a one MHz capacitance bridge. The capacitance transient is captured by a digital storage oscilloscope. Multiple transients are averaged by the oscilloscope reducing noise, before the data are transferred to a computer for analysis. The transient is fit to an exponential function determining the time constant of the decay. Figure 1 shows the stress dependence of the transient time constant for stress applied in the [100] and [110] directions. The [100] data extends to higher stress since GaAs is inherently stronger in the [100] than the [110] direction due to stress concentration on the (110) cleavage planes.

When measuring the DLTS peak, it is important to ascertain that the peak is indeed $EL2(+/+)$ and is not due to Fe or some other transition metal contamination. Distinguishing this main hole trap from Fe is not necessarily trivial. Identical DLTS energy levels at 0.54 eV have been reported for both Fe [13] and $EL2(+/+)$ [9]. Verifying the presence of $EL2$ by checking for the DLTS signal of the first ionization level, $EL2(+/0)$, at elevated temperatures is not possible in p-type material. The large electron capture cross section of the first ionization transition reduces the magnitude of the DLTS signal in p-type material approximately by two orders of magnitude. To check that the level was not due to Fe contamination, we measured the photon capture cross section of the defect level. Both Fe and $EL2(+/+)$ show an initial ionization edge at 0.54 eV but Fe has an additional edge at 0.83 eV [13]. Our sample showed a smooth change in the photon capture cross section over this energy range indicating the level was not due to Fe but rather the second ionization level of $EL2$.

RESULTS AND DISCUSSION

Ultimately, one would like to know the lattice coupling of a particular charge state of a defect in order to determine the microscopic interaction of the defect wave function with the surrounding atoms, i.e. how does the total energy of a particular charge state change as a function of lattice configuration. Unfortunately, DLTS is an ionization spectroscopy and can measure only the energy difference of initial and final states. It can not measure the pressure dependence of a particular charge state. All pressure dependences are the sum of the pressure dependences of both charge states and the valence band. Thus we determine the pressure derivative of the ionization level. For the stressed DLTS experiment on p-type material we measure the time constant of the thermal emission of holes to the valence band. To interpret the raw emission data as an absolute pressure derivative, several effects must be treated quantitatively. First, the heavy and light hole branches of the valence band split under uniaxial stress complicating the emission process. Second, the carrier capture cross section of the defect can be pressure dependent affecting the DLTS time constant as well. In the following section these complications in the interpretation of the DLTS emission data as a shift in ionization energy will be addressed.

To simplify the problem, the pressure dependent properties of the valence band are approximated by a model which treats the valence band as two independent bands rigidly displacing with increasing stress [14]. The splitting of the light and heavy hole band edge for shear stress is experimentally well known. The normal and shear deformation potentials are $b = -2.0$ eV and $d = -5.4$ eV [15]. The total hole emission probability, is the sum of emission probabilities to both branches of the valence band. This problem has been treated for Si where it has been found that the valence bands can be parametrized in terms of an appropriate effective mass and thermal velocity [14]. One finds in this approach that the effective masses are roughly equal for both bands, $m^* = (m_h + m_l)/2$, and that their values are almost independent of stress. Since the structure of the valence band is similar for GaAs and Si, we can apply the procedure for hole emission in GaAs. To zeroth order we assume a stress independent effective mass. The error introduced by this assumption is only about 5 to 10% of the defect energy shift. Such an error lies well within the sum of other experimental errors.

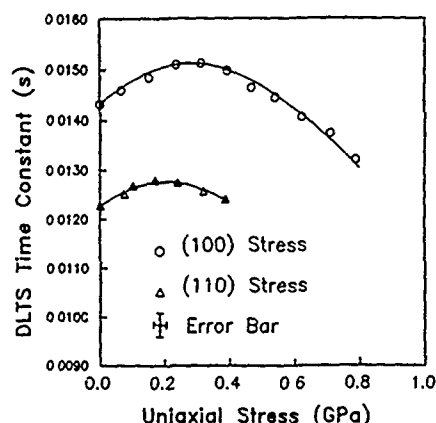


Figure 1. DLTS hole emission time constant for the second ionization level of EL2 in GaAs versus applied uniaxial stress in the [100] (o) and [110] (Δ) direction. The solid line is the fit for the independent band model.

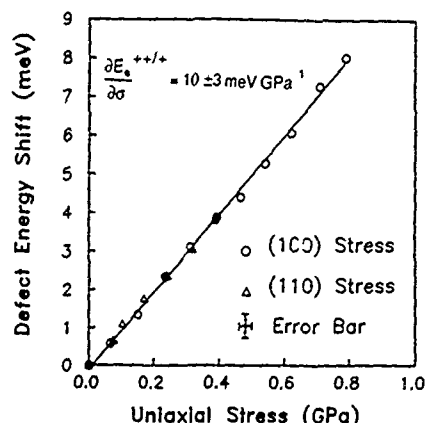


Figure 2. Shift in defect energy relative to the valence band versus applied uniaxial stress using a rigid two band model for the valence band. (o), [100] applied stress. (Δ), [110] applied stress.

Figure 1 gives the experimental result for the pressure dependence of the DLTS emission time constants for EL2(++/+). At low stress, the time constant increases. The splitting of the valence band is much less than kT at these stresses so hole emission is still occurring to both valence bands. The increasing time constant indicates the level is moving away from the bands. At higher stress, the time constant decreases, even becoming less than the zero stress value. This reflects the large splitting of the valence band. The emission is favored by the Boltzmann factor to the band which is approaching the defect level in energy. Figure 2 shows the calculated energy shift of the level relative to the valence band edge versus applied uniaxial stress using the independent band model. The hydrostatic component of the stress is just one third of the applied uniaxial stress. This slope is $10 \pm 3 \text{ meV GPa}^{-1}$ which corresponds to a hydrostatic pressure derivative of $30 \pm 10 \text{ meV GPa}^{-1}$. The pressure derivative of EL2(++/+) can be expressed as,

$$\left[\frac{\partial E_{+}}{\partial p} \right]_{R_{+}} - \left[\frac{\partial E_{vb}}{\partial p} \right]_{R_{+}} - \left[\frac{\partial E_{++}}{\partial p} \right]_{R_{++}} = 30 \pm 10 \text{ meV GPa}^{-1} \quad (1)$$

where the pressure derivatives are evaluated at the relevant equilibrium positions of each charge state. A value of $a_v = -0.7 \text{ eV}$ [16] for the hydrostatic deformation potential of the valence band, as determined using transition metal deep levels as references, corresponds to a pressure derivative of 9 meV GPa^{-1} . Using this value, the absolute pressure derivative of EL2(++/+) becomes,

$$\left[\frac{\partial E_{+}}{\partial p} \right]_{R_{+}} - \left[\frac{\partial E_{++}}{\partial p} \right]_{R_{++}} = 39 \pm 15 \text{ meV GPa}^{-1} \quad (2).$$

The small value of the absolute pressure derivative of the second ionization energy must be contrasted with the large pressure derivative of the first ionization energy. From previous DLTS measurements [17] of EL2(o/+) in n-type material, the absolute pressure derivative was found to be,

$$\left[\frac{\partial E_o}{\partial p} \right]_{R_o} - \left[\frac{\partial E_+}{\partial p} \right]_{R_+} \cong 90 \pm 15 \text{ meV GPa}^{-1} \quad (3).$$

This value of the pressure derivative is much larger than those of any other native defect found in GaAs. In general, this indicates a strong coupling of the defect to the lattice. One can deduce from equations (2) and (3) that the coupling occurs for the neutral state of EL2. This is consistent with the fact that the metastability is observed for the neutral state.

When discussing the large difference in pressure derivatives of two different ionization states of EL2 one has to realize that the emission energy, E_e , determined from a DLTS measurement is the sum of two energies: E_T , the energy separation between the minimum of the appropriate band and the fully relaxed defect occupied by a carrier, plus E_b , the energy barrier for the capture of a carrier from the conduction or valence band by the defect level. The pressure dependence will be the sum of the pressure dependences of these two energies. We measured no pressure dependence of the hole capture barrier for EL2(+/+) to within $\pm 15 \text{ meV GPa}^{-1}$.

Conflicting results, however, have been reported recently for the pressure dependence of the electron capture barrier of EL2(o/+), with one group reporting no pressure dependence of the barrier [18] and another group finding a large pressure dependence [19] of $dE_b/dp = -49 \pm 5 \text{ meV GPa}^{-1}$. If the pressure dependence of the barrier were indeed this large then, from eq. (3) the absolute pressure derivative of the defect equilibrium energy level would be,

$$\frac{\partial E_T}{\partial p} = 41 \pm 15 \text{ meV GPa}^{-1} \quad (4).$$

Therefore we would find the pressure coefficients for the equilibrium excitation energy, E_T , of the first and second ionization levels of EL2 to be very similar.

One can compare these data with the results of theoretical calculations of pressure dependence of energy levels associated with native defects in GaAs [19]. It is predicted in these calculations that the pressure derivatives of energy levels of native defects involving the Ga-site depend only very weakly on the location of the level in the band gap. In particular, for the As_{Ga} antisite defect the energy levels with A1 symmetry located at $-E_v + 0.75$ and at $E_v + 0.57$ are predicted to have pressure derivatives of $\sim 35 \text{ meV GPa}^{-1}$ and 32 meV GPa^{-1} , respectively. Bearing in mind the limited accuracy of the calculations we find that the theoretical values for pressure derivatives of the As_{Ga} levels are in good agreement with the experimental ones determined for the EL2 defect. This result, together with the experimentally found absence of any shear contribution to the pressure dependence of the EL2 energy levels, would appear to be consistent with the As_{Ga} model of the EL2 defect. If, however the capture barrier has little or no pressure dependence then the pressure derivative of the equilibrium energy of EL2(o/+) is large and very different from EL2(+/+). In that case the simple theoretical model reported does not predict the pressure dependence of EL2(o/+).

CONCLUSIONS

In conclusion, we have determined the absolute pressure derivative of the second ionization energy of EL2. We find the small value of the pressure derivative and the lack of orientational dependence consistent with the typical values of simple native defects in GaAs. Comparison of the pressure derivatives of the first and second ionization energies of EL2 gives quite different values. However, the lack of consistent data on the pressure dependence of the electron capture barrier of EL2(o/+) does not allow a strong comparison with theory at this point in time. In order to resolve the conflicting data, studies are being undertaken to measure directly the pressure dependence of both the electron capture barrier, E_b and the thermal equilibrium energy, E_T for EL2(o/+).

ACKNOWLEDGEMENTS

The authors would like to thank Jacek Lagowski for his interest in this work and providing the GaAs material. This work was supported by the Director, Office of Energy Research, Office

of Basic Energy Sciences, Materials Science Division, of the U.S. Department of Energy under Contract No. DE-AC03-76SF00098.

REFERENCES

1. J.F. Wager and J.A. Van Vechten, Phys. Rev. B 35, 2330 (1987).
2. H.J. Bardeleben D. Stievenard, J.C. Bourgoin, and A. Huber, Appl. Phys. Lett. 47, 970 (1985).
3. J. Lagowski, H.C. Gatos, J.M. Parsey, K. Wada, M. Kaminska and W. Walukiewicz, Appl. Phys. Lett. 40, 342 (1982).
4. M. Kaminska, M. Skowronski, and W. Kuszko, Phys. Rev. Lett. 55, 2204 (1985).
5. D.J. Chadi and K.J. Chang, Phys. Rev. Lett. 60, 2187 (1988).
6. J. Dabrowski and M. Scheffler, Phys. Rev. Lett. 66, 2183 (1988).
7. M. Hoinkis, E.R. Weber, W. Walukiewicz, J. Lagowski, M. Matsui, H.C. Gatos, B.K. Meyer, and J.M. Spaeth, Phys. Rev. B. (In Press).
8. E.R. Weber, H. Ennen, U. Kaufmann, J. Windscheif, J. Schneider, and T. Wosinski, J. Appl. Phys. 53, 6140 (1982).
9. J. Lagowski, D.G. Lin, T.P. Chen, M. Skowronski, and H.C. Gatos, Appl. Phys. Lett. 47, 929 (1985).
10. D.D. Nolte, Ph.D. Thesis, University of California, Department of Physics, (1988).
11. J.L. Benton, K.M. Lee, P.E. Freeland, and L.C. Kimmerling, AIME, Thirteenth International Conference on Defects in Semiconductors 14a, 647 (1984).
12. P.M. Henry, J.W. Farmer, and J.M. Meese, Appl. Phys. Lett. 45, 454 (1984).
13. M. Kleverman, P. Omling, L.A. Ledebro, and H.G. Grimmeiss, J Appl. Phys. 54, 814 (1983)
14. D.D. Nolte and E.E. Haller, Phys. Rev. B 38, 9857 (1988).
15. R.N. Bhargava, and M.I. Nathan, Phys. Rev. 161, 695 (1967).
16. D.D. Nolte, W. Walukiewicz, and E.E. Haller, Phys. Rev. Lett. 59, 501 (1987).
17. D.D. Nolte, W. Walukiewicz, and E.E. Haller, Phys. Rev. B 36, 9374 (1987).
18. L. Dobaczewski and A. Sienkiewicz, Acta Phys. Pol. A 71, 341 (1987).
19. P. Dreszer and M. Baj, Acta Phys. Pol. A 73, 219 (1987).
20. S.Y. Ren, J.D. Dow, and D.J. Wolford, Phys. Rev. B 25, 7661 (1982)

THE SYMMETRY OF THE EL2 DEFECT IN GaAs

P. TRAUTMAN AND J.M. BARANOWSKI

Institute of Experimental Physics, Warsaw University, Hoża 69, 00-681 Warszawa, Poland

ABSTRACT

Linear dichroism has been measured in the broad absorption band of the EL2 defect in GaAs under uniaxial stress. In addition, the splittings of the EL2 zero phonon line (ZPL) at 8378 cm^{-1} under uniaxial stress applied along [100], [111], and [110] directions have been measured. Splitting of the ZPL under [100] stress is over one order of magnitude smaller than under [111] stress, on the other hand, the linear dichroism in the broad absorption band is roughly equal for these two directions of stress. This is an evidence for the quenching of the coupling to tetragonal strains due to interaction with trigonal modes of the lattice (the Ham effect). Therefore, it is established, that the excited T_2 state of EL2 is a localized state subject to dynamical Jahn-Teller coupling to trigonal modes of the lattice. The possibility that the excited T_2 state has hydrogenic nature associated with the L minima is ruled out by the present results. The observed splittings of the ZPL together with polarization selection rules clearly indicate the tetrahedral T_d symmetry of the EL2 defect ruling out any other point group in particular trigonal C_{3v} . In view of the presented experimental results, their interpretation, and recent theoretical investigations, the isolated arsenic antisite As_{Ga} most successfully accounts for the properties of the neutral charge state of the EL2 defect.

INTRODUCTION

The EL2 defect in GaAs is currently intensively studied because of its metastability, technological importance, and native origin. Microscopic nature of this defect is still a matter of controversy. From measurements of the splittings of the zero phonon line (ZPL) of EL2 at 8378 cm^{-1} under uniaxial stress Kaminska, Skowronski, and Kuszko [1] have deduced that EL2 is a isolated defect of tetrahedral T_d symmetry. Combining this result with the technological data on dependence of EL2 concentration on crystal growth conditions, they have concluded that EL2 is the arsenic antisite As_{Ga} . On the basis of electron paramagnetic resonance and deep level transient spectroscopy investigations performed on GaAs samples subjected to electron irradiation and heat treatments, von Bardeleben et al. [2,3] have suggested that EL2 is a complex of As_{Ga} and arsenic interstitial As_i . This suggestion has found strong experimental support in optically detected electron nuclear double resonance (ODENDOR) measurements [4,5] which have indicated that EL2 is a $\text{As}_{\text{Ga}}\text{--As}_i$ axial complex. The validity of the interpretation of the piezospectroscopic experiment of Ref.1 has been questioned by Figielski and Wosinski [6]. They have argued that the observed splitting patterns can be explained assuming that EL2 is a center of orthorhombic C_{2v} symmetry. In a recent paper [7], on the basis of independent uniaxial stress experiment, we have confirmed that the ZPL of EL2 is due to the $A\rightarrow T$ electric dipole transition. Therefore the results of uniaxial stress and ODENDOR experiments are incompatible. In aim to overcome this contradiction, Skowronski [8] has proposed that the excited T_2 state has hydrogenic nature associated with the L point minima of the conduction band, so the splitting of the ZPL under uniaxial stress does not necessarily reflect the local symmetry of EL2. This explanation of the origin of the T_2 state gives correct value of the ZPL energy and accounts for more than one

order of magnitude larger splitting of the ZPL under [111] stress than under [100] stress. The purpose of this paper is to present results of measurements of linear dichroism induced by the uniaxial stress in the region of the broad absorption band of EL2. Analysis of this dichroism together with the splittings of the ZPL proves the localized character of the T_2 state, and its coupling to trigonal modes of the lattice which reduces the splitting of the ZPL under [100] stress. Therefore, the T_d symmetry determined from the analysis of the splittings of the ZPL is supported, and is in conflict with the C_{3v} symmetry deduced from ODENDOR experiment.

EXPERIMENTAL

The optical apparatus employed to measure the linear dichroism consisted of the following: halogen lamp, lens, monochromator, compensating polarizer, rotating polarizer, lens, sample in cryostat for measurements under uniaxial stress, lens, and PbS detector. The polarizer rotated in this manner that it passed in succession light of parallel (π) and perpendicular (σ) polarization. The signal from the PbS detector was detected by a lock-in amplifier at the frequency of rotation of the polarizer. The lock-in measured the difference between the intensities of light in π and σ polarizations. The compensating polarizer was used to balance the signal at zero stress. The spectra were collected by an IBM XT clone computer. Measurements were performed at 10 K on crystallographically oriented samples of intentionally undoped semi-insulating (SI) GaAs containing the EL2 defect in concentration approximately 10^{16} cm^{-3} .

In the experimental system described above, we measured the dichroism signal with the sample under 300 MPa of uniaxial stress, also a signal determining the sensitivity of the system was measured with a linear polarizer selecting σ polarization inserted between modulating polarizer and the sample. This signal contains information about the sensitivity of the system including the effect of decrease of the sensitivity in the region where absorption of the sample is large. Knowing in addition the spectrum of transmission of the polarizer, it is possible to calculate the linear dichroism (the difference $\alpha_\pi - \alpha_\sigma$ between the absorption coefficient of light polarized parallel and perpendicularly to the direction of stress).

RESULTS AND DISCUSSION

Curve (b) in Fig.1 shows the spectrum of linear dichroism $\alpha_\pi - \alpha_\sigma$ as determined from measurement under 300 MPa of [100] uniaxial stress. A stress induced dichroism appears only in the region of the intracenter absorption band of EL2 [9] (8378 cm^{-1} – 10800 cm^{-1}). A Gaussian derivative shape of this spectrum indicates that it originates from split absorption band of transitions between localized states of a defect. The [100] uniaxial stress does not differentiate the four L point minima of the conduction band, on the other hand the [111] stress differentiates the L point minima. The dichroism under [111] stress is a superposition of dichroism due to transitions to the L point valleys and dichroism due to the intracenter transitions. The lowest frequency components were removed from the experimentally determined dichroism spectrum under [111] stress by means of Fourier transform analysis. Extracted this way dichroism resulting from the intracenter transitions is shown in Fig.1 (c). Intracenter absorption band obtained by subtraction of absorption due to transitions to conduction band from the total absorption spectrum is shown in Fig.1 (a).

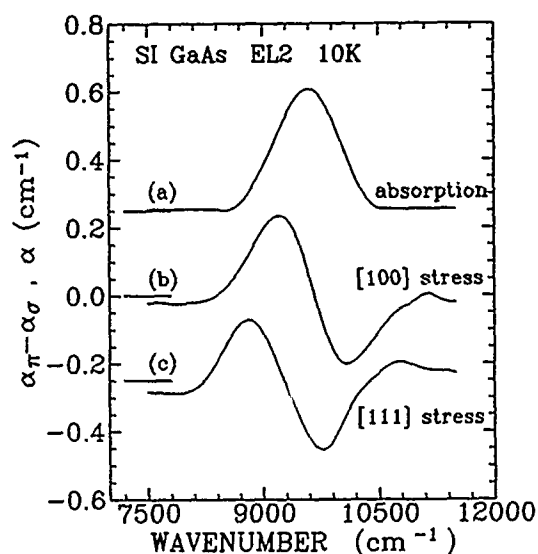


FIG.1.

(a) Spectrum of the intracenter absorption of EL2 after subtraction of the background resulting from the transitions to the conduction band.

(b) Linear dichroism $\alpha_{\pi} - \alpha_{\sigma}$ observed under 300 MPa stress in [100] direction.

(c) Linear dichroism under 300 MPa stress in [111] direction after subtraction of dichroism due to transitions to the conduction band. Vertical scale is arbitrary for this spectrum.

This subtraction was performed assuming that below 8378 cm^{-1} and above 10800 cm^{-1} the absorption is resulting exclusively from transitions to the conduction band; between these points background was assumed to vary linearly in function of the energy. Applying the method of moments, it is possible to determine magnitude of the splitting of the intracenter absorption band under uniaxial stress [10]. In the case of [100] stress the splitting is equal to 1.4 $\text{cm}^{-1}/\text{MPa}$.

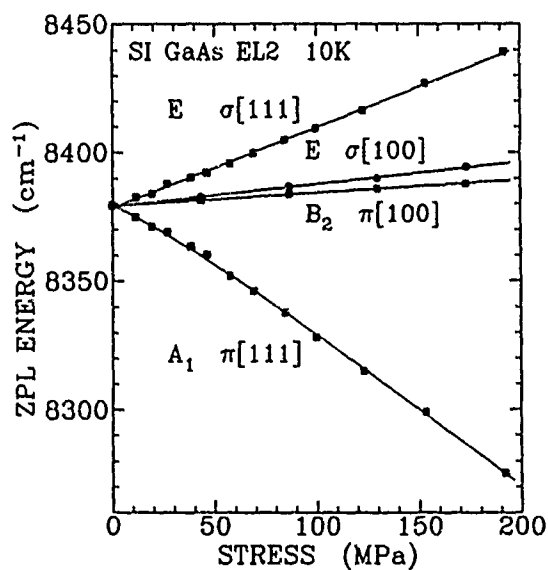


FIG.2. The splitting of the ZPL of EL2 under [100] and [111] stress. Indices [100] and [111] denote components observed under [100] and [111] stress, respectively.

Symbols π and σ indicate components present in π and σ polarization.

The points were experimentally determined. The solid lines represent fit to the theory.

In the case of [111] stress it is not possible to determine accurate value because of the arbitrary method of extracting the dichroism resulting from the intracenter transitions from the total experimental spectrum. The splitting under [111] stress is estimated to be roughly two times smaller than in the case of [100] stress. The sharp line at 8378 cm^{-1} is a ZPL of the band of intracenter absorption peaked at 9600 cm^{-1} [9]. This is supported by the following facts. (1) The ZPL is at the low energy threshold of the intracenter absorption band. (2) The transitions in the ZPL and in the band are leading to the metastable state of EL2, but the transitions below and above the band are not. This holds both in n-type [11] and in Si GaAs [12]. (3) The signs of the splitting of the ZPL and of the band under uniaxial stress are the same, namely the π components shift to lower energy and σ to the higher. (compare Fig.1 and Fig.2). (4) Integrated intensity of the ZPL in relation to the band determines the value of the Huang-Rhys factor $S=8$. From the value of the Franck-Condon shift $d_{FC}=1200\text{ cm}^{-1}=S\cdot\hbar\omega$, the value of the effective phonon energy $\hbar\omega=150\text{ cm}^{-1}$ is obtained. This value of the phonon energy is larger than the energy of the apparent phonon in the fine structure of EL2 absorption (11 meV or 90 cm^{-1}) [9]. This discrepancy indicates that higher energy phonons are also involved as observed experimentally [13].

The large difference in the magnitude of the splitting of the ZPL and the band under [100] stress is an evidence for the Ham effect [14]. Jahn-Teller coupling of the T_2 electronic triplet to lattice modes of T_2 symmetry induces trigonal distortion of the lattice around the defect. In the dynamical limit the fourfold degenerate manifold of distorted states is split into the T_2 ground vibronic level and A_1 level lying above it. Interaction with trigonal modes of the lattice quenches the coupling of the vibronic T_2 state to tetragonal (E) perturbations (like [100] uniaxial stress) reducing only slightly coupling to trigonal T_2 perturbations (like [111] uniaxial stress) [14]. This is a consequence of the fact that in the static limit the four distorted configurations are equivalent with respect to a [100] uniaxial stress which thus causes no splitting, while a [111] stress distinguishes one of the four inducing large splitting. This coupling does not affect the splitting of the band [15]. Jahn-Teller effect coherently explains character of the splitting of both the ZPL and the band, while hydrogenic model of the origin of the T_2 state [8] is incompatible with the observed strong splitting of the band under [100] stress. The ratio of the splitting coefficient of the ZPL to the splitting coefficient of the band under [100] stress determines the value of the Ham quenching factor $K(E)=0.025$. The other quantity characterizing the strength of Jahn-Teller coupling is the value of the tunnelling splitting Δ between the lowest A_1 and T_2 states. Fitting the theoretical eigenvalues to the experimentally determined energy of the ZPL under [110] stress [7], we have determined that $\Delta=65\pm 10\text{ cm}^{-1}$ (see Fig.3). There is no analytical solution of the dynamical Jahn-Teller coupling between electronic triplet and trigonal distortions of the lattice. Caner and Engelman [16] have numerically studied the problem and found the dependence of the eigenvalues and quenching factors on the strength k of the coupling. Comparing the experimental value of the reduction factor $K(E)$ with their results we obtained the magnitude of the coupling $k=2.4$, while employing the dependence of $K(E)$ on k estimated by Ham [14] we obtained $k=1.6$. Knowing the magnitude of the coupling k and the tunneling splitting Δ , it is possible to calculate the energy $\hbar\omega_T$ of phonon of the T_2 vibrational mode and Jahn-Teller energy E_{JT} . Value of $k=2.4$ leads to unreasonably large phonon energy $\hbar\omega_T=900\text{ cm}^{-1}$ and $E_{JT}=3400\text{ cm}^{-1}$ which are both exceeding maximum possible values of $\hbar\omega_{T\max}=300\text{ cm}^{-1}$ (energy of the most energetic phonon in GaAs) and $E_{JT\max}=d_{FC}=1200\text{ cm}^{-1}$ (this limitation results from the fact that d_{FC} is a sum of relaxation energies due to coupling to lattice modes of T_2 and A_1 symmetry).

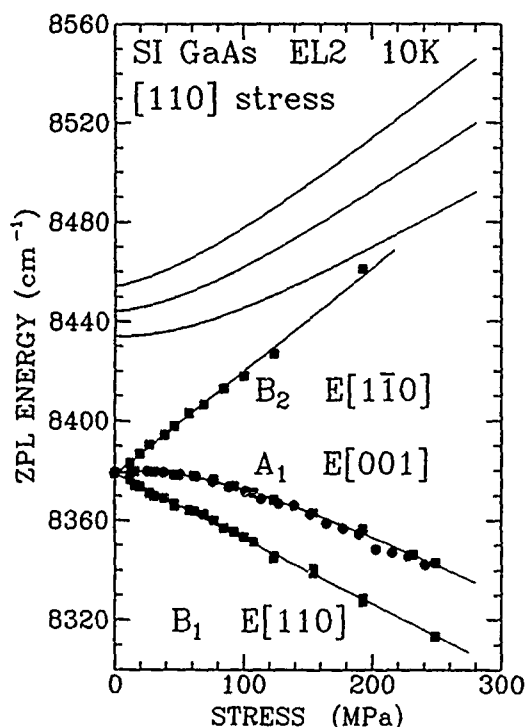


FIG.3. The splitting of the ZPL of EL2 under [110] stress. The symbol E[hkl] denotes that incident light was polarized in the [hkl] direction. The points were experimentally determined. The solid lines represent fit to the theory. The three upper curves represent the variation of the position of the upper A₁ state for three different values of the tunneling splitting Δ equal to 55, 65, and 75 cm⁻¹. The values 55 and 75 cm⁻¹ are the limits of the experimental uncertainty of Δ .

Value of $k=1.6$ leads to $\hbar\omega_T=220$ cm⁻¹ and $E_{JT}=380$ cm⁻¹, this value of E_{JT} is small in comparison with $d_{FC}=1200$ cm⁻¹. The most reasonable values $\hbar\omega_T=300$ cm⁻¹, and $E_{JT}=660$ cm⁻¹ were obtained for $k=1.8$. There is no good agreement between Caner and Engelman calculations and the experimental values but these calculations took into account interaction with only one mode of T_2 symmetry, what is not the case for a real defect in the crystal. The Jahn-Teller interaction with trigonal distortions of the lattice describes semi-quantitatively the splitting of the ZPL under uniaxial stress including the origin and interaction with the lowest A₁ vibronic state. The strong splitting of the band under [100] stress indicates that there is no inherent presumably trigonal structure in EL2 which would result in strong splitting under [111] stress and only weak splitting under [100] stress. The large splitting of the band under [100] stress and the dominating interaction with trigonal modes necessary to describe the Jahn-Teller effect are not in contradiction. Uniaxial stress experiment measures the coupling to long wavelength modes of the lattice, while Jahn-Teller effect results from the coupling to localized (short wavelength) modes. This two sorts of coupling do not have to have similar magnitudes. We have repeated the uniaxial stress experiment of Ref.1 [7] (see Figs. 2 and 3). The ZPL was observed to split into 2, 2, and 3 components under stress applied along [100], [111], and [110] directions, respectively. Exactly one stress split component of the ZPL was observed in each polarization including three unequivalent polarizations in the case of [110] stress. This pattern of splitting indicates unequivocally that the ZPL is due to A \rightarrow T electric dipole transition in tetrahedral T_d symmetry.

Three recent theoretical studies [17, 18, 19] of the isolated arsenic antisite As_{Ga} indicate the presence of distorted metastable configuration of this defect. In view of these theoretical findings and confirmed in the present paper tetrahedral symmetry of EL2, As_{Ga} most successfully accounts for the neutral charge state of the EL2 defect.

CONCLUSION

Piezospectroscopic study of the ZPL and associated with it broad absorption band indicates that the neutral charge state of EL2 has tetrahedral T_d symmetry. The excited T_2 state, transitions to which are giving rise to the ZPL of EL2, is resulting from localized electronic triplet coupled to trigonal modes of the lattice. These results and current theoretical studies support the identification of EL2 with isolated arsenic antisite As_{Ga} .

ACKNOWLEDGEMENT

This work has been supported by the Program CPBP 01.05 of the Polish Ministry of National Education.

REFERENCES

1. M. Kaminska, M. Skowronski, and W. Kuszko, Phys. Rev. Lett. **55**, 2204 (1985).
2. H.J. von Bardeleben, D. Stievenard, J.C. Bourgoin, and A. Huber, Appl. Phys. Lett. **47**, 970 (1985).
3. H.J. von Bardeleben, D. Stievenard, D. Deresmes, A. Huber, J.C. Bourgoin, Phys. Rev. B **34**, 7192 (1986).
4. B.K. Meyer, D.M. Hofman, J.R. Niklas, and J.M. Spaeth, Phys. Rev. B **36**, 1332 (1987).
5. B.K. Meyer, D.M. Hofmann, and J.M. Spaeth, J. Phys. C **20**, 2445 (1987).
6. T. Figielski and T. Wosinski, Phys. Rev. B **36**, 1269 (1987).
7. P. Trautman, J.P. Walczak, and J.M. Baranowski, accepted for publication in Phys. Rev. B.
8. M. Skowronski, in Defects in Electronic Materials, edited by M. Stavola, S.J. Pearton, and G. Davies (Mater. Res. Soc. Proc. **104**, Pittsburgh, PA 1986) pp. 405-408.
9. M. Kaminska, M. Skowronski, J. Lagowski, J.M. Parsey, and H.C. Gatos, Appl. Phys. Lett. **43**, 302 (1983).
10. S.E. Schnatterly, Phys. Rev. **140**, A1364 (1965).
11. W. Kuszko, and M. Kaminska, Acta Phys. Pol. **A69**, 427 (1986).
12. F. Fuchs, and B. Dischler, Appl. Phys. Lett. **51**, 2115 (1987).
13. W. Kuszko, P.J. Walczak, P. Trautman, M. Kaminska, J.M. Baranowski, Materials Science Forum **10-12**, 317 (1986).
14. F.S. Ham, Phys. Rev. **138**, A1727 (1965).
15. C.H. Henry, S.E. Schnatterly, C.P. Slichter, Phys. Rev. **137**, A583 (1965).
16. M. Caner, and R. Engelman, J. Chem. Phys. **44**, 4054 (1966).
17. J. Dabrowski, and M. Scheffler, Phys. Rev. Lett. **60**, 2183 (1988).
18. D.J. Chadi, and K.J. Chang, Phys. Rev. Lett. **60**, 2187 (1988).
19. E. Kaxiras, and K.C. Pandey, Phys. Rev. B **40**, 8020 (1989).

RECOVERY FROM THE METASTABLE *EL2* DEFECT IN *GaAs* UNDER MONOCHROMATIC LIGHT ILLUMINATION.

M. O. MANASREH* and D. W. FISCHER**

*Electronic Technology Laboratory (WRDC/ELRA), Wright Research and Development Center, Wright-Patterson Air Force Base, Ohio 45433-6543

**Materials Laboratory (WRDC/MLPO), Wright Research and Development Center, Wright-Patterson Air Force Base, Ohio 45433-6533.

ABSTRACT

The infrared absorption technique is used to study the recovery of the *EL2* metastable state in semi-insulating *GaAs* under monochromatic light illumination. The induced optical recovery is monitored after low intensity ($\leq 2 \text{ mW/cm}^2$) irradiation in the energy range $0.7 \leq h\nu \leq 1.5 \text{ eV}$. The data exhibit a complex structure consisting of a broad band around 0.9 eV and a set of multiple sharp peaks between 1.44 and 1.5 eV . This recovery is strongly dependent on the sample, temperature and illumination time. The present results suggest that a) the existing data and theoretical predictions for the isolated As_{Ga} antisite structure are not compatible with the optical recovery data, b) *EL2* is affected dramatically by other defects (traps) present in the sample and c) the peaks observed in the optical recovery data are coincident with the arsenic vacancy energy levels and therefore the present results support the proposed complex models involving an arsenic vacancy.

INTRODUCTION

The atomic structure of the mid-gap defect known as *EL2* in *GaAs* and how its constituent atom(s) rearrange during the transformation of this defect from the normal state (*EL2*⁰) to the metastable configuration (*EL2*^{*}) in response to photo-excitation at low temperatures ($T \leq 100 \text{ K}$) are issues which have initiated some very active controversies in recent years. The presence of an optically induced metastable configuration is the most unusual aspect of this defect. The key to reaching a clearer understanding of the nature of the *EL2* defect is therefore to understand its metastable state which apparently exhibits no experimentally observed properties of its own. A few attempts have been made recently to transform the *EL2* defect from *EL2*^{*} to *EL2*⁰ by photon irradiation. Such photo-induced recovery has been reported for photoluminescence¹, photoconductivity², photocapacitance³, infrared (IR) absorption⁴⁻⁷, and electron paramagnetic resonance⁸ (EPR). Even though all these studies have established that the optical recovery from *EL2*^{*} can be induced, they disagree on some important aspects such as the amount of optical recovery and the spectral dependence of the recovery.

In this article we present photo-induced recovery properties of the *EL2* defect. Optical recovery from *EL2*^{*} was found to be sample dependent indicating the existence of interactions between *EL2* and other defects and traps present in the samples. The current results will be tested against the isolated arsenic antisite model as well as other more complex models. The recovery data are in good agreement with the calculated arsenic vacancy energy levels lending support to models containing this point defect.

EXPERIMENTAL TECHNIQUE

Several semi-insulating *GaAs* samples (doped and undoped) grown by the liquid-encapsulated Czochralski (LEC) technique and obtained from several manufacturers were investigated. In the present paper, we report the measurements that were obtained for selected samples that show noticeable differences in the *EL2* properties. Infrared (ir) absorption measurements were made with a CARY 2300 spectrometer. Its probing light was weak enough that no observable photoquenching or photo-induced recovery occurred during long sample

quart-halogen lamp provided the secondary irradiation. A wide range of photon energies (0.7 - 1.51 eV) was available with this monochromator. A cut-off filter with 50% transmittance at 1.46 eV was placed at the output of the monochromator to prevent illumination with photon energies larger than the band gap. The intensity of the monochromator output was measured with a calibrated thermopile and it was kept constant ($\sim 1.9 \text{ mW/cm}^2$) by adjusting the voltage on the light source at each photon energy over the range of $0.7 \rightarrow 1.4 \text{ eV}$. The intensity decreased from 1.9 mW/cm^2 at 1.4 eV to $\sim 0.4 \text{ mW/cm}^2$ at 1.50 eV .

RESULTS AND DISCUSSIONS

Optical recovery from EL2^* was monitored as follows. After a complete photoquenching of EL2^0 at 9 K using 1.125 eV light, the sample was heated to 77 K and illuminated with monochromatic light in the range of $0.7 - 1.51 \text{ eV}$ for 25 min and it was found that the recovery factor $R = (\alpha/\alpha_0) \times 100\%$ shows a very complex structure as shown in Fig. 1 for an annealed sample (sample No.1). Here, α is the absorption coefficient measured at either 1.18 or 1.40 eV

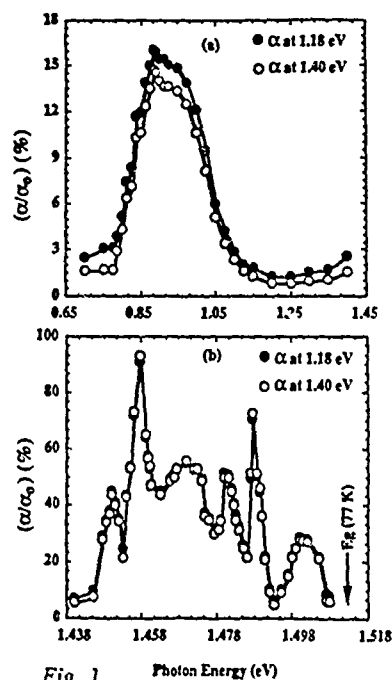


Fig. 1

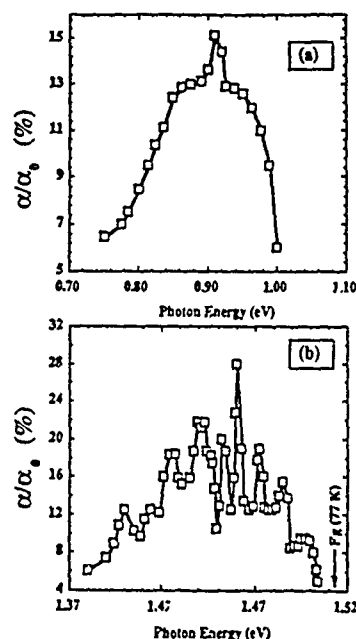


Fig. 2

Fig. 1. Photo-induced $\text{EL2}^* \rightarrow \text{EL2}^0$ recovery for sample #1 as a function of photon energy (a) in the $0.7 \rightarrow 1.4 \text{ eV}$ range and (b) in the $1.44 \rightarrow 1.51 \text{ eV}$ range. The optical recovery was determined at both the 1.18 eV (\bullet) and 1.40 eV (\circ) energy positions in the IR absorption spectrum after illumination for 25 min with monochromatic light of energy indicated by each pair of data points. Sample was illuminated at 77 K then cooled to 9 K to measure the absorption coefficients

Fig. 2. The same key as in Fig. 1, but for sample #2. The illumination time was 50 min . Here we have shown only the recovery factor at 1.18 eV position.

position after photon irradiation and α_0 is the initial absorption coefficient measured after cooling the sample in the dark to 9 K and before photoquenching.

A few points should be noted here. First, the 1.18 and 1.40 eV positions were chosen to measure the absorption coefficient because two broad absorption peaks were obtained at these positions when a base line correction was made. Second, thermal recovery is insignificant ($< 1\%$) at 77 K for the illumination period of 25 min used in this study. Third, optical recovery was observed at 9 K but with a slower rate as compared to the recovery rate at 77 K using 1.46 eV monochromatic light (see Ref. 7). Fourth, the recovery factor, R , may be larger than the data reported in the region above 1.4 eV in Fig. 1 because the light intensity is not constant in this region. Fifth, a temperature dependence is observed in the photo-induced $EL2^* \rightarrow EL2^0$ recovery of the ir absorption⁷ indicating that the photo-induced recovery process itself is thermally activated.

The recovery factor, R , was found to exhibit more complex structure in unannealed samples. Sample No. 2 is taken as an example for which R is plotted as a function photon energy as shown in Fig. 2. It should be pointed out that the same conditions were applied to both samples No. 1 (Fig. 1) and No. 2 (Fig. 2) except that the illumination time used for sample No. 2 was 50 min. Despite the fact that a longer illumination time was used, the amount of R in Fig. 2 is smaller than that obtained in Fig. 1. The complex structure in Fig. 2 consists of a peak and two shoulders [Fig. 2(a)] around 0.9 eV and a number of multiple sharp peaks between 1.38 and 1.51 eV [Fig. 2(b)].

The recovery factor, R , was also studied as a function of time at 77 K using 1.461 eV light for three different samples as shown in Fig. 3. The data in this figure were found to be fitted by the following analytical expression $R = A[1 - B \times \exp(-t/\tau)]$ where A and B are constants depending on the initial and final concentrations of $EL2^*$, t is the illumination time, and τ is a time constant which is inversely proportional to the cross section of the $EL2^* \rightarrow EL2^0$ transformation. Both A , B , and τ were used as fitting parameters in Fig. 3. It is well known that LEC grown GaAs can exhibit variations in properties due to variations in growth conditions and thermal history. If so, sample dependences observed for some $EL2$ properties such as optical recovery characteristics should not be surprising.

The recovery data in Figs. 1 and 2 were evaluated with respect to the well known models proposed for the metastable $EL2$ defect, namely, arsenic antisite-gallium vacancy¹⁰, arsenic split-interstitial¹¹, arsenic antisite-arsenic vacancy¹², and arsenic antisite-divacancy¹³ (gallium vacancy-arsenic vacancy). The optical recovery was also compared with the energy levels of point defects reported in the literature¹⁴ for GaAs. It appears that the one point defect which has electronic energy levels which coincide with the peaks observed in the recovery data (Figs. 1 and 2) is the arsenic vacancy (V_{As}). V_{As} was found to possess an S-like energy level near midgap and a P-like energy level close to the conduction band in apparent agreement with the present optical recovery data. The EPR measurements, however, seem to be in conflict with

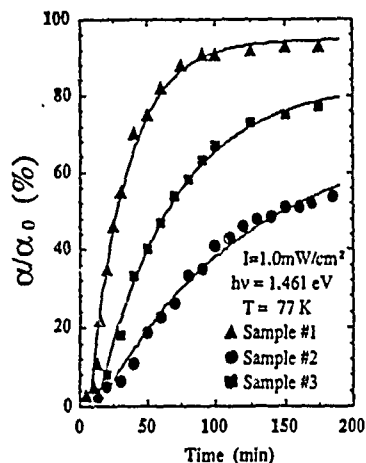


Fig. 3. Photoinduced $EL2^* \rightarrow EL2^0$ recovery as a function of time at 77 K for samples #1 (\blacktriangle), #2 (\bullet), and #3 (\blacksquare). The solid lines are the results of fitting the experimental data by using the analytical expression of R where A , B , and τ are the fitting parameters.

the $\text{As}_{\text{Ga}} - \text{V}_{\text{As}}$ model. von Bardeleben *et al.*¹⁵ found that $g = 1.97$ and $A = 6.8 \times 10^{-2} \text{cm}^{-1}$ for the $(\text{As}_{\text{Ga}} - \text{V}_{\text{As}})$ pair defect in disagreement with $g = 2.04$ and $A = 8.9 \times 10^{-2} \text{cm}^{-1}$ of EL2. It should be pointed out the EPR measurements were performed only on electron irradiated GaAs materials and a definitive identification of the $\text{As}_{\text{Ga}} - \text{V}_{\text{As}}$ defect requires additional measurements using different materials (for example as grown LEC GaAs) and techniques. The above disagreement can be resolved as follows. EL2^* can be represented by $\text{V}_{\text{As}} + \text{X}$ where X could be As_{Ga} while EL2^0 has a different atomic structure. The metastable state, EL2^* , is inaccessible directly by EPR because it is not a paramagnetic state or by the ir absorption technique because of the presence of a large lattice relaxation, but its energy levels nonetheless exist in the gap and are V_{As} derived states.¹⁴

The question of whether the peaks observed in Figs. 4 and 5 are due to splitting in the V_{As} energy levels or to the fact that EL2 is a family of slightly different levels¹⁶ is still open. However, the presence of what appears to be two peaks around 0.9 eV in Fig. 1(a) and three peaks in Fig. 2(a) and the fact that an S-like energy level (A_1) does not split under crystal or strain fields may suggest that the data in Figs. 1 and 2 are due to both splitting in the p-like levels (T_2) and the existence of a family of energy levels.

CONCLUSIONS

We have shown some new and different photo-induced $\text{EL2}^* \rightarrow \text{EL2}^0$ recovery data obtained by the ir absorption technique. Various features of this recovery have been discussed and are summarized as follows. a) For the first time optical recovery has been shown to occur in the 1.4 \rightarrow 1.51 eV region. b) The recovery in the 1.4 \rightarrow 1.51 eV region is more efficient and more complex than that previously reported for the 0.9 eV region. c) The peaks observed in the optical recovery are EL2-related energy levels. d) The small magnitude of the recovery factor around 0.9 eV as compared to that in the 1.4 \rightarrow 1.51 eV region can be understood in terms of competition between quenching and recovery around 0.9 eV. e) The peaks observed in the optical recovery were interpreted as being V_{As} (which is part of EL2^* complex) related energy levels in good agreement with the available theoretical calculations.¹⁴ f) The photoinduced recovery data strongly support the concept of a "family" of EL2 defects.

REFERENCES

1. M. Tajima, Jpn. J. Appl. Phys. **23**, L690 (1984); **24**, L47 (1985).
2. S. Nojima, J. Appl. Phys. **57**, 620 (1985); **58**, 3485 (1985); S. Nojima and H. Asahi, J. Appl. Phys. **61**, 1073 (1987).
3. Y. Mochizuki and T. Ikoma, Jpn. J. Appl. Phys. **24**, L895 (1985).
4. M. Tajima, H. Saito, T. Iino, and K. Ishida, Jpn. J. Appl. Phys. **27**, L101 (1988).
5. J. C. Parker and R. Bray, Phys. Rev. B **37**, 6368 (1988).
6. D. W. Fischer, Appl. Phys. Lett. **50**, 1751 (1987).
7. D. W. Fischer and M. O. Manasreh, Appl. Phys. Lett. **54**, 2018 (1989).
8. H. J. von Bardeleben, N. T. Bagraev, and J. C. Bourgoin, Appl. Phys. Lett. **51**, 1451 (1987).
9. D. W. Fischer, Phys. Rev. B **37**, 2988 (1988).
10. J. Dabrowski and M. Scheffler, Phys. Rev. Lett. **60**, 2183 (1988).
11. C. Delerue, M. Lannoo, D. Stievenard, H. J. von Bardeleben, and J. C. Bourgoin, Phys. Rev. Lett. **59**, 2875 (1987); C. Delerue and M. Lannoo, Phys. Rev. B **38**, 3966 (1988).
12. G. A. Baraff and M. Schluter, Phys. Rev. Lett. **55**, 2340 (1985).
13. J. F. Wager and J. A. Van Vechten, Phys. Rev. B **35**, 2330 (1987).
14. M. O. Manasreh and D. W. Fischer, Phys. Rev. B **40**, 15 December 1989 (to appear) and references therein.
15. J. C. Bourgoin, H. J. von Bardeleben, and D. Stievenard, J. Appl. Phys. **64**, R65 (1988); H. J. von Bardeleben, J. C. Bourgoin, A. Miret, Phys. Rev. B **34**, 1360 (1986); H. J. Bardeleben, A. Miret, H. Lim, and J. C. Bourgoin, J. Phys. C **20**, 1353 (1987).
16. M. Taniguchi and T. Ikoma, J. Appl. Phys. **54**, 6448 (1983); M. Taniguchi and T. Ikoma, Appl. Phys. Lett. **45**, 69 (1984).

EL-2 DEFECT FORMATION AND CARBON INCORPORATION IN GaAs GROWN BY ORGANOMETALLIC VAPOR PHASE EPITAXY

R. Venkatasubramanian, Research Triangle Institute, Research Triangle Park, NC 27709;

J.M. Borrego and S.K. Ghandhi, Electrical Computer and Systems Engineering Dept., Rensselaer Polytechnic Institute, Troy, NY 12180.

ABSTRACT

The anti-site defect As_{Ga} , EL-2, is used to understand the nature of arsenic surface species during the Organometallic Vapor Phase Epitaxy (OMVPE) of GaAs. The concentration of EL-2 in unintentionally doped n-GaAs, measured by Deep Level Transient Spectroscopy, is presented as a function of AsH_3 partial pressure, TMGa partial pressure and the growth temperature. Based on this data, a model for EL-2 incorporation in OMVPE GaAs is developed in which all surface species As-H, are converted to As_2 at around 765°C . Under the same set of growth conditions, relative carbon levels measured by 4K Photoluminescence, suggest that the increase in carbon levels with growth temperature is due to the gas-phase loss of H radical from the As-H species.

Introduction

EL-2 is a deep donor located at $E_c - 0.82\text{ eV}$, with a relatively high electron capture cross-section of about $4 \times 10^{-15}\text{ cm}^2$ [1]. Although its exact electronic nature is far from clear, it is known that the anti-site defect (As_{Ga}) is involved. Although this level is regularly observed in OMVPE n-GaAs, there has been no discussion of the EL-2 defect formation mechanism in the OMVPE process, along the lines of the probable nature of the growth mechanism [2]. There have been a number of studies on the concentration of this level as a function of arsine (AsH_3) and trimethylgallium (TMG) partial pressure ratio, but the results vary considerably [3,4]. Analysis of these results is complicated by the fact that the electron concentration depends on the AsH_3 /TMG ratio, and thermodynamically can affect the EL-2 concentration since the EL-2 is a donor-like specie. Further, an oxygen-related level is expected to be close to the energy position of EL-2, possibly affecting interpretation [5].

We have addressed these issues by studying arsine partial pressure dependencies at growth temperatures where intrinsic carrier levels exist, to isolate the EL-2 concentration dependence on AsH_3 /TMG ratio. Oxygen-related levels were minimized by incorporating molecular-sieves on the AsH_3 source. The concentration of EL-2 was measured by Deep-Level Transient Spectroscopy (DLTS) as a function of AsH_3 partial pressure (p_{AsH_3}), TMG partial pressure (p_{TMG}) and growth temperature. A model for

the nature of arsenic species and EL-2 formation in OMVPE GaAs, is developed, based on these results.

Since carbon incorporation in OMVPE GaAs is closely tied to the nature of arsenic species, either on the growing GaAs surface or in its vicinity, we have also studied the carbon incorporation in the same set of samples. Carbon levels were evaluated by 4K photoluminescence (PL).

Experimental

The GaAs layers were grown in an atmospheric, horizontal-flow OMVPE reactor, using TMG and AsH₃. All the layers considered here were n-type, with a typical thickness of 3 μm . The samples were grown at rates of 0.05 to 0.10 $\mu\text{m}/\text{min}$. The arsine was passed through a molecular-sieve to reduce its level of moisture content. This should reduce the effects of any oxygen-related level near EL-2, or of an oxygen-related exciton-peak near the PL energy of the carbon peak.

The DLTS measurement set-up used in this study, and the evaluation of trap concentration N_t , are described in Ref.6. The excitation for PL at 4.5 K consisted of the 6328 Å line of a 1 mW He-Ne laser. The luminescence was analysed through a 3/4-meter spectrometer with a resolution of $\sim 1\text{\AA}$. A liquid-nitrogen cooled S-1 photocathode was used to detect the PL signal.

Results

van der Pauw Hall-effect measurements on all the GaAs samples, independent of the growth conditions considered here, indicated a free-electron concentration in the range 1 to $4 \times 10^{15} \text{ cm}^{-3}$, smaller, by a factor of ten or more, than the intrinsic carrier concentration at the growth temperatures considered in this study.

EL-2 was observed in the DLTS spectra as a peak around 370 K. The EL-2 concentration, for a constant TMG partial pressure of 0.1 Torr., was observed to follow the dependence $[\text{EL-2}] \propto (p_{\text{AsH}_3})^n$, with $n \sim 1.0$ and 0.5 at growth temperatures of 730 and 765 °C, respectively. This is shown in Figure 1. Also, for a given AsH₃ partial pressure, the EL-2 concentration varied inversely with TMG partial pressure at 730 °C. However, at 765 °C, the dependence of EL-2 concentration on TMG partial pressure can be described by the relation $[\text{EL-2}] \propto (p_{\text{TMG}})^{-0.5}$ and is shown in Figure 2. Also, as shown in Figure 3, it was observed that the EL-2 concentration showed a monotonic fall with growth temperature and appeared to saturate at $\sim 2.5 \times 10^{14} \text{ cm}^{-3}$ for growth temperatures 775 °C and higher.

A typical 4.5 K PL spectra of the GaAs layers, shown in Figure 4, consisted of an excitonic region transition ($\sim 1.514 \text{ eV}$) and the others a (C_{As}, e) free-to-bound carbon acceptor peak at around 1.494 eV, a D-A pair related to carbon at 1.491 eV and a weak (Zn_{Ga}, e) zinc-related peak at 1.484 eV. Figure 5 shows the intensity of the carbon acceptor peak normalised to the total bound exciton intensity, as a function of growth temperature. We use this ratio as a measure of carbon level to circumvent the sample-to-sample variation in surface properties (ie, surface recombination velocity)

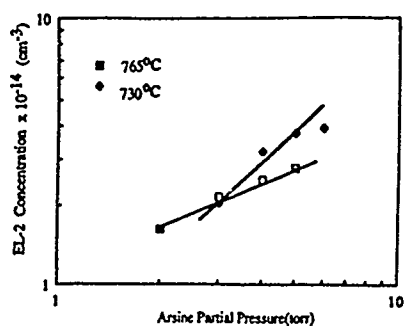


FIG. 1. EL-2 concentration as a function of AsH_3 partial pressure, for $p_{\text{TMG}}=0.1$ Torr.

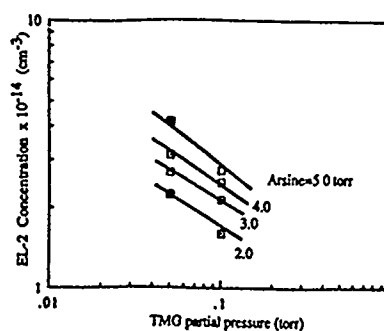


FIG. 2. EL-2 concentration as a function of p_{TMG} partial pressure, for various p_{AsH_3} at 765°C

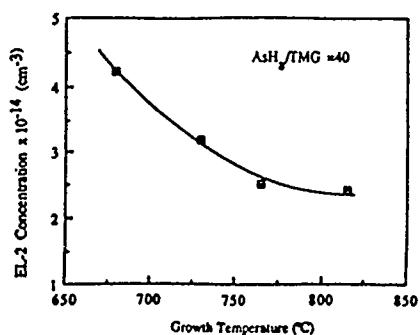


FIG. 3. EL-2 concentration as a function of growth temperature for a fixed AsH_3/TMG ratio

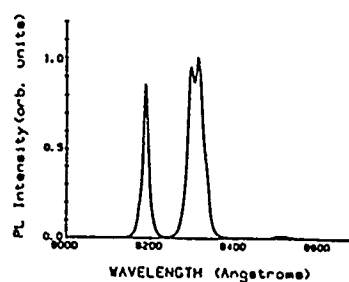


FIG. 4. Typical 4.5 K PL spectra obtained on a n-GaAs sample grown at 680°C

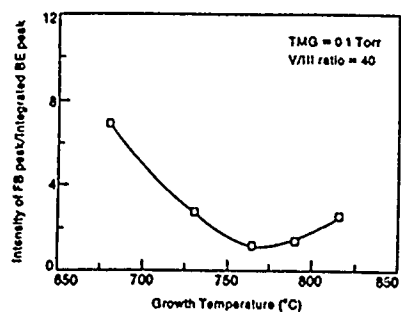


FIG. 5. Carbon level as indicated by the PL intensity ratio, in GaAs, as a function of growth temperature

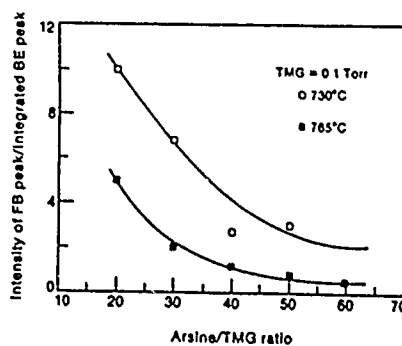
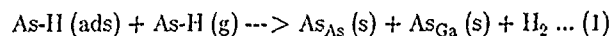


FIG. 6. Carbon level as indicated by the PL intensity ratio, in GaAs, as a function of p_{AsH_3}

which can affect the excess carrier concentration. This ratio also minimizes the error due to the overlap of the D-A peak and the $(\text{Zn}_{\text{Ga}}, \text{e})$ peak, with the $(\text{C}_{\text{As}}, \text{e})$ free-to-bound carbon acceptor peak. This ratio is shown in Figure 6 as a function of AsH_3/TMG ratio, at growth temperatures of 730°C and 765°C . In each case, there is a monotonic fall in carbon level followed by a near saturation, with increasing AsH_3/TMG ratio. Also, this near-saturation is pronounced at the higher growth temperature of 765°C , compared to 730°C . This effect has been noted in an earlier study of carbon-incorporation in OMVPE GaAs [7].

Discussion

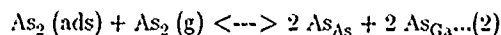
The growth model of OMVPE n-GaAs [2] suggests that the incident species of AsH_3 and TMG are As-H and GaCH_3 respectively. At a growth temperature of 730°C , the growth rate was a linear function of the TMG partial pressure ie, $R_{\text{GaAs}} \propto p_{\text{TMG}}$. This is a well-observed phenomenon in the OMVPE of GaAs. Also due to strong As-H adsorption, the surface-coverage of As-H ($\theta_{\text{As-H}}$) is near unity. This is supported by the independence of GaAs growth rate on AsH_3 partial pressure[2]. Hence, following an EL-2 formation reaction of the type



and noting that the reaction is between an adsorbed specie and a gas-phase specie, we get $R_{\text{EL-2}} \propto p_{\text{AsH}}$ ie, the rate of EL-2 formation is linearly proportional to the input partial pressure of As-H or AsH_3 . Hence, combining with the linear dependence of GaAs growth rate on p_{TMG} , we can explain the linear dependence of EL-2 concentration on AsH_3/TMG ratio at 730°C . We note here a Langmuir-Rideal absorption-model for EL-2 formation and is to be compared with the Langmuir-Hinshelwood model for the GaAs growth [2].

We note that the EL-2 concentration shows a $(\text{AsH}_3/\text{TMG})^{0.5}$ dependence at 765°C . A complete discussion of this result is beyond the scope of this paper and is presented elsewhere [8]. To explain this, a model, in which the dominant surface-species are As_2 and a thermodynamic equilibrium reaction occurs between an adsorbed As_2 and a gas-phase As_2 for EL-2 formation, is required. Here, the As_2 is formed on the GaAs surface from the reaction of two adsorbed As-H species, as discussed elsewhere [9]. Also, the As_2 so formed, can desorb from the GaAs surface [9].

Essentially, with the near conversion of all the As-surface species from As-H to As_2 , an equilibrium reaction of the type



is suggested for the EL-2 formation at high growth temperatures in OMVPE.

The H_2 release associated with EL-2 formation in reaction (1), compared to the reaction (2) at higher growth temperatures, is thought to favour the formation of more EL-2 at lower growth temperatures as seen in Fig.3. It is interesting to note that the EL-2 concentration is lower with As_2 as the dominant arsenic surface-species at the

higher growth temperatures, in the model proposed here, similar to the fact that in MBE-grown GaAs (where As_2 and As_4 are the dominant arsenic species) EL-2 is seldom observed.

With the above nature of surface arsenic species, the trend of carbon incorporation with temperature can be understood as follows. In raising the growth temperature from 680 to 730 °C, in addition to any possible increase in As-H surface coverage more towards the unity mark, the increased conversion of input AsH_3 molecules to excess As-H gas-phase molecules can more effectively scavenge the methyl radicals from the GaCH_3 species, on a growing GaAs surface. This will reduce the carbon incorporation level with growth temperature. This increase in concentration of the gas-phase As-H species probably explains the fall in carbon level from 730 °C to 780 °C, even though the surface-species are proposed to be As_2 based on the EL-2 study. Therefore, the increase in carbon level with growth temperature from about 780 °C onwards, is probably due to the gas-phase loss of H-radical from the As-H species (in contrast to a reaction between two adsorbed As-H species forming H_2 and As_2 on the GaAs surface) so that the CH_3 radical attached to the Ga atom can be incorporated as carbon.

This stresses the importance of reducing unwanted gas-phase heating of input AsH_3 molecules, through proper reactor design, in reducing carbon levels in GaAs. This is important, especially for high minority-carrier lifetime in n-GaAs, where carbon-related levels have been attributed to lowering of lifetimes [10]. This is also of concern during the growth of AlGaAs, where usually high temperature growth is employed.

Summary

In summary, the dependence of EL-2 concentration on AsH_3 partial pressure, TMG partial pressure and growth temperature, in OMVPE n-GaAs were described. The trend of carbon levels, monitored by 4K PL, for similar variation in growth conditions, were also mentioned. A model for the EL-2 formation in OMVPE GaAs was presented, which is consistent with the near conversion of all surface species in OMVPE GaAs, from As-H to As_2 at around 765 °C. Based on this model and the trend of carbon incorporation with temperature, it is concluded that the increase in carbon level with temperature is due to gas-phase loss of the H radical from the As-H species.

Acknowledgement

The authors would like to thank J. Barthel for technical assistance on this program. Technical discussions with Dr. R.J. Field of ITT and Prof. I. Bhat of RPI are most appreciated. This work was sponsored by contract No. XL-5-05018-2 from the Solar Energy Research Institute, Golden, Colorado. Additional funds were provided by Agreement No. 970-ERER-ER-87 with the New York State Energy Research and Development Authority. This support is hereby acknowledged. One of the authors (R.V) would like to thank Dr. Michael L. Timmons of RTI, for his kind support.

References

1. P.K. Bhattacharya, J.W. Ku, S.J.T. Owen, V. Aebi, C.B. Cooper and R.L. Moon, Appl. Phys. Lett., 36, 304 (1980).
2. D.H. Reep and S.K. Ghandhi, J. Electrochem. Soc., 130, 675 (1983).
3. L. Samuelson, P. Omling, H. Titze and H.G. Grimmeis, J. Cryst. Growth, 55, 164 (1981).
4. He-Zhong Zhu, Yoshio Adachi and Toshiaki Ikoma, J. Cryst. Growth, 55, 154 (1981).
5. J. Lagowsky, D.G. Lin, T. Aoyama and H.C. Gatos, Appl. Phys. Lett., 44, 336 (1984).
6. D. Verity, F.J. Bryant, C.G. Scott and D. Shaw, J. Cryst. Growth, 59, 234 (1982).
7. T.F. Kuech and E. Veuhoff, J. Cryst. Growth, 68, 148 (1984).
8. R. Venkatasubramanian, J.M. Borrego and S.K. Ghandhi. To be published in the J. Cryst. Growth.
9. R.J. Field and S.K. Ghandhi, J. Cryst. Growth, 74, 551 (1986).
10. L.W. Molenkamp, G.L.M. Kampschoer, W. de Lange, J.W.F.M. Maes, and P.J. Roksnoer, Appl. Phys. Lett., 54, 1992 (1989).

The role of EL2 for the mobility-lifetime product of photoexcited electrons in GaAs

G. C. Valley
Hughes Research Laboratories
Malibu, Ca 90265 - USA

H.J. von Bardeleben
Groupe de Physique des Solides de l'École Normale Supérieure
Centre national de la Recherche Scientifique
Tour 23, 2 place Jussieu
75251 Paris Cedex 05, France.

H. Rajbenbach
Laboratoire Central de Recherches
Thomson-CSF
Domaine de Corbeville
91404 Orsay Cedex, France

abstract

The mobility lifetime products for photo-electrons in semi-insulating GaAs, which fit successfully the results of photorefractive studies undertaken in the presence of electric fields are three orders of magnitude smaller than those inferred from transport measurements or from the photorefractive effect with no applied electrical field. Consideration of enhanced recombination via EL2 effective-mass states linked to the L-conduction band minimum allows us to fit the dependence of the photorefractive beam coupling gain coefficient on the grating period for both AC fields and moving gratings. A cascade-capture process, which is three orders of magnitude faster than recombination by multiphonon emission from the Γ band to EL2, leads to greatly reduced mobility-lifetime products for field strengths greater than 1 kV/cm. Our results establish the dominant influence of the EL2 defect properties on the recombination processes essential for modelling and optimizing the photorefractive effect in semi-insulating GaAs.

Undoped semi-insulating GaAs is an important electronic material and since 1984 has been shown to have very promising properties for beam coupling, phase conjugation and optical data processing [1-7]. EL2 is the dominant native defect in this material with a concentration of typically $2 \cdot 10^{16} \text{ cm}^{-3}$. It dominates the extrinsic absorption spectrum by the photoionisation from the valence band and to the conduction band. Without an external applied field, however, coupling coefficients in photorefractive experiment are rather small in GaAs because of its small electro-optic coefficient. To increase the coupling coefficient many researchers have applied external DC and AC fields to enhance charge transport and

obtain large internal space-charge field grating [3,4,6,7]. This has led to larger coupling coefficients, but the results are in disagreement with theoretical predictions based on photorefractive theories and intrinsic properties of semi-insulating GaAs [7-9]. Here we explicitly demonstrate this discrepancy between theoretical prediction and experimental result in measurements made on undoped GaAs in which the defect responsible for the photorefractive effects in EL2. The results can be consistently interpreted in terms of enhanced recombination in the presence of large electric fields.

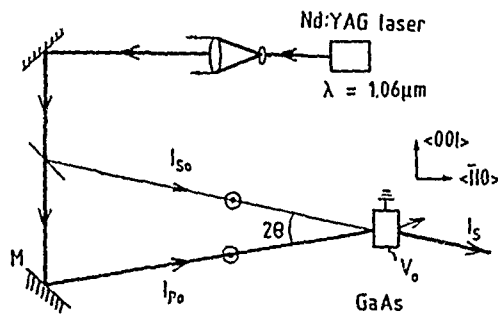


Fig.1: Photorefractive two-beam coupling experiment (ref.15). The optical beams photoinduce a phase volume grating in GaAs and a portion of the pump energy is transferred to the signal beam.

Consider first a typical experiment of two beam coupling as shown in Fig.1. Signal and pump beams interfere in the crystal volume and photoinduce a space charge field that spatially modulate the index of refraction. This grating leads to an energy redistribution that amplifies the transmitted signal beam. The amplification is characterized by the exponential gain coefficient Γ given by:

$$I_S = I_{S_0} \exp(\Gamma - \alpha) d, \quad (1)$$

where α is the absorption coefficient and d is the interaction length. The theoretical expression for beam coupling gain in the presence of an externally applied square-wave AC field E_0 is given by [10]:

$$\Gamma = k r_{\text{eff}}^3 E_q \frac{[1 + E_D E_M / E_o^2 (1 + E_D / E_M)]}{[1 + E_M (E_D + E_q) (1 + E_D / E_M) / E_o^2]} \quad (2)$$

where k is the optical wavenumber, r_{eff} is the effective electro-optic coefficient, and n is the refractive index. E_q , E_D and E_M are the limiting space charge field, the diffusion field and the Maxwellian field defined by $E_q = e N_E / (k_g \epsilon \epsilon_o)$, $E_D = k_g K_B T / e$, and $E_M = 1 / (k_g \mu \tau_R)$. Finally, e is the charge on the electron, N_E is the effective photorefractive trap density, k_g is the grating wavenumber, ϵ is the dielectric constant, ϵ_o is the permittivity of free space, K_B is Boltzmann's constant, T is the temperature, μ is the mobility, and τ_R is the electron recombination time. This expression is valid for the case of photoconduction by one type of carriers only. For illumination at $1.06 \mu\text{m}$ the effects of mixed electron and hole conduction are small in these undoped crystals and thus are neglected in Eq. (2).

The EL2 concentration can be determined by optical absorption and Electron Paramagnetic Resonance measurements. The dielectric constant, electro-optic coefficient and refractive index are known for GaAs so that the only remaining parameter is the mobility-lifetime product. The mobility is known from Hall measurements [2,7] on adjacent samples to be about $5000 \text{ cm}^2/\text{V}\cdot\text{s}$ while the electron lifetime is given by $1/(v \sigma_e N_E)$ where v is the thermal velocity (known) and σ_e is the electron recombination cross section. This cross section is given by Martin and Makram-Ebeid [11] as $4 \times 10^{-16} \text{ cm}^2$. For a thermal velocity of $4 \times 10^7 \text{ cm/sec}$ we obtain a mobility-lifetime product of $\mu \tau_R = 3 \times 10^{-4} \text{ cm}^2/\text{V}$. The three upper curves in Fig.2 are calculated for this mobility-lifetime product. The fit of the experimental data shown in the lower curves of figure 2 requires however a mobility-lifetime product of $2 \times 10^{-8} \text{ cm}^2/\text{V}$ that is four orders of magnitude smaller !

To test the influence of the electric field, we used a photorefractive method to obtain $\mu \tau_R$ without electric field; the results confirmed the value of $\sim 10^{-4} \text{ cm}^2/\text{V}$. [12]

In Fig.3 we show beam coupling data taken using a DC field and the moving fringe technique in a crystal of GaAs with electronic properties very similar to the crystal used for the AC field studies. These data were obtained using the experimental configuration described in detail in ref. 6. In this technique, one of the beams reflects from a piezomirror and is shifted in frequency by $\delta\omega$. The theoretical gain coefficient is given by a formula similar to Eq.(2): [6,8]

$$\Gamma = k n^3 r_{\text{eff}} E_q / (1 + E_M E_q / E_o^2). \quad (3)$$

Results based on this formula and mobility-lifetime products of $3 \times 10^{-4} \text{ cm}^2/\text{V}$ are shown by the straight line in Fig.3, which obviously does not fit the data. The curve that fits the data is based on $\mu \tau_R = 5 \times 10^{-8} \text{ cm}^2/\text{V}$. The calculations presented in Figs. 2 and 3 clearly imply that the mobility-lifetime product in semi-insulating GaAs:EL2 in the presence of

electric fields of 2.5 kV/cm or more is about four orders of magnitude smaller than that with zero field. This decrease in the mobility lifetime product can be attributed to two effects : (i) the transfer of electrons from the high mobility Γ band to the low mobility L band due to the electric field [13] and (ii) the increase in recombination cross section because the capture processes changes from non-radiative multiphonon emission to a cascade process in the presence of the applied field [14].

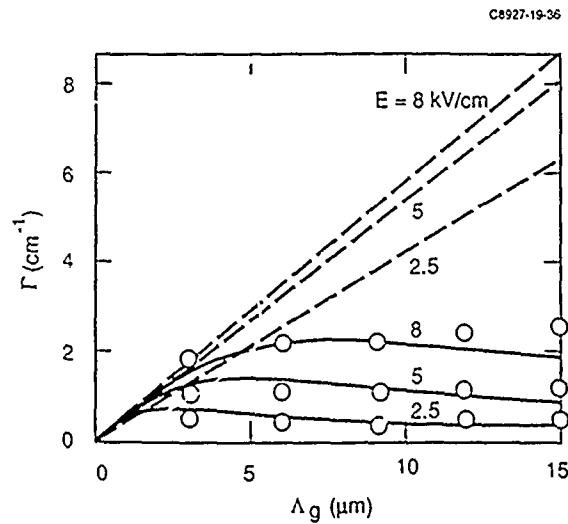


Fig.2: Measurements of beam coupling gain as a function of grating period with an AC field of 2.5, 5, and 8 kV/cm. Theoretical calculations for the same field strengths and a mobility-lifetime product of $3 \times 10^{-4} \text{ cm}^2/\text{V}$ (dotted curves) and $2 \times 10^{-8} \text{ cm}^2/\text{V}$ (dashed curves).

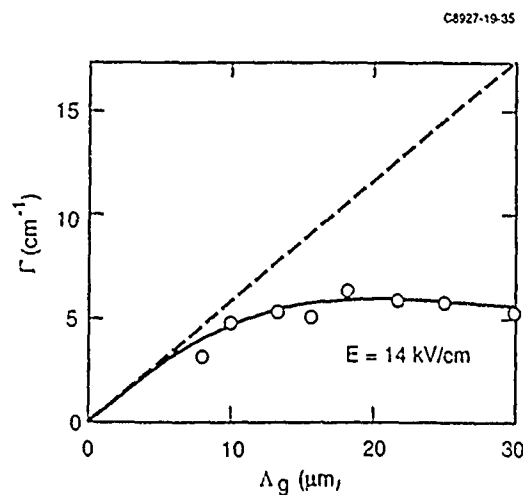


Fig.3: Measurements of beam coupling gain as function of grating period with a DC field of 14 kV/cm and a frequency shift applied to one of the beams. The frequency shift is chosen at each point to optimize the gain. Theoretical calculation are given for mobility-lifetime products of $3 \times 10^{-4} \text{ cm}^2/\text{V}$ (dashed line) and $5 \times 10^{-8} \text{ cm}^2/\text{V}$ (solid line).

The semi-insulating and photorefractive properties of the GaAs material used for our measurements are determined by the deep level defect EL2, which has a concentration of about 10^{16} cm^{-3} . The conduction band electrons responsible for both the photoconductivity and the charge transport that gives rise to the photorefractive effect are obtained by optical excitation from the EL2^0 level 0.76 eV below the conduction band. This excitation at 1.17 eV (1.06 μm) transfers the electrons in the L band (0.35 eV above the bottom of the Γ band), but with no applied field they relax (within a few picoseconds) to the bottom of the Γ valley where the effective mass [13] is $0.067 m_0$ (m_0 is the electron rest mass) and the mobility [2] about $5000 \text{ cm}^2/\text{V.s}$. In the presence of large electric fields, however, the effective temperature of the electrons increases [13] and up to 70 % of the electrons are in the L band where the effective mass is $0.55 m_0$ and the mobility about $100 \text{ cm}^2/\text{V.s}$. This leads to an effective mobility $\langle\mu\rangle$ of

$$\langle\mu\rangle = (n_{\Gamma}\mu_{\Gamma} + n_L\mu_L)/(n_{\Gamma} + n_L) = 0.3 \times 5000 + 0.7 \times 100 = 1570 \text{ cm}^2/\text{V.s}. \quad (4)$$

The electron capture cross-section σ_e of the EL2 defect also depends on the electric field. For $E_0 = 0$, σ_e is: [11]

$$\sigma_e = \sigma_{00} \exp(-E_b/kT) + \sigma_{n0} \quad (5)$$

with σ_{00} , σ_{n0} , and E_b given by $\sigma_{00} = 0.6 \times 10^{-14} \text{ cm}^2$, $\sigma_{n0} = 5 \times 10^{-19} \text{ cm}^2$ and $E_b = 0.066 \text{ eV}$; this gives at 300 K a value of $\sigma_e \sim 5 \times 10^{-16} \text{ cm}^2$. From its value and temperature dependance, it is inferred that the capture process at $E_0 = 0$ proceeds via nonradiative multiphonon emission [14]. On the other hand, at $E_0 = 10 \text{ kV/cm}$ Prinz and Rechkunov [14] measured a recombination cross section of $\sigma_e \sim 10^{-13} \text{ cm}^2$ at 300 K and found that the cross section increased with decreasing temperature, indicative of a cascade process.

Taken together, the reduced mobility ($5000 \rightarrow 1570 \text{ cm}^2/\text{V.s}$) and increased cross section ($5 \times 10^{-16} \rightarrow 10^{-13} \text{ cm}^2$) yield a decrease in the mobility-lifetime product of 1.6×10^{-3} compared to the zero field value. Our best fits to the data shown in Figs. 2 and 3 are obtained with a reduction of about 10^{-4} in the mobility-lifetime product, an agreement that we regard as satisfactory at this point because of both the difficulties in making the recombination cross section measurements and the simplifications and uncertainties involved in the photorefractive modelling.

In conclusion, the consideration of the electric field dependence of the EL2 properties provides a satisfactory explanation for the reduction by a factor 10^3 of the mobility lifetime product. This reduction is consistent with the mobility lifetime product inferred from photorefractive two beam coupling experiments.

References

1. A.M. Glass, A.M. Jonhson, D.H. Olson, W.Simpson and A.A.Ballman, Appl. Phys. Lett. 44, 948 (1984).
2. M.B.Klein, Opt. Lett. 9, 350 (1984)
3. G.Albanese, J.Kumar, and W.H.Steier, Opt. Lett. 11, 650 (1986).
4. J.Kumar, G.Albanese, W.H.Steier, J. Opt. Soc. Am. B, 4, 1079 (1987).
5. L-J.Cheng, G.Gheen, T.-H Chao, H.-K.Liu, A.Partovi, J.Katz, and E.M.Garmire, Opt. Lett. 12, 705 (1987)
6. B.Imbert, H.Rajbenbach, S.Mallick, J.P.Herriau, and J.P.Huignard, Opt. Lett. 13, 327 (1988).
7. M.B.Klein, S.W.McCahon, T.F.Bogges, and G.C.Valley, J. Opt. Soc. Am. B5, 2467 (1988).
8. G.C.Valley, J. Opt. Soc. Am. B1, 868 (1984).
9. J.Kumar, G.Albanese and W.Steier, Opt. Com. 63, 191 (1987).
10. S.I.Stepanov and M.P.Petrov, Opt. Com. 53, 292 (1985).
11. G.M. Martin and S. Makram-Ebeid, in *deep Centers in Semiconductors, a State-of-the-Art Approach*, S.T.Pantelides, e. (Gordon & Breach, New York, 1986) Chap.6, pp.399-487.
12. G.C.Valley, H.Rajbenbach and H.J.Bardeleben, submitted to Appl. Phys. Lett. (1989).
13. S.M.Sze, *Physics of Semiconductor Devices*, p.645-648, John Wiley and Sons, New York (1981).
14. V.Ya Prinz and S.N.Rechkunov, Phys. Stat. Sol. (b) 118, 159 (1983).
15. For a review see for example, *Photorefractive Materials and Their Applications*, P.Gunter and J.P.Huignard, eds (Springer Verlag, vol.61 and 62, Berlin 1989)

PART XIII

Doping in III-Vs

ELECTRON SCATTERING BY NATIVE DEFECTS IN UNIFORMLY AND MODULATION DOPED SEMICONDUCTOR STRUCTURES

W. WALUKIEWICZ

Center for Advanced Materials, Materials and Chemical Sciences Division, Lawrence Berkeley Laboratory, 1 Cyclotron Road, Berkeley, CA 94720

ABSTRACT

Formation of native defects in GaAs is described in terms of the amphoteric native defect model. It is shown that Fermi energy induced formation of gallium vacancies is responsible for the limitations of maximum free electron concentration in GaAs. The effect of the defects on electron mobility in heavily doped n-GaAs is quantitatively evaluated. Defect scattering explains the abrupt reduction of electron mobility at high doping levels. Also, it is demonstrated that native defects are responsible for the mobility reduction in inverted modulation doped GaAs/AlGaAs heterostructures. The amphoteric defect model also explains a distinct asymmetry in defect formation in n- and p-GaAs. In p-GaAs the Fermi level induced reduction of the defect formation energy is much smaller, and therefore the concentration of the native defects is negligible compared with the hole concentration.

I. INTRODUCTION

Native (or intrinsic) defects play a very significant role in determining electrical and optical properties of semiconductors. Numerous characteristics of semiconductor devices are critically affected by the presence of native defects introduced during crystal preparation and/or device fabrication. This issue is especially important in compound semiconductors where a large variety of different native defects can exist.

One of the long standing and poorly understood problems in semiconductors is the extent to which native defects affect free carrier mobilities. Carrier scattering by native defects is very often invoked to explain unusually low mobilities observed in semiconductor crystals. However, since in most cases the nature of the defects as well as their concentrations are not known, such explanations are only qualitative. A quantitative treatment would require a knowledge of the microscopic potential introduced by the defect as well as the concentration and distribution of the defects in the crystal. Dislocations were among the most extensively studied carrier scattering centers [1-4]. Both charged and neutral dislocations were considered in these early studies. In most cases, however, it was difficult to ascertain a detailed form of the potential necessary for a description of the scattering process. The situation is even more unclear in the case of scattering by point defects where both the microscopic nature of the defects and their concentrations are hardly ever known.

In this paper we present model calculations of the effects of native defects on carrier mobility in GaAs. We utilize the recently developed concept of amphoteric native defects [5,6] to calculate the concentration of ionized native defects in heavily doped GaAs crystals. We find a large difference in the defect formation in n- and p-type GaAs. This has important consequences for the limitations of free carrier concentration and carrier mobility in heavily doped material. We also consider the effect of native defects on electron and hole mobilities in modulation doped heterostructures. Free electron induced generation of native defects is found to be responsible for reduced two-dimensional electron-gas mobility in n-GaAs/AlGaAs inverted-modulation-doped-heterostructures. In normal-modulation-doped heterostructures mobilities are high because defect formation during epitaxy is not enhanced by free carriers.

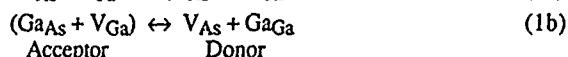
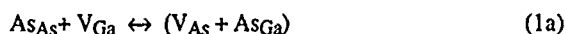
II. NATIVE DEFECTS IN HEAVILY-DOPED GaAs

It has been known for more than two decades that heavy doping of GaAs with donors to levels higher than $\sim 2 \times 10^{18} \text{ cm}^{-3}$ leads to a considerable reduction of the intensity of band edge luminescence [7,8]. The reduction of the luminescence intensity is always associated with the appearance of a broad luminescence line at about 1.2 eV [8]. Extensive annealing studies have

led to the conclusion that the center responsible for the deep luminescence is associated with Ga deficiency in the crystals. On the basis of these studies it has been proposed that the deep center is a donor-gallium vacancy complex (D-V_{Ga}) [9]. This identification of the deep center appears to be consistent with measurements of local vibrational mode absorption in Si-doped MBE grown GaAs, which indicates the presence of a large concentration of complexes with Si_{Ga} and an unidentified native defect on one of the next nearest neighbor sites [10]. Recent studies of MOCVD grown GaAs have confirmed that gallium deficiency promotes formation of the deep centers [11]. An increase in the concentration of deep centers is always associated with reduction of the concentration of electrically active donors [7,11] and electron mobility [11]. All these results are consistent with the assumption that the D-V_{Ga} complex is acting as a deep acceptor, compensating intentionally introduced donors and contributing to the electron scattering.

The doping induced formation of the deep centers in n-type GaAs can be contrasted with p-type material where it has been found that doping to the levels close to 10^{20} cm^{-3} does not significantly affect the band-edge luminescence [12]. Also, no prominent deep level luminescence is detected in p-type material [12]. This indicates that unlike in n-type GaAs, the acceptor doping does not induce the formation of compensating native defects. Such a conclusion is consistent with the very high electrical activity observed for acceptors in heavily doped p-GaAs [13].

In principle, a quantitative evaluation of the effects of native defects on free carrier concentration and/or carrier mobility requires a detailed knowledge of the defect formation energy. It has been shown recently that formation of native defects can be described in terms of the so-called amphoteric native defect (AND) model [5,6]. According to the model, incorporation of simple vacancy-like defects is controlled by the defect reactions



Both reactions involve a jump of a single atom between adjacent lattice sites. The most important feature of these reactions is that they lead to the transformation of an acceptor-like native defect (LHS of 1a and 1b) into a donor-like defect (RHS of 1a and 1b). Therefore one expects that the formation energy of the defects and directions of reactions (1a) and (1b) will depend on the location of the Fermi energy. Based on calculations of the total defect energies [14], one obtains in good approximation the formation energy of the defects given by reaction (1a):

$$E_f[D_{\pm}] = U_f^0 \pm 3E_F \quad (2)$$

where $D_{-} \equiv \text{V}_{\text{Ga}}$, $D_{+} \equiv (\text{As}_{\text{Ga}} + \text{V}_{\text{As}})$, E_F is the Fermi energy measured with respect to the Fermi level stabilization energy, i.e., the energy at which $E_f(D_{-}) = E_f(D_{+}) = U_f^0$. For reaction (1a) E_{FS} is located in the band gap at about 0.6 eV above the valence band edge [6].

The Fermi level stabilization energy E_{FS} plays a crucial role in the amphoteric native defect model. It is an energy reference to calculate the Fermi level induced reduction of the defect formation energy. The location of E_{FS} with respect to the conduction and the valence band edges determines the propensity of the semiconductor to form acceptor- or donor-like native defects, which compensate intentionally introduced shallow donors or acceptors, respectively. Since, as is seen from eq. (2) the defect formation energy strongly depends on the Fermi level position, one expects that defect incorporation will be strongly affected by the type of doping and the doping level.

In the following we consider reaction (1a), which corresponds to arsenic-rich conditions. It should be noted, however, that similar considerations are applicable to reaction (1b) as well. According to eq. (2) in n-type GaAs, $E_F > E_{FS}$ with:

$$[\text{V}_{\text{Ga}}] = C \exp\left(\frac{3E_F}{kT}\right) \quad (3)$$

where C' is a constant dependent on U_F^0 . The presence of triply ionized V_{Ga} acceptors reduces the free carrier concentration which is given by:

$$n = N_D^+ - 3[V_{Ga}] \quad (4)$$

where N_D^+ is the concentration of ionized shallow donors. A standard relationship between n and E_F is:

$$n = N_c F_{1/2} \left[(E_F - E_c) / kT \right] \quad (5)$$

Equation (5) completes the set of equations required to find $[V_{Ga}]$ and n as functions of the doping level N_D^+ . In eq. (5) E_c and N_c are the conduction band edge energy and the density of states, respectively, and $F_{1/2}(2)$ is the Fermi-Dirac integral.

In order to solve the set of equations 3 to 5 one needs to know the location of E_c with respect to E_{FS} at elevated temperatures. As has been discussed previously [15] the major contribution to temperature dependence of the energy difference $E_c - E_{FS}$ comes from the lattice dilation. It has been found [15] that $d(E_c - E_{FS})/dT = -1.7 \times 10^{-4}$ eV/K. Since the temperature coefficient of the GaAs energy gap is -4.8×10^{-4} eV/K one obtains the value of -3.1×10^{-4} eV/K for the temperature coefficient of the energy difference ($E_{FS} - E_v$).

In heavily doped semiconductors the location of the conduction (valence) band edge, E_c (E_v) is modified by Coulomb interactions so that $E_{c,v} = E_{c,v}^0 + \Delta E_{c,v}$. There are two contributions to the band edge shifts, $\Delta E_{c,v}$:

- i) the shift of the conduction band edge due to electron-electron interaction [16]

$$\Delta E_1 = -\frac{2e^2 k_F}{\pi \epsilon_0} - \frac{e^2 \lambda}{2\epsilon_0} \left[1 - \frac{4}{\pi} \tan^{-1} \left[\frac{k_F}{\lambda} \right] \right] \quad (6)$$

where the Fermi wave vector is given by the relation $k_F^3 = 3\pi^2 n$, $\lambda = 2e\hbar (3n/\pi)^{1/6} (m^*/\epsilon_0)^{1/2}$ is the Thomas-Fermi screening parameter, m^* is the electron hole effective mass at the Fermi energy, or $\epsilon_0 = 12.9$ is the static dielectric constant, and n is either the electron or hole concentration.

- ii) The second contribution to the band edge shifts comes from electron-ionized impurity interaction [16]

$$\Delta E_2 = -\frac{4\pi n e^2}{\epsilon_0 a_0 \lambda^3} = -\frac{e\hbar}{2} \left(\frac{\pi n}{\epsilon_0 m^*} \right)^{1/2} \quad (7)$$

where $a_0 = \epsilon_0 \hbar^2 / m^* e^2$ is the effective Bohr radius.

Using eqs. (6) and (7) one can calculate the location of E_c and E_v with respect to E_{FS} , and then with the help of eq. (5) determine the location of the Fermi energy as a function of electron or hole concentration. The results of the calculation are presented in fig. 1. The calculations were performed for $T=900$ K, which is the temperature typical for the MBE growth of GaAs. It is seen from fig. 1 that for low electron (hole) concentration, E_F is determined by the intrinsic concentration and located at about 0.3 eV above E_{FS} . In n-type GaAs E_F moves upward in energy and at $n=10^{19}$ cm $^{-3}$, it reaches the value of ~ 0.8 eV. This rapid shift of the Fermi level in n-type GaAs can be contrasted with a much slower dependence of E_F on the hole concentration. As is shown in fig. 1, even at the highest hole concentrations $\sim 10^{21}$ cm $^{-3}$ ($E_{FS} - E_F$) is smaller than 0.6 eV. The asymmetry in the Fermi level behavior in

n- and p-type GaAs has important consequences for the relative abundance of native defects in the two types of materials.

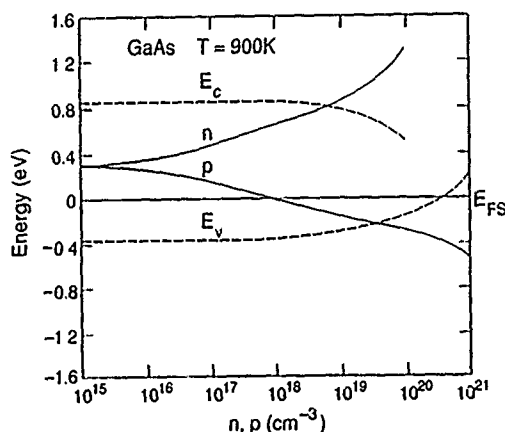


FIG. 1. Fermi energy, measured with respect to E_{FS} , as a function of free carrier concentration in n- and p-type GaAs (solid lines). Renormalized conduction (E_c) and valence (E_v) band edges are also shown.

It has been known from extensive studies [17,20] of GaAs that there is a limit on the maximum electron concentration which can be achieved by doping with shallow donors. Independently of the doping technique the portion of electrically active donors is considerably reduced for the doping level, exceeding about 10^{18} cm^{-3} . This reduction of electrical activity is not strongly dependent on the donor species and is very similar for amphoteric donors, such as Si and Sn, and for group VI donors S, Se, etc. This phenomenon can be easily understood within the amphoteric concept of Fermi-level induced formation of native defects.

To calculate the donor activation efficiency in GaAs we solve eqs. 3 to 5 to obtain $n(N_D^+)$. Fig. 2 shows the results of such calculations. It is seen that at low doping levels, when $[V_{Ga}]$ is small, $n=N_D^+$ and all donors are electrically active. With increasing doping levels an upward shift of the Fermi energy lowers the formation energy of $[V_{Ga}]$, which compensates shallow donors. This leads to a sublinear dependence in $n(N_D^+)$. At high doping levels one obtains $n \sim (N_D^+)^{1/3}$. The characteristic 1/3 power dependence reflects the fact that the compensating native defects are triply ionized acceptors. The calculations are in reasonably good agreement with experimental data on the activation of Se [17] and S [18] in GaAs.

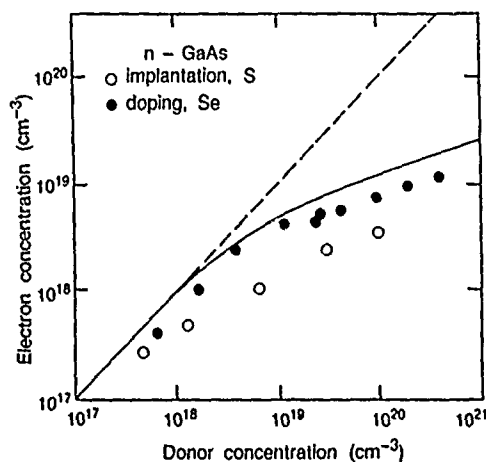


FIG. 2. Calculated electron concentration as a function of donor concentration in n-GaAs (solid line). Dashed line represents the case where all donors are electrically active. Experimental data was taken from Ref. 17 (Se) and Ref. 18 (S).

One can compare this with the case of p-type GaAs where it is known that shallow acceptors exhibit high activation efficiency even for very high doping levels exceeding 10^{20} cm^{-3} [13]. This is consistent with our present model since as is seen in fig. 1 holes produce a much smaller shift of the Fermi energy away from E_{FS} . Thus, for a hole concentration of about 10^{20} cm^{-3} $|E_{FS}-E_F|$ is less than half of the value of $|E_F-E_{FS}|$ in n-type GaAs, with the hole concentration of 10^{18} cm^{-3} .

III. ELECTRON AND HOLE MOBILITIES IN UNIFORMLY-DOPED GaAs

We have argued above that at high doping levels in n-type GaAs gallium vacancies compensate intentionally introduced donors. Since both compensating defects and donors are acting as ionized scattering centers, one expects that the increased incorporation of V_{Ga} will affect the electron mobility.

Calculations of electron mobility in n-GaAs are performed adopting standard procedure based on the variational solution of the Boltzman equation [21]. At high doping levels the electron mobility is largely determined by charged center scattering with a small contribution from the phonon scattering. The inverse electron mobility is

$$\mu^{-1} = \mu_{cc}^{-1} + \mu_{ph}^{-1} \quad (8)$$

where μ_{ph} is the room temperature phonon mobility limit $\sim 8500 \text{ cm}^2/\text{V} \cdot \text{s}$.

The mobility of electrons scattered by charged centers is [22]

$$\mu_{cc} = \frac{3\pi}{2} \frac{\epsilon_0^2 \hbar^3}{e^3} \frac{n}{N_{cc} m^{*2} F_{cc}} \quad (9)$$

where $F_{cc} = \ln(\xi + 1) - \frac{\xi}{\xi + 1}$ and $\xi = 2k_F/\lambda$, and N_{cc} is the total concentration of

scattering centers. The nonparabolicity of the conduction band has been incorporated in the calculation via an energy dependent effective mass m^* [23]. Such an approach slightly overestimates the nonparabolicity effects by neglecting mixing of the valence and conduction band wavefunctions [22].

The concentration of the scattering centers N_{cc} depends not only on N_D^+ and V_{Ga}^{3-} , but also on their distribution in the crystal lattice. Thus, as has been discussed in the previous section, the positively charged donors tend to form complexes with negatively charged V_{Ga} [10,24]. Since such complexes act as doubly-charged centers, the total concentration of scattering centers is

$$N_{cc} = N_D^+ + 3[V_{Ga}] \quad (10)$$

The concentration of V_{Ga} was determined using eqs. 2 to 5. The calculations of the electron mobility, μ , were carried out using expression (10) for the concentration of charged scattering centers. The results of the calculations along with the experimental data on electron mobility in MBE grown n-GaAs [25,26] are shown in fig. 3. A rapid decrease of the electron mobility can be explained quantitatively by native defect scattering, assuming $U_i^0 = 3.5 \text{ eV}$ for the formation energy of $[V_{Ga}]$ in eq. (2). The calculations also show that contrary to previous suggestions [25], the nonparabolicity effects are not very significant and cannot explain the abrupt decrease of the electron mobility. As is seen in fig. 3, conductivity in n-GaAs reaches a maximum value of about $2.4 \times 10^3 \Omega^{-1} \text{ cm}^{-1}$ at $n \sim 1 \times 10^{19} \text{ cm}^{-3}$. This appears to be a basic limit of electrical conductivity achievable in n-GaAs.

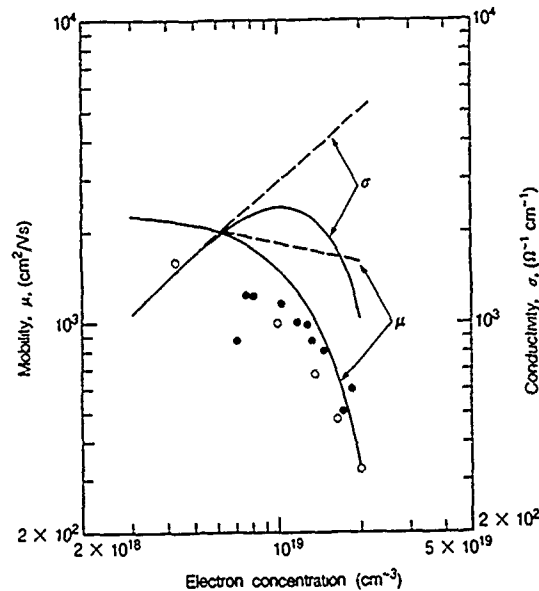


FIG. 3. Electron mobility and conductivity in heavily doped n-GaAs. The solid lines represent the calculations in which effects of native defects were included. The broken curves correspond to the standard case in which the concentration of charged scattering centers is equal to the carrier concentration. The experimental points represent the data of Ref. 25 (○) and Ref. 26 (●).

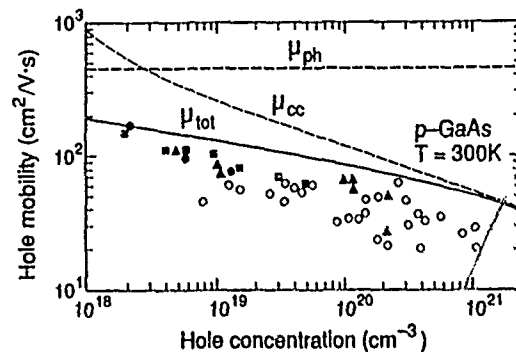


FIG. 4. Hole mobility in heavily doped p-GaAs. μ_{ph} and μ_{cc} are the mobilities due to phonon and charged center scattering, respectively. The combined hole mobility is represented by μ_{tot} . The experimental data for C (○ Ref. 13) and Be (●-Ref. 13, □-Ref. 28, ▲-Ref. 29) doped GaAs is also shown.

Examination of the results in figs. 2 and 3 shows that the effects of $[V_{Ga}]$ on the free electron concentration and mobility are becoming noticeable for electron concentration $n \approx 3$ to $5 \times 10^{18} \text{ cm}^{-3}$. We find from fig. 1 that in n-GaAs this corresponds to $|E_F - E_{FS}| \approx 0.7 \text{ eV}$. In p-GaAs the value of $|E_F - E_{FS}|$ is much smaller and does not reach this level even for the highest hole concentration of 10^{21} cm^{-3} . This indicates that the concentration of the native donor ($As_{Ga} + V_{As}$) defect is always negligible compared with the free carrier concentration. This explains why acceptors show a much higher activation efficiency in GaAs. Also, it suggests that the contribution of the native defects to hole scattering should be negligible.

To test this suggestion we have calculated the hole mobility in p-GaAs. We use a model of partially coupled valence bands [27]. In this model the intra- and inter-band scatterings are included to calculate light- and heavy-hole mobilities. The mobilities are then combined in a standard way to obtain Hall mobility [27], which can be compared with experiments. The results of the calculations are shown in fig. 4. It is seen that at room temperature the phonon mobility limit is about $450 \text{ cm}^2/\text{V}\cdot\text{s}$. This value of the mobility is determined mostly by the deformation potential and the polar optical phonon scatterings. The contribution of acoustic phonons is relatively insignificant. We have also calculated the mobilities resulting from scattering by charged centers. Assuming that the concentration of charged centers is equal to the

concentration of free holes, one finds that μ_{cc} depends very weakly on the hole concentration. For $p \geq 10^{19} \text{ cm}^{-3}$ one finds $\mu_{cc} \sim p^{-1/3}$. This is the same dependence as that found for the mobility in heavily doped, uncompensated n-GaAs. It is also seen in fig. 4 that this weak dependence of the mobility on the hole concentration correctly predicts the experimentally observed mobilities for samples in a very wide concentration range [13,28,29]. This again confirms our finding that native defects do not play any significant role in p-GaAs. Discrepancies between the experimental and theoretical mobilities at very high hole concentrations can be attributed to the limitation of our model calculations which do not properly account for the anisotropy and energy dependence of the valence band effective masses at very high doping levels.

IV. ELECTRON MOBILITY IN MODULATION DOPED HETEROSTRUCTURES

In the case of uniformly doped n-type GaAs, the native defects are formed in heavily doped regions containing high concentrations of electrons and ionized impurities. However, since the formation of the defects is controlled by the Fermi energy, which depends on the electron concentration only, one can also expect an enhancement of defect formation in the systems in which electrons are separated from the impurities. Excellent examples of such systems are modulation doped heterostructures (MDH) [30], in which electrons confined in the quantum well are spatially separated from donors located in the barrier [31]. There are two kinds of MDHs [32]. In a normal-MDH (N-MDH), the undoped, well-forming layer is grown prior to the heavily doped barrier, whereas in an inverted-MDH (I-MDH), the heavily doped barrier is grown first followed by the undoped quantum well-forming layer. The basic difference between those two types of heterostructures is that in I-MDH the nominally undoped well is grown in the presence of a high concentration of free electrons transferred from the barrier forming layer. In N-MDH the electrons are transferred after the well is fully grown. Early studies of charge transport in AlGaAs/GaAs MDHs have shown that electron mobilities in I-MDH are always significantly lower than those in N-MDHs [32]. There were several attempts to explain this phenomenon either in terms of interface roughness [32] or impurity diffusion [33,34]. Here we show that the difference in the mobility values in these two structures can be understood easily in terms of the increased scattering by native defects formed in I-MDH.

In I-MDH the GaAs well is grown in the presence of electrons transferred from the AlGaAs barrier. This leads to the situation where $E_F \gg E_{FS}$, i.e., a condition which favors the formation of native defects. Such defects act as electron scattering centers. To estimate the effect of the defects on electron mobility we consider I-MDH with 2D electron gas density n_{2D} . The equivalent 3D density in the quantum well is $n = n_{2D}/W$, where $W = 2(n^2 \epsilon_0 / 33\pi e^2 m^* n_{2D})^{1/3}$ is an effective width of the triangular quantum well [35]. The concentration of V_{Ga} is calculated using eqs. 3 to 5. For a typical I-MDH with $n_{2D} = 5 \times 10^{11} \text{ cm}^{-2}$ we obtain $[V_{Ga}] \approx 6 \times 10^{14} \text{ cm}^{-3}$. Here we use the same value of the parameter $U_i^0 = 3.5 \text{ eV}$ as the one determined for uniformly doped GaAs. Since the free electron concentration is much lower than in the case of uniformly doped GaAs, we can neglect the conduction band edge renormalization given by eqs. (6) and (7). The concentration of V_{Ga} in I-MDH is much lower than the free carrier concentration, therefore, the compensating effect of the defects is negligible. However, since in MDH, charged impurities are spatially separated from the electrons, the presence of even this small concentration of charged native defects in the quantum well can very significantly affect the 2D-electron gas mobility.

The electron mobility has been calculated using the method presented in Ref. 36. Acoustic and optical phonons, alloy disorder, remote and background charged center scattering are included in the calculations. Since the native defects are located in the quantum well they contribute to the background charged center scattering. The results presented in fig. 5 were obtained for the calculated concentration of V_{Ga} equal to $6 \times 10^{14} \text{ cm}^{-3}$. This corresponds to a background concentration of charge scattering centers of $5.4 \times 10^{15} \text{ cm}^{-3}$. It is seen in fig. 5 that this low concentration of native defects very profoundly affects the mobility. The low temperature mobility in a I-MDH is about an order of magnitude lower than the mobility in an equivalent N-MDH in which background defect scattering is negligible. This is in general agreement with experimental data which show that mobilities in N-MDH are considerably higher than those measured in a I-MDH. Lower mobilities in AlGaAs/GaAs I-MDH were previously explained by assuming additional scattering by charged centers located at the interface [37]. Without elaborating on the nature of the charged centers the authors of Ref. 37 concluded that

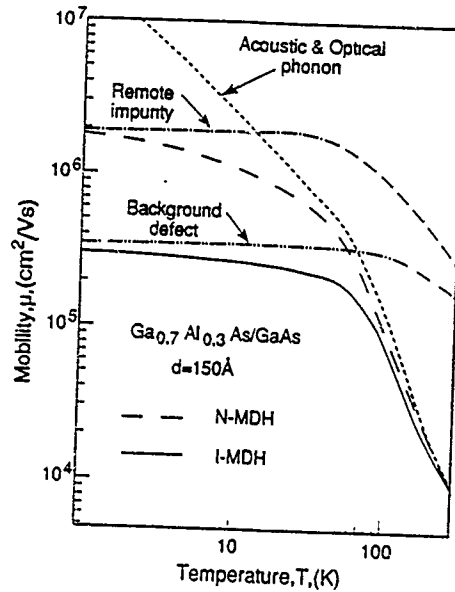


FIG. 5. Temperature dependent 2D-electron gas mobilities in $\text{Al}_{0.3}\text{Ga}_{0.7}\text{As}/\text{GaAs}$ MDHs with the spacer width $d = 150\text{\AA}$. The broken and solid lines represent electron mobilities in normal- and inverted-MDHs, respectively. Contributions to the total mobilities resulting from different scattering mechanisms are also shown.

the interface charge density required to account for the experimental data has to be in the range $5 \times 10^9 \text{ cm}^{-2}$ to $3 \times 10^{10} \text{ cm}^{-2}$. Since there is a great similarity between interface charge and background charge scatterings [36,38], the results of ref. 37 can be interpreted also in terms of scattering by background charged defects uniformly distributed in the well. The equivalent concentration of the background charges is $5 \times 10^{15} \text{ cm}^{-3}$ to $3 \times 10^{16} \text{ cm}^{-3}$. It should be noted that our estimate of the effective charged center concentration of $N_{cc} = 5.4 \times 10^{15} \text{ cm}^{-3}$ lies in this concentration range.

In the present calculations we have assumed $n_{2D} = 5 \times 10^{11} \text{ cm}^{-2}$, which is a typical concentration of 2-D electron gas in $\text{GaAs}/\text{AlGaAs}$ MDH. A more detailed analysis of the native defect formation in I-MDH would require a proper description of the charge transfer from doped AlGaAs to the GaAs quantum well at the growth temperature. Such an analysis can be easily done for a specific structure with known doping levels and spacer width. The single most important factor controlling defect formation is the location of the Fermi energy in 2-D quantum wells. Therefore, the strategy to obtain an I-MDH with a low defect concentration is to lower the doping level and thus also the concentration of 2-D electron gas. Recently, a new type of I-MDH has been devised [39] which consists of an undoped $\text{GaAs}/\text{AlGaAs}$ superlattice and a thick undoped GaAs layer. The electrons in the quantum well originate from planar doping in GaAs at a distance of 2500\AA away from the quantum well. It has been shown that the 2-D electron concentration can be controlled by the gate voltage and mobilities as high as $2 \times 10^6 \text{ cm}^2/\text{V}\cdot\text{s}$ can be achieved in such a structure. This result provides strong support for our explanation of the lower mobilities in I-MDH. In this new structure the GaAs quantum well is grown without any electrons present. Therefore, it resembles the case of N-MDH where the doping is performed only after the well is fully grown.

All the above considerations apply to n-type $\text{AlGaAs}/\text{GaAs}$ MDHs in which there is a substantial Fermi level induced reduction of the defect formation energy. As has been shown in section II, there is no significant reduction of the defect formation energy in p-type GaAs . Therefore, one does not expect any difference in the native defect scattering in p-type I-MDH and N-MDH. This provides an opportunity to differentiate the effects of native defect scattering from other scattering mechanisms [33,34] which were suggested to be responsible for lower mobilities in I-MDHs. Unlike the native defect scattering, the effectiveness of scattering processes due to interface roughness [33] and scattering by impurities diffusing from the heavily doped region [34] into the well, does not depend on the type of doping and therefore they should play an equally important role in p- and n-type MDHs. Unfortunately, to our knowledge, no comparative studies of mobilities in inverted and normal p-type $\text{AlGaAs}/\text{GaAs}$ MDHs have been reported.

Besides the extensive studies of AlGaAs/GaAs MDHs, much information is available on InP/InGaAs MDHs. In the well-forming $\text{In}_{0.47}\text{Ga}_{0.53}\text{As}$ layer, the Fermi level stabilization energy $E_{\text{FS}} \approx E_c - 0.25 \text{ eV}$ is located close to the conduction band edge. Thus, for the typical carrier concentration the effect of the Fermi level induced defect formation is very small. Consequently, one does not expect any difference in the mobility values in I-MDH and N-MDH. This conclusion is in agreement with results of a recent study [40] which has shown that practically the same mobilities are observed in inverted and normal InP/InGaAs MDHs. This again indicates that, at least in this system, the interface roughness and impurity diffusion effects appear not to be important.

CONCLUSIONS

The model of amphoteric native defects has been used, in recent years, to understand a large variety of phenomena in semiconductors [6] and at metal-semiconductor interfaces [5]. The most important feature of the model is that it provides the basis for a quantitative analysis of the native defect formation process. The incorporation of native defects is controlled by the location of the Fermi level measured with respect to the Fermi level stabilization energy, E_{FS} . Therefore, the location of E_{FS} with respect to the band edges determines how the native defect formation process depends on the type of doping and the doping level.

It has been shown previously that the model accounts well for the Schottky barrier heights at metal-semiconductor interfaces and explains pinning of the Fermi level by native defects during metal deposition on a semiconductor surface [5]. The Fermi level dependent formation of native defects has been used to explain the doping enhanced superlattice intermixing [6,41] and saturation of the free carrier concentration in semiconductors [6]. Also, an analysis of the effects of doping on supersaturation of native defects has provided the basis for a semi-quantitative treatment of the long-standing and controversial issue of doping induced suppression of dislocation formation in semiconductors [42,43].

In this paper we have demonstrated that within the same concept of amphoteric defects, one can calculate the contribution of native defects to carrier scattering. In particular, the calculations indicate that the abrupt reduction of electron mobility in heavily doped n-GaAs results from the Fermi-level induced formation of ionized gallium vacancies.

An interesting case is represented by modulation doped heterostructures in which electrons are spatially separated from the parent donors. The native defects are formed in the quantum well. There they act as very efficient scattering centers and play a dominant role in limiting the electron mobility in GaAs/AlGaAs inverted-modulation doped heterostructures.

It is found that there is a distinct asymmetry in defect formation in n- and p-GaAs. Even in very heavily doped p-GaAs the reduction of the defect formation energy and thus also an enhancement of the defect concentration is small and does not produce any of the effects observed in n-GaAs. Although the present considerations were limited to GaAs based systems, the concept of amphoteric native defects has a much broader scope. The known location of E_{FS} can be used, in principle, to describe the formation of defects in any semiconductors and semiconductor structures.

ACKNOWLEDGEMENTS

The author would like to thank E.E. Haller for useful discussions and comments. This work was supported by the Director, Office of Energy Research, Office of Basic Energy Sciences, Materials Science Division, of the U.S. Department of Energy under Contract No. DE-AC03-76SF00098.

REFERENCES

- [1] G.L. Pearson, W.T. Read and F.J. Morin, *Phys. Rev.* **93**, 666 (1954).
- [2] W.T. Read, *Phil. Mag.* **46**, 111 (1955).
- [3] V.L. Bonch-Bruyevich and V. Glasko, *Sov. Phys. Sol. State* **3**, 26 (1961).
- [4] F. Düster and R. Labusch, *Phys. Stat. Solidi (b)* **60**, 151 (1973).
- [5] W. Walukiewicz, *J. Vac. Sci. Technol. B* **6**, 1357 (1988).

- [6] W. Walukiewicz, Appl. Phys. Lett. **54**, 2094 (1989).
- [7] C.J. Hwang, J. Appl. Phys. **40**, 1983 (1969).
- [8] C.J. Hwang, J. Appl. Phys. **40**, 4584 (1969).
- [9] E.W. Williams, Phys. Rev. **68**, 922 (1968).
- [10] J. Maguire, R. Murray, R.C. Newman, R.B. Beall and J.J. Harris, Appl. Phys. Lett. **50**, 516 (1987).
- [11] T. Lideikis and G. Treideris, J. Cryst. Growth **96**, 790 (1989).
- [12] Y. Okano, H. Seto, H. Katahama, S. Nishine, I. Fujimoto and T. Suzuki, Jap. Jour. Appl. Phys. **28**, 6151 (1989).
- [13] Y. Yamada, E. Tokumitsu, K. Saito, T. Akatsuka, M. Miyauchi, M. Konagai and K. Takahashi, J. Cryst. Growth **95**, 145 (1989).
- [14] G.A. Baraff and M. Schlüter, Phys. Rev. Lett. **55**, 1327 (1985).
- [15] W. Walukiewicz, Proceedings of the MRS Symposium, San Diego CA, 1989, to be published.
- [16] K.F. Berggren and B.E. Sernelius, Phys. Rev. **B24**, 1971 (1981).
- [17] L.J. Vieland and J. Kudman, J. Phys. Chem. Solids **24**, 437 (1963).
- [18] F. Sette, S.J. Pearton, J.M. Poate, and J.E. Rowe, Nucl. Instrum. Methods **B19/20**, 408 (1987).
- [19] M. Heiblum, W.I. Wang, L.E. Osterling and V. Deline, J. Appl. Phys. **54**, 6751 (1983).
- [20] E.M. Omelyanovskii and S.P. Grishina, Sov. Phys. Semicon. **1**, 813 (1968).
- [21] W. Walukiewicz, J. Lagowski, L. Jastrzebski, M. Lichtensteiger and H.C. Gatos, J. Appl. Phys. **50**, 889 (1979).
- [22] see e.g. W. Zawadzki, in Handbook on Semiconductors, edited by W. Paul (North Holland Publ., 1982) Vol 1, p. 713.
- [23] J.S. Blakemore, J. Appl. Phys. **53**, R123 (1982).
- [24] J.K. Kung and W.J. Spitzer, J. Appl. Phys. **45**, 4477 (1974).
- [25] R. Sacks and M. Shen, Appl. Phys. Lett. **47**, 374 (1985).
- [26] H. Ito and T. Ishibashi, Japan. J. Appl. Phys. **27**, L707 (1988).
- [27] W. Walukiewicz, L. Pawlowicz, J. Lagowski, and H.C. Gatos, Proc. of the Conf. on Semi-Inst III-V Materials, Evian 1982, edited by Sherif Makram-Ebeid and Brian Tuck (Shiva Nantwich, U.K., 1982) p. 121.
- [28] M. Hegems, J. Appl. Phys. **48**, 1278 (1977).
- [29] R. Mellet, R. Azoulay, L. Dugrand, E.V.K. Rao, and A. Mircea, Inst. Phys. Conf. Ser. **63**, 583 (1982).
- [30] R. Dingle, H.L. Störmer, H.C. Gossard and W. Wiegmann, Appl. Phys. Lett. **33**, 665 (1978).
- [31] L.C. Witkowski, T.J. Drummond, C.M. Stanchok and H. Morkoc, Appl. Phys. Lett. **37**, 1033 (1980).
- [32] H. Morkoc, T.J. Drummond and R. Fisher, J. Appl. Phys. **53**, 1030 (1982).
- [33] L. Gonzalez, J.B. Clegg, D. Hilton, J.P. Growers, C.T. Foxon and B.A. Joyce, Appl. Phys. **A41**, 237 (1986).
- [34] S. Sasa, J. Saito, K. Nanbu, T. Ishikawa and S. Hiyamizu, Japan. J. Appl. Phys. **23**, L573 (1984).
- [35] F.F. Fang and W.E. Howard, Phys. Rev. Lett. **16**, 797 (1966).
- [36] W. Walukiewicz, H.E. Kuda, J. Lagowski, H.C. Gatos, Phys. Rev. **B30**, 4571 (1984).
- [37] U. Meirav, M. Heiblum and F. Stern, Appl. Phys. Lett. **52**, 1268 (1988).
- [38] K. Hess, Appl. Phys. Lett. **35**, 484 (1979).
- [39] T. Sajoto, M. Santos, J.J. Heremans, M. Shayegan, M. Heiblum, M.V. Weckwerth, and U. Meirav, Appl. Phys. Lett. **54**, 840 (1989).
- [40] D. Grützmacher, R. Meyer, P. Balk, C. Berg, T. Schäpers, H. Lüth, M. Zachau and F. Koch, J. Appl. Phys. **66**, 697 (1989).
- [41] T.Y. Tan and U. Gösele, J. Appl. Phys. **61**, 1841 (1987).
- [42] W. Walukiewicz, Phys. Rev. **B39**, 8776 (1989).
- [43] W. Walukiewicz, Appl. Phys. Lett. **54**, 2009 (1989).

ACCEPTOR DELTA-DOPING IN GaAs

W. S. Hobson*, S. J. Pearton*, C. R. Abernathy* and G. Cabaniss**

*AT&T Bell Laboratories, 600 Mountain Ave, Murray Hill, NJ

**Solecon Laboratories, San Jose CA.

ABSTRACT

We have investigated the formation and diffusion of delta-doped layers in GaAs employing the acceptors Zn, Cd, and C. Organometallic Vapor Phase Epitaxy was used for the growth of the Zn and Cd δ -doped layers while Metalorganic Molecular Beam Epitaxy was utilized to achieve C δ -doping. The narrowest atomic profiles for Zn had full width at half maxima of 80 Å for peak Zn concentrations of $\leq 3 \times 10^{18} \text{ cm}^{-3}$, as measured by SIMS. An effective diffusion coefficient of $\leq 7 \times 10^{17} \text{ cm}^2/\text{s}$ is estimated for a growth temperature of 625°C, based on multiple Zn δ -doped layers. For carbon, a doping spike of $7 \times 10^{19} \text{ cm}^{-3}$ with a full width at half maximum of 50 Å, as measured by electrochemical capacitance voltage profiling, was achieved and represents the highest doping level yet reported for planar doping. By contrast, it was difficult to achieve doping levels $\geq 4 \times 10^{17} \text{ cm}^{-3}$ for Cd due to its high vapor pressure.

INTRODUCTION

GaAs device technology will require increasingly stringent control over the spatial distribution of dopant atoms within the device structure. The limit of such localization occurs when the dopants are confined to a few atomic planes, so-called atomic-planar doping or δ -doping.⁽¹⁻³⁾ This concept was first demonstrated by Wood et al.⁽⁴⁾ using Ge doping of GaAs by molecular beam epitaxy. Subsequently most attention has been focussed on n-type impurities, especially Si which is the most common donor dopant in GaAs⁽⁵⁻¹²⁾. Much less attention has been paid to δ -doping with p-type dopants. Kobayashi et al.⁽¹³⁾ reported the growth of narrow (58 Å) carrier profiles using C acceptors by flow-rate modulation epitaxy⁽¹³⁾. Peak carrier concentrations of $2 \times 10^{18} \text{ cm}^{-3}$ were obtained, and the C diffusion coefficient was estimated to be $\sim 2 \times 10^{-16} \text{ cm}^2 \cdot \text{s}^{-1}$ at 800°C, a very low value for a p-type impurity in GaAs. The spatial control of the other acceptor dopants is expected to be a much more challenging problem because of their rapid, concentration-dependent diffusivities. We report here an investigation of Zn and Cd δ -doping by organometallic vapor phase epitaxy (OMVPE), and C δ -doping by metalorganic molecular beam epitaxy (MOMBE).

EXPERIMENTAL

All of the Zn and Cd δ -doped GaAs layers were grown in a barrel-type OMVPE reactor operated at atmospheric pressure. Ultra-high purity helium was used as the carrier gas. Trimethylgallium (TMGa), diethylzinc (DEZn) or dimethylcadmium (DMCd), and arsine were employed as the source reagents. Growth temperatures of 575°C to 625°C were utilized. Mole fraction ratios of AsH₃ to TMG were varied from 37 to 174. For the majority of the growth runs the growth rate was 260 Å min⁻¹. Typically, 2000 Å of GaAs was deposited on (100) or 2° off (100) oriented p⁺ and semi-insulating GaAs substrates. The δ -doped layer was then formed as follows. First, the TMG was switched to the vent line, stopping growth for 10s. This was followed by introducing the DEZn (or DMCd) for durations of 5 to 60s, and then switching back to vent, allowing 10s before resuming growth of an additional 1000 Å. Multiple δ -doped layers were also grown in a similar fashion.

The carbon δ -doped samples were grown in a Varian Gas-Source Gen II MOMBE System. Triethylgallium (TEGa) and As₄ were used for the growth of undoped GaAs while TMGa was utilized as the C dopant precursor. The growth temperature was 500°C as measured by the substrate thermocouple and typical growth rates were 0.7 - 1.5 $\mu\text{m/hr}$. TEGa was introduced into the chamber by means of a hydrogen carrier gas while the TMGa was transported by helium.

RESULTS AND DISCUSSION

The results obtained from electrochemical capacitance-voltage (ECV) profiling of two multiple Zn δ -doped samples are given in Figure 1. One of the samples consisted of a staircase structure with each δ -doped layer being formed by varying the Zn pulse durations while the other utilized identical δ -doping times for all four layers. A growth temperature of 625°C, a V/III ratio of 37, and a growth rate of 260 Å min⁻¹, were used for both samples. For the staircase structure, maximum hole concentrations, P_{\max} , of 2.3×10^{17} cm⁻³ at 950 Å, 9.6×10^{17} cm⁻³ at 1930 Å, 2.8×10^{18} cm⁻³ at 2950 Å, and 2.5×10^{18} cm⁻³ at 3880 Å were determined. As expected, P_{\max} increased with longer pulse durations and reached a saturation value of $\leq 3 \times 10^{18}$ cm⁻³ for this particular growth temperature. While not studied in detail, it is suggested that P_{\max} is limited by the vapor pressure of Zn or ZnAs_x species on the GaAs surface. Furthermore, the length of time allowed to purge the DEZn from the reactor should also effect P_{\max} , since this may allow evaporation of the dopant species from the surface.

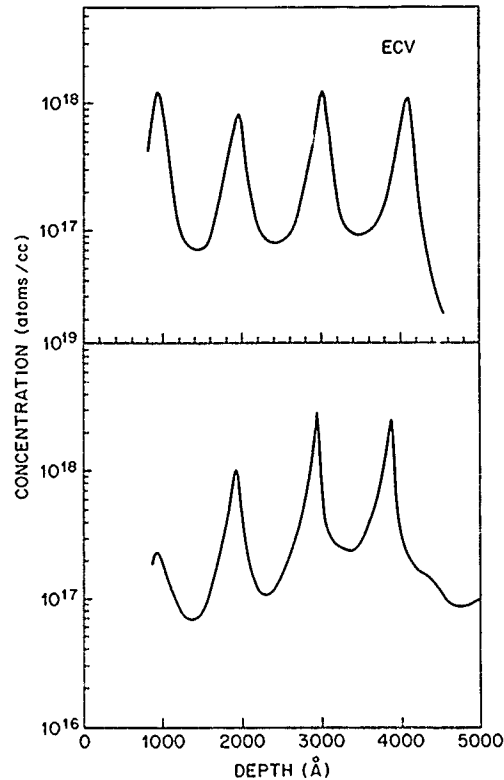


Figure 1 Electrochemical C-V profile of a multiple Zn δ -doped sample with pulse durations of 5, 15, 30 and 60s (bottom) and a sample with four identical pulse durations of 15s (top).

The multiple δ -doped sample with four identical pulse durations of 15s exhibited P_{\max} values of 1.3, 0.82, 1.2, and 1.0×10^{18} cm⁻³ at 960 Å, 1970 Å, 3020 Å, and 4080 Å, respectively. The full width of half maximum (fwhm) of each peak was 150 Å, 205 Å, 160 Å, and 170 Å, respectively. To be noted is the similar fwhm and P_{\max} of each peak, within the experimental error associated with the measurements and the growth conditions. These results can be compared with the SIMS data, given in Figure 2, where maximum values of total Zn concentration of 1.8, 1.4, 1.8, and 1.8×10^{18} cm⁻³ at 930 Å, 1860 Å, 2860 Å, and 3800 Å were obtained, in good agreement with the electrical results. The fwhm of each peak is nearly identical at ~80 - 90 Å. Concentration scales for the SIMS data were obtained from comparison with ion-implanted standards run under the same profiling conditions. The depth scales were

obtained from direct stylus profilometry of the sputtered SIMS crater. The difference in the absolute magnitudes of P_{\max} and FWHM between the SIMS and ECV measurements is due to Debye broadening occurring for the low Zn concentration on the sides of the ECV carrier peaks. Consequently, the SIMS values are assumed to represent the upper limit of the diffusion during growth. Since the instrumental resolution of the SIMS was $\leq 30\text{\AA}$, the Zn dopant atoms are seen to be limited to a few atomic planes. The SIMS and ECV results are consistent in that negligible diffusion occurs after the formation of the δ -doped layers. An estimate of the upper limit to the diffusion coefficient will be presented below.

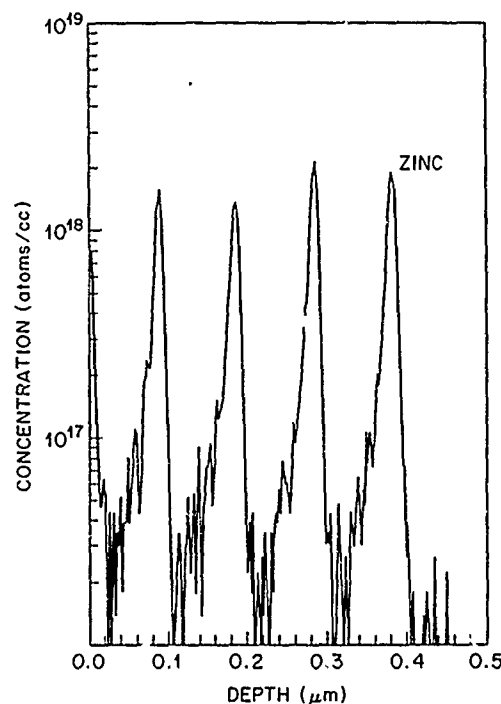


Figure 2 SIMS profile for a multiple δ -doped sample with four identical pulse durations of 15s.

The fwhm of the as-grown peaks include contributions from several factors such as diffusion during subsequent growth, the dopant memory effect, and segregation of the dopant. It is also possible that diffusion can be enhanced while exposing the GaAs surface to the dopant or during the initial stages of growth of the top layer. An indication of these effects can be seen in the half-width at half maximum for the leading and trailing slopes of the peaks. In Fig. 1(top), the average hwhm of the four peaks in the ECV profile on the trailing side was 75\AA while that on the leading side was 95\AA . A memory effect, whereby the dopant desorbs from the reactor walls after termination of the Zn pulse, could explain this asymmetry. Consequently, in order to study bulk diffusion it is necessary to anneal as-grown samples and to examine the broadening of the fwhm. The mean penetration depth of the diffusant can be defined as the difference in the half width at half maximum (hwhm) of the annealed and as-grown samples.⁽⁶⁾ The effective diffusion coefficient, D , can be related to the mean penetration depth Z by $D = (Z/2)^2 \pi/t$, where t is the annealing time.⁽¹⁴⁾ Presented in Fig. 3 are SIMS profiles for a single δ -doped layer annealed at temperatures of 700°C , 800°C , 900°C , or 950°C for 5s using proximity annealing in a SiC-coated graphite susceptor within an RTA system. A pulse duration during growth of 60s was used with other conditions remaining the same as for the previously discussed samples. The fwhm of the annealed samples were 150\AA , 210\AA , 530\AA , and 540\AA and the maximum Zn concentrations, Zn_{\max} , were 5.5, 2.4, 1.2, and 0.8.

respectively. A fwhm of 100\AA and Zn_{max} of $2.2 \times 10^{18} \text{ cm}^{-3}$ were obtained for the as-grown sample. The results are fairly consistent except that the as-grown Zn_{max} is somewhat lower than expected while for the 700°C annealed sample it is larger in value. The apparent variation in Zn peak position may be related to small nonuniformities in the overlayer thickness or to variations in the sputter rate during the SIMS profiling. This has been observed previously⁽⁶⁾. Calculation of D for diffusion times of 5s at the respective temperatures yield $9.8 \times 10^{-15} \text{ cm}^2/\text{s}$ (700°C), $4.7 \times 10^{-14} \text{ cm}^2/\text{s}$ (800°C), $7.3 \times 10^{-13} \text{ cm}^2/\text{s}$ (900°C), and $7.6 \times 10^{13} \text{ cm}^2/\text{s}$ (950°C). No correction has been made for the effective diffusion times in the RTA apparatus since this would require knowledge of the activation energy for the diffusion process. However, assuming this energy is approximately 2.0 eV, a reasonable estimate for a substitutional diffusant in GaAs, and knowing the heating rate of 170°C s^{-1} and cooling rate of 90°C s^{-1} from the annealing temperature to 500°C , we can estimate that the D values are accurate to $\pm 12\%$.

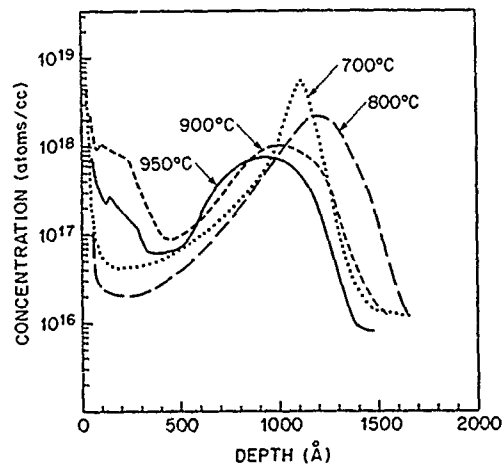


Figure 3 SIMS profiles for δ -doped samples annealed at 700, 800, 900, and 950°C , respectively.

An estimate of the maximum value of D at the growth temperature of 625°C for the as-grown sample can be obtained by considering the δ -doped layer nearest to the substrate in the multiple δ -doped sample of Fig. 2. This layer was exposed to the growth temperature for approximately 1000s. Assuming an uncertainty in the hwhm of the SIMS measurement as $\leq 30\text{\AA}$, a value for D of $7 \times 10^{-17} \text{ cm}^2/\text{s}$ is calculated. The actual value may well be below this estimate to the upper limit. This especially low value of the as-grown δ -doped layer is consistent with recent results by Kuech et al.⁽¹⁵⁾ These authors have calculated values of $\leq 5 \times 10^{-18} \text{ cm}^2/\text{s}$ at 700°C for Zn concentrations $\leq 10^{19} \text{ cm}^{-3}$. Our value is less than that estimated by Enquist et al.⁽¹⁶⁾ Based on their values for D_0 and E_A of $1.0 \times 10^{-9} \text{ cm}^2/\text{s}$ and 0.9 eV, respectively, a value for D of $9 \times 10^{-15} \text{ cm}^2/\text{s}$ at 625°C is estimated. However, the experimental conditions of these authors were different from ours and emphasize the sensitivity of Zn diffusivity in GaAs to parameters such as interstitial and substitutional Zn concentration, the doping level and conductivity type of adjacent layers, and the method of annealing.

The ECV profile of a Cd δ -doped sample is shown in Figure 4. The peak concentration is $\sim 4 \times 10^{17} \text{ cm}^{-3}$, which is low enough to cause the zero bias depletion region to extend well into the leading edge of the carrier distribution. Because of the high vapor pressure of Cd, it was necessary to use the lowest growth temperature possible (580°C) while still maintaining a featureless surface morphology in order to achieve a measurable peak concentration. An estimate of the FWHM of the carrier profile can be made by dividing the distribution down the middle, then doubling the width of the back half of the profile. This procedure gives an

estimated FWHM of $\sim 220\text{\AA}$, which is considerably broader than the reported values for Si and Se δ -doping, and indicates that the Cd ions have diffused or segregated during the growth of the $0.1\text{ }\mu\text{m}$ thick overlayer. However, it was noted during SIMS profiling that an In spike with a peak concentration of $2 \times 10^{19}\text{ cm}^{-3}$ and FWHM of $\sim 50\text{\AA}$ was present at the intended Cd doping plane. Upon further investigation it was determined that the source of the In was the DMCD source. Consequently, it is possible that the presence of In at such a level could influence the diffusion of Cd.

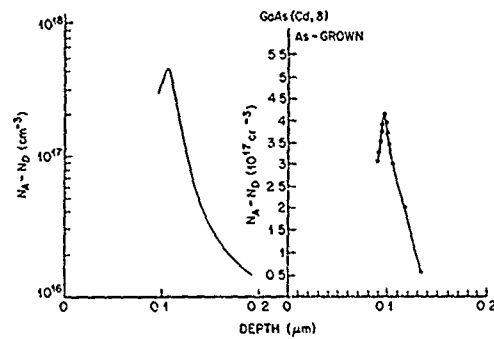


Figure 4 Carrier profiles in Cd δ -doped GaAs grown by OMVPE at 580°C , shown on both log (at left) and linear (at right) scales.

By contrast with the results for Cd, C δ -doped layers grown by MOMBE exhibited peak carrier concentrations of $7 \times 10^{19}\text{ cm}^{-3}$ with FWHM of 50\AA in the ECV profile. This is the highest peak carrier concentration obtained by δ -doping by any growth technique. The SIMS profile for a double C δ -doped layer is given in Figure 5. Peak atomic concentrations of $\sim 1.5 \times 10^{20}\text{ cm}^{-3}$ with FWHM of 65\AA and 80\AA , respectively, were obtained.

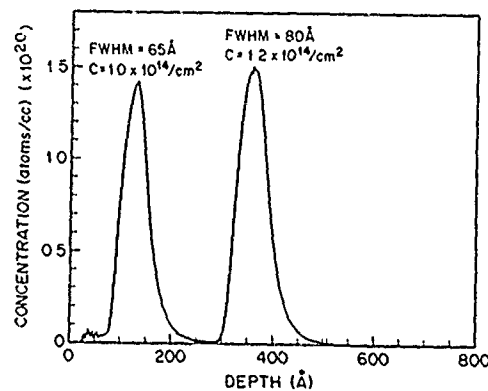


Figure 5 SIMS profile of atomic C distribution in a double δ -doped sample. The background C signal was subtracted from the profile.

CONCLUSIONS

In summary, we have demonstrated Zn δ -doped layers grown by OMVPE. The narrowest profiles had FWHM of 80\AA for Zn_{max} of $\leq 3 \times 10^{18} \text{ cm}^{-3}$. The as-grown width of these profiles is most likely due to a combination of dopant memory effect and growth-related diffusion during the actual formation of the δ -doped layer. An effective diffusion coefficient, D , of $\leq 7 \times 10^{-17} \text{ cm}^2/\text{s}$ is estimated for $T_G = 625^\circ\text{C}$. Rapid thermal annealing at 900°C for 5s of several samples grown under various conditions led to calculated values of $D \sim 0.5 - 1.0 \times 10^{-12} \text{ cm}^2/\text{s}$.

Due to the high vapor pressure of Cd, it was not possible to obtain peak carrier concentrations above $4 \times 10^{17} \text{ cm}^{-3}$. On the other hand, C δ -doped layers by MOMBE exhibited peak carrier concentrations of $7 \times 10^{19} \text{ cm}^{-3}$.

ACKNOWLEDGEMENTS

The authors are indebted to A. S. Jordan for his support and encouragement throughout this work, and to L. J. Oster for his expert technical assistance.

REFERENCES

- [1] F. Koch and A. Zrenner, *Mater. Sci. Eng.* B1, 221 (1989).
- [2] K. Ploog, M. Hauser, and A. Fischer, *Appl. Phys.* A45, 233 (1988).
- [3] B. Ullrich, E. F. Schubert, J. B. Stark, and J. E. Cunningham, *Appl. Phys.* A47, 123 (1988).
- [4] C. E. C. Wood, G. Metzger, J. Berry, and L. F. Eastman, *J. Appl. Phys.* 51, 383 (1980).
- [5] R. B. Beall, J. B. Clegg, and J. J. Harris, *Semicond. Sci. Technol.* 3, 612 (1988).
- [6] T. H. Chin, J. E. Cunningham, B. Tell, and E. F. Schubert, *J. Appl. Phys.* 64, 1578 (1988).
- [7] N. Kobayashi, T. Makimoto, and Y. Horikoshi, *Jpn. J. Appl. Phys.* 25, L746 (1986).
- [8] A.-M. Lanzillotto, M. Santos, and M. Shayegan, *Appl. Phys. Lett.* 55, 1445 (1989).
- [9] H. Ohno, E. Ikeda, and H. Hasegawa, *Jpn. J. Appl. Phys.* 23, L369 (1984).
- [10] M. Santos, T. Sagoto, A. Zrenner, and M. Shayegan, *Appl. Phys. Lett.* 53, 2504 (1988).
- [11] S. Sasa, S. Muto, K. Kondo, H. Ishikawa, and S. Hiyamizu, *Jpn. J. Appl. Phys.* 24, L602 (1985).
- [12] E. F. Schubert, T. H. Chin, J. E. Cunningham, B. Tell, and J. B. Stark, *J. Electron. Mater.* 17, 527 (1988).
- [13] N. Kobayashi, T. Makimoto, and Y. Horikoshi, *Appl. Phys. Lett.* 50, 1435 (1987).
- [14] B. L. Sharma, *Diffusion in Semiconductors* (Trans Tech, Clausthal - Zellerfeld, Germany, 1970), p. 13.
- [15] I. F. Kuech, P.-J. Wang, M. A. Tischler, R. Potemski, G. J. Scilla, and F. Cardone, *J. Cryst. Growth* 93, 624 (1988).
- [16] P. Enquist, J. A. Hutchby, and T. J. de Lyon, *J. Appl. Phys.* 63, 4485 (1988).

PRECIPITATION PHENOMENA ASSOCIATED WITH ULTRA-HIGH Be DOPING IN $\text{Ga}_{0.47}\text{In}_{0.53}\text{P}$ LAYERS GROWN BY MBE

C.M. COTELL, M.B. PANISH, R.A. HAMM, L.C. HOPKINS, AND J.M. GIBSON
AT&T Bell Laboratories, 600 Mountain Avenue, Murray Hill, NJ 07974

ABSTRACT

Ultra-high Be doping of $\text{Ga}_{0.47}\text{In}_{0.53}\text{As}$ layers grown by gas source molecular beam epitaxy has shown that for each growth temperature, there exists a maximum hole concentration ($\geq 1 \times 10^{20} \text{ cm}^{-3}$). Increasing the Be flux above that which produces the maximum hole concentration results in a degradation of the crystalline quality of the films. The degradation of film quality results from precipitation of a Be-rich phase on the surface during growth and nucleation of dislocations at each precipitate. Below that concentration, some of the Be segregates and floats on the growing surface.

INTRODUCTION

Ultra-high Be doping of $\text{Ga}_{0.47}\text{In}_{0.53}\text{As}$ by low temperature molecular beam epitaxy has recently been reported.[1] Carrier concentrations, N_A-N_D , as high as $5.6 \times 10^{20} \text{ cm}^{-3}$, as determined by room temperature Hall measurements, were achieved at a growth temperature of 365°C . The effect of growth temperature on the maximum doping level has been characterized. For each temperature, a value for N_A-N_D is reached for which a further increase in Be flux results in an abrupt deviation of N_A-N_D below that expected from the temperature dependence of the vapor pressure of Be. It has been suggested [1] that some precipitation-related phenomenon may explain the abrupt drop in carrier concentration with Be flux at high doping levels. In this paper, we report the results of characterization of highly-Be-doped samples by transmission electron microscopy (TEM), and secondary ion mass spectrometry (SIMS).

EXPERIMENTAL

All of the samples for this study were grown by hydride source molecular beam epitaxy (HSMBE). [2,3] In this version of gas source MBE, decomposed AsH_3 and PH_3 were used for the generation of As_2 and P_2 beams, and effusion cells containing the elements were used to generate atomic beams of Ga, In, and Be. [2,3] The growth on semi-insulating substrates and substrate temperature monitoring procedures are described in ref. [1]. The growth rate for the ternary was $1.2 \mu\text{m/hr}$ and layer thicknesses ranged from 500 to 4000 Å. The range of growth temperatures studied was 365°C to 505°C .

The microstructures of the samples were characterized in planar- and cross-section using a Philips 430 transmission electron microscope operating at 300 kV. The chemical composition of the samples was studied with secondary ion mass spectrometry (SIMS) using a Cameca IMS-3F instrument operating at 8 keV with an O_2^+ primary beam. The raster area was $250 \times 250 \mu\text{m}^2$ and secondary ions were extracted from a $60 \mu\text{m}$ -diameter region at the center of the crater. The Be^+ signal was monitored and referenced to the As^+ signal. The vertical scale was calibrated with a standard sample of Be-implanted GaInAs. The horizontal scale was based on a sputter rate of 3-5 Å/s for GaInAs, as determined by profilometer measurements of the sputter-induced craters in the Be-implanted GaInAs standard. Additional SIMS spectra were determined using an Atomika A-DIDA-3000-30 instrument equipped with an Extranuclear Laboratories quadrupole spectrometer and also operated with an O_2^+ primary beam. The analyzed area was a $300 \times 300 \mu\text{m}^2$ region in the center of a $900 \times 900 \mu\text{m}^2$ raster.

RESULTS AND DISCUSSION

Plan view TEM specimens were prepared from a number of GaInAs samples grown at different temperatures and different Be fluxes. The samples could be divided microstructurally into two categories: those that showed precipitation and those free from precipitation. An example of each is shown in fig. 1. Figure 1(a) shows a section through a 3000 Å-thick Be-doped GaInAs layer ($9.25 \times 10^{19} \text{ cm}^{-3}$) grown at 448°C. The precipitates visible in fig. 1(a) were about 100 Å in size. Figure 1(b) shows a sample free from precipitation. The sample in fig. 1(b) is a section through a 500 Å-thick layer of Be-doped GaInAs ($2.75 \times 10^{20} \text{ cm}^{-3}$) grown at 411°C.

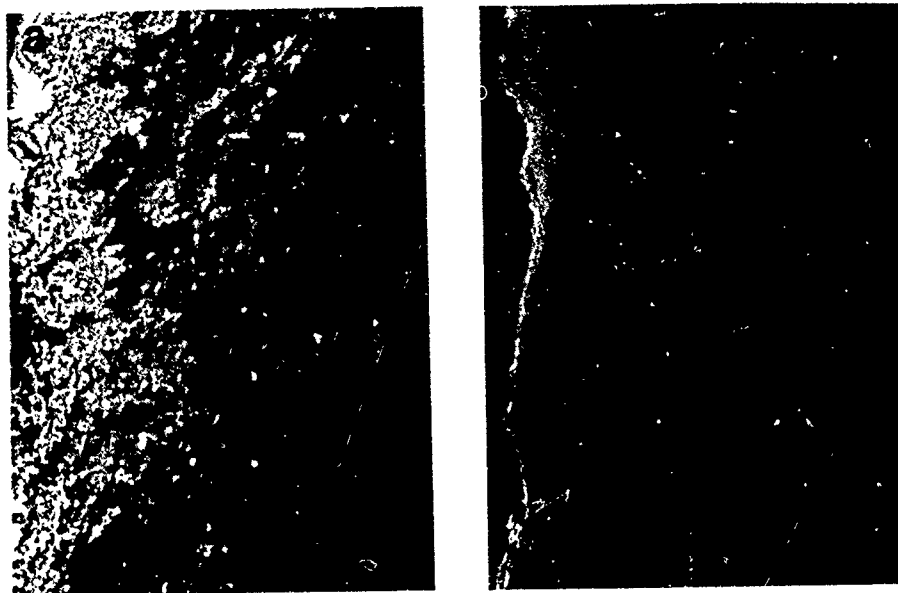


Figure 1: Weak beam (220) TEM images of plan-view sections of (a) 3000 Å Be-doped ($9.25 \times 10^{19} \text{ cm}^{-3}$) $\text{Ga}_{0.47}\text{In}_{0.53}\text{As}$ grown on InP at 448°C and (b) 500 Å Be-doped ($2.75 \times 10^{20} \text{ cm}^{-3}$) $\text{Ga}_{0.47}\text{In}_{0.53}\text{As}$ grown on InP at 411°C.

Figure 2 is a modification of a figure from reference [1] and summarizes the results of study of the samples by plan-view TEM. Figure 2 shows the net carrier concentration plotted against the reciprocal of the Be cell temperature for substrate temperatures ranging from 365°C to 505°C. [1] The slope of the solid line through the experimental points in fig. 2 is that expected from the temperature dependence of the vapor pressure of Be. The shaded points in fig. 2 indicate those samples that were examined in the TEM. The lightly shaded points represent samples in which precipitation was observed while the darkly shaded points represent samples free from precipitation. With the exception of the sample grown at the lowest substrate temperature (366 °C), all of the samples whose Be concentrations did *not* follow the relationship with Be source temperature indicated by the solid line in fig. 2 (i.e., those samples grown "off" the curve) showed precipitation. All other samples free from precipitates were samples grown under conditions "on" the curve.

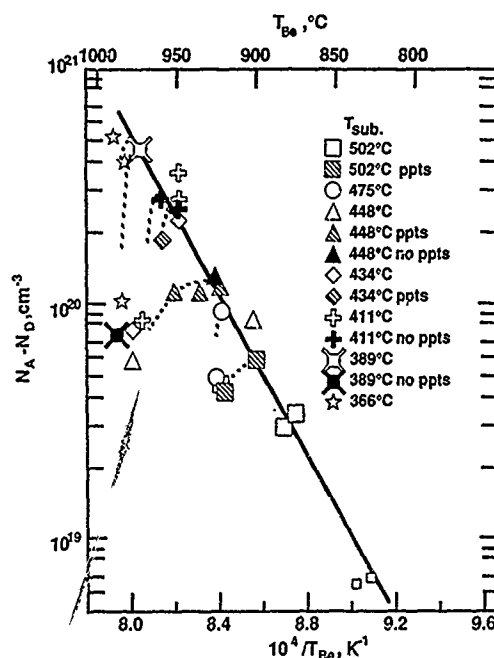


Figure 2: Net hole concentration vs. Be oven temperature at several growth temperatures. The darkly-shaded points indicate samples that were free from precipitation while the lightly-shaded points indicate samples in which precipitation was observed.

Figure 3 compares the microstructure in cross section and composition of a sample that showed precipitation. Figure 3(a) is a weak beam TEM photomicrograph and shows in cross section the sample from fig. 1(a). Between the substrate and the 3000 Å-thick Be-doped GaInAs layer, an undoped buffer layer about 1500 Å thick had been grown. The precipitates were found at a uniform distance of 2500 Å from the substrate; that is, a distance of 1000 Å from the initiation of growth of Be-doped GaInAs. At each precipitate a dislocation was nucleated. Figure 3(b) is a SIMS sputter depth profile taken in the Atomika SIMS from the sample in fig. 3(a). Figure 3(b) shows that the Be concentration is approximately uniform from the surface to a depth which corresponds to the distance from the surface at which precipitation is seen in fig. 3(a). At this depth, the Be concentration increases sharply, then drops off sharply to a concentration lower than the concentration in the region near the surface. There is then a gradual decrease in Be concentration as the InP substrate interface is approached. Clearly, from fig. 3(b) it can be concluded that the precipitates are rich in Be and that there is segregation of Be at the dislocations that are nucleated at each precipitate.

A series of samples was grown in which the thickness of Be-doped GaInAs grown on InP substrates directly without a buffer layer was varied between 500 and 3000 Å. The Be flux was such as to have given a doping level of $p=3 \times 10^{20} \text{ cm}^{-3}$, if the Be were uniformly incorporated as acceptors, as extrapolated from Hall measurements at lower flux. The substrate temperature was 448 °C. These are the same conditions under which the sample in fig. 1(a) was grown ("off" the curve in fig. 2). After the desired thickness of Be-doped GaInAs had been grown, the sample was cooled to 350 °C and a 1000 Å-thick cap of undoped GaInAs was grown at this temperature. Figure 4 shows bright field TEM photomicrographs from several of the samples in this series.

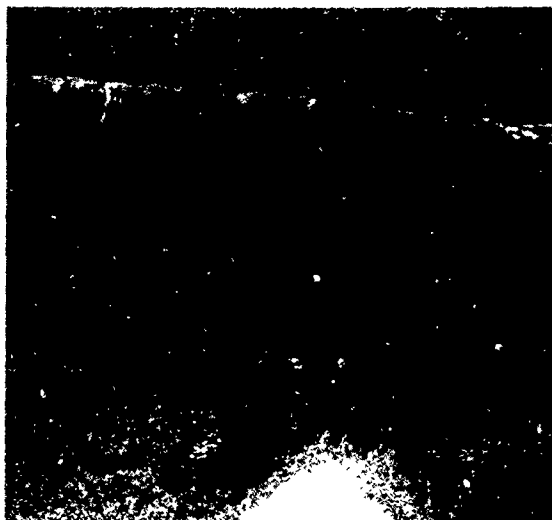
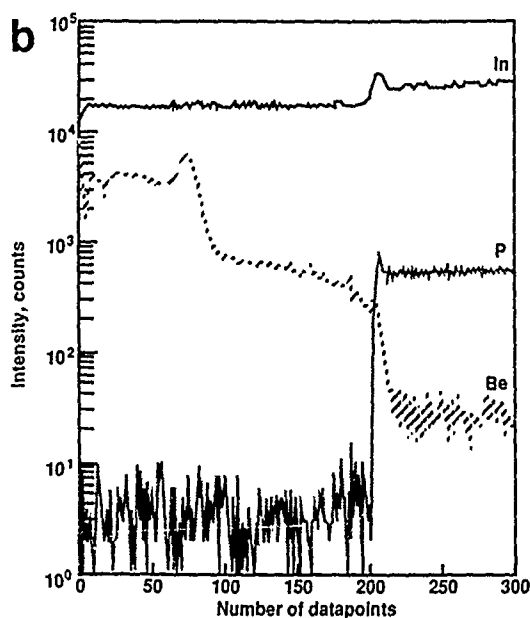


Figure 3: (a) Weak beam (220) TEM image of a transverse section of the sample in fig. 1(a); and (b) SIMS sputter depth profile through the same sample. The photomicrograph in (a) shows that precipitation occurs at a uniform distance from the substrate interface and that dislocations are nucleated at each precipitate.



Precipitation occurred reproducibly at a distance of 1000 \AA from the substrate interface as seen in figs. 4(a-c) in which the GaInAs thicknesses were 3000, 1500 and 1000 \AA , respectively. The precipitates are marked by mismatch Moire fringes. The microstructures in figs. 4(a) and (b) are similar to that in fig. 3(a); that is, a dislocation is associated with each precipitate. In fig. 4(c) the precipitates occurred at the interface between the 1000 \AA -thick Be-doped GaInAs and the undoped cap layer, which is, as expected, of poor crystalline quality in all the samples shown in fig. 4. No evidence for precipitates was found in any of the samples of thicknesses less than 1000 \AA , as seen in figs. 4 (d) and 4(e), in which the GaInAs thicknesses were 700 and 500 \AA , respectively.

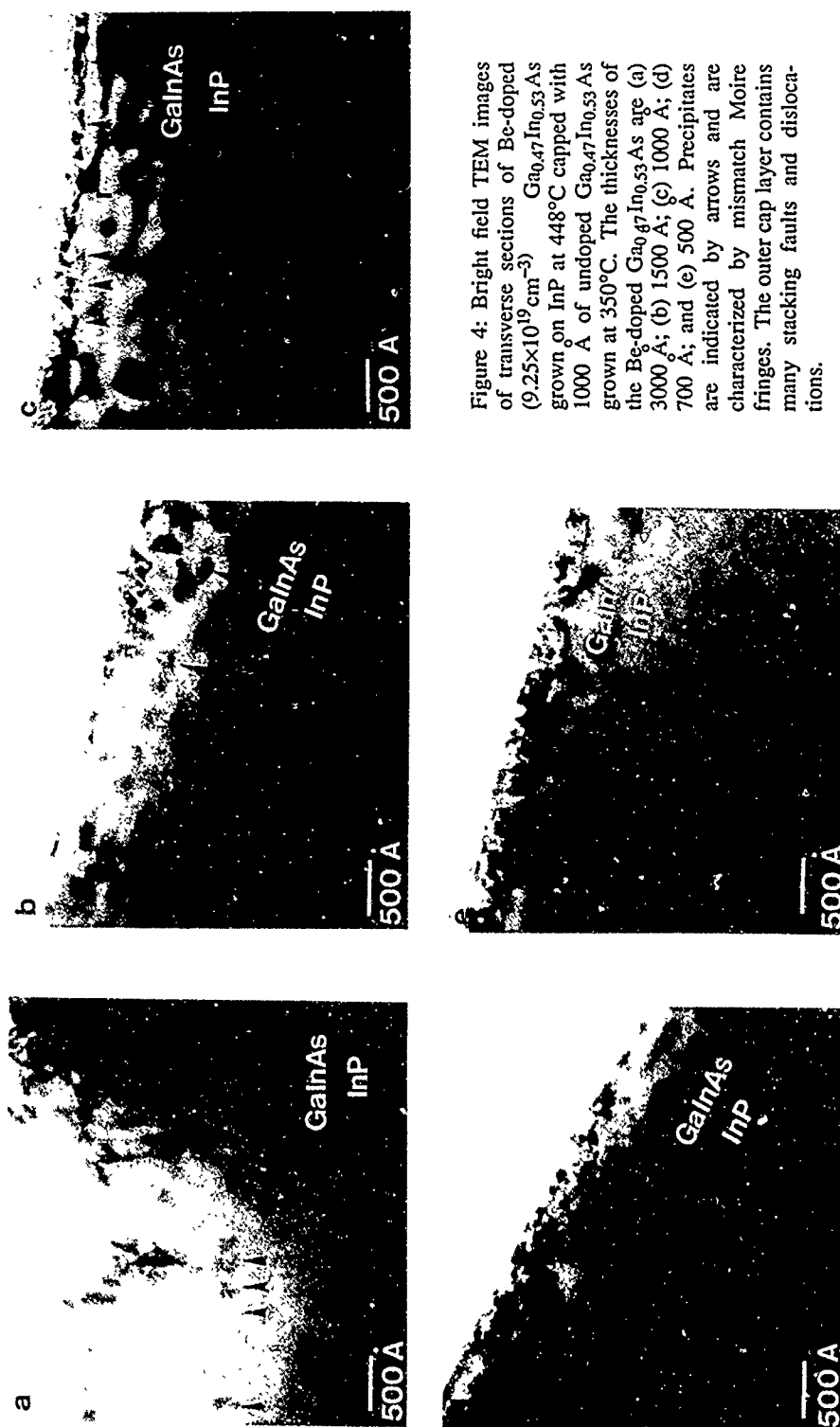


Figure 4: Bright field TEM images of transverse sections of Be-doped $\text{Ga}_{0.47}\text{In}_{0.53}\text{As}$ ($9.25 \times 10^{19} \text{ cm}^{-3}$) grown on InP at 448°C capped with 1000 \AA of undoped $\text{Ga}_{0.47}\text{In}_{0.53}\text{As}$ grown at 350°C . The thicknesses of the Be-doped $\text{Ga}_{0.47}\text{In}_{0.53}\text{As}$ are (a) 3000 \AA ; (b) 1500 \AA ; (c) 1000 \AA ; (d) 700 \AA ; and (e) 500 \AA . Precipitates are indicated by arrows and are characterized by mismatch Moiré fringes. The outer cap layer contains many stacking faults and dislocations.

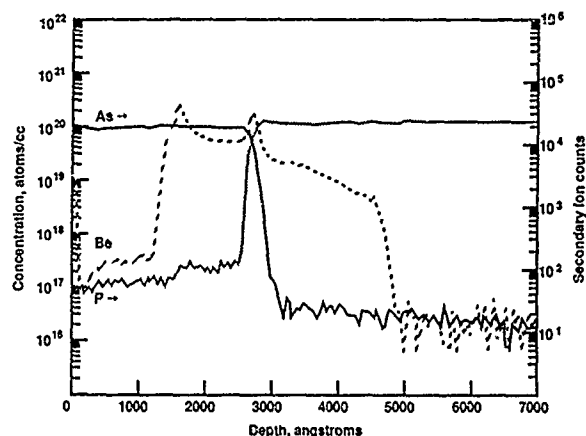


Figure 5: SIMS sputter depth profile through the sample in fig. 4(d).

The SIMS sputter depth profiles from the samples in figs. 4(a) and 4(b) were qualitatively similar to the profile in fig. 3(b); a peak in Be concentration occurred at the location of the precipitates and the Be concentration above the precipitates was higher than that between the precipitates and the substrate. Also, there was evidence for diffusion of Be into the undoped cap layer. The SIMS sputter depth profiles from the samples in figs. 4(c-e) resembled that shown in fig. 5, which is the SIMS sputter depth profile from the sample in fig. 4(d). The SIMS sputter depth profile in fig. 5 was taken with the Cameca SIMS, which has a greater sensitivity for Be. The high Be concentration at the substrate interface is believed to have resulted from residual Be on the source shutters in the reactor. There is evidence for diffusion of Be into the substrate. Within the GaInAs, a peak in Be concentration is found at the interface between the Be-doped GaInAs and the undoped GaInAs cap layer. In the case of the sample in fig. 4(c), this peak corresponds to precipitates, but no precipitation was observed in the samples in figs. 4(d) and 4(e). This indicates that Be segregates and floats on the growing GaInAs until the critical layer thickness of 1000 Å is reached, at which time the surface excess precipitates into a Be-rich phase, as yet unidentified, with a lattice parameter different from that of $\text{Ga}_{0.47}\text{In}_{0.53}\text{As}$. The lattice mismatch results in dislocations that degrade the quality of the layers greater than 1000 Å in thickness. The results of ref. [1] suggest that this critical thickness must also be growth temperature dependent.

ACKNOWLEDGMENTS

The authors would like to acknowledge the assistance of D. Bahnck in the preparation of plan-view TEM specimens and the assistance of N. Ha, J. Kovalchick, and H. Luftman in the study of the samples by SIMS. Valuable discussions with S. Nakahara are also gratefully acknowledged.

REFERENCES

- [1] R. A. Hamm, M. B. Panish, R. N. Nottenburg, Y. K. Chen, and D. A. Humphrey, *Appl. Phys. Lett.*, **54** (25), 2586 (1989).
- [2] M. B. Panish and H. Temkin, *Ann. Rev. Mat. Sci.*, **19**, 209 (1989).
- [3] M. B. Panish, *J. Cryst. Growth*, **81**, 249 (1987).
- [4] M. B. Panish, H. Temkin, and S. Sumski, *J. Vac. Sci. Tech.*, **B3**, 657 (1985).

CHARACTERISTICS OF DOPING AND DIFFUSION OF HEAVILY DOPED N AND P TYPE InP AND InGaAs EPITAXIAL LAYERS GROWN BY METAL ORGANIC CHEMICAL VAPOR DEPOSITION

C.J. Pinzone¹, N. T. Ha², N. D. Gerrard³, R. D. Dupuis¹ and H. S. Luftman²

¹ Microelectronics Research Center; The University of Texas; Austin, Texas 78712-1084

² AT&T Bell Laboratories; 600 Mountain Avenue; Murray Hill, N.J. 07974

³ STC Defense Systems; Paignton, Devon TQ4 7BE; United Kingdom

ABSTRACT

Electronic and photonic device applications of the InGaAs/InP materials system often require the growth of epitaxial material doped to or near the solubility limit of the impurity in the host material. These requirements present an extreme challenge for the crystal grower. To produce devices with abrupt dopant profiles, preserve the junction during subsequent growth, and retain a high degree of crystalline perfection, it is necessary to understand the limits of dopant incorporation and the behavior of the impurity in the material.

In this study, N-type doping above 10^{19} cm^{-3} has been achieved in InP and InGaAs using Sn as a dopant. P-type Zn doping at these levels has also been achieved in these materials but p type activation above $\sim 3 \times 10^{18} \text{ cm}^{-3}$ in InP has not been seen. All materials were grown by the metalorganic chemical vapor deposition (MOCVD) crystal growth technique. Effective diffusion coefficients have been measured for Zn and Sn in both materials from analysis of secondary ion mass spectra (SIMS) of specially grown and annealed samples.

INTRODUCTION

InP and InGaAs electronic and photonic devices such as heterostructure bipolar transistors (HBT's)[1], photodiodes[2], lasers and reflectors [3], are of increasing interest for high-speed applications and the possibility of integrated optical, digital, and analog circuits. For these devices, high performance operation requires a reduction in contact resistance. For example, in the case of HBT's, a reduction in the emitter series resistance of the device is required to lower the emitter capacitance for high speed operation. These requirements are met by maximizing the n-type dopant incorporation in the emitter contact and at the emitter base junction. Furthermore, a wider range of device performance can be exploited by expanding the range of n- and p-type doping.

Increasing the dopant incorporation in epitaxially grown device structures can lead to degradation of the device performance caused by displacement of the electrical and/or the metallurgical junction caused by diffusion of the dopant species upon further heating of the material as subsequent layers are grown. This problem is more severe in devices that exploit quantum-confinement effects since often the doped layers in such structures are extremely thin ($< 300 \text{ \AA}$). It is therefore necessary to investigate the limits of n- and p-type doping and the dopant behavior in the InGaAs/InP lattice.

We have recently reported results for n-type doping with Sn of InP and InGaAs grown by MOCVD using tetraethyltin (TESn) as the dopant source material [4,5,6]. In this study, we were able to achieve net electron carrier concentrations of $N_d - N_a \sim 3.3 \times 10^{19} \text{ cm}^{-3}$ for the binary and $N_d - N_a \sim 6.1 \times 10^{19} \text{ cm}^{-3}$ for the ternary compound. For a p-type dopant we chose to use Zn from diethylzinc. In this paper we report the growth conditions associated with the growth of heavily doped n- and p-type InP and lattice matched InGaAs by MOCVD, and the results of the electrical characterization of these layers. We also report our investigation of the

dopant diffusion behavior in these films by analysis with secondary ion mass spectroscopy (SIMS) taken on as-grown and thermally annealed epitaxial layers.

CRYSTAL GROWTH

All of the material in this study were grown by the MOCVD technique in a non-commercial atmospheric pressure system similar to that previously described [7]. The reaction chamber was vertically oriented and was inductively heated. This reactor employed a vent/run gas delivery scheme but was not optimized for fast gas switching or low dead volume. Group III sources were trimethylindium (TMIn) and trimethylgallium (TMGa), while the group V sources were 10% arsine (AsH_3) in hydrogen, and 10% phosphine (PH_3) in hydrogen. As noted above, Zn and Sn were from DEZn and TESn, respectively. Palladium diffused hydrogen was used as a carrier to transport the metalorganic vapors to the growth chamber. Total flow rates of H_2 and all reactants was ~ 14 slm and the growth temperature was $\sim 660^\circ\text{C}$. V/III ratios of ~ 50 -65 were used for InP and ~ 13 -17 for InGaAs. Dopant gas flows were typically from 1 to 50 sccm with the source material being held in constant temperature baths which could be adjusted from -25°C to 25°C as desired in order to control the source vapor pressure and hence the vapor phase dopant mole fraction in the growth chamber. All growth was performed on InP (100) oriented substrates doped with iron, tin or sulfur, the only preference being that iron-doped substrates were used for all samples which were to be electrically characterized by Hall measurements.

CHARACTERIZATION

Single layers of doped InP and InGaAs grown on semi-insulating InP:Fe were characterized at 300 and 77K by the van der Pauw technique.[8] In:Cd alloy was used for contacts to p-type material and all samples were measured as previously reported. [6]

Sn and Zn atomic concentrations and distributions were measured in selected samples by SIMS. These spectra were obtained using a Cameca 3f instrument with a 14.5 KeV Cs^+ primary ion source. Ion currents from 45-80 nA were used yielding sputtering rates of ~ 11 -17 $\text{\AA}/\text{sec}$ for InP and ~ 5.5 $\text{\AA}/\text{sec}$ for InGaAs. Sputtered crater depths were measured with a Dektak II profilometer. Calibration was made from known implant standards.

RESULTS

Table I shows the measured hole concentrations of Zn doped InP and InGaAs layers. Results for Sn doped layers have been previously reported.[6] Undoped runs were made between these experiments and background carrier concentrations of the order of $n_{77\text{K}} \sim 7 \times 10^{14} \text{ cm}^{-3}$ with $\mu_{77\text{K}} \sim 115,000 \text{ cm}^2/\text{V-sec}$ for InP and $n_{77\text{K}} \sim 8 \times 10^{14} \text{ cm}^{-3}$ with $\mu_{77\text{K}} \sim 45,000 \text{ cm}^2/\text{V-sec}$ for InGaAs were routinely obtained. Our work was focused on achieving high levels of doping but we believe that with appropriate dilution lines, low levels should also be possible. An experiment where DEZn vapor was aspirated into the metalorganic delivery manifold by flowing 5 sccm of H_2 past the open bubbler inlet and outlet instead of through it resulted in an InGaAs p-type layer with $p_{77\text{K}} = 1.28 \times 10^{16} \text{ cm}^{-3}$ and $\mu_{77\text{K}} = 630 \text{ cm}^2/\text{V-sec}$.

We observed a limit of electrically active Zn in InGaAs of $p_{300\text{K}} \sim 3.74 \times 10^{19} \text{ cm}^{-3}$, close to the highest atomic concentration, $4.0 \times 10^{19} \text{ cm}^{-3}$, measured by SIMS analysis. However, for InP, atomic Zn concentrations as high as $1 \times 10^{19} \text{ cm}^{-3}$ were measured but we were not able to measure p-type carrier concentrations above $p_{300\text{K}} = 2.54 \times 10^{18} \text{ cm}^{-3}$ in samples grown with similar Zn mole fractions. The electrical results for Zn doping in InP

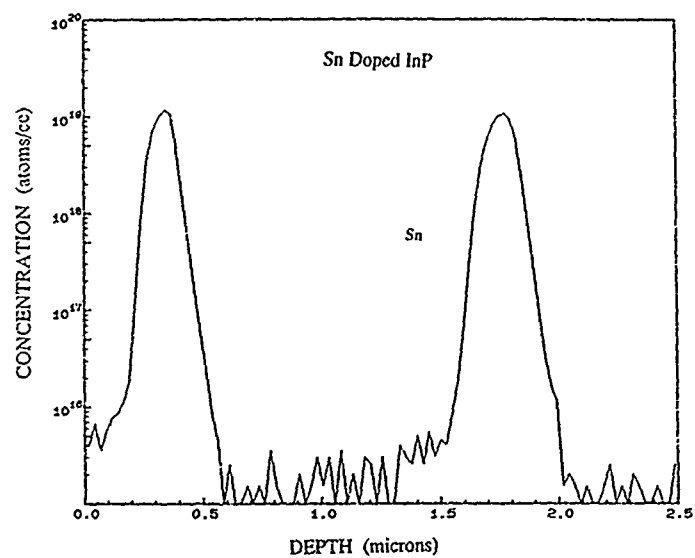


Figure 1

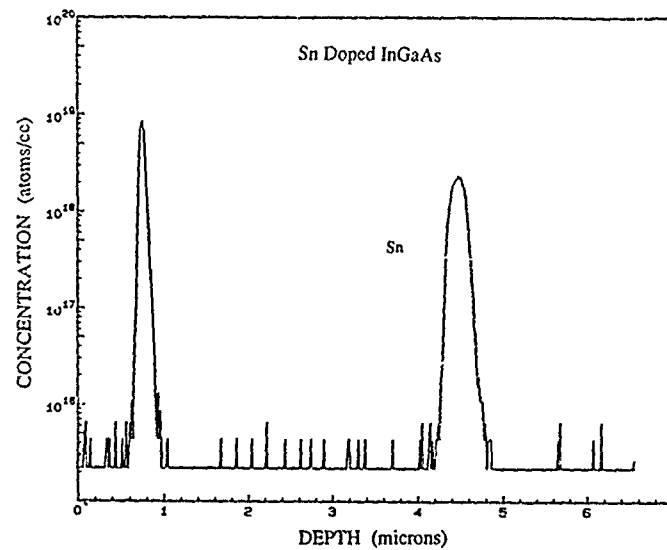


Figure 2

Table I
InP:Zn van der Pauw-Hall Results

Wafer #	M _{Zn} /M _{total}	P300K cm ⁻³	μ300K cm ² /V-sec	P77K cm ⁻³	μ77K cm ² /V-sec
1173	1.2x10 ⁻⁵	2.48x10 ¹⁸	64	1.55x10 ¹⁷	288
1024	1.9x10 ⁻⁶	2.10x10 ¹⁸	57	6.25x10 ¹⁷	62
1169	4.9x10 ⁻⁷	2.54x10 ¹⁸	56	2.75x10 ¹⁷	130
1205	9.4x10 ⁻⁸	1.54x10 ¹⁸	80	2.05x10 ¹⁷	153
InGaAs:Zn van der Pauw-Hall Results					
1164	2.0x10 ⁻⁵	2.84x10 ¹⁹	62	2.44x10 ¹⁹	102
1091	1.0x10 ⁻⁶	3.74x10 ¹⁹	51	2.95x10 ¹⁹	91
1030	5.0x10 ⁻⁶	2.29x10 ¹⁹	54	1.97x10 ¹⁹	87
1168	2.0x10 ⁻⁶	2.39x10 ¹⁹	61	2.00x10 ¹⁹	104
1220	1.9x10 ⁻⁶	1.34x10 ¹⁹	62	1.32x10 ¹⁹	88
1216	4.9x10 ⁻⁷	4.10x10 ¹⁸	82	5.57x10 ¹⁸	78
1212	9.8x10 ⁻⁸	3.94x10 ¹⁸	83	5.52x10 ¹⁸	73

show that there is little change in the high range values of electrically active Zn even with a large change in Zn mole fraction introduced into the reactor. This has been previously reported [9] and suggests a saturation limit for Zn on substitutional Group III lattice sites. N-type doping with Sn on the other hand, shows a fairly linear response of carrier concentration to increase in Sn mole fraction in the vapor phase. SIMS analysis of the highest doped InGaAs layer does show an atomic Sn concentration of $1 \times 10^{20} \text{ cm}^{-3}$, so it is reasonable to assume that $6.3 \times 10^{19} \text{ cm}^{-3}$ is the electrical saturation limit for Sn in InGaAs grown at 660° C. We have also measured atomic Sn concentrations as high as $7 \times 10^{19} \text{ cm}^{-3}$ in InP but have not measured carrier concentrations above $3.3 \times 10^{19} \text{ cm}^{-3}$ which we assume to be the electrical saturation limit for InP:Sn at this growth temperature.

Samples were grown to elucidate the diffusion behavior of heavily doped layers. By placing two doping spikes in the layer we can look at the difference in the full width at half maximum (FWHM) for each spike to determine the diffusion length. The time difference between the start of growth of the first spike and that of the second is taken to be the diffusion time. Representative spectra for Si- and Zn spike doped samples are shown in Figures 1, 2, and 3. For Zn in InP, we used a variation of a technique used by Nelson and Westbrook.[10] Three seconds before the start of a doping pulse, a small amount of TMGa vapor is introduced into the gas stream and then switched off three seconds after the start of the pulse. An "end" marker is formed in a similar way. Three seconds before the dopant is switched off the TMGa is again switched in and then three seconds after the dopant is turned off the TMGa is switched off. This method gives us easily measured markers showing where we intended to put the dopant. The displacement of the dopant from the gallium marker and the time of heating after the center of the gallium pulse can be used to measure the diffusion for the dopant profile. We were concerned as to whether the addition of the small amount of gallium would change the doping behavior due to increased strain in the lattice but it appears from double-crystal X-ray rocking curves on other samples uniformly doped with Ga that no increase in strain is present. This method gives us the added benefit of being able to quantify the difference in dopant diffusion towards the surface (outdiffusion) and towards the substrate (indiffusion). An example of this is shown in Figure 4.

By measuring the difference in the FWHM of the doping peaks of dopant spiked layers and defining the mean penetration depth z as half that value [11] we can then determine the effective diffusion coefficient D from the relationship [12]:

$$z = (Dt/\pi)^{1/2} \quad (1)$$

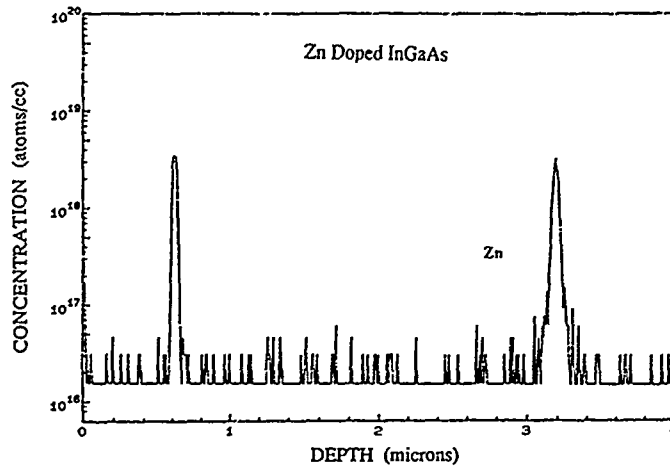


Figure 3

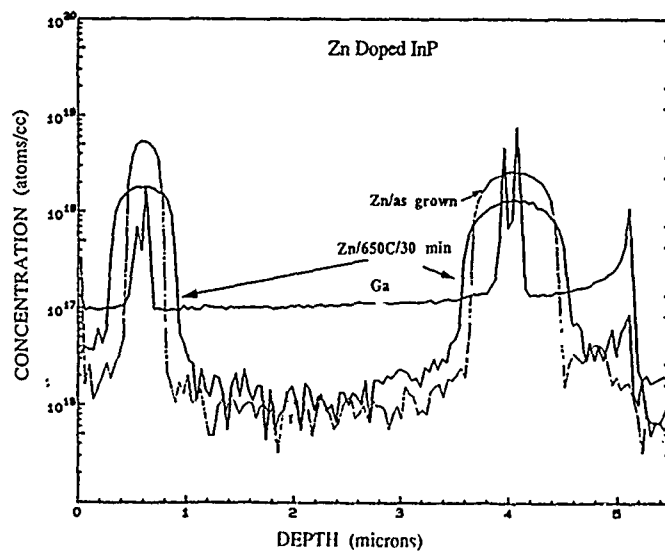


Figure 4

The values calculated from SIMS profiles of different samples are given in Table II.

Table II

Sample #	$M_{\text{dopant}}/M_{\text{total}}$	$D_{\text{out}} (\text{cm}^2/\text{s})$	$D_{\text{in}} (\text{cm}^2/\text{s})$	D_{average}
<u>D_{eff} for Zn in InP</u>				
1099	1.01×10^{-5}			1.18×10^{-13}
1261	8.88×10^{-7}	2.41×10^{-13}	3.75×10^{-13}	3.08×10^{-13}
1206	9.36×10^{-8}	3.49×10^{-14}	4.85×10^{-14}	4.17×10^{-14}
<u>D_{eff} for Zn in InGaAs</u>				
1272	2.03×10^{-6}			6.84×10^{-13}
1184	5.87×10^{-7}			1.77×10^{-14}
1286	9.76×10^{-8}			1.29×10^{-15}
<u>D_{eff} for Sn in InP</u>				
1288	1.15×10^{-6}			4.73×10^{-15}
<u>D_{eff} for Sn in InGaAs</u>				
1289	1.19×10^{-6}			4.81×10^{-14}

The values for Zn in InP are in reasonable agreement with those previously reported.[10]. The values for Zn in InGaAs indicate that the diffusion is less than in the binary, while for Sn the reverse is true, i.e. the diffusion is less in the ternary than in the binary. Assuming that the diffusion is governed by a substitutional-interstitial mechanism, the degree of diffusion can be explained in a manner similar to that proposed by van Gurp, et. al., to explain Zn and Cd diffusion differences in InP, GaAs and InGaAsP.[13] By taking the covalent radii of In, Ga, Zn and Sn as 1.44, 1.26, 1.31, and 1.40 Å, respectively,[14] an averaged In-Ga radii for InGaAs would be 1.39 Å. The covalent radius of Zn is smaller than that of In and the In-Ga averaged radii with the difference being greater between Zn and In in InP. Thus the free energy of formation of a Zn interstitial would be larger in InGaAs than in InP. Therefore there would be fewer interstitials in InGaAs than InP, and as a result, lower diffusion due to interstitials would be expected, as we see here. The covalent radius of Sn is smaller than that for InP but larger than the In-Ga averaged radii so the preceding argument would predict higher diffusion coefficients for Sn in the binary than in the ternary contrary to what is observed. We conclude then that the observed Sn diffusion is not due to a substitutional-interstitial mechanism.

CONCLUSION

P type doping of InGaAs up to a limit of $p_{300K} = 3.7 \times 10^{19} \text{ cm}^{-3}$ and $p_{300K} = 2.5 \times 10^{18} \text{ cm}^{-3}$ for InP has been reported. It is seen that atomic Zn is incorporated up to an atomic concentration of $1 \times 10^{19} \text{ cm}^{-3}$. Analysis of SIMS profiles for doped layers of these materials has shown an effective diffusion coefficient of the order of $10^{-13} \text{ cm}^2/\text{sec}$ for the highest doped InP and of the order of $10^{-14} \text{ cm}^2/\text{sec}$ for the highest doped InGaAs. The diffusion coefficient is seen to decrease with a decrease in Zn concentration supporting diffusion models using a concentration dependent mechanism. The diffusion of Zn is observed to be greater in InP than in InGaAs which supports proposed models of interstitial-substitutional diffusion for Zn in these materials. Analysis of Zn doped InP shows that diffusion towards the surface may be slightly higher than towards the substrate. SIMS profiles

for heavily Sn doped InP and InGaAs yield effective diffusion coefficients of 4.8×10^{-15} and 4.9×10^{-14} cm²/sec respectively. This would imply that Sn diffusion is not governed by the same diffusion kinetics as Zn. These values point out the utility of Sn as an n-type dopant for MOCVD.

ACKNOWLEDGEMENTS

We would like to acknowledge the help and support of, and insightful discussions with A. C. E. Brittany, J. M. Brown, D. L. Coblenz, F. C. Hause, W. S. Hobson, A. C. Jones, A. T. Macrander, S. J. Pearton, P. Simms, B. G. Streetman, L. Taylor and H. H. Wade. Special thanks to Cal, Dana, and Marie.

All work was performed at AT&T Bell Laboratories, Murray Hill, New Jersey.

REFERENCES

- [1] J. R. Hayes, R. Bhat, H. Schumacher and M. Koza, *Electron. Lett.* 2 (1987) p. 931
- [2] H. Temkin, R. E. Frahm, N. A. Olsson, C. A. Burrus, and R. J. McCoy, *Electron. Lett.*, 22 (1986) p. 1267
- [3] D. G. Deppe, N. D. Gerrard, C. J. Pinzone, R. D. Dupuis, E. F. Schubert, to be published in *Appl. Phys. Lett.*
- [4,5,6] C. J. Pinzone, N. D. Gerrard, R. D. Dupuis, N. T. Ha, and H. S. Luftman presented at the 31st Electronics Materials Conference, Cambridge, Mass., June 21-23 1989, Paper R7; *Electron. Lett.* 25 19 (1989) p. 1315; accepted for publication *J. Appl. Phys. Manuscript* No. R-5407
- [7] R. D. Dupuis, L. A. Moudy, P. D. Dapkus in *Gallium Arsenide and Related Compounds 1978*, edited by C. M. Wolfe (Institute of Physics, Bristol, 1979) p. 1
- [8] L. J. van der Pauw, *Philips Research Reports*, 13 1 (1958)
- [9,10] A. W. Nelson and L. D. Westbrook, *J. Appl. Phys.* 55 8 (1984) p. 3103; *J. Cryst. Growth* 68 (1984) p. 102
- [11] T. H. Chiu, J. E. Cunningham, B. Tell, and E. F. Schubert, *J. of Appl. Phys.*, 64 3 (1988) p. 1578
- [12] B. L. Sharma *Diffusion in Semiconductors*, Trans Tech Publication, Germany, 1970 p. 13
- [13] G. J. van Gurp, T. van Dongen, G. M. Fontijn, J. M. Jacobs, and D. L. A. Tjaden, *J. Appl. Phys.* 65 2 (1989) p. 553
- [14] C. Kittel, *Introduction to Solid State Physics* 5th edition; J. Wiley and Sons, N.Y., 1976, p. 100

EFFECTS OF SI INCORPORATION AND ELECTRICAL ACTIVATION ON INTERSUBBAND OPTICAL ABSORPTION IN MBE-GROWN GaAs/AlGaAs MULTIPLE QUANTUM WELL STRUCTURES

J.D. Ralston, H. Ennen, M. Maier, M. Ramsteiner, B. Dischler, P. Koidl, and P. Hiesinger, Fraunhofer-Institut für Angewandte Festkörperphysik, Eckerstrasse 4, 7800 Freiburg, West Germany.

ABSTRACT

Using SIMS profiling, temperature-dependent Hall measurements, electronic Raman scattering, and infra-red absorption, a detailed study is presented examining the effects of Si dopant behaviour on intersubband absorption in GaAs/Al_{0.32}Ga_{0.68}As MQW's. The samples were grown by molecular beam epitaxy at substrate temperatures ranging from 520 to 680°C with Si doping in the GaAs quantum wells only. SIMS profiling reveals that, with increasing substrate temperature, substantial Si migration into the Al_{0.32}Ga_{0.68}As barrier layers occurs during epitaxial growth. Hall measurements indicate that both at elevated growth temperatures and under reduced incident As₄ beam fluxes, the electron sheet concentration is reduced in the QW's. In both cases, loss of free carriers is attributed to enhanced Si compensation. Shifts in the absolute frequency of the infra-red absorption resonance, determined by electronic Raman scattering, as well as variations in the integrated absorption intensity, are both shown to directly reflect the growth-induced variations in the free-carrier concentration in the quantum wells.

INTRODUCTION

In the past five years, several groups have successfully demonstrated efficient infra-red (IR) detection at 8-12 μm based on intersubband absorption in GaAs/AlGaAs quantum wells (QW's) [1-3]. However, no studies have been presented detailing the important role played by MBE growth conditions in determining the IR optical properties of such structures. The GaAs quantum wells are typically 40-80 Å wide, doped with Si to a level on the order of 10^{18} cm^{-3} , and confined between undoped Al_{0.32}Ga_{0.68}As barrier layers with an Al mole fraction $x > 0.3$. In order to achieve the optical and electrical quality required for detector applications, substrate temperatures exceeding 600°C are generally necessary during MBE growth. A substantial body of literature exists which indicates that at the above doping levels and substrate temperatures, Si introduced in such a spatially localized fashion undergoes migration during MBE growth over distances on the order of tens to hundreds of Angstroms [4-7]. The resulting unintended doping of the AlGaAs barrier layers may lead to substantial reductions in the actual free-carrier population in the QW's. Such behaviour is expected to arise from enhanced autocompensation [6,8,9] and/or the formation of deep donor levels [6,10,11] in Si-doped AlGaAs. Furthermore, variations in substrate temperature and incident As flux during MBE growth can also alter the net free carrier concentration in GaAs for a fixed Si concentration [12]. The purpose of the present work was to study the effects of Si doping behaviour on the energy and intensity of the intersubband absorption in doped GaAs/Al_{0.32}Ga_{0.68}As QW's. The photon energy at which the maximum intersubband absorption occurs is carrier-density-dependent, due to the depolarization shift induced by coupling between the bare intersubband transition and the free-carrier plasma in the QW's [13]. The importance of the free carrier density in determining the absolute frequency of the intersubband absorption peak in GaAs/Al_{0.32}Ga_{0.68}As MQW's has recently been clearly demonstrated [14]. The integrated absorption is also expected to be a function of the doping level in the QW's [1].

EXPERIMENTAL

Six samples of identical design were grown on undoped (100) GaAs substrates in a Riber 3200 MBE machine. Each sample contained an undoped superlattice buffer grown at 690°C, followed by a 10 period MQW region, consisting of 140 Å undoped Al_{0.32}Ga_{0.68}As barrier layers and 70 Å GaAs QW's doped in the center 50 Å with Si at a concentration of $2 \times 10^{18} \text{ cm}^{-3}$. The samples were capped with 50 Å of undoped GaAs. Layer thicknesses were calibrated prior to growth using the RHEED oscillation technique. The Si-doped MQW region was grown at a different substrate temperature for each sample. Three samples were grown in each of two separate growth runs, the first using substrate temperatures of 520, 560, and 600°C for the MQW region, and the second using temperatures of 620, 650, and 680°C. In the first growth run, the As₄:Ga and As₄:(Ga+Al) beam pressure ratios were 10:1 and 8:1, respectively, during growth of the Si-doped MQW region. In the second growth run, the corresponding pressure ratios were 15:1 and 12:1, respectively, in order to compensate for increased As desorption at the higher substrate temperatures. Beam pressures were measured with an ion gauge in the substrate growth position and were not corrected for relative ionization efficiencies. SIMS depth profiles of Si, Al, and As (for reference purposes) were measured in an Atomika spectrometer using 3 keV Cs primary ions impinging onto the sample at an angle of 45° with a current density of $4 \mu\text{A}/\text{cm}^2$. Negative secondary ions of AsSi, AsAl, and As (mass 104, 102, and 75, respectively) were recorded. The depth calibration was obtained from the structural dimensions of the samples themselves. DC Hall measurements were made over the temperature range 20-320 K using a magnetic field of 0.5 T. Standard van der Pauw samples with 3 mm cross patterns were fabricated using a single photolithography step followed by wet chemical etching and alloying of Sn ohmic contacts. Raman spectra were excited with the 482.5 and 568.2 nm lines of an Kr-ion laser. The samples were cooled to 10 K in a continuous flow cryostat. The scattered light was filtered and dispersed in a triple monochromator and detected with an intensified silicon diode array. Infra-red absorption was measured at room temperature with a dual-beam grating spectrometer, using both Brewster angle incidence on relatively large samples and a multiple internal reflection geometry with samples whose end faces were bevelled at 45° [3]. For the prism measurements, the surface next to the quantum wells was coated with gold in order to enhance the optical electric field in the active region of the sample [3].

RESULTS AND DISCUSSION

The SIMS results clearly reveal that with increasing substrate temperature the Si doping profile (Fig. 1(a)) broadens extensively and shifts toward the sample surface. This behaviour is attributed to Si diffusion [5] and to segregation on the growing surface [4,6,7], and leads to substantial unintended Si incorporation in the AlGaAs barrier layers. The SIMS results also indicate that, although extensive Si segregation appears to occur through the QW interfaces during MBE growth, no resolvable Al-Ga interdiffusion between the well and barrier layers occurs (Fig. 1(b)). This result agrees with previous experiments [5], which demonstrated that Si doping levels on the order of 10^{19} cm^{-3} are required to generate substantial layer interdiffusion at the growth temperatures used in the present work. Such interdiffusion could have a severe impact on IR detector structures, since modification of the potential well profile, and hence the subband energies, would also shift the intersubband resonance.

Temperature-dependent Hall electron sheet concentrations are plotted in Fig. 2 for all six samples. The sample grown at 620°C has the highest sheet concentration; at higher substrate temperatures the electron concentration is reduced. Whether or not the loss of free carriers at higher substrate temperatures is due solely to Si incorporation in the Al_{0.32}Ga_{0.68}As barrier layers, as revealed by the SIMS profiles of Fig. 1, is not clear. In contrast to measurements on uniformly Si-doped Al_{0.32}Ga_{0.68}As layers [10,11] the temperature-variable Hall data plotted in Fig. 2 show no evidence of carrier freeze-out into deep levels. The activation energies calculated from the temperature dependence of the

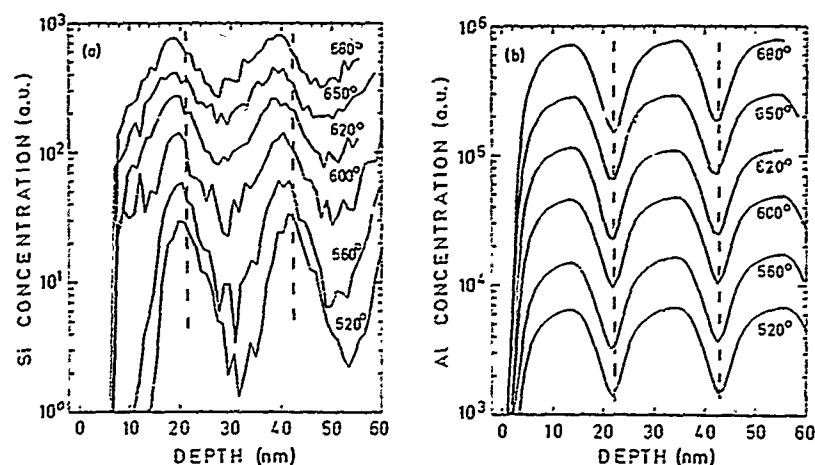


Fig. 1 SIMS depth profiles of (a) Si and (b) Al concentrations in the upper two periods of a ten-period well-doped GaAs/Al_{0.32}Ga_{0.68}As MQW structure grown at substrate temperatures between 520 and 680°C. The curves have been shifted vertically for clarity via multiplication by a constant factor.

carrier concentration between 300 and 100 K in Fig. 2 for the samples grown at 620, 650, and 680°C are only 6, 5, and 4 meV, respectively. The observed temperature dependence corresponds to that of heavily n-doped GaAs in which the conduction is dominated by the formation of an impurity band [15]. Degraded low temperature mobilities were also observed for the samples grown at 650 and 680°C, indicating that Si compensation limits the free electron concentration [16]. Possible compensation mechanisms include Si acceptor incorporation, Si-Si pair formation, and formation of Si-X, a complex of Si with a native defect [17]. All of the above mechanisms may be enhanced both in GaAs and Al_xGa_{1-x}As at elevated growth temperatures. The sharp decrease in electron sheet concentration observed in Fig. 2 for the three low-temperature growths is attributed to the smaller As₄/III flux ratio used. Reduced As₄ fluxes have been shown to enhance Si acceptor incorporation in GaAs [12]. Low temperature mobility data also indicate a substantially greater degree of compensation in the three samples grown under reduced As₄ flux. As discussed next, the above growth-related variations in electron concentration are reproduced in the frequency and integrated intensity of the intersubband absorption resonance.

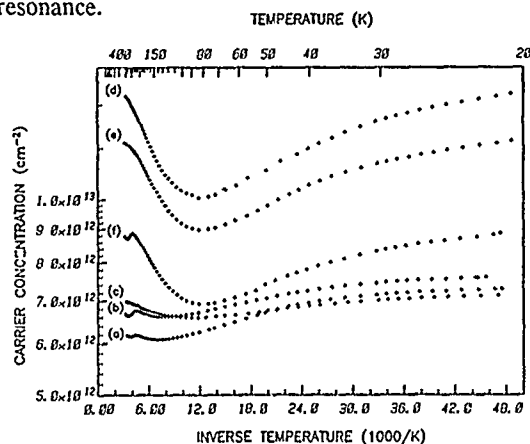


Fig. 2 Temperature-dependent Hall electron sheet concentrations for Si-doped MQW samples grown at substrate temperatures of (a) 520, (b) 560, (c) 600, (d) 620, (e) 650, and (f) 680°C.

Fig. 3 displays (a) depolarized $[x(z',y')\bar{x}]$ and (b) polarized $[x(y',y')\bar{x}]$ Raman scattering spectra from the sample grown at 620°C . The depolarized spectrum shows the single-particle intersubband transition ω_{01} between the first and the second electron subband [18]. In the polarized configuration the collective intersubband plasmon mode ω_{01}^* is observed [18]. The difference in frequency between the single-particle and collective excitations is a direct measure of the depolarization shift [18]. The corresponding infra-red absorption spectrum is shown in Fig. 4, measured using a bevelled structure fabricated from the same sample used for Raman scattering. The multiple internal reflection geometry used is shown schematically in the inset. From the transmission T after four passes through the QW stack the absorption per stack, A , was calculated using the relation $A = 1 - T^{1/4}$.

Fig. 3 Raman spectra showing (a) single particle intersubband excitation, ω_{01} , and (b) collective intersubband plasmon mode, ω_{01}^* , for the Si doped MQW sample grown at 620°C .

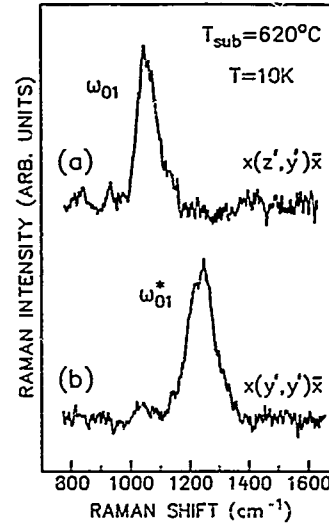
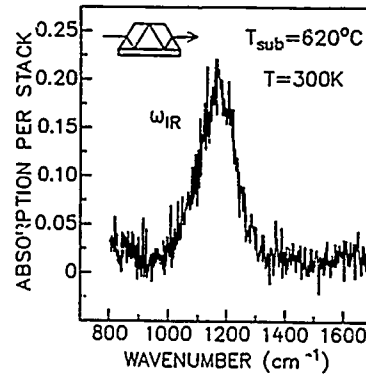


Fig. 4 Intersubband absorption resonance for the same sample as in Fig. 3. The multiple internal reflection geometry, with a gold film deposited on the epilayer side of the bevelled sample, is shown in the inset.

The frequency, ω_{01}^* , of the collective intersubband mode can be expressed as [13]

$$\omega_{01}^{*2} = \omega_{01}^2 + \omega_p^2 \quad (1)$$

where ω_p denotes an effective plasma frequency given by

$$\omega_p^2 = (2e^2/\epsilon_0\epsilon_\infty h)\omega_{01}L_{01}N_s \quad (2)$$

In Eq. 2, ϵ_∞ is the high frequency dielectric constant, N_s the electron sheet concentration, and L_{01} the intersubband transition matrix element. Assuming that the QW-shape-

dependent quantity ω_{01}^* is itself independent of the carrier density, Eq. 2 predicts a linear increase of ω_{01}^* with N_c . Hence the growth-induced variations in carrier concentration should be reproduced in the measured depolarization shift of the intersubband absorption resonance. In Fig. 5 the depolarization shift, $\omega_{01}^* - \omega_{01}$, measured at 10 K by Raman scattering is plotted versus substrate temperature, together with the 20 K Hall electron sheet concentration. The predicted behaviour is indeed observed, including the sharp discontinuity due to the different As_4 fluxes used during sample growth.

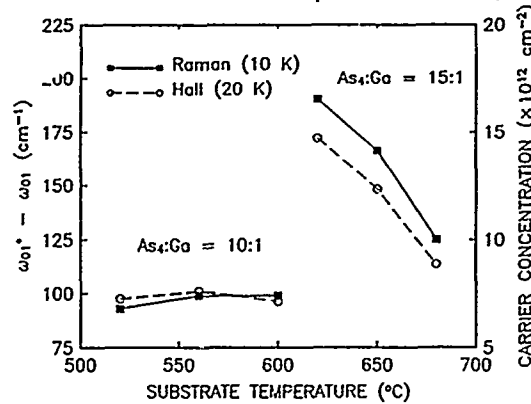


Fig. 5 Depolarization shift, $\omega_{01}^* - \omega_{01}$, of the intersubband absorption resonance as determined via Raman scattering measurements at 10 K, plotted together with the 20 K Hall electron sheet concentration as a function of sample growth temperature for two different incident As_4 fluxes.

Infra-red absorption measurements were made at 300 K using Brewster angle incidence to study the effect of dopant behaviour on absorption strength. According to Ref. 1, the integrated absorption at Brewster's angle should be linearly proportional to the carrier concentration in the QW's. Fig. 6 shows the integrated absorption intensity, calculated from the measured spectra, plotted as a function of substrate temperature, together with the 300 K Hall electron sheet concentration. Again, the variations in carrier concentration due to growth temperature and As_4/III flux ratio are reproduced in the absorption data.

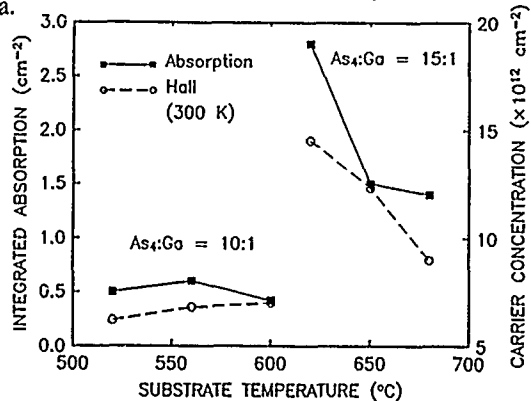


Fig. 6 Integrated 300 K intersubband absorption intensity measured at Brewster angle incidence, plotted together with the 300 K Hall electron sheet concentration as a function of sample growth temperature for two different incident As_4 fluxes.

SUMMARY

The effects of growth-induced variations of Si dopant behaviour on intersubband absorption in MBE-grown GaAs/AlGaAs QW's have been studied. Unintentional Si incorporation in the AlGaAs barrier layers of samples grown at elevated substrate temperatures has been observed via SIMS profiling and attributed to Si migration during the epitaxial deposition. Hall measurements indicate that the free carrier concentration decreases due to enhanced Si compensation in samples grown both at elevated substrate temperatures and under reduced As_4 beam fluxes. The observed growth-induced variations in carrier concentration are reflected directly in both the frequency and the integrated absorption intensity of the infra-red absorption resonance. This work is significant in that it demonstrates the importance of controlled and reproducible spatially localized dopant incorporation and electrical activation in the epitaxial growth of QW intersubband detector structures.

ACKNOWLEDGEMENTS

Discussions with J. Wagner have contributed substantially to this work. The authors gratefully acknowledge the technical assistance of G. Bihlmann, H. Hoffmann, H. Biebl, B. Matthes, T. Fuchs, P. Ganser, and S. Emminger.

REFERENCES

1. L.C. West and S.J. Eglash, *Appl. Phys. Lett.* **46**, 1156 (1985).
2. K.K. Choi, B.F. Levine, C.G. Bethea, J. Walker, and R.J. Malik, *Appl. Phys. Lett.* **50**, 1814 (1987).
3. M.J. Kane, M.T. Emeny, N. Apsley, C.R. Whitehouse, and D. Lee, *Semicond. Sci. Technol.* **3**, 722 (1988).
4. A. Rockett, J. Klem, S.A. Barnett, J.E. Greene, and H. Morkoc, *J. Appl. Phys.* **59**, 2777 (1986).
5. L. Gonzalez, J.B. Clegg, D. Hilton, J.P. Gowers, C.T. Foxon, and B.A. Joyce, *Appl. Phys. A* **41**, 237 (1986).
6. A.-M. Lanzillotto, M. Santos, and M. Shayegan, *Appl. Phys. Lett.* **55**, 1445 (1989).
7. J.J. Harris, R.B. Beall, J.B. Clegg, C.T. Foxon, S.J. Battersby, D.E. Lacklison, G. Duggan, and C.M. Hellon, *J. Cryst. Growth* **95**, 257 (1989).
8. A.K. Saxena and B.B. Singh, *Phys. Rev. B* **28**, 1132 (1983).
9. M. Heiblum, W.I. Wang, L.E. Osterling, and V. Deline, *J. Appl. Phys.* **54**, 6751 (1983).
10. N. Chand, T. Henderson, J. Klem, W.T. Masselink, R. Fischer, Y.-C. Chang, and H. Morkoc, *Phys. Rev. B* **30**, 4481 (1984).
11. H. Künzel, K. Ploog, K. Wüstel, and B.L. Zhou, *J. Electr. Mat.* **13**, 281 (1984).
12. Y.G. Chai, R. Chow, and C.E.C. Wood, *Appl. Phys. Lett.* **39**, 800 (1981).
13. S.J. Allen, Jr., D.C. Tsui, and B. Vinter, *Sol. State. Comm.* **20**, 425 (1976).
14. M. Ramsteiner, J.D. Ralston, P. Koidl, B. Dischler, H. Biebl, J. Wagner, and H. Ennen, submitted for publication.
15. O.V. Emel'yanenko, T.S. Lagunova, D.N. Nasledov, and G.N. Talalakin, *Sov. Phys. Sol. State* **7**, 1063 (1965).
16. C.M. Wolfe and G.E. Stillman, *Appl. Phys. Lett.* **27**, 564 (1975).
17. R. Murray, R.C. Newman, J.L. Sangster, R.B. Beall, J.J. Harris, P.J. Wright, J. Wagner, and M. Ramsteiner, *J. Appl. Phys.* **66**, 2589 (1989).
18. A. Pinczuk and G. Abstreiter, in *Light Scattering in Solids V*, ed. by M. Cardona and G. Guntherodt (Springer, Berlin, 1989), Ch. 4 and references therein.

BERYLLIUM DOPING IN MBE-GROWN GaAs AND AlGaAs

Joseph Pellegrino, National Institute of Standards and Technology, Gaithersburg, Md.;
James Griffin, Leary Myers, and Michael Spencer, Howard University, Materials Science
Research Center of Excellence, Washington, D.C.

ABSTRACT

Beryllium is an effective p-dopant in GaAs and AlGaAs and plays an important role in device characterizations of hetero bipolar transistors. This work addresses the doping and mobility properties for two series of beryllium-doped samples: GaAs and AlGaAs. Within each series the doping ranged between $3 \times 10^{15} \text{cm}^{-3}$ to levels of $5 \times 10^{19} \text{cm}^{-3}$. Mobility and carrier concentrations were obtained through Hall and Polarized measurements. The doping concentration results suggest the onset of carrier compensation at higher doping levels. One possible explanation is that for high doping levels, Be is incorporated as interstitial donors. A thermodynamic model is used to explain the observations.

INTRODUCTION AND THEORY

Heavily doped p-type GaAs and AlGaAs have important technological applications. These include heterojunction bipolar transistors and heterostructure lasers. In this paper we characterize the electrical behavior of heavily doped p-type GaAs and $\text{Al}_x\text{Ga}_{1-x}\text{As}$ and to understand how this behavior can be correlated with the various mechanisms of beryllium incorporation in the gallium arsenide and aluminum gallium arsenide systems. Previous studies of beryllium incorporation in GaAs and AlGaAs have shown the role of interstitial Be at high doping levels⁽¹⁻⁵⁾. Kirchner⁶ et al. used a thermodynamic model for highly n-doped GaAs where the ratio of acceptor to donor concentrations was determined by the Fermi level during growth. We investigate the applicability of a similar model for the case of heavy beryllium-doped GaAs and $\text{Al}_x\text{Ga}_{1-x}\text{As}$. Beryllium can be an acceptor in GaAs if it occupies a gallium site. But beryllium can also behave as a donor if it is incorporated into an interstitial site. At equilibrium the ratio of ionized acceptors to donors is given by:

$$N_A/N_D = K(T)[P_{(A_{(i)})}]^{(1/2)}[N_i]^2/[P]^2 \quad [1]$$

where $K(T)$ is the temperature dependent rate constant. $[N_i/P]$ is the carrier concentration ratio; N_i , the intrinsic carrier concentration which can be expressed as $(N_c N_v)^{(1/2)} \exp(-E_g/2KT)$; N_c , effective density of states in the conduction band; and N_v , effective density of states in the valence band. P is the free hole concentration. Thus, P is proportional to a term which varies as $\exp(-E_g/2KT)$ where E_g = energy gap and T = temperature.

EXPERIMENTAL

Molecular-beam-epitaxial GaAs and $\text{Al}_x\text{Ga}_{1-x}\text{As}$ doped with beryllium is grown with elemental sources at a growth rate of $1 \mu\text{m/h}$ using (100) GaAs substrates. The

MBE system is a Varian Gen 1.5.* During growth the pressure in the growth chamber is approximately 10^{-8} Torr. The GaAs is grown at a substrate temperature of 580 °C, and AlGaAs at 680 °C unless otherwise stated. The material is electrically characterized using Polaron and Hall measurements. A maximum hole concentration of approximately $5 \times 10^{19} \text{ cm}^{-3}$ is observed in GaAs (Fig. 1). Attempts to incorporate more Be than this results in poor morphological surfaces. RHEED patterns monitored during growth indicate the loss of streaking and the onset of spots when more Be is added.

RESULTS

The first graph shows both Hall and Polaron data of the doping concentration of GaAs samples grown at 580 °C as a function of the beryllium cell temperature. The doping behaves quite linearly with beryllium cell temperature for doping levels approaching mid $1 \times 10^{19} \text{ cm}^{-3}$. At the higher levels the doping saturates indicating either a solubility limit has been reached or some kind of compensation is occurring. These data are in agreement with previous experimental results⁷⁻⁸. The data in Fig. 2 reveal that for a given beryllium cell temperature and a GaAs and AlGaAs growth temperature of 680 °C the doping concentration falls off with increasing aluminum mole fraction until the aluminum content is approximately 30 percent. Beyond this x-value the doping concentration varies much less strongly with increasing aluminum for Al values measured up to 45 percent.

The effects of different V/III ratios on the hole concentrations in GaAs and AlGaAs are presented in Fig. 3. These results indicate that the growth conditions involving higher arsenic overpressures, i.e., ($V/III=60$), are more effective in the p-doping of the material. Hall measurements for GaAs and AlGaAs samples ($x = 0 - 0.4$) were recorded for two different V/III ratios, 18 and 60. The data shown in Fig. 4 indicate a slight to moderate increase in the room temperature hole mobility for samples grown at the higher V/III ratio. The liquid nitrogen hole mobility is more markedly increased for those samples grown at the higher V/III=60 ratio.

The doping concentration for different growth temperatures is presented in Fig. 5. The slope of the doping versus Al mole fraction increases at the lower growth temperature (620 °C) in agreement with the model predictions. We would predict that the slope would decrease for the growth temperature of (700-720 °C). This trend is not observed.

DISCUSSION

At lower and intermediate Be furnace temperatures, (750-950 °C), the doping concentration increases linearly with temperature and then begins to saturate at higher temperatures, (greater than 990 °C). The increase in p-type doping seen in the linear part of the graph may be explained as the result of beryllium atoms substituting for

* Certain commercial equipment, instruments, or materials are identified in this paper in order to adequately specify the experimental procedure. Such identification does not imply recommendation or endorsement by the National Institute of Standards and Technology, nor does it imply that the materials or equipment identified are necessarily the best available for the purpose.

gallium atoms in the gallium arsenide. At higher beryllium furnace settings, a saturation, or compensation effect, is observed. We believe that this compensation effect is due to beryllium incorporating interstitially at the high beryllium flux. The beryllium interstitial in GaAs behaves like a donor and this donor-like behavior of the Be interstitial compensates the acceptor-like behavior of beryllium in a gallium lattice site.

The doping efficiency in the AlGaAs samples grown at 680 °C decreases linearly with increasing aluminum mole fraction out until $x=0.3$. For samples with aluminum content greater than 0.3 out to about 0.45, the doping concentration does not change very strongly with the aluminum mole fraction. The doping efficiency strongly depends on the electrochemical potential as demonstrated by the N_A^2/p^2 term in eq [1]. A similar effect has been observed in Mn-doped GaAs⁹. The variation in the hole concentration is proportional to

$$P \text{ proportional to } \exp - ((1.42 + 1.24x)/2KT) \quad [2]$$

The slope of the doping concentration with mole fraction has a theoretical value of -7.6. We observe a slope of -5.08 in the data of Fig. 2. These data are in reasonable agreement with the thermodynamic model.

The data of Fig. 3 shows two curves of doping concentration versus aluminum mole fraction for two different V/III ratios. The material grown under conditions of V/III ratio = 60 demonstrates a higher effective doping concentration than the corresponding material grown under conditions of V/III ratio = 18. As previously stated, eq [1] relates the ratio of acceptors and donors to a term involving the square root of the arsenic dimer pressure. The increase in arsenic overpressure between the two curves is roughly a factor of 3, the square root of which is about 1.7. The observed increase in the p doping is roughly a factor of 2.

The data in Fig. 4 of hole mobility as a function of aluminum mole fraction for two different V/III ratios are obtained from Hall measurements taken at liquid nitrogen and room temperatures. The data for both room-temperature and liquid-nitrogen measurements reveal that the hole mobility decreases with increasing aluminum fraction for aluminum content out to about 20 percent. In Fig. 3 the doping concentration decreases with increasing aluminum concentration. One would expect doping level and mobility to be inversely proportional, i.e., as the doping goes down the mobility should go up. Under conditions of increased arsenic overpressure and increased Al mole fraction, we observed a reduction in the hole mobility and hole concentration. Assuming a fixed number of Be atoms, we believe that the reduction in mobility and concentration are the result of a redistribution of Be atoms among Ga and interstitial sites. It appears that Be in an interstitial site has a more deleterious effect on the scattering of holes and this results in lower mobility.

Finally, the data in Fig. 5 show the doping concentration for various compositions of $\text{Al}_x\text{Ga}_{1-x}\text{As}$ at several different growth temperatures. The slope should be sharper in going to lower temperatures which is observed between the 620 and 680 °C curve but is not observed between the 680 and 720 °C curve. We believe that this is due to the uncertainty in the aluminum concentration due to the reevaporation of Ga at this

growth temperature.

CONCLUSION

We have measured the doping of Be in GaAs and $\text{Al}_x\text{Ga}_{1-x}\text{As}$ MBE samples grown under various conditions. Our results support the idea that at high doping levels Be is incorporated both substitutionally and interstitially. The ratio of substitutional and interstitial species can be explained by a simple thermodynamic model.

ACKNOWLEDGMENTS

The authors wish to acknowledge helpful discussions with Dr. James Comas (NIST). This work was in part supported by the National Science Foundation under Cooperative Agreement R11-8714767.

REFERENCES

1. N. Duhamel, P. Henot, F. Alexandre, and E. V. K. Rao, Appl. Phys. Lett. 39, 49 (1981).
2. B. Tuck and M. A. H. Kadmin, J. Mater. Sci. 7, 585 (1972).
3. V. Gosele and F. Morehead, J. Appl. Phys. 52, 4617 (1981).
4. A. H. van Ommen, J. Appl. Phys. 54, 5055 (1983).
5. L. R. Weisberg and J. Blanc, Phys. Rev. 131 (4), 1548 (1963).
6. P. Kirchner, T. Jackson, G. Pettit, and J. Woodall, Appl. Phys. Lett. 47 (1) (1 July 1985).
7. P. Enquist, L. Lunardi, G. Wicks, L. Eastman, and C. Hitzman, J. Vac. Sci. Technol. B3 (2), 634-635 (March/April 1985).
8. M. Llegems, J. Appl. Phys., Vol. 48 (3), 1278-1287 (March 1977).

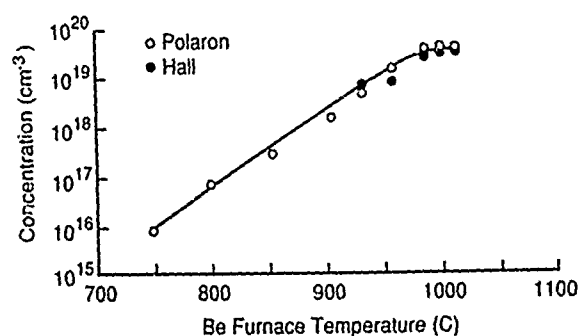


Fig. 1 Hall and Polaron data of the doping concentration of GaAs (580°C) as a function of Be cell temperature.

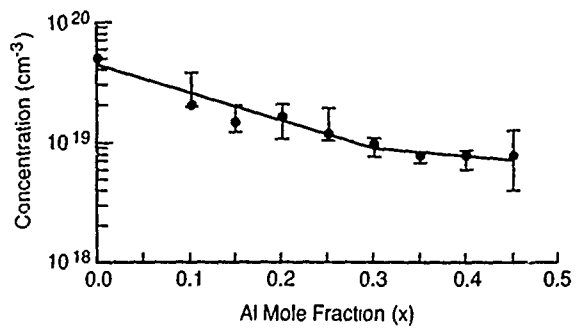


Fig. 2 Doping versus Aluminum mole fraction (680°C)

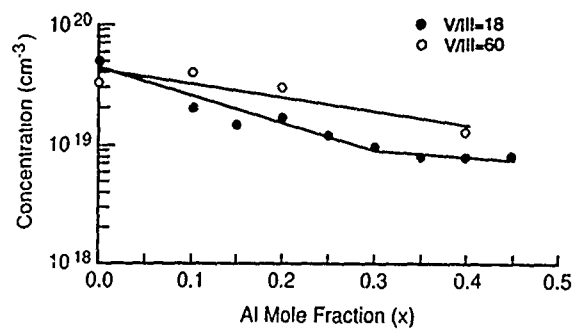


Fig. 3 Two curves of doping concentration versus aluminum mole fraction for two different V/III ratios.

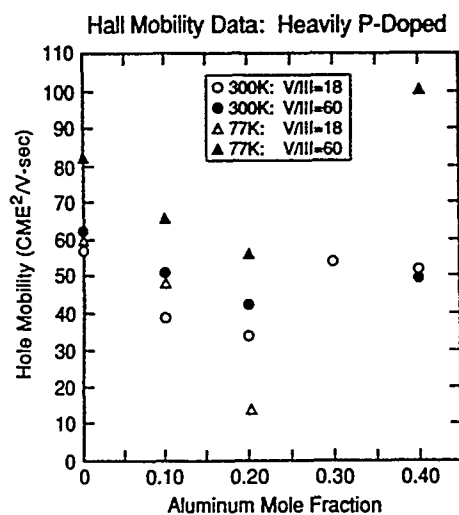


Fig. 4 Hole mobility as a function of aluminum mole fraction for two different V/III ratios from Hall measurements at LN2 and room temperature.

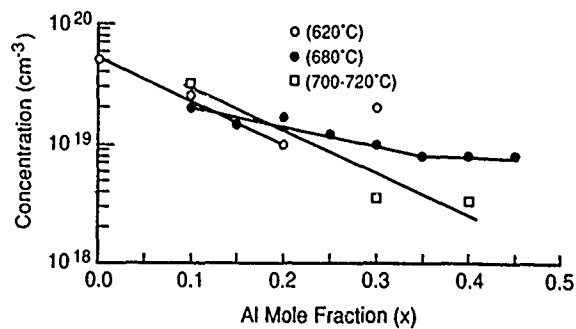


Fig. 5 Doping versus mole fraction for several different growth temperatures

CARBON DOPING IN InGaAs GROWN BY MBE

HIROSHI ITO AND TADAO ISHIBASHI

NTT LSI Laboratories, 3-1, Morinosato Wakamiya, Atsugi-shi, Kanagawa 243-01
JAPAN

ABSTRACT

Carbon doping in $\text{In}_x\text{Ga}_{1-x}\text{As}$ is investigated using solid source MBE. InAs mole fractions, x , from 0 to 1 are tested. Under a constant doping level, hole concentration decreases with increasing x . When x is higher than 0.6, the conduction type is n and electron concentration increases with x . The conduction-type inversion and the behavior of carrier mobilities are explained by a self-compensation mechanism.

INTRODUCTION

Heavily doped semiconductor layers are very important in fabricating various high-speed electron and optoelectronic devices because extremely low contact and sheet resistances are generally required. Be [1] and Zn [2] are widely used as p-type dopants in MBE and MOCVD growth of III-V compound semiconductors since very high carrier concentrations of required levels can be obtained with them. However, diffusion coefficients of these dopants are not sufficiently small [1,3] at the temperatures generally used for epitaxial growth of various devices.

Recently, C has gained popularity as a p-type dopant for GaAs. Its diffusion coefficients in GaAs crystals are 1~2 orders of magnitude smaller than those of Be or Zn. Its maximum available free carrier concentration of $1.5 \times 10^{21} \text{ cm}^{-3}$ [4] is also higher than that of Be or Zn.

InGaAs layers are promising materials for future high speed devices due to high electron mobility and high peak electron drift velocity. Thus, carbon doping for $\text{In}_{0.53}\text{Ga}_{0.47}\text{As}$ lattice matched to InP substrate is of great interest. Only two experiments on C doping for InGaAs have been reported to date. One is by the MOMBE method using metal alkyls as C sources [5]. All the C doped InGaAs layers obtained were n-type, regardless of source material. The other experiment was by the MOCVD method using CCl_4 as the C source, which resulted in p-type InGaAs layers [6]. In the former case, C impurities were highly compensated in InGaAs, which indicated the amphoteric characteristics of C in the (In,Ga)As system at a In mole fraction of 0.53.

This paper reports C doping for InGaAs by solid source MBE. Indium mole fractions in the (In,Ga)As system from 0 (GaAs) to 1 (InAs) were tested.

EXPERIMENTAL

The MBE system used in this study was the RIBER 2300P. Epi-layers were grown directly on (100) oriented semi-insulating GaAs substrates. A graphite filament [7], heated by flowing current directly through the filament, was used as the C source. The growth rate was $1 \mu\text{m/h}$, and the V/III ratio was about 5. Substrate temperatures from 400°C (InAs) to 650°C

(GaAs) were used for the growth, selecting the appropriate value for each In mole fraction. The free carrier concentration and Hall mobility of the grown layers were evaluated using van der Pauw measurements. The temperature of the C filament was measured with an optical pyrometer.

RESULTS AND DISCUSSION

The measured carrier concentrations of GaAs and InAs layers at room temperature, as a function of the reciprocal C filament temperature, are shown in Fig.1. It was found that the conduction type of C doped InAs is n, although that of C doped GaAs is p. This is consistent with reported results that C implanted InAs shows n-type conduction [5]. The free carrier concentration of InAs at the same doping concentration is about an order of magnitude smaller than that of GaAs. The experimental measurements for both materials agree well with the gradient of the C vapor pressure curve shown in Fig.1. This implies that the free carrier concentrations are proportional to the C arrival rate.

The dependence of Hall mobility on free carrier concentration of GaAs and InAs is shown in Fig.2. The mobilities of MBE-grown Be doped GaAs and MBE-grown Si doped InAs [8] are also shown for comparison. Hole mobilities of C doped GaAs are very close to those of Be doped GaAs. This indicates that the compensation ratio of C doped GaAs is comparable to that of Be doped GaAs which is usually very small. On the other hand, electron mobilities of C doped InAs layers are relatively lower than that for Si doped InAs. A possible reason for these low electron mobilities of C doped InAs layers is that the compensation ratio is very high. This relates to the result shown in Fig.1 where the free carrier concentration is very low compared with that of GaAs at the same doping concentration. To check this, C concentrations in GaAs and InAs layers at the same doping concentration were measured using SIMS analysis. It was confirmed that nearly the same

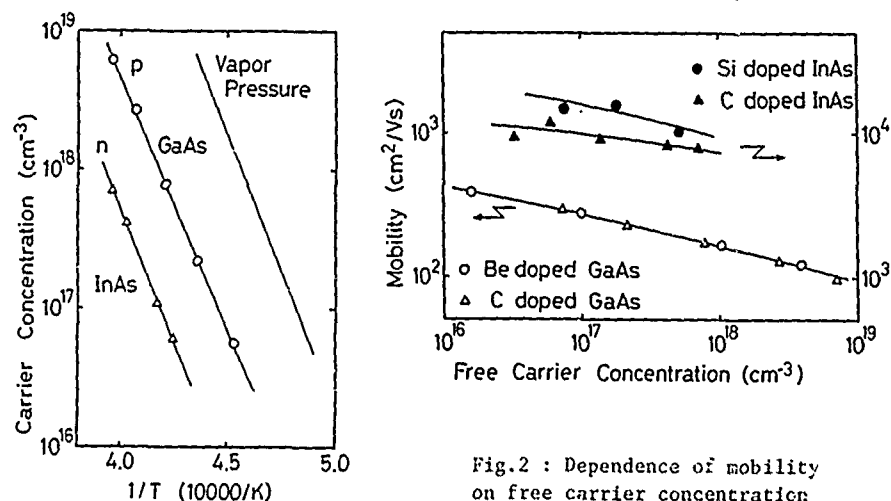


Fig.1 : Free carrier concentrations at room temperature for C doped GaAs and InAs, as a function of reciprocal C filament temperature.

Fig.2 : Dependence of mobility on free carrier concentration of C doped GaAs and InAs layers. Data for Be doped GaAs and Si doped InAs are also shown for comparison.

amount of C atoms were incorporated in both samples, which indicates that the sticking coefficients of C to GaAs and InAs are nearly the same. This result also supports the hypothesis that the compensation ratio in C doped InAs is very high.

The dependence of free carrier concentration and Hall mobility of InGaAs layers in relation to In mole fraction is shown in Fig.3. The doping concentration was kept constant at the point where a free carrier concentration of $6 \times 10^{18} \text{ cm}^{-3}$ can be obtained in the GaAs layer. Free carrier concentration decreases gradually and then more rapidly when the InAs mole fraction increases from 0 to 0.54. In this region, the conduction type is p. Hole mobility also decreases with increasing In mole fraction. When x is greater than 0.68, free carrier concentration increases with an increase in the In mole fraction. The conduction type is n in this region. Electron mobility also increases with increasing InAs mole fraction. As shown here, a conduction-type inversion occurs in C doped InGaAs layers at an InAs mole fraction of about 0.6.

Temperature dependences of Hall mobilities of GaAs, $\text{In}_{0.45}\text{Ga}_{0.55}\text{As}$, and InAs were measured to reveal the activation energy of acceptors or donor in these materials as shown in Fig.4. Each curve is almost temperature-independent, showing that activation energies of C acceptors in GaAs and $\text{In}_{0.45}\text{Ga}_{0.55}\text{As}$ or the C donor in InAs are very small. Therefore, the free carrier concentration reduction at around $x = 0.6$ is not due to the formation of deep acceptor or donor levels in these materials.

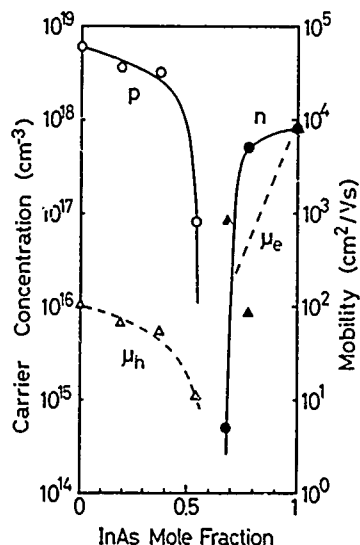


Fig.3 : Dependence of free carrier concentration and mobility on the InAs mole fraction in (In,Ga)As systems.

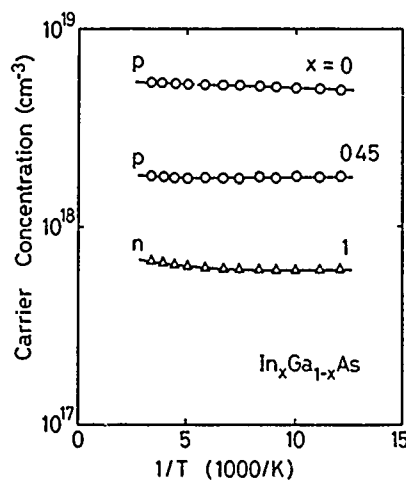


Fig.4 : Temperature dependence of free carrier concentrations in GaAs, $\text{In}_{0.45}\text{Ga}_{0.55}\text{As}$, and InAs layers.

Taking these results into account, the conduction-type inversion which occurs at an InAs mole fraction of about 0.6 must be due to a self-compensation. This amphoteric property of C in an InGaAs layer can be interpreted as follows.

Table I shows average bond strengths for Ga-CH₃, As-CH₃ and In-CH₃ [9]. Although these values do not represent actual binding energies for Ga-C, As-C and In-C on the epilayer surface during MBE growth, the relative

relationship among them is regarded as holding true for the binding energy between C and metals. In the GaAs layer, the binding energy for Ga-C is higher than that for As-C. This may give rise to the fact that C atoms preferably occupy As (acceptor) sites. On the other hand, the binding energy of In-C is lower than that of As-C in an InAs layer. This should make C atoms occupy In (donor) sites more easily. When the In mole fraction is between 0 and 1, the occupation probability of a III or V site by a C atom is thought to change gradually, depending on the binding energy difference among Ga-C, As-C and In-C. This is regarded as the reason for the conduction-type inversion at an InAs mole fraction of about 0.6.

Table I : Average metal-ligand bond strengths for metal alkyls.

Ga-CH ₃	59
As-CH ₃	55
In-CH ₃	47
(kcal/mole)	

CONCLUSIONS

Carbon doping in $\text{In}_x\text{Ga}_{1-x}\text{As}$ has been investigated using solid source MBE. The sticking coefficients of C to GaAs and InAs are found to be nearly the same. Under a constant doping concentration, free carrier concentration decreases as x increases from 0 to 0.54. In this region, the conduction type is p. Hole mobility also decreases with increasing x . When x is higher than 0.68, the conduction type is n. Electron concentration and electron mobility increase with increasing x . These results indicate that the conduction-type inversion which occurs when x is about 0.6 is due to a self-compensation.

ACKNOWLEDGEMENTS

The authors would like to thank Masahiro Hirayama and Kazuo Hirata for their valuable suggestions.

References

1. M. Ilegems, J. Appl. Phys. **48** 1278 (1977).
2. S. J. Bass and P. E. Oliver, Inst. Phys. Conf. Ser. No.33b 1 (1977).
3. C. Dubon, R. Azoulay, M. Gauneau, L. Dugrand, A. Sibille, J. Dangla, A. M. Duchenois, and D. Ankri, Inst. Phys. Conf. Ser. No.74 175 (1985).
4. T. Yamada, E. Tokumitsu, K. Saito, T. Akatsuka, M. Miyauchi, M. Konagai, and K. Takahashi, J. Cryst. Growth **95** 145 (1989).
5. M. Kamp, R. Contini, K. Werner, H. Heinecke, M. Weyers, H. Lüth, and P. Balk, J. Cryst. Growth **95** 154 (1989).
6. G. E. Stillman, B. T. Cunningham, B. Lee, and S. S. Bose, presented at the 16th International Symposium on Gallium Arsenide and Related Compounds, Karuizawa, JAPAN, 1989 (to be published).
7. R. J. Malik, R. N. Nottenberg, E. F. Schubert, J. F. Walker, and R. W. Ryan, Appl. Phys. Lett. **53** 2661 (1988).
8. R. A. A. Kubiak, E. H. C. Parker, S. Newstead, and J. J. Harris, Appl. Phys. **A35** 61 (1984).
9. G. B. Stringfellow, Organometallic Vapor-Phase Epitaxy (Academic Press, San Diego, 1989), p.18.

PART XIV

Ordering in Alloys

ORDERING IN III/V ALLOYS

G.B. Stringfellow
College of Engineering, University of Utah, Salt Lake City, Utah 84112

ABSTRACT

Simple calculations using the delta-lattice-parameter (DLP) model indicate that the enthalpy of mixing is invariably larger than or equal to zero for III/V alloys, and increases with increasing difference in lattice constant for the constituent binary compounds. In terms of the regular solution model this suggests the occurrence of miscibility gaps. Solid phase immiscibility has indeed been observed in a number of systems. Nevertheless, such alloys can be grown by OMVPE, including the highly metastable alloys GaPSb and InPSb. Initially surprising was the occurrence of ordered structures in these same alloys. The regular solution model apparently specifically excludes immiscibility and ordering in the same system. However, when the positive enthalpy of mixing is due to strain energy effects, as in III/V alloys, Hume-Rothery recognized very early that such phenomena should be anticipated. This was later confirmed by detailed first principles calculations. In fact, the tendency for ordering is anticipated to increase as the difference in tetrahedral radii of the elements sharing a common sublattice increases. Thus, it is somewhat surprising that ordering was first observed in the AlGaAs system where Al and Ga have nearly equal sizes. Ordered structures have now been observed in several III/V alloy systems including the ternary systems GaAsSb and GaInP and the quaternaries GaInAsP, GaInAsSb, and AlGaInP. In this paper, ordering in other alloy systems such as GaPSb and InAsSb will be described. Surprisingly, no strong correlation between atomic size difference and the degree of ordering has been observed. Another unexpected observation is that the preferred ordered structure for most ternaries involves ordering along the {111} directions. Both first principles total energy and simple strain energy calculations indicate that such ordered structures are only slightly more stable than the disordered solid solution. Other ordered structures, including L1₀, where ordering occurs along the {100} directions, are considerably more stable. Both phenomena must be explained in terms of the surface kinetic processes occurring during epitaxial growth. Such an explanation is supported by the importance of kinetic parameters such as growth rate, temperature, and substrate orientation in determining both the degree of order and the specific ordered structures observed.

THERMODYNAMIC BACKGROUND

The regular solution model is a semi-quantitative model for the calculation of the free energy of mixing of multicomponent systems. The entropy of mixing is considered to be ideal and the enthalpy of mixing is calculated assuming interactions only between nearest neighbor atom pairs with the atoms residing on a lattice with coordination number Z. For a solution consisting of only A and C atoms, the nearest-neighbor bond energies are designated H_{AC}, H_{AA}, and H_{CC}. The bond energies are commonly thought of as being due to "chemical" interactions, frequently related to charge transfer due to differences in electronegativity, and "strain" energies related to distortions in the lattice due to differences in the sizes of the constituent atoms. Using these assumptions, it is possible to express the enthalpy of mixing of a binary solution A + C in simple terms,

$$\Delta H^M = x(1-x)\Omega \quad (1)$$

where the interaction parameter, Ω , is

$$\Omega = ZN^0 \left[H_{AC} - \frac{1}{2} (H_{AA} + H_{CC}) \right]. \quad (2)$$

N^0 is Avogadro's number.

The regular solution model is not expected to provide significant physical insight into the thermodynamics of mixing of semiconductor solid solutions. However, treated as a purely empirical model, it is useful for the interpolation and extrapolation of phase diagram information in systems for which some experimental data are available. The interaction parameters can be obtained only by fitting the model to experimental free energy or activity coefficient data or by application of the model to the calculation of a phase diagram with the interaction parameter(s) adjusted to provide the best fit to the experimental data.

It is frequently desirable to have a predictive model allowing the calculation of the thermodynamic properties of semiconductor alloys even in systems for which no experimental data exist. This is a difficult problem since the cohesive energies are much larger than mixing enthalpies.

In semiconductors which are nearly covalent like the III-V compounds, the atomization energy, ΔH^{at} , is used as a measure of bonding energy. Using the Phillips-van Vechten model of bonding[1], this quantity can be written[2]

$$\Delta H^{\text{at}} = K a_0^{-2.5} \quad (3)$$

Considering the zero of enthalpy to be infinitely separated atoms, the interaction parameter for the system AC + BC can be calculated from the enthalpy of mixing at $x = 1/2$, yielding[2],

$$\begin{aligned} \Omega^s &= 4K \{ -[(a_A + a_B)/2]^{-2.5} + 1/2(a_A^{-2.5} + a_B^{-2.5}) \} \\ &\approx 99K(a_A - a_B)^2 / (a_A + a_B)^{4.5}, \end{aligned} \quad (4)$$

where a_A and a_B are the lattice constants of AC and BC, and the lattice constant at $x = 0.5$ is obtained using Vegard's law. The value of K was obtained by making a least squares fit of Eqn. (4) to available experimental values of Ω^s . The standard deviation between experimental and calculated results is found to be only 412 cal mol⁻¹[2].

A striking feature of this delta-lattice-parameter or DLP model is that the interaction parameter, hence the enthalpy of mixing, is always positive. The experimental data verify this prediction; not a single III/V alloy has a negative enthalpy of mixing. This is also true, incidentally, for II/VI alloys. Remarkably, for systems with end components having the same interatomic spacing, such as GaAs-AlAs, the solid solution is ideal. In the traditional regular solution model, this is strongly suggestive that the enthalpy of mixing is due to strain, rather than chemical factors. Fedders and Muller[3] performed the strain calculation assuming the virtual crystal model, which yielded interaction parameters more than a factor of 4 too large. This was interpreted as being due to the failure of the virtual crystal approximation (VCA), i.e., the bond distortions are approximately a factor of 4 smaller than deduced from the virtual crystal model. In fact, the virtual crystal model is not a good description of the bond lengths in semiconductor solid solutions. Mikkelsen and Boyce[4] discovered that the bond lengths in the alloy more nearly resemble the bond lengths in the pure binary compounds than the average values anticipated from the virtual crystal model.

As observed by Fedders and Muller, this convergence of two apparently divergent approaches, one beginning with the simplified band structure and the other with the strain energy, is perhaps not surprising considering that both elastic properties and bonding are ultimately determined by the electron energy states in the solid.

Both the DLP and strain energy models discussed above are semiempirical: They each contain a parameter adjusted to fit the experimental data. More recently a number of publications have shown that equally good results can be obtained with no adjustable parameters. Both Fukui[4] and Martins and Zunger[5] have performed calculations of bond lengths and enthalpies of mixing based on the valence force field (VFF) model. The interactions between atoms are considered to be due entirely to strain, i.e., the stretching and bending of the bonds. The bond lengths are calculated by assuming the sublattice on which mixing occurs is uniform, as in the VCA model. More recently Chen and Sher[6] demonstrated that bond lengths and enthalpy of mixing could be accurately calculated considering both strain and chemical effects.

Miscibility Gaps

A feature of both the DLP and strain energy models is that they predict a large positive enthalpy of mixing for systems with a large difference in lattice constant. This can overwhelm the negative entropy of mixing for temperatures below the critical temperature, resulting in a free energy versus composition curve with an upward bowing in the center. This dictates that at equilibrium a random alloy in a certain composition range will decompose into a mixture of two phases, i.e., the phase diagram contains a miscibility gap.

By exploiting the kinetic limitations of atomic rearrangement on the growing surface, techniques such as organometallic vapor phase epitaxy (OMVPE) and molecular beam epitaxy (MBE) can be used to grow these metastable alloys. The extreme case is the growth of GaPSb alloys over the entire composition range by OMVPE even though at a typical growth temperature of 530°C the miscibility gap extends from 0.01 to 0.99[8]. Other less metastable alloys such as GaAsSb[9] and InPSb[10] can also be grown by OMVPE. The key parameter is the V/III ratio, which must be kept near unity for the successful growth of these metastable alloys.

Atomic Ordering

Unexpectedly, long range ordering has been observed in III/V solid solutions with large positive deviations from ideality, including those discussed above which contain large miscibility gaps. The superficial application of the regular solution model suggests that clustering and phase separation will occur in systems with positive interaction parameters, since the AC bonds are less stable than AA and CC bonds[11]. On the other hand, a negative interaction parameter, when AC bonds are more stable, is predicted to produce both short and long range ordering[11].

Short range ordering simply means that more AC bonds exist than for a random alloy. In long range ordering the AC bonds form a pattern with formation of a new superlattice crystal structure having translational symmetry with a period usually double that of the normal lattice. For example, in the GaAsSb system, metastable alloys grown by OMVPE have electron diffraction patterns as seen in Fig. 1[12,36]. The electron diffraction pattern for a disordered GaAsSb epitaxial layer shows only the spots with unmixed indices typical of the zincblende crystal structure. The extra, smaller spots in Fig. 1 are indicative of the formation of ordered phases. In this particular case two ordered structures are formed. For two variants of the $L1_0$ (Cu-Au) ordered structure the periodicity is doubled along the two $\langle 100 \rangle$ directions perpendicular to the growth axis, i.e., the structure consists of alternating layers of GaAs and GaSb along these directions. An additional ordered structure, termed $E1_1$ (chalcopyrite), is also observed which has double the periodicity of the normal lattice along the $\langle 210 \rangle$ directions.

The solution to the apparent dichotomy of ordered structures in systems with large positive deviations from ideality is suggested by early observations for ordered structures in metal systems. Swalin[13] suggests that the regular solution model conclusions related to the preference of a system for clustering or ordering, for a positive or negative interaction parameter, respectively, apply only when the bond energies, H_{AA} , H_{CC} , and H_{AC} are due to chemical factors. If the positive deviation from ideality is due to strain, the atoms tend to be arranged with a larger than random number of unlike nearest neighbor pairs. Four decades ago Hume-Rothery recognized the obvious, that clustering in systems with a large difference in atomic size resulted in large strain energies. He suggested that a size difference would drive both short and long range ordering.[14]

The apparent contradiction is resolved by noting that the phase separation resulting from a large positive enthalpy of mixing involves the formation of two completely incoherent phases. Clustering, on the other hand, involves the formation of coherent regions with dissimilar compositions. The coherency strain energy prevents clustering.[15]

The apparent contradiction is resolved by noting that the phase separation resulting from a large positive enthalpy of mixing involves the formation of two completely incoherent phases. Clustering, on the other hand, involves the formation of coherent regions with dissimilar compositions. The coherency strain energy prevents clustering.[15] In this case, the microscopic strain energy can be reduced by either long or short range ordering.

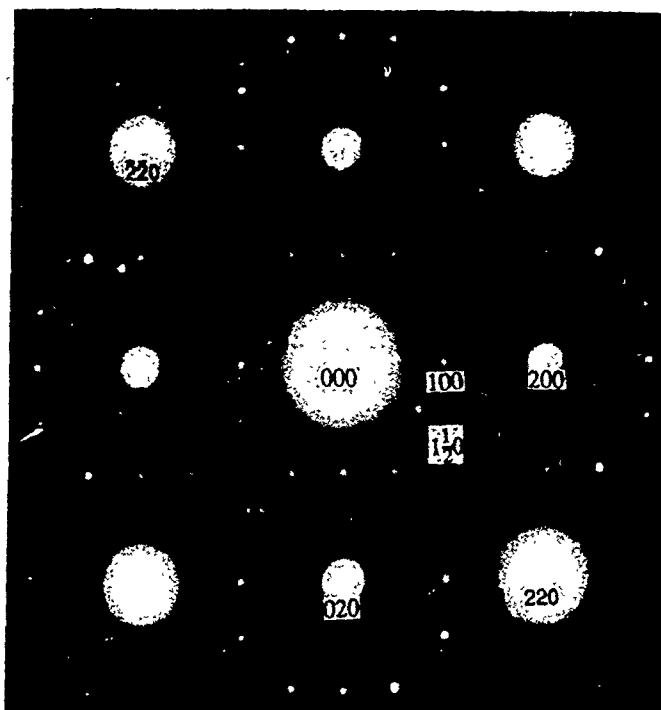


Figure 1. [001] electron diffraction patterns for (001) oriented sample of $\text{GaAs}_{1-x}\text{Sb}_x$ with $x=0.5$. Sample grown at 600°C with L1_0 and E1_1 ordered structures. (after Jen et al [36]).

First principles local density self-consistent total energy minimization calculations in semiconductor alloy systems[16] provided the first detailed rationalization of the ordered structures observed in III/V alloys. The total energy of $\text{Ga}_{0.5}\text{In}_{0.5}\text{P}$ was found to be lower for the L1_0 and E1_1 ordered structures than for a disordered mixture. The L1_0 and E1_1 structures are calculated to have lower energies than for other ordered structures such as the L1_1 or Cu-Pt structure with ordering along $\langle 111 \rangle$ directions in the lattice[17]. However, the energy is still lower for incoherent phase separation. Coherency strain energy and kinetic factors often prevent complete phase separation during epitaxial growth, thus the metastable ordered structures are formed.

An interesting feature of the calculations is that the ordering is shown to be due to strain factors, in accordance with the simple analysis of Hume-Rothery. For AlGaAs alloys where AlAs and GaAs have nearly the same lattice constant, ordering is not predicted[16,17]. However, Kuan et al [18] observed ordering in AlGaAs grown by both OMVPE and MBE. On the other hand, the GaPSb and InPSb systems have very large miscibility gaps due to the large differences in atomic radii between P and Sb. $\text{GaP}_{1-x}\text{Sb}_x$ has a calculated critical temperature of 1996°K : The miscibility gap at 530°C ranges from $x=0.01$ to 0.99 , covering essentially the entire range of solid composition. Nevertheless, epitaxial layers have been grown over nearly the entire composition range [8]. Very little ordering occurs in layers grown on (100) oriented GaAs substrates[19]. This is ascribed to

kinetic effects, since the driving force for ordering should be larger in this material than for most other III/V alloys.

The determination of exactly which of the ordered structures is formed may also be partially determined by kinetic factors. The ordered structure forming most rapidly at the surface during the dynamic epitaxial growth process will be observed. For $\text{GaAs}_{0.5}\text{Sb}_{0.5}$, where the thermodynamic analysis should be similar to that for $\text{Ga}_{0.5}\text{In}_{0.5}\text{P}$ discussed above, the L1_0 structure is formed exclusively during OMVPE growth at low temperatures, and both L1_0 and E1_1 are formed at higher growth temperatures [20]. Several groups have reported ordered structures in MBE-grown $\text{GaAs}_{0.5}\text{Sb}_{0.5}$. In every case the ordered structure is neither L1_0 nor E1_1 , but has ordering along the $\langle 111 \rangle$ directions in the lattice [21], the Cu-Pt structure. The same ordered structure has been reported exclusively for the GaInP system [22], and also for AlInAs [23], GaInAs [24], GaInAsP [24], and GaAsP [34] alloys. Since the ordered structures are formed at the surface, during growth, due to the low diffusion coefficients in the solid, the strain energy of the various ordered structures at the surface may determine the ordered structure(s) formed, i.e., the thermodynamic analysis must involve the "surface phase". In fact, recent calculations of Zunger [25] indicate that the L1_1 structure has the lowest energy at the surface.

In contrast with the GaAsSb results, the similar alloy InAsSb has a completely different ordered structure. The $[110]$ pole diffraction pattern shown in Figure 2 for a sample with $x=0.48$ grown by OMVPE at a temperature of 450°C clearly shows the existence of the Cu-Pt ordered structure [26]. In some samples two of the four Cu-Pt variants are observed, as in Fig. 2. In other areas only a single variant is seen, giving rise to an asymmetric TED pattern.

DISCUSSION

The occurrence of ordered structures over nearly the entire set of III/V alloys, as summarized in Table I, is more than an academic phenomenon. The ordered structures inherently have lower band gaps than for the disordered alloys. In $\text{Ga}_{0.5}\text{In}_{0.5}\text{P}$, the band gap is reduced by nearly 80 meV for the ordered structure [27]. This has the undesirable effect of shifting the emission of laser devices to longer wavelengths. Thus, it is worthwhile to attempt to understand the kinetic aspects of ordering.

The work of Asai [28] indicates that OMVPE growth of GaAs on (100) oriented substrates occurs by the lateral motion of $[110]$ and $[-110]$ steps across the surface. In fact, the steps appear to have $\{111\}$ orientations, which intersect the (100) surface in $[110]$ and $[-110]$ directions. The simple postulate that atoms with a large difference in atomic size will occupy alternate sites along the step, and that the next step will be similar, with a lateral displacement by one atom to allow the smaller atoms to be next to the larger atoms on the previous step, results in the growth of the two variants of the L1_0 structure with ordering directions perpendicular to the growth direction. L1_0 is, of course, one of the ordered structures which is thermodynamically most stable. The two variants expected from this analysis are exactly those observed for GaAsSb, as described above.

The Cu-Pt ordered structure is observed in a wide variety of III/V alloys. As discussed above, such structures result in less reduction in strain energy in the bulk alloy, so are considerably less stable than the L1_0 and E1_1 structures. A combined surface strain energy and kinetic argument related to the model of Asai [28] has been used by Suzuki et al. [29] to justify the existence of the Cu-Pt structure. For growth on (100)-oriented substrates, the strain energy at the surface is minimized when the large and small atoms are placed in alternating rows along the $[110]$ steps. When the relative displacements from layer to layer is constant, this produces Cu-Pt ordering. They suggest the occurrence of $\{111\}$ -oriented microfacets at the step to explain the displacement of rows of large and small atoms from one layer to the next. Such microfacets are unlikely to occur during normal OMVPE growth. An alternate explanation is based on the lowest energy configuration of the "surface phase", which is suggested to favor the Cu-Pt ordered structure [25]. However, any explanation which ignores the kinetics of the growth process will be unable to explain the different ordered structures observed by various workers in the same materials. The significant involvement of kinetic factors is also indicated by the

strong dependence of ordering on growth temperature, growth rate, and substrate orientation[32].

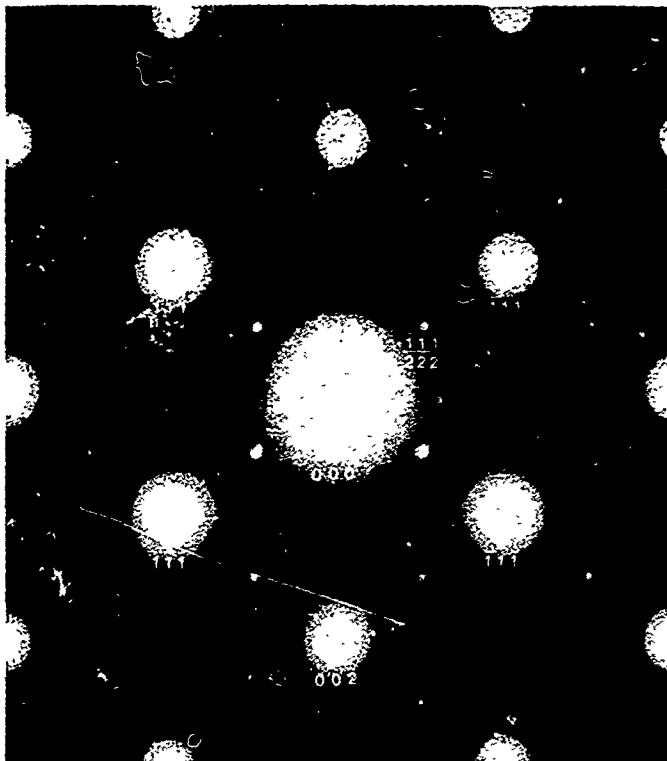


Figure 2. [110] pole transmission electron diffraction pattern for a sample of $\text{InAs}_{0.52}\text{Sb}_{0.48}$ grown by OMVPE at a temperature of 450°C showing the presence of the L1_2 ordered structure. (after Jen et al[26]).

SUMMARY

All III/V alloys are found to have positive values of enthalpy of mixing, with the magnitude increasing as the square of the difference in lattice parameter. In systems such as GaAsSb, InPSb, and GaPSb, this leads to regions of solid immiscibility. In spite of this, such alloys can be grown by OMVPE by using the proper growth conditions. The system attempts to relieve the strain energy by forming either compositional clusters, leading to phase separation, only when the system is not constrained by coherency strain energy effects. In coherent systems, the microscopic strain energy can be relieved by atomic scale ordering. Both strain energy and *ab initio* total energy calculations demonstrate that ordered structures are thermodynamically stable relative to disordered alloys for systems with large differences in lattice constant between the binary constituents. The most stable structures are E1_1 , with ordering along the six $\langle 210 \rangle$ directions, and L1_0 , with ordering along the three $\langle 100 \rangle$ directions in the lattice. Much less stable, but also more stable than the disordered alloy, is the Cu-Pt structure, L1_1 , with ordering along the $\langle 111 \rangle$ directions. Ordering is observed for nearly all III/V alloys. However, the ordered structures are not always those expected from thermodynamic considerations. In GaAsSb grown by OMVPE, the lowest energy L1_0 and E1_1 structures are observed with a high degree of order. For many other systems grown under similar conditions the much less stable Cu-Pt

or L1₁ structure is formed. Kinetic and surface thermodynamic models of the growth of (100) oriented epitaxial layers are considered in an effort to explain the structures observed. However, several phenomena remain unexplained: 1) The extent of order is not related to the lattice constant difference, i.e., ordering is observed for AlGaAs, where $\Delta a = 0$, but not for GaPSb, where Δa is large. 2) Different ordered structures are observed for different alloy systems and, for GaAsSb, for different growth techniques. These anomalies suggest that kinetic effects play a key role.

ACKNOWLEDGEMENTS

The author wishes to thank the Department of Energy for support of this work.

Table 1: SUMMARY OF ORDERING IN III/V ALLOYS

Material/ Technique	$\Delta a/a(\%)$	Substrate Orientation	Ordered Structure	Reference
AlGaAs	0.16	(100),	L1 ₀	Kuan et al
OMVPE		(110)		[18]
GaInAs	6.92	(100)	L1 ₀ , E1 ₁	Nakayama et al
LPE			(DO ₂₂ ?)	[30]
GaInAs	6.92	(110)	L1 ₀	Kuan et al
MBE				[31]
GaInAs(Sb)		(100)	L1 ₀ , E1 ₁	Jen et al
OMVPE				[32]
GaInAs(P)		(100)	L1 ₁	Shahid et al
VLE				[24]
GaInP	7.39	(100)	L1 ₁	Goral et al
OMVPE				[22]
GaInP	7.39	(100)	L1 ₁	Gomyo et al
OMVPE				[27]
GaInP	7.39	(100)	L1 ₁	Ueda et al
OMVPE				[33]
AlGaInP	7.39	(100)	L1 ₁	Suzuki et al
OMVPE				[29]
AlInAs	6.76	(100)	L1 ₁	Norman et al
OMVPE				[23]
GaAsSb	7.54	(100)	L1 ₀ , E1 ₁	Jen et al
OMVPE		(110), (221), (311)		[12]
GaAsSb	7.54	(100)	L1 ₁	Murgatroid et al
MBE				[21]
GaAsSb	7.54	(100)	L1 ₁	Ihm et al
MBE				[21]
InAsSb	6.72	(100)	L1 ₁	Jen et al
OMVPE				[26]
GaPSb	10.7	(100)	L1 ₁	Jen et al
OMVPE				[19]
GaAsP	3.42	(100)	L1 ₁	Jen et al
OMVPE				[34]
InPSb	9.9	(100)	L1 ₁	Jen et al
OMVPE				[35]

REFERENCES

- 1) J.C. Phillips, *Bonds and Bands in Semiconductors* (Academic Press, New York, 1973).

- 2) G.B. Stringfellow, *J. Crystal Growth* 27 21 (1974).
- 3) P.A. Fedders and M.W. Muller, *J. Phys. Chem. Sol.* 45 685 (1984).
- 4) J.C. Mikkelsen and J.B. Boyce, *Phys. Rev. Lett.* 49 1412 (1982).
- 5) T. Fukui, *Japan. J. Appl. Phys.* 23 L208 (1984) and *J. Appl. Phys.* 57 5188 (1985).
- 6) J.L. Martins and A. Zunger, *Phys. Rev. B* 30, 6217 (1984).
- 7) A.B. Chen and A. Sher, *Phys. Rev. B* 32, 3695 (1985).
- 8) M.J. Jou, Y.T. Cherng, H.R. Jen, and G.B. Stringfellow, *Appl. Phys. Lett.* 52 549 (1988).
- 9) M.J. Cherng, R.M. Cohen, and G.B. Stringfellow, *J. Electron. Mater.* 13 799 (1984).
- 10) M.J. Jou, Y.T. Cherng, and G.B. Stringfellow, *J. Appl. Phys.* 64 1472 (1988).
- 11) N.A. Gokcen *Statistical Thermodynamics of Alloys* (Plenum Press, New York, 1986) p. 118.
- 12) H.R. Jen, M.J. Cherng, and G.B. Stringfellow, *Appl. Phys. Lett.* 48 1603 (1986).
- 13) R.A. Swalin *Thermodynamics of Solids*, (New York: John Wiley & Sons, 1972).
- 14) W. Hume-Rothery, *Electrons, Atoms, Metals, and Alloys*, 3rd Edition, (Dover, London, 1963), Chapter 39. The first edition was published in 1948.
- 15) G.B. Stringfellow, *J. Crystal Growth* 65 454 (1983).
- 16) G.P. Srivastava, J.L. Martins, and A. Zunger, *Phys. Rev. B* 31, 2561 (1985).
- 17) A. Zunger and D.M. Wood, *J. Crystal Growth* (to be published).
- 18) T.S. Kuan, T.F. Kuech, W.I. Wang, and E.L. Wilkie, *Phys. Rev. Lett.* 54 201 (1985).
- 19) H.R. Jen, M.J. Jou, and G.B. Stringfellow (unpublished results).
- 20) H.R. Jen, M.J. Jou, Y.T. Cherng, and G.B. Stringfellow, *J. Cryst. Growth* 85 175 (1987).
- 21) J. Murgatroyd, A.G. Norman, and G.R. Booker, Materials Research Society Spring Meeting, Palo Alto, CA, April, 1986; Y.E. Jhm, N. Otsuka, J. Klem, and H. Morkoc, *Appl. Phys. Lett.* 51 2013 (1987).
- 22) A. Gomyo, T. Suzuki, K. Kobayashi, S. Kawata, I. Hino, and T. Yuasa, *Appl. Phys. Lett.* 48 1603 (1987); S. McKernan, B.C. DeCooman, C.B. Carter, D.P. Bour, and J.R. Shealy, *J. Mater. Res.* 3 406 (1988); J.P. Goral, M.M. Al-Jassim, J.M. Olson, and A. Kibbler, *Epitaxy of Semiconductor Layered Structures*, (Materials Research Society, Pittsburg, 1988), pp. 583-589.
- 23) A.G. Norman, R.E. Mallard, I.J. Murgatroyd, G.R. Booker, A.H. Moore, and M.D. Scott, *Inst. Phys. Conf. Ser.* 87 77 (1987).
- 24) M.A. Shahid and S. Mahajan, *Phys. Rev. Lett. B* 38 1344 (1988).
- 25) A. Zunger (private communication).
- 26) H.R. Jen, K.Y. Ma, and G.B. Stringfellow, *Appl. Phys. Lett.* 54 1154 (1989).
- 27) A. Gomyo, T. Suzuki, and S. Iijima, *Phys. Rev. Lett.* 60 2645 (1988).
- 28) H. Asai, *J. Crystal Growth* 80 425 (1987).
- 29) T. Suzuki, A. Gomyo, and S. Iijima, *J. Crystal Growth*, 93 396 (1989).
- 30) H. Nakayama and H. Fujita, *Inst. Phys. Conf. Ser.* 79 289 (1986).
- 31) T.S. Kuan, W.I. Wang, and E.L. Wilkie, *Appl. Phys. Lett.* 51 51 (1987).
- 32) H.R. Jen, M.J. Cherng, and G.B. Stringfellow, *Inst. Phys. Conf. Ser.* 83 159 (1987).
- 33) O. Ueda, M. Takikawa, J. Komeno, and I. Umebu, *Jpn. J. Appl. Phys.* 26 L1824 (1987).
- 34) H.R. Jen, D.S. Cao, and G.B. Stringfellow, *Appl. Phys. Lett.* (submitted).
- 35) H.R. Jen, M.J. Jou, and G.B. Stringfellow (unpublished results).
- 36) H.R. Jen, M.J. Cherng, M.J. Jou, and G.B. Stringfellow, in *Ternary and Multinary Compounds*, ed. S.K. Deb and A. Zunger (Materials Research Society, Pittsburg, 1987) p. 353.

COMPARISON OF ORDERED AND MODULATED STRUCTURES IN InGaP ALLOY SEMICONDUCTORS GROWN BY MOCVD, CHLORIDE-VPE AND LPE METHODS

O. UEDA*, T. KATO**, T. MATSUMOTO**, M. HOSHINO*, M. TAKECHI*, AND M. OZEKI*
 *Fujitsu Laboratories Ltd., 10-1 Morinosato-Wakamiya, Atsugi 243-01, Japan
 **Yamanashi University, 4-3-11 Takeda, Kofu 400, Japan

ABSTRACT

Ordered and modulated structures in InGaP alloy semiconductors grown on (001) GaAs substrates by metalorganic chemical vapor deposition, chloride-vapor phase epitaxy, and liquid phase epitaxy have been systematically studied by transmission electron microscopy. In InGaP grown by metalorganic chemical vapor deposition at 630°C, strong ordering of CuPt-type has been observed, which is associated with an abnormality in the photoluminescence peak energy. For crystals grown by chloride-vapor phase epitaxy, CuPt-type ordered structures have also been observed. However, the degree of ordering is weaker in the latter case and crystals grown at 576-740°C exhibit normal photoluminescence peak energies. On the other hand, in crystals grown by liquid phase epitaxy, no superstructure spots are found in the electron diffraction patterns and the crystals exhibit normal photoluminescence peak energies. Modulated structures do not depend on the growth method since they are observed in all crystals. From these results, it has been concluded that the ordered structures are not generated under thermal equilibrium conditions but rather by the diffusion and reconstruction of deposited atoms on the growth surface.

INTRODUCTION

III-V alloy semiconductors are widely used in the production of optical devices, high-speed devices and so on. To ensure high device performance and reliability, one must eliminate defects and control the thermal stability of the crystal. Regarding the latter point, two phenomena peculiar to these materials have been extensively studied, i.e., generation of ordered structure[1-19] and modulated structure[20-24]. Atomic ordering has been found in AlGaAs[1], In(Al)GaP[2-9], InGaAs(P)[10-12], InAlAs[13,14], GaAsSb[15,16], GaAsP[17,18], and InAsSb[19]. Since the ordering takes place mostly in gas-phase epitaxy, i.e., MOCVD, VPE, and MBE (only one exception of LPE-InGaAs[12]), it is believed that this phenomenon is strongly related to growth kinetics, i.e., migration and reconstruction of deposited atoms on the growth surface[2,7]. However, because of the lack of the direct evidence for the non-existence of ordered structures in most alloy semiconductors grown by LPE, this speculation has not been proved yet.

In this paper, we describe a detailed TEM study on the ordered and modulated structures in InGaP crystals grown by MOCVD, Chloride-VPE, and LPE, and we conclude for the first time that atomic ordering is only associated with growth kinetics and that it is not a bulk phenomenon.

EXPERIMENTAL PROCEDURES

In this study, undoped-InGaP crystals grown by three different growth methods, MOCVD, chloride-VPE(C-VPE), and LPE, were investigated. In the case of MOCVD, crystals are grown on (001) GaAs substrates tilted 2.5° towards <110>, and the growth temperatures are kept at 630°C. TMIn, TMGa, and PH₃ are used as reactants and the V/III partial pressure ratio is kept at 100 (see [2] for detailed growth conditions). Film thickness and lattice mismatch between GaAs and InGaP are 0.4-0.5 μm and (1-2) × 10⁻³,

respectively. Chloride-VPE InGaP crystals are grown on (001) GaAs substrates 2.5° off towards $\langle 100 \rangle$ and at $576\text{--}740^\circ\text{C}$ (detailed growth procedures are described elsewhere [25,26]). They are approximately $1\text{ }\mu\text{m}$ thick and the lattice mismatch between GaAs and InGaP is within $\pm 1 \times 10^{-3}$. The LPE-growth is carried out by using a conventional slide boat [27]. Crystals are grown on (001) GaAs (just) substrates at $630\text{--}698^\circ\text{C}$. They are approximately $1\text{ }\mu\text{m}$ thick and the mismatch is $(1\text{--}5) \times 10^{-3}$. Thin specimens for plan-view and cross-sectional TEM observations were prepared by chemical etching and ion thinning, respectively. TEM observation was carried out in an Akashi ultra-high resolution analytical electron microscope operated at 200 kV.

RESULTS AND DISCUSSION

Ordered structures

Figures 1(a) and 1(b) show transmission electron diffraction (TED) patterns from the (110) and (110) cross-sections of an MOCVD-InGaP crystal grown at 630°C , respectively. Very strong superstructure spots are present in the (110) TED pattern, but not in the (110). Two series of superstructure spots are observed at positions indexed as $h \pm 1/2$, $k \pm 1/2$, $l \pm 1/2$ and $h \mp 1/2$, $k \pm 1/2$, $l \pm 1/2$ for an hkl matrix spot. These superstructure spots are associated with CuPt-type structure [28] which is one of substitutional ordered structures in fcc crystals. The ordering occurs on the (111) plane of column III atoms with doubling in periodicity, i.e., the ordered structure corresponds to a monolayer superlattice of $(\text{InP})_1(\text{GaP})_1$ on the (111) plane. There is asymmetry in the intensity of each series; the intensity of the former series is much stronger than that of the latter series. This is presumably due to the effect of atomic steps descending in the [110] direction on the growth surface, which are believed to act as "phase lockers" during the formation of ordered structure [7]. TED patterns from the (110) and the (110) cross-sections of a C-VPE-InGaP crystal grown at 643°C are shown in Figs. 1(c) and 1(d), respectively. Two series of superstructure spots corresponding to CuPt-type structure with nearly equal intensity, are observed in only the TED pattern from the (110) cross-section. This may be due to the fact that both $\langle 110 \rangle$ - and $\langle 110 \rangle$ -steps are introduced since substrates tilting toward the $\langle 100 \rangle$ direction are used. The superstructure spots are streaky (streaks are present along the $\langle 001 \rangle$ and the $\langle 00\bar{1} \rangle$ direction for each superstructure spot). Maximum intensity is obtained for the crystal grown at 683°C and the intensity becomes weaker as the growth temperature becomes higher or lower than this. It should be noted that the superstructure spot for MOCVD-grown InGaP crystal is spot-like and its intensity is stronger than that of the streaky superstructure spot for C-VPE-grown InGaP. These results suggest that the degree of ordering in C-VPE-grown InGaP is weaker than that in MOCVD-grown InGaP in the whole growth temperature range (see Table 1).

To confirm this, an atomic scale evaluation was carried out on the crystals by high resolution lattice imaging technique. Figure 2(a) illustrates a high resolution TEM image from a (110) cross-section of an MOCVD-grown InGaP at 630°C . Doubling in (111) fringes is clearly observed in a considerably wide region. Thus, the presence of long range ordering is evident. Planar defects where a phase-shift of the (111) fringe is observed are often found. They might be anti-phase boundaries as suggested by Kuan et al. [10]. Similar doubling in (111) fringes is also observed in the high resolution TEM image from the (110) cross-section of C-VPE-grown InGaP at 683°C , as shown in Fig. 2(b). However, the ordered regions are only observed locally, i.e., total volume of ordered regions is smaller than in the case of MOCVD-grown crystal, as suggested from the results of TED patterns. Similar results have also obtained from dark field imaging using one of the superstructure spots (not shown due to lack of space).

The difference in the degree of ordering between MOCVD- and C-VPE-grown

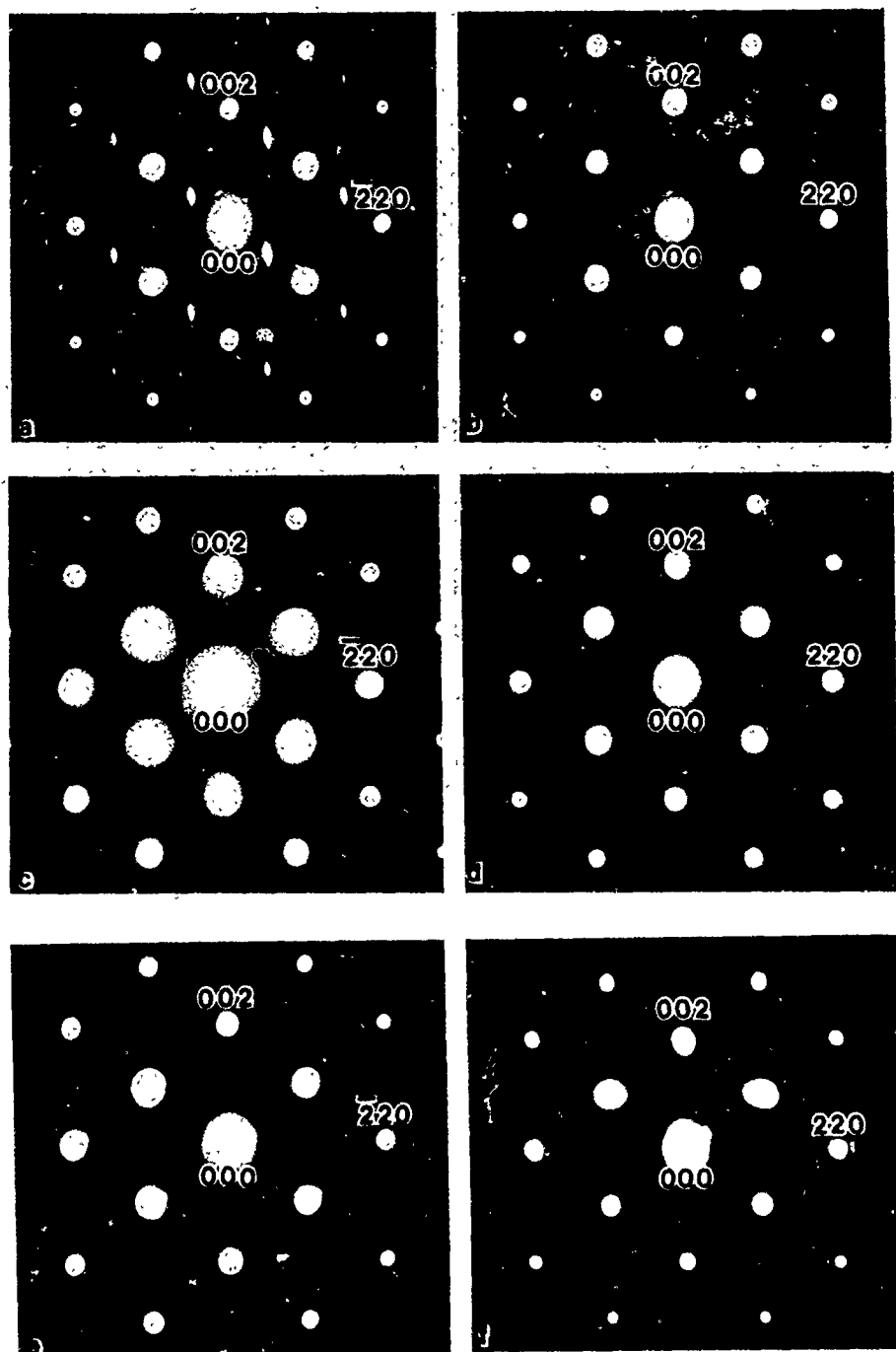


Fig. 1. TED patterns from the (110) and (1 $\bar{1}$ 0) cross-sections of InGaP crystals. (a) (110), MOCVD ($T_g=630^\circ\text{C}$); (b) (1 $\bar{1}$ 0), MOCVD; (c) (110), C-VPE ($T_g=643^\circ\text{C}$); (d) (1 $\bar{1}$ 0), C-VPE; (e) (110), LPE ($T_g=630^\circ\text{C}$); (f) (1 $\bar{1}$ 0), LPE.

Table 1. Summary of results on the PL peak energies and intensities of superstructure spots in the electron diffraction pattern.

Sample No.	Growth method	Growth Temperature(°C)	PL peak energy(eV)	Relative intensity superstructure spots
1	MOCVD	630	1.947	strong, spotty
2	C-VPE	576	1.984	none
3	C-VPE	620	1.977	very weak, streaky
4	C-VPE	683	1.988	medium, streaky
5	C-VPE	740	1.993	very weak, diffused
6	LPE	630	1.984	none
7	LPE	650	1.980	none
8	LPE	688	1.977	none
9	LPE	698	1.984	none

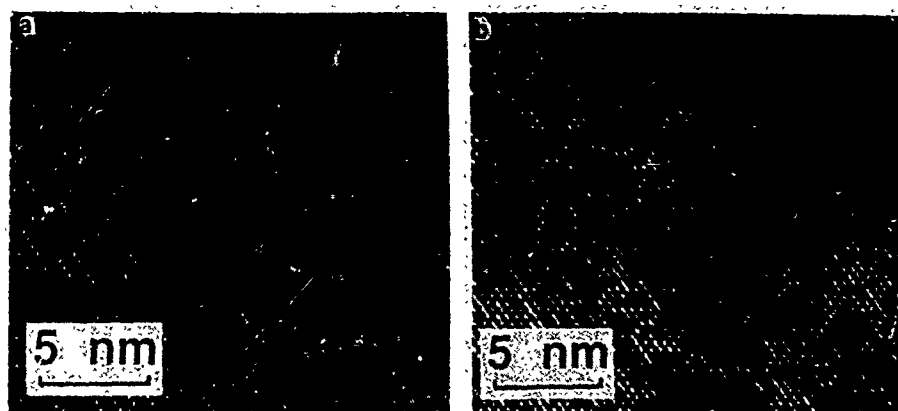


Fig. 2. High resolution TEM images of ordered InGaP crystals.
(a) MOCVD-InGaP($T_g=630^\circ\text{C}$); (b) C-VPE-InGaP($T_g=643^\circ\text{C}$).

crystals, may relate to a difference in the growth mechanism between MOCVD and C-VPE in the following way: In MOCVD, when column III atoms are deposited on the growth surface after rapid decomposition of TMGa and TMI, they can easily migrate and reconstruct so as to minimize the total energy on the surface, thus causing strong ordering. On the other hand, in C-VPE, column III atoms can migrate only in a form of chloride molecules, GaCl and InCl[29], with weak interaction with the substrate, thus causing weaker ordering.

Next, LPE-grown InGaP crystals were evaluated by TED. Figures 1(e) and 1(f) show TED patterns from the (110) and the (110) cross-sections of an LPE-InGaP grown at 630°C , respectively. No superstructure spots are observed in both patterns. In the TED pattern from the (001) plan-view specimen, only fundamental spots are present. This indicates that none of the three types of superstructures, CuPt, AuCu-I, or Chalcopyrite are formed in the crystal. No superstructure spots are observed in the TED patterns from all crystals grown at temperatures in the range $630\text{--}698^\circ\text{C}$ (see also Table 1). In LPE-growth, there is very little chance for each atom to migrate and reconstruct at the liquid-solid interface during growth since the growth rate in LPE is very high compared with MOCVD and C-VPE. Therefore, these findings lead us to the conclusion that the atomic ordering takes place by the diffusion and reconstruction of deposited atoms on the growth surface and that ordered structures are not generated under thermal equilibrium conditions.

Regarding the optical properties of InGaP crystals, several authors have described a detailed growth temperature dependence of the band gap

energy of the crystal by photoluminescence(PL) measurements[4-6]. In most cases, the crystal exhibits abnormal band gap energy with minimum energy approximately 50 meV smaller than the normal value for crystals grown by LPE. Although the exact origins for these abnormalities are not clear, they may be due to (a) the presence of CuPt-type ordered regions, (b) the local atomic configuration at the interface between the ordered and non-ordered regions, or (c) generation of anti-phase boundaries in the ordered region. Theoretical calculations are required for all of these cases. In our experiment, the PL peak energy for MOCVD-grown InGaP at 630°C(sample 1) is also smaller than for crystals grown by LPE(samples 6-9). On the other hand, for the C-VPE-grown crystals, in the whole growth temperature range, the crystals exhibit similar PL peak energies which are normal values at these temperatures. This is presumably due to the fact that the ordered regions are not well ordered (small long range order parameters[10]) or the absence of anti-phase boundaries. Thus, one can conclude that only strong ordering causes a reduction of the band gap energy of the crystal.

Modulated structures

Modulated structures[20-24] are also observed in the crystals. Figures 3(a)-3(c) show typical plan-view dark-field TEM image of modulated structures from MOCVD-, C-VPE-, and LPE-grown InGaP crystals, taken under the 220 reflection, respectively. Coarse and fine modulated structures are present in all of these micrographs. These structures are likely to be generated during growth and/or during the cooling process after growth through surface spinodal decomposition (in MOCVD or C-VPE) or bulk spinodal decomposition (in LPE). Since the compositional variation along the coarse modulated structure has been found to be within few percent by EDX measurement[21], it is expected that they do not have a strong effect on the optical properties of the crystals.

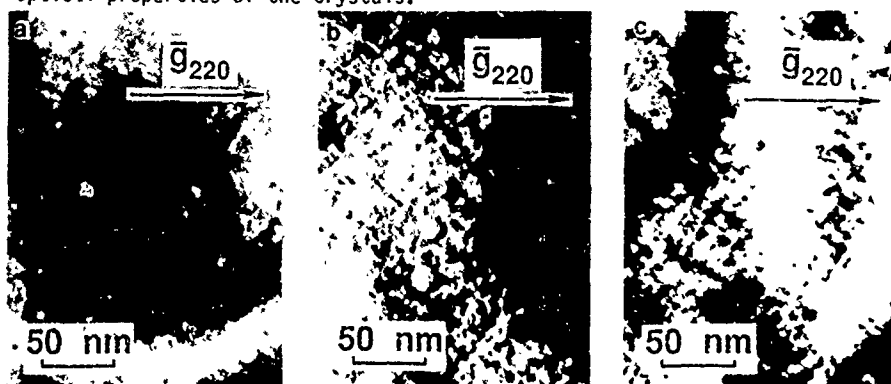


Fig. 3. Plan-view dark-field TEM images of modulated structures. (a) MOCVD-InGaP(630°C); (b) C-VPE-InGaP($T_g=576^\circ\text{C}$); (c) LPE-InGaP($T_g=688^\circ\text{C}$).

CONCLUSIONS

We have presented a detailed TEM study on the modulated and ordered structures in InGaP crystals grown by MOCVD, Chloride-VPE, and LPE. It has been experimentally clarified that ordering takes place only in MOCVD- and C-VPE-grown crystals and not in LPE-grown crystals. The degree of ordering in MOCVD-grown crystals is higher than that in C-VPE-grown crystals. These findings suggest that the ordered structures are not generated under thermal equilibrium condition but rather by the diffusion and reconstruction of deposited atoms on the growth surface. Modulated structures are generated in all of the crystals.

ACKNOWLEDGEMENTS

The authors would like to express their thanks to O. Otsuki for his encouragement throughout this work. Special thanks go to K. Hayashi for the preparation of cross-section TEM specimens.

REFERENCES

1. T. S. Kuan, T. F. Kuech, W. I. Wang, and E. L. Wilkie, *Phys. Rev. Lett.* **54**, 210 (1985).
2. O. Ueda, M. Takikawa, J. Komeno, and I. Umebu, *Japan. J. Appl. Phys.* **26**, L1824 (1987).
3. O. Ueda, M. Takikawa, M. Takechi, J. Komeno, and I. Umebu, *J. Crystal Growth* **93**, 418 (1988).
4. M. Kondow, H. Kakibayashi, and S. Minagawa, *J. Crystal Growth* **88**, 291 (1988).
5. P. Gavrilovic, F. P. Dabkowski, M. Mehan, J. E. Williams, W. Studius, M. A. Shahid, and S. Mahajan, *J. Crystal Growth* **93**, 426 (1988).
6. A. Gomyo, T. Suzuki, and S. Iijima, *Phys. Rev. Lett.* **60**, 2645 (1988).
7. T. Suzuki, A. Gomyo, and S. Iijima, *J. Crystal Growth* **93**, 396 (1988).
8. M. Kondow, H. Kakibayashi, S. Minagawa, Y. Inoue, T. Nishino, and Y. Hamakawa, *J. Crystal Growth* **93**, 412 (1988).
9. M. Kondow, H. Kakibayashi, T. Tanaka, and S. Minagawa, *Phys. Rev. Lett.* **63**, 884 (1989).
10. T. S. Kuan, W. I. Wang, and L. Wilkie, *Appl. Phys. Lett.* **51**, 51 (1987).
11. M. A. Shahid, S. Mahajan, D. E. Laughlin, and H. M. Cox, *Phys. Rev. Lett.* **58**, 2567 (1987).
12. H. Nakayama and H. Fujita, *Inst. Phys. Conf. Ser.* **79**, 289 (1986).
13. A. G. Norman, R. E. Mallard, I. J. Murgatroyd, G. R. Booker, A. H. Moore, and M. D. Scott, *Inst. Phys. Conf. Ser.* **87**, 77 (1987).
14. O. Ueda, T. Fujii, Y. Nakada, H. Yamada, and I. Umebu, *J. Crystal Growth* **95**, 38 (1989).
15. H. R. Jen, M. J. Cherng, and G. B. Stringfellow, *Appl. Phys. Lett.* **48**, 1603 (1986).
16. Y. E. Ihm, N. Otsuka, J. Klem, and H. Morkoc, *Appl. Phys. Lett.* **51**, 2013 (1987).
17. W. E. Plano, D. W. Nam, J. S. Major, Jr., K. C. Hsieh, and N. Holonyak, Jr., *Appl. Phys. Lett.* **53**, 2537 (1988).
18. H. R. Jen, D. S. Cao, and G. B. Stringfellow, *Appl. Phys. Lett.* **54**, 1890 (1989).
19. H. R. Jen, K. Y. Ma, and G. B. Stringfellow, *Appl. Phys. Lett.* **54**, 1154 (1989).
20. P. Henoc, A. Izrael, M. Quillec, and H. Launois, *Appl. Phys. Lett.* **40**, 963 (1982).
21. O. Ueda, S. Isozumi, and S. Komiya, *Japan. J. Appl. Phys.* **23**, 241 (1984).
22. A. G. Norman and G. R. Booker, *J. Appl. Phys.* **57**, 4715 (1985).
23. M. M. Treacy, J. M. Gibson, and A. Howie, *Phil. Mag.* **A51**, 389 (1985).
24. S. N. G. Chu, S. Nakahara, K. E. Strege, and W. D. Johnston, Jr., *J. Appl. Phys.* **57**, 4610 (1985).
25. M. Hoshino, K. Kodama, K. Kitahara, and M. Ozeki, *Appl. Phys. Lett.* **48**, 770 (1986).
26. M. Hoshino, K. Kodama, K. Kitahara, and M. Ozeki, *J. Crystal Growth* **96**, 188 (1989).
27. T. Kato, T. Matsumoto, and T. Ishida, *J. Crystal Growth* **71**, 728 (1985).
28. A. G. Khachaturyan, *Phys. Status Solidi* **B60**, 9 (1973).
29. D. W. Shaw, *J. Crystal Growth* **31**, 130 (1975).

ATOMIC ORDERING AND ALLOY CLUSTERING IN MBE-GROWN $\text{InAs}_y\text{Sb}_{1-y}$ EPITAXIAL LAYERS

TAE-YEON SEONG*, A.G. NORMAN*, G.R. BOOKER*, R. DROOPAD**, R.L. WILLIAMS**, S.D. PARKER**, P.D. WANG** AND R.A. STRADLING**

* Dept. of Metallurgy and Science of Materials, University of Oxford, Parks Road, Oxford OX1 3PH, U.K.

** Dept. of Physics, Imperial College, London SW17 2BZ, U.K.

ABSTRACT

MBE $\text{InAs}_y\text{Sb}_{1-y}$ layers were grown at 370°C across the full composition range. TEM/TED examinations directly showed that separation into two phases had taken place for compositions $0.4 < y < 0.8$ with plates 20 to 200nm thick occurring approximately parallel to the layer surface. The two phases in the individual specimens were tetragonally distorted and their compositions were deduced from the TED results. CuPt-type atomic ordering occurred and was most pronounced in the middle of the composition range. Alloy clustering was also present. Hall measurements showed that the carrier concentration was a maximum, and the mobility was a minimum, for the middle of the composition range.

INTRODUCTION

The pseudo-binary alloy $\text{InAs}_y\text{Sb}_{1-y}$ is of increasing interest for long wavelength infrared detectors. Theoretical calculations have predicted the existence of a miscibility gap for InAsSb for temperatures below $\approx 300^\circ\text{C}$ [1] and difficulty has been experienced in growing layers across the composition range by the near-equilibrium LPE method [2]. However, InAsSb layers across the composition range have been grown by the non-equilibrium MBE and MOCVD methods. So far no structural results have been reported for InAsSb that showed phase separation arising from a miscibility gap. TED studies of MOCVD InAsSb layers grown between 375 and 480°C showed the presence of CuPt-type ordering [3], but no similar studies have yet been reported for MBE InAsSb layers. Electrical measurements have been made for MBE $\text{InAs}_{.33}\text{Sb}_{.67}$ layers [4]. Photoluminescence results for MBE InAsSb layers showed low luminescent efficiency for the middle of the composition range [5].

This paper presents TEM/TED structural results and electrical measurements for MBE InAsSb layers grown across the composition range. The substrates were (001) Cr-doped semi-insulating GaAs. A GaAs buffer layer $\approx 0.5\mu\text{m}$ thick was grown at 550°C, followed by an InAs buffer layer $\approx 100\text{nm}$ thick at 500°C, followed by a $\text{InAs}_y\text{Sb}_{1-y}$ layer $\approx 4\mu\text{m}$ thick at 370°C. Six samples were prepared corresponding to $y=0, 0.2, 0.4, 0.6, 0.8$ and 1.0 . All of the layers were grown nominally undoped. TEM examinations were made of cross-section specimens. Carrier concentrations and mobilities were determined for the layers at 300 and 77K from low-field Hall measurements.

RESULTS AND DISCUSSION

A (110) cross-section TEM 220 dark field (DF) image of the $\text{InAs}_{.2}\text{Sb}_{.8}$ specimen showing the interface region is given in Fig. 1. There is an array of dislocations and moire fringes

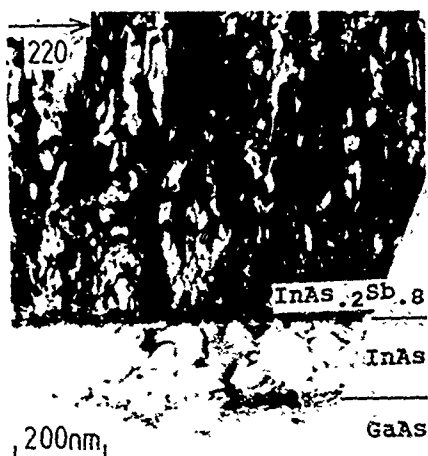


Fig. 1. MBE $\text{InAs}_{0.2}\text{Sb}_{0.8}$ layer/InAs buffer layer/GaAs buffer layer. TEM (110) cross-section, 220 DF image, showing interfaces and threading defects.

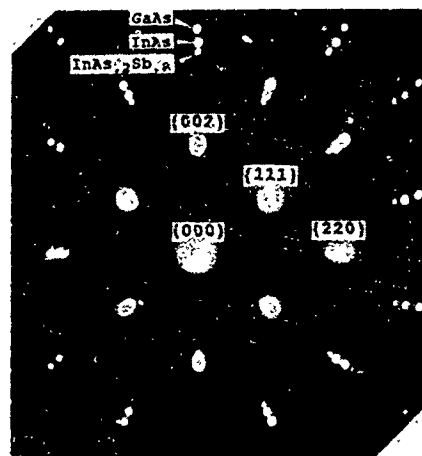


Fig. 3. MBE $\text{InAs}_{0.2}\text{Sb}_{0.8}$ layer/InAs buffer layer/GaAs buffer layer. TED pattern from (110) cross-section showing spots from all three layers.

at the GaAs/InAs and InAs/InAs_{0.2}Sb_{0.8} interfaces. There are threading dislocations in the InAs layer, and threading dislocations, stacking faults and microtwins in the InAs_{0.2}Sb_{0.8} layer.

Similar TEM 002 DF images showing regions in the middle of the four InAs_{1-y}Sb_y layers are given in Fig. 2. The contrast in these images is sensitive to the alloy layer composition. For InAs_{0.2}Sb_{0.8} (Fig. 2a), the layer appeared relatively uniform, with the threading defects providing the main contrast. For InAs_{0.4}Sb_{0.6} (Fig. 2b), the layer showed strong non-uniform bands of contrast approximately parallel to the layer surface. The bands alternated in contrast from bright to dark, and ranged in thickness from ≈ 20 to ≈ 200 nm. For InAs_{0.6}Sb_{0.4} (Fig. 2c), the layer showed similar bands of contrast. For InAs_{0.8}Sb_{0.2} (Fig. 2d), the dark bands were narrower and more irregular. For the InAs_{0.4}Sb_{0.6}, InAs_{0.6}Sb_{0.4} and InAs_{0.8}Sb_{0.2} layers, threading dislocations, stacking faults and microtwins were also observed. The {111} microtwins often started and stopped at interfaces between the bands. When similar TEM 220 DF images were obtained from these three layers, the dark/bright band contrast was not observed, although some dislocations were visible at the positions of the previously observed dark/bright band interfaces. The strong band contrast observed in the 002 reflections indicates that the dark and bright bands within each of these three specimens correspond to plates of material with different alloy compositions, suggesting that phase separation has occurred.

A selected area TED pattern taken from the InAs_{0.2}Sb_{0.8} layer is given in Fig. 3. The pattern arose from a region of the specimen which included the GaAs substrate and the InAs and InAs_{0.2}Sb_{0.8} layers. The higher order 'spots' are split into three spots, corresponding to each of the three materials. On the assumption that the GaAs substrate spots corresponded to undistorted material with the bulk GaAs lattice parameter, the lattice parameters of the InAs and InAs_{0.2}Sb_{0.8} were calculated from the measured spacings of the spots. Moreover, this was done for both the 004 and 440 spots (the latter not shown on the print of Fig. 3), i.e. in the directions perpendicular and

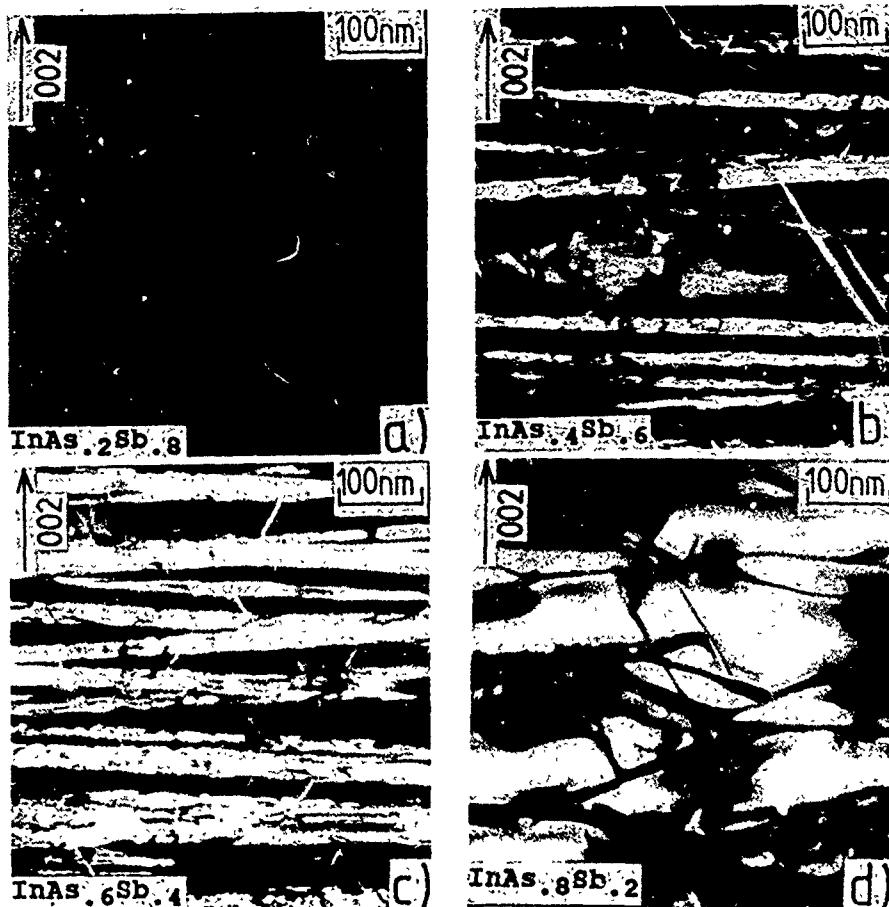


Fig.2. MBE $\text{InAs}_x\text{Sb}_{1-y}$ layers. TEM (110) cross-section, 002 DF images. a) $y=0.2$, b) $y=0.4$, c) $y=0.6$, d) $y=0.8$. Phase separation has occurred in b), c) and d).

parallel respectively to the layer surface. The results showed that the InAs had closely the bulk InAs lattice parameter of 6.06\AA in both of these directions, indicating that the layer was virtually fully relaxed. The $\text{InAs}_{.2}\text{Sb}_{.8}$ layer had a lattice parameter of $c_1=6.44\text{\AA}$ perpendicular to the surface and $a_p=6.36\text{\AA}$ parallel to the surface (see Table I), i.e. although significantly relaxed with respect to the underlying InAs layer, it was tetragonally distorted.

A similar TED pattern from the middle of the $\text{InAs}_{.2}\text{Sb}_{.8}$ layer is given in Fig.4a. Only spots from $\text{InAs}_{.2}\text{Sb}_{.8}$ are now present. A corresponding pattern from the middle of the $\text{InAs}_{.6}\text{Sb}_{.4}$ layer is given in Fig.4b. The higher order 'spots' are split into two spots in the 002 direction, but are not split in the 220 direction. Comparison of the spacings of these spots with the corresponding spots in the GaAs pattern enabled the $\text{InAs}_{.6}\text{Sb}_{.4}$ lattice parameters to be determined. This showed there were two lattice parameters perpendicular to the surface of $c_1=6.44$ and $c_2=6.08\text{\AA}$, and one lattice parameter parallel to the surface of $a_p=6.26\text{\AA}$, i.e. there were two tetragonally distorted phases, one with $c/a>1$ and the other with $c/a<1$. TED

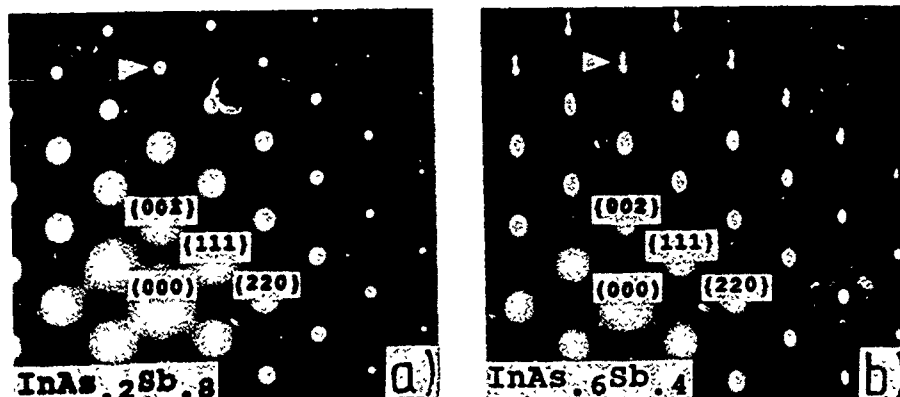


Fig.4 a) MBE InAs_{0.2}Sb_{0.8} layer, b) MBE InAs_{0.6}Sb_{0.4} layer. TED patterns from (110) cross-section. Spots in 002 direction are split into two spots due to phase separation in b), but not in a).

patterns obtained from the InAs_{0.4}Sb_{0.6} and InAs_{0.8}Sb_{0.2} layers showed a similar behaviour again indicating the presence of two tetragonally distorted phases.

For the InAs_{0.2}Sb_{0.8} layer, the determined lattice parameters of $c_1=6.44$ and $a_p=6.36\text{\AA}$ give a deduced completely relaxed cubic lattice parameter of $a_{r1}=6.40\text{\AA}$, which agrees well with the lattice parameter of 6.40\AA for InAs_{0.2}Sb_{0.8}. For the InAs_{0.4}Sb_{0.6} layer, the determined lattice parameters of $c_1=6.37$ and $a_p=6.31\text{\AA}$, and $c_2=6.02$ and $a_p=6.31\text{\AA}$, give completely relaxed cubic lattice parameters of $a_{r1}=6.34$ and $a_{r2}=6.17\text{\AA}$ respectively, which correspond to alloy compositions of InAs_{0.33}Sb_{0.67} and InAs_{0.74}Sb_{0.26} respectively. For the InAs_{0.6}Sb_{0.4} layer, the analogous completely relaxed cubic lattice parameters are 6.35 and 6.17\AA , which correspond to alloy compositions of InAs_{0.31}Sb_{0.69} and InAs_{0.74}Sb_{0.26} respectively, i.e. are almost precisely the same as those of the InAs_{0.4}Sb_{0.6} layer. For the InAs_{0.8}Sb_{0.2} layer, the analogous parameters are 6.27 and 6.11\AA , which correspond to alloy compositions of InAs_{0.50}Sb_{0.50} and InAs_{0.88}Sb_{0.12} respectively.

The behaviour that is occurring can be deduced as follows. At the growth temperature of 370°C , phase separation can occur because of the miscibility gap. When InAs_{0.2}Sb_{0.8} layers are grown, the composition is outside the gap range, and so single

Table I. Electron diffraction results

y	a	m(%)	a_p	c_1	c_2	a_{r1}	a_{r2}	y_1	y_2
0.2	6.3952	5.41	6.36	6.44	-	6.40	-	0.19	-
0.4	6.311	4.08	6.31	6.37	6.02	6.34	6.17	0.33	0.74
0.6	6.2268	2.74	6.26	6.44	6.08	6.35	6.17	0.31	0.74
0.8	6.1426	1.38	6.16	6.38	6.06	6.27	6.11	0.50	0.88

y= nominal InAs_ySb_{1-y} composition; a=relaxed cubic lattice parameter by Vegard's law; m=lattice mismatch with respect to InAs buffer; a_p =measured lattice parameter parallel to interface; c_1 =measured lattice parameter perpendicular to interface of phase 1; c_2 =measured lattice parameter perpendicular to interface of phase 2; a_{r1} =relaxed lattice parameter of phase 1; a_{r2} =relaxed lattice parameter of phase 2; y_1 =composition of phase 1; y_2 =composition of phase 2; columns 2,4-8 in A.

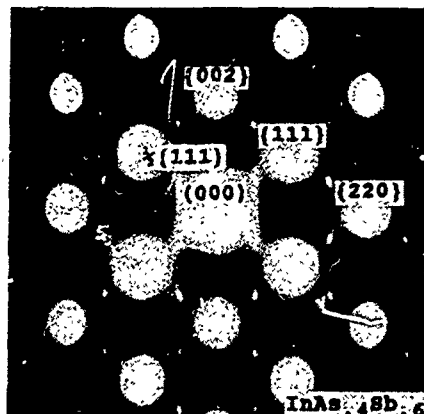


Fig. 5. MBE InAs₄Sb₆ layer. TED pattern from (110) cross-section showing extra half-order spots due to atomic ordering.

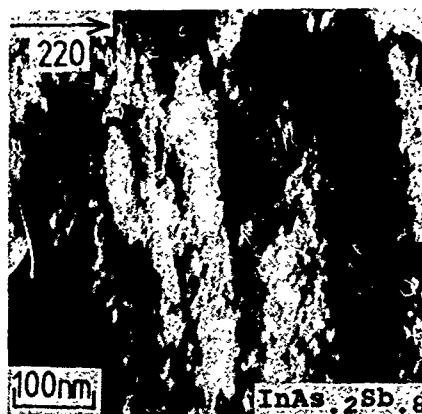


Fig. 6. MBE InAs₂Sb₈ layer. TEM (110) cross-section, 220 DF image, showing fine granular structure due to alloy clustering.

phase material occurs. When InAs₄Sb₆ and InAs₆Sb₄ layers are grown, the compositions are well within the gap range, and so regular two-phase material occurs. When InAs₈Sb₂ layers are grown, the composition is towards one end of the gap range, and so irregular two phase material occurs.

This model is supported by the TEM observations. Thus, for the InAs₄Sb₆ layers, the composition is closer to that of the InAs₃₃Sb₆₇ phase than the InAs₇₄Sb₂₆ phase. Consequently, there should be a greater volume fraction of the InAs₃₃Sb₆₇, i.e. Sb richer, phase. Consideration of structure factors for InAs_ySb_{1-y} alloys shows that those with more Sb will appear darker in TEM 002 DF images. Fig. 2b of the InAs₄Sb₆ layer shows that the darker phase predominates. Conversely, for the InAs₆Sb₄ layer, the composition is closer to the InAs₇₄Sb₂₆ phase, and so there should be a greater volume fraction of the InAs₇₄Sb₂₆, i.e. As richer, phase. Fig. 2c of the InAs₄Sb₆ layer shows that the lighter phase predominates.

A (110) cross-section TED pattern from the InAs₄Sb₆ layer is shown in Fig. 5. Extra spots are present at $(h\pm\frac{1}{2}, k\pm\frac{1}{2}, l\pm\frac{1}{2})$ positions, indicating the presence of atomic ordering of the CuPt-type on both the $(\bar{1}11)$ and $(1\bar{1}1)$ planes. The extra spots are elongated along the [001] growth direction indicating a breakdown of the ordered structure in this direction. A $(\bar{1}10)$ cross-section TED from the same layer showed no such extra spots, indicating no similar atomic ordering on the (111) and $(1\bar{1}\bar{1})$ planes. Examinations of the other three InAs_ySb_{1-y} layers showed analogous behaviours. For the InAs₂Sb₈, InAs₄Sb₆, InAs₆Sb₄ and InAs₈Sb₂ layers, the extra spot intensities were weak, strong, strong and weak, respectively. Hence, the ordering is a maximum at $y\approx 0.5$. The observed change in ordering could be due to a change in either the volume fraction of the ordered material, or a change in the degree of ordering.

A (110) cross-section TEM 220 DF image of the InAs₂Sb₈ layer is shown in Fig. 6. There is a fine granular structure of size ≈ 5 -10nm, which is elongated in the direction perpendicular to the g diffraction vector, i.e. perpendicular to the layer surface. This structure is characteristic of alloy clustering.

Analogous images of the other three $\text{InAs}_y\text{Sb}_{1-y}$ layers showed similar alloy clustering.

The electrical results obtained for the layers are shown in Table II. For the individual $\text{InAs}_y\text{Sb}_{1-y}$ layers, on going from 300 to 77K, the carrier concentration (n) remains relatively unchanged while the mobility (μ) decreases. For measurements at 77K, the carrier concentration is 2 to $3 \times 10^{15} \text{ cm}^{-3}$ for the InSb and InAs layers, and increases to $\approx 1 \times 10^{18} \text{ cm}^{-3}$ for the $\text{InAs}_y\text{Sb}_{1-y}$ layers towards the middle of the composition range. Conversely, the mobility is 3 to $6 \times 10^4 \text{ cm}^2/\text{Vs}$ for the InSb and InAs layers, and decreases to $\approx 1 \times 10^3 \text{ cm}^2/\text{Vs}$ for the $\text{InAs}_y\text{Sb}_{1-y}$ layers towards the middle of the composition range. It is pointed out that the values quoted in Table II are those deduced directly from Hall measurements on the assumption of a single carrier. InSb and InAs grown on GaAs showed parallel conductance effects from high concentrations of low mobility carriers located at either the interface or the layer surface. In these cases, and possibly also with $\text{InAs}_y\text{Sb}_{1-y}$, the bulk mobilities of the layers are substantially higher than the values given in Table II.

Table II. Electrical results

$\text{InAs}_y\text{Sb}_{1-y}$ y	300K		77K	
	n (cm^{-3})	μ (cm^2/Vs)	n (cm^{-3})	μ (cm^2/Vs)
0	2×10^{16}	6×10^4	3×10^{15}	3×10^4
0.2	7×10^{16}	8.5×10^3	4×10^{16}	2.5×10^3
0.4	4×10^{17}	2.0×10^3	3×10^{17}	1.0×10^3
0.6	1×10^{18}	1.0×10^3	1×10^{18}	8×10^2
0.8	2×10^{17}	4.5×10^3	2×10^{17}	2.7×10^3
1.0	8×10^{15}	1.5×10^4	2×10^{15}	6×10^4

In summary, phase separation occurs in MBE $\text{InAs}_y\text{Sb}_{1-y}$ layers grown at 370°C over the composition range $y=0.4$ to 0.8 . Two phases with widely different compositions form as plates approximately parallel to the layer surface and 20 to 200nm thick. Both phases are tetragonally distorted. Such phase separation does not occur for similar layers with $y=0.2$. Atomic ordering of CuPt-type on $\{111\}$ planes occurs in the layers and is most pronounced in the middle composition range. Alloy clustering on the 5 to 10nm scale occurs in all the ternary layers. The carrier concentration is maximum and the mobility is minimum for layers in the middle composition range. The poorer electrical properties in the middle composition range may be associated with the more pronounced phase separation and/or atomic ordering that occurs in this range.

REFERENCES

1. K. Onabe, Jpn. J. Appl. Phys. **21**, 964 (1982).
2. J.L. Zyskind, A.K. Srivastava, J.C. DeWinter, M.A. Pollack and J.W. Sulhoff, J. Appl. Phys. **61**, 2898 (1987).
3. H.R. Jen, K.Y. Ma and G.B. Stringfellow, Appl. Phys. Lett. **54**, 1154 (1989).
4. J.-I. Chyi, S. Kalem, N.S. Kumar, C.W. Litton and H. Morkoc, Appl. Phys. Lett. **53**, 1092 (1988).
5. M.Y. Yen, R. People, K.W. Wecht and A.Y. Cho, Appl. Phys. Lett. **52**, 489 (1988).

PART XV

Processing of
Silicon and Germanium

RAPID THERMAL PROCESS-INDUCED DEFECTS : GETTERING OF INTERNAL CONTAMINANTS

BOUCHAIB HARTITI, WOLFGANG EICHHAMMER, JEAN-CLAUDE MULLER and PAUL SIFFERT
Centre de Recherches Nucléaires (IN2P3), Laboratoire PHASE (UPR du CNRS n°292),
B.P. 20, F-67037 STRASBOURG CEDEX, France

ABSTRACT

We show in this study that RTP-induced defects analysed by Deep Level Transient Spectroscopy (DLTS) are related to residual impurities present in as-grown silicon wafers. For one particular material an activation of a specific residual metallic impurity was observed in the temperature range 800 - 1000°C. This impurity can be returned to an electrically inactive precipitated form by classical thermal annealing (CTA) with a slow cooling rate or neutralized by means of low-energy hydrogen ion implantation.

INTRODUCTION

In recent years, rapid thermal processes (RTP) have been widely studied with the aim to replace conventional thermal processes. As RTP inherently include quenching steps at the end of the thermal cycle, the determination of the origin of RTP-related defects in silicon is of great importance for many device applications.

Metallic impurities are known [1] as major contaminants which degrade the performances of silicon devices. They may be present in the as-grown material or unintentionally introduced during high-temperature processing steps. They induce deep levels which act as efficient recombination centers. The removal of these metallic impurities by a gettering process becomes necessary for most applications as they control the device performance.

In our study, we present results showing that the association of RTP, which electrically activates defects, and of Deep Level Transient Spectroscopy (DLTS), which can detect the associated levels at concentrations as low as 10^{-4} of the dopant level, is an efficient means to reveal residual metallic impurities present in commercially available silicon. We have, in particular, shown in two previous works [2, 3] that residual or externally introduced metallic impurities show the tendency to redistribute inhomogeneously by gettering during the short processing time. This result was obtained by following the defect level by serial sectioning in steps of about 25 μm over the whole thickness of the samples. By this way, we were able to separate the levels of activated impurities from levels which are due to unintentional contamination of the surfaces during the thermal processing step.

EXPERIMENTAL PROCEDURE

The samples used in this study and in the two preceding ones [2, 3] were commercial float-zone (FZ) 380 μm thick, <100> n-type silicon wafers from Wacker with a resistivity of 1-5 Ωcm . All the samples, similarly prepared as before [2, 3], were mechanically damaged on the backside by scratching the whole surface with a diamond scribe, then RCA cleaned and introduced into the RTP furnace. Two temperature cycles of 800°C and 1000°C for 10 s were used, with the cooling rate adjusted at 80°C/s. For the DLTS analysis, Schottky diodes were made by evaporation of 1 nm^2 gold dots on the surfaces. In order to study the distribution of the observed levels below the surface, serial sectioning was performed in steps of roughly 25 μm , starting from both surfaces.

RESULTS AND DISCUSSION

Activation and gettering of an internal impurity

In figure 1 are reported two DLTS spectra recorded after RCA cleaning and RTP annealing at 1000°C/10 s for a sample with a scratched backside. Curves (1) and (2) represent the results obtained on the frontside and after 125 μm sectioning from the frontside, respectively.

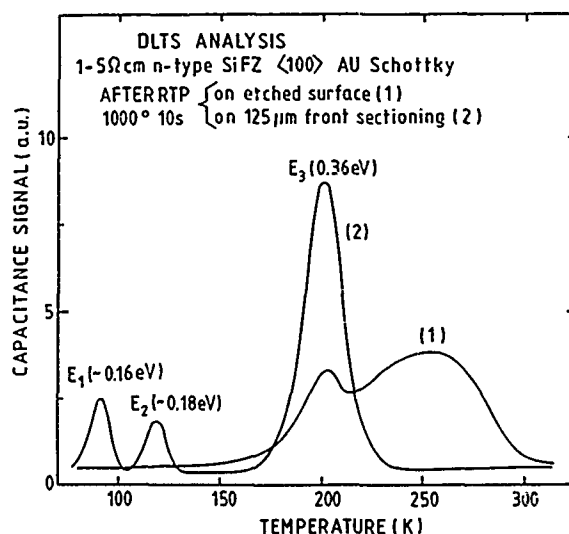


Figure 1 : DLTS spectra recorded after RCA cleaning and rapid annealing at 1000°C/10 s
 (1) : on the etched front surface, (2) : after sectioning 125 μm from the etched frontside.

Two levels E_3 and E_C are detected on the surface and three levels, E_1 , E_2 and E_3 , in the volume. A similar observation is made when the DLTS is performed on the backside or after 125 μm back sectioning. The main peak E_3 whose energy level is 0.36 eV below the conduction band, corresponds to an unknown impurity, electrically activated by the RTP in a concentration of about $1 \times 10^{14} \text{ cm}^{-3}$. As suggested before [3] we believe that the E_3 center can be related to the stable defect at $E_C - 0.37 \text{ eV}$ which has been reported by Ransom et al. [4] after RTP.

The two minor levels E_1 and E_2 also present in the volume as E_3 occur in too low concentrations to be correctly indentified. E_2 could be the level at $E_C - 0.18 \text{ eV}$ which is believed to be the vacancy-oxygen center, as intrinsic gettering mechanisms could have played a role in RTP with a denuded zone at the surface although our material is of the float-zone type which implies a low oxygen content [2].

The broad peak E_C , probably containing more than one defect, is observed in an unreproducible concentration at a temperature of $\approx 260 \text{ K}$, even when RCA cleaning was performed before RTP processing. This can be explained by an enhanced impurity diffusion in RTP, as previously published [5] and by an easier activation of impurities in rapid processing.

The most important point is that spectra recorded after sectioning about 30 μm from the back or frontside of the sample do not show any more the presence of these contaminants. Only the level at $E_C - 0.36 \text{ eV}$ is largely dominant. It can easily be followed by serial sectioning. It decreases first after sectioning from both surfaces and then increases to reach a large maximum near the center of the sample [see curve (2)] measured after removal of 125 μm beginning at the etched front surface.

In figure 2 we have reported the profiles of the E_3 -defect (0.36 eV) as a function of depth after a RTP cycle at 1000°C/10 s. The concentration of this peak is not homogeneous as previously reported for an intentional contamination with gold followed by RTP [2] and in diffusion length studies of RTP induced recombination centers [6]. The general form of the distribution is typically a W-shaped profile with two regions of lower concentration which are about 50 μm below the etched front surface or the scratched backside.

The most important point here is that an extrinsic gettering effect occurs which can be separated by sectioning from an uncontrolled contamination of the surface.

This gettering is typical of one dominant impurity in the present material. No significant levels have been found in another n-type silicon of about the same resistivity and identical processing. This fact confirms that the E_3 level cannot be associated to a fast diffusing contaminant.

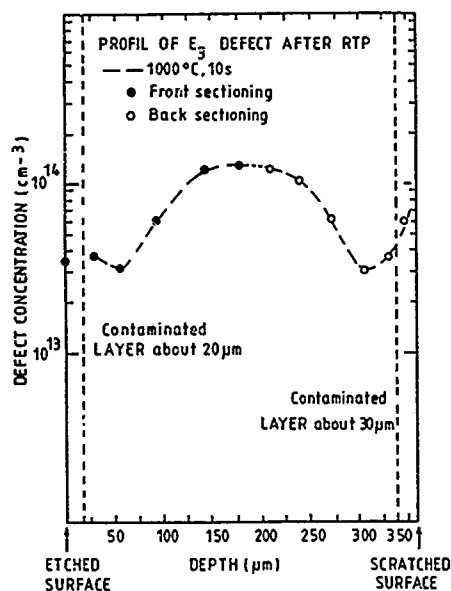


Figure 2 : Concentration of the E_3 level ($E_C - 0.36$ eV) as a function of depth below the surfaces after RTP treatment. The full circles (●) correspond to data points obtained after sectioning starting from the etched front surface, whereas the open circles (○) represent the measurements starting from the diamond scratched backside. The continuous lines are drawn to guide the eye. The vertical dashed lines indicate the limit of influence of the external contamination peak E_C .

Annealing and neutralization of the E_3 defect

We have performed classical thermal annealing (CTA) at 400, 600 and 900°C during one hour with slow cooling at the end of the thermal cycle ($< 0.1^\circ\text{C/s}$) on samples sectioned to a depth of 125 μm which corresponds to the maximum of the E_3 level. For the two lowest temperatures no modification of the E_3 peak occurs. But, as reported on figure 3, the E_3 defect disappears completely at 900°C (curve 2) whereas a small broad contamination level emerges at the position of the E_C -level. Moreover, post-annealing using the RTP furnace in the temperature range 400-650°C with duration from 10 to 300 s, which has been recognized to be able to anneal crystallographic point defects [7], has an influence on the E_3 level. This results confirms the important role of the cooling rate as the solubility of transition metals strongly decreases with the temperature in thermal equilibrium [8], so that they are in a precipitated, electrically inactive form.

On the 125 μm sectioned samples, we have also performed hydrogen ion passivation on one half of a sample under the optimal conditions found for a maximum neutralization of intra and intergrain defects in multicrystalline silicon [9] (H^+ ions of 1 keV, at a fluence of 0.25 mA/cm^2 during 10 mn at a stabilized temperature of 300°C). In order to remove the implantation-related defects, the samples were slightly etched before the deposition of the Schottky diodes. In this case, we obtain a neutralization of the E_3 defect in a region exceeding the zone analysed by DLTS (probably to more than 10 microns). We have verified that the E_3 level, in the second half of the sample which was masked during the H^+ -implantation, was unchanged by the thermal effect associated to the implantation.

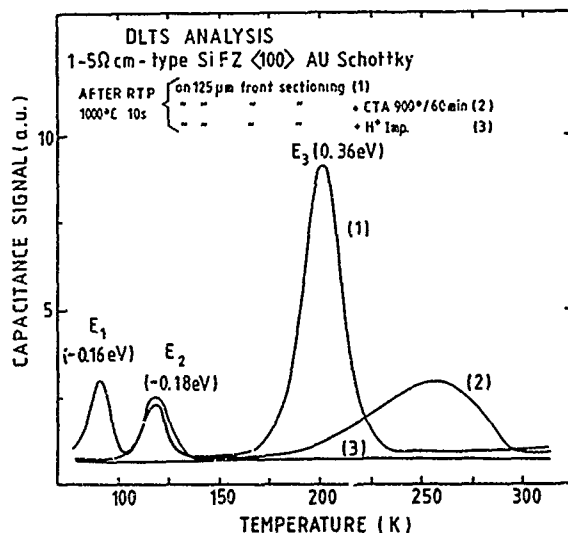


Figure 3 : DLTS spectra recorded after RTP at 1000°C/10 s

(1) after sectioning 125 μm from the etched front side
(2) after CTA at 900°C/1 hr with slow cooling rate (< 0.1°C/s) and
(3) after 1 keV hydrogen ion implantation at 300°C during 10 min.

CONCLUSION

The results of DLTS measurements of rapid thermal processed samples combined with serial sectioning have revealed the influence of a metallic impurity, which was already present in the particular as-grown material used during this study in an inactive form and which has been electrically activated by the RTP in an inhomogeneous distribution. This metallic impurity can be reprecipitated by a classical thermal treatment at 900°C with slow cooling or neutralized by hydrogenation.

ACKNOWLEDGMENTS

This work is funded by the PIFSEM in a program of the AFME (Agence Française pour la Maîtrise de l'Energie) and the CNRS (Centre National de la Recherche Scientifique). The authors would like to thank Dr. Vu Thuong Quat which has initiated this work by diffusion length measurements and S. Barthe for doing the RTP and the elaboration of a great quantity of Schottky diodes.

REFERENCES

1. E.R. Weber, Appl. Phys. **A30**, 1 (1983).
2. B. Hartiti, Vu Thuong Quat, W. Eichhammer, J.C. Muller and P. Siffert, Appl. Phys. Lett. **55**, 873 (1989).
3. B. Hartiti, W. Eichhammer, J.C. Muller, P. Siffert in *Science and Technology of Defects in Silicon*, edited by C.A.J. Ammerlaan, A. Chantre and P. Wagner (Europ. Mater. Res. Soc. Proc. North Holland, Amsterdam, 1989) in press.
4. C.M. Ransom, T.O. Sedgwick and S.A. Cohen, in *Rapid Thermal Processing*, edited by T.O. Sedgwick, T.E. Seidel, B.Y. Tsaur (Mater. Res. Soc. Proc. **52**, Pittsburgh, PA, 1989) p. 153.
5. D.R. Sparks, R.G. Chapman and N.S. Alvi, Appl. Phys. Lett., **49**, 525 (1986).
6. Vu Thuong Quat, W. Eichhammer and P. Siffert, Appl. Phys. Lett., **54**, 187 (1989).
7. B. Hartiti, A. Slaoui, J.C. Muller in *Science and Technology of Defects in Silicon*, edited by C.A.J. Ammerlaan, A. Chantre and P. Wagner (Europ. Mater. Res. Soc. Proc., North Holland, Amsterdam, 1989) in press.
8. E.R. Weber, in *Impurity Diffusion and Gettering in Silicon*, edited by J. Washburn (Mater. Res. Soc. Symp. Proc. **36**, Pittsburgh, PA, 1985) p. 3.
9. J.C. Muller, Vu-Thuong-Quat, P. Siffert, H. Amzil, A. Barhdadi and N. M'Gafad, Solar Cells **25**, 109 (1988).

OXYGEN AND IRON REDISTRIBUTION UPON THERMAL TREATMENT IN IRON IMPLANTED SILICON

B. PIVAC*, A. BORGHESI, L. OTTOLINI**, M. GEDDO, A. PIAGGI AND A. STELLA

Dipartimento di Fisica-Università di Pavia, I-27100 Pavia, Italy

*Permanent Address: R. Boskovic Institute, P.O.B. 1016, YU-41000 Zagreb, Yugoslavia

**Centro di Studio per la Cristallografia Strutturale del C.N.R., I-27100 Pavia, Italy

ABSTRACT

In order to study the iron-oxygen interaction and their redistribution in silicon, different doses of 100 keV iron ions have been implanted into CZ silicon substrates, and subsequently annealed. The redistribution of iron and oxygen upon thermal treatment in nitrogen atmosphere was monitored with SIMS and FTIR measurements. A significant gettering of iron as well as of oxygen into the layer close to the implanted surface has been found only for doses exceeding the critical fluence, therefore indicating that the structural disorder and associated lattice strain field are the main driving forces for gettering mechanism. It has been found, however, that for doses above the critical fluence not all iron ions have been trapped into the damaged region, but a significant part of them have diffused into the bulk of the material, unaffected by gettering oxygen.

INTRODUCTION

Since iron is a fast diffuser in silicon, the control of silicon wafer contamination with iron during technological processes is very difficult. In order to prevent detrimental influence of metallic impurities on device performance, an intrinsic gettering procedure is often used, due to its compatibility with VLSI technology⁽¹⁻³⁾. Although a lot of relevant facts for this kind of gettering is known and used in industrial applications, the understanding of this process is still incomplete and requires further study.

The behavior of iron implanted in FZ silicon upon annealing or oxidation has been already studied⁽⁴⁾ and the existence of a certain critical level of fluences has been found, above which the implanted layer can not be completely recovered upon subsequent thermal annealing.

In order to study the oxygen influence on iron redistribution we implanted CZ wafers with various doses of iron and subsequently annealed them thermally. A systematic study with SIMS and FTIR spectroscopy is presented.

EXPERIMENT

Low boron doped (10^{16} atoms/cm³) and mirror polished on both surfaces CZ silicon wafers of <100> orientation were implanted with 100 keV iron ions at room temperature. Different doses in the range 6.3×10^{11} to 4.5×10^{15} Fe/cm² were implanted and subsequently annealed in a dry nitrogen atmosphere at 1000°C for two hours.

The initial interstitial oxygen concentration in as-received CZ wafer was 9.8×10^{17} atoms/cm³ (ASTM Method F 121-80).

Infrared (IR) measurements were performed with FTIR Bruker 113V spectrometer at room temperature with 4 cm⁻¹ resolution.

SIMS measurements were carried out using a Cameca IMS 4 F ion microprobe. Cs⁺ primary ions with an accelerating voltage of +10 kV and 750 nA current intensity were used to detect oxygen in negative mode, ¹⁶O⁻. To detect iron in positive mode, ⁵⁶Fe⁺, O₂⁺ primary ions with an accelerating voltage +12.5 kV and current intensity of 1.4 μA were used. The depth profile analysis of implanted iron was carried out at high mass resolution (M/ΔM ~ 3000) on all samples, in order to separate the ⁵⁶Fe⁺ signal from ²⁸Si₂⁺ interference due to the matrix.

RESULTS AND DISCUSSION

Profiles of iron implanted with various doses and subsequently annealed are shown in Fig. 1. For the two lower doses, i.e. for 6.3×10^{11} and 6×10^{13} Fe/cm² a rather flat profile across the wafer is obtained, and for the two higher ones, 2×10^{15} and 4.5×10^{15} a pronounced peak close to the surface is observed. Similar results are obtained by Wang et al.^[4] on FZ samples. They identified the existence of the critical fluence (that is 2.5×10^{14} Fe/cm²) above which the damaged layer formed upon implantation is totally amorphised and can not be completely recovered with thermal annealing. The remaining damaged layer acts as a gettering site, i.e. it provides nucleation centers for further iron clustering; therefore iron remains trapped in this region and does not diffuse deeper into the bulk. Our results confirmed the data obtained on FZ material, i.e. the existence of a threshold dose above which iron clusters in the damaged region. However, a difference was observed with respect to the experiment on FZ material, i.e. not all iron was trapped at the damaged region, and a significant tail extends deep into the bulk. This indicates that even for annealing at 1000°C in nitrogen atmosphere there is a certain fraction of iron that diffuses into the bulk.

Oxygen profiles obtained on the same samples after implantation and annealing are shown in Fig. 2. As shown in the figure, the oxygen behavior is similar to that of iron. Namely, for the doses below the threshold value no significant redistribution of oxygen in wafer took place, apart from oxygen pileup close to the surface. But for two doses above the threshold oxygen agglomeration at the damaged layer similar to that of iron took place.

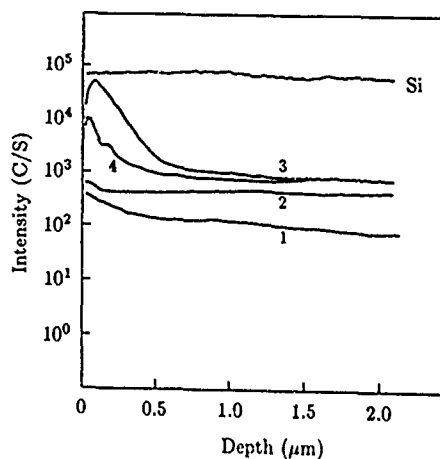


Fig. 1 Iron depth profiles for implanted doses 6.3×10^{11} (curve 1); 6×10^{13} (curve 2); 2×10^{15} (curve 3) and 4.5×10^{15} Fe/cm² (curve 4).

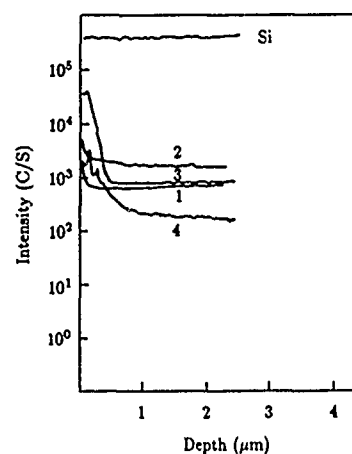


Fig. 2 Oxygen depth profiles for implanted doses 6.3×10^{11} (curve 1); 6×10^{13} (curve 2) and 2×10^{15} Fe/cm² (curve 3). Carbon depth profile obtained for implanted dose 2×10^{15} Fe/cm² is also shown (curve 4).

Redistribution of oxygen in CZ silicon after dopant implantation and subsequent thermal annealing was studied by Magee et al.^[5,6]. They found that after boron implantation and subsequent annealing at 1000°C oxygen diffuses rapidly to the surface, through the implanted region showing negligible or no trapping at all in that region. On the contrary, for the case of arsenic implantation a significant oxygen agglomeration occurs at the depth approximately equal to the projected range R_p of the implanted ions. In the both cases a large pileup of oxygen close to the surface was also observed.

Considerations similar to those for iron can be made also for oxygen. For the doses below the threshold value, the implanted layer was completely recovered, so that oxygen diffused rapidly through this region exhibiting a pileup close to the surface. On the other hand for the doses above the threshold, damaged region was amorphised and as it was not recovered, so it stimulated oxygen to precipitate in large precipitates, that are usually formed upon annealing at 1000°C. Here we should point out that although oxygen precipitated significantly at the damaged layer, as revealed with SIMS, we did not observe any typical SiO_2 -like contribution in IR spectrum, as it one would expect. The coprecipitation of iron and oxygen at the same region (see Figs. 1 and 2) probably caused formation of a new phase that is IR inactive, or at least is not active in this spectral region.

Furthermore, for the highest implanted dose a second oxygen peak can be observed at the depth of approximately $R_p + \Delta R_p$, as found for the case of As implantation^[6]. In addition we can note that the same phenomenon was observed for iron implantation (Fig. 1, curve 4).

In order to understand this phenomenon we must recall models of amorphisation formed upon bombardment-produced defects. Corbett et al.^[7] reviewed proposed models and concluded that the model proposed by Dennis and Hale^[8] is the best so far. This model predicts the existence of a completely amorphous central region surrounded by two partially damaged crystalline regions, the inner one vacancy rich and the outer interstitial rich. It is well known that silicon interstitials ejected during thermal oxidation form stacking faults, to compensate for the volume expansion.

From our results we argue that those stacking faults formed at perimeter of a damaged layer behave as a gettering center for the iron as well as for the oxygen giving rise to the double peak in SIMS profile.

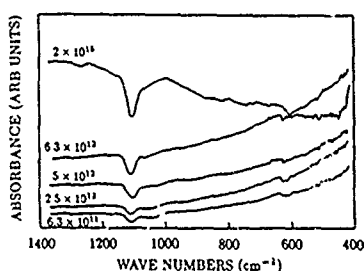


Fig. 3 Differential IR spectra of samples implanted with various doses of iron ions. Unimplanted wafer is taken as a reference.

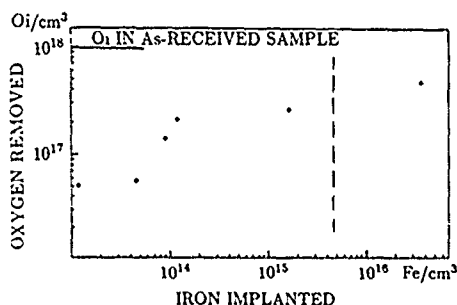


Fig. 4 O, removed as a function of Fe implanted. O, conc. in as-received sample (full line) and iron critical dose (dashed) is shown.

The oxygen behavior in the bulk was also monitored with FTIR spectroscopy. As shown in Fig. 3, with increasing concentration of iron ions implanted and diffused throughout the wafer more and more oxygen is removed from its interstitial position, as revealed with negative peak at 1107 cm^{-1} . Furthermore, it can be noticed that besides peak at 1107 cm^{-1} due to interstitial oxygen also a broad negative peak in the region from 1000 to 1100 cm^{-1} can be observed in all spectra. This broad peak verifies that oxygen precipitates present in as-received material were partially dissolved during the iron diffusion at 1000°C. The same behavior was observed by Colas et al.^[9], but while they observed no change in O, concentration, we saw a decrease in O, with increasing iron concentration.

This evidence supports earlier findings^[9], that besides the iron silicide a new phase is formed in silicon that includes also oxygen. Since iron has more affinity for oxygen

than for silicon, that phase should be more stable. The difference in iron influence on oxygen concentration in our results with respect to ref. [9] can be attributed to different methods of iron introduction into the material. Namely, while in ref. [9] iron was thermally diffused from evaporated films we implanted ions, and therefore introduced a lot of structural damage so that subsequent recovering during thermal annealing could enhance iron-oxygen interaction.

As an illustration of this, in Fig. 4, we showed the concentration of oxygen removed from its equilibrium interstitial position as a function of implanted iron. The line indicating the critical fluence for iron implantation is also shown (dashed line) for convenience. As shown in the figure the concentration of oxygen removed from the bulk exhibits a threshold-like behavior with a threshold value at an implanted dose of approximately 5×10^{12} Fe/cm², that is evidently much lower than the threshold value for iron clustering at damaged layer. This phenomenon is not yet clear and requires a further study.

CONCLUSION

In conclusion, the behavior of implanted iron ions in CZ silicon, upon thermal treatment at 1000°C in N₂, is similar to the one already reported for FZ silicon. The existence of a critical fluence seems to play the most important role in determining the iron behavior. Iron implanted with the doses below the threshold limit distributes rather smoothly throughout the bulk upon thermal annealing, while for the doses above the threshold, the majority remains trapped at the depth equal to projected range. However, there is a significant fraction of iron that diffuses freely into the bulk.

The depth profile of oxygen is found to be similar to the iron one, suggesting that the main driving force for gettering of both elements is structural disorder. It was also found that iron redistributed in the doses below the threshold dissolved oxygen precipitates already existing in as-received material. Furthermore, iron redistributed with annealing seems to remove oxygen from interstitial position and thus a new phase is formed that includes also oxygen. This process exhibits a threshold, like in the case of iron clustering, but its value is two orders of magnitude lower.

REFERENCES

- [1] A. Ourmazd, in Oxygen, Carbon, Hydrogen and Nitrogen in Crystalline Silicon, edited by J.C. Mikkelsen Jr., S.J. Pearton, J.W. Corbett and S.J. Pennycook, MRS, Pittsburgh, 1986, p.331
- [2] A. Borghesi, M. Geddo, A. Stella and Chen Chen-Jia, *J. Appl. Phys.* **63**, 2864 (1988)
- [3] D.K. Sadana, in Impurity Diffusion and Gettering in Silicon, edited by R.B. Fair, C.W. Pearce and J. Washburn, MRS, Pittsburgh, 1985, p.245
- [4] P.W. Wang, H.S. Cheng, W.M. Gibson and J.W. Corbett, *J. Appl. Phys.*, **60**, 1336 (1986)
- [5] T.J. Magee, C. Leung, H. Kawayoshi, B. Furman, C.A. Evans Jr. and D.S. Day, *Appl. Phys. Lett.*, **39**, 260 (1981)
- [6] T.J. Magee, C. Leung, H. Kawayoshi, R. Orman, B.K. Furman, C.A. Evans Jr. and D.S. Day, *Appl. Phys. Lett.*, **39**, 413 (1981)
- [7] J.W. Corbett, J.P. Karins and T.Y. Tan, *Nucl. Instrum. Methods* **182/183**, 457 (1981)
- [8] J.R. Dennis and E.B. Hale, *J. Appl. Phys.*, **49**, 1119 (1978)
- [9] E.G. Colas and E.R. Weber, *Appl. Phys. Lett.*, **48**, 1371 (1986)

ION BEAM ETCHING OF SILICON: IMPLANTATION AND DIFFUSION OF NOBLE GAS ATOMS, AND GETTERING OF COPPER

WILLIAM D. SAWYER*, JÖRG SCHMÄLZLIN† and JÖRG WEBER
 Max-Planck-Institut für Festkörperforschung, Heisenbergstr. 1,
 7000 Stuttgart 80, Federal Republic of Germany
 † Fakultät für Physik, Albert Ludwigs Universität, Hermann Herder Str. 3,
 7800 Freiburg, Federal Republic of Germany
 * Now at Mobil Solar Energy Corporation, 4 Suburban Park Drive, Billerica,
 Mass. 01821-3980

ABSTRACT

Defects introduced into silicon by ion beam etching are investigated by low-temperature photoluminescence (PL) and Rutherford backscattering (RBS) measurements. The RBS results show that during the ion beam etch a highly damaged surface layer is formed which contains a large concentration of Ar atoms. The Ar atoms then diffuse out of the surface and into the crystalline bulk by some form of radiation enhanced diffusion. Annealing of the etched samples at 350°C results in the formation of noble gas defects known from previous PL studies of ion implanted silicon. When the samples are annealed at 650°C PL lines due to new defects are formed. Although little is known about their structure, we show that the new Ar defects getter small copper contaminations very effectively.

INTRODUCTION

Dry etching has become an important process necessary for the production of semiconductor devices. Ion beam etching (IBE) exposes the surface of the material being etched to bombardment by noble gas ions with energies from 100 eV to several keV. Significant semiconductor surface damage is reported [1]. Previous research also gave some indications that the damage created during etching was penetrating the bulk of the material [2]. In this paper we investigate the damage caused by IBE of silicon. Using RBS we show that a large concentration of noble gas atoms is implanted in the surface layer of the material etched. Low temperature PL measurements enable us to characterize the small concentration of defects in a thin region below the surface.

EXPERIMENTAL

Samples cut from polished silicon wafers were cleaned in acetone, propanol and deionized water, and the native oxide was stripped by a short HF dip. They were then immediately mounted in a Veeco 3" Microetch system with good thermal contact to a water cooled stage. The sample temperature was monitored during etching by a thermocouple. A maximum temperature of 40°C was not exceeded. The samples were etched for 15 min in a noble gas ion beam with a constant current density of 0.2 to 0.4 mA/cm², depending on the gas used. The ion beam energy was 1 keV. The samples were annealed in 50°C steps for 30 min under nitrogen gas flow.

Rutherford backscattering measurements were performed in the channeling mode with a 2 MeV He ion beam. Backscattered ions were detected with an Ortec Si detector. Photoluminescence spectra of the samples were recorded at 4.2 K using an unfocused Ar laser, a cooled Ge detector, and conventional lock-in techniques. The surface of some of the samples was anodically oxidized and removed in order to measure the depth profile of the defects. The thickness of the growing oxide was monitored by the voltage drop across the oxide. The absolute oxide thickness was measured by ellipsometry.

NOBLE GAS IMPLANTATION

TRIM calculations [3] show that Ar ions with an energy of 1 keV should have an implantation depth of 30 Å. Figure 1 shows channeled RBS-spectra of a sample that was etched in a 1 keV ion beam (circles) and a virgin sample (triangles). The etched sample shows a wider and higher peak at the energy of helium ions scattered from the surface. This is caused by severe damage to the Si surface during etching. A second scattered He ion peak with an energy maximum at channel number 660 is caused by the scattering of He ions from Ar which was implanted in the surface. The narrow width of the peak is indicative of only a surface layer of Ar in the sample. The area of this peak corresponds to a surface concentration of 1.8×10^{15} atoms/cm².

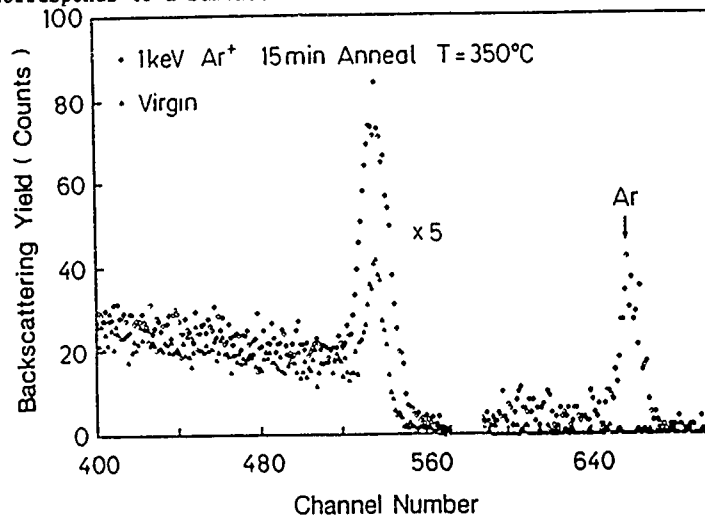


Fig.1: Channeled Rutherford backscattering spectra of a IBE (•) and a virgin (Δ) sample.

In order to determine the depth of the damaged layer which contains a high concentration of Ar, a layer 50 Å thick was removed from the surface of an etched sample. RBS measurements of this sample show no peak due to Ar in the surface. In addition the peak caused by surface damage is the same as in the spectrum of a virgin sample. Thus by removing a layer 50 Å thick from an etched sample, the damage as well as the RBS detectable Ar concentration are removed.

NOBLE GAS DEFECT DEPTH PROFILE

The Ar detection limit of our RBS configuration is 1.0×10^{19} atoms/cm³. This is far too insensitive to detect low-defect concentrations in the Si volume below the highly damaged surface. Davis et al. [4] showed that PL can be used to detect small concentrations of noble gas defects created by the penetration of noble gas ions into Si during IBE. These defects are well known from PL studies of high-energy noble gas implantation in Si [5,6].

The PL signal from the Ar defects created by IBE of Si is generated in the crystalline layer of Si just below the highly damaged surface. In order to determine the depth profile of the Ar defects, we etched samples with (111) and (100) crystallographic orientations with a 1 keV Ar ion beam. One part of the samples was annealed at 350°C before an oxide layer was grown by anodic oxidation. The oxide layers were then removed in a buffered HF solution. On the other part of the samples an oxide layer was grown and removed before it was annealed at 350°C.

The Ar₀ [7] line PL signal is calibrated to the phosphorus bound exciton line detected in the samples. Because the donor concentration is expected to

be homogeneous throughout the samples, the relative Ar_0 line intensity is a measure of the total Ar defect concentration in the samples.

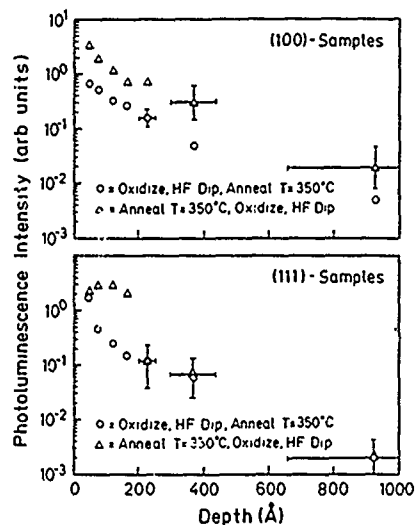


Fig.2: Depth profile of the Ar_0 line PL. (Upper part (100) wafer, lower part (111) wafer)

The PL depth profiles of the Ar defects are shown in Fig. 2. Separate profiles are shown for different crystallographic orientations and different sample treatments, such as removing the layers before or after annealing of the samples. The depth profiles are independent of the sample treatment or crystallographic orientation. The Ar_0 line can be detected even after removing 1000 Å from the sample surface.

The profiles shown in Fig.2 do not directly represent the Ar defect concentration at different depths. The intensity of the Ar_0 line intensity is proportional to the total Ar defect concentration. A decrease in the PL intensity due to removal of a layer from the surface of a sample is caused by the loss of the defects in the layer removed. The inaccuracy in the layer thickness measurement grows larger with the thickness of the oxide layer. Nevertheless, the penetration depth of the Ar ions is much deeper than would be expected from implantation theory [3].

Channelled Ar ions which are implanted at such low energies are able to penetrate into the crystalline substrate. However, the highly damaged sample surface shown in Fig.1a prevents any channeling. Therefore, the only explanation for the large penetration depth seems to be a fast diffusion of the Ar ions. The difference in the depth profile of the samples that were annealed before or after layer removal shows that the 350°C anneal does not cause a substantial diffusion of the defects. The depth profiles are produced during the IBE at room temperature. We estimate the room temperature diffusion constant of the Ar ions to be approximately $10^{-15} \text{ cm}^2/\text{sec}$. This value is comparable to the extrapolated room temperature diffusion constant of transition metals in Si [8]. The Ar diffusion is probably enhanced under IBE conditions because of the high concentration of intrinsic defects created by the ion bombardment.

Gettering of Copper

Annealing of the IBE samples above 500°C destroys the noble gas induced PL-lines. If an etched sample is annealed at 650°C, new defects are formed. Fig.3a shows the PL spectrum generated by the new Ar-associated defects. It consists of a broad band centered at about 1.0 eV with several sharp lines on top. Samples etched with other noble gases which were annealed at 650°C show similar spectra. Ref. 5 and 6 report new defects in samples that were implanted with noble gases and then annealed above 550°C. The energetic position and the number of lines is different from our results. Apparently the creation of the different noble gas complexes at higher temperature depends critically on the implantation conditions and the sample parameters.

The components and structures of the new Ar defects are not known. Fig.3b shows a PL spectrum of the new Ar defect taken under lower laser excitation than the spectrum in Fig.3a. Some of the lines in Fig.3b can be associated with a well known Cu PL signal [9]. The intensity of the Cu spectrum saturates at higher laser excitation power because of the small

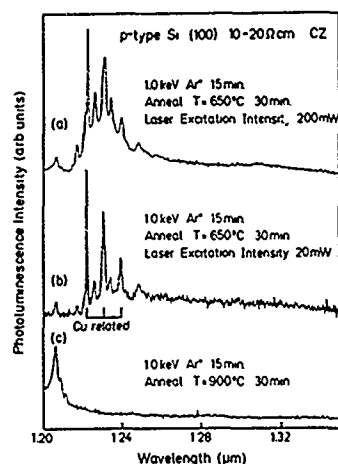


Fig.3: Photoluminescence spectra of Ar IBE samples annealed at 650 and 900°C.

CONCLUSION

We have shown that IBE implants a large concentration of Ar into a surface layer less than 50 Å thick, which causes severe damage. The Ar ions diffuse into the crystalline substrate beneath the surface during the etch. The diffusion is fast due to the high concentration of intrinsic defects created by the ion bombardment. After annealing at 350°C defects are formed as deep as 1000 Å into the substrate. Annealing at 650°C causes the formation of new defects. The PL spectra of these samples shows well known Cu related PL lines. Apparently the damage created during the IBE getters small Cu concentrations very effectively.

ACKNOWLEDGEMENTS

We thank H.J.Queisser and H.-U.Habermeyer for their continued interest in this work.

REFERENCES

1. S.J.Fonash, Solid State Tech, **28**, 201 (1985).
2. J.C.Bean, G.E.Becker, P.M.Petroff and T.E.Seidel, J.Appl.Phys. **48**, 907 (1977).
3. J.F.Ziegler, J.P.Biersack and U.Littmark, in *The Stopping and Range of Ions in Solids*, edited by J.F.Ziegler (Peramon Press, New York, 1985).
4. R.J.Davis, H.-U.Habermeyer and J.Weber, Appl.Phys.Lett. **47**, 1295 (1985).
5. V.D.Tkachev, A.V.Mudryl and N.S. Minaev, Phys.Stat.Solidi (a) **91**, 313 (1984).
6. N.Bürger, K.Thonke, R.Sauer and G.Pensl. Phys.Rev.Lett. **52**, 1645 (1984).
7. The PL line notation used in Ref.6 shall be used in this paper.
8. E.R.Weber, Appl.Phys. A **30**, 1 (1983).
9. J.Weber, H.Bauch and R.Sauer, Phys.Rev. **25**, 7688 (1982).

concentration of Cu defects in the samples. Fig.3c shows that an anneal at 900°C eliminates the Cu and new Ar defect spectra.

The Cu spectrum can only be detected in samples that were etched with Ar and annealed at temperatures above 500°C. Samples that were etched with other noble gases in the same IBE machine and were annealed at temperatures above 500°C do not show the Cu PL lines. This excludes the possibility that the samples were contaminated with Cu during the IBE or by our chemical cleaning of the samples before etching. We suggest that the IBE process getters a residual Cu contamination of Si very efficiently.

ANGLE RESOLVED XPS ANALYSIS OF SURFACE REGION DEFECTS IN RAPID THERMAL ANNEALED ANTIMONY IMPLANTED SILICON

S.N. Kumar, G. Chaussemy and A. Laugier, Laboratoire de Physique de la Matière, Institut National des Sciences Appliquées de Lyon, 69621 Villeurbanne, France
B. Canut, Département de Physique des Matériaux, and M. Charbonnier, Département de Chimie Appliquée, Université Claude Bernard Lyon I, 69622 Villeurbanne, France.

ABSTRACT

Angle-resolved X-ray photoelectron spectroscopy characterization of the surface region of high-dose Sb⁺ ion implanted silicon, after rapid thermal treatments over various temperatures, is reported. The results obtained are compared with the Rutherford backscattering data and the capacitance-voltage measurements on the metal-oxide-semiconductor mesa structures built on them. Rapid anneal at 1100 °C of the 1.4×10^{16} Sb⁺/cm² samples showed an anomalous deep oxygen diffusion inside the implanted region.

INTRODUCTION

High-dose ion implantation of silicon followed by rapid thermal annealing (RTA) is now a well established technique in metal-oxide-semiconductor (MOS) technology. Arsenic or antimony is the usually preferred n⁺ dopant in the fabrication of bipolar integrated circuits. However, for ultrashallow junctions, Sb is more advantageous owing to its reduced range, straggle, and a lower diffusion coefficient. Further, unlike in the case of As, there is a minimal evaporative loss of dopant during the silicidation of the source-drain regions. Electrical measurements [1] on supersaturated solid solutions of antimony in silicon have shown that carrier concentration can greatly exceed the solid solubility limits. The solid phase epitaxial regrowth of the damaged amorphous zone takes place at about 550 °C and the maximum incorporation of electrically active antimony at substitutional sites is complete at about 700 °C [2].

An anomalous depletion behavior of antimony from substitutional sites on annealing above 700°C has been reported by Holland and Fathy [3]. This may be either due to a vacancy assisted Sb diffusion into the precipitates, as deduced from oxidation-retarded diffusion of Sb [4], or by an interstitialcy mechanism [5], due to the existence of a supersaturated interstitial solution upon SPE recrystallization. These contradictory observations thus point out the need for more information of the structural and chemical nature of the near surface region where enhanced Sb depletion is known to occur when annealing is carried out at temperatures higher than 700 °C.

The objective of the present work is to carry out a systematic analysis of the surface region of the high-dose Sb implanted samples after RTA over a wide temperature range, namely, from 500 to 1100 °C. We use the highly surface sensitive technique of angle resolved X-ray photoelectron spectroscopy (ARXPS) to identify the chemical states of Si, O and Sb after various RTA treatments of samples implanted with Sb with a dose in the range of 2×10^{14} to 1.4×10^{16} Sb/cm² with 40, 80 and 120 keV implant energies. These results are compared with the Rutherford backscattering spectrometry (RBS) and capacitance-voltage (C-V) profiles of MOS mesa structures built on them.

EXPERIMENTAL

Wafers of Czochralski-grown boron-doped Si of (100) orientation with a resistivity of about 20 Ω cm were implanted at 40, 80 and 120 keV with four Sb doses: 2×10^{14} , 1.2×10^{15} , 5.4×10^{15} and 1.4×10^{16} Sb⁺/cm². The respective projected ranges were 290, 460 and 630 Å. The implantations were performed at room temperature with a beam current less than 1 μA to limit sample heating and with a 7° incidence to avoid parasitic channeling effects. The RTA treatments were carried out from 500 to 1100 °C for 10 s in a 30 kW incoherent light annealing device. The details of RTA and RBS measurements have been described elsewhere [6]. In the RBS data, algorithmic deconvolution of the observed RBS spectra was performed numerically to reduce the effect of detector resolution. C-V measurements, from 10 kHz - 1 MHz, were performed on MOS mesa structures built on the samples annealed at various temperatures. After lithographic deposition of 1000 Å SiO₂ and aluminum metal front contacts of 0.25 mm² area, mesa structures were obtained by a controlled etching in a solution of HF:HNO₃:CH₃COOH = 1:3:2 (volume ratio) at room temperature. A gallium-indium eutectic served as the back contact.

The ion implanted and subsequently annealed samples were surface characterized by a Riber SIA-200 XPS system. The Al K α X-ray excited photoelectron spectra for Si 2p, O 1s and Sb 3d peaks were recorded at take-off angles of 25°, 65° and 90° with a system pressure at 10⁻⁹ Torr. The binding energy (B.E.) was calibrated with the Au 4f_{7/2} line taken at 83.8 eV as reference. These peaks were smoothed by effectively filtering out the high frequency noise signals by a Fourier transform technique. The area under each peak was obtained after the background correction. By sensing the photoelectrons at low take-off angles, the signal arising from the deeper layers can be effectively quenched. $\theta = 0^\circ$ corresponds to the tangential exit of electrons from the sample surface which gives the maximum "surface sensitivity", while $\theta = 90^\circ$ is used for maximum "bulk sensitivity". One can thus depth profile the states of various elements present and be able to locate the relative abundance of each phase across this shallow region.

RESULTS AND DISCUSSION

XPS Spectra

Figure 1 (a) and (b) show the Si 2p XPS lines from sputter cleaned samples (dose = 1.4×10^{16} Sb/cm² and energy = 40 keV) after RTA at 1100 and 700 °C respectively. The corresponding O 1s spectra are shown in Fig. 2. Spectra (1), (2) and (3) in each correspond to $\theta = 25^\circ$, 65° and 90° respectively. The lower BE line at about 99 eV is due to the elemental Si 2p peak [7]. A gradually increasing positive charge on silicon would shift its core level spectrum (by ΔE) successively towards higher BE values. The second peak at ~102 eV corresponds to the oxide form of silicon. This high energy peak appears well Gaussian so that further deconvolution was not performed. A ΔE of ~3.85 eV between the two lines in Fig. 1(b) corresponds to the oxidation state (4+) of silicon [7] whereas $\Delta E \sim 3$ eV observed in Fig. 1(a) indicates a lower oxidation level. The Ar⁺ cleaning conditions used in the XPS chamber corresponded to a roughly 15 Å sputter etch removal from the sample surface, which is the thickness of the native oxide layer on the silicon surface. The large oxygen concentration in both the samples as well as the considerably intense higher energy line seen in the Si 2p spectra clearly indicate a deeper oxygen penetration in the upper surface region. A lower ΔE value for the 700 °C anneal suggests the existence of a lower oxidation state of Si. Further, a nearly constant value of ΔE among the three Si 2p spectra corresponding to three angles indicates a roughly uniform stoichiometry upto the maximum probed depth.

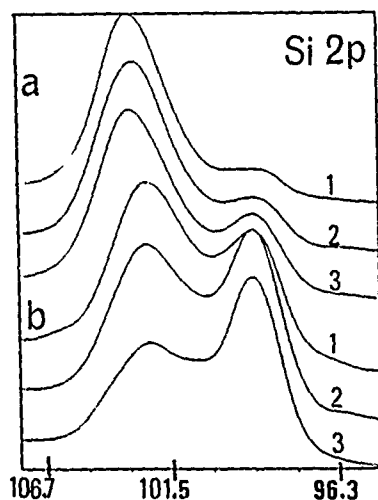


Fig. 1. XPS Si 2p spectra of 1.4×10^{16} Sb/cm², implanted at 40 keV rapidly annealed (a) 1100 °C and (b) 700 °C. Spectra 1, 2 and 3 correspond to $\theta = 25^\circ$, 65° and 90° respectively.

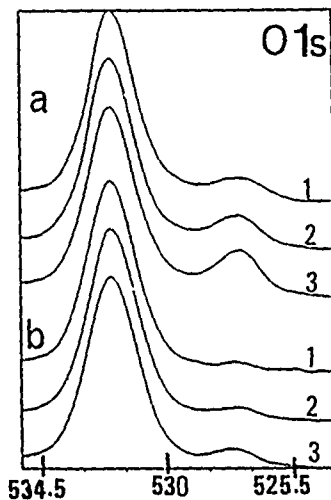


Fig. 2. XPS O 1s spectra of 1.4×10^{16} Sb/cm², implanted at 40 keV rapidly annealed (a) 1100 °C and (b) 700 °C. Spectra 1, 2 and 3 correspond to $\theta = 25^\circ$, 65° and 90° respectively.

Considering that the XPS probed depth is oxidized for all the detection angles, the mean free path of photoelectrons can be taken equal to 37 ± 4 Å [8]. The probed depth for $\theta=25, 65$ and 90° is thus approximately equal to 35, 70 and 105 Å respectively. The Sb 3d XPS spectra (not shown here) for various RTA temperatures, dose and implantation energy conditions clearly indicated that Sb was present only in the elemental form. Thus, the oxygen atoms are bonded only to silicon. Further, within the maximum probed depth of ~ 105 Å of XPS, the SiO_x phase in the 700°C annealed sample exhibits a substoichiometric composition. The ratio of the oxide silicon to elemental silicon is systematically reversed as the analysis angle increases from 25 to 90° . The oxide line intensity rapidly attenuates with increasing probed depth (i.e., $\theta=90^\circ$), thereby suggesting a much smaller oxide layer thickness in the 700°C annealed sample. The 1100°C annealed sample shows, however, a different trend. A constant and higher value of ΔE ($=3.85$ eV) between the spectra taken at three angles indicates that the oxidized fraction of silicon exhibits the maximum oxidation level (Si^{4+}) throughout the probed depth. Further, the oxide signal is stronger than the elemental silicon signal for all the three angles, so that in this case oxygen penetrates much deeper into the implanted zone.

In the O 1s spectra, the peak position of 532.0 eV corresponds to the bonding with Si [7]. Bonding of O with Sb can be ruled out as the O 1s line in Sb_2O_3 and Sb_2O_5 are reported [9] to be at 529.7 and 530.5 eV respectively. The peak at ~ 528 eV is due to the Sb $3d_{5/2}$ emission. In all the spectra the O 1s peak is well gaussian, which again points out to the absence of any oxide with Sb. A higher positive shift (by ~ 0.8 eV) of the higher B.E. Si 2p line for the 1100°C RTA sample, with respect to the 700°C annealed sample, in Fig. 1 indicates a higher oxidation level of Si in the 1100°C sample. Earlier studies on RTA at 1100°C of Sb implanted Si, with dose from 1.2×10^{14} to 1.4×10^{16} Sb/cm², at energies from 40 keV to 120 keV, showed a relatively large concentration of oxygen in the 1.4×10^{16} Sb/cm², 40 keV sample when compared with the value for other doses [10]. Oxygen penetration deeper into the implanted zone in high dose samples may be due to the implantation induced porous structure formation in the surface region which subsequently allows the O atoms to diffuse into the implanted zone. Such a porous structure may be compared with an ordered silicon lattice, wherein the native oxide thickness quickly terminates to ~ 20 Å [11] at room temperature owing to the blocking and inert nature of the non porous oxide formed towards further oxidation.

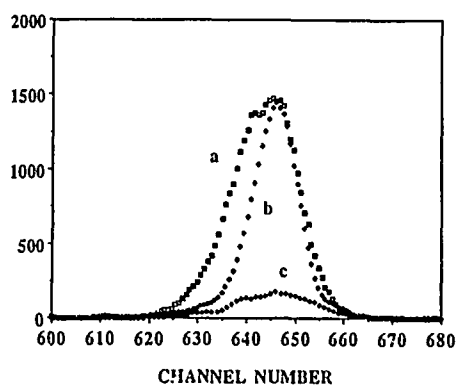


Fig. 3. RBS backscattering yield as a function of channel number for the 120 keV Sb implanted samples at a dose of 5.4×10^{15} Sb/cm²: (a) non annealed, (b) 1100°C RTA and (c) 700°C RTA.

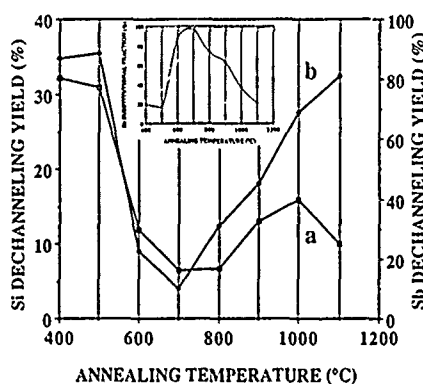


Fig. 4. Variation of Si and Sb dechanneling yields with the RTA temperature for 120 keV Sb implanted sample at a dose of 5.4×10^{15} Sb/cm². The inset shows the dependence of substitutional fraction of Sb on the RTA temperature.

RBS Data

As a typical case, the backscattering yield for Sb (dose = 5.4×10^{15} Sb/cm², 120 keV implant) in the channeling mode as a function of channel number is shown in Fig. 3. It is evident that the 1100°C anneal does not result in any noticeable improvement in the Sb substitutional fraction as compared to that of the unannealed sample. However, in the 700°C annealed sample

the backscattering yield in the channeled mode decreases sharply, thereby indicating that most of the Sb is in substitutional sites. The silicon dechanneling yield χ_{\min}^{Sb} (measured behind the surface peak) and the ratio between the Sb yields in channeled and random geometries, χ_{\min}^{Sb} , are plotted in Fig. 4. The mean substitutional fraction α of the dopant is shown in the inset. It is evident that the substitutional fraction is maximum ($\sim 97\%$) at 700°C . At 1100°C , χ_{\min}^{Si} is $\sim 10\%$. This value is comparable to the value ($\sim 3\%$ for $1.5\text{ MeV }^4\text{He}^+$ analysis) of virgin Si, so that recrystallization of the silicon lattice is largely complete. However, a high value of χ_{\min}^{Sb} after 1100°C RTA indicates a poor activation of antimony. Thus, although the 1100°C RTA seems to fairly well recrystallize the silicon lattice, only a small fraction of Sb is inserted into the substitutional positions.

RBS dose measurements of samples obtained after various doses implanted at 40, 80 and 120 keV and RTA treatments showed that the outdiffusion was not significant for all samples, except the one corresponding to $1.4 \times 10^{16}\text{ Sb/cm}^2$ implant at 40 keV annealed at 1100°C . In the later case, the outdiffusion was comparatively larger and the final dose decreased to $1.1 \times 10^{16}\text{ Sb/cm}^2$.

Preliminary C-V measurements over -10 to $+10\text{ V}$, at 10 kHz , 100 kHz and 1 MHz , on mesa structures constructed on samples ($5.4 \times 10^{15}\text{ Sb/cm}^2$, implanted at 120 keV) annealed at 500 to 1100°C for 10 s have shown that the 1100°C annealed sample exhibits a sharp increase in capacitance at 0 V and 5 V . Further, the capacitance increased by two-orders of magnitude (from 5 nF to 50 pF) between the 10 kHz and 1 MHz measurements. This phenomenon was not observed with the other low temperature annealed samples, wherein the MOS structures exhibited a nearly uniform ($\sim 50\text{ pF}$) capacitance over different frequencies. The reason for this behavior at 1100°C is not clear and further experiments are underway.

CONCLUSIONS

The present XPS, RBS and C-V results have shown that a part of the silicon atoms in the top surface region of about 100 \AA are bonded to the oxygen atoms. The fraction of oxidized silicon in the implanted region after RTA treatment at 1100°C is considerably greater than after the 700°C anneal. Further, a positive shift of about 0.85 eV in the binding energy of the higher energy Si $2p$ XPS line in the 1100°C annealed sample (as compared with the 700°C treated sample) is attributed to the $(4+)$ oxidation state of Si in the surface region.

REFERENCES

- [1] J.S. Williams and K.T. Short, J. Appl. Phys. **53**, 8663 (1982).
- [2] A. Nylandsted-Larsen, F.T. Pederson, G. Weyer, R. Galloni, R. Rizolli and A. Armigliato, J. Appl. Phys. **59**, 1908 (1986).
- [3] O.W. Holland and D. Fathy, J. Appl. Phys. **63**, 5326 (1988).
- [4] D.A. Antoniadis and I. Moskowitz, J. Appl. Phys. **53**, 6788 (1982).
- [5] S.J. Pennycook, J. Narayan and O.W. Holland, J. Appl. Phys. **55**, 837 (1984).
- [6] S.N. Kumar, G. Chaussemy, B. Canut, D. Barbier and A. Laugier, Appl. Surf. Sci. **36**, 545 (1989).
- [7] C.D. Wagner, W.M. Riggs, L.E. Davis, and J.F. Moulder, in *Handbook of X-ray Photoelectron Spectroscopy*, edited by C.D. Wagner (Perkin Elmer, Minnesota, 1979).
- [8] J.M. Hill, D.G. Royce, C.S. Fadley, L.F. Wagner, and F.J. Grunthaner, Chem. Phys. Lett. **44**, 225 (1976).
- [9] J.M. Hill, D.G. W.E. Morgan et. al. Inorg. Chem. **12** (1973), 953.
- [10] S.N. Kumar, G. Chaussemy, B. Canut, M. Charbonnier, A. Laugier and M. Romand, Mater. Sci. and Engg. **B3/4** (1989), in press.
- [11] F. Lukes, Surf. Sc. **30**, 91 (1972).

DEFECTS IN MBE-GROWN SILICON EPILAYERS STUDIED WITH VARIABLE-ENERGY POSITRONS

P.J.SIMPSON, P.J.SCHULTZ, I.V.MITCHELL, T.E.JACKMAN* and G.C.AERS*
Dept. of Physics, University of Western Ontario, London, Ontario N6A 3K7,
Canada.
*Microstructural Sciences Laboratory, National Research Council of Canada,
Ottawa, Ontario K1A 0R6, Canada.

ABSTRACT

Few non-destructive techniques are available which provide information regarding defect type, concentration and depth distribution in semiconductors. The variable-energy positron beam technique has recently demonstrated a sensitivity to near surface defects and impurities at low defect concentrations. In the present study, intrinsic silicon (100) epilayers of ~3000 Å thickness grown by MBE at different temperatures were examined by this method for evidence of changing defect concentration and type.

INTRODUCTION

Molecular beam epitaxy (MBE) is a well established method for growing semiconductor epilayers of high purity and crystal perfection, yet it may still result in defect concentrations that can affect the electronic properties of these epilayers. For example, recent photoluminescence [1] and deep level transient spectroscopy [2] measurements have provided evidence of significant defect concentrations in intrinsic silicon grown at low temperatures ($\leq 500^\circ\text{C}$). It is apparent that the characterization and control of such defects would benefit from improved methods for identifying defect type, concentration and distribution.

As an emerging technique for defect measurement, positron annihilation offers several advantages for studying the near-surface defect distribution [3]. The technique is non-destructive, provides depth-resolved information, and is sensitive to concentrations of point defects as low as 10^{-6} per atom. Qualitative and comparative interpretation of positron beam results is relatively straightforward. Quantitative analysis is more difficult, but progress is being made in its development [4].

In this paper we discuss results of a preliminary study of multilayer silicon samples grown by molecular beam epitaxy (MBE) at the National Research Council of Canada (NRC). The application of the slow positron technique to single semiconductor epilayer structures is well established [5,6]; in this study we apply positron annihilation to one and two epilayer structures, each grown at different temperatures. Data were also obtained using secondary ion mass spectroscopy (SIMS) and electrochemical current-voltage (eCV) profiling as a check on sample impurity content.

EXPERIMENTAL METHOD AND ANALYSIS

Details of the slow positron beam apparatus at the University of Western Ontario are given in reference [7]. Monoenergetic positrons (in the range 0.1 to 60 keV) are implanted into the sample to be studied and lose energy by mechanisms similar to those for electrons. After "thermalization" (i.e. reaching thermal energy), the positron diffuses through the solid until it annihilates, with a typical lifetime of ~200 picoseconds. Annihilation can occur in the defect-free solid, or in a localized defect state within the bulk of the sample, or at the surface. Re-emission from the sample, either as a free positron or as positronium, can in principle occur but is usually negligible for oxide-covered Si surfaces at room temperature.

Upon annihilation of a positron-electron pair, two 511 keV gamma rays are emitted. The gamma rays are Doppler shifted because of the finite momentum of the electron. The gamma ray energy spectrum is analyzed, and a line shape parameter, S , is calculated as a measure of the degree of Doppler broadening of the 511 keV spectral line. S is the ratio of counts in a fixed central region of the peak to the total in the peak. Sensitivity to defects is a result of the modified electron momentum distribution in the region of a defect, and the tendency for positrons to be trapped by defects [3].

In order to obtain depth-resolved defect information, the incident beam energy is varied and a plot of S parameter vs. incident energy is produced. The mean stopping depth of positrons in the sample may then be related to the incident energy.

The positron implantation profile is approximated by the derivative of a Gaussian [3,8]. Trial profiles of defects and electric fields in the sample are adopted, and the diffusion equation for positrons in the solid is solved numerically [4]. For each value of the beam energy the fraction of positrons annihilating at the surface, in defect trapped states, and in the bulk material is calculated. These fractions are used to calculate S parameters for free, surface, and bulk defect annihilations by fitting to the experimental data. Trial values are then adjusted to optimize the fit to the data. All measurements are referenced to the S parameter for free positron annihilation in the undefected Si substrate, S_f , which is observed at high incident energy (>20 keV).

In past positron trapping experiments, defects in MBE-Si have been observed which lead to:

- (1) lineshapes narrower than those for freely diffusing positrons, with $S_d(=S_{\text{defect}})/S_f=1.035\pm 0.01$, associated with defects hereafter called type P1 [6].
- (2) lineshapes broader than those for freely diffusing positrons, with $S_d/S_f=0.93\pm 0.02$, associated with defects hereafter called type P2 [5].
- (3) lineshapes similar to those for free positrons, with $S_d/S_f=1.00\pm 0.01$, associated with defects hereafter called type P3 [6].

Type P1 defects are generally associated with open lattice spaces, which are probably divacancies. Divacancies are expected to be stable at room temperature, annealing out at 500 to 900 K, whereas monovacancies anneal out at 200 to 300 K [9,10]. Type P2 defects have been attributed to oxygen-related defect complexes, due to the similarity of the lineshape parameter to that obtained from Si capped with a native surface oxide ($S_g(=S_{\text{surface}})/S_f=0.91$ to 0.97, depending on the sample). The existence of the recently observed type P3 defect is somewhat controversial, although it has been suggested [6] that substitutional As clusters [11] may be responsible (in samples where As is known to be present) for trapping of positrons with no significant change of lineshape. Recent arguments for a configuration of a single vacancy surrounded by four As atoms, stable at room temperature, are consistent with this proposal [12].

PRESENT STUDY

In the present work, three samples of Si/Si(100) grown using a Vacuum Generators Si MBE facility were studied. The first sample was grown under nominally ideal conditions [4] at $\sim 750^\circ\text{C}$ substrate temperature and consisted of a 5800 Å epilayer (sample #565). The second consisted of a 3000 Å epilayer that was grown at a substrate temperature of 550°C (sample #566A). The deposition was interrupted for ~ 5 minutes as the wafer was partially covered by a shutter and cooled to 400°C , then an additional 2800 Å layer was grown (sample #566B). These two temperatures were chosen to match values where defects have been observed previously [1,2]. Two different pieces from each

sample were studied.

Figure 1 shows the S vs. E data for samples 565 and 566A, together with the best fits to the data. The 750°C layers (sample #565) were fit with a small concentration of type P1 defects (5×10^{-6} /atom) and a relatively weak bipolar field (~ 1000 - 2000 V/cm) centred about and directed toward the growth interface at 5800 Å. This is consistent with previous studies of "good" MBE-grown Si/Si(100) single layers [5] and with SIMS data for sample 565 obtained using a Cameca IMS-4f which confirmed a significant boron spike and carbon at the detectability limit at the substrate interface. No evidence for any other contamination in the layer or at the interface was observed.

The 550°C layers (sample 566A) were fit with a concentration of $\sim 1.5 \times 10^{-5}$ /atom type P1 defects and an electric field of magnitude 1000-2000 V/cm caused by the boron at the interface. The SIMS profile of this sample unexpectedly showed a mass 40 contaminant part way through the layer, correlated with an oxygen spike. High resolution studies at mass 40, examination of other isotope masses and the absence of carbon surprisingly suggested that the contaminant was calcium. The origin of the contaminant (which has not been previously observed in MBE grown material from this system) is unknown as the sample was grown under the same vacuum conditions as sample #565 (2×10^{-8} Pa). An eCV profile demonstrated that the contamination was electrically inactive.

Figure 2 shows the data and fit for sample 566B. Because both 566A and 566B were grown on the same wafer without removal from the MBE vacuum system, a degree of consistency might be expected in the fits for both. However, the eCV profile showed the 400°C (sample 566B) layer to be slightly n-type with a sheet of positive charge at the interface between the two layers, completely changing the electric field distribution from that in sample 566A.

This epilayer also showed the mass 40 spike and oxygen contamination. High resolution electron microscopy did not reveal any evidence for extended defects originating at this interface. Sample 566B was fit assuming an electric field of magnitude $> 1 \times 10^5$ V/cm centred at and directed away from the shallower interface, and concentrations of type P1 defects of 2×10^{-5} /atom in the 550°C layer and 5×10^{-5} /atom in the 400°C layer. Since the increased defect concentration in the overlayer was not correlated with a change in the concentration of the mass 40 contaminant, we presume that they were not related. Detailed models and parameters which led to acceptable fits to the data are contained in table 1.

A source of ambiguity in the fitting procedure lies in the choice of the diffusion coefficient D_+ , and a defect trapping rate ν [4]. We used the value $D_+ = 2.8 \text{ cm}^2/\text{s}$, which we believe to be appropriate for MBE-grown intrinsic Si [4,5]. A defect trapping rate of $3 \times 10^{14} \text{ s}^{-1}$ was used [3]. This value may be too small, which would result in the deduced defect concentrations being inflated.

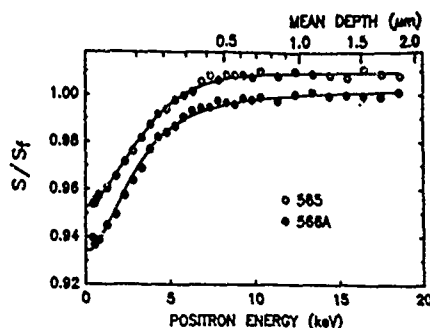


Figure 1: S vs. E curves for samples 565 and 566A. Data for the second sample of each type are shown as points, with the fit shown as a solid line. The data for sample 565 have been shifted upward by 0.01 for clarity.

CONCLUSIONS

We have measured defects and electric fields in several MBE-grown Si layers; results are summarized in table 1. In addition we note the following points:

(1) The concentration of type P1 defects increases with decreasing growth temperature. Specifically, we found concentrations of $\sim 5 \times 10^{-5}$ /atom for 750°C , $\sim 1.5 \times 10^{-5}$ /atom for 550°C and 5×10^{-5} /atom for 400°C .

(2) Defect profiling of multilayer silicon structures by positron annihilation is feasible, but the technique is best used in conjunction with other methods (such as SIMS) which can aid in the analysis of the positron data.

(3) In order to extend the scope and increase the certainty of our modelling procedure, samples with better known characteristics will be required for comparative study. The interdependency of the diffusion coefficient D_+ and the electric field must be resolved, and a more detailed catalogue of defects and their characteristic S parameters must be established.

(4) The use of growth interruptions is of questionable value since significant defects were introduced by this procedure.

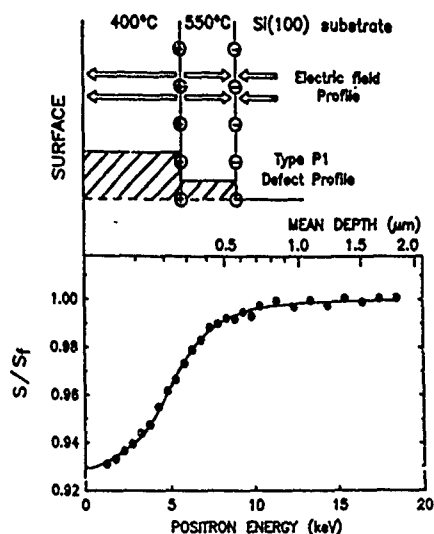


Figure 2: S vs. E data (points) for the second sample of #566B are shown with the fitted curve (solid line). The corresponding model is illustrated above. Arrows indicate the electric field direction; cross hatched boxes indicate relative defect concentrations. Magnitudes are given in table 1.

Table 1: Summary of best fits. C refers to concentration of type P1 defects; E is electric field in V/cm.

Sample	Surface S/S_f	1st overlayer		2nd overlayer	
		C	E	C	E
565-1	0.941	5e-6	2e3		
565-2	0.942	5e-6	1e3		
566A-1	0.969	1.8e-5	1e3		
566A-2	0.931	1.3e-5	1e3		
566B-1	0.940	2e-5	1.2e4	5e-5	2e4
566B-2	0.931	2e-5	1.2e4	5e-5	2.5e4

ACKNOWLEDGEMENTS

Thanks are due to M.Denhoff for growing the samples, S.Rolfe for SIMS, S.Kechang for eCV and J.McCaffrey for XTEM. The assistance of R.W.Hunt is also gratefully acknowledged.

REFERENCES

1. J.P.Noel, J.E.Greene, N.L.Rowell, S.Kechang and D.C.Houghton, Appl. Phys. Lett. 55, 1525 (1989).
2. E.C.Sidebotham, A.R.Peaker, B.Hamilton, M.Hopkinson, R.Houghton, G.Patel, T.E.Whall and E.H.C.Parker in Silicon Molecular Beam Epitaxy II, edited by J.C.Bean and L.J.Schowalter, (Electrochemical Society, Pennington N.J., 1988) pg.355.
3. P.J.Schultz, K.G.Lynn, Rev. Mod. Phys., 60, 701 (1988).
4. E.Tandberg, P.J.Schultz, G.C.Aers and T.E.Jackman, Can. J. Phys. 67, 275-282 (1989).
5. P.J.Schultz, E.Tandberg, K.G.Lynn, Bent Neilson, T.E.Jackman, M.W.Denhoff and G.C.Aers, Phys. Rev. Lett. 61, 187 (1988).
6. T.E.Jackman, G.C.Aers, M.W.Denhoff and P.J.Schultz, Appl. Phys. A49, 335-339 (1989).
7. P.J.Schultz, Nuc. Inst. Meth. B30, 94 (1988).
8. S.Valkealahti and R.M.Nieminen, Appl. Phys A 35, 95 (1984).
9. W.Fuhs, U.Holzhauser and F.W.Richter, Appl. Phys. 22, 415 (1980).
10. R.Würschum, W.Bauer, K.Maier, J.Major, A.Seeger, H.Stoll, H.-D.Carstenjen, W.Decker, J.Diehl and H.-E.Schaefer, in Positron Annihilation, edited by L.Dorikens-Vanpraet, M.Dorikens and D.Segers (World Scientific Publishing, Singapore, 1989) pp.671-673; Motoko-kwete, D.Segers, M.Dorikens, L.Dorikens-Vanpraet, P.Claufs and I.Lemahieu, ibid., pp.687-689.
11. Th.Wichert, M.L.Swanson and A.F.Quenneville, Phys. Rev. Lett. 57, 1757 (1986).
12. K.C.Pandey, A.Erbil, G.S.Cargill III, R.F.Boehme and D.Vanderbilt, Phys. Rev. Lett. 61, 1282 (1988).
13. T.E.Jackman, D.C.Houghton, J.A.Jackman, M.W.Denhoff, S.Kechang, J.McCaffrey and A.Rockett, J. Appl. Phys. 66, 1984 (1989).
14. D.J.Robbins, A.J.Pidduck, J.L.Glasper and J.M.Young, Appl. Phys. Lett. 55, 1229 (1989) and references therein.

A HVEM STUDY OF THE ELECTRON IRRADIATED DEFECTS IN NITROGEN DOPED FZ-Si SINGLE CRYSTAL

Gao Yuzun* and T. Takeyama**

*General Research Institute for Non-Ferrous Metals, Beijing,
100088 China;

**HVEM Lab, Hokkaido University, Sapporo, Hokkaido, Japan

ABSTRACT

High voltage transmission electron microscope (JEM-1000) has been used to investigate the electron irradiated defects in p-type FZ-Si and nitrogen doped p-type FZ-Si. It was found that when the irradiated conditions were the same, the irradiated defects were easier to be produced in the FZ-Si than in nitrogen doped FZ-Si in the temperature range 573-773 K. The defect density was higher in the former. The migration energy of the vacancies in the temperature range 573-773 K was 0.34 and 0.58 eV for FZ-Si and nitrogen doped FZ-Si respectively. It seems to indicate that there was some interaction between vacancies and nitrogen atoms in the nitrogen doped FZ-Si. The results proved that the nitrogen doped FZ-Si has excellent property against electron irradiation.

INTRODUCTION

The nitrogen doped FZ-Si single crystal has excellent strength properties against thermo-mechanical deformation (1). The X ray topograph technique has been used to investigate the defects in FZ-Si single crystal. It was pointed out there was interaction between nitrogen atoms and the defects in Si. Nitrogen affected the electric properties of Si such as the resistivity and the lifetime. Tajima (2) has suggested that nitrogen and vacancies in Si matrix can form deep level defects. But the interaction between nitrogen and the point defects in Si is still not very clear.

In the present work, high voltage transmission electron microscope (JEM-1000) has been used to investigate the electron irradiated defects in p-type (111) FZ-Si and nitrogen doped p-type (111) FZ-Si. The difference of irradiation behaviour of the two type of Si under the same irradiated condition helped us to know the interaction between nitrogen and the point defects.

Experimental

HVEM (JEM-1000) was used to investigate electron irradiated defects in Si. The specimens were p-type (111) FZ-Si and nitrogen doped p-type (111) FZ-Si. The concentration of nitrogen in the latter was 1×10^{15} at/cm³. The specimens were mechanically polished and chemically etched to films with the thickness about 1000 nm.

EM specimens were electron irradiated in HVEM at 573, 623, 673 and 723 K respectively. The specimens were irradiated in the HVEM at 1000 kV with the dose of 0.1 dpa/min.

Results

The electron irradiated defects were easier to be produced in the FZ-Si than in nitrogen doped FZ-Si in the temperature range 573-623 K. When the irradiation temperature was 573 K, the bar-like defects have been observed only with the irradiated time 1 min in the FZ-Si. The defects density was $7 \times 10^9/\text{cm}^2$ at 573 K, 2 min. However there weren't any irradiated defects in nitrogen doped FZ-Si at 573 K, 8 min. The bar-like defects grew along $\langle 110 \rangle$ directions of Si matrix. The EM image of bar-like defects disappeared when the defect was parallel to the direction of diffraction vector at the two beam condition. The defects in the two type of Si is shown in Fig.1a and 1b.

The irradiated defects at 623 K were bar-like defects and dislocation loops. The defect density was $3 \times 10^9/\text{cm}^2$ in FZ-Si at 623 K, 2 min. But there weren't any defects at 623 K, 7 min in nitrogen doped FZ-Si. The relation between defect density and the irradiated time is shown in Fig.2. The irradiated defects at 623 K is shown in Fig.3.

The irradiated defects were formed rapidly at 673 K in the two kinds of Si. Besides the bar-like defects, the irradiated defects were dislocation loops and stacking faults. Some of the bar-like defects became to dislocation loops and stacking faults rapidly. The defect density was higher in the FZ-Si than in the nitrogen doped FZ-Si at the same irradiated condition. The dislocation loops and stacking faults were along $\langle 110 \rangle$ directions and lying on $\{113\}$ planes in the two kinds of Si. The electron irradiated defects at 673 K is shown in Fig.4 a and b.

The migration energy of vacancies was calculated from the slope of the growth speed of bar-like defects versus the irradiated temperature in the temperature range 573-773 K. The migration energy of vacancy was 0.34 and 0.58 eV for the FZ-Si and nitrogen doped FZ-Si respectively.

Discussion

Although the type of the irradiated defects was the same in two kinds of Si single crystals, the electron irradiated defects were easier to be produced in FZ-Si than in nitrogen doped FZ-Si. The incubation time of irradiated defects in nitrogen doped FZ-Si is longer than in FZ-Si.

The formation of the irradiated defects is affected by many factors such as other impurities, the defects in the Si matrix. There were some swirl defects in the Si matrix, but the density of the swirl defects was very low. We didn't find any swirl defects in the irradiated areas. The influence of the surface on the formation of the irradiated defects is important. We should do some experiment about the depth distribution of the irradiated defects.

Conclusions

1. The electron irradiated defects were bar-like defects along $\langle 110 \rangle$ directions, dislocation loops and stacking faults on $\{113\}$ planes in the two kinds of Si.
2. When the irradiated conditions were the same, the irradiated defects were easier to be produced in the FZ-Si than in nitrogen doped FZ-Si in the temperature range 573-773 K.
3. The migration energy of vacancies in the temperature range 573-773 K was 0.34 and 0.58 eV for FZ-Si and nitrogen doped FZ-Si respectively. It seems to indicate that there was some

interaction between vacancies and nitrogen atoms in the nitrogen doped FZ-Si. The results have clearly proved that the nitrogen doped FZ-Si has excellent property against electron irradiation.

Reference

- (1) K.Sumino, et al., J.Appl.Phys.54 (1983), 5016
- (2) M. Tajima, et al., Jpn.Appl.20(1981), L423

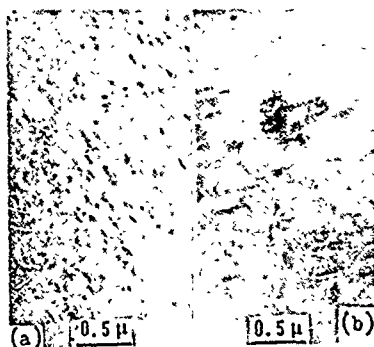


Fig.1. Electron irradiated defects at 573 K, (a) nitrogen doped FZ-Si irradiated 15 min (b) FZ-Si irradiated 4 min.

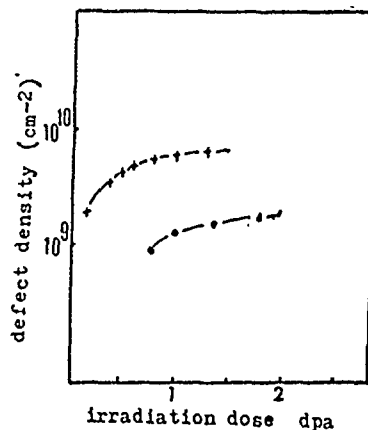


Fig.2. The relation between defects density and the dose at 623 K.

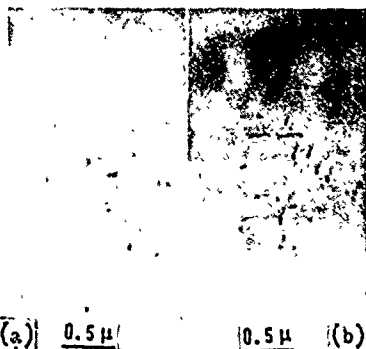


Fig.3. Electron irradiated defects at 623 K, (a) nitrogen doped FZ-Si irradiated 10 min (b) FZ-Si irradiated 2 min.

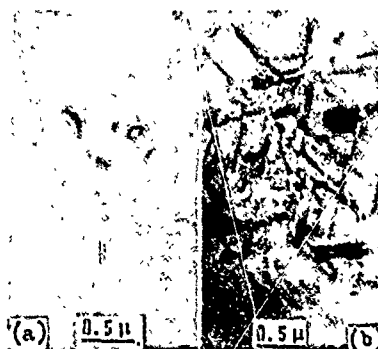


Fig.4. Electron irradiated defects at 673 K, (a) nitrogen doped FZ-Si irradiated 4 min (b) FZ-Si irradiated 3.5 min

MOLECULAR DYNAMICS STUDIES OF DISLOCATIONS IN SI

M.S. DUESBERY*, D.J. MICHEL** AND B. JOOS***

*GeoCenters Inc., Fort Washington, MD 20744

**Naval Research Laboratory, Washington, D.C. 20375

***Ottawa-Carleton Institute for Physics, University of Ottawa
Campus, Ottawa, Ontario, Canada K1N 9B4

ABSTRACT

The mobility of dislocations in a model Silicon lattice is examined at an atomistic level using molecular dynamics. Straight and double-kinked 30° and 90° partial dislocation glide-set dipoles are modelled in a strain-free environment: reconstruction and anti-phase defects are found to be present for 30° partial dislocations. The effects of applied shear strains and of temperatures up to the melting point are considered.

INTRODUCTION

Plasticity in Silicon is typical of elemental and many compound covalent materials, in that dislocation mobility is highly anisotropic and extremely sensitive to dopants, point defects and impurities [1]. Experimental EPR and DLTS [1] and theoretical [2] evidence suggests that this may be due to strong coupling of the dislocation core to the electronic structure, via deep levels localized either along the dislocation line or at secondary defects, such as kinks [3] or anti-phase defects (APDs) [4]. Therefore it is unlikely that any theoretical treatment which does not allow for electron redistribution will provide a completely successful description of the core. Nevertheless, the computational load implicit in a self-consistent electron-ion calculation is sufficiently large that it is worthwhile to pursue the simpler avenue of pure ionic interactions, if only to establish bounds and identify states which merit further examination.

The present paper will be concerned only with mechanical properties, specifically the dislocation mobility, using the valence force field potential developed by Stillinger and Weber [5]. Similar work, with emphasis on the static core energy, has been performed by Nandedkar and Narayan [6,7]; Heggie and Jones [8] have considered static double kinks. Other calculations which place more emphasis on the electronic structure are referenced elsewhere [1,2,9].

METHODOLOGY

The Stillinger-Weber potential [5] defines the total energy E of a covalent solid by an expression of the form

$$E = \epsilon \left\{ \sum f_2(|r_{ij}|) + \lambda \sum f_3(|r_{ij}|, |r_{ik}|, \theta_{jik}) \right\} \quad (1)$$

in which r_{ij} is the vector joining ions i and j , θ_{jik} is the angle between the vectors r_{ij} , r_{ik} and the summations are assumed to run over all enclosed indices. The parameter ϵ normalizes the potential and λ specifies the strength of the angular term. Details of the functional forms of f_2 and f_3 , and of the Si parametrization, are contained in [5].

An advantage of the form (1) is that the strength of the angular term can be varied simply by changing λ . For $\lambda = 0$, the potential reduces to a central pair form. In this limit the diamond cubic lattice is not stable, of course, but for values of λ down to $\lambda = 0.1\lambda_0$, where λ_0 is the value appropriate for Si [5], the diamond cubic structure has lower energy than the competing face-centered cubic structure. Therefore it should be possible in principle to examine the change in core behavior from quasi-metallic forces ($\lambda \ll \lambda_0$) to Si-strength covalent forces ($\lambda = \lambda_0$).

Calculations have been performed for dipoles formed from 30° and 90° glide-set partial dislocations with an arbitrarily chosen separation of $\sqrt{6}a$, where a is the lattice constant, using periodic boundary conditions. Straight dipoles within a periodic cell of dimensions $9\sqrt{3}/2a \times 5\sqrt{3}a$ normal to and a single repeat distance of $a/\sqrt{2}$ parallel to the dislocation line have been considered, together with double-kinked dipoles in periodic cells of size $5\sqrt{3}/2a \times 3\sqrt{3}a$ normal to and $2\sqrt{2}a$ parallel to the dislocation line. In all cases the starting solutions were those prescribed by linear anisotropic elasticity.

Standard constant volume molecular dynamics methods have been used, for temperatures up to the melting point. Time intervals of 1psec, with an integration step of 0.5fsec, were used.

RESULTS

Straight Dislocations

In agreement with earlier calculations [2], little positional relaxation is observed in the core region. Without any externally applied stress, the partials experience an attractive stress $\sim \mu/20$ (taking into account the periodic images), where μ is the shear modulus. However, no motion occurs even for applied shear strains of magnitude ± 0.05 , even at temperatures approaching the melting point of $\sim 1400\text{K}$. This places a conservative lower limit on the first-order Peierls stress of $\sim 0.1\mu$; in contrast, similar calculations for metals give values of order $0.01 - 0.03\mu$ at 0K . Calculations for straight dipoles were performed for $\lambda = \lambda_0$ only.

That dislocation core movement is possible within the model was confirmed by displacing the cores from their symmetrical low-energy sites by $0.25a$; relaxation to the equilibrium sites took place.

Kinked Dislocations

Full three-dimensional calculations are more representative of Si dislocation structure because in this case the model permits bond reconstruction. Figs. 1a and 1b show slip plane projections of double-kinked dipole structures for 30° and 90° partials, respectively, calculated for $\lambda = \lambda_0$ at a temperature of 500K . In each case the atoms in the planes immediately above and below the slip plane are shown, as open and filled circles, respectively. Bonds stretched by less than 20% are indicated as lines joining the bonded atoms. Atoms with dangling bonds are shown as open and filled squares, rather than circles. The dislocation lines pertaining to the starting solutions are drawn in with dashed lines.

For the 30° partial dislocation dipole (fig. 1a), spontaneous reconstruction occurs for bonds within the core and parallel to the dislocation line at the lowest temperature considered (350K). This

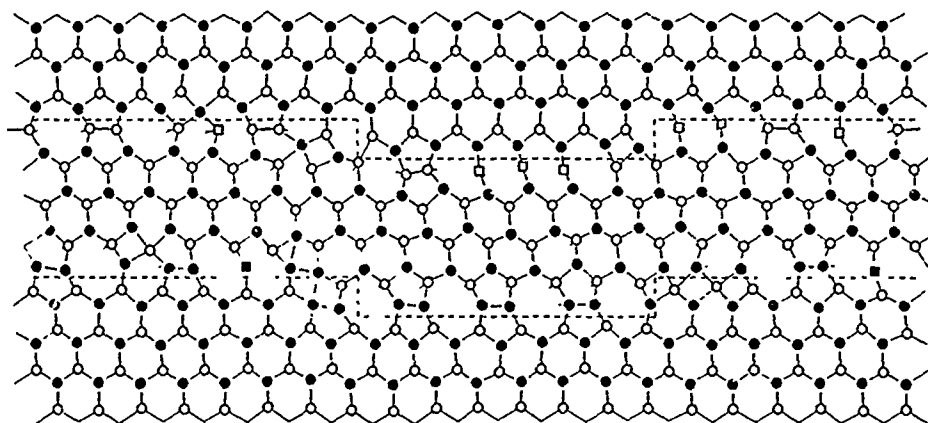
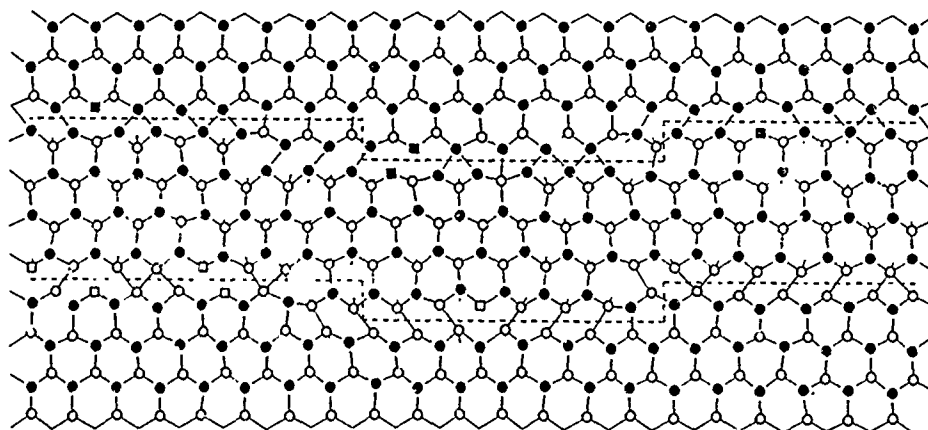
**a****b**

Fig. 1

Atoms immediately above (open circles) and below (closed circles) the slip plane of a double-kinked partial dislocation dipole. The dislocations are shown as dashed lines. 30° (a) and 90° (b) dipoles are shown.

can be seen in fig. 1a, which also shows the presence of APDs. These latter defects exchange quite readily with reconstructed bonds, especially at higher temperatures.

Assuming that the kinks can be treated as short segments of infinite dislocation lines, the attractive stress acting between them is of order 0.01μ . Additional stresses of up to $\pm 0.05\mu$ have also been superimposed. In no case has any kink motion been observed.

The 90° partial dislocation dipoles (fig. 1b) reconstruct also, but less strongly than the 30° partials. No kink motion has been detected for this case, as for the 30° dipoles above.

The same result has been found for reduced angular bond strengths down to $\lambda = 0.75\lambda_0$; below this level, the diamond cubic structure becomes unstable in the vicinity of the dislocation core.

DISCUSSION

The calculations reported above cover only rather small atomistic models and have been performed only for partial dislocation dipoles, rather than true glide dipoles. Nevertheless, it is considered significant that no dislocation or kink motion has been observed even in the most extreme cases of applied stress and elevated temperature. Weakening of the angular bonding leads to local instability of the structure before motion takes place, suggesting that the same factors which stabilize the diamond cubic structure (i.e. the covalent bonding) militate against dislocation motion.

The conclusion pointed to by these results is that valence force-field potentials do not provide an acceptable model of dislocation mobility, and that it is necessary to allow for electron redistribution (change in effective bond strength).

REFERENCES

1. H. Alexander, Dislocations in Solids, edited by F.R.N. Nabarro, vol. 7, (North Holland, New York, 1986), p115.
2. S. Marklund, J. de Physique, 44, C4-25, (1983).
3. P.B. Hirsch, J. de Physique, 40, C6-117, (1979).
4. R. Jones, Phil. Mag., B42, 413, (1980).
5. F.H. Stillinger and T.A. Weber, Phys. Rev. B31, 5262 (1985).
6. A.S. Nandedkar and J. Narayan, Phil. Mag., 56, 625, (1987).
7. A.S. Nandedkar and J. Narayan, Dislocations and Interfaces in Semiconductors, (TMS, Warrendale, 1988) p43.
8. M. Heggie and R. Jones, Intl. Conference on Microscopy of Semiconducting Materials, Oxford, 1987, (Institute of Physics Conference Series 87, London, 1987) p367.
9. M.S. Duesbery and G.Y. Richardson, CRC Critical Reviews in Materials Science, 1990, to be published.

A TEM INVESTIGATION OF SECONDARY DISLOCATIONS IN GRAIN BOUNDARIES IN GERMANIUM

M. GRIESS, M. SEIBT AND H.J. MÖLLER*

IV. Physikalisches Institut, University of Göttingen, 3400 Göttingen, FRG

* Department of Materials Science and Engineering, Case Western Reserve University, Cleveland, Ohio 44106, USA

ABSTRACT

Germanium bicrystals containing dissociated low energy grain boundaries with a common [011] tilt axis were studied. The dislocation structure of a grain boundary with a misorientation of about 28° has been investigated in detail and could be interpreted as a near-coincidence $\Sigma 27$ - tilt grain boundary. Both conventional and high-resolution techniques were applied to analyze the Burgers vectors of the secondary dislocation network. In all cases non - primitive Burgers vectors were observed. The comparison with previous results indicates that the Burgers vectors of the dislocation network may depend on the degree of misorientation of the bicrystal.

INTRODUCTION

The electronic properties of polycrystalline semiconductors are to a great extent determined by the energy levels in the band gap which are introduced by grain boundaries. Structural features like dislocations, steps or precipitates have been related to the electrical activity of the grain boundaries [1-3]. Since the complexity of random grain boundaries hampers their investigation coincidence and near-coincidence grain boundaries in elemental semiconductors have been mainly investigated so far [4]. Of particular importance are dislocations in grain boundaries which seem to introduce not only additional deep levels [5] but can also be attractive sites for segregating impurities [6]. It is therefore desirable to obtain more insight into the structures of secondary grain boundary dislocations. This paper presents a structural investigation of a near - coincidence [011] tilt grain boundary in germanium. The network of the secondary dislocations could be partly analyzed by conventional and high resolution TEM. The problems connected with the analysis of complex dislocation networks in grain boundaries will be discussed.

EXPERIMENTAL PROCEDURE

Bicrystals were grown by the two seed Czochralski technique from high purity germanium. The [011] - oriented seed crystals were rotated around the common [011] axis by about 42° to produce a symmetric near - coincidence $\Sigma 9$ tilt grain boundary. This angle is about 3° off the exact $\Sigma 9$ coincidence orientation at 38.94° . The growth often resulted in a dissociation of the near - $\Sigma 9$ grain boundary into a pure $\Sigma 3$ twin boundary and a grain boundary with a misorientation of approximately 28° which lies between a $\Sigma 19$ and a $\Sigma 27$ coincidence orientation. It was this grain boundary that was used for the further analysis. The deviation of the two grains from the coincidence orientations which had to be measured very accurately was determined in the TEM by measuring the splitting of corresponding diffraction spots in both grains and the shift of corresponding Kikuchi lines. Both methods yielded similar results with an accuracy of 0.1° .

RESULTS OF THE CONVENTIONAL TEM ANALYSIS

In general the grain boundary planes were not planar but contained facets and steps at irregular spacings. Both light optical and TEM investigations showed that the grain boundary plane was approximately symmetric to both grains and the orientation on average close to a $(25\bar{5})$ plane which is the symmetric low energy $\Sigma 27$ grain boundary plane. The symmetric $(13\bar{3})$ plane of the $\Sigma 19$ grain boundary is inclined to the it by 2.53° only which makes it impossible at this point to distinguish between the two grain boundary orientations. The analysis was always carried out

on the macroscopically straight sections of the grain boundaries. A TEM dark field image of the grain boundary plane which shows the complete dislocation network is presented in Fig. 1. Four different sets of dislocations can be distinguished. First a rather irregular set of dislocations running at an average angle of 5° to the $[011]$ direction and with a wide mean spacing between 40 - 400 nm. The different image contrast for various diffraction conditions indicates two different types of dislocations which shall be denoted by 1a and 1b. Furthermore one can observe a second set 2 aligned approximately to the $[10\bar{5}1]$ direction with an average spacing of 160 nm and a third set 3 aligned to the $[5\bar{9}7]$ direction with an average spacing of 7.9 nm, respectively.

It is assumed in the following that all dislocations observed here are related to the angular deviation from a coincidence orientation and are part of the equilibrium structure for this particular misorientation. Since the misorientation of the two grains is such that either the structure of the $\Sigma 27$ (at $\theta = 31.59^\circ$) or the $\Sigma 19$ (at $\theta = 26.53^\circ$) coincidence grain boundary is maintained the analysis had to take into account both possibilities. It turns out, however, that a better agreement can be obtained if one assumes that the Burgers vectors belong to the $\Sigma 27$ - DSC lattice. If we refer to the conventional diamond cubic lattice of germanium (a lattice constant) the basis vectors defining the body-centered orthorhombic unit cell of the $\Sigma 27$ - DSC lattice are given by

$$d_1 = (a/54) [\bar{2} \bar{5} 5] \quad d_2 = (a/27) [5 \bar{1} 1] \quad d_3 = (a/54) [\bar{1} 11 16] = (1/2) \{d'_3 + d_1\}$$

with the common direction $d'_3 = (a/2) [011]$ and d_2 in the grain boundary plane. The unit cell of the CSL is parallel to d_1, d_2, d'_3 . The experiments yielded a main tilt component around the $[011]$ axis $\Delta\theta_3 = -3.2^\circ$ and a second tilt component around the $[5\bar{1}1]$ axis $\Delta\theta_2 = 0.8^\circ$. In addition there was a twist component around the $[\bar{2}55]$ axis normal to the plane by $\Delta\theta_1 = 0.4^\circ$. The experimentally observed tilt deviations mean that the actual tilt axis $p = [p_1 p_2 p_3]$ for the two grains differs from the $[011]$ direction. The components of p and the tilt angle $\Delta\theta_{\text{ult}}$ for this common rotation can be approximated for small rotation angles by

$$\Delta\theta_{\text{ult}} \approx \{ (\Delta\theta_2)^2 + (\Delta\theta_3)^2 \}^{1/2} \quad p_1 \approx 0 \quad p_2 \approx \Delta\theta_2 / \Delta\theta_{\text{ult}} \quad p_3 \approx \Delta\theta_3 / \Delta\theta_{\text{ult}}$$

(p is defined with respect to the CSL unit cell) The rotation axis p lies approximately in the grain boundary plane and the angle α_e between $[011]$ and p is given by $\alpha_e = \arctan(\Delta\theta_2 / \Delta\theta_3)$. The results for the angles are $\Delta\theta_{\text{ult}} = -3.3^\circ$ and $\alpha_e = 14^\circ \pm 2^\circ$.



Fig. 1 TEM dark field image of the dislocation network in a near - $\Sigma 27$ grain boundary.

The compensation of the tilt deviation $\Delta\theta_{\text{tilt}}$ requires a set of dislocations with an edge component lying along the direction of p . Since this component is the largest angular deviation we assume that the dislocations with the narrowest spacing - set 3 - compensate the deviation, although the observed line direction is inclined to the $[011]$ direction by an angle of about 25° which does not quite agree with the direction of p . The difference will be explained later by the fact that a second set of edge dislocations (1b) running inclined to the first one also contributes to the tilt deviation. The observed twist component $\Delta\theta_1$ has to be compensated by a network of screw or near-screw dislocations which will turn out to be the remaining dislocations of set 2 and set 1a.

The edge component of the Burgers vector b_e of set 3 perpendicular to the grain boundary plane (parallel d_1) can be related to the spacing D by $b_e = D / \Delta\theta_{\text{tilt}}$. One obtains for $b_e = 0.43 \pm 0.03$ nm and within the margin of errors $b_e = 6 d_1$. The same analysis can be carried out for the screw component b_s of the set 2 dislocations and one obtains $b_s = 1.1 \pm 0.05$ nm. The dislocations of this set are aligned in a direction which is rotated in the grain boundary plane anticlockwise relative to $[011]$ by an angle of $\beta_s = 70^\circ \pm 5^\circ$. Assuming pure screw dislocations the possible Burgers vectors for the set 2 can be $b_s = n d_2 + d_3$ ($n = 9 - 11$) within the error margin. In the following it is assumed that the shortest Burgers vector ($n=9$) is the most likely one.

The conventional approach to the determination of the Burgers vectors of dislocations by TEM is to apply the extinction criterion. In the case of secondary dislocations in high Σ -grain boundary there is in general a lack of low-index reflections common to both grains so that usually only the reflections of one grain can be strongly excited and used for the analysis. As has been shown recently by computer simulations [7] an analysis utilizing the extinction criterion does not give unambiguous results. However, the simulations have also shown that one can obtain some information on the dislocation type if one analyzes the asymmetry and intensity of the dislocation contrast for various excitation conditions. The complete analysis carried out here will be given in a following paper but the results can be summarized as follows.

The change of contrast of the set 3 dislocations is consistent with the major edge component $b_e = 6 d_1$ normal to the grain boundary plane that has been determined earlier; it also shows an edge component for set 1b. The observed contrasts for the other dislocations (set 1a, 2) are in agreement with a major screw component for both sets. An additional edge component mainly in the direction of d_2 is required for the Burgers vector of set 1a lying along $[011]$.

HIGH RESOLUTION TEM RESULTS

The previous discussion has shown that the combination of conventional TEM Burgers vector analysis and DSC lattice theory does not allow to determine the character of the observed dislocation network completely. Therefore it becomes necessary to apply an additional method which may be suitable to supplement the previous results. As has been shown recently [4,8] high resolution electron microscopy can be used to determine the Burgers vectors of secondary dislocations. The method uses the fact that a secondary dislocation in a grain boundary with a Burgers vector b chosen from the DSC lattice is connected with a displacement x of the CSL and O-lattice by the following equation [9]

$$b = T * x \quad \text{with} \quad T = I - A^{-1}$$

where I is the identity matrix and A the rotation matrix describing the geometrical relationship between lattice 1 and 2 (here for the $\Sigma 27$ or $\Sigma 19$ misorientation). Instead of b one can also determine x and calculate b from this equation. The advantage is in cases of complex grain boundary structures where it is often difficult to locate exactly the position of the secondary dislocations and distinguish them from the undisturbed structure of the coincidence grain boundary, so that a Burgers circuit analysis becomes impossible. But it may be still possible to determine the shift of the O-lattice due to the presence of dislocations.

Fig. 2 shows a part of the near- $\Sigma 27$ grain boundary in high resolution projected along $[011]$. Typically one could not observe any periodicity which could be related to the periodicity of the $\Sigma 27$ or $\Sigma 19$ grain boundary structure as proposed in [10]. The irregular structure is likely to be caused by the presence of the dislocations in the grain boundary plane which are inclined to the $[011]$ projection at various angles: set 1 by an angle of 5° , set 2 by 70° , and set 3 by 25° .

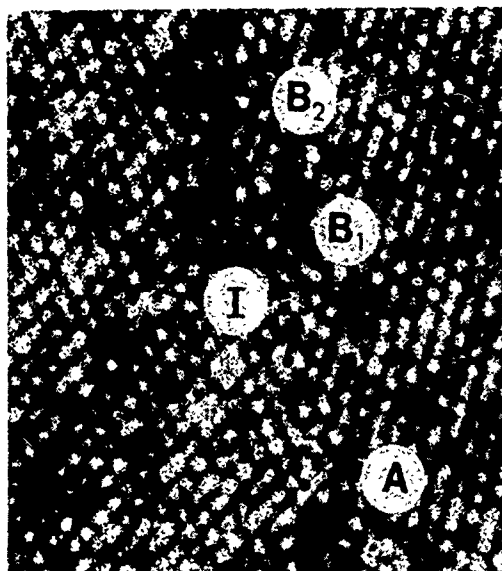


Fig. 2

High resolution image of a section of a near $\Sigma 27$ grain boundary. The trace of the grain boundary is indicated by black dots representing either tunnels or atomic rows of the perfect lattice on both sides of the grain boundary plane. The O - lattice for both lattices is determined first in the lower section of the grain boundary with the left grain being used as the reference lattice. With respect to this grain several shifts of the O - lattice at the points A, B₁ and B₂ can be determined which are related here to the presence of three dislocations lying inclined to the [011] and intersecting the surface somewhere between these points.

The analysis shows that the O - lattice is displaced three times along the imaged section of the grain boundary. The displacement vectors x have been determined at the points A, B₁ and B₂. The displacements x at the points A and B₁ and the corresponding Burgers vector are in agreement with the previously determined Burgers vector for the set 3 dislocations. The displacement x at position B₂ yields $b' = d_1 + 3 d_2$. In view of the contrast experiments which have shown a major component in the direction of d_2 for the set 1a dislocations it is assumed here that b' can be attributed to this set. These dislocations must also have a screw component in the [011] (d'_3) direction which remains undetected in the projection here. The shortest possible vector for set 1a in this direction would be $d'_3 = [011] a/2 = 2 d_3 - d_1$ which gives together with b' a total Burgers vector for the dislocations 1a: $b = 2 d_3 + 3 d_2$

DISCUSSION AND CONCLUSION

It has been shown that the combination of the different techniques allows to determine the Burgers vectors of at least three of the four observed dislocations. The angular tilt and twist deviations are compensated by a set of two edge (set 3, 1b), a screw (2) and a near-screw dislocation (set 1a) with the most likely Burgers vectors

$b = d'_3 + 3 d_2 + d_1$	line direction $\approx d'_3$	(set 1a)
$b = 6 d_1$	line direction $\approx d'_3 (+ 25^\circ)$	(set 3)
$b = d'_3 + 9 d_2$	line direction $\approx d'_3 + 9 d_2$	(set 2)

(with $d'_3 = (a/2) [011]$ the original growth direction of the bicrystal and d_1 normal to the grain boundary plane). For the major edge dislocation (3) the only inconsistency is that these dislocations do not lie exactly along the actual tilt axis p as one should expect. However, the second set (1b) of which the Burgers vector could not be determined but has been shown by the contrast analysis to be predominantly of the edge type, does also contribute to the tilt compensation which may therefore account for the observed deviation of set 3 from the p direction.

An unexpected result is that although the misorientation lies closer to a $\Sigma 19$ coincidence orientation ($\Delta\theta_{\text{tilt}} = 1.9^\circ$ in comparison with $\Delta\theta_{\text{tilt}} = -3.2^\circ$ for the $\Sigma 27$) the Burgers vectors of the edge dislocations (set 3) which are derived both from the dislocation spacing and the displacement of the O - lattice do not agree if they are related to the $\Sigma 19$ coincidence lattice. The reason for this result can be that the energy of the $\Sigma 27$ grain boundary is lower compared to $\Sigma 19$

so that it is energetically more favorable to maintain this structure over a wider range of misorientation angles.

The Burgers vectors found here are all non-primitive DSC vectors. This result seems to contradict a recent investigation of a near - $\Sigma 27$ [11] where only primitive Burgers vectors for the edge and screw dislocations have been found. Since in this case the misorientation $\Delta\theta_{\text{ilt}} = 1.2^\circ$ was smaller, a possible explanation for this discrepancy is that the secondary dislocation structure depends on the misorientation angle and that for larger misorientations longer Burgers vectors become more favorable. Non - primitive Burgers vectors in other grain boundaries have been reported by several authors, too [3,12]. It has also been concluded from an energy calculation [12] carried out for dislocations in a $\Sigma 9$ that non-primitive DSC Burgers vectors may be preferred. This result was explained by noting that a dislocation with a DSC Burgers vector produces a step in the grain boundary plane which depends on the length and the direction of the vector. Since primitive DSC Burgers vectors are frequently associated with large steps which increases the total grain boundary area they may therefore be energetically less favorable. However, so far no general rules seem to exist regarding to which Burgers vectors are selected.

ACKNOWLEDGEMENTS

The authors would like to thank Mr. C. Daum for growing the bicrystals, and Mr. W. Skrotzki for his help in the TEM work and many invaluable discussions. One of the authors (M. Griess) has been partly funded by the Deutsche Forschungsgemeinschaft and acknowledges the support.

REFERENCES

- 1) M. Aucouturier, A. Broniatowski, A. Chari, and J.L. Maurice, in Polycrystalline Semiconductors, ed. by H.J. Möller et.al. (Springer Verlag, Berlin, 1989) p. 64
- 2) X.J. Wu, W. Szielko, and P. Haasen, *J. de Physique* **43**, C1-135 (1982)
- 3) A. Broniatowski, *Phys. Rev B* **36**, 5895 (1987)
- 4) W. Skrotzki, H. Wendt, C. B. Carter, and D.L. Kohlstedt, *Phil. Mag.* **A57**, 383 (1988)
- 5) J. Werner, H. Strunk, *J. Phys.* **43**, C1-89 (1982)
- 6) U. Jendrich and H.J. Möller, *Proc. Int. Conf. on Intergranular and Interphase Boundaries in Mat.*, Paris 1989, in press
- 7) K. Marukawa, and Y. Matsubara, *Trans JIM* **20**, 560 (1979)
- 8) C. d'Anterrosches, and A. Bourret: *J. Phys.* **43**, C1-1 (1982), 783 (1984)
- 9) W. Bollmann, Crystal Defects and Crystalline Interfaces (Springer Publisher, Berlin, 1970)
- 10) M.D. Vaudin, B. Cunningham, and D.G. Ast, *Scripta Met.* **17**, 191 (1983)
- 11) Z. Elgat, PhD Thesis, Cornell University 1985
- 12) H.J. Möller and H.H. Singer, in Defects in Crystals, ed. E. Mizera (World Scientific, 1986) p. 535

AC PHOTOVOLTAIC INSPECTION OF P-N JUNCTIONS HAVING HIGH LEAKAGE CURRENT

N. HONMA, H. SHIMIZU, C. MUNAKATA AND M. OGASAWARA*

Central Research Laboratory, Hitachi Ltd., Kokubunji, Tokyo 185,
Japan

* Device Development Center, Hitachi Ltd., Oume, Tokyo 198,
Japan

ABSTRACT

A focused photon beam chopped at 2 kHz scans p-n junctions in a p-type Si wafer and ac photovoltages are capacitively measured in order to inspect homogeneities of the junctions. It is found that the ac photovoltages are high not only in the junction areas but also in the field oxide regions around the junctions when the junctions are leaky. This indicates that dense positively charged traps exist at the interface between the heavily boron implanted Si substrate and the field oxide layer around the high leakage junction, and that the traps cause the increase in both the junction leakage current and the ac photovoltage.

INTRODUCTION

Junctions are one of the fundamental structures in semiconductor devices, such as MOS memory or solid state image devices. With shrinking geometries and with small charge packet sizes, it is becoming increasingly important to reduce junction leakage in such devices. Junction leakage should be inspected in an early stage of device manufacturing in order to obtain a high yield.

A technique for imaging the distribution of ac photovoltages induced with a chopped photon beam (PB) has been developed [1]. The ac photovoltage (PV) is the product of junction impedance and photocurrent (PC). When leakage current in a junction is large, junction impedance may possibly be reduced. Therefore, the induced PV is expected to decrease. However, measured PV is actually large when junction leakage is high. Experimental results indicate the importance of the peripheral region of the high leakage junction. Here we report that the dense interface traps around a high leakage junction is the cause of the unexpectedly large ac PV as well as the high leakage current.

EXPERIMENTAL

(1) Sample preparation

Many junctions were formed on a p-type (100) Si wafer with a diameter of 127 mm and resistivity of $0.1 \Omega \cdot \text{cm}$. The n-type surface layers were formed by As ion implantation at a dosage of $2 \times 10^{16} \text{ m}^{-2}$. A channel isolation was formed by oxidation of 500 nm thick SiO_2 followed by B ion implantation. The junction depth was $0.2 \mu\text{m}$ and the junction size was $1\text{mm} \times 2\text{mm}$.

(2) Experimental apparatus

A scanning photon microscope (SPM) [2] was used to measure the ac PV distribution in the Si wafer. The SPM has two cathode

ray tubes (CRTs), one provides a blue PB (wavelength $\lambda_p = 450$ nm) and another provides an infrared PB. The maximum viewing size was 150 mm and the PB diameter on a sample wafer was 0.3 mm. The chopping frequency (f) of the PB was 2 kHz. When high resolution was required, a He-Ne laser with wavelength of 633 nm was used as the PB source. The laser beam was modulated at 2 kHz with an acousto-optic modulator. The modulated beam was scanned in the x-y direction using two galvanometer scanners. The induced ac PV in a sample is measured capacitively through the air gap between a transparent electrode and the sample surface. The measured ac PV distribution is stored in an image memory and displayed on a monochrome CRT display.

The leakage current was measured by the conventional technique using a metal probe.

RESULTS

The ac PV image for a Si wafer with junctions is obtained using blue PB from the CRT. Correlation between measured photovoltage ΔV and measured leakage current I_1 on a logarithmic scale is shown in Fig. 1 when bias voltage for leakage current measurement is 0.1 V. The higher I_1 , the greater ac PV.

A different Si wafer, with gettering ability, was also investigated using the SPM. This wafer also had junctions formed in the same way. These junctions did not exhibit any abnormal leakage current. This suggests that the high leakage observed in the junctions on the ordinary wafer is caused by some kinds of contamination.

A more detailed study was made using the high resolution SPM. Figure 2 (a) shows a photograph of the high leakage junction A and a neighboring normal junction B, taken with an optical microscope. The two junctions show no difference in contrast, implying that they have the same optical properties. Conversely in Fig. 2 (b), which shows the ac PV image corresponding to the photograph, the brightness in the junction A is high and uniform. The ΔV distribution along a line b-b' in Fig. 2 (b) is shown in Fig. 2 (c). Figures 2 (b) and (c) show that ΔV is large not only in the region of junction A but also in the region surrounding the junction.

Minority carrier lifetime τ_0 for the substrate was measured using the ac photovoltaic method [3]. For junction A, τ_0 was $3.7 \mu s$, compared to shorter than $1 \mu s$ for a normal junction.

DISCUSSION

(1) Variation of surface potential due to interface traps

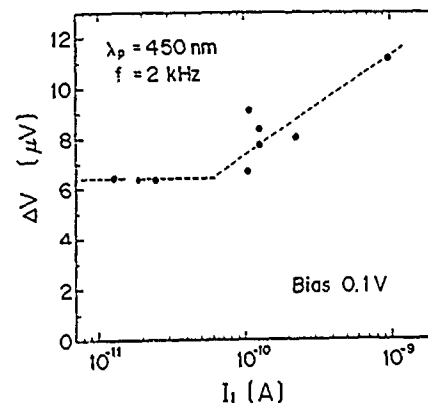


Fig. 1 Correlation between measured photovoltage ΔV and leakage current I_1 of junctions.

Figure 2 (c) shows that ac PV increases in the field oxide

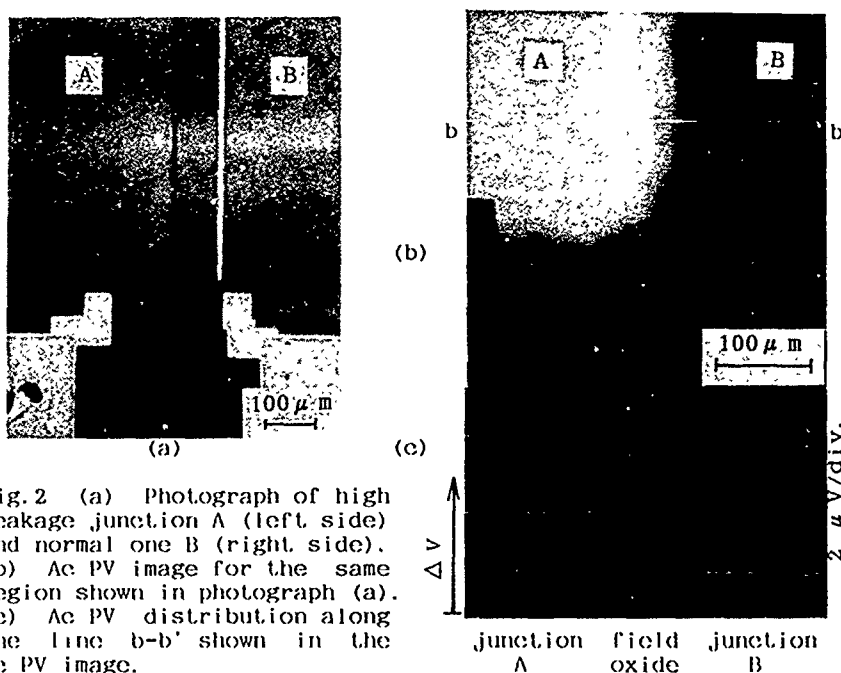


Fig.2 (a) Photograph of high leakage junction A (left side) and normal one B (right side). (b) Ac PV image for the same region shown in photograph (a). (c) Ac PV distribution along the line b-b' shown in the ac PV image.

around a high leakage junction. The large PV at 2 kHz is due to an increase in depletion layer width. As shown in Fig.3 (A), charged traps are considered to be the cause for increasing depletion layer width. It is widely accepted that the generation-recombination current arising from interface traps facing the depletion layer, is one of the causes for high leakage current of a junction [4]. If many interface traps are generated by stress or defects, they become positively charged in the case of depletion condition [5]. Therefore, surface potential increases in vicinity of the junction as shown by the dashed line in Fig.3 (B). This case is very close to a gate-controlled n' p junction [4] to which a positive gate voltage is applied. Thus, the depletion layer width in the peripheral regions widens.

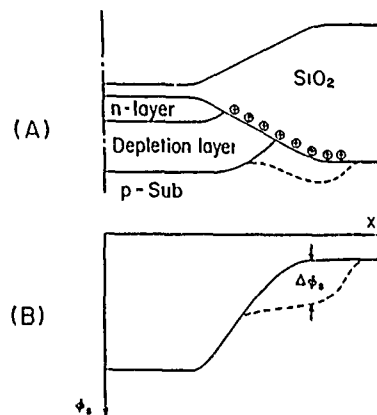


Fig.3 Charge-up effect due to interface traps around the junction. (A) Variation in depletion layer width due to positive charges of the interface traps. (B) Variation of surface potential ϕ_s due to the trap charges.

(2) Generation of photovoltages in high leakage junctions

(2-1) *Peripheral effect*

A measured photovoltage ΔV is given as $\Delta V \propto I_{ph} / (\omega (C_j + C_1))$, where ω is $2\pi f$, I_{ph} is the photocurrent, C_j is a capacitance due to depletion layer for the junction area and C_1 is a capacitance for the peripheral region. When many interface traps, due to defects, have positive charge in the peripheral region of the junction, C_1 becomes small because of the increase in depletion layer width. Therefore, ΔV for a high leakage junction becomes large.

(2-2) *Carrier diffusion effect*

When a junction is irradiated by a PB, minority carriers, generated below the depletion layer, diffuse toward the peripheral region. If they arrive at the depletion layer in the periphery of the junction, they can generate surface photovoltage V_s . This V_s depends on both a minority carrier lifetime τ_0 in the bulk and on the depletion layer width in the periphery of the junction. Since junction A has a longer τ_0 and wider depletion layer width than normal junctions, V_s is larger than that in those junctions. Then, ΔV also becomes large since it is the sum of V_s generated in the peripheral region and a junction photovoltage V_j in the central region.

(3) Photovoltage for H_2 annealed MOS structure

Further experiments were conducted to investigate the cause for high ac PV in high leakage junctions using another set of n'p junctions whose size was 1mm X 1mm. They were annealed in H_2 ambient before the SPM observation. Ac PVs for H_2 annealing at 150 °C (5 minutes) are larger than those for H_2 annealing at 450 °C (5 minutes). This indicates that H_2 annealing at 450 °C reduces ΔV for n'p junctions because the reduction of interface trap density decreases the depletion layer width. Leakage current of a n'p junction annealed in H_2 at 150 °C is one order of magnitude higher than that annealed at 450 °C. This fact supports our model for the increase in ac PV in a high leakage junction.

CONCLUSION

Junction leakage can be inspected nondestructively by the ac photovoltaic method. High leakage junctions exhibit a larger ac photovoltage than normal junctions when the field oxide around the junction is damaged. This is because many interface traps under the damaged oxide in the periphery of the junction in a p-type Si wafer have positive charges which widen the depletion layer. Thus, the wide depletion layer contributes to the increase of the ac photovoltage.

REFERENCES

1. C. Munakata, K. Yagi, T. Warabisako, M. Namba and S. Matubara, Japan. J. Appl. Phys. 21, 624 (1982).
2. K. Kinameri, C. Munakata, N. Honma and H. Shimizu, Scanning Microscopy 2, 1237 (1988).
3. N. Honma, C. Munakata, H. Itoh and T. Warabisako, Japan. J. Appl. Phys. 25, 743 (1986).
4. A.S. Grove, Physics and Technology of Semiconductor Devices, (John Wiley & Sons, New York, 1967) Chap.10.
5. G.A. Scoggan and T.P. Ma, J. Appl. Phys. 48, 294 (1977).

TWINNING STRUCTURE OF {113} DEFECTS IN HIGH-DOSE OXYGEN IMPLANTED SILICON-ON-INSULATOR MATERIAL.

S. Visitserngrakul, J. Barry*, and S. Krause

Department of Chemical, Bio and Material Engineering, Arizona State University, Tempe, AZ 85387

*Electron Microscope Centre, University of Queensland, St. Lucia, Brisbane, Queensland 4067, Australia.

ABSTRACT

Conventional and high resolution electron microscopy (HREM) were used to study the structure of the {113} defects in high-dose oxygen implanted silicon. The defects are created with a density of 10^{11} cm^{-2} below the buried oxide layer in the substrate region. The {113} defects are similar to the ribbon-like defects in bulk silicon. Our HREM observations show that two crystalline phases are present in the defect. Portions of the defects exhibit the original cubic diamond structure which is twinned across {115} planes. The atomic model shows that the {115} interface is a coherent interface with alternating five- and seven-membered rings and no dangling bonds.

INTRODUCTION

Silicon-on-insulator structures can be produced by implantation of a high dose of oxygen to form a buried oxide layer below a thin, top silicon layer - SIMOX (Separation by IMplantation of OXygen). The implantation generates defects not only in the top silicon layer, but also in the silicon substrate beneath the buried oxide layer. It has been previously reported that the defects present in the substrate region of as-implanted SIMOX are {113} defects and stacking faults [1-4]. The {113} defects are very similar in shape to the oxygen-induced ribbon-like defects (RLDs) in the bulk silicon which have been extensively studied in the last decade [5]. Based on computer simulations of high resolution electron microscopy (HREM) images, the {113} defects were initially identified as ribbon of coesite, a high pressure phase of silicon oxide [6,7]. Recently, however, evidence was presented that the defects consist of hexagonal silicon and are thus formed by self-interstitial precipitation [5,8,9]. A proposed nucleation and growth mechanism for the RLD is a pure silicon-interstitial agglomeration as described by Salisbury and Loretto [10] or Tan et al. [11]. More recently, Pirouz et al. [12,13], who had observed the cubic-hexagonal transformation in hot-indented silicon, discussed that hexagonal silicon formation by aggregation of silicon self-interstitials in RLD is unlikely because the hexagonal phase in silicon is not thermodynamically favored. Also, the orientation relationship of $(011)_{\text{Cu}} // (0001)_{\text{hc}}$, $[011]_{\text{Cu}} // [12\bar{1}0]_{\text{hc}}$ is unexpected. It would be preferential to have the more natural orientation relationship of $(111)_{\text{Cu}} // (0001)_{\text{hc}}$, $[1\bar{1}0]_{\text{Cu}} // [11\bar{2}0]_{\text{hc}}$.

In SIMOX, the {113} defects were first discussed by van Ommen et al [1]. They analyzed the diffraction patterns of the substrate region in SIMOX and suggested that the {113} defect is a platelike precipitate of monoclinic silica phase coesite oriented with (010) coesite // (110) silicon. De Veirman et al. [2] also identified {113} defects as coesite by matching with the computed simulations with HREM images. Ravi et al. [4] presented evidence supporting both models. Their HREM images matched well with coesite, but their experimental results showed that the {113} defects are stable up to 850°C in annealed material, suggesting support for the hexagonal silicon phase hypothesis. Hence, the structure of RLDs or {113} defects is still uncertain.

In this paper, we report new HREM observations on {113} defects in SIMOX. It is found that there are two crystalline phases present in the same {113} defect. Besides the possible presence of the hexagonal silicon phase or monoclinic coesite phase, it is possible that some part of the defect can assume the original cubic diamond phase, which can be created through a twin operation across {115} planes. The atomic structure model of the interface will also be discussed.

EXPERIMENTAL

The Si (100) wafers were implanted by a high-current (40 mA) implanter [14], at 575°C, at 200 keV to the dose of $1.8 \times 10^{18} \text{ cm}^{-2}$. They were examined from cross-section samples using a Philips 400T at 120 keV and a JEOL 200CX at 200 keV for high resolution images.

RESULTS AND DISCUSSIONS

The overview of as-implanted SIMOX is shown in Figure 1. The structure consists of three regions: the top silicon layer about 0.3 μm thick, the buried oxide layer about 0.4 μm thick, and the mottled, defect-rich zone below the oxide layer which extends as far as 0.5 μm into the substrate. The interface of the buried oxide and the substrate is not sharp but it appears to have rows of oxide precipitates embedded in a silicon matrix. In the region below, numerous {113} defects and stacking faults are observed. Figure 2 shows this region in greater detail illustrating the elongated zigzag shape of the defects lying in different {113} or {115} planes with a density of 10^{11} cm^{-2} . The defects are 10 to 40 nm long and only few nm wide. Figure 3 shows the atomic structure of the {113} defect in SIMOX. The defect generally lies along a {113} plane and is elongated along the $\langle 011 \rangle$ direction. Some parts of the defect clearly show the crystalline structure with three- or four-layer periodicity. The crystalline structure cannot exist over extended distances along a {113} plane without giving excessive strains. The interfaces between the defect and the matrix, especially the upper interface, are highly distorted because they must accommodate the strain of the defect. The nature of this distortion leads to lattice rotation. When the rotation is not around the beam direction, it will lead to tilts that locally change the imaging conditions, as may be seen from the upper interface of the middle part of the defect. The {111} lattice fringes of the silicon matrix appear along only one direction instead of imaging as cross fringes.

Figure 3b shows an enlargement of the area in the square in Figure 3a. There are two types of crystalline phases in the defect, labelled H and C. It is suggested that the structure of the defect in the region 'C' is twinning across the {115} planes. That is, this part of the {113} defect has assumed the original cubic diamond phase, not a hexagonal or coesite phase. The image of this region shows that a set of the {111} planes in the matrix that are continuous (coherent) with a set of the same {111} planes of the defect, as shown by the traced line on the micrograph. The contrast of the {111} lattice fringes appear evenly in one direction, instead of cross fringes, because of the local tilting mentioned above. Hetherington et al. [15] have shown by HREM image simulation that a 2.0° tilt can change the image of the {111} planes from uniform cross-fringes to an evenly one-direction fringes. The angle between these two sets of planes is 141° and the {115} habit plane bisects them. It has been shown that the {115} interface is a low-index plane in the $\Sigma 9$ coincidence site lattice [11,12]. Figure 4 is a schematic of atomic model for the {115} twinning in the cubic diamond lattice. The model shows that the interface formed by alternating five- and seven-membered rings, identical to the model of Tan et al. [11] for a {113} stacking fault. The absence of dangling bonds shows that this is a coherent interface.

We have observed few other {113} defects that have the same appearance of the {115} twinning. Bourret [5], and Salisbury and Loretto [10] had discussed the instability of the {113} defects during TEM observations. The defects tend to disappear gradually by a reverse phase transformation to the cubic diamond lattice. It is possible that the present {115} twinning is a reverse transformation that occurred at some parts of the defect.

For comparison with experimental HREM images of the region labelled 'H' in Figure 3b, a number of image simulations have been carried out on both hexagonal and coesite phases using the EMS program. Figure 5 shows the schematic atomic structure and simulated images of both structures, for a 200 keV microscope with the electron-optical parameters (e.g. $C_s=1.2 \text{ nm}$) typical of the JEOL 200CX at the optimum defocus of -67 nm. At this value of underfocus, atom pairs appear as dark spots. The experimental images of the 'H' region match well with the hexagonal simulated image, although there is a slight asymmetry of the basal planes in the sense that they are not of equal intensity but have alternate strong and weak contrast. This can be caused by a slight misalignment of the incident beam, or a tilt of the hexagonal crystal only 0.7° from the exact $\langle 011 \rangle$ zone axis [6]. The kinematically forbidden spot of $(001)_{\text{hc}}$ will be strongly excited resulting in a different contrast of the basal planes. However, the experimental images of the {113} defect in SIMOX studied by Ravi et al. [4] match well with the simulated image of

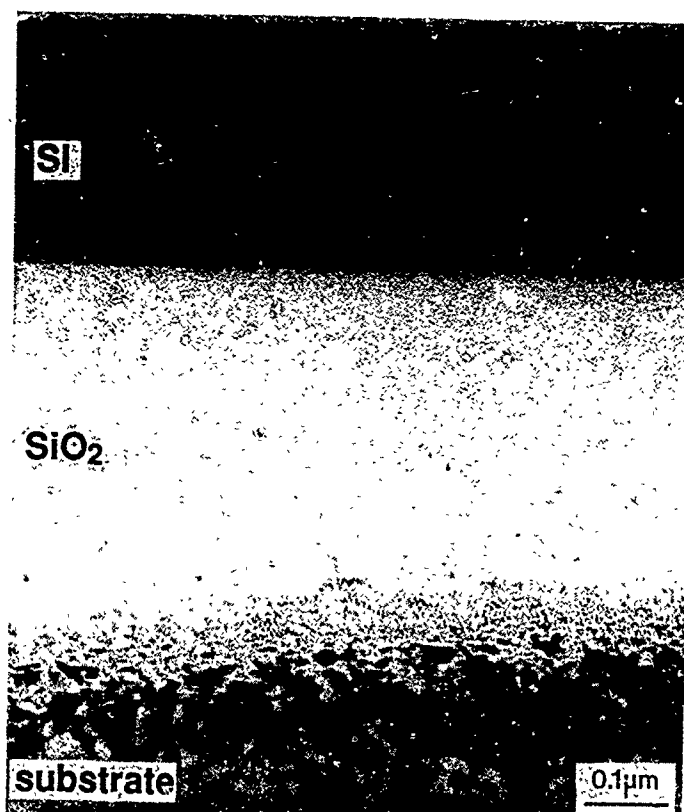


Figure 1. Overview of SIMOX implanted at 575°C, 180 keV, to the dose of $1.8 \times 10^{18} \text{ cm}^{-2}$.

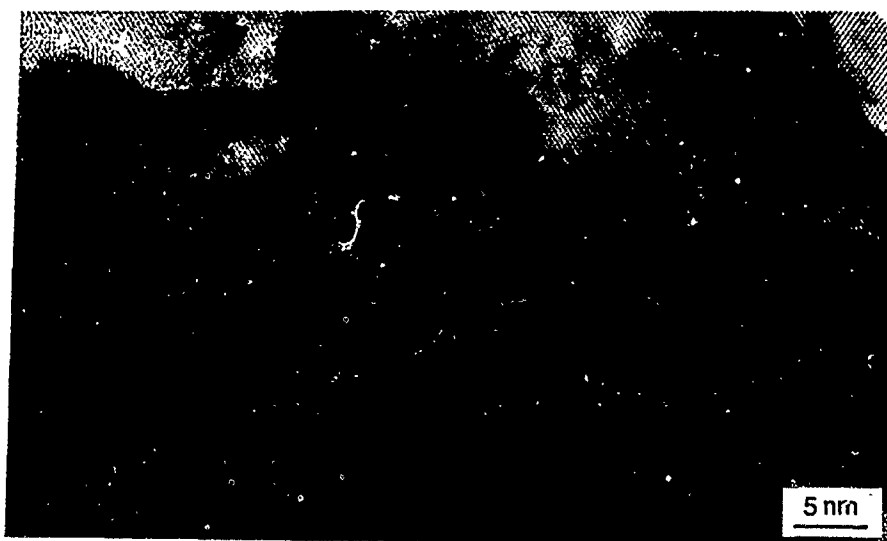


Figure 2. HREM image of the zigzag {113} defects observed below the buried oxide layer in the substrate region.



Figure 3. (a) HREM image of a {113} defect in SIMOX; (b) An enlargement of the portion in the square of (a) showing the atomic structure of the regions "C" and "H".

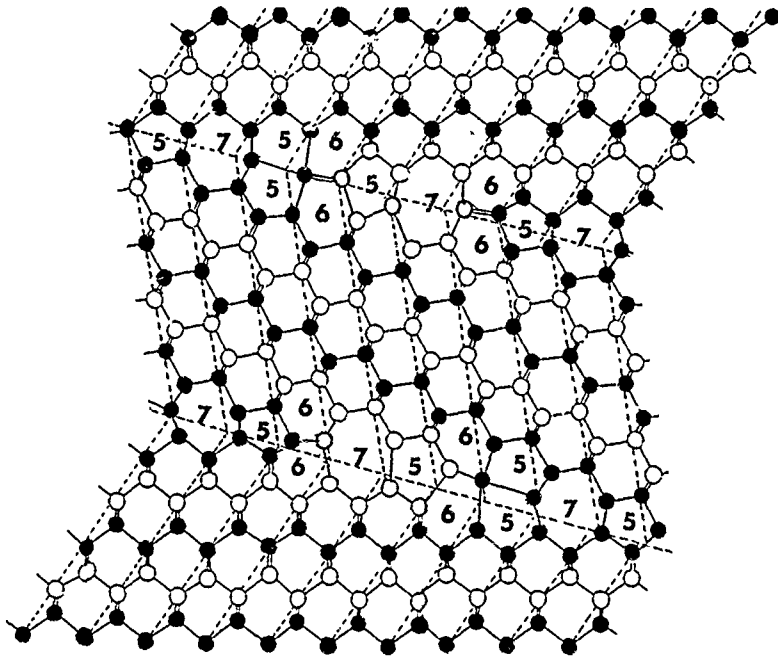


Figure 4. Schematic of atomic model for the $\{115\}$ twinning in cubic diamond lattice.

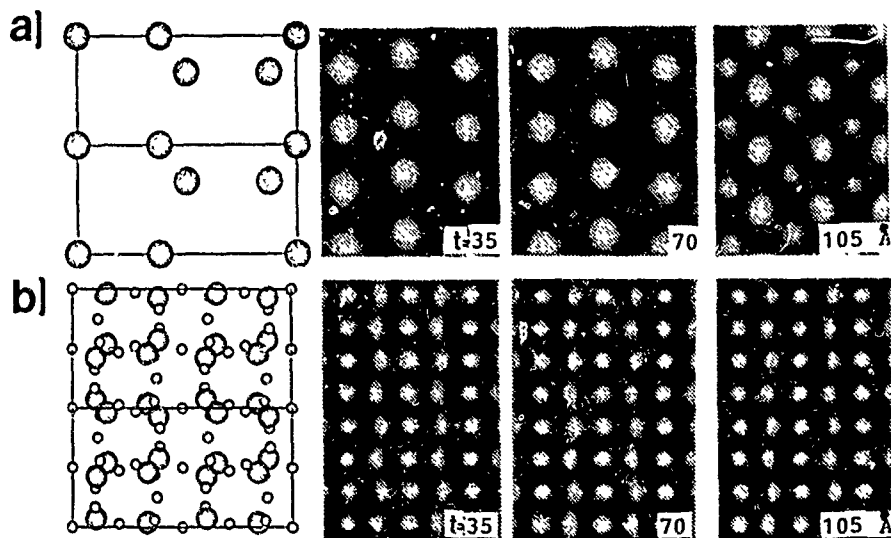


Figure 5. Atomic structure and simulated images of (a) the $\langle 110 \rangle$ hexagonal silicon; (b) the $\langle 100 \rangle$ coesite. The optimum defocus of -67 nm.

coesite. Therefore, it is still not conclusive that the structure of the {113} is hexagonal silicon or coesite or a mixture of the two or more phases.

SUMMARY AND CONCLUSIONS

High-dose oxygen implantation creates a high density of the {113} defects below the buried oxide layer in the substrate region. The {113} defects are similar to the ribbon-like defects in bulk silicon. Our HREM observations show that at least two crystalline phases are present in the defect. Portions of the defect exhibit the original cubic diamond structure as a twin across {115} planes. The atomic model shows that the {115} interface is a coherent interface with alternating five- and seven-membered rings and no dangling bonds.

ACKNOWLEDGEMENTS

We acknowledge staff assistance and facility use in the National Center for High Resolution Electron Microscopy, Arizona State University, supported by national Science Foundation Grant DMR-8611609. Thanks also to B.F. Cordts of the Ibis Technology Corp., Danvers, Massachusetts for providing the SIMOX samples examined in this work, and C.J.D. Hetherington of National Center for Electron Microscopy, Lawrence Berkeley Laboratory for profitable discussions.

REFERENCES

- [1] A.H. van Ommen, B.H. Koek, and M.P.A. Vieggers, *Appl. Phys. Lett.* **49**, 628 (1986).
- [2] A. De Veirman, K. Yallup, J. Van Landuyt, H.E. Maes, and S. Amelinckx, *Inst. Phys. Conf. Ser.* **87**, 403 (1987).
- [3] S. J. Krause, C. O. Jung, T. S. Ravi, S. Wilson, and D. E. Burke in Silicon-on-Insulator and Buried Metals in Semiconductors, edited by J.C. Sturm, C.K. Chen, L. Pfeiffer, P.L.F. Hemment (*Mat. Res. Soc. Proc.* **107**, Pittsburgh, PA 1988) pp 93-104.
- [4] T.S. Ravi, C.O. Jung, D.E. Burke, and S.J. Krause in *Proc. 47th Elect. Mic. Soc. Amer.*, edited G.W. Bailey, San Francisco Press, Inc., (1989) pp 602-603.
- [5] A. Bourret, *Inst. Phys. Conf. Ser.* **87**, 39 (1987).
- [6] A. Bourret, J. Thibault-Desseaux, D.N. Seidman, *J. Appl. Phys.* **55**, 825 (1984).
- [7] H. Bender, *Phys. Stat. Sol. (a)* **86**, 245 (1984).
- [8] M. Reiche and O. Breitenstein, *Phys. Stat. Sol. (a)* **101**, K97 (1987).
- [9] H. Bender and J. Vanhellemont, *Phys. stat. Sol. (a)* **107**, 455 (1988).
- [10] I.G. Salisbury and M.H. Loretto, *Phil. Mag.*, **A39**, 317 (1979).
- [11] T.Y. Tan, H. Foll, and S.M. Hu, *Phil. Mag.* **A44**, 127 (1981).
- [12] P. Pirouz, R. Chaim, and U. Dahmen in Defects in Electronic Materials, edited by M. Stavola, S.J. Pearton, G. Davies (*Mat. Res. Soc. Proc.* **104**, Pittsburgh, PA 1988) p.133.
- [13] P. Pirouz, U. Dahmen, K.H. Westmacott, and R. Chaim, *Acta Metall.* (1989) in press.
- [14] A. Wittkower and M. Guerra, *Nucl. Instr. and Meth.* **B37/38**, 512-517 (1989).
- [15] C.J.D. Hetherington, U. Dahmen, P. Pirouz, and K.H. Westmacott in *Proc. 47th Elect. Mic. Soc. Amer.*, edited G.W. Bailey, San Francisco Press, Inc., (1989) pp 132-133.

STRUCTURAL TRANSITIONS IN TITANIUM/AMORPHOUS-SILICON MULTILAYERS

E. Ma, L.A. Clevenger¹ and C.V. Thompson
 Department of Materials Science and Engineering, Massachusetts Institute of
 Technology, Cambridge, MA 02139

R.R. DeAvillez
 Departamento de Ciencia dos Materiais e Metalurgia, Pontificia Universidade
 Catolica, 22452-Rio de Janeiro, RJ-Brazil

K.N. Tu
 IBM T.J. Watson Research Center, Yorktown Heights, NY 10598

¹ Present address: IBM T.J. Watson Research Center, Yorktown Heights, NY 10598

We report a quantitative investigation of silicidation in Ti/amorphous-Si thin-films using Differential Scanning Calorimetry (DSC), thin-film X-ray diffraction and Cross-sectional Transmission Electron Microscopy (XTEM). Multilayered thin films were used to facilitate calorimetric observation of the heat released or absorbed at many reacting interfaces. It is shown that calorimetric analysis, combined with structural analysis using X-ray diffraction and XTEM, is effective in providing both kinetic and thermodynamic information about interdiffusion reactions in thin films. The present paper describes experimental results for multilayers with an atomic concentration ratio of 1 Ti to 2 Si and modulation periods ranging from 10 to 60 nm. A thin amorphous titanium silicide layer was found to exist between the as-deposited Ti and a-Si layers. Heating the multilayer film caused the amorphous Ti-silicide to grow over a broad temperature range by an exothermic reaction. An endothermic relaxation occurs during the late stage of amorphous silicide growth. Heating to temperatures over 800K causes C49-TiSi₂ to form at the a-silicide/a-Si interface. Temperatures at which all the above structural transitions occur vary with modulation period. Analysis of the DSC data indicates an activation energy of 3.1 eV for the formation of C49-TiSi₂, which is attributed to both the nucleation and the early growth of the silicide. The heat of formation for C49-TiSi₂ from a reaction of a-silicide and a-Si was found to be -30±5KJ/mol. Nucleation appears to be the controlling step in C49-TiSi₂ formation.

INTRODUCTION

Titanium/a-Si thin-film reactions are of importance due to the application of Ti-silicides in integrated circuits [1]. Recent discovery of the growth of a metastable amorphous Ti-silicide has generated further interest in this system [2]. Previous investigations of silicidation processes during thin-film reactions typically rely on analytical tools such as Rutherford Backscattering Spectrometry (RBS), X-ray diffraction, and Transmission Electron Microscopy (TEM). These tools are sensitive only to either compositional changes or structural changes, and generally a large number of separate experiments are required to follow reaction kinetics over a wide temperature range. In our recent work [3-5], it has been demonstrated that Differential Scanning Calorimetry (DSC) is a valuable technique for study of the nucleation and growth of metastable and equilibrium silicides in multilayered thin films. With DSC, which is sensitive to both compositional and structural changes, one can observe all the transitions that occur in a range of temperatures, and simultaneously obtain kinetic and thermodynamic data with one experiment. The present study of Ti/a-Si reactions, with emphasis on the use of calorimetry, is a part of a series of characterizations of thin-film reactions in a number of silicide-forming systems [3-6].

EXPERIMENTAL

For calorimetric analysis, free-standing multilayered thin films were prepared by alternate e-beam evaporation of Ti and Si onto photoresist-coated microscope slides at room temperature in a system with a low 10^{-7} Torr base pressure. Films used in this work consisted of five pairs of Ti and Si layers with various modulation periods, which were designed to yield an overall atomic concentration ratio of 1 Ti to 2 Si. The deposition rates were about 0.8 nm/sec for Ti and 0.3 nm/sec for Si. After deposition, the slides were soaked in acetone to dissolve the photoresist and remove the multilayers. No impurities were detectable in the as-deposited or annealed films when examined using Auger electron spectroscopy [6]. DSC analysis was performed with samples weighing about 2 mg samples and at heating rates from 2.5K/min to 40K/min and in a temperature range from 330 to 900K. After initial heating and data collection, the samples were quenched at 320K/min from 900K back to 330K, and a second run was made without disturbing the sample and with the same heating rate used in the first run. The second DSC trace was used as the baseline and subtracted from the first trace. Analysis of thin-film X-ray diffraction, using a Rigaku diffractometer with a rotating Cu anode, was done for samples annealed in the calorimeter to desired temperatures and quenched at 320K/min back to room temperature for phase identification. Cross-sectional TEM was also used for structural analysis, with multilayer samples deposited on oxidized Si wafers and annealed in a calorimeter to the temperatures of interest. Details of TEM sample preparation have been described elsewhere [6].

RESULTS AND DISCUSSION

In figure 1, we present constant-heating-rate DSC traces for five scan rates of 2.5K/min to 40K/min for multilayers with a fixed modulation period of 30 nm (8.8nm Ti/21.2nm Si). Concentrating on the 20K/min trace, three distinct features can be observed: an increasing exothermic peak below 700K, an endothermic step labeled 1 at about 700K, and an exothermic peak labeled 2 at about 860K. Similar features are observed at other scan rates (Fig. 1) and for other modulation periods shown in Fig. 2, which displays DSC traces for five different modulation periods at a fixed scan rate of 20K/min. To correlate the thermal changes seen in the calorimetric data to structural changes, samples heated to various stages were examined using thin-film X-ray diffraction. The Ti diffraction lines present for the as-deposited sample drop significantly in intensity at point 1, and fade away before peak 2, indicating a progressive reaction consuming Ti. However, no diffraction lines corresponding to a Ti-Si crystalline intermetallic appear up to this point. Clear identification of the C49-TiSi₂ phase was made for samples only after heating to temperatures higher than those of peak 2. The transition from C49-TiSi₂ to C54-TiSi₂ [7] was not observed up to 1000K, the maximum temperature accessible in our calorimeter. For further structural identification, two groups of XTEM samples, with modulation periods of 30 nm and 60 nm respectively, were prepared in the as-deposited state as well as after heating in the calorimeter at 20K/min to various temperatures. The TEM results are consistent with those of X-ray diffraction and give a clear picture of structural evolution. An amorphous silicide layer about 2.5 nm thick is present at the Ti/a-Si interface in the as-deposited sample. Heating to temperatures right before point 1 (670K for the 30nm sample and 750K for the 60nm sample) causes the a-silicide to grow by consuming Ti and Si. Some Ti pure Ti is still left at this point. Further heating to temperatures after the endothermic step but before peak 2 (790K and 810K respectively for the 30nm and 60nm samples) leads to further thickening of the a-silicide. There is no evidence of any new crystalline or amorphous phase formation between points 1 and 2, which rules out a phase transition as a possible explanation for the endothermic step in Figs. 1 and 2. Comparison of TEM pictures for

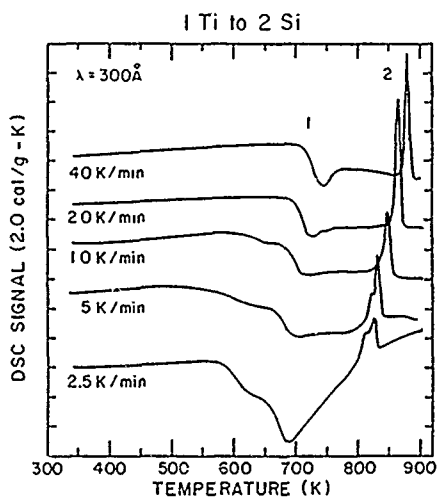


Figure 1

DSC traces for five scan rates for multilayers with an atomic concentration ratio of 1 Ti to 2 Si and a fixed modulation period of 30 nm.

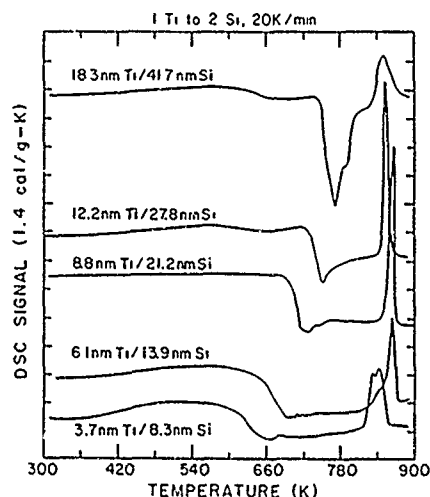


Figure 2

DSC traces for five different modulation periods for multilayers with an atomic concentration ratio of 1 Ti to 2 Si, at a fixed scan rate of 20 K/min.

samples annealed to temperatures at and beyond peak 2 (835 K for the 60 nm sample, 860 K and 890 K for the 30 nm sample) clearly indicate the formation of crystalline TiSi_2 , starting from the a-silicide/a-Si interface. Due to space limitations, the TEM pictures are not shown in this paper. Some of the TEM results can be found in a forthcoming publication [6].

Figure 1 shows that as the heating rate is increased, the endothermic step and exothermic peak shift to higher temperatures. The shift of the exothermic TiSi_2 peak can be related to the activation energy for formation using an analysis originally developed by Kissinger [8] which indicates that:

$$\ln(R/T_p^2) = C - Q/(kT_p)$$

where R is the heating rate, T_p is the peak temperature, C is a constant, k Boltzmann's constant and Q is the activation energy. A Kissinger plot yields a Q value of 3.1 ± 0.1 eV. This value is significantly higher than the 1.8 ± 0.1 eV reported by Hung et al [9]. We note that the Q value we measure here is for the early stage of C49-TiSi_2 formation, to a thickness below 30 nm, and

thus includes both nucleation and initial growth of the silicide, while Hung's value is for diffusion-limited growth only, for TiSi_2 layers over 30 nm thick. We cannot determine an activation energy for the α -silicide growth in these groups of samples, because there is no clear exothermic peak for the α -silicide growth in Fig. 1. The endothermic step begins before all the Ti is consumed to form α -silicide. This endothermic process is tentatively attributed to the relaxation of the α -silicide, as a similar behavior due to homogenization and densification has been observed in α -Si [10].

By integrating the area under peak 2 for about 10 DSC traces, some of which are shown in Fig. 2, the heat of formation of TiSi_2 was determined to be $-30 \pm 5 \text{ kJ/mol}$. Within experimental errors, this value agrees with the previous value [6] ($-25.8 \pm 8.8 \text{ kJ/mol}$) obtained for the traces shown in Fig. 1. The measured heat of formation shows that the thermodynamic driving force for TiSi_2 formation from a reaction of α -Si with amorphous Ti-silicide is much lower than that for its formation as the first phase from elemental materials, which is -132.5 kJ/mol [11]. By using the above heats of formation values for TiSi_2 and the heat of crystallization of α -Si (-11.95 kJ/mol [12]), we estimate the heat of formation for stoichiometric amorphous Ti-silicide to be -126 kJ/mol .

In Fig. 2, the TiSi_2 peak does not shift consistently to higher temperatures as the modulation period is increased, as would be expected for simple thickening [3]. We postulate that this is related to the nucleation-controlled nature of TiSi_2 formation. In fact, in both groups of XTEM samples, it was observed that TiSi_2 did not nucleate at every α -silicide/ α -Si interface at the same time, which indicates that the TiSi_2 nucleation is sensitive to local environment and small temperature variations. The high activation energy and reduced driving force described in the preceding paragraphs also supports an important role of nucleation in the TiSi_2 formation. Similar irregular DSC peak shifts have been observed in the formation of other silicides, NiSi_2 and VSi_2 [4]. In contrast, the endothermic step in Fig. 2 moves towards higher temperatures consistently as the modulation period is increased. This suggests that the relaxation is dependent on a diffusive process which leads to a layer-thickness-dependent time for consumption of constituent materials.

CONCLUDING REMARKS

We have shown that the use of calorimetry is very helpful in following phase transition sequences during Ti/ α -Si thin-film reactions and obtaining quantitative kinetic and thermodynamic data. The endothermic process accompanying the late stage of the amorphous Ti-silicide growth is a new feature that has not been observed in other amorphous-silicide forming systems [3-5]. Also, our calorimetric analysis indicates that the formation of the crystalline Ti-silicide is nucleation limited.

This work is part of an MIT/IBM joint research program supported by IBM.

REFERENCES

1. S.P. Murarka, Silicides for VLSI Applications, (Academic Press, New York, 1983)
2. K. Holloway and R. Sinclair, *J. Appl. Phys.* **61**, 1359 (1987).
3. L.A. Clevenger, C.V. Thompson, R.C. Cammarata and K.N. Tu, *Appl. Phys. Lett.* **52**, 795 (1988).
4. L.A. Clevenger, C.V. Thompson, A. Judas and K.N. Tu, First International Meeting on Advanced Materials **10**, 431 (1989).
5. L.A. Clevenger, R.R. DeAvillez, C.V. Thompson and E. Ma, *J. Vac. Sci. Technol.* in press.
6. R.R. DeAvillez, L.A. Clevenger, C.V. Thompson and K.N. Tu, *J. Mater. Res.* in press.
7. R. Beyers and R. Sinclair, *J. Appl. Phys.* **57**, 5240 (1985).
8. H.E. Kissinger, *Analyt. Chem.* **29**, 1702 (1957); P.G. Boswell, *J. Ther. Anal.* **18**, 353 (1980).
9. L.S. Hung, J. Gyulai, J.N. Mayer, S.S. Lau and M.A. Nicolet, *J. Appl. Phys.* **54**, 5076 (1983).
10. R.R. DeAvillez, L.A. Clevenger and C.V. Thompson, *J. Mater. Res.* **4**(5), 1057 (1989).
11. R. Hultgren, R.L. Orr, P.D. Anderson and K. Kelly, Selected Values of Thermodynamic Properties of Metals and Alloys, (J. Wiley, New York, 1963).
12. E.P. Donovan, F. Spaepen, D. Turnbull, J.M. Poate and D. Jacobson, *J. Appl. Phys.* **57**, 1795 (1985).

STUDIES OF THE EARLY OXIDATION OF SILICON (111) IN ATOMIC OXYGEN*

Bhola N. De, Jane Hruska, Jane Peterkin, Yong Zhao and John A. Wooliam, Center for Microelectronic and Optical Materials Research, and Department of Electrical Engineering, University of Nebraska, Lincoln, NE 68588-0511.

INTRODUCTION

With the growing interest in submicron size, integrated circuit technologies based on silicon, there is continuing attention to the study of ultrathin oxides [1-5]. A number of studies have been conducted on dry oxidation of silicon in the ultrathin regime; however, there is no general agreement on the correct oxidation mechanism. It has been evident that from studies of oxidation kinetics alone, one can not determine the exact oxidation mechanism [6]. However, by examining the dependence of growth (e.g., the growth rate of oxide) on various process parameters (e.g., the pressure or the temperature during oxide growth) one might be able to reduce the list of possible mechanisms of oxide growth.

Studies of oxidation mechanisms of silicon (111) in atomic oxygen, in the ultrathin oxide regime will be discussed in this paper. Particularly, the extent of agreement of experimental results with the recently proposed Murali and Murarka theory [1] will be addressed. Analyses based on other theories will be published elsewhere.

THEORIES OF OXIDATION

The Deal and Grove theory of silicon oxidation has long been used as a practical model for describing thick oxides [7]. According to this theory, the oxidizing species diffuses through the oxide layer and reacts at the silicon dioxide-silicon interface. The (reaction limited) oxide growth for earlier oxidation is described by a linear equation.

Murali and Murarka proposed that at extremely early stages the oxidizing species diffuses through a very thin oxide layer into the silicon substrate due to very low diffusion resistance of a thin oxide layer. Thus, the oxidation takes place over a volume (i.e., reaction zone) rather than only at the interface. At later stages when the oxide thickens, all of the oxidizing species is consumed at the interface due to an increased diffusion resistance of a thick oxide layer. Since initially the oxidation takes place over a reaction zone rather than at the interface, the rate of oxide growth becomes faster. Based on this model and some additional simplifications (see reference 1 for details) the following results were obtained. There is a critical thickness, say x^* of oxide layer below which the oxide growth is given by the relationship: $x = A't + B$, where the constant A' is proportional to the oxygen gas pressure. For thicknesses greater than x^* the growth law is given by a second linear equation: $x = A''t + C$, where A'' is again proportional to the oxygen gas pressure. The relationship between various con-

* Research supported by NASA Lewis Research Center Grant No. NAG-3-95.

stants are: $A' > A''$ and $C > B$. At later stages the growth law approximates to a parabolic equation.

EXPERIMENTAL SETUP AND RESULTS

The details of experimental setup have already been discussed [8]. Briefly, the oxidation was done (without heating the substrate) in a capacitively coupled, 13.56 Mhz RF power-driven pure atomic oxygen plasma (this method of oxidation is also called "ashing") having the atomic oxygen as a dominant species, as discussed in reference 8. Monolayer sensitive, and nondestructive Variable Angle of Incidence Spectroscopic Ellipsometry (VASE) [9-12] was used to measure the oxide thickness. Three angles of incidence: 68, 70 and 72 degrees, and the wavelength range: 3500 - 6500 Angstroms at 100 Angstroms intervals, were used for the VASE measurements.

Three different ashing powers were used: 25, 50 and 100 Watts. The oxygen pressure was 103 microns and the background pressure was 22 microns. To calibrate the asher in terms of atomic oxygen concentration, kapton [13] mass loss experiments at three different powers (25, 50 and 100 watts) were done for various times. Kapton is known to form gaseous products due to reaction with atomic oxygen and therefore kapton mass loss is proportional to the concentration of atomic oxygen (with the implicit assumption that the sputtering rate of kapton is negligible). The kapton mass loss data as a function of ashing time for three different powers were least squares fit to three straight lines from which the rates of kapton mass loss were obtained. A least squares fit of these data plotted as a function of ashing power showed a parabolic increase of atomic oxygen concentration with ashing power.

Next, oxidation of silicon for various ashing times and for three different powers (25, 50 and 100 Watts) were performed using three different samples. The small ashing times were chosen such that the details at early oxidation stages could be followed accurately. The data analyses were performed using the simple model as shown in Fig. 1, and excellent fits were obtained to the ellipsometric data. The results of these analyses are shown in Fig. 2, where the oxide thickness is plotted as a function of ashing time. One should notice the kinks in these three growth curves around 30 Angstroms of oxide thickness.

A least squares fit of the Deal and Grove linear formula for oxide growth to the entire experimental data was not successful. Next, attempts were made to interpret the data according to Murali and Murarka theory. For each power, the oxide thickness data on each side of the kink were fitted to a straight line, and the results are shown in Fig. 2. The agreement between the experimental data and the calculated values is excellent (including the kink). The first segment rapidly

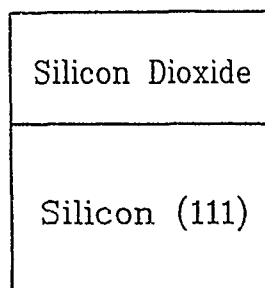


Fig. 1 Model used for analyzing VASE data from oxidized silicon samples.

recedes to small times with increasing ashing power and it becomes difficult to follow the first segment of the growth curve with an RF power of more than about 100 Watts. The interpolation between these two linear segments gives the critical thicknesses, x^* . The values of various model parameters are shown in Table I. Notice that the relationship : $A' > A''$ and $B > C$ (as deduced from the model) are satisfied by the values determined from fits to the data.

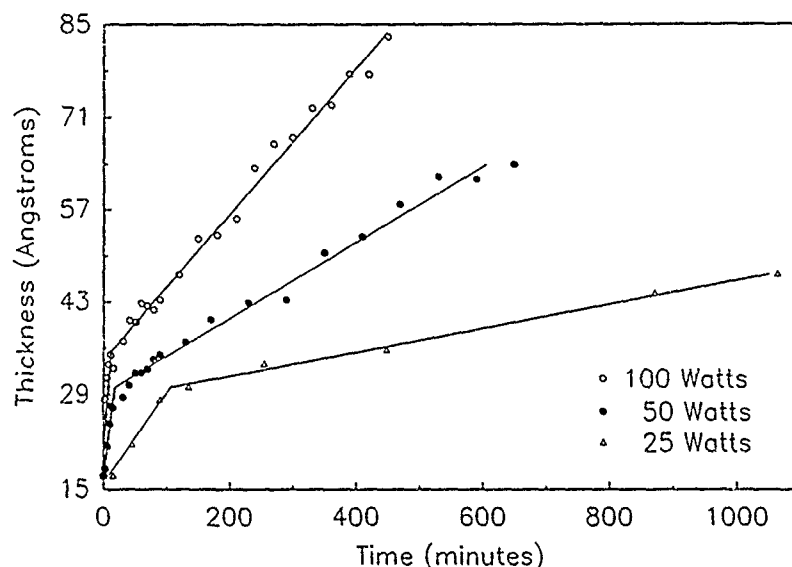


Fig. 2 Plot of silicon dioxide thickness as a function of ashing time for three different ashing powers. Notice the presence of distinct kinks in these three curves.

Table I

Table showing the "best fit" values of oxide growth parameters in the Murali-Murarka model.

Power (Watts)	A' (Angs/min ⁻¹)	B (Angs)	A'' (Angs/min ⁻¹)	C (Angs)	x^* (Angs)
25	16.1	0.1314	28.1	0.0181	30.1
50	16.7	0.7660	29.1	0.0574	30.1
100	20.6	1.863	34.8	0.1083	35.7

However, assuming that the rate of kapton mass loss is proportional to the partial pressure of atomic oxygen, it was found that the rates of oxide growth in the zone reaction and interface reaction regimes were not proportional to the atomic oxygen partial pressure. Instead, the oxide growth rate was found to be proportional to $P^{1.27}$ in the zone reaction regime,

and $P^{0.82}$ in the interface reaction regime. The pressure dependence in the second segment is in close agreement with the published values [2,5]. We believe that the pressure dependence deduced for the first segment has not been reported before.

SUMMARY AND CONCLUSION

In conclusion, the oxidation of silicon (111) in an atomic oxygen plasma environment has exhibited two distinct and linear oxide growth curves for all of the three plasma powers used in ashing (25, 50 and 100 Watts). Initially the oxide growth was faster, and above a certain critical thickness (roughly about 30 Angstroms) the growth rate became slower. The Murali and Murarka theory best describes this phenomenon as a change from the "zone reaction" regime to the "interface reaction" regime. However, the predicted dependence of the growth rate on the oxygen partial pressure does not agree with the present measurements. The exponent to the pressure in the oxide growth rate formula changes from 1.27 to 0.82 as one crosses the critical thickness whereas the theory predicts that this exponent should be 1 for both regimes.

REFERENCES

1. V. Murali and S.P. Murarka, J. Appl. Phys., 60, 2106 (1986).
2. S.M. Hu, J. Appl. Phys., 55, 4095 (1984).
3. H.Z. Massoud, J.D. Plummer and E.A. Irene, J. Electrochem. Soc., 132, 2685 (1985); *ibid.*, 132, 2693 (1985).
4. E. Farrés, J. Sune, I. Placència, N. Barniol and X. Aymerich, phys. stat. sol. (a), 114, 167 (1989).
5. S. Aptekar, M. Fernandes, and D.L. Kwong, J. Electrochem. Soc., 132, 1448 (1985).
6. K.R. Lawless, Rep. Prog. Phys., 37, 231 (1974).
7. B.E. Deal and A.S. Grove, J. Appl. Phys., 36, 3770 (1965).
8. B.N. De, Y. Zhao, P.G. Snyder, J.A. Woollam, T.J. Coutts and X. Li, Surface and Coatings Technology, 1990 (accepted).
9. R.M.A. Azzam and N.M. Bashara, Ellipsometry and Polarized Light (North-Holland, Amsterdam, 1977).
10. P.G. Snyder, M.C. Rost, G.H. Bu Abbud, J.A. Woollam and S.A. Alterovitz, J. Appl. Phys., 60, 3293 (1986).
11. S.A. Alterovitz, J.A. Woollam and P.G. Snyder, Solid State Technol., 31, 99 (1988).
12. G.H. Bu-Abbud, N.M. Bashara and J.A. Woollam, Thin Solid Films, 138, 27 (1986).
13. M. Ash and I. Ash, Eds., Encyclopedia of Plastics, Polymers, and Resins, Vol. II (Chemical Publishing Co., New York, 1982).

ENHANCEMENT OF OXYGEN PRECIPITATION IN QUENCHED CZOCHRALSKI SILICON CRYSTALS

A. HARA, T. FUKUDA, I. HIRAI, AND A. OHSAWA
Fujitsu Laboratories Ltd., Kamikodanaka, Nakahara-ku, Kawasaki,
Japan

ABSTRACT

We studied oxygen precipitation in quenched Czochralski silicon crystals. The larger the cooling rate and the higher the quenching temperature, the more oxygen precipitated. The defects enhancing oxygen precipitation are eliminated by annealing above 900°C. The defects are formed and removed repeatedly by quenching and slow cooling. We think that the aggregation of vacancies is related to those defects.

INTRODUCTION

Intrinsic gettering can improve yield in device manufacturing, but the amount of oxygen precipitation must be controlled. The amount of oxygen precipitation depends on the thermal history of crystal growth [1,2]. There has been much research on oxygen precipitation in slowly cooled crystals to simulate device fabrication process and to study thermal history of crystal growth [1], but not much research has been done in oxygen precipitation in quenched Czochralski silicon crystals [3].

EXPERIMENTAL

To study oxygen precipitation in such crystals, we annealed samples above 1270°C in nitrogen or dry-oxygen to eliminate thermal history during crystal growth and to obtain initially homogeneous crystals and then quenched them. We then annealed samples to precipitate oxygen at 700°C for 360 h or at 700°C for 20 h and then at 1000°C for 10 h. We used a conversion coefficient of $4.81 \times 10^{17} \text{ cm}^{-2}$.

RESULTS

Figure 1 shows relationship between the amount of oxygen precipitation and the cooling rate. Solution annealing was done at 1290°C for 40 min in nitrogen. We changed the cooling rate from 1700°C/min to 8°C/min. Annealing to precipitates oxygen was at 700°C for 360 h. The larger the cooling rate, the more oxygen precipitated. The largest was about 4 times as big as the smallest. This shows that the faster the cooling, the more unknown defects are introduced and cause oxygen to precipitate.

Figure 2 shows how the amount of oxygen precipitated is affected by the temperature at the start of quenching. We annealed samples at 1270°C for 25 min and slowly cooled them at 9°C/min to the quenching temperature (QT). After 15 min at this temperature, we quenched them faster than 1000°C/min. One was quenched directly from 1270°C. We changed quenching temperature from 1270°C to 1100°C. Annealing to precipitate

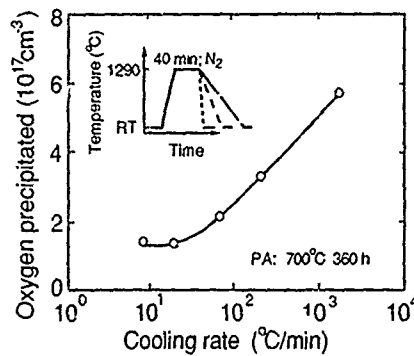


Fig. 1. Relationship between amount of oxygen precipitation and cooling rate. $[O_i] = 1.78 \times 10^{18} \text{ cm}^{-3}$. $\rho(B) = 15 \text{ ohm-cm}$. RT: room temperature. PA: precipitation annealing.

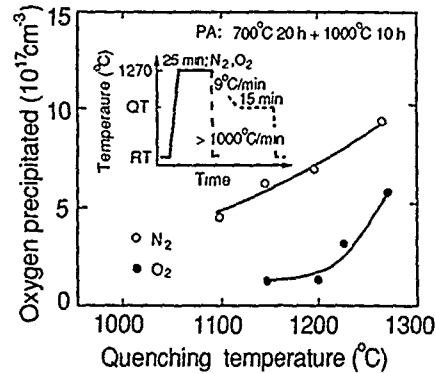


Fig. 2. Amount of oxygen precipitation at different quenching temperatures. $[O_i] = 1.82 \times 10^{18} \text{ cm}^{-3}$. $\rho(B) = 17 \text{ ohm-cm}$. QT: Quenching temperature.

oxygen was done at 700°C for 20 h and then at 1000°C for 10 h. The higher the quenching temperature, the more oxygen precipitated. This shows that the higher the quenching temperature, the more unknown defects, which enhance oxygen precipitation, are introduced.

We studied the properties of unknown defects. We prepared samples made by three different cooling processes involving quenching (Q) and slow cooling (S) (Fig. 3). One sample was quenched from 1270°C faster than 1000°C/min . The second was prepared by the first quenching process, solution annealing at 1270°C and slow cooling at 9°C/min to 1000°C . The third underwent one more quenching process from 1270°C to the second annealing process.

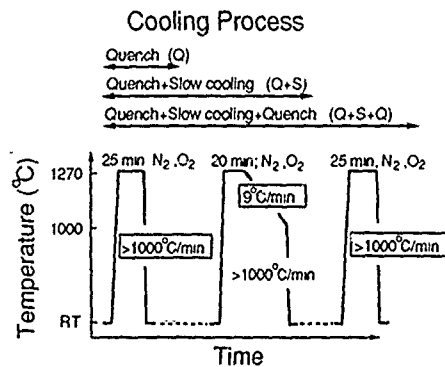


Fig. 3. Three different cooling process involving quenching (Q) and slow cooling (S).

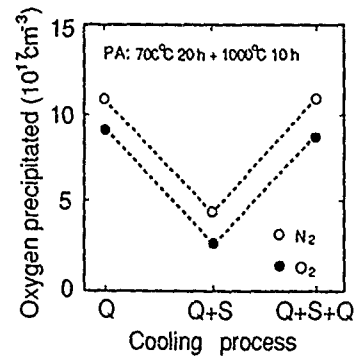


Fig. 4. Oxygen precipitation for three different cooling process. $[O_i] = 1.87 \times 10^{18} \text{ cm}^{-3}$. $\rho(B) = 15 \text{ ohm-cm}$.

Figure 4 shows the oxygen precipitation for the three different cooling processes. Annealing to precipitate oxygen was done at 700°C for 20 h and then at 1000°C for 10 h. The amount of oxygen precipitation depends only on the final cooling process. It was large in quenching (Q) and in quenching + slow cooling + quenching (Q+S+Q), but small in quenching + slow cooling (Q+S). This shows that the unknown defects enhancing oxygen precipitation are eliminated by slow cooling once they are introduced by quenching.

Next, we studied the thermal stability of the unknown defects. First, we quenched samples after annealing them at 1270°C for 25 min. Then, quenched Si crystals were annealed for 15 min between 800°C and 1000°C. We then annealed samples to precipitate oxygen at 700°C for 20 h and then 1000°C for 10 h. Oxygen precipitation begins to disappear rapidly above 900°C. The unknown defects enhancing oxygen precipitation thus disappear above 900°C.

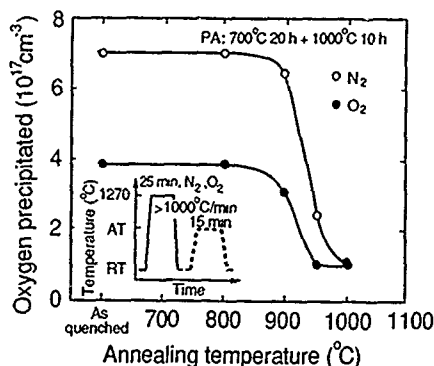


Fig. 5. Thermal stability of unknown defects enhancing oxygen precipitation. $[O_i] = 1.58 \times 10^{18} \text{ cm}^{-3}$. $\rho(B) = 62 \text{ ohm-cm}$. AT: preannealing temperature.

DISCUSSION

Small oxygen precipitates enhance oxygen precipitation. A long annealing time is usually needed to precipitate oxygen. Slowly cooled crystals are annealed longer than quenched crystals during cooling, so these crystals contain many small oxygen precipitates. In our experiment, a lot of oxygen precipitated in quenched samples, showing that the unknown defects are not small oxygen precipitates.

Heavy metal impurities encourage microdefects to form [4]. These impurities usually occur during high-temperature annealing, and usually concentrate more in slowly cooled crystals than in quenched crystals, because they are annealed for long time at high temperature. Once introduced, these impurities cannot be removed from silicon crystals, so they cannot explain decreased oxygen precipitation in slowly cooled and in quenching + slow cooling (Q+S) samples.

Intrinsic point defects can explain our results [5]. The concentration of intrinsic point defects is high in quenched crystals and low in slowly cooled crystals. The concentration is higher when crystals are quenched from a higher temperature. Intrinsic point defects are formed and removed cyclically by quenching and slow cooling after high-temperature annealing.

The unknown defects are not individually saturated intrinsic point defects such as vacancies or self-interstitials and simple complexes such as divacancies or A-centers because these are stable at low temperatures [6]. B and D defects, made

up of aggregations of self-interstitials or vacancies, are stable even at 950°C, which is temperature for Cu decoration. We think that aggregations formed by quenching are related to unknown defects.

Aggregation of intrinsic point defects are stable at 900°C, so they will act as a nucleation site for oxygen precipitates. The supersaturation of self-interstitials emitted from growing oxygen precipitates slows oxygen precipitation [3,7,8]. If aggregations are made up of self-interstitials such as B defects, supersaturation of self-interstitials will be very large with growing of oxygen precipitates, then the growth rate will decrease. If there are many vacancies in the crystals, self-interstitials emitted from growing oxygen precipitates will combine with the vacancies. The growth will then increase. We think that the aggregation of vacancies are related to unknown defects enhancing oxygen precipitation, but more work is necessary to confirm this.

When we did solution annealing in nitrogen, the amount of oxygen precipitation was larger than that of dry-oxygen. We think that nitrogen impurities, which diffused into silicon crystals during high temperature solution annealing, also enhance oxygen precipitation.

SUMMARY

We found that the larger the cooling rate and the higher the quenching temperature, the more oxygen precipitates. The increased oxygen precipitation in the quenched Czochralski silicon is related to the aggregation of vacancies.

ACKNOWLEDGMENT

We thank H. Ishikawa for his discussion and advice, and M. Kobayashi for his encouragement.

REFERENCE

1. Y. Shimanuki, H. Furuya, I. Suzuki, and M. Murai, Jpn. J. Appl. Phys. 24, 1594 (1985)
2. G. Fraundorf, P. Fraundorf, R. A. Craven, R. A. Frederick, J. W. Moody, and R. W. Shaw, J. Electrochem. Soc. 132, 1701 (1985)
3. H. Harada, T. Abe, and J. Chikawa, in "Semiconductor Silicon 1986", edited H. R. Huff, B. Kolbesen, and T. Abe (Electrochem Society, Pennington, N. J. 1986), p. 76
4. F.-G. Kirscht, H. Richter, K. Schmalz, R. Bertoldi, and H. Klose, in "Semiconductor Silicon 1986", edited H. R. Huff, B. Kolbesen, and T. Abe (Electrochem Society, Pennington, N. J. 1986), p. 903
5. A. C. Damask and G. J. Dienes, Point Defects in Metals (Cordon and Breach, New York, 1963).
6. G. D. Watkins, Deep Level in Semiconductors, edited by S. T. Pantelides (Gordon and Breach, New York, 1986), Chap. 3, p. 147.
7. T. Y. Tan and C. Y. Kung, J. Appl. Phys. 59, 917 (1986).
8. W. B. Rogers, H. Z. Massoud, R. B. Fair, U. M. Gosele, T. Y. Tan, G. A. Rozgonyi, J. Appl. Phys. 65, 4215 (1989)

PART XVI

Processing of Compounds

BURIED AMORPHOUS LAYER IN GALLIUM ARSENIDE

D. Sengupta, M.C. Ridgway, J.M. Zemanski and S.T. Johnson

Microelectronics and Materials Technology Centre,
Royal Melbourne Institute of Technology,
Melbourne, Victoria, Australia

INTRODUCTION

Relatively low dose oxygen implant is used for isolation and carrier removal in GaAs. Ion implantation induced damage is a function of ion mass, ion dose, dose rate and substrate temperature. In this paper, we explore the production of such damage leading to amorphisation in single crystal GaAs due to Oxygen ion implantation.

We have also studied the solid state regrowth behaviour of such amorphous layers. It has been previously observed that GaAs implanted with other ion species has a very complex regrowth process [1,2]. Unlike amorphous silicon, that exhibits a regrowth with a planar amorphous-crystalline interface and defect free recrystallized region, lower temperature regrowth of GaAs (less than 600°C) is characterized by formation of heavily twinned regions and thickening of crystal-amorphous interface and in the extreme cases loss of planarity at the crystal-amorphous interface [3]. We encounter some of these behaviours in our recrystallization studies.

EXPERIMENTAL

The substrates used were semi-insulation (100) GaAs. O^+ ions were implanted with energy in the range 100–150 keV. The dose was varied over the range $2 - 7.5 \times 10^{15}/\text{cm}^2$ and the substrate temperature was varied over the range 0° to 150°C. The dose rate was kept reasonably constant at $\sim 1 \mu\text{A}/\text{cm}^2$. The buildup of implantation-induced damage was monitored during implantation by the intensity of scattered laser light from the surface of the crystal (TRR). Typical spectrum is presented in fig. 1. In addition channelled Rutherford backscattering (C-RBS) and transmission electron microscopy was used to characterise the samples.

The thermal regrowth Kinetics were studied over the temperature range 250 to 300°C using a standard TRR set up [4].

RESULTS AND DISCUSSIONS

Figure 1 that summarises the effects of different implant conditions on final damage level. The scattering intensity is minimum for an undamaged crystal (~ 1 in arbitrary units) and maximum for an amorphous layer (~ 33 A.U.). The figure shows that samples implanted at 0°C for doses greater than $2 \times 10^{15}/\text{cm}^2$ forms an amorphous layer, the width of the layer increasing with dose. At 20°C and dose of $3.5 \times 10^{15}/\text{cm}^2$ it was possible to produce buried amorphous layer. The oscillation of TRR signal is a clear indication of the onset of amorphisation at a location where majority of the ions stop. At higher doses the amorphous region spread in both directions, eventually reaching the surface. For implants undertaken at higher sample temperature, it was not possible to produce any amorphous layer due to self annealing and one obtained damaged layer with higher scattered intensity than pure crystal, but less than the amorphous level.

Figure 1
TRR trace for the damage
buildup during implantation
as a function of implant temperature.

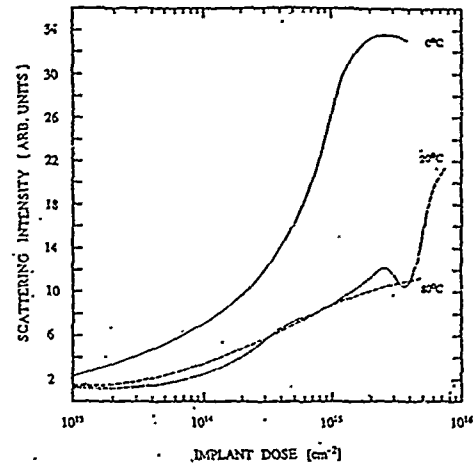


Figure 2
RBS-C spectrum
showing the creation
of amorphous layer
● — unimplanted,
○ — $2.5 \times 10^{15}/\text{cm}^2$
25°C, ▲ — $3.7 \times 10^{15}/\text{cm}^2$
18°C, △ — $10^{16}/\text{cm}^2$
at 20°C, ■ — random (scale:
23Å/channel).

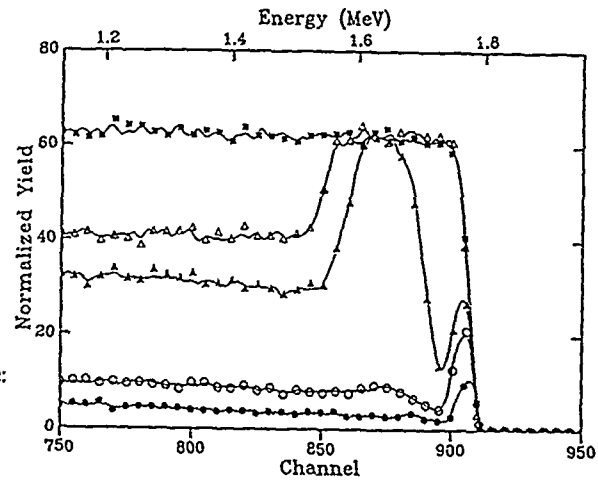
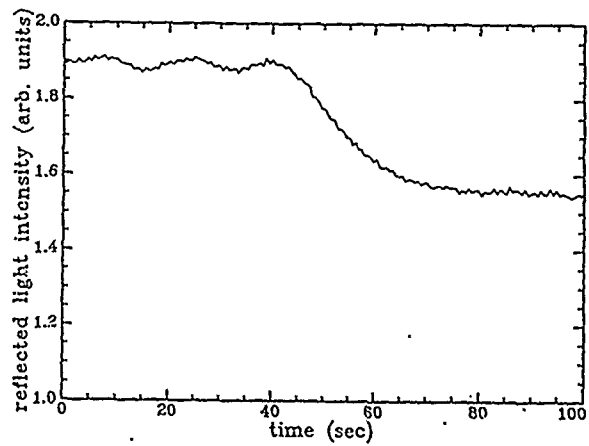


Figure 3
TRR trace showing
the solid state regrowth
of 2000Å thick
amorphous layer.



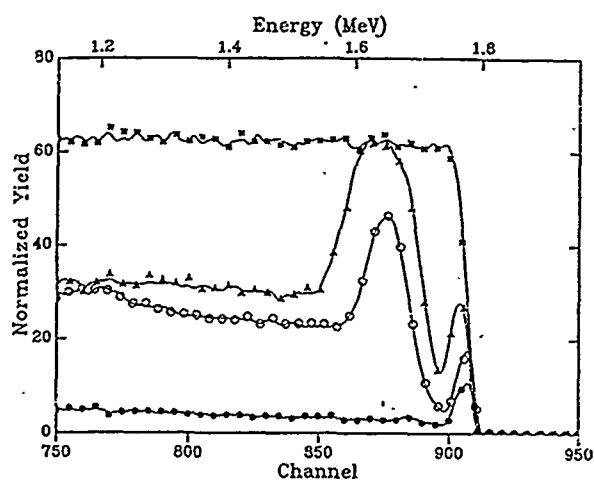


Figure 4
RBS-C Spectrum showing regrowth of buried
amorphous layer, ● – unimplanted, ○ – annealed layer,
■ – random level, (scale $15\text{\AA}/\text{Channel}$).

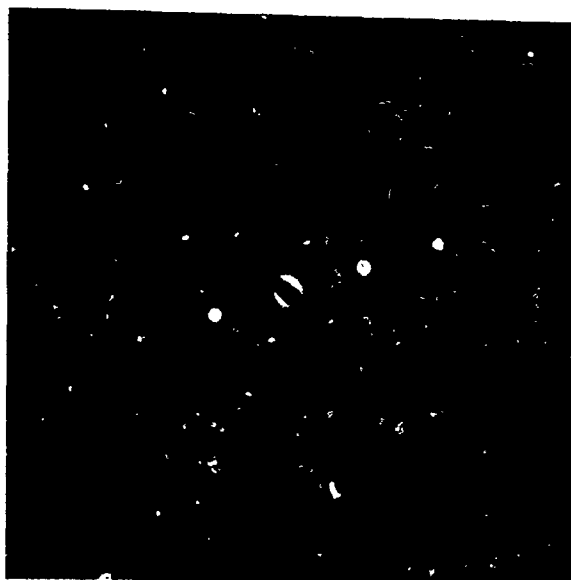


Figure 5
Electron diffraction – pattern from a heavily twinned
region after regrowth.

Fig. 2 shows the RBS-C spectra for three different ion doses at 25°C. Also shown are the unimplanted and random levels. It shows the growth of buried amorphous layer at a dose of $3.7 \times 10^{15}/\text{cm}^2$ and eventual spread of amorphous regions to the surface at higher dose. The amorphous nature of the implanted region has been verified by cross-sectional TEM.

Solid state epitaxial regrowth studies were carried out both with buried layers and layers extending to the surface. The minimum thickness of the layer in the two cases were 1100 Å and 2000 Å respectively. The deposited energy density was of the order $33 \times 10^{21} \text{keV}/\text{cm}^3$, exceeding $10^{22} \text{keV}/\text{cm}^3$ limit required for unretarded regrowth [5]. Consequently, we were expecting incomplete epitaxial growth.

The TRR signal did show oscillation typical of normal regrowth [6] but the amplitude of modulation was less than expected (Fig. 3). As recognised earlier [7] this indicated the presence of interface roughening during regrowth. The ratio of maximum to minimum signal was 1.08. Calculations by LiCoppe et al [7] show this corresponds to an interface roughening of at least 135 Å. In GaAs the regrowth rates are different along (100) and (111) direction. Any twinning present initially leads to interface roughening due to the anisotropic regrowth velocities.

Fig. 4 shows typical RBS-C spectrum of a buried amorphous layers after the regrowth has been completed. The large peak is the characteristic of heavily twinned material. The electron diffraction pattern obtained from TEM samples (Fig. 5) show the clear indication of twinning.

CONCLUSIONS

The optimum condition required for buried amorphous layer formation in GaAs by O^+ implant has been determined. The minimum energy density required for amorphisation using O^+ exceeded the theoretical limit of $10^{22} \text{keV}/\text{cm}^3$ required for planar regrowth. Consequently regrowth was characterised by broadening of crystalline amorphous interface and resulted in a heavily twinned region.

REFERENCES

1. D.J. Mazey and R.S. Nelson, *Rad. Effects* **1**, 229 (1969).
2. S.S. Kujar, B.J. Sealy, K.G. Stephens, D.K. Sadana and G.R. Booker, *Solid St. Elect.* **23**, 831 (1980).
3. J.S. Williams and H.B. Harrison, *Mat. Res. Symp. Proc.* **1**, 209 (1981).
4. G.L. Olson, S.A. Kokorowski, R.A. McFarlane and L.D. Hess, *Appl. Phys. Lett.* **37**, 1019 (1980).
5. Y.I. Nissim, L.A. Christel, T.W. Sigmon, J.F. Gibbons, T.J. Magee and R. Ormond, *Appl. Phys. Lett.* **39**, 598 (1981).
6. C. LiCoppe, Y.I. Nissim and C. Meriadec, *J. Appl. Phys.* **58**, 3084 (1985).
7. C. LiCoppe, Y.I. Nissim, C. Meriadec and P. Krauz, *J. Appl. Phys.* **60**, 1352 (1986).

DEFECT LEVELS IN THE NEAR-SURFACE REGION OF 2.0 MeV $^{16}\text{O}^+$ ION IMPLANTED n-GaAs.

C.C. TIN*, P.A. BARNES*, T.T. BARDIN** AND J.G. PRONKO**

*Department of Physics, 206 Allison Laboratory, Auburn University, AL 36849.

**Lockheed Missiles and Space Company, Inc., Research & Development Div., D91-10, B203, 3251 Hanover Street, Palo Alto, CA 94304.

ABSTRACT

MeV ion implantation in GaAs is known to cause amorphization of the region at the end of the ion range. The near-surface region, however, is still crystalline albeit heavily compensated. We have carried out deep level transient spectroscopy (DLTS) studies of the defect levels in the near-surface region of n-GaAs samples implanted with different doses of 2.0 MeV $^{16}\text{O}^+$ ions.

A comparison between the defect structures in the original and the implanted samples shows that implantation produced a broad range of defect levels ranging from 0.58 to 0.3 eV from the conduction band edge. This broad range of defects has an unusually large capture cross-section. The intensities of the DLTS peaks increase with the dose of $^{16}\text{O}^+$ ions. The presence of EL2, which was present in the original samples, was not observed in the implanted samples.

Results from measurements made on samples that have been implanted at 200°C and on implanted samples subjected to rapid thermal annealing will also be discussed.

INTRODUCTION

Radiation damage by ion-implantation has been widely used to produce semi-insulating (SI) regions for the purpose of electrical isolation in III-V semiconductor devices[1-3]. The creation of the high resistivity region is due to the presence of deep trapping levels, introduced by high energy radiation, which compensate the free carriers in the material. Proton irradiation is a common technique in creating SI layers in III-V compounds because of the large penetration depth by virtue of its low ion mass[4]. However, oxygen ion implantation has proven more effective in producing thermally stable SI layers[5,6] although the penetration depth of $^{16}\text{O}^+$ ions is smaller than that of protons. The need for deep implants and the small range of $^{16}\text{O}^+$ in GaAs necessitate the use of MeV ion implantation in such diverse application as the fabrication of stripe geometry lasers, avalanche and mixer diodes, metal-semiconductor field-effect-transistor (MESFET) and IMPATT diodes.

Radiation damage produces two distinct regions in semiconductors as shown by cross-sectional transmission electron microscopy (XTEM) studies[7,8]. The region at the end of the ion range is amorphous in nature but the near-surface region and the region beyond the end of the ion range are still crystalline. The near surface region is the region where electronic interaction between incident ions and target atoms predominates. The end of the ion range is where nuclear interaction predominates as the ion slows down and elastic nuclear collisions occur. The amorphous region has a large conglomeration of defects and several models[7] have been proposed to explain the phenomenon of amorphization resulting from ion implantation. The near surface region contains relatively less defects but many of these still remain even after annealing. The purpose of the present study is to investigate the nature and behavior of these defects and how they behave after annealing.

Previous studies of deep levels induced in $^{16}\text{O}^+$ irradiated GaAs have been carried out on samples irradiated by ions in the energy range 50-185 keV[9,10]. We have carried out deep-level transient spectroscopy (DLTS)[11] studies on n-GaAs irradiated with 2.0 MeV $^{16}\text{O}^+$ ions with emphasis on the near surface region. Results will be presented for unimplanted samples; those implanted at room temperature and also at 200°C; and finally on implanted samples subjected to rapid thermal annealing (RTA). The results show a broad range of defect levels in the ion-implanted samples. The intensities of the DLTS peaks vary with ion dosage. RTA introduces hole defect levels but these levels are not prominent in those samples that had been irradiated with high ion dosage.

EXPERIMENTAL DETAILS

Samples of nominally undoped n-GaAs with carrier concentration of $\approx 1.9 \times 10^{16} \text{ cm}^{-3}$ were irradiated with different doses of 2.0 MeV $^{16}\text{O}^+$ ions. Three different batches of samples were prepared. One batch was irradiated at room temperature; another batch was irradiated at about 200°C, and the third batch was irradiated at room temperature followed by RTA at about 900°C for approximately 10 seconds with arsenic overpressure. Ohmic contacts were made by alloying AuGe on the back of the samples and Schottky diodes were fabricated using evaporated Au dots. In the case of samples to be heat-treated (hot-implant and RTA), the Au dots were fabricated only after heat treatment to avoid Au diffusion. Degreasing procedure using 1,1,1-trichloroethane, acetone and methanol and oxide removal procedure using dilute HCl solution were followed before each metallization step. DLTS measurements were carried out using a microcomputer-controlled system[12] which employs the correlation technique[13]. To confine our studies to the near-surface regions, DLTS measurements were made using 0 V reverse bias with 5.0 V filling pulse. This means that only those trapping centers present within the zero bias depletion layer created by the Schottky contact will be detected. The equivalent depth from the interface is $\approx 0.23 \mu\text{m}$. The emission rate window for all the DLTS curves given here is 11.6 s^{-1} .

RESULTS AND DISCUSSION

Figure 1 shows the DLTS curves for a series of samples implanted with different doses of $^{16}\text{O}^+$ at room temperature. It can be seen from Figure 1 that the intensities of the peaks increase with increasing dose of $^{16}\text{O}^+$ ions.

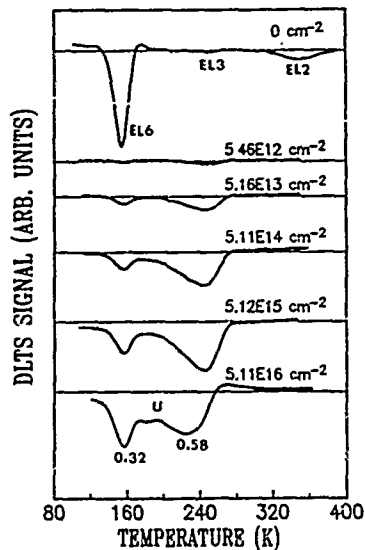


Fig. 1. DLTS curves for samples implanted at room temperature with different doses of $^{16}\text{O}^+$ ions.

not been conclusively determined. However, results from DLTS and photoluminescence studies[20] of GaAs samples under uniaxial stress strongly indicate a relationship between EL6 and the arsenic antisite defect. The DLTS curve for the unimplanted sample in Figure 1 also shows the presence of the EL2 peak at about 350 K. However, this peak is absent in the implanted samples. The results in Figure 1 show that the defect levels originally present in the near-surface region of the unimplanted sample disappear after ion implantation at low dosage. This phenomenon enables the subsequent effects of ion implantation to be clearly seen.

The broad peak between 160 and 250 K indicates the presence of a range of defect centers with closely spaced activation energies. This could be due to a clustering of defect centers induced by irradiation. The position of this broad peak is similar to that of the U band that has been observed in ion implanted samples[14,15]. The presence of the broad band in ion implanted samples sets them apart from electron irradiated samples which show discrete trapping levels[16]. The U band has been attributed to phonon-assisted tunneling of electrons between neighboring defects[15,17]. The origin of the U band is poorly understood. It has been recently proposed[18] that the U band is related to EL2[19]. Besides the U band, there is another major peak at about 158 K. The trapping parameters of this peak agree with those of EL6[19]. This peak is present in both unimplanted and implanted samples. The intensity of this peak increases with $^{16}\text{O}^+$ ion dose. The identity of the EL6 defect has

The DLTS curves for samples that had been implanted at about 200°C are shown in Figure 2. The concentration of the electron trap EL6 again increases with $^{18}\text{O}^+$ ion dose and the broad U band is also present. However, the difference between these curves and those of the samples implanted at room temperature is that a hole peak can be seen at about 260 K which corresponds to an activation energy of $(E_v+0.65)$ eV. The intensity of this hole peak increases with ion dose. The DLTS curve for the unimplanted sample of Figure 2 shows the presence of a broad peak ranging from $\approx 240 - 350$ K. This broad peak covers the temperature range where EL3 and EL2 are usually observed. The positions of EL3 and EL2 are indicated in Figure 2. The position of the peak at about 330 K is affected by the EL2 peak at 350 K. Hence, the trapping parameter of this peak cannot be accurately determined. A comparison between the DLTS curves for the unimplanted samples in Figures 1 and 2 indicate that the broad peak could be caused by heating the wafer at about 200°C for several hours while different regions of the wafer were being irradiated with different doses of $^{18}\text{O}^+$ ion. The DLTS curves of the implanted samples do not show the presence of this broad peak.

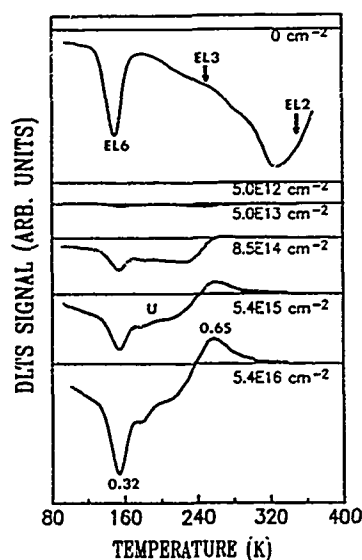


Fig. 2. DLTS curves for samples implanted at 200°C.

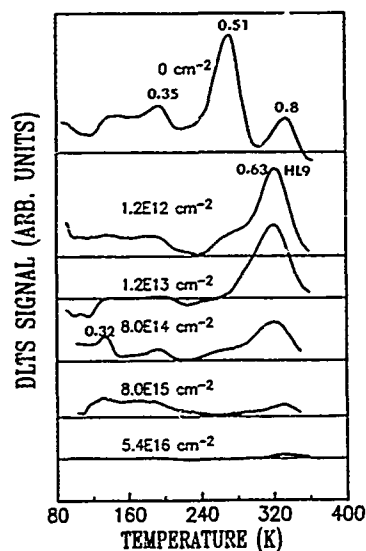


Fig. 3. DLTS curves for samples implanted at room temperature and then subjected to RTA.

The DLTS curves for samples implanted at room temperature and then subjected to RTA at about 900°C for about 10 seconds are shown in Figure 3. These curves differ from those of the other two types of samples. The salient features of Figure 3 are the negligibly small electron peaks and the presence of large hole peaks. The presence of these hole peaks in the DLTS curve for the unimplanted sample indicates that these peaks were introduced by RTA. It should be noted that these peaks occurred in the near-surface region which may be non-stoichiometric after RTA treatment. The main hole peak at about 320 K in Figure 3 corresponds to an energy level of $(E_v+0.63)$ eV. This hole peak is possibly HL9[21]. The intensities of both electron and hole trapping centers decrease with increasing $^{18}\text{O}^+$ ion dose. The gradual disappearance of these peaks as the ion dose increases does not mean the annihilation of the defects responsible for these peaks. Instead, we believe that the defect clusters responsible for these peaks have undergone a transformation into dislocation loops[22] which are not electrically active.

In the light of our results, it is obvious that $^{18}\text{O}^+$ ion implantation induces the clustering of defects. The disappearance of these peaks in RTA samples and the decreasing intensities of the hole peaks are due to localized recrystallization of these defects to form dislocation loops. The samples implanted at 200°C showed the characteristics of the transition between these two types of samples.

CONCLUSION

We have carried out DLTS studies of defect levels in the near-surface region of 2.0 MeV $^{16}\text{O}^+$ ion implanted n-GaAs. The DLTS results show that $^{16}\text{O}^+$ ion implantation causes the formation of the defects responsible for EL6 and the U band. The behavior of these peaks with different ion dose and also with annealing treatment indicates the presence of defect clusters. These defect clusters transform into electrically inactive defects upon annealing which explains the decreasing intensities of the peaks with increasing ion dose for the samples that were subjected to rapid thermal annealing.

ACKNOWLEDGEMENTS

This research was supported by DNA Contract No. 001-85-C-0183 at Auburn University and by the Lockheed Independent Research Fund at Lockheed.

REFERENCES

1. K.G. Stephens, Nucl. Instr. and Meth. 209/210, 589 (1983).
2. S.J. Pearton, J.M. Poate, F. Sette, J.M. Gibson, D.C. Jacobson, and J.S. Williams, Nucl. Instr. and Meth. B19/20, 369 (1987).
3. S.J. Pearton, Solid State Phenomena 1/2, 247 (1988).
4. J.P. Donnelly, Inst. Phys. Conf. Ser. 33b, 166 (1977).
5. P.N. Favennec, J. Appl. Phys. 47, 2532 (1976).
6. T. Itoh, T. Tsuchiya, and M. Takeuchi, Jpn. J. Appl. Phys. 15, 2277 (1976).
7. D.K. Sadana, Nucl. Instr. and Meth. B7/8, 375 (1985).
8. T.T. Bardin, J.G. Pronko, F.A. Junga, W.G. Opyd, A.J. Mardinly, F. Xiong, and T.A. Tombrello, Nucl. Instr. and Meth. B24/25, 548 (1987).
9. D.V. Lang, Inst. Phys. Conf. Ser. 31, 71 (1977).
10. T. Asano, R.D. Atanassov, H. Ishiwara, and S. Furukawa, Jpn. J. Appl. Phys. 20, 901 (1981).
11. D.V. Lang, J. Appl. Phys. 45, 3023 (1974).
12. C.C. Tin and P.A. Barnes, J. Appl. Phys. 66, 223 (1989).
13. G.L. Miller, J.V. Ramirez, and D.A.H. Robinson, J. Appl. Phys. 46, 2638 (1975).
14. G.M. Martin, P. Secordel, and C. Venger, J. Appl. Phys. 53, 8706 (1982).
15. G.M. Martin, E. Esteve, P. Langlade, and S. Makram-Ebeid, J. Appl. Phys. 56, 2655 (1984).
16. D.V. Lang, L.C. Kimerling, and S.Y. Leung, J. Appl. Phys. 47, 3587 (1976).
17. J. Samitier, J.R. Morante, L. Giraudet, and S. Gourrier, Appl. Phys. Lett. 48, 1138 (1986).
18. A. Perez, J. Samitier, A. Romano, and J.R. Morante, in *Semi-insulating III-V Materials, Malmo, 1988*, edited by G. Grossman and L. Ledebø (IOP, England, 1988), p. 81.
19. G.M. Martin, A. Mitonneau, and A. Mircea, Electron. Lett. 13, 191 (1977).
20. M. Levinson, Inst. Phys. Conf. Ser. 91, 73 (1988).
21. A. Mitonneau, G.M. Martin, and A. Mircea, Electron. Lett. 13, 666 (1977).
22. P.W. Hutchinson, R.K. Ball, P.S. Dobson, and P. Leigh, J. Mater. Sci. Lett. 1, 457 (1982).

CORRELATION OF VOID FORMATION WITH THE REDUCTION OF CARRIER ACTIVATION AND ANOMALOUS DOPANT DIFFUSION IN SI-IMPLANTED GaAs

Kei-Yu Ko*, Samuel Chen*, S.-Tong Lee*, Longru Zheng*, and T.Y. Tan**

*Corporate Research Laboratories, Eastman Kodak Company, Rochester, NY 14650

**Dept. of Mechanical Eng. and Materials Sci., Duke Univ., Durham, NC 27706, and Microelectronics Center of North Carolina, Research Triangle Park, NC 27709

ABSTRACT

We report the study of high-dose Si-implanted GaAs containing doses ranging from 1×10^{14} to $1 \times 10^{15} \text{ cm}^{-2}$ and with subsequent anneals at 850°C for 1 hour. At doses $\geq 3 \times 10^{14} \text{ cm}^{-2}$, a severe reduction of carrier concentration and anomalous Si diffusion are observed in the near-surface region. In the same region, small, near-spherical voids are found by transmission electron microscopy. In contrast, for samples implanted with doses $\leq 1 \times 10^{14} \text{ cm}^{-2}$, voids are not found, and both normal carrier activation and Si diffusion profiles are observed. The concurrent onset of these three phenomena in the same region in high-dose samples leads us to conclude that the severe reduction of carrier concentration and anomalous Si diffusion are attributable to the formation of voids.

INTRODUCTION

Ion implantation of Si has been used extensively in GaAs devices and integrated circuit processing, such as the fabrication of n-type channel layers and n^+ regions for good ohmic contacts in MESFET devices. Implantation is usually followed by a high temperature annealing step to activate the implanted species and to remove lattice damage caused by the implantation process. However, it is known that high electrical activation (close to 90%) of implanted Si is obtained only at low dose implants ($\leq 10^{13} \text{ cm}^{-2}$) [1,3]. At higher implant doses ($\geq 10^{14} \text{ cm}^{-2}$), activation $\leq 20\%$ is typical [4,5]. Previous studies showed that this low activation of Si in GaAs in high dose implants could be linked to phenomena such as (1) self compensation by silicon acceptors, Si_{As} [6], (2) formation of $\text{Si}_{\text{Ga}}\text{-Si}_{\text{As}}$ neutral pairs [4,5,7], and (3) compensation by defects related to residual implantation damage after annealing [3,8].

In a recent study Chen *et al.* [9] reported the formation of voids in high dose Si-implanted GaAs and GaAs/AlGaAs superlattices. They postulated that the internal surfaces of voids could trap the Si dopant and they became electrically inactive. Furthermore, surface states associated with the surfaces of voids could also compensate free carriers. In this paper, we present experimental evidence to examine these postulates and show that the occurrence of carrier concentration reductions and Si diffusion anomalies in the near-surface region in high dose implants are related to the formation of voids.

EXPERIMENTAL

$\langle 100 \rangle$ -oriented, undoped, semi-insulating GaAs was used in this study. Room temperature Si implantation was performed in a non-channeling direction at an energy of 220 keV and doses ranging between 1×10^{14} and $1 \times 10^{15} \text{ cm}^{-2}$. The samples were then encapsulated with 1000 Å-thick plasma-deposited silicon nitride film, followed by furnace annealing at 850°C for 1 hour in flowing

H₂/Ar ambient. Microstructural defect characteristics were studied by transmission electron microscopy (TEM) using cross-section specimens. Atomic Si concentration profiles were obtained by secondary ion mass spectrometry (SIMS), and the electron concentration profiles were measured with a Polaron PN4200 electrochemical CV profiler.

RESULTS

Two types of defects were seen in the near-surface region of implanted and annealed GaAs. First, similar to those reported by others [3,4], dislocation loops were observed in samples implanted with doses $\geq 3 \times 10^{13} \text{ cm}^{-2}$. The second type of defects, small (10 to 50 Å in diameter) near-spherical voids, was found in samples implanted with doses $\geq 3 \times 10^{14} \text{ cm}^{-2}$. The identification of voids has been described in a previous report [9]. As shown by the TEM images in Fig. 1, for an implant dose of $3 \times 10^{14} \text{ cm}^{-2}$, voids distribute from the surface to a depth of about 0.25 μm , whereas voids are found to distribute in a buried region between depths of about 0.18 to 0.27 μm in the sample implanted with $1 \times 10^{15} \text{ cm}^{-2}$ of Si. No voids were found in samples implanted with lower doses ($\leq 1 \times 10^{14} \text{ cm}^{-2}$) nor in samples implanted with a dose of $1 \times 10^{15} \text{ cm}^{-2}$ and not annealed.

The effect of voids on the electrical characteristics can be readily seen by comparing the carrier concentration profiles with the distribution of voids. As shown in Fig. 2, at a dose of $1 \times 10^{14} \text{ cm}^{-2}$ where no voids were found, the carrier concentration profile follows the Si distribution (see Fig. 3), showing the normal Si diffusion and low electrical activation of about 54% after annealing. Upon increasing the dose to $3 \times 10^{14} \text{ cm}^{-2}$, an anomalous suppression of n is seen in the near-surface region with a minimum of about $3 \times 10^{17} \text{ cm}^{-3}$ (corresponding to an activation, $n/[\text{Si}]$, of less than 4%) at 0.12 μm . Beyond this depth, n gradually increases to its peak value of $2 \times 10^{18} \text{ cm}^{-3}$ (or about 70% activation) at a depth of 0.35 μm and then follows the Si distribution (Fig. 3). For samples implanted with $1 \times 10^{15} \text{ cm}^{-2}$ of Si, a noticeable dip in n is observed in a region between 0.12 and 0.28 μm with a minimum value of $7 \times 10^{17} \text{ cm}^{-3}$ (or $< 1\%$ activation) at a depth of 0.2 μm . Beyond this region, n is seen to follow the Si profile (Fig. 3) with an activation of about 30%. Note that in both samples where voids formed, the regions of carrier suppression coincide well with the distribution of voids shown in Fig. 1, and normal n profiles are seen outside where voids are found.

Fig. 3 shows the Si atomic concentration profiles. For the void-free, $1 \times 10^{14} \text{ cm}^{-2}$ implanted sample, normal Si diffusion characteristics are seen after annealing. However, for implant doses $\geq 3 \times 10^{14} \text{ cm}^{-2}$ where voids were

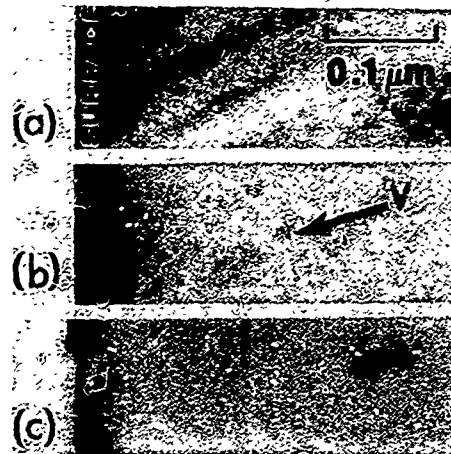


Fig.1 TEM bright field micrographs of the near-surface region of 220 keV Si-implanted GaAs after annealing at 850°C for one hour. Implant doses shown are (a) $1 \times 10^{14} \text{ cm}^{-2}$, (b) $3 \times 10^{14} \text{ cm}^{-2}$, and (c) $1 \times 10^{15} \text{ cm}^{-2}$. Voids, labelled as "V", are seen only in samples implanted at doses $\geq 3 \times 10^{14} \text{ cm}^{-2}$.

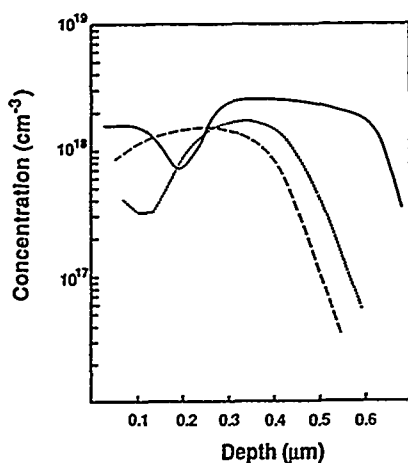


Fig.2 Carrier concentration profiles of Si-implanted and annealed (850°C, 1 h) GaAs containing doses of (---) $1 \times 10^{14} \text{ cm}^{-2}$, (....) $3 \times 10^{14} \text{ cm}^{-2}$, and (—) $1 \times 10^{15} \text{ cm}^{-2}$.

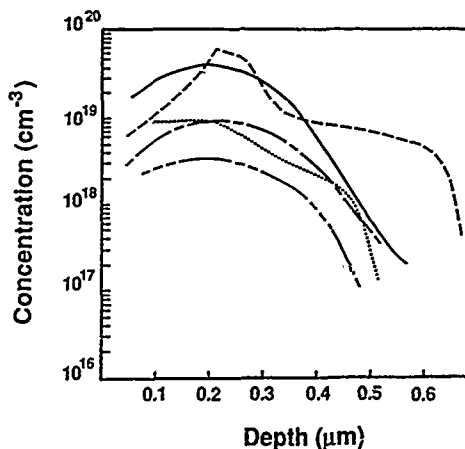


Fig.3 SIMS Si profiles of Si-implanted and annealed (850°C, 1 h) GaAs containing doses of (---) $1 \times 10^{14} \text{ cm}^{-2}$, annealed; (- · -) $3 \times 10^{14} \text{ cm}^{-2}$, as-implanted; (....) $3 \times 10^{14} \text{ cm}^{-2}$, annealed; (—) $1 \times 10^{15} \text{ cm}^{-2}$, as-implanted; and (- - -) $1 \times 10^{15} \text{ cm}^{-2}$, annealed.

found in the near-surface regions, anomalous Si diffusion can be seen in the same regions. For the $3 \times 10^{14} \text{ cm}^{-2}$ implanted and annealed sample, Si concentration is nearly constant within a region of $0.23 \mu\text{m}$ from the surface. This region of constant Si concentration coincides with the distribution of voids found in the same sample (Fig. 1b); and compares with its as-implanted profile, it is a result of Si depletion at larger depths outside where voids are found. For implant dose of $1 \times 10^{15} \text{ cm}^{-2}$, similar comparison clearly shows the formation of a Si accumulation region between 0.19 and $0.29 \mu\text{m}$ after annealing accompanied with two Si depletion regions on two sides. This Si accumulation occurs at the same region where voids are found. Beyond $0.4 \mu\text{m}$ a long tail in Si distribution is seen as a result of normal Si diffusion during annealing. The Si uphill diffusion indicates an effective negative diffusivity of Si in the vicinity where voids are found.

DISCUSSION

While the presence of compensation centers and neutral complexes suggested in the literature can explain the low overall electrical activation in general [3-8], they cannot account for the carrier concentration suppression in the near-surface region we observed in this study. Bhattacharya *et al.* [4] also observed a dip in n under similar implantation and annealing conditions. They attributed this to the formation of neutral neighboring pairs; however, no direct evidence was provided.

The data we presented in the previous section showed a strong correlation between the severe reduction of n and anomalies in Si diffusion with the presence of voids in the same region. We believe that the internal surfaces of voids can possess a lower surface potential than the bulk of the crystal; as a consequence, Si can preferentially segregate there during high temperature annealing. Si trapped by voids is most likely electrically

inactive and thus causes a lowering of electron concentration in the same region. This is evident by the observation of Si accumulation and carrier suppression in the same region where voids distribute. Further, once Si is trapped it may not readily participate in the diffusion process. The uphill diffusion of Si in the highest dose we used is believed to be due to the high absorbence of Si by the void surface and to the inhomogeneous distribution of Ga and As vacancy supersaturation in the vicinity of voids. The lowering in carrier concentration is also responsible for the inhibition of Si diffusion by reducing the concentration of charged vacancy through the Fermi level effect [10,11]. Finally, defect energy levels could also be associated with voids, which would compensate carriers in their vicinity. However, this explanation is still premature until a direct identification of energy traps associated with voids is found.

CONCLUSION

In conclusion, we have presented experimental results which correlate the anomalous Si diffusion and carrier suppression with the formation of voids in high-dose Si-implanted GaAs. Outside the region where voids distribute, normal Si diffusion is observed, and the low electrical activation is believed to be related to self-compensation and neutral complex formation. In regions where voids are found, the electrical activation is as low as 1% and Si shows up-hill diffusion. This can be satisfactorily explained by the trapping of Si by voids and its consequences in electrical activation and Si diffusion.

ACKNOWLEDGEMENT

We would like to thank Dr. J. P. Shepherd for technical discussions of the subject. We also like to acknowledge J. Madathil for technical assistance in ion implantation, P. Fellingner for SIMS measurements, and J. J. DeJohn for TEM sample preparation. One of us (TYT) acknowledges the Duke Endowment for financial support.

REFERENCES

1. Y. K. Yeo, R. L. Hengehold, Y. Y. Kim, A. Ezis, Y. S. Park, and J. E. Ehret, *J. Appl. Phys.* **58**, 4083 (1985).
2. S. G. Liu, E. C. Douglas, C. P. Wu, C.W. Magee, S. Y. Narayan, S. T. Jolly, F. Kolondra, and S. Jain, *RCA Rev.* **41**, 227 (1980).
3. A. Masuyama, M-A. Nicolet, I. Golecki, J. L. Tandon, D. K. Sadana, and J. Washburn, *Appl. Phys. Lett.* **36**, 749 (1980).
4. R. S. Bhattacharya, A. K. Rai, Y. K. Yeo, P. P. Pronko, S. C. Ling, S. R. Wilson, and Y. S. Park, *J. Appl. Phys.* **54**, 2329 (1983).
5. J. L. Tandon, M-A. Nicolet, F. H. Eisen, *Appl. Phys. Lett.* **34**, 165 (1979).
6. S. K. Tiku and W. M. Duncan, *J. Electrochem. Soc.* **132**, 2237 (1985).
7. L. H. Skolnik, W. G. Spitzer, A. Kahan, F. Euler, and R. G. Hunsperger, *J. Appl. Phys.* **43**, 2146 (1972).
8. A. K. Rai, R. S. Bhattacharya, and P. P. Pronko, *Appl. Phys. Lett.* **41**, 1086 (1982).
9. S. Chen, S.-Tong. Lee, G. Braunstein, and T. Y. Tan, *Appl. Phys. Lett.* **55**, 1194 (1989).
10. D. G. Deppe, N. Holonyak, Jr., F. A. Kish, and J. E. Baker, *Appl. Phys. Lett.* **50**, 998 (1987).
11. S. Yu, U. M. Gosels, and T. Y. Tan, *J. Appl. Phys.* **66**, 2952 (1989).

SURFACE AND INTERFACE DAMAGE CHARACTERIZATION OF REACTIVE ION ETCHED MBE REGROWN GaAs

M.W. COLE*, M. DUTTA*, J. ROSSABI**, D.D. SMITH*, AND
J.L. Lehman***

*US Army ETDL, Ft. Monmouth, N.J. 07703

**Quest Tech. Inc., Eatontown, N.J. 07724

***JEOL USA Inc., Peabody, Mass. 01960

ABSTRACT

Damage resulting from reactive ion etching (RIE) and wet etching of MBE grown GaAs and the defects generated in subsequent GaAs regrowth was evaluated by Transmission Electron Microscopy (TEM), photoluminescence (PL), and Raman spectroscopy. The samples were reactively etched with HCl and Cl₂ at two power densities; 0.3 W/cm² and 0.6 W/cm². A wet chemical (H₂O:H₃PO₄:H₂O₂) etched sample was used for comparison. The LO phonon intensities measured by room temperature Raman spectroscopy showed a strong correlation to the relative PL intensities, where the HCl sample was found to be inferior to the others. TEM microstructural evaluation showed both HCl RIE samples to have significant interface roughness, with the sample etched at 0.6 W/cm² showing the most structural damage in the regrowth region. Defect densities for the Cl₂ and wet etched samples were two orders of magnitude lower than that of the HCl etched samples. The extent of disorder in the regrowth region was largest for the HCl sample with respect to the Cl₂ and wet etched samples. These microstructural and optical results suggest that the H⁺ ion plays an important role in the generation of crystal defects during the RIE process.

INTRODUCTION

Reactive ion etching (RIE) is a preferred dry process step for fabrication of submicron III-V semiconductor device structures. This kinetically assisted chemical dry etch process offers several important advantages over other etching methods, namely etch anisotropy, etch rate control, selectivity, accuracy, uniformity across the wafer and reproducibility [1]. As a result of these desirable characteristics, a number of semiconductor device designs involve RIE in their device fabrication process. Some of the more novel designs involve lateral quantum well arrays, whereby fabrication requires molecular beam epitaxial (MBE) regrowth on RIE semiconductors [2,3].

A major drawback of RIE is the potential lattice damage introduced by energetic ion bombardment and contamination. This material damage may lead to deterioration of device performance. It is important to identify and understand this RIE induced damage in order to develop and refine the RIE process, i.e. minimize crystal damage and thus optimize device performance. This study identifies and analyzes the damage associated with various RIE parameters used for quantum well fabrication.

EXPERIMENTAL

One micron of undoped GaAs was grown by MBE (Varion 360 MBE machine) on a semi-insulating GaAs substrate. The growth conditions were adjusted to achieve a growth rate of 1µm/hr with a substrate temperature of 620° C. Preparation of substrates has been described elsewhere [4,5]. Upon comple-

tion of this initial growth the wafer was cleaved into smaller pieces for exposure to different RIE conditions.

A parallel plate Plasma Therm PK 1250 reactive ion etch system at 13.56 MHz was used for all experiments. The system was evacuated to $1.0\text{E-}6$ Torr and then all process pressures were maintained at 10 mTorr with the cathode temperature of 40°C . Parameters which were not kept constant were the type of ion used for etching and etch power density. Specifically, HCl and Cl_2 reactive ion etches were performed at two power densities; $0.3\text{W}/\text{cm}^2$ and $0.6\text{W}/\text{cm}^2$. The samples were remounted and placed back in the MBE chamber to allow $1\mu\text{m}$ of undoped GaAs to be grown on these etched surfaces. For comparison a sample was wet etched in a solution of $50\text{H}_2\text{O}:5\text{H}_3\text{PO}_4:\text{H}_2\text{O}_2$. Material characterization was of two types: microstructural via TEM and optical involving PL and Raman spectroscopy. TEM was chosen in order to identify the nature of lattice defects, their distribution, and density. Photoluminescence was chosen because it's noninvasive, contactless and a well suited technique to qualitatively characterize crystal damage. Raman spectroscopy is also nondestructive and the phonon spectra obtained allows evaluation of the crystal damage and serves as a reliable comparator for the PL data.

The RIE - regrowth samples were prepared in $\{110\}$ cross sections for the TEM investigation. Samples were mechanically polished to $30\mu\text{m}$ then ion milled with an Ar^+ beam at 6 KeV in a liquid nitrogen cooled stage. Microscopy was performed using a Philips 420T STEM at 120 KeV and a JEOL 2010 TEM at 200 KeV. Microstructural evaluation was achieved via bright field, dark field, weak beam, and high resolution crystal imaging techniques.

PL spectra were taken at temperatures varying from 5K to 40K using an Argon laser's green line (514.5 nm) at a power density of $50\text{ mW}/\text{cm}^2$. The laser penetration depth in the sample was 150 nm. The Raman experiments were undertaken using the 514.5 nm line from a Coherent Innova 90 Argon Ion Laser with a power of approximately 150 mW on the sample through a 100x microscope objective. A $Z(\text{XY})Z$ scattering geometry was used for all experiments. This configuration disallows the Transverse Optical (TO) mode by the selection rules based on crystal symmetry. Thus, the appearance of the TO phonons in the spectra are due only to crystal imperfections caused by the RIE conditions.

RESULTS AND DISCUSSION

Microstructural TEM evaluation shows all RIE - regrown samples exhibited lattice damage which emanates from the interface into the GaAs regrowth region. The extent and nature of the damage is dependent on the type of etchant and power density employed. The worse case was that of HCl at $0.6\text{W}/\text{cm}^2$. Material damage was extensive throughout the $1\mu\text{m}$ regrowth region with defect density of $> 1.0\text{E}+11/\text{cm}^2$. The presence of large microtwins, averaging 85 nm in width on $\{111\}$ planes were observed to dominate the regrowth region. When the power density was lowered ($0.3\text{W}/\text{cm}^2$), while keeping the etchant constant (HCl) an appreciable decrease in crystal defects was observed. Figure 1 shows the material quality of the regrowth region for the $0.3\text{W}/\text{cm}^2$ etch. There was a high concentration of material damage in the first 250 nm of the regrowth region. The defect density is $1.3\text{E}+11/\text{cm}^2$ consisting of dislocation tangles and stacking faults and a few narrow microtwins averaging 50 nm in width. Material quality of the $0.3\text{W}/\text{cm}^2\text{Cl}_2$ RIE is superior to that of the HCl etchs. Figure 2 is a dark field micrograph of the GaAs - regrowth region. Lattice damage consists primarily of dislocations and a few narrow

~18 nm $\{111\}$ microtwins and stacking faults with a defect density two orders of magnitude less than that of the HCl etch at a similar power level. The extent of disorder into the regrowth region is 150 nm. Figure 3 shows a $\{110\}$ High Resolution Crystal Image of the Cl_2 RIE surface regrowth region. The $\{002\}$ plane is parallel to the RIE surface. The $\{002\}$ plane spacing is 2.83 Å and the $\{111\}$ plane spacing is 3.26 Å. Planar defects along $\{111\}$ plane shows lattice shifts as stacking faults. The interface roughness is on the order of 6.5 nm. The defect density of the Cl_2 RIE sample is comparable to that of the wet etch.

The PL data of the Cl_2 etched sample at a temperature of 5.4K revealed a strong peak at 1.5153 eV due to the exciton recombination and a smaller peak due to Carbon (1.4945 eV). In Figure 4 a comparison of exciton intensities of the HCl, Cl_2 , and wet etchs vs temperature is presented. It is easily seen that the sample etched with Cl_2 has the highest intensity, thus the best crystal quality. The PL data mirrors the TEM data quite well, further illustrating the undesirable effects of the HCl RIE. Figure 5 compares the Raman spectra of the HCl and Cl_2 RIE at $0.3\text{W}/\text{cm}^2$. TO scattering is ascribed to the presence of defects which destroy the crystal symmetry hence lead to a violation of the selection rule. Twinning and accompanying defects give rise to internal strain resulting in the appearance of the forbidden TO mode [6]. The intensity ratio of TO to LO can be used to qualitatively assess the crystallographic quality of the material [7,8]. A simple comparison of the TO/LO intensity ratio for the HCl and Cl_2 etchs shows the HCl to be larger which is indicative of the high density of twins and stacking fault defects revealed by TEM. Both optical and microstructural results confirm the inferior quality of the HCl vs Cl_2 etched material at equivalent powers.

Mu et al. has shown that RIE's which contain Hydrogen (CF_4/H_2) result in more structural damage to Silicon surfaces vs non Hydrogen plasmas (CF_4) [9]. Similar studies of Silicon exposed to a Hydrogen containing RIE plasma attributes the crystal damage to be caused by the physical bombardment of the surface by Hydrogen ions [10]. The work of Jeng and Oehrlein has also realized that Hydrogen plays an important role in the formation of RIE related damage in Silicon. They compare the RIE damage mechanism to that of ion implantation of light ions. They suggest that light ion bombardment (H^+) causes the accumulation of point defects and point defect clusters similar to the implantation process. During the RIE process the cathode temperature is $30\text{--}40^\circ\text{C}$. It is suggested that this temperature is enough to mobilize the point defects thus enabling them to recombine or diffuse to other clusters in order to form larger and stable defect clusters like stacking faults etc. [11]. Our work seems to fit the above model well, as the Hydrogen containing etch shows more structural damage than the non Hydrogen etch (Cl_2). It is believed that the H^+ ions create more structural damage than Cl^- ions because they move with a greater velocity and penetrate deeper into the crystal [4,5].

CONCLUSIONS

Our results have shown that TEM, PL and Raman spectroscopy are powerful tools for evaluating the damage induced by RIE processing. These characterization methods have revealed that RIE using Cl_2 results in less material damage than that of HCl. The role of Hydrogen in the plasma is directly correlated to the high density of crystal defects observed in the GaAs regrowth region. It is suggested that the velocity of H^+ ions combined with the elevated temperature of the RIE cathode are responsible for the increased damage seen in the HCl etch - regrown GaAs. Future work will examine the crystal quality of RIE - MBE regrown GaAs etched with BCl_3 and SiCl_4 .



Fig. 1 Dark field micrograph of $0.3\text{W}/\text{cm}^2$ HCl RIE.

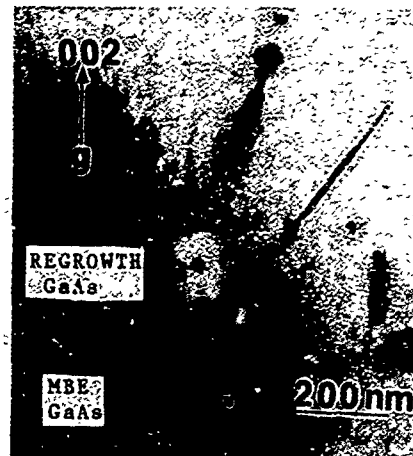


Fig. 2 Dark field micrograph of $0.3\text{W}/\text{cm}^2$ Cl_2 RIE.

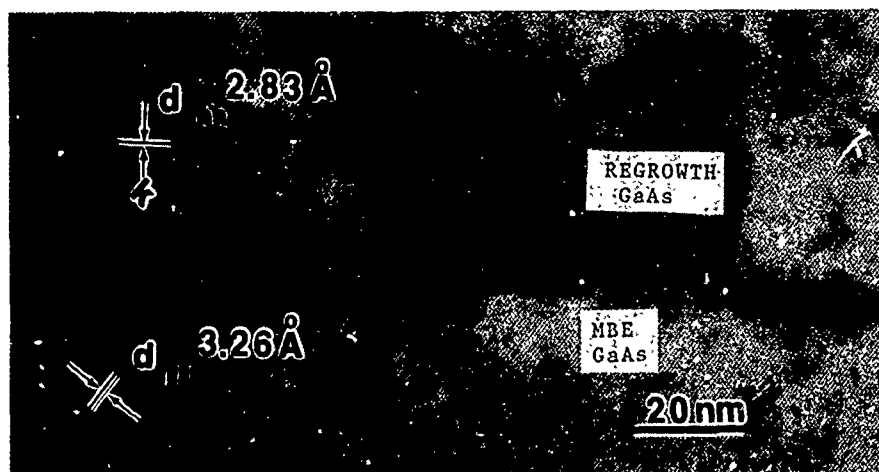


Fig. 3 $[110]$ Crystal image of $0.3\text{W}/\text{cm}^2$ Cl_2 RIE.

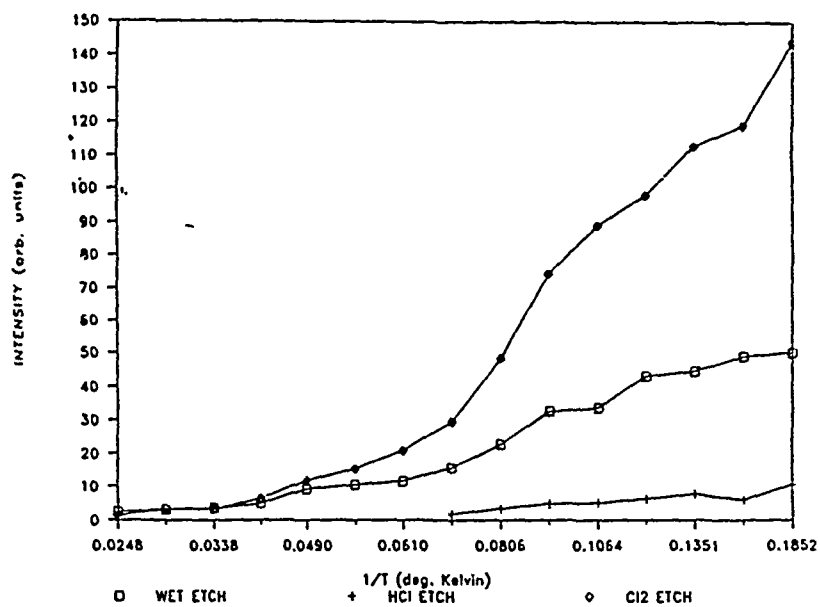


Fig. 4 Comparison of exciton intensities of HCl, Cl₂, and wet etch vs temperature.

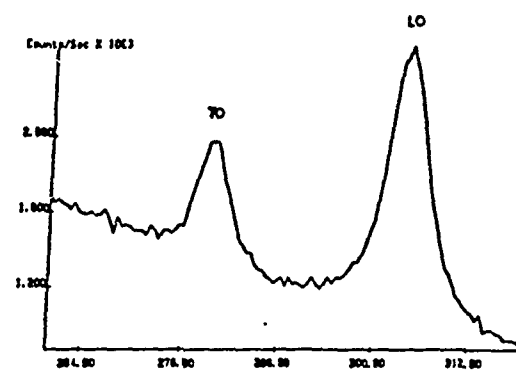
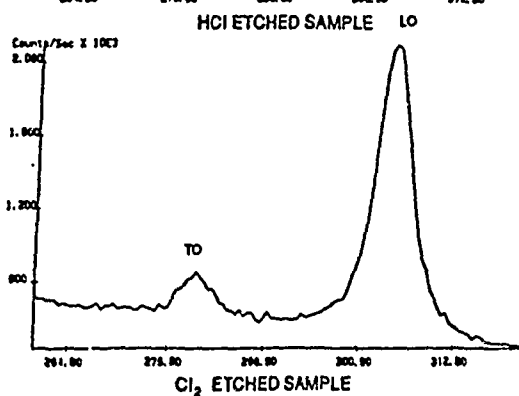


Fig. 5 Raman spectra of HCl and Cl₂ RIE at 0.3W/cm².



REFERENCES

1. S.W. Pang, *Electrochem. Soc.* 133, 784 (1986).
2. D.A.B. Miller, *J. Vac. Sci. Technol.* B5, 313 (1987).
3. G.J. Iafrate, D.K. Ferry, and R.K. Reich, *Surface Sci.* 113, 485 (1982).
4. L.S. Heath, D.D. Smith, M. Dutta, M.A. Taysing-Laura, and T.P. Monahan, *J. Electrochem. Soc.* 136, 495 (1989).
5. J. Kossabi, M. Dutta, M.W. Cole, and D.D. Smith, presented at the 1989 SPIE Fall Meeting, Santa Clara, Ca., 1989.
6. P. Lao, W.C. Tang, A. Madhuker, and P. Chen, *J. Appl. Phys.* 65, 1676 (1989).
7. R.J. Matyi, W.M. Duncan, H. Shichigo, and H.L. Tsai, *Appl. Phys. Lett.* 53, 2611 (1988).
8. C. Fontaine, H. Benarfa, E. Bedel, A. Munoz-Yague, G. Landa, and R. Carles, *J. Appl. Phys.* 60, 208 (1986).
9. X.C. Mu, S.J. Fonash, A. Rohatgi, and J. Rieger, *Appl. Phys. Lett.* 48, 1147 (1986).
10. R.G. Frieser, F.J. Montillo, N.B. Zingerman, W.K. Chu, and S.R. Mader, *J. Electrochem. Soc.* 130, 2237 (1983).
11. S.J. Jeng and G.S. Oehrlein, *Appl. Phys. Lett.* 50, 1912 (1987).

Pd/Au:Be OHMIC CONTACTS TO p-TYPE GaAs

K.M. Schmitz, K.L. Jiao, R. Sharma and W.A. Anderson, Center for Electronic and Electro-optic Materials, Department of Electrical and Computer Engineering, State University of New York at Buffalo, Bonner Hall, Buffalo, NY 14260

G. Rajeswaran and L.R. Zheng, Corporate Research Laboratory, Eastman Kodak Company, Rochester, NY 14650

M.W. Cole and R.T. Lareau, U.S. Army Electronics Technology and Devices Laboratory, Fort Monmouth, NJ 07703

ABSTRACT

Stable, low resistance ohmic contacts to p-type GaAs were studied for use in semiconductor laser applications. Comparison was made between Cr/Au, Au:Be and Pd/Au:Be metallizations. Regions of P^+ were formed in N-type GaAs by a spin-on source which was rapid diffused at 950°C for 6s. Surface doping of $2 \times 10^{20}/\text{cm}^3$ and junction depth of 0.4 μm were determined by SIMS, groove and stain, and electrochemical profile. Metallizations were accomplished by thermal evaporation with a base pressure of 3×10^{-6} Torr. Sintering of the metallizations was done by furnace or RTA at 350°C. This sintering temperature was selected after RBS studies predicted an absence of significant interdiffusion. Pd/Au:Be yielded the best result of $0.3 \mu\Omega\text{-cm}^2$ based upon transmission line, cross-bridge Kelvin and van der Pauw studies. A layer of BeO was revealed on the surface of Au:Be contacts by Auger studies. Cross-section TEM studies on Pd/Au:Be revealed a uniform layer of alloyed Ga-Au with an absence of spiking.

INTRODUCTION

GaAs and its related compounds are becoming widely used in modern optoelectronic devices such as semiconductor lasers. Since high current density is utilized in laser operation, high quality ohmic contacts are required. These contacts must exhibit low resistance, thermal and electrical stability, and be compatible in fabrication with other processing steps. This research involves a GaAs/AlGaAs heterojunction laser with particular emphasis to an ohmic contact to the Zn-diffused p^+ region. Alloyed ohmic contacts have been extensively studied and are the favored contact in present device technology [1]. Most ohmic contacts are based on a GaAs/X/Y/Z configuration. Here, X is a thin metal (eg: Pt, Ti, Cr, Pd) used primarily for adhesion purposes, and Y is an electrically conductive diffusion barrier layer consisting of a eutectic-type metal composition. Layer Z is a thick metal which is typically required for electrical contacts as well as to prevent oxidation of the metallization [2].

Some of the better ohmic contacts have utilized Ti/Pt/Au [3], Zn/Pd/Au [4] or Mn/Au [5]. This work explores the relationship between electrical and structural properties of Pd/Au:Be ohmic contacts to p-GaAs.

DEVICE FABRICATION

Substrates consisted of $1 \times 1 \text{ cm}^2$ slices of (100) n-type GaAs, Si-doped to a carrier concentration of $5 \times 10^{18} \text{ cm}^{-3}$. Wafers were capped with a 2500 Å layer of Si_3N_4 deposited by plasma chemical vapor deposition. Samples were patterned to form transmission line (TL), cross bridge Kelvin (CBK), lateral diffusion (LD) and step coverage (SC) patterns, all of which permit evaluation of the quality of the ohmic contacts. Dry etching was used to remove any barrier material (Si_3N_4) not protected by hardened photoresist. For junction formation, the source was a zinc-silica (Zinc Silica Film 306, Emulsitone Co.) and was spun at a speed of 4000 rpm for 30 seconds. The samples were then post-baked at 150°C for 10 minutes. They were then rapidly diffused for 6 seconds at a temperature of 950°C. The source was then removed by immersing the sample in buffered HF for 30 seconds. A groove and stain evaluation gave a junction depth of about 0.4 μm . This was followed by an electrochemical C-V profile which indicated a surface concentration of $2 \times 10^{20} \text{ cm}^{-3}$ and junction depth of 0.42 μm . Further confirmation by secondary ion mass spectroscopy (SIMS) verified this result. Hall effect studies gave a Hall mobility of 48.9 $\text{cm}^2/\text{V-s}$ and sheet resistance of 92 ohm/sq .

After junction formation, samples were prepared for the photolithography procedures prior to metallization. The thin metal (eg: Pd) was placed in a 0.5 inch triple strand tungsten coil basket and deposited first, followed by the Au:Be deposition. Film thicknesses of about 300 Å

for Pd and 1000 Å for Au:Be were recorded by an in situ thickness monitor. After evaporation, the wafers were immersed in acetone and placed in an ultrasonic cleaner where the metal over photoresist was removed in less than one minute. The completed structure was then heated to promote interdiffusion between the metallization layers and p⁺ GaAs. The sintering techniques utilized in this work fall into two categories: furnace and rapid thermal sintering (RTS). In RTS, the GaAs wafers were rapidly heated in N₂ to 350°C by a quartz lamp for 10 seconds. For furnace sintering, the GaAs samples were heated at 350°C for 15 minutes in 3 LPM of flowing forming gas (15% H₂, 85% N₂). The sintering conditions were chosen after several previous trials at higher temperatures. The higher temperatures produced significant interdiffusion and reaction as indicated by Rutherford backscattering spectroscopy (RBS) data. At 350°C, RBS data followed the non-sintered case indicating no interdiffusion.

EXPERIMENTAL RESULTS

Resistance Data

Quality of the ohmic contacts was compared utilizing resistance measurements, Auger electron spectroscopy (AES) or scanning auger microscopy (SAM), cross-section transmission electron microscopy (TEM) and secondary ion mass spectrometry (SIMS). Resistance measurements required transmission line (TLM) and cross-bridge Kelvin (CBK) patterns to avoid errors found in conventional methods and to permit measurement of low contact resistance values [6]. TLM patterns were spaced at 10, 20, 30, 40 and 50 μm whereas CBK patterns utilized 10, 15 and 20 μm square contact regions. Data shown in Table I represent the lowest values of measurements on many patterns contained on each wafer. Data for 400°C represent a re-heat of the previous 350°C sample. For example, 400°C - CBK data for sample 24 might range from 1.6×10^{-6} to $1.1 \times 10^{-7} \Omega\text{-cm}^2$. This variation in values across a 1x1 cm wafer is attributed to variations in surface doping concentration after utilizing the spin-on source. Repeated testing of an individual pattern would produce little variation in the recorded values.

CBK data of Table I tend to be lower than TLM data. TLM data are known to be less reliable when contact resistance becomes small. Similar tests on samples having higher contact resistance did not reveal differences in results. Au:Be/Pd compared to Au/Cr indicates a contact of about equal quality and perhaps even better. It may be advantageous to avoid Cr in optical devices using GaAs since Cr is a mid-gap acceptor. A comparison of 23R with 23F leads one to conclude the 350°C RTA to be an insufficient sinter whereas the furnace anneal was adequate since a subsequent 400°C furnace anneal did not change ρ_c . Absence of some data points in the table is due to occasional poor adhesion of Au:Be/Pd after lift-off.

TABLE I
Typical Contact Resistance Data, ρ_c (ohm-cm²)

Sample No.	Metal	Sinter	TLM Data		CBK Data	
			350°C	400°C	350°C	400°C
24	Au/Cr	RTA	1.5×10^{-6}	1.5×10^{-6}	8.2×10^{-7}	1.1×10^{-7}
23R	Au:Be/Pd	RTA	--	--	3.6×10^{-6}	3.0×10^{-8}
23F	Au:Be/Pd	FCE	9.4×10^{-7}	--	3.6×10^{-7}	5.0×10^{-7}

Auger Electron Spectroscopy Analysis (AES)

An AES, SAM study was made to evaluate the composition of the as-deposited and sintered Au:Be/Pd contact. Figure 1 shows an AES depth profile of the as-deposited Au:Be/Pd with a focus on the air/Au:Be interface. The surface is rich in Be and deficient in Au. Also, a strong O-signal follows the Be which indicates a Be-oxide formation. Further sputtering leads to the Au:Be/Pd/GaAs interface as shown in Figure 2. A sharp Pd-peak is seen with carbon following the Pd-signal. Some Pd-penetration is seen into the GaAs but Au penetration is not observed. After sintering at 350°C for 15 min in forming gas, the Pd-peak was slightly broadened, Au just began to penetrate the GaAs, and the carbon peak was removed. There was no significant change in the air/Au:Be interface after the sintering step.

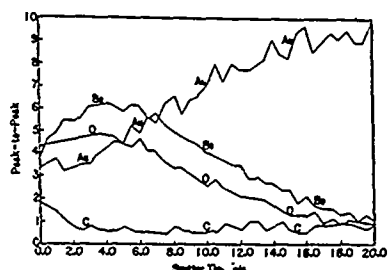


Fig. 1 AES analysis of as-deposited Au:Be/Pd/GaAs with focus on the air/Au:Be interface.

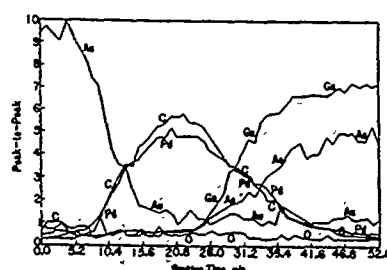


Fig. 2 AES analysis of as-deposited Au:Be/Pd/GaAs with focus on the Pd-region.

Transmission Electron Microscopy Analysis (TEM)

A bright field TEM micrograph of the cross-section of a Au:Be/Pd/GaAs contact is given in Figure 3. The contact was previously heated to 350°C for 15 min in forming gas. Energy dispersive analysis by X-ray was conducted at the numbered probe points with qualitative data shown in Table II. Points 1 and 6 indicate a predominant Au-Ga phase. Point 3 indicates a peak in Pd with a greatly diminished Au signal which agrees with the Auger results. The dark broad band marked by points 3 and 4 is predominantly Ga and As with some Au. This band is 450 Å in thickness. The interface region indicated by point 2 has an accumulation of Au at a level 50% less than in the above region and ~50% less than the amount of Ga in this interface area. Small amounts of Pd were also observed. The sample surface was examined by scanning electron microscopy and contained 1000 Å spherical hillocks. No significant protrusions or spiking into the GaAs was observed which was not the case when Pd was omitted.

TABLE II
EDS Result Corresponding to Points of Figure 3*

Probe Point	Au (%)	Pd (%)	Ga (%)	As (%)
1	41.56	0.98	36.46	20.98
2	22.38	1.54	49.92	26.16
3	3.02	1.72	64.63	30.64
4	3.91	0.92	62.93	32.24
5	2.11	0.60	66.40	30.82
6	43.91	0.99	34.67	20.42

* Energy dispersive spectroscopy (EDS) results do not include Be since EDS cannot detect these light elements. Thus, the numbers are qualitative or relative amounts and do not sum to 100%.

SIMS Study of Au:Be/Pd/GaAs

The final study utilized a Cameca IMS 3f Ion Microanalyzer at ETDL. A focused Cs⁺ ion beam rastered a 125 μm x 125 μm sample surface with analytical data taken in the central 65% of the crater. The matrix masses were monitored following the cluster ions, Cs+Ga and Cs+As, in the positive secondary ion mode. A SIMS profile is given in Figure 4.

The surface is predominantly BeAu, with the modulation of each due presumably to an ion yield variation with the presence of oxygen in the near-surface region. Pd and Au form a eutectic upon annealing which is not the case when Be is absent. A BeAuPd region is then followed by an oxide with mixed low levels of Be, Pd and Au. A larger Pd peak exists at the GaAs surface. Out-diffusion of Zn is seen, but not out to the surface as is the case when Be is absent. The distribution of Zn is consistent with Figure 1. Some carbon is also seen at the BeAuPd/oxide interface.

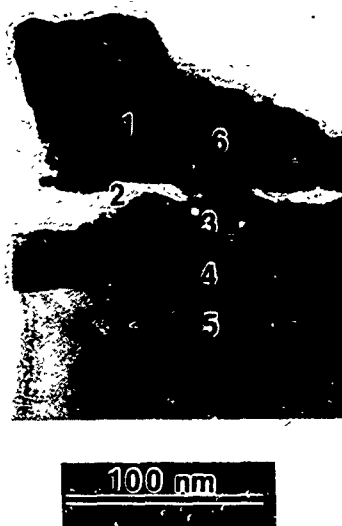


Fig. 3 Bright field TEM micrograph of a section of Au:Be/Pd/GaAs heated to 350°C for 15 min.

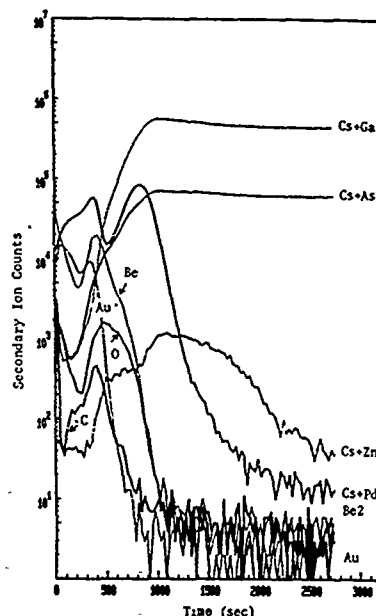


Fig. 4 SIMS profile of heated Au:Be/Pd/GaAs.

DISCUSSION AND CONCLUSIONS

Ohmic contacts to Zn-diffused p-GaAs using a Au:Be/Pd contact utilized Pd to improve adhesion and surface morphology while the Be served as a dopant for increased surface carrier concentration. Studies revealed a surface concentration of $2 \times 10^{20}/\text{cm}^3$, junction depth of $0.42 \mu\text{m}$, mobility of $48.9 \text{ cm}^2/\text{V-s}$ and sheet resistance of 92 ohms/sq . Contact resistance in the low $10^{-7} \Omega\text{-cm}^2$ range was measured by both TLM and CBK using 350°C anneals. AES analysis revealed a Be-oxide/Au/Pd/GaAs profile with little change after sintering of the contact. SIMS analysis revealed a BeAuO-region followed by BeAuPd and another oxide region. A strong Pd-peak was adjacent to the GaAs. TEM analysis showed a smooth boundary between metal and semiconductor with an absence of spiking. Phases rich in Au and Ga were observed at points 1, 2, 3 and 6. The interface region indicated by point 2 has an accumulation of Au at a level 50% less than in the above region and ~50% less than the amount of Ga in the same lateral area. Small amounts of Pd were also observed.

ACKNOWLEDGMENT

Financial support from Eastman Kodak Company and the Center for Electronic and Electro-optic Materials is gratefully acknowledged.

REFERENCES

1. M.J. Howes and D.V. Morgan, Gallium Arsenide Materials, Devices and Circuits, John Wiley and Sons, New York 1985.
2. J.L. Tandon, K.D. Douglas, G. Vendura, E. Kolawa, FCT So and M. Nicolet, Metallization Systems for Stable Ohmic Contacts, Proceedings from Materials Research Society 1985.
3. J.R. Shealy and S.R. Chin, *Appl. Phys. Lett.* **47**, 410 (1985).
4. R.C. Brooks, C.L. Chen, A. Chu, L. Mahoney, J. Mavroides, M. Manfra and M. Finn, *Elect. Dev. Lett.*, EDL-6, (10), 525 (1985).
5. C. Dupon-Chevallier, A. Duchenois, J. Breese, D. Ankri, *J. Appl. Phys.* **52**, 3783 (1986).
6. W.M. Loh, S.E. Swirhun, T.A. Schreyer, R.M. Swanson, and K.C. Saraswat, *IEEE Trans. Elec. Dev.*, ED-34, 512 (1985).

IMPROVED HOLE DIFFUSION LENGTHS IN BULK n-TYPE GaAs FOR HIGH EFFICIENCY SOLAR CELLS

D. WONG, T. E. SCHLESINGER AND A. G. MILNES

Department of Electrical and Computer Engineering, Carnegie Mellon University,
Pittsburgh PA15213

ABSTRACT

A method for wafer annealing which is effective in suppressing defects and raising minority carrier diffusion lengths in n-type bulk GaAs is described. The beneficial effect of the annealing is shown to be associated with the proximity surface with measurements of photoresponse as a function of depth. The concentration of the hole trap HCX ($E_v + 0.29\text{eV}$) varies as a function of depth from the surface, qualitatively, as might be expected of the concentration of the dominant recombination center in the material. The impact of improving the material in this manner on the performance of Zn diffused solar cells is demonstrated.

INTRODUCTION

Annealing can greatly alter the defect structure in bulk GaAs [1,2]. Given the correct anneal conditions, beneficial effects such as defect suppression [3], uniformity of electronic properties [4] and improved device performance [5] may be obtained. In earlier reports [6,7] we have shown that proximity wafer annealing of n-type GaAs in sealed quartz ampoules results in defect suppression and increases in hole diffusion length (L_p) of up to a factor of 3. Such improvements can be obtained in Liquid encapsulated Czochralski (LEC) and horizontal Bridgman (HB) wafers, regardless of choice of dopant (Si or Te) and independently of whether the material has been boule annealed. Deep level transient spectroscopy (DLTS) measurements of the defect structure in the specimens show that the dominant recombination center in bulk n-type GaAs manifests itself as a hole trap at $E_v + 0.29\text{eV}$ (HCX). In the present work we have further characterized the effects of proximity anneals in order to ascertain the nature of the mechanism responsible for the changes observed.

EXPERIMENTAL PROCEDURE

All the specimens discussed here were cut from wafers from the same crystal of Te-doped ($1 \times 10^{17} \text{ cm}^{-3}$) LEC GaAs. Annealing was done in evacuated ampoules made from high purity quartz tubing. The proximity annealed specimens were placed with their polished faces together during annealing. We have described the specimens which were not stacked with their polished faces protected in this manner during annealing as having had "exposed surface" anneals.

L_p in the specimens was determined using a cleaved diode electron beam induced current (EBIC) technique. Photoresponse measurements were made using the electrochemical cell unit from a commercial semiconductor profiler (Polaron 4100). Photocurrent was measured as a function of depth by making successive measurements on the same specimen following each of a sequence of chemical etches. For profiling of defect concentrations as a function of depth, several different pieces of each specimen were chemically etched for different lengths of time. p^+n junctions for characterization of minority carrier traps by DLTS were then fabricated by solid phase diffusion of Zn. Further details of the procedures used for material characterization are given elsewhere [6,8].

Solar cells were fabricated using a vapor phase Zn diffusion from a ZnGaAs source [9]. The two cells characterized in this work had been placed in the same quartz ampoule for the diffusion step to ensure that their junction depths were

essentially identical (about $0.2 \mu\text{m}$). A square gold grid served as the front surface metallization, and the active area ($5 \text{ mm} \times 5 \text{ mm}$) of each cell was defined by mesa etching in a 5:1:1 $\text{H}_2\text{SO}_4\text{:H}_2\text{O}_2\text{:H}_2\text{O}$ solution using a photoresist mask.

RESULTS

EBIC data obtained from proximity and exposed surface annealed specimens is shown in fig. 1. The control specimen was not given any wafer anneal, whereas the

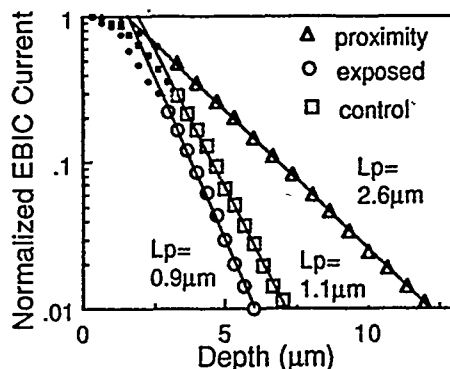


Fig. 1 : EBIC plots showing the effect of annealing on L_p . The control specimen had been given no wafer anneal, while the other specimens had been annealed for 16 hours at 950°C in the same ampoule.

other two specimens were annealed in the same ampoule for 16 hrs at 950°C . Proximity annealing results in substantial increases in hole diffusion length whereas exposed surface annealing does not.

Fig. 2 contains plots of electrochemical cell photoresponse as a function of depth for three specimens given 16 hour proximity anneals at 900°C , 950°C and 1000°C and a control specimen which had not been subjected to any wafer annealing. The photoresponse for the annealed specimens was in all cases higher than that for the control specimen, with the photocurrents being highest at the proximity surfaces of the annealed specimens and falling off with depth.

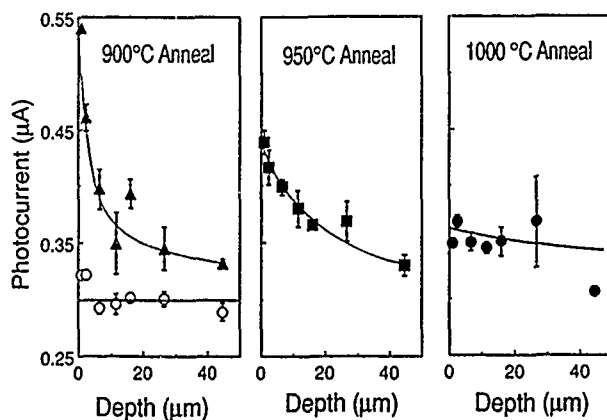


Fig. 2 : Electrochemical cell photocurrent as a function of depth for specimens given 16 hr proximity anneals at different temperatures. The open circles represent data from a control specimen which had not been wafer annealed.

DLTS measurements revealed the presence of three deep levels in the material used in the present work - a hole trap HCX ($E_v + 0.29 \text{ eV}$), and two electron traps ECX ($E_c - 0.34 \text{ eV}$) and EL2. ECX was reduced to below the DLTS detection levels by proximity annealing at 950°C for 16 hours. This anneal also resulted in decreases in the concentrations of HCX and EL2 and these are plotted in fig. 3 as a function of

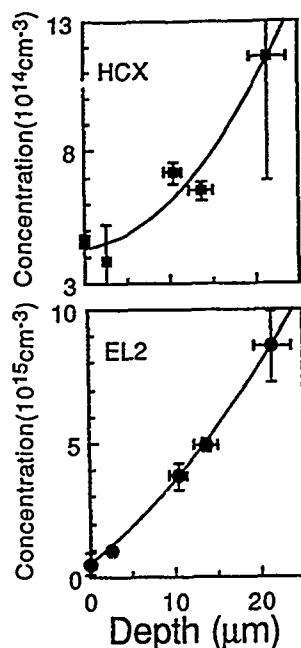
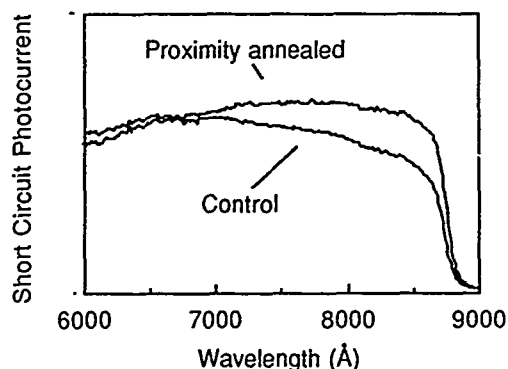


Fig. 3 : Defect concentrations as a function of depth from the (proximity) surface in a specimen given a 16 hr 950 °C proximity anneal.

Fig. 4 : Spectral response plots for two solar cells, one fabricated from proximity annealed (16hr 950°C) material and the other from material from the same crystal which had not been given any wafer anneal. The vertical axis is plotted in arbitrary current per photon units.



depth from the proximity surface.

To demonstrate a practical application of the anneal procedure, two solar cells were fabricated, one from a piece of the proximity annealed material and the other from a piece of material which had not been given any wafer anneal (control). The spectral response plots of these cells are shown in Fig. 4. The long wavelength response of the cell made from proximity annealed material is substantially higher than that of the cell made from material which had not been wafer annealed.

DISCUSSION

From fig. 1 it can be seen that it is necessary to provide proximity protection for the specimen surface to achieve increases in L_p . Annealing with the polished face exposed results in the introduction of a hole trap HCZ ($E_v + 0.57$ eV) at the surface [6]. This is probably the reason for the low hole diffusion length in such specimens.

The electrochemical cell photocurrent measurements are useful as a qualitative description of the L_p profiles as a function of depth since a larger photocurrent implies a larger L_p . From the photocurrent profiles it can be seen that the enhancement of L_p as a result of proximity annealing is associated with the proximity surface, and that this improvement extends some tens of micrometers into the bulk of the specimen.

There is evidence that the hole trap HCX is the center which controls the hole lifetimes in bulk n-type material [7,8]. The profile of HCX concentration as a function of depth (fig. 3) and the photoresponse profiles of fig. 2 are qualitatively consistent with HCX being the dominant recombination center in the material.

The HCX concentration close to the surface does not decrease monotonically

with increasing anneal time [6]. Fig. 3 shows that the photocurrent at the surface (0 μm depth) of specimens annealed for 16 hours at different temperatures decreases with increasing anneal temperature. These two experimental results suggest a situation involving a "limited source" diffusion process [10]. We propose the following model: The suppression of the dominant recombination center (HCX) occurs at the immediate surface of the specimen in the early part of the anneal. This is perhaps the result of changes in stoichiometry at the surface due to arsenic loss during the time that the ampoule is warming to its anneal temperature and the equilibrium arsenic overpressure in the ampoule is being built up. Once the equilibrium overpressure in the ampoule has been established, no further suppression of HCX occurs at the surface, and there is a net diffusion of HCX to the surface, driven by the concentration gradient of the defect. The diffusion coefficient of HCX rises with increased anneal temperature. Thus, the higher the anneal temperature, the more complete the redistribution of HCX for a given anneal time, and the profile showing a reduction in HCX extends further into the bulk of the material while the residual suppression of HCX in the immediate surface region (0 μm) is reduced.

CONCLUSIONS

A simple method of increasing hole diffusion lengths (L_p) in n-type bulk GaAs by proximity wafer annealing has been described. Hole diffusion lengths of up to 2.6 μm have been obtained in $1 \times 10^{17} \text{ cm}^{-3}$ doped material, and the impact of improving the material in this manner on the performance of Zn diffused GaAs solar cells has been demonstrated. The beneficial effect of the anneal treatment is associated with the proximity protected surface, and extends several micrometers into the bulk of the material. The mechanism responsible for the increases in diffusion length is associated with a "limited source" diffusion process. The concentration-depth profile of the hole trap HCX ($E_v + 0.29\text{eV}$) in proximity annealed specimens is consistent with this trap being the dominant recombination center in bulk n-type GaAs.

ACKNOWLEDGEMENTS

This work was supported by a Solar Energy Research Institute contract, number XB-6-06005-3.

REFERENCES

1. S. Y. Chiang and G. L. Pearson, J. Appl. Phys. **46**, 2986 (1975).
2. M. Kuzuhara and T. Nozaki, J. Appl. Phys. **59**, 3131 (1986).
3. Zhao-Qiang Fang, T. E. Schlesinger and A. G. Milnes, J. Appl. Phys. **61**, 5047 (1987).
4. A. K. Chin, I. Camlibel, R. Caruso, M. S. S. Young, and A. R. von Neida, J. Appl. Phys. **57**, 2203 (1985).
5. Hilda Kander and D. C. Wang, IEEE Electron Dev. Lett. **EDL-8**, 263 (1987).
6. D. Wong, T. E. Schlesinger and A. G. Milnes, to appear in Solar Cells.
7. D. Wong, T. E. Schlesinger and A. G. Milnes, presented at the International Conference on the Science and Technology of Defects in Semiconductors, Yokohama, Japan, 1989.
8. D. Wong, H. K. Kim, Z. Q. Fang, T. E. Schlesinger and A. G. Milnes, J. Appl. Phys. **68**, 2002 (1989).
9. H. C. Casey Jr. and M. B. Panish, Trans. Metallurgical Soc. - AIME **242**, 406 (1968).
10. Sorab K. Ghandi, VLSI Fabrication Principles (Wiley-Interscience, New York, 1983), pp. 143-146.

THE STUDY OF CONTAMINATION OF CARBON, BORON, AND OXYGEN IN LEC-GaAs

Y. Itoh, M. Takai*, H. Fukushima**, and H. Kirita**

The Institute of Physical and Chemical Research, Hirosawa, Wako,
Saitama 351-01, Japan

*Faculty of Engineering Science, Osaka University, Toyonaka,
Osaka 560, Japan

**Japan Analysis Center, Sannou, Chiba 281, Japan

ABSTRACT

Carbon in LEC GaAs was found to be introduced as CO from the ambient atmosphere; the oxygen concentration in the crystals decreased with increase in the duration of melting. An equilibrium segregation coefficient of oxygen in GaAs crystals was found by charged particle activation analysis to be 0.1, the value of which was smaller by a factor of 3~4 than that reported before.

INTRODUCTION

It is important to control and suppress residual impurities such as carbon, boron and oxygen in a LEC-GaAs crystal[1]. To date, however, the role of such impurities in the crystal has not been clarified because of the lack of accurate and precise analytical methods for the determination of such impurities.

In this study, the concentrations of carbon, boron and oxygen in LEC(Liquid Encapsulated Czochralski)-GaAs by a newly modified CPAA(charged particle activation analysis) method[2,3]. In the case of the LEC method, usually, the molten GaAs is covered with a boric oxide encapsulant in pyrolytic BN crucible, and heated by a graphite heater. In this case, carbon, boron and oxygen get into or out of the GaAs melt, and are not segregated into the GaAs crystal according to the normal freezing process. Therefore, it is difficult to estimate the behavior of these impurities, such as segregation during LEC processes. However, the segregation behavior of carbon, boron and oxygen is important to control these concentrations in LEC GaAs crystal. We investigated the incorporation of carbon and the equilibrium segregation coefficients of carbon, boron and oxygen in the GaAs crystal. The reactions used were $^{12}\text{C}(\text{d},\text{n})^{13}\text{N}$, $\text{natB}(\text{d},\text{xn})^{11}\text{C}$ and $^{16}\text{O}(\text{He}, \text{p})^{18}\text{F}$ for carbon, boron, and oxygen, respectively.

EXPERIMENTAL PROCEDURES

Sample preparation

The samples used were LEC-GaAs crystals pulled from a melt of 99.99999 % arsenic and 99.9999 % gallium in a pyrolytic BN(boron nitride) crucible. Three different parameters were used under following conditions : different ambience of CO concentrations; different melting durations; for segregation coefficients, the GaAs ingot was cooled down rapidly at the solidified fraction of 0.5 and cut from the tail portion of the GaAs single crystal ingot and the remainder. Samples were cut in the shape of rectangular plates (20 x 20 x 1 mm³), and the surfaces of their <100> planes were mirror-polished.

Establishment of Conditions in C, B and O Analysis

Samples were bombarded for 10 min with a deuteron beam (8 MeV, 5 μ A) for carbon and boron, and 60 min with a helium ($^3\text{He}^{++}$) beam (12 MeV, 5 μ A) for oxygen from the cyclotron at the Institute of Physical and Chemical Research. The reactions used were $^{12}\text{C}(\text{d},\text{n})^{13}\text{N}$ (9.98 min half life), $^{10}\text{B}(\text{d},\text{xn})^{11}\text{C}$ (20.4 min half life), and $^{16}\text{O}(\text{He},\text{p})^{18}\text{F}$ (109.8 min half life) for C, B, and O, respectively. The surface of the bombarded sample (15 μm thickness) was removed by etching with $\text{H}_2\text{SO}_4\text{-H}_2\text{O}_2\text{-H}_2\text{O}$ for the elimination of the surface contamination.

Separation of Carbon(^{13}N) and Boron(^{11}C):

The bombarded sample was fused with copper drops in a helium stream by radio-frequency heating, and the stream was passed through a heated CuO column, an Ascarite column, and a heated titanium sponge column. The experimental conditions for the quantitative separation of ^{13}N and ^{11}C in pure states were as follows; flow rate of helium gas, which carried ^{13}N and ^{11}C , 100 ml min^{-1} . The fusion temperature was 1500 $^\circ\text{C}$. The length of the titanium sponge column with 0.6 cm diameter was 1.5 cm and temperature was 830 $^\circ\text{C}$. The ^{13}N trapped in the titanium sponge and ^{11}C trapped in Ascarite were measured by a pair of BGO detectors operated in coincidence and an NaI well-type detector, respectively. Graphite and B_2O_3 plates were used as the activation comparators.

Separation of Oxygen(^{18}F)

The separation method of ^{18}F was improved from our previous method[2,3] as shown with double parentheses in Fig. 1. Moreover a suction pump is used in all filtration procedures. In order to prevent the adsorption of ^{70}As and ^{72}As into KBF_4 precipitate, arsenite as a hold-back carrier was added. The filter paper of TOYO No.5C was changed for membrane filter of 0.45 μm pore size. Resultantly, the decay curve of ^{18}F agreed

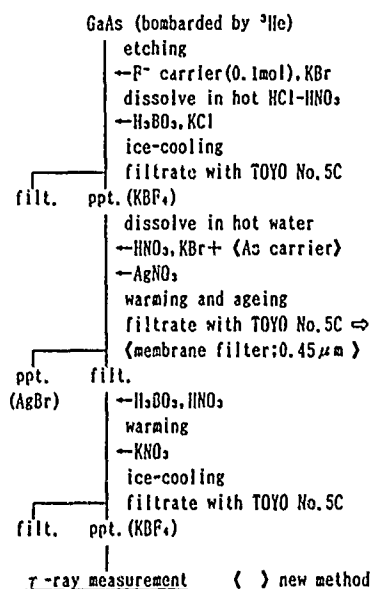


Fig.1 Scheme of chemical separation for ^{18}F

with a half life of 109.8 min. As an activation comparator, quartz plate was used.

RESULTS AND DISCUSSION

Carbon and oxygen concentration

Figure 2 shows the decay curves of ^{13}N and ^{11}C separated from GaAs, indicating complete radiochemical purity for carbon and boron. As for the separation of ^{18}F for the oxygen concentration of lower than 10^{15} atoms cm^{-3} , radiochemical impurities were difficult to be ignored previously. Therefore, the procedure of the separation for ^{18}F from GaAs was newly improved as shown in Fig. 1. As a result of this improvement, the decay of the activity in a precipitate of KBF_4 agrees with a half life of ^{18}F , 109.8 min as shown in Fig. 3. The reliabilities and the detection limits of the determination of carbon, boron, and oxygen in a GaAs crystal by CPAA are shown in Table I.

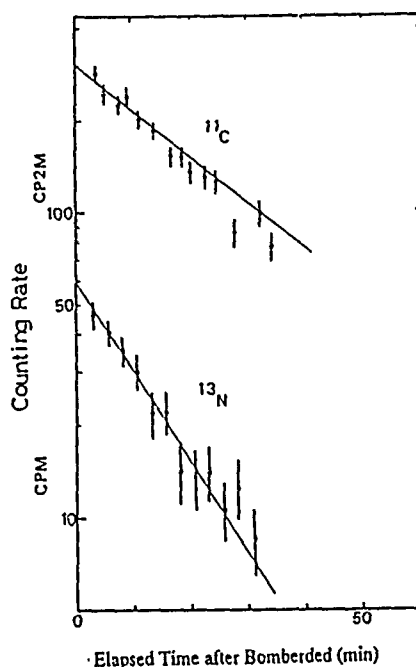


Fig. 2 Decay curves of ^{13}N and ^{11}C separated from GaAs

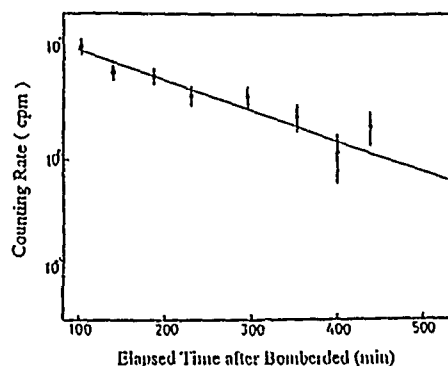


Fig. 3 Decay curves of ^{18}F separated from GaAs

Table I. Detection limit and reliability of determination of C, B, and O in LEC-GaAs

Element	Detection limit atoms $\cdot \text{cm}^{-3}$	Reliability
C	$\sim \times 10^{15}$	$\pm 10 \%$
B	$\sim \times 10^{15}$	$\pm 10 \%$
O	$\sim \times 10^{14}$	$\pm 20 \%$

Figure 4 shows the carbon concentration in LEC-GaAs as a function of CO concentration in a furnace. The open circles show the value from CPAA. The solid circles show the value obtained from infrared (IR) spectrophotometry. The carbon concentration increases with increase in CO concentration in a furnace. This result suggests that carbon in the crystal was introduced with a form of CO from a graphite heater in the furnace.

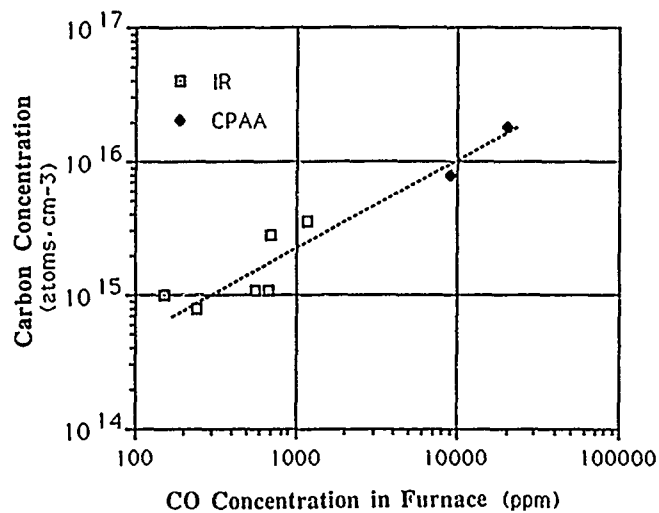


Fig.4 Carbon Concentration in LEC-GaAs versus CO concentration in a furnace

The concentrations of oxygen in GaAs crystal pulled at different melting durations were determined to study the behavior of oxygen in LEC-GaAs crystal. Fig. 5 shows the oxygen concentration as a function of melting duration during LEC-processes. The scatter in data points presumably arises from different ingots origin. The oxygen concentration in LEC-GaAs decreases with increase in melting duration.

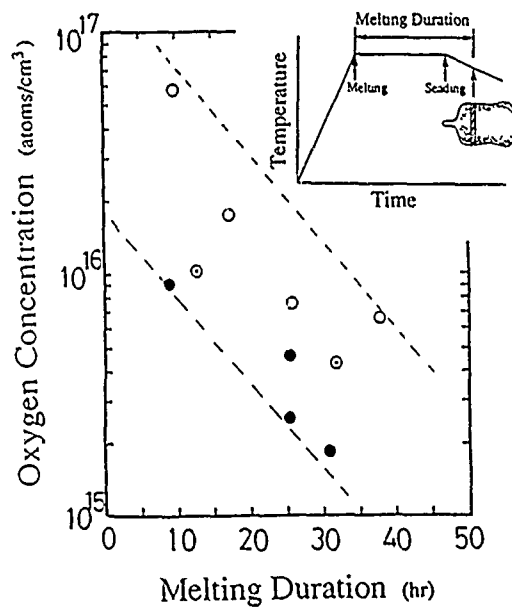


Fig. 5 Oxygen concentrations versus melting duration

Equilibrium segregation coefficient (k_0)

The equilibrium segregation coefficient (k_0) can be obtained from the impurity concentrations of the tail portion (C_s) and the remainder (C_L), i.e. $k_0 = C_s/C_L$. Carbon and boron concentrations were measured by FTIR[4] and SIMS, respectively, calibrated by our CPAA method. Oxygen concentration was directly determined by CPAA method. Table II shows the results of the impurity analysis and the equilibrium segregation coefficients of carbon, boron and oxygen, i.e. k_0 of 2 for carbon, k_0 of 1~4 for boron and k_0 of 0.06~0.13 for oxygen. Recently, Clemans and Conway reported the segregation coefficient of carbon as k_0 of 2.1 ± 0.6 using the GaAs crystal grown by the vertical gradient freeze (VGF) growth method[5]. The good agreement of the segregation coefficient for carbon suggests that our method for the determination of the equilibrium segregation coefficients of boron and oxygen in LEC-GaAs crystal is reliable. The value for oxygen obtained by our direct measurements was smaller by a factor of 3~4 than that reported before[6]. Since the previous value was the segregation coefficient of oxygen in GaAs crystal grown by a HB(Horizontal Bridgman) method, oxygen decomposed from As_2O_3 and gallium melt in quartz ampoule reacts with silicon and oxygen. Then, residual excess oxygen can distribute at the crystal-melt interface by segregation, and oxygen is incorporated into the crystal according to the normal-freeze equation[7]. Borisova et al.[8] reported K_{eff} of 0.13 obtained by extrapolating their data to the melting temperature of GaAs, 1238 °C, but detailed growth and doping parameters were not known. Therefore, The present value of 0.06~0.13 seems to be a directly measured and credible value for LEC-GaAs crystal.

Table II. Segregation coefficients for a carbon, boron, and oxygen

Impurity	Method	Concentration (atoms/cm ³)	Segregation Coefficient
Carbon	FTIR	Crystal 1.0×10^{14}	2
		Remainder 0.4×10^{15} 0.5×10^{15}	
Boron	SIMS	Crystal 2.8×10^{16} 2.9×10^{16}	1 ~ 4
		Remainder 6.1×10^{15} 2.2×10^{16}	
Oxygen	CPAA	Crystal 7.2×10^{15} 1.1×10^{16}	0.06 ~ 0.13
		Remainder 8.6×10^{16} 9.1×10^{16} 1.3×10^{17}	

CONCLUSIONS

1. High sensitive determination of carbon, boron and oxygen in LEC-GaAs by CPAA. ($\sim 10^{15} \cdot \text{cm}^{-3}$ for carbon and boron, $\sim 10^{14} \cdot \text{cm}^{-3}$ for oxygen) was established.
2. Carbon was incorporated in LEC-GaAs as CO from the ambient.
3. Oxygen concentration decreased with melting duration.
4. Segregation coefficient of oxygen was found by direct CPAA to be 0.06~0.13, the value of which was smaller by a factor 3~4 than that reported before.

ACKNOWLEDGMENTS

Authors wish to thank Mr. K. Ogiwara for operating the cycrotron accelerator for this work.

REFERENCES

1. L. B. Ta, H. M. Hobgood, A. Rehatgi, and R. N. Thomas, J. Appl. Phys. 53, 5771 (1982).
2. Y. Itoh, Y. Kadota, T. Nozaki, H. Fukushima, and K. Takeda, Jpn. J. Appl. Phys. 28, 210 (1989).
3. H. Fukushima, T. Kimura, H. Hamaguchi, T. Nozaki, Y. Itoh, and Y. Ohkubo, J. Radioanal. Nucl. Chem. Artic., 112, 415 (1987).
4. Y. Kadota, K. Sakai, T. Nozaki, Y. Itoh, and Y. Ohkubo, Semi-Insulating III-V Materials (Ohmusha, Tokyo, 1986) p. 201.
5. J. E. Clemans and J. H. Conway, Conf. on Semi-Insulating III-V Materials (Ohmusha, Tokyo, 1988) p. 28.
6. K. Shikano, K. Kobayashi, and S. Miyazawa, Appl. Phys. Lett. 46, (4), 391 (1985).
7. W. R. Wilcox, in Fractional Solidification, edited by M. Zief and W. R. Wilcox (Mar Dekker, 1967), Chap. 3, p. 69.
8. L. A. Borisova, Z. L. Akkermann, and A. N. Dorokhov, Neorg. Mater. 13, 908 (1977).

IN-SITU SYNTHESIS AND MAGNETICALLY STABILIZED KYROPOULOS GROWTH OF UNDOPED INDIUM PHOSPHIDE

STEPHEN BACHOWSKI, BRIAN S. AHERN, & ROBERT M. HILTON, Rome Air Development Center, Hanscom AFB, MA 01731; AND JOSEPH A. ADAMSKI, Parke Mathematical Laboratories, Carlisle, MA 01741

Abstract

The Kyropoulos growth technique has been combined with in-situ synthesis to yield high purity undoped crystals of 300 to 700 gm charges of InP. Etched wafers show a uniform dislocation density across 70mm diameter in contrast with the "W" pattern created by LEC. Use of an axial magnetic field in Kyropoulos growth reduces the dislocation density by an order of magnitude, to $1 \times 10^4 \text{ cm}^{-2}$. By combining Kyropoulos growth with in-situ synthesis of the indium phosphide, high mobility (4.6×10^4 at 77 C) undoped single crystals have been obtained.

Introduction

High purity low dislocation density indium phosphide is becoming an increasingly important substrate material for optoelectronic devices. High mobility indium phosphide can be obtained by in-situ synthesis. Low and uniform dislocation density wafers may be obtained by magnetic liquid encapsulate Kyropoulos growth.

The vapor pressure of phosphorus (27.5 atm) at the melting point of InP (1070 C) [1] presents a major obstacle to obtaining stoichiometric charges. Several methods have been employed to obtain stoichiometric polycrystalline InP. The two best known synthesis routes are enclosing indium and phosphorus in a sealed ampoule within a horizontal pressure furnace and using a very high pressure autoclave systems [2,3]. These methods result in polycrystalline InP ingots which are then remelted for use in Czochralski growth.

In-situ synthesis yields purer material but is complicated by the fact that phosphorus changes phase when it is heated. Red phosphorus sublimates as yellow phosphorus which is highly unstable and tends to explode on reheating. Farges attempted to overcome this problem by using a dual heating system for his injector and crucible [4]. We have chosen to modify an approach first used by CrystaComm, Inc [5], in which a quartz container holds the phosphorus and injects it into the indium.

Liquid Encapsulated Czochralski (LEC) is currently the dominant method for growth of InP boules. However, because of convection currents in the melt and a large thermal gradient near the B_2O_3 /gas interface, LEC growth of III-V materials tends to result in high dislocation densities. The vertical gradient freeze (VGF) method has been used to surmount these problems [6], but in-situ synthesis prior to crystal growth is difficult.

We are exploring the Liquid Encapsulated Kyropoulos (LEK) technique [7,8] because it combines many of the attractive features of LEC and VGF growth. Like LEC, LEK is top-seeded, so in-situ synthesis followed by crystal growth is practical. Like VGF, LEK is not characterized by large thermal gradients:

the LEK crystal is never pulled through the B_2O_3 encapsulant.

Experimental

Undoped indium phosphide crystals were grown by the Czochralski and Kyropoulos techniques with and without axial magnetic field stabilization. InP charges were prepared by injecting phosphorus into an indium melt. Typically, 110gm of red phosphorus is placed into a quartz injector. The phosphorus is then injected into 300gm of indium. Thus, the InP charge was not exposed to outside contamination before growth. A pressure of 550 psi of nitrogen over boron oxide was maintained during crystal growth to compensate for the high vapor pressure of the phosphorus. A uniform axial 2 KGauss magnetic field was employed to promote melt stability. A (111) seed was used in all cases; the fused silica crucible was 70mm in diameter and 80mm deep.

Liquid Encapsulated Kyropoulos (LEK) and the associated Magnetic Liquid Encapsulated Kyropoulos (MLEK) use the same furnace configuration as LEC. However, LEK differs from LEC in that the crystal is crowned off to the sides of the crucible and then directionally cooled. The crown is kept as flat as possible so the crystal is not removed from the encapsulant. Keeping the melt interface below the encapsulant results in a lower thermal gradient than in LEC and minimizes loss of phosphorus.

In order to compare growth techniques, care was taken to maintain similar environment for both Czochralski and Kyropoulos growth. Thus, for LEC and MLEC the pull rate was 12 mm/hr with counter-rotation of 4 rpm for the seed and crucible. For LEK and MLEK, the seeded crystal and susceptor were slowly moved together out of the hot zone at a rate of 12 mm/hr with synchronous rotation of 4 rpm. A 1 cm thickness of dry boron oxide was used as the encapsulant.

Wafers were sliced to 30 mils and mechanically polished, using 15 micron diamond polish. The resulting wafers were chemically polished using a 1% bromine/methanol solution. Dislocations were revealed by applying Hubers Etch for 2 minutes on the (111) face of the crystals [9]. Dislocation densities were determined by taking a series of photographs across the face of the wafer using Nomarski Interference Contrast Microscopy. A four point Hall measurement technique was used to determine carrier density and mobility.

Our first goal was to achieve stoichiometric charges. Temperature and overpressure are the main control variables. The phosphorus must reach a critical temperature, its vapor pressure inside the injector is sufficient to overcome the pressure inside the furnace. The injector is radiatively heated by the crucible. At an overpressure of 500psi, phosphorus loss from the InP through the boron oxide was a problem. The pressure inside the furnace was therefore raised to 600 psi and the injector was insulated so less direct heat would be required. Once the injector is lowered into the top of the indium layer, phosphorus begins to transport. The rate of injection is controlled by lowering the injector deeper into the charge, providing a steady increase in injector temperature. Finally, when the injector touches bottom and it reaches a constant temperature, the furnace chamber overpressure is reduced by 30-50 psi. The remaining phosphorus

inside the injector now has a higher vapor pressure than the external environment and more phosphorus is forced into the melt. The entire injection takes about 30-40 minutes.

Observation of the melt interface was difficult because of particulates in the boron oxide. Upon isolating these particulates, analysis determined the brownish powder to be an oxide of indium. Our previous research suggested that this might be a contaminant in the indium.[10] Therefore, we used indium which was vacuum packed on shipping and found no particulates in the boron oxide layer. Seeding and single crystal growth became much more reproducible.

Results and Discussion

Our first LEK crystals had much larger dislocation densities than LEC crystals of the same size. This surprising result was due to pressure build-up from the expansion of InP on solidification [11]. A capillary-sized hole was machined in the bottom of the crucible, permitting excess liquid InP to bleed out of the crucible as the LEK crystal grew.

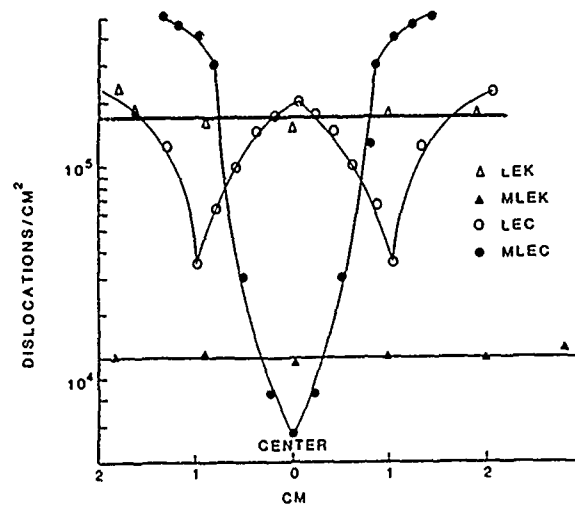
Figure 1 compares the dislocation profiles for (111) wafers from the middle of boules for LEC, MLEC, LEK and MLEK. The LEC wafers shows the expected 'W' pattern with dislocation densities comparable to densities in commercial wafers. The 70mm LEK wafers have dislocation densities comparable to those of LEC crystals but the distribution for LEK is nearly uniform across the wafer. Application of an axial magnetic field lowered the dislocation density by an order of magnitude, while preserving the uniform distribution.

We attribute the lower dislocation densities in MLEK crystals to the reduction in small scale turbulence of the melt at the solid/liquid interface. The uncontrolled fluctuations in temperature and composition may have been reduced below a critical, but as yet undetermined value for nucleation of dislocations. The uniformity in dislocation density results from lower thermal gradients

Table 1 shows mobility data obtained for our crystals. Runs 1 - 4 were grown from poly charges prepared from our in-house synthesized InP. The material was premelted to combine charges and handled before growth. Runs 5 - 6, in-situ growth runs, resulted in higher electron mobilities. Runs 7-8, in-situ runs using vacuum packed indium, yielded the highest mobilities.

Conclusion

Kyropoulos growth of InP has been shown to give uniform dislocation patterns. Addition of a 2 KGauss axial magnetic field lowered the dislocation density by an order of magnitude. This technique has potential for producing wafers having very low uniform dislocation densities that will be required for advanced electronic devices. Dislocation densities comparable to VGF should be possible by further reducing the thermal and mechanical stress. Future work will be directed at improving our hot zone and refining growth parameters.



SAMPLE	RT MOBILITIES		CARRIER CONC	
	77	77	77	77
1. LEK	3100	6100	4.3×10^{16}	3.1×10^{15}
2. LEC	3100	16000	6.1×10^{15}	4.1×10^{15}
3. MLEC	3300	16000	5.3×10^{15}	9.1×10^{15}
4. MLEK	3300	8800	1.9×10^{16}	1.4×10^{16}
5. LEC	2900	39000	6.1×10^{15}	3.3×10^{15}
6. MLEC	4000	40000	4.1×10^{15}	2.9×10^{15}
7. LLK	3900	46000	3.5×10^{15}	2.4×10^{15}
8. MLEK	3300	45000	4.1×10^{15}	2.3×10^{15}

FIGURE 1 (top): DISLOCATIONS ALONG (111) PLANE FOR INDIUM PHOSPHIDE

TABLE 1: (bottom): HALL MEASUREMENTS

References

- ¹K.J. Bachman and E. Buchler, J. Electrochem Soc, 121 (1974) 835.
- ²W.A. Bonner, J. Crystal Growth, 54 (1981) 21.
- ³J.E.Wardill d.J. Dowling S.F.Lovett, D.A.E. Crouch and A.J.Thompson, in: Proc. 1980 NATO Sponsored InP Workshop, 1980, p 65.
- ⁴J.P. Farges, J. of Crystal Growth, 59 (1982) pp. 665-668.
- ⁵CrystaComm, Inc, Final Technical Report N00014-82-C-2372 to Naval Research Laboratory, "Development of High Purity InP Crystals", September 1983.
- ⁶J. E. Clemans, W. A. Gault and E. M. Monberg, AT&T Technical Journal, 65, Jul 1986, pp. 86-97.
- ⁷Marc Duseaux, J.of Crystal Growth, 61, (1983) pp. 576-590.
- ⁸G. Jacob, J.of Crystal Growth, 58, (1982) pp. 455-459.
- ⁹V.M.Glazov, S.N. Chizhevskaya, and S.B.Evgen'ev, Russian Journal of Physical Chemistry, 43, (2) 1969 p. 201-205.
- ¹⁰J. Adamski, J. of Crystal Growth, 64, 1983 pp. 1-9.
- ¹¹G.T. Brown, B. Cockayne and W. R. MacEwan The Institute of Physics Conference Series No. 60; Section 7, April 1981.

DEEP-LEVEL DOMINATED CURRENT-VOLTAGE CHARACTERISTICS OF NOVEL SEMICONDUCTOR HETEROSTRUCTURES

K. DAS, Department of Materials Science and Engineering, North Carolina State University, Raleigh, North Carolina 27695-7907

ABSTRACT

Current-voltage characteristics of Au contacts formed on buried implanted oxide silicon-on-insulator structures and molecular beam epitaxially grown GaAs on (10 $\bar{1}2$) sapphire and silicon-on-sapphire substrates indicate that the dominant transport mechanism in these films is space-charge-limited current conduction in the presence of deep-level states. The deep-level parameters, determined using an analysis of the current-voltage characteristics, appear to be sensitive to the nature of crystallographic defects present in the grown layers. Conduction in the GaAs film on SOS was dominated by one discrete state located $\sim 0.28\text{eV}$ below the conduction band-edge, which is close to the E1 center uniquely observed in the molecular beam epitaxially grown GaAs-on-Si. Discrete levels are also observed in annealed buried implanted oxide silicon-on-insulator films. In contrast, the GaAs films deposited directly on (10 $\bar{1}2$) sapphire substrates and rapid-thermally annealed high-dose As implanted buried oxide SOI films appear to have a continuous distribution of states. The distributed states in GaAs films deposited directly on sapphire probably arise from the electrical activity of the double-position boundaries present in this material system.

INTRODUCTION

Heteroepitaxial GaAs films have received a great deal of attention for the potential monolithic integration of optoelectronic and electronic devices [1]. The advantages of insulating sapphire and silicon-on-insulators (SOI) such as silicon-on-sapphire (SOS) and buried implanted oxide structures in silicon are potentially numerous and include: (1) dielectric isolation, (2) extreme radiation hardness, and (3) the excellent physical and optical transmission properties afforded by sapphire.

The present study involves an assessment of the electrical characteristics of the material systems utilizing photolithographically-defined metal-semiconductor contacts. The current-voltage (I-V) characteristics of these contacts indicate that the dominant transport mechanism is space-charge-limited current conduction and is influenced by the presence of deep-level states. An analysis of the I-V characteristics has been employed to determine the position and concentration of the deep states in implanted oxide SOI and heteroepitaxial GaAs films deposited on (10 $\bar{1}2$) sapphire and silicon-on-sapphire (SOS) substrates. The procedure, as outlined below, can serve as a technique for the rapid electrical assessment of the films prior to device fabrication.

EXPERIMENTAL PROCEDURE

GaAs films have been grown directly on (10 $\bar{1}2$) sapphire and commercially-available chemical vapor deposited (CVD) (100) silicon-on-sapphire (SOS) substrates by molecular beam epitaxy (MBE) under identical growth conditions [2]. The native oxide present on the SOS sample was desorbed by heating the substrates to a temperature of 800°C for 20 minutes. The substrate temperature was then lowered to 515°C and an As primer prelayer deposited. After the initial growth of a thin layer of GaAs at this temperature, the growth sequence was interrupted. The temperature was increased to 625°C and the epitaxial layer annealed for 10 minutes in an As overpressure. Growth was then resumed at a temperature of 600°C with a V/III ratio of 10 and silicon doping calibrated to yield $\sim 10^{17}\text{cm}^{-3}$ carrier concentration. Subsequent deposition was carried out for a period of 2 hours with fluxes established for a growth rate of 1 $\mu\text{m/hr}$, estimated for homoepitaxial GaAs layers.

A buried oxide layer was formed in a 100 mm diameter, 3-4 $\Omega\text{-cm}$, n-type nominally (100) silicon wafer by implanting $1.7 \times 10^{18}\text{cm}^{-2}$ oxygen ions at 150 KeV using an Eaton NV-200 high current oxygen implantation system. The substrate was maintained at a temperature of 570°C during implantation. Following an RCA cleaning step, the implanted wafer was capped

with a 2500Å thick layer of low temperature CVD SiO₂. Several small samples of 1 cm² were cut from the wafer and subsequently annealed at a temperature of 1200°C for 3 hr in a nitrogen ambient. One sample was also annealed for 10 min at 1200°C. Following the anneal, the capping oxide layer was removed by etching in a buffered HF solution. Some of the annealed samples were implanted with two different doses of As, viz. 1.5X10¹²cm⁻² and 6X10¹³cm⁻² both at 60 KeV. The implanted As was activated by rapid thermal annealing (RTA) at 1050°C for 10s.

A layer of gold ~2000Å in thickness was deposited by thermal evaporation on the samples to form a metal-semiconductor contact. By employing photolithography and gold etching in a solution of 4g KI + 1g I₂ + 40ml H₂O, 100 μm diameter active device areas were delineated. These active devices were separated from the field region by a 100 μm wide annular ring. The structure of these devices were similar to those reported by Ioannou et al. [3]. A measurement of current-voltage between the active device and the field region was carried out using an HP 4145A semiconductor parameter analyzer. Capacitance measurements at 1MHz were carried out using a Keithley 590 CV analyzer.

RESULTS AND DISCUSSION

Extensive microstructural and optical analysis that has been reported elsewhere indicates that the heteroepitaxial GaAs films deposited on silicon-on sapphire are superior to those layers grown directly on (1012) sapphire [2]. In particular, threading dislocations, microtwins and antiphase domain boundaries (APBs) are the predominant defects observed in the (100) GaAs epitaxial films grown on SOS. In contrast, threading dislocations, microtwins and the formation of double-position boundaries (DPBs) were observed in the (111) GaAs films grown on (1012) sapphire.

The current-voltage characteristics of the metal-semiconductor contacts fabricated on the GaAs layers shown in Figs. 1 (a) and 2 (a) exhibit asymmetric (rectifying) behavior. Diode polarities in the GaAs film grown on SOS indicate the presence of small p-type areas in a nominally n-type film. In contrast, the GaAs film grown on sapphire appeared to be high resistivity p-type which was verified directly from room-temperature Hall measurements. Interestingly, Hall measurements at 77K showed the GaAs film on sapphire to switch to n-type conductivity [2]. In logarithmic plots of the forward characteristics (Figs. 1(b) and Fig. 2 (b)), an ohmic slope at low biases is an indication of non-thermionic behavior. In particular, the features in the I-V characteristics strongly indicate a space-charge-limited current (SCLC) conduction mechanism in the presence of deep-level states at higher biases.

The transition from an ohmic regime to a sharply rising current regime is an indication of deep traps. A sharp rise to a true SCLC level is obtained when all the deep traps are filled, the voltage at which this occurs is designated by V_{TFL}, where TFL denotes the trap-filled-limit. The hole occupancy of the traps or the concentration of traps not occupied by electrons, p_{to}, is obtained from the experimentally determined V_{TFL} and is given by [4]

$$V_{TFL} \approx \frac{qp_{to}L^2}{\epsilon\epsilon_0} \quad (1)$$

where, L is the thickness of the active region, determined from the measured zero-bias capacitance, (assuming that parallel plate capacitors having the same area as the contact dots were formed), q is the electronic charge, ε is the dielectric constant, and ε₀ is the permittivity of free space. The effective carrier concentration in the active region of the device, n₀, is given by the approximate relation [4]:

$$\frac{J(2V_{TFL})}{J(V_{TFL})} \approx \frac{p_{to}}{n_0} \quad (2)$$

where J is the current density at the designated voltage. From the value of n₀ the effective position of the Fermi level can be estimated. The position of the deep level is taken as being

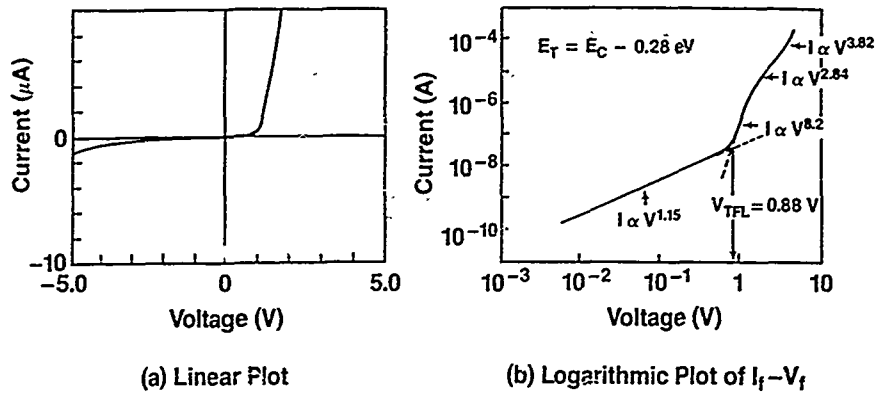


Fig. 1. Current-voltage characteristics of Au contacts fabricated on GaAs films on SOS.

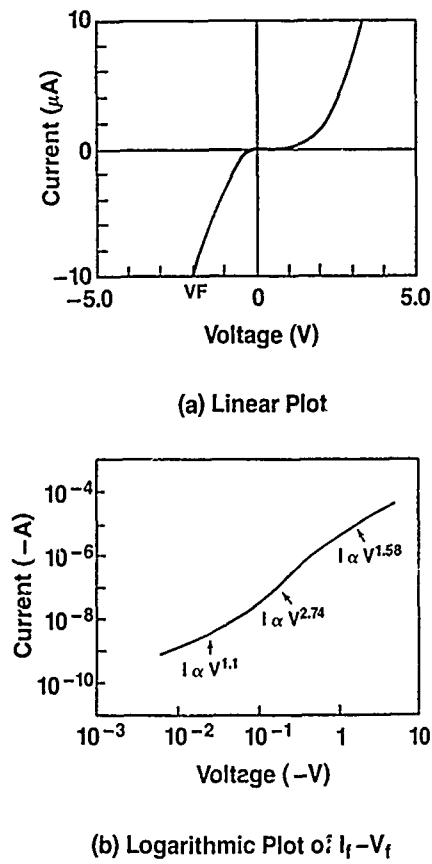


Fig. 2. Current-voltage characteristics of Au contacts fabricated on GaAs films on $(10\bar{1}2)$ sapphire. The change in polarity for the film on sapphire indicates p-type conduction.

close, within kT , to the effective Fermi level [4]. Concentration of the unoccupied states, located approximately at the estimated Fermi level will be given by p_{10} . The I-V characteristics of the film deposited on the SOS substrates ($L=2.45 \times 10^{-3}$ cm) analyzed in this manner indicate the effect of one discrete deep-level located 0.28 eV below the conduction band-edge, which is close to the E1 center unique to MBE grown GaAs-on-Si [5]. Corresponding effective carrier concentrations and concentrations of unoccupied traps in these samples are of the order of 10^{13} cm^{-3} and 10^{16} cm^{-3} , respectively.

For the implanted oxide SOI, the I-V characteristics (Fig. 3 (a) and (b)) of the samples annealed at 1200°C indicate the effect of one discrete deep-level located 0.33 eV and 0.37 eV below the conduction band-edge in the 10 min ($L=6.8 \times 10^{-3}$ cm) and the 3 hr ($L=2 \times 10^{-4}$ cm) annealed samples, respectively. Corresponding carrier concentrations and concentrations of unoccupied traps in these samples are of the order of 10^{13} cm^{-3} and 10^{15} cm^{-3} , respectively, however for the longer anneal time lower values were obtained. The sample implanted with $1.5 \times 10^{12} \text{ cm}^{-2}$ As yields a carrier concentration of $\sim 2 \times 10^{15} \text{ cm}^{-3}$ and unoccupied trap concentration of $\sim 6 \times 10^{16} \text{ cm}^{-3}$ located 0.25 eV below the conduction band-edge.

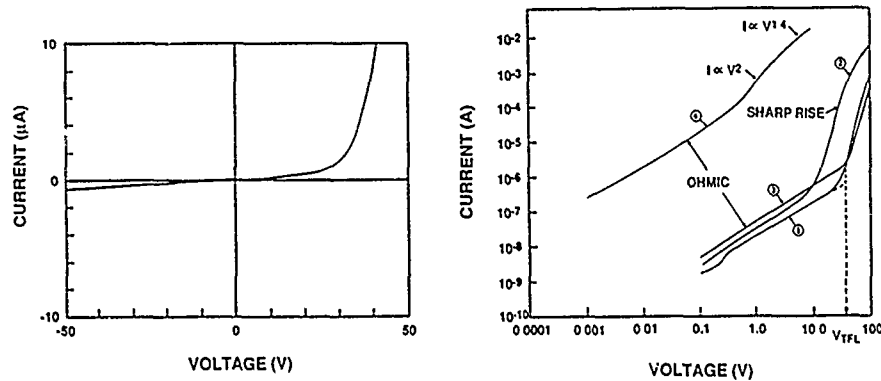


Fig. 3. Current-voltage characteristics of Au contacts on fabricated on buried implanted oxide SOI. (a) Linear I-V plot for sample annealed for 10 min at 1200°C . (b) Log-log plots of the forward characteristics: 1. 1200°C , 10 min anneal; 2. 1200°C , 3 hr. anneal; 3. 1200°C , 3 hr + low dose As ion implant + RTA; 4. 1200°C , 3 hr + high dose As ion implant + RTA.

In contrast, the films deposited on the sapphire substrate did not show as rapid a rise in current following the ohmic regime (where $I \propto V^{2.74}$). At a bias of 0.4V the slope dropped to 1.58, this corresponds to the regime where SCLC characterized by a slope of 2.0 would normally be expected. This behavior is probably due to a continuous distribution of traps above the valence band-edge. Filling of these traps arrests the sharp rise in current, although eventually the traps are filled and current tends to attain space-charge-limited value although the ideal slope of 2.0 is not reached. This non-ideal slope in the SCLC regime may be due to high-level injection and/or bulk resistance effects. Traps distributed in energy can be conveniently described by an exponential function of the type [6]:

$$N(E) \sim N_0 e^{-E/\Delta}$$

where $N(E)$ the density of trap states at an energy E above the valence band, N_0 is the density of trap states at the valence band-edge, and Δ a thermal energy parameter characterizing the trap distribution.

The SCLC, in this case in the range between 0.1V and 0.4V ($I \propto V^{2.74}$), is given by [6]

$$I_{\text{SCLC}} = A q \mu N_c \left(\frac{\epsilon \epsilon_0}{q N_0 \Delta} \right)^{\frac{\Delta}{kT}} \left(\frac{V^{\frac{\Delta}{kT}+1}}{L^{\frac{2\Delta}{kT}+1}} \right) \quad (3)$$

where A is the contact area, μ is the carrier mobility, N_c/N_v is the effective density of states in the conduction/valence band and $\Delta/kT+1$ is equal to m , the observed exponent of the experimental I-V curve, i.e. $I \propto V^m$. A characteristic temperature, such that $\Delta = kT_t$, has been defined [4]. However, the physical significance of this temperature T_t is not clear. A value of N_0 of $6.3 \times 10^{19} \text{ cm}^{-3} \text{ eV}^{-1}$ is obtained with eqn. (3) using the following parameters: $\Delta = (m-1)kT = (2.74-1)kT = 1.74kT = 0.045 \text{ eV}$, $I = 1 \times 10^{-7} \text{ A}$, $V = 0.016 \text{ V}$, $A = 7.8 \times 10^{-5} \text{ cm}^2$, $\mu = 0.84 \text{ cm}^2/\text{V s}$ (experimentally determined Hall mobility), $N_v = 7 \times 10^{18} \text{ cm}^{-3}$ and $L = 1.06 \times 10^{-5} \text{ cm}$. It is quite possible that the integrated-effect of the distribution of states in the GaAs-on-sapphire overcompensates the n-type Si dopant activity at room-temperature. We hypothesize that some proportion of this distribution of states, in particular those furthest from the valence band-edge, become ineffective at low temperatures due to the lack of thermal energy necessary to ionize them. Hence n-type conduction dominates in GaAs-on-sapphire at low temperatures.

Deep-level states distributed in energy were also observed in implanted oxide SOI samples implanted with an As dose of $6 \times 10^{13} \text{ cm}^{-2}$. These samples had a higher carrier concentration and conducted a much higher current at lower voltages, as shown in Fig. 2; however, did not show a sharp rise in current, indicative of a discrete level, following the ohmic regime, where $I \propto V^2$. At a bias of 1.2V the slope dropped to 1.3, this corresponds to the regime where SCLC characterized by a slope of 2.0 would normally be expected. A value of N_0 of $1.0 \times 10^{18} \text{ cm}^{-3} \text{ eV}^{-1}$ is obtained with eqn. (3) using the following parameters: $\Delta = (m-1)kT = (2.0-1)kT = kT = 0.026 \text{ eV}$, $I = 4.1 \times 10^{-4} \text{ A}$, $V = 1.0 \text{ V}$, $A = 7.8 \times 10^{-5} \text{ cm}^2$, $\mu = 63 \text{ cm}^2/\text{V s}$ (experimentally determined Hall mobility), $N_c = 1.5 \times 10^{19} \text{ cm}^{-3}$, and $L = 1.8 \times 10^{-5} \text{ cm}$.

It is interesting to note that similar deep-level effects have also been observed in heteroepitaxial β -SiC films grown on Si(100) substrates [7]. β -SiC films grown on off-axis Si(100) substrates show discrete deep-level dominated characteristics similar to those of GaAs films on SOS and implanted oxide SOI. In contrast, the distributed deep-level characteristics of GaAs films deposited directly on (1012) sapphire are similar to those of β -SiC films grown on nominally (100) oriented silicon substrates. In comparison, the heteroepitaxial β -SiC films on nominal Si(100) display antiphase domain boundaries (APBs) whereas the GaAs layers deposited directly on (1012) sapphire substrates contain double-position boundaries (DPBs) [1]. It appears that the presence of these defects introduce a distribution of deep states in the band-gap close to the band-edges in the respective heteroepitaxial films. However, in contrast, although APBs were observed in GaAs films on SOS, the I-V characteristics do not indicate the presence of a distribution of near-edge states. Further work is in progress in order to develop an understanding of the mechanism(s) and role of microstructural defects in introducing deep and shallow level states in the grown films and their subsequent effect on device performance.

CONCLUSION

Space-charge-limited current conduction, influenced by deep-level traps, appear to be the dominant carrier transport mechanism in the materials studied. The deep-level parameters, determined from an analysis of the I-V characteristics, appear to be sensitive to the type and nature of microstructural defects in the films, anneal conditions employed and subsequent processing. Discrete levels are observed in GaAs films on silicon on sapphire and annealed buried implanted oxide SOI films. In contrast, an exponential distribution of traps is observed in the GaAs grown directly on (1012) sapphire and also in RTA annealed high-dose As implanted buried oxide SOI. The distributed states in GaAs films deposited directly on sapphire probably arise from the electrical activity of the double-position boundaries present in this material system.

ACKNOWLEDGEMENTS

The author is grateful to his colleagues and associates Drs. Trevor P. Humphreys (NCSU, MBE growth), John B. Posthill, (RTI, TEM studies), Nalin R. Parikh (UNCCH, RBS characterization) and Richard T. Kuehn (NCSU Microelectronics Laboratory), E. D. Richmond

(NRL, SOS wafers), and Eaton Corporation (implanted oxide wafers), for making the study possible.

REFERENCES

1. T. P. Humphreys, K. Das, J. B. Posthill, J. C. L. Tarn, B. L. Jaing, J. J. Wortman, and N. R. Parikh, *Jpn. J. Appl. Phys.*, 27, 1458, (1988).
2. T. P. Humphreys, N. R. Parikh, K. Das, J. B. Posthill, R. J. Nemanich, M. K. Summerville, C. A. Sukow, and C. J. Miner, *Mat. Res. Soc. Symp. Proc.*, Advances in Materials, Processing and Devices in III-V Compound Semiconductors, Eds., D. K. Sadana, L. Eastman, and R. Dupuis, Vol. 144, in press.
3. D. E. Ioannou, N. A. Papanicolaou, and P. E. Nordquist, Jr., *IEEE Trans. Electron Devices*, ED-34, 1694 (1987).
4. M. A. Lampert, M. A. and P. Mark, 'Current injection in solids', Academic Press, New York (1970).
5. K. Nauka, G. A. Reid, S. J. Rosner, S. M. Koch, and J. S. Harris, *Mat. Res. Soc. Symp. Proc.*, 91, 225 (1987).
6. H. P. D. Lanyon, *Phys. Rev.*, 130, 134 (1963).
7. K. Das, H. S. Kong, J. B. Petit, J. W. Bumgarner, R. F. Davis, and L. G. Matus, submitted for publication (1989).

SURFACE STRUCTURE OF SULFUR COATED GaAs

YOSHIHISA FUJISAKI AND SHIGEO GOTO

Hitachi Ltd., Central Research Laboratory, 1-280 Higashikoigakubo, Kokubunji, Tokyo 185, Japan

ABSTRACT

Surface structure of $(\text{NH}_4)_2\text{S}$ treated GaAs is investigated using PL (Photoluminescence), XPS (X-ray Photoelectron Spectroscopy) and RHEED (Reflection of High Energy Electron beam Diffraction). The data taken with these techniques show the strong dependence upon the crystal orientations coming from the stabilities of chemical bonds of Ga-S and As-S on GaAs crystals. The greater enhancement of PL intensity, the clearer RHEED patterns and the smaller amount of oxides on (111)A than (111)B implies the realization of a more stable structure composed mainly of the Ga-S chemical bond.

INTRODUCTION

Recently, sulfur passivation of GaAs crystals has received a great attention since it improves the quality of GaAs surfaces. It is thought to be attributed to the termination of dangling bonds on the surface by sulfur atoms. However, the detailed surface structure has not been clarified enough. Actually, two models have been proposed on the termination of free bonds [1],[2]. In this study, the surface structure of sulfur coated GaAs is investigated by changing the crystal orientations.

EXPERIMENTS

Photoluminescence measurements were performed at 4.2K using a 514.5nm light source with $500\text{mW}/\text{cm}^2$ lasing intensity. The XPS analyses were carried out with Al and Mg K_α X-ray sources under the background pressure of 2×10^{-10} torr. The RHEED observations were performed with 30KeV electron beams. Just before the RHEED observations, specimens were heated up to 150°C to stick them to a holder using indium solder. In every experiment, specimens were exposed to the air before they were inserted into the analysis chambers.

The specimens used in this study were (100), (111)A, and (111)B oriented GaAs crystals. They were, at first, etched chemically with $4\text{H}_2\text{SO}_4/\text{H}_2\text{O}_2$ solution for a few seconds. Sulfur treatment was performed using $(\text{NH}_4)_2\text{S}$ solution for 20-30 hours at room temperature and 10 minutes at 50°C . In order to evaporate the thick amorphous sulfur layer on the crystal, specimens were then heated for 30 minutes at 390°C in pure hydrogen atmosphere.

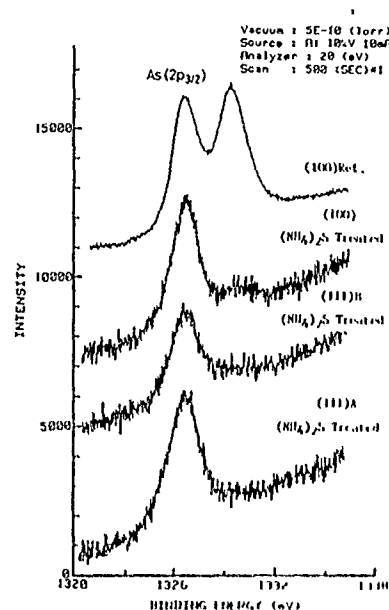


Fig. 1 XPS spectrum around As $2p_{3/2}$. Signals found at about 3eV higher energy than As $2p_{3/2}$ correspond to As_2O_3 .

RESULTS AND DISCUSSIONS

The XPS spectra around As $2p_{3/2}$ peak are shown in Figure 1. The main peaks near 1327eV correspond to As $2p_{3/2}$ coming from the As atoms in the bulk GaAs crystal. The peak near 1329eV which is clearly found in the spectrum of a reference specimen originates from As_2O_3 . This peak is clearly found only for the reference specimen, but are not so obvious for the $(NH_4)_2S$ treated specimens. This is due to the etching ability of $(NH_4)_2S$ for both gallium and arsenic oxides. However, some differences are found among the $(NH_4)_2S$ treated specimens. The spectra for the (100) and (111)B surfaces show that a small amount of oxides still exist on them. To the contrary, the oxides seem to be removed almost completely from the (111)A surface.

The angle resolved O_{1s} peak intensity is shown in Figure 2. The signal intensities which reflect the total density of the oxides ($Ga_2O_3 + As_2O_3$) are normalized with the total peak intensity of $Ga_{3d} + As_{3d}$. The horizontal axis is the angle made by the sample surface and the photo-electron detector. The smaller angle corresponds to the information mainly from the surface of the specimen. The tendency mentioned in the previous paragraph is quantitatively disclosed in this figure, i.e., larger amount of oxides are found on (111)B than (111)A. Since $(NH_4)_2S$ solution has a strong etching ability for both gallium and arsenic oxides, they are removed almost completely from crystal surfaces just after the $(NH_4)_2S$ treatment. Therefore, the major chemical bond created after the $(NH_4)_2S$ treatment on the (111)B surface is As-S. However, sulfur atoms are thought to be replaced by oxygen atoms through the air exposure process after the $(NH_4)_2S$ treatment. This means that the As-S chemical bond is rather unstable in the air. To the contrary, Ga-S chemical bond is thought to be rather strong compared with As-S and this results in the difference between the density of oxides on the (111)A and (111)B surfaces.

This estimation that a Ga-S chemical bond is stronger and more stable in the air than an As-S bond is also confirmed from the data shown in Figure 3. Four curves are also the angle resolved XPS data for Ga_{3d} peaks normalized $Ga_{3d} + As_{3d}$ peak intensities. As is clear from the figure, the upmost atomic layers of $(NH_4)_2S$ treated GaAs surfaces becomes Ga rich regardless of the surface orientation. The comparison between the $(NH_4)_2S$ treated (100) and the (100) Ref., which is the untreated with $(NH_4)_2S$, shows the drastic change in the density of Ga atoms in the upmost atomic plane.

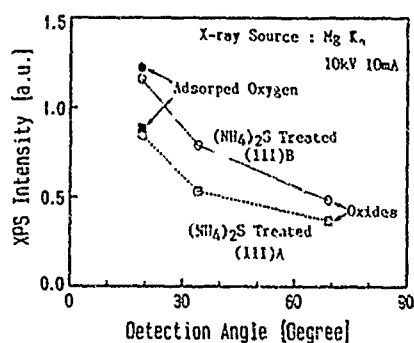


Fig. 2 Difference between the amount of oxides and adsorbed oxygen on $(NH_4)_2S$ treated (111)A and (111)B.

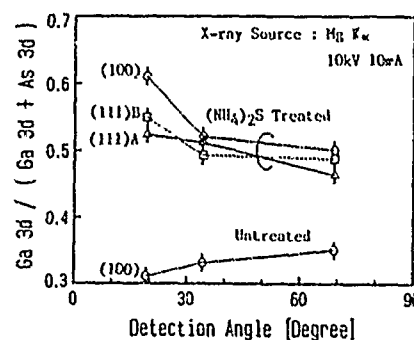


Fig. 3 The angle resolved XPS data for $(NH_4)_2S$ treated (100), (111)A, (111)B, and untreated (100) GaAs. The tendency is found that data at low angles for the $(NH_4)_2S$ treated become Ga rich.

In order to realize the surface structure, RHEED observations were

performed on sulfur treated (111)A and (111)B specimens. The RHEED patterns observed for the (111)A and (111)B samples are shown in Figures 4 and 5. In both cases, the patterns are made clearer with the $(\text{NH}_4)_2\text{S}$ treatment. The patterns for the $(\text{NH}_4)_2\text{S}$ treated (111)A specimen become a clear streak 1×1 . This fact together with the XPS data explained in the previous two paragraphs imply the monolayer coverage of sulfur atoms just above the gallium atoms combined with the stable Ga-S chemical bond. To the contrary, the RHEED patterns of the $(\text{NH}_4)_2\text{S}$ treated (111)B specimen are not so clear which reflects the structure of bulk crystals. Generally speaking, the upmost surface should be arsenic rich in the case of a (111)B surface. Due to the XPS data, however, the uppermost surface layer of the $(\text{NH}_4)_2\text{S}$ treated (111)B surfaces is Ga rich. Therefore, the surface structure seem rather complex and is thought to be covered with amorphous sulfur or sulfides. The rather vague RHEED pattern on the (111)B surfaces can be understood if it is covered with amorphous sulfur or amorphous gallium sulfides.

 $\langle 1\bar{1}0 \rangle$ $\langle 1\bar{1}2 \rangle$ Without $(\text{NH}_4)_2\text{S}$ Treatment $\langle 1\bar{1}0 \rangle$ $\langle 1\bar{1}2 \rangle$ Without $(\text{NH}_4)_2\text{S}$ Treatment $\langle 1\bar{1}0 \rangle$ $\langle 1\bar{1}2 \rangle$ $(\text{NH}_4)_2\text{S}$ Treated and Baked $\langle 1\bar{1}0 \rangle$ $\langle 1\bar{1}2 \rangle$ $(\text{NH}_4)_2\text{S}$ Treated and Baked

Fig. 4 Change in the RHEED patterns due to $(\text{NH}_4)_2\text{S}$ treatment. Specimens are (111)A oriented GaAs. Patterns were observed from $\langle 1\bar{1}0 \rangle$ and $\langle 1\bar{1}2 \rangle$ azimuths.

Fig. 5 Change in the RHEED patterns due to $(\text{NH}_4)_2\text{S}$ treatment. Specimens are (111)B oriented GaAs. Patterns were observed from $\langle 1\bar{1}0 \rangle$ and $\langle 1\bar{1}2 \rangle$ azimuths.

Due to the XPS and RHEED analyses, the $(\text{NH}_4)_2\text{S}$ treated (111)A surface is expected to have more desirable properties than (111)B does. To investigate the electrical quality, a PL measurement was carried out at 4.2K. The change in PL intensities through the $(\text{NH}_4)_2\text{S}$ treatment is shown in Figure 6. Both reference samples show approximately the same intensity, however, the great enhancement of luminescence due to the $(\text{NH}_4)_2\text{S}$ treatment is found only for the (111)A specimen. The enhancement is rather small in the case of (111)B compared with (111)A. This enhancement is attributable to the reduction of surface states through the $(\text{NH}_4)_2\text{S}$ treatment. Therefore, the surface quality of (111)A can be said to be better than that of (111)B since the (111)A surface has a smaller amount of surface states. This difference in the surface electrical quality is reasonably understood if the XPS and RHEED data are taken into account. The surface dangling bonds on the (111)A surface is expected to be reduced greatly due to the formation of the stable Ga-S chemical bonds which act as a passivation film on the crystal surface. To the contrary, the free bonds of As and Ga on the (111)B surface cannot be suppressed enough since the film on the crystal seems to be amorphous rather

than a rigid structure.

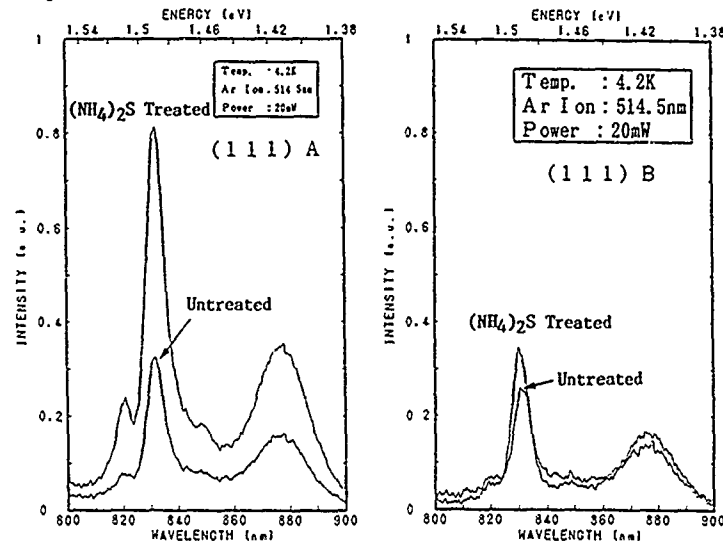


Fig. 6 Change in PL intensities due to (NH₄)₂S treatment.

CONCLUSION

The enhancement of PL intensity was remarkable for the sulfur treated (111)A wafer, but it was not so obvious for the (111)B wafers. Due to RHEED observations, the sulfur treated (111)A surface has a 1×1 non-reconstructed structure. This non-reconstructed structure implies the termination of Ga dangling bonds on the A surfaces, which decreases the surface state density of a crystal and enhances the PL intensity. To the contrary, both patterns corresponding to sulfur treated and untreated (111)B surfaces were halo. This is due to the thick oxides and amorphous sulfur upon the (111)B surface.

The major chemical bond created through the (NH₄)₂S treatment is a Ga-S, which is stable in the air and protect the GaAs surface from oxygen atoms. The structure realized through the (NH₄)₂S treatment is expected to be 1×1 with the sulfur atoms placed just above the Ga atoms on the upmost atomic plane of GaAs.

ACKNOWLEDGMENT

The authors wish to thank Miss Akiko Muto and Dr. Shinichiro Takatani for giving them useful comments on the XPS analysis. The authors also wish to thank Dr. Ryotaro Irie for supporting the analysis from the theoretical aspects.

References

1. C.J. Sandroff, M.S. Hegde, L.A. Farrow, C.C. Chang, and J.P. Harbison, *Appl. Phys. Lett.* **54**, 362 (1989).
2. B.A. Cowans, Z. Dardas, W.N. Delegass, M.S. Carpenter, and M.R. Melloch, *Appl. Phys. Lett.* **54**, 365 (1989).

ELECTRICAL AND MATERIAL CHARACTERIZATION OF THE STABILITY OF ALGAS AND GAS PLANAR DOPED STRUCTURES

Larry P. Sadwick* and Dwight C. Streit**

*Department of Electrical Engineering, Merrill Engineering Building, University of Utah,
Salt Lake City, Utah 84112

** TRW Electronic Systems Group, One Space Park, Redondo Beach, California 90278

ABSTRACT

In this work we have studied the effects of silicon planar doping on the electrical and optical properties of GaAs, and the effects of rapid thermal annealing on AlGaAs planar-doped structures. MBE-grown GaAs epilayers with multiple planar-doped layers displayed a 1.2 eV photoluminescence peak, presumably due to gallium vacancy - donor complexes, for samples with nominal silicon sheet densities much greater than measured charge densities. The Hall mobilities of these samples were also reduced compared to both uniformly-doped and planar-doped structures whose silicon areal densities were more nearly equal to measured sheet charge densities, although X-Ray rocking curves were nearly identical in all cases. Planar-doped AlGaAs Schottky diodes had nearly ideal electrical characteristics. Rapid thermal annealing of the planar-doped structures before fabrication increased the diode ideality factor from $n=1.06$ to $n=1.60$, seriously degraded the saturation current and breakdown voltage, and increased the doping profile FWHM from 60Å to 170Å.

INTRODUCTION

The demonstrated improvement in device performance for planar-doped HEMTs has prompted renewed interest in this material structure. Recently Schubert et. al. [1,2] have used planar-doped structures as a tool to study the diffusion of atomic silicon in GaAs and AlGaAs by capacitance-voltage (C-V) measurements on as-grown and annealed samples. In this work we use the C-V technique to investigate silicon diffusion in AlGaAs planar-doped samples, and also characterize the electrical parameters of the diodes before and after rapid thermal annealing. In addition we measure the effects of planar-doping on the Hall mobility, photoluminescence spectra, and X-Ray rocking curves of MBE-grown GaAs.

EXPERIMENTAL

Two sets of planar-doped samples were grown and analyzed for this study. The epilayers were all grown at 600C under arsenic stabilized conditions in Varian GenII MBE systems. The first set of samples were designed for analysis by photoluminescence, double-crystal X-Ray diffraction and Hall-effect measurements. All of these samples are 5000Å thick GaAs epilayers, bound by thin AlGaAs cladding layers so as to minimize surface, interface and substrate contributions to the photoluminescence spectra, and were grown on semi-insulating GaAs substrates. The second set of samples were designed for C-V and I-V characterization before and after rapid thermal annealing, and were grown on n+ GaAs substrates.

Planar-doped GaAs

The structure of the first set of samples is summarized in Table I, along with the Hall-effect results. Sample 1 is a nominally-undoped reference sample against which the X-Ray rocking curves and photoluminescence spectra for the doped samples could be compared. Thick undoped samples grown in the same MBE system under the same conditions were p-type with free-carrier concentrations in the mid- 10^{13} cm^{-3} range. The remaining samples of the first set were doped in various configurations, including single planar doped, multiply planar doped, and uniformly doped for comparison purposes. Sample 2 with a single plane of silicon doping in the middle of the 5000Å thick GaAs epilayer had the highest Hall mobility, comparable to other published results [3], and its 10K PL spectra was virtually identical to that of the reference sample, as shown in Figure 1. As the doping level was increased, either through multiple planar doping or through uniform doping, the measured Hall mobility decreased and the free-exciton peak was extinguished. Samples 3 and 4 have the same net donor concentration, but the doping is uniform in sample 3 and distributed in 50 planes of silicon 100Å apart in sample 4. The planar-doped sample has a slightly higher mobility, with slightly lower measured sheet charge. When these 2 sample structures are merged, 50 silicon planes superimposed on a uniform background doping of $6 \times 10^{18} \text{ cm}^{-3}$, the Hall mobility drops considerably, as does the measured sheet charge. Whether a silicon sheet concentration of $6 \times 10^{14} \text{ cm}^{-2}$ is distributed in 50 planes 100Å apart or in 100 planes 50Å apart makes no difference in the Hall measurements, as seen in samples 6 and 7.

A 1.2 eV defect peak appears in the 10K photoluminescence spectra for the highest-doped samples, as shown in Figure 1. This transition is most likely associated with a gallium vacancy - donor complex, and has been observed in melt-grown GaAs.[4] To our knowledge this defect has not been seen before in MBE-grown GaAs. The integrated PL intensity is about the same for the undoped and the single planar-doped samples, but is reduced to less than 8% of the original value for the highly doped samples with multiple planes of silicon.

X-Ray rocking curves were recorded using Cu K alpha radiation in the (+-) parallel mode from the 004 reflection, and are shown in Figure 2 for the undoped reference sample and sample 6, doped $50 \times 1.2 \times 10^{13} \text{ cm}^{-2}$. Interference fringes are typical of structures of the form ABA, and are clearly seen. The main peaks are identical, but some slight difference is seen in the quality of the interference fringes.

Table I Hall-Effect Results on Planar-Doped Structures

Sample	Structure	Nominal $n(\text{cm}^{-2})$	Measured $n(\text{cm}^{-2})$	$\mu(\text{cm}^2/\text{Vs})$
1	reference undoped			
2	PD $1 \times 6 \times 10^{12} \text{ cm}^{-2}$	6×10^{12}	5.98×10^{12}	2250
3	uniform $6 \times 10^{18} \text{ cm}^{-3}$	3×10^{14}	3.03×10^{14}	1620
4	PD $50 \times 6 \times 10^{12} \text{ cm}^{-2}$	3×10^{14}	2.83×10^{14}	1670
5	3 and 4 combined	6×10^{14}	2.63×10^{14}	1320
6	PD $50 \times 1.2 \times 10^{13} \text{ cm}^{-2}$	6×10^{14}	2.45×10^{14}	1310
7	PD $100 \times 6 \times 10^{12} \text{ cm}^{-2}$	6×10^{14}	2.45×10^{14}	1310

Fig. 1 10K PL spectra of planar-doped GaAs with AlGaAs cladding. Structures are identified in Table I.

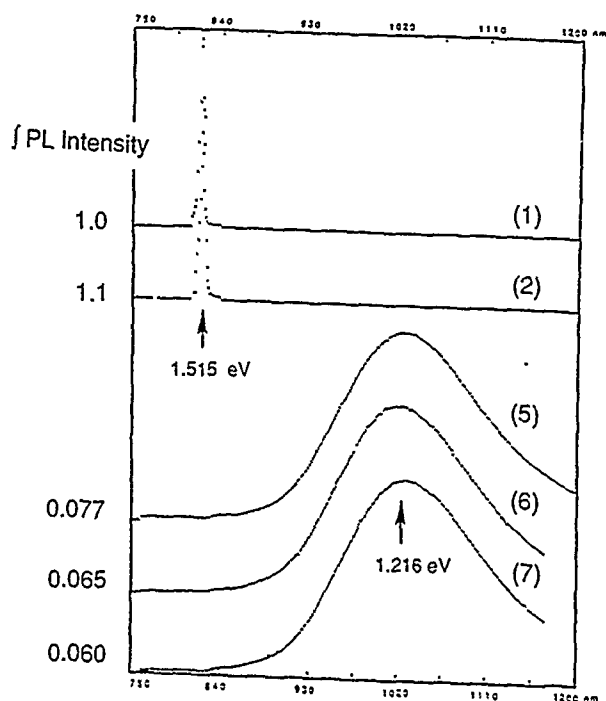
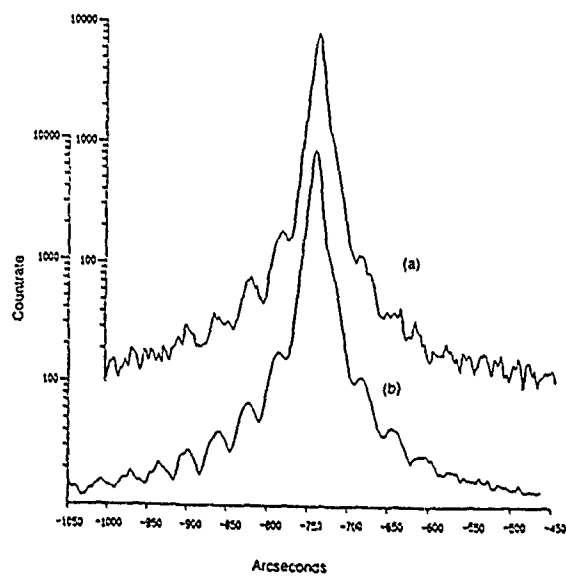


Fig. 2 X-Ray rocking curves for 5000Å thick GaAs films cladded with thin AlGaAs layers. (a) sample 6, with 50 planar-doped layers (b) sample 1, reference undoped



Planar-doped AlGaAs

The samples designated for CV and IV measurements had 3000Å thick epilayers with a single planar-doped region in the center, and were grown on n+ substrates. Portions of these samples were rapid-thermal annealed at 800C for 5 seconds. Following annealing the samples recieved AuGe back contacts, which were annealed at 450C for 1 minute to assure good ohmic characteristics. Schottky contacts were then deposited on the front surface, and consisted of 250 μm diameter dots of 400Å Ti with a 5000Å Au overlayer.

All C-V measurements were done at 1MHz, and care was taken that the phase angle was close to 90°. Doping profiles extracted from these measurments are shown in Figure 3 for a $6 \times 10^{12} \text{ cm}^{-2}$ silicon plane in AlGaAs, with an Al mole fraction of 0.25. The as-grown full-width half maximum was 60Å. After annealing the FWHM had increased to 170Å. These figures compare with those of Schubert et. al. [2] of 118Å for as grown at 600C and 145Å for 500C growth and a similiar 800C, 5 second anneal schedule. The calculated diffusion length of 56.6Å yields a diffusion coefficient of $6.3 \times 10^{-14} \text{ cm}^2/\text{s}$, similiar to the $3 \times 10^{-14} \text{ cm}^2/\text{s}$ value of reference 4.

There is a dramatic change in the Schottky diode I-V characteristics for annealed versus as-grown samples, as shown in Figures 4 and 5 for typical forward and reverse characteristics, respectively. The as-grown planar-doped AlGaAs samples have a remarkably linear log current versus voltage curve, with a straight-line fit over 10 decades of current. The barrier height is 1.00 V, the ideality factor $n=1.06$, and the saturation current density $J=4 \times 10^{-12} \text{ A/cm}^2$. Following the 800C, 5 second anneal the ideality factor has degraded to $n=1.60$, the saturation current density has increased 4 orders of magnitude to $J=4 \times 10^{-8} \text{ A/cm}^2$, and the barrier height has been reduced to 0.775 V. Under reverse bias the breakdown voltage decreases from 7V to 3V for the annealed sample.

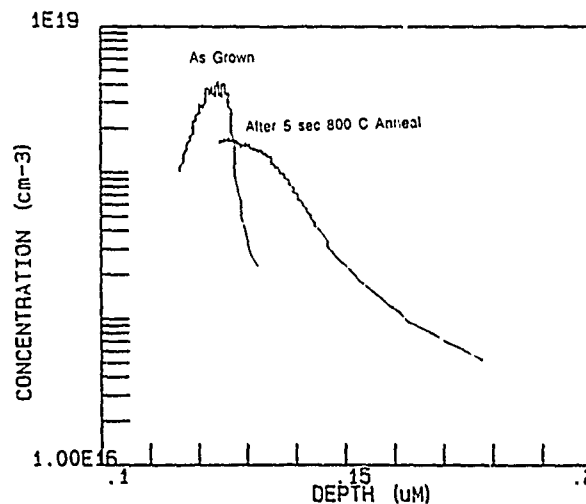


Fig. 3 Doping profiles from C-V measurements for AlGaAs planar-doped with silicon $n = 6 \times 10^{12} \text{ cm}^{-2}$, before and after rapid thermal annealing on initial structures.

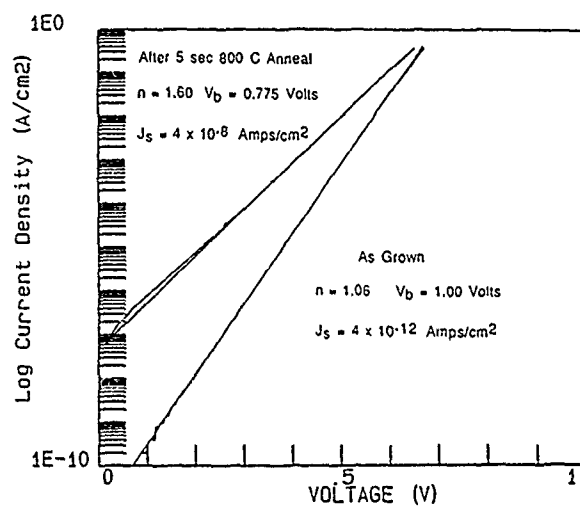


Fig 4. Forward I-V curves for AlGaAs planar-doped Schottky barriers before and after rapid thermal annealing on initial structures.

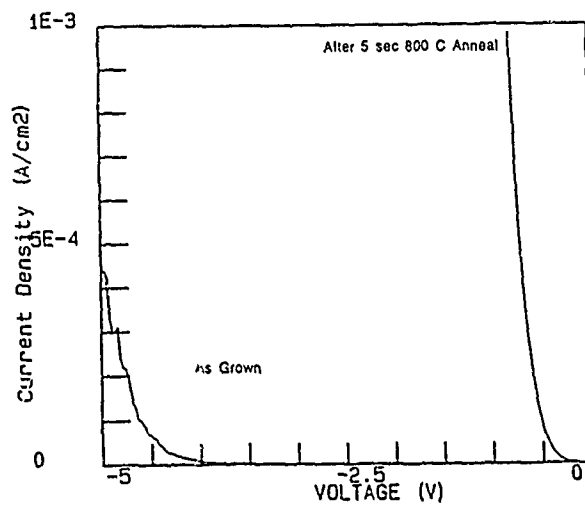


Fig. 5 Reverse characteristics for the diodes of Fig 4.

Table II AlGaAs Planar-Doped Schottky-Diode Electrical Data

Sample	n	V(barrier) volts	J(sat) A/cm ²	V(breakdown) volts	FWHM Å
as grown	1.06	1.00	4×10^{-12}	7	60
annealed	1.60	0.775	4×10^{-8}	3	170

CONCLUSIONS

While single planes of silicon show high activation in GaAs, attempting to obtain higher doping densities using multiple planar-doping schemes than is possible with uniform doping does not appear feasible, and results in reduced carrier concentrations and reduced Hall mobilities. A 1.2 eV defect line presumably due to gallium vacancy - donor complexes is seen in the photoluminescence spectra of MBE planar-doped GaAs with silicon concentrations far exceeding the measured free electron concentrations, indicating the damage caused by over-doping, although this is not readily seen in the X-Ray rocking curves of the same structures.

The sensitivity of planar-doped AlGaAs structures is seen in the degraded electrical properties of Schottky diodes fabricated in such structures that have been subjected to rapid thermal annealing. The diffusion of atomic silicon at 800C in AlGaAs grown at 600C has been measured and is only slightly higher than in AlGaAs grown at 500C as measured in reference 2.

We would like to thank J. Velebir, W. Jones, E. Reihlen and C.W. Kim for their assistance in the preparation and measurement of these samples.

REFERENCES

1. E.F. Schubert, T.H. Chiu, J.E. Cunningham, B. Tell, and J.B. Stark, J. Electron. Mater. 17, 527 (1988).
2. E.F. Schubert, C.W. Tu, R.F. Kopf, J.M. Kuo, and L.M. Lunardi, Appl. Phys. Lett. 54, 2592 (1989)
3. G. Gillman, B. Vinter, E. Barbier, and A. Tardella, Appl. Phys. Lett. 52, 972 (1988).
4. E.W. Williams, Phys. Rev. 168, 922 (1968).

PHOTOLUMINESCENCE STUDIES OF IMPURITIES AND DEFECTS IN MERCURIC IODIDE

X.J. BAO*, T.E. SCHLESINGER*, R.B. JAMES**, A.Y. CHENG*** AND C. ORTALE***

*Carnegie Mellon University, Department of Electrical and Computer Engineering, Pittsburgh, PA 15213

**Sandia National Laboratories, Advanced Materials Division, Livermore, CA 94450

***EG&G Energy Measurements, Inc., Goleta, CA 93116

ABSTRACT

We have studied the effects of chemical etching in potassium iodide(KI) aqueous solution, vacuum exposure and bulk heating on the photoluminescence(PL) spectra of mercuric iodide(HgI_2). Different contact materials deposited onto HgI_2 were also investigated, such as Pd, Cu, Al, Ni, Sn, In, Ag and Ta. These processing steps and the choice of a suitable electrode material are very important in the manufacturing of high-quality mercuric iodide nuclear detectors. Comparisons are made between the front surface photoluminescence and transmission photoluminescence spectra.

INTRODUCTION

Mercuric iodide has gained increasing attention because it can be used to fabricate high efficiency nuclear detectors operated at ambient temperature, as compared with conventional Si(Li) and Ge(Li) nuclear detectors that have to be kept cool at all times[1]. However, defects that are introduced during detector fabrication as well as due to the interaction of the contact material with the HgI_2 severely limit the manufacturing yield of high quality HgI_2 nuclear detectors[2]. Characterization of the processing steps and various contact materials can provide guidance in the optimization of fabrication processes and the proper choice of a contact material.

RESULTS AND DISCUSSIONS

HgI_2 has a bandgap of 2.4eV at 4.2K and produces strong PL at low temperatures. Many workers[3-6] have studied HgI_2 by PL measurement. In this work, an Argon laser tuned to 4880Å was used for excitation source in the PL measurement. Several processing steps were separately studied by PL. These steps include KI etch, vacuum exposure and bulk heating. The effect of KI etching is shown in Fig.1. It can be seen that KI etch effectively exposes a fresh surface that is quite different from the "degraded" surface before the etch. This "degraded" surface can be formed within a day for samples stored in a dessicator. Since the PL spectra taken from a degraded surface resemble those taken from freshly etched samples that are relatively iodine poor (see Fig.2), the degradation was attributed to iodine loss due to sublimation and/or interaction of the HgI_2 with air. The effect of vacuum exposure was similar to KI etch in that it removes a layer of material from the surface. Instead of inducing a preferential loss of iodine or mercury, the vacuum does not produce a significant deviation of stoichiometry as measured with a PL technique. Bulk heating to 100°C in a helium ambient for 10 to 60 minutes was found to decrease P2 to P3 and band 2 to P3 ratios. These changes were attributed to the creation of native defects at elevated temperatures. In Fig.2, P2 to P3 and band 2 to P2 ratios for nine different samples are plotted as a function of their color number. The color numbers come from the visual observation of the redness of the vapor in each

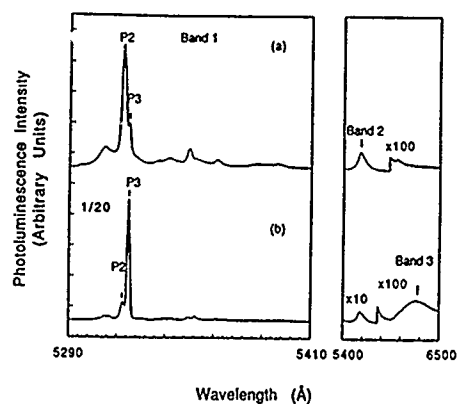


Figure 1: 4.2K PL spectra taken (a) before and (b) immediately after a 10% KI etch for about 3 minutes. The sample had been stored in a dessicator for 30 days prior to this experiment. P2 to P3 and band 2 to P3 ratios were decreased after KI etch primarily due to the increase of the absolute intensity of P3.

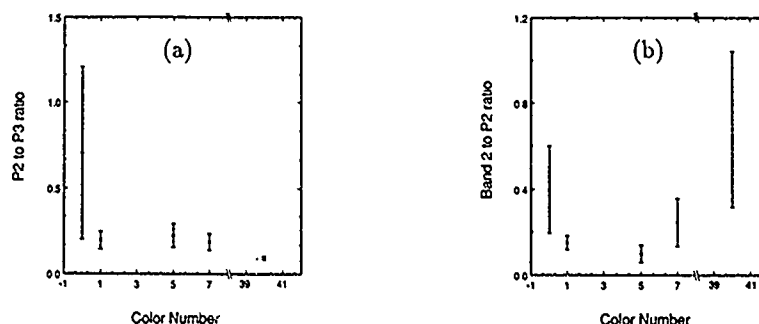


Figure 2: (a) P2 to P3 ratio and (b) Band 2 to P2 ratio as a function of color number for nine samples. All PL spectra were taken immediately after a KI treatment to expose a fresh surface. A larger color number is assumed to represent a larger iodine content. The P2 to P3 ratio is then related to the relative stoichiometry of the crystal.

ampoule during crystal growth, and it is qualitatively related to the abundance of iodine in the vapor. A larger color number is assumed to represent a larger iodine content in the crystal. It then appears that large P2 to P3 ratios can be roughly correlated to an iodine deficiency in the crystal. The band 2 to P2 ratio clearly shows a U-shape with a minimum at 3 to 5.

Various contact materials were studied by depositing a semitransparent layer of the material onto HgI_2 . PL spectra were then taken from the contacted area and compared with PL spectra taken from the as-grown crystal. The PL spectra from samples with semitransparent Pd, Cu, Al, Ni, Sn, In, Ag and Ta contacts as well as from an as-grown crystal are shown in Fig.3. It is clear that almost every metal introduces some distinct feature in the PL spectra. As-grown crystals usually have a well resolved band 1 in the near-bandgap photoluminescence (between 5290 and 5410Å), which we found consisted of at least 26 emission lines. At longer wavelengths there are three other broad bands labeled as band 2(5595Å), band 3(6200Å) and band 4(7550Å). In and Sn contacts introduce a similar broad band superimposed on band 1 and another broad band centered at about 6820Å. The broad band around band 1 was found to be detrimental to HgI_2

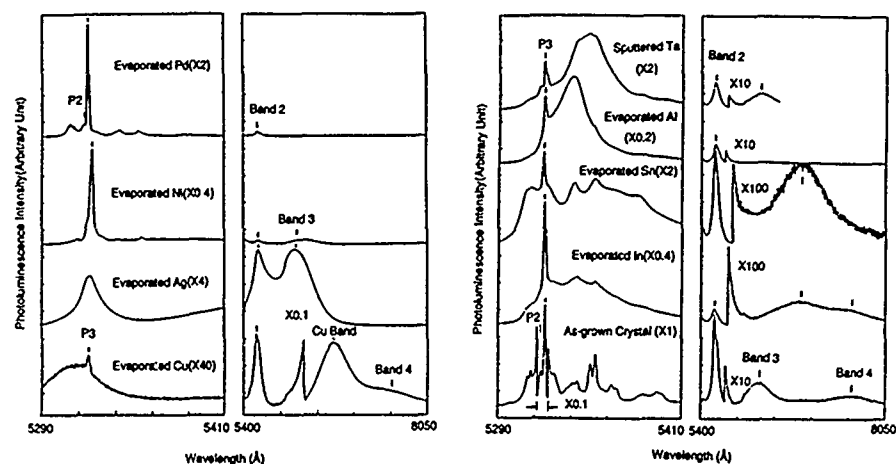


Figure 3: PL spectra taken from an as-grown HgI_2 crystal and from various semitransparent metal contacts deposited on HgI_2 substrates.

photodetectors with indium-tin-oxide (ITO) transparent contacts[3]. Al and Ta contacts introduce two different bands centered at about 5340 and 5350 Å, respectively in the band 1 region. Ag and Cu metals suppress the overall band 1 emission considerably. Ag introduces a new broad band at about 5500 Å. This band often appears as a shoulder on the shorter wavelength side of band 2. Cu contacts generate a very strong new band at about 6720 Å, which we have labeled as the Cu band. From a back doping experiment, it was found that Cu was a fast diffuser in bulk HgI_2 . Nuclear detectors with Cu electrodes were tested and the performance indicated that Cu is unacceptable as a contact material for detector applications[4]. This is not surprising given the changes in PL spectra caused by Cu deposition. Ni induces little change in the PL spectra, except it may have slightly broadened P3. Ni-contacted nuclear detectors have yet to be tested. Pd contact is the "best" among these metals in that it produces the least changes in the PL spectra. In addition it is the most used contact material in the manufacture of nuclear detectors; although, problems related to Pd contacts do exist.

Fig.4 shows two PL spectra taken in two different configurations. Spectrum(a) was taken in the conventional way, as all of the other PL spectra shown above. Spectrum(b) was taken in a transmission configuration. P2 and P3 have both been assigned as bound excitons by many workers[5,6]. From the transmission spectrum, it is clear that P3 was almost completely re-absorbed and there is a deep valley at the wavelength position where P3 usually is observed in a reflection spectrum. On the other hand, P2 appeared as a well resolved peak indicating a much smaller absorption than P3. The large absorption of P3 is readily explained if P3 is an exciton from a direct bandgap bound to an impurity. Since phonon participation is not required to conserve the crystal momentum in creating such an exciton, the emission from the radiative annihilation of this exciton can be re-absorbed. P2 must then be of a different origin. One possibility is that P2 is a phonon replica due to another line at a shorter wavelength. But no such line has been found. Another possibility is that P2 is due to an exciton from an indirect bandgap bound to an impurity. Since phonon participation is needed to conserve the crystal momentum for an indirect bandgap, the emission from the annihilation of such an exciton can not be re-absorbed. As a matter of fact, in the ordinary absorption spectra of HgI_2 , continuous absorption was observed[5,7], which is characteristic of an indirect bandgap material. However in the extraordinary absorption spectra, sharp resonant absorption lines were observed[5,7],

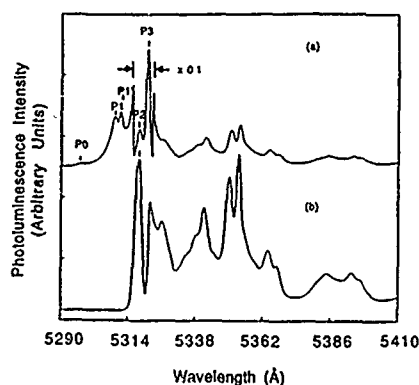


Figure 4: 4.2K PL spectra obtained in (a) reflection and (b) transmission mode.

which are characteristic of a direct bandgap material. Therefore, we postulate that HgI_2 may have two conduction band minima that are very close in energy with one directly above and the other indirectly above the valence band maximum.

CONCLUSIONS

In conclusion, we found that processing steps can modify the defect structure of HgI_2 crystals. A degraded surface can be developed as quickly as one day, which can be removed by either KI etch or vacuum exposure. Heating to 100°C appears to modify the concentration of native defects in the bulk. Different contact materials introduce distinct features in the PL spectra, which can be correlated to their capability as an electrode material for detector applications. The spectra also provide useful insights as to the nature of the interaction between the contact materials and HgI_2 . Some of these features can be used as signatures to identify the existence of the corresponding metal as a dopant in HgI_2 . Comparison between reflection and transmission PL spectra allows us postulate that HgI_2 may have two conduction band minima that are very close in energy.

REFERENCES

1. M. Schieber, Nucl. Instr. Meth. **213**, 1 (1983).
2. A. Holzer and M. Schieber, IEEE Trans. Nucl. Sci. **NS-27**, 266 (1980).
3. R.B. James, X.J. Bao, T.E. Schlesinger, J.M. Markakis, A.Y. Cheng and C. Ortale, J. Appl. Phys. **66**, 2578 (1989).
4. X.J. Bao, T.E. Schlesinger, R.B. James, R.H. Stulen, C. Ortale, L. van den Berg, to be published.
5. B.V. Novikov and M.M. Pimonenko, Sov. Phys. Semicond. **4**, 1785 (1971).
6. J.L. Merz, Z.L. Wu, L. van den Berg and W.F. Schnepple, Nucl. Instr. Meth. **213**, 51 (1983).
7. I. Akopyan, B. Novikov, S. Permogorov, A. Selkin and V. Travnikov, Phys. Stat. Sol.(b) **70**, 353 (1975).

DEPTH SENSITIVE IMAGING OF DEFECTS IN EPILAYERS AND SINGLE CRYSTALS USING WHITE BEAM SYNCHROTRON RADIATION TOPOGRAPHY IN GRAZING BRAGG-LAUE GEOMETRY.

M. DUDLEY,* G.-D. YAO,* J. WU,* AND H.-Y. LIU,**

* Dept. of Materials Science & Engineering, State University of New York at Stony Brook, Stony Brook NY 11794.

** Materials Science Laboratory, Texas Instruments Inc., P.O. Box 655936, Mail Stop 147, Dallas, TX 75265.

ABSTRACT.

The technique of Synchrotron White Beam topographic imaging in grazing Bragg-Laue geometries has been developed at the Stony Brook synchrotron topography station at the NSLS. This technique enables imaging of defects in subsurface regions of thickness which can range from hundreds of Angstroms to hundreds of microns as determined by the penetration depth of the X-rays. This penetration depth, which is shown to be determined by the kinematical theory of X-ray diffraction, can be conveniently varied, in a controlled manner, by simple manipulation of the diffraction geometry, thereby enabling a depth profiling of the defect content.

The fundamentals of the technique are described, and its advantages and disadvantages compared to existing techniques are discussed in detail. Examples of application of the technique in the characterization of defects in thin epitaxial films of GaAs on Si, are given, and the general applicability of the technique is discussed.

INTRODUCTION.

The characterization of the defect content in thin subsurface layers of single crystals has importance in many branches of Materials Science, ranging from technologically important areas such as characterization of semiconductor and superconductor heterostructures, respectively, to areas of more esoteric but nonetheless fundamental importance such as characterization of organic single crystals undergoing UV induced solid state reactions (which are often near surface reactions). This paper addresses primarily the former of these applications. Examples of applications in the other areas will be published in separate papers.

Among the techniques capable of imaging and characterizing the defect and strain content in thin subsurface layers, X-ray topographic imaging is the most strain sensitive, with a capability of detecting strains ($\Delta d/d$) in the range of 10^{-5} and smaller. Transmission X-ray topography and reflection X-ray topography in the Conventional-Bragg geometry have been routinely used to characterize the defect content in bulk semiconductor crystals for many years. However, when it comes to characterizing thin epitaxial films, the transmission technique has very limited depth sensitivity (based on subtle contrast variations), and even the conventional-Bragg geometry reflection technique has limitations in determining the position of a defect with respect to the crystal surface. In these latter geometries, (e.g. the Berg-Barrett technique), as in all reflection type geometries, it is well known that information can only be obtained from the volume defined by the effective area of the incident beam on the crystal surface and the penetration depth of the X-ray beam. Clearly, on topographs recorded in such geometries, it can be stated that defects imaged lie within the sampled volume, thus lending some depth sensitivity.

However, penetration depths in conventional Bragg geometries tend to be of the order of a few microns and greater. For epitaxial layers of thickness smaller than the penetration depth, it becomes impossible to determine the depth of a particular defect in the crystal. Kuo et al [1] utilized white beam synchrotron radiation topography in a conventional Bragg geometry to study the defect structure as a function of depth in a GaAs on GaAs specimen. The variation of absorption coefficient with wavelength was exploited so as to vary the penetration depth in the range from 3 to several hundred μm . Unfortunately, the lower end of this range is larger than the thickness of many epitaxial films. In any case, however, the crystal utilized in this study appeared hopelessly defective rendering any conclusions regarding the location of, for example, individual dislocations with respect to the entrance surface extremely difficult.

This penetration depth problem can be overcome by employing grazing Bragg-Laue geometries for imaging experiments. Imaging in these geometries was pioneered by Afanasiev and coworkers [2], who developed a technique using conventional radiation. Working in these geometries one can realize the possibility of studying the crystallographic perfection (defect content and state of strain) of very thin (a few hundred to a few thousand \AA thick) subsurface layers. This becomes possible since in grazing Bragg-Laue geometries (where incidence angles are typically a few degrees, and are usually chosen to be greater than the critical angle for total external reflection), the penetration depth of the X-rays can be readily varied, and in fact easily manipulated down to around a few thousand \AA and less. However, long exposure times and practical difficulties encountered with the complicated translation mechanisms which are necessary, limit the applicability of the technique to the characterization of very thin epitaxial films.

In this paper we report on the development of a white beam synchrotron radiation grazing Bragg-Laue imaging technique. Examples of its application to the characterization of defects in epitaxial layers of GaAs on Si substrates are presented. Factors determining the depth resolution capability of the technique are discussed in detail.

EXPERIMENTAL TECHNIQUES.

The Grazing Bragg - Laue Geometry.

It is well known that the loci of possible diffracted and incident beam directions lie on the surface of a cone of axis parallel to the g vector of the diffracting plane, and of apex angle $(90 - \theta_B)$, where θ_B is the Bragg angle. Such a cone, known as the Bragg cone, can be generated by rotation of the crystal, set for Bragg diffraction from the planes of interest, about the g vector. In the grazing Bragg-Laue geometry this cone is partially embedded in the specimen surface [3], and one can make the transition from the Bragg case to the Laue case via a small rotation about the g vector. This is the origin of the name "grazing Bragg-Laue" geometry.

When white radiation is used, one can also change the glancing angles by changing the diffraction geometry so as to select a different wavelength. This wavelength selectivity also has other extremely useful attributes pertaining to the separation of contributions from epilayer and substrate in heterosystems. One can also use the Laue patterns themselves as an on-line indication of the orientation of the beam to the crystal surface, provided the specimen surface orientation is accurately known. This enables the glancing angles of the incident and diffracted beams with the specimen surface, Φ_0 and Φ_h , respectively, to be accurately determined. The surface orientation was accurately determined by setting the crystal so that the transmission Laue pattern indicated that the beam was incident parallel to the lowest index direction closest to the surface normal, and then noting the orientation in space of the reflection angle of a low power laser

directed at the specimen surface in a direction parallel to the incident beam direction.

Penetration Depth.

X-ray Penetration depths in single crystals are a function of the the diffraction geometry and the degree of perfection of the crystal. For distorted or mosaic single crystals, the kinematical theory of X-ray diffraction holds, and penetration depth is determined by consideration of the length of path in the crystal beyond which photoelectric absorption reduces the diffracted intensity to less than $1/e$ times the incident intensity. On the other hand for near perfect single crystals, extinction effects can lead to attenuation at a much more rapid rate than absorption, and the penetration depth is determined by the extinction length. Detailed expressions for penetration depths can be found in [4].

The variation of dynamical and kinematical penetration depths with wavelength and incident glancing angle can be conveniently represented on three dimensional graphs, as illustrated in figure 1, which represents the penetration depths calculated for GaAs.

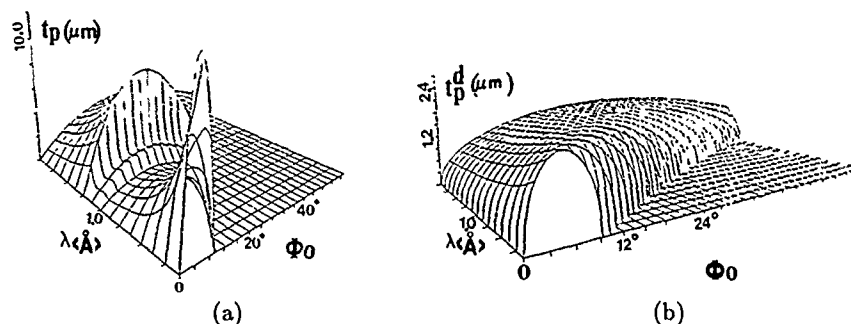


Figure 1. Three dimensional plots of penetration depth, calculated according to (a) kinematical theory, and (b) dynamical theory, respectively, versus wavelength, λ and incident glancing angle Φ_0 . (333) reflection, (100) GaAs crystal.

The penetration depths vary from fractions of microns to several tens of microns depending on the wavelength and glancing angle.

RESULTS.

The detailed discussion of the scientific results of these experiments will be published in separate papers. The emphasis here will rest upon demonstrating the ability of this technique in depth profiling the defect structure in the near surface region of a $3.2 \mu\text{m}$ thick, MBE grown, (100) GaAs epilayer on Si. Figure 2 shows 022 and 022 synchrotron white beam topographs recorded in the transmission geometry. The dominant contrast features on these images, marked S, arise from the specimen identification numbers scribed on the Si side of the specimen by Texas Instruments. The features of interest are the dislocation images which can be seen between and around these scribe marks. The three most obvious segments of dislocation visible on figure are marked A, B and C. Line direction analyses, performed using the algorithm of Miltat and Dudley [5], show that dislocations A and B have line direction $[1\bar{1}0]$, and $[101]$, respectively, and that dislocations C have line direction $[0\bar{1}1]$. The lengths of the various segments indicate that dislocations A and B are substrate threading dislocations, and that dislocations C are parallel to the crystal surface. Burgers vector analysis was performed and showed that dislocations A and B have Burgers vectors, $1/2[101]$ and $1/2[110]$, respectively, so that they are of 60° type, whereas, dislocation C have Burgers vector $[011]$, so that

they are of edge type. This overall structure is similar to that observed by Petroff and Sauvage [6], except that in this case the preponderance of the edge dislocations, which are formed from a reaction between $[0\bar{1}1]$ segments of dislocations A and B left behind after glide in the $[0\bar{1}1]$ direction, via the mechanism of Matthews, Mader and Light [7]. This reaction is more probable in this crystal than in the one studied by Petroff and Sauvage since the dislocation density is higher, and also since in our case the intersection between the (111) and $(1\bar{1}\bar{1})$ slip planes lies in the plane of the interface (the crystal is misoriented by 3 degrees away from (100) about an axis parallel to the edge dislocation line directions. This latter point differs from the case of Petroff and Sauvage in that their specimen was misoriented about an axis which was not parallel to the interfacial dislocation line direction, so that this intersection direction made a small angle with the interface plane, i.e. the two sets of interfacial dislocations produced from the two sets of threading dislocations were not exactly parallel, so that reaction between them was only occasionally observed.

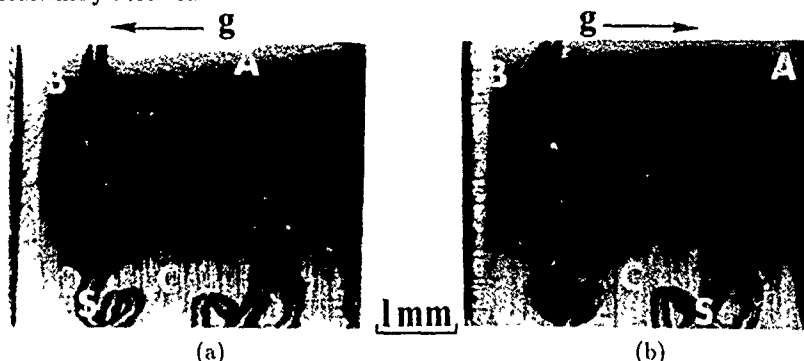


Figure 2. Synchrotron white beam transmission topographs recorded with the substrate on the X-ray exit surface. (a) $g=0\bar{2}2$, $\lambda=0.67$ Å, and (b) $g=022$, $\lambda=0.67$ Å.

Figure 3 shows synchrotron white beam topographs recorded in the grazing Bragg-Laue geometry (harmonic contents are indicated in the caption).

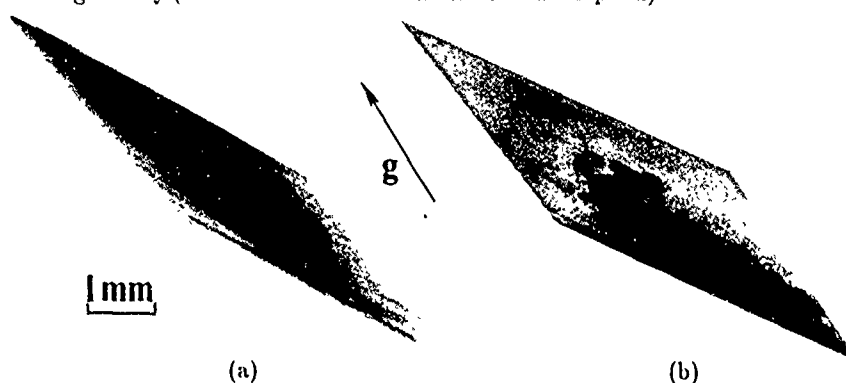


Figure 3. Grazing Bragg-Laue images recorded from the epilayer. (a) $\Phi_0=6.67^\circ$, $g=1\bar{1}1$, $\lambda=1.85$ Å, and $g=3\bar{3}3$, $\lambda=0.62$ Å, $I_{111}/I_{333}=0.2$, (b) $\Phi_0=0.46^\circ$, $g=1\bar{1}1$, $\lambda=1.68$ Å, and $g=3\bar{3}3$, $\lambda=0.56$ Å, $I_{111}/I_{333}=1.5$.

In Figure 3, contributions from the substrate are attenuated in the epilayer. Note the presence of the long straight $[011]$ dislocation images on figure 3(a) and their conspicuous absence on figure 3(b). This disappearance of the dislocation images is effected by the

simple changes in diffraction geometry indicated which in turn induce slight changes in penetration depth.

DISCUSSION.

The ability to determine the depth of a defect with respect to the crystal surface in reflection X-ray topography rests solely on whether or not the effective penetration depth of the X-ray beam can be accurately determined. It was recently shown [4] that penetration depth is a function of the local distortion. In the case studied, that of a region of crystal containing a surface threading dislocation, kinematical theory considerations, based on normal photoelectric absorption effects, were shown to determine penetration depth. This is to be expected since the dislocation images obtained from the crystals were of the Direct or kinematical type. Therefore those regions of the incident beam, at the wavelength of interest, which contribute to the dislocation image, are outside the perfect crystal acceptance angle (i.e. the perfect crystal rocking curve width), while being inside the beam divergence at that wavelength. Therefore these rays do not undergo extinction, and their penetration depth is determined by kinematical theory. Normally they would pass through the crystal until they were attenuated, and they would only be diffracted should they meet a region of lattice with suitable effective misorientation, for example surrounding a dislocation line.

For the example presented here, we have edge dislocations which are expected to be located at the interface between epilayer and substrate. According to the criterion of Zachariasen [8], the epilayer is expected to diffract dynamically since the parameter $\pi t/L_{ex}$, where t is crystal thickness and L_{ex} is extinction length, is greater than unity. In the geometries employed here, L_{ex} is small so that values for this parameter for a $3.2 \mu\text{m}$ thick crystal, are typically of the order of 10-20. Therefore, extinction contrast effects, arising from the differences in diffracted intensity from regions diffracting dynamically and kinematically, respectively, are possible. Therefore, the visibility of the dislocation depends on whether the rays which contribute to the dislocation image survive X-ray absorption before they meet the volume surrounding the dislocation line which has the correct effective misorientation to diffract them. Figure 4 shows a section through this latter volume.

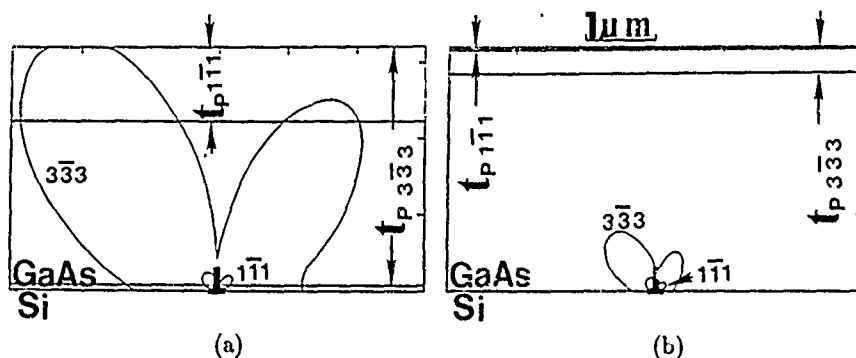


Figure 4. Plots of equi-effective misorientation surrounding an edge dislocation in GaAs located $3.2 \mu\text{m}$ below the surface (i.e. at the interface) for the $1\bar{1}1$, and $3\bar{3}3$ reflections. Also shown are the corresponding kinematical penetration depths.

This section is delineated by the contour for which the effective misorientation is equal to the rocking curve width, which was calculated using the approach of Miltat and

Bowen [9]. The corresponding kinematical penetration depths are also shown.

If the rays of interest pierce this volume then the dislocation will be visible, if not, it will be invisible. By making controlled changes to the diffraction geometry, which change both the kinematical penetration depth and the size of the contributing volume surrounding the dislocation line, and noting the point at which the dislocation image disappears, the position of the defect with respect to the surface can be accurately determined. As the incident glancing angle is reduced, the volume contributing to the dislocation image shrinks, and the kinematical penetration depth is reduced. The fact that these two parameters retreat in opposite directions leads to increased depth sensitivity. Comparison of figure 4 with the corresponding series of grazing Bragg-Laue images, shown in figure 3, confirms that this approach successfully accounts for the visibility of dislocation images on the topographs, and also confirms that the dislocations are located at the interface between epilayer and substrate.

CONCLUSIONS.

The development of the technique of white beam synchrotron topographic imaging in grazing Bragg-Laue geometries has been described. This technique enables the defect structure in thin subsurface layers of single crystals to be imaged exclusively. The visibility of dislocation images on topographs recorded in these geometries, is shown to be determined by the degree of overlap between the volume defined by the area of the incident beam and the kinematical penetration depth, and the volume defined by the contour on which the effective-misorientation is equal to the rocking curve width. The success of this model enables the technique to be used to determine the position with respect to the surface of dislocations in subsurface layers of thickness of the order of a few thousand Å.

REFERENCES.

- [1] C.L. Kuo and J.C. Bilello, *J. Appl. Phys.*, 62, 137, (1987).
- [2] A.M. Afanasiev, P.A. Aleksandrov, R.M. Imamov, E.M. Pashaev and V.I. Polovinkina, *Phys. Status Solidi*, (a)90, 419, (1985).
- [3] S.J. Miles, G.S. Green, B.K. Tanner, M.A.G. Halliwell and M.H. Lyons, *Mat. Res. Symp. Proc.*, 143, (1989).
- [4] M. Dudley, J. Wu and G.-D. Yao, *Nucl. Instr. & Meth.*, B40/41, 388, (1989).
- [5] J. Miltat and M. Dudley, *J. Appl. Cryst.*, 13, 555, 1980.
- [6] J.F. Petroff and M. Sauvage, *J. Cryst. Growth*, 43, 628, (1978).
- [7] J.W. Matthews, S. Mader and T.B. Light, *J. Appl. Phys.*, 41, 3800, (1970).
- [8] W.H. Zachariasen, "Theory of X-ray Diffraction in Crystals", Wiley, NY, (1945).
- [9] J. Miltat and D.K. Bowen, *J. Appl. Cryst.*, 8, 657, (1975).

Acknowledgements.

Research supported in part by the NSF under grant # DMR 8506948, and by Texas Instruments, and carried out at the Stony Brook Synchrotron Topography Facility at the NSLS, which is supported by DOE under grant # DE-FG02-84ER45098. The authors are indebted to Dr. Y.-C. Kao of Texas Instruments for providing the GaAs/Si samples.

Author Index

- Abernathy, C.R., 477, 855
 Adamski, Joseph A., 1007
 Aers, G.C., 931
 Agarwal, Anuradha M., 543
 Ahern, Brian S., 1007
 Ahrenkiel, Richard K., 781
 Akiyama, I., 139
 Alaya, S., 163, 747
 Allen, E.L., 685
 Altelarra, H., 785
 Anderson, Robert A., 431, 455
 Anderson, W.A., 993
 Antonelli, A., 523
 Arora, B.M., 185, 203
 Arriga, O., 139
 Asakura, H., 115
 Aucouturier, M., 401
 Awadelkarim, O.O., 283, 377

 Baba, T., 741
 Bachowski, Stephen, 1007
 Bajaj, K.K., 313
 Bakry, Assem M., 781
 Ballutaud, D., 401
 Banerjee, S., 185
 Bao, X.J., 1027
 Baraff, G.A., 805
 Baranowski, J.M., 821
 Barbier, D., 567
 Barczynska, J., 179
 Bardin, T.T., 979
 Barnes, P.A., 979
 Barry, J., 955
 Beckett, D.J.S., 221
 Bedair, S.M., 647
 Benson, B.W., 295
 Benyattou, Taha, 69
 Bergman, J.P., 325, 337
 Bernholc, J., 523
 Beye, A.C., 115, 121, 139
 Bliss, D.E., 815
 Bode, M., 639
 Booker, G.R., 907
 Borenstein, J.T., 633
 Borghesi, A., 919
 Borrego, J.M., 831
 Bosch, J., 785
 Bourgoin, J.C., 163, 747, 799
 Breitschwerdt, A., 395
 Brennan, T.M., 773
 Brower, K.L., 145
 Brown, A.R., 555
 Brown, G.J., 157, 809
 Brown, Robert A., 615
 Buda, F., 383

 Budil, Matthias, 535

 Cabaniss, G., 855
 Canut, B., 927
 Car, R., 383
 Carmo, M.C., 273
 Carter, C.B., 709
 Caruso, R., 489
 Chadi, D.J., 765
 Chakrabarti, U.K., 489
 Chandvankar, S.S., 203
 Charasse, Marie-Noelle, 69
 Charbonnier, M., 927
 Chaussemy, G., 927
 Chen, Samuel, 983
 Chen, W.M., 303, 377
 Cheng, A.Y., 1027
 Cheng, K.Y., 193
 Chevallier, J., 793
 Chiarotti, Guido L., 383
 Clarke, D.R., 425
 Clevenger, L.A., 961
 Cole, M.W., 987, 993
 Compaan, A., 759
 Corbett, J.W., 633
 Cotell, C.M., 861
 Cowern, N.E.B., 605

 Das, K., 1011
 Dautremont-Smith, W.C., 501
 Davies, G., 273
 De Mierry, P., 401
 De, Bhola N., 965
 Deal, Michael D., 653, 685, 691
 DeAvillez, R.R., 961
 Deicher, M., 245
 Deleo, G.G., 367
 Dischler, B., 875
 Dörnen, A., 21, 239
 Dow, John D., 349
 Droopad, R., 907
 Dubé, C., 459
 Dudley, M., 1031
 Duesbery, M.S., 941
 Dunham, Scott T., 543
 Dupuis, R.D., 867
 Dutta, M., 987

 Eichhammer, Wolfgang, 915
 Elcess, K., 197
 Emanuelsson, P., 307
 Ennen, H., 875
 Estle, T.L., 407

- Fahey, P., 529
 Fang, Zhaoqiang, 189
 Feng, S.L., 747
 Fischer, D.W., 827
 Florez, L.T., 709
 Fowler, W.B., 367
 Franciosi, A., 665
 Fujisaki, Yoshihisa, 1017
 Fujisawa, T., 741
 Fukuda, T., 969
 Fukushima, H., 1001

 Gaiduk, P., 601
 Galtier, Pierre, 69
 Garone, P.M., 591
 Geddo, M., 919
 Gehlhoff, W., 307
 Gerrard, N.D., 867
 Ghandhi, S.K., 95, 831
 Gibson, J.M., 861
 Gislason, H.P., 127
 Glaser, E., 753
 Goldman, L.M., 627
 Goldys, E., 179
 Gösele, Ulrich M., 671, 715
 Gossard, A.C., 325, 331, 337
 Goto, Shigeo, 1017
 Griess, M., 945
 Griffin, James, 881
 Grimmeiss, H.G., 3, 51, 307
 Grossmann, G., 51
 Grünebaum, D., 21
 Guido, L.J., 697
 Guillot, Gerard, 69
 Gürer, E., 295

 Ha, N.T., 501, 867
 Haegel, N.M., 63
 Haller, E.E., 15, 133, 815
 Hallin, C., 337
 Hamm, R.A., 861
 Hanak, Thomas R., 781
 Hara, A., 969
 Harbison, J.P., 709
 Harrison, Joseph G., 89
 Hartiti, Bouchaib, 905
 Hashimoto, Fumio, 291
 Haugstad, G., 665
 Heinrich, Michael, 535
 Henry, A., 283, 303
 Henry, M.O., 273, 299
 Herman, M.H., 197
 Herrero, C.P., 395
 Heyman, J., 15
 Hiesinger, P., 875
 Higgs, Victor, 57
 Hilton, Robert M., 1007
 Hirai, I., 969
 Hjalmarson, Harold P., 361, 773

 Hobson, W.S., 63, 489, 855
 Holonyak, Jr., Nick, 697
 Holtz, P.O., 325, 331, 337
 Honma, N., 951
 Hopkins, L.C., 861
 Hoshino, M., 901
 Hruska, Jane, 965

 Ichimura, Masaya, 549
 Ishibashi, Tadao, 887
 Ishituka, K., 121
 Ito, Hiroshi, 887
 Itoh, Y., 1001
 Iyer, S.S., 343

 Jackman, T.E., 931
 Jackson, Koblar, 89
 Jackson, S.L., 193
 Jacobson, D.C., 621
 Jäger, W., 659
 James, R.B., 1027
 Janssen, K.T.F., 605
 Janzén, E., 169, 207, 303
 Jendrich, U., 579
 Jeng, Nanseng, 543
 Jeong, J., 151
 Jiao, K.L., 993
 Johnson, S.T., 975
 Joos, B., 941
 Jos, H.F.F., 605

 Kahen, K.B., 677, 681
 Kalejs, J.P., 459
 Kamijoh, K., 139
 Kaminski, Pawel, 75
 Kamiura, Yoichi, 291
 Kao, Y.J., 63
 Katayama-Yoshida, H., 81
 Kato, T., 901
 Keilmann, F., 133
 Keller, R., 245
 Kennedy, T.A., 33, 753
 Kiefl, R.F., 407
 Kienle, R., 21, 239
 Kightley, P., 57
 Kim, Y., 639
 Kimerling, L.C., 151
 Kirita, H., 1001
 Kleverman, M., 3, 51, 169, 207
 Ko, Kei-Yu, 983
 Koch, U., 609
 Koidl, P., 875
 Kopf, R.F., 793
 Kozuch, D.M., 367, 477
 Krause, S., 955
 Kringhøj, P., 585
 Kukimoto, H., 741
 Kumar, S.N., 927
 Kürner, W., 239
 Kurtz, S.R., 773

Kutsuwada, N., 115, 139

Lambert, G., 109

Lareau, R.T., 993

Larsen, A. Nylandsted, 585, 601

Larsen, K. Kyllsbech, 601

Latushko, Ya.I., 277

Laugier, A., 927

Lawrence, D.J., 677

Lee, J.W., 501

Lee, K.M., 151

Lee, S.-Tong, 983

Legoues, F.K., 437

Legros, R., 793

Lehman, J.L., 987

Lever, R.F., 561

Lightowlers, E.C., 57, 273, 299

Lindelfelt, U., 287

Lindström, J.L., 283, 377

Linnarsson, M., 127, 169, 207

Liu, H.-Y., 1031

Liu, Joyce C., 437

Lopata, J., 367, 477, 489, 501

Luftman, H.S., 501, 867

Lundgren, K.R., 221

Luysberg, Martina, 659

Ma, E., 961

Maaref, H., 163, 747

Magno, R., 789

Maier, M., 875

Makita, Y., 115, 121, 139

Manasreh, M.O., 175, 809, 827

Maroudas, Dimitrios, 615

Marrakchi, G., 163

Marwick, A.D., 437

Mathiot, D., 401

Matlock, J.H., 597

Matsumori, T., 121, 139

Matsumoto, T., 901

Mayer, K.M., 115, 121, 139

McCollum, M.J., 193

McDermott, B.T., 647

McGuigan, K.G., 273, 299

Mehrer, H., 659

Mei, P., 709

Merk, E., 15

Merz, J.L., 325, 331, 337

Michel, D.J., 941

Michel, J., 151

Milnes, A.G., 189, 997

Mitchel, W.C., 157

Mitchell, I.V., 931

Mizuta, M., 741, 753

Möhrle, Martin, 495

Möller, H.J., 579, 945

Molnar, B., 753

Moncorge, Richard, 69

Monemar, B., 39, 85, 127, 169,

207, 257, 261, 265, 283,

303, 325, 331, 337, 377

Monteiro, Teresa, 215

Mooney, Patricia M., 729

Morante, J.R., 785

Morehead, F.F., 561

Mori, M., 121

Mostefaoui, R., 793

Muller, Jean-Claude, 915

Munakata, C., 951

Murray, Jeffrey J., 691

Murray, R., 555

Myers, Leary, 881

Myers, N.C., 609

Nakayama, Y., 121

Narasimhan, K.L., 269

Nazare, M.H., 299

Newman, R.C., 555

Nichols, C.S., 425

Nissen, M.K., 221

Nolte, D.D., 815

Norman, A.G., 907

Northrop, G.A., 27, 343

Nygren, E., 627

Oda, T., 139

Oehrlein, G.S., 377

Ogasawara, M., 951

Oguchi, T., 81

Ohnishi, N., 115, 121

Ohsawa, A., 969

Olajos, J., 3

Omling, P., 307

Ortale, C., 1027

Ottolini, L., 919

Ourmazd, A., 639

Ozeki, M., 901

Pajot, Bernard, 465

Palmstrom, C., 709

Panish, M.B., 861

Pantelides, Sokrates T., 511

Park, B., 621, 627

Park, In-Shik, 211

Parker, S.D., 907

Parrinello, M., 383

Pearah, P.J., 175, 197

Pearton, S.J., 367, 477, 489, 501, 855

Pederson, Mark R., 89

Pellegrino, Joseph, 881

Pensl, G., 21

Pereira, Estela, 215

Perez, A., 785

Perret, M., 659

Peterkin, Jane, 965

Petersen, J.W., 585

- Peterson, D.L., 677
 Petrov, V.V., 277
 Pfeiffer, W., 245
 Piaggi, A., 919
 Pinzone, C.J., 867
 Pivac, B., 919
 Plano, M.A., 193
 Plummer, J.D., 685
 Poate, J.M., 621
 Pötzl, Hans W., 535
 Premchandran, V., 269
 Pronko, J.G., 979

 Radzimski, Zbigniew, 449
 Raisanen, A., 665
 Rajbenbach, H., 837
 Rajendran, S., 459
 Rajeswaran, G., 677, 993
 Ralston, J.D., 875
 Ramdani, J., 647
 Ramsteiner, M., 875
 Ren, Shang Yuan, 349
 Reynolds, Donald C., 313
 Ridgway, M.C., 975
 Robinson, H.G., 653
 Ronay, Maria, 573
 Rossabi, J., 987
 Rozgonyi, George A., 449
 Rune, G.C., 331

 Sadwick, Larry P., 1021
 Samitier, J., 785
 Sarkar, D., 269
 Sasaki, T., 81
 Sawyer, William D., 923
 Schad, R.G., 573
 Schlesinger, T.E., 189, 997, 1027
 Schlette, A., 239
 Schmälzlin, Jorg, 923
 Schmid, U., 609
 Schmitz, K.M., 993
 Schneider, J.W., 407
 Schultz, P.J., 931
 Schwab, C., 407
 Schwartz, P.V., 591
 Schwarz, S.A., 591, 709
 Seager, Carleton H., 431, 455
 Seghier, Djelloul, 69
 Seibt, M., 945
 Sengupta, D., 975
 Seong, Tae-Yeon, 907
 Shan, Lei, 189
 Sharma, D.K., 203, 269
 Sharma, R., 993
 Shelby, R., 789
 Shen, Jun, 349
 Shibata, H., 115, 121, 139
 Shimizu, A., 139
 Shimizu, H., 951

 Shin, Ki-Chul, 211
 Siffert, Paul, 915
 Simpson, P.J., 931
 Skudlik, H., 245
 Smith, D.D., 987
 Smith, L.M., 65
 Sopori, Bhushan, 449
 Spaepen, F., 621, 627
 Spencer, Michael, 881
 Srivastava, A.K., 185, 203, 269
 Stavola, Michael, 367, 477
 Steiner, D., 245
 Stella, A., 919
 Stevenson, David A., 653, 691
 Stillman, G.E., 193, 483
 Stockman, S.A., 193
 Stolwijk, N.A., 21, 659
 Stolz, P., 21
 Stradling, R.A., 907
 Streit, Dwight C., 1021
 Stringfellow, G.B., 893
 Sturm, J.C., 591
 Stutzmann, M., 395
 Suezawa, Masashi, 233
 Sugiyama, H., 139
 Sugiyama, Y., 121
 Sumino, Koji, 233
 Sundaram, M., 325, 331, 337
 Sveinbjörnsson, E.Ö., 127
 Svensson, B.G., 261
 Svensson, J.H., 261, 265
 Swaminathan, V., 489
 Szafraneck, I., 193, 483

 Tacano, M., 121
 Takahashi, T., 121
 Takai, M., 1001
 Takechi, M., 901
 Takeda, Akihiro, 549
 Takeda, Michihiko, 549
 Takeyama, T., 937
 Tan, T.Y., 715, 983
 Tan, Teh Y., 671
 Tanoue, H., 139
 Theiler, T., 133
 Theis, Thomas N., 729
 Theodore, N.D., 709
 Thewalt, M.L.W., 221, 303
 Thilderkvist, A., 51
 Thompson, C.V., 961
 Thonke, K., 21, 239
 Timmons, Michael L., 781
 Tin, C.C., 979
 Trautman, P., 821
 Trombetta, J.M., 33
 Tsai, Min-Hsiung, 349
 Tu, C.W., 793
 Tu, K.N., 961
 Tucker, J.H., 555

Tulchinski, D., 633

Jeda, O., 901

Uekusa, S., 139

Urban, K., 659

Valley, G.C., 937

Van de Walle, Chris G., 419

Van Vechten, J.A., 609

Venkatasubramanian, R., 95,
831

Visitserngtrakul, S., 955

von Bardeleben, H.J., 163,
747, 799, 837

Wachters, A.J.H., 605

Wada, Takao, 549

Wagner, A.V., 627

Wall, A., 665

Walukiewicz, W., 815, 845

Wang, P.D., 907

Ward, I.D., 197

Watkins, G.D., 367

Weber, Jörg, 443, 923

Weman, H., 257

Wichert, Th., 245

Wijaranakula, W., 597

Williams, R.L., 907

Wittmer, M., 529

Wolford, D.J., 27, 95, 343

Wong, D., 997

Woollam, John A., 965

Wu, D.T., 627

Wu, J., 1031

Xiao, Zhigang, 449

Xu, Hongqi, 287

Yamada, A., 115, 121, 139

Yao, G.-D., 1031

Yao, H.D., 759

Yoneta, Minoru, 291

Yoshino, J., 741

Yu, Shaofeng, 671, 715

Yuzun, Gao, 937

Zaidi, M.A., 163

Zazoui, M., 747

Zemanski, J.M., 975

Zemon, S., 109

Zhang, S.B., 765

Zhao, Q.X., 337

Zhao, Yong, 965

Zheng, Longru, 983, 993

Zhou, Tian-Qun, 449

Zhu, J., 567

Zundel, T., 443

Subject Index

- absorbance, infrared, 367
- absorption
 - high-resolution, 15
 - infrared, 277, 465, 477, 556, 809, 827, 919
 - intersubband, 875
 - intracenter, 321
 - model, Langmuir-Ridcal, 831
 - optical, 21, 179, 265, 805, 827
 - vibrational, 477
- acceptor(s), 483
 - double, 21, 169
 - like defect, shallow, 193
 - shallow, 331
 - zinc, 15
- activation
 - analysis, 1001
 - energies, 511
 - thermal, 781
- AES, 697, 993
- Al, 277
- AlGaAs, 109, 729, 747, 765, 773, 781, 793, 799, 881, 893, 1021
- AlGaInP, 893
- alloy clustering, 907
- amorphous layer, 975
- amphoteric
 - defect model, 845
 - impurity, 115
- annealing, 175, 233, 489, 523, 997
 - classical thermal, 915
 - furnace, 585
 - induced activation, 139
 - pulsed-laser, 759
- anti-
 - bonding site, 465
 - phase boundary, 901
- antisite, 39, 151
 - arsenic, 821, 827
- ashing, 965
- atomic
 - layer epitaxy (ALE), 647
 - order, 893
 - ordering, 907
- Auger
 - depth profile, 437
 - effect, 69
 - recombination, 265
- B-acceptor pair, 443
- band-to-band, 95
- bandgap narrowing, 759
- Be-
 - doping, 653, 881
 - ultra-high, 861
 - implanted, 151
- beam-coupling gain, 837
- bicrystals, 579
 - Ge, 945
- binding energy, 437
- bond-centered location, 465
- boron, 269, 367
- bound
 - excitons, 21, 221, 295, 303, 313, 325, 331, 343
 - multi-exciton complex, 221
- Bragg-Laue geometry, grazing, 1031
- bulk moduli, 425
- buried layer, 543
 - antimony, 597
 - marker, 529
- capacitively measured, 951
- capture
 - cross section, 781, 793
 - hot-electron, 729
 - rates, 729
- carbon, 197, 291, 887
 - group V pairing, 295
 - incorporation, 831
- carrier
 - activation, 983
 - compensation, 881
 - lifetime, minority, 95, 189, 951
 - scattering, 845
- $\text{Cd}_{1-x}\text{Mn}_x\text{Te}$, 665
- CdTe , 665
- charged particle activation
 - analysis (CPAA), 1001
- chemical etching, 1027
- chemo-mechanical polishing, 245
- chloride-VPE, 901
- cluster formation, 605
- clustering
 - effects, 383
 - model, dynamic, 605
- compensation, 133
- complex
 - defect, 139, 269, 303
 - formation, 633

- complexes, 39
 - S-related, 303
 - substitutional, 39
 - vacancy-
 - impurity, 39
 - phosphorus, 287
- compositionally graded
 - region, 489
- compound semiconductors, 845
- compression, 425
- concerted exchange, 511, 523
- conductance, source drain, 789
- configuration
 - coordinate diagram, 163, 295, 729
 - local atomic, 741
- constant-force-of-
 - interaction, 615
- contact(s)
 - metals, 1027
 - ohmic, 993
- contaminants, 197
 - internal, 915
- Cr, 567
 - B pairs, 239
 - interstitial, 239
- critical temperature, 893
- cross-bridge Kelvin (CBK), 993
- crystal-field splitting, 21
- Cu(-), 197, 273
 - diffused, 169
 - doped, 221, 295
 - pairing, 239
 - precipitation, 579
- CuBr, 407
- CuCl, 407
- Cu₃Si, 573
- CV
 - measurement, 1021
 - profiling, 855, 927
 - etch, 685
- damage characterization, 987
- dangling bonds, 1017
- decay time, 325
- deep levels, 27, 75, 157, 185, 277, 343, 729
- defect(s), 85, 927, 997, 1027
 - {113}, 955
 - axial isoelectronic, 295
 - characterization, 1031
 - dopant-related, 709
 - E₁, 915
 - E₂, 915
 - E₃, 915
 - E_c, 915
 - electron irradiation, 937
 - extended, 257
 - Ge-related, 179
 - hydrogen-induced, 449
 - intrinsic, 845
 - levels, 979
 - native, 845
 - noble-gas, 923
 - process-induced, 915
 - reactions, 845
 - rod-like, 291
 - Sn-vacancy, 261
- delta
 - doped, 855
 - lattice parameter (DLP)
 - model, 893
- depletion layer width, 951
- deuterium diffusion profile, 401
- diamagnetic shift, 313
- diamond, 89
- differential
 - scanning calorimetry (DSC), 961
 - transient spectroscopy (DITS), 785
- diffusion, 601, 639, 653, 677, 855
 - Al-Ga inter-, 697
 - anomalous, 605, 681
 - dopant, 983
 - vacancy, 597
- arsenic, 535
- asymmetric, 529
- atomic, 609
- Au, 609, 627
- B, 605
- Be, 715
- coupled defect-impurity, 561
- dopant impurity, 511
- enhanced, 529
 - O, 555
- hydrogen, 395, 401, 633
- impurity, 523
- inter-, 621, 639, 715
- low-temperature, 529
- Mn, 665
- nonequilibrium condition, 535
- one-sided, 609
- self, 511, 523, 573, 715
- Si, 671, 677, 691, 715
- Si-Si pair, 671
- Sn, 685
- substitutional interstitial, 653
- transient, 605
- volume, 549
- Zn, 659, 681, 715

- diffusion
 - coefficient, 383, 511, 535, 621, 627, 697, 715
 - lengths, hole, 997
 - model, 401
 - modeling, 535
 - profiles, calculated, 401
- diffusivity, 567
 - Ga-vacancy, 677
 - interstitial, 543
 - tensor, 615
- direct-gap semiconductor, 95
- dislocated, 459
- dislocation(s), 57, 941, 1007
 - edge, 1031
 - loops, 659
 - partial, 941
 - secondary, 945
- disordering
 - dopant-induced, 715
 - superlattices, 715
- dissociation energy, 465
- DLTS, 163, 277, 291, 567, 729, 741, 781, 785, 789, 815, 915, 979, 997
- donor(s)
 - generation, oxygen, 597
 - neutral, 313
 - new, 291
 - OH, 133
 - shallow, 33, 133, 753
 - substitutional, 729
- dopant atoms
 - Group-V, 277
 - substitutional, 529
- doping, 881, 887
 - electron-beam, 549
 - heavy, 759
 - n-type, 867
 - p-type, 867, 881
- DX center, 729, 741, 747, 753, 759, 765, 773, 781, 785, 789, 793, 799
- EBIC, 459
- EDX, 901
- effective-mass
 - hole, 21
 - state, 747, 799
- EL2, 211, 799, 805, 809, 815, 821, 827, 831, 837, 979
 - formation, 831
 - like defect, 175
- EL3, 211, 979
- EL6, 163, 979
- electrical
 - neutralization, 465
 - properties, 121
- electron
 - beam electroreflectance (EBER), 197
 - gas, 2-dimensional, 337
 - irradiation, 261, 265, 277, 367
 - microscopy, analytical, 659
 - electronic
 - structure, 81
 - transitions, 261
 - emission
 - barrier, electron, 741
 - rates, 729
 - EPR, 233, 307, 407, 419, 799
 - Er-doped, 69
 - exchange broadening, 33
 - excited states, 15, 21
 - excitons, 95, 109, 115, 273
- Fermi
 - energy, 845
 - level
 - effect, 671, 697
 - stabilization energy, 845
 - resonance, 367
- Fick's second law, 653
- first-principles calculations, 419, 425, 511
- fourier transform
 - photoluminescence spectroscopy (FTPLS), 221
- Frank-Condon shift, 261
- free
 - excitons, 325, 361
 - heavy-hole, 313
 - to-bound, 313
- FTIR, 169, 207, 221, 919
- GaAs, 95, 109, 115, 121, 127, 163, 169, 175, 189, 193, 207, 221, 349, 407, 465, 477, 483, 549, 653, 659, 671, 677, 681, 685, 691, 715, 759, 765, 799, 809, 815, 821, 827, 837, 845, 855, 867, 881, 975, 979, 983, 987, 993, 997, 1001, 1011, 1021
- heavily
 - Be-doped, 121
 - Ge-doped, 115
- LEC, 197
- semi-insulating, 75, 157, 189
- undoped, 211
- GaAs/AlGaAs, 313, 325, 331, 337
- GaAs/Ge, 647
- GaAs/InP, 489
- GaAsSb, 893

- GaAs/Si, 1031
- GaInP, 893
- GaP, 145, 179, 215, 407
 - S-doped, 145
- GaPSb, 893
- gas bubbles, 449
- Ge, 133, 407
 - amorphous, 621
 - ultra-pure, 133
- gettering, 915, 951, 969
- gradient, electric field, 245
- grain boundary, 211, 579, 945
- Green's function, 511
- H₂
 - molecules, 401
 - pairing, 401
- H-band luminescence, 337
- Hall measurement, 203, 881, 1021
- HClX, 997
- heat of solution, 425
- HEMTS, 789
- heterojunctions, 337
 - GaAs/Ge, 647
- heterostructures, 1011
 - GaAs/AlGaAs, 753
 - modulation-doped, 845
 - Si/Ge, 523
 - Si/SiGe, 343
- high-
 - dose, 931
 - resolution spectroscopy, 3
- hole-hole coupling, 21
- homoelectronic, 95
- hot carriers, 85
- HREM, 955
- Huang-Rhys factor, 261
- HVEM, 937
- hydrogen, 245, 383, 401, 419, 425, 437, 443, 459, 511
 - acceptor pairs, 245, 483
 - B pairs, 395, 401
 - bond, 465
 - charge state, 425
 - complexes, 465
 - diffusion, 455, 465
 - donor complexes, 477
 - impurity complexes, 465
 - isolated, 407
 - O interaction, 555
 - pairs, 443
 - passivation, 245, 367, 431, 459, 477, 489
 - plasma, 555
 - neutralization, 465
 - related complexes, 377
 - segregation, 437
 - shallow-acceptor, 443
 - Sn complex, 477
 - hydrogenated, 483
 - hydrogenation, 431, 449, 455, 465
 - DX center, 793
 - ion-beam, 455
 - plasma, 489, 501
 - hydrogenic states, 729
 - hyperfine parameters, 419
 - immiscibility, 893
 - implantation, 139, 621
 - hydrogen, 915
 - iron, 919
 - MeV, 979
 - oxygen, 975, 979
 - Sb, 931
 - Si, 983
 - Sn, 585, 685
 - impurities, 197, 927, 1027
 - metal, 915
 - impurity-induced layer
 - disorder (IILD), 697
 - In₁₁₁, 245
 - InAsSb, 893, 907
 - In-Cu pairs, 245
 - indiffusion, Mn, 665
 - in-doped, isoelectronic, 189
 - infrared
 - far, 133, 221
 - mid, 221
 - InGaAs, 495, 861, 887
 - InGaAs/InP, 203
 - InGaAsP, 893
 - InGaAsSb, 893
 - InGaP, 901
 - InP, 33, 139, 185, 465, 501, 861, 867, 1007
 - semi-insulating, 75
 - InPSb, 893
 - interaction potential, 615
 - interface(s), 437, 951
 - (115), 955
 - Al/Si, 437
 - GaAs/AlGaAs, 337, 639
 - roughness, 361
 - traps, 951
 - interfacial luminescence, 489
 - interstitial(s), 561, 639
 - Al, 277
 - Be, 881
 - donor, 881
 - iron, 51
 - mechanism, 523
 - mediated, 511
 - self, 609, 715
 - Zn, 681
 - ion
 - beam etching, 923
 - implantation, 601, 653
 - transit, 431

- ionization energy, 747
- iron, 51, 185, 919
 - B pairs, 233
 - indium pairs, 307
- isothermal transient spectroscopy (ITS) 785
- isotope
 - effect, 465
 - shift, 367
- Jahn-Teller, 169
- junction
 - impedance, 951
 - leakage current, 951
 - p-n, 951
- Kaufman plasma, 449
- kick-out
 - mechanism, 549, 659, 715
 - model, 609
- kinetic model, 633
- Kyropoulos growth, 1007
- laser applications, 993
- lattice
 - image, 437
 - relaxation, 81, 729, 799, 805
 - large, 747, 773
- lifetime, 95
- measurement, 215
- light-emitting-diode, blue, 81
- limited-reaction processing, 591
- lithium, 81, 127
- local density
 - approximation (LDA), 89
 - functional formalism, 81
- LPE, 901, 907
- magnetic field, axial, 1007
- MBE, 69, 115, 121, 193, 875, 887, 893, 907, 927, 1021
 - gas-source, 861
 - hydride-source, 861
 - regrown, 987
- membrane structure, 543
- mercuric iodide (HgI_2), 1027
- metal contamination, 57
- metastability, 295, 407, 799, 815
- metastable, 827
 - properties, 265
- Mg, 653
- migration energy, 937
- miscibility gaps, 893, 907
- mixing, 709
 - luminescence, 215
- Mn, 185, 197, 207, 215
- mobilities, 881, 887, 907, 1007
 - free-carrier, 845
- mobility-lifetime product, 837
- MOCVD, 63, 867, 901, 907
- modulated structure, 901
- molecular dynamics, 941
 - simulations, ab initio, 383
- moment analysis, 615
- monohydride groups, 383
- Monte-Carlo simulation, 609
 - dynamic, 615
- Mössbauer spectroscopy, 579, 585
- MQW, GaAs/AlGaAs, 875
- multilayers, 961
 - artificial, 621, 627
- muon, 407
 - spin
 - resonance, 419
 - rotation, 407
- muonium, 419
 - centers, 407
- Murali and Murarka theory, 965
- neutralization, 443
- $(\text{NH}_4)_2\text{S}$, 1017
- nitridation, 535
- nitrogen, 89
- nondestructive inspection, 951
- nonradiative, 69
- nuclear
 - detectors, 1027
 - resonant reaction, 437
- ODMR, 33, 39, 81, 145, 151, 303, 377, 753
 - donor-acceptor pair, 33
- OMMBE, 855
- OMVPE, 831, 855, 893
- optical ionization, 15
- ordered
 - alloy, 741
 - structures, 893, 901
- ordering
 - CuPt-type, 901, 907
 - short-range, 893
- oscillator strength, giant, 361
- oscillatory structure, 63
- oxidation, 543
 - dry, 965
 - mechanism of, 965
- oxides, ultra thin, 965
- oxygen, 151, 919, 969, 975, 979, 1001
 - atomic, 965

- pair
 - correlation function, 383
 - recombination, 33
- pairing
 - Cr-B, 567
 - defect-impurity, 561
 - reaction, 567
 - SiGa-VGa, 677
- Pankove model, 367
- passivation, 633
 - acceptor, 483, 501
 - dopant, 455
 - nonradiative center, 489
 - Zn-acceptor, 495
- pattern recognition, vector, 639
- Pd/Au:Be, 993
- Pd₂Si, 529
- PECVD, 501
- penetration depth, kinematical, 631
- perturbed angular correlation, 239
- phase
 - separation, 907
 - volume grating, 827
- phonon density of states, 383
- phosphorus, 89, 221, 269
- photo-
 - capture, 773
 - induced
 - changes, 809
 - transient spectroscopy (PITS), 75
 - thermal ionization spectroscopy (PTIS), 3, 133
- photoconductivity, 133, 179, 239, 809
 - persistent, 773
 - spectral, 157
- photocurrent, 951, 997
- photoelectron spectroscopy, x-ray, 931
- photoemission, 665
- photoionization, 773
 - cross section, 793
- photoluminescence, 27, 33, 57, 69, 109, 115, 121, 127, 139, 157, 163, 169, 185, 193, 203, 207, 215, 221, 239, 257, 269, 273, 277, 295, 303, 313, 325, 331, 337, 343, 361, 377, 483, 489, 549, 697, 747, 759, 907, 923, 1017, 1021, 1027
- D-band, 57
- decay, 325
- 0.8 eV band, 163
- excitation, 63, 69, 139, 221
 - magneto-, 221
 - resonant, 313
 - temperature-dependent, 313
 - time-resolved, 95
- photon beam, chopped, 951
- photoquenching, 809, 827
- photorefractive effect, 837
- photovoltage
 - AC, 951
 - surface, 951
- planar
 - defects, (111), 449
 - doped structures, 1021
- plastically deformed, 57
- platelets, 257
- point(-)defect(s), 3
 - charged, 691
 - gradient model, 671
 - native, 639
 - nonequilibrium, 715
- polaron measurement, 881
- polycrystalline, 579
- Poole-Frenkel, 747, 785
- positron, 927
 - annihilation, 927
 - slow, 927
- potential well, strain-induced, 257
- preannealing, low-temperature, 291
- precipitates, 257, 659, 861, 915, 969
 - oxygen, 597
- pressure
 - hydrostatic, 27, 523, 741, 747, 799, 805, 815
 - uniaxial, 805
- pseudo-donor model, 265
- pseudopotential method
 - ab initio self-consistent, 765
 - norm-conserving, 81
- quantum(-)well(s), 313, 325, 331, 349, 875
 - heterostructures (QWH), 697
- quasi-steady-state, 561
- quenching, 969
- radiation
 - damage, 343
 - induced, 277
- radiative efficiency, 95
- radioactive acceptor, 245
- Raman scattering, 875, 987

- rapid thermal
 - annealing (RTA), 585, 601, 681, 931, 1021
 - processing (RTP), 591, 915
- reaction kinetics, first-order, 233
- recombination
 - nonradiative, 145
 - radiative, 295
- recovery, 827
- reflectance spectroscopy, infrared, 395
- regrowth kinetics, 975
- regular solution model, 893
- ReSi₂, 573
- RHEED, 1017
- RIE, 495, 987
- rocking curve, 1031
- Rutherford backscattering (RBS), 585, 601, 923, 931, 961, 975
- Rydberg series, 51
- S-diffused, 303
- scanning photon microscope (SPM), 951
- Schottky barrier, 1021
- segregates, 861
- segregation coefficient, 1001
- selectively doped, 741
- SEM, 697
- SEM/EBIC, 449
- semi-magnetic semiconductor, 665
- Si
 - compensation, 875
 - dopant behavior, 875
- SiGe alloys, 591
- silicidation, 961
- silicides, 573
 - metal, 579
 - transition-metal, 529
- silicon, 15, 27, 51, 57, 221, 233, 239, 261, 269, 277, 287, 291, 303, 307, 367, 377, 383, 395, 401, 407, 419, 425, 431, 437, 449, 455, 459, 511, 523, 535, 543, 549, 561, 567, 573, 579, 585, 591, 597, 601, 605, 609, 633, 915, 923, 927, 931, 937, 941, 965, 969
 - amorphous, 621, 627, 961
 - on-insulator, 955, 1011
 - on-sapphire, 1011
- SIMOX, 955
- SIMS, 401, 437, 501, 529, 591, 605, 633, 647, 653, 685, 691, 697, 855, 861, 867, 919, 927, 983
- Si/SiGe, 343
- Sn, 261, 867
- snow-plow effect, 529
- solar cells, 997
- solid solubility, 585
- spectrophotometry, infrared
 - multiple internal reflection, 449
- spin
 - density functional, 419
 - Hamiltonian, 377
- spinodal decomposition, 901
- spreading resistance
 - measurement (SRM), 659
- Stillinger-Weber potential, 941
- Stokes shift, 765
- strain, 523
 - binding, 273
 - energy, 893
 - heteroepitaxial, 753
 - hydrostatic, 273
- stress, 465, 789
 - uniaxial, 273, 815, 821
- substitutionality, 585
- subsurface layers, thin, 1031
- sulfur-coated, 1017
- superlattices, 343
 - GaAs/AlGaAs, 709
 - monolayer, 901
- supersaturation, 715
 - interstitial, 535
 - oxygen, 591
 - vacancy, 535
- surface
 - alloys, non-equilibrium, 665
 - ambient interaction, 697
 - electric field, 449
 - potential, 951
 - protection, 501
 - reaction, 665
 - recombination velocity, 95
 - structure, 1017
- synchrotron white beam, 1031
- TED, 907
- TEM, 579, 585, 659, 697, 709, 861, 893, 901, 907, 937, 945, 961, 975, 979, 983, 987, 993
- tension, 425
- ternary alloy, 785

- thermal
 - (-)donor, 291, 597
 - formation, 555
 - neutron(s), 179
 - irradiation, 175
 - treatment, 919
- thermally stimulated current (TSC), 189
- thermodynamic equilibrium reaction, 831
- tight(-)binding, 349
- theory, 287
- tilt grain boundary, 945
- titanium, 961
- topographic imaging, 1031
- total
 - energies, 81
 - energy
 - calculations, 89, 425
 - surfaces, 511
- transformation, 809
- transient
 - capacitance, 789
 - current, 789
- transition
 - metal films, 573
 - state, 729
- transmission, 3, 51
 - line model (TLM), 993
 - topographs, 1031
- transmittance, 477
- transmuted Ge, 179
- transport equation, 615
- transverse electric fields, 337
- trapping, 109
- traps, 189
 - positively charged, 951
- TRR, 975
- twinning, 955
- two-beam experiment, 69
- undersaturation, 715
- vacancies, 561, 609, 639, 845, 937, 969
 - Ga, 677
- vacancy
 - mechanism, 523
 - mediated, 511
- valence force field (VFF) model, 893
- Van der Pauw, 121
- vanadium, 63
- variable angle of incidence spectroscopic ellipsometry (VASE), 965
- variational calculation, 361
- virtual crystal approximation (VCA), 893
- void formation, 983
- XPS, 1017
- x-ray(s), 1031
 - diffraction, 621, 627
 - rocking, 1021
- Zeeman, 133
 - measurements, 273, 295
 - spectroscopy, 51, 207
- zero-
 - field splitting, 307
 - phonon line, 805, 821
- zinc, 21, 33, 867
 - substitutional, 681
- ZnSe, 81, 349

MATERIALS RESEARCH SOCIETY SYMPOSIUM PROCEEDINGS

ISSN 0272 - 9172

- Volume 1—Laser and Electron-Beam Solid Interactions and Materials Processing, J. F. Gibbons, L. D. Hess, T. W. Sigmon, 1981, ISBN 0-444-00595-1
- Volume 2—Defects in Semiconductors, J. Narayan, T. Y. Tan, 1981, ISBN 0-444-00596-X
- Volume 3—Nuclear and Electron Resonance Spectroscopies Applied to Materials Science, E. N. Kaufmann, G. K. Shenoy, 1981, ISBN 0-444-00597-8
- Volume 4—Laser and Electron-Beam Interactions with Solids, B. R. Appleton, G. K. Celler, 1982, ISBN 0-444-00693-1
- Volume 5—Grain Boundaries in Semiconductors, H. J. Leamy, G. E. Pike, C. H. Seager, 1982, ISBN 0-444-00697-4
- Volume 6—Scientific Basis for Nuclear Waste Management IV, S. V. Topp, 1982, ISBN 0-444-00699-0
- Volume 7—Metastable Materials Formation by Ion Implantation, S. T. Picraux, W. J. Choyke, 1982, ISBN 0-444-00692-3
- Volume 8—Rapidly Solidified Amorphous and Crystalline Alloys, B. H. Kear, B. C. Giessen, M. Cohen, 1982, ISBN 0-444-00698-2
- Volume 9—Materials Processing in the Reduced Gravity Environment of Space, G. E. Rindone, 1982, ISBN 0-444-00691-5
- Volume 10—Thin Films and Interfaces, P. S. Ho, K.-N. Tu, 1982, ISBN 0-444-00774-1
- Volume 11—Scientific Basis for Nuclear Waste Management V, W. Lutze, 1982, ISBN 0-444-00725-3
- Volume 12—In Situ Composites IV, F. D. Lemkey, H. E. Cline, M. McLean, 1982, ISBN 0-444-00726-1
- Volume 13—Laser-Solid Interactions and Transient Thermal Processing of Materials, J. Narayan, W. L. E. own, R. A. Lemons, 1983, ISBN 0-444-00788-1
- Volume 14—Defects in Semiconductors II, S. Mahajan, J. W. Corbett, 1983, ISBN 0-444-00812-8
- Volume 15—Scientific Basis for Nuclear Waste Management VI, D. G. Brookins, 1983, ISBN 0-444-00780-6
- Volume 16—Nuclear Radiation Detector Materials, E. E. Haller, H. W. Kraner, W. A. Higinbotham, 1983, ISBN 0-444-00787-3
- Volume 17—Laser Diagnostics and Photochemical Processing for Semiconductor Devices, R. M. Osgood, S. R. J. Brueck, H. R. Schlossberg, 1983, ISBN 0-444-00782-2
- Volume 18—Interfaces and Contacts, R. Ludeke, K. Rose, 1983, ISBN 0-444-00820-9
- Volume 19—Alloy Phase Diagrams, L. H. Bennett, T. B. Massalski, B. C. Giessen, 1983, ISBN 0-444-00809-8
- Volume 20—Intercalated Graphite, M. S. Dresselhaus, G. Dresselhaus, J. E. Fischer, M. J. Moran, 1983, ISBN 0-444-00781-4
- Volume 21—Phase Transformations in Solids, T. Tsakalakos, 1984, ISBN 0-444-00901-9
- Volume 22—High Pressure in Science and Technology, C. Homan, R. K. MacCrone, E. Whalley, 1984, ISBN 0-444-00932-9 (3 part set)
- Volume 23—Energy Beam-Solid Interactions and Transient Thermal Processing, J. C. C. Fan, N. M. Johnson, 1984, ISBN 0-444-00903-5
- Volume 24—Defect Properties and Processing of High-Technology Nonmetallic Materials, J. H. Crawford, Jr., Y. Chen, W. A. Sibley, 1984, ISBN 0-444-00904-3
- Volume 25—Thin Films and Interfaces II, J. E. E. Baglin, D. R. Campbell, W. K. Chu, 1984, ISBN 0-444-00905-1

MATERIALS RESEARCH SOCIETY SYMPOSIUM PROCEEDINGS

- Volume 26—Scientific Basis for Nuclear Waste Management VII, G. L. McVay, 1984, ISBN 0-444-00906-X
- Volume 27—Ion Implantation and Ion Beam Processing of Materials, G. K. Hubler, O. W. Holland, C. R. Clayton, C. W. White, 1984, ISBN 0-444-00869-1
- Volume 28—Rapidly Solidified Metastable Materials, B. H. Kear, B. C. Giessen, 1984, ISBN 0-444-00935-3
- Volume 29—Laser-Controlled Chemical Processing of Surfaces, A. W. Johnson, D. J. Ehrlich, H. R. Schlossberg, 1984, ISBN 0-444-00894-2
- Volume 30—Plasma Processing and Synthesis of Materials, J. Szekeley, D. Apelian, 1984, ISBN 0-444-00895-0
- Volume 31—Electron Microscopy of Materials, W. Krakow, D. A. Smith, L. W. Hobbs, 1984, ISBN 0-444-00898-7
- Volume 32—Better Ceramics Through Chemistry, C. J. Brinker, D. E. Clark, D. R. Ulrich, 1984, ISBN 0-444-00898-5
- Volume 33—Comparison of Thin Film Transistor and SOI Technologies, H. W. Lam, M. J. Thompson, 1984, ISBN 0-444-00899-3
- Volume 34—Physical Metallurgy of Cast Iron, H. Fredriksson, M. Hillerts, 1985, ISBN 0-444-00938-8
- Volume 35—Energy Beam-Solid Interactions and Transient Thermal Processing/1984, D. K. Biegelsen, G. A. Rozgonyi, C. V. Shank, 1985, ISBN 0-931837-00-6
- Volume 36—Impurity Diffusion and Gettering in Silicon, R. B. Fair, C. W. Pearce, J. Washburn, 1985, ISBN 0-931837-01-4
- Volume 37—Layered Structures, Epitaxy, and Interfaces, J. M. Gibson, L. R. Dawson, 1985, ISBN 0-931837-02-2
- Volume 38—Plasma Synthesis and Etching of Electronic Materials, R. P. H. Chang, B. Abeles, 1985, ISBN 0-931837-03-0
- Volume 39—High-Temperature Ordered Intermetallic Alloys, C. C. Koch, C. T. Liu, N. S. Stoloff, 1985, ISBN 0-931837-04-9
- Volume 40—Electronic Packaging Materials Science, E. A. Giess, K.-N. Tu, D. R. Uhlmann, 1985, ISBN 0-931837-05-7
- Volume 41—Advanced Photon and Particle Techniques for the Characterization of Defects in Solids, J. B. Roberto, R. W. Carpenter, M. C. Wittels, 1985, ISBN 0-931837-06-5
- Volume 42—Very High Strength Cement-Based Materials, J. F. Young, 1985, ISBN 0-931837-07-3
- Volume 43—Fly Ash and Coal Conversion By-Products: Characterization, Utilization, and Disposal I, G. J. McCarthy, R. J. Lauf, 1985, ISBN 0-931837-08-1
- Volume 44—Scientific Basis for Nuclear Waste Management VIII, C. M. Jantzen, J. A. Stone, R. C. Ewing, 1985, ISBN 0-931837-09-X
- Volume 45—Ion Beam Processes in Advanced Electronic Materials and Device Technology, B. R. Appleton, F. H. Eisen, T. W. Sigmon, 1985, ISBN 0-931837-10-3
- Volume 46—Microscopic Identification of Electronic Defects in Semiconductors, N. M. Johnson, S. G. Bishop, G. D. Watkins, 1985, ISBN 0-931837-11-1
- Volume 47—Thin Films: The Relationship of Structure to Properties, C. R. Aita, K. S. Sreeharsha, 1985, ISBN 0-931837-12-X
- Volume 48—Applied Materials Characterization, W. Katz, P. Williams, 1985, ISBN 0-931837-13-8
- Volume 49—Materials Issues in Applications of Amorphous Silicon Technology, D. Adler, A. Madan, M. J. Thompson, 1985, ISBN 0-931837-14-6

MATERIALS RESEARCH SOCIETY SYMPOSIUM PROCEEDINGS

- Volume 50—Scientific Basis for Nuclear Waste Management IX, L. O. Werme, 1986, ISBN 0-931837-15-4
- Volume 51—Beam-Solid Interactions and Phase Transformations, H. Kurz, G. L. Olson, J. M. Poate, 1986, ISBN 0-931837-16-2
- Volume 52—Rapid Thermal Processing, T. O. Sedgwick, T. E. Seidel, B.-Y. Tsaur, 1986, ISBN 0-931837-17-0
- Volume 53—Semiconductor-on-Insulator and Thin Film Transistor Technology, A. Chiang, M. W. Geis, L. Pfeiffer, 1986, ISBN 0-931837-18-9
- Volume 54—Thin Films—Interfaces and Phenomena, R. J. Nemanich, P. S. Ho, S. S. Lau, 1986, ISBN 0-931837-19-7
- Volume 55—Biomedical Materials, J. M. Williams, M. F. Nichols, W. Zingg, 1986, ISBN 0-931837-20-0
- Volume 56—Layered Structures and Epitaxy, J. M. Gibson, G. C. Osbourn, R. M. Tromp, 1986, ISBN 0-931837-21-9
- Volume 57—Phase Transitions in Condensed Systems—Experiments and Theory, G. S. Cargill III, F. Spaepen, K.-N. Tu, 1987, ISBN 0-931837-22-7
- Volume 58—Rapidly Solidified Alloys and Their Mechanical and Magnetic Properties, B. C. Giessen, D. E. Polk, A. I. Taub, 1986, ISBN 0-931837-23-5
- Volume 59—Oxygen, Carbon, Hydrogen, and Nitrogen in Crystalline Silicon, J. C. Mikkelsen, Jr., S. J. Pearton, J. W. Corbett, S. J. Pennycook, 1986, ISBN 0-931837-24-3
- Volume 60—Defect Properties and Processing of High-Technology Nonmetallic Materials, Y. Chen, W. D. Kingery, R. J. Stokes, 1986, ISBN 0-931837-25-1
- Volume 61—Defects in Glasses, F. L. Galeener, D. L. Griscom, M. J. Weber, 1986, ISBN 0-931837-26-X
- Volume 62—Materials Problem Solving with the Transmission Electron Microscope, L. W. Hobbs, K. H. Westmacott, D. B. Williams, 1986, ISBN 0-931837-27-8
- Volume 63—Computer-Based Microscopic Description of the Structure and Properties of Materials, J. Broughton, W. Krakow, S. T. Pantelides, 1986, ISBN 0-931837-28-6
- Volume 64—Cement-Based Composites: Strain Rate Effects on Fracture, S. Mindess, S. P. Shah, 1986, ISBN 0-931837-29-4
- Volume 65—Fly Ash and Coal Conversion By-Products: Characterization, Utilization and Disposal II, G. J. McCarthy, F. P. Glasser, D. M. Roy, 1986, ISBN 0-931837-30-8
- Volume 66—Frontiers in Materials Education, L. W. Hobbs, G. L. Liedl, 1986, ISBN 0-931837-31-6
- Volume 67—Heteroepitaxy on Silicon, J. C. C. Fan, J. M. Poate, 1986, ISBN 0-931837-33-2
- Volume 68—Plasma Processing, J. W. Coburn, R. A. Gottscho, D. W. Hess, 1986, ISBN 0-931837-34-0
- Volume 69—Materials Characterization, N. W. Cheung, M.-A. Nicolet, 1986, ISBN 0-931837-35-9
- Volume 70—Materials Issues in Amorphous-Semiconductor Technology, D. Adler, Y. Hamakawa, A. Madan, 1986, ISBN 0-931837-36-7
- Volume 71—Materials Issues in Silicon Integrated Circuit Processing, M. Wittmer, J. Stimmell, M. Strathman, 1986, ISBN 0-931837-37-5
- Volume 72—Electronic Packaging Materials Science II, K. A. Jackson, R. C. Pohanka, D. R. Uhlmann, D. R. Ulrich, 1986, ISBN 0-931837-38-3
- Volume 73—Better Ceramics Through Chemistry II, C. J. Brinker, D. E. Clark, D. R. Ulrich, 1986, ISBN 0-931837-39-1
- Volume 74—Beam-Solid Interactions and Transient Processes, M. O. Thompson, S. T. Picraux, J. S. Williams, 1987, ISBN 0-931837-40-5

MATERIALS RESEARCH SOCIETY SYMPOSIUM PROCEEDINGS

- Volume 75—Photon, Beam and Plasma Stimulated Chemical Processes at Surfaces, V. M. Donnelly, I. P. Herman, M. Hirose, 1987, ISBN 0-931837-41-3
- Volume 76—Science and Technology of Microfabrication, R. E. Howard, E. L. Hu, S. Namba, S. Pang, 1987, ISBN 0-931837-42-1
- Volume 77—Interfaces, Superlattices, and Thin Films, J. D. Dow, I. K. Schuller, 1987, ISBN 0-931837-56-1
- Volume 78—Advances in Structural Ceramics, P. F. Becher, M. V. Swain, S. Sōmiya, 1987, ISBN 0-931837-43-X
- Volume 79—Scattering, Deformation and Fracture in Polymers, G. D. Wignall, B. Crist, T. P. Russell, E. L. Thomas, 1987, ISBN 0-931837-44-8
- Volume 80—Science and Technology of Rapidly Quenched Alloys, M. Tenhover, W. L. Johnson, L. E. Tanner, 1987, ISBN 0-931837-45-6
- Volume 81—High-Temperature Ordered Intermetallic Alloys, II, N. S. Stoloff, C. C. Koch, C. T. Liu, O. Izumi, 1987, ISBN 0-931837-46-4
- Volume 82—Characterization of Defects in Materials, R. W. Siegel, J. R. Weertman, R. Sinclair, 1987, ISBN 0-931837-47-2
- Volume 83—Physical and Chemical Properties of Thin Metal Overlayers and Alloy Surfaces, D. M. Zehner, D. W. Goodman, 1987, ISBN 0-931837-48-0
- Volume 84—Scientific Basis for Nuclear Waste Management X, J. K. Bates, W. B. Seefeldt, 1987, ISBN 0-931837-49-9
- Volume 85—Microstructural Development During the Hydration of Cement, L. Struble, P. Brown, 1987, ISBN 0-931837-50-2
- Volume 86—Fly Ash and Coal Conversion By-Products Characterization, Utilization and Disposal III, G. J. McCarthy, F. P. Glasser, D. M. Roy, S. Diamond, 1987, ISBN 0-931837-51-0
- Volume 87—Materials Processing in the Reduced Gravity Environment of Space, R. H. Doremus, P. C. Nordine, 1987, ISBN 0-931837-52-9
- Volume 88—Optical Fiber Materials and Properties, S. R. Nagel, J. W. Fleming, G. Sigel, D. A. Thompson, 1987, ISBN 0-931837-53-7
- Volume 89—Diluted Magnetic (Semimagnetic) Semiconductors, R. L. Aggarwal, J. K. Furdyna, S. von Molnar, 1987, ISBN 0-931837-54-5
- Volume 90—Materials for Infrared Detectors and Sources, R. F. C. Farrow, J. F. Schetzina, J. T. Cheung, 1987, ISBN 0-931837-55-3
- Volume 91—Heteroepitaxy on Silicon II, J. C. C. Fan, J. M. Phillips, B.-Y. Tsaur, 1987, ISBN 0-931837-58-8
- Volume 92—Rapid Thermal Processing of Electronic Materials, S. R. Wilson, R. A. Powell, D. E. Davies, 1987, ISBN 0-931837-59-6
- Volume 93—Materials Modification and Growth Using Ion Beams, U. Gibson, A. E. White, P. P. Pronko, 1987, ISBN 0-931837-60-X
- Volume 94—Initial Stages of Epitaxial Growth, R. Hull, J. M. Gibson, David A. Smith, 1987, ISBN 0-931837-61-8
- Volume 95—Amorphous Silicon Semiconductors—Pure and Hydrogenated, A. Madan, M. Thompson, D. Adler, Y. Hamakawa, 1987, ISBN 0-931837-62-6
- Volume 96—Permanent Magnet Materials, S. G. Sankar, J. F. Herbst, N. C. Koon, 1987, ISBN 0-931837-63-4
- Volume 97—Novel Refractory Semiconductors, D. Emin, T. Aselage, C. Wood, 1987, ISBN 0-931837-64-2
- Volume 98—Plasma Processing and Synthesis of Materials, D. Apelian, J. Szekely, 1987, ISBN 0-931837-65-0

MATERIALS RESEARCH SOCIETY SYMPOSIUM PROCEEDINGS

- Volume 99—High-Temperature Superconductors, M. B. Brodsky, R. C. Dynes, K. Kitazawa, H. L. Tuller, 1988, ISBN 0-931837-67-7
- Volume 100—Fundamentals of Beam-Solid Interactions and Transient Thermal Processing, M. J. Aziz, L. E. Rehn, B. Stritzker, 1988, ISBN 0-931837-68-5
- Volume 101—Laser and Particle-Beam Chemical Processing for Microelectronics, D.J. Ehrlich, G.S. Higashi, M.M. Oprysko, 1988, ISBN 0-931837-69-3
- Volume 102—Epitaxy of Semiconductor Layered Structures, R. T. Tung, L. R. Dawson, R. L. Gunshor, 1988, ISBN 0-931837-70-7
- Volume 103—Multilayers: Synthesis, Properties, and Nonelectronic Applications, T. W. Barbee Jr., F. Spaepen, L. Greer, 1988, ISBN 0-931837-71-5
- Volume 104—Defects in Electronic Materials, M. Stavola, S. J. Pearton, G. Davies, 1988, ISBN 0-931837-72-3
- Volume 105—SiO₂ and Its Interfaces, G. Lucovsky, S. T. Pantelides, 1988, ISBN 0-931837-73-1
- Volume 106—Polysilicon Films and Interfaces, C.Y. Wong, C.V. Thompson, K-N. Tu, 1988, ISBN 0-931837-74-X
- Volume 107—Silicon-on-Insulator and Buried Metals in Semiconductors, J. C. Sturm, C. K. Chen, L. Pfeiffer, P. L. F. Hemment, 1988, ISBN 0-931837-75-8
- Volume 108—Electronic Packaging Materials Science II, R. C. Sundahl, R. Jaccodine, K. A. Jackson, 1988, ISBN 0-931837-76-6
- Volume 109—Nonlinear Optical Properties of Polymers, A. J. Heeger, J. Orenstein, D. R. Ulrich, 1988, ISBN 0-931837-77-4
- Volume 110—Biomedical Materials and Devices, J. S. Hanker, B. L. Giammara, 1988, ISBN 0-931837-78-2
- Volume 111—Microstructure and Properties of Catalysts, M. M. J. Treacy, J. M. Thomas, J. M. White, 1988, ISBN 0-931837-79-0
- Volume 112—Scientific Basis for Nuclear Waste Management XI, M. J. Apted, R. E. Westerman, 1988, ISBN 0-931837-80-4
- Volume 113—Fly Ash and Coal Conversion By-Products: Characterization, Utilization, and Disposal IV, G. J. McCarthy, D. M. Roy, F. P. Glasser, R. T. Hemmings, 1988, ISBN 0-931837-81-2
- Volume 114—Bonding in Cementitious Composites, S. Mindess, S. P. Shah, 1988, ISBN 0-931837-82-0
- Volume 115—Specimen Preparation for Transmission Electron Microscopy of Materials, J. C. Bravman, R. Anderson, M. L. McDonald, 1988, ISBN 0-931837-83-9
- Volume 116—Heteroepitaxy on Silicon: Fundamentals, Structures, and Devices, H.K. Choi, H. Ishiwara, R. Hull, R.J. Nemanich, 1988, ISBN: 0-931837-86-3
- Volume 117—Process Diagnostics: Materials, Combustion, Fusion, K. Hays, A.C. Eckbreth, G.A. Campbell, 1988, ISBN: 0-931837-87-1
- Volume 118—Amorphous Silicon Technology, A. Madan, M.J. Thompson, P.C. Taylor, P.G. LeComber, Y. Hamakawa, 1988, ISBN: 0-931837-88-X
- Volume 119—Adhesion in Solids, D.M. Mattox, C. Batich, J.E.E. Baglin, R.J. Gottschall, 1988, ISBN: 0-931837-89-8
- Volume 120—High-Temperature/High-Performance Composites, F.D. Lemkey, A.G. Evans, S.G. Fishman, J.R. Strife, 1988, ISBN: 0-931837-90-1
- Volume 121—Better Ceramics Through Chemistry III, C.J. Brinker, D.E. Clark, D.R. Ulrich, 1988, ISBN: 0-931837-91-X

MATERIALS RESEARCH SOCIETY SYMPOSIUM PROCEEDINGS

- Volume 122—Interfacial Structure, Properties, and Design, M.H. Yoo, W.A.T. Clark, C.L. Briant, 1988, ISBN: 0-931837-92-8
- Volume 123—Materials Issues in Art and Archaeology, E.V. Sayre, P. Vandiver, J. Druzik, C. Stevenson, 1988, ISBN: 0-931837-93-6
- Volume 124—Microwave-Processing of Materials, M.H. Brooks, I.J. Chabinsky, W.H. Sutton, 1988, ISBN: 0-931837-94-4
- Volume 125—Materials Stability and Environmental Degradation, A. Barkatt, L.R. Smith, E. Verink, 1988, ISBN: 0-931837-95-2
- Volume 126—Advanced Surface Processes for Optoelectronics, S. Bernasek, T. Venkatesan, H. Temkin, 1988, ISBN: 0-931837-96-0
- Volume 127—Scientific Basis for Nuclear Waste Management XII, W. Lutze, R.C. Ewing, 1989, ISBN: 0-931837-97-9
- Volume 128—Processing and Characterization of Materials Using Ion Beams, L.E. Rehn, J. Greene, F.A. Smidt, 1989, ISBN: 1-55899-001-1
- Volume 129—Laser and Particle-Beam Modification of Chemical Processes on Surfaces, A.W. Johnson, G.L. Loper, T.W. Sigmon, 1989, ISBN: 1-55899-002-X
- Volume 130—Thin Films: Stresses and Mechanical Properties, J.C. Bravman, W.D. Nix, D.M. Barnett, D.A. Smith, 1989, ISBN: 1-55899-003-8
- Volume 131—Chemical Perspectives of Microelectronic Materials, M.E. Gross, J. Jasinski, J.T. Yates, Jr., 1989, ISBN: 1-55899-004-6
- Volume 132—Multicomponent Ultrafine Microstructures, L.E. McCandlish, B.H. Kear, D.E. Polk, and R.W. Siegel, 1989, ISBN: 1-55899-005-4
- Volume 133—High Temperature Ordered Intermetallic Alloys III, C.T. Liu, A.I. Taub, N.S. Stoloff, C.C. Koch, 1989, ISBN: 1-55899-006-2
- Volume 134—The Materials Science and Engineering of Rigid-Rod Polymers, W.W. Adams, R.K. Eby, D.E. McLemore, 1989, ISBN: 1-55899-007-0
- Volume 135—Solid State Ionics, G. Nazri, R.A. Huggins, D.F. Shriver, 1989, ISBN: 1-55899-008-9
- Volume 136—Fly Ash and Coal Conversion By-Products: Characterization, Utilization and Disposal V, R.T. Hemmings, E.E. Berry, G.J. McCarthy, F.P. Glasser, 1989, ISBN: 1-55899-009-7
- Volume 137—Pore Structure and Permeability of Cementitious Materials, L.R. Roberts, J.P. Skalny, 1989, ISBN: 1-55899-010-0
- Volume 138—Characterization of the Structure and Chemistry of Defects in Materials, B.C. Larson, M. Ruhle, D.N. Seidman, 1989, ISBN: 1-55899-011-9
- Volume 139—High Resolution Microscopy of Materials, W. Krakow, F.A. Ponce, D.J. Smith, 1989, ISBN: 1-55899-012-7
- Volume 140—New Materials Approaches to Tribology: Theory and Applications, L.E. Pope, L. Fehrenbacher, W.O. Winer, 1989, ISBN: 1-55899-013-5
- Volume 141—Atomic Scale Calculations in Materials Science, J. Tersoff, D. Vanderbilt, V. Vitek, 1989, ISBN: 1-55899-014-3
- Volume 142—Nondestructive Monitoring of Materials Properties, J. Holbrook, J. Bussiere, 1989, ISBN: 1-55899-015-1
- Volume 143—Synchrotron Radiation in Materials Research, R. Clarke, J. Gland, J.H. Weaver, 1989, ISBN: 1-55899-016-X
- Volume 144—Advances in Materials, Processing and Devices in III-V Compound Semiconductors, D.K. Sadana, L. Eastman, R. Dupuis, 1989, ISBN: 1-55899-017-8

Recent Materials Research Society Proceedings listed in the front.

MATERIALS RESEARCH SOCIETY CONFERENCE PROCEEDINGS

Tungsten and Other Refractory Metals for VLSI Applications, Robert S. Blewer, 1986; ISSN 0886-7860; ISBN 0-931837-32-4

Tungsten and Other Refractory Metals for VLSI Applications II, Eliot K. Broadbent, 1987; ISSN 0886-7860; ISBN 0-931837-66-9

Ternary and Multinary Compounds, Satyen K. Deb, Alex Zunger, 1987; ISBN 0-931837-57-X

Tungsten and Other Refractory Metals for VLSI Applications III, Victor A. Wells, 1988; ISSN 0886-7860; ISBN 0-931837-84-7

Atomic and Molecular Processing of Electronic and Ceramic Materials: Preparation, Characterization and Properties, İlhan A. Aksay, Gary L. McVay, Thomas G. Stoebe, J.F. Wager, 1988; ISBN 0-931837-85-5

Materials Futures: Strategies and Opportunities, R. Byron Pipes, U.S. Organizing Committee, Rune Lagneborg, Swedish Organizing Committee, 1988; ISBN 1-55899-000-3

Tungsten and Other Refractory Metals for VLSI Applications IV, Robert S. Blewer, Carol M. McConica, 1989; ISSN 0886-7860; ISBN 0-931837-98-7

Tungsten and Other Advanced Metals for VLSI/ULSI Applications V, S. Simon Wong, Seiji Furukawa, 1990; ISSN 1048-0854; ISBN 1-55899-086-2

High Energy and Heavy Ion Beams in Materials Analysis, Joseph R. Tesmer, Carl J. Maggiore, Michael Nastasi, J. Charles Barbour, James W. Mayer, 1990; ISBN 1-55899-091-7

Physical Metallurgy of Cast Iron IV, Goro Ohira, Takaji Kusakawa, Eisuke Niyama, 1990; ISBN 1-55899-090-9